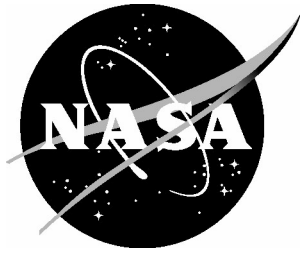


NASA/TM-2006-214276



Collected Papers in Structural Mechanics Honoring Dr. James H. Starnes, Jr.

Compiled by:

Norman F. Knight, Jr.

General Dynamics – Advanced Information Systems, Chantilly, Virginia

Michael P. Nemeth

Langley Research Center, Hampton, Virginia

John B. Malone

Langley Research Center, Hampton, Virginia

February 2006

The NASA STI Program Office . . . in Profile

Since its founding, NASA has been dedicated to the advancement of aeronautics and space science. The NASA Scientific and Technical Information (STI) Program Office plays a key part in helping NASA maintain this important role.

The NASA STI Program Office is operated by Langley Research Center, the lead center for NASA's scientific and technical information. The NASA STI Program Office provides access to the NASA STI Database, the largest collection of aeronautical and space science STI in the world. The Program Office is also NASA's institutional mechanism for disseminating the results of its research and development activities. These results are published by NASA in the NASA STI Report Series, which includes the following report types:

- **TECHNICAL PUBLICATION.** Reports of completed research or a major significant phase of research that present the results of NASA programs and include extensive data or theoretical analysis. Includes compilations of significant scientific and technical data and information deemed to be of continuing reference value. NASA counterpart of peer-reviewed formal professional papers, but having less stringent limitations on manuscript length and extent of graphic presentations.
- **TECHNICAL MEMORANDUM.** Scientific and technical findings that are preliminary or of specialized interest, e.g., quick release reports, working papers, and bibliographies that contain minimal annotation. Does not contain extensive analysis.
- **CONTRACTOR REPORT.** Scientific and technical findings by NASA-sponsored contractors and grantees.

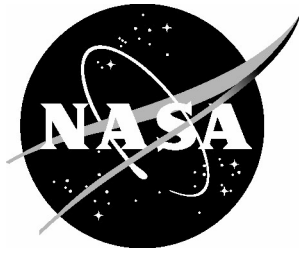
- **CONFERENCE PUBLICATION.** Collected papers from scientific and technical conferences, symposia, seminars, or other meetings sponsored or co-sponsored by NASA.
- **SPECIAL PUBLICATION.** Scientific, technical, or historical information from NASA programs, projects, and missions, often concerned with subjects having substantial public interest.
- **TECHNICAL TRANSLATION.** English-language translations of foreign scientific and technical material pertinent to NASA's mission.

Specialized services that complement the STI Program Office's diverse offerings include creating custom thesauri, building customized databases, organizing and publishing research results ... even providing videos.

For more information about the NASA STI Program Office, see the following:

- Access the NASA STI Program Home Page at [*http://www.sti.nasa.gov*](http://www.sti.nasa.gov)
- E-mail your question via the Internet to [*help@sti.nasa.gov*](mailto:help@sti.nasa.gov)
- Fax your question to the NASA STI Help Desk at (301) 621-0134
- Phone the NASA STI Help Desk at (301) 621-0390
- Write to:
NASA STI Help Desk
NASA Center for AeroSpace Information
7121 Standard Drive
Hanover, MD 21076-1320

NASA/TM-2006-214276



Collected Papers in Structural Mechanics Honoring Dr. James H. Starnes, Jr.

Compiled by:

Norman F. Knight, Jr.

General Dynamics – Advanced Information Systems, Chantilly, Virginia

Michael P. Nemeth

Langley Research Center, Hampton, Virginia

John B. Malone

Langley Research Center, Hampton, Virginia

National Aeronautics and
Space Administration

Langley Research Center
Hampton, Virginia 23681-2199

February 2006

Available from:

NASA Center for AeroSpace Information (CASI)
7121 Standard Drive
Hanover, MD 21076-1320
(301) 621-0390

National Technical Information Service (NTIS)
5285 Port Royal Road
Springfield, VA 22161-2171
(703) 605-6000



Dr. James H. Starnes, Jr.
March 3, 1939 – October 27, 2003

Dedication

This publication is dedicated to the memory of Dr. James H. Starnes, Jr. Dr. Starnes was born in California and graduated from Granby High School in Norfolk, Virginia. He graduated from Georgia Tech in 1961 with a BS in Engineering Mechanics and completed his MS in 1963 in Engineering Mechanics. He received his PhD in Aeronautical Engineering from California Institute of Technology in 1970, and joined the staff of the NASA Langley Research Center later that year. Soon, he became the head of the Structural Mechanics Branch, which he led for 18 years. At the time of his death, Dr. Starnes was the Senior Engineer of Structures and Materials at the NASA Langley Research Center.

During his 33 years of NASA civil service, he received 32 NASA Achievement Awards including the NASA Exceptional Engineering Achievement Medal in 1995 for developing reliable composite structures design technology for commercial transport aircraft. He was a Fellow of AIAA, a Fellow of ASME, a Fellow of ASC, and Member of the Georgia Institute of Technology Academy of Distinguished Engineering Alumni.

This page left blank intentionally.

Preface

This special publication contains a collection of structural mechanics papers honoring Dr. James H. Starnes, Jr. presented at the 46th AIAA/ASME/ASCE/AHS/ASC Structures, Structural Dynamics, and Materials Conference held in Austin, Texas, April 18-21, 2005. Contributors to this publication represent a small number of those influenced by Dr. Starnes' technical leadership, his technical prowess and diversity, and his technical breadth and depth in engineering mechanics. These papers cover some of the research areas Dr. Starnes investigated, which included buckling, postbuckling, and collapse of structures; composite structural mechanics, residual strength and damage tolerance of metallic and composite structures; and aircraft structural design, certification and verification. He actively pursued technical understanding and clarity, championed technical excellence, and modeled humility and perseverance.

As compilers of this volume honoring Dr. Starnes, we appreciate the efforts made by the contributors to this publication and also acknowledge that these colleagues represent only a small number of those influenced by Dr. Starnes.

This page left blank intentionally.

Table of Contents

Dedication.....	iii
Preface.....	v
Reflections on Jim Starnes' Technical Contributions R. Haftka (AIAA Paper No. 2005-1872)	1
James H. Starnes, Jr.'s Four Decades of Structural Stability and Collapse Contributions (1966-2003) J. Arbocz (AIAA Paper No. 2005-1873)	11
Utilization of the Building-Block Approach in Structural Mechanics Research M. Rouse, D. Jegley, D. McGowan, H. Bush, and W. Waters (AIAA Paper No. 2005-1874).....	21
Contributions to Damage Tolerance and Residual Strength Technologies for Composite Structures D. Ambur, P. Chunchu, N. Jaunky, and C. Rose (AIAA Paper No. 2005-1875)	41
Jim Starnes' Contributions to Residual Strength Analysis Methods for Metallic Structures R. Young, C. Rose, and C. Harris (AIAA Paper No. 2005-1876)	57
Safety and Certification Initiatives for Composite Airframe Structures L. Ilcewicz and B. Murphy (AIAA Paper No. 2005-1877)	85
Damage Tolerance – A Status Report R. Sierakowski (AIAA Paper No. 2005-2003)	97
NASA Research in Composite Structure Damage Tolerance and Composite Applications in the Oil Industry J. Williams (AIAA Paper No. 2005-2004)	103
Thin-Ply Composites S. Tsai, S. Sihn, and R. Kim (AIAA Paper No. 2005-2005)	143
Spatial Parametric Resonance and Novel Buckling Problems Inspired by James H. Starnes, Jr. I. Elishakoff (AIAA Paper No. 2005-1931)	149
Optimum Design of Stiffened Panels with Substiffeners D. Bushnell and C. Rankin (AIAA Paper No. 2005-1932)	159

Buckling Behavior of Composite Laminated Stiffened Panels Under Combined Shear and Axial Compression H. Abramovich, T. Weller, C. Bisagni (AIAA Paper No. 2005-1933)	213
Residual Strength Calculations of Stiffened Metal Panels Containing Cracks C. Rankin, E. Riks, and F. Brogan (AIAA Paper No. 2005-2007)	231
Failure Analysis of Large Stiffened Metallic Fuselage Panels Subjected to Compression Loading V. Britt and F. Simmons (AIAA Paper No. 2005-2008)	251
Failure Analysis of Discrete Damaged Tailored Extension-Shear-Coupled Stiffened Composite Panels D. Baker (AIAA Paper No. 2005-2367)	269
Mechanical Behavior of Inplane-Loaded Unsymmetrically Laminated Plates M. Majeed and M. Hyer (AIAA Paper No. 2005-2099)	289
Simulation of Progressive Failure in Multidirectional Composite Laminated Panels S. Basu, A. Waas, and D. Ambur (AIAA Paper No. 2005-2368)	325
Buckling and Failure of Compression-Loaded Composite Cylindrical Shells with Reinforced Cutouts M. Hilburger and M. Nemeth (AIAA Paper No. 2005-2370)	363
Stress Analysis of Composite Cylindrical Shells with an Elliptical Cutout E. Oterkus, E. Madenci, and M. Nemeth (AIAA Paper No. 2005-1824)	387
Global Buckling and Face Wrinkling Response of Sandwich Panels Under Transient Loads J. Hohe, L. Librescu, and S. Oh (AIAA Paper No. 2005-2100)	409
Plastic Thermal Buckling of Uniformly Heated Rectangular Plates with Temperature-Dependent Material Properties R. Jones (AIAA Paper No. 2005-1935)	421
Nonlinear Dynamic Buckling of a Composite Shell C. Chamis and G. Abumeri (AIAA Paper No. 2005-1936)	457
Dynamic Thermal Stress Creep Buckling, Probabilistic Failures and Survival Times of Viscoelastic Columns with Follower Loads H. Hilton (AIAA Paper No. 2005-2144)	469
Behavior of Composite Laminates and Sandwich Panels Subject to Compression and Fire V. Birman, G. Kardomateas, and G. Simites (AIAA Paper No. 2005-2101)	489

Preliminary Design of Piezo-Activated Composite Sandwich Fins for Projectile Maneuverability J. Arters, J. Vinson, T. Bogetti, P. Weinacht, W. Drysdale, M. Leibowitz, and O. Rabinovitch (AIAA Paper No. 2005-2102)	509
Evaluation of Composite Bonded Joint Designs for Space Applications K. Kedward, Y. Zhu, and S. Kiefer (AIAA Paper No. 2005-2098)	533
A High Fidelity Composite Bonded Joint Analysis Validation Study – Part I: Analysis S. Engelstad, G. Renieri, G. Mabson, L. Deobald, E. Nottorf, and S. Clay (AIAA Paper No. 2005-2166)	551
Validation and Certification of Aircraft Structures M. Mohaghegh (AIAA Paper No. 2005-2162)	567
Consistent Structural Integrity in Preliminary Design Using Experimentally Validated Analysis C. Collier and P. Yarrington (AIAA Paper No. 2005-2366)	585
A Perspective on Design and Certification D. Veley and C. Clay (AIAA Paper No. 2005-2163)	615
Design Tailoring of Laminated Composite Structures – A Tribute to Dr. James H. Starnes, Jr. Z. Gurdal (AIAA Paper No. 2005-2164)	625
Accelerated Insertion of Materials – Composites C. Saff, G. Hahn, J. Griffin, R. Ingle, and K. Nelson (AIAA Paper No. 2005-2165)	635
Increasing Design Load and Reducing Weight of Structures by Error Reduction E. Acar, R. Haftka, B. Sankar, and X. Qiu (AIAA Paper No. 2005-2167)	659
Overview of the Structures Investigation for the American Airlines Flight 587 Investigation B. Murphy, J. O’Callaghan, M. Fox, L. Ilcewicz, and J. Starnes (AIAA Paper No. 2005-2251)	679
Fractographic Examination of the Vertical Stabilizer and Rudder from American Airlines Flight 587 M. Fox, C. Schultheisz, and J. Reeder (AIAA Paper No. 2005-2252)	689

NASA Langley Inspection of Rudder and Composite Tail of American Airlines Flight 587 W. Winfree, E. Madaras, K. Cramer, P. Howell, K. Hodges, J. Seebo, and J. Grainer (AIAA Paper No. 2005-2253)	701
Structural Analysis for the American Airlines Flight 587 Accident Investigation – Global Analysis R. Young, A. Lovejoy, M. Hilburger, and D. Moore (AIAA Paper No. 2005-2254)	723
NASA Structural Analysis Report on the American Airlines Flight 587 Accident – Local Analysis of the Right Rear Lug I. Raju, E. Glaessgen, B. Mason, T. Krishnamurthy, and C. Davila (AIAA Paper No. 2005-2255)	747
Appendix – List of Publications Authored or Co-authored by Dr. James H. Starnes, Jr.	769

Reflections on Jim Starnes' Technical Contributions[†]

Raphael T. Haftka (Haftka@ufl.edu)
University of Florida
Gainesville, FL 32611

Abstract: For my generation of aerospace researchers NASA has played a crucial role in translating industry needs to research problems, orchestrating research progress in government laboratories, universities and industry, and helping transition that research to applications. Jim Starnes may have played this role better than any other NASA researcher, greatly advancing in the process our understanding of how composite materials should be best utilized for aerospace applications. This paper provides a view from a close university research collaborator on how he accomplished this remarkable feat. In particular it focuses on his vision that reducing the uncertainty in predicting failure of composite structures is key to more efficient utilization of such structures.

I. Introduction

When Norm Knight asked me to write the lead paper for the session that will give tribute to Jim's contributions to our community I was at a loss of how to respond. I recognized his claim that I may have worked with Jim closely over more than 30 years, and so I was a reasonable candidate for the job. Furthermore, even though I am a professor, I spent about five years (counting only intervals of one month or more) at NASA Langley Research Center, and during that time I had close interaction with Jim. During that time I had ample opportunity to observe Jim's interaction with his branch and research associates. Finally, Jim had profound impact on my own work, and so I was in position to give first hand testimonial on Jim's contributions by influencing the research direction of others. With that in mind I accepted Norm's assignment, and set out to write a paper, which leads a session where several of Jim's close collaborators attempt to do justice to the contributions of a very remarkable individual.

How do you measure the impact of the life's work of an individual on the technical community or communities in which he operated, and on the state of the art? There are some bean counting measures that are now commonly in use in academe, notably the number of references to the publications of this individual. I will make use of this device. It is more applicable to professors who live by publishing in archival journals than to a researcher in a government laboratory who disseminates ideas often by other type of publications. However, Jim's contributions were prominent enough, so that even by this professorial yardstick he fares well.

There are testimonials from many of Jim's colleagues that reflect on his extraordinary abilities in leadership, motivation, and most important—vision. I have solicited such contributions and will make use of them to attempt to provide an indication of his profound impact on the work of others.

[†] Copyright 2005 by Raphael T. Haftka. Printed by NASA with permission.

Finally, there is the question of how you assess the contribution of an individual to the state of the art in a technical field. I believe that Jim has contributed more than any other individual to the increased utilization of composite materials in aerospace structures. He has done so through coordinated attack on the uncertainties associated with the complex failure modes, which are characteristic of structures made of composite materials. He complemented this attack by sponsoring studies on the use of design optimization for taking advantage of the flexibility of composite material design. The last part of the paper is focused on the relationship of these two aspects of his life work on composite materials.

In this paper, I will make extensive use of the part of my own work that has been done in collaboration with Jim or that has been shaped by our conversations. I would have attempted to put into this paper many other examples coming from his interactions with other members of his research family. However, these are amply covered by other papers in this session.

II. Citation analysis

My citation analysis is based on the Science Citation Index that is heavily biased towards journal publications. Therefore, citations in conference proceedings and NASA reports are not included. In addition, my analysis is only approximate, in that I could not view some of the records to ascertain who were co-authors, but these were only for publications with one or two citations so that they would not influence the analysis much.

With this in view I will concentrate on citations for Jim's papers. Jim was an author on 83 Journal publications, and 173 conference papers, which is a reasonable average for an engineering professor in his early 60s. My department head for example, gives faculty members a desirable target of three journal papers per year. Keeping in mind that this was a side activity for Jim, it is remarkable. Jim's main co-authors on these journal papers are university professors, including Isaac Elishakoff (17), Ahmed Noor (10), and Raphael Haftka (10). The leading NASA colleague as a co-author is Michael Nemeth (9).

When we measure impact by the number of citations for these journal papers, there is a total of about 560 citations or almost seven citations per paper. Of this total, 161 are for papers with Haftka, 84 for papers with Knight, 77 for papers with Elishakoff, 69 for papers with Nemeth, and 44 for papers with Noor.

Jim was not the main author on most of these papers, and I cannot assess his contribution to all of them. However, I would like to discuss two of my papers. The first is Starnes, J. H., Jr. and Haftka, R.T. (1979), It has received 86 citations, which is the most of any of my research papers (review papers tend to be more cited than research papers). We worked together on this paper, exchanging ideas and analyzing results, with Jim contributing most of the physical understanding. A big part of my share constituted in that I wrote the computer program for obtaining the results. My second most cited research paper, with 62 citations is Le Riche, R. and Haftka, R.T. (1993). My PhD student, Rodolphe Le Riche, spent 2 months working with Jim who provided motivation and critique of the work. I am

giving this example to indicate that Jim's name was not added to a paper based just on minor contributions.

Most of us who knew Jim understood how he accomplished this feat of being an accomplished published and cited researcher at the same time that he has discharged his many other obligations at NASA, including management, advocacy and a host of investigations of the causes of spectacular structural failure. He was very effective in what he was doing, and he worked at least 50% longer hours than most of his collaborators including myself.

III. Testimonials

I have worked with several branches at NASA, and I always marveled at how well Jim could motivate the people who worked for him. I knew that part of it was his character, and part was the personal example that he set with long hours on the job and commitment to his work. The following excerpts from two of the people who worked for him summarize this influence.

Jim maintained a balance between giving direction and mentoring, between pointing the way and clearing the path – always ready to help when needed, but also always eager to watch you succeed on your own.,...

Basic research in nonlinear mechanics was one of Jim's great loves. Many times Jim would say "we do this research to be always ready when the agency calls on us for some special task."
(Norm Knight)

Jim was a great inspiration and role model to those with whom he worked. Honesty, truth, respect, fairness, discipline, integrity, are words which characterized his life whether describing his pursuit of scientific understanding or in personal relationships. As a manager, he motivated people to put forth their best effort through a relationship in which you never worked for Jim; you worked with him. (Jerry Williams)

For me, Jim was amazingly effective in the role that I believe is central to a researcher in a government laboratory. He provided a vital link between industry needs and long range research by combining the resources of industry, government and academe. Jim played this role to perfection through a combination of vision, persistence, personal leadership, and skill in obtaining resources for programs he believed in. In particular, he has large impact on the development of the field of the prediction of failure and damage propagation in composite structures and the optimum design of such structures. I would time and again come to Jim for guidance as to what areas in this field deserved attention because they stymie engineers in industry now or are going to become important in the future. I knew that he had the vision to stick to a long range program rather than just cater to the fad of the day.

Jim's persistence in pursuing long-range goals was of great value to me, as he often needed to repeatedly goad me into tackling a research topic until I finally saw the wisdom of doing it. I will use as an example the last research topic that he urged on me. After

resisting for a couple of years I finally tackled reluctantly and discovered that it was one of the more exciting and rewarding research endeavors of my career.

Over the last few years, I have moved into the area of structural design for reliability, focusing on the computational aspect of the problem. For a couple of years, at every meeting that we had (on average 4-5 times a year), Jim kept drawing a three dimensional chart that he wanted me to pursue. He said that I should find a way to generate a surface that links safety, weight and cost as the three variables. He believed that such charts are essential for understanding the usefulness of probability based design.

When I finally saw the light and accepted the challenge, I was still at a loss of how to get cost data, so I was content by investigating the effect of a number of measures that reduce uncertainty with the understanding that others can estimate better than me or my students the cost of such measures. This topic will be illustrated in detail in the next section.

III. Effect on composite design:

While composite materials have the potential to allow tailored stiffness and strength that can greatly reduce the weight or enhance the performance of aerospace structures, they are prone to much more complex failure modes. Damage, such as delamination may be more difficult to observe, so that inspections may be less effective for improving safety. Furthermore, because of the inherent redundancy of these structures, the ultimate failure of a composite structure is the culmination of progressive damage that is computationally difficult to predict. Finally, environmental effects, such as humidity, degrade composite properties in a more complex way than they degrade the properties of aluminum alloys.

The reaction of aerospace designers to these complexities when Jim entered the fray was to produce what he and others called *black aluminum*. This refers to working with quasi-isotropic or almost quasi-isotropic laminates. These offered double comfort to designers. First, because like aluminum they possessed strength in every direction, they did not require the extra analyses for a myriad of off-design conditions, and they allowed to test these almost isotropic laminates extensively to explore failure modes associated with this limited class of structures. In addition, aerospace companies imposed extremely conservative allowables, in order to promote damage tolerance. During many years, for example, Boeing limited the design strain on composite laminates to 0.004.

As Jim explained time and again to me, these practices eliminated most of the benefits of composite materials. First, the use of almost isotropic laminates reduced substantially possible weight savings that would derive from laminates that would be better tailored to loads. Second, the conservative allowables would further increase the weight.

Jim recognized that designers were paying the price for uncertainty, and that it was paramount to reduce this uncertainty through basic research into predicting failure in composite structures. Jim's work was particularly focused on the behavior of composite structures in compression and particularly the postbuckling behavior. He realized that in

many aerospace applications composite panels buckle at low strain levels, so that if postbuckling strength was not taken into account, the design becomes very conservative and heavy. So he has made his mark in very thorough investigation of this postbuckling regime (e.g., Starnes et al., 1985, Noor et al., 1995). While buckling and postbuckling behavior was his pet topic, he recognized that damage propagation, especially as a result of impact was of primary concern to aerospace designers, and to he made important contribution to better understanding and modeling of damage and damage propagation (e.g., Rhodes et al., 1981, Prasad et al., 1994)

While I was not involved in the substantial research that he conducted and orchestrated into predicting failure, we worked together on testing the tailored designs that my students and I produced to demonstrate the benefits of breaking with the black-aluminum paradigm.

The first lesson that I received from Jim on that score was in the mid 1980s, when he asked me to design a plate under compressive loads with a hole so as to protect it from pre-mature failure due to the hole. Since the dimensions were associated with strength failure, I followed the standard process from metals structures by designing a thicker region near the hole. Jim followed by building and testing my designs, only to show me that the extra thickness that I had added near the hole did not have almost any effect on the failure load. He pointed out to me that the weak resin could not transfer loading fast enough from the thin to the thick region. That is, shear lag proved to be more of a problem for composite laminates than for a comparable metal plate.

This failure prompted us to explore alternatives, and to our delight we found that the opposite approach worked quite well. That is, instead of protecting the hole by adding material, we could do a better job by removing the main load-carrying zero plies from a region that included the hole, thus shunting the loads away from the hole. The design and the agreement between analysis and experiments (from Haftka and Starnes, 1988) are shown in Figures 1 and 2.

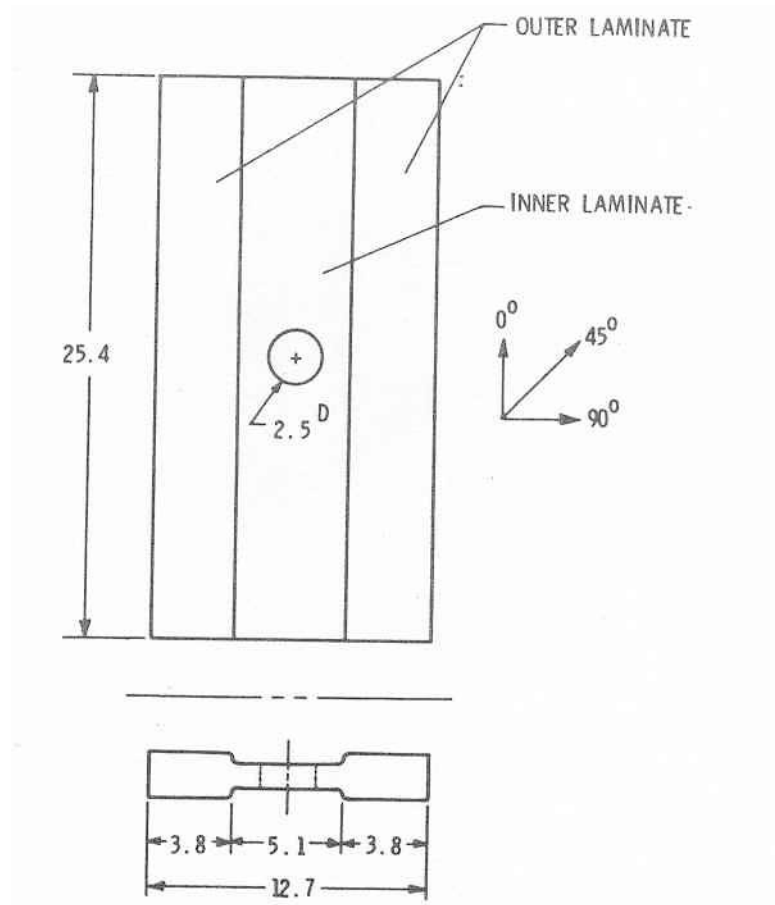


Figure 1: Tailored-stiffness plate geometry (dimensions are in cm), from Haftka and Starnes, 1988.

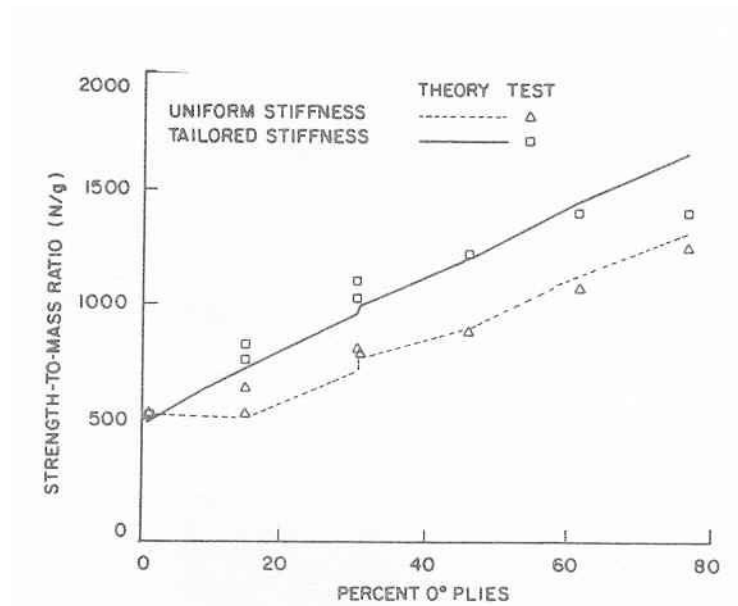


Figure 2: Failure strength-to-mass ratio for all-graphite-epoxy plates (From Haftka and Starnes, 1988).

This design concept clearly indicated that for a panel with a hole, a stiffened panel may make sense, and my students and I followed with several studies of stiffened panels. Here we ran into both the benefits and challenges of composite structure design. The requirement of integer number of plies and of orientations limited to multiple of 45-degrees lead to a formidable optimization challenge. Our first study compared designs obtained with traditional optimization algorithms (Nagendra et al., 1991) to designs obtained with genetic algorithms (Nagendra et al., 1996). The traditional continuous optimization led to designs of 26.1 lbs., the first generation of genetic algorithms improved upon this to 25.2 lbs, and the advanced genetic algorithm reduced this further to 24.1 lbs. Furthermore, the genetic optimization produced 10 substantially different designs in the weight range of 24.1 and 24.6 lbs. Three of these designs were then built and tested and all failed slightly above the design load (Park et al., 2001).

IV. Legacy: Quantifying the Benefits of Uncertainty Control

Jim realized very early in his career how uncertainty about failure exacted a very high price on structural design by making them much heavier than they needed to be. For most of his career he has worked assiduously to reduce the uncertainty about the failure of composite materials, in what many project managers regarded as “basic research.” The characterization of *basic research* implies that it is long range research unlikely to bear fruit in the near future to serve the goals of a particular project. However, often the benefits of improved understanding of failure are immediate, and it is the fault of researchers engaged in such basic research for not quantifying the benefits of their work.

My first foray into attempting to quantify the effect of reducing uncertainty about failure was influenced by Jim’s focus on reducing uncertainty about the buckling behavior of cylindrical shells. He realized that the knockdown factor used to compensate for variability in the behavior of such shells was responsible for large weight penalties, and he set out to find out how to reduce the scatter. He undertook investigation into better characterization of the scatter and relating it to manufacturing imperfections (e.g., Li et al., 1997, Arbocz et al., 2002). I realized then that probability based design furnishes an ideal setting for assessing the impact of reducing scatter on the weight of structures.

The following example is from Qu et al. (2003), work partially funded by Jim and which we discussed at length. It deals with the design of composite liquid hydrogen tanks, and it was partly motivated by the failure of such tanks on the X-33 project, failure that led to the cancellation of that project. The failed design was a prominent example of the failure of the black aluminum philosophy. At cryogenic temperatures, quasi-isotropic laminates suffer from excessive residual stresses due to the mismatch between the coefficients of thermal expansion of resin and fibers. Safe designs must have small angles between plies to reduce these thermal stresses, and the optimum design that we obtained was a $\pm 25^\circ$ laminate.

The weight of the laminate was very sensitive to variability in material characteristics as shown in Figure 3. The figure shows the large effect on weight of uncertainty reduction.

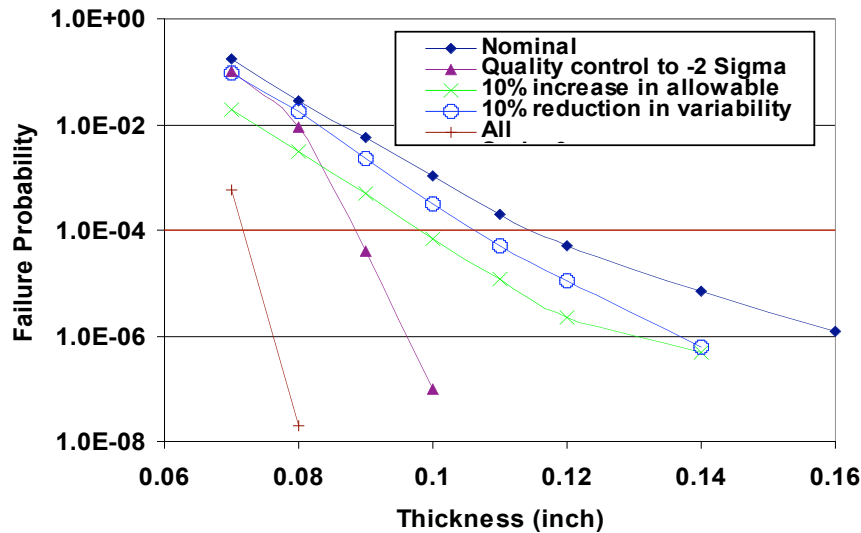


Figure 3: Effect of uncertainty control on the weight and probability of failure of composite laminates for cryogenic hydrogen tanks (from Qu et al., 2003). Three improvements in the transverse failure strain are considered: (a) quality control rejecting material batches two standard deviations from specification (about 2 percent); (b) reducing the standard deviation from 9% to 8.1%; (c) increasing the failure strain by 10%.

For example, reducing the standard deviation of the transverse failure strain from the nominal of 9% to 8.1% (a 10% reduction) reduces the thickness (hence weight) from 0.16 to less than 0.14 when designing for a probability of failure of 10^{-6} .

It is similarly possible to take each of Jim's contributions to improved accuracy in failure prediction to reduced weight. The methodology for performing this calculation is outlined in Erdem et al. (2005). They show that reducing errors in stress predictions from a maximum of 50% to a maximum of 10% leads to weight savings of about 25% (see Figure 4.) If these errors appear excessive, consider Figure 5 that compares the effect of neglecting chemical shrinkage (which is commonly done) (ERDEM, get reference from Billy or Lucian) on calculating the residual stresses in the X-33 laminate and the $\pm 25^\circ$ laminate.

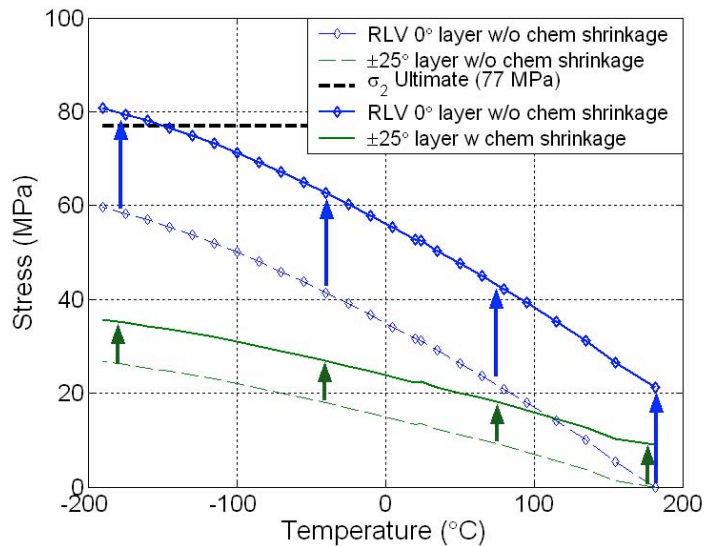


Figure 5: Effect of chemical shrinkage during cure on residual stresses in the X-33 laminate (RLV) and optimal angle ply laminate (From ...ERDEM)

Concluding Remarks:

Jim Starnes has advanced our understanding of failure of composite aerospace structures by his personal research as well as research he directed and sponsored. His vision is responsible for substantial improvements in the performance of composite aerospace structures and substantially contributed to their increased utilization. For me his main legacy was in showing how basic research into the failure of composite structures can translate to improvements in weight and safety. It may be useful in the future to use probability based design to quantify the impact of individual improvement in accuracy in predicting failure.

References:

Arbocz, Johann; and Starnes, James H., Jr.: On a High-Fidelity Hierarchical Approach to Buckling Load Calculations. In "Calladine Festschrift," S. Pellegrino, Ed., Wolters Kluwer Academic Publishers. Dordrecht, The Netherlands, 2002.

Haftka, R. T. and Starnes, J. H., Jr., "Stiffness Tailoring for Improved Compressive Strength of Composite Plates with Holes," *AIAA Journal*, Vol. 26, No. 1, pp. 72-77, 1988.

Le Riche, R. and Haftka, R.T., "Optimization of Laminate Stacking Sequence for Buckling Load Maximization by Genetic Algorithm," *AIAA Journal*, 31 (5), pp. 951-956, 1993.

Li, Yi-Wei; Elishakoff, Isaac; Starnes, James H., Jr.; and Bushnell, David: Effect of the Thickness Variation and Initial Imperfection on Buckling of Composite Cylindrical Shells: Asymptotic Analysis and Numerical Results by BOSOR4 and PANDA2. *International Journal of Solids and Structures*, Vol. 34, No. 28, 1997, pp. 3755-3767.

Nagendra, S., Haftka, R. T., Gürdal, Z., and Starnes, J. H., "Design of Stiffened Composite Plate with a Hole," *Composite Structures*, Vol. 18, pp. 195-219, 1991.

Nagendra, S., Jestin, D., Gürdal, Z., Haftka, R.T., and Watson, L.T., "Improved genetic Algorithms for the Design of Stiffened Composite Panels," *Computers & Structures*, Vol. 58, No. 3, pp. 543-555, 1996.

Noor, A. K.; Starnes, J. H., Jr.; and Peters, J. P.: Mechanics of Postbuckling of Multilayered Composite Panels with a Cutout. *Composite Structures*, Vol. 30, No. 4, 1995, pp. 369-388.

Park, O., Haftka, R.T., Sankar, B.V., Starnes, J.H., and Nagendra, S., "Analytical-Experimental Correlation for a Stiffened Composite Panel Loaded in Axial Compression," *Journal of Aircraft*, **38 (2)**, 379-387, 2001.

Prasad, Chunchu B.; Ambur, Damodar R.; and Starnes, James H., Jr.: Response of Laminated Composite Plates to Low-Speed Impact by Different Impactors. *AIAA Journal*, Vol. 32, No. 6, June 1994, pp. 1270-1277.

Qu, X., Haftka, R.T., Venkataraman, S., and Johnson, T.F., "Deterministic and Reliability-Based Optimization of Composite Laminates for Propellant Tanks," *AIAA Journal*, **41(10)**, pp. 2029-2036, 2003.

Rhodes, Marvin D.; Williams, Jerry G.; and Starnes, James H., Jr.: Low-Velocity Impact Damage in Fiber-Reinforced Laminated Epoxy Structures. *Polymer Composites*, Vol. 2, No. 1, January 1981, pp. 36-44.

Starnes, J. H., Jr. and Haftka, R.T., "Preliminary Design of Composite Wings for Buckling, Strength and Displacement Constraints," *Journal of Aircraft*, Vol. 16 (8), pp. 564-570, 1979.

Starnes, James H., Jr.; Knight, Norman F., Jr.; and Rouse, Marshall: Postbuckling Behavior of Selected Flat Stiffened Graphite-Epoxy Panels Loaded in Compression. *AIAA Journal*, Vol. 23, No. 8, August 1985, pp. 1236-12

James H. Starnes Jr.'s Four Decades of Structural Stability and Collapse Contributions (1966-2003)

by

Johann Arbocz*
Delft University of Technology, The Netherlands

Abstract

During his four decades long professional career at the Structures Directorate of Nasa Langley Research Center Dr. James H. Starnes has worked on and/or initiated and supported research and development work in five distinct areas such as

- Structural Stability and Collapse Contributions
- Utilization of the Building Block Approach in Structural Mechanics
- Contributions to Residual Strength Analysis Methods for Metallic Structures
- Contributions to Damage Tolerance and Residual Strength Technologies for Composite Structures
- Safety and Certification Initiatives for Composite Airframe Structures

Each of these areas will be covered by separate sessions.

The present paper describes Dr. James H. Starnes seminal contributions covering the effect of cutouts on structural stability and collapse, the numerical simulation of complex structural stability and collapse problems and his leading role in introducing the new high-fidelity analysis approach for buckling critical structures.

Introduction

James Starnes' first encounter with structural stability problems occurred in 1966 when the California Institute of Technology in Pasadena accepted him as a Ph.D. student in the School of Aeronautics. Jim chose to work with Prof.Dr. E.E. Sechler, Head of the Solid Mechanics Group and one of the leading authorities in shell stability problems.

During his four year stay at Caltech Jim has assimilated Ernie Sechler's philosophy well, which says that theoretical and experimental investigations must go hand in hand. Then without theory, there is no understanding and without experiment there is no discovery. During all his long and successful professional career Jim always adhered to his approach and he maintained that one can only claim that one has a workable method if the results of theoretical calculations agree well with the experimental verifications.

Jim's professional interests covered a wide and varied range of topics but no topic was dearer to his heart than the

Effect of Cutouts on Structural Stability and Collapse

In his Ph.D. thesis¹ Jim presented the results of a detailed study of the effects of circular cutouts on the buckling of cylinders loaded by axial compression, bending and torsion. Mylar was selected as one of the specimen materials because Mylar shells could be buckled many times without any noticeable degradation of the test specimens. The shells were loaded to buckling before any holes were cut into their sides in order to provide the reference buckling loads. A series of concentric circular cutouts was

* Professor Emeritus, Faculty of Aerospace Engineering, Fellow AIAA
Copyright 2005 by Johann Arbocz. Printed by NASA with permission

then cut into the cylinder wall at midlength, and the shell buckling load was measured for each cutout size and desired loading condition. This procedure was continued until the largest desired hole was cut into the shell and all desired loading conditions had been applied. To correlate the experimental results the following nondimensional parameter was used

$$\bar{r} = \frac{r}{\sqrt{Rt}} \quad (1)$$

where for circular cutouts the characteristic hole dimension r was taken to be equal to the cutout radius, R is the shell radius and t is the shell thickness.

The effects of circular cutouts on the buckling loads of 16 Mylar cylinders are summarized in Fig. 1 by the curves representing the boundaries of the experimental results

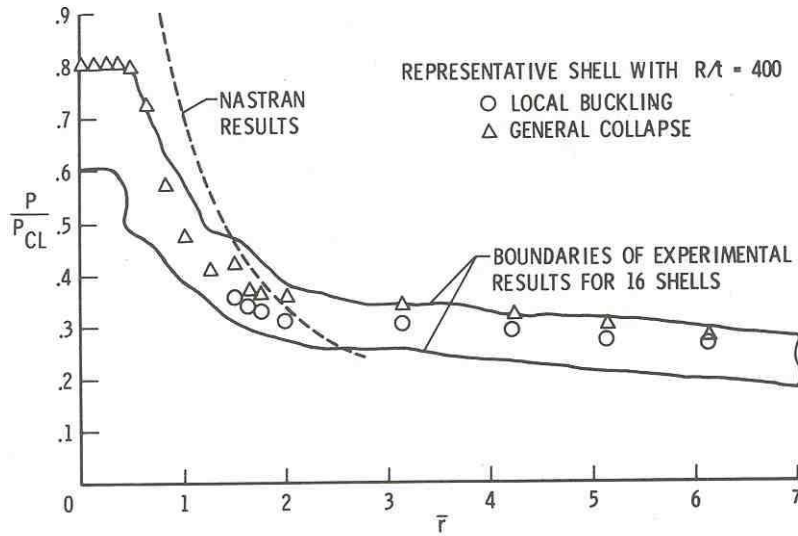


Fig. 1 The effect of circular cutouts on the buckling of circular cylinders loaded by central axial compression (from Ref. 3).

The measured experimental buckling loads P have been nondimensionalized by the classical theoretical buckling load P_{CL} for a cylinder without a cutout to provide a constant reference for comparing results for different shells. The normalized measured experimental buckling loads are plotted as a function of the nondimensional geometric parameter \bar{r} . The dashed curve in Fig. 1 represents the results of a finite element analysis.

In Reference 2 experimental results from tests performed on seamless electroformed copper shells with circular holes are presented. These results confirmed that the character of the shell buckling was indeed dependent on the nondimensional geometric parameter \bar{r} as indicated in Fig. 1. For small values of \bar{r} , there was no apparent effect of the hole on the buckling load. For slightly larger values of \bar{r} , the shells still buckled into a general collapse configuration, but the buckling loads were sharply reduced as the parameter \bar{r} increased. For still larger values of \bar{r} , the buckling loads were further reduced, and the shells buckled into a stable local buckling configuration.

A detailed summary of the results obtained by nearly a decade of combined experimental and analytical (numerical) investigation of the effect of circular and rectangular cutouts on the buckling of thin cylinders loaded by axial compression, bending and torsion is presented in Ref. 3. Some of the interesting results are shown in Fig. 2.

The rectangles cut into each shell were oriented with their long sides either in the shell longitudinal or circumferential direction with a given orientation maintained for a particular shell. The rectangles had

aspect ratios ranging from about 1.2 to 2.0 for each configuration orientation, with the majority equal to 1.5 or greater.

The characteristic hole dimension r in the correlation parameter \bar{r} was taken to be equal to one-half of the side length for the squares and the average of the half-side lengths for the rectangles. Even for such diversely different configurations as longitudinal and circumferential rectangles with aspect ratios equal to 2.0, all the experimental results for the cylinders with square and rectangular cutouts fell within the relatively narrow scatterband of Fig. 2 when plotted with respect to \bar{r} . From these results, it is possible to identify approximate ranges of \bar{r} with different buckling characteristics as mentioned above for the results plotted in Fig. 1 for circular cutouts.

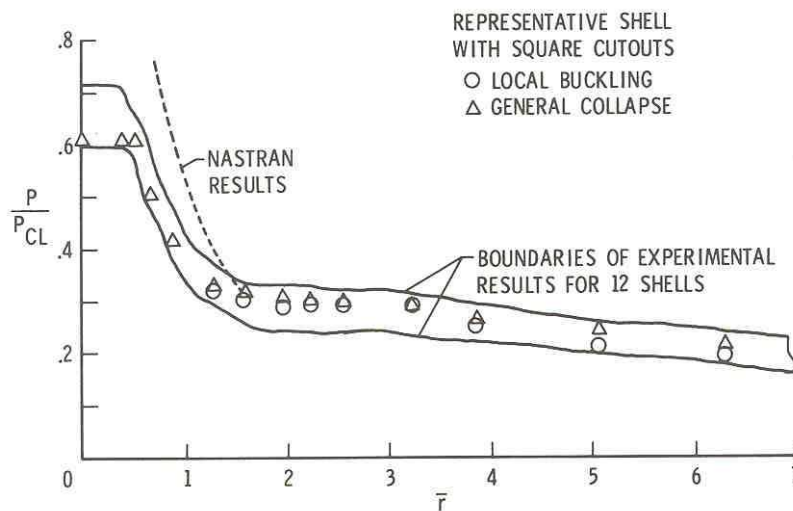


Fig. 2 The effect of square and rectangular cutouts on the buckling of circular cylinders loaded by central axial compression (from Ref. 3).

Jim's attention to structural details that may influence the stability behavior is illustrated in Ref. 4, where the findings of a systematic experimental program dealing with the influence of intentionally introduced perturbations from the hole shape was reported. The results of this study indicated that with small local variations around the hole there was little or no effect on the buckling loads; however when the departure from the initial hole shape was large enough and appropriately located to influence the stress field in the hole region, there were noticeable effects on the buckling loads.

Over the years the effect of cutouts on the buckling load of thin-walled structures remained one of Jim's principal interest.

Numerical Simulation of Complex Structural Stability and Collapse Problems

After joining NASA Langley Research Center in 1970 Dr. James Starnes got involved with investigating the nonlinear analysis capabilities of the new generation of computer codes developed by B.O. Almroth and his colleagues at Lockheed Palo Alto Research Laboratories⁵.

Initially Jim worked on the nonlinear collapse behavior of long cylindrical shell structures subject to combined bending and pressure loads⁶. In order to determine the maximum strength two modes of nonlinear collapse were investigated. One mode of collapse is described by circumferential flattening of the cylinder cross-section, the so-called Brazier effect. Axial wrinkling in the region of maximum compression represents the other mode. Results for unpressurized long cylinders are presented in Fig. 3.

The dashed curves show the moment plotted as a function of cross-sectional flattening for various values of the length-to-radius ratios. The envelope of the collapse moments is shown by the solid curve. It is seen that this envelope approaches both the expected classical value of $M = M_{CL}$ ⁸, where $M_{CL} = 0.6\pi R t^2 E$ corresponds to an applied load amplitude of $N_b = 0.6 E t^2 / R$ when $\nu = 0.3$, for short

cylinders and the Brazier solution⁹ of $0.55M_{C\ell}$ at $\Delta W/t$ equal to 22.2. Collapse for these results is due to an interaction between the Brazier effect and the short wave axial buckling mode, although Brazier flattening becomes the dominant effect as values of L/R increase.

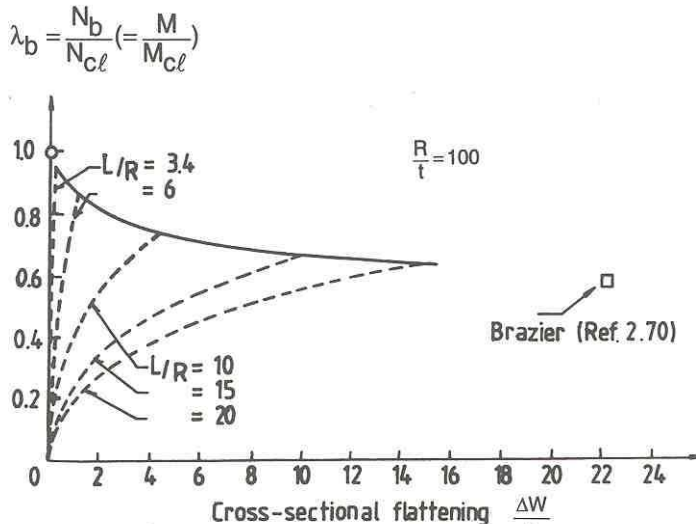


Fig. 3 Comparison of collapse moments of unpressurized cylinders with classical results (from Ref. 6).

Interaction curves for all results studied are presented in Fig. 4 where $M/M_{C\ell}$ is plotted as a function of p/p_e . Here p_e is the buckling pressure for cylinders with an elastic end ring restraint. These rings are stiff enough to approximate a condition for which the end plane rotates and translates with undisturbed cross section and with a minimum of warping of the cross section.

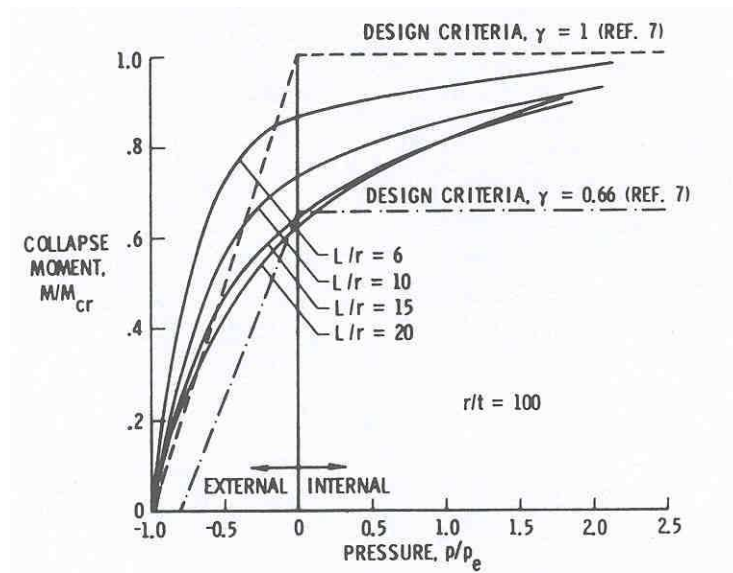


Fig. 4 Interaction curves for the collapse of cylindrical shells under bending and pressure (from Ref. 6).

The solid curves correspond to collapse moments of constant values of L/R . The dashed curve which passes through the points $M/M_{C\ell}$ and p/p_e equal to unity is the classical design criteria relation expressed by the linear relation $R_b + R_p = 1$, where R_b is the ratio of the collapse bending moment for the cylinder subject to combined loads to the allowable bending moment of the cylinder when subjected only to bending and therefore $R_b = M/M_{Cr}$.

Similarly, R_p is the ratio of the pressure on the cylinder subjected to combined loads to the allowable external pressure of the cylinder when subjected only to external pressure. Here R_p is given by $R_p = p/p_e$, where p_e is the buckling pressure for cylinders with elastic end ring restraint described previously.

In practical applications, a conservative design requires the use of an empirical factor γ which correlates experimental results with theoretical results. These differences in experimental and theoretical results are primarily due to small initial imperfections. In Ref. 7 it is recommended that M_{cr} be multiplied by γ and p_e be multiplied by $\sqrt{\gamma}$. For $R/t=100$ the value of γ is 0.66. Using this value, the design criteria curve is replotted and is shown by the dash-dot curve. For a conservative design, this curve should represent a lower bound to the analytical (numerical) results, and indeed it does except for a small region for large L/R values around zero pressure. This small discrepancy is not too surprising since the experimental data used to determine the empirical factor γ is based on studies using lower value of L/R than those studied in Ref. 6.

Beginning in the late 1970-ties with the availability of advanced nonlinear analysis capabilities and the growing interest in composite structures the buckling and postbuckling behavior of flat and curved composite panels and cylinders with circular holes was extensively investigated. A joint paper with N.F. Knight published in 1985¹⁰ is probably the best example of Jim's philosophy of how one should approach the vexing problems of structural stability and collapse that occur so frequently with thin-walled aerospace structures. In this paper the results of an experimental and analytical (numerical) study of the effects of circular holes on the postbuckling behavior of graphite-epoxy cylindrical panels loaded in axial compression are presented. The analytical modeling and solution strategy details necessary to predict accurately the buckling and postbuckling response are described at length. It was found that analytical results obtained by using STAGSC-1 computer code¹¹ correlate well with the typical postbuckling test results provided local failures do not occur and the moderate-rotation limitation of the analysis is not violated. Further, it appears that reliable postbuckling strength predictions for curved panels require an accurate local analysis procedure that accounts for large rotations associated with severe local bending gradients and for local laminate failures and subsequent failure propagation.

Further highlights of numerical simulation of complex structural stability and collapse problems can be found in Ref. 12, describing the response of composite shells with cutouts subjected to internal pressure and axial compression and in Ref. 13, where the results of an extensive and very detailed investigation of the effects of initial geometric imperfections on the nonlinear response of the Space-Shuttle super lightweight liquid-oxygen tank is presented.

High-Fidelity Analysis for Buckling Critical Structures

In the last ten years or so Dr. James Starnes was one of the leaders of a movement trying to improve the shell design capabilities of the aerospace community¹⁴. Jim realized that to make the development of an advanced space transportation system a success and to achieve the very ambitious performance goals (like every generation of vehicles being ten times cheaper and ten times more reliable than the previous one), one must make full and efficient use of the technical expertise accumulated in the past, and combine it with the tremendous computational power now available. Jim felt that with the strict weight constraints used in space applications these performance goals can only be achieved with an approach often called "high fidelity analysis", where the uncertainties involved in a design are simulated by refined and accurate numerical methods.

To provide the means for such a refined computer-supported design approach, Jim has supported the development of DISDECO, The **D**elft **I**nteractive **S**hell **D**esign **C**ode¹⁵. This hierarchical, interactive computer code includes three levels of fidelity for the analysis. Level-1 assumes that the shell buckling load can be predicted by the classical solution with simply supported boundary condition, and with a linear membrane prebuckling solution. Level-2 includes the effects of a nonlinear prebuckling solution and the effects of boundary conditions. Level-3 includes the nonlinear interaction between nearly simultaneous buckling modes and the effects of boundary imperfections. Jim has co-authored several

publications^{16,17,18} where it is demonstrated how the hierarchical, high-fidelity analysis approach can be used in the design process to rapidly converge to an accurate and reliable prediction of the expected buckling load of a thin shell.

One can consider the last paper that Jim has co-authored as part of his legacy. In Reference 19 a robust and accurate approach for predicting the nonlinear response and stability characteristics of compression loaded thin-walled composite shell structures is described. For this experimental and analytical (numerical) study of the effects of imperfections of unstiffened thin-walled graphite-epoxy cylindrical shells three different shell-wall laminates are used. The results for the nonlinear prebuckling, buckling, transient collapse and post collapse response of geometrically perfect shells and shells with measured imperfections are presented. The results identify the effects of traditional initial geometric shell-wall midsurface imperfections and the effects of other non-traditional imperfections on the nonlinear response and buckling loads of the shells. These non-traditional imperfections include shell-wall thickness variations, material property variations, shell-end geometric imperfections, local shell-wall ply-gaps associated with the fabrication process, variations in the loads applied to the end of the shell and elastic boundary support conditions.

A high-fidelity nonlinear shell analysis procedure is used to predict the nonlinear response of the shells, and the analysis procedure accurately accounts for the effects of the traditional and non-traditional imperfections and elastic boundary conditions on the nonlinear response and buckling loads of the shell. In addition, upper and lower bounds to the nonlinear response of the shells have been determined based on a combinational analysis of the effects of uncertainties or variations in several shell parameters.

Analytically predicted and experimentally measured load-shortening curves are presented in Fig. 5 for shells C1, C2 and C3. Values of the axial load P and end-shortening Δ are normalized by the linear bifurcation buckling load of the quasi-isotropic shell C3 P_{bif}^{quasi} and the nominal shell wall thickness t_{nom} . The solid and dashed lines in the figure represent experimentally measured and analytically predicted results, respectively. Each shell has two predicted response curves representing analytically (numerically) calculated upper and lower bounds to the response based on specimen parameter uncertainties. Notice that for the most part the measured load-shortening response curves of the shells fall on or within the analytically predicted response bounds. Thus the measured response curves tend to correlate well with the analytically predicted lower bounds for each shell.

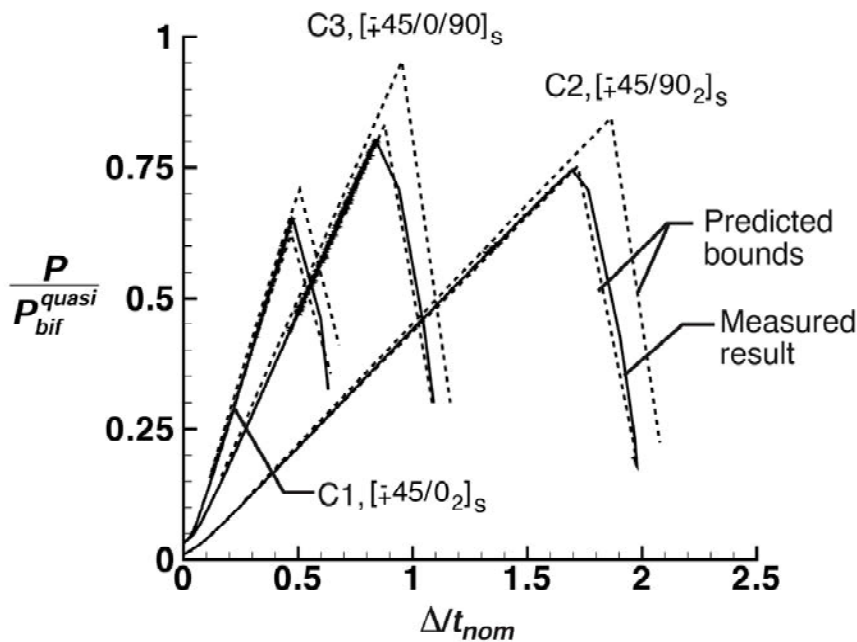


Fig. 5 Numerically predicted and experimentally measured load-shortening response curves; predicted results represent response bounds (from Ref. 19).

A comparison of results from the traditional shell design approach and from the present nonlinear high-fidelity shell design approach is shown in Fig. 6 for shell C3. Values of the axial load P and end-shortening Δ in the figure are normalized by the predicted linear bifurcation load for the quasi-isotropic shell C3, $P_{bif}^{quasi} = 42,590$ lbs and the nominal shell-wall thickness $t_{nom} = 0.04$ in, respectively.

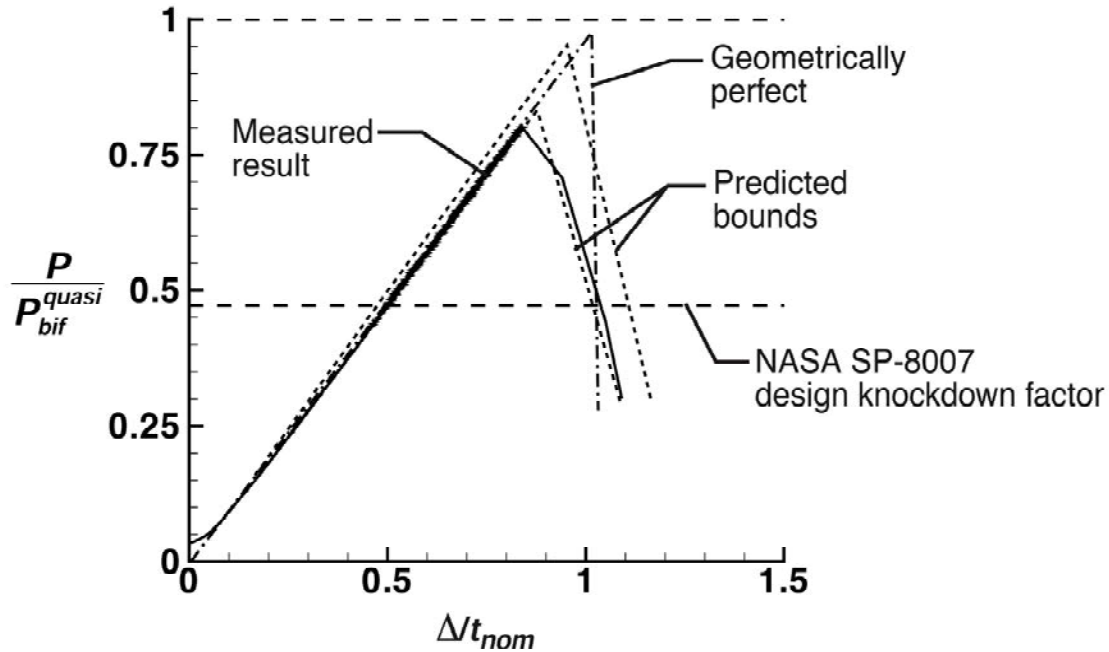


Fig. 6 Numerically predicted and experimentally measured load-strain response curves for quasi-isotropic shell C-3 (from Ref. 19).

The traditional approach to shell design is to predict the shell buckling load using a linear bifurcation buckling analysis with the nominal structural dimensions and material properties of an idealized geometrically perfect shell. This predicted buckling load for the shell is then reduced by an empirical "knockdown" factor based on a design criterion such as the lower-bound design recommendation reported in NASA SP-8007⁷. The quasi-isotropic shell C3 has a nominal radius-to-shell-wall-thickness ratio equal to 200 and the design knockdown factor from NASA SP-8007 for an equivalent isotropic shell is approximately equal to 0.470 as indicated in Fig. 6. This traditional design approach is an overly conservative design for this shell.

The normalized experimentally measured buckling load and the normalized analytically predicted buckling load from the lower response bound curve calculated by the nonlinear analysis procedure are 0.803 and 0.832, respectively. These results are 33% and 36% greater than the results based on the traditional design approach.

Thus the modern high-fidelity analysis approach offers a promising alternative to relying on historical test data for shells that do not represent the configuration, material system, or fabrication process for a particular composite shell design of interest. It is suggested that a design analysis procedure based on a high-fidelity analysis approach should be used with a selected number of carefully conducted experiments that would be used to verify the design and analysis results. This approach would make it possible to avoid testing the large number of replicates of a design needed to develop empirical design factors.

This nonlinear analysis procedure could be used as a parameter tool in the early stages of a design development program to determine the sensitivity of the response characteristics of a specific design to a number of different types of imperfections or differences in the idealized as-designed shell structure and the actual as-manufactured shell structure.

Conclusions

With Dr. James Starnes' untimely death the Aerospace Community has not only lost a person of vision but also a person whose remarkable knowledge of how to solve structural stability and collapse problems will be severely missed in the future. How did John Hutchinson say in his acceptance speech of the 2002 Timoshenko Medal:

"Buckling problems of all kinds arise continually in many areas of technology. Sometimes I wonder where the expertise on buckling will reside when all of us aging bucklers cross the bar. ABAQUS can solve buckling problems, but it can't pose or understand them. I'm afraid it would not take long to count the number of courses on buckling now taught in this country."

I suppose these words describe the dilemma we are facing quite accurately. The least we can do is to work very hard to continue Jim's legacy of preserving our technical/scientific heritage and make the High-Fidelity Analysis Approach a success.

References

- ¹Starnes, J.H. Jr., "The Effect of a Circular Hole on the Buckling of Cylindrical Shells," Ph.D. Thesis, California Inst. of Tech., Pasadena, 1970.
- ²Starnes, J.H. Jr., "Effect of a Circular Hole on the Buckling of Cylindrical Shells Loaded by Axial Compression," AIAA Journal, Vol. 10, No. 11, November 1972, pp. 1466-1472.
- ³Starnes, J.H. Jr., "The Effects of Cutouts on the Buckling of Thin Shells," in: Thin-Shell Structures, Theory, Experiment and Design. Edited by Y.C. Fung and E.E. Sechler, Prentice-Hall, Inc. Englewood Cliffs, New Jersey, 1974, pp. 289-304.
- ⁴Starnes, J.H. Jr., "Effect of a Slot on the Buckling Load of a Cylindrical Shell with a Circular Cutout," AIAA Journal, Vol. 10, No. 2, February 1972, pp. 227-229.
- ⁵Almroth, B.O., Brogan, F.A. and Marlowe, M.B., "Collapse Analysis for Shells of General Shape," Vol. I: Analysis, AFFDL-TR-71-8, August 1972, Air Force Flight Dynamics Lab., Wright-Patterson Air Force Base, Ohio.
- ⁶Stephens, W.B., Starnes, J.C. Jr. and Almroth, B.O., "Collapse of Long Cylindrical Shells under Combined Bending and Pressure Loads," AIAA Journal, Vol. 13, No. 1, January 1975, pp. 20-25.
- ⁷Anonymous, "Buckling of Thin-Walled Circular Cylinders," NASA SP-8007, August 1968.
- ⁸Seide, P. and Weingarten, V.I., "On the Buckling of Circular Cylindrical Shells under Pure Bending," Journal of Applied Mechanics, Vol. 28, 1961, pp. 112-116.
- ⁹Brazier, L.G., "On the Flexure of Thin Cylindrical Shells and Other 'Thin' Sections," Proceedings of the Royal Society, Series A, Vol. CXVI, 1926, pp. 104-114.
- ¹⁰Knight, N.F. Jr. and Starnes, J.H. Jr., "Postbuckling Behavior of Axially Compressed Graphite-Epoxy Cylindrical Panels with Circular Holes," Transactions of the ASME - Journal of Pressure Vessel Technology, Vol. 107, November 1985, pp. 394-402.
- ¹¹Almroth, B.O., Brogan F.A. and Stanley, G.M., "Structural Analysis of General Shells, Vol. II, User Instructions for STAGSC-1," Report No. LMSC-D633873, Lockheed Palo Alto Research Laboratory, Palo Alto, CA, December 1982.
- ¹²Hilburger, M.W., Waas, A.M. and Starnes, J.H. Jr., "Response of Composite Shells with Cutouts to Internal Pressure and Compression Loads," AIAA Journal, Vol. 37, No. 2, February 1999, pp. 232-237.
- ¹³Nemeth, M.P., Young, R.D., Collins, T.J. and Starnes, J.H. Jr., "Effects of Initial Geometric Imperfections on the Non-linear Response of the Space Shuttle Superlightweight Liquid-Oxygen Tank," International Journal of Non-Linear Mechanics, Vol. 37, 2002, pp. 723-744.
- ¹⁴Nemeth, M.P. and Starnes, J.H. Jr., "The NASA Monographs on Shell Stability Design Recommendations - A Review and Suggested Improvements," Proceedings 38th AIAA/ASME/ASCE/AHS/ASC Structures, Structural Dynamics and Materials Conference, April 7-10, 1997, Kissimmee, Florida, (Paper AIAA-1997-1302).
- ¹⁵Arbocz, J., and Hol, J.M.A.M., "Shell Stability Analysis in a Computer-Aided-Engineering (CAE) Environment," Proceedings 34th AIAA/ASME/ASCE/AHS/ASC Structures, Structural Dynamics and Materials Conference, April 19-22, 1993, La Jolla, California, pp. 300-314.

¹⁶Arbocz, J., Starnes, J.H. Jr. and Nemeth, M.P., "On a High-Fidelity Hierarchical Approach to Buckling Load Calculations," Proceedings 42nd AIAA/ASME/ASCE/AHS/ASC Structures, Structural Dynamics and Materials Conference, April 16-19, 2001, Seattle, Washington, pp. 1534-1554.

¹⁷Arbocz, J., Starnes, J.H. Jr., "Buckling Load Calculations of the Isotropic Shell A-8 using a High-Fidelity Hierarchical Approach," Proceedings 43rd AIAA/ASME/ASCE/AHS/ASC Structures, Structural Dynamics and Materials Conference, April 22-24, 2002, Denver, Colorado, pp. 2396-2423.

¹⁸Arbocz, J., Starnes, J.H. Jr., "A Hierarchical High-Fidelity Analysis Procedure for Buckling Critical Structures," Proceedings 44th AIAA/ASME/ASCE/AHS/ASC Structures, Structural Dynamics and Materials Conference, April 7-10, 2003, Norfolk, Virginia, (Paper AIAA-2003-1844).

¹⁹Hilburger, M.W. and Starnes, J.H., "Effects of Imperfections on the Buckling Response of Compression-Loaded Composite Shells," International Journal of Non-Linear Mechanics, Vol. 37, 2002, pp. 623-643.

This page left blank intentionally.

Utilization Of The Building-Block Approach In Structural Mechanics Research

Marshall Rouse,^{*} Dawn C. Jegley[†] David M. McGowan,^{*} Harold G. Bush[†]
NASA Langley Research Center Hampton, VA 23681

and

W. Allen Waters[§]
Lockheed Martin Corp. Hampton, VA 23681

In the last 20 years NASA has worked in collaboration with industry to develop enabling technologies needed to make aircraft safer and more affordable, extend their lifetime, improve their reliability, better understand their behavior, and reduce their weight. To support these efforts, research programs starting with ideas and culminating in full-scale structural testing were conducted at the NASA Langley Research Center. Each program contained development efforts that (a) started with selecting the material system and manufacturing approach; (b) moved on to experimentation and analysis of small samples to characterize the system and quantify behavior in the presence of defects like damage and imperfections; (c) progressed on to examining larger structures to examine buckling behavior, combined loadings, and built-up structures; and (d) finally moved to complicated subcomponents and full-scale components. Each step along the way was supported by detailed analysis, including tool development, to prove that the behavior of these structures was well-understood and predictable. This approach for developing technology became known as the “building-block” approach. In the Advanced Composites Technology Program and the High Speed Research Program the building-block approach was used to develop a true understanding of the response of the structures involved through experimentation and analysis. The philosophy that if the structural response couldn’t be accurately predicted, it wasn’t really understood, was critical to the progression of these programs. To this end, analytical techniques including closed-form and finite elements were employed and experimentation used to verify assumptions at each step along the way. This paper presents a discussion of the utilization of the building-block approach described previously in structural mechanics research and development programs at NASA Langley Research Center. Specific examples that illustrate the use of this approach are included from recent research and development programs for both subsonic and supersonic transports.

I. Introduction

In the last 20 years NASA has worked in collaboration with industry to develop enabling technologies needed to make aircraft safer and more affordable, extend their lifetime, improve their reliability, better understand their behavior, and reduce their weight. To support these efforts, research programs starting with ideas and culminating in full-scale structural testing were conducted at the NASA Langley Research Center. Each program contained development efforts that (a) started with selecting the material system and manufacturing approach; (b) moved on to experimentation and analysis of small samples to characterize the system and quantify behavior in the presence of defects like damage and imperfections; (c) progressed on

^{*} Senior Aerospace Engineer, Mechanics of Structures and Materials Branch, Mail Stop 188E, Senior Member, AIAA.

[†] Senior Aerospace Engineer, Mechanics of Structures and Materials Branch, Mail Stop 188E, Associate Fellow, AIAA.

[§]Senior Aerospace Engineer. Senior Member, AIAA.

to examining larger structures to examine buckling behavior, combined loadings, and built-up structures; and (d) finally moved to complicated subcomponents and full scale components. Each step along the way was supported by detailed analysis, including tool development, to prove that the behavior of these structures was well-understood and predictable. This approach for developing technology became known as the “building-block” approach and was used successfully in programs such as the Advanced Composites Technology Program (ACT)¹⁻³⁸ and the High Speed Research Program (HSR).³⁹⁻⁴³ Analysis techniques including closed-form and finite elements were employed. The intent was to always verify that the analysis and experimental data agreed because otherwise the behavior of the structure was not adequately understood.

In the 1980’s Jim Starnes and others at NASA Langley saw the need for a major initiative to promote the use of light-weight composites on commercial transport aircraft. At the time, Langley’s current programs were winding down and many issues involving the use of composites were yet to be resolved. Many discussions with industry and other government agencies resulted in the understanding that technical, cost, certification and manufacturing roadblocks all existed and must be overcome before any manufacturer would consider relying on composite primary structures for carrying passengers. The airlines also demanded that maintenance, safety, and cost issues be addressed before they would consider buying transports with composite primary structures. With these thoughts in mind, the Advanced Composites Technology (ACT) program was born. Jim led much of the initial work in organizing the program and implementing the program. The defined goal was to reduce the structural weight of a commercial transport aircraft by 30 to 50 % while also reducing manufacturing costs by 20 to 25% and ensuring that the resulting structures behaved in a predictable manner, would meet FAA requirements for certification including the area of damage tolerance, and be repairable in a way that the airlines would find acceptable.

In 1989 fifteen contracts were awarded in Phase A of the program.³ Phase A was defined to be “technology innovation” where work in the areas of manufacturing techniques such as resin transfer molding, fiber placement and stitching technology were developed. Contracts were awarded to industry (Boeing Commercial Airplanes, Hercules, Lockheed Aeronautical Systems, Grumman, Rockwell International, BASF, Dow Chemical, McDonnell Douglas, Sikorsky, and Northrop) and universities (Stanford, University of Utah, University of Delaware and University of California-Davis). Phase A represents the first part of the building-block approach—initial investigations and characterizations. Phase B was considered “technology development” and represented the next step in both size and complexity of the structures. The program became more narrowly focused and by Phase C, “technology verification,” ACT was focused on two prime contractors and two concepts. Each step was necessary for the following step to be successful. The results of these efforts are described in the following sections. Those original contracts helped develop the basic technology and understanding of material behavior and structural response. The building-block philosophy was critical to the success of this program.

In the mid 1990’s, feasibility studies indicated that a High Speed Civil Transport (HSCT) with the capability to fly between Mach 2.0 and 2.5, with a capacity of 200 to 250 passengers and a range of 5,000 nautical miles might be economically feasible. These studies indicated that to be economically viable, the HSCT would have to provide a return on investment that was competitive with subsonic transport aircraft. Advancements in the current state of technologies were shown to be necessary to meet the manufacturing, maintenance, and operational cost requirement for a HSCT aircraft. In 1994, NASA initiated the High Speed Research (HSR) program to address these challenges. The goal of the HSR program was to develop the technologies needed to build a commercial transport aircraft capable of flying at Mach 2.4 for 5000 nautical miles at an altitude of 60,000 ft. The target vehicle was to be capable of carrying 300 passengers from California to the Pacific Rim in half the time and at only 1.2 times the cost of conventional subsonic vehicles. The vehicle weight goal was a 30% reduction as compared to the Concorde supersonic transport.

In 1994, Phase I of the HSR program, trade studies were conducted to develop a configuration for a vehicle to meet the market requirements. In 1995, Phase II was initiated to develop the technology necessary for a HSCT vehicle. One area of technology development that was pursued was Material and Structures Technology Development. The Material and Structures Technology Development was further divided into elements or tasks which consisted of: Metallic Materials; Composite Materials; Materials Durability; Wing Structures; Fuselage Structures; Aeroelasticity; Acoustics; and Design Integration Trade Studies. These tasks were integrate together to develop the material processes, structural concepts and airplane configuration that met the design criteria and environmental constraints. This paper concentrates on aspects of the impact of building-block tests on the development of Wing and Fuselage Structures technology.

II. Material Characterization

The first step in applying the building-block approach to the development of composite structure is to be able to quantify the mechanical properties of the composite material being considered. Compression, tension, and shear stiffnesses and strengths must be determined. In addition, failure mechanisms and nonlinear material responses must be quantified. Some typical material characterization tests are described herein, although these tests are only meant to be representative of the many tests needed to fully understand and predict the behavior of specimens constructed from new material systems.

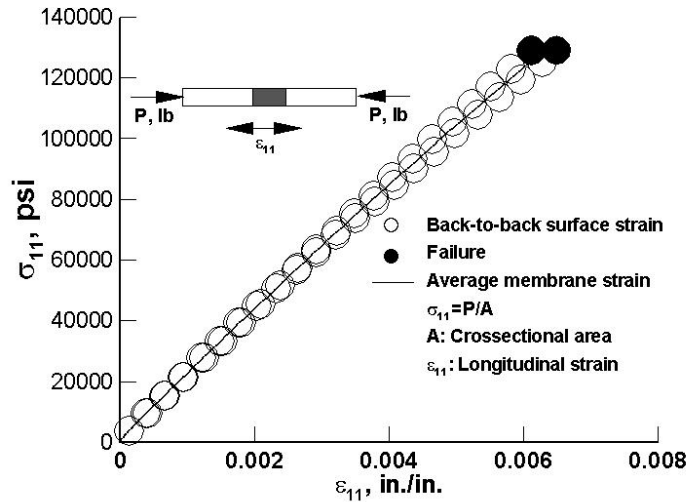
A. IITRI

A typical method used to determine the compressive property of polymer matrix composite material is the IITRI test method. The IITRI can be used to determine the compressive



a) Photograph of typical specimen.

strength and stiffness of a polymer matrix material. The method is describe in Ref. 44. An IITRI specimen and typical results for AS4/3502 graphite-epoxy uni-directional tape are shown in Fig. 1. A photograph of a IITRI specimen is shown in Fig. 1a. Typical stress-strain results for a IITRI test specimen that was tested to failure are presented in Fig. 1b. The



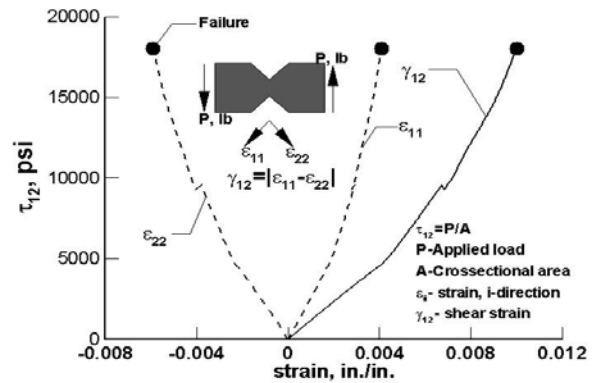
b) Typical strain results.

Figure 1. Summary of IITRI test results.



a) Photograph of typical specimen.

applied stress is shown as a function of the surface strain results obtained from back-to-back strain gages oriented in the longitudinal direction and is represented by the open symbols. The filled symbols indicate failure of the specimen. The average membrane strain in the longitudinal direction is representation by the solid line.

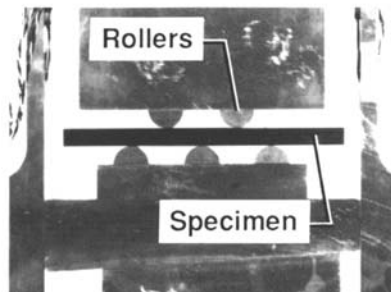


b) Typical strain gage results.

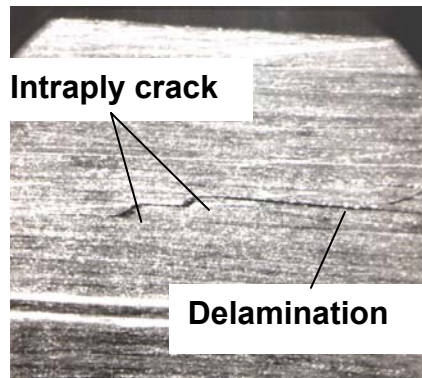
Figure 2. Summary of isopescu test.

B. Isopescu

The isopescu shear test is used to determine the shear strength and stiffness of a polymer matrix material. The method is described in Ref. 45. Typical results for AS4/3502 graphite-epoxy uni-directional tape are shown in figure 2. A photograph of an isopescu specimen is shown in Fig. 2a. Typical stress-strain results for an isopescu test specimen that was tested to failure are presented in Fig. 2b. The applied shear stress is shown as a function of the average memberane strain results taken from back-to-back strain gages oriented in the ± 45 degrees to longitudinal axis and is represented by the dashed lines. The filled symbols indicates failure of the specimen. The average membrane shear strain in the longitudinal direction is represented by the solid line.



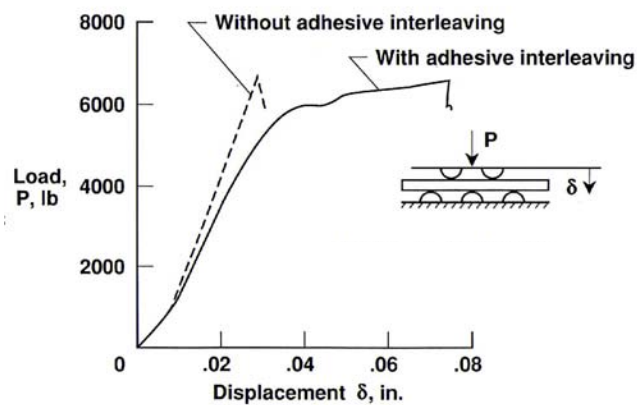
a) Photograph of test set-up.



b) Cracks and delaminations.

C. Multi-Point Bending Tests

Since layered composite structures have failure modes not seen in isotropic structures, certain types of testing became more critical than in a traditional aircraft development program. One such test was a multi-span beam shear test. In the simplest case, this test is a 3-point bend test. However, a 3-point test does not apply the same stress state through the thickness of the structure as a 4- or 5-point test, and different failure mechanisms can be activated.⁴⁶ The test set-up and typical results are shown in figure 3 for a 5-point-bend test. This set-up shows five rollers and a graphite-epoxy beam specimen in figure 3a. The failure mode of delaminations between plies and intraply cracks shown in Fig. 3b are typical of a layered composite constructed from a brittle resin system. The white layers in the photograph are layers of an adhesive which was added to improve the damage tolerance capability of the specimen. Depending on the location of the layers, the number of adhesive layers and the overall stacking sequence, failure loads, and displacements at final failure could be increased. Such an adhesive layer had the effect of increasing the failure displacement, failure load, or both. Changes in load and displacement as cracking progresses in a typical laminate are shown in Fig. 3c. Since brittle resin systems were common in the early 1980's and 1990's, these mechanisms were examined as they related to damage due to impact, external surface damage, stress concentrations and repair. This testing technique was valuable as an initial screening test in determining the damage tolerance of composite material systems—a necessary step in evaluating a material system's usefulness in aircraft structural applications.⁴⁷



c) Typical load-displacement relationship.

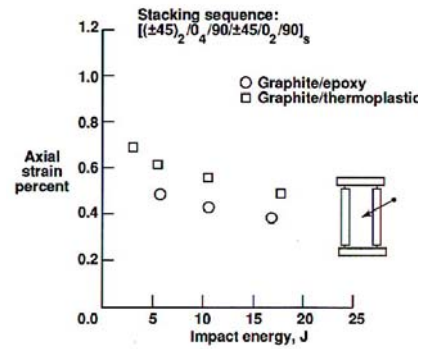
Figure 3. Multi-span beam shear test.

III. Simple Plates and Shells

Evaluating the behavior of damaged structures is part of any design process. Structures must withstand damage due to tool drops, hail stones, runway stones, and engine damage resulting in thrown debris. Compression after impact, tension after impact, flat and curved panels with holes or sawcut-type damage



a) Impact panel prior to testing.



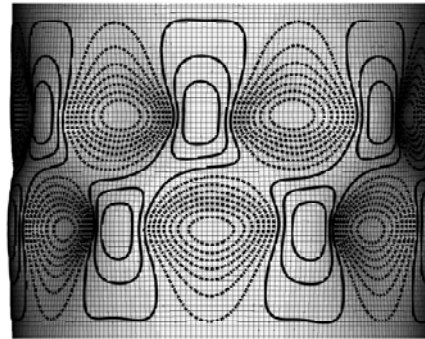
b) Failure strain.

Figure 4. Impact damage evaluation

and with pressure, shear and combined loadings in the presence of damage all have to be considered. Typical impact experimentation is done by inflicting damage to a panel by dropping weights or shooting projectiles at it at specified velocities to inflict damage, and then loading the panels to study its response. A typical flat panel in the test fixture is shown in Fig. 4a and the resulting series of results of strain at failure versus impact energy for compression-loaded graphite-epoxy panels is shown in figure 4b. In this case, graphite-epoxy panels (represented by circles) and graphite-thermoplastic panels (represented by squares) were evaluated to determine the improvement in damage tolerance by using a thermoplastic resin.⁴⁸ Panels were first impacted by shooting a 0.5-inch diameter aluminum sphere at the center of the panel then each panel was loaded to failure in compression. The axial strain in the panel at failure was recorded. The improvement in performance can be seen by noting that the thermoplastic panels have higher axial strain at



a) Experimental post-buckling deformations.



b) Predicted post-buckling deformations.

Figure 5. Typical compression-loaded cylinder.

failure than the graphite-epoxy panels for each impact energy considered. Similar studies were conducted for panels subjected to pressure or shear loadings in the presence of impact or discrete source damage. Discrete source damage can result from debris like fan blades being thrown through a wing or fuselage skin. Such damage can sever a stringer, frame or other stiffening element, supporting the need for clear understanding of changing load paths and load redistribution.

Curvature can also influence the panel behavior. Cylindrical panels and full cylinders must be tested and analyzed to predict their behavior. A typical cylinder subjected to compressive loading past the initial buckling load is shown in Fig. 5a.⁴⁹ A shadow moiré interferometry technique was used to capture the out-of-plane displacement pattern shown. Finite element analysis using the Structural Analysis of General Shells (STAGS)⁵⁰ computer code was used to predict the initial buckling load and the post-buckling behavior. The corresponding buckle pattern predicted for this cylinder is shown in Fig. 5b. The black curves represent the contours of the out-of-plane displacement predicted.

IV. Focused Technology Development Programs

There were two parts to Phase C of the ACT program. NASA and McDonnell Douglas Aerospace (now Boeing Phantom Works) were to address technologies applicable to the wing of the airplane, while NASA and Boeing were to address technologies applicable to the fuselage. Differences in structural and manufacturing requirements for the wing and fuselage meant that these parts of the aircraft would require different approaches to achieve the goals of the program; however, the high stiffness and light weight of composite materials made composites the obvious choice for both parts of the program. The first step in addressing the goals of the ACT program was to select the most promising material system and manufacturing technique. For the wing program, through-the-thickness stitching was selected to improve the damage tolerance of the wing by reducing damage growth and reduce part count by eliminating the need for rivets by stitching the stiffeners to the skin. A resin film infusion technique was selected to be cost-efficient and allow for the infiltration of resin into the stitched perform. For the fuselage program, a skin/stringer configuration was selected for the crown quadrant of the fuselage and sandwich configurations were selected for the side and keel quadrants of the fuselage. The stiffened-skin configuration consisted of skin that was fabricated using automated fiber placement. The hat section stringers were fabricated using a tape laying machine and occurred to the skin. The circumferential frames were J-section braided resin transfer molded and cobonded to the skin.

The approach used in the HSR program was to integrate design requirements from various disciplines leading to the development of wing and fuselage structural concepts. Analysis and sizing methodologies were developed for combined thermal and mechanical structural loads and then these methodologies were verified by test. Selected structural concepts were verified by test using a building-block approach from coupons to structural elements to components. These concepts were more structurally efficient and cost effective than state-of-the art aircraft structures. Materials durability testing was conducted to determine the durability of metallic and composite materials subjected to supersonic vehicle loadings. Also, accelerated tests method were developed to study the long term effects of composite structures subjected to thermal and mechanical loading. The prime industry partners in the HSR program were Boeing, McDonnell Douglas Aerospace, and Northrop-Grumman.

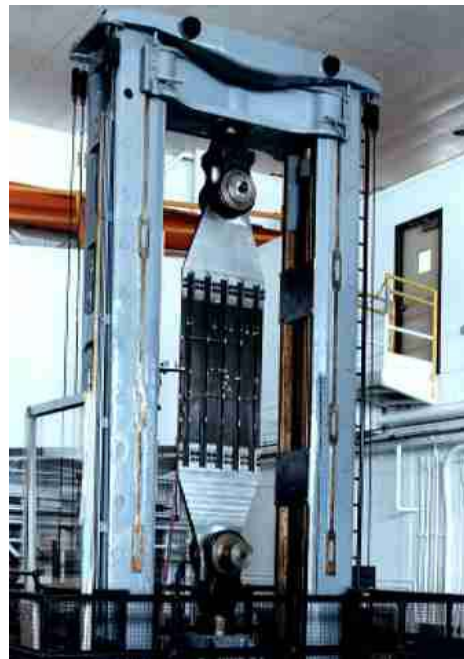


Figure 6. Tension-loaded design development test article.

A. ACT Wing Program

After the basic concept development work was completed in Phase A of the ACT program, the follow-on work was focused on either a wing or fuselage. McDonnell Douglas focused on developing the technology and verification work needed to promote the use of a composite wing on a 220-passenger commercial transport aircraft. In addition to the typical material characterization activities, since the new stitching technology was to be employed in the ACT wing program, small flat panels were built to define

the stitching requirements. These small specimens were used to determine how many stitches per inch were needed to prevent damage growth under tensile or compressive loading and then to determine the influence of the stitches on the material in-plane properties. Specimens were then built to investigate the ability of stitches to hold stiffener flanges to the panel skin in the presence of shear or tensile loads. In addition to stitching, a Resin-Film-Infusion (RFI) process was developed to simplify the infusion process for large structures. Characterization studies were conducted to quantify the behavior of these RFI specimens.

In order to develop a full-scale stitched composite wing, the next step in the building-block approach was to look at “Design Development Test Articles.” These articles included multi-stringer panels with access door holes, 2-bay discrete source damage, spliced stringer repairs, tension and compression loading changes in skin thicknesses, and specimens focusing on the landing gear region, shear-loaded spars and stiffener terminations.^{9,11,13}

A 40-inch-wide, 10-foot-long 5-stringer panel subjected to discrete source damage and tensile loading is shown in figure 6. This panel was subjected to a series of tests leading up to an evaluation of its ability to withstand loading in the presence of discrete source damage. Discrete source damage can result from debris like fan blades being thrown through a wing or fuselage skin. Such damage can sever a stringer, frame or other stiffening element, requiring the need to develop a clear understanding of changing load paths and load redistribution supported by both testing and analysis. This tension panel failed through the damage site at a load of 140% of Design Limit (DLL) twice that required by the FAA for commercial transport aircraft with this type of damage.

A similar 5-stringer panel with a bolted patch repair to be loaded with compressive loading is shown in Fig. 7. Repairs involving patching the skin and spicing a severed stringer can be performed with little equipment. The panel shown in Fig. 7 supported a load greater than Design Ultimate Load (DUL = 1.5 * DLL) when loaded in compression.

Also in this phase of the program was the need to prove that a full scale

wing box could be built and that it would withstand the necessary loading conditions. The progression through the building-block approach next led to the design of a subscale wing box, also known as the stub box. In designing the stub box, design details such as stiffener runouts, changes in skin thicknesses and the interaction of these design details with impact damage were examined. In each case, a detailed finite element model was created to predict the failure load, mode and location. To build wing cover panels, automated stitching technology had to be developed and a resin film infusion method refined to allow the manufacturing goals to be met. Building the “stub box” was a challenge in itself because each cover panel was larger than any piece of stitched structure previously built. Nevertheless, the 12-foot-long, 8-foot-wide stub box with all-composite cover panels, ribs and spars was constructed using the stitched resin film infusion technology and loaded in a way to simulate a 2.5 G pull-up flight maneuver.



Figure 7. Compression-loaded repair panel panel.



Figure 8. Wing stub box prior to testing.

The wing-stub-box test article consists of a metallic load-transition structure at the wing root, the composite wing stub box, and a metallic extension structure at the wing tip, as shown in Fig. 8. The load-transition structure and the wing-tip extension structure are metallic end fixtures required for appropriate load introduction into the composite wing stub box during the test. The load-transition structure is located inboard of the composite wing stub box (between the composite wing stub box and the vertical reaction structure at the wing-stub-box root), and the wing-tip extension structure is located outboard of the composite wing stub box. The load-transition structure is mounted on a steel and concrete vertical reaction structure resulting in a nominally clamped end condition. A 300-kip actuator was positioned under the tip of the metal extension box. A series of four tests were conducted where the structure was loaded with and without impact damage. Prior to the final test, the stub box was subjected to drop weight impacts with 100 ft-lb energy, causing barely visible impact damage. Failure occurred at a load of 154 kips, which corresponds to 93% of DUL. Failure occurred though a known impact-damage site near a stiffener termination on the upper cover panel, as shown in Fig. 9. The success of the stub box tests led to moving on to the next step in the program, the fabrication, analysis and testing of a full-scale stitched RFI semi-span wing.

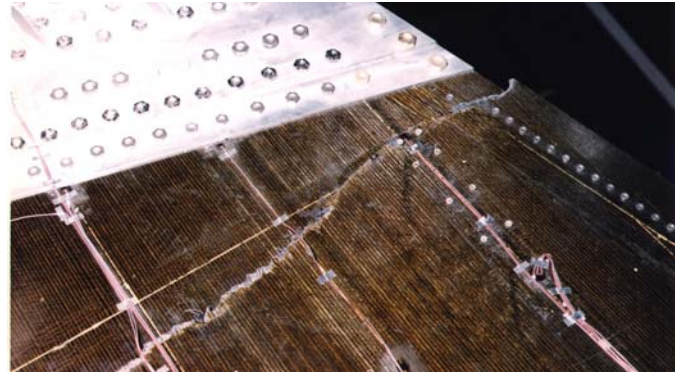
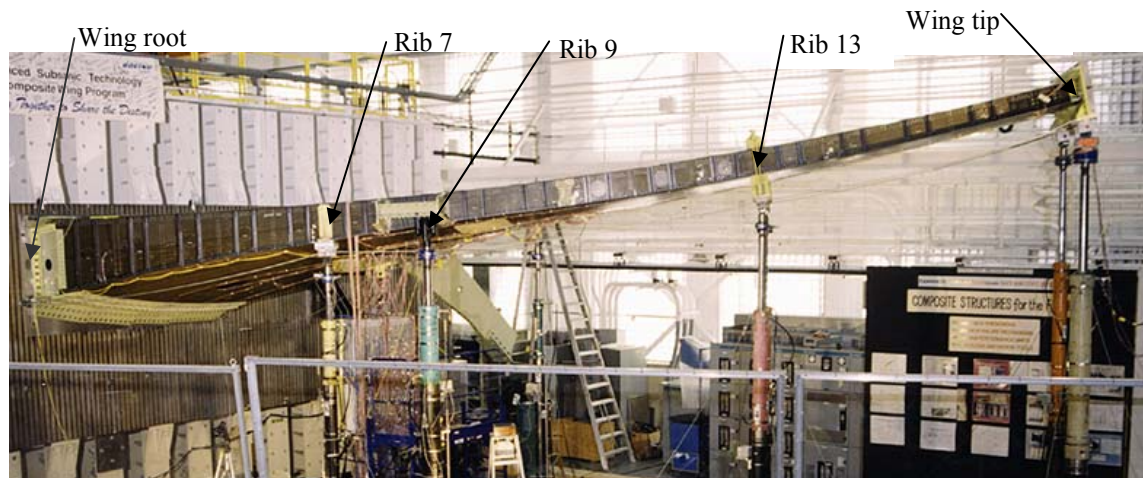


Figure 9. Failed upper cover stub box panel.

A major effort in fabricating the semi-span wing test article was to use the stitched resin-film infusion manufacturing technique to build a series of 40-foot-long stiffened panels with complex curvature. Two of these panels were assembled together with spars, ribs and load introduction structures to create a semi-span wing box representing the first 40 feet out from the root of a 220-passenger commercial transport aircraft wing. A detailed finite element analysis of the semi-span wing box was

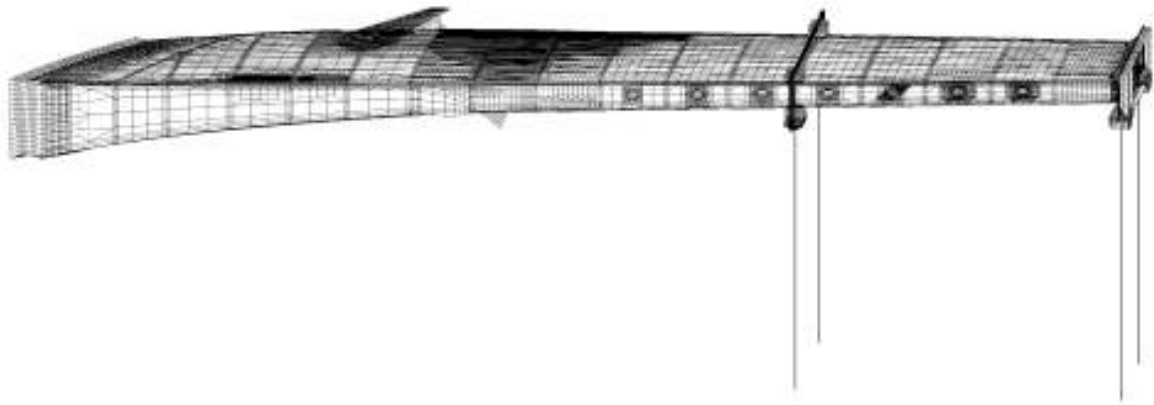


(a) Stitched semi-span wing subjected to 95% design ultimate load.

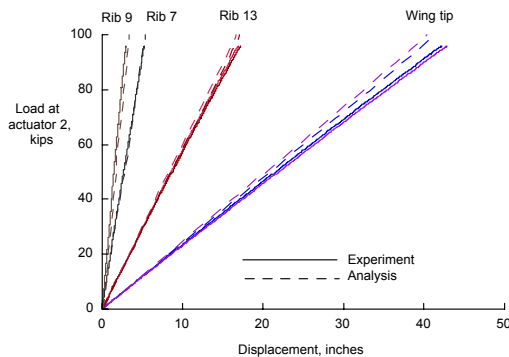
conducted using the STAGS computer code to understand behavior at design details such as stiffener runouts, splices and unsupported regions. Nine actuators were used to subject the wing box to a series of loadings including a brake-roll condition in which load was introduced through a simulated landing gear leg, a pull down flight condition of $-1G$ and a pull up flight conditions of $2.5G$. During this series of tests, discrete source damage was inflicted to both the upper and lower cover panels, the wing subjected to DLL, and the damage repaired. Prior to the final test, the upper and lower cover panels were each subjected to three 100-ft-lb impacts to cause barely visible damage at critical locations. In the final test the semi-span wing was subjected to loading in the $2.5G$ upbending condition. The wing box supported 97% of DUL

prior to failure through a lower cover panel access door. A photograph of the wing box subjected to 95% of its DUL in the 2.5G loading condition is shown in Fig. 10a. The finite element model of the wing box is shown in Fig. 10b. This model contains approximately 71,000 nodes, 76,000 elements and 428,000 degrees of freedom. A comparison of test data and predictions of deflections are shown in Fig. 10bc and the failure across the lower cover panel is shown in Figure Fig. 10d.

By withstanding 97% of DUL in the most severe loading condition and in the presence of damage and repair, the stitched wing program was declared a successful technology development program and NASA turned further development over to industry. Further information about the stitched semi-span wing test program can be found in references 23-25.



b) Finite element model.



c) Measured and predicted displacements at load points.



d) Failure across lower cover panel.

Figure 10. Stitched semi-span wing.

B. ACT Fuselage Program

The primary objective of the ACT fuselage program was to develop composite primary structure for commercial airplanes with 20-25% less cost and 30-50% less weight than equivalent metallic structure. In order to develop advanced structural concepts for aircraft fuselage, a pressurized aft fuselage section of a wide body generic wide body airplane with a diameter of 244 inches was chosen as the area of study for development of composite fuselage structural concepts. This section was chosen since it contained most of the structural details and critical manufacturing issues present in fuselage structures. The fuselage section was divided into four circumferential quadrants, the crown, the left and right sides, and keel. Details of the aft fuselage section are described in Fig. 11. A three step approach was used to identify and evaluate structural concepts for each quadrant of the fuselage section. First, the baseline concept selection was determined to be the concept that was judged to have the greatest potential for cost and weight savings with considerations for acceptable risk. Second, a global evaluation was conducted to develop preliminary designs in sufficient detail such that cost and weight differences between the baseline concept and other

low-cost/low-weight concepts could be developed. The final step involved selecting the concepts with the largest weight-saving potential for local optimization. This step involved optimizing the design elements while considering the impact of any design changes on overall cost. This approach resulted in a skin/stringer configuration for the crown quadrant and sandwich construction for the keel and side

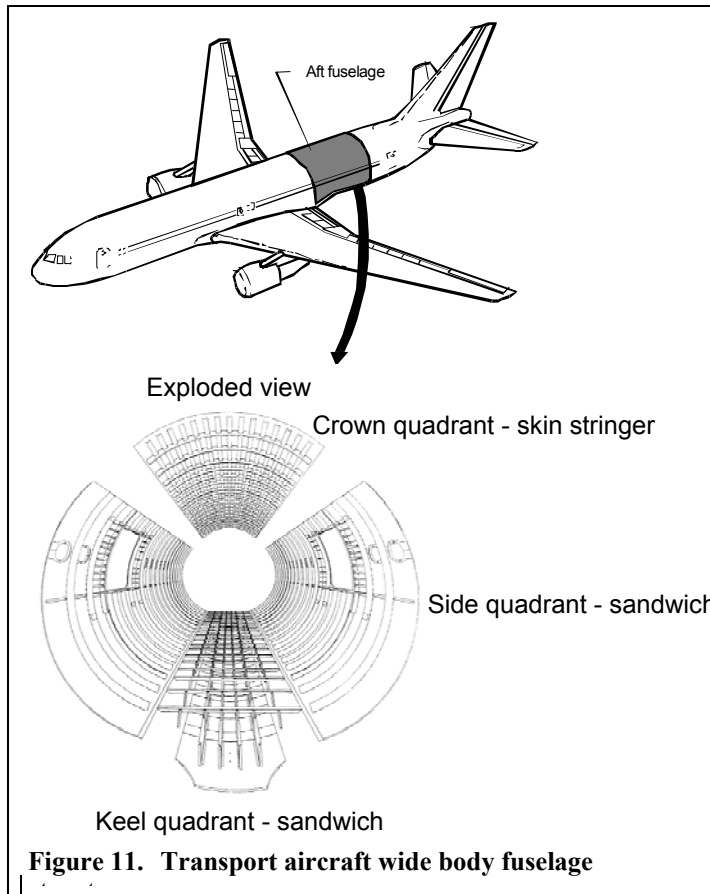


Figure 11. Transport aircraft wide body fuselage



Figure 12. Photograph of a typical benchmark crown panel.

quadrants.³⁴

Structural stability was also an important consideration for evaluating structural concepts for fuselage structures. Overall cylinder buckling was a consideration for all quadrants of the fuselage section as well as local and torsional buckling of the circumferential frames. Local skin buckling and column buckling of stringers were also assessed. Facesheet wrinkling, dimpling, and crimping were considered for side and keel structures. A series of building-block tests were conducted to evaluate the structural stability of crown fuselage concepts. Crippling test were conducted on single skin/stringer elements to understand the local stability behavior of stringers. Finally, three-stringer panels with two frames and five-stringer panels with four frames were tested to evaluate the skin buckling. The effect of barely visible impact damage on the buckling and failure behavior was also studied during the tests.

Fuselage Crown Panel Evaluation.

A series of benchmark crown panels were formulated to gain additional understanding of the structural performance of thin gage fuselage structures fabricated from composite materials. Five curved stiffened panels representative of fuselage crown design concepts were fabricated to provide test specimens for a pressure-box test fixture (described subsequently) and for frame/skin bondline strength evaluations. These panels also provided the opportunity to investigate alternate design concepts in addition to alternate damage scenarios such as circumferentially-oriented notches and barely visible impact damage. A summary of the different panel configurations is given in Table 1. A photograph of a typical benchmark crown panel is shown in Fig. 12. The stiffened graphite-epoxy fuselage crown panel shown in Fig. 12 was tested in a pressure-box test machine to study its response characteristics when subjected to internal pressure and biaxial tension. The panel has a 122-in. radius, a 72-in. length, and a 63-in. arc width. The material type

and material properties for this panel are presented in Ref. 35. The panel skin is tow-placed using a fiberglass-graphite-epoxy hybrid material system to improve the damage tolerance characteristics of the panel. The panel frames are made of triaxially braided graphite fiber preform impregnated with an epoxy resin and cured using a Resin Transfer Molding process. The stringers pass through cutouts machined into the frames, and no clips are used to attach the stringers to the frames. This design detail reduces the structural part count and the cost associated with panel fabrication.

Table 1. Summary of benchmark crown panel tests.

Panel Designation	Ultimate		Limit	
	Load Case	Damage	Load Case	Damage
TCAPS 5	18.2 psi pressure	None	8.85 psi	Severed skin/frame
TCAPS 1	Combined 13.8 psi pressure and 5,000 lb/in tension	Failed due to critical damage at frame/skin interface	Combined 8.85 psi and 3,370 lb/in	
ATCAS 12	18.2 psi pressure	None	8.85 psi	Severed skin/frame
TCAPS 4	18.2 psi pressure	None	8.85 psi	Severed skin/frame
TCAPS-3	18.2 psi pressure	Low-speed impact damage	8.85 psi cycle loading	Low-speed impact damage

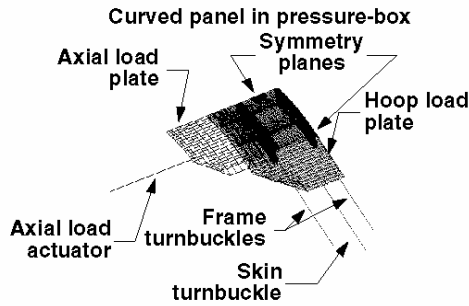
As part of the ACT fuselage program, several curved panels were fabricated by Boeing Commercial Airplane Group and tested in a specially designed pressure-box test fixture. The fixture is capable of testing curved panels subjected to internal pressure and bi-axial tension by using axial actuators and



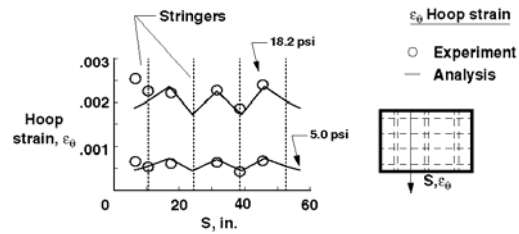
Figure 13. Photograph of pressure-box test fixture.

turnbuckle or hoop restraint rods. This fixture is described in Refs. 51 and 52. A photograph of the pressure-box test machine is shown in Fig. 13. In support of these tests, nonlinear structural analyses of a cylindrical shell with internal pressure as well as the pressure-box test fixture with a curved panel subjected to internal pressure were performed using the STAGS finite element code. The analysis of the cylindrical shell ensured that the load state that was applied to the pressure-box panel was representative of that in a full cylinder. A quarter model of the pressure-box test fixture with a curved panel has been developed for analysis using shell, rod, and beam elements as shown in Fig. 14. The turnbuckles or hoop restraint rods and hydraulic actuator rods are also included in the model to account for their rigid-body rotational degrees of

freedom as the panel translates when internally pressurized. This model has approximately 10,000 elements with approximately 62,000 degrees of freedom. The experimental hoop strain results along an axis oriented in the axis s from the experiment are compared with analysis results in Fig. 14 for a fuselage panel subjected to internal pressure conditions of 5 psig and 18.2 psig in the pressure box test fixture. The correlation between the results is excellent. This comparison suggests that the finite element model represents the test well.



a) Finite element model of crown

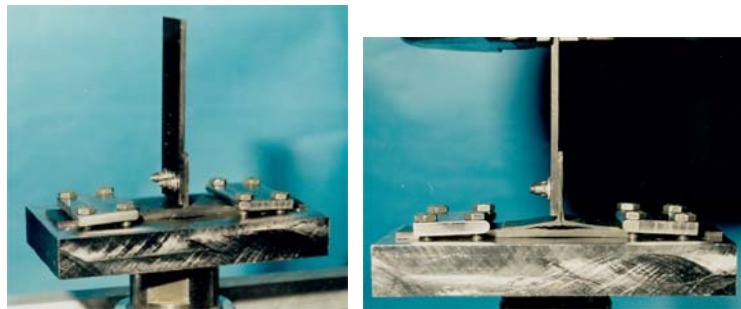


b) Comparison of analytical and experimental hoop strain results
Figure 14. Finite element model of crown panel.

panel.

C. HSR program

As part of the HSR fuselage program, several sizes of structural specimens were fabricated to support the development of stiffened-skin concepts for the fuselage structure. Specimens ranged from simple stiffener pull-off and stiffener crippling specimens to full-scale panels designed for vehicle loads. Examples of stiffener pull-off and stiffener crippling specimens are given in figures 15 and 16, respectively. A typical stiffener pull-off specimen is shown in Figure 15(a), and a typical stiffener pull-off failure mode is shown in figure 15(b). These tests were used to verify the integrity of the skin-stiffener interface, which is important in postbuckled designs as well as fuselage over-pressure conditions. A typical stiffener crippling specimen is shown in Figure 16(a), and a photograph of the shadow moiré interferometry out-of-plane displacement pattern at an applied load of 33.6 kips is shown in figure 16(b). These tests were used to investigate the stability of the stiffener design and to understand the strength characteristics of the skin-stiffener combination.

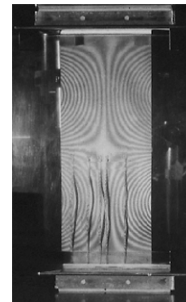


(a) stiffener pull-off specimen. (b) Stiffener pull-off failure mode

Figure 15. Typical stiffener pull-off specimen and test.

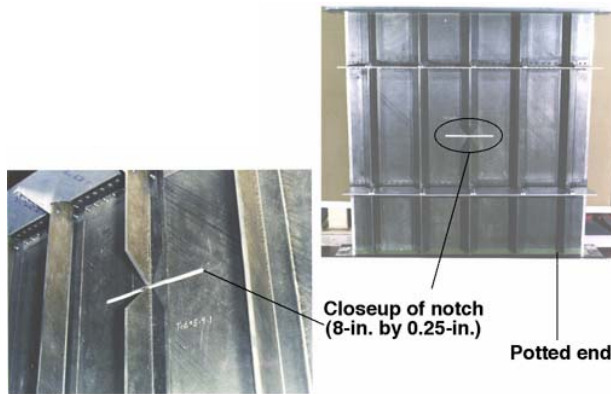


(a) stiffener crippling



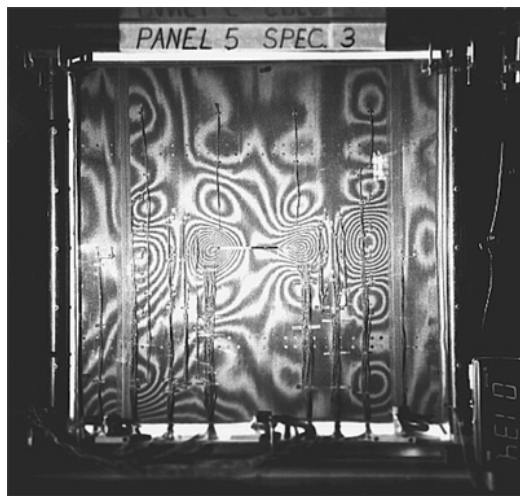
(b) out-of-plane displacement

Figure 16. Typical stiffener crippling specimen and test.



(a) Five-stringer2-frame notched-compression subcomponent

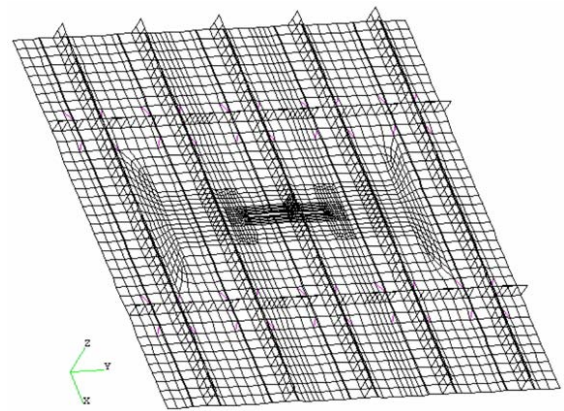
sub-component scale panels were tested. The panels were tested in uniaxial compression to evaluate the response of the different skin layup designs as well as the effect of impact damage and discrete-source damage. Experimental and analytical results are compared in Fig. 17 for a compression sub-component panel built for the HSR fuselage program by McDonnell Douglas Aerospace (now Boeing Phantom Works Division). The sub-component panel is shown in Fig. 17a and it measures 40-in-wide by 40-in-long and has five stringers spaced at 8 inches and two frames located



(c) An experimental out-of-plane displacement pattern at an applied load of 134 kips.

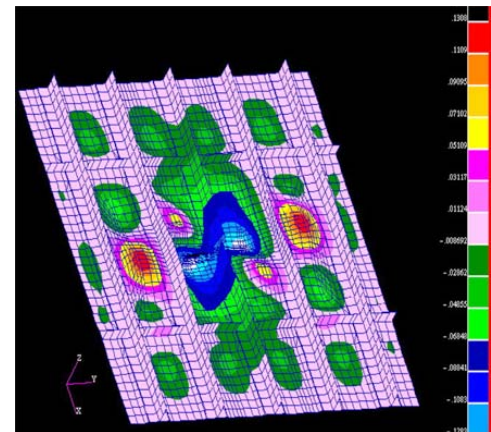
by 0.25-in-wide machined notch through the center stringer to simulate discrete-source damage. Knife-edge supports were applied to the unload edges, and frame restraints were used to restrict global bending response.

The loaded edges were encased in potting material and



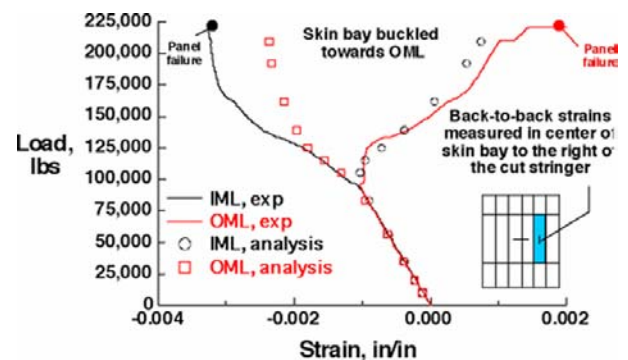
(b) Finite element model of the notched 5-stringer subcomponent panel.

Following these element tests, a series of



(d) An analytical out-of-plane displacement pattern at an applied load of 138 kips.

10 inches above and below the horizontal centerline of the panel. There is an 8-in-long



(e) Comparison of surface strain results in a skin-bay adjacent to the cut skin bay.

Figure 17. Typical results for a HSR fuselage panel loaded in compression.

A

geometrically nonlinear structural analysis of this subcomponent was also performed using the STAGS finite element code. The finite element model used for the analysis, shown in Fig. 17b consists of 3,596 nodes, 3,492 shell elements, and 21,776 active degrees of freedom. A photograph of the shadow moiré interferometry out-of-plane displacement pattern at an applied load of 134 kips is shown in Fig 17c. The out-of-plane displacement contours at an applied load of 138 kips predicted using the STAGS analysis are shown in Fig. 17d. The correlation between the measured and predicted displacement patterns is very good. A comparison between measured and predicted load versus surface strain results in a skin bay

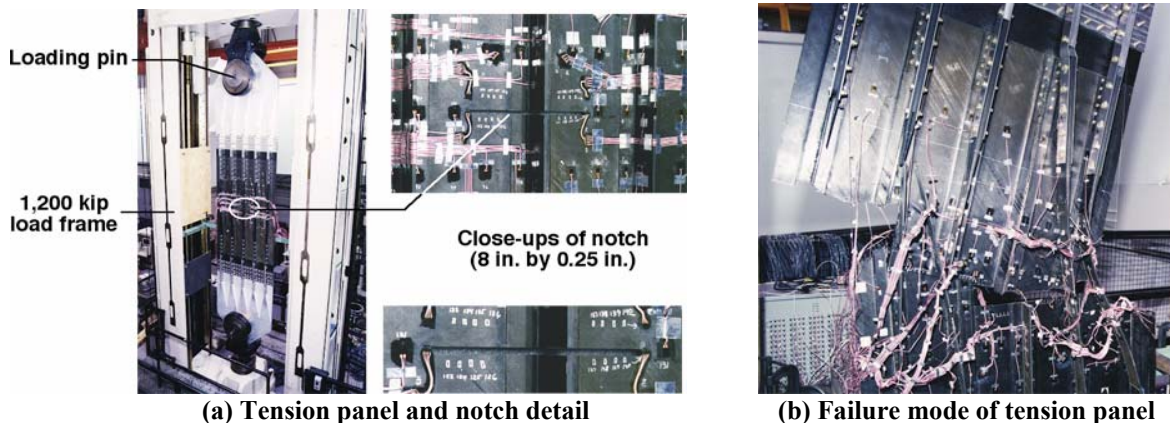


Figure 18. Five-stringer fuselage tension panel with discrete source damage.

adjacent to the cut skin bay is presented in Fig. 17e. The good correlation between the experimental values (i.e., the solid lines) and the predicted values (i.e., the open symbols), suggest that the analysis model represents the test well. Failure is indicated by the filled symbols.

The results from these element and sub-component tests were then utilized by McDonnell Douglas to design full-scale fuselage panel test articles to be tested under uniaxial loads in an un-pressurized configuration. Both tension and compression full-scale fuselage panels were designed and tested. One of

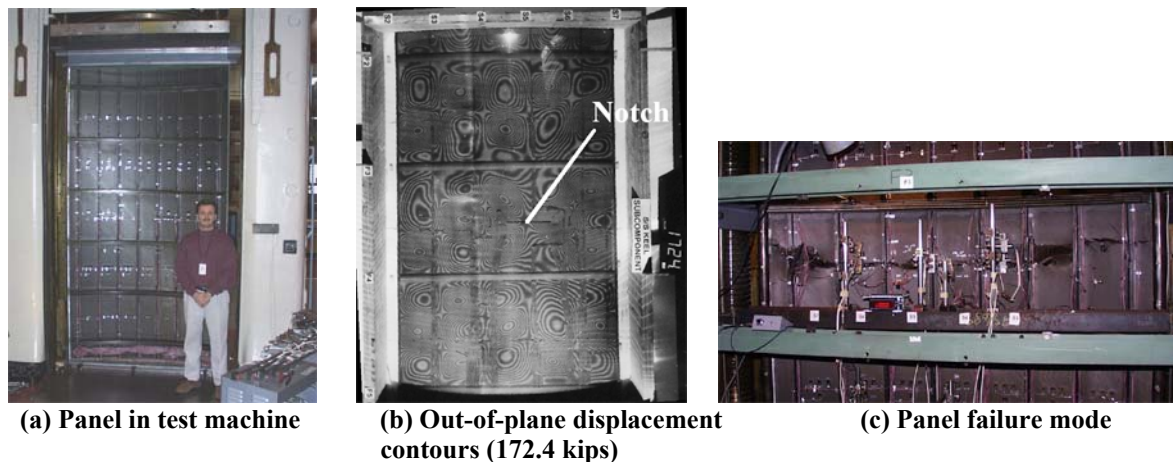


Figure 19. Five stringer fuselage compression panel with barely visible impact damage and discrete-source damage

the five-stringer fuselage panel tension test articles is shown in figure 18. These test panels were 80-inches-long and 40-inches-wide, and had an eight-inch stringer spacing. A special load introduction fixture was designed by McDonnell Douglas to directly introduce load into the stringers. The purpose of the tension test series was to evaluate the adequacy of the skin-stringer design to support the required design loads in the presence of discrete source damage. The discrete source damage was simulated with a notch that was machined through the center stringer and spanning one full skin-bay width. A typical test panel is shown in the 1.2 million-pound test machine at NASA Langley in figure 18. A close-up of the notch is also shown in figure 18(a), and the failure mode of the panel is shown in figure 18(b). The failure initiated at

the notch tip, propagated to the adjacent stringers, and then ran parallel to the stringers causing failure of the panel. The panel supported all design loads.

The final full-scale fuselage compression panel tested in this series of tests is shown in figure 19. This curved panel is 120-inches-long with an arc length of 60 inches and a radius of curvature of 60 inches. This panel was tested in uniaxial compression to assess its stability characteristics and to study its response

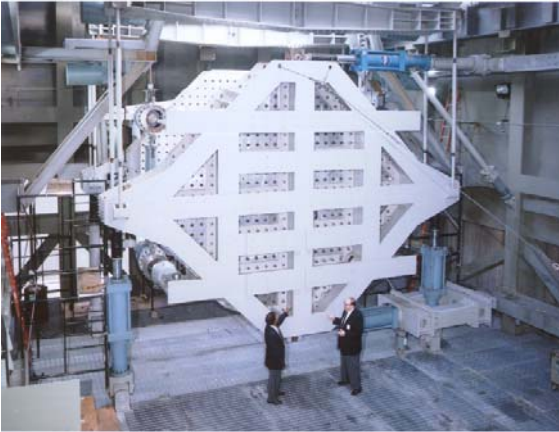


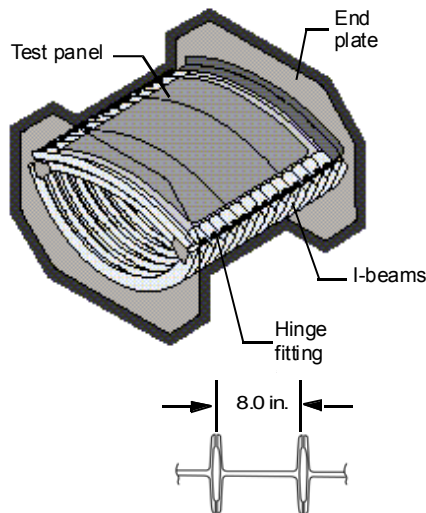
Figure 20. NASA combined loads test machine.

in the presence of both barely visible impact damage as well as discrete source damage. A photograph of the shadow moiré interferometry out-of-plane displacement pattern just prior to failure at an applied load of 172.4 kips is shown in Fig 19b. The location of the notch is shown in this figure as well. The panel was well into the post-buckled range at this load level. The failure mode of the panel is shown in figure 19c. The failure initiated as a local failure at the notch tip in the post-buckled configuration and then propagated across the width of the panel. This panel supported all required design loads as well.

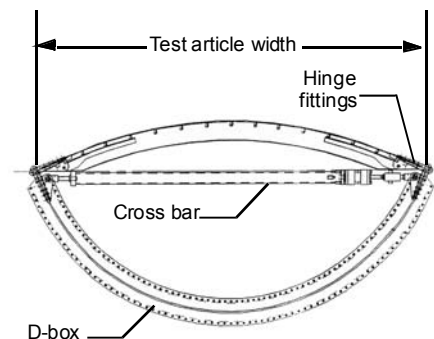
Combined Loads Test HSR Fuselage Panels

A majority of the testing conducted in the HSR Program consisted of coupons, elements and panels. These building-block tests were used to develop

material property database that could be used to size and analytical predict the responses of larger structures. However, large full scale panels with sufficient details were tested in order to validate structural concepts. Some typical results for composite curved fuselage panels that were tested in the Combined Loads Test machine (COLTS) will be described in this section.



a) Overall configuration



b) Cross-sectional view

Figure 21. D-box fixture for testing curved stiffened panels.

curved panel to provide a stress state that is representative of a cylindrical shell. This requirement is particularly important when investigating the failure of a curved panel.

The D-box test fixture shown in Fig. 21a was used to apply mechanical and internal pressure loads to the test panel. The small axial stiffness of the D-box test fixture allows a test panel to experience most of the applied axial load and minimizes the shift in the center-of-pressure of the assembly if the test panel buckles. The low axial stiffness of the D-box test fixture is the result of an assembly of curved I-beams

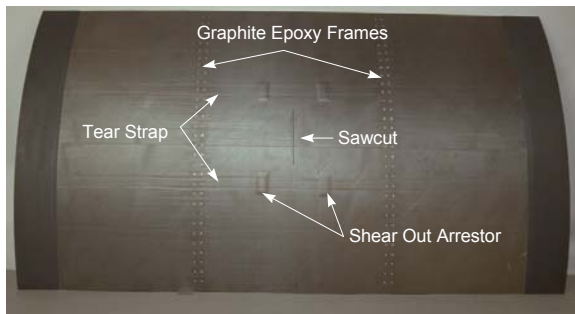


Figure 22. Photograph of curved sandwich fuselage panel.

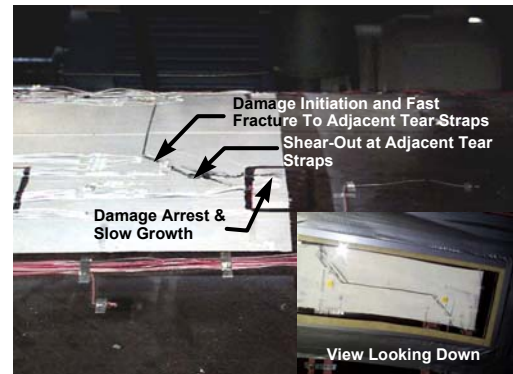


Figure 23. Photograph of failed fuselage panel.

with the cross-section shown in the inset. The I-beam sections are 8.0-inches deep and 15 of these sections are used to make the D-box test fixture. This D-box test fixture is designed to test curved panels with 60- to 130-inch radii and 20- to 22-inch frame spacings. The panels are attached to the D-box test fixture with the hinge fittings as indicated in Figure 21b. A cross-section of the D-box test fixture is presented in Fig 21b that shows the details of the hinge fittings. Thirteen of these hinge fittings are provided between the I-beams for this purpose. When the D-box assembly is internally pressurized, the assembly expands in a manner that causes the hinge supports to move inward. This deformation will cause the test panel to bend in a way that is not representative of the response of an internally pressurized shell. To prevent this undesirable deformation, cross bars are mounted between the hinge points as shown in the figure such that the distance between the hinge points can be held constant or adjusted as needed to induce the appropriate stress state in the test panel. A detailed description of the D-box test fixture is presented in Ref. 53.

A curved sandwich fuselage panel with a centrally located circumferential sawcut through the facesheet and honeycomb core of the panel was subjected to internal pressure, shear and axial loading using the D-box test fixture in the COLTS combined loads test machine (Ref. 54). The sandwich facesheets were fabricated from IM7/PETI-5 uni-directional tape with longitudinal tear straps, and the core is a titanium honeycomb core. The basic facesheet was a 12-ply laminate. The panel contained longitudinal tear straps spaced 10-in. apart that were 20-ply laminates. The panel also had transverse patch doublers at four locations. The facesheet of the patch doublers was a 30-ply laminate. A 12-inch-long notch was machined through the longitudinal tear strap at the center of the panel to simulate discrete-source damage in the panel prior to testing. A detailed description of the test panel is presented in Ref. 54. A photograph of the panel is shown in Fig. 22.

The panel was initially loaded to 7.2 psi internal pressure followed by axial and shear loading. The damage initiated at the tip of the notch and propagated at a 40° path toward the adjacent tear straps. The damage progressed beyond the doublers at an applied of 7.2 psi internal pressure, 3,900 lb/in. axial load, and 888 lb/in. shear load. A photograph of the failed panel is shown in Fig. 23.

V. Concluding Remarks

NASA Langley Research Center and its industry partners advanced the understanding of the behavior of composite structures through large focused programs in the 1990s. The building-block approach to research in structural mechanics was vital to the success of the composite technology development programs. Examples that highlight the development of unique testing capabilities to support the building blocks include the Advanced Composites Technology Program, which began in 1989 and ended in 2000, and the High Speed Research Program, which began in 1994 and ended in 1999. Building block elements involving analysis and experimentation including coupons, stiffened and unstiffened panels, subcomponents, design detail articles and large full-scale components supported technology development. Verified tools and new approaches to composite design and fabrication and the development of new experimentation capabilities were critical parts of each program.

VI. References

- ¹Chen, V. L., Hawley, A. V., Klotzsche, M., Markus, A. M., and Palmer, R. J., "Composites Technology for Transport Primary Structure," First NASA Advanced Composites Technology Conference," NASA CP-3104, Part 1, 1991, pp.71-126.
- ²Davis, J. G. Jr., "Overview of the ACT Program," Ninth DoD/NASA/FAA Conference on Fibrous Composites in Structural Design—Second NASA ACT Conference, NASA CP 3154, June 1992, pp. 3-25.
- ³Davis, J. G. Jr., "Overview of the ACT Program," Proceedings of the Ninth DoD/NASA/FAA Conference on Fibrous Composites in Structural Design, 1991, pp. 577-599.
- ⁴Davis, J. G. Jr., "Advanced Composites Technology Program," Third NASA Advanced Composites Technology Conference, NASA CP-3178, Part 1, 1993, pp. 49-78.
- ⁵Markus, A., Thrash, P., and Grossheim, B., "Manufacturing Development and Requirements for Stitched/RTM Wing Structure," NASA CP 3229, 1993, pp. 503-523.
- ⁶Hawley, A., "Preliminary Design of a Transport Aircraft Composite Wing," Proceedings of the Fifth NASA/DoD Advanced Composites Technology Conference. NASA CP-3294, Volume 1, Part 2, pp. 717-772.
- ⁷Hawley, A. V., "Development of Stitched/RTM Primary Structures for Transport Aircraft," NASA CR-191441, 1993.
- ⁸Marcus, A., Thrash, P., and Rohwer, K., "Progress in Manufacturing Large Primary Aircraft Structures Using the Stitching/RTM Process," Third NASA Advanced Composites Technology Conference. NASA CP-3178, Part 1, 1993, pp. 453-479.
- ⁹Jegley, D. C. and Waters, W. A. Jr., "Test and Analysis of a Stitched RFI Graphite-Epoxy Panel with a Fuel Access Door.," NASA TM 108992, March, 1994.
- ¹⁰Sutton, J., Kropp, Y., Jegley, D., and Banister-Hendsbee, D., "Design, Analysis and Tests of Composite Primary Wing Structure Repairs," Presented at the 5th ACT Conference, Seattle, Washington, August 1994. NASA CP 3294, Vol. 1, Part 2, pp. 879-912.
- ¹¹Hinrichs, S., Chen, V., Jegley, D., Dickinson, L., and Kedward, K., "Effect of Impact on Stitched/RFI Compression Panels," Presented at the 5th ACT Conference, Seattle, Washington, August 1994 NASA CP 3294, Vol. 1, Part 2, pp. 913-934.
- ¹²Hinrichs, S., Kropp, Y., and Jegley, D., "Manufacturing, Analysis And Tests Of Stitched/RFI Subcomponents," Presented at the 6th ACT Conference, Anaheim, CA, August 1995. NASA CP 3326 Volume 1, Part 1, pp. 209-231.
- ¹³Sutton, J., Kropp, Y., Jegley, D., and Banister-Hendsbee, D.: Design, Analysis and Tests of Composite Primary Wing Structure Repairs. Presented at the 5th ACT Conference, Seattle, Washington, August 1994. NASA CP 3294, Vol. 1, Part 2, pp 879-912.
- ¹⁴Jegley, Dawn, "Analysis of Selected Compression Splice Joint Locations in a Graphite-Epoxy Transport Wing Stub Box," NASA TM 110170, October 1995.
- ¹⁵Hinrichs, S. C., Kropp, Y., and Jegley, D. C., "Analysis and Testing of Stitched/RFI Subcomponents," Sixth NASA/DOD Advanced Composites Technology Conference. NASA CP-3326, Vol. 1, Part 1, 1996, pp. 209-233.
- ¹⁶Hinrichs, S., Jegley, D. C., and Wang, J. T., "Structural Analysis and Test of a Stitched Composite Wing Box," Sixth NASA/DOD Advanced Composites Technology Conference. NASA CP-3326, Vol. 1, Part 1, 1996, pp. 279-309.
- ¹⁷Hawley, A. V., "Detail Design Development of a Transport Aircraft Composite Wing," Sixth NASA/DOD Advanced Composites Technology Conference. NASA CP-3326, Vol. 1, Part 1, 1996, pp. 131-154.
- ¹⁸Drenth, S. E., and Renieri, M. P., "Cover Panel and Substructure Design for a Full-Scale Composite Transport Wing," 11th DOD/NASA/FAA Conference on Fibrous Composites in Structural Design—Seventh NASA ACT Conference, Aug. 1996.
- ¹⁹Rohwer, K., Ghumman, A., and Markus, A., "Stitched/Resin Film Infusion (S/RFI) Manufacturing Technology Development," Proceedings of the 11th DOD/NASA/FAA Conference on Fibrous Composites in Structural Design. Report number WL-TR-97-3009 pp. XIII-93-116.
- ²⁰Wang, John T., Jegley, Dawn C, Bush, Harold G, and Hinrichs, Stephen C. "Correlation of Structural Analysis and Test Results for the McDonnell Douglas Stitched/RFI All-Composite Wing Stub Box." NASA TM 110267, July, 1996.

- ²¹Jegley, D. and Bush, H., "Test Documentation and Results of the Structural Test on the All-Composite Wing Stub Box." NASA TM 110204, April, 1997.
- ²²Jegley, D. C., "Behavior of Compression-Loaded Panels with Stringer Terminations and Impact Damage." *Journal of Aircraft*. Vol. 35, No. 12, pp.942-948, Nov.-Dec., 1998.
- ²³Jegley, D. C., and Bush, H. G., "Structural Testing of a Stitched/Resin Film Infused Graphite-Epoxy Wing Box." NASA TM 210846, April, 2001.
- ²⁴Karal, M., "AST Composite Wing Program - Executive Summary," NASA CR 2001-210650.
- ²⁵Jegley, D. C., Bush, H. G. and Lovejoy, A. E., "Evaluation of the Structural Response and Failure of a Full Scale Stitched Graphite-Epoxy Wing." *Journal of Aircraft*. Vol. 40, No. 6, pp. 880-886, November-December, 2003.
- ²⁶Dow, M. B. and Dexter, B. H., "Development of Stitched, Braided and Woven Composite Structures in the ACT Program and at Langley Research Center (1985-1997) Summary and Bibliography." NASA TP 97-206234, Nov. 1997.
- ²⁷McGowan, D. M. and Ambur, D. R., "Structural Response of Composite Sandwich Panels Impacted With and Without Compression Loading". *Journal of Aircraft*, Vol. 36, No. 3, May-June 1999, pp. 596-602.
- ²⁸Dávila, C. G., Ambur, D. R., and McGowan, D. M., Analytical Prediction of Damage Growth in Notched Composite Panels Loaded in Axial Compression. *Journal of Aircraft*, Vol. 37, No. 5, September–October 2000, pp. 898-905.
- ²⁹McGowan, D. M., Ambur, D. R., Hanna, T. G., and McNeill, S. R., "Evaluation of the Compressive Response of Notched Composite Panels Using a Full-Field Displacement Measurement System". *Journal of Aircraft*, Vol. 38, No. 1, January–February 2001, pp. 122-129.
- ³⁰McGowan, D. M., Young, R. D., Swanson, G. D., and Waters, W. A., "Compression Tests and Nonlinear Analyses of a Stringer- and Frame-Stiffened Graphite Epoxy Fuselage Crown Panel," Presented at the Fifth NASA/DoD/ARPA Advanced Composites Technology Conference, Seattle, WA, August 22-25, 1994.
- ³¹McGowan, D. M., and Ambur, D. R., "Compression Response of a Sandwich Fuselage Keel Panel With and Without Damage," Presented at the Sixth NASA/DoD/ARPA Advanced Composites Technology Conference, Anaheim, CA, August 7-11, 1995.
- ³²Walker, T., Scholz, D., Flynn, B., Dopker, B., Bodine, J., Ilcewicz, L., Rouse, M., McGowan, D., and Poe, Jr., C., "Damage Tolerance of Composite Fuselage Structure," Presented at the Sixth NASA/DoD/ARPA Advanced Composites Technology Conference, Anaheim, CA, August 7-11, 1995.
- ³³Murphy, D., Dopker, B., Ilcewicz, L., Biornstad, R., and McGowan, D., "Composite Structural Analyses Supporting Affordable Manufacturing and Maintenance," Presented at the Sixth NASA/DoD/ARPA Advanced Composites Technology Conference, Anaheim, CA, August 7-11, 1995.
- ³⁴Walker, T. H., Minguet, P. J., Carbery, D. J., Swanson, G. D., and Ilcewicz, L. B., "Advanced Technology Composite Fuselage – Structural Performance," NASA CR-4732.
- ³⁵Walker, T. H., Minguet, Ilcewicz, L., Bodine, J.B., Murphy, D. P., Dost, E. F., "Benchmark Panels, " NASA CR-194969.
- ³⁶McGowan, D. M., and Ambur, D. R., "Damage-Tolerance Characteristics of Composite Fuselage Sandwich Structures With Thick Facesheets," Presented at the 11th DoD/NASA/FAA Conference on Fibrous Composites in Structural Design, Fort Worth, TX, August 26-29, 1996.
- ³⁷Ambur, D. R., McGowan, D. M., Baker, D. J., Hanna, T. G., and McNeill, S. R., "Compression Response of Notched Stiffened Composite Panels: Analyses and Experiments," Presented at the 1999 Society for Experimental Mechanics Conference on Theoretical, Experimental and Computational Mechanics, Cincinnati, OH, June 7 – 9, 1999.
- ³⁸McGowan, D. M., Dávila, C. G., and Ambur, D. R., "Damage progression in Buckle-Resistant Notched Composite Plates Loaded in Uniaxial Compression." Presented at the 40th Structures, Structural Dynamics and Materials Conference, Seattle, WA, April 16-19, 2001. AIAA Paper No. 2001-1482.
- ³⁹McGowan, D.M., "Skin/Stringer Large-Notch Compression Structural Tests and Analyses," Presented at the HSR Fuselage Structures Semi-Annual Review, St. Louis, MO, September 1998.
- ⁴⁰McGowan, D.M., "Skin/Stringer Large-Notch Tension Structural Tests and Analyses," Presented at the HSR Fuselage Structures Semi-Annual Review, Los Angeles, CA, January 1998.
- ⁴¹McGowan, D.M., "Skin/Stringer Large-Notch Compression Structural Tests and Analyses," Presented at the HSR Fuselage Structures Semi-Annual Review, Los Angeles, CA, January 1998.
- ⁴²McGowan, D. M., "PMC 3 Bay Panel and Crippling Tests & Analyses," 2nd Annual HSR Aircraft Materials and Structures Workshop, Hampton, VA, February 1996.

- ⁴³“High Speed Research Program Summary Report for Task 16 Materials and Structures Damage Tolerance and Task 25 Fuselage Structures,” January 1995 to September 1999.
- ⁴⁴ASTM Standard D 3410/D3410M-0 (1995), "Compressive Properties of Polymer Matrix Composite Materials with Unsupported Gage Section by Shear Loading," American Society for Testing and Materials, West Conshohocken, PA.
- ⁴⁵ASTM Standard D 5379/D 5379M-98, "Test Method for Shear Properties of Composite Material by the V-notched Beam Method," American Society for Testing and Materials, West Conshohocken, PA.
- ⁴⁶Williams, J.G., "The Multi-Span-Beam Shear Test Method For Studying Composite Transverse Shear Failure Characteristics," Presented at the 26th AIAA/ASME/ASCE/AHS/ASC Structures, Structural Dynamics and Materials (SDM) Conference, Orlando, FL, April 1985.
- ⁴⁷Williams, J.G. and Rhodes, M. D., "Effect of Resin on Impact Damage Tolerance of Graphite/Epoxy Laminates. Composite Materials: Testing and Design (Sixth Conference)," ASTM STP 787, pp. 450-480, 1982.
- ⁴⁸Jegley, D. C., "Compression Behavior of Graphite-Thermoplastic and Graphite-Epoxy Panels with Circular Holes or Impact Damage." NASA TP 3071, March 1991.
- ⁴⁹Hilburger, M. and Starnes, J. H. Jr., "Parametric Study on the Response of Compression-Loaded Composite Shells with Geometric and Material Imperfections," NASA TM 2004-212676. Sept. 2004.
- ⁵⁰Rankin, C. C., Brogan, F. A., Loden, W. A., and Cabiness, H. D., "STAGS User Manual, Version 3.0," Lockheed Martin Missiles & Space Co., Inc., Rept. LMSC P032594, March 1999.
- ⁵¹Rouse, M., and Ambur, D. R., "Fuselage Response Simulation of Stiffened Panels Using a Pressure-Box Test Machine," AIAA-95-1362-CP, April 1995.
- ⁵²Ilcewicz, L. B., Smith, P. J., and Horton, R. E., "Advanced Composite Fuselage Technology". NASA CP 3178, 1992, pp. 97-156.
- ⁵³Ambur, D. R., Cerro, J. A., and Dickson, J., "Analysis of a D-box Fixture for Testing Curved Stiffened Aircraft Fuselage Panels In Axial Compression and Internal Pressure," AIAA-94-1345-CP, April 1994.
- ⁵⁴Mahler, M., Ley, R., Chandu, S., and Weichuan, L., "Propagation and Control of Crack-Like Damage In Curved Composite Panels Under Combined Loads," AIAA-2000-1534, April 2000.

This page left blank intentionally.

Contributions to Damage Tolerance and Residual Strength Technologies for Composite Structures

Damodar R. Ambur*
NASA Glenn Research Center
Cleveland, OH 44135

Prasad B. Chunchu•
Eagle Aeronautics
Hampton, VA 23669

Navin Jaunky§
National Institute of Aerospace
Hampton, VA 23666

Cheryl A. Rose‡
NASA Langley Research Center
Hampton, VA 23681

Abstract

The research and technology work conducted at the NASA Langley Research Center over the past two decades on damage tolerance of composite structures is summarized. Only a few topics such as the effects of manufacturing defects, response to low-speed impact that is representative of manufacturing tool drops, failure initiation and growth in unstiffened flat and curved panels with a circular cutout, stiffened flat plates with and without discrete-source damage in the form of notches subjected to compression and inplane shear loading are presented and discussed. Over the years, a better understanding of these physical phenomena led to the development of tougher polymeric material systems, damage tolerant material forms and structural concepts, measurement techniques and test methods for assessing structural response and failure modes, and analysis methods for predicting damage initiation and growth to facilitate structural system prognostics and residual strength prediction.

I. Introduction

Aerospace structural design requires several considerations. One that centers on safety is design for damage tolerance. Damage tolerant design, in general, encompasses considerations for manufacturing anomalies, low-speed impact, notch sensitivity, and fatigue life, depending on the aerospace structure. The damage tolerance criteria used for structural design are worked in the context of inspection intervals, repair, and replacement for the damage tolerance principles became a significant consideration in design during the late 70's; such knowledge base for polymer matrix composites was very limited then. Many key researchers began efforts to add scientific understanding to the damage tolerance of composite structures, which held great promise for lightweight air vehicles.

* Chief, Structures Division. Associate Fellow, AIAA.

• Research Engineer, Member AIAA.

§ Research Engineer, Member AIAA.

‡ Senior Aerospace Engineer. Senior Member, AIAA.

Dr. James H. Starnes, Jr. was one such key researcher from NASA Langley Research Center that was responsible for nurturing this research area to study the low-speed impact response, compression-after impact strength, and notch sensitivity of both stiffened and unstiffened laminated composite plates (Ref. 1-5). These research activities addressed the airgun impact damage tolerance of laminated quasi-isotropic and orthotropic composite plates to identify the energy threshold for plate catastrophic failure. This effort also helped define the size of the compression-after-impact test specimen to be 10-in. long and 5-in. wide for a 48-ply laminate. Activities were also conducted on stiffened plates to address damage to stiffeners, which was used to develop stiffened panel sizing methods that account for damage tolerance. Subsequent to this, several of Dr. Starnes' colleagues developed several standard test methods to evaluate the damage tolerance of different tough material systems with T300, AS4, and Celeron fiber reinforcements.

Additional efforts were conducted by his colleagues and successors to study the effects of manufacturing defects, low- and high-speed impact response, and the failure initiation and growth from local stress risers such as dropped plies, terminated stiffeners, cutouts, and notches. Determination of the residual strength of structures with such features both in the buckle-resistant and post-buckled structures was also pursued together with developing design features that can arrest damage growth so that the full potential of composite structures can be realized in aerospace applications. The present paper summarizes the work done over the past one-and-a-half decades [6-15] on composite structures and materials to study low-speed impact response, discrete-source damage, and failure arising from regions of stiffness discontinuities and the damage growth. Impact response of composite structures is a complex phenomenon since it involves different damage modes and possible localized strain rate effects which are influenced by the impactor mass, size, and speed, specimen or target geometry, hybrid materials, lamination sequence, boundary or support conditions, the relative magnitudes of impactor and target masses, and the nonlinear response of thin structures. The objective was to obtain scientific understanding of the low-speed impact response phenomenon for thin and thick structures so that the strain allowables could be increased to result in reduced structural weight. This knowledge is currently being utilized to develop scaling laws so that with a combination of small specimen testing and analysis one could accurately infer the impact damage resistance and tolerance of a given practical structure. Analytical methods are also being developed which eventually can help do certification by analyses. Dr. Starnes' inspiration also led to the development of damage initiation and progressive failure methodologies. These tools have been validated on large-scale structures by determining the residual strength of flat and curved polymeric composite plates [16-21] and full-scale built-up and sandwich structures with discrete-source damage in the form of a notch and with stiffness discontinuities that lead to stress gradients. Some of these large structures were subjected to combined pressure, axial tension/compression and shear in the Langley Combined Loads Test System (COLTS) facility with the capability to simulate actual flight loading conditions.

The knowledge gained through these research efforts and the capabilities developed have been instrumental in assisting the National Transportation Safety Board in the investigation of the American Airlines 587 accident, the assessment of X-33 cryogenic tank failure, the NASA Agency on Columbia Accident Investigation, the detailed work associated with Shuttle return-to-Flight, and the Helios Unpiloted Aerial Vehicle failure. This capability also will help to develop advanced aircraft with optimized, active flexible wing structures for load alleviation; strength and stiffness tailored, unconventional geometry fuselage structures; advanced launch vehicle structures including cryogenic tanks, large space and planetary habitats subjected to extreme operating conditions, space radiation, and micrometeoroid impact, to name a few.

II. Summary of Technical Contributions

Effect of manufacturing defects in the form of delaminations

When designing laminated composite structures, delaminations are a major concern since they can grow when subjected to critical loading conditions. Delaminations in a structure can occur in a

number of ways including through impact damage, manufacturing flaws, and free edge stresses. Delamination growth can result in significant degradation in structural performance. The effect of a circular delamination in flat and curved composite panels subjected to axial compression loading has been investigated. The analytical results are compared below with experimental results.

The finite element model of the test specimen configuration is shown in Figure 1 and consisted of both flat and curved plates. The test specimen is 10-in. by 5-in. in size. With clamped loaded conditions and simply supported unloaded conditions along the 10-in. long side, the unsupported specimen size measures 9 inches by 4.5 inches. Each AS4/3501-6 panel had a $[(\pm 45/90/0)_2/\pm 60/\pm 15]_s$ lay-up and each was fabricated with a 64 mm (2.5 in.) diameter circular delamination between either the 4th and 5th or 5th and 6th plies. Three different test configurations were tested: a flat panel, a 15-inch-radius cylindrical shell, and a 30-inch-radius cylindrical shell. The curvature was always in the shorter direction and the compression load was always applied in the long straight direction. When the specimen was curved, the delamination was always placed on the convex side of the panel. As the test specimens were loaded in compression, the load, end shortening and strain at different locations were recorded. In addition, a full-field deformation measurement system shown in Figure 2 was used that required a random speckle pattern be applied to the specimen [22, 23]. This technique provided a convenient way to observe the buckling of the delaminated region, and to track the progression of delamination growth.

The effect of three different modeling parameters were investigated in this study: 1) element choice (2D shell vs. 3D brick), 2) style of boundary condition (simplified vs. extended), 3) method for delamination prediction (Virtual Crack Closure Technique-VCCT vs. Interface element). The ABAQUS finite element program was used to conduct the analyses. The analytical local and global buckling results are presented in Figure 3. The delamination growth is when the strain energy release rate at any point along the boundary of the delamination exceeds the critical strain energy rate for the material. These results suggest that local buckling occurs first for both flat and curved laminates followed by delamination growth when the delamination is placed closer to the convex or concave surface of the plate. Also, the results for the curved plate are skewed with respect to the centerline of the plate thickness. This is a plate curvature effect. The influence of plate radius on delamination initiation and growth are shown in Figure 4. The delamination growth is determined using either VCCT or by incorporating an interface element between the plies of interest. These results suggest that for flat plates the delamination initiation occurs at a lower load and grows gradually whereas, for the plates with curvature, the delamination growth begins at a higher load but progresses more rapidly.

Low-speed impact response

In order to systematically study the low-speed impact response of composite structures, it was necessary to develop test equipment that provided all the necessary data accurately. The dropped-weight impactor and a static indentation test setups shown in Figure 5 were developed for this purpose [6]. These test setups are designed for accurately delivering the impacts and accessing response information of both the target and the force-inducing device. The nonlinear response phenomena associated with low-speed impact response, which is a quasi-static loading condition that is representative of a dropped-tool impact, was identified during 1993 [7]. To study this effect further, the response of flat and curved panels to a lateral force was studied analytically. The results summarized in Figure 6 confirmed the softening geometric nonlinearity earlier identified during low-speed impact response studies. Further studies were conducted to study the influence of impactor and target parameters on impact response. The results from a study on the influence of impactor mass on damage state and compression-after-impact strength for a flat plate are summarized in Figure 7. The 48-ply-thick, $[45/0/-45/90]_{6s}$ quasi-isotropic flat plate test specimens used in this experimental study were fabricated from Hercules, Inc. AS4 graphite fibers preimpregnated with Hercules, Inc. 3502 epoxy resin. As the impact energy level is increased from 7-25 ft-lbs, the damage area increases as a function of the impactor mass with the damage area following an S-curve. The general trend is that for a given impactor mass the damage area increases and then decreases as the energy is increased. The damage area curve with a larger mass stacks on top of the previous lower mass damage area curve. The leveling off of the damage area is due to more penetrating damage at the

impact site. The compression-after-impact strength results are presented in Figure 7(b), which suggests that the residual strength is a function of the impactor mass with a larger mass impact for a given energy level resulting in reduced strength. Additional results are available in Reference 11. The influence of plate radius on the impact response of thin (16-ply quasi-isotropic) laminated composite plate that are representative of fuselage structure skins are presented in Figure 8 for an impact energy level of 1.5 ft-lb. For high-velocity impacts that are representative of hailstone or runway debris impacts, the impact duration is short (~50 micro-seconds) and has a highly localized influence. For this reason, as shown in Figure 8(a), the influence of plate radius on the contact force for a given impact energy level for such an event is negligible. The dropped-weight impact, on the other hand, is a longer duration event (~1 to 5 milli-seconds) and is experienced by a larger part of the structure. The maximum force response results shown in this figure suggest that the peak contact force exhibits a reduction for plate radii around 30-inches. This behavioral trend is due to nonlinear deformation of the plate associated with the radius [25]. The compression-after-impact strength information for these panels is presented in Figure 8(b). The strengths of 16-ply-thick quasi-isotropic curved plates with inflicted damage from impact tests conducted with a 2.5 lb. impactor (at 9.6, 10.6, 8.4, and 8.2 ft-lbs. of energy for plate radii of 15-, 30-, 60-in. and flat, respectively) are compared with plates that are statically loaded with a central force equal in magnitude to the maximum value of the contact force obtained from the impact tests. The objective was to evaluate the applicability of statically indented plate compression tests to assess the compression-after-impact strength of thin plates with different sizes. The results suggest that the residual strength is a function of the plate radius, particularly for smaller radii. The compression strength results for statically indented 9-in. by 5-in. size plates appear to agree more favorably with the results for dropped-weight impacted plates of the same size. There appears to be up to a 40% difference in the strength results when the plate radius approaches that for a flat plate suggesting that the static indentation test results should not be used to assess the strength of impact damaged larger size thin plates.

The influence of plate anisotropy on the impact response and compression strength is presented in Figures 9 and 10. The analytical maximum contract force results for a 16-ply-thick AS4/3501-6 graphite-epoxy curved plates [10] with different types of coupled response and impacted at 1.5 ft-lb of dropped-weight impact energy are summarized in Figure 9. These results are obtained by artificially setting the in-plane and/or out-of-plane coupling stiffnesses to zero. When compared to the $[45/0/-45/90]_{2s}$ quasi-isotropic laminate contact force results, the results for plates with different types of coupling have reduced maximum contact force values, depending on the plate radius. If the magnitude of the contact force for a given impact energy is an indicator of the extent of damage created in the plate made if the same material system, then the plates with anisotropic properties, particularly with no in-plane coupling, should have lesser damage and higher compression-after-impact strength. The failure strain results for the above quasi-isotropic plate is compared with a tailored anisotropic plate (with A_{16} , A_{26} , D_{16} , and D_{26} terms) in Figure 10. Both of these plates are impacted at energy levels that result in barely visible damage. These preliminary results for plate with anisotropy suggest a marginally higher strength than the quasi-isotropic plate with larger radii, corroborating the above hypothesis of anisotropy contributing to plate softening and, hence, improved compression-after-impact strength.

The currently ongoing effort utilizes the knowledge acquired from the studies on low-speed impact response of composite plates to develop scaling laws where information from impacting small-scale specimens can be scaled to assess the impact response and, eventually, the residual strength of composite structures [13]. Approximate closed-form analysis methods were developed earlier to obtain contact force profiles for curved plates with different boundary conditions, preloading conditions, and degrees of anisotropy [9, 25]. The contact force results for quasi-isotropic curved plates that are scaled for target and impactor parameters are presented in Figure 11 for impact energies that are low enough not to result in plate damage. The contact force magnitude for the reference 8-ply-thick plate is approximately 100 lbs. whereas the magnitude for the plates that are geometrically scaled to be 16-ply-thick laminates is approximately 450 lbs. For the 16-ply-thick plates, ply-level geometric scaling requires that each ply thickness in the 8-ply quasi-isotropic laminate is doubled $[45_2/0_2/-45_2/90_2]_s$ and the

sublamine geometric scaling requires that the 8-ply stack be repeated $[45/0/-45/90]_{28}$. When scaled using the linear scaling factors presented in the literature and in this paper, the force profiles for the 16-ply-thick plates map exactly suggesting that the previously suggested scaling laws are valid for thin plates that exhibit nonlinear impact response. Similar results are obtained as shown in Figure 12 when the impact energy levels are increased to a level that initiates damage in the plates.

Response of stiffened plates with discrete-source damage

There was no analytical method available which has been thoroughly validated using either finite element analysis or experimental results to determine stress distributions around an inclined narrow elliptical notch in finite anisotropic plates subjected to combined in-plane loading conditions. The objective of this work is to present and discuss a validated analysis procedure which can be used to determine stress concentrations and stress and strain distributions around a narrow elliptical notch in finite anisotropic composite laminated plates and three-stiffener panels loaded in axial compression. The present analysis method was validated by comparing the analytical stress and strain results with finite element analysis and experimental results for square laminated plates with notches oriented in two different angles to the loading direction [15]. The present analysis results and finite element analysis results are also compared with the experimental results for three-stiffener panels with long elliptical notches. The test specimen with an inclined notch and the test specimen with speckle interferometry instrumentation are shown in Figure 13. References 15 and 22 provide details on the analysis methodology, test specimens, and experimental methods. The finite element model with different degrees of element discretization to capture the stress gradient at the notch tip region is shown in Figure 14 (a). Due to the inclined orientation of the notch, a combined stress state exists at the notch tip region for an applied axial loading condition. A comparison of the finite element and present analysis results for in-plane shear strain with the experimental results is presented in Figure 14 (b). The present analysis method provides results corresponding to a linear response whereas the finite element results capture the nonlinear specimen response with no failure. All three data agree well with each other until the load value approaches 10,000 lbs. suggesting the accuracy of the present analysis results. Beyond this load value, nonlinear response is indicated from the finite element analysis results whereas failure initiation and growth is suggested by the experimental results.

Failure initiation, growth and residual strength results for flat, curved, and stiffened panels with and without cutouts and notches

The work performed to address the above subject is presented in detail in References 16-20. The goal here was to understand the failure modes, develop failure criteria and analysis tools to predict the initiation and growth of interlaminar and intralaminar failure modes, and the residual strength of flat, curved, and stiffened panels subjected to uniaxial compression and in-plane shear loading conditions. Sample results for thin curved composite panels that are representative of fuselage skins with and without a centrally located hole are presented in Figures 15 and 16. Since the curved plates are sensitive to geometric imperfections, analysis was conducted with and without the measured values for geometric imperfection to assess the sensitivity of this parameter on panel response and failure. Details of the failure criteria and the stiffness degradation models are presented in References 16 and 19. The analytical predictions for the load end-shortening response compared well with the experimental results when the geometric imperfections are included. FV1, FV2 and FV3 designated by the open symbols represent analytical predictions for matrix, fiber-matrix shear, and fiber failure modes, respectively. The analysis results suggest that these failure modes occur either at or after the collapse of the specimen, depending on whether geometric imperfections are not included or included. The residual strength of the panel is also predicted accurately by the analysis, particularly when the geometric imperfections are included. The load end-shortening results for the 16-ply-thick quasi-isotropic curved plate with a centrally located hole with the hole diameter to panel width ratio of 0.2 are presented in Figure 16. Once again, the panel response is accurately predicted by the analysis results when the geometric imperfections are included.

The experimental results are not captured after the panel collapse and, therefore, the residual strength could not be compared here with the analytical results.

The analytical and experimental results for a flat panel with a diagonal notch and subjected to in-plane shear loading condition in a picture frame fixture are presented in Figures 17 and 18. The panel configuration is shown in Figure 17 (a) together with the location for the notch (discrete source damage) and the loading direction. The load end-shortening results presented in Figure 17 (b) suggest excellent comparison between the analytical and experimental results for the maximum load to failure. The load drop obtained from the experiment suggests panel catastrophic failure. The analysis results suggest that all the three failure modes occurred around 10,000 lbs. The analytical results did not converge beyond an applied displacement value of 0.22 in. The analytical and experimental failure results are compared in Figure 18. The analytical contours for accumulated FY3 mode, fiber failure, through the panel thickness are shown in Figure 18 (a). A 100% failure is predicted around and approximately perpendicular to the notch tip. The experimental failure mode shown in Figure 18 (b) illustrates a failure pattern that is consistent with the analytical prediction.

The results from a study conducted on a bead-stiffened composite panel made of a thermoplastic material system are summarized in Figure 19. The panel is made using thermal forming technology to shape a stiffening bead. The panel makes a part of the wing rib web structure that experiences predominantly in-plane shear loading. The panel was tested during 1988 using a picture frame shear test fixture and analyzed using the methodology described and referenced above. The geometric imperfection data was not available for this panel to include in the analysis. The back-to-back surface strain results from the experiment at a point centrally located on the panel on top of the bead are compared with the analysis results in Figure 19 (b). The progressive failure analysis results predict initial failure around 12,000 lbs. and the final failure at 28,000 lbs. with the strain results closely comparing with the experimental results.

III. Concluding Remarks

NASA Langley Research Center and their collaborators have conducted a significant amount of research in the area of polymeric composite structures damage tolerance and residual strength during the past more than 20 years, which is summarized in this paper. We pay our tribute to Dr. James H. Starnes, Jr. who was inspirational in initiating and conducting some of this work. This collective effort has significantly contributed to advancing the state-of-the-art in the damage tolerance and residual strength of composite structures and, consequently, increasing the confidence of the aerospace industry to use polymer matrix composites in primary structural applications. There is a need for additional work in developing validated analysis tools to understand, quantify, and apply damage tolerance and residual strength methodologies for highly-loaded, tailored composite structures and nanomaterial systems based structural concepts such as light-weight functionally-graded and multifunctional structures subjected to extreme space environmental conditions.

IV. References

1. Rhodes, M. D., Williams, J. G., and Starnes Jr., J. H., "Effect of Impact Damage on the Compression Strength of Filamentary-Composite Hat-Stiffened Panels." *Selective Application of Materials for Products and Energy*, 23rd National SAMPE Symposium and Exhibition, Disneyland Hotel, Anaheim, CA, May 2-4, 1978, pp. 300-319.
2. Starnes, Jr., J. H., Rhodes, M. D., and Williams, J. G., "The Effect of Impact Damage and Circular Holes on the Compression Strength of a Graphite-Epoxy Laminate." NASA TM-78796, 1978.
3. Starnes, Jr., J. H. and Haftka, R. T., "Preliminary Design of Composite Wing-Box Structures for Global Damage Tolerance." AIAA Paper No. 80-0755, 1980.
4. Rhodes, M. D., Williams, J. G., and Starnes Jr., J. H., "Low-Velocity Impact Damage in Graphite-Fiber Reinforced Epoxy Laminates." *Polymer Composites*, Vol. 2, No. 1, January 1981, pp. 36-44.

5. Williams, J. G., Starnes Jr., J. H., and Waters, W. A., "Damage Tolerance Characteristics of Kevlar Epoxy Laminates Loaded in Compression," Ninth AFWAL Annual Mechanics of Composites Review, Dayton, OH, October 24-26, 1983, pp. 12-25.
6. Prasad, C. B., Ambur, D. R., and Starnes, J. H., Jr., "Response of Laminated Composite Plates to Low-Speed Impact by Different Impactors." *AIAA Journal*, Vol. 32, No. 6, June 1994, pp. 1270-1277.
7. Ambur, D. R., Starnes, J. H., Jr., and Prasad, C. B., "Influence of Impact Parameters on the Response of Laminated Composite Plates." *Composite Materials: Fatigue and Fracture – Fifth Volume*, ASTM STP 1230, edited by R. H. Martin, 1995, pp. 389-404.
8. Ambur, D. R., Starnes, J. H., Jr., and Prasad, C. B., "Low-Speed-Impact Damage-Initiation Characteristics of Selected Laminated Composite Plates." *AIAA Journal*, Vol. 33, No. 10, October 1995, pp. 1919-1925.
9. Ambur, D. R., Starnes, J. H., Jr., Kapania, R. K., and Stoumbos, T., "Influence of Large-Deformation Effects on the Impact Response of Flat and Curved Composite Plates." AIAA Paper No. 95-1412, 1995.
10. Ambur, Damodar R., and Starnes, James H., Jr., "Low-Speed Impact Damage Tolerance of Anisotropic Composite Plates." Invited presentation at the 14th U.S. National Congress of Theoretical and Applied Mechanics, Blacksburg, VA, June 23-28, 2002.
11. Ambur, D.R., and Kemmerly, H.L., "Influence of Impactor Mass on the Damage Characteristics and Failure Strength of Laminated Composite Plates." AIAA Paper No. 98-1784, 1998.
12. Ambur, D. R., Starnes, J. H., Jr., and Waters, W. A., "Effects of Low-Speed Impact Damage on the Compression Strength of a Graphite-Epoxy Laminated Plate with a Skewed Thickness Taper." AIAA Paper No. 94-1403, 1994. Accepted for publication in the *Journal of Aircraft*.
13. Ambur, D. R., Chunchu, P. B., Rose, C. A., Feraboli, P., and Jackson, W. C., "Scaling the Nonlinear Impact Response of Flat and Curved Composite Panels." AIAA Paper No. 2005-2224, April 2005.
14. McGowan, D. M. and Ambur, D. R., "Structural Response of Composite Sandwich Panels Impacted with and without Compression Loading." AIAA Paper No. 99-1276, April 1999.
15. Ambur, D. R., and McGowan, D. M., "Response of Composite Plates with Inclined Elliptical Notches and Subjected to Axial Compression." *Journal of Aircraft*, Vol. 36, No. 3, May-June 1999, pp. 596-602.
16. Jaunky, N., Ambur, D. R., Dávila, C. G., and Hilburger, M. W., "Progressive Failure Studies of Composite Panels with and without Cutouts." NASA/CR-2001-211223 ICASE Report No. 2001-27.
17. Ambur, D. R., Jaunky, N., Dávila, C. G., and Hilburger, M. W., "Progressive Failure Studies of Composite Panels with and without Cutouts." AIAA Paper No. 2001-1182, 2001.
18. Camanho, P.P., Dávila, C.G., and Ambur, D.R., "Numerical Simulation of Delamination Growth in Composite Materials." NASA-TP-2001-211041, Hampton, VA, August 2001.
19. Goyal, V. K., Jaunky, N., Johnson, E. R., and Ambur, D., "Intralaminar and Interlaminar Progressive Failure Analysis of Composite Panel." AIAA Paper No. 2002-1745, 2002.
20. Ambur, D., Jaunky, N., and Hilburger, M. W., "Progressive Failure of Stiffened Panel Subjected to Shear Loading." AIAA Paper No. 2002-1404, 2002.
21. Ambur, D. R., Jaunky, N., Lawson, R. E., and Knight, Jr., N. F. "Numerical Simulations for High-Energy Impact of Flat Plates." *International Journal of Impact Engineering*, Vol. 25, No. 7, August 2001, pp. 683-702.
22. Helm, J. D., "Improved Three-Dimensional Image Correlation for Surface Displacement Measurement." *Optical Engineering*, Vol. 35, 1996, pp. 1911-1920.
23. Reeder, J. R., Song, K., Chunchu, P. B., and Ambur, D. R., "Post Buckling and Growth of Delaminations in Composite Plates Subjected to Axial Compression." AIAA Paper No. 2002-1746, 2002.
24. Ambur, D. R. and Chunchu, P. B., "Impact Damage Tolerance of Thin, Curved Composite Plates." Presented at the RLV/SOV Meeting, November 19-22, 2002, Hampton, VA.
25. Ambur, D. R., Starnes, J. H., Jr., and Chunchu, P. B., "Influence of Target and Impactor Parameters on the Nonlinear Response and Residual Strength of Curved Thin Composite Plates." AIAA Paper No. 2000-1591, 2000.

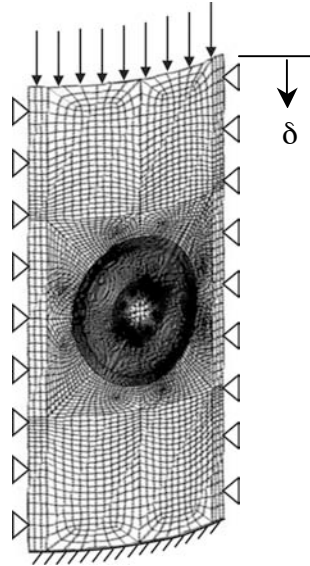


Figure 1. Finite element model of the curved plate.

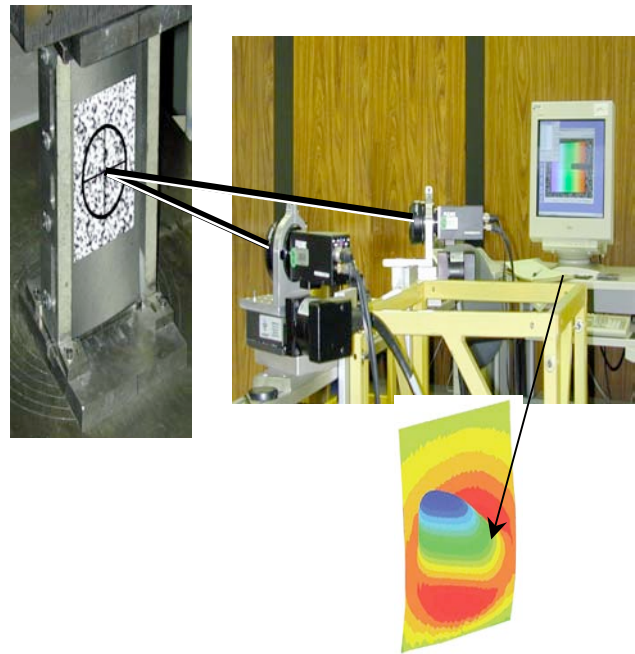


Figure 2. Experimental setup for measuring the full-field displacements of a postbuckled curved plate.

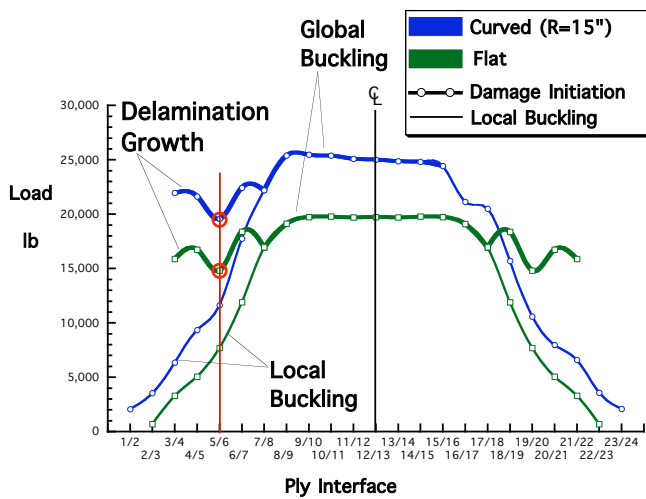


Figure 3. Summary of flat and curved composite plate response with a central delamination.

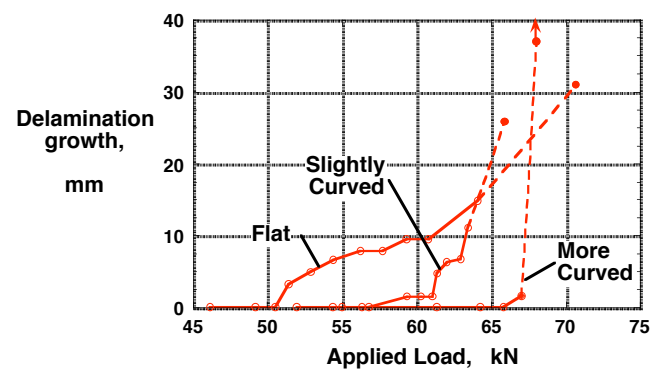
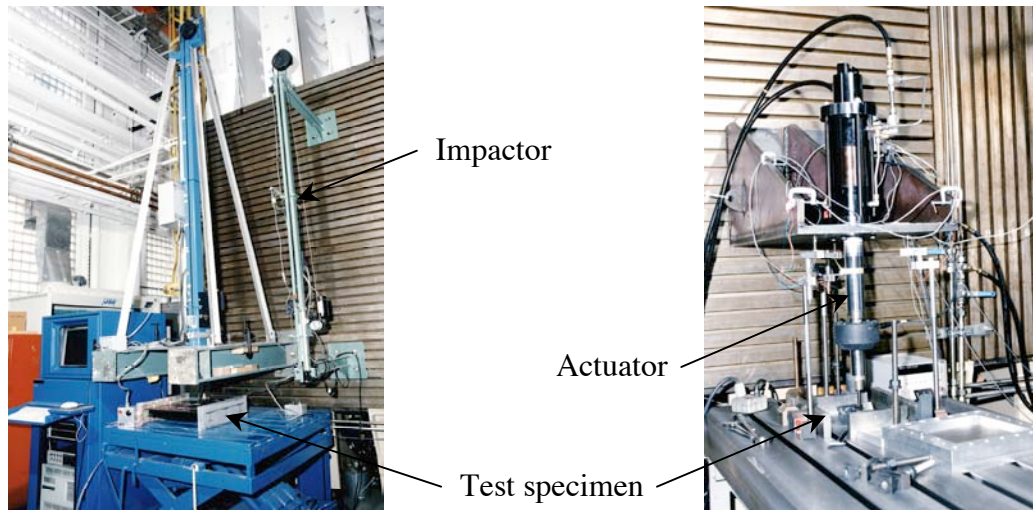


Figure 4. Influence of plate radius on the damage initiation and growth.

(from Reeder, Song, Chunchu, and Ambur [23])



a. Dropped-weight impact

b. Static indentation

Figure 5. Experimental capability for testing flat and curved plates.

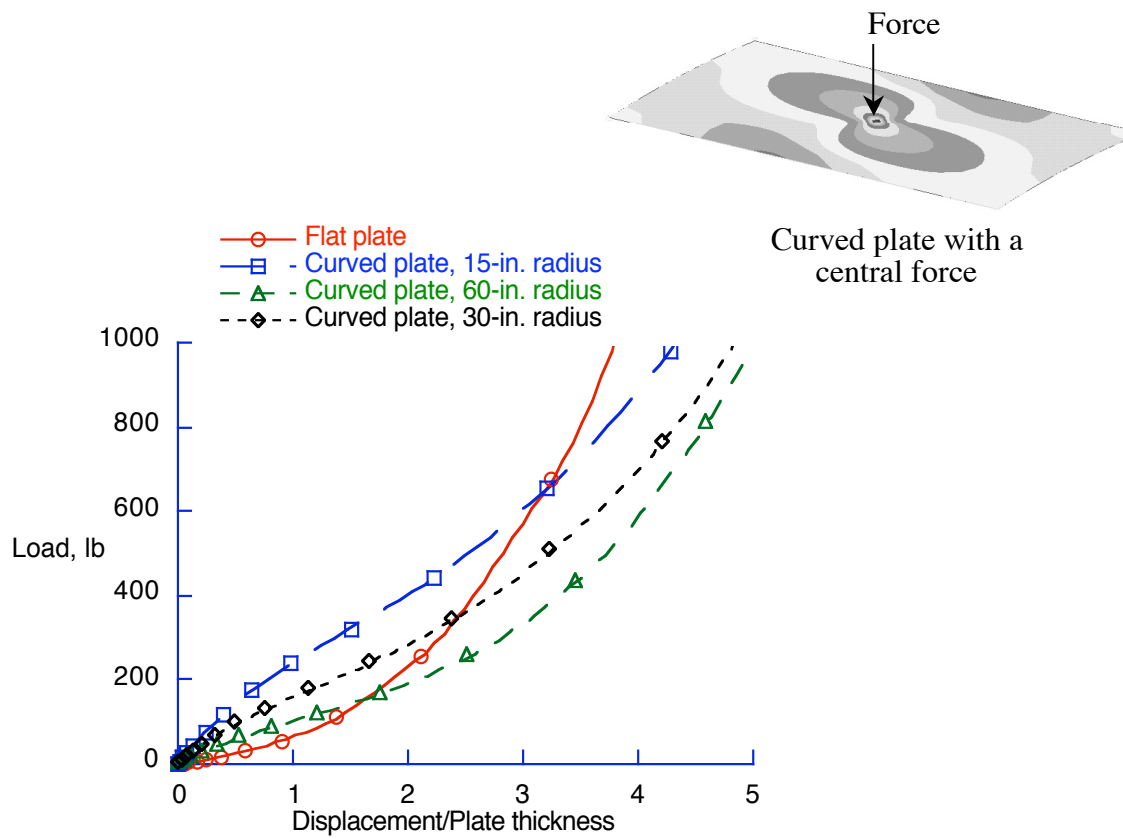
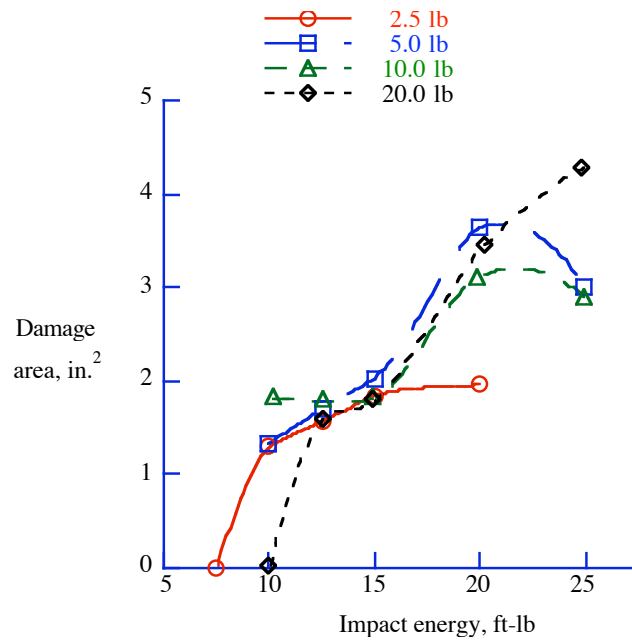
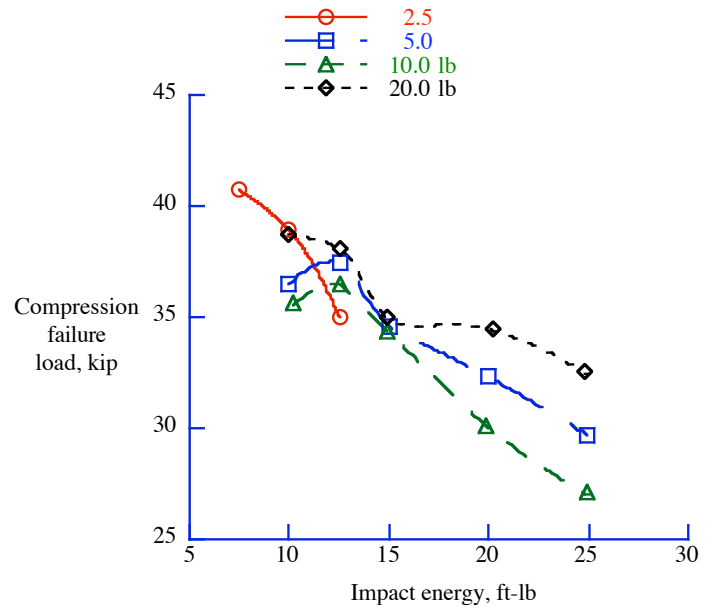


Figure 6. Load vs. center deflection plots for plates with different radii.

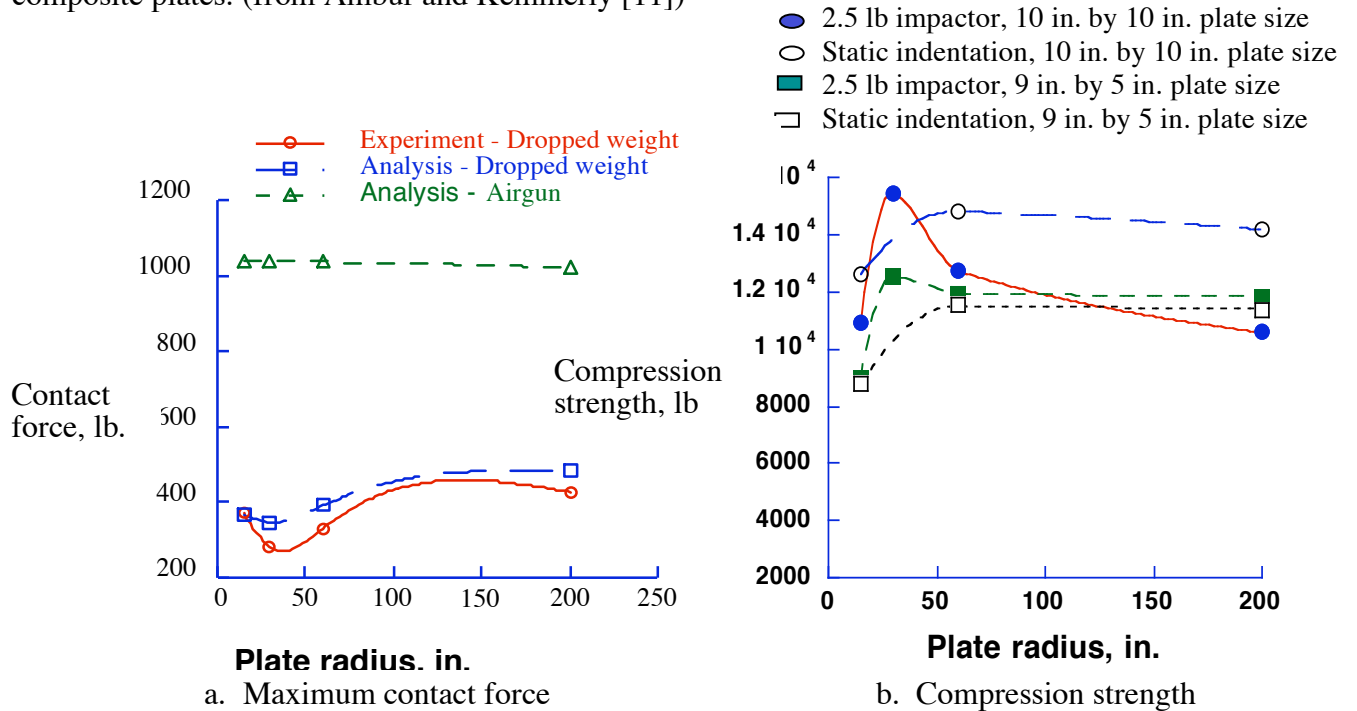


a. C-scan damage area.



B. Compression strength.

Figure 7. Influence of impactor mass on the sustained damage and compression strength of flat composite plates. (from Ambur and Kemmerly [11])



a. Maximum contact force

b. Compression strength

Figure 8. Influence of plate radius on the impact response of composite plates. (from Ambur, Starnes, and Chunchu [9])

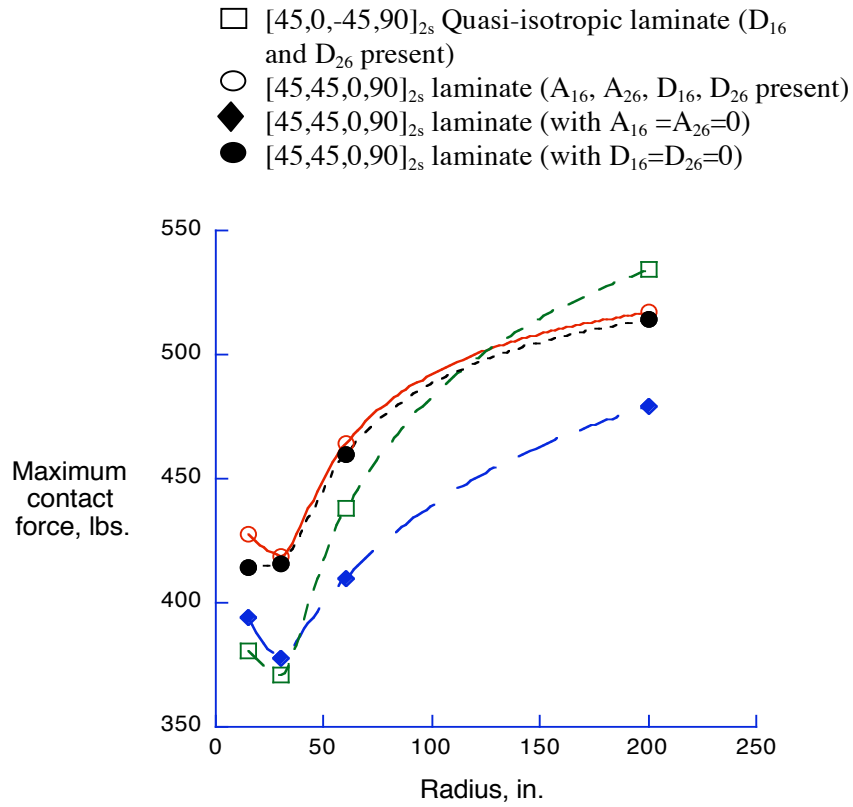


Figure 9. Analytical contact force results for 16-ply-thick AS4/3502 graphite/epoxy laminates with different degrees of anisotropy impacted at 1.5 ft-lb of energy. (from Ambur and Starnes [10])

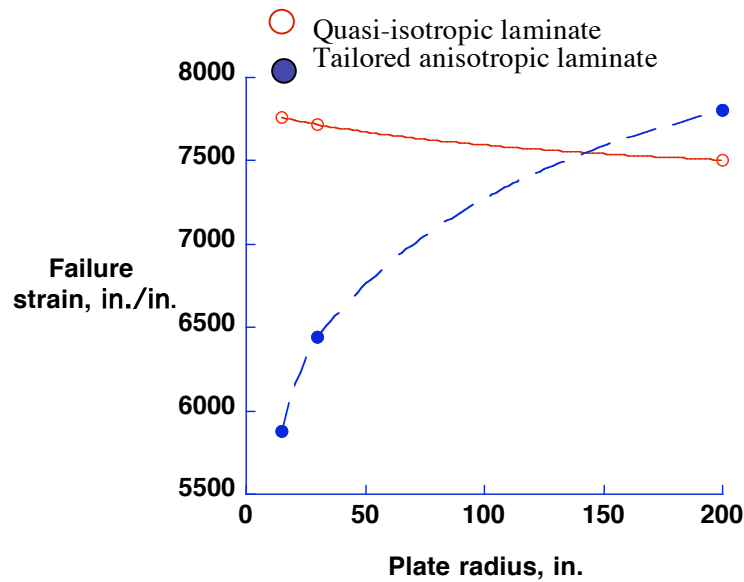


Figure 10. Influence of plate anisotropy on the compression-after-impact strength of laminated composite plates. (from Ambur and Chunchu [24])

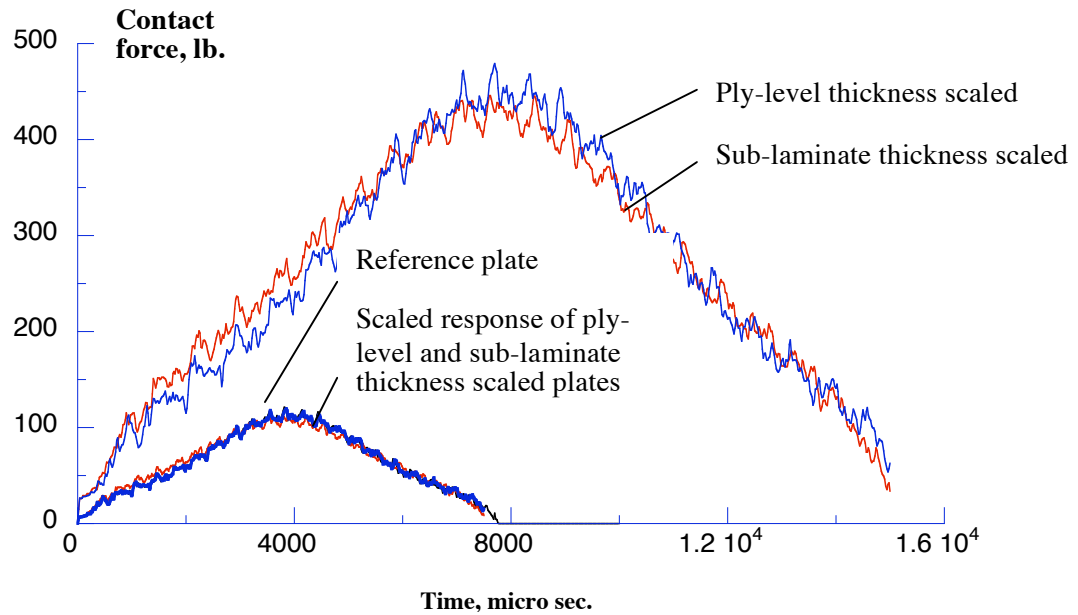


Figure 11. Analytical contact force profiles for curved panels centrally impacted at 0.35 ft-lb and 2.8 ft-lb of nominal impact energy for the reference and scaled-up configurations, respectively.

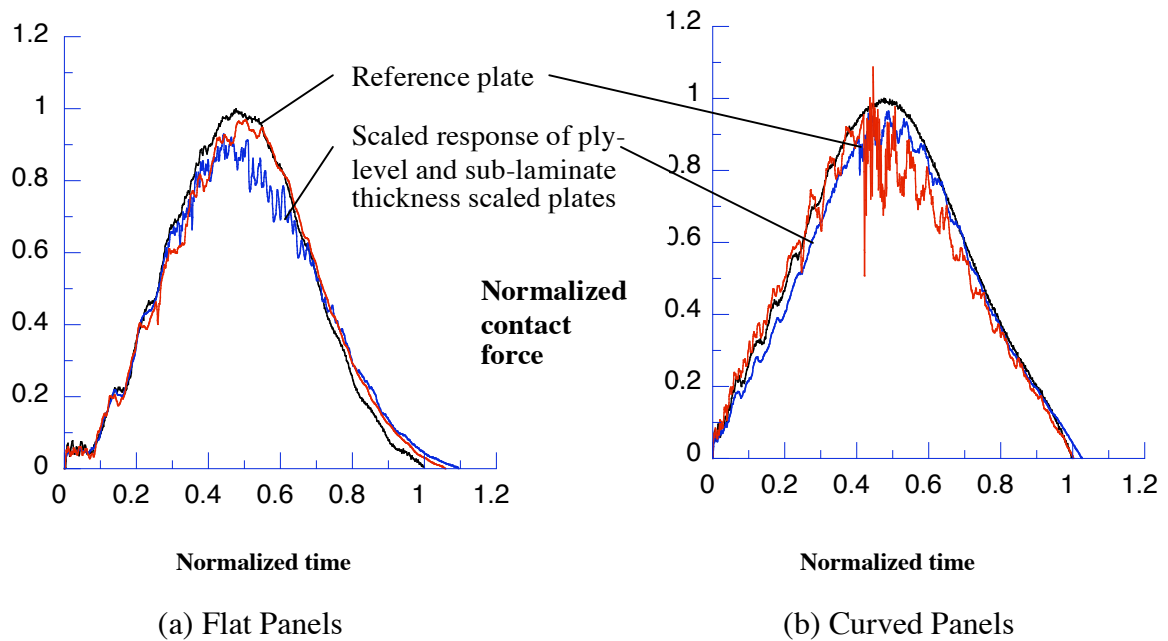
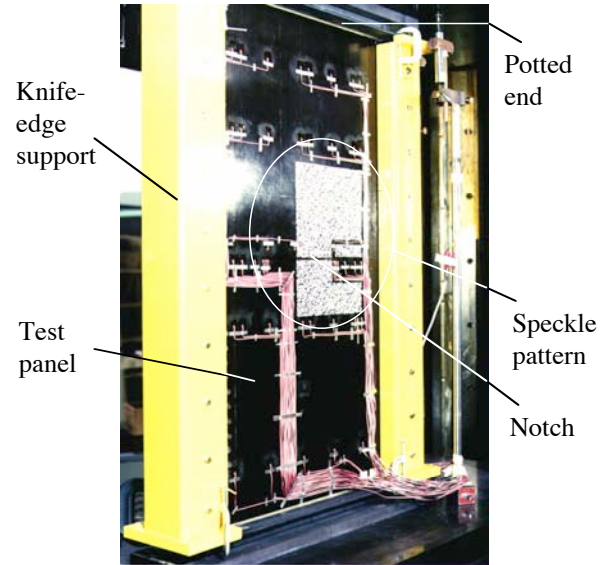
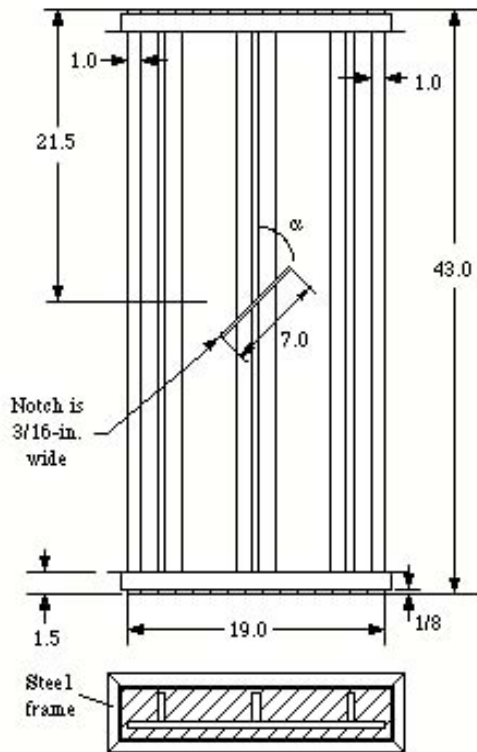


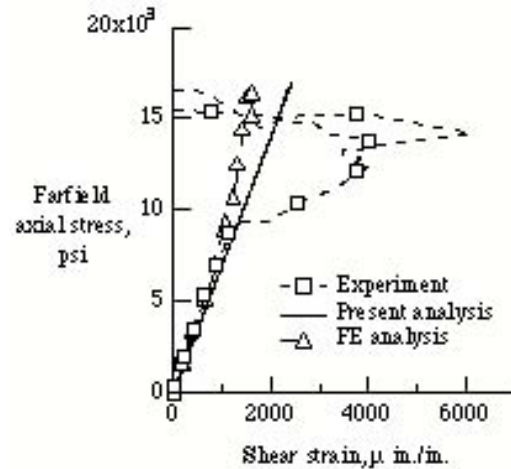
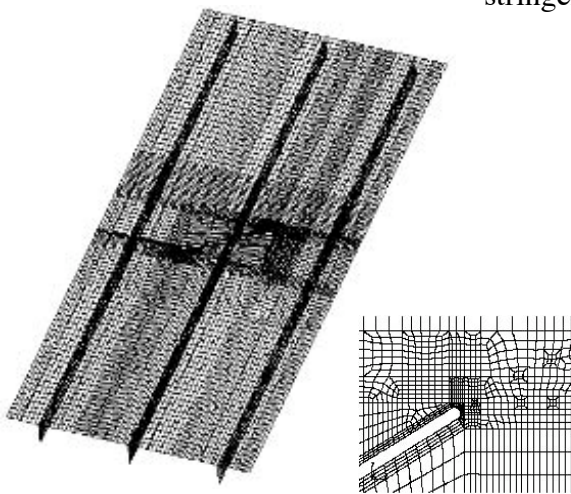
Figure 12. Experimental normalized and adjusted contact-force profiles for the flat and curved panels impacted at 1.125 ft-lb and 9.0 ft-lb of nominal impact energy for the reference and scaled configurations, respectively.

(from Ambur, Chunchu, Rose, Feraboli and Jackson [13])



a. Schematic of the panel (dimensions in inches) b. Photograph of the test setup

Figure 13. Stitched, graphite-epoxy panel with a centered notch through the center stringer.



a. Panel finite element model

b. Shear strain results near notch tip

Figure 14. Comparison of analysis and experimental in-plane stress results for a panel with a notch inclination of 60° .

(from Ambur and McGowan [15])

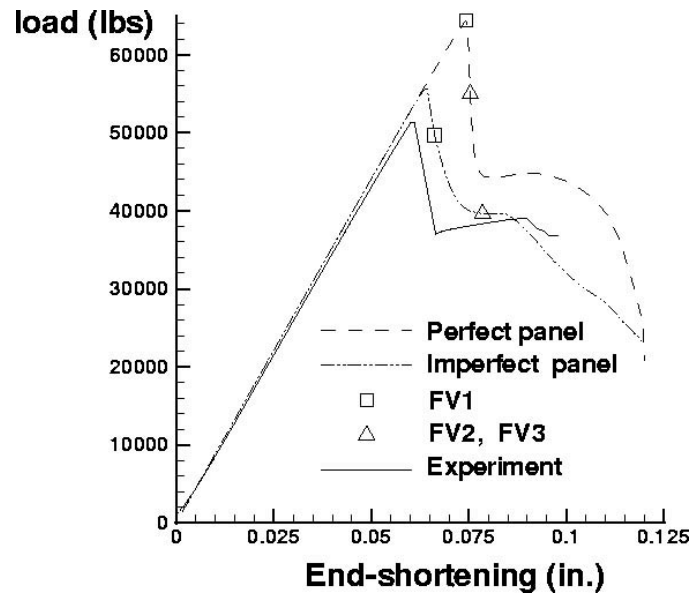


Figure 15. Comparison of experimental and analytical compression response results for a curved composite panel without a cutout.

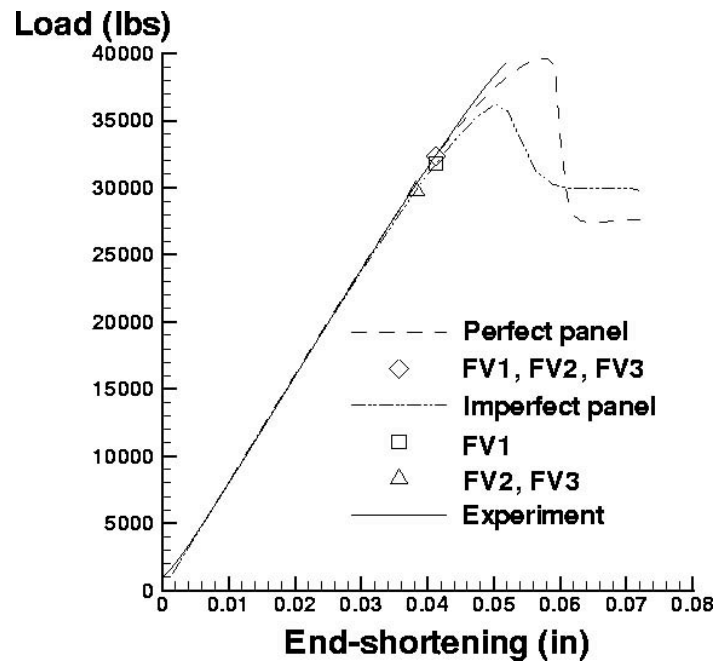


Figure 16. Comparison of experimental and analytical compression response results for a curved composite panel with a circular cutout ($d/w=0.2$).

(from Jaunky, Ambur, Davila, and Hilburger [16])

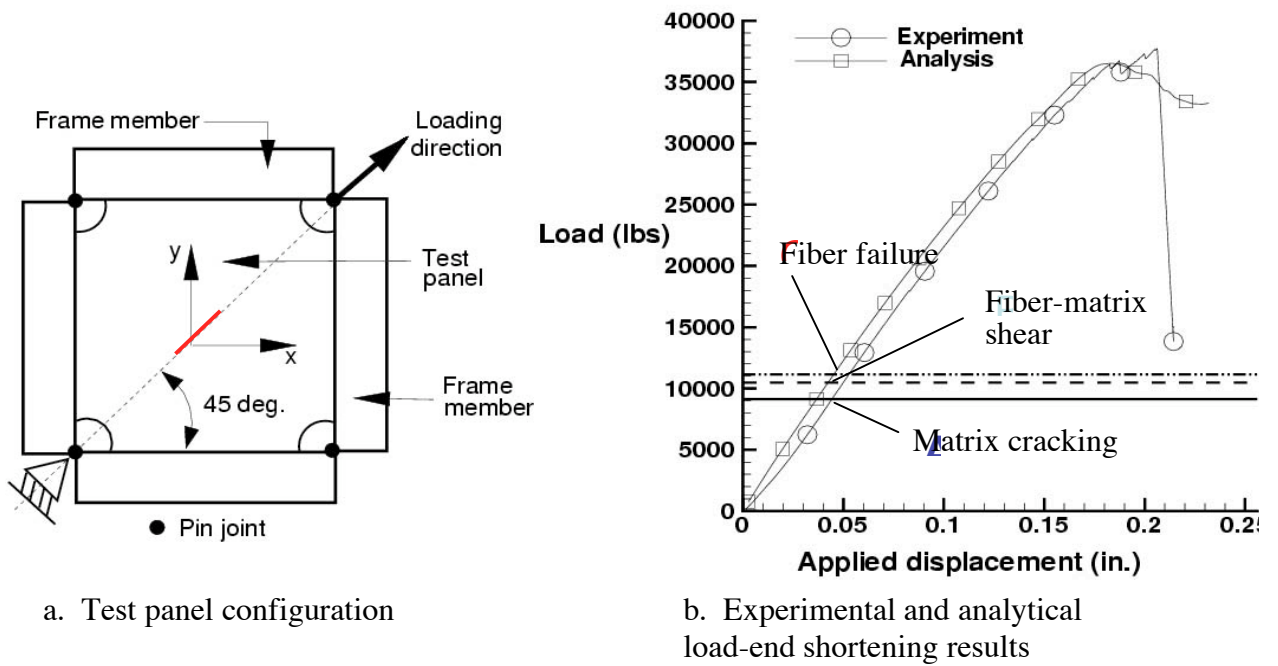


Figure 17. In-plane shear test and analysis results for a flat plate with the centrally-located notch.

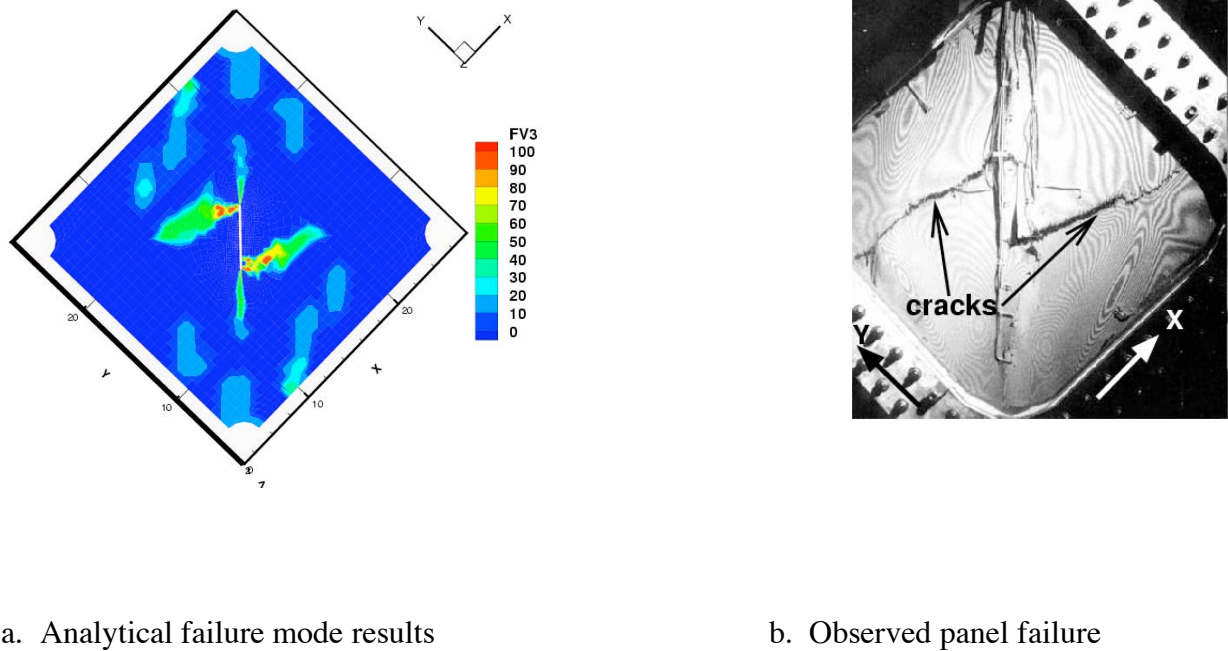
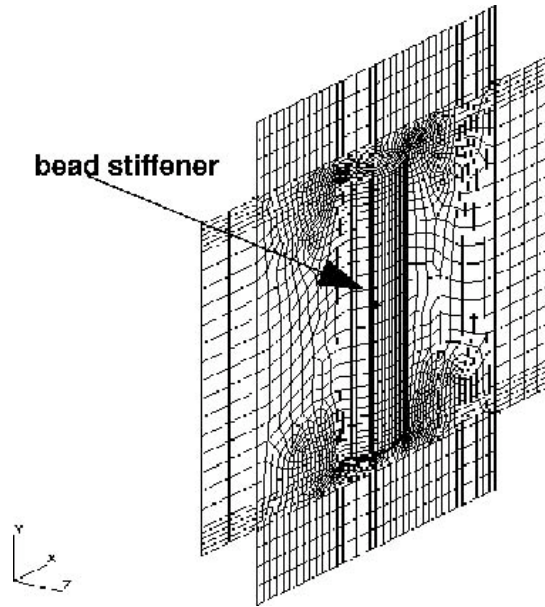
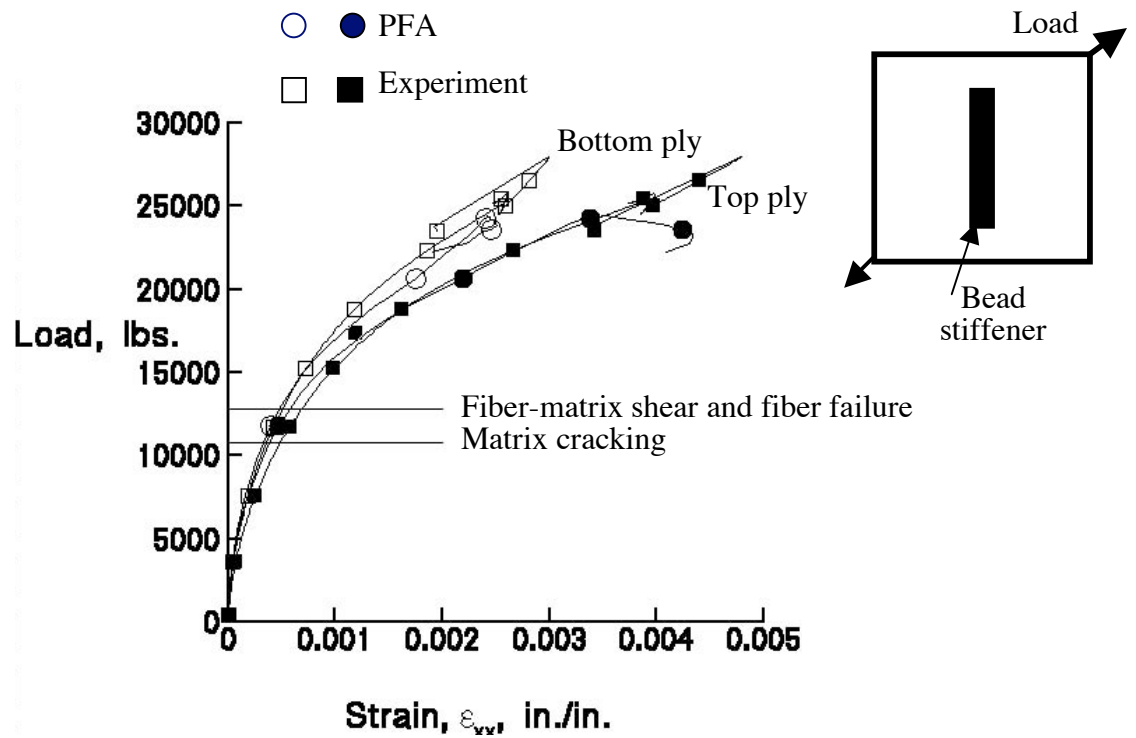


Figure 18. Comparison of test and analysis results for a flat plate with a notch and subjected to uniform in-plane shear. (from Ambur, Jaunky and Hilburger [20])



a. Finite element model of the bead-stiffened test panel



b. Experimental and analytical load-end shortening response

Figure 19. In-plane shear response of a bead-stiffened flat composite panel.
(from Ambur, Jaunky, Dávila and Hilburger [17])

Jim Starnes' Contributions to Residual Strength Analysis Methods for Metallic Structures

Richard D. Young,^{*} Cheryl A. Rose,^{*} and Charles E. Harris[†]
NASA Langley Research Center, Hampton, Va 23681-2199

A summary of advances in residual strength analyses methods for metallic structures that were realized under the leadership of Dr. James H. Starnes, Jr., is presented. The majority of research led by Dr. Starnes in this area was conducted in the 1990's under the NASA Airframe Structural Integrity Program (NASIP). Dr. Starnes, respectfully referred to herein as Jim, had a passion for studying complex response phenomena and dedicated a significant amount of research effort toward advancing damage tolerance and residual strength analysis methods for metallic structures. Jim's efforts were focused on understanding damage propagation in built-up fuselage structure with widespread fatigue damage, with the goal of ensuring safety in the aging international commercial transport fleet. Jim's major contributions in this research area were in identifying the effects of combined internal pressure and mechanical loads, and geometric nonlinearity, on the response of built-up structures with damage. Analytical and experimental technical results are presented to demonstrate the breadth and rigor of the research conducted in this technical area. Technical results presented herein are drawn exclusively from papers where Jim was a co-author.

I. Introduction

The present paper summarizes advances in residual strength analyses methods for metallic structures that were realized under the leadership of Dr. James H. Starnes, Jr. Dr. Starnes, respectfully referred to herein as Jim, had a passion for studying complex response phenomena and dedicated a significant amount of research effort toward advancing damage tolerance and residual strength analysis methods for metallic structures. In this research area, Jim's efforts were focused on understanding damage propagation in built-up fuselage structure with widespread fatigue damage, and on understanding the effects of damage on the structural response of built-up fuselage structure, with the goal of ensuring safety in the aging international commercial transport aircraft fleet.

The majority of research led by Jim Starnes in the area of damage tolerance and residual strength analysis of metallic structures was conducted in the 1990's under the NASA Airframe Structural Integrity Program (NASIP). This program, headed by Dr. Charles E. Harris, covered a wide range of topics including fatigue and fracture of materials, nondestructive inspection methods, and residual strength analysis methods for built-up structures with damage. Jim led the structures element of the program, and within this activity Jim supervised, mentored, and collaborated with junior researchers Ms. Vicki O. Britt, and Drs. Richard D. Young and Cheryl A. Rose. Jim also worked closely with Dr. James C. Newman, 'champion' of the critical Crack-Tip-Opening Angle (CTOA) fracture criterion for elasto-plastic fracture, to incorporate the elasto-plastic criterion in residual strength analysis methods, and to help define laboratory scale experiments and critical loading scenarios for validation of the criterion. In addition, Jim supported and collaborated with Dr. Charles Rankin at Lockheed, Palo Alto, to incorporate crack modeling and residual strength analysis methodologies into the STAGS (STructural Analysis of General Shells) general-purpose finite element code.¹

Jim's approach to research in damage tolerance and residual strength analysis methods for metallic structures was typical of his approach to solving complex problems. The first step in the approach was defining the overall research problem. Several components contributed to the problem definition. First, there was a motivational component, or a driving force for solving the problem. Typically, the driving force was a problem experienced by the aeronautics industry. Jim's connection with industry was invaluable; he had the respect and confidence of manufacturers and operators, and they often conveyed to him issues or failures that were occurring that they didn't understand. He then relied

^{*} Senior Research Engineer, Mechanics of Structures and Materials Branch.

[†] Principal Engineer, NASA Engineering and Safety Center.

upon his intuition and extensive expertise in structural mechanics to define preliminary studies to characterize the problem. The preliminary studies were typically tests or simplified analyses of complex built-up configurations, conducted to obtain qualitative information on relevant structural parameters, fundamental structural response characteristics and failure scenarios, and to identify critical loading conditions. Jim would consider results from these studies, and factor in industry input, to formulate the overall problem definition, and then form a vision toward a solution. This vision often consisted of multiple research elements, and the integration of the individual elements. Each research element addressed a critical component of the larger problem, and was defined by breaking the complex response of built-up structure down into contributing factors to be studied separately. Research of each element consisted of detailed numerical and experimental studies of a simplified structural configuration conducted to develop a quantitative understanding of critical response mechanisms identified in the preliminary studies. Each research element provided a stand-alone technical result for a simple application and provided insight into understanding the response characteristics of a more complex configuration. In addition, the individual research elements often resulted in the development of new analysis capabilities that were eventually integrated to develop high-fidelity analysis capabilities for quantitative characterization of the real-world built-up structure.

In the present paper results of research activities in residual strength analysis methods for metallic structures that were conducted in collaboration with Jim are presented following an outline based upon the research approach described above. First, the motivation for the research and the overall problem definition is described. Then results of selected research activities that were defined based upon fuselage structure response characteristics observed in the preliminary studies conducted to define the problem, are presented. The research activities described are presented in order of increasing complexity. First results of a numerical study of nonlinear bulging factors in unstiffened aluminum shells is presented. This study examined the effect of geometric nonlinearity and combined loading conditions on the crack-tip stress intensity factor in an unstiffened shell. The second study extended the previous study's efforts in unstiffened shells to stiffened structure, including detailed modeling of stringer and fastener parameters. The final section presents a summary of research activities that were specifically focused on the development and validation of a high-fidelity residual strength analysis methodology for aircraft aluminum fuselage structures with cracks and subjected to combined internal pressure and mechanical loads. The method accounts for all of the complexities present in a fuselage shell structural response that must be represented to predict accurately fuselage structure residual strength. The methodology is based upon the critical crack-tip-opening-angle (CTOA) elastic-plastic fracture criterion to represent stable crack growth and fracture in ductile materials, and a geometric and material nonlinear shell analysis code to perform the structural analysis.

II. Problem Definition

Commercial transport are designed with a damage tolerant design philosophy that requires the aircraft to maintain adequate structural integrity in the presence of discrete source damage or fatigue cracks. As economic and market conditions encourage the use of commercial airplanes beyond their original design service life, it is important to be able to predict the fatigue life and residual strength of fuselage structures with cracks. Widespread fatigue damage (WFD) is a significant concern for the aging aircraft fleet because the residual strength of structure with a long crack might be significantly reduced by the existence of adjacent smaller cracks.² The accident of the Aloha aircraft, shown in Fig. 1, made aging aircraft a national priority. The Aloha aircraft accident is an example of widespread fatigue damage, where several short fatigue cracks along a fuselage lap joint linked together and unzipped an 18-foot-long section of the crown of the fuselage. One flight attendant was killed, but, amazingly, the pilot was able to land the aircraft. Another example demonstrating the threat to the structural integrity of aging aircraft is shown in Fig. 2. The aircraft shown in this figure was damaged when a fatigue crack from a manufacturing flaw caused engine failure during take-off. Uncontained engine debris from the engine penetrated the fuselage, killing two passengers and significantly compromising the structure.

The Aloha aircraft resulted in the launching of NASA and FAA initiatives in aging aircraft. One of the objectives of the NASA Airframe Structural Integrity Program (NASIP) was to develop an analysis methodology for predicting failure of damaged fuselage structures in the presence of widespread fatigue damage. The structural response of a stiffened fuselage with long cracks, such as mid-bay cracks or splice joint cracks after MSD link-up, is extremely complex, and is influenced by local stress and displacement gradients near the crack, and by the internal load distribution in the shell. This complex response needed to be understood in order to develop a residual strength analysis methodology for fuselage structures with cracks.



Figure 1. Wide-spread fatigue damage causes in-flight fuselage crown panel separation. Aloha Airlines Boeing 737, April 28, 1988.

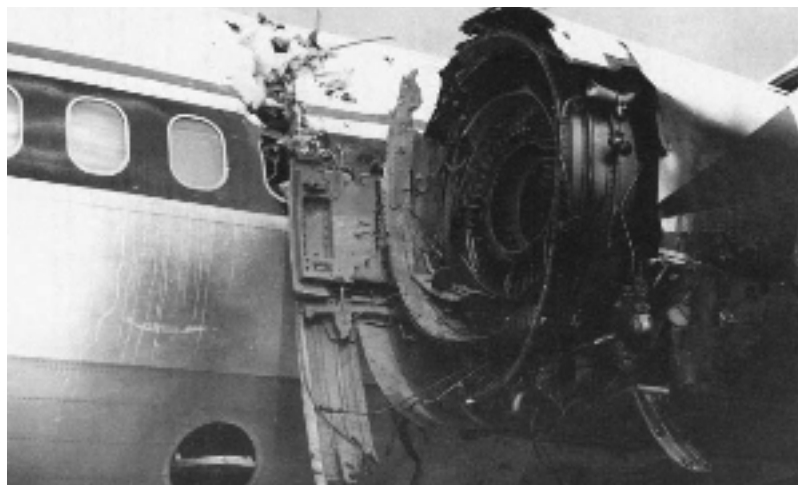


Figure 2. Engine failure during take-off with uncontained debris penetrating fuselage. Delta Airlines, MD-88, July 6, 1996.

Early work conducted in the NASIP program and led by Jim Starnes focused on developing an understanding of the effects of combined loads and geometric nonlinearity on the response of complex built-up fuselage structure.³⁻⁵ Analytical studies of the nonlinear response of stiffened shells with long cracks were conducted using relatively coarse models of a stiffened shell to obtain qualitative information on the effects of crack location, crack orientation, and various combinations of internal pressure and mechanical loads on the response characteristics. Results from a typical early study are shown in Fig. 3. In this case, an analytical study was conducted for a full-barrel fuselage with a longitudinal crack in the crown, and subjected to internal pressure loading, and internal pressure plus up-bending and down-bending moments. The crack edges are loaded in axial compression when an up-bending moment is applied and in axial tension when a down-bending moment is applied. The results shown in Fig. 3 indicate that the local crack deformations are symmetric, so fracture is governed by the symmetric crack-opening stress-intensity factor. In addition, the results indicate that the symmetric crack-opening stress-intensity factor is the largest for the up-bending moment case, where there is local axial compression along the crack edges, and is the smallest for the down-bending moment case. These results demonstrate sensitivity to combined loads and also represent a geometrically nonlinear response, as linear analyses do not indicate such a combined load effect.

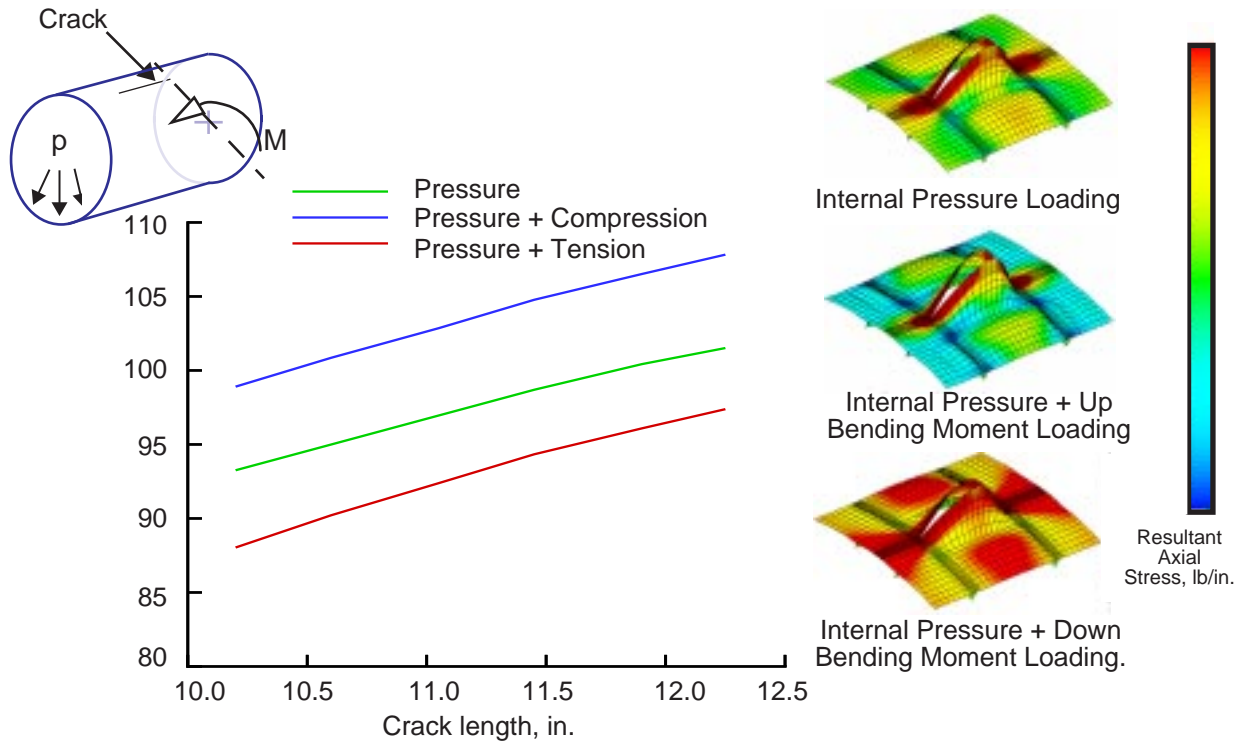


Figure 3. Crack-opening stress-intensity factor for a longitudinal crack in a fuselage shell subjected to internal pressure loading, and internal pressure loading plus an up-bending and a down-bending moment.

Additional preliminary studies were conducted to determine the effect of crack location within the fuselage structure, and the effect of shear and torsion fuselage loadings on the local crack deformations and stress-intensity factors. Results from these studies indicated that torsion loads can cause an increase in the crack-shearing stress-intensity associated with a crack. Results also showed that the crack-growth trajectory can be influenced by the crack location and the loading condition. A typical result from a study of the effects of loading condition and crack location on crack-growth trajectories is shown in Fig. 4. Crack growth trajectories are shown in Fig. 4 for three longitudinal crack locations and loading conditions. The crack is either located midway between two stringers or 1.2 inches from a stringer. The crack-growth trajectory for a crack located midway between two stringers in a panel that is subjected to internal pressure, up-bending and vertical shear loads is shown in Fig. 4a. The crack-growth trajectory for this case is self-similar due to the symmetry of the loading and the geometry. The crack-growth trajectory for a crack located 1.2 in. from a stringer in a panel that is subjected to internal pressure, up-bending and vertical shear loads is shown in Fig. 4b. In this case the crack-growth trajectory is non-self-similar due to the nonsymmetry of the geometry. The crack-growth trajectory for a crack that is located midway between two stringers in a panel that is subjected to internal pressure and torsion loads is shown in Fig. 4c. The crack-growth trajectory for this case is non-self-similar due to the nonsymmetry of the loading condition.

These and additional preliminary results demonstrated important aspects of the response of a long crack in a stiffened fuselage shell and several general conclusions were drawn from these initial studies. First, long cracks can change the internal load distribution in a stiffened shell. Second, the pressure only loading case, which is typically used as the critical design condition in practice, can result in unconservative predictions for the fuselage shell residual strength. Therefore, the effects of combined loads must be considered. Third, the local shell response is geometrically nonlinear, as evidenced by the effect of combined loads on the crack-tip stress-intensity. Local displacements near a crack can be large compared to the fuselage thickness, and these displacements can couple with internal stresses resultants in the shell to amplify magnitudes of the local stresses and displacements near the crack. Fourth, the crack behavior is strongly influenced by structural stiffening elements. Furthermore, fracture of fuselage structures made from ductile aluminum alloys exhibit a large degree of plasticity near the crack tip. Thus, a fracture criterion that accounts for elastic-plastic material nonlinearity would be also be required. All of these complexities are present in a

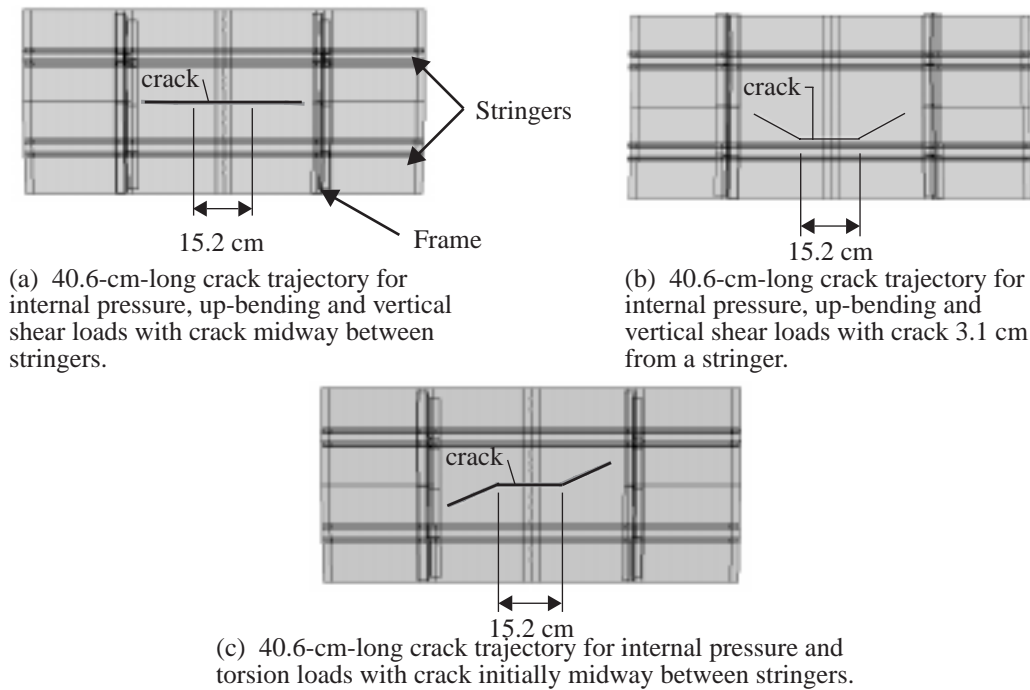


Figure 4. Effect of fuselage loading condition and crack location on crack growth trajectories.

fuselage shell structure with damage and must be addressed in residual-strength analysis methods for fuselage structure.

Jim Starnes integrated information from these preliminary analyses, from industry experience, and from his own expertise to formulate a general problem statement for research in residual strength analyses methods for metallic structures with damage. The goal of this research was to develop, and verify by experiment, a residual strength analysis methodology for fuselage structures that incorporates the inherent response characteristics described above. Jim was a strong advocate for high-fidelity analysis methods, believing that eliminating empiricism whenever possible would increase general understanding of relevant parameters and reduce the chance for applying empirical factors inappropriately.

Jim's vision for addressing the general research problem described above consisted of separating the complex general problem into several research elements, each designed to consider part of the more-general problem. In the next two sections of this paper, results from two such research elements are summarized. These results are drawn from references that contain complete details of each research element.

III. Nonlinear Bulging Factors

A study on nonlinear bulging factors for pressurized fuselage shells is described in Ref. 6. The objective of this study was to establish a solid understanding of the effects of curvature, combined loads, and geometric nonlinearity on linear elastic fracture parameters for unstiffened shell structures. The study was motivated by the traditional approach to residual strength analyses and damage tolerant design that relied primarily on geometrically linear analyses and fracture analyses based on linear elastic fracture mechanics. Linear elastic fracture mechanics suggests that the crack-tip stress intensity factor is an indicator of the likelihood of fracture. The conventional engineering approach used in design practice was to predict the crack-tip stress intensity factors for a crack in a fuselage shell by applying a so-called "bulging factor," in combination with additional design factors that account for stiffener elements, to the stress intensity factor for a flat plate subjected to similar loading conditions. Results of the preliminary studies described previously suggested that residual strength predictions based on the pressure-only loading case may be unconservative if the loading has axial compression.

The bulging factor accounts for the fundamental difference in behavior of a crack in a curved shell compared to the behavior of a crack in a flat plate. In a cracked shell, the local region around the crack deforms out-of-plane as a

result of the curvature induced coupling between the membrane and bending displacements, and the internal pressure, where, in a plate, the crack deforms in plane. These out-of-plane displacements in the neighborhood of a crack in a shell increase the crack opening and crack-tip stress intensity compared to those of a cracked plate with the same crack geometry. The bulging factor, β , amplifies the flat-plate stress intensity factor and is defined as the ratio of the stress intensity factor K_s in a shell with a crack, to the stress intensity factor K_p in a flat plate of the same material, thickness, crack length, and in-plane remote stress, σ , acting perpendicular to the crack line:

$$\beta = \frac{K_s}{K_p} \quad (1)$$

Many studies have been conducted to characterize bulging cracks, and both analytical⁷⁻¹⁴ and empirical formulas¹⁵⁻²⁰ for the bulging factor have been developed. Analytical expressions for the bulging factor in shells were developed using formulations based on linear shallow shell theory. These analytical expressions depend on the shell curvature parameter, λ , where, for an isotropic shell, λ is defined as:

$$\lambda = \frac{a}{\sqrt{Rt}} \sqrt[4]{12(1-\nu^2)} \quad (2)$$

and:

$$\begin{aligned} \nu &= \text{Poisson's ratio} \\ a &= \text{half crack length} \\ R &= \text{radius of the shell} \\ t &= \text{thickness of the shell} \end{aligned}$$

The analytical bulging factors based on linear shallow shell theory tend to overestimate the physical bulging effect, unless the cracks are very short, or the applied load is very small, so that geometric nonlinear effects are not significant. For longer cracks or higher loads, tensile membrane stresses develop along the crack edges as the crack bulges. These tensile stresses increase the resistance to additional crack bulging and crack opening, and result in a reduction in the bulging factor.²¹⁻²² Empirical formulas, which attempt to account for the nonlinear character of the bulging response, were also developed for determining bulging factors in shells with longitudinal cracks.¹⁷⁻²⁰ These empirical formulas were developed for specific materials, geometries and loading conditions, and thus, the formulas are valid for limited applications.

A more general investigation of the geometrically nonlinear response of pressurized cylindrical shells with longitudinal cracks was conducted by Budiman and Lagace.^{23,24} Budiman and Lagace, under a grant sponsored by Jim Starnes, demonstrated that the nonlinear response of cylindrical shells with longitudinal cracks, subjected to internal pressure loading, can be characterized by two nondimensional parameters: the shell curvature parameter, λ , as defined in Eq. (2); and a loading parameter, η , which depends on the applied internal pressure, material properties, and shell geometry. Research conducted by Young, Rose, and Starnes^{25,26} extended the study conducted by Budiman and Lagace by investigating the geometrically nonlinear response of pressurized cylindrical shells with long longitudinal and circumferential cracks and the effects of combined loads on the bulging factor. A comprehensive numerical parametric study of the geometrically nonlinear response of unstiffened aluminum shells with centrally located longitudinal and circumferential cracks subjected to combined internal pressure and mechanical loads was conducted using the STAGS nonlinear finite element analysis code. Major results of the study were contour plots for the bulging factor, β , and empirical expressions for estimating the bulging factor for longitudinal and circumferential cracks in both the linear and nonlinear region of the response. Contour plots of the bulging factor are presented in terms of three nondimensional parameters: the curvature parameter λ , a pressure loading parameter, η , defined as:

$$\eta = \sqrt{\frac{\sigma_y R}{E t}} \sqrt[4]{12(1-\nu^2)} \quad (3)$$

where σ_y is the farfield circumferential stress, and the biaxial loading parameter,

$$\chi = \sigma_x / \sigma_y. \quad (4)$$

Longitudinal crack

Typical results obtained in the study for the bulging factor for a longitudinal crack in a cylindrical shell, β^L , as a function of the shell curvature parameter, λ , and the pressure loading parameter, η , are presented as contour plots in Fig. 5. Bulging factors for $\chi = 0.0, 0.5, 1.5$, and 6.0 , are shown in Fig. 5a, 5b, 5c, and 5d, respectively. The solid lines in the figure are contour lines, or lines through points with a common value of the bulging factor. There are some

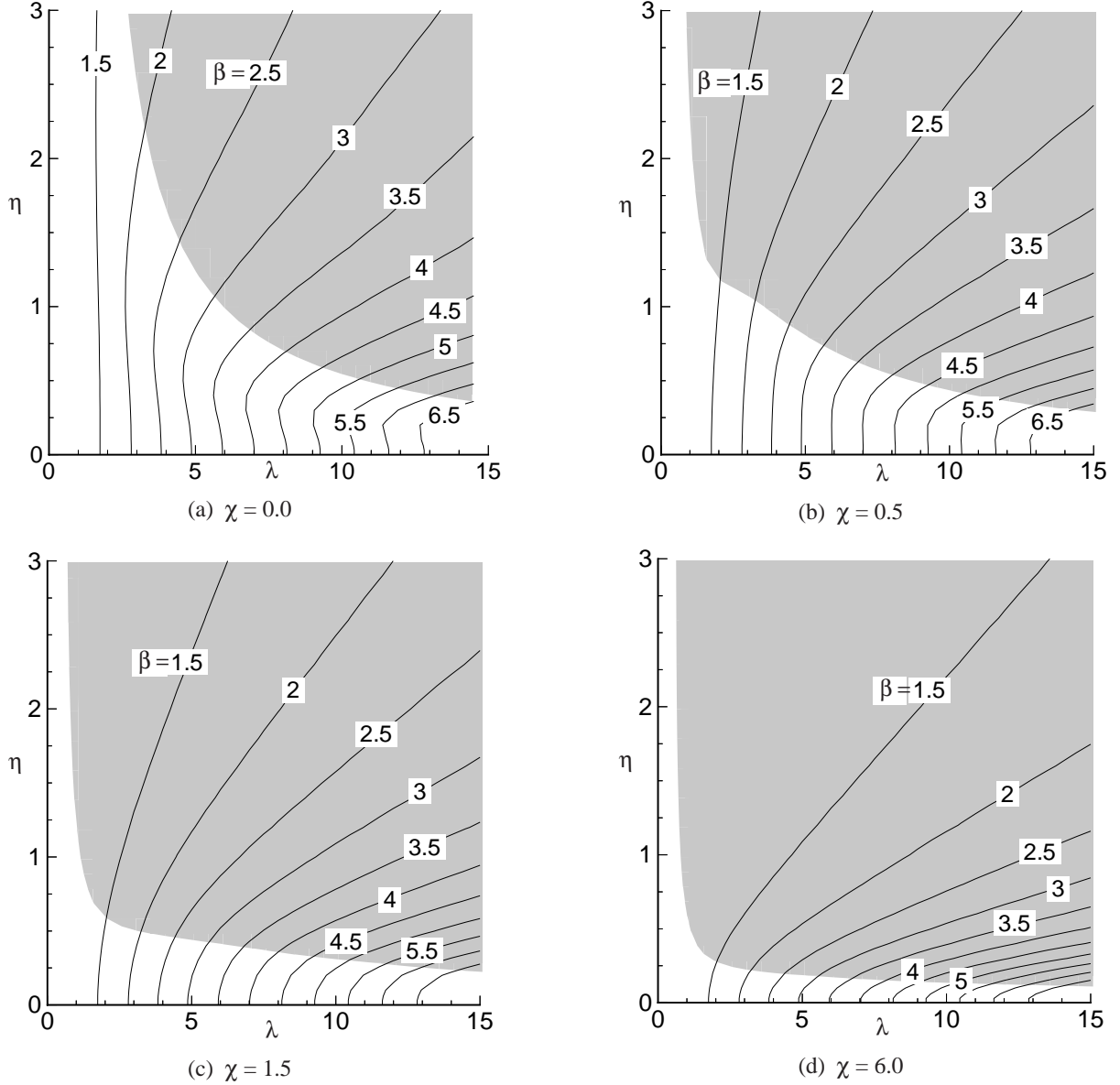


Figure 5. Contour plot of the bulging factor for a longitudinal crack, β^L , from STAGS analyses, and the linear (unshaded) region of the bulging factor response, as a function of the shell curvature parameter, λ , and the pressure loading parameter, η , for several values of the biaxial loading parameter, χ .

general trends indicated by the contour plots. For a given value of χ , the bulging factors monotonically increase with increasing values of λ , and generally decrease with increasing values of η . In each contour plot, the bulging factor for very small values of η , i.e., for locations near the λ -axis, corresponds to the linear bulging factor, β_{lin}^L as reported by Erdogan and Kibler¹², and does not vary with changes in χ . For small values of η , the contour lines are nearly perpendicular to the λ -axis, indicating that the bulging factor for small values of η is primarily a function of λ only and can be approximated by β_{lin}^L . The unshaded areas of the contour plots in Fig. 5 indicate the linear region of the response where the difference between β^L and β_{lin}^L is less than 10%. For higher values of η , the bending deformations become sufficiently large and cause nonlinear membrane stiffening. The bulging factors decrease with increasing η , and the contour lines bend to the right and asymptotically approach lines which extend radially from the origin. The shaded areas of the contour plots in Fig. 5 indicate the nonlinear region of the response where the difference between β^L and β_{lin}^L is greater than 10%. The largest differences between β^L and β_{lin}^L occur when λ and η are both large, where β_{lin}^L overpredicts β^L by 45% when $\chi = 0$, and by 400% when $\chi = 6$. Comparison of the contour plots for different values of χ indicates that increasing the biaxial loading parameter promotes tensile membrane behavior, causing

the contour lines to bend to the right at lower values of η , thus reducing the size of the linear response region. A simple expression for representing the bulging factor behavior shown in Fig. 5, that can be easily used in a design environment, is obtained by characterizing the linear and nonlinear regions of the response separately.

The linear region of the response is accurately described by the linear bulging factor for a longitudinal crack, β_{lin}^L . A simple expression for the linear bulging factor is obtained by examining the behavior of the numerical data and determining that the data can be approximated closely by the function

$$\beta_{lin}^L = \sqrt{1 + (0.5)\lambda^{1.725}} \quad (5)$$

An expression for estimating the bulging factor in the nonlinear region of the response, β_{nl}^L , is obtained by utilizing the fact that the contour lines of the bulging factor asymptotically approach radial lines through the origin. For a given value of χ , the value of the bulging factor can be uniquely related to the slope of the radial line, i.e., λ/η , which is approached asymptotically by a contour line. To obtain an expression which relates the nonlinear bulging factor to the ratio λ/η and the biaxial loading ratio, χ , the relationship between the nonlinear bulging factor and the ratio λ/η is first established for each value of χ . Then, the variation in this relationship is described as a function of χ . By numerical processing of the data represented in Fig. 5, it was determined that β_{nl}^L can be closely approximated by the equation

$$\beta_{nl}^L = \sqrt{1 + [c_1(\chi)][\lambda/\eta]^{c_2(\chi)}} \quad (6)$$

where the coefficients $c_1(\chi)$ and $c_2(\chi)$ are given by

$$c_1(\chi) = 0.15 + 1.75e^{-0.8\chi}, \text{ and} \quad (7)$$

$$c_2(\chi) = 1.4 - 0.52e^{-0.43\chi} \quad (8)$$

By using Eqs. (7) and (8) with Eq. (6), the nonlinear bulging factor for a longitudinal crack in a cylindrical shell, β_{nl}^L , is expressed in terms of the shell curvature parameter, the pressure loading parameter, and the biaxial loading parameter. The expression for β_{nl}^L in Eq. (6) will overpredict the bulging factor in the linear region of the response, while the expression for β_{lin}^L in Eq. (5) will overpredict the bulging factor in the nonlinear region of the response. The bulging factor over the entire linear and nonlinear regions of the response, for any value of λ , η and χ , is approximated by taking the minimum of the linear bulging factor estimated by Eq. (5), and the nonlinear bulging factor, estimated by Eq. (6).

$$\beta_{approx}^L = \min(\beta_{lin}^L, \beta_{nl}^L) \quad (9)$$

The accuracy of Eq. (9) in representing the bulging factors from the STAGS analyses is demonstrated by the contour plots of the bulging factors for $\chi = 0.0$ and 6.0 shown in Fig. 6a and 6b, respectively. In Fig. 6, the bulging factors from the STAGS analyses are shown as solid lines, and the estimates from Eq. (9) are shown as dashed lines. The largest discrepancies between Eq. (9) and the STAGS analyses occur in the transition region between the linear and the nonlinear regions of the response. For $\chi = 0$, the discrepancies are less than 10% over the entire area. For $\chi = 6$, the shaded area in the contour plot indicates the region where the discrepancies are greater than 10%. The shaded area is small, and the worst case situation for Eq. (9) overpredicts the bulging factor by 22%.

Circumferential Crack

Results obtained for a circumferential crack demonstrated that the bulging factor for cylindrical shells with circumferential cracks, β^C , has a mild dependence on the biaxial loading parameter. The bulging factors for $\chi = 0.5$ are a good estimate for $0.25 < \chi < 6$, and the largest discrepancies are conservative. Thus, the circumferential bulging factor will be characterized for $\chi = 0.5$. The bulging factor results from the STAGS analyses of cylindrical shells with circumferential cracks, β^C , are presented as a function of the shell curvature parameter, λ , and the pressure loading parameter, η , in Fig. 7. The solid lines in the figure are contour lines, or lines through points with a common value of the bulging factor. The results in the contour plot indicate that the bulging factors monotonically increase with increasing values of λ , and monotonically decrease with increasing values of η . This behavior is consistent with the results shown in Fig. 5. The contour plot of the bulging factors for the circumferential crack with $\chi = 0.5$ in Fig. 7 is similar to the contour plot of the bulging factors for the longitudinal crack with $\chi = 0.5$ shown previously in Fig. 5(b). The primary differences between the bulging factor contour plots for the two crack orientations are that the bulging factor for the circumferential crack is smaller in amplitude, and the contour lines are concentrated nearer to the abscissa of the plot. The contour lines are perpendicular to the λ -axis for very small loads, but the contours bend to the right almost

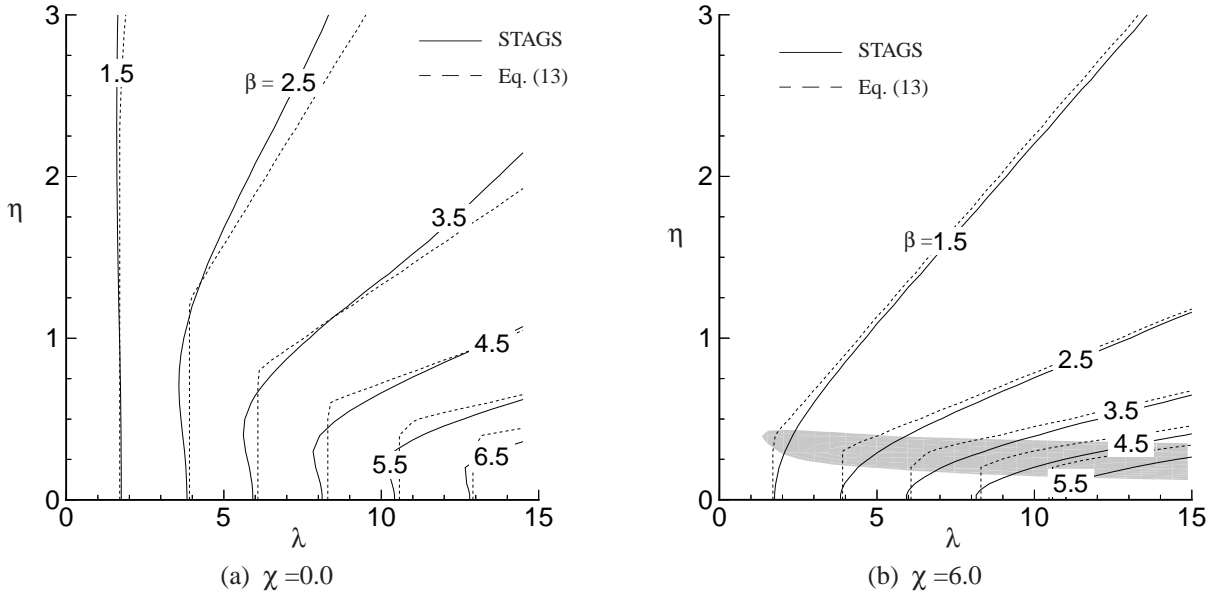


Figure 6. Contour plot showing the bulging factors for a longitudinal crack, β^L , as computed using STAGS and approximated by Eq. (13), as a function of the shell curvature parameter, λ , and the loading parameter, η .

immediately as η is increased, and asymptotically approach lines which extend radially from the origin. The shaded area of the contour plot in Fig. 7 signifies the nonlinear region of the response where the difference between β^C and β_{lin}^C is greater than 10%. This shaded region is closer to the λ -axis than it was for the longitudinal crack with $\chi = 0.5$, indicating that the transition from the linear bending response to the nonlinear membrane response occurs at smaller values of load for a shell with a circumferential crack than for a shell with a longitudinal crack. The largest differences between β^C and β_{lin}^C occur when λ and η are both large, which results in β_{lin}^C overpredicting β^C by 100%.

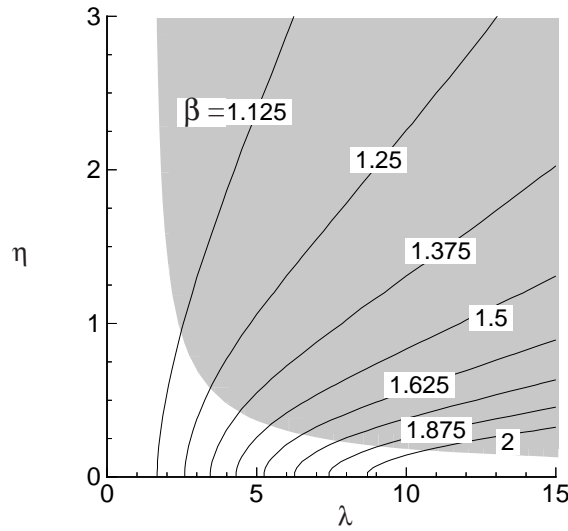


Figure 7. Contour plot of the bulging factor for a circumferential crack, β^C , from STAGS analyses, and the linear (unshaded) region of the bulging factor response, as a function of the shell curvature parameter, λ , and the pressure loading parameter, η .

By applying numerical procedures similar to those applied for the longitudinal crack case, simple expressions that can be easily used in a design environment were generated for a circumferential crack case. The bulging factor for a circumferential crack over the entire linear and nonlinear regions of the response, for any value of λ , η and χ , can be approximated by the expression:

$$\beta_{approx}^C = \min(\beta_{lin}^C, \beta_{nl}^C) \quad (10)$$

where

$$(\beta_{lin}^C)^2 = 0.955 + 0.110\lambda + 0.0637\lambda^2 - 0.00534\lambda^3 + 0.000144\lambda^4 \quad (11)$$

and

$$(\beta_{nl}^C)^2 = 1.05 + 0.122\left(\frac{\lambda}{\eta}\right) - 0.00161\left(\frac{\lambda}{\eta}\right)^2 + 9.27E-6\left(\frac{\lambda}{\eta}\right)^3 \quad (12)$$

The bulging factors obtained by applying Eq. (10) are compared to the bulging factors from the STAGS analyses in Fig. 8. The bulging factors from the STAGS analyses are shown in Fig. 8 as solid lines, and the estimates from Eq. (10) are shown as dashed lines. The largest discrepancies between Eq. (10) and the STAGS analyses occur in the transition region between the linear and the nonlinear regions of the response. The worst case situation for Eq. (10) overpredicts the bulging factor by 9%.

Summary Remarks

The results presented in this study demonstrated the ranges of the shell curvature and loading parameters for which the effects of geometric nonlinearity are significant, and showed the effect of biaxial loads on the value of the bulging factor. Simple empirical expressions for the bulging factor, derived from the numerical results, were shown to predict accurately the nonlinear response of shells with longitudinal and circumferential cracks. The primary outcome of this research was accurate nondimensional representation of a complex nonlinear response phenomena, that accounts for combined load effects, and presents a direct improvement to current design methodology for damage tolerance of curved shell structures. The results illustrated that for longitudinal and circumferential cracks, the linear bulging factor is generally overconservative, and using the linear factor may result in designs that are significantly overweight. For circumferential cracks, the bulging factor is insensitive to biaxial loads. For longitudinal cracks, the nonlinear bulging factor is a function of biaxial loading, and designing with the nonlinear result for the pressure-only case is unconservative if the actual loading has axial compression, i.e., $\chi < 0.5$.

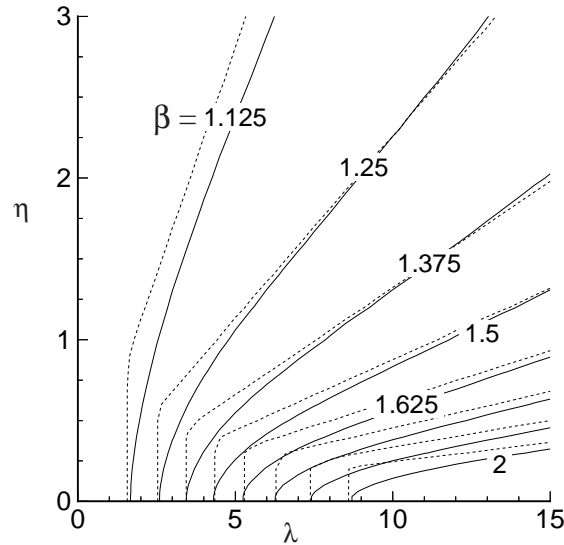


Figure 8. Contour plot showing the bulging factors for a circumferential crack from the STAGS analysis, and from Eq. (16), as a function of the shell curvature parameter, λ , and the pressure loading parameter, η .

IV. Skin, Stringer, and Fastener Loads in Buckled Fuselage Panels

The study described in Ref. 27 extended previous efforts in modeling and understanding the response of unstiffened shells subjected to internal pressure and mechanical loads to more complex built-up structure representative of fuselage structure. Typical metallic fuselage structure consists of built-up stiffened panels with a thin skin attached to longitudinal stringers and circumferential frames. To maximize structural efficiency, fuselage shells are usually designed to allow the fuselage skin to buckle in compression and shear at a load level that is below the design limit load condition for the shell. Thus, it is assumed that cracks may exist in the structure during the service life of the aircraft, and that loading conditions could occur that would cause the fuselage skin with cracks to buckle.

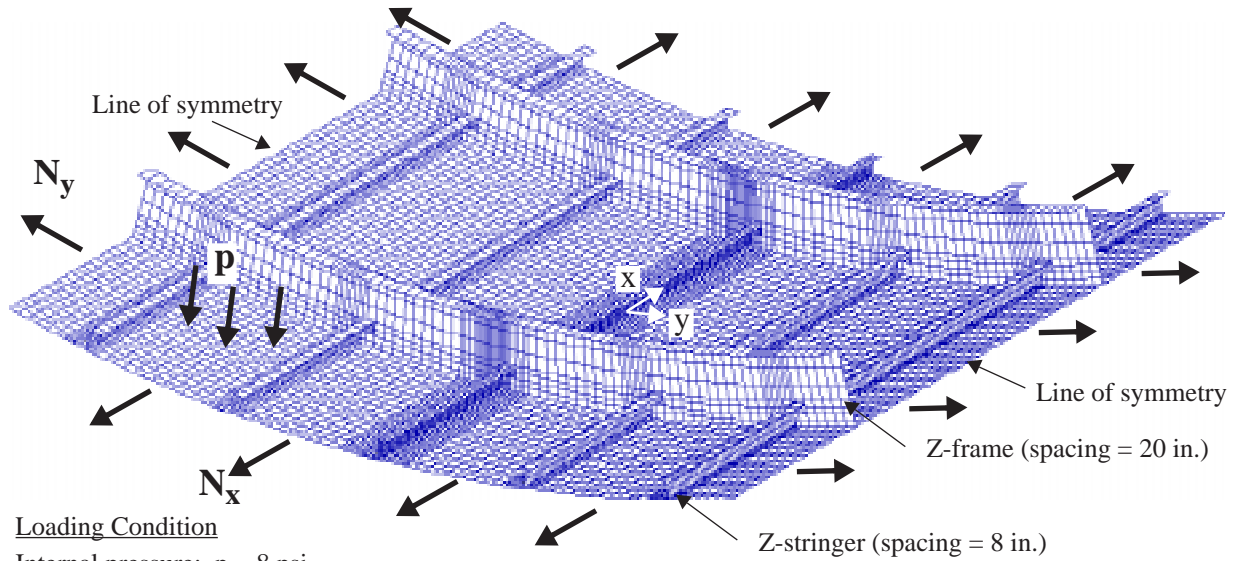
Skin buckling causes nonlinear deformations and changes in the stress distribution in the skin, the internal structure, and the fasteners connecting the skin and the internal structure. Failure initiation and propagation in the built-up structure may involve crack initiation in the skin or stiffening elements, or fatigue or strength failure of the fastener elements connecting the skin to the stiffening elements. The structural integrity of a built-up structure subjected to combinations of internal pressure and mechanical flight loads can be studied analytically with a nonlinear structural analysis capability, but a high-fidelity modeling and analysis methodology must be applied to obtain accurate predictions of the state of stress in each component of the structure. Most residual-strength analysis studies reported in the literature for fuselage shells with cracks^{7,11,12,18,19,21-24} have been limited to internal pressure loads only, where the shell is in biaxial tension. The results of analytical studies of the nonlinear response of unstiffened aluminum shells with longitudinal cracks and subjected to internal pressure and axial compression loads^{6,17,28-29} have indicated that the crack-growth characteristics of longitudinal cracks are influenced by the biaxial-loading ratio, χ , defined as the ratio of the longitudinal stress resultant to the circumferential stress resultant. The influence of biaxial loading on cracked stiffened panels was reported in Refs. 30 and 4, but skin buckling was not considered in either reference. Rose, Young and Starnes²⁸ studied the effect of initial cracks on the nonlinear response of a cylindrical shell and found that the buckling load can be significantly reduced by the presence of a crack, and that the buckling load decreases as the crack length increases for a given pressure load. In addition, results of a fatigue test of an A300B fuselage³¹ indicated that compressive stress directioned parallel to a crack may increase the stress intensity factor by 40%.

A numerical study was conducted to assess the effect of skin buckling on the internal load distribution in a pristine stiffened fuselage panel, and in a stiffened fuselage panel with longitudinal cracks. In addition, the impact of changes in the internal loads on the fatigue life and the residual strength of a fuselage panel were assessed. Geometrically nonlinear response was considered, and the assessment was simplified by considering linear-elastic material behavior and examining linear-elastic fracture parameters to provide a qualitative measure of the effect of skin buckling on residual strength and life. The STAGS finite element code, which has special features for modeling fastener elements, contact between built-up components, and cracks in shell structures, was used to conduct the analyses.¹ Stress intensity factors for symmetric and anti-symmetric membrane (K_I , K_{II}) and bending (k_1 , k_2) modes can be computed within STAGS.³²⁻³³ The total stress intensity factor K_T is calculated from the total strain-energy-release rate, G :

$$K_T = \sqrt{EG} \quad (13)$$

The structural configuration considered in this study is shown in Fig. 9, and is a generic narrow-body fuselage panel. It is constructed entirely of 2024-T3 aluminum alloy, with a 74.-in. skin radius, a 0.040-in. skin thickness, Z-stringers with an 8.-in spacing, and Z-frames with a 20.-in. spacing. A finite element model of the stiffened fuselage panel with two frame-to-frame longitudinal skin bays and five circumferential stringer bays is shown in Fig. 9. The origin of the (x,y) coordinate system shown in Fig. 9 is located on the center stringer, and midway between the frames. The model was defined to include one half of a skin-bay beyond the last stiffening member on each edge of the panel. The circumferential edges of the skin and frames have symmetry boundary conditions. The longitudinal edges of the panel have the rotational constraints of a line of symmetry and multi-point constraints to enforce a uniform longitudinal edge displacement. The Young's modulus, E , for the aluminum alloy is equal to 10.5 msi and Poisson's ratio, ν , is equal to 0.33.

The loading condition for the fuselage panel consists of an applied internal pressure, p (which generates a circumferential stress resultant reaction, N_y), and an axial stress resultant, N_x , which is the sum of the bulkhead pressure load, and an applied mechanical load. The stress resultants, N_x and N_y , represent the average load in pounds per inch along the longitudinal and circumferential edges of the panel, respectively. A biaxial loading ratio, χ , is defined as the ratio of the axial load to the circumferential load, $\chi = N_x/N_y$. A biaxial loading ratio $\chi = 0.5$ corresponds to the



Loading Condition
 Internal pressure: $p = 8$ psi
 Axial load: $N_x = \chi N_y$ ($\chi = -1.2$ to $+2$)

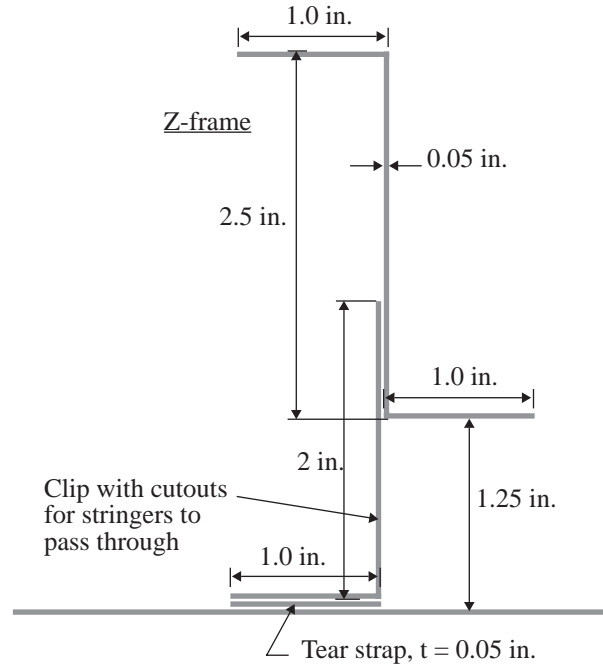
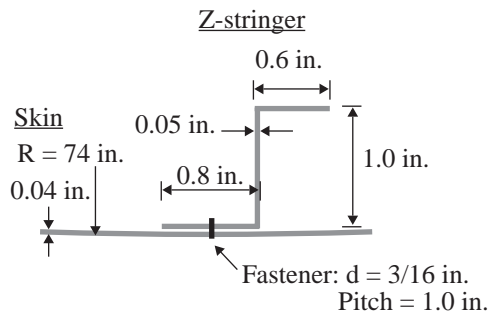


Figure 9. Geometry and finite element model of stiffened fuselage shell.

internal-pressure-only loading condition. The maximum compression load considered corresponded to a biaxial loading ratio $\chi = -1.2$, which was two times the axial compressive load required to buckle the skin of the fuselage panel.

Pristine Panel

Nonlinear analyses were conducted for the fuselage panel with no damage. Solutions were obtained for an internal pressure load of 8 psi, and a range of axial loading values corresponding to biaxial loading ratio values $\chi = 2.0$ to -1.2 . Contour plots of the fuselage-skin radial displacement for $\chi = 0.5$ and -1.0 are shown in Fig. 10. The case with $\chi = 0.5$ corresponds to the bulkhead tension load for a nominal pressure load only. The radial displacement result for $\chi = 0.5$, shown in Fig. 10a, shows that the internal pressure on the skin deforms the skin radially outward, and the displacements are smaller where the skin is attached to the stiffening structure. The circumferential stiffness of the

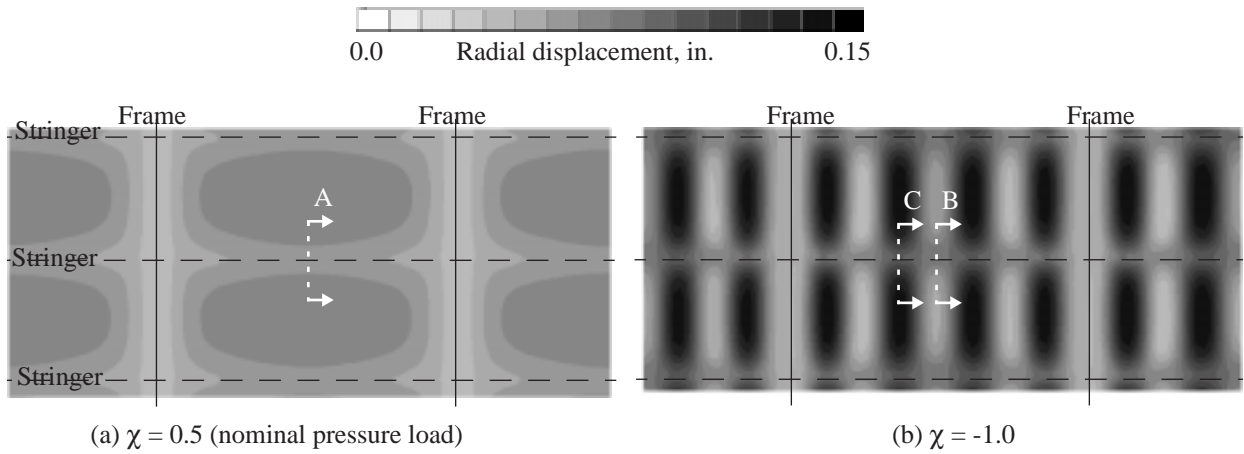


Figure 10. Fuselage-skin radial displacement for biaxial loading ratio values of $\chi = 0.5$, and -1.0 .

frames strongly resists the radial deformation, thus the skin's radial displacement is the smallest near the frames. The stringers resist radial deformation because they are attached to the frames. The stringers provide some radial support to the skin through the bending stiffness of the stringers. The stringers bend along their length and deflect outward more than the frames, and the skin on each side of the stringer deflects outward more than the stringer. The skin radial displacement for $\chi = -1.0$, shown in Fig. 10b, displays a fully-developed buckled skin pattern that is symmetric with respect to each stringer and each frame. The symmetry in the response is attributed to the strong influence of the bending boundary layer on each side of the frames and the presence of the internal pressure load. Changes in the structural configuration would likely influence the deformation shape and symmetry of the response.

Panel cross sections 'A', 'B' and 'C' are identified in Fig. 10. For each cross section, the deformed shape of the skin-stringer attachment area is shown amplified by a factor of 10 in Fig. 11. For the case with nominal pressure load, $\chi = 0.5$, the deformed shape of cross section 'A', shown in Fig. 11a, indicates a small amount of outward deformation in the skin on each side of the stringer, and a small amount of twisting in the stringer deformation due to the asymmetry of the stringer Z cross section. For the case with the postbuckled skin and $\chi = -1.0$, the deformed shape of cross section 'B' shows the skin deformed toward the stringer and bent over the stringer, with contact evident in the skin-stringer interface. At cross section 'C' of the postbuckled skin with $\chi = -1.0$, the deformed shape shown in Fig. 11c shows the skin pulled away from the stringer, which causes the asymmetric stringer to twist. The skin and stringer separate on one side of the fastener row (see Fig. 11c), and the bending response of the skin is most severe in this region. There are significant bending stresses associated with the skin bending shown in Figs. 11b and 11c. The large stress values located in the skin-stringer attachment region will increase the likelihood of damage initiation and propagation in this region.

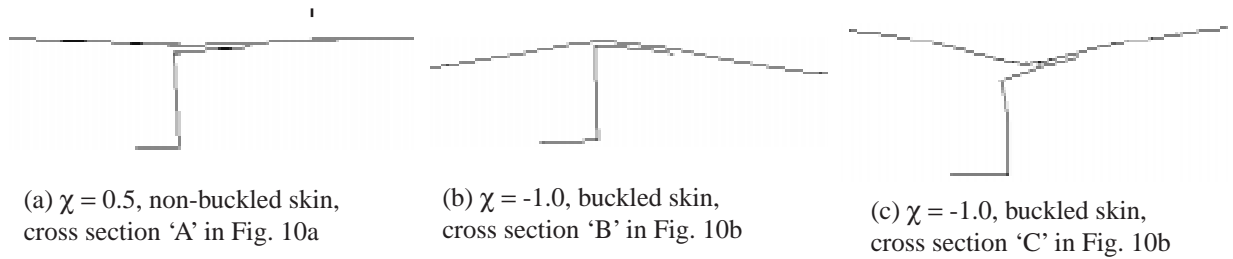


Figure 11. Deformed shape (10x) of the stringer cross section for biaxial loading ratio values of $\chi = 0.5$ and -1.0 .

Centered 4-In.-Long Longitudinal Crack

The effects of cracks on the response was studied by modifying the finite element model to include a 4-in.-long longitudinal crack in the panel skin. The crack was located midway between frames, centered on $x = 0$ in Fig. 9, and adjacent to the line of skin-stringer attachment. Nonlinear analyses were conducted for an internal pressure load of 8 psi, and a range of axial load values corresponding to biaxial loading ratio values $\chi = 2.0$ to -1.2 . The 4-in.-long crack is large enough to influence the panel's overall response. Contour plots of the fuselage-skin radial displacement for biaxial loading ratio values $\chi = 0.5$ and -1.0 are shown in Fig. 12. The displacement results indicate that the presence of the 4-in.-long crack influences the radial displacement in one skin bay on each side of the center stringer. The influence is not confined to the skin bay on the side of the stringer where the crack is located, because the crack unloads the circumferential tension load in the skin, and the stringer is not stiff enough in the circumferential direction to prevent the adjacent skin bay from also unloading.

For cases with all values of the biaxial loading ratio, the radial displacement is larger than in the pristine panel in the two skin bays adjacent to the crack, and the shape of the buckling deformation is different from the deformation in the remainder of the panel. The internal pressure causes outward bulging of the skin near the crack, and these bulging deformations are magnified when the panel is subjected to compressive loads. The deformations associated with the 4-in.-long crack dominate the local panel response and skin buckling deformation. The deformed shapes (3x magnification) of the center stringer near the 4-in.-long crack for biaxial loading ratio values of $\chi = 0.5$ and -1.0 are shown in Fig. 13. The deformed shapes have significant displacements in the skin, but distortion of the stiffener cross-section appears to be minimal. The results of the analyses indicate that the stringer did not yield or collapse, and was able to support the additional loads developed by the crack.

The effects of combined loads and buckling deformations on fastener forces were also assessed. The maximum forces in the fasteners that connect the skin to the center stringer are reported in Table 1 for biaxial loading ratio values $\chi = 0.5$ and -1.0 . The maximum fastener loads are considerably larger than the values for the pristine panel. Compared to the pressure-only case, $\chi = 0.5$, cases with pressure plus axial tension, $\chi > 0.5$, have smaller fastener forces. When axial compression is applied and the skin buckles, as is the case for $\chi = -1.0$, all of the fastener loads become significantly larger.

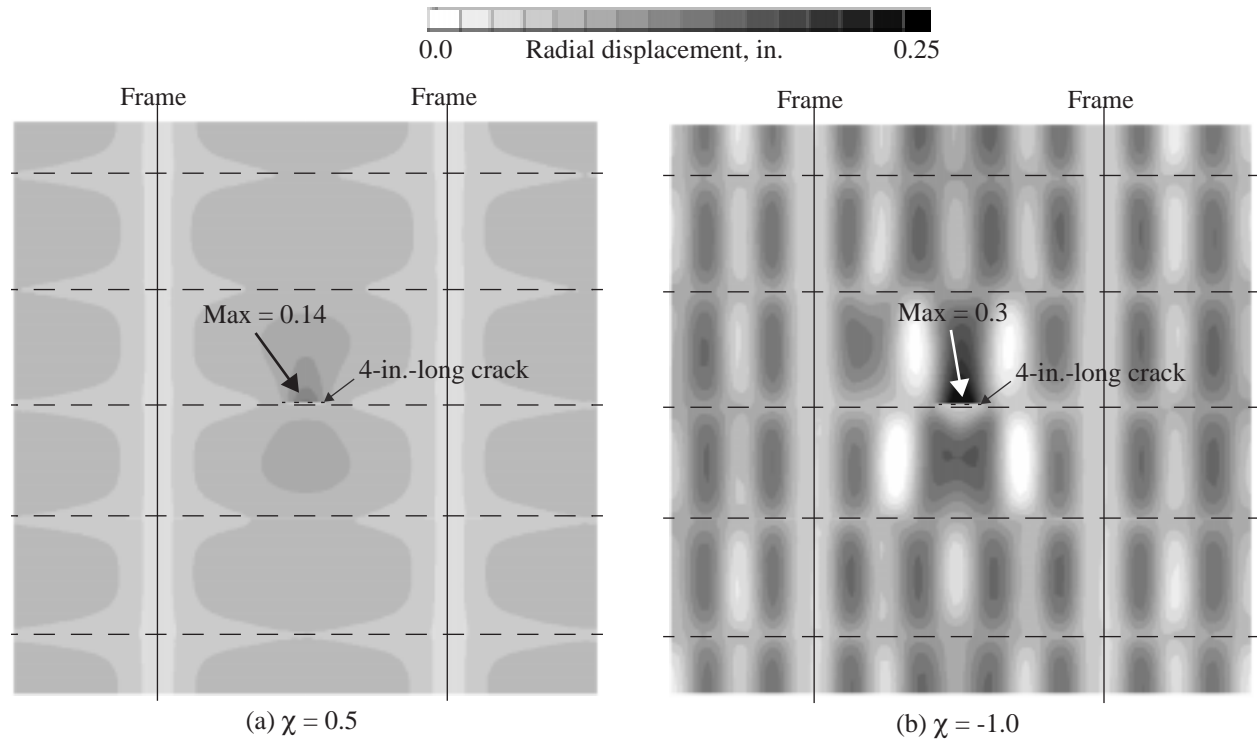


Figure 12. Radial displacement of fuselage-skin with a 4-in.-long longitudinal crack located midway between frames ($x = 0.0$) and adjacent to the center stringer, for biaxial loading ratio values of $\chi = 0.5$ and -1.0

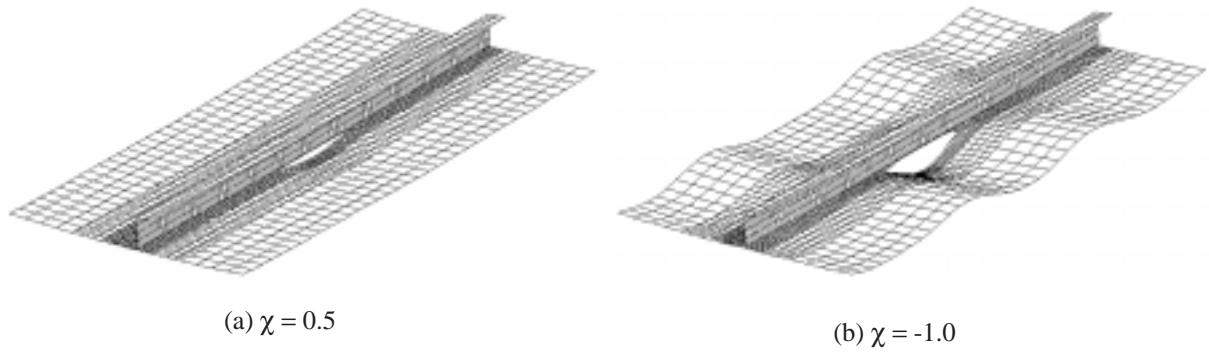


Figure 13. Deformed shape (3x) of the center stringer near a 4-in.-long crack for biaxial loading ratio values of $\chi = 0.5$ and -1.0 .

Table 1. Maximum fastener forces along the center stringer in a panel with a 4-in.-long longitudinal crack.

Biaxial loading ratio, χ	Tension, lb.	Axial shear, lb.	Side shear, lb.	Bending moment, in-lb.
0.5	18	58	55	3
-1.0	81	328	115	8

Stress intensity factors for the 4-in.-long longitudinal crack are shown in Fig. 14 for biaxial loading ratio values of $\chi = 2$ to -1.2 . In this figure, stress-intensity factors are normalized by the total stress intensity factor for the standard pressure-only condition. Results are shown for \bar{K}_T , the symmetric and asymmetric membrane components, \bar{K}_I and \bar{K}_{II} , respectively, and the asymmetric bending component, \bar{k}_2 . For the pressure-only case, $\chi = 0.5$, and cases with pressure plus axial tension, $\chi > 0.5$, the crack-tip response is dominated by \bar{K}_I , and the response is not very sensitive to

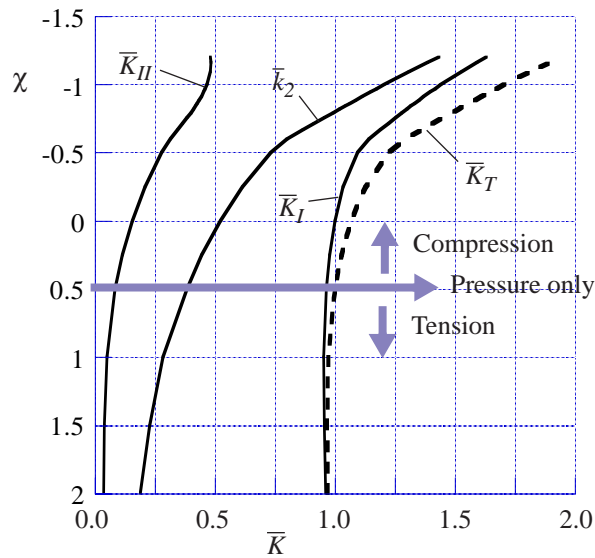


Figure 14. Stress intensity factors for a 4-in.-long longitudinal crack centered between frames ($x = 0$) and adjacent to the center stringer, for biaxial loading ratio values of $\chi = 2$ to -1.2 ; normalized by $K_T = 36$ ksi $\sqrt{\text{in.}}$ for $\chi = 0.5$.

variations in the biaxial loading ratio. When axial compression load is applied, $\chi < 0.5$, the stress intensity factors increase in magnitude in a manner that is typical of a limit-load response, rather than a bifurcation buckling response. That is, the bulging deformation near the crack develops gradually with increasing compression load, rather than changing suddenly when the skin buckles. For the maximum compression load considered, $\chi = -1.2$, \bar{K}_I is 70% larger than \bar{K}_I for the pressure-only case. Similarly, \bar{k}_2 and \bar{K}_{II} are 270% and 460% larger, respectively, for $\chi = -1.2$, than their respective values for a pressure load only, $\chi = 0.5$. These elevated stress intensity factors can be related to accelerated crack growth rates and reduced residual strength.²⁷

Summary Remarks

The results of this study indicate that nonlinear analyses of the stiffened-shell model can provide predictions of the geometric-nonlinear response of the buckled skin, cross section deformation of the stiffening components, and skin-stringer attachment forces associated with discrete fasteners. The numerical results indicate that compression loads and skin buckling can have a significant effect on the circumferential stress in the skin, and fastener loads, which will influence damage initiation. Compression loads and skin buckling have a comparable effect on stress intensity factors for cases with cracks, which will influence damage propagation rates and the residual strength of the panel.

V. Advances in Residual Strength Analyses from Laboratory Coupons to Structural Components

This section describes the residual strength analysis methodology developed at NASA Langley Research Center for aluminum aircraft fuselage structures with cracks and subjected to combined internal pressure and mechanical loads.³⁴ This methodology is applicable to complex built-up structure and accounts for combined loads, geometric nonlinearity, and material nonlinearity associated with elastic-plastic fracture. The methodology is based on the critical crack-tip-opening-angle (CTOA)³⁵⁻⁴³ fracture criterion and the STAGS nonlinear finite element shell analysis code.¹ The critical CTOA criterion assumes that crack growth will occur when the local crack opening angle reaches a critical value. An elastic-plastic finite element analysis that allows cracks to propagate is needed to implement the criterion. The STAGS nonlinear shell analysis code has been developed to implement the criterion and to automatically extend a crack while the shell is in a nonlinear equilibrium state. The STAGS nonlinear shell analysis code is used with the critical CTOA criterion to perform the residual strength analyses for structures with geometric and material nonlinear behavioral characteristics.

Several studies have been conducted to confirm the use of the CTOA criterion in the STAGS analysis to predict the residual strength of a structure. The validation studies ranged in complexity from simple coupon tests, to unstiffened cylinder tests, up to complex built-up fuselage structure tests.⁴⁴⁻⁴⁸ In the first validation effort, geometrically nonlinear elastic-plastic analyses were conducted to predict the response of compact-tension, C(T), and middle-crack-tension, M(T), panels, with and without buckling constraints. The experimental and predicted crack extension results for 2024-T3 C(T) and M(T) panels are shown in Fig. 15 as a function of the applied load. These results verify the selection of CTOA_{cr} for this material and indicate that the analyses with STAGS accurately predict the reduction in strength of the panels caused by the geometrically nonlinear effect of panel buckling. Results for small-scale pressurized shells, flat stiffened panels, and curved stiffened panels were also obtained and are described below.

Pressurized Cylindrical Shell Tests

Unstiffened cylindrical shells were fabricated from 0.04-inch-thick 2024-T3 aluminum-alloy sheet, with the rolling direction orientated circumferentially. The shells were 39-inches long, 18 inches in diameter, and had a 1.5-inch-wide double lap splice with 0.04-inch-thick splice plates and a single row of rivets on each side of the splice. Each shell had a longitudinal crack that was simulated by a 0.01-inch-wide saw cut at the specimen mid-length, diametrically opposite to the lap-splice. Specimens with initial crack lengths of 2, 3, and 4 inches were loaded by internal pressure until failure occurred.⁴⁵ The crack length extension was recorded using crack wire gages.

The finite element models used to simulate the response of the cracked shells subjected to internal pressure took advantage of the symmetry of the problem and only a quarter of the shell was modeled. Self-similar crack growth (straight cracks) was assumed. The critical CTOA value used in the fracture analysis was the same as that used for the C(T) and M(T) panels of the same material and thickness.

The experimental measurements and the STAGS finite element predictions for the pressurized cylindrical shells with initial crack lengths of 2, 3, and 4 inches are shown in Fig. 16. The analyses predicted the maximum pressure to within 4% of the measured values, but tended to overpredict the pressure required to initiate crack growth. The use of saw cuts would generally cause the analysis to underpredict the pressure required to initiate the crack growth, since a

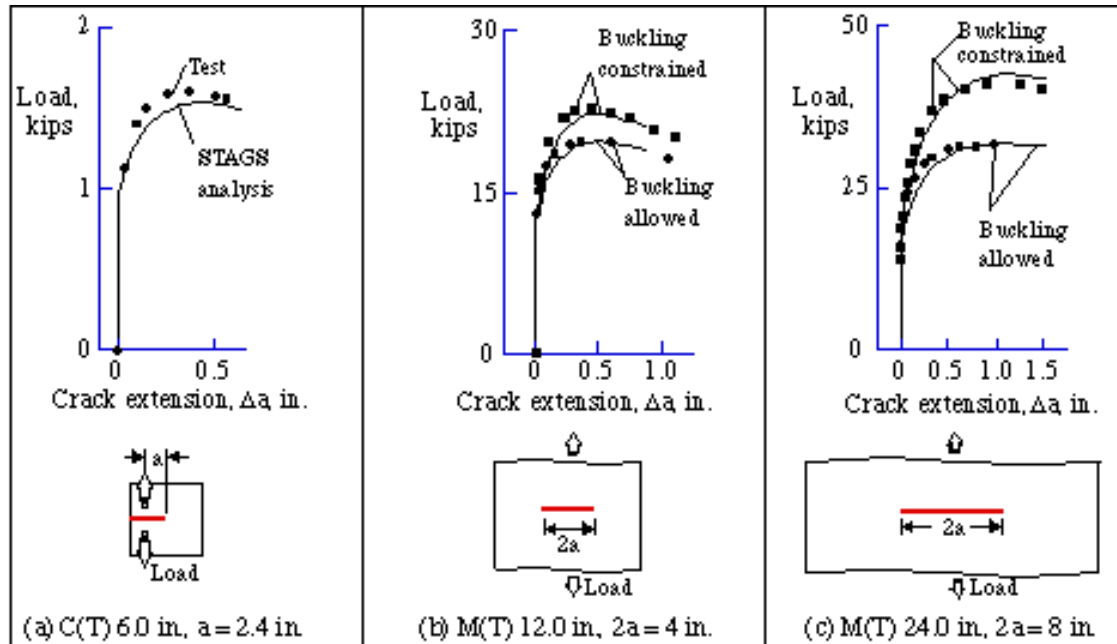


Figure 15. Load versus crack extension results from C(T) and M(T) tests, and nonlinear STAGS analyses with $CTOA_{cr} = 5.0$ deg. and $h_c = 0.04$ in.

saw cut would require higher loads to initiate crack growth than a sharp fatigue crack.⁴⁹ One possible explanation for the overprediction of the pressure for initial crack growth could be that the intense crack-tip deformations might have caused the crack wire gages to register crack growth before the growth actually occurred.

Flat Stiffened Panel Tests

Fracture tests were conducted on 40-inch-wide, 0.063-inch-thick, 2024-T3 aluminum alloy, flat, stiffened panel specimens.⁴⁴ The stiffeners were made from 7075-T3 aluminum alloy and riveted to the specimens. The stiffeners were 1.6-inches wide and placed on both sides of the specimen, as illustrated in Fig. 17. The crack configuration of

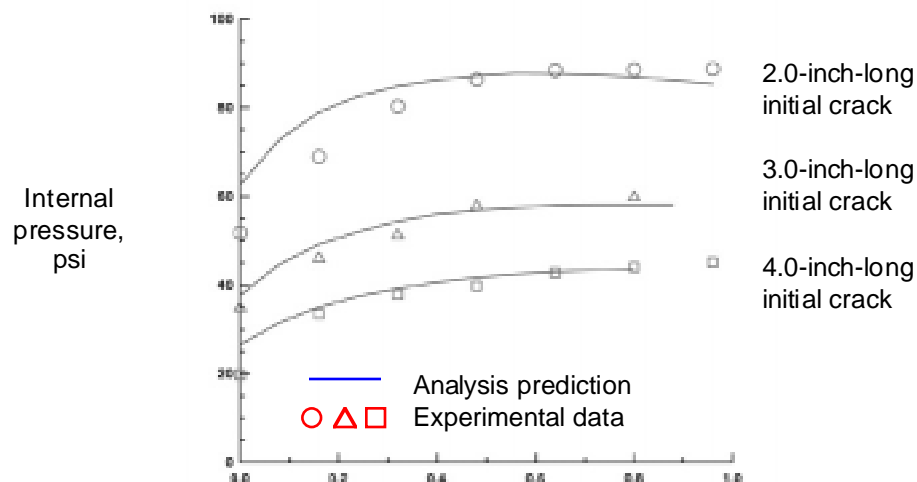


Figure 16. Comparison of analytical and experimental total crack extension results for 0.040-inch-thick internally pressurized shells.

the specimens consisted of a single 8-inch-long center crack with an array of twelve 3/16-inch-diameter holes on either side of the center crack. Specimens with and without MSD were tested. The MSD crack length was 0.05 inches from the edge of the hole. The specimens were tested without guide plates to allow out-of-plane displacements.

Predictions of the fracture behavior were conducted with the STAGS analysis code using a critical CTOA value obtained from smaller panel C(T) and M(T) tests. The configuration and loading condition were symmetric, so only a quarter of the sheet and stiffeners were modeled. The minimum element size along the line of crack extension was 0.04 inches. The analysis did not explicitly model the holes, but assumed that the holes with MSD cracks could be approximated with a crack with a length equal to the sum of the MSD crack lengths and the hole diameter. The rivet connections between the stiffener and sheet were modeled with nonlinear spring fastener elements with six degrees-of-freedom. A bifurcation buckling analysis was conducted to determine the first buckling mode shape, and this shape was introduced as an initial geometric imperfection with an amplitude of 10% of the panel thickness for the nonlinear analysis. To prevent element interpenetration, contact elements and multi-point constraint conditions were used to allow the panel sheet and stiffener surfaces to contact or separate during the response of the panel. The experimental measurements and finite element predictions for the stiffened panels with a single center crack are shown in Fig. 18. The results indicate that the analysis methodology represents the behavior of this specimen very well. Additional results in Ref. 44 indicate similar correlation was achieved for stiffened panels with MSD. The results from these tests and analyses confirm a residual strength prediction capability for flat stiffened panels with MSD.

Curved Stiffened Panel Tests

Three stringer- and frame-stiffened aluminum fuselage panels with longitudinal cracks were tested and analyzed at the NASA Langley Research Center using the analysis methodology described above.^{46,47} These curved stiffened panels are referred to as Panels ASIP1, ASIP2, and ASIP3. Typical results are presented herein for Panels ASIP2 and ASIP3.

Panel ASIP2 has four stringers and three frames, and is shown prior to testing in Fig. 19a.⁴⁶ The overall dimensions of this panel include a 122-in. radius, a 72-in. length, and a 63-in. arc width. The skin is 0.063-in.-thick 2024-

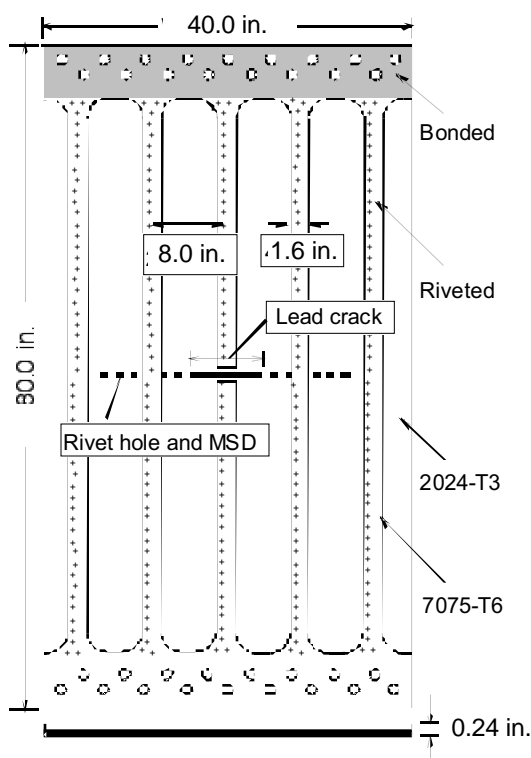


Figure 17. Wide stiffened flat panel and MSD configuration.

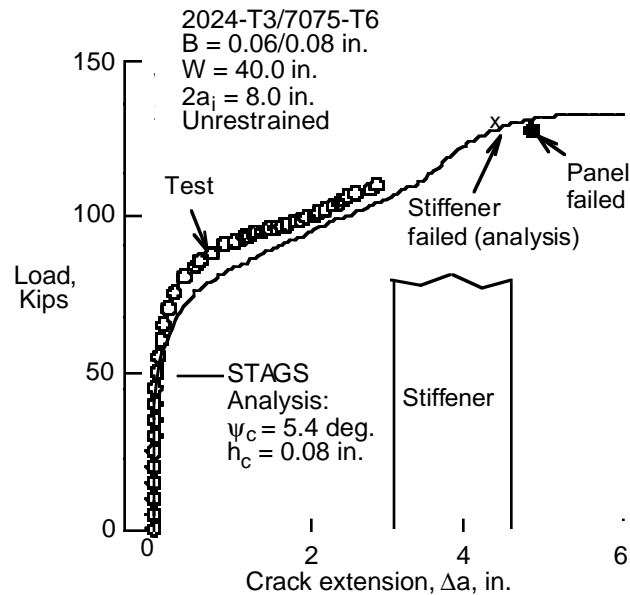


Figure 18. Experimental fracture measurements and STAGS finite element predictions for a 40-inch-wide, 2024-T3 aluminum alloy unrestrained stiffened panel with a single crack.

T3 aluminum alloy with the sheet rolling direction parallel to the stringers. The stringers are 2024-T3 aluminum-alloy inverted hat-section stringers with a stringer spacing of 14 in. The frames are 2024-T3 aluminum-alloy Z-section frames with a frame spacing of 22 in. There are 0.040-in.-thick 2024-T3 aluminum-alloy waffle tear straps, bonded to the skin, and located under the stringers and frames, but there are no tear straps midway between the frames. The stringers and frames are riveted to the skin and tear straps, and the frames are connected to the stringers by riveted stringer clips. Aluminum-alloy doublers are fastened to the curved ends of the panel between the stringers and along the sides of the panel between the frames to distribute the loads from the axial and circumferential or hoop load introduction plates of the test fixture into the panel skin. There is a lap joint in this panel under the second stringer from the left as the panel is shown in Fig. 19a. In the lap joint, the skin from the right side of the panel is the outer skin and overlaps at a greater radius over the inner skin from the left side of the panel. The layers of the lap joint are connected with three rows of 0.125-in.-diameter countersunk fasteners. The fastener pitch in the longitudinal direction is 1.0 in., and the three rows of fasteners are spaced 1.33 in. in the circumferential direction with the middle row of fasteners centered on a hat-section stringer. The initial damage for panel ASIP2 consisted of a 10-in.-long longitudinal lead crack and MSD cracks along the edge of the lap joint. The 10-in.-long lead crack was located adjacent to the second stringer and centered on a severed frame, as indicated in Fig. 19a. A schematic of the lap joint, shown in Fig. 19b, indicates that the lead crack was along the third row of fasteners in the lap joint. The MSD cracks were introduced prior to panel assembly by making small longitudinal cuts in the outer skin of the lap joint that extend 0.05 in. on each side of the fastener countersink for each fastener in the third row of fasteners. The resulting initial damage state was a 10-in.-long longitudinal lead crack with 0.33-in.-long MSD cracks in the outer skin, spaced ahead of the lead crack with a 1-in. pitch. The lead crack and MSD cracks were defined to be along the ‘critical third row of fasteners’ which is where lap joint eccentricity, pressure pillowing of the skin, and the fastener countersink combine to promote crack growth in the outer skin.

Panel ASIP3 has 12 stringers and five frames, and is shown prior to testing in Fig. 20. The overall dimensions of the panel include a 122-in. radius, a 120-in. length, and a 120-in. arc width. The initial damage for panel ASIP3 was a 10-in.-long longitudinal crack, located midway between stringers and centered on a severed frame, as indicated in

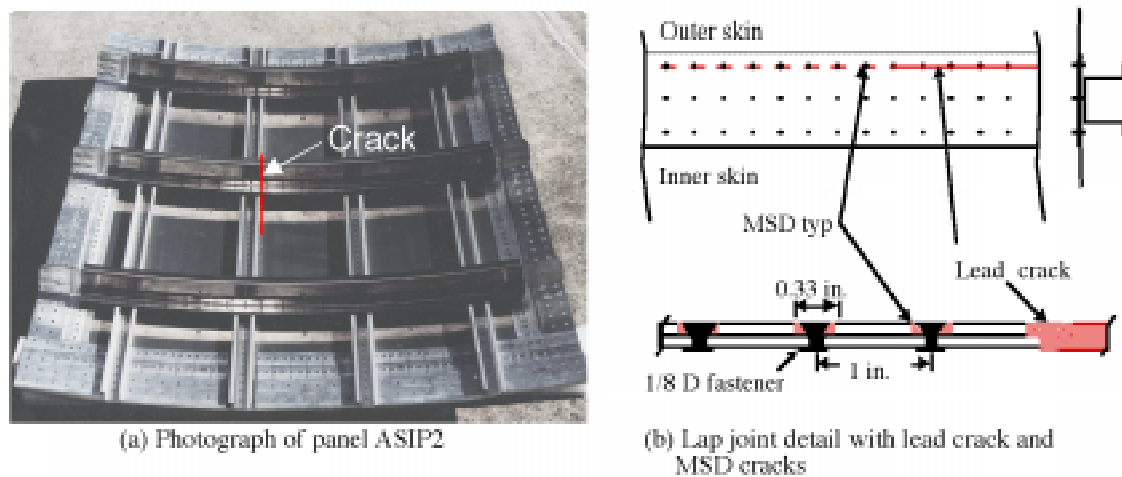


Figure 19. Panel ASIP2 prior to testing.

Fig. 20. Details of panel ASIP3 are given in Ref. 47.

Panel ASIP2 was tested in a pressure-box test machine indicated in Fig. 21. The pressure-box test machine is capable of applying axial tensile loads of up to 7,000 lb/in. and internal pressure loads of up to 20 psi. Axial loads are applied at each end of the panel by two 225-kip hydraulic actuators connected to curved steel load introduction plates. Pressure is applied to the concave side of the panel using a 100-psi air supply source and a pneumatic control system. Circumferential or hoop loads that develop in the skin of the panel are reacted by flat steel load introduction plates attached to the straight edges of the panel, and two steel rods that connect each load introduction plate to the rigid steel frame of the pressure-box test machine. Circumferential or hoop loads that develop in the frames of the panel are reacted by steel rods that connect each end of the panel frames to the rigid steel frame of the test machine. Each steel rod that reacts the circumferential loads includes a turnbuckle device that can be adjusted to ensure that circumferential loads of proper magnitudes are introduced in the panel frames and skin for a given loading condition. The reaction loads in the circumferential rods are measured by load cells built into the rods. A continuous rubber seal is connected to the bottom of the axial and circumferential load plates and to the top of the steel pressure containment box to permit the panel to float freely when pressurized and to minimize air leakage. The loading condition for panel ASIP2 was a combination of internal pressure plus axial tension loads. The axial load was prescribed to be equivalent to the bulk-

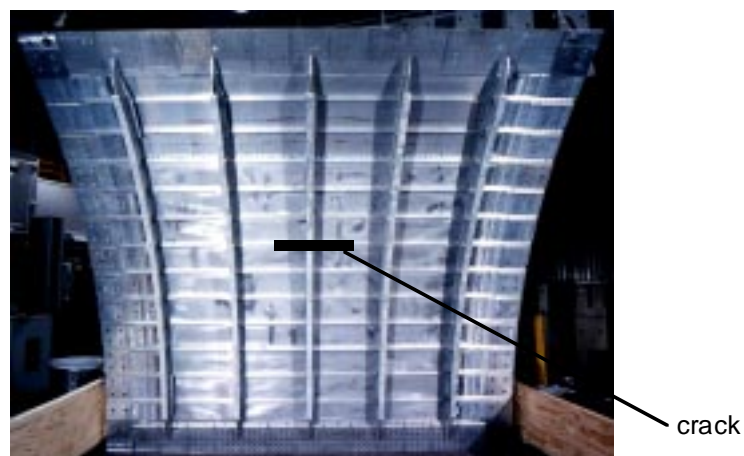


Figure 20. Panel ASIP3 prior to testing

head pressure load in a closed pressurized cylinder, and was applied during the test in proportion to the internal pressure load. Strain gages, linear variable displacement transducers, and video cameras were used to measure the panel response. Panel ASIP3 was tested in the COLTS combined loads test machine indicated in Fig. 22. The panel was attached to the D-box test fixture shown in the figure, and the panel was subjected to internal pressure, axial compression and torsion loads. Details of the test fixture for ASIP3 are given in Ref. 47.

The test results for panel ASIP2 indicate that the panel failed as a result of MSD crack link up. When panel ASIP2 was tested in the pressure-box test machine, the video record did not show any visible crack growth for pressure levels less than 9.95 psig. When the pressure reached 9.95 psig, the lead crack suddenly extended on each end of the crack, and linked up with the series of MSD cracks ahead of the lead crack. The crack extended in the longitudinal direction in a fast fracture mode, and extended over the entire panel length in an instant. The crack growth behavior was symmetric with respect to the central severed frame. Photographs which characterize the failure of panel ASIP2

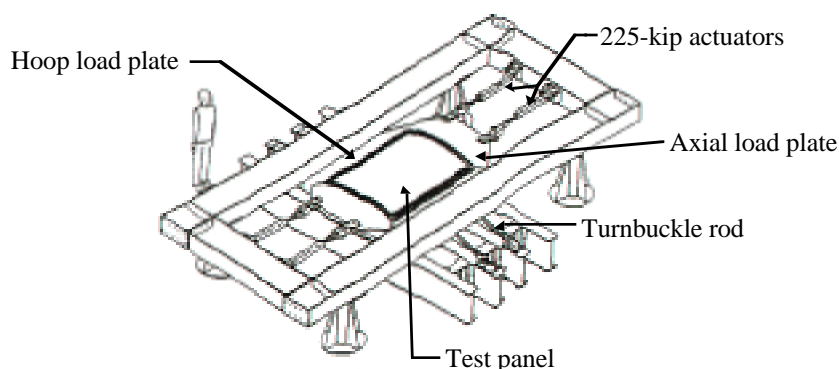


Figure 21. Pressure-box test machine.

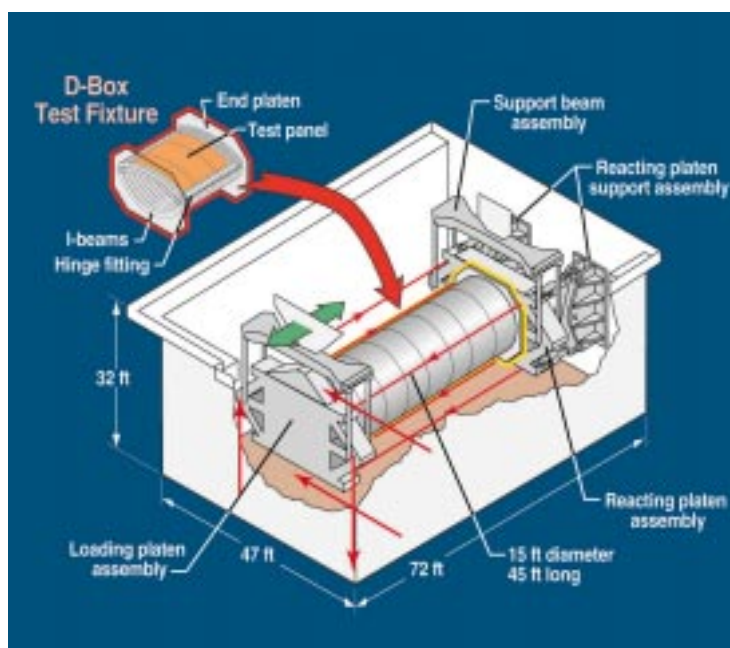
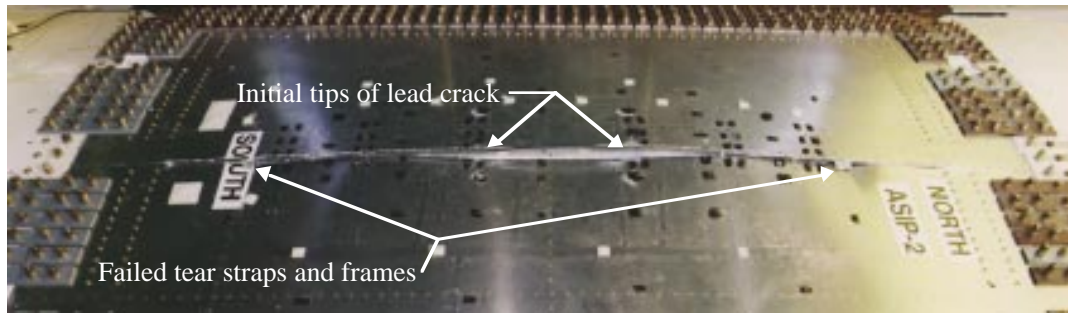


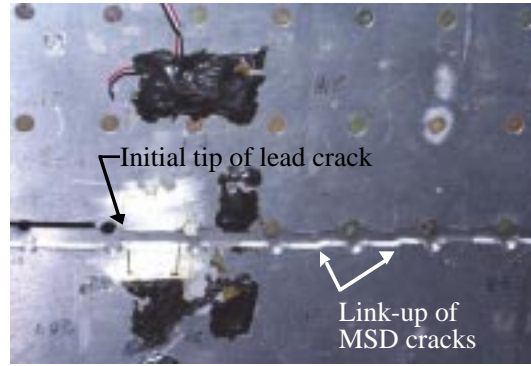
Figure 22. Combined loads test machine.



(a) Self-similar crack growth over the entire length of panel, failing adjacent tear straps and frames



(b) Failed tear strap and frame



(c) Crack trajectory with link-up of MSD cracks

Figure 23. Panel ASIP2 after testing.

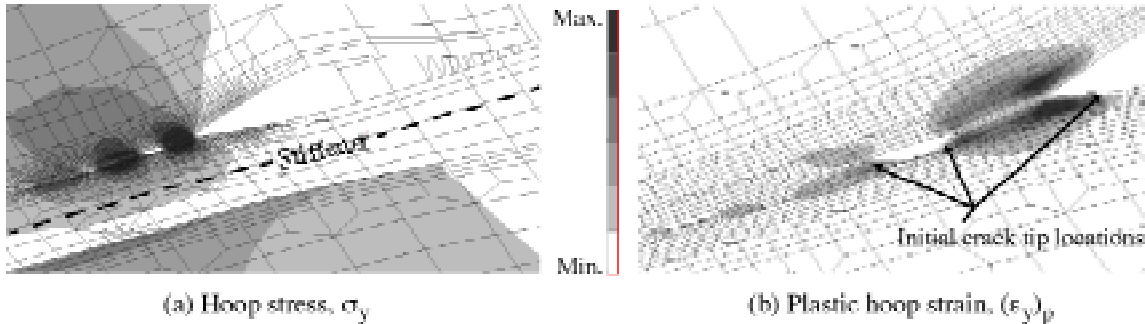


Figure 24. Typical analysis results for panel ASIP2 showing crack growth in the lead crack and MSD cracks.

are shown in Fig. 23. A view of the outer surface of the panel is shown in Fig. 23a, which shows that the skin crack has extended the full length of the panel. A view of the inner surface of the panel is shown in Fig. 23b which shows that the skin crack has extended past the adjacent frame and tear strap, failing each of these components at fastener hole locations. A close-up of the crack trajectory is shown in Fig. 23c which shows the link-up of the MSD cracks along the row of fasteners with the lead crack growing to the right, and the MSD cracks growing to the left and right so that link-up occurs midway between the fasteners. A typical solution with crack growth in the lead crack and the MSD cracks is shown in Fig. 24. The contour plot of the hoop stress in the region around the crack tip region, shown in Fig. 24a, indicates the high stress regions near the crack tips of the lead crack and the MSD cracks. A contour plot of the plastic strains in the hoop direction is shown in Fig. 24b which indicates that there are regions of plastic deformation.

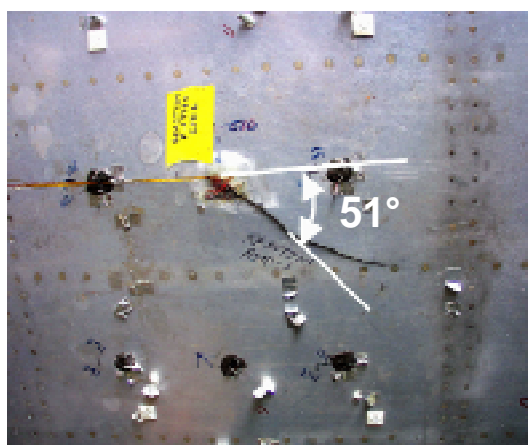
mation emanating from the lead crack and from the MSD crack tips, and that for the solution shown, the plastic zones from the lead crack and the first MSD crack have coalesced. The deformed shape shown in these plots indicates that the deformation on the side of the crack attached to the stiffener is much smaller than the deformation on the other side of the crack, demonstrating that the crack is not tearing due to a symmetric loading condition. The asymmetric loading could promote curvilinear crack growth, but it is assumed in the analysis that interaction between the lead crack and the MSD cracks will cause self-similar crack growth. The opening of the MSD cracks is also evident in the deformed shapes. The analysis predicted the residual strength of panel ASIP2 to within 11% of the experimentally observed value. For details on test and analysis correlation see Ref. 46.

The test results for panel ASIP3 indicate that the panel failed as a result of non-self-similar crack propagation. The loading condition for this panel included internal pressure, axial compression and torsion loads. The loading sequence for the panel consisted of applying the internal pressure load, followed by the axial compression load, and then followed by the torsion load. No crack growth was observed when the internal pressure and axial compression loads were applied. The torsion load was increased in magnitude until the crack propagated. A comparison of the analytically predicted crack growth trajectory and the test results for panel ASIP3 is shown in Fig. 25 indicating that the CTOA criterion and the nonlinear STAGS analysis predicted the crack growth trajectory very well for this combined loading condition. Details of the test and analysis results for panel ASIP3 are given in Ref. 47.

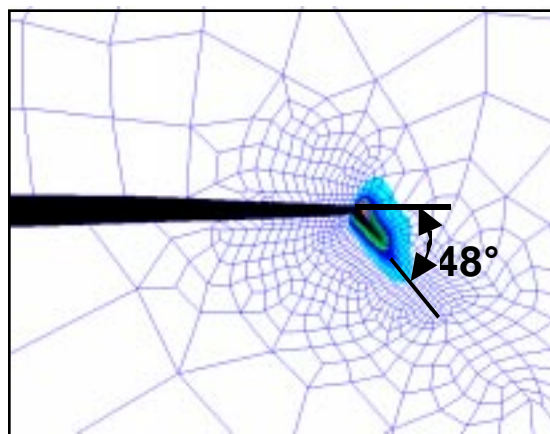
Summary Remarks

The results presented in this section demonstrate the fidelity of the residual strength analysis methodology developed at NASA Langley Research Center for aluminum aircraft fuselage structures with cracks and subjected to combined internal pressure and mechanical loads. The methodology is based on the critical crack-tip-opening-angle fracture criterion that characterizes the fracture behavior of a material of interest, and a geometric and material nonlinear finite element shell analysis code that performs the structural analysis of a fuselage structure of interest. The results indicate that elastic-plastic effects in a thin sheet can be effectively represented by a critical-crack-tip-opening-angle fracture criterion. The results also indicate that geometric and material nonlinear structural analyses can accurately represent the changes in internal load distributions, local stress and displacement gradients, and crack growth behavior in stiffened fuselage shells that are subjected to combined internal pressure and mechanical loads and have long cracks. In addition, nonlinear fracture analysis and structural analysis methods provide higher fidelity results than traditional linear-elastic engineering analysis approximations for structures with significant plastic yielding and nonlinear out-of-plane deformations associated with internal pressure loads. Numerical models and structural analysis methods must accurately represent the multiple length scales associated with simulating the global response of a large stiffened shell structure, the local deformations, and the internal load redistribution as damage propagates in the structure.

The results presented in this section represent what is currently possible with a state-of-the-art residual strength analysis methodology. This analysis methodology is possible today because verified high-fidelity nonlinear structural



(a) Experimental results.



(b) Analytical results.

Figure 25. Panel ASIP3 crack growth trajectory.

analysis tools are emerging; high-capacity computing engines are becoming affordable; insight into the complex structural response and failure characteristics of structures subjected to combined loads is developing; physics-based failure initiation and propagation analyses are emerging; and the underlying scientific basis for high-fidelity analysis and design technology is emerging.

VI. Concluding Remarks

Results from research efforts in residual strength analysis of metallic fuselage structures have been presented. These efforts were led by Jim Starnes and were the product of his vision for solving this complex problem. Jim's major contributions to advances in residual strength analysis methods for metallic structures were in identifying the effect of combined internal pressure and mechanical loads and geometric nonlinearity on the response of built-up structure with damage. Through Jim's leadership, research was conducted that demonstrated that the linear pressure-only case often used by industry may be unconservative in some cases, and over-conservative in other cases.

In addition, a residual strength analysis methodology for fuselage structure with cracks has been developed and verified by experiments. Fifteen years ago, the aircraft industry would not consider using nonlinear analysis for structures with cracks. Today, personal communications indicate that the verified analysis methodology and analysis code described in this paper have been used by the aircraft industry to realize improved analyses and design capability. A few examples include Boeing's use of nonlinear parametric analyses to update their damage tolerance design guide for stiffened panels, and using nonlinear residual strength analyses to predict the strength of a DC-9 aft bulkhead and KC-135 fuselage panels. In addition, Lockheed Marietta has used this analysis methodology to improve life predictions and refine inspection schedules for Strategic Airlift Aircraft (C-5). The residual strength analysis methodology is currently being incorporated into the ABAQUS commercial finite element code. The CTOA fracture criterion has already been implemented in the ABAQUS code and efforts are underway to adopt residual strength solution algorithms from STAGS for use in ABAQUS.

In 1999, NASA recognized this research with a "Turning Goals into Reality" Award for valuable contributions to the NASA Airframe Structural Integrity Team and exceptional progress toward aviation safety. The success of this research can be largely attributed to the technical guidance and vision that Jim Starnes provided for the research team. The research effort spanned several years, involved many complex phenomena, and required contributions from several disciplines and many researchers. Through Jim's vision, he was able to address the complex research problem through a series of smaller problems, and then integrate the research findings into a general capability for solving real-world fuselage problems.

Jim's contributions to this research activity, and to the many other research activities he led, go well beyond the technical results that were generated. His knowledge and his vision provided direction, sometimes direction not fully appreciated, and while assembling this paper it was realized that our understanding of Jim's vision continues to grow. His never ending enthusiasm kept us going and striving to learn more. Perhaps teaching of his research approach was his largest contribution as we now apply his approach to guide us in our research.

VII. References

¹Rankin, C. C., Brogan, F. A., Loden, W. A. and Cabiness, H. D., "STAGS User Manual, Version, 5.0," Lockheed Martin Missiles & Space Co., Inc., Rept. LMSC P032594, January 2005.

²Swift, T., "Damage Tolerance in Pressurized Fuselages," *New Materials and Fatigue Resistant Aircraft Design*, D. L. Simpson, Ed., EMAS Ltd., 1987, pp.1-77.

³Starnes, J. H., Jr., Britt, Vicki O., and Rankin, C. C., "Nonlinear Response of Damaged Stiffened Shells Subjected to Combined Internal Pressure and Mechanical Loads," AIAA Paper 95-1462, April 1995.

⁴Starnes, J. H., Jr., Britt, V. O., Rose, C. A., and Rankin, C. C., "Nonlinear Response and Residual strength of Damaged Stiffened Panels Subjected to Combined Loads," AIAA Paper No. 96-1555, April 1996.

⁵Starnes, J. H., Jr., Rose, C. A., Young, R. D., and Rankin, C. C., "Effects of Combined Loads on the Nonlinear Response of Stiffened Shells with Long Cracks," Presented at the 19th International Committee on Aeronautical Fatigue Symposium, Edinburgh, Scotland, UK, June 18-20, 1997

- ⁶Young, R. D., Rose, C. A., and Starnes, J. H., Jr., "Nonlinear Bulging Factors for Longitudinal and Circumferential Cracks in Cylindrical Shells Subjected to Combined Loads," Proceedings of the 41st AIAA/ASME/ASCE/AHS/ASC Structures, Structural Dynamics and Materials Conference, Atlanta, GA, April 2000, AIAA Paper No. 2000-1514.
- ⁷Folias, E. S., "An Axial Crack in a Pressurized Cylindrical Shell," *International Journal of Fracture Mechanics*, Vol. 1, No. 2, 1965, pp. 104-113.
- ⁸Folias, E. S., "A Circumferential Crack in a Pressurized Cylindrical Shell," *International Journal of Fracture Mechanics*, Vol. 3, 1967, pp. 1-12.
- ⁹Folias, E. S., "On the Effect of Initial Curvature on Cracked Flat Sheets," *International Journal of Fracture Mechanics*, Vol. 5, No. 4, December 1969, pp. 327-346.
- ¹⁰Folias, E. S., "Asymptotic Approximations to Crack Problems in Shells," *Mechanics of Fracture - Plates and Shells with Cracks*, G. C. Sih, H. C. van Elst, and D. Broek, eds., Noordhoff International, Leyden, 1977, pp. 117-160.
- ¹¹Copely, L. G., and Sanders, J. L., Jr., "A Longitudinal Crack in a Cylindrical Shell under Internal Pressure," *International Journal of Fracture Mechanics*, Vol. 5, No. 2, June 1969, pp. 117-131.
- ¹²Erdogan, F., and Kibler, J. J., "Cylindrical and Spherical Shells with Cracks," *International Journal of Fracture Mechanics*, Vol. 5, No. 3, September 1969, pp. 229-237.
- ¹³Erdogan, F., and Ratwani, M., "Fatigue and Fracture of Cylindrical Shells Containing a Circumferential Crack," *International Journal of Fracture Mechanics*, Vol. 6, No. 4, September 1970, pp. 379-392.
- ¹⁴Duncan-Fama, M. E., and Sanders, J. L., Jr., "A Circumferential Crack in a Cylindrical Shell under Tension," *International Journal of Fracture Mechanics*, Vol. 8, No. 1, March 1972, pp. 15-20.
- ¹⁵Peters, Roger W., and Kuhn, Paul, "Bursting Strength of Unstiffened Pressure Cylinders with Slits," NACA TN 3993, April 1957.
- ¹⁶Anderson, Robert B., and Sullivan, Timothy L., "Fracture Mechanics of Through-Cracked Cylindrical Pressure Vessels," NASA TN D-3252, February 1966.
- ¹⁷Chen, D., "Bulging of Fatigue Cracks in a Pressurized Aircraft Fuselage," Ph.D. Thesis, Delft University of Technology, Delft, The Netherlands, Report LR-647, October 1990.
- ¹⁸Jeong, D. Y., and Tong, P., "Nonlinear Bulging Factor Based on R-Curve Data," Proceedings of the FAA/NASA International Symposium on Advanced Structural Integrity Methods for Airframe Durability and Damage Tolerance, September 1994, pp. 327-338.
- ¹⁹Bakuckas, J. G., Ngugen, P. V., and Bigelow, C. A., "Engineering Fracture Parameters for Bulging Cracks in Pressurized Unstiffened Curved Panels," Proceedings of the FAA-NASA Symposium on Continued Airworthiness of Aircraft Structures, DOD/FAA/AR-97/2, 1996.
- ²⁰Bakuckas, J. G., Jr., Nguyen, P. V., Bigelow, C. A., and Broek, D., "Bulging Factors for Predicting Residual Strength of Fuselage Panels," Presented at the International Conference on Aeronautical Fatigue, Edinburgh, Scotland, June 18-20, 1997.
- ²¹Riks, E., "Bulging Cracks in Pressurized Fuselages: A Numerical Study," NLR Report NLR-MP-87058 U, NLR National Aerospace Laboratory, The Netherlands, 1978.
- ²²Riks, E., Brogan, F. A., and Rankin, C. C., "Bulging Cracks in Pressurized Fuselages: A Procedure for Computation," in *Analytical and Computational Models of Shells*, Noor, A. K., Belytschko, T., and Simo, J. C., eds., The American Society of Mechanical Engineers, ASME-CED, Vol. 3, 1989.
- ²³Budiman, H. T., and Lagace, P. A., "Nondimensional Parameters for Geometric Nonlinear Effects in Pressurized Cylinders with Axial Cracks," *Journal of Applied Mechanics*, Vol. 64, 1997, pp. 401-407.
- ²⁴Budiman, H. T., "Mechanisms of Damage Tolerance and Arrest in Pressurized Composite Cylinders," Ph.D. Thesis, Department of Aeronautics and Astronautics, Massachusetts Institute of Technology, Cambridge, MA, 1996.
- ²⁵Young, R. D., Rose, C. A., and Starnes, J. H., Jr., "Nonlinear Local Bending Response and Bulging Factors for Longitudinal and Circumferential Cracks in Pressurized Shells," Proceedings of the 3rd Joint FAA/DoD/NASA Conference on Aging Aircraft, Albuquerque, NM, September 20-23, 1999.
- ²⁶Rose, C. A., Young, R. D., and Starnes, J. H., Jr., "Nonlinear Local Bending Response and Bulging Factors for Longitudinal Cracks in Pressurized Cylindrical Shells," Proceedings of the 40th AIAA/ASME/ASCE/AHS/ASC Structures, Structural Dynamics, and Materials Conference, St. Louis, MO, April 12-15, 1999, AIAA Paper No. 99-1412.

- ²⁷Young, R. D., Rose, C. A., and Starnes, J. H., Jr., "Skin, Stringer, and Fastener Loads in Buckled Fuselage Panels," Proceedings of the 42nd AIAA/ASME/ASCE/AHS/ASC Structures, Structural Dynamics and Materials Conference, Seattle, WA, April 2001, AIAA Paper No. 2001-1326.
- ²⁸Rose, C. A., Young, R. D., and Starnes, J. H., Jr., "The Nonlinear Response of Cracked Aluminum Shells Subjected to Combined Loads," Proceedings of the 42nd AIAA/ASME/ASCE/AHS/ASC Structures, Structural Dynamics and Materials Conference, Seattle, WA, April 2001, AIAA Paper No. 2001-1395.
- ²⁹Starnes, J. H., Jr., and Rose, C. A., "Nonlinear Response of Thin Cylindrical Shells with Longitudinal Cracks and Subjected to Internal Pressure and Axial Compression Loads," Proceedings of the 38th AIA/ASME/ASCE/AHS/ASC Structures, Structural Dynamics and Materials Conference, April 1997, AIAA Paper No. 97-1144, April 1997.
- ³⁰Ratwani, M. M., and Wilhem, D. P., "Influence of Biaxial Loading on Analysis of Cracked Stiffened Panels," *Engineering Fracture Mechanics*, Vol. 11, 1979, pp. 585-593.
- ³¹Gökgöl, O., "Crack Free and Cracked Life of the Pressurized Cabin of the A300B – Calculation, Tests and Design Measurements to Improve Damage Tolerance," *Aeronautical Journal*, January 1979.
- ³²Rybicki, E. F., and Kanninen, M. F., "A Finite Element Calculation of Stress Intensity Factors by a Modified Crack Closure Integral," *Engineering Fracture Mechanics*, Vol. 9, 1977, pp. 931-938.
- ³³Hui, C. Y., and Zehnder, A. T., "A Theory for the Fracture of Thin Plates Subjected to Bending and Twisting Moments," *International Journal of Fracture*, Vol. 61, No. 3, 1993, pp. 211-229.
- ³⁴Starnes, J. H., Jr., Newman, J. C., Jr., Harris, C. E., Young, R. D., Rose, C. A., and James, M. A., "Advances in Residual Strength Analyses from Laboratory Coupons to Structural Components," Proceedings of the ICAF 2001 International Committee on Aeronautical Fatigue 21st Symposium, Toulouse, France, June 2001.
- ³⁵Newman, J. C., Jr., "An Elastic-Plastic Finite Element Analysis of Crack Initiation, Stable Crack Growth, and Instability," ASTM STP 833, 1984, pp. 93-117.
- ³⁶Dawicke, D. S., Sutton, M. A., Newman, J. C., Jr., and Bigelow, C. A., "Measurement and Analysis of Critical CTOA for an Aluminum Alloy Sheet," NASA TM-109024, September 1993.
- ³⁷Dawicke, D. S. and Newman, J. C., Jr., "Residual Strength Predictions for Multiple Site Damage Cracking Using a Three-Dimensional Finite Element Analysis and a CTOA Criterion," In *Fatigue and Fracture Mechanics: 29th Volume*, ASTM STP 1332, 1998, pp. 815-829.
- ³⁸Dawicke, D. S. and Sutton, M. A., "Crack Tip Opening Angle Measurements and Crack Tunneling Under Stable Tearing in Thin Sheet 2024-T3 Aluminum Alloy," NASA CR-191523, September 1993.
- ³⁹Shivakumar, K. N. and Newman, J. C., Jr., "ZIP3D - An Elastic-Plastic Finite-Element Analysis Program for Cracked Bodies," NASA TM-102753, 1990.
- ⁴⁰Dawicke, D. S. and Newman, J. C., Jr., "Residual Strength Predictions for Multiple Site Damage Cracking Using a Three-Dimensional Finite Element Analysis and a CTOA Criterion," In *Fatigue and Fracture Mechanics: 29th Volume*, ASTM STP 1332, T. L. Panontin and S. D. Sheppard, Eds. American Society for Testing and Materials, 1998.
- ⁴¹Dawicke, D. S., Newman, J. C., Jr., and Bigelow, C. A., "Three-Dimensional CTOA and Constraint Effects During Stable Tearing in a Thin-Sheet Material," In *Fracture Mechanics: 26th Volume*, ASTM STP 1256, 1995, pp. 223-242.
- ⁴²Newman, J. C., Jr., "Finite Element Analyses of Fatigue Crack Propagation -- Including the Effects of Crack Closure," Ph.D. Thesis, Virginia Polytechnic Institute and State University, Blacksburg, VA, May 1974.
- ⁴³Dawicke, D. S., "Residual Strength Predictions Using a Crack Tip Opening Angle Criterion," FAA-NASA Symposium on the Continued Airworthiness of Aircraft Structures, DOT/FAA/AR-97/2, Vol. II, July 1997, pp. 555-566.
- ⁴⁴Seshadri, B. R., Newman, J. C., Jr., Dawicke, D. S., and Young, R. D., "Fracture Analysis of the FAA/NASA Wide Stiffened Panels," Proceedings of the FAA-NASA Symposium on the Continued Airworthiness of Aircraft Structures," DOT/FAA/AR-92/2, 1997, pp. 513-524.
- ⁴⁵Starnes, James H., Jr., and Rose, Cheryl A., "Stable Tearing and Buckling Response of Unstiffened Aluminum Shells with Long Cracks," Proceedings of the Second Joint NASA/FAA/DOD Conference on Aging Aircraft, Williamsburg, VA, August 31-September 3, 1998. NASA/CP-1999-208982/Part 1, pp. 610-626, January 1999.
- ⁴⁶Young, Richard D., Rouse, Marshall, Ambur, Damodar R., and Starnes, James H., Jr., "Residual Strength Pressure Tests and Nonlinear Analyses of Stringer- and Frame-Stiffened Aluminum Fuselage Panels with Longitudinal Cracks," Proceedings of the Second Joint NASA/FAA/DOD Conference on Aging Aircraft, Williamsburg, VA, August 31-September 3, 1998. NASA/CP-1999-208982/Part 1, pp. 408-426, January 1999.

⁴⁷Ambur, Damodar R., Rouse, Marshall, Young, Richard D., and Perez-Ramos, Carlos, "Evaluation of an Aluminum Panel with Discrete-Source Damage and Subjected to Combined Loading Conditions," Proceedings of the 40th AIAA/ASME/ASCE/AHS/ASC Structures, Structural Dynamics, and Materials Conference, St. Louis, MO, April 12-15, 1999. AIAA Paper AIAA-99-1439, 1999.

⁴⁸Dawicke, David S., Newman, James C., Jr., Starnes, James H., Jr., Rose, Cheryl A.; Young, Richard D. and Seshadri, B. R., "Residual Strength Analysis Methodology: Laboratory Coupons to Structural Components," Proceedings of the Third Joint FAA/DOD/NASA Conference on Aging Aircraft, Albuquerque, NM, September 20-23, 1999.

⁴⁹Dawicke, D. S., Newman, J. C., Jr., Sutton, M. A., and Amstutz, B. E., "Influence of Crack History on the Stable Tearing Behavior of a Thin-Sheet Material with Multiple Cracks," NASA CP 3274, FAA/NASA International Symposium on Advanced Structural Integrity Methods for Airframe Durability and Damage Tolerance, Part 1, 1994, pp. 193-212.

This page left blank intentionally.

Safety & Certification Initiatives for Composite Airframe Structure

Larry B. Ilcewicz *

Federal Aviation Administration, Renton, WA, 98055

and

Brian Murphy†

National Transportation Safety Board, Washington, D.C., 20594

The use of advanced composite materials in airframe structures has steadily increased since the 1970s. Currently, the applications have expanded to include empennage, fuselage, wing and dynamic components of small airplanes, transport aircraft and rotorcraft. Composite safety and certification initiatives (CS&CI) were derived to address technical areas important to the development and certification of composite aircraft structures. This paper will summarize some background related to important contributions from the National Aeronautics and Space Administration (NASA) and recent work for composite airframe structures, including highlights of Dr. Jim Starnes' contributions.

I. □ Background

Use of advanced composite materials in commercial and military airframe structures has steadily increased since the 1970s. As this occurred, the expectation has been that any new technology will perform as well or better than existing metal structure. Considerable research helped establish an initial understanding and early applications provided proof of composite designs, which could be safely applied to airframe structure. Technology advancements and solutions to a few problems that occurred over time have helped to further evolve the state-of-the-art in composite applications.

Early applications of composites were limited to secondary structure, which were not critical to safety of flight. Over time the applications expanded to include most structures on small airplanes, including wings and pressurized fuselage. Transport aircraft applications evolved to include control surfaces and empennage structures for many different aircraft models by the end of the 1900s. New transport aircraft designs are currently being developed for composite wing and fuselage structure. Propeller and rotor blades for helicopters have long been using composite materials. More recently, composite structural components have been implemented in the rotor drive system of some helicopters. Future reusable launch vehicles for space applications also plan to use composite airframe structure.

NASA Langley Research Center (LaRC) provided leadership for early composite applications to aircraft structure. Several prototype programs in the 1970s and 1980s led the development and certification of composite aircraft structure that flew many years on a limited number of transport airplanes. For example, the NASA Aircraft Energy Efficiency (ACEE) program resulted in Boeing, McDonnell Douglas and Lockheed prototype empennage structure. Dr. Jim Starnes was one of the key technical focal representing NASA LaRC in these efforts. Since the NASA prototype programs preceded production applications, they became a basis for early certification guidance available for composite airframe structure.

The NASA ACEE Program was very successful in providing a good basis for the use of composite materials in transport aircraft applications such as the Boeing 777 empennage structure¹. Figure 1 shows the structural arrangement of the composite Boeing 737 horizontal stabilizer and a schematic diagram of the building block

* Chief Scientific & Technical Advisor for Advanced Composites, 1601 Lind Ave. SW, ANM-115N, Renton, WA, 98055, New AIAA Member.

† Aircraft Structures Engineer, Office of Aviation Safety, 490 L'Enfant Plaza, Washington, DC, 20594, New AIAA Member.

approach used to develop and certify this airframe structure². Five shipsets of Boeing 737 horizontal stabilizers entered service in 1984. These airframe structures have accumulated many flight hours of commercial service.

Developed and certified under NASA Aircraft Energy Efficiency, ACEE, program (1977-1982)

NASA ACEE 737 Horizontal Stabilizer Structural Arrangement

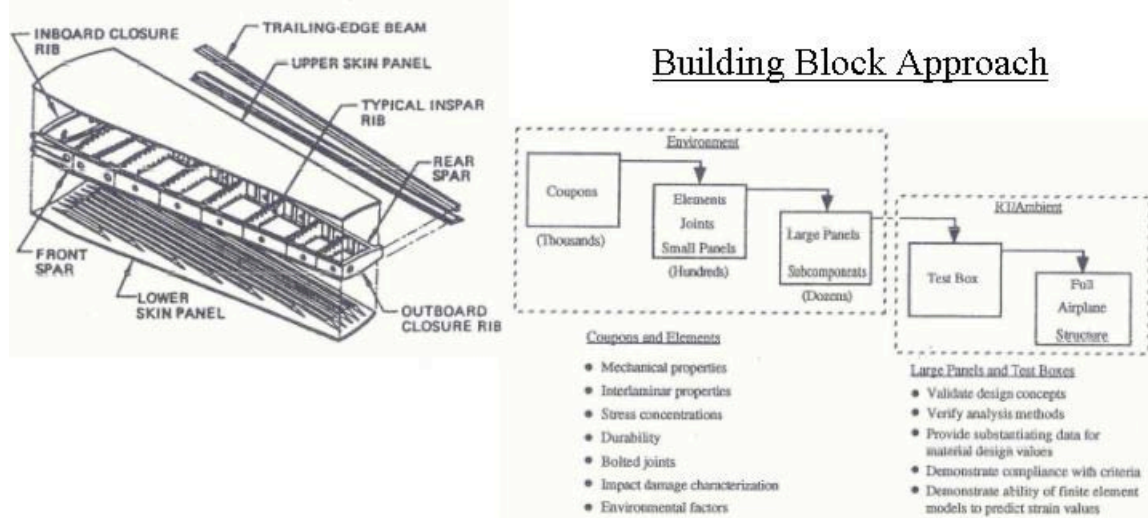


Figure 1. Boeing 737 Composite Horizontal Stabilizer Development and Certification Under the NASA ACEE Program^{1,2}.

A summary of the maintenance program and service experiences of the composite Boeing 737 horizontal stabilizer has been documented³. The most significant service-induced damage to these stabilizers has been a result of accidental impact events. As designed, the structure was damage tolerant to such events, which included fan blade penetration of the lower skin and severe impact of the front spar from engine run-up at the edge of a runway (resulting in impact of the stabilizer leading edge by large chunks of runway debris).

Figure 2 shows a summary of the service history for the five shipsets of composite Boeing 737 horizontal stabilizers. Shipset numbers 4 and 5 were recently retired and have become the subject of joint FAA and Boeing research, which includes nondestructive inspection (NDI), physical & chemical property measurements, destructive evaluation using microscopy and mechanical testing². To date, inspections have found little deterioration due to wear, fatigue, or environmental factors. Production NDI results indicated that today's factory "standard", which is applied to Boeing 777 composite empennage structure, is advanced beyond that of early 1980s. Figure 3 shows the results of ultrasonic scans using both methods. Subsequent microscopic cross-sections indicate that the NDI indications from the higher frequency ultrasonic methods used today relate to significant amounts of porosity, which was present in the 737 horizontal stabilizer structure during eighteen years of service.

Teardown inspections performed to date have revealed additional information on the state of retired, composite Boeing 737 horizontal stabilizers². Fasteners and liquid shim were noted to be in good condition during torque box disassembly. The corrosion and lightning strike protection schemes were also found to be durable and performed as intended throughout the life of the airframe. An apparent small drop in the composite glass transition temperature is currently under study. Figure 4 shows the results of some mechanical tests performed with samples cut from the skin panels².

Shipset	Production Line Number	Entry into Service	Status as of October 31, 2004
1	1003	2 May 1984	In service (58000 hours, 43000 flights)
2	1012	21 March 1984	In service (58000 hours, 44000 flights)
3	1025	11 May 1984	Damaged beyond repair 1990; partial teardown of stabilizers completed 1991 (17300 hours, 19300 flights).
4	1036	17 July 1984	Stabilizers removed from service 2002 (approx. 39000 hours, 55000 flights); partial teardown of right hand unit
5	1042	14 August 1984	Stabilizers removed from service 2002 (approx. 52000 hours, 48000 flights); teardown of left hand unit reported here; right hand unit donated to the FAA Tech Center (FAATC) for their teardown activities being conducted at the National Institute for Aviation Research (NIAR) at Wichita State University

Figure 2. Boeing 737 Composite Horizontal Stabilizer Service Experience [2].

Factory Ultrasonic Scans of Skin Panels

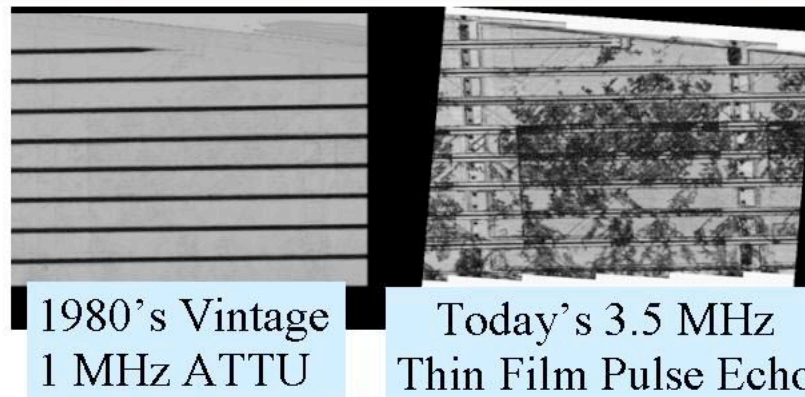


Figure 3. Boeing 737 Composite Horizontal Stabilizer Teardown Inspection Using Ultrasonic Methods from 1980 and Current Day [2].

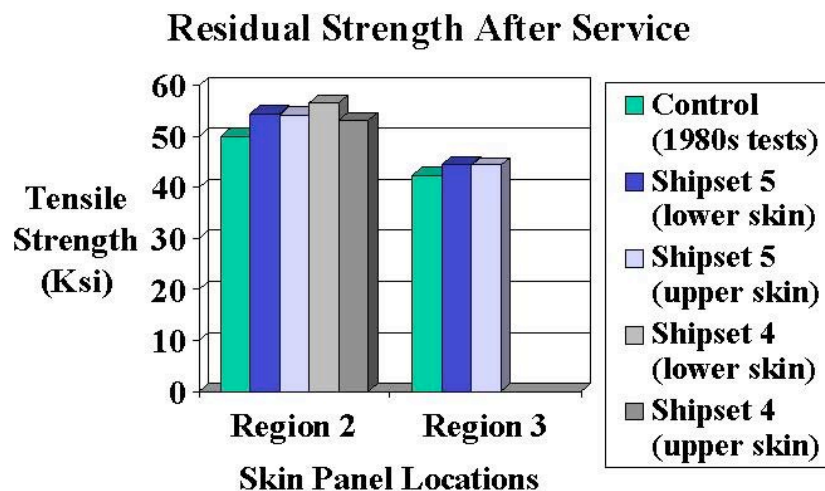


Figure 4. Mechanical Testing of Samples Taken from the Boeing 737 Composite Horizontal Stabilizer After Many Years of Service [2].

Following ACEE, the NASA Advanced Composite Technology (ACT) Program started in the late 1980s and lasted through much of the 1990s. As part of the ACT program, McDonnell Douglas and Boeing studied transport composite wing and fuselage structure, respectively. Dr. Jim Starnes was again one of the key technical focal representing NASA LaRC in technical oversight of the ACT program. His influence on the design, structural analysis and testing of composite airframe structure led to numerous advances, which are important to the current development of Boeing 787 composite structures. Boeing's ACT achievements in composite fuselage development are documented^{4,5}.

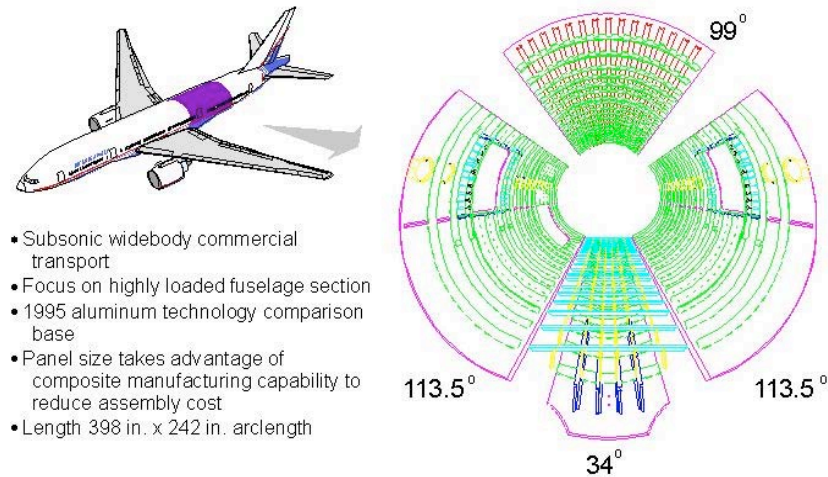


Figure 5. NASA/Boeing ACT Composite Fuselage Development Program.

In recent years, composite applications have expanded at an increased rate, while the technology continues evolving to reduce costs. Figure 6 summarizes the current state of applications to transport aircraft, rotorcraft and small airplanes. Expanding applications have justified a need to document engineering guidelines and update rules, policies and guidance used for FAA certification. With increased applications, also come the needs to standardize, when possible, and provide sufficient training for the workforce. Joint efforts between industry, government agencies and academia are needed to help ensure safe and efficient deployment of composite technologies used in existing and future aircraft. NASA LaRC was recently involved in such efforts for small airplanes through the program called Advanced General Aviation Transport Experiments (AGATE). The Mil-Handbook-17 and other standards organizations, such as ASTM and SAE, continue to provide a forum for composite technical issues and expanding applications.



Figure 6. Existing State-of-the-Art in Composite Aircraft Structures.

II. □ Composite Safety and Certification Initiatives

The FAA has developed composite safety and certification initiatives (CS&CI) for regulatory work with industry, government agencies and academia. One objective of CS&CI is to ensure safe and efficient deployment of composite technologies used in existing and future aircraft structure. Another objective is to update related policies, advisory circulars, training and the detailed background, which is used to support standardized composite engineering practices.

Figure 7 illustrates the approach used for CS&CI. Moving from left to right in the figure, internal policies are evolved into mature certification practices over time. The FAA derives initial regulatory policies for composites based on past certification programs and service experiences. Focused research and other industry interfaces are used to transition the initial, often unwritten policies, into documented procedures and guidance for review by regulatory agencies and the aviation industry. Another factor affecting the directions taken with CS&CI are new technology considerations of interest to the industry.

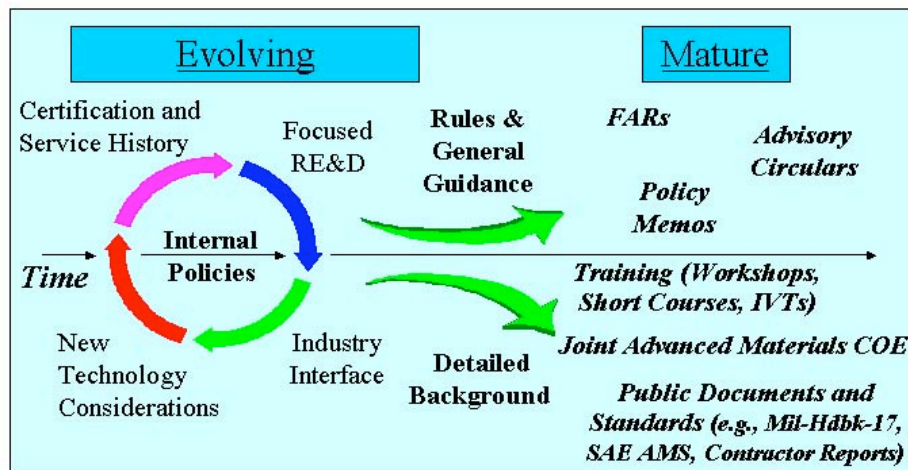


Figure 7. FAA Approach to Composite Safety & Certification Initiatives.

As shown in Figure 7, detailed background is developed to complement and facilitate technology transfer of the composite regulatory practices. Detailed background includes research reports, engineering standards and training. The FAA Joint Advanced Materials and Structures Center of Excellence (JAMS COE), which is comprised of several U.S. universities (see Figure 8) and numerous partners from the aviation industry, support CS&CI in research and training activities.

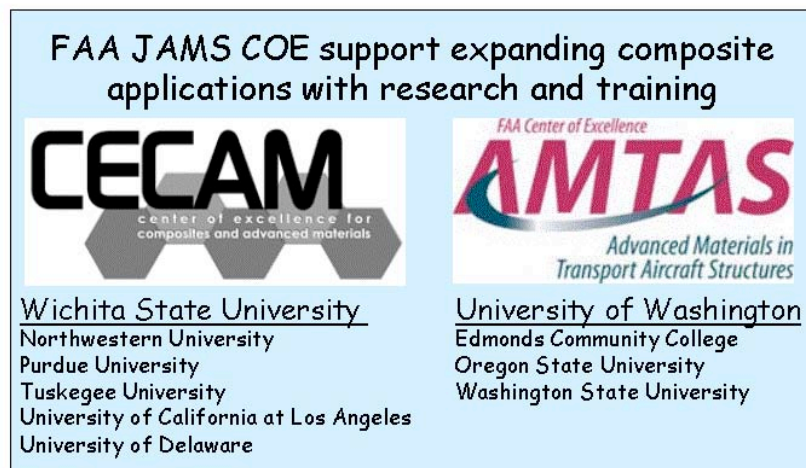


Figure 8. FAA Joint Advanced Materials & Structures Center of Excellence.

III. □ Critical Technical Issues

The CS&CI, which are currently active for composite aircraft structures, address the technical areas listed in Figure 9. Initiatives have been established for these technical areas because they often require considerable attention in development and certification. Advances in engineering practices and future trends in these areas also require the joint efforts of regulatory agencies and industry.

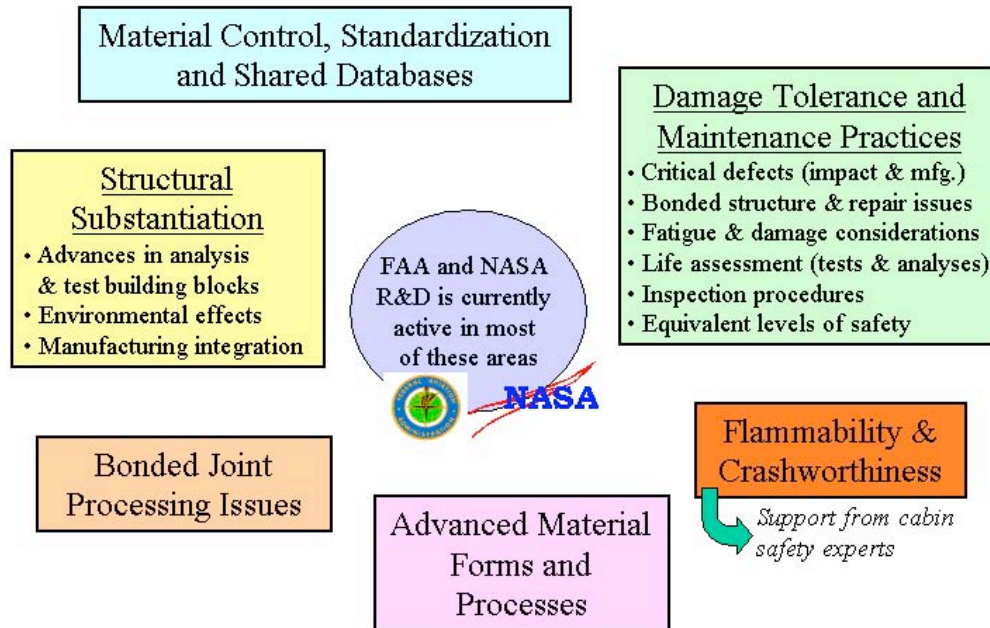


Figure 9. Technical Thrust Areas for Composite Safety & Certification Initiatives.

Composite aircraft manufacturers are faced with a more complicated endeavor in achieving material & process qualification and control than exists for metal structures. Composite materials typically don't chemically advance to a final, usable state until relatively large parts are fabricated and cured. Often times, bonding uses additional curing to assemble previously fabricated composite parts into larger components of the airframe. As a result, composite manufacturing processes have more implications to structural performance and methods of substantiation. Shared material databases and the standardization of material & process control procedures also don't exist for composite applications like they do for metals. Advances in Mil-Handbook-17 over the years and recent AGATE thrusts have led to some significant advances in the areas of material standardization and shared databases, which led to new CS&CI policies and guidance.

Composite airframe structures have proven to be more fatigue resistant than the metal counterparts for design strain levels used in applications. However, composites are more sensitive to accidental damage such as foreign object impact, which together with the effects of design details (e.g., bolted joints and cutouts), limit the operating strain levels. Impact damage becomes a threat to composite residual strength in compression and shear, as well as tension. These unique sensitivities have led to distinct differences in the procedures used to substantiate the fatigue and damage tolerance of composite versus metal structures. The flammability and crashworthiness of composite transport wing and fuselage structures have not been studied to the same level as existing metal structure because such applications are relatively new. As shown in Figure 9, support from cabin safety experts will be sought as the CS&CI take on future tasks in these areas.

Significant progress of relevance to different aircraft product types has been gained to date for the thrust areas shown in Figure 9. The progress achieved for CS&CI since 1999 will be summarized in the subsequent section. Dr. Jim Starnes played an important role in developing the technical plans used for CS&CI, including joint research by FAA, NASA and industry groups. An e-mail received from Dr. Jim Starnes in the summer of 2003, which relates to CS&CI, is shown in Figures 10 ⁶. Figure 11 shows program elements from a proposal contained in this e-mail. Note that one of the program elements addresses certification technology for composite structures. Figure 12 gives some details on the NASA LaRC research areas, which directly support CS&CI.

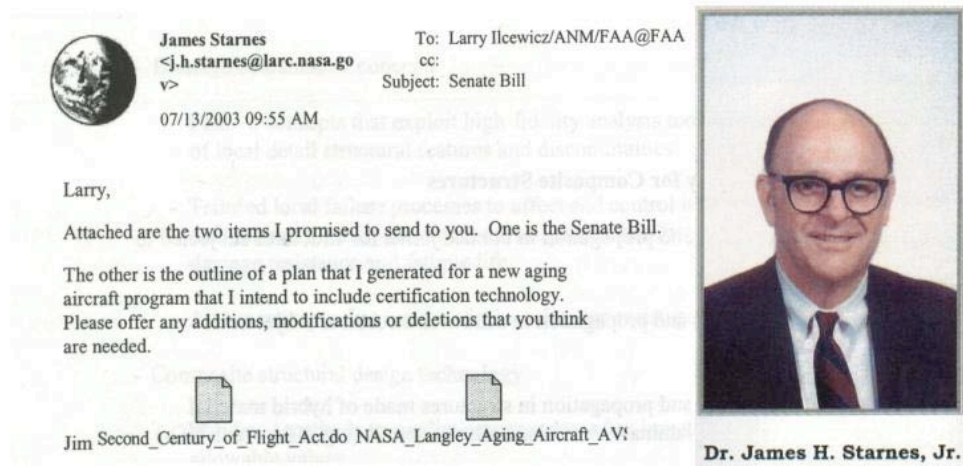


Figure 10. July 13, 2003 Communication from Dr. Jim Starnes [6].

NASA Langley Research Center Research and Development Topics for
**Strength Degradation Prediction Methods and
 Damage Science for Aging Airframe Structures**
 James H. Starnes
 Structures and Materials Competency
Program Focus
 Program focus is on both metallic & composite structures and materials

Program Elements

- Advanced NDE methods for aging aircraft
- Determination of environmental effects on damage initiation
- Structural integrity, durability and residual strength of built-up structures subjected to combined loads
- Reliability based design and analysis technology
- ***Certification technology for composite structures***

Figure 11. Dr. Jim Starnes Proposal for NASA Research⁶.

As shown in Figure 12, support on certification technology from NASA LaRC addressed many areas. Recently, a large NASA program addressing the fourth bullet in the figure was initiated at Wichita State University, which is one of the universities leading the FAA JAMS COE. This effort is called the National Center for Advanced Material Performance (NCAMP). Dr. Jim Starnes was a strong advocate for principles of composite material and process control, which advance the current state-of-the-art practiced by industry into standards that ensure repeatable design, manufacturing and maintenance implementation of airframe structures. He believed that rigorous material and process control was a cornerstone for advances in composite technology such as more rigorous analysis methods to predict the strength, durability and damage tolerance of built-up airframe structures. The NCAMP plans were recently discussed at March 2005 Mil-Handbook-17 Meetings, with an emphasis on the material and process controls needed for *design, manufacturing and maintenance*.

Certification Technology for Composite Structures

- Damage initiation and propagation in bonded joints for structures subjected to combined loads
- Damage initiation and propagation in sandwich structures subjected to combined loads
- Damage initiation and propagation in structures made of hybrid material systems including laminates with dissimilar materials (e.g., Glare and TiGr)
- Advanced building-block design approach that links multiple dimensional length scales and includes the effects of structural and material parameter variability

Figure 12. Dr. Jim Starnes Proposal for NASA Research on Certification Technology for Composite Structures⁶.

Some barriers to expanded composite applications, which may add to safety concerns, include issues related to manufacturing costs, maintenance technology, training and lack of standardization. The industry is currently pursuing advanced material forms and processes, which don't have the service experience of proven composite technology, in hopes of reducing manufacturing costs. Safety concerns listed in Figures 9 and 12 must be addressed for these new materials and processes to prepare for expanding applications. Composite maintenance procedures must also continue to evolve to efficiently meet the needs of expanding applications. This includes sufficient training to add to the limited resources (engineers, inspectors and technicians), which are proficient in composites, and standardization to facilitate the teaching of more common engineering practices.

I had many discussions with Dr. Jim Starnes on the gap that exists between much of the composite research and training available in college curriculum and the needs of industry. Both of us believe that this relates to proprietary industry practices for composites and a lack of standards, which are typically not visible to those in academic institutions. As a result, most college graduates entering the job market for composites used in aerospace are faced with a transition period where on-the-job training is needed to supplement their formal education. This is also an issue for the existing work force, which is expected to take on more tasks involving composites as applications expand. Although such is common with other emerging aircraft technologies, the overall visibility of industry practices for composite airframe applications is far behind that of metal. Joint FAA and NASA efforts in CS&CI were committed to overcoming some of these shortcomings in education by benchmarking industry practices in workshops and developing associated standards and training for use by the industry. It is our hope that universities will adopt some of these efforts. The FAA JAMS COE will help lead the way.

IV. Status of Composite Safety and Certification Initiatives

General guidance for certification of composite airframes has been documented in Advisory Circular 20-107A (Composite Aircraft Structure), which was last updated on 4/25/84⁷. As discussed previously, the NASA ACEE program provided a good basis for this early guidance material, which is still applied for composite certification. Since that timeframe other advisory circulars have also been developed for composites including AC 21-26 (Quality Control for the Manufacture of Composite Structures, 6/26/89)⁸ and AC 145-6 (Repair Stations for Composite and Bonded Aircraft Structure, 11/15/96)⁹.

Currently, expanding applications of composites are driving a need for more definitive guidance and policy to support certification, operations and maintenance. The active CS&CI are striving to meet these needs based on certification experiences and service history. As a result, the interface with industry in such activities, as well as knowledge on their pursuit of new technologies, provides a starting point for all CS&CI. Focused research is used to fill the gaps between the different means of certification compliance used in applications, service experiences and

findings uncovered in accident or incident investigations. The overall approach is to evolve internal, unwritten policies applied in past programs into mature, documented policies and guidance with detailed background captured in engineering reports and standards. This is followed by the development of associated training curricula for the government and industry workforce. Figure 7 showed a schematic summarizing the CS&CI approach.

Significant progress has been achieved in CS&CI since 1999. Dr. Jim Starnes has played a supporting role in many of these accomplishments. Policy and training for composite material qualification and equivalency testing for shared databases was initially developed in 2000 and updated in 2003¹⁰. Policy and training for composite static strength substantiation was developed in 2001 based on small airplane certification experiences¹¹. A new rule and advisory circular was drafted for damage tolerance and fatigue evaluation of composite rotorcraft structure in 2002^{12,13}. In 2003, an advisory circular on material procurement and process specifications for polymer matrix composite systems (AC 23-20) was released¹⁴. Revision F to Mil-Handbook-17 was released in 2002¹⁵. Workshops were held in each of the years from 2000 to 2004 on the subjects of material control, structural substantiation, bonded structure and new material forms & processes. Finally, research progress has been achieved in structural substantiation, bonded joints, damage tolerance and repair to support the development of future policy, guidance and training.

The CS&CI efforts in 2004 and 2005 were focused on bonded joints and attachments used in aircraft structure. An industry survey and two workshops were held in 2004 to benchmark bonded structures technology used in aircraft applications and provide a basis for initial regulatory guidance, which is scheduled for release in 2005. Future directions in CS&CI for bonded structures were also derived from the 2004 studies. Research and detailed background development for the CS&CI on bonded aircraft structures have been ongoing since 1999. Some of these research efforts were supported by NASA under the direction of Dr. Jim Starnes¹⁶.

The primary objective of the two FAA Bonded Structures Workshops held in 2004 was to collect and document technical details that need to be addressed for bonded structures, including critical safety issues and certification considerations. There were also several secondary objectives for the workshops. Invited speakers were asked to give examples of proven engineering practices for the technical subjects addressed in the workshop. Participants were asked to identify future needs in engineering guidelines, standard tests, and shared databases & specifications. Finally, participants were asked to provide directions for bonded structure research and technology development, which supports safety and certification.

The first FAA Bonded Structures Workshop was held in Seattle, WA immediately following Mil-Handbook-17 Meetings on June 16 to 18, 2004. There were more than 150 participants in attendance at this workshop, which proved to be very useful for CS&CI on bonded structures. The workshop addressed applications in many different aircraft product types, including small airplanes, business jets, transport aircraft, fighter jets, rotorcraft and propellers. Commercial and military applications of composite and metal bonding were reviewed. Workshop sessions spent time gaining agreement on the technical issues for material & process control, design development, structural substantiation, manufacturing implementation, maintenance practices and service experiences. There were numerous presentations by industry and military bonding experts from around the world.

In order to increase European participation in the CS&CI, another FAA Bonded Structures Workshop was held in London on October 26 and 27, 2004. The Civil Aviation Authority (CAA) hosted this workshop near Gatwick Airport. The CAA organized the speakers from European industry and helped run the workshop, which had an agenda similar to that used by the U.S. workshop. There were about 50 participants for this workshop, which provided valuable information that was in general agreement with insights collected at the U.S. workshop.

Figure 13 summarizes the technical scope of the Bonded Structures Workshop. The main technical subjects are given in boxes appearing in the four corners of the figure. Regulatory considerations are listed in the center of the figure. The workshop covered all facets of structural bonding from material & process definition through structural design development and certification, manufacturing implementation and maintenance practices. Although these subjects were covered separately, experts participating in the workshop understood the importance of integrated teamwork for successful bonding applications.

Presentations and other related materials from 2004 FAA Bonded Structures Workshops in both Seattle and London can be viewed, downloaded and printed at:

<http://www.niar.twsu.edu/faa/>

Note that this website also contains materials from previous FAA workshops held on material control in 2002 and 2003. The CS&CI information collected at workshops and published in FAA Technical Center Documents contains considerable amounts of technical data and insights derived from industry applications to composite aircraft structures, which are not found in any other public information. A report summarizing the industry survey and workshops for bonded structures was recently drafted¹⁷. This information can be used by the FAA JAMS COE and other universities or educational groups in developing training for the expanding composite workforce.

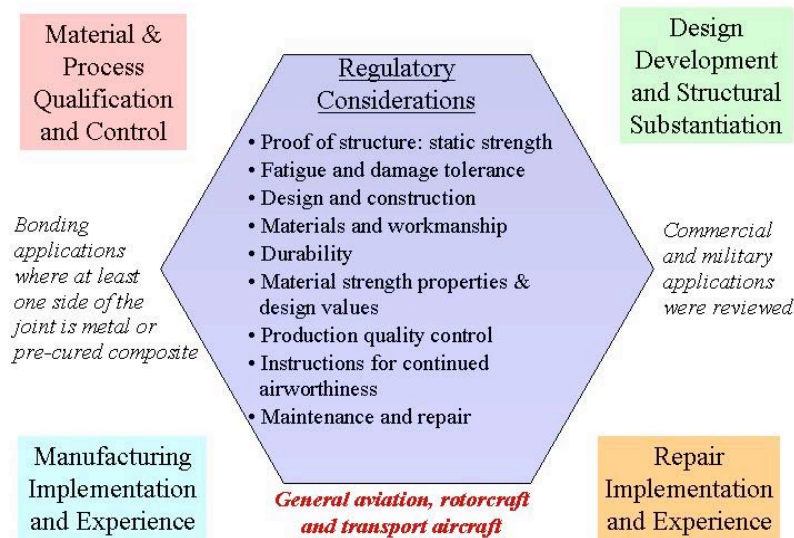


Figure 13. Technical Scope of 2004 FAA Bonded Structures Workshops.

Progress in CS&CI is periodically reviewed in meetings held by composite engineering organizations such as Mil-Handbook-17, SAE Committee P-17, SAE Commercial Aircraft Composite Repair Committee (CACRC) and ASTM D-30. The interface with these groups is important to the development of standards, training and documentation of detailed engineering practices, which support certification, operations and maintenance of composite aircraft structure. The JAMS COE, which was recently established by the FAA, will also continue to play an important role in CS&CI research and education in the future.

V. □ American Airlines Flight #587 Accident Investigation

On November 12, 2001, American Airlines Flight 587 (AA587) crashed into a neighborhood in Belle Harbor, New York, several minutes after taking off from Kennedy International Airport. The airplane, which was an Airbus A300-600, was on a scheduled flight to Santo Domingo, Dominican Republic. All 260 persons aboard the airplane were fatally injured, as were five on the ground. The plane's vertical stabilizer, rudder and both engines separated from the aircraft before it impacted the ground. The vertical stabilizer structure was constructed mostly from composite materials. It was recovered largely intact because it failed at fin root attachment details and landed in water.

Structural evaluations supporting the National Transportation Safety Board (NTSB) AA587 accident investigation were performed at NASA LaRC. This NASA facility and its engineering resources were selected to support the investigation based on available laboratory facilities, equipment and past experiences with composite airframe structures. Dr. Jim Starnes led the efforts of the NASA LaRC AA587 investigation team. This team created in-depth photographic records and performed nondestructive evaluations of the failed vertical stabilizer, rudder and fuselage attachment details. Laboratory failure analyses were also performed, including fractographic investigation of failed composite and metal surfaces, to judge whether fatigue had contributed to the failure. Some of the primary tasks performed by the NASA team were in structural analyses and aeroelastic stability. These analyses were used to evaluate design and certification procedures, accident load cases and potential failure scenarios. Advanced progressive failure analyses were also used to predict structural failures and to support subcomponent tests at Airbus for the critical attachment detail.

A detailed fault tree was constructed at the start of the NTSB AA587 accident investigation to guide the efforts at NASA LaRC. At the highest level, the fault tree had two main branches as shown in Figure 14. Through the course of the investigation, evidence showed that the primary factors contributing to the accident were related to vertical fin loads much greater than expected. Some of the structures working group efforts focused on analyses and tests confirming that the AA587 loads derived from digital flight data recorders and flight simulations would cause failures similar to those observed in the accident. A special session of the 46th AIAA/ASME/ASCE/AHS/ASC Structures, Structural Dynamics, and Materials Conference provides some details on these studies, as well as the

inspections and laboratory failure analyses performed with the help of NASA LaRC. Based on nearly three years of accident investigation, the NTSB Safety recommendations were released at the end of 2004.

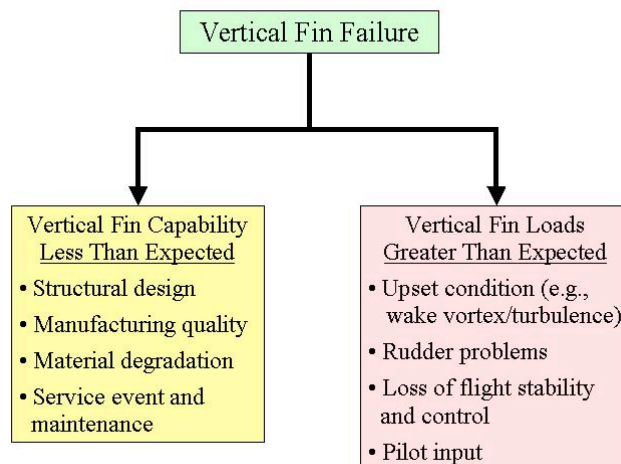


Figure 14. Two Main Branches of the Fault Tree Studied for the AA587 Accident.

Composite structures work performed in support of the AA587 accident investigation will have an effect on future CS&CI in several ways. Laboratory failure and structural analysis methods that were applied for the accident investigation have been documented for reference in future investigations involving composite structure. It is also desirable to use this information to develop training for composite failure analysis. In addition, candidate failure scenarios that were determined not to be the cause of the AA587 accident but remain a legitimate safety concern will continue to be studied in the interest of future accident risk mitigation.

VI. □ Conclusion

Use of advanced composite materials in commercial and military airframe structures has steadily increased since the 1970s. Throughout his career, Dr. Jim Starnes made many research contributions on structural analysis and testing important to composite airframe applications. He also worked with NASA LaRC engineers, the industry and FAA on other composite developments needed for applications to commercial aircraft structure in programs such as ACEE, ACT and AGATE. Highlights from these NASA programs are provided as background for current composite applications. The technical advice and leadership of Dr. Jim Starnes went beyond developments needed for initial applications to his support for accident investigation and technologies important to certification.

Expanding applications of composite airframe structures continue to evolve for small airplanes, rotorcraft and transport aircraft. Composite safety and certification initiatives for related technical issues depend on a strong interface between the FAA, industry, other government agencies (e.g., NASA, NTSB and DoD) and academia. The status of these initiatives, including plans and progress achieved to date, were reviewed in this paper. These efforts are continuously updated based on experiences from certification and service, as well as insights derived from accident or incident investigations. Focused research is used to advance a technical understanding of the issues and fill gaps between applications. Deliverables include policy, guidance, standards and training.

Dedication to Dr. James H. Starnes, Jr.

Dr. James H. Starnes had a brilliant career at NASA Langley Research Center (LaRC), where he contributed to the development and advancement of aeronautical and space structures for more than thirty years. His numerous contributions in thin shell stability and strength theory helped transform the industry from a strong dependence on empirical design methods to a balanced approach that included a combination of analysis and tests. Jim and his colleagues made this possible with an interface in real applications and careful attention to the associated structural details, including combined loads, damage, environmental effects, cutouts, and variations in stiffening element & skin geometry. As analysis procedures improved, his team sought further advancements to support design optimization, structural tailoring and insights on the effects of manufacturing variations. Jim's technical skills, willingness to share insights and practical regard for applications made him an excellent resource for accident investigation and certification technology development over the years.

References

- ¹Ilcewicz, L. B., Hoffman, D. J., and Fawcett, A. J., "Composite Applications in Commercial Airframe Structures," Chapter 6.07 from *Comprehensive Composites* Volume 6, published by Elsevier Science LTD, 2000.
- ²Hoffman, D. J., Kollgaard, J. and Miller, M., "Structural Teardown Inspection of an Advanced Composite Stabilizer for Boeing 737 Aircraft," 8th Joint FAA/DoD/NASA Aging Aircraft Conference, January 2005.
- ³Mabson, G.E., Fawcett, A. J. and Oakes, G.D., "Composite Empennage Primary Structure Service Experience," CANCOM Conference, Montreal, Canada, August 2001.
- ⁴Ilcewicz, L. B., "Scaling Crucial to Integrated Product Development of Composite Aerospace Structures: Part 1," *Composites Part A: Applied Science and Manufacturing*, 30, 1999, pp. 385-393.
- ⁵Ilcewicz, L. B., "Composite Technology Development for Commercial Airframe Structures," Chapter 6.08 from *Comprehensive Composites* Volume 6, published by Elsevier Science LTD, 2000.
- ⁶Starnes, J. H. Jr., "Strength Degradation Prediction Methods and Damage Science for Aging Airframe Structures," Structures & Materials Competency, NASA LaRC, attached to a July 13, 2005 e-mail to Larry Ilcewicz.
- ⁷"Composite Aircraft Structure," FAA Advisory Circular 20-107A, April 1984.
- ⁸"Quality Control for the Manufacture of Composite Structures," FAA Advisory Circular 21-26, June 1989.
- ⁹"Repair Stations for Composite and Bonded Aircraft Structure," FAA Advisory Circular 145-6, November 1996.
- ¹⁰"Material Qualification and Equivalency for Polymer Matrix Composite Material Systems," FAA Policy Memorandum PS-ACE100-2002-006, September 2003.
- ¹¹"Static Strength Substantiation of Composite Airplane Structure," FAA Policy Memorandum PS-ACE100-2001-006, December 2001.
- ¹²"Damage Tolerance and Fatigue Evaluation of Composite Rotorcraft Structure," Federal Aviation Administration FAR 27.573 and 29.573, Drafted in 2002 (pending Federal Registrar Process).
- ¹³"Substantiation of Composite Rotorcraft Structure," Advisory Circular 29-2C, MG8, Updated in 2002 for the new rules (pending Federal Registrar Process).
- ¹⁴"Acceptance Guidance on Material Procurement and Process Specifications for Polymer Matrix Composite Systems," FAA Advisory Circular 23-20, September 2003.
- ¹⁵"Composite Materials Handbooks, Mil-17, Volume 1 to 5," Revision F, ASTM International, 2002.
- ¹⁶Kim, H., Kwon, H. and Keune, J., "Buckling Initiation and Disbond Growth in Adhesively Bonded Composite Flanges," Proceedings of the 44th AIAA/ASME/ASCE/AHS/ASC Structures, Structural Dynamics, and Materials Conference, AIAA-2003-1996, April, 2003.
- ¹⁷Tomblin, J., Davies, C., Ilcewicz, L., Strole, K., Dodosh, G., "Assessment of Industry Practices for Aircraft Bonded Joints and Structures," DOT/FAA/AR-05/13, May 2005.

Damage Tolerance: A Status Report

Dr. Robert L. Sierakowski*

Air Force Research Laboratory Munitions Directorate
101 W. Eglin Blvd, Ste 105, Eglin Air Force Base, Florida 32542, USA

Abstract

The introduction of new materials such as advanced composites, leads to not only new attributes for aerospace structures, but also introduces new technological elements to be considered. Historically, structural aircraft design has progressed from wood structures (homogenous, anisotropic materials), to metallic structures (homogenous, isotropic materials), to advanced composite structures (homogenous, anisotropic materials). While the progression has come full circle so to speak, our technical knowledge in developing, understanding, and modeling the behavior of these materials has increased exponentially. For example, the Wright Brothers used wood structurally without understanding the nuances of anisotropy. As design experience changed to metallic structures, our understanding and modeling at the phenomenological level of homogeneity and isotropy in successful design practice became documented. With the introduction of advanced composite materials, the inherent anisotropy of such materials has led to new classes of failure mechanisms unlike previous experience with metallic materials. In addition to inherent anisotropy, such materials can be brittle, and the initiation and growth of damage remains to a degree as work in progress. This has led to a design approach which can be considered semi-empirical and relies on our continued and developing experience for design/certification. In this paper, we will explore the damage tolerance issues based on design requirements, current state of the art design and analysis, some selected examples, and concluding remarks.

I. Introduction

All aerospace vehicles must be designed such that the structural integrity of the platform is ensured. When we speak of structural integrity we infer the following¹:

$$\boxed{\text{Strength}} + \boxed{\text{Stiffness}} + \boxed{\text{Durability}} + \boxed{\text{Safety}}$$

or

$$\boxed{\text{Fatigue}} \quad \boxed{\text{Damage Tolerance}}$$

That is, at all times the strength, stiffness, durability, and damage tolerance of the structure are preserved. In the following presentation, focus is directed toward damage tolerance issues for structures.

Damage tolerance design for aerospace platforms can be dramatically illustrated through such recent events as the Aloha Airlines Boeing 737 aircraft structural failure in 1988 and the Delta Airlines MD-88 uncontained engine failure in 1996. Each of these events was attributed to accumulated undetectable fatigue damage². This can be graphically depicted in the accompanying Figure²:

*Chief Scientist, Air Force Research Laboratory Munitions Directorate, 101 W. Eglin Boulevard, Ste 105, Eglin Air Force Base, Florida, 32542, AIAA Member Grade of Fellow

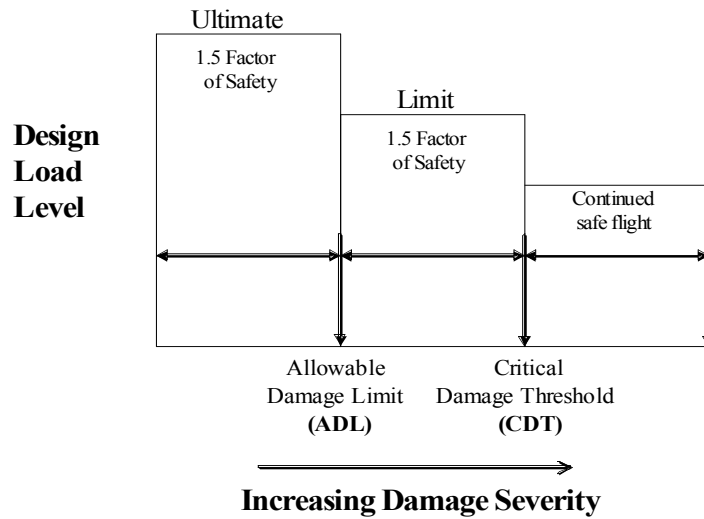


Figure 1. Definitions of durability and damage tolerance for commercial aircraft and associated design requirements (Mil-Hbk-17)²

What is clear in the above figure is that damage is accepted and the accompanying changes in material properties must be such as to ensure platform safety over the entire flight regime. While the above can be considered a generic statement, the introduction of new materials such as advanced composites, leads to not only new attributes for aerospace structures, but also introduces new technological elements to be considered. Historically, structural aircraft design has progressed from wood structures (homogenous, anisotropic materials), to metallic structures (homogenous, isotropic materials), to advanced composite structures (homogenous, anisotropic materials). While the progression has come full circle so to speak, our technical knowledge in developing, understanding, and modeling the behavior of these materials has increased exponentially. For example, the Wright Brothers used wood structurally without understanding the nuances of anisotropy. As design experience changed to metallic structures, our understanding and modeling at the phenomenological level of homogeneity and isotropy in successful design practice became documented. With the introduction of advanced composite materials, the inherent anisotropy of such materials has led to new classes of failure mechanisms unlike previous experience with metallic materials. In addition to inherent anisotropy, such materials can be brittle, and the initiation and growth of damage remains to a degree as work in progress. This has led to a design approach which can be considered semi-empirical and relies on our continued and developing experience for design/certification. In this paper, we will explore the damage tolerance issues based on design requirements, current state of the art design and analysis, some selected examples, and concluding remarks.

II. Design Requirements

In design of civil infrastructure, weight is an important design metric, however, this factor does not weigh as heavily in design as that for aerospace structural components. For example, some metrics for aircraft structures suggest a safety factor of 1.5 between the design limit load and design ultimate load for large transport commercial aircraft^{3,4}. This factor is attributed to the code for federal regulations² for aeronautics and space, Title 14, which states that it is required that a structure maintain no permanent deformation at the design limit load. There is thus a driver to meet minimum weight requirements with design margins taken to the lowest levels for design ultimate load levels. Thus, the factor of safety between the design limit load and design ultimate load retains importance as one drives to minimize design margins in order to ensure safety in structural behavior. This begs the question of where do safety factors come from. A very recent book addresses this question with a question in its title, "Safety Factors and Reliability: Friends or Foes?"⁵. This book discusses the relationship between safety factors and structural reliability, as well as showing that safety factors are more comprehensible if they are viewed in a probabilistic context. The latter is a subject for separate discussion, however, the point that can be made is that safety and damage tolerance are inherently related. Returning to damage tolerance requirements for transport commercial aircraft^{3,4}, it is

useful to construct a definition for damage tolerance. This definition can be qualified by the ability of the structure to sustain design limit loads in the presence of damage caused by: Fatigue; Environmental Effects; Accidental Events; Corrosion; Other sources.

For manned spacecraft systems^{2, 6}, NASA has defined damage tolerance as the ability to resist failure due to the presence of cracks during its entire service life, multiplied by a required service life factor. This factor for all NASA space flight hardware is 4. In addition, for the case of composite materials which may contain hidden damage, the damage level assumed for evaluation should be considered as representative of a credible damage threat, after inspection and prior to flight service. It has been observed, based on numerous test programs, that a significant reduction in residual strength can occur even in the case of undetectable damage⁷⁻¹². Examples of strength reduction are shown in the accompanying Figure 2 which is an indicator of damage severity associated with inherent or introduced damage states.

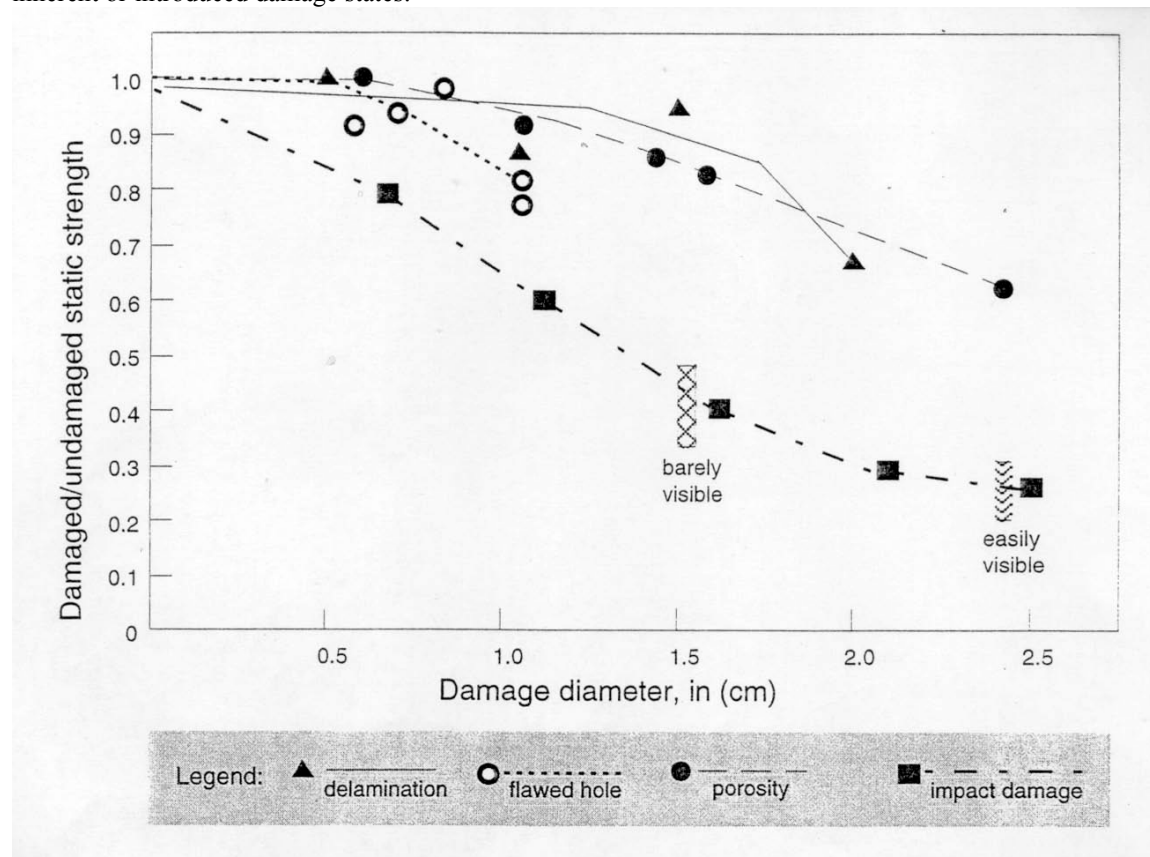


Figure 2, Defect damage severity¹.

Since inherent manufacturing and introduced damage states are commonplace occurrences, knowledge of the strength reduction associated with these occurrences is equally important. This has led to the Compression after Impact (CAI) test as a means to determine the strength reduction for structures, as a standard measure for developing design allowables used to meet limit load requirements. The general design approach for damage tolerance can be summarized as noted in reference 2:

- Catalog the location of fracture critical components
- Assess potential damage states in the structural component
- Determine the damage size associated with initial manufacturing quality assurance and subsequent in service inspections
- Assume that undetected damage exists in each critical component at the most critical locations
- Determine the residual strength of the structure at the required design limit load and critical damage state
- Determine the residual strength of the structure at the required design limit load and critical damage state

- Insure that undetectable damage can survive a source damage event ensuring that damage remains less than design limit loads
- Maintain an in-service inspection program to ensure that damage does not reach a critical damage threshold.

III. Current State of the Art in Design and Analysis

Over the past several decades, improvements have been made in the areas of structural design and analysis of structures, particularly those composed of new materials. For design with these new materials, some of the standard practices associated with analysis are based upon some combination of empirical, semi-empirical, finite element and advanced computer models. The models include routines to evaluate the stress, strain and displacement fields in complex structures based upon techniques such as automated mesh generation, mesh refinement, post processing algorithms, and improved graphics as some representative examples of recent techniques. While these methods contribute to the prediction of the key stress, strain, displacement fields; the understanding of complex failure modes, ultimate strength, residual strength, and fatigue life of structures composed of composite materials are still sought after-goals of the designer. Attempts to bridge this discrepancy include the introduction of high fidelity models, which provide a rigorous assessment of local stresses and stress gradients, which would enable the prediction of structural failure.

As one example of use of an advanced design and analysis methodology, reference² discusses the damage tolerance of a primary aircraft structure, a composite wing structure containing a sawcut which simulates a discrete source of damage as well as undetectable impact damage. The wing box was designed by a contractor to satisfy the requirements for a 220 passenger commercial transport aircraft. A full-scale wing box was then used for a test program in coordination with the NASA Langley Research Center. For the damage tolerance test program, the wing box was subjected to foreign object damage at several locations. In addition, saw cuts through the sandwich construction core panels were introduced to simulate discrete source damage. A number of design limit load tests were performed for verification of the FEM predictive codes. Failure occurred at 97% of the design ultimate load with unrepaired impact damage and was observed to occur at an unreinforced access port on the lower core panel that was not near any impact damage site. The failure load was well within the predictive capability of the FEM codes used as well as for the material properties data used as input to the code. This is one representative example of the damage-tolerance design methodology in current use for primary structures used in aircraft.

As another example of the NASA Advanced Subsonic Technology Program, the development of design and manufacturing technology of fuselage structures was studied. Due to requirements associated with technology readiness levels for composite fuselage structures being much lower than for wing structures, the fuselage program did not include full-scale testing. The program was focused on the design of the crown region of the fuselage which is directed by tension loads. Design details were established by damage tolerance design criteria for this region, in particular, the discrete source damage requirement. This technology was demonstrated by conducting tests on curved, stiffened panels. Two methods were pursued, one on adoption of a semi-empirical method developed for metallic structures, while the second was a more rigorous progressive damage method. The curved stiffened panel was tested under combined bi-axial loads at NASA Langley. The stable damage growth exhibited by the panel before catastrophic failure displayed a behavior similar to panels fabricated from ductile aluminum alloys. Results of the methodologies employed strongly suggest that a semi-empirical method can be used for structural design and analysis.

IV. Concluding Remarks

As mentioned in reference 1, the subject of damage tolerance can be traced back to the 15th century and DaVinci's notebook on flying machines. The premise of DaVinci's work was a fail safe approach with built-in redundancy in the design. This design philosophy was maintained through the 1960s and led to design approaches for metallic structures. The basic tenet of this approach was that damage induced over the flight history of the platform could be detected at regularly scheduled inspection intervals and that the structural integrity of the platform would not be comprised below a threshold. A change in this approach occurred in the 1970s with the inclusion of damage associated with manufacturing as well as in service damage considered as integral in an approach to evolving a damage tolerance concept. Thus has evolved a definition of damage tolerance which for structural components can be stated as the ability of the structure to sustain anticipated loads in the presence of fatigue, corrosion, or accidental damage until such damage is detected through inspections and repaired.

For design, the key damage tolerance issues are:

- The acceptance that damage will occur. That an adequate inspection system is created to detect the damage; and that adequate strength in the presence of damage can be maintained

The above can be illustrated in the accompanying Figure 3, in which (3a) shows the time period associated with damage growth from the initial to the critical size which (3b) shows the retained residual static strength available for a structural component in the process of damage during in-service deployment.

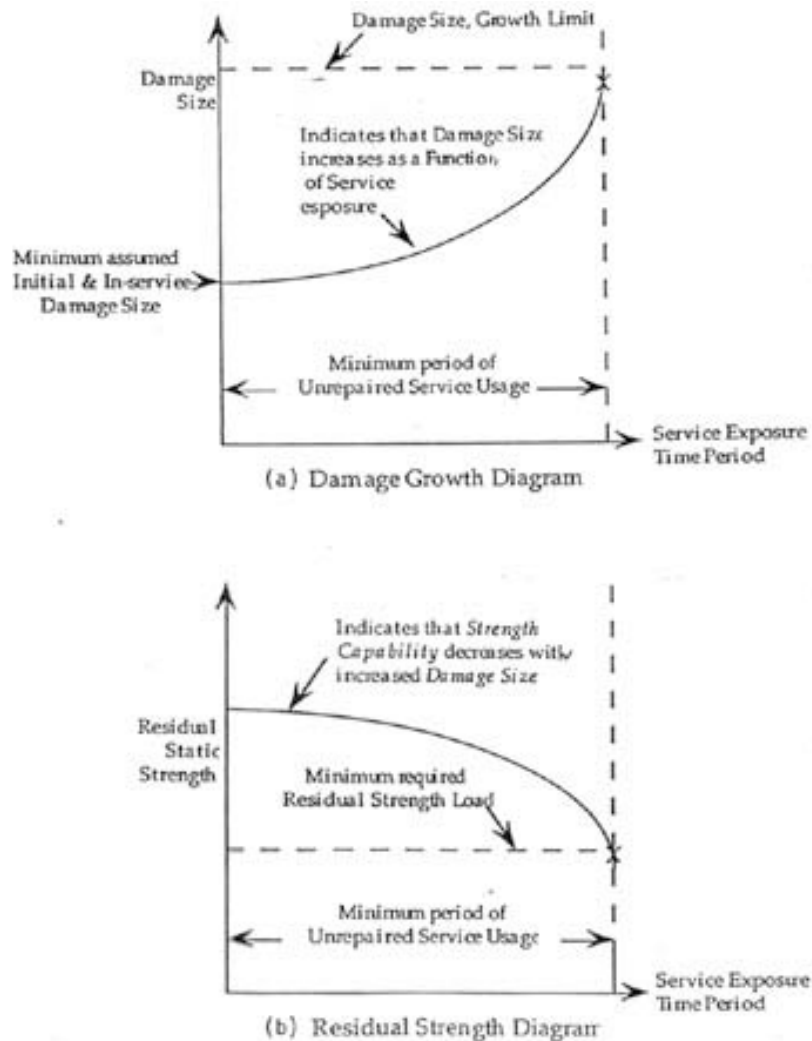


Figure 3a, b. Damage Size/Residual Strength versus Time

At the present time, the current state of the art in damage tolerant design remains semi-empirical, relying on a building block approach for design and certification². In particular, while advances have been made in damage tolerant design and analysis, the methodology for composite structures appears less than mature for application to all aircraft structural components. A number of research issues require further studies including:

- Understanding the initiation and growth of material level damage at meso and macro levels
- Understanding the complex failure modes of component materials at meso and macro levels
- Understanding how the material parameters GI, II, III relate to damage tolerance
- Developing a capability to predict critical damage metrics for damaged components
- Developing predictive techniques for establishing static failure loads in the presence of damage

- Developing accurate, reliable user-friendly computational tools to address current deficiencies in existing algorithms
- Developing standardized laboratory test methods to assess damage independent of specimen geometry
- Developing standardized test methods for assessing damage characterization.

Finally, several comments related to damage tolerant design philosophy include:

- Semi-empirical methods coupled with FEM analyses represent useful design tools
- Computational methods relying on physics based understanding of damage initiation, growth and residual strength represent a significant tool for damage tolerant design.

With all said, the requirements associated with damage threat design represent a challenge to the materials and mechanics community.

References

- ¹ Sierakowski, R. L., "Impact Damage Tolerant Composite Structural Design," Chapter 4, in "Impact Behavior of Fibre-Reinforced Composite Materials and Structures," Editors, Reid, S. R., and Zhou, G., Woodhead Publishing Limited, Cambridge, England, 2000
- ² Harris, Charles E., Starnes, James H., Jr., and Stuart, Mark J., *Advanced Durability and Damage Tolerance Design and Analysis Methods for Composite Structures - Lessons Learned from NASA Technology Development Programs*, NASA TM 2003-212420, June 2003.
- ³ Anon., *Aeronautics and Space, Code of Federal Regulations, title 14*, published by the Office of the Federal Register, National Archives and Records Administration, U.S. Government Printing Office, Mail Stop SSOP, Washington DC 20402, 1996.
- ⁴ Polymer Matrix Composites, Mil-Handbook-17, Volume 3, Chapter 7, Damage Resistance, Durability, and Damage tolerance, Department of Defense, U.S.A., December 12, 2001. (Copies may be obtained from the Standardization Document Order Desk, Bldg. 4D, 700 Robbins Avenue, Philadelphia PA 19111-5094.)
- ⁵ Elishakoff, I., "Safety Factors and Reliability: Friends or Foes?", Springer Publishers, August 2004.
- ⁶ Anon., General Fracture Control Requirements for Manned Spacecraft Systems, NASA-STD-5007, National Aeronautics and Space Administration, George C. Marshall Space Flight Center, Huntsville AL 35812, March 13, 2001.
- ⁷ Rhodes, M. D., J. G. Williams, and J. H. Starnes, Jr., "Effect of Low-Velocity Impact Damage on the Compression Strength of Graphite-Epoxy Hat-Stiffened Panels," NASA TN D-8411, National Aeronautics and Space Administration, Hampton VA 23681, April 1977.
- ⁸ Rhodes, M. D., J. G. Williams, and J. H. Starnes, Jr., "Effect of Impact Damage on the compression Strength of Filamentary-Composite Hat-Stiffened Panels," *The Science of Advanced Materials and Process Engineering Series*, Vol. 23, "Selected Applications of Materials for Products and Engineering" pp. 300-319, SAMPE, 1978.
- ⁹ Starnes, J. H., Jr., M. D. Rhodes, and J. G. Williams, "Effect of Impact Damage and Holes on the Compressive Strength of a Graphite-Epoxy Laminate," *Nondestructive Evaluation and Flaw Criticality for Composite Materials*, ASTM STP 696, R. B. Pipes, Ed., American Society for Testing and Materials, 1979, pp. 145-171.
- ¹⁰ Williams, J. G., M. S. Anderson, M. D. Rhodes, J. H. Starnes, Jr., and W. J. Stroud, Recent Developments in the Design, Testing, and Impact-Damage Tolerance of Stiffened Composite Panels," *Fibrous Composites in Structural Design*, E. M. Lenoe, D. W. Oplinger, and J. J. Burke, Eds., Plenum Press, New York, 1980, pp. 259-291.
- ¹¹ Rhodes, M. D., J. G. Williams, and J. H. Starnes, Jr., "Low-Velocity Impact Damage in Fiber-Reinforced Laminated Epoxy Structures," *Polymer Composites*, Vol 2, No. 1, January 1981, pp. 36-44.
- ¹² Starnes, J. H., Jr. and J. G. Williams, "Failure Characteristics of Graphite-Epoxy Structural Components Loaded in Compression," *Mechanics of Composite Materials: Recent Advances*, Z. Hashin and C. T. Herakovich, Eds., Plenum Press, New York, 1983, pp. 283-306.

NASA Research in Composite Structure Damage Tolerance and Composite Applications In the Oil Industry

Jerry G. Williams*

Petroleum Composites, The Woodlands, TX, 77380

Many factors influence the successful introduction of composite materials into structural applications including a recognized need for improvement over existing technology, material property advantages, innovative structural concepts, advanced design capability, and cost. Motivation to use composite structures in the aerospace industry is driven primarily by weight saving which provide enhanced performance benefits. Weight saving is also an important factor for special applications proposed for the oil industry, especially deepwater developments. Other assets of composites are also important including fatigue and corrosion resistance. Consideration of reliability and safety is especially important in both industries. Composites exhibit unique failure modes compared to metals and it is important to understanding the reductions in strength caused by damage. Early pioneering work at NASA on composites established that compression; and especially the reduction in compression strength following damage, placed severe limits on the design allowables for highly loaded components such as aircraft wing and fuselage structure. Research by NASA established important design constraints for composite structures which were subsequently integrated into guidelines for the design of composites for commercial aircraft. Early research concentrated on establishing the limitations imposed by the effect of damage on compression strength and to develop innovative ways to improve performance. Approaches studied included: damage tolerant resins and innovative design concepts such as soft-skin stiffened panels, hybrid composites, bonded and bolted stiffeners, and laminate stitching. In addition, test methods were developed to access improvement advancements including: open hole compression, open hole tension, and compression after impact. Optimization design methods were exercised to develop minimum-weight composite comparisons with aluminum designs including consideration of the limitations imposed by damage. Many of the foundation principles in composites developed at NASA have been applied to applications in the oil industry. The paper discusses the pioneering work in damage tolerance conducted at NASA and describes how the technology developed has been applied in the development of composites technology for applications in the oil industry such as spoolable high pressure composite pipe, composite risers, carbon fiber tendons and synthetic fiber mooring ropes. The paper is intended as a memorial to Dr. James H. Starnes, Jr. with whom the author worked closely at NASA in composites mechanics and structural design for 15 years.

Nomenclature

A	Planform area of stiffened panel
a	Hole diameter
e	Amplitude of overall bow at panel midlength
L	Panel length
N_x, N_y, N_{xy}	Stress resultants
N_x / L	Load index
t	Thickness
W	Mass of stiffened panel
w	Panel width
$(W/A)/L$	Mass index
Δ	Amplitude of eccentricity at panel midwidth
ϵ	Strain

* Copyright 2005 by Jerry G. Williams.
Printed by NASA with permission.

I. Introduction

Structures and materials research at the NASA Langley Research Center began in the early 1970's to emphasize the importance of newly emerging high performance composite materials including boron, carbon, and aramid fiber¹. The Structural Mechanics Branch of the newly formed Structures and Dynamics Division shifted emphasis from research in metallic shell structures² to advancing computational methods using the rapidly expanding capability of the modern computer and to understanding the benefits and limitations of composite materials for space and aeronautical applications. The current paper highlights research activities of the period 1970-1985 during which the author was a colleague of Dr. James H. Starnes, Jr. and other personnel at NASA engaged in research on the topic of composite damage tolerance with particular emphasis on the effects of damage on compression behavior and the technology proposed to improve the performance of composite structures for highly loaded aircraft primary structure such as wing and fuselage. In 1985, the author began focus on the application of composites to the oil industry. The technology developed at NASA served to guide the development of new applications described in the second topic of this paper.

Some of the earliest work on composite material characterization for aircraft design was conducted on fiberglass laminates in the 1950's by the Forest Products Laboratory.³⁻⁹ Capabilities introduced by the modern computer permitted the opportunity to evaluate the weight saving potential of composite structures using optimization algorithms in which the variables of selected configurations including cross-sectional dimensions and thicknesses and composite material properties and fiber angle orientation are subject to constraints including strength, stiffness, stability, and property limitations such as maximum strain or minimum gage. This analytical approach was in sharp contrast to the experimental assessment program conducted by the National Advisory Committee for Aeronautics (NACA) in the 1940's¹⁰⁻¹⁴ in which thousands of aluminum stiffened panels of selected designs were tested to establish optimum structural performance of stiffened compression panels. Figure 1 taken from Ref. 15 summarizes graphically the results of the structural efficiency from many of these NACA compression panel tests. The panel weight per unit area per unit length

(W/AL) is plotted as a function of the load index (N_X/L). Similar structural efficiencies for graphite/epoxy hat-stiffened panels showing weight savings of approximately 50 percent established using the analytical optimization method are presented for comparison. Similar analytical optimization results presented for an aluminum hat-stiffened panel provide a lower bound for the experimental data. A few "Y" configuration panels fall below the optimized aluminum hat results as predicted by the NACA reports.

Having established the merits of using the computer to establish minimum weight composite structure designs; it was considered essential to validate the analytical methods and optimization procedures¹⁶⁻²¹ with representative experiments. In response, selected composite configurations and designs were fabricated and an

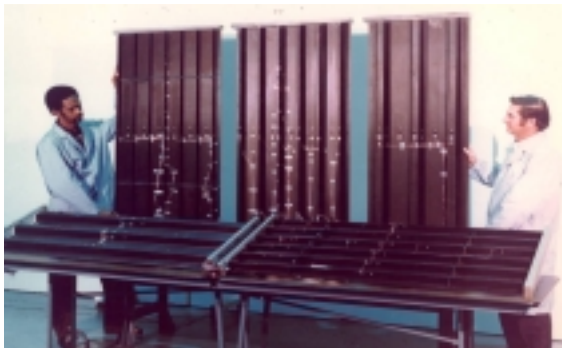


Figure 2. Composite compression panels.

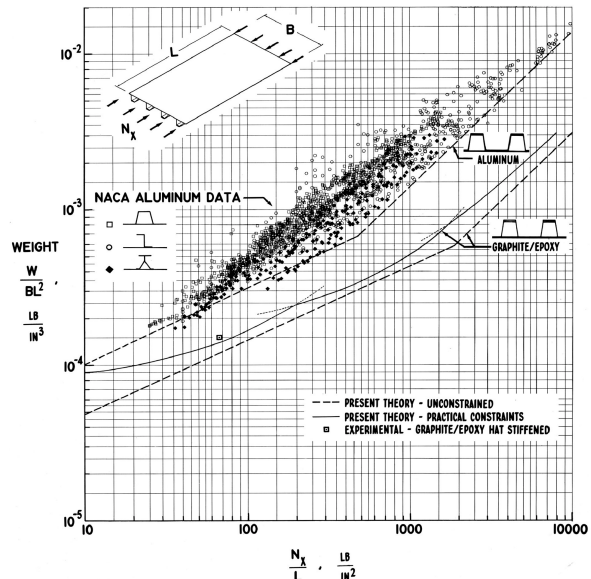


Figure 1. Stiffened panel structural efficiency.

extensive compression panel experimental program conducted. Representative hat- and blade-stiffened panel test specimens are presented in Fig. 2.

Commercial aircraft typically utilize aluminum at a maximum design strain of from 0.4 to 0.5 percent. One criterion studied for structurally efficient composite wing structure designed to meet similar stiffness requirements is to allow approximately the same maximum allowable strain level. The graph of Fig. 3 provides a comparison of the structural efficiency of commercial aircraft wings constructed of aluminum with analytical predictions for comparable composite compression panels with maximum strain values of 0.3%, 0.4% and 1%²². At higher load index

values, the maximum allowable strain can be seen to influence the associated weight savings which can be achieved. The experimental results shown in Fig. 4 for carbon/epoxy hat and blade stiffened panels¹⁵ are in close agreement with analytical predictions demonstrating that potential weight saving of approximately 50 percent can be achieved under ideal circumstances.

In the mid 1970's apprehension began to emerge concerning how tolerant composite structures were to the effects of damage and inclusions such as defects and cutouts. To address the issue, impact tests were conducted on composite compression panels prior to loading and some while under load as shown in Fig. 5. The results showed impact damage could cause not only local damage, but could result in the propagation of damage to the free edges of the panel as shown in Fig. 5. Impact under load was found to be only a slightly worse condition than impact followed by loading. The projectile in these tests was a 1/2-inch diameter aluminum sphere propelled using an air gun at velocities up to 500 feet per second. A velocity detector installed at the end of the gun barrel measured the projectile velocity as it exited just prior to impact. The impact test

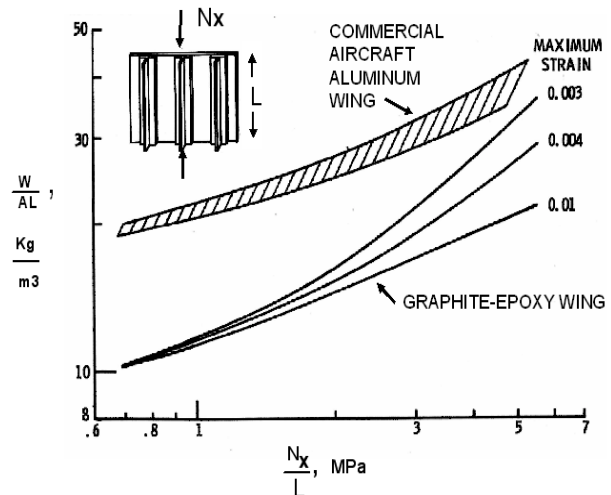


Figure 3. Structural efficiency of commercial aircraft wing and composite compression panels.

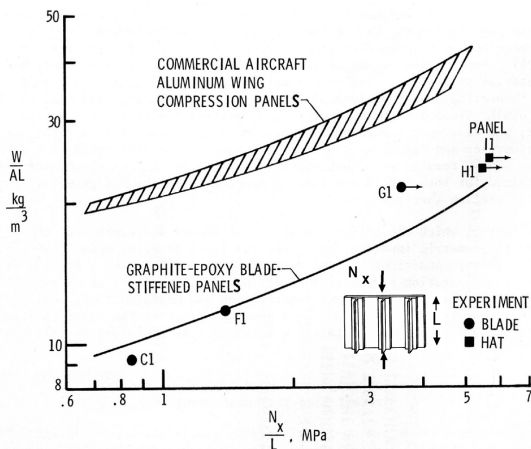


Figure 4. Structural efficiency of composite compression panels.

research efforts to quantify the effect of damage on composite structure performance with emphasis on compression behavior and the ensuing approaches developed to make improvements. Finally, a discussion is presented on how composites technology has been transferred into specific applications in the oil industry with discussion of related damage tolerance issues. Interest in composites in the oil industry is driven by deepwater developments in which weight saving becomes an economic enabling factor as well as by the other assets one normally associates with composites including corrosion resistance.

simulated the threat which might be expected from runway debris kicked up during landing of an aircraft.

The effect of damage on composite structural performance was found to be more severe for compression loading than tension. This is in sharp contrast to metal structures where tension fatigue typically governs performance. In response to the impact issue, a comprehensive experimental program was launched to scope the magnitude of the problem and to innovate ways to improve the performance. This paper summarizes the early

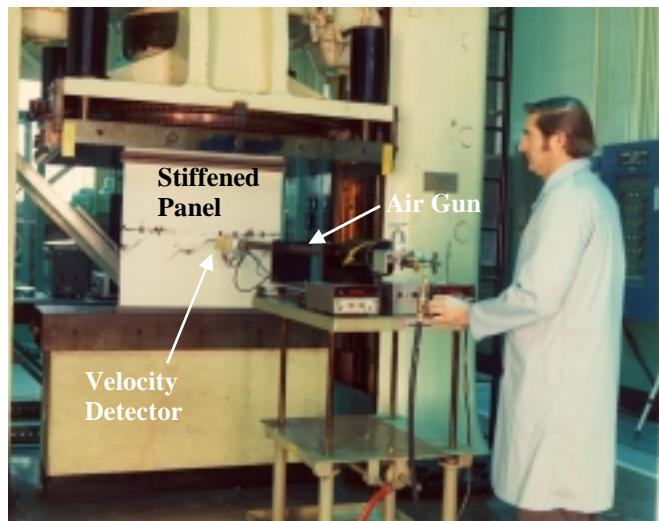


Figure 5. Stiffened panel impact test.

II. NASA COMPOSITE DAMAGE TOLERANCE RESEARCH 1970-1985

A. Damage Characterization

Following the discovery that impact damage could cause significant reductions in the performance of composite compression loaded panels a comprehensive program was initiated to quantify and characterize the issues: of impact damage,²³⁻⁴¹ basic inclusions including holes,⁴²⁻⁶² and the response of structural configurations⁶³⁻⁷⁶ to damage. These studies also included efforts to improve the tolerance to damage of the matrix and fiber and to develop damage tolerant structural configurations. Fundamental studies to understand composite material damage tolerance and advancing improvements in structural performance is a topic of continuing interest.⁷⁷⁻¹¹⁰ The NASA effort initiated with an extensive test program later complimented by optimization studies to quantify the effect of limiting design allowables to provide safe component designs. Because composites can be designed to have an infinite range of laminate anisotropic properties, strain rather than stress was found to be a convenient parameter for measuring and comparing performance. Some of the initial tests were conducted on pseudo-isotropic laminates with a portion of the lamina loaded directly in axial compression. As will be shown, the axial compressive strain in the fibers is an important consideration in composite compression behavior and failure. Initial experiments were conducted on commonly available carbon fibers and resins. As will be shown, the properties of both the fiber and resin influence the compression behavior and damage tolerance.

The test specimen initially used to characterize compression damage tolerance was a 48 ply T300 carbon/5208 epoxy laminate including axially oriented fibers loaded in the test fixture shown in Fig. 6. The specimen is 10-inches long and 5-

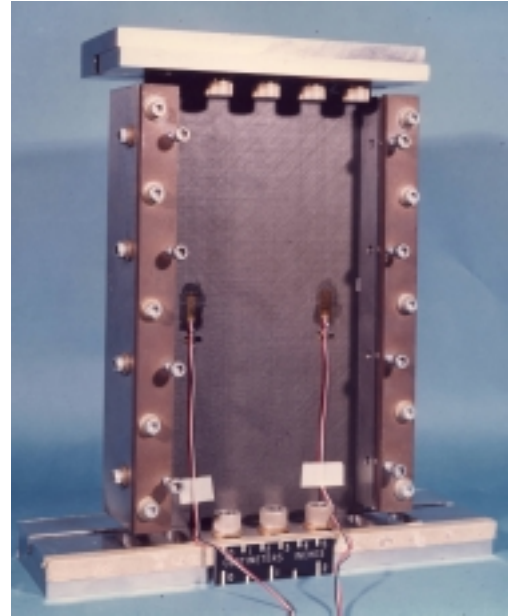


Figure 6. Plate compression fixture.



Figure 8. Composite plate specimens following impact. Front surface painted white and back surface with brittle coating.

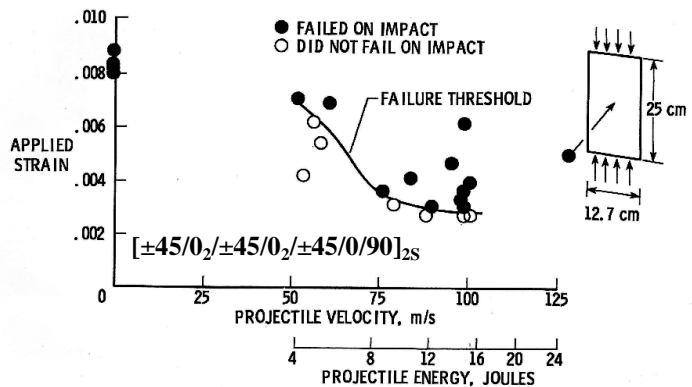


Figure 7. Effect of damage on compression strength.

inches wide and approximately 0.25-inch thick. Impact damage was inflicted using a 1/2-inch diameter aluminum sphere propelled by the air gun shown in Fig. 5. The data of Fig. 7 shows representative test results in which specimens were impacted at selected levels of imposed strain and impact energy. The line represents a threshold boundary between specimens which failed on impact (open circles) and those which survived (filled circles). At the higher energy levels the residual strength of specimens which survived impact were only slightly above the threshold curve. The failures for specimens without impact damage are due to buckling of the panel and do not represent the undamaged strength of the

material. The test results suggested a limiting strain on approximately 0.3 percent for brittle resin material systems commonly used at the time. The design strain of commercial aircraft control surfaces are typically less than 0.3 percent, however, as discussed above the design strain for efficient wing structure is significantly higher.

Photographs of the impact side and back side of a failed plate are shown in Fig. 8. A series of moiré fringe photographs representing the delamination growth of the damage as represented by the out-of-plane deformation of the surface of the panel in the vicinity of the impact during a residual strength test is presented in Fig. 9. High speed photography tests conducted at California Institute of Technology²⁵ recorded the propagation of the delamination mode of damage involving delamination in the vicinity of the impact followed by local buckling of the delaminated lamina initiating damage propagation to the free edge of the specimen. The 0.25-inch thick carbon-epoxy specimen was impacted by the ½-inch diameter aluminum sphere at 65 m/s and the propagation recorded by photographing the moiré fringe pattern on the back of the specimen as well as the lateral free edge. The time for the damage to propagate to the free edge of the 5-inch wide panel was approximately 360 microseconds. Following contact of the 0.25-inch thick composite plate by the projectile, a transient local deformation response occurs followed in time by a global structural deformation response as illustrated in Fig. 10. Less damage occurs for very thick plates in which the bending stiffness is sufficiently great to resist the transient local deformation response.

These results suggested that suppressing delamination caused by impact would suppress the subsequent lamina local buckling mode of damage propagation. To investigate this hypothesis an experiment was conducted using a much wider plate specimen (15-inches wide) with intermediate rigid vertical supports designed to arrest the lamina local buckling and thus the damage propagation. Instead of arresting the damage; however, the damage propagated upon impact through the lateral support to the free edge of the compression loaded specimen as shown in the photograph of Fig. 11.

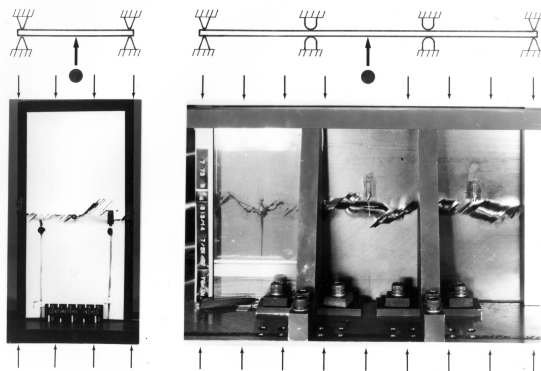


Figure 11. Impact test on plate with intermediate supports.



Figure 9. Moiré fringe contours representing progressive delamination growth with load.

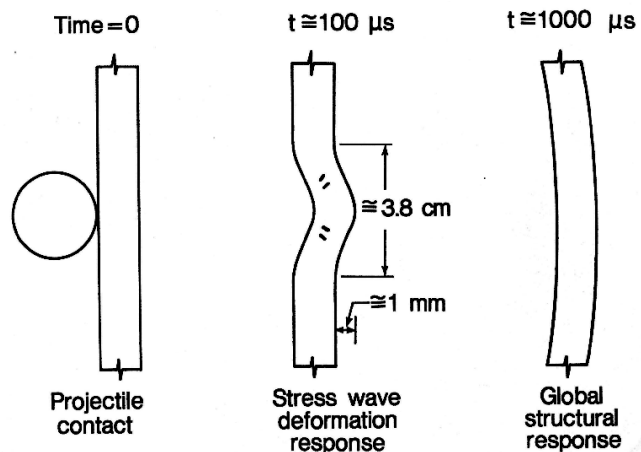


Figure 10. Response of composite plate to impact.

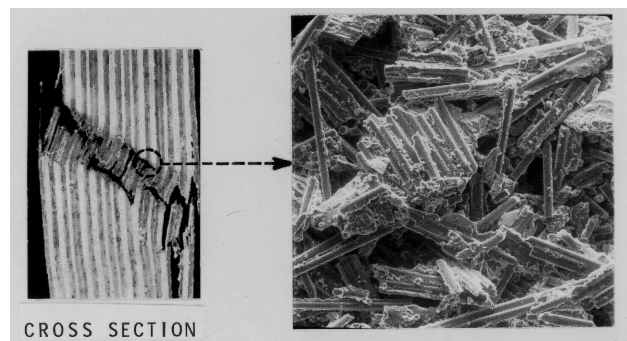


Figure 12. Shear crippling mode of failure for compression loaded panel following impact.

Further study revealed a second mode of damage propagation in addition to delamination, namely shear crippling as illustrated in Fig. 12. Shear crippling of the compression loaded 0-degree lamina allows the damage to traverse through the lateral deformation constraint and continue to propagate in the delamination mode on the other side. The shear crippling mode becomes the primary mode of damage propagation when delamination is suppressed as will be shown for composites constructed using advanced formulation tough resins.

B. Open Hole Compression

The study of the compressive strength characteristics of composite plates and structures with open holes⁴⁸⁻⁶² showed, like impact damage; the failure modes were controlled by (1) delamination due to a strength failure of the matrix and (2) micro buckling of the fibers due to the low stiffness of the matrix. Experimental results for the compression failure strain of quasi-isotropic laminates constructed of two different resins systems and containing a range of centrally located holes sizes (a/w) hole sizes is presented in Fig. 13. Unlike ductile metals, composite materials loaded in compression are highly notch sensitive. Failure prediction techniques were explored to describe analytically the effect of the presence of discontinuities such as holes or damage. The theoretical failure curve in Fig. 13 drawn through the data is based on the point stress failure criterion described in Ref. 54 using the method presented in Ref. 45. The data shows a significant reduction in performance with increasing hole size in excess of the notch insensitive line (net area reduction); approaching the notch sensitive lower bound at higher a/w ratios. As is shown below, BP907 exhibited improved performance in impact tests versus the control epoxy material 5208, but as shown in these tests, did not show improved performance in open hole tests. The explanation for the difference in performance is the damage mode, which was found to initiate first with shear crippling of the axial oriented plies in the stress concentration in the vicinity of the hole followed by delamination.

The photographs of Fig. 14 show the progression of failure for an open hole specimen loaded in compression. At 92.8% of the ultimate load, moire fringe photographs show no evidence of delamination around the hold boundary. At 95.2 %, local fringes appear and grow in size with increasing load. One might conclude based on this evidence that the initiating failure mode for open hole specimens is delamination; however, further investigation revealed that microscopic shear crippling occurs in the vicinity of the hole boundary in advance of delamination. This response is illustrated in Fig. 15 in which in a similar test a specimen was loaded to a load level just prior to the initiation of delamination (approximately 92% of ultimate) and unloaded. A small block of material adjacent

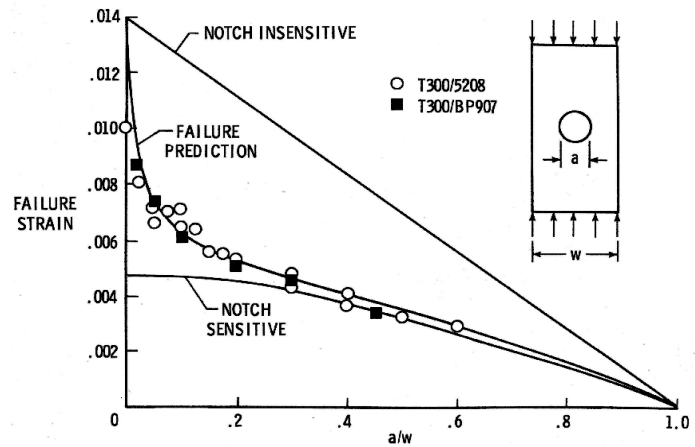


Figure 13. Open hole compress test data.

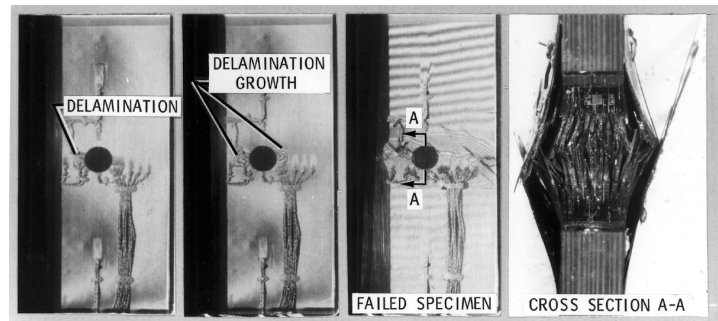


Figure 14. Open hole compression test damage propagation with increasing load.

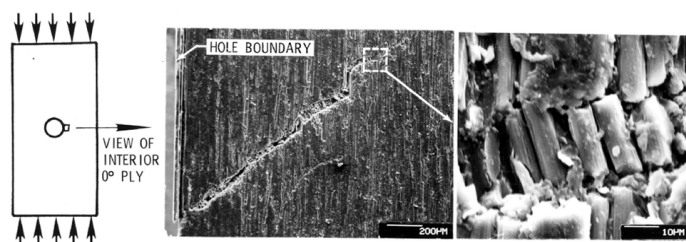


Figure 15. Shear crippling failure exhibited near hole prior to delamination.

to the hole boundary was cut from the specimen and the surface material sanded away to expose an interior 0-degree layer. A scanning electron photomicrograph (right photo of the Fig.) shows the broken carbon fibers following micro buckling in the high strain concentration region adjacent to the hole.

It was found that slightly higher failure strains for specimens with holes were achieved for carbon fibers with higher ultimate strain allowables. The higher failure strain corresponding to plates constructed with higher ultimate strain fibers supports the hypothesis that high bending strain in a buckled fiber initiates a local micro buckling initiated shear crippling failure mode. Several material properties govern fiber micro buckling and failure including the fiber extensional and bending stiffness and strength as well as the stiffness and strength properties of the matrix.

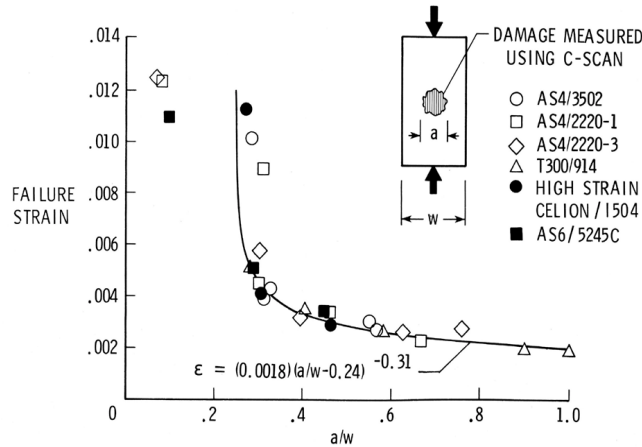


Figure 16. Shear crippling failure exhibited near the hole prior to delamination.

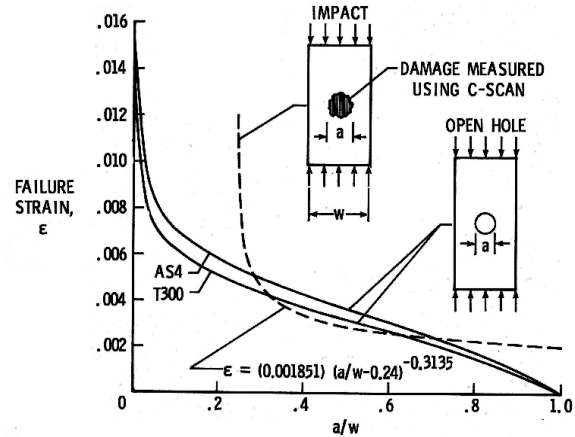


Figure 17. Comparison of effect of impact damage and open holes on composite plate compression strength .

Failure strain data for quasi-isotropic laminates loaded in compression which failed in a residual strength test following damage by impact for several different material systems is plotted in Fig. 16 as a function of the size of damage. The damage size was measured using the C-scan non-destructive test method following impact at selected energies. For these laminates and impact conditions, the size of damage appears to be a parameter that reduces the test data for all of the material systems studied to a common curve. A two-parameter curve asymptotic to $a/w = 0.24$ has been drawn to match the test data. A large reduction occurs around $a/w = 0.24$ while the failure strain for $a/w < 0.24$ is governed by conditions other than impact such as plate buckling.

A comparison of the effect of holes and impact damage on plate strength is presented in Fig. 17 using the curve fit to impact data of Fig. 16 and experimentally validated failure prediction curves for open hole data for AS4 and T300. AS4 has a higher ultimate tensile strain value than T300 (0.015 vs. 0.012) and a slightly larger fiber diameter (8 μm versus 7.5 μm), characteristics which should improve comparative resistance to micro buckling. For the five inch wide panels, the open hole causes the greatest reduction in strength for $a/w < 0.3$ and slightly greater reductions in failure strain due to impact damage for $a/w > 0.3$.

C. Tough Resin Formulations

Numerous approaches were investigated at the materials level to develop approaches to improve the damage tolerance of composite materials to impact damage and defects or inclusions such as holes. The first approach investigated was to determine if a more ductile resin than the brittle class of resins initially studied might help. A tough resin BP907 was selected for the study. As shown in the impact failure threshold curves of Fig. 18; significant improvements in resistance to impact compared to the 5208 epoxy resin were demonstrated with the same T300 carbon fiber. However, as was shown in Fig. 13, when the same material comparisons were made for open hole compression tests; there was no similar improvement. The explanation proposed for this

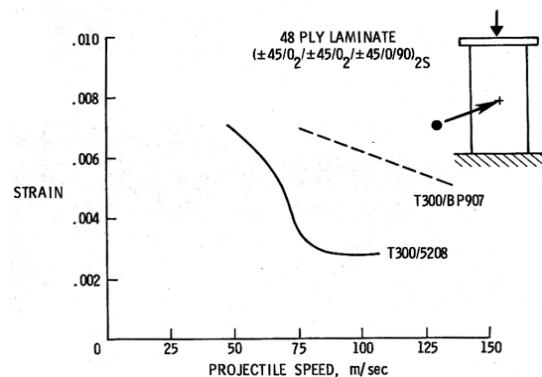


Figure 18. Impact Damage Failure Threshold Curves.

conundrum was that the tough resin suppressed the brittle resin delamination mode of failure in the case of impact, but the shear crippling mode of failure governs the failure mechanism in both cases responding to the stress concentration in the vicinity of the open hole.

D. Transverse Stitching

Another approach investigated for suppressing delamination in carbon-epoxy laminates was to provide transverse reinforcement to the laminate by stitching. Dr. C. T. Sun (Purdue University) engaged students to hand stitch precured plates including some which were perpendicular and others stitched at 45-degrees relative to the plane of the plate. A comparison of the impact damage failure threshold data for T300/5208 and T300/BP907 laminates with and without transverse stitching is presented in Fig. 19. Transverse stitching significantly increased the failure threshold strains for the delamination prone T300/5208 laminates, but had no effect on the failure threshold strains for the delamination resistant T300/BP907 laminates.^{27,30} Both stitching and tough resins help suppress delamination in the laminate, but cannot address the shear crippling mode of failure. Additional papers on the topic of stitching and fabric can be found in Ref. 111-113.

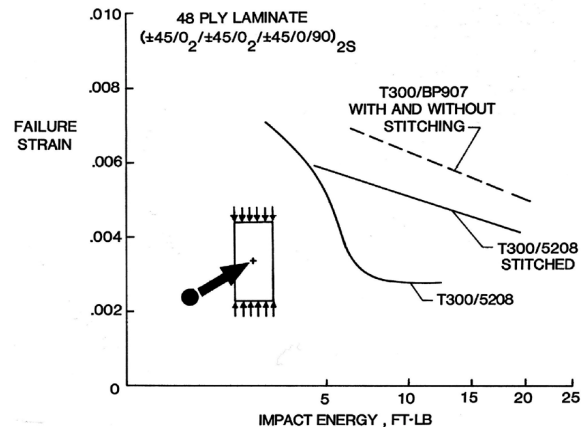


Figure 19. Impact Damage Failure Threshold Curves with/without transverse stitching.

E. Aramid

E.I. DuPont introduced a new low density, high modulus ($E = 20 \times 10^6$ psi and $\rho = 0.053$ lb/in³) aramid polymeric fiber and made it available to NASA and the aircraft industry for evaluation in the early 1970's. Initially called PRD-49, it is currently known as Kevlar[®] in several different formulations. It was soon demonstrated that the material could provide substantial weight saving as a substitution for glass fiber in pressure vessel applications. It also appeared attractive for aircraft secondary structure applications. The performance in compression was less well known and NASA conducted compression characterization studies including the effect of impact damage and open holes in thermoset epoxy resins. Characterization studies were also conducted using specimens fabricated by Boeing using a PRD-49/thermoplastic resin (phenoxy 8080) tow over wound onto aluminum cylinders and with NOL rings. The NOL ring tests showed the 54 percent fiber content uniaxial composite to possess an ultimate strength of 190,000 psi and a tensile modulus of 7,900,000 psi. The 90° wound tube was found to have a shear modulus of 512,000 psi and an ultimate shear strength of 2400 psi. Two cylinders were tested in axial compression and failed by crippling of the inner 0.020-inch aluminum skin as it was plastically yielded. These limited studies demonstrated that PRD 49/thermoplastic composites could be successfully fabricated and exhibit high performance structural properties.

In the late 1970's, a potential hazard surfaced as an issue related to the shorting of electrical equipment derived from the highly conductive electrical properties of free carbon fibers. A comprehensive study was initiated by NASA to assess the potential problem associated with free floating carbon fibers during processing or released in a fire. The potential issue with carbon fiber provided an incentive to look more seriously at aramid as a substitute for carbon in aerospace structural applications. The results of the electrical hazard study concluded that electrical shorting due to the release of carbon fibers was not a serious concern for structural applications in which the fibers were encapsulated in a resin.¹¹⁴⁻¹¹⁵

Open hole failure strain data for Kevlar[®]/epoxy laminates loaded in compression is presented in Fig. 20 for several different ratios of a/w (hole size/plate width) for a 5-inch wide specimen. Laminates without 0° plies (axial) have significantly higher failure strains than laminates containing 0° plies.

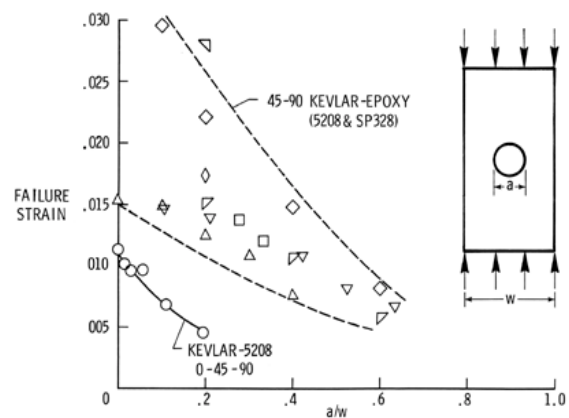


Figure 20. Open hole compression data for Kevlar[®]/Epoxy laminates with/without axial oriented fibers.

Aramid zero plies loaded in compression have a characteristic fibril failure mode initiating at a strain of approximately 0.004. To avoid this characteristic compressive failure mode, aramid fibers cross-ply laminates (absent of 0-degree plies) were evaluated $[(\pm 45/\pm 45)_2/90]_2/\pm 45/\pm 45]_S$ in greater detail. Figure 21 shows an impact test conducted with the specimen impacted three times while subjected to high magnitudes of strain (0.009, 0.011, and 0.013). The specimen did not fail and each case was loaded again and ultimately failed at a strain level of 0.016. The the C-scan damage signature insert shows that damage resulted from each of the impacts by the 1/2-inch diameter sphere with an impact energy of over 9 ft-lb.

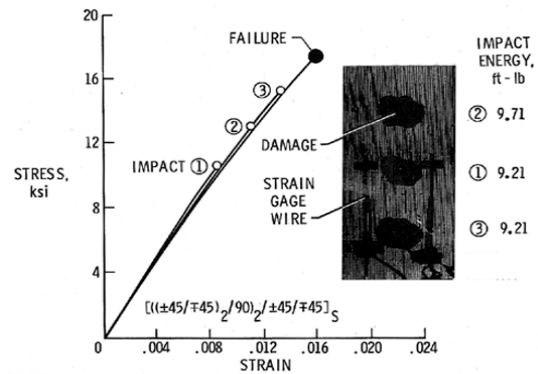


Figure 21. Impact damage test for aramid laminate without 0° (axial) plies.

F. Damage Tolerance Standards

NASA initiated the Composites Flight Service program in 1972 to evaluate the long term performance of composites in actual aircraft environments.¹¹⁶⁻¹¹⁷ In addition, NASA in 1976 initiated the Aircraft Energy Efficiency (ACEE) program¹¹⁸⁻¹²⁶ and in 1988 the Advanced Composites Technology program to encourage advancement of technology aimed at reducing weight and saving fuel on commercial aircraft.

As one of it's activities, the ACEE program office coordinated a program with the commercial aircraft industry to develop standardized damage tolerance tests to evaluate alternative resin and fiber materials for high performance structural applications.¹²⁷⁻¹³² A summary of one element of the study involving twenty-six different resin formulations and seven manufacturers is summarized in Fig. 22. Studies were also conducted in which different carbon fibers were evaluated. A standard set of test methods (Fig. 23) was

DAMAGE-TOLERANT RESIN EVALUATION NASA-INDUSTRY STUDY

GUIDELINES	PREPREG SUPPLIERS
• IMPROVE DAMAGE TOLERANCE	AIR LOGISTICS (1)
• IGNORE PROCESSING AND ENVIRONMENTAL FACTORS	AMERICAN CYANAMID (4)
• FORMULATIONS MAY BE EXPERIMENTAL	CIBA-GEIGY (7)
• RECOMMEND PROCESSING CYCLE	FIBERITE (1)
• USE THORNEL 300 FIBER	HEXCEL (3)
	NARMCO (5)
	U.S. POLYMERIC (2)
	VOLUME FRACTION VARIATION (3)
	TOTAL (26)

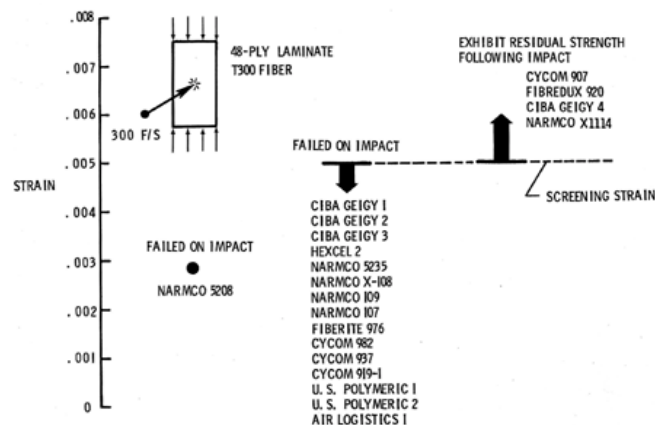


Figure 23. Screening test to identify damage tolerant materials.

plate loaded at a strain level of 0.005 identified four materials which did not fail on impact (Fig. 22) demonstrating the viability of making improvement through tough resin formulations. A more recent discussion of an open hole compression test is presented in Ref. 133.

G. Multi-Span Beam Transverse Shear Test

The multi-span beam transverse shear test shown in Fig. 24 was another procedure developed to better understand damaged composite failure modes and evaluate proposed material performance

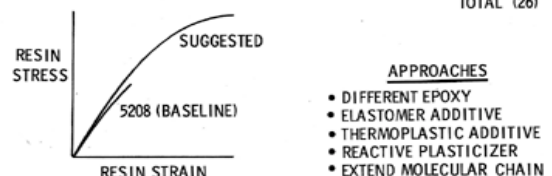


Figure 22. NASA ACEE/Industry investigation of damage tolerant resins.

formulated by the Aircraft Energy Efficiency (ACEE) Project Office in cooperation with industry to help evaluate important material parameters.¹³³ In addition to the compression-after-impact and open hole compression tests, the standard included: edge delamination tension test used to calculate interlaminar fracture toughness G_c , double cantilever beam test to calculate the critical strain-energy release rate, and open hole tension test. The standard impact test (ST-1) conducted with the composite

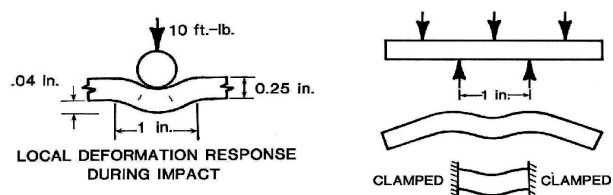


Figure 24. Simulation of impact condition with multi-span beam.

improvements.^{30,134-140} The test was designed to simulate the impact generated transient stress wave deformation response illustrated in Fig. 10. Quasi-isotropic laminate test specimens $[45/0/-45/90]_{6S}$ approximately 4-inches long, 1-inch wide, and $\frac{1}{4}$ -inch thick were transversely loaded using five sets of line loads imposed by $\frac{1}{2}$ -inch diameter half cylinder pins spaced 1-inch apart (three on one side of the specimen and two on the other). The center span is the highest stressed region and the deformation approximates in 2-dimensions the transient deformation response during impact. A moiré fringe interferometry method was used to characterize the complex state of strain on the edge of the specimen.¹³⁴ Fig. 25 from Ref. 134 shows that the center region of the mid bay section between loading pins is in a state of high transverse shear strain and near zero axial and normal strains. The strain in the vicinity of

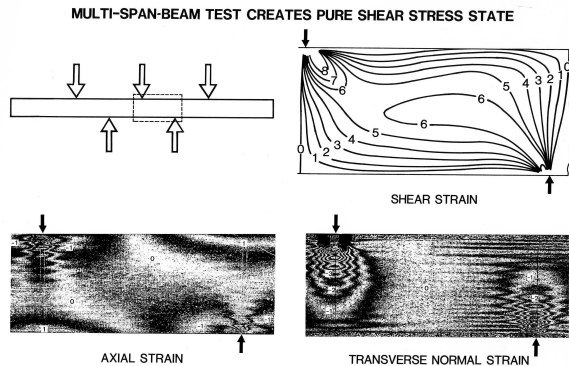


Figure 25. Simulation of impact condition with multi-span beam.

the region of loading exhibits a complex state of high axial, shear and transverse compressive normal strain.

Numerous different resin material systems were tested and the two characteristic load / crosshead-displacement responses shown in Fig. 26 were typically of the responses exhibited. For comparison purposes, the residual compression failure strain for several different material systems from the compression-after-impact test at selected impact energies is presented in Fig. 27. Damage tolerant resins identified by solid symbols in the compression-after-impact residual strength tests exhibited significantly higher loads and crosshead displacements in the multi-span beam tests. During tests, a long-distance microscope was used to identify the failure mode in the cross-section in the sequence in which it occurred. For the brittle resin materials, the first incidence of damage was a localized failure of the resin in a 90-degree ply oriented at 45° to the plane of the plate in the region of highest transverse shear strain shown in Fig. 28. At slightly higher loads the damage was observed to propagate in a delamination mode initiating at the location of the original damage. This mode of failure was suppressed for damage tolerant resins for which the initial failure occurred at higher loads and displacements in the region close to the region of load introduction. The shear ductility of the damage tolerant resin appears to be a key material property important to providing the improved resistance to impact damage.

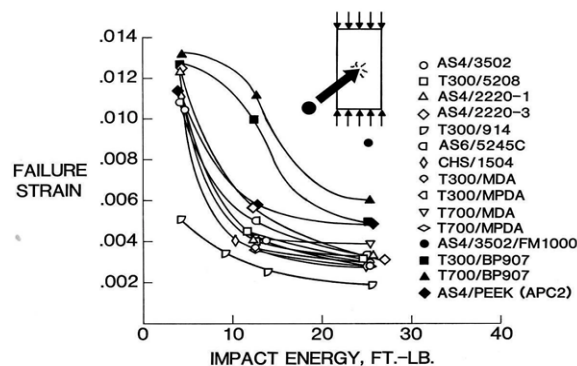


Figure 27. Compression after impact test residual strength test for selected materials.

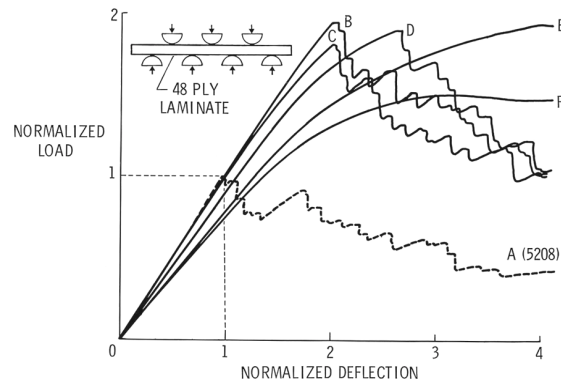


Figure 26. Load-deformation response for multi-span beam test.

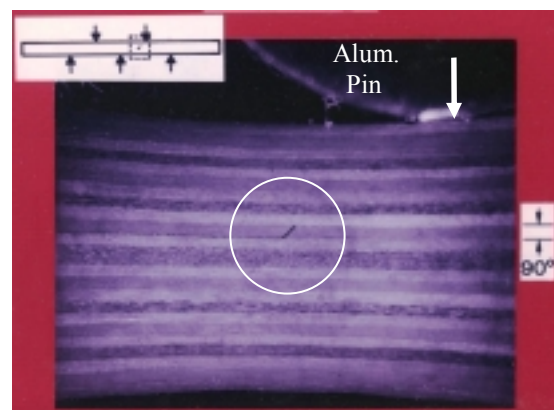


Figure 28. First failure in 90 ply in region of maximum shear strain.

The single test labeled AS4/3502/FM1000 (filled circle) in Fig. 27 was a specimen in which a lower modulus high strain film FM 1000 was placed between lamina in the composite plate. As can be seen, the impact damage tolerance was significantly improved compared to the AS4/3502 specimen without interleaving (open circle). The material with interleaving also changed the AS4/3502 material load-displacement response for the multi-span beam test from the baseline 5208 response (Fig. 26) to a response like a damage tolerant resin. Although the film increased the specimen thickness, thus providing a correspondingly higher bending stiffness; it is believed the primary improvement was derived from the high shear deformation capability between plies derived from interleaving. Evidence to further support this hypothesis is the set of photographs presented in Figure 29 for a test designed to investigate the resistance of different materials systems to bolt push-through.⁴⁰ The loading in 3-dimensions for the bolt push-through is similar to the multi-span beam test in 2-dimensions. The damage shown for the symmetrical loading is intra laminar fracture of the resin at 45° to the plane of the plate in both 0° and 45° oriented fibers. With the FM 1000 interleaf layer, the damage did not propagate as delamination between plies while this was a characteristic failure mode for the same laminate (fiber and brittle resin) without the FM 1000. The composites industry has continued to investigate interleaving and several damage tolerant material systems are currently commercially available.

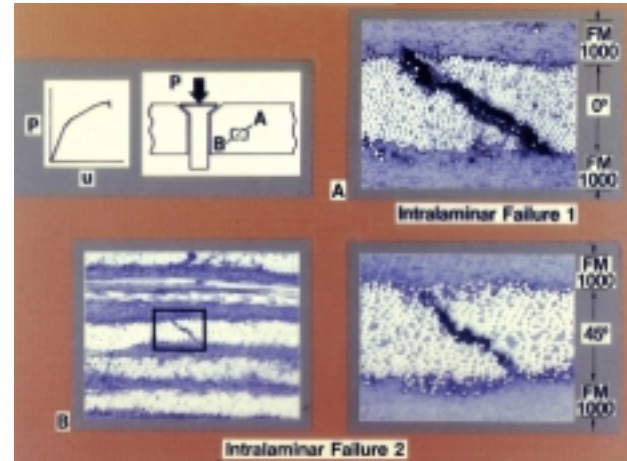


Figure 29. Bolt push-through test of laminate with FM 1000 interleaving between plies.

H. Damage Tolerant Stiffened Panel Design Concepts

Debris on the runway, hail, dropped tools, or engine rotor burst are some of the potential sources of damage to aircraft structure. Conventional minimum-weight stiffened panel designs such as shown in Fig. 2 with laminate containing axial 0° oriented carbon fibers and an epoxy resin have been loaded to axial compression strains as high as 0.008 without failing. When subjected to low-velocity impact damage; however, similar brittle resin panels failed at axial strains as low as 0.0035²² as shown in Fig. 30. Filled circles represent the imposed strain level during impact and the vertical line displays the residual

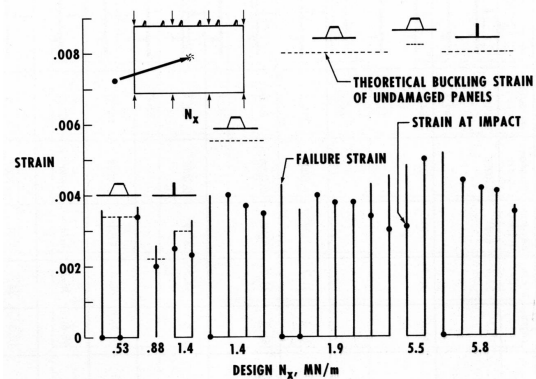


Figure 30. Stiffened panel strength reduction caused by impact damage.



Figure 31. Hat stiffened compression panel failure initiated by local impact.

strain for panels which survived impact. The performance of lightly loaded panels ($N_x/L < 200$) is usually not as adversely affected by impact damage since typical applications like aircraft control surfaces carry the required loads at relatively low strains (less than 0.003). The vulnerability to impact damage is demonstrated in the test shown in Fig. 31 for a hat-stiffened panel in which local skin damage imposed by impact has propagated laterally to the free edges of the panel. Numerous concepts for improving the damage tolerance of composite compression panels were evaluated⁶⁸ including: (1) fabric material form versus tape, (2) transverse through-the-thickness stitching including the stiffener attachment, (3) plate with alternating regions with and without 0° plies, (4) metal strip skin discontinuities, (5) bonded

stiffeners, and (6) mechanical fastening. Improvements anticipated by tough resin and other material improvement approaches discussed above were also evaluated for stiffened panels. The emphasis of the investigation reviewed in this section is on the technology studied to improve the damage tolerance of highly loaded stiffened compression panels such as might be applied in a wing or fuselage structure.

Various methods for attaching the stiffener were evaluated including coccured, bonded, bolted and stitched. Bonding stiffeners to the skin was successful in arresting damage propagation for designs in which the stiffener and stiffener flange were sufficiently stiff to restrict the transverse deformations of the propagating skin delamination. Isolation of the stiffener from the skin with bonded or bolted stiffeners avoids propagation of delamination and shear crippling damage from one into the other. Cross-section stiffness tailoring was studied in which the stiffener and skin have different laminate constructions designed with the skin providing high shear stiffness and primary axial stiffness concentrated in the stiffener. This approach was based on laminated flat plate data described above which showed an increase in the ultimate compression strain for a cross-ply laminate without 0° plies following impact from a range of 0.004 or less to greater than 0.006. One concept studied involved a design in which the panel skin is composed of all $\pm 45^\circ$ and 90° lamina. The 90° plies increase both the axial and transverse panel stiffness. The design of a stiffened panel utilizing an aramid skin constructed without 0° plies was also evaluated. An isogrid design was evaluated based on the expectation that the redundant load path would allow redistribution of load without collapse. Several design approaches were evaluated for arresting the propagation of damage including a hybrid design consisting of an axial discontinuity in the skin consisting of a metal strip.⁶⁸ Although beyond the scope of the present paper, significant research was also conducting in understanding the damage tolerance of stiffened panels loaded into the postbuckled state with potential application to aircraft fuselage structure.¹⁴¹⁻¹⁴² The results described below illustrate several of these advanced damage tolerant design concepts. Structural efficiency studies show damage tolerant designs can be configured which impose a small penalty on structural efficiency.

1. Bonded Blade-Stiffened Panel With $\pm 45^\circ$ Skin

The blade-stiffened compression panel is attractive for structural applications because it is a structurally efficient design, easy to fabricate and more accessible for inspection than closed section stiffeners. The test specimen shown in Fig. 32 is a blade-stiffened configuration with bonded stiffeners in which the skin is composed totally of $\pm 45^\circ$ oriented plies (relative to the 0° load direction). For a wing-panel application this skin orientation provides the primary shear stiffness, while axial stiffness is primarily provided by 0° plies located in the stiffeners. The cross-section proportions for the panel were optimized using the Langley-developed design code, PASCO^{143,144} which included extensional and shear stiffness requirements typical of commercial aircraft aluminum wing panels and included the effect of a bow-type initial imperfection and a maximum allowable strain. The 23 inches wide test panel was initially loaded to 350,000 pounds or 0.0035 strain and impacted under load with a 1/2 Inch diameter aluminum sphere at 300 feet/sec.

The panel survived with only local damage as shown in the C-scan photograph top center. A subsequent load cycle was applied, and the sequence of events which occurred is shown in the moiré fringe photographs at the bottom and the load-strain diagram at the upper right. At a strain of 0.0034 the skin was buckled into 3 halfwaves between stiffeners (bottom center). At a strain of 0.0042 the damage propagated rapidly across the skin, but was contained at two adjacent stiffener interfaces as shown by the moiré fringe pattern, lower right. The panel was then loaded to 500,000 pounds or 0.0050 strain without further damage propagation, and the test was terminated. C-scan inspection confirmed that skin damage did not extend beyond the stiffeners. This test demonstrated the potential of a structural configuration to provide damage containment in a compression loaded carbon/epoxy structure.

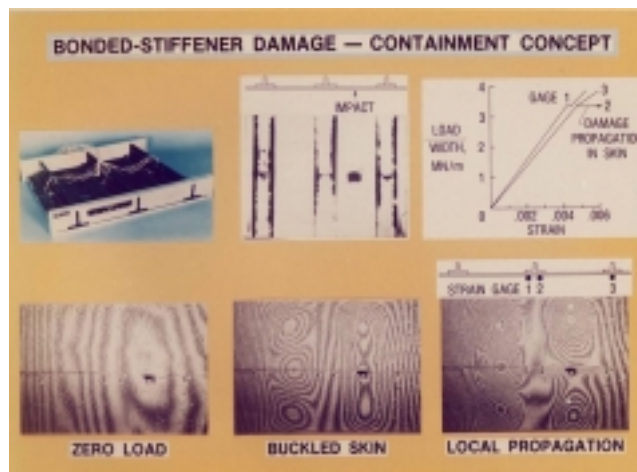
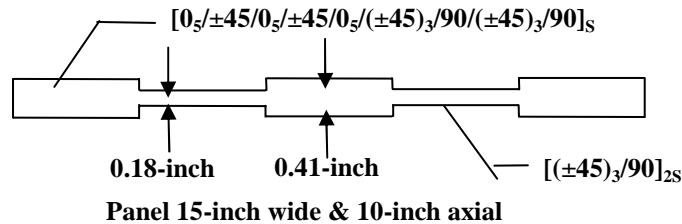


Figure 32. Impact test results for blade-stiffened panel with bonded stiffeners and $\pm 45^\circ$ skin.

2. Plate With Alternating Regions With And Without 0° Plies

Plates constructed with alternating regions with and with axial (0°) plies shown in the sketch below were impact tested following proof testing to strain levels in excess of 0.006.⁶⁸



One specimen was damaged by impact in the low axial stiffness $[(\pm 45)_3/90]_{2S}$ region without load and a second specimen was similarly damaged while the plate was loaded to a strain of about 0.0053. Both had easily detectable visible damage and were subsequently proof loaded to a strain of 0.0060 without propagation of the damage or increase in damage size. The first panel was subsequently damaged in the high stiffness region (with 0° plies) while loaded to an applied strain of 0.0044. No propagation of damage occurred and the specimen was subsequently loaded to a strain of about 0.0055 at which the damage propagated within the high-stiffness region but arrested at the low axial stiffness boundary. The second test plate was damaged while loaded at an applied axial strain of about 0.0054 in the high stiffness region. Upon impact, the high-axial-stiffness region failed similar to the damage propagation of the first panel arresting at the low stiffness boundary.

3. ARAMID Skin/Carbon Stiffener Panel

A plate laminate composed of $\pm 45^\circ$ oriented carbon or Kevlar® (aramid) fibers was shown above to be capable of carrying loads at considerably higher strain with damage than laminates containing axially loaded 0° plies. An all ± 45 -degree laminate is an optimum configuration to carry shear loads but has a low axial stiffness. These characteristics have lead to the development of the so-called “soft skin” stiffened panel configuration in which the skin is composed of ± 45 - and 90-degree (for transverse stiffness) plies and the stiffener has a high percentage of 0-degree oriented material. The skin provides shear stiffness and arrests the propagation of damage while the stiffener provides the panel axial stiffness.

Damage tolerance studies were conducted on a compression panel constructed using Kevlar®-epoxy material for the skin. Kevlar®-epoxy has a relatively high structural efficiency when used for tension application since the axial strength and tension modulus exhibit relatively high values. Although not as efficient as carbon-epoxy for carrying shear loads, a $[\pm 45]$ Kevlar®-epoxy laminate has a specific shear modulus 44 percent higher than the value for aluminum. On the other hand, the structural efficiency for compression loads is relatively low because the material exhibits a nonlinear stress-strain response at strains in excess of 0.0035 and behaves almost like a perfectly-plastic material. It is Kevlar®-epoxy's nonlinear compression response that suggests it may have intrinsic damage-tolerance characteristics and provided the motivation for this study. It was hypothesized that a damage- tolerant structurally efficient hybrid compression panel could be constructed using a predominantly ± 45 -degree Kevlar®-epoxy layup for the skin and a predominantly 0-degree carbon-epoxy laminate for the stiffeners. The Kevlar®-epoxy skin would provide the required shear stiffness and serve to arrest damage initiating in the skin or stiffener.

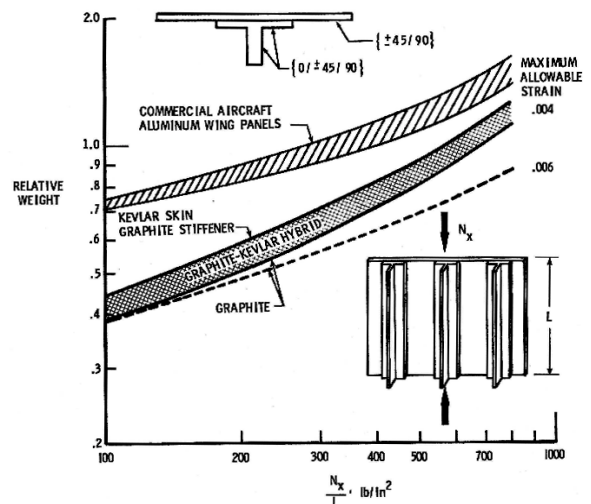


Figure 33. Structural efficiency comparison, skin laminate with $\pm 45^\circ$ & 90° Kevlar® and carbon/epoxy stiffeners versus all carbon.

The results of a structural efficiency study conducted using the stiffened panel optimization code PASCO^{143,144} for a soft-skin configuration designed to meet typical commercial aircraft wing requirements are presented in Fig. 33. These results demonstrate that significant weight savings can be achieved using a soft-skin configuration both with all carbon-epoxy construction and with Kevlar®-epoxy as the skin material when compared to an aluminum

design. Using Kevlar[®]-epoxy for the skin material imposes a weight penalty of approximately 12 percent compared to the all carbon-epoxy design for identical maximum design strains. Even greater weight savings would be achieved if the maximum allowable strain were increased from 0.004 to 0.006.



Figure 34. Blade stiffened compression panel constructed with Kevlar skin and carbon stiffener.

Two heavily-loaded (16,000 lb/in compressive load) stiffened panels with $\pm 45^\circ$ Kevlar[®]-epoxy skins and carbon/epoxy stiffeners were constructed based on the PASCO^{143, 144} design program including typical wing panel requirements. The stiffeners in one specimen were bonded to the skin and in the other were bolted as shown in Fig. 34. The first test involved impacting the Kevlar[®] skin between stiffeners at a design strain of 0.005 using a 1/2-inch diameter aluminum sphere impacting with an energy of approximately 30 ft-lb. The skin sustained local damage but did not propagate in either panel. Next each of the panels was loaded to the design load of 16,000 lb/in corresponding to a strain of 0.0042 and impacted with the same condition of 30 ft-lb in the blade of the carbon/epoxy "T" stiffener. A plywood shield insured that the reflected projectile hit only the stiffener blade. The stiffener sustained sever damage in both cases, but the skin in the bonded design separated from the stiffener and the buckled skin caused separation of the skin from the stiffener and failure of the stiffeners as shown in Fig. 35. On the other hand, the panel with bolted stiffeners survived the major damage to the stiffener. These test results highlight the importance of the interface between the skin and stiffener in stiffened panel design.



Figure 35. Impact tests of blade stiffened compression panels shown in Fig. 34.

4. Damage Containment for Damaged Stiffener Using Tough Resin

Experimental results for plate specimens demonstrated that the strength of impact-damaged laminates could be improved by using tough resin formulations. To compare the performance of two different resin systems in stiffened panel performance, two honeycomb-blade stiffened carbon/epoxy panels designed to meet heavily loaded aircraft wing panel requirements were constructed and tested with damage in one of the stiffeners. One specimen was fabricated using a delamination-prone brittle resin (Narmco 5208) that had been used by industry for several years and the other specimen was fabricated using a tough, delamination-resistant resin (American Cyanamide BP907) that has been shown on the coupon level to be less sensitive to impact damage. To simulate damage,

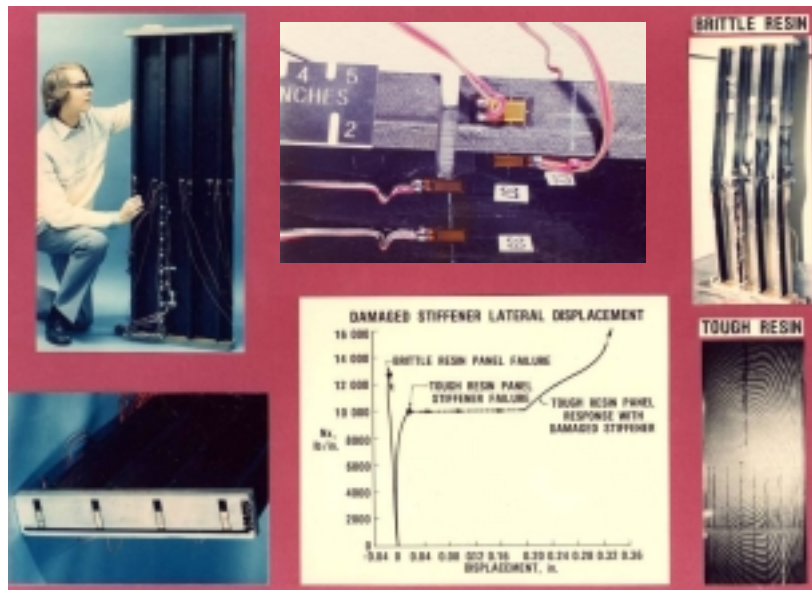


Figure 36. Honeycomb blade stiffened panels constructed of brittle and tough resins tested with damaged stiffener..

identical saw cuts 0.5-inch deep were made in the cap of the second stiffener of the four stiffener wide panels at the stiffener mid-length as shown in Fig. 36.

The saw cut removed locally approximately 59 percent of the stiffener cap axial stiffness and created a high strain concentration in the predominantly 0° cap laminate. The strain concentration resulted in local failure of the stiffener in both the brittle and tough resin panels at a recorded strain of approximately 1.1% measured by the strain gage located adjacent to the saw cut (Fig. 37). The corresponding far field strain was approximately 0.28%. The stiffener of both panels failed locally in a microbuckling shear crippling mode. Globally, however, the response of the two panels was entirely different. For the brittle resin panel (Fig. 36, upper right) the damage propagated in the honeycomb web to the skin/stiffener interface and because the material delaminates easily; the damage was not contained but continued to propagate into and across the skin region resulting in total failure of the panel (see photograph upper right). For the tough resin panel (Fig. 36, lower right), the damage in the stiffener also propagated in the honeycomb web to the skin/stiffener interface following the local cap failure, however, the delamination-resistant tough resin skin laminate was capable of suppressing propagation into the skin. The tough resin panel stiffener failure resulted in a major load redistribution and produced a panel lateral deflection at the stiffener midlength of approximately 0.2-inch as indicated on the graph in Fig. 36. The tough resin panel with damage was capable of carrying greater than 15,000 lb/in axial compression load without failure. For comparison the brittle resin panel failed catastrophically at an applied load of approximately 13,000 lb/in. Arresting the local damage in the tough-resin panel allowed a major internal load redistribution and large out-of-plane deformations of the skin to occur without failing the panel (moiré pattern in lower right represents out-of-plane deflection contours and the graph at the lower middle of the chart compares the out-of-plane deflections for the two specimens). The peak amplitude is approximately 0.32-inch. Repair methods developed for composite panels are discussed in Ref. 145-146. These results indicate that both damage tolerant structural concepts and tough material systems are important factors to consider in the damage tolerant design of heavily-loaded structural components.

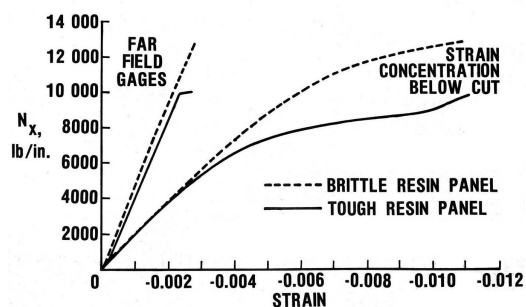


Figure 37. Far field and strain concentration at saw cut in honeycomb blade stiffened panels.

5. Isogrid

An isogrid design in which a grid network of stiffeners oriented at $[\pm 45/90]$ was another configuration studied for damage tolerance assessment. The isogrid test panel shown on the left of Fig. 38 failed when impacted in the skin with the panel loaded to the design load. The performance was significantly improved when the stiffeners were overwrapped with fabric extending onto the skin as shown on the right of Fig. 38. The interface of the stiffener to skin is a common weakness in stiffened panel design and over wrapping is one method of providing resistance to disbonding of the stiffener from the skin. Although limited study of the isogrid concept was conducted, it appeared to merit further consideration as a damage tolerant concept.



Figure 38. Isogrid Far field and strain concentration at saw cut in honeycomb blade

III. Oil Industry Composite Applications

The interest in composites in the oil industry initiated in the late 1970's with consideration of the use of aramid fiber for mooring ropes and fiberglass for pipe applications¹⁴⁷⁻¹⁴⁸. During the 1980's, interest in exploring and developing deepwater reservoirs encouraged several oil companies to assign personnel specifically to explore the potential of composites for applications in the oil industry. In 1994, several oil and oil service companies, the Minerals Management Service and the Department of Energy became charter members of the Composites

Engineering and Applications Center (CEAC) at the University of Houston focused on advancing composites technology for applications in petroleum industry exploration and production (E&P) operations. Another industry/government consortium, the Offshore Technology Center, was chartered in 1988 at Texas A&M University to address a broad range of deepwater E&P issues and in the 1990's began to focus some of its programs on the application of composite materials. European research organizations which have contributed to the advancement of composites technology for the petroleum industry include the Marinetech/Advanced Research Partnership program, Centre for Composite Materials Engineering (University of Newcastle upon Tyne), and Sintef Materials Technology (Norway). The National Research Council's Marine Board sponsored programs to study marine applications of composites including the organization of a national conference in 1990.¹⁴⁹

In January 1995, representative of the petroleum industry submitted a white paper¹⁵⁰ to the National Institute of Standards and Technology (NIST) advocating a program to encourage development of composites technology directed toward petroleum industry applications. Based on the needs and opportunities identified, NIST in 1995 established a focused program on manufacturing composite components for the oil industry and seven programs including: composite production riser, composite drilling riser, composite drill pipe, offshore fiberglass pipe, spoolable composite pipe, flexible composite pipe and pultruded composite shapes addressed oil exploration and production applications. Much like the NASA Aircraft Energy Efficiency Program (ACEE) program, NIST support helped create a critical mass of interested parties involving all the stake holder, the end users (oil companies), technology developers (industry and universities), and potential suppliers (materials and manufacturers). Consideration was made for a 2nd NIST focus program on composites for the oil industry¹⁵¹ in 1998, but NIST was in the process of changing to a general solicitation method. The Composites Engineering and Applications Center has sponsored three international conferences (1993, 1997, and 2000 with a 4th conference planned for the fall of 2005) focused on composites for petroleum applications. Numerous papers present the opportunities to use composites in oil industry applications.¹⁵²⁻¹⁷⁵ In the late 1980's support to develop technology to apply composites to oil industry components also began in Europe and a number of projects have been sponsored by oil companies and the European Union. In the late 1990's, oil company mergers and restructuring reduced emphasis on inhouse research adversely affecting the availability of funds for composites research.

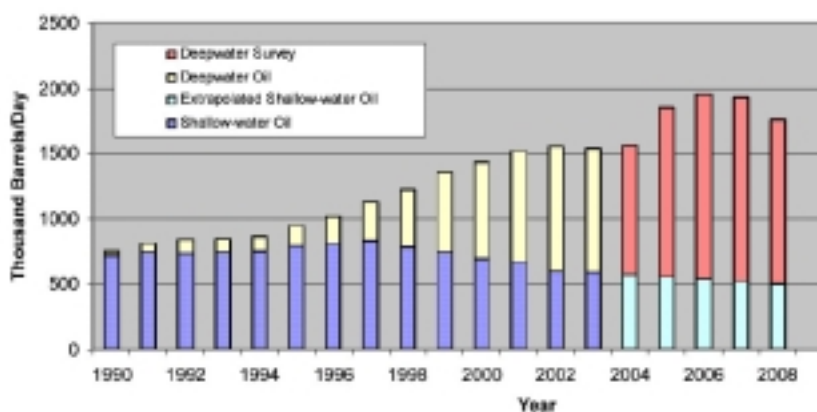


Figure 39. Total Gulf of Mexico Oil Production. (MMS Report 2004-065, page 12¹⁷⁶)

Several factors have converged to make composite materials attractive solutions for primary structural applications on offshore platforms. First, large reserves of oil and gas have been discovered beneath deepwater basins in the Gulf of Mexico (GOM), West Africa, and in other parts of the world. A graph showing recent production from the GOM and projections through 2008¹⁷⁶ is presented in Fig. 39. Deepwater is increasingly providing the majority of United States offshore oil production. The Minerals Management Service (MMS) defines deepwater as water depths greater than 1000 feet and *ultra deepwater* as water depths greater than 5000 ft. A schematic illustrating the variety of offshore operations is presented in Fig. 40. In shallow water, fixed platforms are used with structure extending from the water surface to the seabed while floating platforms are used in deep water. Subsea facilities have also become an important method of production with tie back via pipelines to a platform or a ship. Dynamical positioning is used to hold drill ships on location during ultra deepwater drilling operations. A variety of configurations are currently used in offshore service including: (1) Tension Leg Platform (TLP), (2) semi-submersible, (3) SPAR, and (4) Floating Production Storage and Offloading platform (FPSO). Current water depth records in the Gulf of Mexico include drilling in 10,011 ft. of water with a recent discovery in 9743 ft of water.¹⁷⁷ The current water depth record for production from a TLP is 3800 ft, from a SPAR is 5400 ft. and from subsea facilities is 7591 ft. of water.¹⁷⁷

A listing of some of the applications proposed for composites is provided in Appendix A. Applications highlighted in *italics* have been introduced into products. Some composite applications including: fiberglass pipe

used onshore and offshore,¹⁷⁸⁻¹⁹⁵ topside facilities,¹⁹⁶⁻¹⁹⁸ tanks,¹⁹⁹⁻²⁰⁰ high-pressure accumulator vessels used to support riser tensioners,²⁰¹ and spoolable composite pipe,²⁰¹⁻²³⁴ have been commercially produced and used. Other applications such as composite risers,²³⁵⁻²⁵⁶ composite drill pipe, and composite tendons²⁵⁷⁻²⁶⁸ show promise but are still in development or field trial studies. One application of composite materials which has become a highly important advancement for deepwater development is dry synthetic fiber, primarily polyester, used in mooring ropes for station keeping of deepwater floating platforms.²⁶⁹⁻²⁷⁷

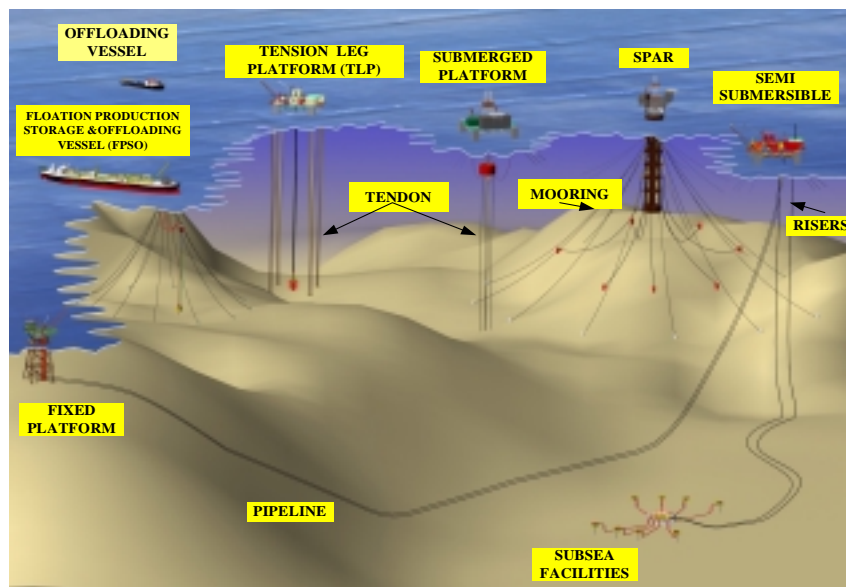


Figure 40. Offshore oil and gas exploration and production operations.

Steel is the primary material used in the construction of offshore platforms and supporting infrastructure; and tubulars are the most common structural element with products ranging from the transport of fluids to framework construction. Corrosion control and weight savings are the two main factors motivating the interest and growth of the use of composite components in offshore oil and gas exploration and production operations. Controlling and inhibiting corrosion and periodic replacement of metal components costs the oil industry large amounts of money; while composite materials can usually be chosen²⁷⁸ which will resist corrosion and be compatible with saltwater and the chemicals used downhole and offshore. Reducing the weight of deep (> 1000 ft.) and ultra deepwater (> 5000 ft.) floating platforms has become a high priority and the low density of composites yields the most effective solution. The total weight saving benefits often include indirect savings¹⁶⁹ as summarized in Table 1 and to be captured must be considered in the initial design of the platform. For example, saving weight on a TLP using a composite riser results in an additional indirect 185% weight savings contributed by the reduced need for the platform to provide buoyancy to carry the weight of the riser and from reduced pretension requirements. Composites can also provide enhanced safety such as the application of fiberglass firewater pipe²⁷⁹⁻²⁸⁸ to replace steel pipe with associated corrosion problems including clogging the deluge system nozzles. Composites also provide unique advantages for special downhole operations in which tubulars and other products benefit from composite material's electromagnetic transparency and from the ability to integrate electrical wiring and fiber optics into the composite structure as energy and signal carriers or for structural monitoring.²⁸⁸⁻²⁹¹ Some applications also benefit from the damping and fatigue resistant properties of composites. Lower thermal conductivity can provide advantages for pipelines where it is important to keep the fluid temperature elevated to avoid solidification and lighter weight components often makes it easier to conduct offshore operations.

Table 1 - Weight Savings Leverage for TLP in 4000 Ft. Water Depth.¹⁶⁹

Component	Hull (ton)	Deck (ton)	Payload (ton)	Riser (ton)	Tether Pretension (ton)	Total Savings (ton)
Hull	1.0	0	0	0	0.32	1.32
Deck	0.47	1.0	0	0	0.47	1.94
Payload	0.72	0.5	1.0	0	0.71	2.93
Riser	0.69	0.5	0	1.0	0.66	2.85

Weight savings of approximately 50% is the upper bound in most aluminum aircraft applications with many of the savings captured in the range of 30 percent. With oil field components, weight savings on the order of 100 percent are possible due to the larger difference in density for steel compared to composite. The greater magnitude

of the potential structural efficiency weight savings provides greater flexibility to build in higher safety factors to account for the uncertainties associated with new oil industry applications. Ultimately, the incentive to use composites or metal in the oil industry is cost. In many cases the initial cost will be higher in composites than metals, but significant life cycle costs can be demonstrated.

The technology needed to safely and economically develop deepwater petroleum bearing reservoirs is extremely complex and important advancements have been made in several technologies including: seismic, directional drilling, multiple completions, subsea systems, and advanced production techniques. Composite materials is another technology which could provide important enabling solutions for safe, affordable deepwater development. Floating platforms are the only practical configurations for deepwater and are commonly used in combination with subsea wells. Floating platforms are tied to the ocean floor by moorings or tethers, or for drilling can be dynamically positioned using thrusters. Saving weight is an important design consideration for floating platforms with more cost benefit for some configurations such as Tension Leg Platforms (TLPs) than others and corrosion prevention is also important. Successful introduction of secondary composites on recent GOM TLPs and NIST ATP research programs have positioned the oil industry to be more receptive to using composite components.

Like the aircraft industry, the risk of structural failure for many proposed oil industry applications can have serious consequences and establishment of specific requirements including environmental risk factors, qualified materials data base, reliable design methodology is critical to safe performance. Damage tolerance factors include the same kind of issues aerospace faces including manufacturing defects, inclusions, impact damage, chemical degradation, and fire resistance. The oil industry can draw on the extensive technology developed for aerospace, but some of the technology must be developed independently to address different requirements. One of these issues is in the development of standards of practice and risk assessment to meet the requirements of operators and regulatory authorities. Although the oil industry has come to accept composite materials; there is a cost associated with proving reliability and a cultural bias toward familiarity with steel.

The approach used to measure structural integrity or damage is integrally associated with the topic of damage tolerance. Almost all of the methods adapted to aerospace applications have been investigated. As with aerospace, visual inspection is a preliminary method particularly underwater using an ROV. Ultrasonic methods have been used but in contrast to aerospace is not a primary method. Fiber optics are becoming an important tool in the oil industry for communication downhole and the ability to integrate optical fibers into the composite structure for structural monitoring is an important emerging technology. Plastic optical fibers are being investigated for the large strains experienced in mooring ropes.²⁷⁶⁻²⁷⁷ Measurements of changes in strain over time has been found to be a useful structural integrity assessment monitoring tool. Acoustic emission has been used successfully to monitor the structural integrity of tanks onshore and has been investigated for application offshore. Advanced methods such as X-ray computed tomography are also being studied.²⁵⁶

The remainder of this section highlights a few of the innovative ways composite materials have been used in the design of applications of interest to the oil industry with special emphasis on issues related to damage tolerance.

A. Fiberglass Pipe for Fire Protection

Filament wound fiberglass pipe was first introduced into the oil field in the late 1950's. The lighter weight, fatigue and corrosion resistance and associated low life cycle costs make FRP components very attractive for expanded offshore applications. Glass fibers are inert to most chemicals and resin materials are available which are compatible with most environments experienced in the oil industry. FRP components are from one-third to one-fifth as heavy as equivalent steel components and the lighter weight permits FRP products to be more easily handled and installed. FRP connections eliminate the hazards associated with welding and the experience level required to make quality connections can be learned very quickly. The net result is that FRP composites can provide significant cost savings relative to metal. There has been significant increase in the use of FRP offshore in the last twenty years in the Gulf of Mexico, Middle East, Far East, Africa and the North Sea. An example is the low pressure pipe



Figure 41. Fiberglass pipe used in offshore operations.

used in Dubai in the water injection system with pipe ranging in size up to 36-inch in diameter as shown in Fig. 41. Environmental concerns also encourages the use of fiberglass pipe for low pressure water transport. An emerging design philosophy is to use non-corrosive composites to permit elimination of chemicals such as corrosion inhibitors required to protect steel pipe.

One of the most interesting applications for FRP pipe offshore is the use in the transport of water in fire protection systems. Although not intuitive, extensive fire testing has shown that FRP pipe is as safe if not safer in this critical safety related application than steel pipe.^{279,283,284}

The problem with steel pipe is that corrosion particles clogs the nozzles of the deluge system and even repetitive testing cannot insure that sufficient water will be delivered. Following the disastrous fire in the North Sea on Piper Alpha in 1988, the oil industry worked with regulatory agencies to establish the test criteria to quality FRP pipe for this safety critical application.^{175,285,292}

The United States Coast Guard published criteria for using FRP for the firewater ring main and deluge pipe in Policy File Memorandum PFM 1-98 16714. A firewater pipe installation penetrating through the floor of a phenolic resin fiberglass grating^{286,287} is shown in Fig. 42.



Figure 42. Fiberglass firewater pipe passing through phenolic resin fiberglass grating.

B. Composite Riser

A program to develop a composite riser was first initiated by Institut Francais du Petrole and Aerospatiale in 1985.²³⁵⁻²³⁸ The program resulted in a successful prototype, but it was early in the deepwater development activity and the estimated cost was considered too expensive for the market. The drop in the cost of advanced composites and the accelerated pace of deepwater development in recent years renewed interest in a composite production riser. Two joint industry projects, in part supported by the National Institute of Standards and Technology (NIST) Advanced Technology Program (ATP), focused on the development of composite risers. One led by Lincoln Composites (presently part of General Dynamics) focused on a production riser²⁴¹ and the other led by ABB Vetco Gray focused on a larger diameter drilling riser.²⁴⁰

The 10.75-inch Lincoln Composites production riser is a hybrid construction composed of carbon and S-glass fibers



Figure 43. Composite production riser.

embedded in an epoxy matrix. The composite body transfers load into a metal end coupling using a "trapped lock" design commonly used in the aerospace industry. The Lincoln program involved an extensive test program with over sixty, 12 feet long specimens tested under different load conditions simulating the environment experienced in service including internal and external pressure and axial tension and fatigue.^{241,245,246,249} The average burst pressure for 6 specimens was 11,635 psi and the average axial load at failure for 6 specimen was 942 kip. A photograph showing a 50-ft long section of production riser built by Lincoln Composites is shown in Fig. 43. The weight of the riser in air is 1450 pounds which represents a 41 percent weight savings compared to steel. The corresponding weight savings in water is 68 percent. This weight savings provides a significant impact on the platform design considering the long length from the platform to the sea bed and the large number of risers deployed on a typical deepwater platform.

The most recent evaluation program for a composite riser is a joint venture between Norske Conoco A/S and Kvaerner Oilfield Products.²⁵⁵⁻²⁵⁷ Several composite drilling risers were fabricated and extensively tested both in the laboratory and in drilling operations on the Heidrun platform in the North Sea.²⁵⁵ The composite design is compatible with properties characteristic of the current titanium drilling riser and the design includes a titanium liner. The requirements for the 22-inch diameter composite drilling riser are more demanding than for a production riser. Not only is the diameter much larger, but large bending loads are imposed. Also, an impact damage criterion was considered based on simulation of a dropped riser. A series of laboratory tests were conducted to evaluate methods proposed to monitor the structural integrity in service. Measurement of axial and hoop strains using fiber optics and strain gages were found to correlate with progressive damage in the composite riser imposed at high load levels.²⁵⁵ An X-ray tomography system is also being developed for in service monitoring of tubular structural integrity.

In another study, a Comparative Risk Analysis assessment is being conducted by OTRC at Texas A&M University to compare the risks associated with the use of a composite versus a steel production riser.

C. Spoolable High Pressure Pipe

A new class of product is being introduced into the oil industry based on a technology developed to design and fabricate continuous lengths of composite pipe which can be bent to a relatively small radius of curvature and placed on a cylindrical spool for storage and transport.²⁰¹⁻²³⁴

Composite tubing can be tailored to exhibit unique anisotropic characteristics which optimally address combined burst and collapse pressures and tensile and compression loads, as well as the high strains imposed by bending. Composites can be designed to be more resistant to fatigue than steel coiled tubing, especially when combined

loads impose strains which force the steel tubing into plastic deformation. Composite tubes can weigh 1/3 as much as comparable steel tubes, which for some operations provides significant service advantages. Composite pipe is near neutrally buoyant in produced fluids which can be beneficial in moving the pipe in deviated or horizontal wells or pipelines. One emerging application to use this capability is for pipeline cleanout. By tailoring the cross-section to optimally carry pressure, tension, compression and bending loads; it is possible to wind a high pressure composite pipe onto a relatively small-diameter spool. The composite pipe is tailor designed to be able to repeatedly experience large strains without failure. The basic concept for the pipe is illustrated in Fig. 44. Several cross-ply laminates constructed of glass, carbon or aramid in an epoxy or other resin are wound onto a thermoplastic liner constructed of high density polyethylene, polyamid, PVDF or other polymeric material. The process for making

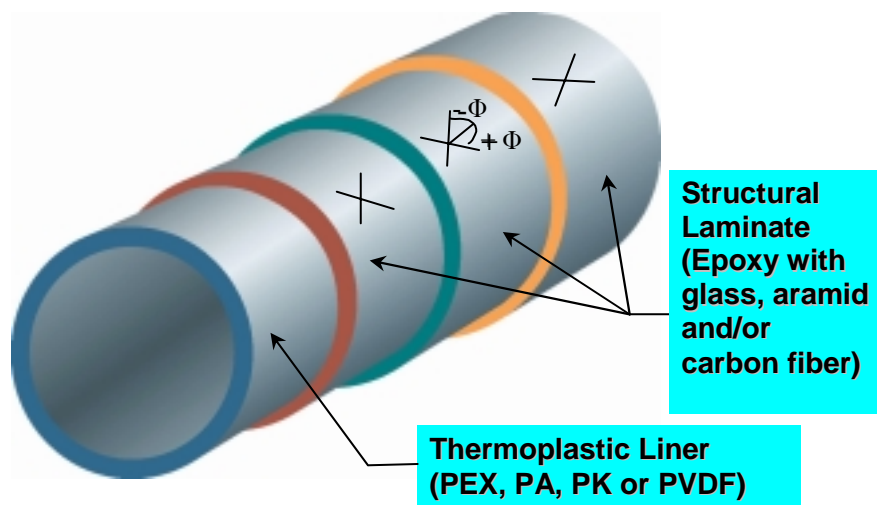


Figure 44. Spoolable pipe basic design.

spoolable pipe is different from conventional filament winding in that instead of the pipe rotating to apply the fibers, small spools of fiber articulate around the pipe using ring winders or braiders such as illustrated in Fig. 45.

Conoco initiated an inhouse program to study spoolable pipe for flowlines applications in the late 1980's and in 1993 sponsored a composite coiled tubing development project²³⁴ with Fiberspar Tubular Products in the United States and Compipe a/s in Norway. Hydril developed similar products sponsored by a Joint Industry Project (JIP) in a NIST ATP program.²¹¹ The Conoco effort initially evaluated the concept using Kevlar[®] fiber and epoxy as a water injection line, but later focused the technology on the development of a design based on carbon fiber which would meet the rigid requirements of coiled tubing applications.^{202,204,205}

Several innovative configurations were developed for special needs²³⁴ including the formation of cells, selective reinforcement, and integration of fiber optics and energy carriers into the composite wall; concepts illustrated in Fig. 46. Several applications are being explored to use spoolable composite tubulars including: onshore and offshore pipelines, subsea injection lines, well workover/intervention services, flowline cleanouts and surveys, wellbore completions and coiled tubing drilling. A design utilizing anisotropic tailoring of the composite tube construction to allow pressure variations in the pipe to cause the pipe to twist and help keep it from becoming stuck during downhole operations is another advanced concept. Large-diameter (> 6-inch), long-length, composite pipe is also being considered for future development as flexible risers and subsea pipelines.

The concept of manufacturing continuous composite pipe to meet oil industry needs was influenced by the performance demonstrated in NASA research on $\pm 45^\circ$ laminates loaded in compression.^{59,62,71,72,74} The classical design of composite pipe to carry internal pressure is with a fiber angle relative to axial of $\pm 54^\circ$ corresponding to the 2:1 hoop to longitudinal stress ratio. Axial strains of 3% are commonly imposed on the pipe during spooling. Winding the fiber at from $\pm 40^\circ$ to $\pm 60^\circ$ keeps the strain in the fiber low during bending onto the spool. For example, for a $\pm 45^\circ$ carbon laminate, the strain in the carbon fiber is only 12 percent of the imposed axial strain.

The test procedures developed to assess the performance of composite spoolable pipe for the downhole coiled tubing application included a full reversal cyclical bending test illustrated in Fig. 47



Figure 45. Multiple rotating winding stations used to manufacture long length spoolable pipe.

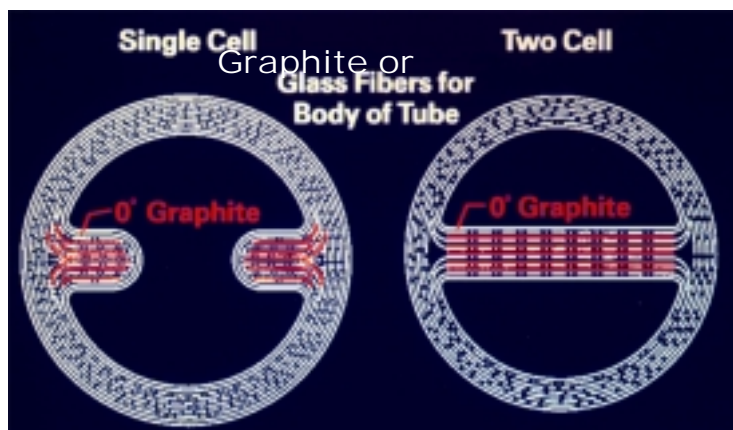


Figure 46. Spoolable composite pipe selective reinforcement and cells.

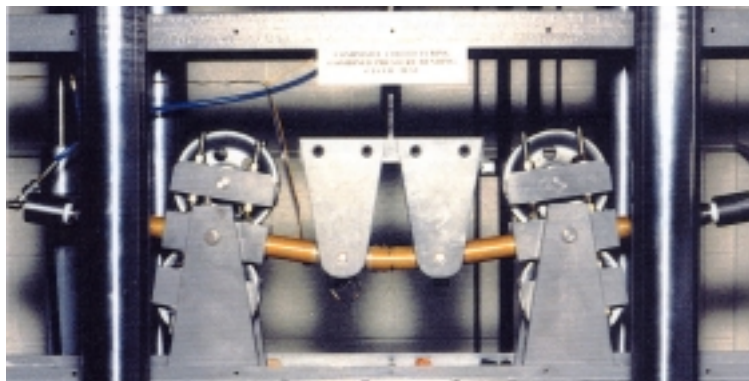


Figure 47. Spoolable composite pipe reversible bending with or without pressure applied.

with and without the tube pressurized. Additional tests included ultimate internal pressure, ultimate axial tension, ultimate axial compression, combined pressure and tension, external differential pressure, rapid decompression and a dropped weight impact test. For the coiled tubing application, some operational conditions require the pipe to be inserted into a pressurized well. The combination of axial compression and internal pressure imposed as the pipe as it is forced through a pressure seal stripper by the rotating chain blocks of a coiled tubing injector is one of the most difficult design requirements that can be imposed on any composite. The diametrical expansion of the composite at the point of entry into the stripper limits the maximum pressure differential which can be successfully imposed on the tube by the well internal pressure. Fiberspar Corporation manufactured a composite coiled tubing drill string over 20,000 feet long for Halliburton who conducted drilling field tests in a project called Anaconda.²³³ The design requirements for typical onshore line pipe for hydrocarbon and water service are much less compelling and most of the commercial success to date of spoolable pipe products has been in this type of application. ASTM D2992 long-term pressure test procedure is one of the test methods used to qualify spoolable pipe for onshore line pipe service.

D. Composite Tendon

Aerospace studied the use of high stiffness boron fiber in the early 1970's as selective reinforcement of aluminum²⁹³⁻²⁹⁵ for wing box and other structural applications. The photograph of Fig. 48 shows an extruded "T" shaped aluminum stiffener with three circular holes. The holes were subsequently filled with longitudinal boron fibers and the space between fibers filled with resin in a vacuum infiltration process. Another concept for using boron was to bond boron tape to a metal stiffener. One critical design problem associated with such a high stiffness material (modulus 58 msi (400 GPa)) is the transfer of load in regions of reinforcement run-out back into the metal component. For bonded configurations, the plies were stepped to avoid shear failure in the region of reinforcement run out. For the infiltrated stiffener concept, a method of machining a taper in the boron stiffener in the end region was found to be effective in reducing the shear stress concentration.²⁹⁶ Boron fibers are manufactured in a vapor deposition process as individual fibers onto a tungsten substrate and are thus inherently expensive, so boron became of less interest as lower cost carbon fibers became more readily available.

An analogous application of unidirectional oriented fibers in the oil industry is the use of pultruded carbon rods such as shown in Fig. 48 for application as a tendon for a Tension Leg Platform (TLP). An assembly of multiple small diameter unidirectional rods efficiently provides the high strength/stiffness structure required for the application. Deepwater TLP tendons are primarily stiffness critical rather than strength driven. The potential economic benefits anticipated from using carbon fiber tendons are associated with composites low density which reduces the need for buoyancy and the availability of low-cost manufacturing processes. Steel tendons are limited by fatigue loading whereas a composite tendon designed to meet stiffness requirements is relatively insensitive to fatigue. Neutrally buoyant steel tubular tendons currently used in deepwater are considerably more expensive in ultra deepwater due the need to resist collapse from high external pressure loading. To resist collapse in deepwater; either rings and stiffeners must be added to the steel tube, the tube must be internally pressurized, or the diameter-to-thickness ratio of the tubular must be reduced below 30 thus making the tendon heavier than water. The wet weight of the tendon must be carried by the buoyancy of the hull or expensive buoyancy modules.

Carbon rod tendons can be spooled since the individual rods can be bent without damage and slide one relative to the other in a rope assembly. For example, the strain imposed a 5 mm diameter composite rod bent to a 2 meter radius is only 0.25 percent. Although carbon fibers are available with modulus values as high as four times the modulus of steel, high modulus carbon fibers are more expensive and exhibit low strain to failure. Based on current economics, a composite rod constructed of carbon fiber encapsulated in a vinyl ester or epoxy resin binder will have an axial

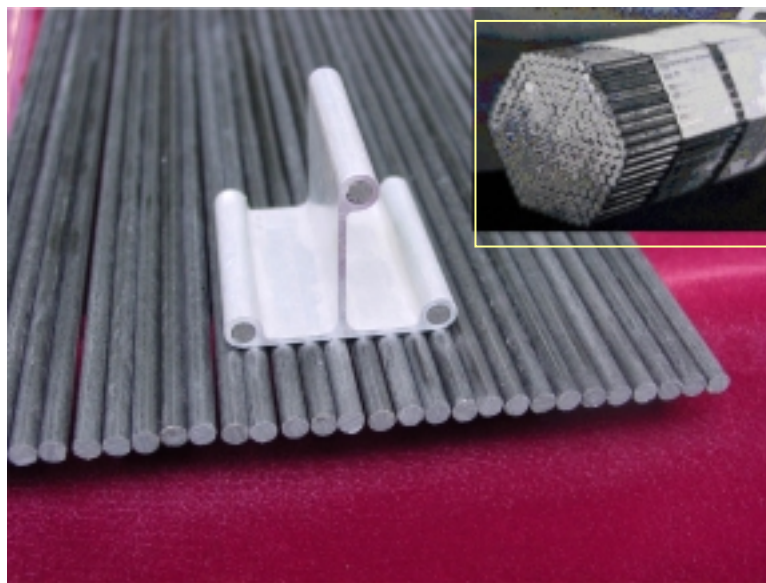


Figure 48. Boron stiffened aluminum and pultruded carbon fiber rods.

modulus of elasticity around two-thirds the modulus of steel. To match the stiffness of the steel, additional cross-sectional area must be provided to the composite tendon. However, the areal profile to ocean currents and associated loads will still be less for the smaller composite rope than for an equivalent stiffness neutrally buoyant steel tubular supported by buoyancy modules.

Carbon rod tendons were first studied in an experimental program including static and fatigue tests in the late 1980's in a program sponsored by Conoco U.K. with Bridon Ropes.²⁵⁸⁻²⁶⁰ More recently Deepwater Composites has advanced the technology.²⁶⁸

E. Mud Motor Torque Shaft

Composite properties can provide efficient engineering solutions for applications in which torque is a significant design load requirement. In the late 1980's Conoco and DuPont designed, fabricated and tested a mud motor composite torque shaft. The problem addressed was to prolong the life of the universal joint in the mud motor which at the time of the development was the major weak link in the mud motor assembly. The design used carbon fiber and a PEEK thermoplastic resin. Loads include not only torque to drive the drill bit, but also bending as the drive shaft articulates in a nonconcentric rotation. Test specimens were successfully laboratory tested in a dynamometer under representative field conditions including bending, compression, and torsion. The composite mud motor torque shaft is shown during assembly into the mud motor in Fig. 49.



Figure 49. Mud motor torque shaft.

Although the shaft passed dynamometer tests with loads higher than the design loads; it failed during a subsequent field test. It was believed the tube was damaged during the field make-up of the mud motor assembly when larger loads were imposed than the shaft was designed to carry. The development of the composite torque shaft was dropped when mud motor manufacturers developed alternative solutions to the torque shaft failure problem. One of the uncounted benefits of new technology is that it often motives improvements in existing technology.

F. Synthetic Fiber Mooring Rope

Synthetic fiber ropes constructed of polyester are providing an important enabling technology for mooring deep-water drilling and production platforms. To date, synthetic fiber mooring ropes have been successfully deployed in Brazil and have recently been deployed in new installations in the Gulf of Mexico. Forty years ago polyester fiber was proposed for applications in expandable space structures including airlocks and lunar shelters²⁹⁷ and NASA conducted mechanical and abrasion fatigue tests to evaluate polyester damage tolerance.²⁹⁸

Saving weight is the primary driver encouraging operators to use synthetic fiber moorings for station keeping on deepwater floating platforms. Synthetic fiber mooring ropes have high strength-to-weight ratios and possess adequate stiffness, but they are much more susceptible to damage than their steel wire rope counterparts. Steel wire rope mooring systems become very expensive in deep water because of the need to provide expensive buoyancy to support the weight of the mooring and due to related operational complexities such as an extended footprint which may interfere with adjacent

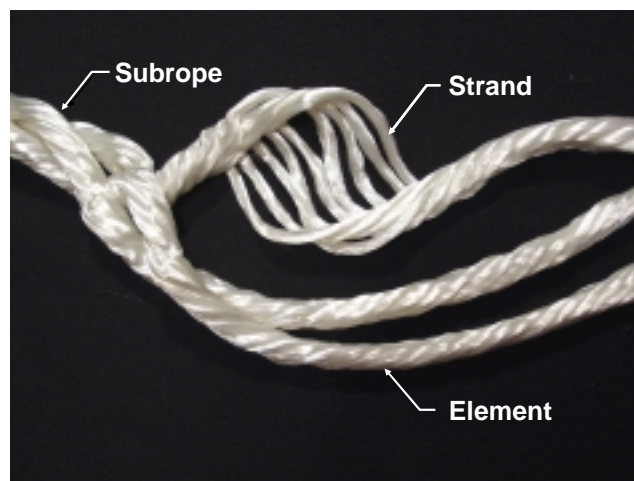


Figure 50. Subrope, elements, and strands.

operations or extend outside the operators lease. Petrobras (Brazil) pioneered the introduction of polyester fiber mooring ropes in deep water service.²⁷¹⁻²⁷² For water depths on the order of 3000-5000 feet, polyester is the most economical material to meet typical mooring requirements. Greater axial stiffness and strength requirements for ultra deepwater may drive the designer to prefer higher performance materials such as aramid fiber or to carbon rod ropes such as that proposed for TLP tendons.

The GOM marine environment is much more severe than waters off the coast of Brazil including large loop currents and strong hurricane conditions. The threats of damage to mooring ropes include cuts and abrasions during installation or service as well as damage from dropping the rope onto the seafloor during installation. Sand particles can be introduced into the body of the rope as a result of exposure on the seabed and lead to progressive damage through internal abrasion, wear, or cutting mechanisms. In addition, small marine organisms have been found to grow within the body of the rope at shallow water depths.

Numerous studies have been conducted on the effects of damage and to analytically model the performance of mooring ropes. Small scale tests were conducted at the University of Houston²⁷⁵ on the subrope constructions shown in Fig. 50 taken from the mooring rope shown in Fig. 51. Polyester exhibits strain capability in excess of 10 percent as shown in the stress-strain plot in Fig. 52. Tests on subropes with cut fibers such as shown in Fig. 53 were conducted and subsequently correlated with an analytical model to predict the behavior of damaged ropes being developed at the University of Texas. Full scale experiments on polyester mooring ropes are being conducted in a program coordinated by the Offshore Technology Research Center at Texas A&M University to determine the effect of damage on the residual strength of mooring ropes.

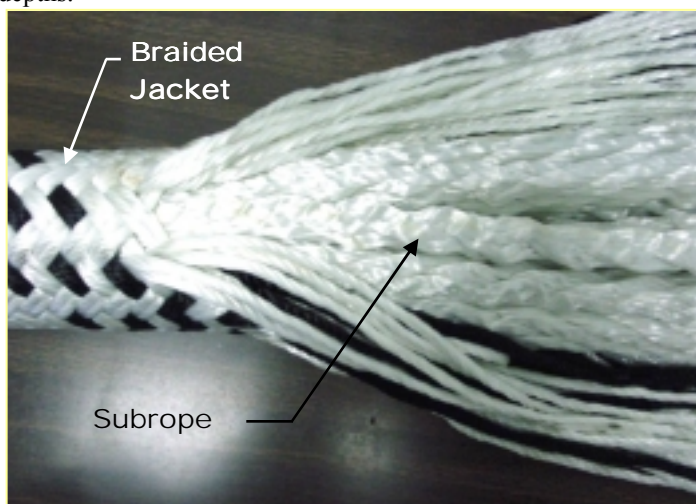


Figure 51. Mooring rope construction with twisted subropes.

The most common current method to monitor the integrity of synthetic fiber ropes is visual inspection. This method has major deficiencies since it tells nothing about the load-strain history of the rope or the state of internal wear or degradation. Lacking a better method, Petrobras has approached the inspection issue by (1) using an ROV to inspect the ropes visually and (2) placing short sections of mooring rope in the string near the surface and periodically removing and testing them for residual strength. This approach is also being adopted in initial installations approved by the MMS for Gulf of Mexico operations. Mooring ropes proposed for offshore platforms, for example, may be a foot or more in diameter and carry 3 to 5 million pounds (1.3 to 2.3 kilotonnes) of load. For such large ropes, one cannot visually detect internal wear and damage. In addition, it is difficult to reliably inspect long length mooring ropes *in situ* using ROV technology. Future safe deployment of synthetic fiber mooring ropes would be significantly enhanced if a reliable technique were available to monitor the performance of the ropes in service and thus provide an early warning of the loss of structural integrity.

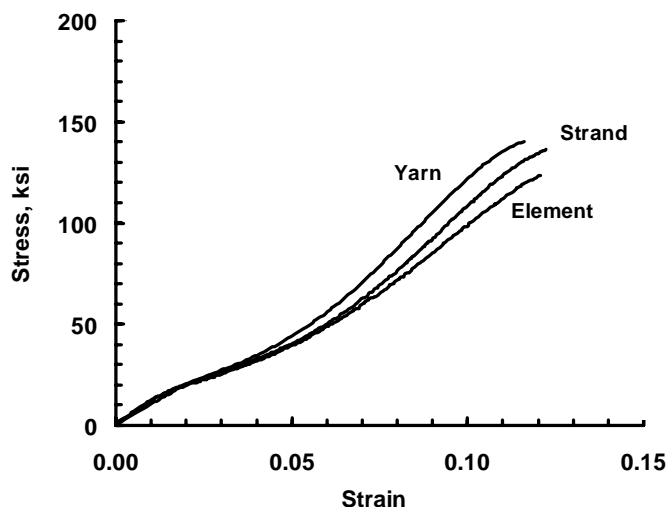


Figure 52. Polyester stress-strain.

Reference 299 states, “The tensile fatigue behavior of nylon and polyester single fibers and yarn is characterized as a simple process of accumulation of creep strain and failure occurs at a strain that is similar to the static strain to failure”. Measurement of the state of strain in the rope, including accumulated strain, should provide a reliable benchmark with which to estimate the remaining life of the rope and allow the establishment of meaningful criteria for rope recertification or retirement. Such measurements would be particularly useful following installation and hurricanes or other major disturbances. Fiber optics has been proposed as a method for making measuring mooring rope strain.



Figure 53. Damaged element of subrope.

A direct method to measure mooring rope strain is being developed based on the placement of high strain plastic optical fibers parallel to the polyester fibers along the axis of the rope and the use of Optical Time Domain Reflectometry (OTDR) instrumentation to measure changes in its length as the optical fiber and rope are stressed.²⁷⁶⁻²⁷⁷ The concept illustrated in Fig. 54 shows plastic optical fibers located within the mooring rope of a taut leg platform. A portion of the light signal is reflected at interfaces placed along the axis of the fiber to allow measurement of strain within discrete gage lengths. Strains measured in polymeric optical fibers exhibit good one-to-one correlation with applied strains within the test range studied (10% or less, typically). The integrated polymeric optical fiber has been shown to withstand large numbers of repeated cycles to high strains without failure and to accurately track the hysteresis exhibited by polyester rope as shown in Fig. 55 for a polyester subrope. Periodic interrogation would allow measurement of changes in the accumulated strain for comparison with pre-established design guidelines and; if needed, remediation action could be taken.

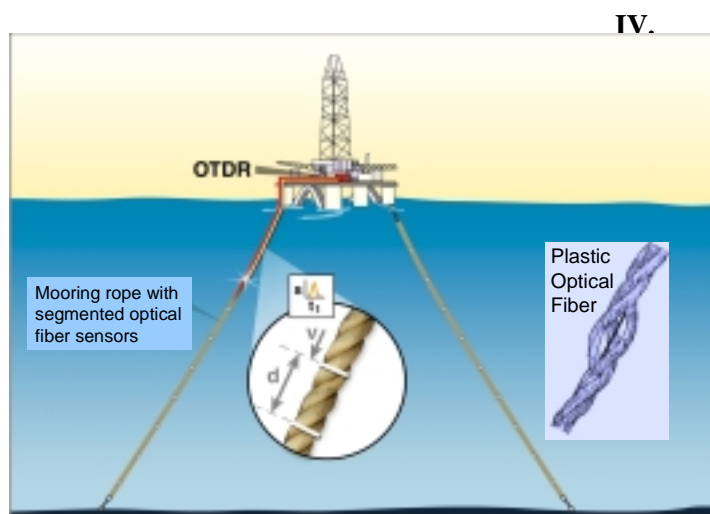


Figure 54. Monitoring strain in a floating offshore platform using plastic optical fibers and Optical Time Domain Reflectometry instrumentation.

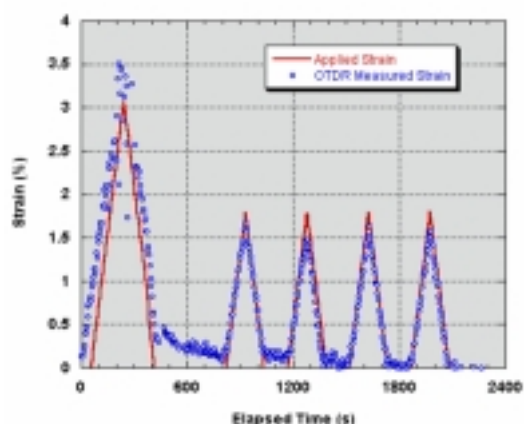


Figure 55. Applied and OTDR measured strain comparison for 5 cycles of mooring rope loading.

IV. Conclusion

Composite materials continue to be applied to new products including primary structure used in the aerospace and oil industries. Weight saving is the primary motivation to use composites, but other assets such as corrosion resistance, electromagnetic transparency, ability to integrate fiber optics and energy carriers are sometimes even more important. Performance is important, but the ultimate decision to use composites in many applications is cost savings. Often the cost savings are magnified by consideration in the initial design phase rather than as retrofit. Deployment of composites in critical applications by industry and acceptance by regulatory authorities depends on understanding the characteristic limitations of material systems and structural concepts derived from basic research and critical laboratory and field demonstrations of the technology. The tolerance of composite materials and structures to damage, imperfections, and inclusions is one of these key technology areas. Early analytical structural efficiency studies and experiments showed weight savings of approximately 50% could potentially be achieved using composites in primary aircraft wing structure. Additional experimental studies, however, showed that impact damage could significantly reduce the strength of composites and in contrast to metals; compression strength was often the most critical limitation. Development of basic understanding of the response of composite materials and structures, especially to compression loading, was the focus of a research effort initiated at NASA-Langley in the mid 1970's.

The basic compression failure modes at the materials level are delamination and shear crippling involving the microbuckling of fibers. Both the matrix and fiber properties were found to affect the failure modes and strength. Suppliers were encouraged to develop "tough" resin formulations and the NASA Aircraft Energy Efficiency (ACEE) program orchestrated the development of industry standards to evaluate potential improvements. Structural optimization programs were exercised to investigate the effect limiting the allowable strain would have on potential weight savings. Advanced structural configurations were developed and evaluated with improvements demonstrated in the laboratory. Considerable advancement has been made in both materials and structural configurations since these initial studies to characterize the damage tolerance of composites to impact damage and inclusions. These advancements have allowed the aerospace industry to introduce additional applications of composite materials into aircraft.

The oil industry also sees benefit in the use of composite materials in applications where weight saving is important such as in deep water offshore oil and gas exploration and production operations and in applications where corrosion resistant is an asset. Fire resistant fiberglass products have been introduced offshore, including critical applications such as firewater pipe and gratings. These successful introductions have come about through intensive testing and a close interaction with regulatory agencies. Advanced composite applications include high pressure accumulator bottles used to adjust the tension on risers, spoolable pipe, and synthetic fiber moorings while other high payoff applications such as composite risers and tendons are still awaiting deployment.

Composites technology resulting in products for use in the oil industry has drawn on the extensive composites technology developed by the National Aeronautics and Space Administration and the Department of Defense. Technology transfer is an important fringe benefit of government sponsored research. The design issues for products in the oil industry are often different from aerospace, however, and independent research is necessary to address unique issues, i.e., the large strains imposed on spoolable pipe or mooring ropes or the application of fiber optics technology. Some of the technology developed in support of the oil industry may even be of interest to the aerospace industry. Organizations such as CEAC at the University of Houston, OTRC at Texas A&M University, and counterpart organizations in Europe have conducted studies and coordinated research programs to advance composites technology to meet the challenging requirements defined by the oil industry. United States government organization including the Minerals Management Service, the Coast Guard, the Department of Energy, and the National Institute of Standards and Technology have been helpful in defining regulatory requirements and sponsoring research programs related to oil industry composite applications.

Appendix A

Proposed Oil Industry Applications for Composites.

- **Facilities**
 - *Fiberglass pipe – water transport*
 - *Storage Tanks*
 - *High Pressure Vessels*
 - *Process Equipment*
- **Platform Structure**
 - *Primary Deck Structure (Beams, Girders)*
 - *Secondary Deck Structure (Gratings, Hand Rails)*
 - *Buoyancy Modules*
 - *Drilling Derrick & Flare Boom*
 - *Stress Joint / Keel Joint*
 - *Accommodation Modules*
 - *Blast Walls*
- **Risers**
 - *Production*
 - *Drilling (Field tests)*
 - *High Pressure Accumulator Bottles*
 - *Tubing*
 - *Choke & Kill Lines*
- **Downhole**
 - *Tubing*
 - *Tools*
- *Drill Pipe (Field tests)*
 - **Integrated Energy Carrier/Fiber Optics**
 - **Mud Motor Torque Shaft**
- **Station Keeping**
 - **Carbon Fiber Tendons**
 - *Synthetic Fiber Mooring Rope*
- **Spoolable Composite Pipe**
 - **Coiled Tubing**
 - *Hydrocarbon Flow Lines (onshore)*
 - *Water/CO₂ Injection lines (onshore)*
 - **Large Diameter Subsea Lines**
 - *Drill Pipe (Field tests)*
 - *Tubing (onshore)*
 - **Subsea Pipeline Remediation**
 - **Subsea Injection Lines**
- **Subsea**
 - **Structure**
 - **Pipe lines**

Acknowledgments

The author wishes to express appreciation to NASA and to Conoco Inc. for supporting a research environment conducive to the advancement of technology and for the opportunity to work with so many talented and professional engineers and scientists. It was the author's privilege to have worked with Dr. James H. Starnes, Jr. for 15 years at the NASA Langley Research Center sharing an interest in composites technology with special interest in understanding damage tolerance issues and seeking materials and structural design improvements. Numerous people have made contributions in advancing the understanding of composite damage tolerance and many of their names appear in the reference list. Dr. Starnes received his Ph.D. at the California Institute of Technology in 1970 with a dissertation on the topic "The Effects of a Circular Hole on the Buckling of Cylindrical Shells"³⁰⁰ and successfully contributed to advancing technology in topics of composites, panel and shell analysis, stability, and damage tolerance for the rest of his career. Dr. Starnes was a national resource and his achievements are well documented; but his greatest legacy is in the large number of people he touched and encouraged to capture the adventure and excitement of making scientific discoveries and using them to make a better world. This paper is intended as a tribute to the memory of a great friend.

References

- ¹Heldenfels, R. R.: Recent NASA Progress In Composites. USAF/NASA Symposium on Composites, An Assessment of the Future, Washington, D. C., NASA TM X-72713. June 11-12, 1975.
- ²Anon.: Collected Papers on Instability of Shell Structures – 1962. NASA TN-D-1510, December 1962.
- ³Werren, Fred: Mechanical properties of Plastic Laminates. United States Department of Agriculture Forrest Products Laboratory. Report 1820. February 1951.
- ⁴Werren, Fred: Mechanical Properties of Plastic Laminates. United States Department of Agriculture Forrest Products Laboratory. Report 1820-A. February 1953.
- ⁵Werren, Fred: Mechanical Properties of Plastic Laminates. United States Department of Agriculture Forrest Products Laboratory. Report 1820-B. September 1955.
- ⁶Youngs, Robert L.: Mechanical Properties of Plastic Laminates. United States Department of Agriculture Forrest Products Laboratory. Report 1820-C. November 1956.
- ⁷Freas, Alan D.; and Werren, Fred: Mechanical Properties of Cross-Laminated and Composite Glass-Fabric-Base Plastic Laminates. United States Department of Agriculture Forrest Products Laboratory. Report 1821. February 1951.
- ⁸Freas, Alan D.; and Werren, Fred: Mechanical Properties of Cross-Laminated and Composite Glass-Fabric-Base Plastic Laminates. United States Department of Agriculture Forrest Products Laboratory. Report 1821-A. March 1953.
- ⁹Boller, K. H.: Fatigue Tests of Glass-Fabric-Base Laminates Subjected to Axial Loading. United States Department of Agriculture Forrest Products Laboratory. Report 1823. May 1952.
- ¹⁰Schuetz, Evan H.; Barab, Saul; and McCracken, Howard L.: Compression Strength of 24S-T Aluminum- Alloy Flat Panels With Longitudinally Formed Hat-Section Stiffeners. NACA TN 1157, 1946.
- ¹¹Hickman, William A., and Dow, Norris F.: "Compressive Strength of 24S-T Aluminum-Alloy Flat Panel With Longitudinal Formed Hat-Section Stiffeners Having Four Ratios of Stiffener Thickness to Skin Thickness," NACA TN 1553, 1948.
- ¹²Hickman, William A.; and Dow, Norris F.: Data on the Compressive Strength of 75S-T6 Aluminum-Alloy Flat Panels Having Small Thin, Widely Spaced, Longitudinal Extruded Z-Section Stiffeners. NACA TN 1978. 1949.
- ¹³Hickman, William A.; and Dow, Norris F.: Data of 75S-T6 Aluminum-Alloy Flat Panels With Longitudinal Extruded Z-Section Stiffeners. NACA TN 1824. 1949.
- ¹⁴Dow, Norris F.; and Hickman, William A.: Design Charts for Flat Compression Panels Having Longitudinal Extruded Y-Section Stiffeners and Comparison With Panels Having Formed Z-Section Stiffeners. NACA TN 1389. 1947.
- ¹⁵Williams, Jerry G. and Mikulas, Martin M., Jr.: Analytical and Experimental Study of Structurally Efficient Composite Hat-Stiffened Panels Loaded in Axial Compression. ASME/AIAA/SAE 16th Structures, Structural Dynamics, and Materials Conference, AIAA Paper 75-754, May 1975.
- ¹⁶Tripp, L. L., Tamekuni, M., and Viswanathan, A. V.: User's Manual-BUCLASP-2. A Computer Program for Instability Analysis of Biaxially Loaded Composite Stiffened Panels and Other Structures. NASA CR-112226. 1973.
- ¹⁷Halstead, David W., Tripp, L. L., Tamekuni, M., and Baker, L. L.: User's Manual BUCLAP2. A Computer Program for Instability Analysis of Laminated Long Plates Subjected to Combined Inplane Loads. NASA CR-132298. 1973.
- ¹⁸Williams, Jerry G.; and Stein, Manuel: Buckling Behavior and Structural Efficiency of Open-Section Stiffened Composite Compression Panels. AIAA Journal, Vol. 14, No. 11, November 1976. pp. 1618-1626.
- ¹⁹Williams, Jerry G.; and Stein, Manuel: Buckling Behavior and Structural Efficiency of Open-Section Stiffened Composite Compression Panels. Proceedings of AIAA/ASME/SAE 17th Structures, Structural Dynamics, and Materials Conference. Valley Forge, PA, May 5-7, 1976.
- ²⁰Stein, Manuel; and Williams, Jerry G.: Buckling and Structural Efficiency of Sandwich-Blade Stiffened Composite Compression Panels. NASA TP-1269, September 1978.

- ²¹Anderson, M. S.; and Stroud, W. J.: General Panel Sizing Computer Code and Its Application to Composite Structural Panels. *AIAA Journal*, Vol. 17, Number 8, August 1979.
- ²²Williams, Jerry G.; Anderson, Melvin S.; Rhodes, Marvin D.; Starnes, James H., Jr.; and Stroud, W. Jefferson: Recent Developments in the Design, Testing and Impact-Damage Tolerance of Stiffened Composite Panels. *Fibrous Composites in Structural Design*, E. M. Lenoe, D. W. Oplinger, and J. J. Burke, Eds., Plenum Press, New York, 1980, pp. 259-291. Also available as NASA TM 80077, April 1979.
- ²³Rhodes, M. D.; Williams, J. G.; and Starnes, J. H., Jr.: "Low-Velocity Impact Damage in Graphite-Fiber Reinforced Epoxy Laminates". Presented at the 34th Annual Conference Reinforced Plastics/Composite Institute, The Society of the Plastics Industry, Inc. in New Orleans, Louisiana, January 29 - February 2, 1979.
- ²⁴Starnes, J. H., Jr.; Rhodes, M. D.; and Williams, J. G.: Effect of Impact Damage and Holes on the Compression Strength of a Graphite-Epoxy Laminate. *ASTM STP 696*, 1979, pp. 145-171.
- ²⁵Knauss, W. G.; Babcock, C. D. and Chai, H.: Visualization of Impact Damage of Composite Plates by Means of the Moiré Technique. NASA Contractor Report 159261, California Institute of Technology. April 1980.
- ²⁶Rhodes, Marvin D.; Williams, Jerry G.; and Starnes, James H., Jr.: Low velocity Impact Damage in Fiber-Reinforced Laminated Epoxy Structures. *Polymer Composites*, Vol. 2, No. 1, January 1981, pp. 36-44.
- ²⁷Williams, Jerry G. and Rhodes, Marvin P.: The Effect of Resin on the Impact Damage Tolerance of Graphite-Epoxy Laminates. NASA TM 83213, October 1981.
- ²⁸Rhodes, Marvin D.; and Williams, Jerry G.: Lacquer Reveals Impact Damage in Composite Wing Structure. Presented at NASA ACEE Program Review. November 1981.
- ²⁹Freeman, S. M.: "Characterization of Lamina and Interlaminar Damage in Graphite/Epoxy by the Depty Technique. Composite Materials". *Composite Materials: Testing and Design* (Sixth Conference), edited by I. M. Daniel, ASTM STP 787, 1982, pp. 50-62.
- ³⁰Williams, Jerry G.; and Rhodes, Marvin D.: "Effect of Resin On Impact Damage Tolerance of Graphite-Epoxy Laminates". *Composite Materials: Testing and Design* (6th Conference), ASTM STP 787, I. M. Daniel, Ed., American Society for Testing and Materials, December 1982, pp. 450-480.
- ³¹Noor, Ahmed K.; Shuart, Mark J.; Starnes, James H., Jr.; and Williams Jerry G. (Editors): Failure Analysis and Mechanisms of Failure of Fibrous Composite Structures. Conference held March 23-25, 1982. NASA CP-2278. 1983.
- ³²Williams, Jerry G.: "Microbuckling Initiated Failure in Tough Resin Laminates." *Proceedings of the Eighth Annual Mechanics of Composites Review*, Dayton, OH, October 5-7, 1982. AFWAL-TR-83-4005, April 1983, pp. 46-57.
- ³³Chai, H.; Knauss, W. G.; and Babcock, C. D.: "Observation of Damage Growth in Compressively Loaded Laminates." *Experimental Mechanics*. September 1983. pp. 329-337.
- ³⁴Williams, Jerry G.; and Waters, W. Allen: "Failure Mechanisms Characteristics of Compression Loaded Laminates Containing Local Discontinuities." Paper Presented at the ASTM Symposium on Delamination and Debonding of Materials, Pittsburgh, PA, November 8-10, 1983.
- ³⁵Williams, Jerry G.: Effect of Impact-Damage and Open Holes on the Compression Strength of Tough Resin/High Strain Fiber Laminates. NASA Langley Tough Composite Materials Workshop, May 26-26, 1983. NASA TM 85756, February 1984.
- ³⁶Hahn, H. T.; and Williams, Jerry G.: "Compression Failure Mechanisms in Unidirectional Composites." Presented at the ASTM Seventh Symposium on Composite Materials: Testing and Design, Philadelphia, PA, April 2-4, 1984. Also available as NASA TM 85834, August 1984.
- ³⁷Hahn, H. T. and Williams, Jerry G.: "The Effect of Constituent Properties On Compressive Failure Mechanisms In Unidirectional Composites." Tenth Annual Mechanics of Composite Review. Dayton, Ohio. October 15-17, 1984.
- ³⁸Shuart, Mark J.; and Williams, Jerry G.: "Investigating Compression Failure Mechanisms in Composite Laminates with a Transparent Fiberglass/Epoxy Birefringent Material." *Experimental Techniques*. NASA TM-86306, August 1984.
- ³⁹Hahn, H. T.; and Williams, Jerry G.: "Compressive Failure Mechanisms in Unidirectional Composites." Presented at the Tenth Annual Mechanics of Composites Review, Dayton, OH, October 15-17, 1984. Published in 1985 AFWAL-TR.
- ⁴⁰Waters, William Allen; and Williams, Jerry G.: Failure Mechanisms of Laminates Transversely Loaded by Bolt Push-Through. NASA TM-87603. September 1985.
- ⁴¹Mohsen M. Sohi; Hahn, H. Thomas; and Williams, Jerry G.: The Effect of Resin Toughness and Modulus On Compressive Failure Modes of Quasi-Isotropic Graphite/Epoxy Laminates. NASA TM-87604. March 1986.
- ⁴²Howland, R. C. J.: "On the Stresses in the Neighborhood of a Circular Hole In a Strip Under Tension." *Philos. Trans. R. Soc., London, Ser. Q*, Vol. 229, January 6, 1930, pp. 49-86.
- ⁴³Foye, R. L.: "Compression Strength of Unidirectional Composites." AIAA 3rd Aerospace Sciences Meeting, AIAA Paper No. 66-143, January 24-26, 1966.
- ⁴⁴Waddoups, M. E., Eisenmann, J. R., and Kaminski, B. E.: "Macroscopic Fracture Mechanics of Advanced Materials." *Journal of Composite Materials*, Vol. 5, 1971, pp. 446-654.
- ⁴⁵Whitney, J. M. and Nuismer, R. J.: "Stress Fracture Criteria for Laminated Composites Containing Stress Concentrations." *Journal of Composite Materials*, Vol. 8, July 1974, pp. 253.
- ⁴⁶Nuismer R. J. and Whitney J. M.: "Uniaxial Failure of Composite Laminates Containing Stress Concentrations." *Fracture Mechanics of Composites*, ASTM STP 593, American Society for Testing and Materials, 1975, pp. 117-142.
- ⁴⁷Garbo, S. P. and Ogonowski, J. M.: "Strength Predictions of Composite Laminates with Unloaded Fastener Holes." MCAIR 79-010, Presented at the AIAA/20th Structures, Dynamics and Materials Conference held in St. Louis, Missouri on April 4-6, 1977.

- ⁴⁸Knauss, J. F.; Starnes, J. H., Jr.; and Henneke, E. G.: "The Compressive Failure of Graphite/Epoxy Plates with Circular Holes." VPI-E-78-5. Interim Report Number 11, NASA-VPI&SU Composites Program, NASA Grant NGR 47-004-129, February 1978.
- ⁴⁹Starnes, James H., Jr.; Rhodes, Marvin D.; and Williams, Jerry G.: "Effect of Impact Damage and Holes on the Compressive Strength of a Graphite-Epoxy Laminate." *Nondestructive Evaluation and Flaw Criticality for Composite Materials*, ASTM STP 696, R. B. Pipes, Ed., American Society for Testing and Materials, 1979, pp. 145-171. Also available as NASA TM 78796.
- ⁵⁰Starnes, J. H., Jr.; Rhodes, M. D.; and Williams, J. G.: "Effect of Impact Damage and Holes on the Compressive Strength of a Graphite/Epoxy Laminate." *Nondestructive Evaluation and Flaw Criticality for Composite Materials*, ASTM STP 696, R. B. Pipes, Ed., American Society for Testing and Materials, 1979, pp. 145-171.
- ⁵¹Hong, C. S. and Crews, J. H. Jr.: Stress-Concentration Factors for Finite Orthotropic Laminates with a Circular Hole and Uniaxial Loading. NASA Technical Paper 1469, May 1979.
- ⁵²Starnes, J. H., Jr.: "Compressive Strength of Graphite-Epoxy Structural Components with Cutouts." Proceedings of the Fifth Annual Mechanics of Composites Review Technical Report AFWAL-TR-80-4020, January 1980, pp. 125-133.
- ⁵³Garbo, S. P.: "Compression Strength of Laminates with Unloaded Fastener Holes." MCAIR 80-005, Presented at the 21st Structures, Structural Dynamics and Materials Conference held in Seattle, Washington on May 12-14, 1980.
- ⁵⁴Mikulas, Martin M., Jr.: Failure Prediction Techniques for Compression Loaded Composite Laminates With Holes. Special Review of ACEE Composites Programs. Seattle, Washington. August 11-13, 1980. NASA CP 2142.
- ⁵⁵Williams, Jerry G.: Proposed Compression Loaded Composite Impact and Hole Test Methods. Presented at ACEE Workshop on Standardization of Test Methods for Damage Tolerance. Presented at ACEE Project review. Seattle, WA, December 1981.
- ⁵⁶Rhodes, M. D., Mikulas, M. M. Jr., and McGowan, P. E., "Effect of Orthotropic Properties and Panel Width on the Compression Strength of Graphite-Epoxy Laminates with Holes," AIAA Paper 82-0749, 1982.
- ⁵⁷Williams, Jerry G.: "NASA LCPAS Materials Test Results for Compression Loaded Panels with Impact Damage and Open Holes." Presented at ACEE Sponsored NASA/Manufacturers Workshop. NASA Langley Research Center. December 15, 1982.
- ⁵⁸Williams, Jerry G.: Effect of Impact Damage and Open Holes On The Compression Strength Of Tough Resin/High Strain Fiber Laminates. NASA TM-85756. February 1984.
- ⁵⁹Shuart, Mark J.; and Williams, Jerry G.: "Compression Failure Characteristics of +45° Dominated Laminates with a Circular Hole or Impact Damage." Proceedings of the AIAA/ASME/ASCE/AHS 25th Structures, Structural Dynamics and Materials Conference, Palm Springs, CA, May 14-16, 1984. AIAA Paper No. 84-0848.
- ⁶⁰Haftka, Raphael T.; and Starnes, James H., Jr.: "Use of Optimum Stiffness Tailoring to Improve the Compressive Strength of Composite Plates with Holes." Presented at the AIAA/ASME/ASCE/AHS 26th Structures, Structural Dynamics and Material Conference, Orlando, FL, April 15-17, 1985. AIAA Paper No. 85-0721-CP
- ⁶¹Burns, Stephen W.; Herakovich, Carl T.; and Williams Jerry T.: "Compressive Failure of Notched Angle-Ply Composite Laminates; Three-Dimensional Finite Element Analysis and Experiment." Virginia Tech Center for Composite Materials and Structures Publication CCMS-85-11, VPI-E-85-22. November 1985.
- ⁶²Shuart, Mark J.; and Williams, Jerry G.: "Compression Behavior of ±45°-Dominated Laminates with a Circular Hole or Impact Damage." AIAA Journal. Vol. 24, No. 1, January 1986. pp 115-122.
- ⁶³Rhodes, Marvin D.; Williams, Jerry G.; and Starnes, James H., Jr.: Effect of Low Velocity Impact Damage on the Compressive Strength of Graphite-Epoxy Hat-Stiffened Panels. NASA TN D-8411, April 1977.
- ⁶⁴Rhodes, Marvin D.; Williams, Jerry G., and Starnes, Jr., James H.: "Effect of Impact Damage on the Compression Strength of Filamentary Composite Hat-Stiffened Panels." The Science of Advanced Materials and Process Engineering Series, Vol. 23, Selected Applications of Materials for Products and Engineering, SAMPE, May 1978, pp. 300-319.
- ⁶⁵Rhodes, M. D.: Impact Tests on Fibrous Composite Sandwich Structures, NASA Technical Memorandum 78719, October 1978.
- ⁶⁶Williams, Jerry G.: "Composite Structures Research and Component Experiences Applicable to General Aviation Aircraft." Presented at the 1980 SAE Turbine Powered Executive Aircraft Meeting, Scottsdale, AZ, April 9-11, 1980.
- ⁶⁷Rhodes, M.D.: Damage Tolerance Research on Composite Compression Panels. Selected NASA Research in Composite Materials, and Structures, NASA CP 2142, 107-142, Aug. 1980.
- ⁶⁸Rhodes, M. D.; and Williams, J. G.: "Concepts for Improving the Damage Tolerance of Composite Compression Panels." Proc. 5th DOD/NASA Conf. on Fibrous Composites in Structural Design, New Orleans, LA, January 1981 Vol. 2, pp. 301-341. Also available as NASA TM 85748.
- ⁶⁹Starnes, Jr., James H. and Williams, Jerry G.: Failure Characteristics of Graphite-Epoxy Structural Components Loaded In Compression. NASA TM 84552. September 1982.
- ⁷⁰Starnes, James H., Jr.; and Williams, Jerry G.: "Failure Characteristics of Graphite-Epoxy Structural Components Loaded in Compression." *Mechanics of Composite Materials: Recent Advances*, Z. Hashin and C. T. Herakovich, Pergamon Press, New York, 1983, pp. 283-306.
- ⁷¹Williams, Jerry G.; Starnes, James H., Jr.; and Waters, Allen W.: "Applications of Kevlar-Epoxy in Damage Tolerant Compression Loaded Structures." Presented at the DOD/NASA 6th Conference on Fibrous Composites in Structural Design, New Orleans, LA, January 24-27, 1983.

- ⁷²Williams, Jerry G.; Starnes, James H., Jr.; and Waters, W. Allen: "Damage Tolerance Characteristics of Kevlar-Epoxy Laminates Loaded in Compression." Presented at the Ninth Annual Mechanics of Composites Review, Dayton, OH, October 24-26, 1983. Published in 1984 AFWAL-TR.
- ⁷³Williams, Jerry G.: "Damage Tolerance Research on Composite Compression Panels." Presented at the ACEE Composite Structures Technology Conference, Seattle, WA, August 13-16, 1984.
- ⁷⁴Williams, Jerry G.; Starnes, James H., Jr.; and Waters, W. Allen: "Damage-Tolerance Characteristics of Kevlar-Epoxy Laminates Loaded in Compression." Paper presented at the Ninth Annual Mechanics of Composites Review, Dayton, OH, October 24-26, 1983.
- ⁷⁵Williams, Jerry G.; Palmer, Raymond J.; and Tucci, Allan T.: Continuous Filament Isogrid Composite Panel. NASA Tech Brief LAR-12975, 1984.
- ⁷⁶Williams, Jerry G.: "Damage Tolerance Research on Composite Compression Panels." Presented at the ACEE Composite Structures Technology Conference, Seattle, WA, August 13-16, 1984.
- ⁷⁷Curry, James M.; Johnson, Eric R.; and Starnes, James H., Jr.: "Effect of Ply Drop-Offs on the Strength of Graphite-Epoxy Laminates." Report Number CCMS-86-07, VPI-E-86-27, Virginia Polytechnic Institute and State University, Blacksburg, VA, December 1986.
- ⁷⁸Poe, C. C.: Simulated Impact Damage In A Thick Graphite/Epoxy Laminate Using Spherical Indenters. NASA TM-100539. January 1988.
- ⁷⁹O'Brien, T. Kevin: Towards A Damage Tolerance Philosophy for Composite Materials and Structures. NASA TM 100548. March 1988.
- ⁸⁰Nagendra, S.; Haftka, R. T.; Gurdal, Z.; and Starnes, James H., Jr.: "Design of a Stiffened Composite Plate with a Hole." Report Number CCMS-89-17, Virginia Polytechnic Institute and State University, Blacksburg, VA, August 1989.
- ⁸¹Portanova, M. A. and Poe, Jr., C. C.: "Open Hole and Post-Impact Compression Fatigue of Stitched and Unstitched Carbon/Epoxy Composites." NASA TM-10276. June 1990.
- ⁸²Starnes, James H., Jr.: "Effects of Low-Speed Impact Damage on Compression-Loaded Composite Structures." Invited lecture at the National Conference on the Use of Composite Materials in Load Bearing Marine Structures, National Research Council, Arlington, VA, September 25-26, 1990.
- ⁸³NASA Workshop On Impact Damage to Composites. Compiled by C. C. Poe, Jr. NASA Conference Publication 10075. July 1991.
- ⁸⁴Starnes, James H., Jr. and Shuart, Mark J.: "Behavior of Composite Structures Subjected to Compressive Loading." Presented at the AGARD 73rd Structures and Materials Panel Meeting Workshop on the Utilization of Advanced Composites in Military Aircraft, San Diego, CA, October 7-8, 1991.
- ⁸⁵Nagendra, S.; Haftka, R. T.; Gurdal, Z.; and Starnes, James H., Jr.: "Design of a Blade-Stiffened Composite Panel with a Hole." *Composite Structures*, Vol. 18, 1991, pp. 195-219.
- ⁸⁶Nagendra, S.; Gurdal, Z.; Haftka, R. T.; and Starnes, J. H., Jr.: "Buckling and Failure Characteristics of Compression Loaded Stiffened Composite Panels with a Hole." Proceedings of the American Society for Composites Seventh Technical Conference, University Park, PA, October 13-15, 1992, pp. 650-661.
- ⁸⁷Ambur, Damodar R.; Starnes, James H., Jr.; and Prasad, Chunchu B.: Influence of Transverse Shear and Large Deformations Effects on the Low-Speed Impact Response on Graphite-Epoxy Plates. NASA TM-107753, April 1993.
- ⁸⁸Prasad, C. B.; Ambur, D. R.; and Starnes, James H., Jr.: "Response of Laminated Composite Plates to Low-Speed Impact by Airgun-Propelled and Dropped-Weight Impactors." Presented at the AIAA/ASME/ASCE/AHS/ASC 34th Structures, Structural Dynamics and Materials Conference, La Jolla, CA, April 19-21, 1993. AIAA Paper No. 93-1402.
- ⁸⁹Ambur, Damodar R.; Starnes, James H., Jr.; and Prasad, Chunchu B.: "Influence of Large Deformations and Transverse Shear Effects on the Low-Speed Impact Response on Graphite-Epoxy Plates." Presented at the Ninth International Conference on Composite Materials, Madrid, Spain, July 12-16, 1993. *Composites Properties and Applications*, Vol. 5, July 1993, pp. 456-464.
- ⁹⁰Ambur, Damodar R.; Starnes, James H., Jr.; and Prasad, C. B.: "Low-Speed-Impact Damage-Initiation Studies for Selected Laminated Composite Plates." Presented at the AIAA/ASME/ASCE/AHS/ASC 35th Structures, Structural Dynamics and Materials Conference, Hilton Head, SC, April 18-20, 1994. AIAA Paper No. 94-1402.
- ⁹¹Prasad, Chunchu B.; Ambur, Damodar R.; and Starnes, James H., Jr.: "Response of Laminated Composite Plates to Low-Speed Impact by Different Impactors." *AIAA Journal*, Vol. 32, No. 6, June 1994, pp. 1270-1277.
- ⁹²Ambur, Damodar R.; Starnes, James H., Jr.; Stourmbos, T.; and Kapania, Rakesh: "Effects of Large Deformations on the Impact Response of Flat and Curved Graphite-Epoxy Panels." Presented at the AIAA/ASME/ASCE/AHS/ASC 36th Structures, Structural Dynamics and Materials Conference, New Orleans, LA, April 10-13, 1995. AIAA Paper No. 95-1205.
- ⁹³Ambur, Damodar R.; Starnes, James H., Jr.; and Prasad, C. B.: "Low-Speed-Impact Damage-Initiation Characteristics of Selected Laminated Composite Plates." *AIAA Journal*, Vol. 33, No. 10, October 1995, pp. 1919-1925.
- ⁹⁴Ambur, Damodar R.; Starnes, James H., Jr.; and Prasad, Chunchu B.: "Influence of Impact Parameters on the Response of Laminated Composite Plates." *Composite Materials: Fatigue and Fracture - Fifth Volume*, ASTM STP 1230, R. H. Martin, Ed., American Society for Testing and Materials, 1995, pp. 389-404.
- ⁹⁵Madenci, E.; Ileri, L.; and Starnes, J. H., Jr.: "Analysis of Pin-Loaded Holes in Composite Laminates Under Combined Bearing-Bypass and Shear Loading." *International Journal of Solids and Structures*, Vol. 32, No. 14, 1995, pp. 2053-2062.

- ⁹⁶Hilburger, Mark W.; Starnes, James H., Jr.; and Waas, Anthony M.: "The Response of Cylindrical Shells with Rectangular Cutouts Subject to an Axial Compression Load." University of Michigan Department of Aerospace Engineering Solid Mechanics Report No. UMSM96-1, Ann Arbor, MI, February 16, 1996.
- ⁹⁷Hilburger, Mark W.; Starnes, James H., Jr.; and Waas, Anthony M.: "Numerical Study of the Response of Generally Orthotropic Cylindrical Shells with Rectangular Cutouts Under an Applied Axial Compression Load." University of Michigan Department of Aerospace Engineering Solid Mechanics Report No. UMSM96-2, Ann Arbor, MI, March 28, 1996.
- ⁹⁸Stoll, Frederick; Gurdal, Zafer; and Starnes, James H., Jr.: "Improvements to a Method for the Geometrically Nonlinear Analysis of Compressively Loaded Stiffened Composite Panels." Report Number CCMS-96-04, VPI-E-96-03, Virginia Polytechnic Institute and State University, Blacksburg, VA, May 1996.
- ⁹⁹Ambur, Damodar R.; and Starnes, James H., Jr.: "Nonlinear Response and Damage-Initiation Characteristics of Curved Composite Plates Subjected to Low-Speed Impact." Presented at the AIAA/ASME/ASCE/AHS/ASC 38th Structures, Structural Dynamics, and Materials Conference, Kissimmee, FL, April 7-11, 1997. AIAA Paper No. 97-1058.
- ¹⁰⁰Hilburger, M. W.; Waas, A.; and Starnes, J. H., Jr.: "The Response of Composite Cylindrical Shells with Rectangular Cutouts Under an Applied Axial Compression Load." Presented at the 1996 ASME Mechanics and Materials Conference, The Johns Hopkins University, Baltimore, MD, June 12-14, 1996.
- ¹⁰¹Hilburger, M. W., Starnes, J. H., Jr., Waas, A. M.: "The Response of Composite Cylindrical Shells with Rectangular Cutouts Subjected to an Applied Axial Compression Load." Presented at the XIX International Congress of Theoretical and Applied Mechanics Conference, Kyoto, Japan, August 25-31, 1996.
- ¹⁰²Ambur, Damodar R.; Starnes, James H., Jr.; and Phillips, Eric A.: "Response of Composite Panels with Stiffness Gradients due to Stiffener Terminations and Cutouts." Presented at the AIAA/ASME/ASCE/AHS/ASC 38th Structures, Structural Dynamics, and Materials Conference, Kissimmee, FL, April 7-11, 1997. AIAA Paper No. 97-1386.
- ¹⁰³Ambur, Damodar R.; and Starnes, James H., Jr.: "Effect of Curvature on the Impact Damage Characteristics and Residual Strength of Composite Panels." Presented at the AIAA/ASME/ASCE/AHS/ASC 39th Structures, Structural Dynamics and Materials Conference, Long Beach, CA, April 20-23, 1998. AIAA Paper No. 98-1881.
- ¹⁰⁴Hilburger, Mark W.; Starnes, James H., Jr.; and Waas, Anthony M.: "The Response of Composite Cylinders with Cutouts and Subjected to Internal Pressure and Axial Compression Loads." Presented at the AIAA/ASME/ASCE/AHS/ASC 39th Structures, Structural Dynamics and Materials Conference, Long Beach, CA, April 20-23, 1998. AIAA Paper No. 98-1768.
- ¹⁰⁵Hilburger, Mark W.; Starnes, James H., Jr.; and Waas, Anthony M.: "A Numerical and Experimental Study of the Response of Selected Compression-Loaded Composite Shells with Cutouts." Presented at the AIAA/ASME/ASCE/AHS/ASC 39th Structures, Structural Dynamics and Materials Conference, Long Beach, CA, April 20-23, 1998. AIAA Paper No. 98-1988.
- ¹⁰⁶Ambur, Damodar R.; and Starnes, James H., Jr.: "Influence of Target and Impactor on the Nonlinear Response and Residual Strength of Curved Thin Composite Plates." Presented at the AIAA/ASME/ASCE/AHS/ASC 41st Structures, Structural Dynamics and Materials Conference, Atlanta, GA, April 3-6, 2000. AIAA-2000-1591, April 2000.
- ¹⁰⁷Hilburger, Mark W.; Nemeth, Michael P.; and Starnes, James H., Jr.: "Effective Width of Compression-Loaded Plates With a Cutout." NASA/TP-2000-210538, October 2000.
- ¹⁰⁸Starnes, James H., Jr.; Newman, James C., Jr.; Harris, Charles, E.; Piascik, Robert S.; Young, Richard D.; and Rose, Cheryl A.: "Advances in Structural Integrity Analysis Methods for Aging Metallic Airframe Structures with Local Damage." Proceedings of the NATO Research and Technology Organization Applied Vehicle Technology Panel Specialists' Meeting on Life Management techniques for Aging Air Vehicles, Manchester, UK, October 8-11, 2001.
- ¹⁰⁹Hilburger, Mark W.; and Starnes, James H., Jr.: "Buckling and Failure of Compression-Loaded Composite Cylindrical Shells with Reinforced Cutouts." Presented at the AIAA/ASME/ASCE/AHS/ASC 43rd Structures, Structural Dynamics and Materials Conference, Denver, CO, April 22-25, 2002. AIAA Paper No. 2002-1516, April 2002.
- ¹¹⁰Starnes, James H., Jr.; and Hilburger, Mark W.: "Effects of Reinforced Cutouts on the Buckling of Composite Shells." Invited paper, Proceedings of the Fifth World Congress on Computational Mechanics (WCCM5), July 6-12, 2002, Vienna, Austria, Eds. Mang, H. A., Rammesdorfer, F. G., and Eberhardstein, J., Publisher, Vienna University of Technology, Austria (ISBN 3-9501554-0-6).
- ¹¹¹Pontanova, M. A.; Poe, C. C., Jr., and Whitcomb, John D.: Open Hole and Post-Impact Compression Fatigue of Stitched and Unstitched Carbon/Epoxy Composites. NASA TM 102676. June 1990.
- ¹¹²Dow, Marvin B.; and Smith, Donald L.: "Damage-Tolerant Composite Materials Produced by Stitching Carbon Fabrics". SAMPE Conference Series Vol. 21, September 1989, pp. 595-605.
- ¹¹³Lubowinski, S. J.; and Poe, C. C. Jr.: "Fatigue Characterization of Stitched Graphite/Epoxy Composites". Fiber-Tex 1987 Conf. Proceedings, Nov. 3-6, 1987. Also NASA CP-3001, June 1988, pp. 253-271.
- ¹¹⁴Pride, R. A.: Carbon Fiber Counting. NASA TM 80117. August 6, 2000.
- ¹¹⁵Pride, R. A.: Large-Scale Carbon Fiber Tests. NASA TM 80218. August 12, 2001.
- ¹¹⁶Dexter, H. Benson; and Chapman, Andrew J.: "NASA Service Experience With Composite Components." 12th National SAMPE Technical Conference, Seattle, WA. October 7-9, 1980.
- ¹¹⁷Vaughn, R. L.: "Flight Service Evaluation of an Advanced Composite Empennage Component On Commercial Transport Aircraft." NASA Contractor Report 159286, April 15, 1976.
- ¹¹⁸Dexter, Benson H.: Composite Components On Commercial Aircraft. NASA TM 80231. March 1980.
- ¹¹⁹Davis, G. W.; and Sakata, I. F.: Design Considerations for Composite Fuselage Structure of Commercial Transport Aircraft. NASA Contractor Report 159296. March 1981.

- ¹²⁰Bohon, H. L.; Chapman, A. J., III; and Leybold, H. A.: Ground Test Experience With Large Composite Structures for Commercial Transports. NASA TM 84627. March 1983.
- ¹²¹Griffin, C. F.: Fuel Containment and Damage Tolerance in Large Composite Primary Aircraft Structures. NASA CR-166083. March 1983.
- ¹²²Nelson, W. D.; Bunin, B. L.; and Hart-Smith, L. J.: Critical Joints in Large Composite Aircraft Structures. NASA CR-3710. August 1983.
- ¹²³ACEE Composite Structures Technology – Papers by Boeing Commercial Airplane Company. NASA Contractor Report 172358. August 1984.
- ¹²⁴McCarty, J. E.; and Roeseler, W. G.: Durability and Damage Tolerance of Large Composite Primary Aircraft Structure (LLCPAS). NASA CR-3767. January 1984.
- ¹²⁵ACEE Composite Structures Technology - Papers by Douglas Aircraft Company. NASA Contractor Report 172359. August 1984.
- ¹²⁶ACEE Composite Structures Technology – Papers by Lockheed-California Company. NASA Contractor Report 172360. August 1984.
- ¹²⁷Williams, Jerry G.: “Proposed Compression Loaded Composite Impact and Hole Test Methods.” Presented at ACEE Workshop on Standardization of Test Methods for Damage Tolerance. Presented at ACEE Project review. Seattle, WA, December 1981.
- ¹²⁸Williams, Jerry G.: “NASA Impact and Hole Compression Tests.” Presented at ACEE sponsored Key Technology Mini-Workshop. Long Beach, CA; September 28, 1982.
- ¹²⁹Anon.: Standard Tests for Toughened Resin Composites. NASA RP 1092, May 1982. Revised July 1983.
- ¹³⁰Williams, Jerry G.; O’Brien, Kevin T.; and Chapman, A. J., III: Damage Tolerance Test Results for Key Technology Program Tough Composite Specimens. ACEE Contractor Review. NASA-Langley. May 23, 1984.
- ¹³¹Williams, Jerry G.; O’Brien, T. Kevin; and Chapman, A. J., III: “Comparison of Toughened Composite Laminates Using NASA Standard Damage Tolerance Tests.” Proceedings of the ACEE Composite Structures Technology Conference, Seattle, WA, August 13-16, 1984, NASA CP 2321, pp. 51-73.
- ¹³²Anon.: NASA/Aircraft Industry Standard Specification for Graphite Fiber/Toughened Thermoset Resin Composite Material. Compiled by ACEE Composites Project Office. NASA Reference Publication 1142. 1985.
- ¹³³Adams, Donald F.: *Open-Hole Compression Testing*. High-Performance Composites. March 2005. pp. 12-13.
- ¹³⁴Post, Daniel; Czarnek, Robert; Joh, Duksung; and Wood, Judy: Deformation Measurements of Composite Multi-Span Beam Shear Specimens by Moiré Interferometry. NASA Contractor Report 3844. November 1984.
- ¹³⁵Williams, Jerry G.: “The Multi-Span-Beam Shear Test Method for Studying Composite Transverse Shear Failure Characteristics.” 26th Structures, Structural Dynamics and Materials Conference. Orlando, FL, April 15-17, 1985.
- ¹³⁶Jegley, Dawn C.; and Williams, Jerry G.: Multispan-Beam Shear Test For Composite Laminates. NASA LAR-13605. 1987.
- ¹³⁷Jegley, Dawn C.; and Williams, Jerry G.: Studying Composite Laminates Using the Multi-Span-Beam Shear Test. NASA Technical Brief LAR 13065, April 1988, pp. 57-58.
- ¹³⁸Jegley, Dawn C.: Effect of Adhesive Interleaving and Discontinuous Plies on Failure of Composite Laminates Subjected to Normal Loads. NASA TM 101507, January 1989.
- ¹³⁹Jegley, Dawn C.: “A Study of Graphite-Epoxy Laminate Failures Due to High Transverse Shear Strains Using the Multi-Span-Beam Shear Test Procedure.” Presented at the SEM 1989 Spring conference on Experimental Mechanics, Cambridge, MA, May 28-June 1, 1989.
- ¹⁴⁰Jegley, Dawn C.: Effect of Adhesive Interleaving and Discontinuous Plies On Failure of Composite Laminates Subject To Transverse Normal Loads. NASA TM 101507. January 1989.
- ¹⁴¹Starnes, J. H.; Knight, N. F.; and Rouse, M.: Postbuckling Behavior of Selected Flat Stiffened Graphite-Epoxy Panels Loaded in Compression. Proc. AIAA/ASME/ASCE/AHS 23rd Structures, Structural Dynamics and Material Conf., Atlanta, Georgia. 1981.
- ¹⁴²Starnes, J. H.; and Rouse, M.: Postbuckling and Failure Characteristics of Selected Flat Rectangular Graphite-Epoxy Plates Loaded In Compression. Proc. AIAA/ASME/ASCE/AHS 22nd Structures, Structural Dynamics and Materials Conf., Atlanta, Georgia. 1981.
- ¹⁴³Stroud, W. J. and Anderson, M. S.: “PASCO: Structural Panel Analysis and Sizing Code, Capability and Analytical Foundations:”. NASA TM-80181, November 1981.
- ¹⁴⁴Anderson, M. S. and Stroud, W. J.: “PASCO: Structural Panel Analysis and Sizing Code, User’s Manual”. NASA TM-177985, 1985.
- ¹⁴⁵Deaton, Jerry W.: A Repair Technology Program At NASA On Composite Materials. NASA TM 84505. August 1982.
- ¹⁴⁶Deaton, Jerry W.: “A Process For Repairing Graphite/Epoxy Structures”. Presented at the 6th Conference on Fibrous
- ¹⁴⁷Salama, M. M.: “Lightweight Materials for Deepwater Offshore Structures,” Proc. Of Offshore Technology Conference, OTC paper 5185. 1986.
- ¹⁴⁸Williams, Jerry G.: Oil Industry Experiences With Fiberglass Components. Offshore Technology Conference. Houston, TX. Paper 5380. April 27-30, 1987. pp. 211-220.
- ¹⁴⁹Williams, J.G.: Opportunities for Composites in the Offshore Oil Industry. National Conference on the Use of Composite Materials in Load-Bearing Marine Structures, Arlington, VA September 25-26, 1990; Volume II: Conference Proceedings, National Academy Press, Washington, D.C. 1991.

- ¹⁵⁰Cole, B.W.; Lo, K.L.; Williams, J.G.; and Wang, S.S.: White Paper Proposal for a Focus Program On Advanced Composites Offshore. Submitted to NIST ATP. January 6, 1994.
- ¹⁵¹Williams, Jerry G.: Advanced Composites Technology Development For Ultra Deepwater Petroleum Production in the Twenty-First Century. White Paper Submitted to National Institute of Standards and Technology, Composites Engineering and Applications Center for Petroleum Exploration and Production. June 1, 1998.
- ¹⁵²Williams, J. G.: Oil Industry Experiences With Fiberglass Components. 19th Offshore Technology Conference, Houston, Texas, April 1987.
- ¹⁵³Williams, J. G.: Opportunities for Composites In The Offshore Oil Industry. National Conference on the Use of Composite Materials In Load-Bearing Marine Structures. National Academy Press, Washington, D.C. 1991. pp. 41-65.
- ¹⁵⁴Williams, J. G.: Developments in Composite Structures for the Offshore Oil Industry. Offshore Technology Conference Paper 6579, Houston, TX. May 1991.
- ¹⁵⁵Dismukes, John P., and Luton, Michael J.: Polymer Composite Materials Performance Criteria for Offshore Petroleum Production: An Overview. *Composite Materials for Offshore Operations*. Proceedings of the First International Workshop. University of Houston. October 26-28, 1993. S. S. Wang and D. W. Fitting, Eds., NIST Special Publication 887. August 1995. pp. 149-160.
- ¹⁵⁶Salama, M.M., "Advanced Composites for the Offshore Industry: Applications and Challenges". *Revue De L'Institut Français Du Pétrole*, International Conference on Composite Materials in the Petroleum Industry, Ruell-Maimaison, November 3-4, 1994. Vol. 50. No. 1, January/February 1995.
- ¹⁵⁷Croquette, J.: "Potential Applications of Composites Offshore", *Revue De L'Institut Français Du Pétrole*, International Conference on Composite Materials in the Petroleum Industry, Ruell-Maimaison, November 3-4, 1994. Vol. 50. No. 1, January/February 1995.
- ¹⁵⁸Robertson, Gordon G.: Composite Materials for Offshore Operations, Industry Perspective. *Composite Materials for Offshore Operations*. Proceedings of the First International Workshop. University of Houston. October 26-28, 1993. S. S. Wang and D. W. Fitting, Eds., NIST Special Publication 887. August 1995. pp. 83-90.
- ¹⁵⁹Cole, B. W.; Lo, K. H.; Williams, J. G.; and Wang, S. S.: Advanced Composites Offshore: Current Status and a Proposed Research and Development Program. *Composite Materials for Offshore Operations*. Proceedings of the First International Workshop. University of Houston. October 26-28, 1993. S. S. Wang and D. W. Fitting, Eds., NIST Special Publication 887. August 1995. pp. 7-17.
- ¹⁶⁰Williams, Jerry G.: "Petroleum Industry Applications of Composites in E&P Operations". *Composite Materials for Offshore Operations*. Proceedings of the First International Workshop. University of Houston. October 26-28, 1993. S. S. Wang and D. W. Fitting, Eds., NIST Special Publication 887. August 1995. pp. 77-90.
- ¹⁶¹Cole, B. W.: "Petroleum E&P Industry Perspective on the Use of Composites in Offshore Operations". *Composite Materials for Offshore Operations*. Proceedings of the First International Workshop. University of Houston. October 26-28, 1993. S. S. Wang and D. W. Fitting, Eds., NIST Special Publication 887. August 1995. pp. 71-76.
- ¹⁶²Salama, Mamdouh M.: Advanced Composites for the Offshore Industry: Applications and Challenges. *Composite Materials for Offshore Operations*. Proceedings of the First International Workshop. University of Houston. October 26-28, 1993. S. S. Wang and D. W. Fitting, Eds., NIST Special Publication 887. August 1995. pp. 269-288.
- ¹⁶³Barnes, Frazer J.: "Composite Materials in the UK Offshore Oil & Gas Industry", *SAMPE Journal*, Vol. 32, No. 2, March/April, 1996.
- ¹⁶⁴Medlicott, P.A.C.: "Using Composite Materials to Minimize Weight and Maintenance and Maximize Safety". *Offshore Platforms*. 1996.
- ¹⁶⁵Salama, Mamdouh M.: Some Challenges and Innovations for Deepwater Developments. Offshore Technology Conference Paper 8455. May 1997.
- ¹⁶⁶F. Botros, J. G. Williams, and E. Coyle: "Applications of Composite Materials In Deep Water Offshore Platforms". Offshore Technology Conference Paper 8500, Houston, Texas, May 1997.
- ¹⁶⁷Fisher, F.J. and Salama, M.M.: "Emerging and Potential Composite Applications for Deep Water Offshore Operations". *Composite Materials for Offshore Operations – 2*. Proceeding Second International Conference On Composite Materials For Offshore Operations. University of Houston. October 28-30, 1997. S. S. Wang, J. G. Williams and K. H. Lo, Eds., American Bureau of Shipping, 1999. pp. 33-49.
- ¹⁶⁸Williams, J. G.: "Advanced Composites Technology Development For Ultra Deepwater Petroleum Production In The Twenty-First Century". CEAC-TR-98-0106, CEAC, University of Houston, 1998.
- ¹⁶⁹Vennett, R. M.; Williams, J. G.; Lo, K. H.; and Ganguly, P.: "Economic Benefits of Using Composites For Offshore Development And Operations". *Composite Materials for Offshore Operations – 2*. Proceeding Second International Conference On Composite Materials For Offshore Operations. University of Houston. October 28-30, 1997. S. S. Wang, J. G. Williams and K. H. Lo, Eds., American Bureau of Shipping, 1999. pp. 3-16.
- ¹⁷⁰Karayaka, Metin: Integration of Advanced Material Components to Deepwater Platforms. Offshore Technology Conference, Houston, Texas, May 1-4, 2000.
- ¹⁷¹Lo, K. H.; Williams, J. G.; Karayaka, M.; and Salama, M. M.: "Progress, Challenges and Opportunities in the Application of Composite Offshore". *Composite Materials for Offshore Operations – 3*. Proceeding Third International Conference On

Composite Materials For Offshore Operations. October 31 –November 2, 2000. S. S. Wang, J. G. Williams and K. H. Lo, Eds. University of Houston. 2001. pp. 3-17.

¹⁷²Hsu, T. M.; Skogsberg, Jim; and Karayaka, Metin: Composites Utilization On a SPAR Platform-Potential Economic Impact and Technical Gaps. *Composite Materials for Offshore Operations* – 3. Proceeding Third International Conference On Composite Materials For Offshore Operations. October 31 –November 2, 2000. S. S. Wang, J. G. Williams and K. H. Lo, Eds. University of Houston. 2001. pp. 19-43.

¹⁷³Peterson, Robert H.: Development Opportunities in the Deepwater Gulf. *Composite Materials for Offshore Operations* – 3. Proceeding Third International Conference On Composite Materials For Offshore Operations. October 31 –November 2, 2000. S. S. Wang, J. G. Williams and K. H. Lo, Eds. University of Houston. 2001. pp. 45-58.

¹⁷⁴Dodds, N.; Speake, S. D.; and Gibson, A. G.: Highlights and Advances in the ARP Composites Offshore Programme. *Composite Materials for Offshore Operations* – 3. Proceeding Third International Conference On Composite Materials For Offshore Operations. October 31 –November 2, 2000. S. S. Wang, J. G. Williams and K. H. Lo, Eds. University of Houston. 2001. pp. 59-73.

¹⁷⁵Oditt, Lietenant Kevin L.: The U.S. Coast Guard's Perspective on the Use of Composite Materials Within the Marine and Offshore Oil & Gas Industry. *Composite Materials for Offshore Operations* – 3. Proceeding Third International Conference On Composite Materials For Offshore Operations. October 31 –November 2, 2000. S. S. Wang, J. G. Williams and K. H. Lo, Eds. University of Houston. 2001. pp. 85-89.

¹⁷⁶Gulf of Mexico Oil and Gas Production Forecast: 2004-2013. Minerals Management Service Publication MMS 2004-065. October 2004.

¹⁷⁷Deepwater Gulf of Mexico 2004: America's Expanding Frontier. Minerals Management Service Publication MMS 2004-021. May 2004.

¹⁷⁸Williams, Jerry G.: Oil Industry Experiences With Fiberglass Components. NACE 1987 South Central Region Meeting. Lafayette, Louisiana. November 17, 1987.

¹⁷⁹Oney, Charles L.: Special Considerations Needed For Fiberglass Tubing. *Petroleum Engineer International*, December 1987.

¹⁸⁰Oswald, Kenneth J.: The Effect Of 25 Years Of Oil Field Flow Line Service On Epoxy Fiberglass Pipe. Edited Version of Paper No. 167, CORROSION/88 St. Louis, MO. 1988.

¹⁸¹Oswald, Kenneth J.: Carbon Dioxide Resistance Of Fiberglass Oil Field Pipe Made From Aromatic Amine Cured Epoxy, Vinyl Ester And Isophthalic Polyester Resins. Paper No. 171, CORROSION/88, St. Louis, MO, March 1988.

¹⁸²Huntoon, G. G. and Alkire, J. D.: Design And Performance Properties Of Oilfield Fiberglass Tubulars. 64th Annual Technical Conference and Exhibition of the Society of Petroleum Engineers, San Antonio, TX, October 1989.

¹⁸³Robbe, C.: A New Look at the Use of Glass-Fiber Reinforced Piping. *Materials Performance*, June 1990.

¹⁸⁴Aubert, C.F.P., "The Use of GRP Materials in Piping Systems: The Experience of Total", OMAE Conference, Vol. III-A, *Materials Engineering*, ASME, 1993.

¹⁸⁵Winkel, John, "Economic Performance of Glass Fiber Reinforced Plastic (GRP) Piping at Ekofisk", *Engineering Solutions to Industrial Problems*, NACE International, June 7-9, Sandefjord, Norway, Paper No. 43. 1993.

¹⁸⁶Uralil, Francis S.: Impact Damage Tolerance of FRP Composites in Offshore Applications. *Composite Materials for Offshore Operations*. Proceedings of the First International Workshop. University of Houston. October 26-28, 1993. S. S. Wang and D. W. Fitting, Eds., NIST Special Publication 887. August 1995. pp. 185-191.

¹⁸⁷Zelic, M.: Application Of Fiberglass Pipes In Oil And Gas Gathering Technology. *NAFTA* 46 (9), pp. 379-385, 1995.

¹⁸⁸Lea, R.H. et al.: Sea Water Corrosion Resistance of Composite Pipe Systems in the Marine Industry. Presented at 51st Annual Conference SPI, Cincinnati, OH, February, 1996.

¹⁸⁹Wang, S. S.; and Lu, X.: Leakage Failure of Threaded Fiber-Composite Joints Under Combined Internal Pressure, Axial and Makeup Loading: Experiments and Analyses. *CEAC-TR-96-0102*. December, 1996.

¹⁹⁰Wang, S. S.; and Srinivasan, S.: Long-Term Leakage Failure of Filament-Wound Fiberglass Composite Laminate Tubing Under Combined Internal Pressure and Axial Loading. *CEAC-TR-96-0101*. December, 1996.

¹⁹¹Turnipseed, Stephen P.; Koster, Michael D.; and Aghar, Hani Y.: Use Of Large Diameter Fiberglass Lined Tubing In Highly Deviated Offshore Water Injection Wells. Paper No. 78, *NACE, Corrosion/97*, 1997.

¹⁹²Folkers, J.; Friedrich, R.; and Fortune, M.: High Performance Phenolic Piping for Oilfield Applications. *Corrosion/97* Paper No. 83. New Orleans, LA, March 1997.

¹⁹³Drake, Steve and Cagle, Larry: General Utility Pipe for Offshore Applications. *Composite Materials for Offshore Operations* – 2. Proceeding Second International Conference On Composite Materials For Offshore Operations. University of Houston. October 28-30, 1997. S. S. Wang, J. G. Williams and K. H. Lo, Eds., American Bureau of Shipping, 1999. pp. 179-182.

¹⁹⁴Frost, Simon R.: The Development of Reinforced Thermoplastic Pipes for Use in the Oil Industry. *Composite Materials for Offshore Operations* – 2. Proceeding Second International Conference On Composite Materials For Offshore Operations. University of Houston. October 28-30, 1997. S. S. Wang, J. G. Williams and K. H. Lo, Eds., American Bureau of Shipping, 1999. pp. 341-360.

¹⁹⁵Soden, Peter D.; Reid, Steve R.; Ashton, J. N.; Peng, C.; Heaton, M.; Li, S.; and Hinton, M. J.: Strength and Long-Term Behavior of Impact-Damaged GRE Pipes. *Composite Materials for Offshore Operations* – 2. Proceeding Second International Conference On Composite Materials For Offshore Operations. University of Houston. October 28-30, 1997. S. S. Wang, J. G. Williams and K. H. Lo, Eds., American Bureau of Shipping, 1999. pp. 463-484.

- ¹⁹⁶Godfrey, P. R.; and Davis, A. G.: The use of GRP Materials In Platform Topsides Construction and the Regulatory Implications. Proceedings of the Ninth International Conference On Offshore Mechanics and Arctic Engineering. Houston, TX. Volume III - Part A. Feb. 18-23, 1990. pp. 15-20.
- ¹⁹⁷Miravete, A.: "A Preliminary Design Study of Composite Flare Boom". CEAC-TR-98-0105, University of Houston, 1998.
- ¹⁹⁸Houghton, C. J.: Composites Use on Platform Topsides: A recent Case History and Future Prospects. *Composite Materials for Offshore Operations* – 2. Proceeding Second International Conference On Composite Materials For Offshore Operations. University of Houston. October 28-30, 1997. S. S. Wang, J. G. Williams and K. H. Lo, Eds., American Bureau of Shipping, 1999. pp. 17-32.
- ¹⁹⁹Oney, C.: Water Storage Tanks Rank High in Fiberglass Tank Use. *Pet. Engr. Int.*, p. 61, March 1988.
- ²⁰⁰Anisdahl, Lars; Wang, Dag T.; and Stokke, Reidar: Study of the Design & Use of GRP Tanks and Vessels Offshore. *Composite Materials for Offshore Operations* – 2. Proceeding Second International Conference On Composite Materials For Offshore Operations. University of Houston. October 28-30, 1997. S. S. Wang, J. G. Williams and K. H. Lo, Eds., American Bureau of Shipping, 1999. pp. 261-274.
- ²⁰¹Moe, Tore Wood; Aanonsen, Torbjorn; and Williams, Jerry G.: Spoolable, Composite Piping for Chemical and Water Injection and Hydraulic Valve Operation. 11th International Conference on Offshore Mechanics and Arctic Engineering, Vol. III, Part A, Materials Engineering. June 1992. pp. 199-207.
- ²⁰²Sas-Jaworsky, Alex; and Williams, Jerry G.: Development of Composite Coiled Tubing for Oilfield Services. SPE paper 26536 presented at 68th Annual Technical Conference and Exhibition of the Society of Petroleum Engineers, Houston, TX, October 1993.
- ²⁰³Moe, T. W.; and Williams J. G.: Spoolable Composite Pipes. NACE Paper No. 45, Engineering Solutions to Industrial Corrosion Problems. Sandefjord Norway. 1993.
- ²⁰⁴Sas-Jaworsky, Alexander; and Williams, Jerry G.: Enabling Capabilities and Potential Applications Of Composite Tubing. World Oil Coiled Tubing Exhibition, Amsterdam 2nd International Conference and Exhibition on Coiled Tubing. Amsterdam. The Netherlands. June 28-30, 1994.
- ²⁰⁵Sas-Jaworsky, A. and Williams, J. G.: Advanced Composites Enhance Coiled Tubing Capabilities. *World Oil Magazine*, Vol. 214, No. 4, April 1994. pp. 57-69.
- ²⁰⁶Austigard, E.; and Tomter, R.: Composites Subsea: Cost Effective Products – An Industry Challenge. Subsea 94 International Conference. 1994.
- ²⁰⁷Sas-Jaworsky, A.; and Teel, M. E.: Coiled Tubing 1995 Update: Production Applications. *World Oil*, June 1995, pp. 97-105.
- ²⁰⁸Sas-Jaworsky II, Alex: Developments Position CT For Future Prominence. *The American Oil & Gas Reporter*. March 1996. pp. 87-92.
- ²⁰⁹Sas-Jaworsky II, Alex: Innovative Applications Stimulate Coiled Tubing Development. *World Oil*. June 1996. pp. 61-69.
- ²¹⁰Hansen, Allan Boye; Williams, J. G.; and Asdal, Bent: Spoolable Composite Service and Injection Lines for Oilfield Installations. International Conference on Oilfield Engineering With Polymers – Cost Effective Technology. Westminster, London, UK. October 28-29, 1996.
- ²¹¹Lundberg, C. A.; Walsh, T. J.; Peterman C. P.; and Reynolds, H. A.: Advances in Manufacturing Technology for Spoolable Composite Tubing. *Composite Materials for Offshore Operations* – 2. Proceeding Second International Conference On Composite Materials For Offshore Operations. University of Houston. October 28-30, 1997. S. S. Wang, J. G. Williams and K. H. Lo, Eds., American Bureau of Shipping, 1999. pp. 289-302.
- ²¹²Silverman, Seth A.: Spoolable Composite Pipe for Offshore Applications. *MP*, January 1997, pp. 48-50.
- ²¹³Fowler, H.: Update On Advanced Composite Spoolable Pipe Developments. SPE paper 38414 presented at the 2nd North American Coiled Tubing Roundtable, Montgomery, TX. April 1997.
- ²¹⁴Hansen, A. Boye; and Asdal, B.: Qualification and Verification of Spoolable High Pressure Composite Service Lines for the Åsgard Field Development Project. OTC paper 8436, Presented at the Offshore Technology Conference, Houston, TX, May 1997.
- ²¹⁵Quigley, P. A.; Nolet, S. C.; Williams J. G.; and Sas-Jaworsky, A.: Development And Application Of A Novel Coiled Tubing String For Concentric Workover Services. Offshore Technology Conference Paper 8456, Houston, TX, May 1997.
- ²¹⁶Quigley, Peter; Fowler, Hampton; Nolet, Stephen; and Berning, Scott: Update on Composite Coiled Tubing Developments and Horizontal Well Applications. *Composite Materials for Offshore Operations* – 2. Proceeding Second International Conference On Composite Materials For Offshore Operations. University of Houston. October 28-30, 1997. S. S. Wang, J. G. Williams and K. H. Lo, Eds., American Bureau of Shipping, 1999. pp. 303-318.
- ²¹⁷Berning, S. and Fowler, H.: Update On Composite Coiled Tubing Developments and Horizontal Well Applications. PNEC 6th International Conference on Coiled Tubing Technologies. Houston, TX. October 1997.
- ²¹⁸Frost, Simon R.: The Development of Reinforced Thermoplastic Pipes for Use in the Oil Industry. *Composite Materials for Offshore Operations* – 2. Proceeding Second International Conference On Composite Materials For Offshore Operations. University of Houston. October 28-30, 1997. S. S. Wang, J. G. Williams and K. H. Lo, Eds., American Bureau of Shipping, 1999. pp. 341-360.

- ²¹⁹Lundberg, Chris A.; Walsh, Thomas J.; Reynolds, Harris A.; and Peterman, Charles P.: Spin-off Technologies from Development of Continuous Composite Tubing Manufacturing Process. Offshore Technology Conference Paper 8620. Houston, TX. May 1998.
- ²²⁰Fowler, Hampton; Feechan, Michael; and Berning, Scott: Development Update and Applications of an Advanced Composite Spoolable Tubing. Offshore Technology Conference Paper 8621, Houston, Texas. May 1998.
- ²²¹Haug, P. A. and Ekeberg, K. I.: Dynamic Umbilical With Composite Tube (DUCT). Offshore Technology Conference Paper 8887, 1998.
- ²²²Lundberg, C. A.; Walsh, T. J.; Peterman C. P.; and Reynolds, H. A.: Advances in Manufacturing Technology for Spoolable Composite Tubing. *Composite Materials for Offshore Operations – 2*. Proceeding Second International Conference On Composite Materials For Offshore Operations. University of Houston. October 28-30, 1997. S. S. Wang, J. G. Williams and K. H. Lo, Eds., American Bureau of Shipping, 1999. pp. 289-302.
- ²²³Quigley, Peter; Fowler, Hampton; Nolet, Stephen; and Berning, Scott: Update on Composite Coiled Tubing Developments and Horizontal Well Applications. *Composite Materials for Offshore Operations – 2*. Proceeding Second International Conference On Composite Materials For Offshore Operations. University of Houston. October 28-30, 1997. S. S. Wang, J. G. Williams and K. H. Lo, Eds., American Bureau of Shipping, 1999. pp. 303-318.
- ²²⁴Wolfe, Donald and Baron, John: Unbonded, Multiple-Layer, Flexible Composite Pipe. *Composite Materials for Offshore Operations – 2*. Proceeding Second International Conference On Composite Materials For Offshore Operations. University of Houston. October 28-30, 1997. S. S. Wang, J. G. Williams and K. H. Lo, Eds., American Bureau of Shipping, 1999. pp. 319-328.
- ²²⁵Wolfe, Donald and Baron, John: Unbonded, Multiple-Layer, Flexible Composite Pressure Pipe. *Composite Materials for Offshore Operations – 2*. Proceeding Second International Conference On Composite Materials For Offshore Operations. University of Houston. October 28-30, 1997. S. S. Wang, J. G. Williams and K. H. Lo, Eds., American Bureau of Shipping, 1999. pp. 329-340.
- ²²⁶Wang, S. S.; Yui, T. P.; and Lo, K. H.: Coupled Geometric and Material Nonlinear Analysis and Failure Prediction of Thick-Wall Spoolable Composite Laminate Tubing. *Composite Materials for Offshore Operations – 2*. Proceeding Second International Conference On Composite Materials For Offshore Operations. University of Houston. October 28-30, 1997. S. S. Wang, J. G. Williams and K. H. Lo, Eds., American Bureau of Shipping, 1999. pp. 413-430.
- ²²⁷Koshak, W. E.; Feechan, Michael; Berning, Scott; Headrick, Dick; and Fowler, Hampton: A Summary of Recent Successes and Challenges in the Development of Spoolable Composite Tubulars. Paper 54506 presented at 1999 SPE/ICoTA Coiled Tubing Roundtable held in Houston, Texas. May 1999.
- ²²⁸McClatchie, D. M.; Reynolds, H. A.; Walsh, T. J. and Lundberg, C.: Applications Engineering For Composite Coiled Tubing. Offshore Technology Conference Paper 54507. Houston, Texas. May 1999.
- ²²⁹Haug, Per Arne; and Asdal, Bent: High-Pressure Spoolable Composite Pipe. OMAE Conference. St. Johns, New Foundland, Canada. July 1999.
- ²³⁰Haug, Per Arne; and Andersen, Stig: The Åsgard Spoolable Composite Lines – The World's First Spoolable Composite Lines Used for Subsea Methanol Injection. Deep Offshore Technology. October 1999.
- ²³¹McClatchie, D. W. Reynolds, H. A. Walsh, T. L. Lundberg, C.: Applications Engineering For Composite Coiled Tubing. SPE 54507. 1999.
- ²³²Melve, Bjørn; Meland, Thor; Bergh, Paal Angell; and Kløfjell, Karl: Continuous Composite Lines For Methanol Injection On The Asgard Field – Experiences from Production and Installation. ETCT/OMAE 2000 Joint Conference Energy for the New Millennium. New Orleans, Louisiana. February 2000.
- ²³³Marker, Roy; Haukvik, John; Terry, James B.; Paulk, Martin D.; Coats, Alan; Wilson, Tom; Estep, Jim; Farabee, Mark; Berning, Scott A.; and Song, Haoshi: Anaconda: Joint Development Project Leads to a Digitally Controlled Composite Coiled Tubing Drilling System. 2000 SPE/ICoTA Coiled Tubing Roundtable, Paper 60750, Houston, TX. April 2000.
- ²³⁴Williams, J. G. and Sas-Jaworsky II, Alex: Composite Spoolable Pipe Development, Advancements, and Limitations. Offshore Technology Conference Paper 12029, Houston, Texas. May 2000.
- ²³⁵Ordu, P. and Guichard : "Design and Tests of High Performance Composite Tubes for Use in Deepwater Drilling and Production Systems". Proc. of OMAE Specialty Symposium on Offshore and Arctic Frontiers. M. M. Salama, ed., ASME, pp. 353-359. 1986.
- ²³⁶Sparks, C.; Odru, P.; Bono, H.; and Metivaud, G.: Mechanical Testing of High Performance Composite Tubes for TLP Production Risers. 20th Annual OTC Conference Paper OTC 5797. 1988.
- ²³⁷Sparks, C. P. and Schmitt, J.: "Optimized Composite Tubes for Riser Application". Proceeding of the Ninth International Conference On Offshore Mechanics and Arctic Engineering. Houston, TX. Vol. III. – Part A. Feb 18-23, 1990. pp. 1-8.
- ²³⁸Sparks, C.; Odru, P.; Metivaud, G.; and Le Floch, C.: Composite Riser Tubes: Defect Tolerance Assessment and Nondestructive Testing. 24th Annual OTC Conference. Paper OTC 6894. 1992.
- ²³⁹Fischer, F. J.: "Composite Production Risers for Deepwater Offshore Structures", Revue de L Institut Francais du Petrole, Vol. 50, No. 1. 1995. pp.35-43.
- ²⁴⁰Anderson, W. F.; Anderson J. J.; Mickelson, C. C.; and Sweeney, T. F.: "The Application of Advanced Composite Technology To Marine Drilling Riser Systems: Design, Manufacturing and Test". Prof. of Offshore Technology Conference, Paper 8433, SPE. 1997.
- ²⁴¹Baldwin, D.D., Newhouse, N.L., Lo, K.H., and Burden, R.C.: "Composite Production Riser Design". Offshore Technology Conference, OTC 8431, 1997.

- ²⁴²Burgdorf, O., Andersen W.: "Comparative Analysis of 12,500 ft Water Depth Steel and Advanced Composite Drilling Risers". Offshore Technology Conference. 1998.
- ²⁴³Karayaka, M.; Wu, S.; Wang, S. S.; Lu, X.; and Ganguly, P.: "Composite Production Riser Dynamics and Its Effects on Tensioners, Stress Joints, and Size of Deep Water Tension Leg Platforms". Offshore Technology Conference, OTC 8666. 1998.
- ²⁴⁴Hill, R.T.; Hatton, S.; and Karayaka, M.: "Deepwater Riser Technology: Current Status and Developments". Deepwater '98, New Orleans, Louisiana, 1998.
- ²⁴⁵Salama, M. M.; Johnson, D. B.; and Long, R.: "Composite Production Riser - Testing and Qualification," SPE Journal of Production & Facilities, Society of Petroleum Engineers, August Issue. 1998. pp. 170-177.
- ²⁴⁶Baldwin, D.; Newhouse, N.; and Lo, K. H.: Composite Production Riser Development. *Composite Materials for Offshore Operations* – 2. Proceeding Second International Conference On Composite Materials For Offshore Operations. University of Houston. October 28-30, 1997. S. S. Wang, J. G. Williams and K. H. Lo, Eds., American Bureau of Shipping, 1999. pp. 115-128.
- ²⁴⁷Salama, M.M.; Murali, J.; Baldwin, D.D.; Jahnsen, O.; Johnson, D.B., Meland, T.: "Design Consideration for Composite Drilling Riser". OTC10565, Proceedings of the Offshore Technology Conference. 1999.
- ²⁴⁸Salama, M. M.; Echtermeyer, A.; and Lindefjeld, O.: "Composite Risers for Deepwater Applications, Proc. of Deep Offshore Technology Int. Conf. And Exhibition. Vol.2, Paper 25-3, Oct. 19-21, Stavanger Norway. 1999.
- ²⁴⁹Johnson, D.B.; Baldwin, D.D.; Long, J.R.: "Mechanical Performance of Composite Production Risers". OTC10568, Proceedings of the Offshore Technology Conference. 1999.
- ²⁵⁰Murali, J.; Salama, M. M.; Jahnsen O.; and Meland, T.: Composite Drilling Riser – Qualification Testing and Field Demonstration. *Composite Materials for Offshore Operations* – 2. Proceeding Second International Conference On Composite Materials For Offshore Operations. University of Houston. October 28-30, 1997. S. S. Wang, J. G. Williams and K. H. Lo, Eds., American Bureau of Shipping, 1999. pp. 129-149.
- ²⁵¹Furlow, William: "Three-Phase Roll Out for Composite Riser," Offshore Magazine, Vol. 60, No. 4. April 2000.
- ²⁵²Johnson, D.; Baldwin, D.; and Slaughter, L.: "Composite Choke and Kill Line Development and Test Results". *Composite Materials for Offshore Operations* – 3. Proceeding Third International Conference On Composite Materials For Offshore Operations. October 31 –November 2, 2000. S. S. Wang, J. G. Williams and K. H. Lo, Eds. University of Houston. 2001. pp. 125-141.
- ²⁵³Hanna, S. Y.; Salama, M. M.; and Hannus, H.: "New Tendon and Riser Technologies Improve TLP Competitiveness in Ultra-Deep Water". Proc. of Offshore Technology Conference, Paper 12963, SPE. 2001.
- ²⁵⁴Salama, M. M.; Martinussen E.; Spencer, B.; Hanna, S.; Hsu, T. M.; Stjern, G.; Franco, E.; Storhaug, T.; and Echtermeyer, A.: "Composite Risers Are Ready for Field Applications - Status of Technology, Field Demonstration and Life Cycle Economics. "Proc. of 13th Annual Deep Offshore Technology Conference (DOT 2001), October 17-19,2001, Rio de Janeiro, Brazil. 2001.
- ²⁵⁵Salama, M. M.; Stjem, G.; Storhaug, T.; Spencer, B.; and Echtermeyer, A.: "The First Offshore Field Installation for a Composite Riser Joint". Prof. of Offshore Technology Conference, SPE Paper 14018. May 6-9, 2002.
- ²⁵⁶Salama, Mamdouh M.; Echtermeyer, Andreas T.; Tore, Odd; Storhaug, Turid; Spencer, Brian; and Stjern, Gisle: In-Service Integrity Monitoring of Deepwater Composite Riser. 14th International Deep Offshore Technology Conference (DOT 2002), New Orleans, Louisiana. November 13-15, 2002.
- ²⁵⁷Salama, M. M.: "Lightweight Materials for Mooring Lines of Deepwater Tension Leg Platform ". Marine Technology. Vol. 21, No. 3. 1984. pp. 234-241.
- ²⁵⁸Yeung, Y. C.: Composite Tension Members for Structural Applications. Proceedings of the 4th Int. Conference on Composite Materials. Paisley. 1987. pp. 1.309-1.320.
- ²⁵⁹Walton, J. J. and Yeung, Y. C.: "Flexible Tension Members from Composite Material". Proc. of 6th Int. OMAE Symposium. (M. M. Salama, et. al, eds.) ASME, V. 3. 1987. pp.7-14.
- ²⁶⁰Yeung, C. T.: "Composite Tension Members for Structural Applications". Proceedings of the 4th International Conference on Composite Structures Paisley. 1987. pp. 1.309-1.320.
- ²⁶¹Hanna, S. Y.; Thomason, W. H.; and Williams, J. G.: Influence of Tension, Weight, and Hydrostatic Pressure On Deepwater TLP Tendons. 19th Annual Offshore Technology Conference, Houston, Texas. OTC Paper 5610, April 27-30, 1987.
- ²⁶²Kim, K. S.; Hahn, H. T.; and Williams Jerry G.: Application of Composites in TLP Tethers. Proceedings of the Seventh International Conference on Offshore Mechanics and Arctic Engineering. Volume III, pp. 1-7. February 8-11, 1988.
- ²⁶³Williams, Jerry G.; and Salama, Mamdouh: Effects of Environmental Factors on the Strength of Composite Materials for TLP Tendons. Presentation OMAE Conference, The Hague, The Netherlands. March 1989.
- ²⁶⁴Kim, K.S.; Hahn, H. T.; and Williams, Jerry G.: Design of a Mechanical Joint for Pultruded Composite Rods. Proceedings of ICCM/7 International Conference on Composite Materials. Fall 1989.
- ²⁶⁵Chisholm, J. M.; Hahn, H. T.; and Williams, Jerry G.: Diametrical Compression of Pultruded Composite Rods As A Quality Control Test. Composites. Volume 20. Number 6. November 1989.
- ²⁶⁶Chisholm, J. M.; Kallas, M. N.; Hahn, H. T.; and Williams, J. G.: The Effect of Seawater Absorption In Pultruded Composite Rods. 8th International Conference On Composite Materials. (ICCM/VIII) Sheraton Waikiki Hotel, Honolulu, HI, July 15-19, 1991.
- ²⁶⁷Hanna, S. Y.; Salama, M. M.; and Hannus, H.: "New Tendon and Riser Technologies Improve TLP Competitiveness in Ultra-Deep Water". Proc. of Offshore Technology Conference, Paper 12963. SPE. 2001.

- ²⁶⁸Botker, S.; Salama, M. M.; and Storhaug T.: "Composite Tethers and Risers in Deepwater Field Development: Step Change Technology," Proc. of Offshore Technology Conference, Paper 13183, SPE. 2001.
- ²⁶⁹Salama, M. M.: "Material for Mooring systems". Materials for Marine and Structures. Treatise of Materials Science and Technology. Academic Press, Vol. 28. 1988. p. 411.
- ²⁷⁰Lo, K.H. and Su, H.: Polyester Rope Mooring Design Considerations. Textile Research Institute, Proceedings International Offshore and Polar Engineering Conference, June 1999.
- ²⁷¹Del Vecchio, C. and Meniconi, L. C.: Deep Water Mooring Systems Using Fiber Ropes. Composite Materials for Offshore Operations – 2. Proceeding Second International Conference On Composite Materials For Offshore Operations. University of Houston. October 28-30, 1997. S. S. Wang, J. G. Williams and K. H. Lo, Eds., American Bureau of Shipping, 1999. pp. 231-249.
- ²⁷²Del Vecchio, C.; Costa, L.; Souse C.; and Meniconi, L. C.: Petrobras Experiences With Deep Water Polyester Moorings. Composite Materials for Offshore Operations – 3. Proceeding Third International Conference On Composite Materials For Offshore Operations. October 31 –November 2, 2000. S. S. Wang, J. G. Williams and K. H. Lo, Eds. University of Houston. 2001. pp. 495-502.
- ²⁷³Anon.: API RP 2SM: "Recommended Practice for Design, Manufacture, Installation, and Maintenance of Synthetic Fiber Ropes for Offshore Moorings", First Edition, American Petroleum Institute, March 2001.
- ²⁷⁴Shu, Hongbo; Loeb, David; and Bergeron, Billy: Polyester Rope Mooring Field Trial in 6200 ft. Water Depth. Composite Materials for Offshore Operations – 3. Proceeding Third International Conference On Composite Materials For Offshore Operations. October 31 –November 2, 2000. S. S. Wang, J. G. Williams and K. H. Lo, Eds. University of Houston. 2001. pp. 529-539.
- ²⁷⁵Williams, Jerry G.; Miyase, Akira; Donghui, Li; and Wang S. S.: Small-Scale Testing of Damaged Synthetic Fiber Mooring Ropes. Offshore Technology Conference Paper 14308. May 6-9, 2002.
- ²⁷⁶Smith, D. Barton and Williams, Jerry G.: Direct Measurement of Large Strains in Synthetic Fiber Mooring Ropes Using Polymeric Optical Fibers. Offshore Technology Conference, paper 14242. May 6-9, 2002.
- ²⁷⁷Smith, D. Barton and Williams, Jerry G.: Monitoring Axial Strain In Synthetic Fiber Mooring Ropes Using Polymeric Optical Fibers. Paper No. OMAE2003-37402, Proceedings of 22nd International Conference on Offshore Mechanics and Arctic Engineering, Cancun, Mexico. June 8-13, 2003.
- ²⁷⁸Williams, J. G.: Composite Material Offshore Corrosion Solutions. International Workshop on Corrosion Control of Marine Structures and Pipelines. Galveston, TX, February 1999.
- ²⁷⁹Thon, Harald; and Stokke, Reidar: Performance of GRP Pipes in Fire Situations. Senter for Industriforskning Report 85-02-021. Oslo, Norway. January 1, 1987.
- ²⁸⁰Hunter, J. The advantages of Glass Reinforced Phenolics In Demanding Construction Applications. 3rd International Conference Polymers In Offshore Engineering. June 1988. pp. 25/1-25/15.
- ²⁸¹Thon, Harald; Haanes, Havard; and Stokke, Reidar: Glass Fibre Reinforced Plastic (GRP) Pipes In The Fire Water System Offshore. Senter for Industriforskning Report No. 890210-3. October 1991.
- ²⁸²Anon.: Specifications and Recommended Practice For The Use of GRP Piping Offshore. Part 1 - Philosophy and Scope. UKOOA. March 1994.
- ²⁸³Sorathia, U.: Flammability and Fire Safety of Composite Materials. Composite Materials for Offshore Operations. *Composite Materials for Offshore Operations*. Proceedings of the First International Workshop. University of Houston. October 26-28, 1993. S. S. Wang and D. W. Fitting, Eds., NIST Special Publication 887. August 1995. pp. 309-317.
- ²⁸⁴Folkers, Joie: Fire Testing and Performance of Fiber Glass Pipe. *Composite Materials for Offshore Operations – 2*. Proceeding Second International Conference On Composite Materials For Offshore Operations. University of Houston. October 28-30, 1997. S. S. Wang, J. G. Williams and K. H. Lo, Eds., American Bureau of Shipping, 1999. pp. 169-177.
- ²⁸⁵Anon.: Policy File Memorandum On The Fire Performance Requirements For Plastic Pipe Per IMO Resolution A.753(18). PSM 1-98, The United States Coast Guard, 1998.
- ²⁸⁶Anon.: Policy File Memorandum On The Use Of Fiber Reinforced Plastic (FRP) Gratings And Cable Trays. PSM 2-98, The United States Coast Guard, 1998.
- ²⁸⁷Carlson, T.; Lo, K. H.; and Myskowski, C. S.: Fire Performance And Regulatory Approval Of Glass Fiber Reinforced Composite Grating. Composites in Fire Conference, University of New Castle, 1999.
- ²⁸⁸Ciaraldi, Stephen W.: Safety Philosophy for the Use of Composite Materials Offshore. Composite Materials for Offshore Operations. Proceeding of the First International Workshop. NIST SP 887. pp. 319-325.
- ²⁸⁹Read, David T.; Kriz, Ronald D.; and Williams, Jerry G.: Multimode Optical Fibers as Damage Sensors in Composite Rods. Proceedings of the Ninth International Conference On Offshore Mechanics and Arctic Engineering. Vol. III - Part A. Feb. 1990. pp. 41-47.
- ²⁹⁰Measures, R. M.; LeBlanc, M.; Liu, K.; Ferguson, S.; Valis, T.; Hogg, D.; Turner, R.; and McEwen, K.: Fiber Optic Sensors for Smart Structures. Optics and Lasers In Engineering 16, 1992. pp. 127-152.
- ²⁹¹Parnas, Richard; Dunkers, J. P.; and Neff, Raymond A.: Optical Fiber Sensors for Composites. *Composite Materials for Offshore Operations – 2*. Proceeding Second International Conference On Composite Materials For Offshore Operations. University of Houston. October 28-30, 1997. S. S. Wang, J. G. Williams and K. H. Lo, Eds., American Bureau of Shipping, 1999. pp. 655-663.

²⁹²Patel, Rayman: HSE Perspective On Composites Utilization Offshore. Proceeding Third International Conference On Composite Materials For Offshore Operations. October 31 –November 2, 2000. S. S. Wang, J. G. Williams and K. H. Lo, Eds. University of Houston. pp. 77-84.

²⁹³Peterson, James P.: Structural Efficiency of Aluminum Multiweb Beams and Z-Stiffened Panels Reinforced With Filamentary Boron-Epoxy Composite. NASA TN D-5856. 1970.

²⁹⁴Suarez, J. A.; Whiteside, J. B.; and Hadcock, R. N.: The Influence of Local Failure Modes on the Compressive Strength of Boron/Epoxy Composites. Composite Materials: Testing and Design (Second Conference), ASTM STP 497, American Society for Testing and Materials. 1972. pp. 237-256.

²⁹⁵Roy, Paul A.; McElman, John A.; and Henshaw, Jim: Development of Lightweight Aluminum Compression Panels Reinforced by Boron-Epoxy Infiltrated Extrusions. NASA CR-2145. January 1973.

²⁹⁶Williams, Jerry G.; and Agarwal, Banarsi L.: Load Introduction Techniques for Boron Infiltrated Aluminum Panels. 2nd Air Force Conference On Fibrous Composites In Flight Vehicle Design, Dayton, Ohio. May 1974.

²⁹⁷Tynan, Charles I.; Williams, Jerry G.; and Osborne, R. S.: Expandable Structures Technology for Manned Space Applications. AIAA Paper 71-399. 1971.

²⁹⁸Williams, Jerry G.: Mechanical Properties and Abrasion Resistance of Polyester Cord. NASA TM X-72806. January 1966.

²⁹⁹Mandell, J. F.: Modeling of Marine Rope Fatigue Behavior. Textile Research Institute. June 1987. pp. 318-329.

³⁰⁰Starnes, James H., Jr.: The Effects of a Circular Hole on the Buckling of Cylindrical Shells. Ph.D. Dissertation, California Institute of Technology, May 1970.

Thin Ply Composites[†]

Stephen W. Tsai
Stanford University, Stanford, CA 94305-4035

and
Sangwook Sihn and Ran Y. Kim
University of Dayton Research Institute, Dayton, OH 45469-0168

Large tows of carbon fiber can be spread by a simple, non-intrusive process from which plies down to 1/6 of the conventional 5-mil thickness can be obtained. Laminates made from such plies showed remarkable resistance to micro cracking, delamination and splitting under both static and fatigue loading. With thick-thin ply hybrids, superior performance, lower cost and lower minimum gage can all lead to applications not feasible with 5-mil thick plies.

I. □ Introduction

THIS presentation covers some recently obtained results of the processing and property determination of carbon fiber reinforced composite laminates made from thin plies. The premature failure modes by micro cracking and delamination have imposed severe limitations on the more effective utilization of the fiber strength. For example, traditional threshold for micro cracking is 0.5 percent strain while most modern fibers have a failure strain about 2 percent. Thus if micro cracking can be suppressed or prevented, a composite laminate can be designed to carry load up to 2 percent, four times the micro cracking threshold. It will be shown that thin plies in a laminate do not lead to micro cracking and delamination. It is therefore possible to load the laminates to a much higher level than what has been accepted thus far.

II. □ Test Data of Thin Ply Laminates

A tow spreading process has been developed by Kawabe of Fukui Technology Center. He blew air across a 12k or 24k tow to create thin plies down to 1/6 of the conventional 0.12-mm (5-mil) ply thickness. Because the spreading process does not induce any stress to the fibers so they are not damaged.

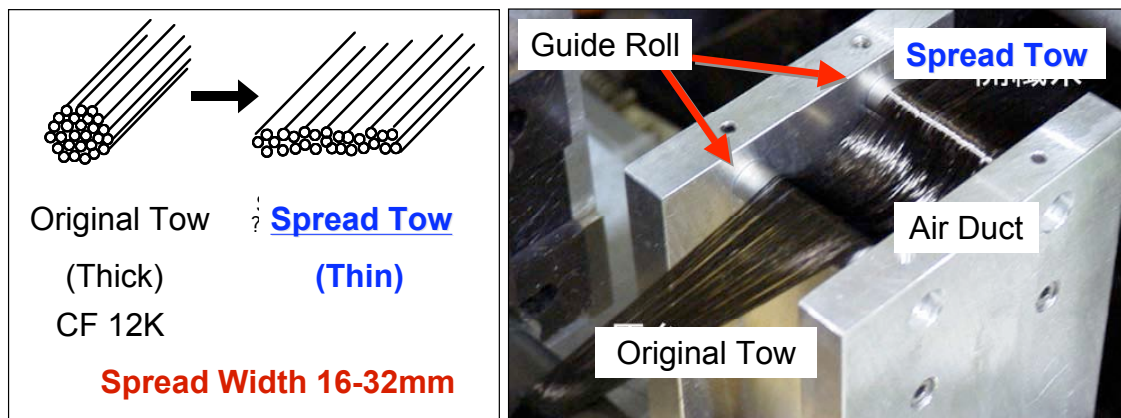


Figure 1. Thin plies are made from a tow spreading process.

[†] Copyright 2005 by S. W. Tsai. Printed by NASA with permission.

When laminates made from these thin plies, all the anticipated ply properties are recovered. When plies were made into cross-ply, quasi-isotropic and other laminates, tests showed that micro cracking and delamination were suppressed up the ultimate strength. The stress-strain curves were different so were the failure modes varied from massive delamination for regular thick ply ($T = 5.00$ mil) coupons to a clean break for thin ply ($T/6 = 0.83$ mil) coupons. The dramatic difference in the coupon failure modes can be seen in the photos below:

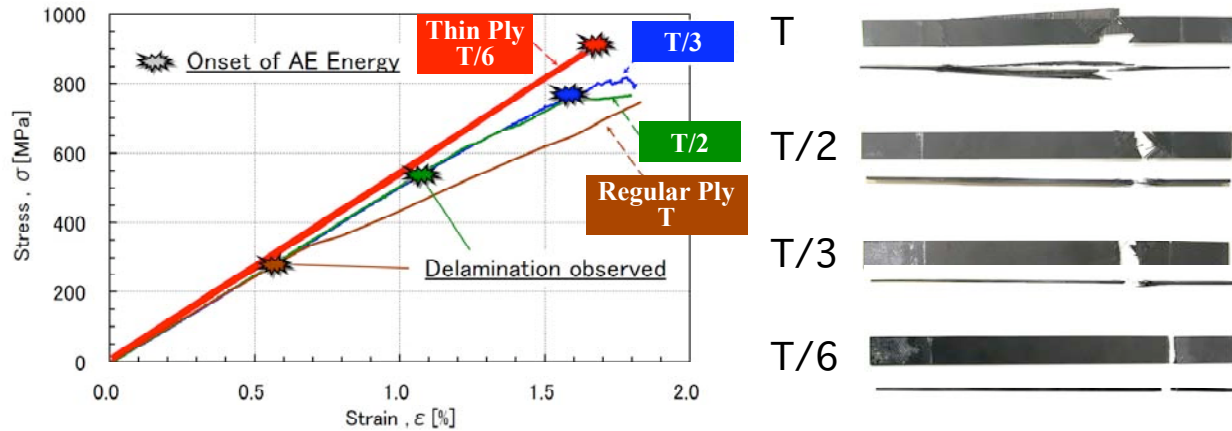
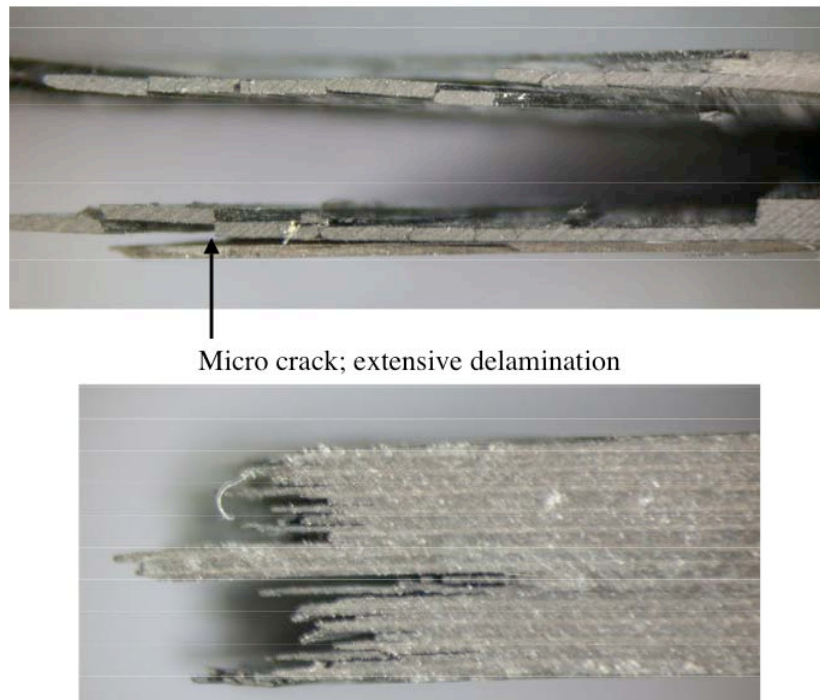


Figure 2. Stress-strain curves of thick and thin ply quasi-isotropic laminates and their failure modes.

Closed up photos of the coupon failures in Figure 2 are shown in the following two photos, in Figures 3. The upper photo shows the failure mode of thick ply (5 mil) quasi-isotropic laminates where extensive micro cracking and delamination were evident. The lower photo, on the other hand, shows a thin ply ($T/6$) laminate where a clean failure was seen. The gross fracture was highly localized with no micro cracking and delamination away from the fracture surface.



Micro crack; extensive delamination

No micro crack; no delamination

Figure 3. The upper photo is the failure of a thick ply laminate; the lower photo, a thin ply laminate.

. When thick and thin ply laminates with open hole were tested, X-ray photos showed massive micro cracking in thick ply laminates while the thin ply stayed clean. The tensile load was 90 percent of the ultimate load. The failure modes were very different with the thin ply laminate having a clean fracture with no delamination, consistent with earlier coupon tests. Fatigue tests also showed massive micro cracking and delamination along all free edges for thick ply laminates while the thin ply laminates stayed clean.

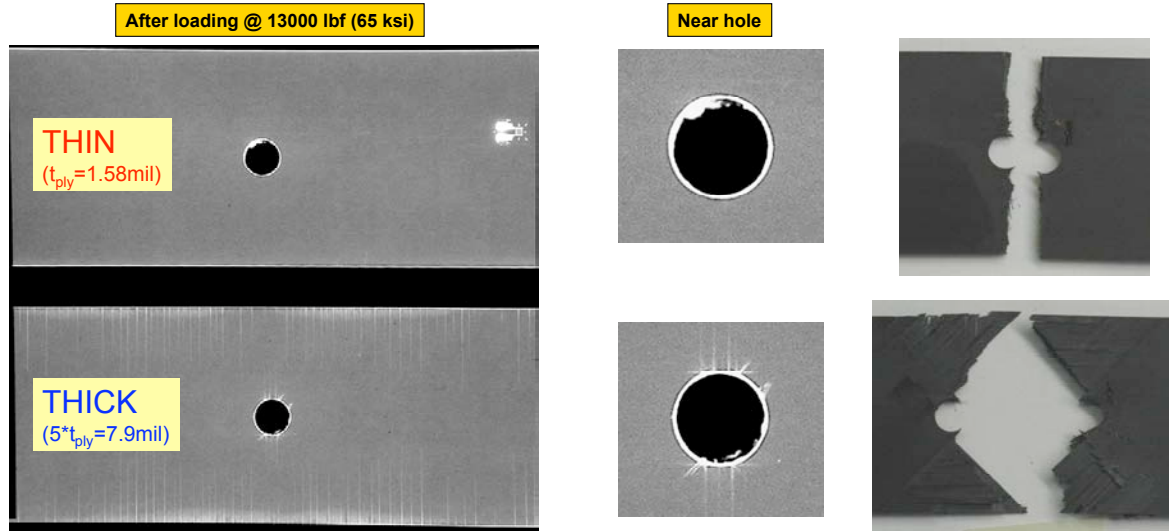


Figure 4. Static test of thick and thin open hole laminates. Local damage and gross failures were different.

The same quasi-isotropic specimens can be tested under fatigue loading. In the figures below we show the X-ray image of laminates with open hole subjected to tensile-tensile fatigue of 51 ksi after 100,000 cycles. Edge delamination and micro cracking began to appear after 20,000 cycles in the thick ply laminate on the right, while the thin ply laminate stayed clean. Even up to 100,000 cycles, thin ply laminates stayed amazingly resilient and free of damage. The thick ply laminates had massive damages far beyond the point of practical utility as a structure.

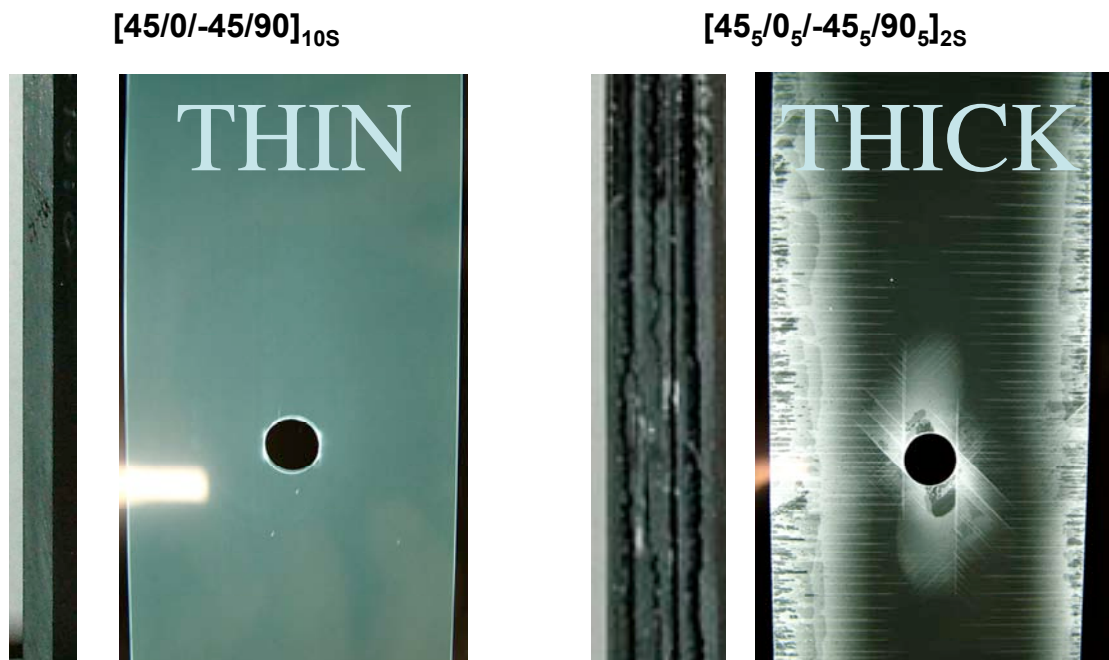


Figure 5. Fatigue test of thin and thick ply open hole laminates. The extent of damage was very different.

For hard laminates where [0] plies are 50 percent of the laminate, tension-tension fatigue at a stress level of 70 ksi after 73,000 cycles for thin and thick ply laminates. The extent of damage along the interior and outside edges was drastically more severe for the thick ply.

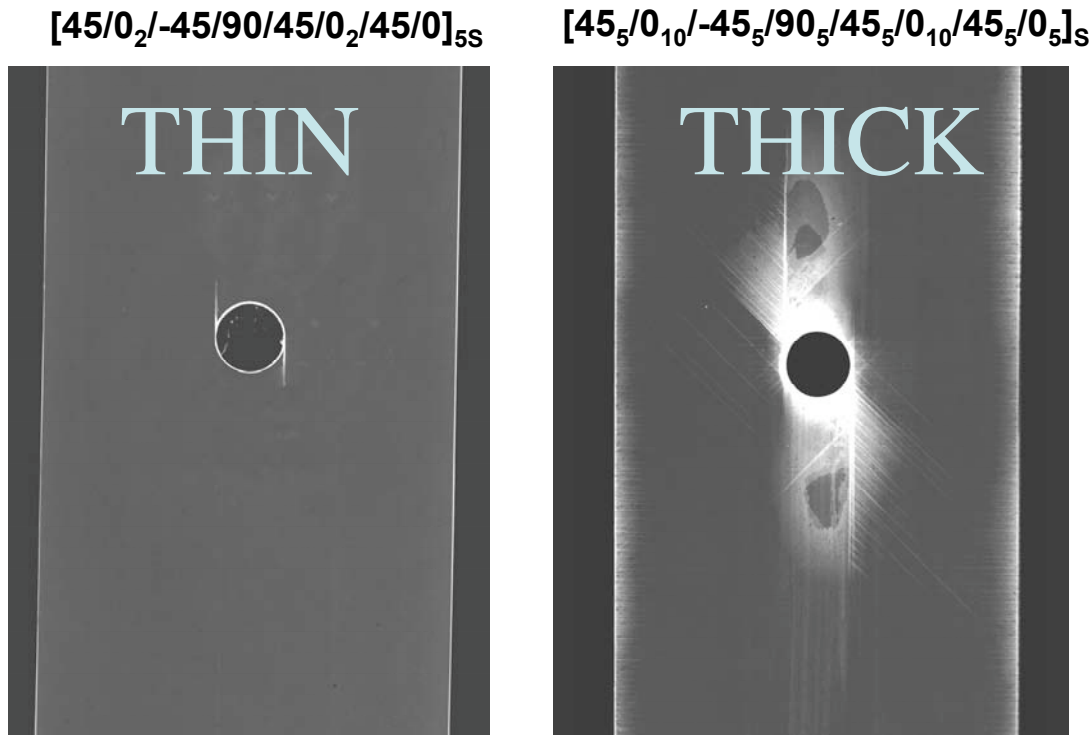


Figure 6. Fatigue of thin and thick laminates with 50 percent [0]. Again failure modes were different.

III. Conclusions

We therefore realized that thin plies have much to offer. Laminates and structures can be made strong and damage tolerant without any special resin or 3D reinforcement. Lower weight and/or lower cost is possible from having higher design allowable. The fear of premature failure by micro cracking and delamination may be a thing of the past. Designers now have more options to select the best combinations of materials and processes.

The increased cost of more layup process can be offset of a new automated lamination machine that can provide bi- and tri-directional hybrid sublaminates with thick and thin plies. This machine was invented by Mitsuya Company, also located in Fukui, Japan. A picture of this machine is shown in Figure 7.

One-meter wide sublaminates with continuous length will be available soon. Such material can have major impact how composite structures are made. The lay-up and ply drop can also be simplified in both the design and assembly processes.

While work is continuing in process development, analytical modeling of failure processes, and design methodology, we firmly believe that thin ply technology is transformational because it is simple, cost-effective and opens to new concepts not feasible with thick plies.

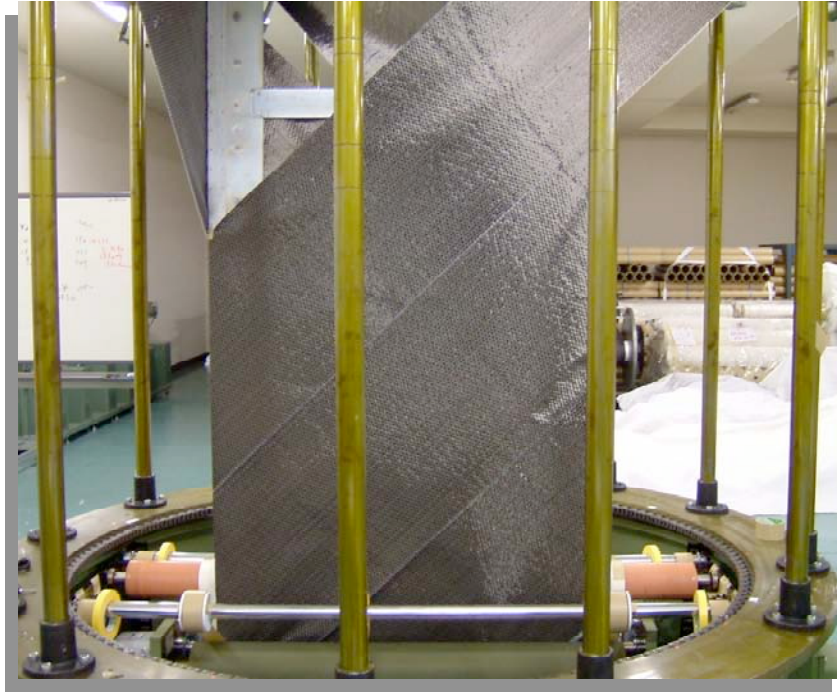


Figure 7. An automated multidirectional lamination machine.

This page left blank intentionally.

Spatial Parametric Resonance and Other Novel Buckling Problems Inspired by James H. Starnes, Jr.¹

Isaac Elishakoff
Department of Mechanical Engineering
Florida Atlantic University
Boca Raton, FL 33431-0991

Abstract

This brief note is devoted to the apparently new phenomenon in buckling of shells, namely a spatial parametric resonance due to thickness variation in isotropic and composite cylindrical shells. This problem was posed and inspired by late Dr. James H. Starnes, Jr. whose tremendous impact on the research on thin walled structures in the U.S.A. yet has to be properly ascertained. Paper also contains some personal observations on the future of buckling research.

1. Introduction

This paper is devoted to some problems in structural mechanics inspired by the late Dr. James H. Starnes, Jr. As the head of Aircraft Structures Branch, he had a great influence on the research that was conducted at the universities and within NASA. The outcome of our joint work is reported in References 1-18.

I recall that we agreed that I give him a 'private' lecture at the SDM conference about my research in stochastic analysis of initial imperfections, that culminated in papers [19,21] paving the way of introducing the initial-imperfection concept, developed by Koiter [22] in the deterministic context, into design. Indeed, we skipped one of the lunches and had a working session instead where during one hour I expanded on the importance of stochastic analysis of shell imperfections. Discussions with Dr. Starnes were always fruitful and motivating as he had the big picture vision for shell buckling and structural mechanics in his mind. Following our discussion, he mentioned that he would think about some problem that would be closely related to the research that I was proposing. After a week he contacted me and informed that he was interested in the influence of thickness imperfections in isotropic and composite shells. I suggested that I would contemplate about this problem, and if I could come with some sensible ideas I would communicate them to him.

After some thoughts, the following germ of an idea occurred, during the discussion of this topic with Professor W.T. Koiter. Since cylindrical shells are extremely sensitive to initial geometric surface imperfections that are co-configurational to the mode shape for classical buckling, one could anticipate that if the thickness distribution of the shell has a component that is proportional to such a bucking mode shape, then the thickness

¹ Copyright 2005 by I. Elishakoff. Printed by NASA with permission.

variation (or thickness imperfection) ought to influence the buckling behavior of the shells.

After getting a research assignment on this topic, we embarked on this research intensively. Fortunately, I was invited as a visiting professor at the Delft University of Technology during that summer of 1993 and had a chance to discuss this matter extensively with Professor Warner T. Koiter. He expressed his interest in participating in the research. Since then we had a very intense exchange of ideas between Dr. Starnes, Professor Koiter, as well as my student, now Dr. Yiwei Li, and myself. Derivations and calculations have been conducted on the both sides of Atlantic. I must note that Professor Koiter performed all derivations and calculations by hand, whereas we extensively used the symbolic algebraic packages.

2. Spatial Parametric Resonance

It turned out that our anticipation that the unfavorable thickness imperfections were proportional to the classical buckling mode were not incorrect; still, later on we characterized our conjecture as naïve. The effect of thickness imperfections on shell buckling turned out to be more subtle than anticipated. It was found that when the thickness variation took the form similar to the classical buckling mode shape, it may have a remarkable effect on the classical buckling load, namely the classical buckling load is decreased by over 6 percent when the imperfection amplitude is 15 percent.

Namely, if the axisymmetric thickness imperfection pattern is

$$h(x) = h_0 \left(1 - \varepsilon \cos \frac{p_0 x}{R} \right) \quad (1)$$

where h_0 = nominal thickness, ε = thickness variation amplitude, p_0 corresponds to the top of Koiter's semi-circle, then the expression for the buckling load reduction factor α is

$$\alpha = 1 - \frac{\nu}{2} \varepsilon - \frac{832 + 464\nu - 23\nu^2}{512} \varepsilon^2 \quad (2)$$

where ν = Poisson's ratio. The first two terms correspond to the formula obtained by Koiter by hand evaluation.

However, if

$$h(x) = h_0 \left(1 - \varepsilon \cos \frac{2p_0 x}{R} \right) \quad (3)$$

then the buckling load reduction formula takes a different form

$$\alpha = 1 - \varepsilon - \frac{25}{32} \varepsilon^2 \quad (4)$$

The symbolic algebra derivation provided an additional term whose influence is very small for small thickness variation amplitudes. Again, expression (4) was obtained by using symbolic calculation package, while Professor Koiter obtained the first two terms by hand calculation.

The formula (4) signifies that the most detrimental thickness variation is the one with wave number twice that corresponding to the classical buckling mode. In this situation even if the amplitude of the thickness variation is as small as 0.1, the thickness variation reduces the buckling load by 10 percent from its counterpart of the shell with uniform thickness. Thus, it turned out in the absence of initial geometric surface imperfection, this particular kind of thickness variation may constitute the most important factor in the buckling load reduction for axially compressed cylindrical shells.

A key finding was that the thickness imperfection whose wave number is twice the wave number of the classical buckling mode is reminiscent of a parametric resonance. It has a *spatial* character, which is in contrast to classical parametric resonance problems. This paper was published in the *International Journal of Solids and Structures* [2].

At this stage, Dr. Starnes suggested further work on the presence of both geometric and thickness imperfections. His style was using the word AND instead of the word BUT. He mentioned to the effect that “AND now we should move to the geometrically imperfect shell case.” This type of approach in leadership is usually referred as NEURO-LINGUISTIC PROGRAMMING. Thus, I found that Dr. Starnes had some natural magnificent leadership skills, that allowed to “squeeze”, as it were, more and more useful results from ourselves.

Let us return to the effect of initial imperfections. The fundamental study on the effect of a geometric imperfection in cylindrical shells was conducted by Professor Koiter in 1963. Hence I suggested that we take the Koiter solution as the basic one and superimpose on it the terms stemming due to deviation due to the thickness imperfections. The resulting work [17] had two components: asymptotic analysis via the energy criterion; and numerical analysis.

The following two asymptotic formulas were derived

$$(1 - \alpha) \left(1 - \frac{1}{2} \nu \varepsilon - \alpha \right) - \frac{3c}{2} \alpha \mu = 0 \quad (5)$$

and

$$(1 - \alpha)(1 - \varepsilon - \alpha) - \frac{3c}{2}\alpha\mu = 0 \quad (6)$$

where μ = amplitude of the thickness coefficient, $c = \left[3(1 - \nu^2)\right]^2$ (ν is the Poisson's ratio). Eq. (6) corresponds to the case when thickness imperfections are co-configurational to the buckling mode, whereas Eq. (6) is associated with the case when thickness imperfection wave number is twice the wave number of the axisymmetric buckling mode.

It turned out that when initial geometric surface imperfections are present, the combination of initial geometric surface imperfections and thickness imperfections reduce the buckling load even more drastically. When the thickness variation amplitude is 0.2 times the nominal thickness while initial geometric surface imperfection amplitude is just 0.02, the thickness variation causes an 11-percent further decrease in the critical buckling load. This reduction is in addition to the reduction from the initial geometric imperfection, which is 20 percent. Thus, the decrease in load-carrying capacity of the shell due to both initial geometric surface imperfections and thickness imperfections amounts to 31 percent.

This study illustrated that despite the fact that the initial geometric surface imperfections stand out as the main factor for the reduction of the critical buckling load and the effect of thickness variation is of certain patterns is less significant in many cases, the thickness variations of certain kinds may cause further notable decrease in the critical buckling load. Neglect of thickness variation, therefore, is not on the safe side, for design purposes. This one example illustrates the tremendous engineering foresight of the late Dr. Starnes.

At this stage Dr. Starnes posed the problem of comparison of the results with commercially available software. This task was accomplished by our cooperation with the computer genius Dr. David Bushnell—another pillar of the shell buckling research [14]. Further inspiration was again provided by Starnes, suggesting on generalizing the results to composite shells. This was performed in Ref. 6. In his private communication to this writer, Professor W.T. Koiter expressed his “happiness” with the results derived in Ref. 6.

3. Recent Research

From the recent studies, the paper by Gusik, Combescure and Jullien [23] stands out. They used FE analysis to study the “influence of harmonic thickness variations in the circumferential direction on the bifurcation pressure of thin cylindrical shell.” They also derived analytical formulas, extending our Eqs (1-4) to the external pressure case

$$\alpha = 1 - 1.5\varepsilon - 0.703\varepsilon^2 \quad (7)$$

Authors also found that the most detrimental imperfection mode depends on the Batdorf parameter

$$Z = \sqrt{1 - \nu^2} \left(\frac{L}{R} \right)^2 \frac{R}{h_0} \quad (8)$$

They also showed that there is a transitional value of the thickness imperfection amplitude at which the worst decrease of the buckling load takes place.

The critical imperfection amplitude, corresponding to the transition reads

$$\varepsilon_{cr} = 0.0032 + \frac{2.45}{(n_w - 1)^{2.5}} \quad (9)$$

where n_w is the Windenburg parameter.

Other important papers include those by Papadopoulos and Papadrakakis [24] and, Bathe, Chappelle and Lee [25]. Professor J. Arbocz utilized formulas (5)-(6) to investigate their effect on reliability estimates (unfortunately, this writer cannot locate this reference, presented at some EUROMECH symposium). The novel line of research reported recently by Bodner and Rubin [26] appears necessary to pursue, especially with its combination with probabilistic modeling [27].

Some pertinent comments appear to be needed on several recent studies. In the study by Schenk and Schüeller [28] the thickness imperfections are not yet included; they assert that “the Kahrunen-Loève expansion proves to be most instrumental for replacing the traditional Fourier series representation”; they also mention “advantages of using the Kahrunen-Loève expansion.” Naturally, the Fourier series and Kahrunen-Loève expansion should yield the same results, therefore, no need exists in replacing the Fourier representation. Note also that the reading and study of an interesting review paper by Arbocz and Starnes [29] ought be supplement with the review paper [21] and monograph [16] to get a comprehensive view on the subject. Likewise, some questionable statements appeared in the recent literature dealing with axial load randomness. One ought also to ask what importance is in reliability estimation based on asymptotic deterministic theories. It appears that for highly reliable structures one needs extremely accurate numerical codes. It is gratifying to read many recent papers based on our previous study [27]. Still, many papers use low-order second-moment method; it appears that the analysis based on Hasofer-Lind index ought be implemented. It appears that FE method based general program is needed for the attendant reliability analysis.

In many other occasions, our joint research and my personal views were tremendously affected by his experience and great questions that were posed by Dr. Starnes; he had an incomparable ability to pose most pertinent questions. Our cooperation resulted in the monograph titled *Non-Classical Problems in the Theory of Elastic Stability* published by the Cambridge University Press [16]. We were both gratified and humbled by the extremely positive reviews it has received in the open literature; only to salute Dr. Starnes’s memory some quotes will be reproduced here. The journal *Current Engineering*

Practice wrote “This substantial and attractive volume is well-organized and superbly written one that should be warmly welcomed by both theorists and practitioners... [Authors] have given us a jewel of a book.” *AIAA Journal* wrote: “...excellent presentation...It is well written, with the material presented in an informational fashion as well as to raise questions related to unresolved or questionable challenges...In the vernacular of film critics, “thumbs up”.” Journal *Ocean Engineering* characterized this monograph as follows: “...outstanding book...elegant...unique book...will be of enormous use...” Without the timely questions, constant encouragement, critical attitude and the divine gifts given to Dr. Starnes, of feeling what is important and what is not, the monograph would not have nearly an equal impact.

Many other research efforts were inspired by Dr. Starnes. Some of these efforts include: studying the effect of limited data on the prediction of the variability of the buckling loads and natural frequencies; efforts related to the enhancement of safety factors approach based upon reliability concept; and others.

This writer can humbly testify about many research programs that his branch supported resulted in extremely beautiful works in mechanics, with attendant feeling of a need to attend a lecture whose author or co-author was Dr. Starnes – and these were many. Dr. Starnes was a true lighting lamp for many research activities conducted at many universities via the association with NASA Langley Research Center. May this light continue to inspire more and more collaborative research activities between the academia and NASA.

4. Thoughts on the Future

Dr. James H. Starnes was a great giant in the buckling research. We see that in modern times the research support for buckling is reduced considerably; in very few universities the course on stability is given. There is a danger that the knowledge base would disappear.

On top of this government organizations fell in love with establishing research centers of excellence, which perhaps makes financial management a lot easier. Yet the research is mostly an individual endeavor, brilliant researchers being available in great schools as well the schools that do not (yet) possess such adjectives. It makes sense for NASA to concentrate on individual researches and abandon support of fewer but bigger projects.

Likewise, in order to reduce universities “appetite” for funds and financial pressure, it appears to this writer that the overhead percentages ought be reduced significantly to about 10%. This will allow to support more researchers, yet as a smaller scale: It appears that we can learn much from Canada in this respect.

Finally, it is humbly suggested the NASA Langley Research Center to be renamed into NASA Langley-Starnes Research Center and becomes a world center of buckling research.

5. References

1. Elishakoff, I.; Li, Y. W.; and Starnes, James H., Jr.: A Deterministic Method to Predict the Effect of Unknown-But-Bounded Elastic Moduli on the Buckling of Composite Structures. *Computer Methods in Applied Mechanics and Engineering*, Vol. 111, 1994, pp. 155-167.
2. Koiter, W. T.; Elishakoff, I.; Li, Y. W.; and Starnes, J. H., Jr.: Buckling of an Axially Compressed Cylindrical Shell of Variable Thickness. *International Journal of Solids and Structures*, Vol. 31, No. 6, 1994, pp. 797-805.
3. Elishakoff, I.; Cai, G. Q.; and Starnes, James H., Jr.: Probabilistic and Convex Models of Uncertainty in Buckling of Structures. In *Structural Safety & Reliability*, Schuëller, G. I.; Shinozuka, M. and Yao, J. T. P., Editors, A. A. Balkema, Rotterdam, The Netherlands, 1994, pp. 761-766.
4. Elishakoff, I.; Cai, G. Q.; and Starnes, James H., Jr.: Non-linear Buckling of a Column with Initial Imperfection via Stochastic and Non-stochastic Convex Models. *International Journal of Non-Linear Mechanics*, Vol. 29, No. 1, 1994, pp. 71-82.
5. Li, Y. W.; Elishakoff, I.; Starnes, J. H., Jr.; and Shinozuka, M.: Nonlinear Buckling of a Structure with Random Imperfection and Random Axial Compression by a Conditional Simulation Technique. *Computers & Structures*, Vol. 56, No. 1, 1995, pp. 59-64.
6. Li, Y. W.; Elishakoff, I.; and Starnes, J. H., Jr.: Axial Buckling of Composite Cylindrical Shells with Periodic Thickness Variation. *Computers & Structures*, Vol. 56, No. 1, 1995, pp. 65-74.
7. Li, Y. W.; Elishakoff, I.; and Starnes, J. H., Jr.: Buckling Mode Localization in a Multi-span Periodic Structure with a Disorder in a Single Span. *Journal of Chaos, Solutions and Fractals*, Vol. 5, No. 6, 1995, pp. 955-969.
8. Elishakoff, I.; Li, Y. W.; and Starnes, J. H., Jr.: Buckling Mode Localization in Elastic Plates due to Misplacement in the Stiffener Location. *Journal of Chaos, Solutions and Fractals*, Vol. 5., No. 8, 1995, pp. 1517-1531.
9. Elishakoff, I.; Marcus, S.; and Starnes, J. H., Jr.: On Vibrational Imperfection Sensitivity of Augusti's Model Structure in the Vicinity of a Nonlinear Static State. *International Journal of Non-Linear Mechanics*, Vol. 31, No. 2, 1996, pp. 229-236.
10. Li, Y. W.; Elishakoff, I.; Starnes, J. H., Jr.; and Shinozuka, M.: Prediction of Natural Frequency and Buckling Load Variability Due to Uncertainty in Material Properties by Convex Modeling. *Fields Institute Communications*, American Mathematical Society, Vol. 9, 1996, pp. 139-154.

11. Zhu, L. P.; Elishakoff, I.; and Starnes, J. H., Jr.: Derivation of Multi-Dimensional Ellipsoidal Convex Model for Experimental Data. *Mathematical Computing and Modeling*, Vol. 24, No. 2, 1996, pp. 103-114.
12. Elishakoff, I.; Li, Y. W.; and Starnes, J. H., Jr.: Imperfection Sensitivity Due to the Elastic Moduli in the Roorda-Koiter Frame. *Journal of Chaos, Solutions and Fractals*, Vol. 7., No. 8, 1996, pp. 1179-1186.
13. Qiu, Zhiping; Elishakoff, I.; and Starnes, James H., Jr.: The Bound Set of Possible Eigenvalues of Structures with Uncertain But Non-Random Parameters. *Journal of Chaos, Solutions & Fractals*, Vol. 7, No. 11, 1996, pp. 1845-1857.
14. Li, Yi-Wei; Elishakoff, Isaac; Starnes, James H., Jr.; and Bushnell, David: Effect of the Thickness Variation and Initial Imperfection on Buckling of Composite Cylindrical Shells: Asymptotic Analysis and Numerical Results by BOSOR4 and PANDA2. *International Journal of Solids and Structures*, Vol. 34, No. 28, 1997, pp. 3755-3767.
15. Elishakoff, I.; Li, Y. W.; and Starnes, James H., Jr.: Passive Control of Buckling Deformation Via Anderson Localization Phenomenon. *Journal of Chaos, Solutions & Fractals*, Vol. 8, No. 1, 1997, pp. 59-75.
16. Elishakoff, Isaac; Li, Y. W.; and Starnes, James H., Jr.: *Nonclassical Problems in the Theory of Elastic Stability*, Cambridge University Press, New York. January 2001.
17. Koiter, W.T., Elishakoff I., Li, Y.W. and Starnes J.H.Jr.: Buckling of an Axially Compressed Imperfect Cylindrical Shell of Variable Thickness, *Proceedings of 35th AIAA/ASME/ASCE/AHS/ASC Structures, Structural Dynamics and Materials Conference*, Hilton Heat, SC, AIAA Press, Washington, DC, pp.277-289, 1994.
18. Elishakoff I.; Arbocz, J. and Starnes, J.H., Jr.: Buckling of Stiffened Shells with Random Initial Imperfections, Thickness and Boundary Conditions, *Proceedings 33rd AIAA/ASME/ASCE/AHS/ASC Structures, Structural Dynamics and Materials Conference*, Dallas, TX, 1992, pp.95-100.
19. Elishakoff, I.: How to Introduce Initial-Imperfection Sensitivity Concept into Design, *Collapse: The Buckling of Structures in Theory and Practice* (J.M.T. Thompson and G.W. Hunt, eds.), Cambridge University Press, 1983, pp.345-357.
20. Elishakoff, I.: How to Introduce Initial-Imperfection Sensitivity Concept into Design 2, *M. Stein Memorial Volume*, NASA CP, 1998, pp.206-280.
21. Elishakoff, I.: Uncertain Buckling: Past, Present and Future, *International Journal of Solids and Structures*, Vol. 37, 2000, pp.6869-6889.

22. Koiter, W.T.: On the Stability of Elastic Equilibrium, *Ph.D. Dissertation*, Delft University, 1945 (in Dutch; English translations: (a) NASA TT-F-10, 833, 1967; (b) AFFDL-TR-70-25, 1970).
23. Gusic, G.; Combescure, A. and Jullien, J.F.: The Influence of Circumferential Thickness Variations on Buckling of Cylindrical Shells under External Pressure, *Computers and Structures*, Vol. 74, 2000, pp.461-477.
24. Papadopoulos, V. and Papadrakakis, M.: The Effect of Material and Thickness Variability on the Buckling Load of Shells with Random Initial Imperfections, *Computer Methods in Applied Mechanics and Engineering*, Vol. 194, 2005, pp.1405-1426.
25. Bathe, K-J.; Chapelle, D. and Lee, P-S.: A Shell Problem “Higly Sensitive” to Thickness Changes, *International Journal for Numerical Methods in Engineering*, Vol. 57, 2003, pp.1039-1052.
26. Bodner, S.R. and Rubin, M.B.: Modeling the Buckling of Axially Compressed Elastic Cylindrical Shells, *AIAA Journal*, Vol. 42(1), 2005, pp.103-110.
27. Elishakoff, I.; Van Manen, S.; Vermeulen, P.G. and Arbocz, J.: First-Order Second-Moment Analysis of the Buckling of Shells with Random Initial Imperfections, *AIAA Journal*, Vol. 25, 1987, pp.1113-1117.
28. Schenk, C.A. and Schuëller, G.I.: Buckling Analysis of Cylindrical Shells with Random Geometric Imperfections, *International Journal of Non-Linear Mechanics*, Vol. 38, 2003, pp.1119-1132.
29. Arbocz, J. and Starnes, J.H., Jr.: Future Directions And Challenges in Shell Stability Analysis, *Thin-Walled Structures*, Vol. 40, 2002, pp.729-754.
30. Cederbaum, G. and Arbocz J., Reliability of Shells via Koiter Formulation, *Thin-Walled Structures*, Vol. 24, 1996, 178-187.
31. Cederbaum, G. and Arbocz J., On the Reliability of Imperfection-Sensitive Long Isotropic Cylindrical Shells, *Structural Safety*, Vol. 18, 1996, 1-9.
32. Cederbaum, G. and Arbocz, J., Reliability of Imperfection-Sensitive Composites Shells via the Koiter-Cohen Criteria, *Reliability Engineering and System Safety*, Vol. 56, 1997, 257-263.
33. Nguen, T. H. L. and Tran, H. T., Influence of Variable Thickness on Stability of Rectangular plate under Compression, *Mechanics Research Communication*, Vol. 32, 2005, pp. 139-146.

This page left blank intentionally.

OPTIMUM DESIGN OF STIFFENED PANELS WITH SUBSTIFFENERS

David Bushnell,* Fellow, AIAA, Retired
Charles Rankin, Associate Fellow, AIAA
Rhombus Consultants Group, Inc.
Suite B100, 1121 San Antonio Rd., Palo Alto, CA 94303

ABSTRACT

The capability of the computer program PANDA2 to generate minimum-weight designs of stiffened panels and cylindrical shells is enhanced to permit the adding of substiffeners with rectangular cross sections between adjacent major stringers and rings. As a result many new buckling margins exist that govern buckling over various domains and subdomains of the doubly stiffened panel or shell. These generally influence the evolution of the design during optimization cycles. The substiffeners may be stringers and/or rings or may form an isogrid pattern. The effects of local, inter-ring, and general buckling modal imperfections can be accounted for during optimization. Perfect and imperfect cylindrical shells with external T-shaped stringers and T-shaped rings and with and without substringers and subrings and under combined axial compression, external pressure, and in-plane shear are optimized by multiple executions of a "global" optimizer called SUPEROPT. It is found that from the point of view of minimum weight there is little advantage of adding substiffeners. However, with substiffeners present the major stringers and rings are spaced farther apart at the optimum design than is so when there are no substiffeners. The weight of a cylindrical shell with substiffeners is much less sensitive to the spacing of the major T-shaped stringers than is the case for a cylindrical shell without substiffeners. The optimum designs obtained by PANDA2 are evaluated by comparisons with buckling loads obtained from a general-purpose finite element program called STAGS. Predictions from STAGS agree well with those from PANDA2.

INTRODUCTION

Local and overall buckling and optimization of panels can be determined with the PANDA2 [1], POSTOP [2], VICONOPT [3], and PASCO [4] computer programs. These four programs are capable of obtaining optimum designs, and PANDA2, POSTOP, and VICONOPT can do so including the effect of local postbuckling of the panel skin and/or parts of the stringers.

Other contributions to the field of buckling and postbuckling of panels include works by Weaver and his colleagues [5-7], Hilburger, et al [8], Baruch and Singer [9], the creators of the STAGS general purpose program, Almroth, Rankin, Brogan, and Riks [10-12], Arbocz and his colleagues [13-15], Stein [16], Leissa [17], Arnold and Parekh [18], Starnes, Knight, and Rouse [19], Spier [20,21], Khot and Bauld [22,23], Zhang and Matthews [24], Gurdal and his colleagues [25-30], Haftka and his colleagues [30-32], Librescu and his colleagues [33-35], Sridharan and his colleagues [36,37], Myers and Hyer [38], Nemeth [39], and Noor, Starnes, and Peters [40], to identify but a few in a vast literature.

PURPOSE OF THIS PAPER

The purpose of this paper is to report on an enhancement to PANDA2 that permits the optimization of flat and/or cylindrical panels and shells with the "usual" stringers and rings and also with "substiffeners". That is, the skin between the "usual" stringers and rings can be further stiffened by additional members, called "substiffeners" in this work. The substiffeners must be of rectangular cross section. The "usual" stiffeners (stringers and rings) can, as always, have a variety of cross sections, such as rectangular, Tee, Jay, Zee, Hat, Truss-Core, as described in [1]. The new version of PANDA2 is used to find minimum weight designs of cylindrical shells with T-shaped stringers and T-shaped rings and with rectangular substringers and subrings. Figure 1 shows a STAGS model of a piece of a cylindrical shell with major T-shaped stringers, major T-shaped rings and rectangular (blade) substringers and

* Copyright © 2005 by David Bushnell. Published by NASA with permission

subbrings.

Thermal loading is not included in cases that involve substiffeners. Also, local postbuckling is not permitted in such cases. The objective of this research is to determine if the minimum-weight designs of cylindrical shells with the more complex "double" stiffening scheme are significantly lighter than those optimized with just T-shaped stringers and T-shaped rings.

The substiffeners can also form an isogrid pattern between major axial stiffeners (stringers) and circumferential major stiffeners (rings). If the major stiffeners form an isogrid there cannot be any substiffeners. If there are substiffeners present, there can be no post-local buckling analysis (no "Koiter" analysis,[1,45]). There are no discretized single module models of a segment of panel skin with one substiffener, as with the major stiffeners [1]. In the skin-stringer and skin-ring discretized modules, the substiffeners are smeared out in the manner of Baruch and Singer [9]. Hence, in these discretized module models the new panel "skin" between major stiffeners is the actual panel skin plus smeared substringers and smeared subbrings.

Only the panel skin can have substiffeners. As of this writing there can be no substiffeners attached to the webs or outstanding flanges of major stiffeners. The substiffeners cannot be laminated composite. They are modelled as if they were of a single orthotropic material with user-specified E1, E2, G, nu, density, and maximum allowable stress components.

No attempt has yet been made to account properly for THERMAL loading in cases that have substiffeners.

This paper is a summary of a section of the file called .../panda2/doc/panda2.news called "Item no. 600" [1b]. Please see that file for details about input data, output data, and "how to.." directions and suggestions with regard to obtaining optimum designs with the new version of PANDA2. (NOTE: This paper has been updated to account for changes to PANDA2 since panda2.news Item No. 600 was written. However, Item No. 600 has not been updated.)

DESCRIPTION OF PANDA2

PANDA2 is a computer program for the minimum weight design of stiffened, composite, flat or cylindrical, perfect or imperfect panels and shells subjected to multiple sets of combined in-plane loads, normal pressure, edge moments, and temperature. For most configurations the panels can be locally postbuckled. Previous work on PANDA2 is documented in [1]. PANDA2 incorporates the theories of earlier codes PANDA [41] and BOSOR4 [42]. The optimizer used in PANDA2 is called ADS [43,44]. Panels are optimized subject primarily to buckling and stress constraints.

PANDA2 Processors and Types of Analysis

As described in [1], the PANDA2 system consists of several processors, BEGIN, SETUP, DECIDE, MAINSETUP, PANDAOPT, CHOOSEPLOT, CHANGE, STAGSMODEL, STAGSUNIT, etc. The functions of these processors are as follows:

BEGIN	User establishes starting design, material properties, prebuckling and buckling boundary conditions.
SETUP	System sets up BOSOR4-type templates for stiffness and load geometric matrices.
DECIDE	User chooses decision variables and bounds and sets up equality and inequality constraints.
MAINSETUP	User chooses analysis type, loading, and solution strategies.
PANDAOPT	Analysis type is performed (e.g. optimization).

CHOOSEPLOT	User chooses what to plot.
DIPLOT	The system obtains plots (postscript files).
CHANGE	User changes selected variables and constants.
AUTOCHANGE	A new starting design is automatically generated in a random manner.
SUPEROPT	An attempt is made to find a global optimum design.
PANEL	A BOSOR4 input file is generated for inter-ring buckling of panel skin and stringers, with stringers modelled as flexible shell branches.
PANEL2	A BOSOR4 input file is generated for inter-ring buckling of panel skin+smeared stringers with rings modelled as flexible shellbranches.
STAGSMODEL	Input files for STAGS [10-12] are generated (one finite element unit, only stringers are permitted).
STAGSUNIT	Input files for STAGS are generated (multiple shell units, both stringers and rings are permitted).
CLEANPAN	Delete all files except files containing user-provided input data for BEGIN, DECIDE, MAINSETUP, CHANGE, PANEL, PANEL2, STAGSMODEL and STAGSUNIT.

PANDA2 can be run in five modes:

1. optimization
2. simple analysis of a fixed design
3. test simulation
4. design sensitivity
5. load-interaction (N_x, N_y), (N_x, N_{xy}), (N_y, N_{xy})

Types of Buckling Included in PANDA2 Before Substiffeners Added

PANDA2 computes general, inter-ring, and local skin buckling loads and mode shapes. General buckling is buckling in which both stringers (or isogrid stiffeners) and rings participate; panel (inter-ring) buckling is buckling between adjacent rings in which stringers (or isogrid stiffeners) participate but the lines of intersection of ring web roots with the panel skin do not translate; local buckling is buckling of the panel skin between adjacent stringers (or isogrid stiffeners) and rings. PANDA2 includes the following buckling models:

1. A discretized single skin-stringer module. This model is used for local buckling, local postbuckling, and wide column buckling of the panel region between adjacent rings (transverse stiffeners).
2. Simple models for the buckling of the panel skin and stiffener segments of the type described in [41]. Typical buckling modes of the panel skin and stiffeners are shown in Figs. 5 and 6 of [41]. In the panel skin the buckling nodal lines are assumed to be straight, as shown in Fig. 9 of [41]. This type of buckling model is used in some of the software written by Arbocz and Hol [13-15] and by Khot and his colleagues [22,23]. These models are called "PANDA-type (closed form)" in PANDA2 jargon because they are the only ones used in the original PANDA program [41], which was superseded by PANDA2 [1] many years ago. Over the years an elaborate strategy has been developed in order to ensure that for each type of buckling in this PANDA-type category, the most critical (lowest) buckling load factor is not missed. The critical eigenvalue is determined from several searches over various regions in the (m, n, slope) domain, where m is the number of axial halfwaves, n is the number of circumferential halfwaves, and slope is the slope of the buckling nodal lines (non-zero when there is in-plane shear loading and/or shell wall anisotropy). More details are given in the panda2.news file identified in [1].

For sandwich panels and shells PANDA2 computes load factors for additional types of buckling that only occur for sandwich walls: face sheet wrinkling, buckling over the diameter of a single cell of a honeycomb core, and core crimping [1].

Three additional buckling models were fairly recently added to PANDA2 as described in [1]:

3. Local buckling between adjacent stringers and rings of a cylindrical or flat panel obtained from a Ritz model in which the buckling modal displacement components, u , v , w , are expanded in double trigonometric series. The local region is assumed to be simply supported on all four edges.

4. General buckling of a cylindrical panel in which stringers and rings are treated as discrete beams with undeformable cross sections. Again, the general buckling modal displacement components, u , v , w , are expanded in double trigonometric series. The edges of the domain are assumed to be simply supported and to have discrete stiffeners of half the user-specified modulus. The domain for this model is an M-bay by N-bay subdomain of the entire panel in which M and N are determined by PANDA2.

5. A discretized single module model for a cylindrical panel in which the ring segments and panel skin-with-smear-stringers are discretized. In this "branched shell" model the cross sections of the rings can deform in the buckling mode, since they are subdivided into finite elements of the type used in BOSOR4[42].

Buckling loads corresponding to a given type of buckling (such as local buckling of the skin between stringers or general buckling) may be computed by more than one model in order to verify results and to provide appropriate knockdown factors to account for anisotropy, inherent unconservativeness in smearing stiffeners, the presence of in-plane shear loading, and variation of in-plane loading within the domain that buckles. The effect of transverse shear deformation (t.s.d.) is accounted for as described in [1].

PANDA2 can optimize imperfect stiffened panels and shells [1]. Imperfections are assumed to be in the shapes of the general, inter-ring, and local buckling modes obtained from the PANDA-type model identified as Item No. 2 above. Imperfections in stiffened panels and shells have two major effects:

a. The imperfect panel or shell bends as soon as any loading is applied. This bending causes significant redistribution of stresses between the panel skin and the various stiffener parts, thus affecting significantly many buckling and stress constraints in the optimization problem.

b. The "effective" curvature of a cylindrical panel or shell depends on the amplitude of the initial imperfection and on the circumferential wavelength of the critical buckling mode of the perfect shell. This "effective" curvature is larger than the nominal radius of curvature because it corresponds to the radius of a typical inward circumferential lobe of the initial and subsequently load-amplified buckling modal imperfection. In PANDA2 this larger local radius of curvature is assumed to be the governing radius in the buckling equations pertaining to the imperfect shell.

Local post buckling analysis

An analysis branch exists in which local post buckling of the panel skin is accounted for [1]. In this branch a constraint condition that prevents stiffener pop-off is introduced into the optimization calculations. The postbuckling theory incorporated into PANDA2 is similar to that formulated by Koiter for panels loaded into the far-postbuckling regime [45].

Stress constraints

In addition to buckling constraints, PANDA2 computes stress constraints including local postbuckling deformations and thermal loading by both curing and applied temperature distributions. For laminated composite walls PANDA2 generates stress constraints corresponding to maximum tension along fibers, maximum compression along fibers, maximum tension transverse to fibers, maximum compression transverse to fibers, and maximum in-plane shear

stress for each different material in a stiffened panel. For isotropic material PANDA2 generates stress constraints based on the von Mises effective stress.

Global optimizer called SUPEROPT introduced into PANDA2

Global optimum designs can be obtained with PANDA2 by means of multiple sequential executions of a processor called SUPEROPT, which is described in more detail in [1]. At intervals during the optimization process new starting designs are automatically generated as follows:

$y(i) = x(i)[1 + dx(i)]$, $i = 1, 2, 3, \dots$ number of decision variables, in which $x(i)$ is the old value of the i th decision variable, $y(i)$ is the new value, and $dx(i)$ is a random number between -0.5 and +1.5 if the decision variable is other than a stiffener spacing and a random number between -1.0 and +1.0 if the decision variable is a stiffener spacing. Stiffener spacings are treated differently from other decision variables because an increase in a stiffener spacing always makes the structure weaker. In order to obtain global optimum designs it is almost always necessary to execute SUPEROPT several times in succession, not just once or twice.

Frequent use of "knockdown" factors in PANDA2

As mentioned in previous PANDA2 literature, in PANDA2 knockdown factors are used often. There are knockdown factors for weakening due to transverse shear deformation (t.s.d.), to compensate for the inherent unconservativeness of smearing stiffeners, to compensate for anisotropic effects and the application of in-plane shear loading, to compensate for initial imperfections, and to compensate for possible truncation error in the double trigonometric series expansions used in the alternative buckling models.

DESCRIPTION OF STAGS

STAGS (SStructural Analysis of General Shells) is a finite element code for general-purpose nonlinear analysis of stiffened shell structures of arbitrary shape and complexity. Its capabilities include stress, stability, vibration, and transient analyses with both material and geometric nonlinearities permitted in all analysis types. STAGS includes enhancements, such as a higher order thick shell element, more advanced nonlinear solution strategies, and more comprehensive post-processing features such as a link with STAPL [1b].

Research and development of STAGS by Brogan, Almroth, Rankin, Stanley, Cabiness, Stehlin and others of the Computational Mechanics Department of the Lockheed Palo Alto Research Laboratory has been under continuous sponsorship from U.S. government agencies and internal Lockheed funding for the past 30 years. During this time particular emphasis has been placed on improvement of the capability to solve difficult nonlinear problems such as the prediction of the behavior of axially compressed stiffened panels loaded far into their locally postbuckled states. STAGS has been extensively used worldwide for the evaluation of stiffened panels and shells loaded well into their locally postbuckled states. See [12], for example.

A large rotation algorithm that is independent of the finite element library has been incorporated into STAGS [46]. With this algorithm there is no artificial stiffening due to large rotations. The finite elements in the STAGS library do not store energy under arbitrary rigid-body motion and the first and second variations of the strain energy are consistent. These properties lead to quadratic convergence during Newton iterations.

Solution control in nonlinear problems includes specification of load levels or use of the advanced Riks-Crisfield path parameter [12] that enables traversal of limit points into the post-buckling regime. Two load systems with different histories (Load Sets A and B) can be defined and controlled separately during the solution process. Flexible restart procedures permit switching from one strategy to another during an analysis. This includes shifts from bifurcation buckling to nonlinear collapse analyses and back and shifts from static to transient and transient to static analyses with modified boundary conditions and loading. STAGS provides solutions to the generalized eigenvalue problem for buckling and vibration from a linear or nonlinear stress state.

Quadric surfaces can be modeled with minimal user input as individual substructures called "shell units" in which the analytic geometry is represented exactly. "Shell units" can be connected along edges or internal grid lines with partial or complete compatibility. In this way complex structures can be assembled from relatively simple units. Alternatively, a structure of arbitrary shape can be modeled with use of an "element unit".

Geometric imperfections can be generated automatically in a variety of ways, thereby permitting imperfection-sensitivity studies to be performed. For example, imperfections can be generated by superposition of several buckling modes determined from previous STAGS analyses of a given case.

A variety of material models is available, including both plasticity and creep. STAGS handles isotropic and anisotropic materials, including composites consisting of up to 60 layers of arbitrary orientation. Four plasticity models are available, including isotropic strain hardening, the White Besseling (mechanical sublayer model), kinematic strain hardening, and deformation theory.

Two independent load sets, each composed from simple parts that may be specified with minimal input, define a spatial variation of loading. Any number of point loads, prescribed displacements, line loads, surface tractions, thermal loads, and "live" pressure (hydrostatic pressure which remains normal to the shell surface throughout large deformations) can be combined to make a load set. For transient analysis the user may select from a menu of loading histories, or a general temporal variation may be specified in a user-written subroutine.

Boundary conditions (B.C.) may be imposed either by reference to certain standard conditions or by the use of single- and multi-point constraints. Simple support, symmetry, antisymmetry, clamped, or user-defined B.C. can be defined on a "shell unit" edge. Single-point constraints which allow individual freedoms to be free, fixed, or a prescribed non-zero value may be applied to grid lines and surfaces in "shell units" or "element units". A useful feature for buckling analysis allows these constraints to differ for the prestress and eigenvalue analyses. Lagrangian constraint equations containing up to 100 terms may be defined to impose multi-point constraints.

STAGS has a variety of finite elements suitable for the analysis of stiffened plates and shells. Simple four node quadrilateral plate elements with a cubic lateral displacement field (called "410" and "411" elements) are effective and efficient for the prediction of postbuckling thin shell response. A linear (410) or quadratic (411) membrane interpolation can be selected. For thicker shells in which transverse shear deformation is important, STAGS provides the Assumed Natural Strain (ANS) nine node element (called "480" element). A two node beam element compatible with the four node quadrilateral plate element is provided to simulate stiffeners and beam assemblies. Other finite elements included in STAGS are described in the STAGS literature [10-12].

THEORY AND MODIFICATIONS TO PANDA2 TO PERMIT SUBSTIFFENERS

With the introduction of substiffeners between major stiffeners, there are many new buckling constraints introduced into the optimization problem, such as buckling of the panel skin between substiffeners including rolling of the substiffeners, buckling of the panel skin with smeared substringers between adjacent subrings, buckling of the substringers, buckling of the subrings, and buckling from the alternative theory (double trigonometric series expansions) of various "patches" involving segments of the panel skin with discrete substiffeners.

These new constraints are generated in PANDA2 by means of new coding that is analogous to that previously existing for buckling of segments of the major stiffeners and for buckling of sections of the panel skin stiffened by major stiffeners.

In the case of a panel with substiffeners that form an isogrid pattern between adjacent major stringers and rings, a new capability has been implemented with regard to buckling of the triangular portion of panel skin between adjacent isogrid members. Previously, the buckling theory was based on the assumption that the triangular piece of panel skin between adjacent isogrid members was simply supported along its three edges. The contributions of stiffener rolling to the strain energy and work done by prebuckling stiffener resultants during buckling modal rotations were neglected. Now, provided that the stiffeners are of rectangular cross section (as is always the case with substiffeners), these contributions are included. For panels in which the major stiffeners form an isogrid pattern, if the major stiffeners are of rectangular cross section, their rolling during buckling modal rotations is now

included. If the major stiffeners form an isogrid pattern, substiffeners are not allowed.

There are new stress constraints that involve the substiffeners.

EXAMPLE

The numerical results presented here are all derived from an example of an aluminum cylindrical shell, the dimensions, material properties, loading, boundary conditions, and imperfection for which are listed in Table 1. Table 2 lists the names and definitions of all the variables that may or may not be decision variables in optimization problems. Variable No. 2, the stringer base B2(STR), is always equal to one tenth the stringer spacing in this study, and the properties of the wall in the stringer base are the same as those in the wall midway between stringers; there is no stringer faying flange. The width of the ring base, B2(RNG), is always zero in this study.

The new variables pertaining to the substiffeners are called TSUB (thickness), HSUB (height), and BSUB (spacing). In the examples presented here there are always both substringers and subrings.

Table 3 lists the starting design and optimum designs for perfect and imperfect shell with and without substiffeners. One can see from the weights listed that there is little advantage of adding substiffeners from the point of view of weight alone.

RUNSTREAM TO OBTAIN THE "GLOBAL" OPTIMUM DESIGN

The runstream to produce a "global" optimum design is listed in Table 4. The case name is "testax4p". "Global" is in quotes because there is no guarantee that the optimum is truly a global optimum design. The more sets of "superopt/chooseplot/diplot" the user executes, the more likely it is that a truly global optimum design will result. In the "global" optimization in this case, there were four executions of the sequence SUPEROPT /CHOOSEPLOT/DIPILOT.

Each execution of SUPEROPT must be followed by an execution of CHOOSEPLOT because CHOOSEPLOT is where the total number of design iterations gets reset to zero between executions of SUPEROPT. This must always be done before the next execution of SUPEROPT.

Figure 2 shows a plot of the objective function vs design iterations after the first execution of SUPEROPT for the perfect shell with substiffeners. The final optimum design of the perfect shell is listed in Column 3 of Table 3.

RESULTS CORRESPONDING TO THE "GLOBAL" OPTIMUM DESIGN: PERFECT SHELL WITH SUBSTIFFENERS

With substiffeners present there exist many new margins. Table 5 lists the margins corresponding to the optimized perfect cylindrical panel with T-shaped major stringers and T-shaped rings and with rectangular substringers and subrings (case name = "testax4p"). In Table 5 the last six margins correspond to six inequality expressions provided by the PANDA2 user in DECIDE. These six inequality conditions impose the following constraints on the optimum design:

1. The stringer spacing must be at least 3 times the substringer spacing.
2. The ring spacing must be at least 3 times the subring spacing.
3. The substringer height must be less than 10 times the substringer thickness.
4. The subring height must be less than 10 times the subring thickness.
5. The major stringer web height must be less than 20 times the major stringer web thickness.
6. The major ring web height must be less than 20 times the major ring web thickness.

There is one linking constraint: the stringer base width, B2(STR), must equal $0.1 \times$ (stringer spacing B(STR)). In this case the stringer base has the same thickness and properties as the skin between stringers; there are no faying

flanges in any of the cases explored here.

A few of the margins in Table 5 are negative. PANDA2 accepts designs that are "ALMOST FEASIBLE", that is, for which there may be some slightly negative margins, specifically, any margin greater than -0.05.

The optimum dimensions of the perfect shell are listed in Column 3 of Table 3.

The new margins pertaining to substiffeners are listed in Table 6.

In PANDA2 the new margins involving substiffeners are computed in a manner analogous to similar margins involving major stiffeners. For example, Margin 21 in Table 6 is computed from the PANDA-type (closed-form) theory in which the effect of rolling of the substiffeners along the edges of a local region of skin between adjacent substiffeners is included. In PANDA2 models with IQUICK=1 (no discretized skin-stringer module model) and no alternative solution and no substiffeners and major stiffeners with rectangular cross sections, there is an analogous margin:

"buck.(SAND);rolling with local buck.; M=1;N=1;slope=0.2236;FS=1.

computed from the same subroutines.

Margins 22 and 23 in Table 6 are computed from the same subroutines as those for the analogous margins that involve major stiffeners. For example, the "old" margin pertaining to a major stringer (Table 5),

7 1.76E+00 buckling margin stringer Iseg.3 . Local halfwaves=8 .MID.;FS=1.

is computed in SUBROUTINE STFEIG. (In this particular case there is no buckling of ring "Iseg.3" because there exists only tension along the axis of the ring web).

The new margins pertaining to a substringer and subring,

22 -4.04E-04 buckling:simp-support of substring.M=1;FS=1.

23 1.14E+01 buckling:simp-support of subrings N=1;FS=1.

are computed from statements taken from SUBROUTINE STFEIG and inserted in the proper place in SUBROUTINE BUCPAN.

The new margins 24, 25, and 27 in Table 6, computed from the alternative buckling theory described in [1]:

24 -2.86E-02 buckling:simp-support altsoln4 intermajorpatch; FS=0.999

25 3.21E-01 buckling:simp-support altsoln5 skin+edgsubroll; FS=0.999

27 5.78E-02 buckling:simp-support altsoln6 inter-subring ; FS=0.999

are calculated in the same subroutine, ALTSOL, used for computation of the "old" margins (Table 5):

12 1.53E-01 buck.(SAND);simp-support smearsbstf; (0.95*altsol);FS=0.999

13 -3.84E-03 buck.(SAND);simp-support inter-ring; (1.00*altsol);FS=0.999

15 2.35E-03 buck.(SAND);simp-support general buck;(0.85*altsol);FS=0.999

The new alternative buckling models are analogous to the old. The new margin (Table 6),

25 3.21E-01 buckling:simp-support altsoln5 skin+edgsubroll; FS=0.999

is analogous to the "old" one (Table 5),

12 1.53E-01 buck.(SAND);simp-support smearsbstf; (0.95*altsol);FS=0.999

In the new margin (Margin 25) the buckling domain is the panel skin between adjacent substiffeners with rolling of the substiffeners along the edges of the domain included in the model. In the old margin, (Margin 12 in Table 5) the domain is the panel skin + smeared substiffeners between adjacent major stiffeners.

The new margin (Table 6),

27 5.78E-02 buckling:simp-support altsoln6 inter-subring ; FS=0.999
is analogous to the "old" one (Table 5),

13 -3.84E-03 buck.(SAND);simp-support inter-ring; (1.00*altsol);FS=0.999

In the new margin (Margin 27) the buckling domain is the panel skin plus substringers between subrings. A 6-substringer-bay model is used. In the "old" margin (Margin 13) the domain is the panel skin + smeared substiffeners between adjacent major rings. A 6-major-stringer-bay model is now used. (See panda2,news Item No. 603. Previously it was a 3-major-stringer bay model.)

The new margin (Table 6),

24 -2.86E-02 buckling:simp-support altsoln4 intermajorpatch; FS=0.999

is analogous to the "old" one (Table 5),

15 2.35E-03 buck.(SAND);simp-support general buck;(0.85*altsol);FS=0.999

In the new margin (Margin 24) the buckling domain is an N-substringer-bay x M-subring-bay "patch", in which N can be as high as 6 and M can be as high as 5. In the "old" margin (Margin 15) the buckling domain is an N-major-stringer bay x M-major-ring-bay "patch", in which N can be as high as 6 and M can be as high as 5, with substringers and subrings smeared. (See panda2.news Item No. 603 for the recent modification of the way in which the "old" Margin 15 is now computed with a larger "patch" than was previously used. The old "patch" had 3-major-ring bays x 3-major-stringer bays.)

The two new margins pertaining to substiffeners (Table 6),

28 5.77E+00 buck.(SAND);rolling with smear subrng;M=39;N=1;slope=0.01;FS=0.999

29 6.91E-01 buck.(SAND);rolling only of substring;M=20;N=0;slope=0.;FS=1.6

are analogous to the two "old" margins pertaining to major stiffeners (Table 5):

16 5.72E+00 buck.(SAND);rolling with smear rings; M=52;N=1;slope=0.01;FS=0.999

17 6.94E-03 buck.(SAND);rolling only of stringers;M=16;N=0;slope=0.;FS=1.6

The two new margins pertaining to substiffeners (Table 6),

26 2.18E-01 buck.(SAND);rolling with smear substr;M=1;N=2;slope=16.67;FS=0.999

30 8.00E+00 buck.(SAND);rolling only of subrings; M=0;N=4;slope=0.;FS=1.6

are analogous to similar "old" margins pertaining to major stiffeners. However, the "old" margins, although computed, are not recorded as constraints on the design because they are both superceded by the discretized skin-with-smeared-stringers/ring single module model that yields the margin (Table 5),

4 2.53E-02 Inter-ring bucklng, discrete model, n=6 circ.halfwaves;FS=0.999

With the NPRINT index set equal to 2 in the *.OPT file, PANDA2 prints messages such as the following:

“Inter-ring buckling with smeared stringers and ring rolling is not recorded as a margin because this type of buckling

has been superceded by the results from the discretized inter-ring module model, for which inter-ring buckling load factors have been computed in the range from $n = 1$ to $n = 70$ circumferential halfwaves. The critical inter-ring-buckling-with-ring-rolling model has 7 circ. half waves, which lies within this range.”

“Ring rolling without participation of the panel skin is not recorded as a margin because this type of buckling has been superceded by the results from the discretized "skin"-ring module model, for which buckling load factors have been computed in the range from $n = 1$ to $n = 70$ circ. halfwaves. The critical ring-rolling-without-participation-of-the-panel-skin model has 7 circ. half waves, which lies within this range.”

Please see panda2.news Item No. 463 [1] for more about the discretized module model that involves the panel skin with smeared major stringers and a single discretized major ring cross section and how this model supercedes several buckling constraints that involve major ring rolling. Note that there exists no analogous discretized skin-with-smeared-substringers/subring module model. Therefore, margins such as Margin No. 26 and Margin No. 30 are recorded and not superceded by any other buckling model.

Table 7 lists margins in which the substringers and subrings are smeared in the manner of Baruch and Singer [9].

Margins 1-3 in Table 7:

- 1 2.53E-02 Local buckling from discrete model-1., $M=2$ axial halfwaves; $FS=0.99$
- 2 2.23E-01 Bending-torsion buckling; $M=2$; $FS=0.999$
- 3 3.24E-01 ($m=2$ lateral-torsional buckling load factor)/(FS)-1; $FS=0.999$

are from the discretized "skin"-major-stringer single module model. In Margin 1 the term "local" means "local buckling of the "skin" between major stringers. In the presence of substiffeners, what used to be called the panel skin is now the panel skin-with-smeared-substiffeners. Margins 2 and 3 are computed from the same discretized single module model with smeared substiffeners.

With substiffeners present there exist buckling modes more local than that corresponding to Margin 1. For example, the margin,

- 21 4.60E-01 buck.(SAND);rolling with skin buckl.; $M=1$; $N=1$; $slope=0.1939$; $FS=0.999$

(Table 6) involves local buckling of the panel skin between adjacent substiffeners, with rolling of the substiffeners included in the model.

Margins 4 and 13 in Table 7,

- 4 2.53E-02 Inter-ring buckling, discrete model, $n=6$ circ.halfwaves; $FS=0.999$
- 13 -3.84E-03 buck.(SAND);simp-support inter-ring; $(1.00*\text{altsol})$; $FS=0.999$

are computed with substiffeners smeared and major stringers smeared.

Margin 12 in Table 7,

- 12 1.53E-01 buck.(SAND);simp-support smearsbstf; $(0.95*\text{altsol})$; $FS=0.999$

used to be called "buck.(SAND);simp-support local buckling; $(0.95*\text{altsol})$ ". It is generated from the same alternative buckling theory (double trigonometric series expansion) as before when there existed only skin between adjacent stringers and rings. Now the domain between adjacent major stringers and rings includes smeared substiffeners.

Margins 14 and 15 in Table 7,

- 14 -2.02E-02 buck.(SAND);simp-support general buck; $M=6$; $N=0$; $slope=0.4637$; $FS=.999$
- 15 2.35E-03 buck.(SAND);simp-support general buck; $(0.85*\text{altsol})$; $FS=0.999$

are derived from two different models of general instability, a closed form PANDA-type model in which all stiffeners (major and sub) are smeared out (Margin 14) and an alternative (double trig series expansion) model in which the substiffeners are smeared out and the major stiffeners are treated as discrete beams in a 6-major stringer bay by 5-major-ring-bay "patch" (Margin 15).

Margin 16 in Table 7,

16 5.72E+00 buck.(SAND);rolling with smear rings; M=52;N=1;slope=0.01;FS=0.999

is generated from a model in which the substiffeners as well as the major rings are smeared out and the major stringers are treated as discrete beams that run along the two generators at the straight edges of the long, narrow domain that includes the entire length of shell between two adjacent major stringers.

GENERATING AN OPTIMUM DESIGN THAT CAN BE ANALYZED WITH STAGS

It is important to evaluate the optimum design obtained by PANDA2 by use of a general-purpose finite element program operating on the same design. The general-purpose finite element program STAGS [10-12] was used. The PANDA2 processor STAGSUNIT [1] had to be modified to work for panels with substiffeners [1b].

In order to generate a PANDA2 model that, via STAGSUNIT, produces suitable input files, *.bin and *.inp, for STAGS, it is necessary first to find an optimum design with PANDA2 in which there are integral numbers of major stiffeners over the entire domain of the STAGS model and integral numbers of substiffeners between adjacent major stiffeners. This is done by the following steps:

1. Use the PANDA2 processor called CHANGE to reset the variables, B(STR), B2(STR), B(RNG) BSUB(substring), BSUB(substrings) so that there are integral numbers of each kind of stiffener in the appropriate domains. Choose values that are close to those found in the optimum designs listed in Table 3. (See Table 8 for appropriate values of the stiffener spacings for STAGS models).

2. Use the PANDA2 processor called DECIDE. The stiffener spacings B(STR), B2(STR), B(RNG) BSUB(substring), BSUB(substrings), should no longer be decision variables, and the therefore inappropriate inequality constraints,

- a. The stringer spacing must be at least 3 times the substringer spacing.
- b. The ring spacing must be at least 3 times the subring spacing.

should be eliminated.

3. Execute SUPEROPT/CHOOSEPLOT/DILOT at least once to find a new "global" optimum design for which there are integral numbers of major stiffeners and substiffeners in the appropriate domains.

4. Execute PANDAOPT once more for a fixed design: the optimum design.

New optimum designs suitable for analysis by STAGS are listed in Table 8. The margins corresponding to the perfect shell with substiffeners (second column in Table 8) are listed in Table 9.

CREATION OF STAGS MODELS

STAGS models, such as that shown in Fig. 1, are generated via the PANDA2 processor called STAGSUNIT. The purpose of STAGSUNIT is to generate the two input files, *.bin and *.inp, for the STAGS general purpose finite element program. In this example "*" stands for the case name, "testax4p". Typical input data files for STAGSUNIT are listed in several tables in [1b].

As described in [1], the processor STAGSUNIT is written in such a way that "patches" of various portions of a complete panel or shell can be analyzed with STAGS. The correct prebuckled state of a perfect panel is preserved independently of the size of the "patch" to be included in the STAGS model. The minimum size "patch" must contain at least one major stiffener spacing in each direction, and major stringers are always included along the two straight edges of the "patch". There may or may not be rings running along the two curved edges of the "patch", depending on input to STAGSUNIT provided by the user of PANDA2. Stiffeners that run along the four boundaries of the "patch" have half the stiffness of those that lie within the "patch". Figure 1 shows a STAGS "patch" model that includes only three bays between major stringers (four major stringers) and one bay between two major rings.

Substiffeners always lie within the patch. There must always be integral numbers of uniformly spaced substiffeners (substringers and/or subrings) between adjacent major stiffeners. The substiffeners that are closest to the major stiffeners are one half a substiffener spacing away from the major stiffeners. Substringers and subrings never occur along coordinate lines where there exist major stringers and/or major rings. As of this writing STAGSUNIT cannot handle isogrid stiffening or substiffening.

The STAGS models are constructed by the PANDA2 processor STAGSUNIT in such a way that all stiffeners (major and sub) are connected only to the panel skin. That is, where stiffeners intersect they simply pass through each other with no constraints between them along their lines of intersection. This is a conservative model with respect to buckling.

There can be gaps between the roots of the stiffeners and the reference surface of the panel skin. For example, if the reference surface of the panel skin is the middle surface, there are gaps equal to half the skin thickness. The user can elect to have what in STAGS jargon are called "fasteners" that relate the nodal displacement components on the skin reference surface to those at the root of a stiffener web. The STAGS model shown in Fig. 1 has fasteners. They can barely be seen as tiny black dots at nodal points along the roots of all the stiffeners.

Several examples of input data for the PANDA2 processor, STAGSUNIT, are given in [1b]. Detailed instructions on running STAGSUNIT followed by running STAGS are also listed there.

RESULTS FROM STAGS

The execution of STAGS produces a number of files. The user must inspect the *.out1 and *.out2 files if the STAGS run bombs. The user must inspect the *.out2 file if the run finishes in a normal fashion.

Table 10 lists the most important part of the testax4p.out2 file generated from the successful STAGS run to which Fig. 3 corresponds: a three-axial-bay by nine- circumferential-bay "patch" in which all of the major stiffeners and substiffeners are modelled as shell units and in which the "480" STAGS finite element is used throughout the STAGS model. The middle surface is used as the reference surface of the cylindrical skin and there exist fasteners that connect this middle surface to the roots of the stiffeners.

The buckling modes corresponding to the eigenvalues (buckling load factors) listed in Table 10 are all mixtures of the types corresponding to the following margins from PANDA2 (Table 9):

- 1 1.24E-01 Local buckling from discrete model-1.,M=2 axial halfwaves;FS=0.99
- 2 3.38E-01 Bending-torsion buckling; M=2 ;FS=0.999
- 3 4.50E-01 (m=2 lateral-torsional buckling load factor)/(FS)-1;FS=0.999
- 4 1.03E-02 Inter-ring buckling, discrete model, n=6 circ.halfwaves;FS=0.999
- 13 -3.76E-03 buck.(SAND);simp-support inter-ring; (1.00*altsol);FS=0.999
- 17 -2.58E-02 buck.(SAND);rolling only of stringers;M=14;N=0;slope=0.;FS=1.6
- 24 -4.18E-02 buckling:simp-support altsoln4 intermajorpatch; FS=0.999

The numbers listed under "TYPES OF BUCKLING" in Table 10 correspond to the PANDA2 margins from Table 9 and repeated just above.

According to PANDA2, the three types of buckling

- 1 1.24E-01 Local buckling from discrete model-1.,M=2 axial halfwaves;FS=0.99
- 2 3.38E-01 Bending-torsion buckling; M=2 ;FS=0.999
- 3 4.50E-01 (m=2 lateral-torsional buckling load factor)/(FS)-1;FS=0.999

are not critical. In contrast, these three modes play a prominent role in the STAGS model of buckling. In PANDA2 the domain used for these three types of buckling includes only the axial dimension between adjacent major rings. Therefore, the string "M=2" means "two axial halfwaves between major rings". In the STAGS model the axial wavelength of the "bending-torsion" buckling or "lateral-torsional" buckling (sideways of the major stringers) is not restricted to the distance between adjacent major rings because the stiffeners are allowed to deform relative to each other where they intersect. The PANDA2 model that leads to the margin,

17 -2.58E-02 buck.(SAND);rolling only of stringers;M=14;N=0;slope=0.;FS=1.6

also allows the stringers to deform relative to the major rings because the domain is the entire axial length of the panel. Therefore, the string "M=14" means "14 axial halfwaves over the entire axial length of the panel". The inclusion of this type of buckling prevents PANDA2 from yielding an unconservative design in this case because the buckling domain is longer than one major ring spacing.

Figure 3 shows the buckling mode from STAGS corresponding to the lowest eigenvalue (buckling load factor), 0.97738. Figure 4 shows the "same" STAGS model and buckling mode except that the STAGS 410 finite element is used for the panel skin and the major stiffeners and the STAGS 210 finite element is used for the substiffeners. If any stiffeners (major or sub) are modelled as beams (210 element), then the user has no choice: the STAGS 410 element MUST be used for all shell units since this element is compatible with the STAGS 210 beam element.

Figure 5 shows the fundamental buckling mode from the same model that produced Figure 3 except that the substiffeners are smeared out in the manner of Baruch and Singer [9]. The buckling modes from STAGS are similar to those corresponding to the STAGS models in which the substiffeners are treated as shell units except that there is little evidence of the type of buckling from PANDA2's margin 24: "intermajorpatch".

GENERAL BUCKLING MODE(S) FROM STAGS

Of particular interest is the determination of the general buckling load factor according to STAGS. In this case one must include the entire cylindrical shell in the STAGS model. Because of the presence of uniform in-plane shear loading, N_{xy} , (Table 1) there are no planes of symmetry. In the STAGS model of the entire shell the substiffeners are smeared out and the major stiffeners are treated as shell units. The STAGS "480" finite element is used throughout. The outer surface of the panel skin is used as the reference surface and there are no fasteners in this particular model.

In order to find the lowest long-wavelength general buckling mode in this case it is necessary to make several STAGS runs, each successive run with a slightly higher initial eigenvalue "shift". This has to be done because there are many "inter-ring" buckling modes that have eigenvalues (buckling load factors) that bracket the lowest eigenvalue corresponding to the general buckling mode. "Inter-ring" is in quotation marks here because most of these short-wavelength modes involve significant in-plane bending of the major rings, as will be seen later. This places them in the "general buckling" category. Three STAGS runs were required in this case to obtain the lowest long-wavelength general buckling mode (Mode 19).

There are results from two sets of three runs each listed in Table 600.24 of [1b]. The first set of three runs corresponds to a model in which the outer surface of the shell skin is used as a reference surface and there are no fasteners. The second set of three runs corresponds to a model in which the middle surface of the shell skin is used as a reference surface and there are fasteners. The effect of this difference in modeling is minor: The buckling load factors from the model with fasteners are from one to two per cent lower than those without fasteners.

The general buckling load factor, 1.0511, for the "no fasteners" model, corresponds to the 19th eigenvalue. This general buckling mode has three circumferential waves. The general buckling load factor, 1.04201, for the

"fasteners" model, also corresponds to the 19th eigenvalue for that model and also has three circumferential waves.

The buckling mode corresponding to the lowest eigenvalue, 1.022198E+00, is shown in Fig. 6 and the buckling mode for the lowest eigenvalue corresponding to long-wavelength general instability, 1.051100E+00, is shown in Fig. 7. Both of these modes are for the STAGS model with no fasteners. The modes for the STAGS model with fasteners, corresponding to the first eigenvalue, 1.008428, and to the 19th eigenvalue, 1.042010, are essentially the same.

All of the other eigenvalues correspond approximately to "inter-ring" buckling modes similar to that in Fig. 6. In these relatively short wavelength buckling modes the axes of the stringers deform and the rings primarily twist. However, for most of the rings the axes of the rings also deform, as shown in Fig. 8. Figure 8 is produced by elimination of all the shell units except the two shell units that correspond to the web and outstanding flange of the fourth ring from the left end of the model shown in Fig. 6. In Fig. 8 the buckling modal deformations for the same mode (Mode No. 1) as that shown in Fig. 6 are plotted to the same scale as is shown in Fig. 6. Because there is significant bending in the plane of this and in the planes of the other rings, these "inter-ring" modes may also be considered to have significant components of general buckling: a short-wavelength general buckling mode similar in type to that shown in Figs. 21, 26, 27, 29 of the paper, "Additional buckling solutions in PANDA2" [1].

For a complete (360 degrees) cylindrical shell the converged eigenvalues (buckling load factors) occur in pairs. This is typical in STAGS models of complete (360-degree) cylindrical shells. The buckling mode corresponding to each eigenvalue in a pair is the same except that one mode in the pair is rotated around the shell circumference relative to the other.

RESULTS FROM STAGS MODELS OF THE COMPLETE CYLINDRICAL SHELL WITH ALL STIFFENERS (MAJOR AND SUB) SMEARED

STAGS produces the results listed in Table 11. The critical buckling mode is shown in Fig. 9 and the buckling mode corresponding to the third eigenvalue, 1.371375, is shown in Figs. 10 and 11. The axisymmetric buckling load factor, 1.371375, is not far above the critical buckling load factor, 1.288339, which corresponds to a general buckling mode with three circumferential waves, essentially the same buckling mode as that shown in Fig. 7.

A similar STAGS model was run with use of the "410" finite element rather than the "480" finite element. For that model, the same nodal point density leads to a prediction of general buckling at a load factor (eigenvalue) of 1.340773, reasonably close to the 1.288339 obtained from the model with use of the 480 finite element. The order of the n=2 and n=0 modes is reversed compared to that for the model in which the STAGS "480" finite element was used (Table 11).

Although the critical general buckling mode according to STAGS has long wavelengths (one halfwave in the axial direction and three full waves over the entire circumference), a model in which all stiffeners are smeared produces a prediction that is unacceptably unconservative (Table 11). Compare the STAGS buckling load factor, 1.288339, from the smeared stiffener model with the STAGS buckling load factor from the model in which the sub stiffeners are smeared but the major stiffeners are modelled as shell units and fasteners are included: lowest eigenvalue = 1.04201. The model in which all stiffeners are smeared is unconservative by about 24 per cent.

With use of the "410" finite element rather than the "480" finite element in the STAGS model, the unconservativeness of the smeared model: general buckling load factors = 1.340773E+00 vs 1.042010E+00, is even more pronounced. The conclusion is that even though the general buckling mode in Fig. 7 appears to be smooth, it does not seem to be good practice to smear the major stiffeners for optimized shells. Models with smeared stiffeners may well lead to unacceptably unconservative designs.

COMMENTS ON DIFFERENCES IN BUCKLING MODES FROM STAGS AND PANDA2 FOR THE PERFECT SHELL

STAGS is a general-purpose finite element program. Therefore, the buckling modes obtained from STAGS do not necessarily have to fall into a classification such as "general" or "inter-ring" or "local" or "stiffener rolling without participation of the panel skin", etc. For example, a buckling mode from STAGS may be a combination of "general" and "inter-ring". The buckling load factors listed in Table 10 correspond to buckling modes of this "mixed" type. Also, the buckling mode shown in Figs. 6 and 8 is a mixture of general and inter-ring buckling.

What may be termed a "general buckling" mode from STAGS for descriptive purposes is not always a "pure" general buckling mode. The AIAA Paper 2002-1408 [1] shows examples of "pure" and "not so pure" general buckling modes. Figure 25 of that paper shows a "pure" general buckling mode; Figure 24 shows a "somewhat impure" general buckling mode; and Figure 23 shows a "very impure" general buckling mode. The "impure" general buckling modes have differing degrees of short-wavelength deformation superposed on what is basically a general buckling mode. (Incidentally, Figures 20-22 of AIAA Paper 2002-1408 show an "inter-ring" buckling mode similar in nature to the "inter-ring" modes in the present case; there is considerable deformation of at least one ring in its plane, as displayed in Fig. 22 of that paper, making the mode a combination of "inter-ring" buckling and "general buckling".)

The classifications of "general", "inter-ring", "local", etc. ARE meaningful in the PANDA2 "universe", however. PANDA2 arrives at reasonable optimum designs with reasonable computer execution times through the use of many different simplified models for the prediction of buckling and stress. In applying PANDA2, one expects that the appropriate combination of these simplified models will lead to reliable preliminary optimum designs that are not too conservative and for which all the "holes have been plugged", that is, there are not any critical modes of failure that have been overlooked. Over the many years that PANDA2 has been evolving, many such "holes" have been discovered and eliminated. (See the file, ..panda2/doc/panda2.news [1]).

Table 600.30 in [1b] lists results from PANDA2 computations for the types of buckling that are seen to occur in the STAGS models of the complete (360-degree) cylindrical shell to which the results shown in Figs. 6-11 correspond. Results from ten different buckling models are listed there, including three models of inter-ring buckling, two models of general buckling, and five models of stiffener buckling. Several comments, "<--NOTE...", and several paragraphs of comments have been added to the standard PANDA2 output listed in Table 600.30 in [1b] in order to help give the reader a physical "feel" for what is going on. The information given in that table, which is too long to include in this paper, should be absorbed by any researcher interested in using PANDA2 and interested in understanding how it tries to solve difficult shell problems reasonably accurately through the use of many different approximate models. (NOTE: panda2.news ITEM No. 600 was written during February and early March, 2005. Since then there have been many changes in PANDA2, documented in panda2.news items 601 – 621. This paper has been updated accordingly. However, panda2.news ITEM No. 600 was not updated. Therefore some of the results listed there are not what one would obtain currently. The overall conclusions and the basic philosophy and approach to solving the various buckling problems remains unchanged. Therefore panda2.news ITEM No. 600 remains a useful teaching tool.

The critical STAGS buckling mode for short-wavelength "general" buckling is shown in Fig. 6 and the critical STAGS buckling mode for long-wavelength general buckling is shown in Fig. 7. As seen from Fig. 8 the short-wavelength "general" buckling mode has five circumferential waves around the 360-degree circumference of the cylindrical shell. The long-wavelength general buckling mode has three circumferential waves.

PANDA2 uses two models for general instability, to which the following two margins, taken from Table 9, correspond:

14 -3.66E-02 buck.(SAND);simp-support general buck;M=6;N=0;slope=0.473;FS=0.999
15 6.26E-04 buck.(SAND);simp-support general buck;(0.85*altsol);FS=0.999

The first margin, Margin No. 14, is computed from the closed-form PANDA-type model [41]. In that model all

stiffeners are smeared out and transverse shear deformation (t.s.d.) is neglected. PANDA2 makes an elaborate search over (m,n,slope) = (MWAVEX,NWAVEX,SLOPEX) space for the critical (lowest) buckling load factor, EIGMNC, in which MWAVEX = number of axial halfwaves over the entire shell, NWAVEX = number of circumferential halfwaves over 180 degrees of circumference (the "width" of the panel = $\pi \times r$), and SLOPEX = the slope of the buckling nodal lines, non-zero in this case because of the presence of in-plane shear loading, $N_{xy} = 20000$ lb. The search over (m,n,slope) space must be thorough because there often are multiple minima of buckling load factor vs (m,n,slope). The following lines are typical PANDA2 output giving the results of this thorough search:

```
EIGMNC= 1.52E+00 1.52E+00 1.69E+00 1.93E+00 1.69E+00 1.52E+00 1.48E+00
SLOPEX= 6.81E-01 6.81E-01 1.00E-02 1.32E-01 0.00E+00 6.81E-01 4.73E-01
MWAVEX= 1 1 7 6 7 1 6
NWAVEX= 3 3 2 4 2 3 0
```

In this particular case there are at least four minima in (m,n,slope) space, corresponding to (m,n) = (1,3), (7,2), (6,4), and (6,0) and various nodal line slopes. [Question: Why do we write, "at least four minima", instead of, "four minima"? Answer: For given (m,n) there are often two minima over the practical range of nodal line slope]. PANDA2 chooses the smallest EIGMNC as the critical buckling load factor and mode shape for general buckling from the closed-form PANDA-type theory [41].

Notice that in this particular case the general buckling load factors corresponding to the buckling modes (m,n,slope) = (1,3,0.681) and (6,0,0.473) are fairly close: 1.52 and 1.48, respectively. The (1,3,0.681) buckling mode is similar to the STAGS mode from the smeared stiffener model shown in Fig. 9. The (6,0,0.473) buckling mode is similar to the STAGS mode from the smeared stiffener model shown in Figs. 10 and 11 (axisymmetric mode).

PANDA2 "knocks down" the most critical buckling load factor from PANDA-type theory as follows:

```
Buckling load factor before t.s.d.= 1.4820E+00 After t.s.d.= 1.4019E+00
Buckling load factor BEFORE knockdown for smeared stringers= 1.4019E+00
Buckling load factor AFTER knockdown for smeared stringers = 1.3147E+00
```

General buckling load factor before and after knockdown:

```
EIGGEN(before modification by 2 factors below) = 1.3147E+00
Knockdown factor from modal imperfection(s) = 9.4144E-01
Knockdown factor for smearing rings on cyl. Shell = 7.7761E-01
```

```
Final buckling load factor from closed-form PANDA theory = 9.6249E-01
```

Note that there is a knockdown factor for modal imperfection(s) even though in this particular example the shell is perfect. Why? Because the ratio, (ARBOCZ/PANDA2) is equal to 0.94144. The ratio, (ARBOCZ/PANDA2) is the ratio of buckling loads from ARBOCZ theory [13] to PANDA-type (closed form) theory [41] for general buckling of a perfect cylindrical shell.

After knockdown, EIGENVALUE = 9.6249E-01. This buckling load factor should be compared to those predicted from STAGS, given in Fig. 6 (pcr = 1.0222) and Fig. 7 (pcr = 1.0511). The EIGENVALUE, 9.6249E-01, is the buckling load factor from which Margin No. 14 in Table 9 is derived:

$$\text{margin} = (\text{buckling load factor})/(\text{factor of safety}) - 1.0 \\ = 0.96249/0.999 - 1.0 = -3.66E-02.$$

The most critical general buckling mode from PANDA2 probably would have corresponded to the (m,n) = (1,3) mode if the knockdown factor for smearing rings, which depends on the number of circumferential waves in the buckling mode, had been applied before PANDA2 decided which mode was the most critical. Then the long-wavelength general buckling mode shape from STAGS (Fig. 7) would have agreed with that from PANDA2. However, this is not the way PANDA2 works, and it is not feasible to change the order of computations in PANDA2.

The other model of general instability in PANDA2 is the so-called "alternative buckling theory" in which the buckling load factor is computed from a double trigonometric series expansion of the buckling modal displacements over a "patch" of the cylindrical shell [1]. This is the theory from which Margin No. 15 in Table 9 is computed. The mode shape corresponding to the buckling load factor derived from this alternative buckling theory resembles an inter-ring buckling mode, although there are components of buckling modal displacements that give rise to some in-plane bending of the rings. In the alternative theory model for general buckling the substiffeners are smeared.

The short-wavelength STAGS buckling mode shown in Figs. 6 and 8 seems to be a combination of inter-ring buckling of the type covered by PANDA2 in Margin No. 4 of Table 9,

4 1.03E-02 Inter-ring buckling, discrete model, $n=6$ circ.halfwaves;FS=0.999

and general buckling from the alternative theory covered by Margin No. 15 of Table 9,

15 6.26E-04 buck.(SAND);simp-support general buck;(0.85*altsol);FS=0.999

Thus, by the use of several approximate models that cover the same or similar buckling phenomena, PANDA2 produces margins that guide the design toward an optimum similar to one that might be produced by STAGS if STAGS were used in an optimization context.

STAGS MODEL FOR LOCAL BUCKLING

It is best to determine local buckling behavior from a rather small "patch". In this case the STAGS "patch" includes only one bay between major rings, with a major ring at each end of the "patch", and three bays between major stringers, with a major stringer running along each straight edge (generator) of the "patch". Hence, the "patch" is 37.5 inches long in the axial direction and 43.836 inches long in the circumferential direction. The major stiffeners that run along the four boundaries of the "patch" have half the stiffnesses of those that lie within the "patch". As mentioned previously, all of the substiffeners lie within the "patch". Figures 1, 12, 13, and 14 show the STAGS "patch" model suitable for a local buckling survey. The STAGS 480 finite element is used, the reference surface is the middle surface of the panel skin, and there are fasteners connecting this reference surface to the roots of all of the stiffeners. The fasteners are seen as tiny black dots at the stiffener roots shown in Figs. 1, 12, 13, and 14.

The purpose of the STAGS model with use of a small "patch" is to compare predictions with the various models that PANDA2 uses for the many types of buckling that can be classified as "local" in this case. The buckling margins from Subcase 1 in Table 9 that seem to apply best in this context are as follows:

1 1.24E-01 Local buckling from discrete model-1, $M=2$ axial halfwaves;FS=0.99
2 3.38E-01 Bending-torsion buckling; $M=2$;FS=0.999
3 4.50E-01 ($m=2$ lateral-torsional buckling load factor)/(FS)-1;FS=0.999
7 1.45E+00 buckling margin stringer Iseg.3 . Local halfwaves=8 .MID.;FS=1.
8 -3.99E-03 buckling margin stringer Iseg.4 . Local halfwaves=8 .MID.;FS=1.
9 4.64E-01 buckling stringer Isegs.3+4 together. $M=9$; $C=0.$;MID.;FS=1.4
10 7.63E-02 buckling stringer Iseg 4 as beam on foundation. $M=198$;MID.;FS=3.
11 1.43E+01 buckling ring Iseg 4 as beam on foundation. $M=140$;MID.;FS=3.
12 2.95E-01 buck.(SAND);simp-support smearsbstf; (0.95*altsol);FS=0.999
13 -3.76E-03 buck.(SAND);simp-support inter-ring; (1.00*altsol);FS=0.999
17 -2.58E-02 buck.(SAND);rolling only of stringers; $M=14$; $N=0$;slope=0.;FS=1.6
18 7.89E-01 buck.(SAND);hiwave roll. of stringers; $M=84$; $N=0$;slope=0.;FS=1.2
19 1.43E+00 buck.(SAND); STRINGERS: web buckling; $M=9$; $N=1$;slope=0.;FS=1.
20 1.51E+01 buck.(SAND); RINGS: web buckling; $M=2$; $N=1$;slope=0.;FS=1.
21 4.86E-01 buck.(SAND);rolling with skin buckl.; $M=1$; $N=1$;slope=0.1978;FS=0.999
22 6.44E-03 buckling:simp-support of substring. $M=1$;FS=1.
23 1.41E+01 buckling:simp-support of subbrings $N=1$;FS=1.
24 -4.18E-02 buckling:simp-support altsoln4 intermajorpatch; FS=0.999

25 3.18E-01 buckling:simp-support altsoln5 skin+edgsubroll; FS=0.999
 26 1.21E-01 buck.(SAND);rolling with smear substr;M=1;N=2;slope=20.;FS=0.999
 27 1.16E-02 buckling:simp-support altsoln6 inter-subring ; FS=0.999

Many buckling modes were generated via five STAGS runs, each successive run made with use of a slightly higher eigenvalue "shift" in the STAGS input file, testax4p.bin. Table 600.32 of [1b] lists the abridged testax4p.out2 files from each of the five STAGS executions. Figure 1 shows the buckling mode and eigenvalue (buckling load factor) corresponding to the critical (lowest) buckling load, 0.98903. Figures 12 - 14 show selected higher buckling modes, modes that display especially well some of the idealized buckling modes of the type computed by PANDA2 and listed above and in Table 9.

DESCRIPTION OF PANDA2 MODELS OF VARIOUS MODES OF LOCAL BUCKLING

Table 600.33 in [1b] is analogous to Table 600.30 in [1b]. Table 600.33 in [1b] lists output from PANDA2 corresponding to thirteen models of local buckling that PANDA2 includes as design constraints. The local buckling modes from STAGS listed in Table 600.32 of [1b] are combinations of the simplified buckling models listed in Table 600.33 of [1b]. This table is too long to include here. As with Table 600.30 in [1b] its information should be absorbed by researchers interested in using PANDA2.

Figures 1 and 12 - 14 show selected buckling modes from the STAGS "patch" model. Figure 1 shows buckling of the panel skin and substiffeners together with some deformation of the major stringers, a mode covered by PANDA2 margins 1 and 24. Figure 12 shows mainly buckling between subrings with subring rolling and substringers participating in the buckling mode. This type of buckling is covered by PANDA2 margins 26 and 27. Figure 13 shows mainly rolling of the stringers, a mode covered by PANDA2 Margin No. 17. Figure 14 displays a combination of local buckling modes covered by PANDA2 margins 21, 22, and 25.

OPTIMUM DESIGN INCLUDING INITIAL BUCKLING MODAL IMPERFECTION

A general buckling modal imperfection with amplitude Wimp_{g2} equal to 1.0 inch is assumed. The case is the same as before except it is called "testax4" instead of "testax4p" (the "p" in testax4p is for "perfect").

The testax4.BEG and testax4.DEC files, listed in [1b], are the same as those for testax4p. The new testax4.OPT file is listed in Table 600.35 of [1b]. There are two load cases, the first with a positive general buckling modal imperfection (+1.0 inch) and the second with a negative general buckling modal imperfection (-1.0 inch). The optimum design is listed in Column 4 of Table 3. This optimum design was obtained via the runstream listed in Table 4.

In order to obtain a new (close) optimum design that is suitable for analysis by STAGS, we must ensure that there are integral numbers of equally spaced major stiffeners over the entire shell and integral numbers of equally spaced substiffeners between adjacent major stiffeners, just as we did with the perfect shell (testax4p). The final optimum design suitable for analysis by STAGS is listed in the third column of Table 8. As before, this optimum design is obtained with the use of two load cases: the first with an initial general buckling modal imperfection with amplitude Wimp_{g2} = +1.0 inch and the second with imperfection amplitude Wimp_{g2} = -1.0 inch. The margins corresponding to Load Case 1, Subcase 1 are listed in Table 12.

In the STAGS runs the imperfection is not present. If we wish to compare the behavior of the newly optimized shell with the imperfection neglected, we must execute PANDAOPT again for the same design, this time with the imperfection amplitude set equal to zero. This was done and the new margins for Load Case 1, Subcase 1 are listed in Table 13.

PANDA2 generates two estimates of general buckling, one from a PANDA-type (closed form) theory (Margin No. 16 in Load Set 1, Subcase 1 in Table 12 and Margin No. 14 in Load Set 1, Subcase 1 in Table 13) and the other from the alternative, double trigonometric series expansion, theory (Margin No. 17 in Load Set 1, Subcase 1 in Table 12 and Margin No. 15 in Load Set 1, Subcase 1 in Table 13). These margins are given by

a. Including the initial general buckling modal imperfection (Table 12, Wimp=1.0 inch):

16 -1.35E-02 buck.(SAND);simp-support general buck;M=1;N=2;slope=25.;FS=0.999
 17 4.01E-02 buck.(SAND);simp-support general buck;(0.85*altsol);FS=0.999

b. Neglecting the initial buckling modal imperfection (Table 13, Wimp=0.0):

14 1.96E-01 buck.(SAND);simp-support general buck;M=1;N=2;slope=25.;FS=0.999
 15 4.78E-01 buck.(SAND);simp-support general buck;(0.85*altsol);FS=0.999

Note that the initial general buckling modal imperfection has a much smaller influence on the buckling margin derived from the PANDA-type (closed form) theory (Margin 16 with the imperfection and Margin 14 without the imperfection) than on the buckling margin derived from the alternative (double trig series expansion) theory (Margin 17 with the imperfection and Margin 15 without the imperfection). This difference in behavior is explained in Table 600.42 in [1b]. In the PANDA-type (closed form) model the redistribution of stress from stiffeners to skin during prebuckling bending of the imperfect shell has no influence on the predicted buckling load or mode because all stiffeners are smeared out in the PANDA-type model. Hence, this simplified theory makes use only of the overall applied stress resultants which are the same whether there is or is not an initial imperfection. In the alternative theory, in which the major stiffeners are treated as discrete beams and only the substiffeners are smeared out, the redistribution of stress from major stiffeners to skin-with-smeared-substiffeners during prebuckling bending of the imperfect shell does have an influence on the predicted buckling load and mode shape. This influence is apparent from the output from PANDA2 listed in Table 600.42 in [1b] and from a comparison of Margin No. 17 with Margin No. 15 listed just above.

RESULTS FROM STAGS FOR THE CASE testax4 WITH IMPERFECTION ABSENT

The STAGS model includes the entire shell. The major stiffeners are treated as shell units, the substiffeners are smeared, and the STAGS "480" finite element is used. The outer surface of the panel skin is the reference surface and there are no fasteners connecting this reference surface to the roots of the major stiffener webs.

Figure 15 shows the general instability buckling mode from the STAGS model with only the substiffeners smeared, and Fig. 16 shows the same mode with all stiffeners (major and sub) smeared. Note that smearing the major stiffeners raises the buckling load factor from 1.4468 to 1.8058, about 25 per cent. Even though the critical general buckling mode is smooth and has long wavelengths a model in which the major stiffeners are smeared yields an unacceptably unconservative prediction for general buckling.

With neglect of the initial general buckling modal imperfection, PANDA2 obtains the following general buckling margin (from Table 13):

14 1.96E-01 buck.(SAND);simp-support general buck;M=1;N=2;slope=20.;FS=0.999
 (buckling load factor = (buckling margin + 1.0)*(factor of safety, FS).
 buckling load factor = (0.196 + 1.0)*(0.999) = 1.1948)

The PANDA2 prediction is about 17 per cent conservative compared to the STAGS prediction, and PANDA2 predicts buckling with two rather than three circumferential waves. The PANDA2 buckling load factor for general buckling is computed as follows:

```
-----
EIGMNC= 2.07E+00 2.07E+00 2.10E+00 3.91E+00 2.10E+00 2.07E+00 1.00E+17
SLOPEX= 4.00E-02 4.00E-02 0.00E+00 1.32E-01 0.00E+00 4.00E-02 2.31E+00
MWAVEX= 1      1      1      6      1      1      1
NWAVEX= 2      2      2      5      2      2      0
```

Buckling load factor before t.s.d.= 2.0713E+00 After t.s.d.= 1.9586E+00
 Buckling load factor BEFORE knockdown for smeared stringers= 1.9586E+00
 Buckling load factor AFTER knockdown for smeared stringers= 1.8367E+00

General buckling load factor before and after knockdown:
 EIGGEN(before modification by 2 factors below) = 1.8367E+00
 Knockdown factor from modal imperfection(s) = 8.9150E-01
 Knockdown factor for smearing rings on cyl. shell = 7.2989E-01

14 1.19515E+00 buckling load factor simp-support general buck;M=1;N=2;slope=20.

A second STAGS model includes three major ring bays and nine major stringer bays for the case called testax4. All the stiffeners, major as well as sub, are treated as shell units, there are fasteners, and the STAGS "480" finite element is used. This is the same type of model as that used for the optimized perfect shell and shown in Fig. 3.

Figure 17 shows the second buckling mode from the STAGS 3 x 9 bay "patch" model. The second mode rather than the first is shown because the modal deformations show up better in the plot. (The first two eigenvalues are practically identical).

A third STAGS model includes one major ring bay and three major stringer bays for the case called testax4. All the stiffeners, major as well as sub, are treated as shell units, there are fasteners, and the STAGS "480" finite element is used. This is the same type of model as that used for the optimized perfect shell and shown in Figs. 1 and 12-14.

Figures 18 and 19 show buckling modes from the STAGS 1 x 3 bay "patch". The buckling mode corresponding to the lowest eigenvalue, 1.2757, is displayed in Fig. 18, and the buckling mode corresponding to the third eigenvalue, 1.3099, is displayed in Fig. 19.

Figure 18 is a combination of the PANDA2 modes from Table 13,

2 2.21E-01 Long-axial-wave bending-torsion buckling; M=2 ;FS=0.999
 17 7.94E-02 buck.(SAND);rolling only of stringers;M=12;N=0;slope=0.;FS=1.6

and Fig. 19 is a combination of the PANDA2 modes from Table 13,

8 1.35E-01 buckling margin stringer Iseg.4 . Local halfwaves=8 .MID.;FS=1.
 9 7.26E-01 buckling stringer Isegs.3+4 together.M=8 ;C=0. ;MID.;FS=1.4
 12 2.71E-01 buck.(SAND);simp-support smearsustf; (0.95*altsol);FS=0.999
 13 7.45E-02 buck.(SAND);simp-support inter-ring; (1.00*altsol);FS=0.999
 22 3.87E-02 buckling:simp-support of substrng.M=1;FS=1.
 24 1.94E-01 buckling:simp-support altsoln4 intermajorpatch; FS=0.999
 26 6.03E-01 buck.(SAND);rolling with smear substr;M=1;N=1;slope=14.29;FS=0.999
 27 5.63E-01 buckling:simp-support altsoln6 inter-subring ; FS=0.999
 25 4.39E-01 buckling:simp-support altsoln5 skin+edgsubroll; FS=0.999
 27 3.49E-01 buckling:simp-support altsoln6 inter-subring ; FS=0.999

RESULTS FOR A SIMILAR STIFFENED SHELL WITHOUT SUBSTIFFENERS

The name of the case for the externally T-stiffened cylindrical shell with the same overall dimensions (Table 1) but without any substiffeners is "testax3". It is of interest to optimize this shell and to compare the optimized weights of perfect and imperfect shells without substiffeners with the optimized weights of perfect and imperfect shells with substiffeners.

There are two inequality conditions in testax3.DEC (Table 600.51 in [1b] not present in the preceeding cases, testax4p and testax4, in which substiffeners are present. The first of these two new inequality constraints requires that the width of the flange of the T-ring be less than the ring spacing. The second new inequality constraint requires that the spacing of the T-stringers be less than five times the spacing of the T-rings. After several preliminary optimizations it became clear that these two additional inequality conditions were required for the following reasons:

1. to prevent impossible designs in which the rings become so closely spaced or their outstanding flanges so wide that the outstanding flanges overlap.

2. to prevent "bombs" from SUPEROPT caused by a requirement that for an IQUICK = 0 type of analysis the stringers must be closer together than a distance equal to five times the ring spacing. This condition is built into PANDA2; the user has no choice. When it is violated SUPEROPT bombs because PANDA2 demands a change of model from IQUICK = 0 to IQUICK = 1 and then exits from the mainprocessor, not completing the rest of the SUPEROPT run.

The difficulties leading to the need for these two new inequality constraints arise because, without any substiffeners present, optimum designs tend to correspond to configurations in which the T-shaped stiffeners are close together.

The optimum design of the perfect shell is listed in the fifth column of Table 3. This optimum results from the runstream listed in Table 4. The fourth column of Table 8 lists the optimum design of the perfect shell without substiffeners that is suitable for analysis by STAGS (integral numbers of equally spaced stringers and rings over the entire shell). The corresponding margins for Load case 1, Subcase 1 are listed in Table 14.

COMPARISON OF THE OPTIMIZED DESIGNS OF THE PERFECT SHELLS WITH AND WITHOUT SUBSTIFFENERS

The weights of the optimized perfect shells with and without substiffeners are listed in columns 3 and 5, respectively, of Table 3. It is disappointing that the difference in optimized weights of the perfect cylindrical shells with and without substiffeners is insignificant. For the optimized perfect cylindrical shell with substiffeners the weight of the shell skin plus the weight of the substiffeners is close to the weight of the shell skin in the optimized cylindrical shell without substiffeners. The weights of the major stringers and the weights of the major rings are approximately the same in the two cases. It is not worthwhile including substiffeners just to save weight.

However, substiffeners may be considered if it is important that the number of major stringers be minimized. The spacing of the major stringers in the optimized cylindrical shell with substiffeners is given in Table 3 by $B(\text{STR}) = 14.775$ inches. In contrast, the spacing of the stringers in the optimized cylindrical shell without substiffeners is $B(\text{STR}) = 5.2141$ inches.

There is a somewhat less dramatic effect on the spacing of the major rings:

39.157 B(RNG):major ring spacing perfect shell WITH substiffeners
22.208 B(RNG):major ring spacing perfect shell WITHOUT substiffeners.

Optimized designs of the perfect, externally T-stiffened cylindrical shells with and without substiffeners were determined for a range of spacing of the major stringers. The results are shown in Fig. 20, generated via a plotting routine "plots" written by W. D. Bushnell [1]. From Fig. 20 one can see that the weight of the optimized cylindrical shells without substiffeners is much more sensitive to spacing of the major stringers than is the case for the optimized cylindrical shells with substiffeners. This seems to be the only advantage of adding substiffeners of rectangular cross section to the panel skin.

Other loadings, such as external hydrostatic compression ($N_x = p \cdot r/2$; $N_y = p \cdot r$) and load combinations with more in-plane shear N_{xy} , were investigated with the same conclusion: there is very little if any advantage of adding substiffeners of rectangular cross section in order to decrease minimum weight as long as the stringer spacing is permitted to vary widely during optimization cycles. Also, the advantage of adding substiffeners of rectangular cross section disappears if stresses become critical.

Different conclusions might be drawn if the substiffeners have other than rectangular cross section. PANDA2 is not yet capable of handling substiffeners with non-rectangular cross sections. Also, it may be that adding substiffeners to other parts of the structure than the panel skin would be advantageous. Perhaps lighter-weight shells could be made if substiffeners were added to webs and outstanding flanges of the major stiffeners. There are no plans at this time to expand PANDA2's capability to handle any of these new geometries.

RESULTS FROM STAGS FOR THE OPTIMIZED PERFECT SHELL WITHOUT SUBSTIFFENERS

The fourth column of Table 8 lists the optimum design of the perfect shell without substiffeners that is suitable for analysis by STAGS (integral numbers of equally spaced stringers and rings over the entire shell). The corresponding margins for Load case 1, Subcase 1 are listed in Table 14.

The PANDA2 processor STAGSUNIT was used to generate a STAGS model corresponds to a "patch" that includes three ring bays and nine stringer bays. The middle surface of the panel skin is the reference surface and there are fasteners that connect the roots of the stiffener webs to this reference surface (tiny black dots in Fig. 21). The critical buckling mode for the "patch" is displayed in Fig. 21. This mode is similar in character to the buckling modes shown for a similar "patch" of the optimized perfect shell with substiffeners in Figs. 3-5.

An endview plot of the same buckling mode appears in Fig. 22, which shows clearly that there are five circumferential halfwaves in the nine-stringer-bay "patch". This patch spans 47.124 inches of shell circumference [$9 \times (B(STR)=5.236 \text{ in Col. 4 of Table 8}) = 47.124 \text{ inches}$]. The 47.124-inch-wide "patch" represents 1/13.333th of the 360-degree shell circumference. Hence, the same buckling pattern over the entire circumference would have 66.667 half waves over 360 degrees or about 33 halfwaves over 180 degrees. This mode is in very good agreement with that predicted by PANDA2 for inter-ring buckling from the PANDA-type (closed form) analysis (PANDA2 buckling mode type 5 listed in Table 14):

5 1.57E-01 Inter-ring buckling, discrete model, n=32 circ.halfwaves;FS=0.999

STAGSUNIT was used to generate a STAGS model of the optimized, perfect, complete cylindrical shell. The T-shaped stringers and T-shaped rings are modeled as shell units, and the STAGS "480" finite element is used. The outer surface of the shell skin is used as the reference surface and there are no fasteners. At the optimum design of the perfect shell the T-shaped stringers are very closely spaced; there are 120 of them over the entire (360-degree) circumference. There are 15 T-rings over the 300-inch length of the cylindrical shell. Since each T-shaped stringer consists of two shell units and each T-shaped ring consists of two shell units, there are $1 + (2 \times 120) + (2 \times 15) = 271$ shell units in this very large STAGS model. This STAGS model has about 580000 degrees of freedom.

The STAGS model predicts general buckling in a mode with three circumferential waves at a load factor of 1.060638. This general buckling mode corresponds to the 25th eigenvalue. Figure 23 shows the general buckling mode from STAGS. All the other eigenvalues correspond to inter-ring buckling in which the stringers bend. The lowest eigenvalue (buckling load factor) is 1.0512. The corresponding buckling mode is displayed in Fig. 24. It was difficult to find the one general buckling mode hidden like a needle in a haystack among a thicket of short-wavelength buckling modes of the type shown in Fig. 24. (See ACKNOWLEDGMENTS).

With the stringers and rings smeared out and with use of the 480 finite element, the lowest eigenvalue corresponds to general buckling at a load factor of 1.170279, an increase of about 10 per cent over that for the more accurate model: 1.060638. The general buckling mode is the same as that found for the STAGS model in which all stiffener parts were modelled as shell units. With use of the 410 finite element in the smeared stiffener model the lowest eigenvalue increases from that computed with use of the 480 element, eigenvalue=1.170279, to eigenvalue=1.194869.

Note that for this shell without substiffeners, in which the T-shaped stringers and T-shaped rings are more closely spaced than is the case for the optimized shell with substringers, the degree of unconservativeness caused by smearing the major stiffeners is significantly less than for the optimized shell with substringers. In those cases (testax4p for the perfect shell and testax4 for the imperfect shell) smearing the major stiffeners raises the buckling load factor for general instability from 1.0511 to 1.2883 for the optimized PERFECT shell with substiffeners and from 1.4468 to 1.8058 for the optimized IMPERFECT shell with substiffeners.

Notice in Table 14 that the margin corresponding to general buckling from the closed-form PANDA-type theory [41],

13 -3.53E-02 buck.(SAND);simp-support general buck;M=8;N=0;slope=0.335;FS=0.999

shows that the critical buckling mode from PANDA2 has $(m,n) = (MWAVEX,NWAVEX) = (8,0)$ halfwaves in the (axial, circumferential) directions. This is similar to the critical general buckling mode from PANDA2 discussed at some length for the optimized perfect shell with substiffeners. In that case PANDA2 predicts the critical $(m,n) = (6,0)$. As with the optimized shell with substiffeners, in the present case the critical long-wavelength general buckling mode predicted by STAGS for the shell without substiffeners, shown in Fig. 23, is very different from that predicted by PANDA2. According to STAGS the critical long-wavelength buckling mode has one axial halfwave and three circumferential waves.

For the optimized perfect shell without substiffeners PANDA2 yields the following results from the exhaustive search over $(m,n,slope) = (MWAVEX,NWAVEX,SLOPEX)$ space:

```
EIGMNC= 1.30E+00 1.30E+00 1.27E+00 1.54E+00 1.35E+00 1.30E+00 1.00E+17
SLOPEX= 2.77E+00 2.77E+00 3.35E-01 1.32E-01 0.00E+00 2.77E+00 0.00E+00
MWAVEX= 1      1      8      8      9      1      0
NWAVEX= 3      3      0      4      1      3      0
```

Notice that the buckling load factors, EIGMNC for $(m,n,slope) = (1,3,2.77)$ and $(8,0,0.335)$ are close: EIGMNC = 1.30 and 1.27, respectively. As mentioned in this context previously, if the knockdown factor for smearing rings had been applied before PANDA2 chooses which mode is critical, PANDA2's prediction of buckling mode shape probably would have agreed with that from STAGS. What is important in this computation of buckling is not the buckling mode shapes but the buckling load factors. They are what control the evolution of the design of the perfect shell during optimization cycles.

RESULTS FOR THE OPTIMIZED IMPERFECT SHELL WITHOUT SUBSTIFFENERS

The optimum design resulting from the runstream listed in Table 4 is listed in the last column in Table 3. The optimum design suitable for analysis by STAGS is listed in the last column in Table 8. As with the imperfect shells with substiffeners, the optimum designs without substiffeners were obtained with application of two load cases:

1. Load Case 1: general buckling modal imperfection amplitude, Wimp_{g2} = +1.0 inch,
2. Load Case 2: general buckling modal imperfection amplitude, Wimp_{g2} = -1.0 inch.

The margins corresponding to the optimized design suitable for analysis by STAGS are listed in Tables 15 and 16.

COMPARISON OF OPTIMUM DESIGNS OF IMPERFECT EXTERNALLY T-STIFFENED CYLINDRICAL SHELLS WITH AND WITHOUT SUBSTIFFENERS

As is the case for the perfect optimized shells with substiffeners, a comparison of the optimum weights of the imperfect shells with and without substiffeners reveals that the weight saving by introduction of substiffeners is small (6.2 percent from Table 3 and 5.6 percent from Table 8). (Compare weights in columns 4 and 6 of Table 3 and columns 3 and 5 of Table 8).

As with the optimized perfect shells with and without substiffeners, the major stiffeners weigh about the same amount for the optimized imperfect shells with and without substiffeners. The panel skin for the optimized imperfect cylindrical shell without substiffeners weighs about 8.3 per cent more than the skin plus substiffeners of the optimized cylindrical shell with substiffeners.

The spacing of the major stringers in the optimized imperfect cylindrical shell with substiffeners is given in Table 3 as $B(\text{STR}) = 11.424$ inches. In contrast, the spacing of the major stringers in the optimized imperfect cylindrical shell without substiffeners is given by $B(\text{STR}) = 5.760$ inches. Hence, as with the perfect shells, the presence of substiffeners of rectangular cross section permits the major stringers to be spaced at much wider intervals around the cylindrical shell.

There is a much less dramatic effect on the spacing of the major rings:

42.874 B(RNG):major ring spacing, imperfect shell with substiffeners
28.291 B(RNG):major ring spacing, imperfect shell without substiffeners.

Probably the spacing of the major rings would be influenced more by the presence of substiffening for loading by hydrostatic compression, in which the hoop compression is twice the axial compression, in contrast to the cases explored here, in which the axial compression is five times the hoop compression.

RESULTS FROM STAGS FOR THE DESIGN LISTED IN COLUMN 5 OF TABLE 8 (testax3)

The linear buckling analysis by STAGS for a three-ring-bay by nine-stringer-bay "patch" of the optimized shell yields a buckling load factor of 1.3252 (initial imperfection not present in the STAGS model). With the amplitude of the general buckling modal imperfection set equal to zero, PANDA2 obtains the following margins (among other margins) for that design:

- 2 3.86E-01 Long-axial-wavw bending-torsion buckling; M=1; FS=0.999
- 4 4.53E-01 (m=1 lateral-torsional buckling load factor)/FS-1; FS=0.999
- 5 7.76E-01 Inter-ring buckling, discrete model, n=33 circ.halfwaves;FS=0.999
- 13 1.72E-01 buck.(SAND);simp-support inter-ring; (1.00*altsol);FS=0.999
- 17 1.44E-01 buck.(SAND);rolling only of stringers;M=12;N=0;slope=0.;FS=1.6

The circumferential width of the "patch" in the STAGS model is 51.8796 inches, which corresponds to 1/12.111th of the 360-degree circumference of the shell. The lowest buckling load factor from STAGS, 1.3252, is associated with a buckling mode that has five circumferential halfwaves over the 51.8796-inch width of the "patch". This mode translates into $5 \times 12.111/2 = 30$ full circumferential waves over the entire 360-degree circumference of the shell. This mode is in agreement with the buckling mode associated with the 5th margin in the PANDA2 model:

- 5 7.76E-01 Inter-ring buckling, discrete model, n=33 circ.halfwaves;FS=0.999

which has 33 circumferential halfwaves over 180 degrees of the circumference of the shell. The three buckling margins from PANDA2, Margins 2, 4, 5, 13, and 17, cover the type of buckling observed in the STAGS model.

PANELS WITH SUBSTIFFENERS THAT FORM AN ISOGRID

The "substiffener" capability in PANDA2 was extended to include panels with axial and circumferential major stiffeners and a skin that may be reinforced by substiffeners of rectangular cross section that form an isogrid pattern between adjacent major stringers and rings. Results from optimizations of perfect and imperfect cylindrical shells with external T-shaped stringers and external T-shaped rings and with external subisogrid stiffening are given in [1b]. Also presented in [1b] is the improvement to the theory for local buckling of the triangular piece of panel skin between adjacent isogrid or subisogrid members. The improved theory includes the contribution of the isogrid members to the total potential energy, provided that the cross section of the isogrid members is rectangular.

As with the cases involving axial and circumferential substiffeners, for the various loadings investigated it was found that there is no weight saving from introduction of subisogrid stiffening. The optimized weight of the perfect shell with an external subisogrid is 17392 lb, which is greater than the optimized weight of the perfect shell with no substiffeners (16846 lb) and greater than the optimized weight of the perfect shell with axial and circumferential substiffeners (16712 lb). The optimized weight of the imperfect shell with an external subisogrid is 21560 lb, which is less than the optimized weight of the imperfect shell without substiffeners (21620 lb) and greater than the optimized weight of the perfect shell with axial and circumferential substiffeners (20560 lb).

With subisogrid stiffening the optimum designs have major stiffeners spaced farther apart than for the optimum designs without any substiffeners, although the difference in spacing between the case with substiffeners and that without is less pronounced than for the cases involving axial and circumferential substiffeners.

OTHER SUBSTIFFENING CONFIGURATIONS

Cases involving substringers and subrings on opposite sides of the panel skin and involving internal substringers and internal subrings combined with external major T-shaped stringers and external T-shaped major rings were explored. Some results are presented in [1b], especially for the case of a perfect cylindrical shell with external major stringers and major rings and internal substringers and subrings. The optimized weight of this perfect cylindrical shell is 16612 lb, slightly less than the 16712 lb for the optimized weight of the perfect cylindrical shell with external substringers and subrings.

NONLINEAR COLLAPSE

In the paper, AIAA 2002-1408 [1], nonlinear collapse is computed for a ring and stringer stiffened cylindrical shell with general and local buckling modal imperfections. Figures 27 and 28 of that paper show the results from such an analysis. Collapse occurs because both the general and local imperfections grow as the load is increased. Unfortunately, it was not possible to perform a similar analysis in the effort leading to the present paper for the following reasons:

1. The entire shell must be included in the model because there are no planes of symmetry due to the presence of in-plane shear loading, $N_{xy} = 20000$ lb/in.
2. In the example of the optimized imperfect shell without substiffeners, the T-shaped stiffeners are so close together that a converged finite element model would contain too many degrees of freedom to capture the local component of collapse, which is seen as small dimples in Fig. 27 of AIAA Paper 2002-1408 [1]. It was barely possible to compute the general buckling mode from linear theory for a similar model (Fig. 23). A nonlinear collapse analysis requires far more computer resources. Also, as Fig. 24 demonstrates, the very large STAGS model is probably not large enough to capture accurately either inter-ring buckling or local buckling between adjacent stringers and rings.
3. In the example of the optimized imperfect shell with substiffeners one might well conduct a nonlinear collapse analysis in a model in which the substiffeners are smeared, such as that shown in Fig. 15. However, an analysis of this type would simply be a repeat of the type of study that produced Figs. 27 and 28 in AIAA Paper 2002-1408. It would not reveal the effect of prebuckling bending of the globally imperfect shell on the local buckling behavior of panel skin and substiffeners, such as that displayed in Figs 1, 12, and 14 of the present work. A model of the complete cylindrical shell that would capture the complex local behavior of shell skin and substiffeners would require far more degrees of freedom (d.o.f.) than the approximately 580000 d.o.f. model needed to predict the general buckling mode shown in Fig. 23.

CONCLUSIONS

Adding substiffeners of rectangular cross section between major stiffeners does not lead to significantly lower optimum weights. However, with substiffeners present the optimum weights correspond to configurations in which the major stiffeners are spaced farther apart than is the case for optimized cylindrical shells without substiffeners.

ACKNOWLEDGMENTS

The author (D. Bushnell) is most grateful for the help of Dr. Frank Weiler, a friend and colleague at Lockheed Martin in Palo Alto, California. Dr. Weiler frequently helped Bushnell whenever any problems arose in connection with executing STAGS on various computers at the Lockheed Martin Advanced Technology Center. Dr. Weiler ran and reran and reran and reran the 580000-degree-of-freedom STAGS model generated by the file listed in Table 600.62 of [1b] and shown in Figs 23 and 24. Several reruns at different "eigenvalue shifts" were required in order to capture the lowest general buckling mode, which was buried like a needle in a haystack among a thicket of local

buckling modes. Each run required about 40 minutes on the computer. (Dr. Weiler had to use a special computer with enhanced memory and disk capacities. That computer, a Pentium 4 desktop with two gigabytes of memory, was available to him only.) The author, David Bushnell, also very much appreciates the help of his son, Bill Bushnell, in obtaining proper formats for Tables 2 – 16.

REFERENCES

- [1] D. Bushnell, "PANDA2-Program for minimum weight design of stiffened, composite, locally buckled panels", *Computers and Structures*, Vol. 25 (1987) pp. 469-605. See also: "Optimization of composite, stiffened, imperfect panels under combined loads for service in the postbuckling regime", *Computer Methods in Applied Mechanics and Engineering*, Vol. 103, pp 43-114, 1993; "Recent enhancements to PANDA2" 37th AIAA SDM Conference, April 1996; "Approximate method for the optimum design of ring and stringer stiffened cylindrical panels and shells with local, inter-ring, and general buckling modal imperfections", *Computers and Structures*, Vol. 59, No. 3, 489-527, 1996; "Optimum design via PANDA2 of composite sandwich panels with honeycomb or foam cores", AIAA Paper 97-1142, AIAA 38th SDM Conference, April 1997; "Additional buckling solutions in PANDA2", AIAA 40th SDM Conference, p 302-345, April 1999; "Minimum-weight design of a stiffened panel via PANDA2 and evaluation of the optimized panel via STAGS", *Computers and Structures*, Vol. 50, 569-602 (1994); "Optimization of perfect and imperfect ring and stringer stiffened cylindrical shells with PANDA2 and evaluation of the optimum designs with STAGS", AIAA Paper 2002-1408, pp 1562-1613, Proceedings of the 43rd AIAA SDM Meeting, April, 2002;
- [1b] D. Bushnell, .../panda2/doc/panda2.news, a continually updated file distributed with PANDA2 that contains a log of all significant modifications to PANDA2 from 1987 on. In particular, see ITEM No. 600 in that file, which contains more details about the "substiffener" project..
- [2] J. N. Dickson, S. B. Biggers, and J. T. S. Wang, "Preliminary design procedure for composite panels with open-section stiffeners loaded in the post-buckling range," in: *Advances in Composite Materials*, A. R. Bunsell, et al, editors, Pergamon Press Ltd., Oxford, England, 1980, pp 812-825. Also see, J. N. Dickson and S. B. Biggers, "POSTOP: Postbuckled open-stiffened optimum panels, theory and capability", NASA Langley Research Center, Hampton, Va., NASA Contractor Report from NASA Contract NAS1 -15949, May 1982.
- [3] Butler, R. and Williams, F. W., "Optimum design features of VICONOPT, an exact buckling program for prismatic assemblies of anisotropic plates," AIAA Paper 90-1068-CP, Proceedings 31st AIAA/ASME Structures, Structural Dynamics, and Materials Meeting, pp 1289-1299. Also see Williams, F. W., Kennedy, D., Anderson, M.S., "Analysis features of VICONOPT, an exact buckling and vibration program for prismatic assemblies of anisotropic plates," AIAA Paper 90-0970-CP, Proceedings 31st AIAA/ASME Structures, Structural Dynamics, and Materials Meeting, pp 920-929
- [4] M. S. Anderson and W. J. Stroud, "General panel sizing computer code and its application to composite structural panels," *AIAA Journal*, 17, (1979) pp. 892-897. Also see W. J. Stroud and M. S. Anderson, "PASCO: Structural panel analysis and sizing code, capability and analytical foundations," NASA TM-80181, NASA Langley Research Center, Hampton, Va., 1981. Also see W. J. Stroud, W. H. Greene and M. S. Anderson, "Buckling loads of stiffened panels subjected to combined longitudinal compression and shear: Results obtained with PASCO, EAL, and STAGS computer programs," NASA TP 2215, Nasa Langley Research Center, Hampton, Va., January 1984.
- [5] Wong, K. F. W. and Weaver, P. M., "Approximate solution for the compression buckling of fully-anisotropic cylindrical shells", 45th AIAA Structures, Structural Dynamics & Materials Conference, April 2004, Palm Springs, California
- [6] Weaver, P. M., "On optimisation of long anisotropic flat plates subject to shear buckling loads", 45th AIAA SDM Conference, April 2004
- [7] Diaconu, C. G. and Weaver, P. M., "Approximate solution and optimum design for postbuckling of infinite laminated composite plates subjected to compression loading", 45th AIAA SDM Conference, April 2004

- [8] Hilburger, M. W., Nemeth, M. P., Riddick, J. C., and Thornburgh, R. P., "Effects of elastic edge restraints and initial prestress on the buckling response of compression-loaded composite panels", 45th AIAA SDM Conference, April 2004
- [9] Baruch, M. and Singer, J., "Effect of eccentricity of stiffeners on the general instability of stiffened cylindrical shells under hydrostatic pressure," *Journal of Mechanical Engineering Science*, 5, (1) (1963) pp.23-27.
- [10] Almroth, B. O. and Brogan, F. A., "The STAGS computer code", NASA CR-2950, NASA Langley Research Center, Hampton, VA, 1978.
- [11] Rankin, C. C., Stehlin, P., and Brogan, F. A., "Enhancements to the STAGS computer code", NASA CR-4000, NASA Langley Research center, Hampton, VA, 1986.
- [12] Riks, E., Rankin C. C., Brogan F. A., "On the solution of mode jumping phenomena in thin walled shell structures", First ASCE/ASM/SES Mechanics Conference, Charlottesville, VA, June 6-9, 1993, in: *Computer Methods in Applied Mechanics and Engineering*, Vol.136, 1996.
- [13] Arbocz, J., "The effect of initial imperfections on shell stability - An updated review", Delft University Faculty of Aerospace Engineering Report LR-695, September 1992.
- [14] Arbocz, J. and Hol, J. M. A. M., "On the reliability of buckling load predictions", AIAA Paper 94-1371, Proc. 35th AIAA Structures, Structural Dynamics, and Materials Conference, Hilton Head SC, 514-527 (1993).
- [15] Arbocz, J. and Hol, J., "Shell stability analysis in a computer aided engineering (CAE) environment", AIAA Paper 93-133, Proc. 34th AIAA Structures, Structural Dynamics, and Materials Conference, La Jolla, CA, 300-314 (1993).
- [16] Stein, M., "The phenomenon of change of buckling patterns in elastic structures," NASA Technical report R-39, NASA (1959)
- [17] A. W. Leissa, "Buckling of laminated composite plates and shell panels," AFWAL-TR-85-3069, Air Force Wright Aeronautical Laboratories, Wright-Patterson AFB, Ohio 45433, June, 1985.
- [18] R. R. Arnold and J. C. Parekh, "Buckling, postbuckling, and failure of flat and shallow-curved, edge-stiffened composite plates subject to combined axial compression and shear loads", Presented at 27th SDM Meeting, San Antonio, Tx., April 1986, AIAA Paper No. 86-1027-CP, 1986, Proceedings pp. 769-782.
- [19] J. H. Starnes, Jr., N. F. Knight, Jr. and M. Rouse, "Postbuckling behavior of selected flat stiffened graphite-epoxy panels loaded in compression," AIAA Paper 82-0777, presented at AIAA 23rd Structures, Structural Dynamics, and Materials Conference, New Orleans, May, 1982. See also, AIAA J., 23, (8) (1985) pp.1236-1246.
- [20] E. E. Spier, "On experimental versus theoretical incipient buckling of narrow graphite/epoxy plates in compression," Proc. AIAA 21st SDM Conference, AIAA Paper 80-0686-CP, May, 1980.
- [21] E. E. Spier, "Local buckling, postbuckling, and crippling behavior of graphite-epoxy short thin-walled compression members," Naval Air Systems Command, Washington, D. C., NASC-N00019-80-C-0174, July 1981.
- [22] N. R. Bauld, Jr. and N. S. Khot, "A numerical and experimental investigation of the buckling behavior of composite panels", *Computers and Structures*, 15 (1982) pp. 393-403.
- [23] N. S. Khot and N. R. Bauld, Jr., "Further comparison of the numerical and experimental buckling behaviors of composite panels," *Computers and Structures*, 17, (1983) pp. 61-68.
- [24] Y. Zhang and F. L. Matthews, "Postbuckling behavior of anisotropic laminated plates under pure shear and shear combined with compressive loading", *AIAA Journal*, 22, (2), (1984) pp 281-286.

- [25] Stoll, F. and Gurdal, Z., "Nonlinear analysis of compressively loaded linked-plate structures," AIAA Paper 90-0968-CP, Proceedings 31st AIAA/ASME Structures, Structural Dynamics, and Materials Meeting, pp 903-913 (1990).
- [26] Stoll, F. and Gurdal, Z., and Starnes, J. H., Jr., "A method for the geometrically nonlinear analysis of compressively loaded prismatic composite structures," VIPSU Center for Composite Materials and Structures Report CCMS-91-03 (VPI-E-91-01), February, 1991
- [27] Shin, D. K., Gurdal, Z., and Griffin, O. H., Jr., "Minimum weight design of laminated composite plates for postbuckling performance," AIAA Paper 91-0969-CP, Proceedings 32nd AIAA/ASME Structures, Structural Dynamics, and Materials Meeting, pp 257-266 (1991)
- [28] Ley, R.P., Gurdal, Z., and Johnson, E.R. (1993). Optimal design of imperfect, anisotropic, ring-stiffened cylinders under combined loads. AIAA Paper 93-1526-CP, Proceedings of 34th AIAA Structures, Structural Dynamics, and Materials Conference, Part 4, pp 1881-1889.
- [29] Ley, R.P., Johnson, E.R., and Gurdal, Z. (1992). Buckling of imperfect, anisotropic, ring-stiffened cylinders under combined loads. AIAA Paper 92-2232-CP, Proceedings of 33rd AIAA Structures, Structural Dynamics, and Materials Conference, Part 1, pp 86-94.
- [30] Nagendra, S., Haftka, R. T., and Gurdal, Z. (1992). Stacking sequence optimization of simply supported laminates with stability and strain constraints. AIAA Paper 92-2310-CP, Proceedings of 33rd AIAA Structures, Structural Dynamics, and Materials Conference, Part 5, pp. 2526-2535.
- [31] Le Riche, R. and Haftka, R. T. (1992). Optimization of laminate stacking sequence for buckling load maximization by genetic algorithm. AIAA Paper 92-2314-CP, Proceedings of 33rd AIAA Structures, Structural Dynamics, and Materials Conference, Part 5, pp. 2564-2575.
- [32] Lombardi, M., Haftka, R. T., and Cinquini, C. (1992). Optimization of composite plates for buckling by simulated annealing. AIAA Paper 92-2313-CP, Proceedings of 33rd AIAA Structures, Structural Dynamics, and Materials Conference, Part 5, pp. 2552-2563.
- [33] Librescu, L. and Chang, M.-Y. (1993). Effects of geometric imperfections on vibration of compressed shear deformable laminated composite curved panels. *Acta Mechanica*, 96, 203-224.
- [34] Librescu, L. and Souza, M. A. (1991). Postbuckling behavior of shear deformable flat panels under the complex action of thermal and in-plane mechanical loadings. AIAA Paper 91-0913-CP, Proceedings of 32nd AIAA Structures, Structural Dynamics, and Materials Conference, Part 2, pp. 917-925.
- [35] Librescu, L. and Stein, M. (1991). A geometrically nonlinear theory of transversely isotropic laminated composite plates and its use in the post-buckling analysis. *Thin-Walled Structures*, 11, 177-201.
- [36] Graves-Smith, T.R. and Sridharan, S., "A finite strip method for the post-locally-buckled analysis of plate structures," *Int. J. Mech. Sci.*, Vol. 20, pp 833-843 (1978)
- [37] Peng, M-H and Sridharan, S., "Optimized design of stiffened panels subject to interactive buckling," AIAA Paper 90-1067-CP, Proceedings 31st AIAA/ASME Structures, Structural Dynamics, and Materials Meeting, pp 1279-1288
- [38] Meyers, C. A. and Hyer, M. W. (1992). Thermally-induced, geometrically nonlinear response of symmetrically laminated composite plates. AIAA Paper 92-2539-CP, Proceedings of 33rd AIAA Structures, Structural Dynamics, and Materials Conference, Part 2, pp. 1027-1037.
- [39] Nemeth, M. P. (1992). Buckling behavior of long symmetrically laminated plates subjected to compression, shear, and inplane bending loads. AIAA Paper 92-2286-CP, Proceedings of 33rd AIAA Structures, Structural

Dynamics, and Materials Conference, Part 2, pp. 274-282.

[40] Noor, A. K., Starnes, J. H., Jr., and Peters, J. M. (1992). Thermomechanical buckling and postbuckling of multilayered composite panels. AIAA Paper 92-2541-CP, Proceedings of 33rd AIAA Structures, Structural Dynamics, and Materials Conference, Part 2, pp. 1052-1068.

[41] Bushnell, D., "Theoretical basis of the PANDA computer program for preliminary design of stiffened panels under combined in-plane loads", Computers and Structures, v. 27, No. 4, pp 541-563 (1987).

[42] D. Bushnell, "BOSOR4: Program for stress, buckling, and vibration of complex shells of revolution," Structural Mechanics Software Series - Vol. 1, (N. Perrone and W. Pilkey, editors), University Press of Virginia, Charlottesville, 1977, pp. 11-131. See also Computers and Structures, Vol. 4, (1974) pp. 399-435; AIAA J, Vol. 9, No. 10, (1971) pp. 2004-2013; Structural Analysis Systems, Vol. 2, A. Niku-Lari, editor, Pergamon Press Oxford, 1986, pp. 25-54, and Computers and Structures, 18, (3), (1984) pp. 471-536.

[43] Vanderplaats, G. N., "ADS--a FORTRAN program for automated design synthesis, Version 2.01", Engineering Design Optimization, Inc, Santa Barbara, CA, January, 1987

[44] Vanderplaats, G. N. and Sugimoto, H., "A general-purpose optimization program for engineering design", Computers and Structures, Vol. 24, pp 13-21, 1986

[45] Koiter, W. T., "Het Schuifplooiveld by Grote Overschrijdingen van de Knikspanning", National Luchtvaart Laboratorium, The Netherlands, Report X295, November 1946 (in Dutch).

[46] STAGS Brochure (2002) available online by request: crankin@rhombuscgi.com (pdf format).

Table 1 Geometry, Material Properties, and Loading

Geometry (cylindrical shell):

Length = 300 inches
Radius = 100 inches
External T-shaped major stringers
External T-shaped major rings

Material properties (aluminum):

Young's modulus = 10 msi
Poisson ratio = 0.3
Maximum allowable stress = 1.0 msi (set high to avoid active stress constraints)

Loading used for all cases:

-100000.0 \$ Axial Resultant (lb/in), Nx(1) Load Set A
-20000.00 \$ Hoop Resultant (lb/in), Ny(1) Load Set A
20000.00 \$ In-plane shear (lb/in), Nxy(1) Load Set A
-200.0000 \$ Uniform pressure, (psi), p(1) Load Set A
Zero loading in Load Set B

Boundary conditions:

Simple support

Imperfection:

General buckling modal imperfection amplitude, Wimp_{g2} = +1.0 inch and -1.0 inch.

Imperfect shells have two load cases:

Load Case 1: Wimp_{g2} = +1.0 inch
Load Case 1: Wimp_{g2} = -1.0 inch

Table 2 Definitions of variables used in PANDA2 examples

Variable Number	Variable Name	Definition	Structural Part
1	B(STR)	stiffener spacing, b: STR	stringer
2	B2(STR)	width of stringer base, b2 (must be > 0)	stringer
3	H(STR)	height of stiffener (type H for sketch), h:	stringer
4	W(STR)	width of outstanding flange of stiffener, w:	stringer
5	T(1)(SKN)	thickness for layer index no.(1): SKN seg=1	panel skin
6	TSUB,substr	thickness, TSUB, of substiffener set(1):	substringer
7	HSUB,substr	height, HSUB, of substiffener set(1): SKN	substringer
8	BSUB,substr	spacing, BSUB, of substiffener set(1): SKN	substringer
9	TSUB,subrng	thickness, TSUB, of substiffener set(2):	subring
10	HSUB,subrng	height, HSUB, of substiffener set(2): SKN	subring
11	BSUB,subrng	spacing, BSUB, of substiffener set(2): SKN	subring
12	T(2)(STR)	thickness for layer index no.(2): STR seg=3	stringer web
13	T(3)(STR)	thickness for layer index no.(3): STR seg=4	stringer flange
14	B(RNG)	stiffener spacing, b: RNG	ring
15	B2(RNG)	width of ring base, b2 (zero is allowed):	ring
16	H(RNG)	height of stiffener (type H for sketch), h:	ring
17	W(RNG)	width of outstanding flange of stiffener, w:	ring
18	T(4)(RNG)	thickness for layer index no.(4):RNG seg=3	ring web
19	T(5)(RNG)	thickness for layer index no.(5):RNG seg=4	ring flange

Table 3 Starting design and optimum designs from PANDA2 with and without substiffeners
(dimensions in inches)

		Perfect Shell With Substiffeners	Imperfect Shell With Substiffeners	Perfect Shell Without Substiffeners	Imperfect Shell Without Substiffeners
Variable Name	Starting Design	Optimum Design	Optimum Design	Optimum Design	Optimum Design
B(STR)	20.0	14.775	11.461	5.2141	5.7718
B2(STR)	2.0	1.4775	1.1461	0.52141	0.57718
H(STR)	10.0	4.5048	4.9955	2.7194	3.8575
W(STR)	10.0	2.9341	3.5908	2.1716	2.9305
T(1)(SKN)	1.0	0.30150	0.36755	0.49158	0.55232
TSUB,substr	1.0	0.23625	0.15374	-----	-----
HSUB,substr	5.0	1.1934	0.82430	-----	-----
BSUB,substr	5.0	2.8821	2.4256	-----	-----
TSUB,subrng	1.0	0.24665	0.20833	-----	-----
HSUB,subrng	5.0	2.4665	2.0833	-----	-----
BSUB,subrng	5.0	7.0617	4.9854	-----	-----
T(2)(STR)	1.0	0.52520	0.49773	0.25874	0.33045
T(3)(STR)	1.0	0.27664	0.31908	0.17386	0.23108
B(RNG)	20.0	39.157	42.874	22.208	28.291
B2(RNG)	0.0	0.0	0.0	0.0	0.0
H(RNG)	10.0	11.046	9.5948	8.2778	8.7430
W(RNG)	10.0	4.661	8.0986	3.4935	6.2876
T(4)(RNG)	1.0	0.55228	0.95512	0.41389	0.72687
T(5)(RNG)	1.0	0.25829	0.54145	0.26031	0.43056
WEIGHT	-----	16712 lb	21480 lb	16846 lb	22820 lb

Table 4 Runstream for finding the "global" optimum design

Command	Meaning of the command	Input file(s)	Output file(s)
panda2log	activate PANDA2 command set	.	.
begin	user provides starting design	testax4p.BEG	testax4p.OPB
setup	PANDA2 sets up matrix templates	none	many files
decide	user chooses decision variables	testax4p.DEC	testax4p.OPD
mainsetup	user chooses loading, strategy	testax4p.OPT	none
.	.	.	.
superopt	PANDA2 finds "global" optimum	testax4p.OPT	testax4p.OPM, -.OPP
chooseplot	user chooses what to plot	testax4p.CPL	testax4p.OPL
diplot	user obtains plot hard copies	.	testax4p.5.ps, etc.
.	.	.	.
superopt	PANDA2 finds "global" optimum	testax4p.OPT	testax4p.OPM, -.OPP
chooseplot	user chooses what to plot	testax4p.CPL	testax4p.OPL
diplot	user obtains plot hard copies	.	testax4p.5.ps, etc.
.	.	.	.
superopt	PANDA2 finds "global optimum	testax4p.OPT	testax4p.OPM, -.OPP
chooseplot	user chooses what to plot	testax4p.CPL	testax4p.OPL
diplot	user obtains plot hard copies	.	testax4p.5.ps, etc.
.	.	.	.
superopt	PANDA2 finds "global optimum	testax4p.OPT	testax4p.OPM, -.OPP
chooseplot	user chooses what to plot	testax4p.CPL	testax4p.OPL
diplot	user obtains plot hard copies	.	testax4p.5.ps

Table 5 Margins computed by PANDA2 for Load Case No. 1, Subcase No. 1 for the optimized perfect shell with substiffeners (Case name = testax4p)

Mar. No.	Margin Value	Margin Definition
1	2.53E-02	Local buckling from discrete model-1.,M=2 axial halfwaves;FS=0.99
2	2.23E-01	Bending-torsion buckling; M=2 ;FS=0.999
3	3.24E-01	(m=2 lateral-torsional buckling load factor)/(FS)-1;FS=0.999
4	2.53E-02	Inter-ring buckling, discrete model, n=6 circ.halfwaves;FS=0.999
5	4.28E+00	eff.stress:matl=1,SKN,Iseg=2,at:n=1,layer=1,z=-0.1507;MID.;FS=1.
6	5.49E+00	matl=2 ; substiffener effective stressSTRCON MID.;FS=1.
7	1.76E+00	buckling margin stringer Iseg.3 . Local halfwaves=8 .MID.;FS=1.
8	5.68E-03	buckling margin stringer Iseg.4 . Local halfwaves=8 .MID.;FS=1.
9	7.44E-01	buckling stringer Isegs.3+4 together.M=9 ;C=0. ;MID.;FS=1.4
10	1.27E-01	buckling stringer Iseg 4 as beam on foundation. M=212;MID.;FS=3.
11	1.18E+01	buckling ring Iseg 4 as beam on foundation. M=169;MID.;FS=3.
12	1.53E-01	buck.(SAND);simp-support smearsustf; (0.95*altsol);FS=0.999
13	-3.84E-03	buck.(SAND);simp-support inter-ring; (1.00*altsol);FS=0.999
14	-2.02E-02	buck.(SAND);simp-support general buck;M=6;N=0;slope=0.4637;FS=.999
15	2.35E-03	buck.(SAND);simp-support general buck;(0.85*altsol);FS=0.999
16	5.72E+00	buck.(SAND);rolling with smear rings; M=52;N=1;slope=0.01;FS=0.999
17	6.94E-03	buck.(SAND);rolling only of stringers;M=16;N=0;slope=0.;FS=1.6
18	1.28E+00	buck.(SAND);hiwave roll. of stringers;M=86;N=0;slope=0.;FS=1.2
19	1.73E+00	buck.(SAND); STRINGERS: web buckling;M=9;N=1;slope=0.;FS=1.
20	1.35E+01	buck.(SAND); RINGS: web buckling;M=2;N=1;slope=0.;FS=1.
21	4.60E-01	buck.(SAND);rolling with skin buckl.; M=1;N=1;slope=0.1939;FS=0.999
22	-4.04E-04	buckling:simp-support of substring.M=1;FS=1.
23	1.14E+01	buckling:simp-support of subrings N=1;FS=1.
24	-2.86E-02	buckling:simp-support altsoln4 intermajorpatch; FS=0.999
25	3.21E-01	buckling:simp-support altsoln5 skin+edgsubroll; FS=0.999
26	2.18E-01	buck.(SAND);rolling with smear substr;M=1;N=2;slope=16.67;FS=0.999
27	5.78E-02	buckling:simp-support altsoln6 inter-subring ; FS=0.999
28	5.77E+00	buck.(SAND);rolling with smear subrng;M=39;N=1;slope=0.01;FS=0.999
29	6.91E-01	buck.(SAND);rolling only of substring;M=20;N=0;slope=0.;FS=1.6
30	8.00E+00	buck.(SAND);rolling only of subrings; M=0;N=4;slope=0.;FS=1.6
31	6.43E+01	(Max.allowable ave.axial strain)/(ave.axial strain) -1; FS=1.
32	4.15E-01	1.-3.V(8)^1+V(1)^1-1 inequality constraint no. 1
33	4.59E-01	1.-3.V(11)^1+V(14)^1-1 inequality constraint no. 2
34	9.80E-01	1.+10.V(6)^1-V(7)^1-1 inequality constraint no. 3
35	0.00E+00	1.+10.V(9)^1-V(10)^1-1 inequality constraint no. 4
36	1.33E+00	1.-V(3)^1+20.V(12)^1-1 inequality constraint no. 5
37	-3.62E-05	1.-V(16)^1+20.V(18)^1-1 inequality constraint no. 6

Table 6 New margins in the case testax4p pertaining to substringers and subbrings

Mar. No.	Margin Value	Margin Definition
6	5.49E+00	matl=2 ; substiffener effective stressSTRCON MID.;FS=1.
21	4.60E-01	buck.(SAND);rolling with skin buckl.; M=1;N=1;slope=0.1939;FS=0.999
22	-4.04E-04	buckling:simp-support of substring.M=1;FS=1.
23	1.14E+01	buckling:simp-support of subbrings N=1;FS=1.
24	-2.86E-02	buckling:simp-support altsoln4 intermajorpatch; FS=0.999
25	3.21E-01	buckling:simp-support altsoln5 skin+edgsubroll; FS=0.999
26	2.18E-01	buck.(SAND);rolling with smear substr;M=1;N=2;slope=16.67;FS=0.999
27	5.78E-02	buckling:simp-support altsoln6 inter-subring ; FS=0.999
28	5.77E+00	buck.(SAND);rolling with smear subrng;M=39;N=1;slope=0.01;FS=0.999
29	6.91E-01	buck.(SAND);rolling only of substring;M=20;N=0;slope=0.;FS=1.6
30	8.00E+00	buck.(SAND);rolling only of subbrings; M=0;N=4;slope=0.;FS=1.6

Table 7 Margins in the case testax4p for which the substiffeners are smeared out

Mar. No.	Margin Value	Margin Definition
1	2.53E-02	Local buckling from discrete model-1.,M=2 axial halfwaves;FS=0.99
2	2.23E-01	Bending-torsion buckling; M=2 ;FS=0.999
3	3.24E-01	(m=2 lateral-torsional buckling load factor)/(FS)-1;FS=0.999
4	2.53E-02	Inter-ring buckling, discrete model, n=6 circ.halfwaves;FS=0.999
12	1.53E-01	buck.(SAND);simp-support smearsbstf; (0.95*altsol);FS=0.999
13	-3.84E-03	buck.(SAND);simp-support inter-ring; (1.00*altsol);FS=0.999
14	-2.02E-02	buck.(SAND);simp-support general buck;M=6;N=0;slope=0.4637;FS=.999
15	2.35E-03	buck.(SAND);simp-support general buck;(0.85*altsol);FS=0.999
16	5.72E+00	buck.(SAND);rolling with smear rings; M=52;N=1;slope=0.01;FS=0.999

Table 8 Optimum designs suitable for analysis with STAGS (dimensions in inches)

.	Perfect Shell With Substiffeners	Imperfect Shell With Substiffeners	Perfect Shell Without Substiffeners	Imperfect Shell Without Substiffeners
Variable Name	Optimum Design	Optimum Design	Optimum Design	Optimum Design
B(STR)	14.612	11.424	5.2360	5.7644
B2(STR)	1.4612	1.1424	0.52360	0.57644
H(STR)	4.2569	5.1430	2.6734	3.8010
W(STR)	3.1474	3.3240	2.2670	2.9990
T(1)(SKN)	0.30574	0.38290	0.48975	0.56340
TSUB,substr	0.24266	0.15810	-----	-----
HSUB,substr	1.2074	0.87730	-----	-----
BSUB,substr	2.9224	2.2848	-----	-----
TSUB,subrng	0.26422	0.20290	-----	-----
HSUB,subrng	2.6422	2.0290	-----	-----
BSUB,subrng	7.5000	4.7619	-----	-----
T(2)(STR)	0.46728	0.52520	0.25758	0.32390
T(3)(STR)	0.29086	0.29530	0.18523	0.23430
B(RNG)	37.500	42.857	21.429	27.273
B2(RNG)	0.0	0.0	0.0	0.0
H(RNG)	10.486	9.6990	9.0944	7.9770
W(RNG)	5.2204	7.7940	2.0981	6.3630
T(4)(RNG)	0.52429	0.93330	0.45472	0.72520
T(5)(RNG)	0.32008	0.50620	0.091261	0.47750
WEIGHT	16750 lb	21780 lb	17020 lb	23020 lb

Table 9 Margins for the optimized perfect shell with substiffeners. Stiffener spacings are suitable for an analysis with STAGS (Case name = testax4p, Subcase 1 only)

Mar. No.	Margin Value	Margin Definition
1	1.24E-01	Local buckling from discrete model-1.,M=2 axial halfwaves;FS=0.99
2	3.38E-01	Bending-torsion buckling; M=2 ;FS=0.999
3	4.50E-01	(m=2 lateral-torsional buckling load factor)/(FS)-1;FS=0.999
4	1.03E-02	Inter-ring buckling, discrete model, n=6 circ.halfwaves;FS=0.999
5	4.26E+00	eff.stress:matl=1,SKN,Iseg=2,at:n=1,layer=1,z=-0.1529;-MID.;FS=1.
6	5.39E+00	matl=2 ; substiffener effective stressSTRCON MID.;FS=1.
7	1.45E+00	buckling margin stringer Iseg.3 . Local halfwaves=8 .MID.;FS=1.
8	-3.99E-03	buckling margin stringer Iseg.4 . Local halfwaves=8 .MID.;FS=1.
9	4.64E-01	buckling stringer Isegs.3+4 together.M=9 ;C=0. ;MID.;FS=1.4
10	7.63E-02	buckling stringer Iseg 4 as beam on foundation. M=198;MID.;FS=3.
11	1.43E+01	buckling ring Iseg 4 as beam on foundation. M=140;MID.;FS=3.
12	2.95E-01	buck.(SAND);simp-support smeasubstf; (0.95*altsol);FS=0.999
13	-3.76E-03	buck.(SAND);simp-support inter-ring; (1.00*altsol);FS=0.999
14	-3.66E-02	buck.(SAND);simp-support general buck;M=6;N=0;slope=0.473;FS=0.999
15	6.26E-04	buck.(SAND);simp-support general buck;(0.85*altsol);FS=0.999
16	6.26E+00	buck.(SAND);rolling with smear rings; M=50;N=1;slope=0.01;FS=0.999
17	-2.58E-02	buck.(SAND);rolling only of stringers;M=14;N=0;slope=0.;FS=1.6
18	7.89E-01	buck.(SAND);hiwave roll. of stringers;M=84;N=0;slope=0.;FS=1.2
19	1.43E+00	buck.(SAND); STRINGERS: web buckling;M=9;N=1;slope=0.;FS=1.
20	1.51E+01	buck.(SAND); RINGS: web buckling;M=2;N=1;slope=0.;FS=1.
21	4.86E-01	buck.(SAND);rolling with skin buckl.; M=1;N=1;slope=0.1978;FS=0.999
22	6.44E-03	buckling:simp-support of substring.M=1;FS=1.
23	1.41E+01	buckling:simp-support of subrings N=1;FS=1.
24	-4.18E-02	buckling:simp-support altsoln4 intermajorpatch; FS=0.999
25	3.18E-01	buckling:simp-support altsoln5 skin+edgsubroll; FS=0.999
26	1.21E-01	buck.(SAND);rolling with smear substr;M=1;N=2;slope=20.;FS=0.999
27	1.16E-02	buckling:simp-support altsoln6 inter-subring ; FS=0.999
28	6.04E+00	buck.(SAND);rolling with smear subrng;M=39;N=1;slope=0.01;FS=0.999
29	7.09E-01	buck.(SAND);rolling only of substring;M=18;N=0;slope=0.;FS=1.6
30	9.28E+00	buck.(SAND);rolling only of subrings; M=0;N=3;slope=0.;FS=1.6
31	6.33E+01	(Max.allowable ave.axial strain)/(ave.axial strain) -1; FS=1.
32	2.33E+00	0.3333 *(Stringer spacing, b)/(Stringer base width, b2)-1;FS=1.
33	1.01E+00	1.+10.V(6)^1-V(7)^1-1
34	-2.38E-07	1.+10.V(9)^1-V(10)^1-1
35	1.20E+00	1.-V(3)^1+20.V(12)^1-1
36	-1.79E-07	1.-V(16)^1+20.V(18)^1-1

Table 10 Abridged and edited version of the output file, testax4p.out2 from STAGS for a "patch" model containing three axial bays and nine circumferential bays between major stiffeners

threexninebays.testax4p.allshells.fasteners.480.out2 (name of STAGS case)

shift=0.98, one negative buckling mode

CONVERGENCE HAS BEEN OBTAINED FOR EIGENVALUES 1 THROUGH 8 Critical load factor

.	.	.	.	Types of buckling
NO.	Eigenvalue	Load set A	@DOF	.
1	9.773792E-01	9.773792E-01	27287	<--1st mode 4, 13, 17 (See Fig. 3)
2	9.816915E-01	9.816915E-01	17321	<--2nd mode 4, 13, 17
3	1.012336E+00	1.012336E+00	4731	<--3rd mode 1, 2, 3, 4, 13, 17
4	1.017679E+00	1.017679E+00	5335	<--4th mode 1, 2, 3, 4, 13, 17, 24
5	1.024645E+00	1.024645E+00	6877	<--5th mode 1, 2, 3, 4, 13, 17, 24
6	1.025765E+00	1.025765E+00	114463	<--6th mode 1, 2, 3, 17, 24
7	1.028083E+00	1.028083E+00	27275	<--7th mode 1, 2, 3, 17, 24
8	1.029080E+00	1.029080E+00	4605	<--8th mode 1, 2, 3, 17, 24

Table 11 Abridged and edited version of the output file, testax4p.out2 from STAGS for a model of the complete cylindrical shell with all stiffeners smeared and with use of the 480 finite element

entireshell.testax4p.allstiffsmear.480.out2

shift=1.05, zero negative buckling modes

MAXIMUM NUMBER OF ITERATIONS

CONVERGENCE HAS BEEN OBTAINED FOR EIGENVALUES 1 THROUGH 5

CONVERGENCE CRITERION HAS NOT BEEN SATISFIED FOR EIGENVALUES 6 THROUGH 6

.	Critical load factor	Critical load factor	.	Types of buckling
NO.	Eigenvalue	Load set A	@DOF	.
1	1.288339E+00	1.288339E+00	12879	<--n=3 circ.waves, Fig. 9
2	1.288339E+00	1.288339E+00	12663	.
3	1.371375E+00	1.371375E+00	18375	<--n=0 circ.waves, Figs.10, 11
4	1.371375E+00	1.371375E+00	18333	.
5	1.382606E+00	1.382606E+00	12735	<--n=2 circ.waves
6	1.382625E+00	1.382625E+00	12543	<--not converged

Table 12 Margins for the optimized imperfect shell with substiffeners. Stiffener spacings are suitable for an analysis with STAGS (Case name = testax4)

Mar. No.	Margin Value	Margin Definition
1	3.51E-01	Local buckling from discrete model-1.,M=5 axial halfwaves;FS=0.99
2	1.59E-01	Long-axial-wave bending-torsion buckling; M=2 ;FS=0.999
3	2.41E-01	(m=2 lateral-torsional buckling load factor)/(FS)-1;FS=0.999
4	-2.96E-02	Ring sidesway buk., discrete model, n=7 circ.halfwaves;FS=0.999
5	8.23E-02	Hi-n Ring flang buckl.discrete model,n=52 circ.halfwaves;FS=0.999
6	5.02E+00	eff.stress:matl=1,SKN,Iseg=1,at:n=1,layer=1,z=0.1914;-MID.;FS=1.
7	6.93E+00	matl=2 ; substiffener effective stressSTRCON MID.;FS=1.
8	1.61E+00	buckling margin stringer Iseg.3 . Local halfwaves=8 .MID.;FS=1.
9	5.19E-02	buckling margin stringer Iseg.4 . Local halfwaves=8 .MID.;FS=1.
10	6.43E-01	buckling stringer Isegs.3+4 together.M=8 ;C=0. ;MID.;FS=1.4
11	2.04E-01	buckling stringer Iseg 4 as beam on foundation. M=190;MID.;FS=3.
12	2.81E+00	buckling margin ring Iseg.3 . Local halfwaves=1 .MID.;FS=1.
13	-2.37E-02	buckling ring Iseg 4 as beam on foundation. M=105;MID.;FS=3.
14	8.89E-02	buck.(SAND);simp-support smearsbstf; (0.95*altsol);FS=0.999
15	2.27E-03	buck.(SAND);simp-support inter-ring; (1.00*altsol);FS=0.999
16	-1.35E-02	buck.(SAND);simp-support general buck;M=1;N=2;slope=25.;FS=0.999
17	4.01E-02	buck.(SAND);simp-support general buck;(0.85*altsol);FS=0.999
18	6.67E+00	buck.(SAND);rolling with smear rings; M=64;N=1;slope=0.01;FS=0.999
19	1.58E-02	buck.(SAND);rolling only of stringers;M=12;N=0;slope=0.;FS=1.6
20	1.16E+00	buck.(SAND);hiwave roll. of stringers;M=75;N=0;slope=0.;FS=1.2
21	1.62E+00	buck.(SAND); STRINGERS: web buckling;M=8;N=1;slope=0.;FS=1.
22	2.98E+00	buck.(SAND); RINGS: web buckling;M=1;N=1;slope=0.2017;FS=1.
23	1.56E+00	buck.(SAND);rolling with skin buckl.; M=1;N=1;slope=0.11;FS=0.999
24	-4.82E-03	buckling:simp-support of substring.M=1;FS=1.
25	3.62E+00	buckling:simp-support of subrings N=1;FS=1.
26	-9.47E-03	buckling:simp-support altsoln4 intermajorpatch; FS=0.999
27	1.34E+00	buckling:simp-support altsoln5 skin+edgsubroll; FS=0.999
28	4.58E-01	buck.(SAND);rolling with smear substr;M=1;N=2;slope=16.67;FS=0.999
29	3.92E-01	buckling:simp-support altsoln6 inter-subring ; FS=0.999
30	8.81E+00	buck.(SAND);rolling with smear subrng;M=39;N=1;slope=0.02;FS=0.999
31	8.08E-01	buck.(SAND);rolling only of substring;M=29;N=0;slope=0.;FS=1.6
32	8.13E-01	buck.(SAND);hiwave roll. of substring;M=31;N=0;slope=0.;FS=1.6
33	1.06E-01	buck.(SAND);rolling only of subrings; M=0;N=3;slope=0.;FS=1.6
34	8.04E+01	(Max.allowable ave.axial strain)/(ave.axial strain) -1; FS=1.
35	2.33E+00	0.3333 *(Stringer spacing, b)/(Stringer base width, b2)-1;FS=1.
36	7.04E-01	$1 + 10.V(6)^1 - V(7)^1 - 1$
37	0.00E+00	$1 + 10.V(9)^1 - V(10)^1 - 1$
38	1.04E+00	$1 - V(3)^1 + 20.V(12)^1 - 1$
39	9.25E-01	$1 - V(16)^1 + 20.V(18)^1 - 1$

Table 13 Margins for the optimized imperfect shell with substiffeners. Stiffener spacings are suitable for an analysis with STAGS. The design is the same as that for Table 12 but the amplitude of the initial imperfection has been set equal to zero.

Mar. No.	Margin Value	Margin Definition
1	3.31E-01	Local buckling from discrete model-1.,M=5 axial halfwaves;FS=0.99
2	2.21E-01	Long-axial-wave bending-torsion buckling; M=2 ;FS=0.999
3	3.14E-01	(m=2 lateral-torsional buckling load factor)/(FS)-1;FS=0.999
4	5.34E-01	Inter-ring buckling, discrete model, n=8 circ.halfwaves;FS=0.999
5	5.63E+00	eff.stress:matl=1,SKN,Iseg=2,at:n=1,layer=1,z=-0.1914;-MID.;FS=1.
6	7.11E+00	matl=2 ; substiffener effective stressSTRCON MID.;FS=1.
7	1.72E+00	buckling margin stringer Iseg.3 . Local halfwaves=8 .MID.;FS=1.
8	1.35E-01	buckling margin stringer Iseg.4 . Local halfwaves=8 .MID.;FS=1.
9	7.26E-01	buckling stringer Isegs.3+4 together.M=8 ;C=0. ;MID.;FS=1.4
10	2.99E-01	buckling stringer Iseg 4 as beam on foundation. M=190;MID.;FS=3.
11	2.54E+01	buckling ring Iseg 4 as beam on foundation. M=105;MID.;FS=3.
12	2.71E-01	buck.(SAND);simp-support smeasubstf; (0.95*altsol);FS=0.999
13	7.45E-02	buck.(SAND);simp-support inter-ring; (1.00*altsol);FS=0.999
14	1.96E-01	buck.(SAND);simp-support general buck;M=1;N=2;slope=25.;FS=0.999
15	4.78E-01	buck.(SAND);simp-support general buck;(0.85*altsol);FS=0.999
16	6.90E+00	buck.(SAND);rolling with smear rings; M=64;N=1;slope=0.01;FS=0.999
17	7.94E-02	buck.(SAND);rolling only of stringers;M=12;N=0;slope=0.;FS=1.6
18	1.29E+00	buck.(SAND);hiwave roll. of stringers;M=75;N=0;slope=0.;FS=1.2
19	1.71E+00	buck.(SAND); STRINGERS: web buckling;M=8;N=1;slope=0.;FS=1.
20	7.05E+01	buck.(SAND); RINGS: web buckling;M=1;N=1;slope=0.;FS=1.
21	2.99E+00	buck.(SAND);rolling with skin buckl.; M=1;N=1;slope=0.1756;FS=0.999
22	3.87E-02	buckling:simp-support of substring.M=1;FS=1.
23	1.82E+01	buckling:simp-support of subrings N=1;FS=1.
24	1.94E-01	buckling:simp-support altsoln4 intermajorpatch; FS=0.999
25	2.69E+00	buckling:simp-support altsoln5 skin+edgsubroll; FS=0.999
26	6.03E-01	buck.(SAND);rolling with smear substr;M=1;N=1;slope=14.29;FS=0.999
27	5.63E-01	buckling:simp-support altsoln6 inter-subring ; FS=0.999
28	1.02E+01	buck.(SAND);rolling with smear subrng;M=43;N=1;slope=0.02;FS=0.999
29	7.72E-01	buck.(SAND);rolling only of substring;M=29;N=0;slope=0.;FS=1.6
30	7.77E-01	buck.(SAND);hiwave roll. of substring;M=31;N=0;slope=0.;FS=1.6
31	1.16E+01	buck.(SAND);rolling only of subrings; M=0;N=3;slope=0.;FS=1.6
32	8.04E+01	(Max.allowable ave.axial strain)/(ave.axial strain) -1; FS=1.
33	2.33E+00	0.3333 *(Stringer spacing, b)/(Stringer base width, b2)-1;FS=1.
34	7.04E-01	1.+10.V(6)^1-V(7)^1-1
35	0.00E+00	1.+10.V(9)^1-V(10)^1-1
36	1.04E+00	1.-V(3)^1+20.V(12)^1-1
37	9.25E-01	1.-V(16)^1+20.V(18)^1-1

Table 14 Margins for Load case 1, Subcase 1 for the perfect optimized externally T-stiffened cylindrical shell without substiffeners for the optimum design suitable for analysis by STAGS (case name = testax3)

Mar. No.	Margin Value	Margin Definition
1	2.12E-01	Local buckling from discrete model-1.,M=1 axial halfwaves;FS=0.99
2	2.37E-01	Bending-torsion buckling; M=1 ;FS=0.999
3	5.73E+00	eff.stress:matl=1,STR,Dseg=5,node=11,layer=1,z=0.2449; MID.;FS=1.
4	3.07E-01	(m=1 lateral-torsional buckling load factor)/(FS)-1;FS=0.999
5	1.57E-01	Inter-ring buckling, discrete model, n=32 circ.halfwaves;FS=0.999
6	5.73E+00	eff.stress:matl=1,SKN,Iseg=1,at:n=1,layer=1,z=0.2449;-MID.;FS=1.
7	1.27E+00	buckling margin stringer Iseg.3 . Local halfwaves=8 .MID.;FS=1.
8	4.52E-02	buckling margin stringer Iseg.4 . Local halfwaves=8 .MID.;FS=1.
9	2.65E-01	buckling stringer Isegs.3+4 together.M=7 ;C=0. ;MID.;FS=1.4
10	1.48E-01	buckling stringer Iseg 4 as beam on foundation. M=292;MID.;FS=3.
11	3.53E-01	buck.(SAND);simp-support local buck.; (0.95*altsol);FS=0.999
12	2.58E-03	buck.(SAND);simp-support inter-ring; (1.00*altsol);FS=0.999
13	-3.53E-02	buck.(SAND);simp-support general buck;M=8;N=0;slope=0.335;FS=0.999
14	1.52E-01	buck.(SAND);simp-support general buck;(0.85*altsol);FS=0.999
15	1.28E+01	buck.(SAND);rolling with smear rings; M=152;N=1;slope=0.01;FS=0.999
16	5.13E-02	buck.(SAND);rolling only of stringers;M=18;N=0;slope=0.;FS=1.6
17	4.74E-01	buck.(SAND);hiwave roll. of stringers;M=123;N=0;slope=0.;FS=1.2
18	5.32E+01	buck.(SAND);rolling only axisym.rings;M=0;N=0;slope=0.;FS=1.6
19	1.27E+00	buck.(SAND); STRINGERS: web buckling;M=8;N=1;slope=0.;FS=1.
20	7.73E+03	buck.(SAND); RINGS: web buckling;M=1;N=8;slope=0.;FS=1.
21	7.37E+01	(Max.allowable ave.axial strain)/(ave.axial strain) -1; FS=1.
22	2.33E+00	0.3333 *(Stringer spacing, b)/(Stringer base width, b2)-1;FS=1.
23	9.27E-01	1.-V(3)^1+20.V(6)^1-1
24	-5.96E-08	1.-V(10)^1+20.V(12)^1-1

Table 15 Margins for Load case 1, Subcase 1 for the imperfect optimized externally T-stiffened cylindrical shell without substiffeners for the optimum design suitable for analysis by STAGS (case name = testax3)

Mar. No.	Margin Value	Margin Definition
1	3.73E-01	Local buckling from discrete model-1.,M=1 axial halfwaves;FS=0.99
2	3.75E-01	Bending-torsion buckling; M=1 ;FS=0.999
3	6.72E+00	eff.stress:matl=1,STR,Dseg=5,node=11,layer=1,z=0.2812; MID.;FS=1.
4	3.54E-01	(m=1 lateral-torsional buckling load factor)/(FS)-1;FS=0.999
5	4.74E-01	Ring flang buckling,discrete model,n=51 circ.halfwaves;FS=0.999
6	5.10E-02	Lo-n Ring sidesway, discrete model, n=8 circ.halfwaves;FS=0.999
7	6.39E+00	eff.stress:matl=1,RNG,Iseg=3,at:TIP,layer=1,z=0.3626;-MID.;FS=1.
8	1.09E+00	buckling margin stringer Iseg.3 . Local halfwaves=7 .MID.;FS=1.
9	7.63E-03	buckling margin stringer Iseg.4 . Local halfwaves=7 .MID.;FS=1.
10	2.06E-01	buckling stringer Isegs.3+4 together.M=7 ;C=0. ;MID.;FS=1.4
11	1.80E-01	buckling stringer Iseg 4 as beam on foundation. M=221;MID.;FS=3.
12	3.00E+00	buckling margin ring Iseg.3 . Local halfwaves=1 .MID.;FS=1.
13	6.61E-02	buckling ring Iseg 4 as beam on foundation. M=114;MID.;FS=3.
14	8.69E-01	buck.(SAND);simp-support local buck.; (0.95*altsol);FS=0.999
15	1.03E-01	buck.(SAND);simp-support inter-ring; (1.00*altsol);FS=0.999
16	3.15E-02	buck.(SAND);simp-support general buck;M=1;N=3;slope=3.4427;FS=0.999
17	3.86E-03	buck.(SAND);simp-support general buck;(0.85*altsol);FS=0.999
18	1.75E+01	buck.(SAND);rolling with smear rings; M=110;N=1;slope=0.01;FS=0.999
19	-4.77E-03	buck.(SAND);rolling only of stringers;M=12;N=0;slope=0.;FS=1.6
20	4.47E-01	buck.(SAND);hiwave roll. of stringers;M=92;N=0;slope=0.;FS=1.2
21	1.03E+00	buck.(SAND); STRINGERS: web buckling;M=7;N=1;slope=0.;FS=1.
22	3.27E+00	buck.(SAND); RINGS: web buckling;M=1;N=1;slope=0.1864;FS=1.
23	9.45E+01	(Max.allowable ave.axial strain)/(ave.axial strain) -1; FS=1.
24	2.33E+00	0.3333 *(Stringer spacing, b)/(Stringer base width, b2)-1;FS=1.
25	7.04E-01	1.-V(3)^1+20.V(6)^1-1
26	8.18E-01	1.-V(10)^1+20.V(12)^1-1

Table 16 Margins for Load case 2, Subcase 1 for the imperfect optimized externally T-stiffened cylindrical shell without sub stiffeners for the optimum design suitable for analysis by STAGS (case name = testax3)

Mar. No.	Margin Value	Margin Definition
1	2.59E-02	Local buckling from discrete model-1.,M=1 axial halfwaves;FS=0.99
2	2.77E-02	Bending-torsion buckling; M=1 ;FS=0.999
3	6.85E+00	eff.stress:matl=1,SKN,Dseg=2,node=6,layer=1,z=0.2812; MID.;FS=1.
4	8.51E-02	(m=1 lateral-torsional buckling load factor)/(FS)-1;FS=0.999
5	5.46E-02	Inter-ring buckling, discrete model, n=37 circ.halfwaves;FS=0.999
6	6.39E+00	eff.stress:matl=1,RNG,Iseg=3,at:TIP,layer=1,z=0.3626;-MID.;FS=1.
7	1.56E+00	buckling margin stringer Iseg.3 . Local halfwaves=7 .MID.;FS=1.
8	3.71E-01	buckling margin stringer Iseg.4 . Local halfwaves=7 .MID.;FS=1.
9	5.53E-01	buckling stringer Isegs.3+4 together.M=7 ;C=0. ;MID.;FS=1.4
10	6.06E-01	buckling stringer Iseg 4 as beam on foundation. M=221;MID.;FS=3.
11	3.00E+00	buckling margin ring Iseg.3 . Local halfwaves=1 .MID.;FS=1.
12	6.61E-02	buckling ring Iseg 4 as beam on foundation. M=114;MID.;FS=3.
13	4.09E-02	buck.(SAND);simp-support local buck.; (0.95*altsol);FS=0.999
14	2.69E-02	buck.(SAND);simp-support inter-ring; (1.00*altsol);FS=0.999
15	3.15E-02	buck.(SAND);simp-support general buck;M=1;N=3;slope=3.443;FS=0.999
16	7.52E-02	buck.(SAND);simp-support general buck;(0.85*altsol);FS=0.999
17	7.39E-01	buck.(SAND);rolling with smear string;M=1;N=14;slope=33.33;FS=0.999
18	1.68E+01	buck.(SAND);rolling with smear rings; M=112;N=1;slope=0.01;FS=0.999
19	3.10E-01	buck.(SAND);rolling only of stringers;M=12;N=0;slope=0.;FS=1.6
20	9.10E-01	buck.(SAND);hiwave roll. of stringers;M=92;N=0;slope=0.;FS=1.2
21	9.09E-02	buck.(SAND);rolling only of rings; M=0;N=8;slope=0.;FS=1.6
22	6.24E-01	buck.(SAND);hiwave roll. of rings; M=0;N=45;slope=0.;FS=1.2
23	1.32E+00	buck.(SAND); STRINGERS: web buckling;M=7;N=1;slope=0.;FS=1.
24	3.27E+00	buck.(SAND); RINGS: web buckling;M=1;N=1;slope=0.1864;FS=1.
25	9.45E+01	(Max.allowable ave.axial strain)/(ave.axial strain) -1; FS=1.

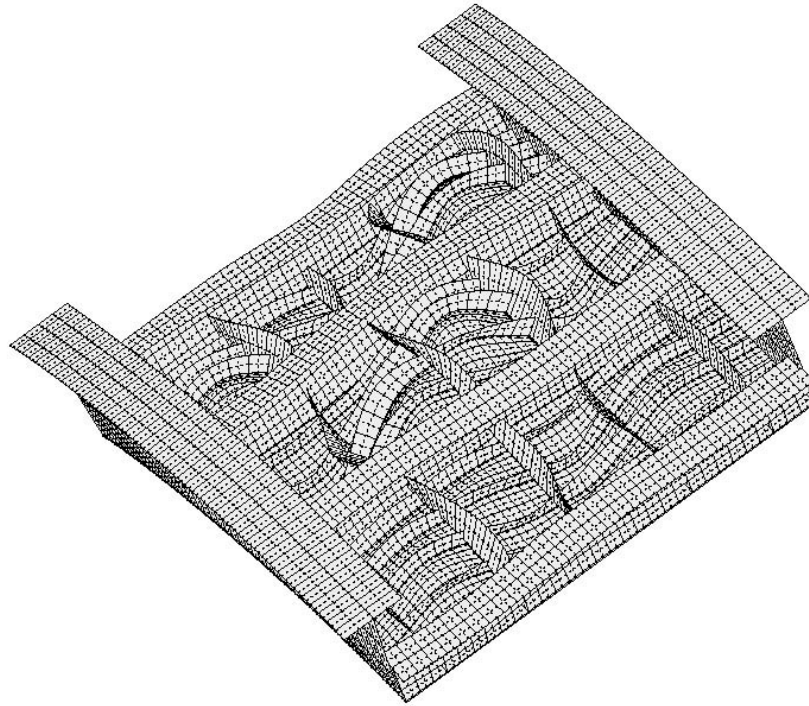


Fig. 1 STAGS model interring testax4p.allshells.1x3bays, mode 1, Pcr = .98903

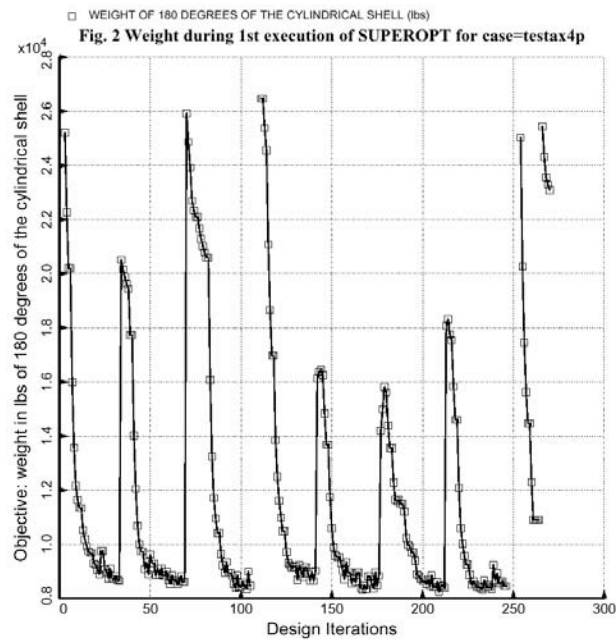


Fig. 2 Weight during 1st execution of SUPEROPT for case=testax4p

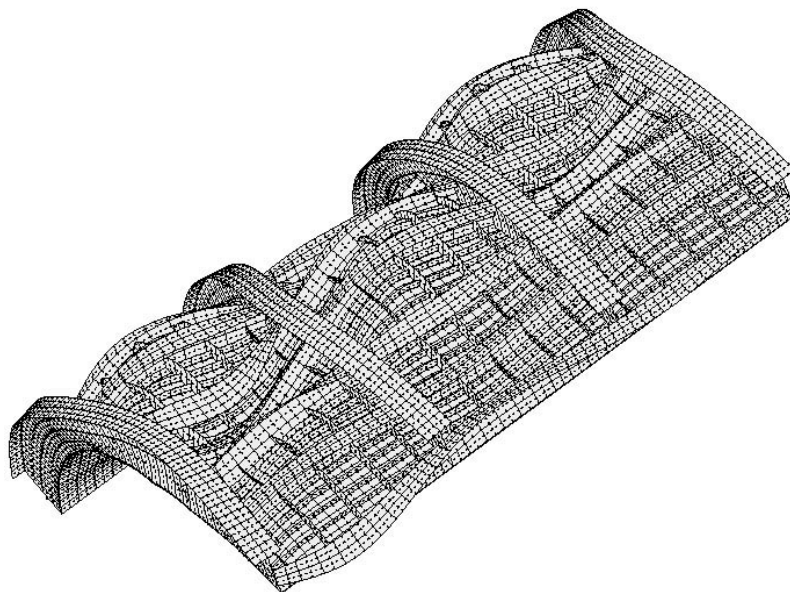


Fig. 3 STAGS model, threexninebays.testax4p.allshells.fasteners, mode 1, Pcr = .97738

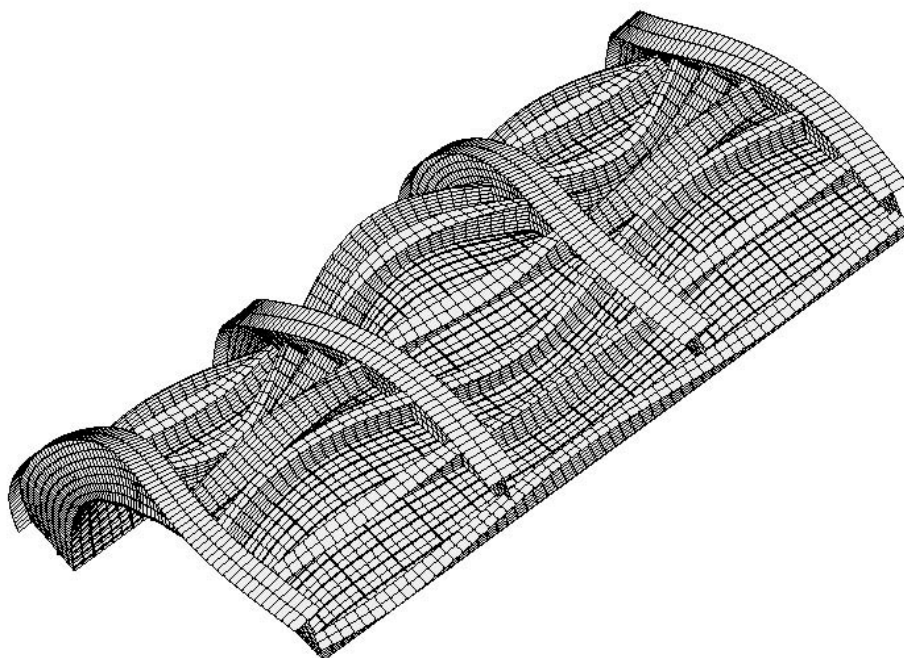


Fig. 4 STAGS model, threexninebay.testax4p.substiffbeams.majorstiffshells.410, mode 1, Pcr = 1.0259

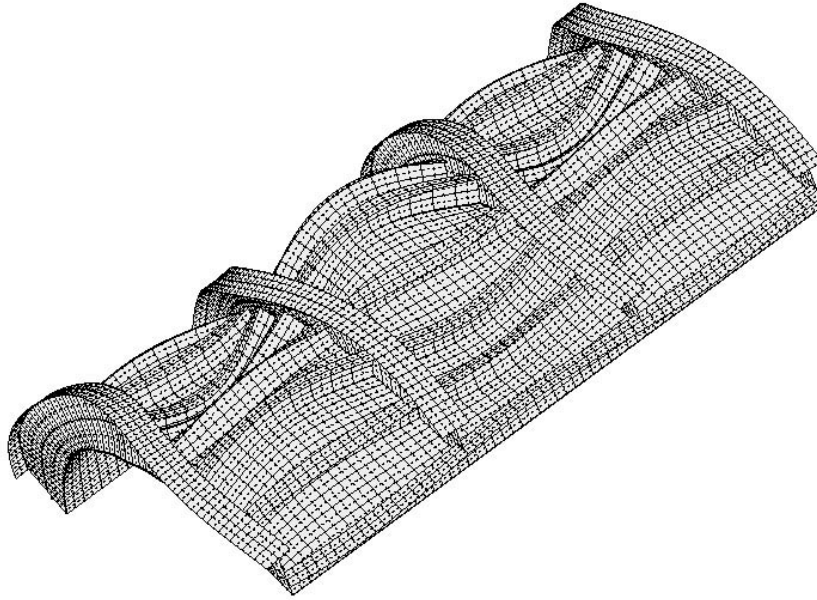


Fig. 5 STAGS model, threexninebay.testax4p.substiffsmearred.majorstiffshells.480, mode 1, Pcr = .98903

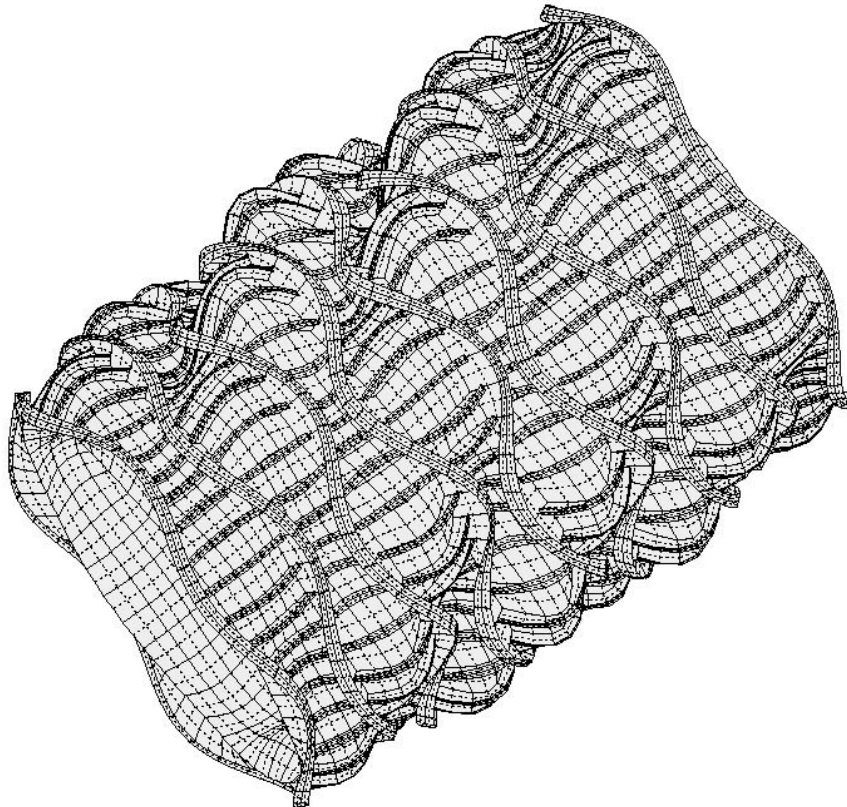


Fig. 6 STAGS model, entireshell.testax4p.substiffsmearred.majorstiffshells.480, mode 1, Pcr = 1.0222

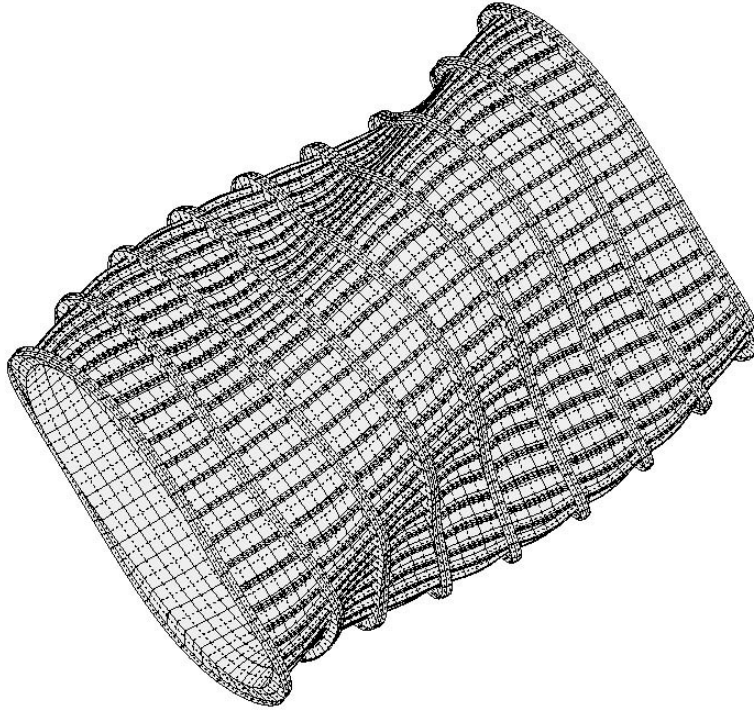


Fig. 7 STAGS model, entire shell, entire shell, testax4p.substiffsmearred.majorstiffshells.480, mode 19, $P_{cr} = 1.0511$

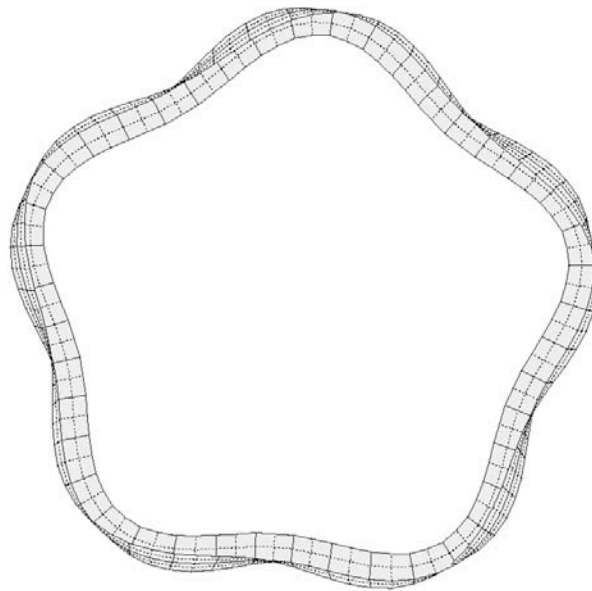


Fig. 8 STAGS model, fourth ring, entire shell, testax4p.substiffsmearred.majorstiffshells.480

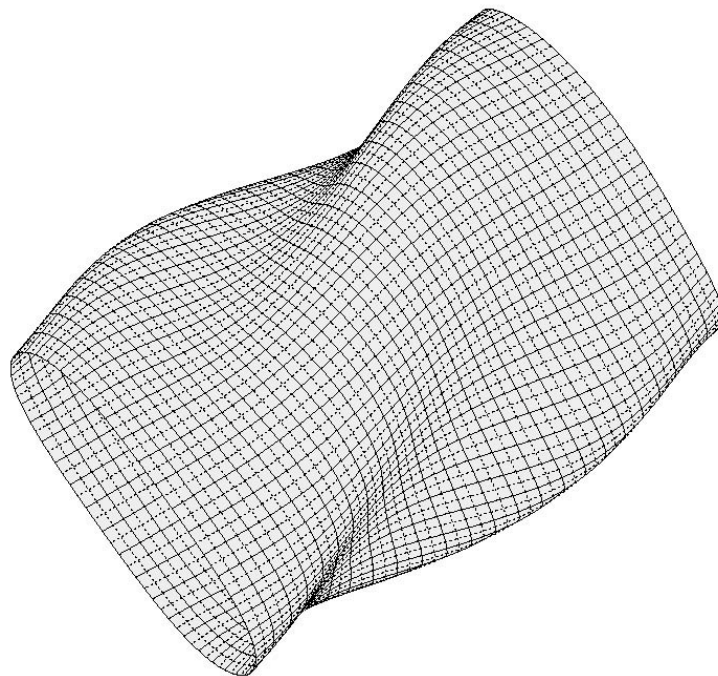


Fig. 9 STAGS model, entireshell.testax4p.allstiffsmear.480, mode 1, $P_c = 1.2883$

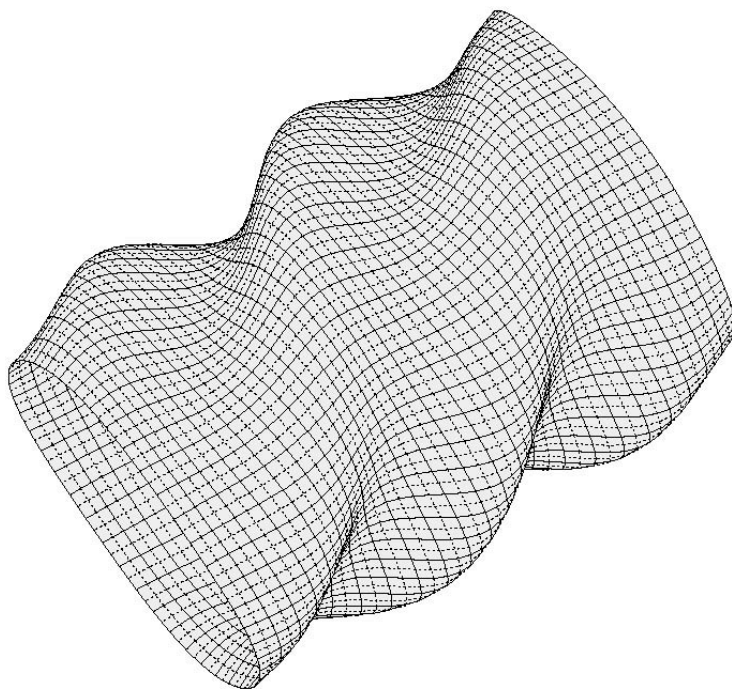


Fig. 10 STAGS model, entireshell.testax4p.allstiffsmear.480, mode 3, $P_c = 1.3714$

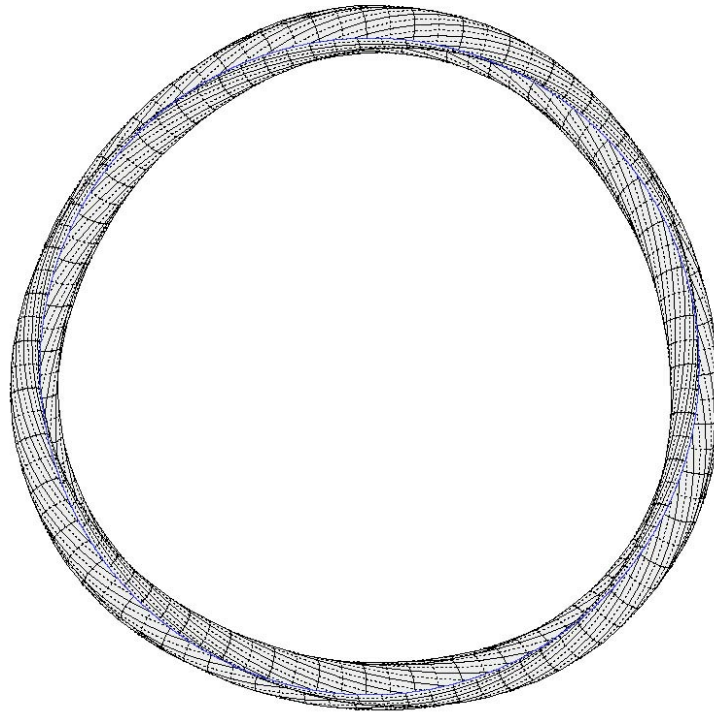


Fig. 11, End view of model in Fig. 10

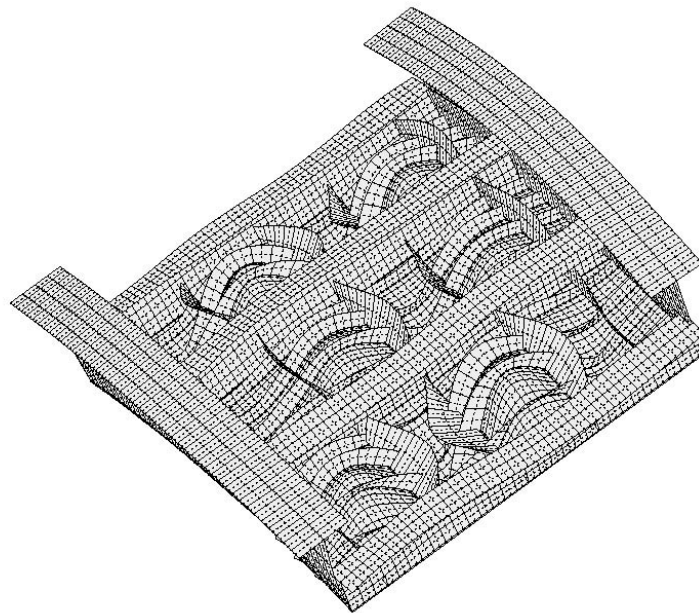


Fig. 12 STAGS model, interring.testax4p.allshells.1x3bays.fasteners.480, mode 4, $P_{cr} = 1.0278$

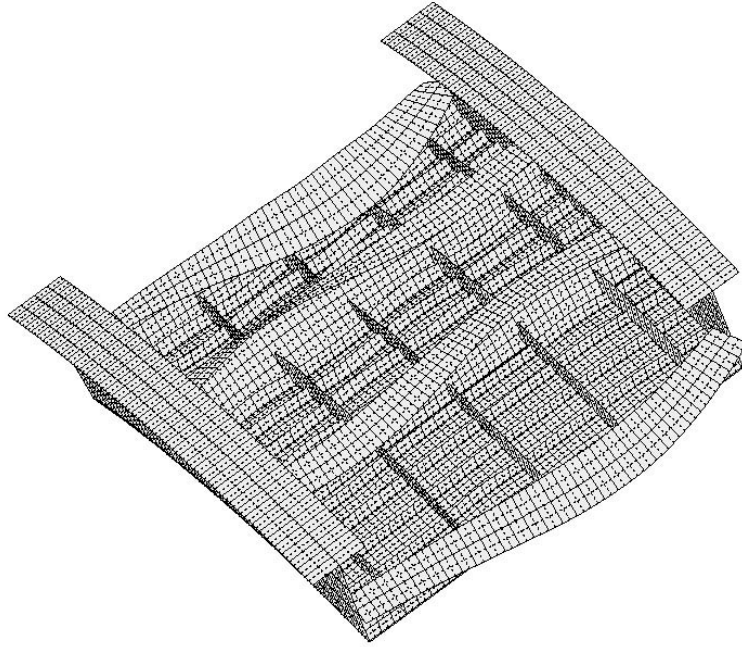


Fig. 13 STAGS model, interring.testax4p.allshells.1x3bays.fasteners.480 mode 16, $P_{cr} = 1.1668$

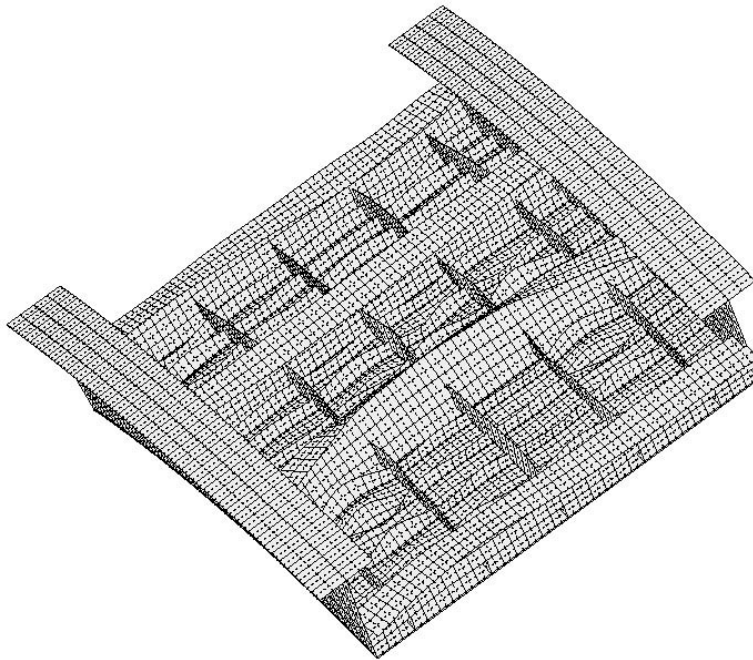


Fig. 14 STAGS model, interring.testax4p.allshells.1x3bays.fasteners.480 mode 34, $P_{cr} = 1.3113$

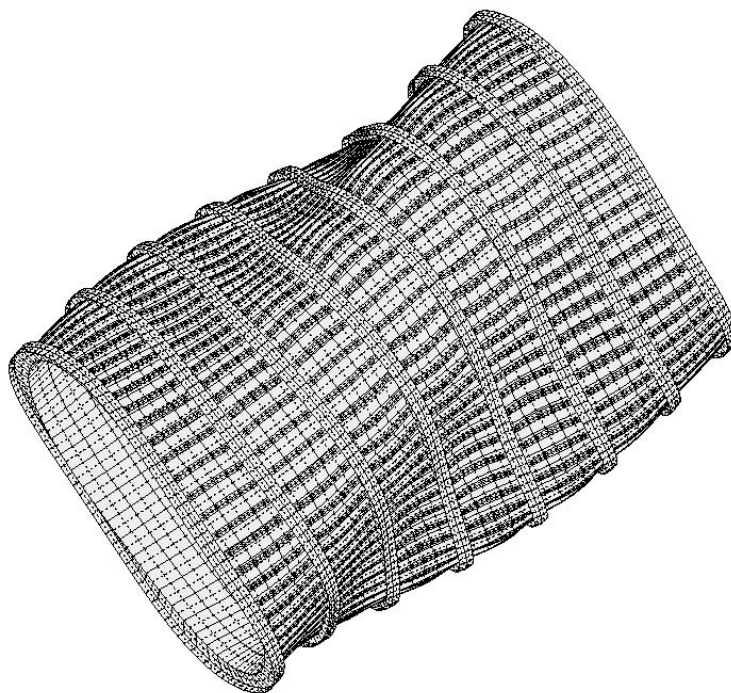


Fig. 15 STAGS model, entireshell.testax4.substiffsmearred.majorstiffshells.480, mode1, Pcr = 1.4468

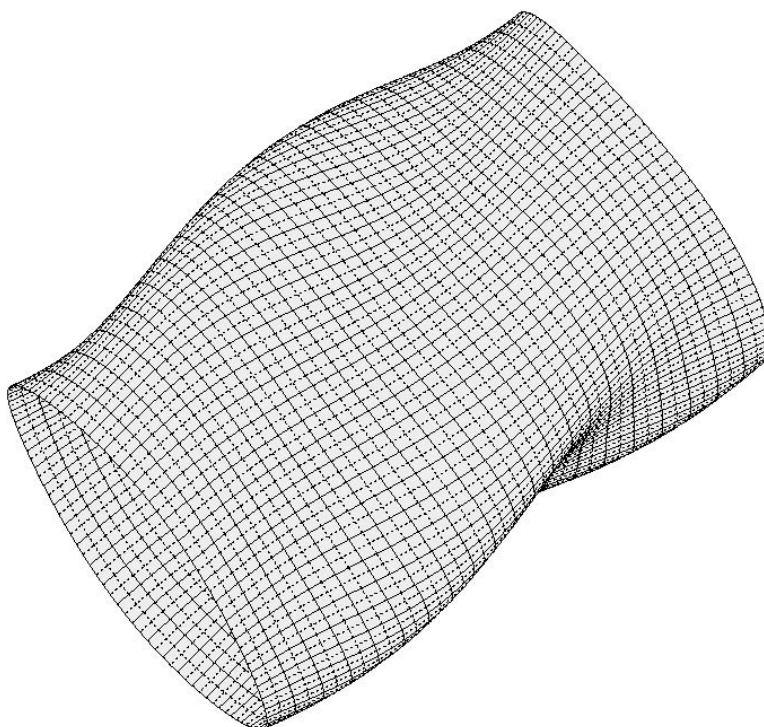


Fig. 16 STAGS model, entireshell.testax4.allstiffsmearred.480, mode 1, Pcr = 1.8058

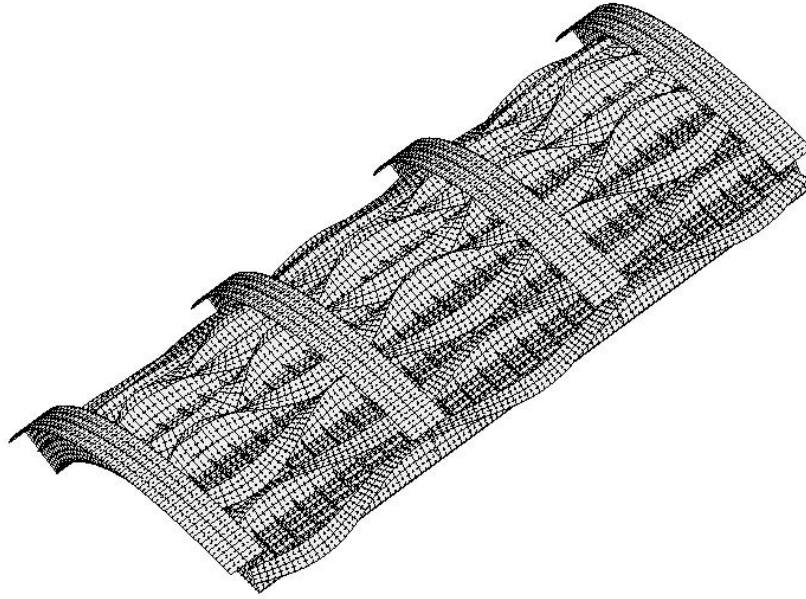


Fig. 17 STAGS model, threexninebays.testax4.allshells.fasteners.480, mode 2 $P_{cr} = 1.2557$

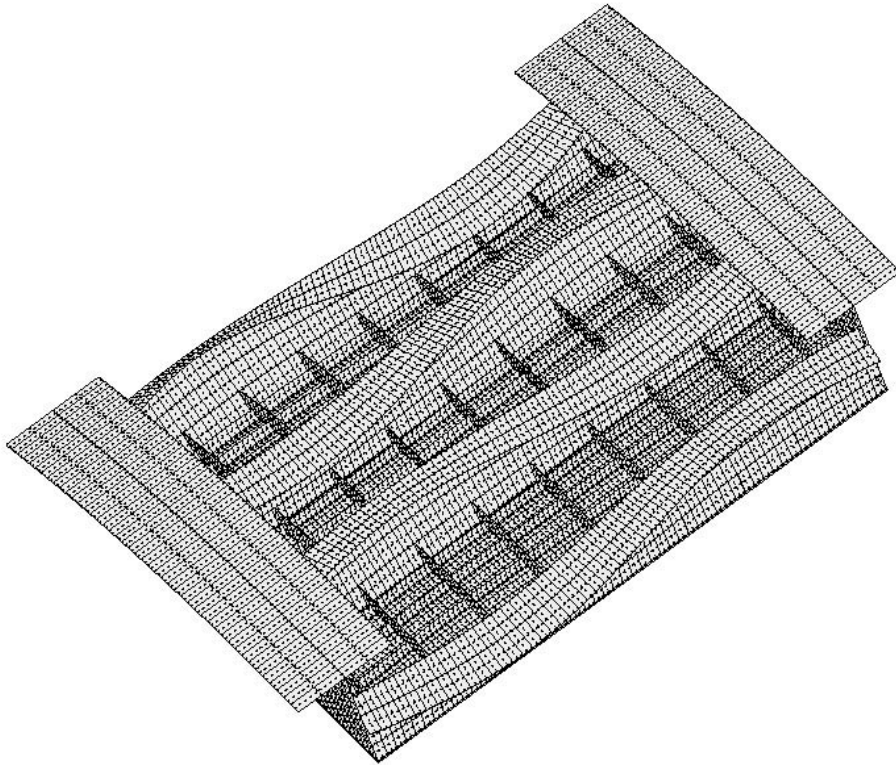


Fig. 18 STAGS model, interrering.testax4.allshells.1x3bays.fasteners.480, mode 1, $P_{cr} = 1.2757$

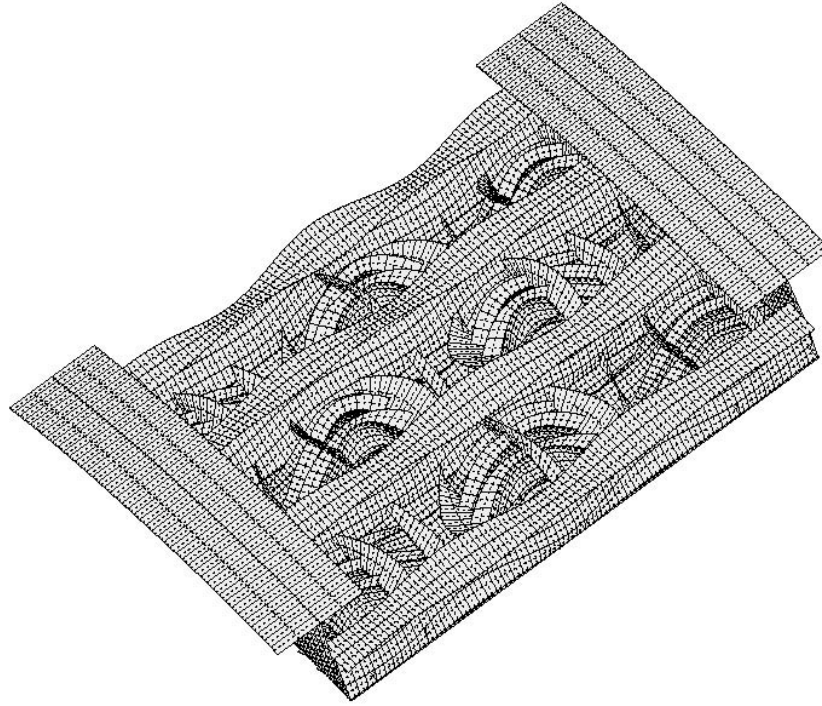


Fig. 19 STAGS model, interring.testax4.allshells.1x3bays.fasteners.480, mode 3, Pcr = 1.3099

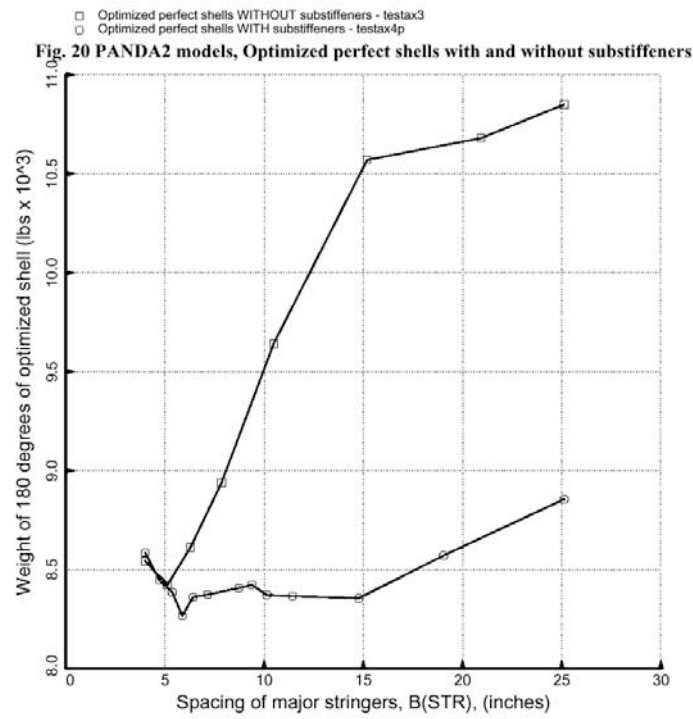


Fig. 20 PANDA2 models, optimized perfect shells with and without stiffeners

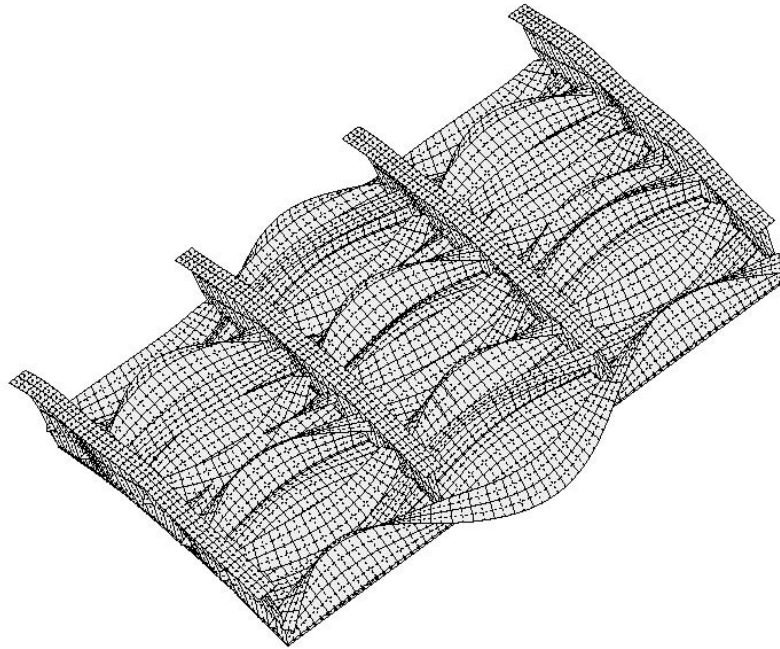


Fig 21 STAGS model, threexninebays.testax3.allshells.fasteners.480, mode 1, Pcr = 1.0042

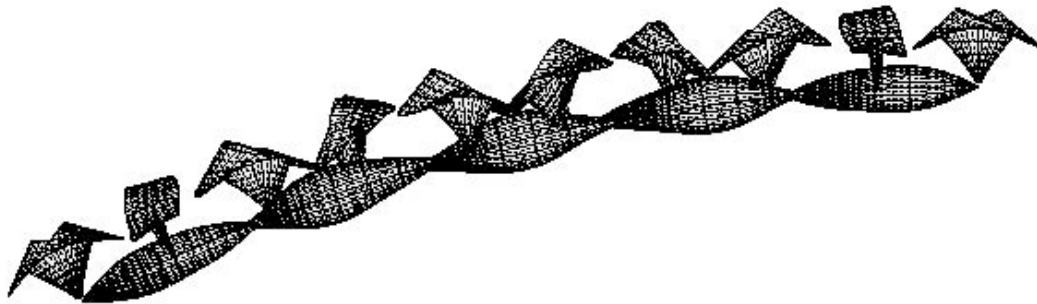


Fig 22, STAGS model, threexninebays.testax3.allshells.fasteners.480.perfect, mode 1, Pcr = 1.0042

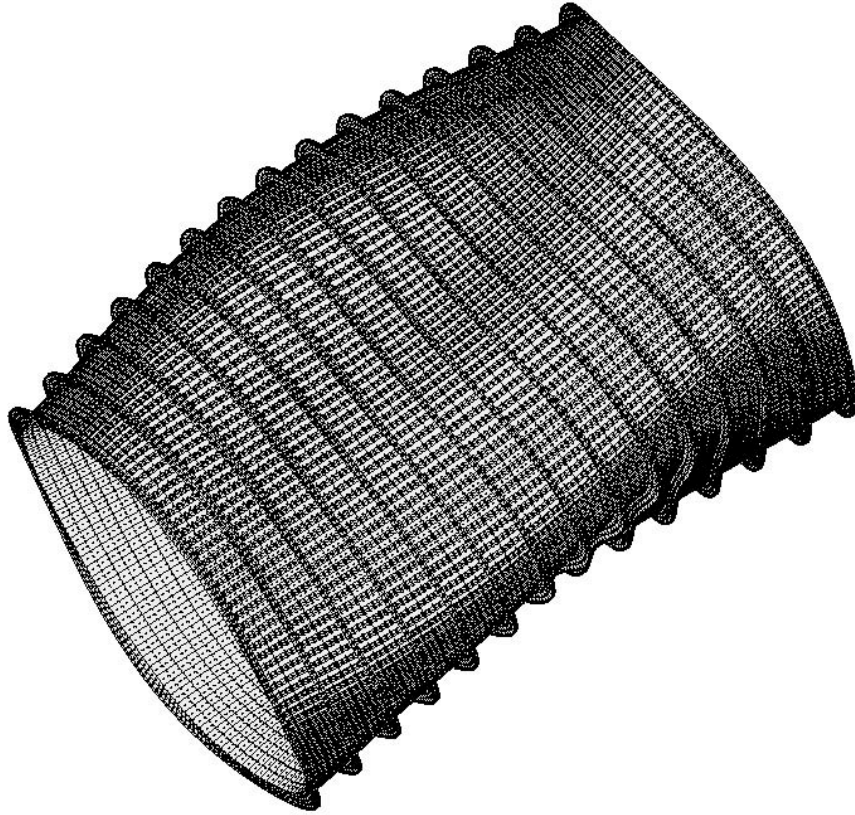


Fig. 23 STAGS model, testax3.perfect.allshells.480, mode 25, $P_{cr} = 1.0606$



Fig. 24 STAGS model, testax3.perfect.allshells.480, mode 1, $P_{cr} = 1.0512$

Buckling Behavior of Composite Laminated Stiffened Panels under Combined Shear and Axial Compression

H. Abramovich^{*} and T. Weller[†]
Technion, I.I.T., Haifa, Israel, 32000

and

C. Bisagni[‡]
Politecnico di Milano, Milano, Italy, 20156

Experimental results on the behavior of four torsion boxes, each comprising of two stringer stiffened cylindrical graphite-epoxy composite panels that have been subjected to torsion, axial loading and their combinations are reported. The buckling and post buckling behavior of these torsion boxes demonstrated consistent results. Prior to performing the buckling tests, the initial geometric imperfections of the boxes were scanned and recorded. The tests were complemented by finite element calculations, which were performed for each box. These detailed calculations have also assisted in identifying critical regions of the boxes and the boxes were reinforced accordingly to avoid their premature failure. The tests indicated that: the torsion carrying capacity is laminate lay-up dependent; axial compression results were in very good agreement with previous tests performed with single identical panels; and that the boxes have a very high post-buckling carrying capacity.

Nomenclature

CCW	=	counter clockwise direction of the applied torque
CW	=	clockwise direction of the applied torque
E_{11}	=	Young's modulus in the principal direction
E_{22}	=	Young's modulus in the minor direction
G_{12}	=	shear modulus
L	=	total length
L_{al}	=	arc length
L_n	=	nominal length
P_{const}	=	constant axial compression
P_{cr}	=	critical axial compression
R	=	panel radius
T_{const}	=	constant torque
T_{cr}	=	critical torque
ν_{12}	=	major Poisson's ratio

I. Introduction

L OADING of single curved panels, which represent a non-symmetric structure, in buckling tests poses a tough

^{*} Professor, Faculty of Aerospace Engineering, Technion City, AIAA Senior Member.

[†] Professor, Faculty of Aerospace Engineering, Technion City, AIAA Associate Fellow.

[‡] Professor, Department of Aerospace Engineering, Via La Masa 34, and AIAA Member .

problem, particularly when they represent a segment of a structure, e.g. fuselage and conclusions from the tests have to be drawn for the full structure. Therefore, though being much more complicated in testing, it is more appropriate to test symmetric closed type structures, which consist of two or more identical panels. This approach has been adopted in the present test program.

Experimental and theoretical investigations on buckling and post-buckling behavior of composite-stiffened-curved panels and shells are quite scarce (all of which are concerned with aerospace applications) and are barely documented in the open literature. Among these are the analytical and experimental studies carried out at the Aircraft Division of the Northrop Corporation, Hawthorne, California, by Agarwal¹; at the NASA Langley Research Center by Knight and Starnes²; the joint programs of NASA Langley Research Center, Lockheed Engineering and Sciences Company and Boeing Commercial Airplane group and the Douglas Aircraft Company in California and the ALENIA Company in Italy which were reported by McGowan et al.³ and by Bucci and Mercuria⁴; the studies conducted by Israel Aircraft Industries together with the Aerospace Structures Laboratory, Technion, Israel that are discussed in Chapter 14 of (Ref. 5) and the other studies cited in this reference; and the recent studies performed within the framework of the POSICOSS consortium funded by the 5th EU initiative program, that were reported in (Refs. 6-14).

The present study presents the results of tests on four torsion boxes under various combinations of axial and shear loads, the local buckling of their skins; their behavior in post-buckling under combined loading and their collapse under torsion. These tests have also been conducted within the framework of the POSICOSS consortium. The tests aimed at demonstrating the safe operation of post-buckled composite cylindrical stiffened panels, as well as providing a data base for the development of "fast tools" for the design of this type of structures.

II. Specimens and Test Set-up

Within the framework of the POSICOSS effort, Israel Aircraft Industries (IAI) has designed and manufactured 12 Hexcel IM7 (12K)/8552(33%) graphite-epoxy stringer stiffened composite panels, using a co-curing process. The nominal radius of each panel was $R=938$ mm and its total length $L=720$ mm (which included two end supports having the height of 30 mm, each). The nominal test length was $L_n=680$ mm and the panel arc-length was $L_{al}=680$ mm. The skin lay-up was quasi-isotropic ($0^\circ, \pm 45^\circ, 90^\circ$)_s. Each layer had a nominal thickness of 0.125 mm. Eight of these panels were used to form 4 torsion boxes, with co-cured stringers. Each box consisted of two curved stringer-stiffened curved panels that were connected together by two flat non-stiffened aluminum side plates.

Two of the boxes comprised of panels with blade type stringers (see Fig. 1a), one box had short flange "J" type stringers (see Fig. 1b) and the 4th box had long flange "J" type stringers (see Fig. 1c). The dimensions and properties of the panels are given in Table 1.

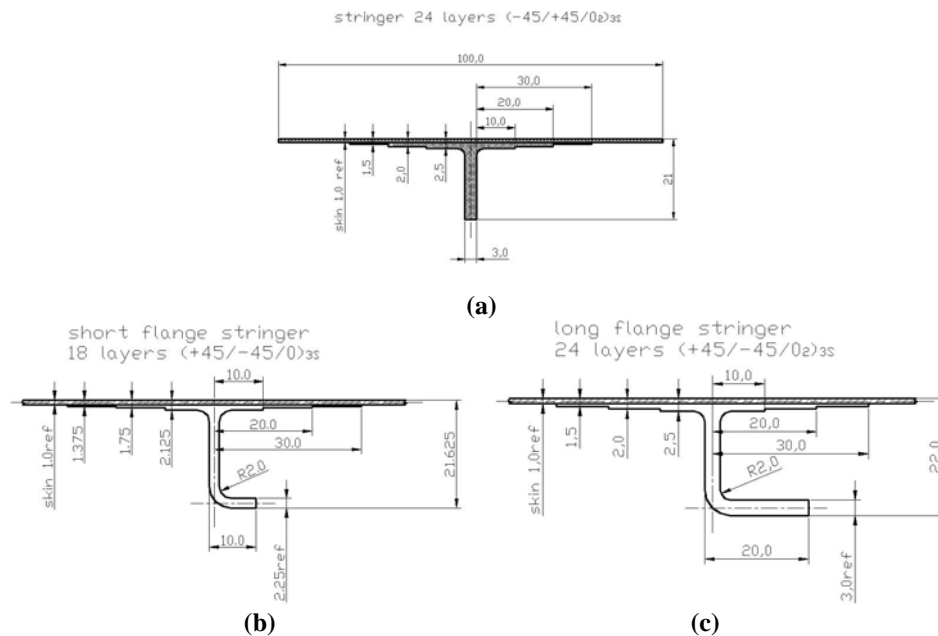


Figure.1 Dimensions, geometry and lay-ups of panels:

(a) BOX 1 and BOX 2, (b) short flange stringer ,BOX 3, (c) long flange stringer , BOX 4

Table 1- Data used for load calculations of torsion boxes BOX 1 - BOX 4

	Stringer type		
	Blade	Small flange "J"	Large flange "J"
Specimens	BOX1, BOX2	BOX3	BOX4
Total panel length	720mm	720mm	720mm
Free panel length	660mm	660mm	660mm
Radius	938mm	938mm	938mm
Arc length	680mm	680mm	680mm
Number of stringers	5	5	4
Stringer distance	136mm	136mm	174mm
Laminate lay-up of skin	[0,45,-45,90] _s	[0,45,-45,90] _s	[0,45,-45,90] _s
Laminate lay-up of stringer	[45,-45,0 ₂] _{3s}	[45,-45,0] _{3s}	[45,-45,0 ₂] _{3s}
Ply thickness	0.125mm	0.125mm	0.125mm
Type of stringer	blade	J-stringer	J-stringer
Stringer height	20mm	20.5mm	20.5mm
Stringer feet width	60mm	60mm	60mm
Stringer flange width	---	10mm	20mm
E ₁₁	147300 N/mm ²	147300 N/mm ²	147300 N/mm ²
E ₂₂	11800 N/mm ²	11800 N/mm ²	11800 N/mm ²
G ₁₂	6000 N/mm ²	6000 N/mm ²	6000 N/mm ²
ν ₁₂	0.3	0.3	0.3

Each panel was stiffened by 5 stringers, except for the panel with the long flange "J" type stringers which had only 4 stringers. Since each pair of panels was tested as a part of a closed box, it is assumed that by applying a torque to the box, the two panels were subjected to "identical" shear. Various tests were performed with each box before reaching its collapse under torsion, including combined axial compression and torsion loadings. For each box, the first buckling load was observed in the skin, for axial compression only, torsion only and combinations of axial compression and torsion, while the collapse test was normally performed under torsion only.

The four torsion boxes were tested at the laboratory of Politecnico di Milano employing their controlled position and loading equipment [6] (see Fig. 2).

The way the shear stresses were introduced into the torsion boxes is schematically depicted in Fig. 3. Four aluminum blocks were bolted to the upper and lower heavy loading plates of the loading machine. The blocks were closely tightened against the aluminum loading end pieces of the boxes. Thus, when rotating the lower loading plate of the machine, the loading blocks bolted to it reacted against the lower box end pieces and thus introduced torsion into the lower end of the box. At the same time the aluminum loading blocks, which were bolted to the fixed upper machine loading plate, reacted against the upper box end pieces and prevented the upper end of the box from rotating. Thus the box was exposed to a couple that introduced a torque into it and consequently uniform shear stresses into the curved panels.

Prior to performing the buckling tests, a comprehensive failure analysis of the torsion boxes was conducted, indicating high local stresses at the corners of each panel. Those corners were subsequently reinforced locally, outside and inside, by bonded aluminum patches (see Fig. 4).

During the tests, the values of axial displacement, rotation, axial compression load and torque of the box were measured by LVDT's and a load cell.

Eighty strain gages were bonded back to back, both on the skin and on the stringers of each panel. The strain gages map and the LVDT's locations are shown in Fig. 5, while Fig. 6 depicts a photo of the panel with the bonded strain gages.

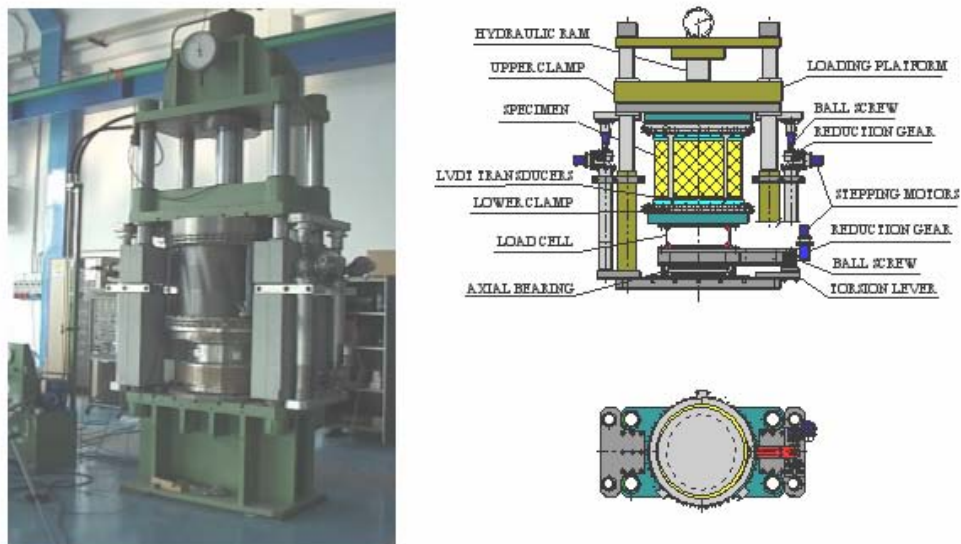


Figure 2- The loading equipment at the laboratory of Politecnico di Milano

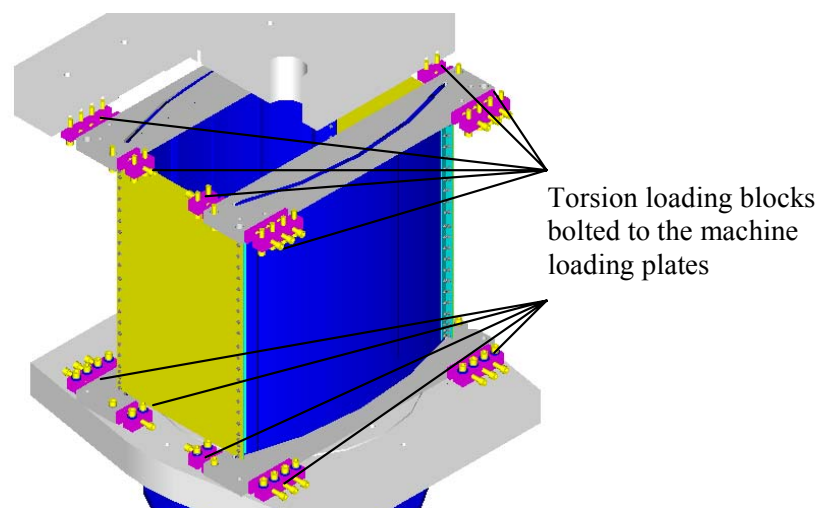


Figure 3- Schematic drawing of the torsion box, indicating the way torsion is transferred into the curved stringer stiffened panels

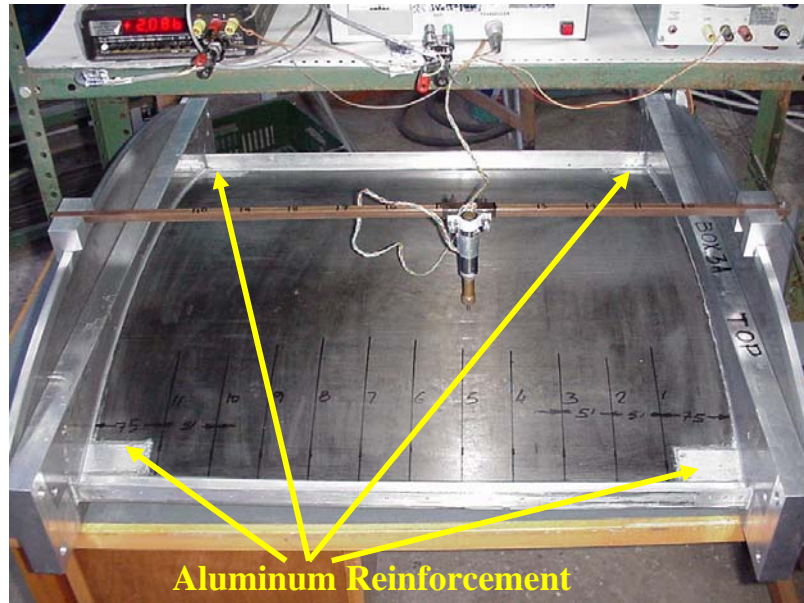


Figure 4- Panel A of Box-3 in the set up for measurement of initial geometric imperfections. Note the four aluminum reinforcements at the corners of the panel.

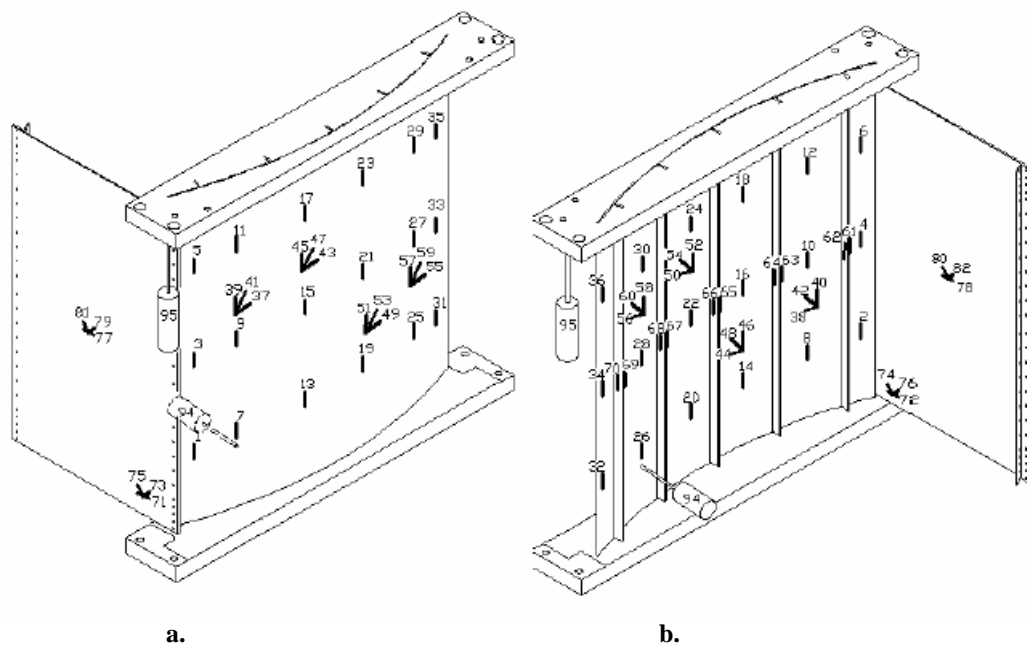


Figure 5– Typical strain gages and LVDT's locations: a. external view, b. internal view



Figure 6- Panel with side aluminum plate and bonded strain gages

III. Results

Tables 2-5 summarize the experimentally observed buckling loads of the four torsion boxes.

Typical results experienced in the tests are presented next. The experimental and numerical interaction curves obtained for the first buckling loads of BOX 1-BOX 4 (skin buckling) are presented in Figs. 7a-d. One should note the asymmetry of the numerical interaction curve calculated using the MSC NASTRAN finite element code, even for the blade type stringer stiffened panels. This asymmetry was barely experienced during the tests on the torsion boxes having blade type stringers, BOX 1 and BOX 2. It was more noticeable in the tests with BOX 3, with the smaller "J" stiffeners (see Fig. 7c) and quite pronounced in the tests of BOX 4 with large J stringers (see Fig. 7d).

Typical measurements of the strain gages are given in Fig. 8. It presents the results experienced by three pairs of strain gages (for reference see Fig. 5) of panel A BOX 1: gages 25 and 26 on the skin closer to the lower edge of the panel, gages 29 and 30 on the skin near the upper end of the panel and gages 63 and 64 located at the middle of the fifth blade type stringer. The results (see Table 2) are presented for axial compression only (Test 1), clockwise torsion only (Test 3) and combined axial compression and counter clockwise torsion (Test 6) in Figs 8a-c, respectively. For comparison, the counterpart strain gages readings of panel B BOX-1 are also presented in Figs. 8d-f at the same combinations of loading. Note that to make a correct comparison for the case of torsion only (Test 3), the readings of strain gages 7-8, 11-12, 69-80 of panel B were compared with their counterpart strain gages 25-26, 29-30 and 63-64 (see Fig. 5), respectively. As one can see, the readings of the strain gages on both panels, A and B of BOX 1 seem very similar, thus indicating that introduction of the loads into both panels was equal and balanced.

Moiré fringes, as shown in Fig. 9, were used to detect and identify the buckling and post-buckling patterns of each panel. Figs. 9a-h present the behavior and the associated changes in deformation patterns that was observed with increase in load.

Fig. 10 presents the typical collapse mode that was observed for panel A of Box 1.

Readings of the twist angle vs. the applied torsion that was observed in the collapse test of BOX 1 are presented in Fig. 11.

The experimental results were compared with predictions obtained by the finite element analyses performed using the ABAQUS code. Fig. 12 shows the moment as a function of the circumferential displacement (representing the twist angle), obtained by the ABAQUS code. The mode shapes at various critical points were also calculated. The numerical first skin buckling torque for BOX 1 and BOX 2 was evaluated at 13.2 kNm. It is in good agreement with the experimental ones, measured at 12.5 kNm and 14 kNm, respectively (see Tables 2 & 3). Collapse for this type of boxes was numerically obtained at 50 kNm, which is comparable with the experimental value experienced at 47.4 kNm for BOX 1(see Table 2).

To increase the accuracy of the numerical predictions, the refined F.E. model of Fig. 13 was used. This model was employed for the numerical predictions of Figs. 7a-d. It is simulating the connections and the stiffening of the side flat aluminum panels as can be seen in Fig. 14.

To simulate the connections and the stiffening of the side flat aluminum panels (see Fig. 14), four rows of nodes (three rows of elements) at the bottom part of the composite panels were clamped, whereas four rows of nodes at the upper part of the panel (three rows of elements) were connected together to form a rigid body with a reference node at the center of the box (see Fig. 13). The axial force and the torsion moment were applied at this reference node. The side flat aluminum panels were 3.3 mm thick and were connected with the composite panels 7 mm beneath the rigid body, so that no direct axial force was introduced into them during loading (see detail I and view A of Fig. 13). All of the elements of the model were "CQUAD4" shell type elements. For BOX 1 and BOX 2 11096 elements were used, while for BOX 3 and BOX 4 11816 elements and 10872 elements were employed, respectively. In general, the FE predictions yielded by this model that were applied in the present test program were found to be in good correlation with the experimental observed results for all of the loading combinations.

Table 2- Experimental Buckling Loads – BOX 1

Test No.	Initial P const. (kN)	Initial Tconst. (kNm)	Panel A Pcr(kN) or Tcr (kNm)	Panel B Pcr(kN) or Tcr (kNm)	Remarks
1	0	0	$P_{cr}=240.6$	$P_{cr}=268$	Pure axial compression test
2	11	0	-	$T_{cr}=12.5$ ($P_{const.}=10.5$)	CCW* "pure" torsion test
3	11	0	-	$T_{cr}=13.0$ ($P_{const.}=13.3$)	CW** "pure" torsion test
4	0	9 (CCW)	$P_{cr}=54.5$ ($T_{const.}=9$)	$P_{cr}=34$ ($T_{const.}=9$)	Constant torsion, buckling under axial compression
5	0	6 (CCW)	-	$P_{cr}=85$ ($T_{const.}=6$)	Constant torsion, buckling under axial compression
6	0	3 (CCW)	-	$P_{cr}=190$ ($T_{const.}=3$)	Constant torsion, buckling under axial compression
7	85	0	-	$T_{cr}=5.2$ ($P_{const.}=85$)	Constant axial compression, buckling under torsion (CCW)
8	34	0	-	$T_{cr}=7.6$ ($P_{const.}=34$)	Constant axial compression, buckling under torsion (CCW)
9	12	0	$T_{cr}=47.4$ ($P_{const.}=18.5$)	$T_{cr}=47.4$ ($P_{const.}=18.5$)	Collapse under torsion (CCW) with a small axial compression

*CCW –Counter clockwise; **CW - Clockwise

Table 3- Experimental Buckling Loads – BOX 2

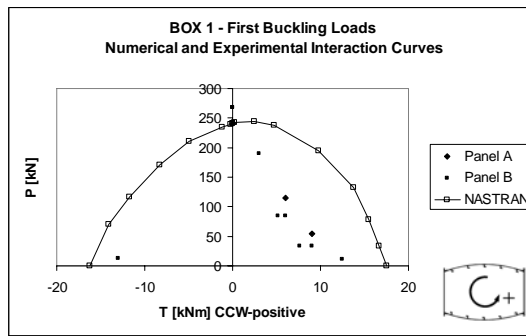
Test No.	Initial P const. (kN)	Initial Tconst. (kNm)	Panel A Pcr(kN) or Tcr (kNm)	Panel B Pcr(kN) or Tcr (kNm)	Remarks
1	0	0	$P_{cr}=231.0$	-	Pure axial compression test
2	15	0	-	$T_{cr}=14.0$ ($P_{const.}=16.2$)	CCW "pure" torsion test
3	15	0	-	$T_{cr}=18.0$ ($P_{const.}=18.0$)	CW "pure" torsion test
4	60	0	$T_{cr}=12.0$ ($P_{const.}=60$)	$T_{cr}=12.0$ ($P_{const.}=60$)	Constant axial compression, buckling under torsion (CCW)
5	120	0	$T_{cr}=7.4$ ($P_{const.}=120$)	$T_{cr}=7.4$ ($P_{const.}=120$)	Constant axial compression, buckling under torsion (CCW)
6	180	0	$T_{cr}=4.0$ ($P_{const.}=180$)	-	Constant axial compression, buckling under torsion (CCW)
7	180	0	$T_{cr}=48.0$ ($P_{const.}=182$)	$T_{cr}=48.0$ ($P_{const.}=182$)	Collapse under torsion (CCW) with a large axial compression

Table 4- Experimental Buckling Loads – BOX 3

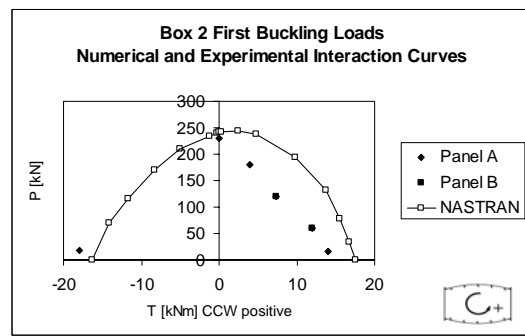
Test No.	Initial P const. (kN)	Initial Tconst. (kNm)	Panel A Pcr(kN) or Tcr (kNm)	Panel B Pcr(kN) or Tcr (kNm)	Remarks
1	15	0	$T_{cr}=12.8$ ($P_{const.}=13.5$)	-	CCW "pure" torsion test
2	15	0	$T_{cr}=15.0$ ($P_{const.}=16.2$)	$T_{cr}=20.0$ ($P_{const.}=16.3$)	CW "pure" torsion test
3	0	0	$P_{cr}=150.0$	$P_{cr}=200$	Pure axial compression test
4	0	4 (CCW)	$P_{cr}=87.0$ ($T_{const.}=4$)	-	Constant torsion, buckling under axial compression
5	0	7.5 (CCW)	$P_{cr}=65.0$ ($T_{const.}=7.5$)	$P_{cr}=68.0$ ($T_{const.}=7.5$)	Constant torsion, buckling under axial compression
6	0	11 (CCW)	$P_{cr}=50.6$ ($T_{const.}=7.5$)	$P_{cr}=50.6$ ($T_{const.}=7.5$)	Constant torsion, buckling under axial compression
7	16	0	$T_{cr}=51.2$ ($P_{const.}=21.3$)	$T_{cr}=51.2$ ($P_{const.}=21.3$)	Collapse under torsion (CCW) with a small axial compression

Table 5- Experimental Buckling Loads – BOX 4

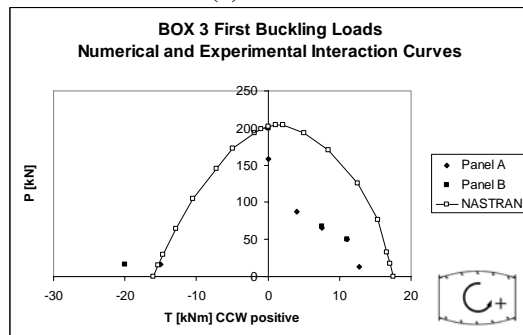
Test No.	Initial $P_{const.}$ (kN)	Initial $T_{const.}$ (kNm)	Panel A P_{cr} (kN) or T_{cr} (kNm)	Panel B P_{cr} (kN) or T_{cr} (kNm)	Remarks
1	0	0	$P_{cr}=115.0$	$P_{cr}=115.0$	Pure axial compression test
2	10	0	$T_{cr}=8.0$ ($P_{const.}=10.0$)	$T_{cr}=8.0$ ($P_{const.}=10.0$)	CCW "pure" torsion test
3	10	0	$T_{cr}=22.0$ ($P_{const.}=10.0$)	$T_{cr}=16.0$ ($P_{const.}=10.0$)	CW "pure" torsion test
4	0	4 (CCW)	$P_{cr}=70.0$ ($T_{const.}=4$)	$P_{cr}=50.0$ ($T_{const.}=4$)	Constant torsion, buckling under axial compression
5	0	2 (CCW)	$P_{cr}=80.0$ ($T_{const.}=2$)	$P_{cr}=74.0$ ($T_{const.}=2$)	Constant torsion, buckling under axial compression
6	0	6 (CCW)	$P_{cr}=50.0$ ($T_{const.}=6$)	$P_{cr}=60.0$ ($T_{const.}=6$)	Constant torsion, buckling under axial compression
7	60	0	$T_{cr}=5.4$ ($P_{const.}=60$)	$T_{cr}=3.0$ ($P_{const.}=60$)	Constant axial compression, buckling under torsion (CCW)
8	0	8 (CW)	$P_{cr}=130.0$ ($T_{const.}=8$)	$P_{cr}=121.0$ ($T_{const.}=8$)	Constant torsion, buckling under axial compression
9	0	12 (CW)	$P_{cr}=126.0$ ($T_{const.}=12$)	$P_{cr}=70.0$ ($T_{const.}=12$)	Constant torsion, buckling under axial compression
10	0	4 (CW)	$P_{cr}=120.0$ ($T_{const.}=4$)	$P_{cr}=130.0$ ($T_{const.}=4$)	Constant torsion, buckling under axial compression
11	10	0	$T_{cr}=69.0$ ($P_{const.}=15$)	$T_{cr}=69.0$ ($P_{const.}=15$)	Collapse under torsion (CCW) with a small axial compression



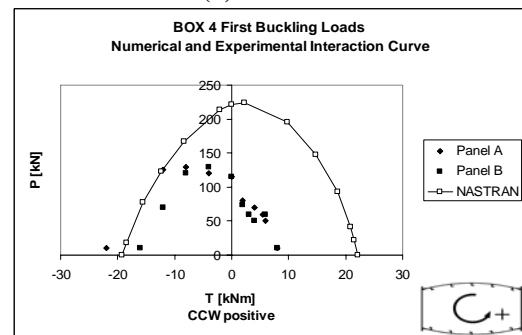
(a)



(b)

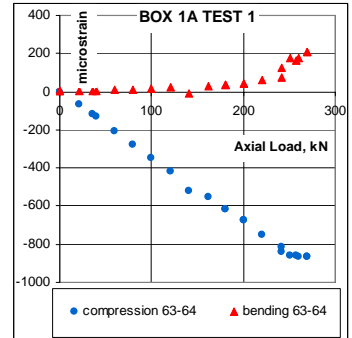
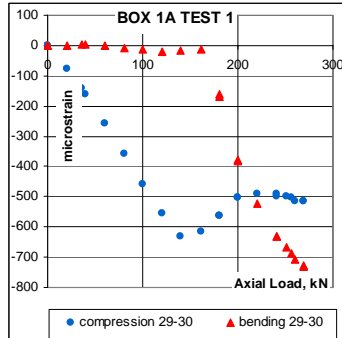
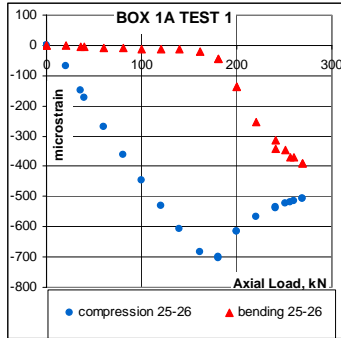


(c)

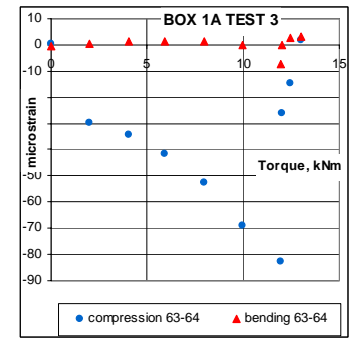
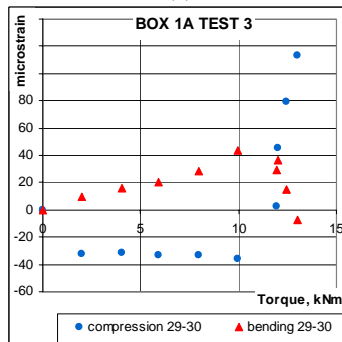
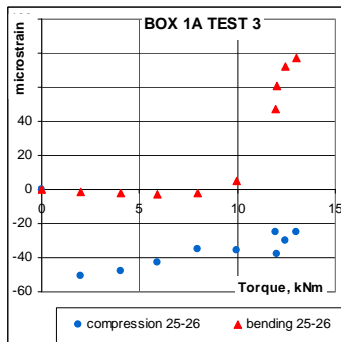


(d)

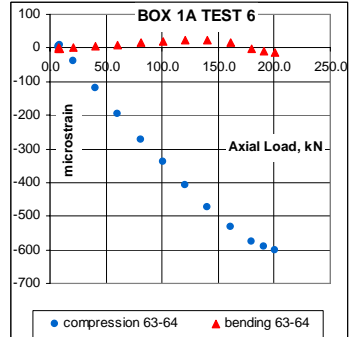
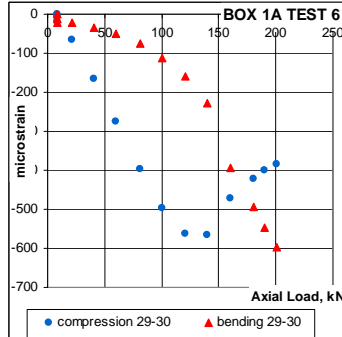
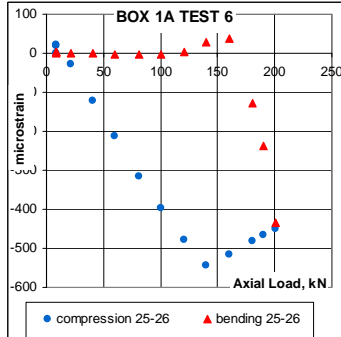
Figure 7– Typical experimental and numerical interaction curves: (a) BOX 1, (b) (a) BOX 2, (c) BOX 3, (d) BOX 4



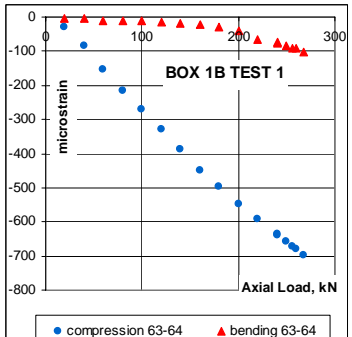
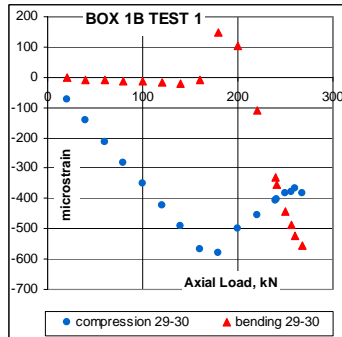
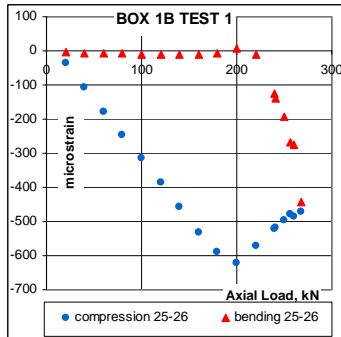
(a)



(b)



(c)



(d)

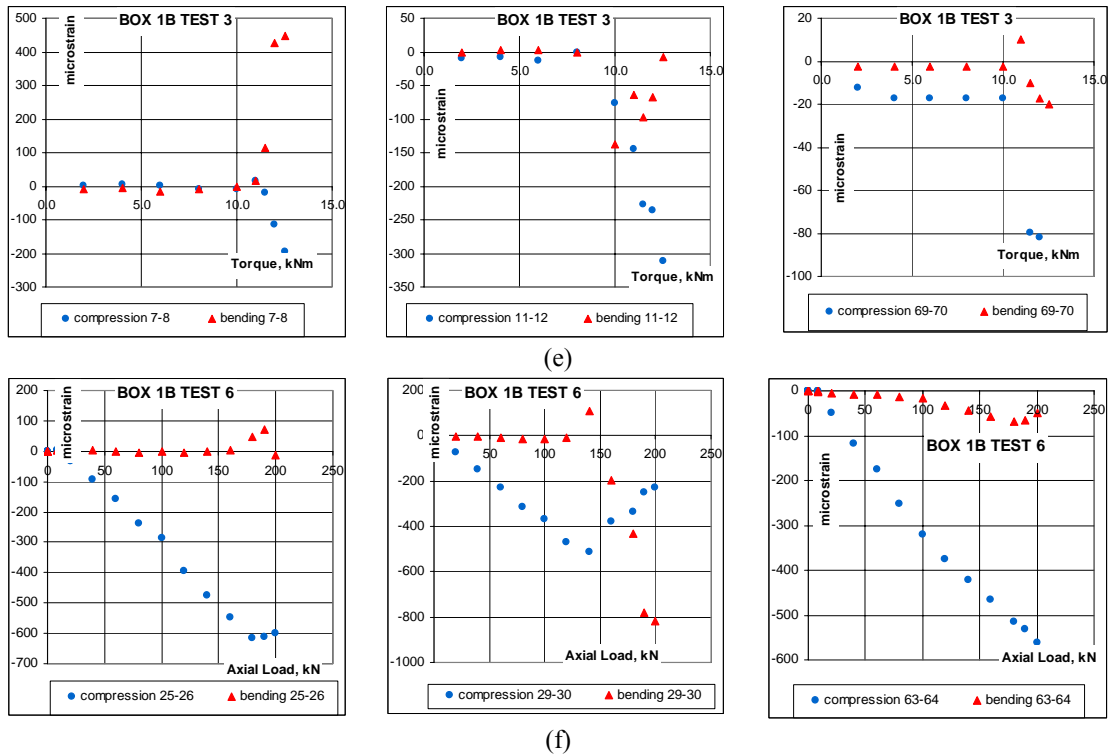


Figure 8- Typical strain gages measurements for axial compression and torsion:
a. Test 1, b. Test 3, c. Test 6— panel A BOX 1; d. Test 1, e. Test 3, f. Test 6— panel B BOX 1

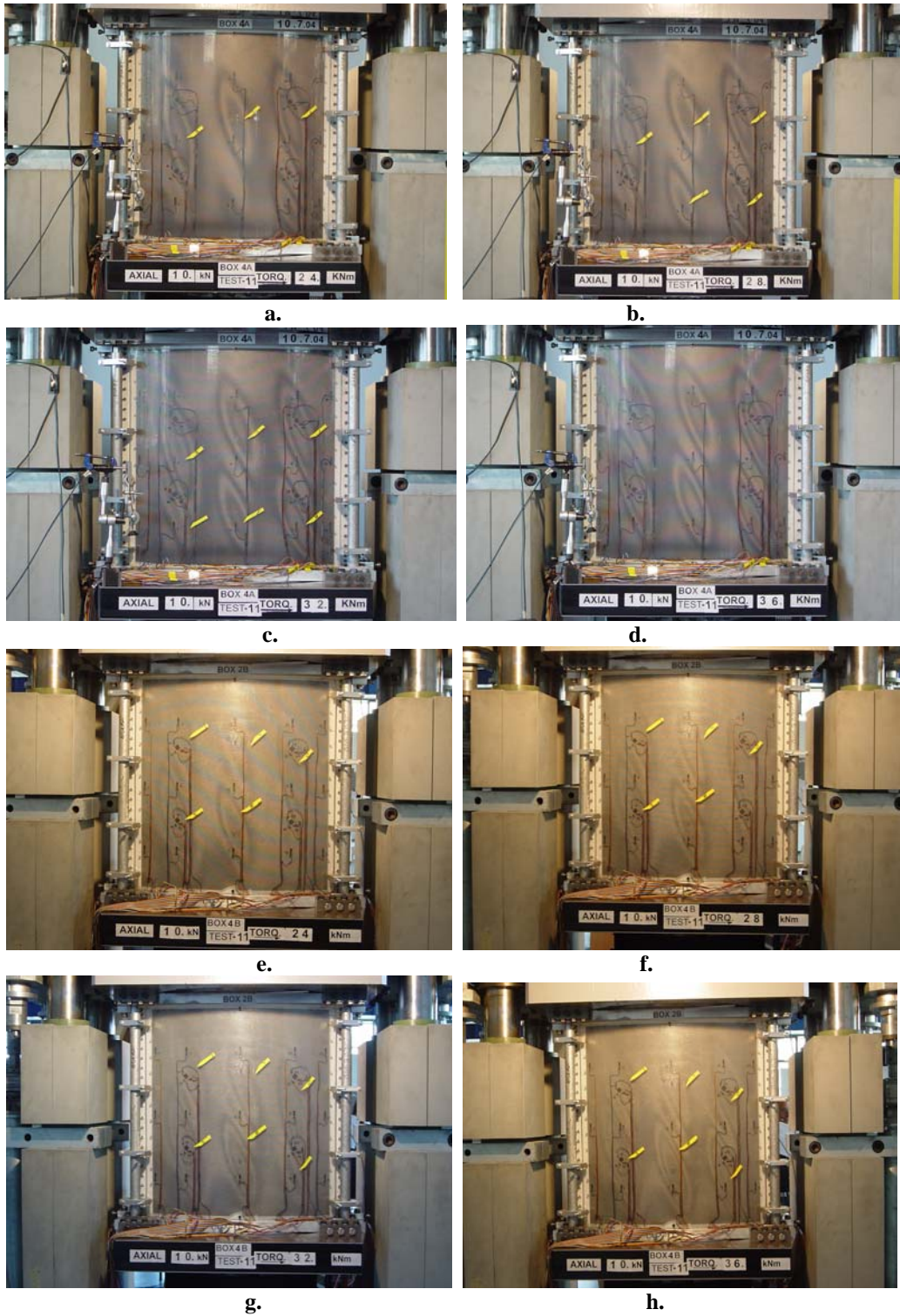


Figure 9- Typical post-buckling patterns in Test 11 of BOX 4, constant axial compression 10 kN and increasing torque: a-d panel A at 24, 28, 32 and 36 kN-m, f-h panel B at 24, 28, 32 and 36 kN-m, respectively.



Figure 10- Typical collapse pattern –BOX 1

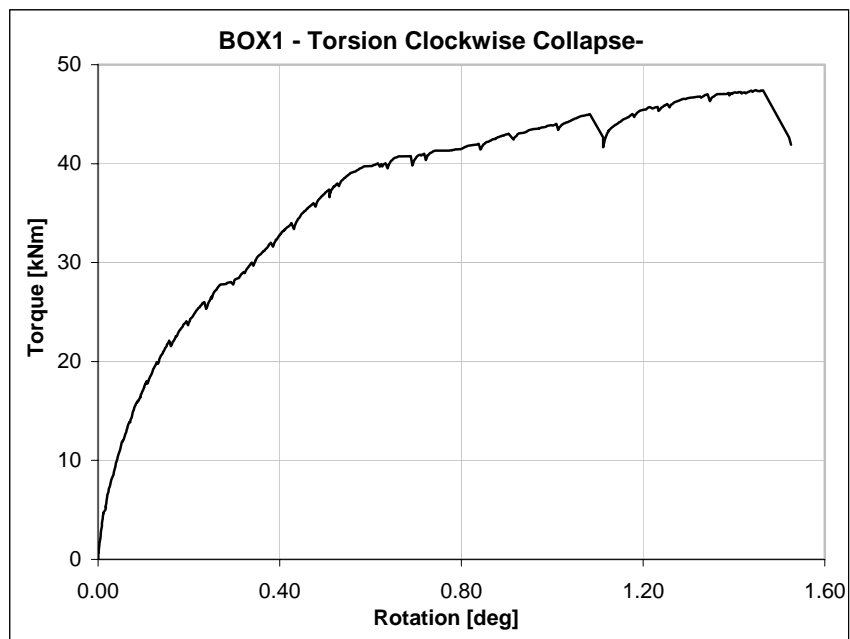


Figure 11- Torque vs. rotation angle – BOX 1

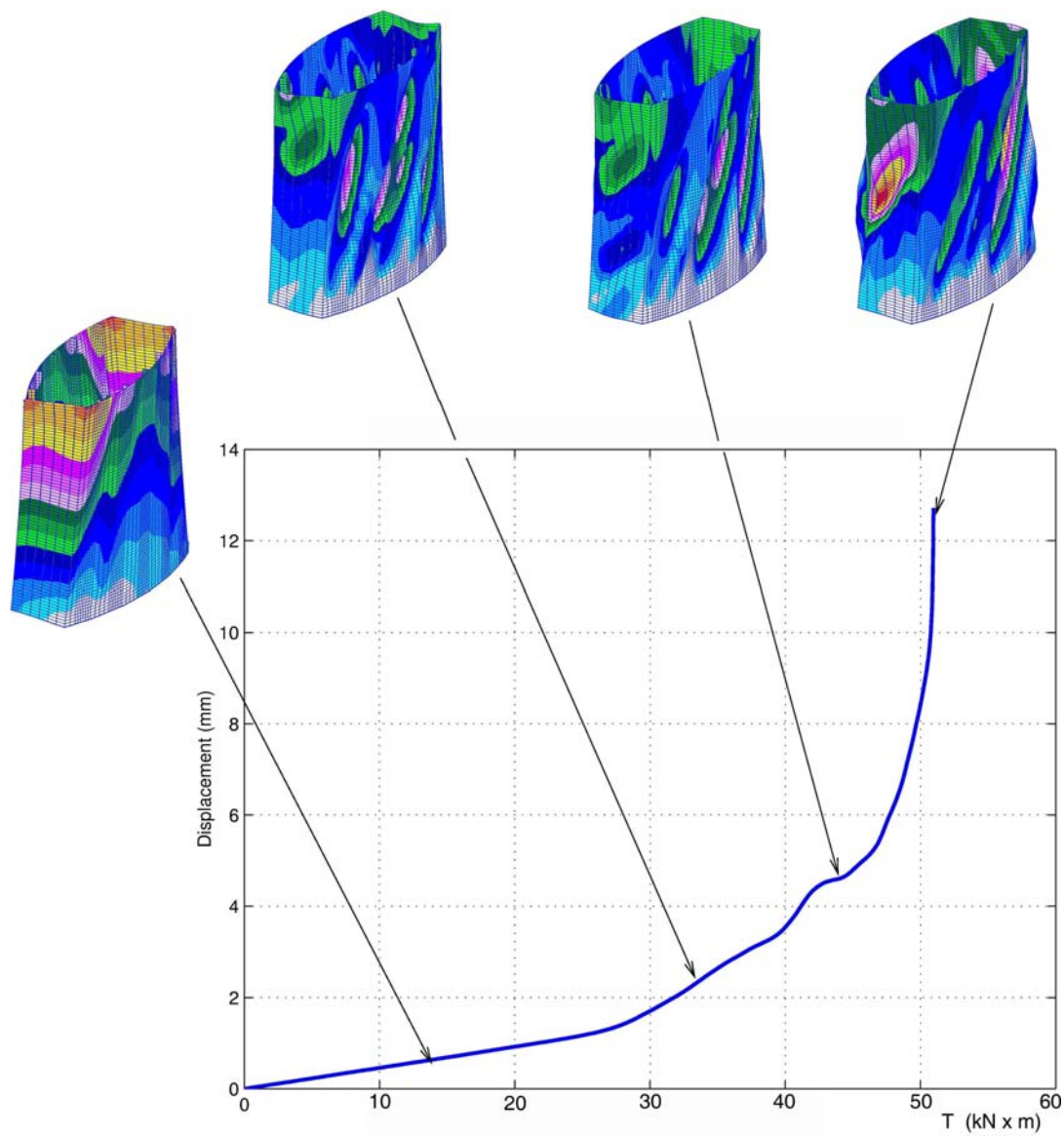


Figure 12- ABAQUS results: torque vs. circumferential displacement and associated mode shapes at various critical points – BOX 1 and BOX 2

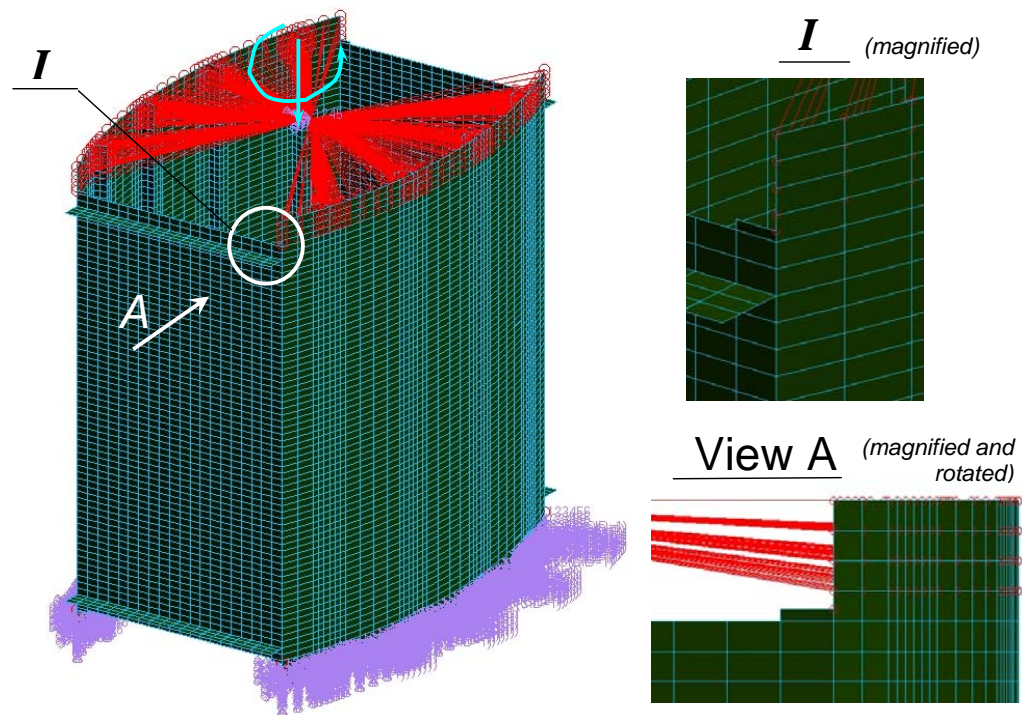


Figure 13- Refined finite element model

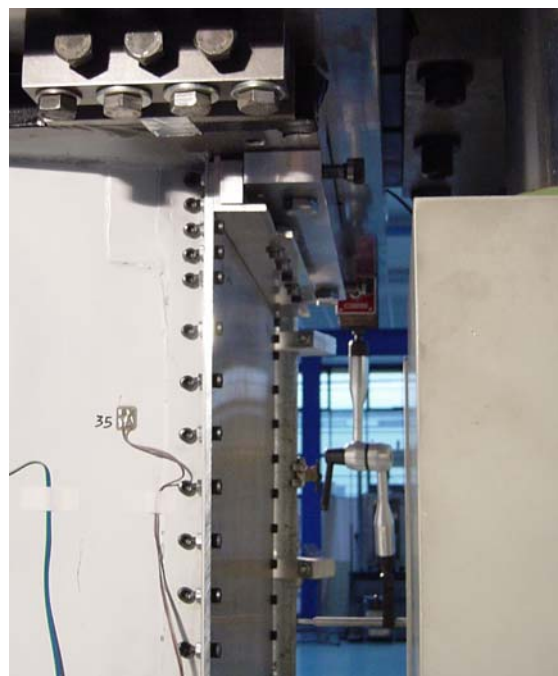


Figure 14- Details of the stiffening and the connections of the side flat aluminum plate

IV. Conclusions

The behavior of four torsion boxes, each comprising of two stringer stiffened cylindrical graphite-epoxy composite panels that have been subjected to torsion, axial loading and their combinations, have been investigated both experimentally and numerically.

The buckling and post buckling behavior of these torsion boxes demonstrated consistent results.

Detailed finite element calculations have assisted in identifying critical regions of the boxes and the boxes were reinforced accordingly to avoid their premature failure.

The tests indicated that the torsion carrying capacity is laminate lay-up dependent, axial compression results were in very good agreement with previous tests performed with single identical panels and that the boxes have a very high post-buckling load carrying capacity.

Comparisons of the experimentally experienced buckling loads with those predicted numerically by finite element analyses were found to be in good agreement.

Acknowledgement

This work was partly supported by the European Commission, Competitive and Sustainable Growth Programme, Contract No. G4RD-CT-1999-00103, project POSICOSS (<http://www.posicoss.de>). The information in this paper is provided as is and no guarantee or warranty is given that the information is fit for any particular purpose. The user thereof uses the information at its sole risk and liability.

References

- 1 Agarwal, B.L., Postbuckling Behavior of Composite-Stiffened Curved Panels Loaded in Compression, *Experimental Mechanics*, Vol. 22, 1982, pp.231-236.
- 2 Knight, N.F., Jr. and Starnes, J.H., Jr., Postbuckling Behavior of Selected Curved Stiffened Graphite-Epoxy Panels Loaded in Axial Compression, *AIAA Journal*, Vol. 26, No. 3, March 1988, pp.344-352.
- 3 McGowan, D.M., Young, R.D., Swancon, G.D. and Waters, W.A., Compression Tests and Nonlinear Analysis of a Stringer-and Frame-Stiffened Graphite Epoxy Fuselage Crown Panel, 5th NASA/DoD Advanced Composite Technology Conference, Seattle, Wash., August 22-25 1994, Paper No. A94-33140.
- 4 Bucci, A and Mercuria, U., CFRP Stiffened Panels under Compression, in : *The Utilization of Advanced Composites in Military Aircraft*, AGARD-785, San Diego, Calif., Oct. 7-11, 1996, 12-1-12-14.
- 5 Singer, J., Arbocz, J., and Weller, T., *Buckling Experiments – Experimental Methods in Buckling of Thin-Walled Structures*, Vol. 2, 2002, John Wiley & Sons Inc.
- 6 Abramovich, H., Grunwald, A., Pevsner, P., Weller T., David, A., Ghilai, G., Green, A., and Pekker, N., Experiments on Axial Compression Postbuckling Behavior of Stiffened Cylindrical Composite Panels, *Proceeding of 44th AIAA/ASME/ASCE/AHS Structures, Structural Dynamics and Material Conference*, Norfolk, VI, USA, AIAA paper No. 2003-1793.
- 7 Bisagni, C., and Cordisco, P., An Experimental Investigation into the Buckling and Post-Buckling of CFRP Shells under Combined Axial and Torsion Loading, *Composite Structures*, Vol. 60, 2003, pp. 391-402.
- 8 Gal, E., Levy, R., Abramovich, H. and Pevsner, P., Buckling of Composite Stiffened Panels: Analysis and Experiment, *International Conference on Buckling and Postbuckling Behavior of Composite Laminated Shell Structures March 1 – 2, 2004 Hilton Queen of Sheba Hotel, Eilat, Israel*.
- 9 Zimmermann, R. and Rolfes, R., POSICOSS - Improved Postbuckling Simulation for Design of Fibre Composite Stiffened Fuselage Structures, *International Conference on Buckling and Postbuckling Behavior of Composite Laminated Shell Structures March 1 – 2, 2004 Hilton Queen of Sheba Hotel, Eilat, Israel*.
- 10 Bisagni, C., and Cordisco, P., Buckling and Postbuckling Tests of Stiffened Composite Cylindrical Shells, *International Conference on Buckling and Postbuckling Behavior of Composite Laminated Shell Structures March 1 – 2, 2004 Hilton Queen of Sheba Hotel, Eilat, Israel*.
- 11 Abramovich, H., Pevsner, P., Weller, T., Pecker, N. and Ghilai, G., Axial Buckling of Laminated Composite Stringer Stiffened Curved Panels – Tests vs. FE Predictions, *International Conference on Buckling and Postbuckling Behavior of Composite Laminated Shell Structures March 1 – 2, 2004 Hilton Queen of Sheba Hotel, Eilat, Israel*.
- 12 Klein, H., Zimmermann, R., and Kling, A., Buckling and Postbuckling of Stringer Stiffened Fibre Composite Curved Panels – Tests and Computations, *International Conference on Buckling and Postbuckling Behavior of Composite Laminated Shell Structures March 1 – 2, 2004 Hilton Queen of Sheba Hotel, Eilat, Israel*.

13. Abramovich, H., Pevsner, P., Weller, T. and Bisagni, C., The Behavior of Laminated Composite Stringer Stiffened Curved Panels under Torsion Moments - Tests vs. FE Predictions, International Conference on Buckling and Postbuckling Behavior of Composite Laminated Shell Structures March 1 – 2, 2004 Hilton Queen of Sheba Hotel, Eilat, Israel.
14. Thomson, R. S. and Scott, M. L., A Review of Postbuckling Composite Aerospace Structures Research in Australia, International Conference on Buckling and Postbuckling Behavior of Composite Laminated Shell Structures, March 1 – 2, 2004 Hilton Queen of Sheba Hotel, Eilat, Israel.
15. Falzon, B.G., Efficient and Robust Modelling of Postbuckling Stiffened Composite Aerostructures Undergoing Mode-Jumping, International Conference on Buckling and Postbuckling Behavior of Composite Laminated Shell Structures, March 1 – 2, 2004 Hilton Queen of Sheba Hotel, Eilat, Israel.

This page left blank intentionally.

Residual Strength Calculations of Stiffened Metal Panels Containing Cracks

Charles Rankin^{*}
Rhombus Consultants Group, Inc.
Palo Alto, CA 94303

Eduard Riks[†]
Retired University of Delft
04100 Manosque, France

Francis Brogan[‡]
Retired Lockheed Martin
Menlo Park, CA

Paper Category: Structures

**For the special sessions on
Perspectives on Residual Strength and Damage Tolerance for Metallic Structures
In honor of Dr. James Starnes**

Summary

This paper reviews simulation methods for the evaluation of the residual strength of stiffened panels in fuselage shell structures that are damaged by through cracks. Two example problems - a single and a multiple crack case - are used to demonstrate the effectiveness of these capabilities.

^{*}Consultant Specialist, Associate Fellow AIAA

[†]Consultant, Aeronautics

[‡]Consultant

Copyright 2005 by Charles Rankin. Printed by NASA with permission.

1. Introduction

Historical notes

This paper is about shells with cracks and their behavior under load. It presents an overview of methods and modeling features by which residual strength issues concerning shell structures damaged by through cracks can be analyzed.

The methods that we want to discuss are imbedded in the STAGS¹, the finite element code that for so many years was supported (and used) by the structures group at NASA Langley under the leadership of Dr. James Starnes. Jim Starnes and his co-workers contributed enormously to its development over a period of many years, in particular, the crack analysis package. This review is therefore dedicated to his involvement in the creation of this set of methods.

Jim Starnes interest in the STAGS program (Structural Analysis of General Shells) began early, that is in the years that the first versions of it appeared under the leadership of the late Bo Almroth, at the Lockheed Missiles and Space Co., Palo Alto in 1971². At first the development was exclusively focused on the analysis of shell buckling problems. Indeed, for many years STAGS was considered “the shell stability” code amongst the solid mechanics computer codes then in existence.

At about 1986, STAGS had undergone several stages of evolution the most important of which was the transition from finite difference schemes to finite elements for the modeling part. It must have been about this time that the development of STAGS as an analysis tool took a turn into broader direction.

The first analysis carried out with STAGS that involved a shell with cracks appeared in^{3, 4}. It took place at the NLR* where the C1 version of the code was used to verify the (then) growing suspicion that the available methods of those days overestimated the crack tip intensity factors for (long) through cracks in pressurized cylindrical shells considerably.

Although this initial investigation was primitive and based on a great deal of improvisation, the results were convincing and they led to a number of important conclusions of which we mention here two. First of all, it was shown that - for problems of this kind - it was imperative that the analysis be embedded in a full geometrical nonlinear setting in order to get reliable results. Secondly, the STAGS code as it stood was not really equipped to deal with crack problems routinely and needed badly some extensions to facilitate analysis. The latter conclusion ultimately led to a co-operation between the NLR (later Delft University, the Netherlands) and the developers of STAGS at the (then) Lockheed Missiles and Space Co. in Palo Alto in the ensuing years.

At first this joint effort was aimed at the development of methods that could determine the crack tip stress intensity factors routinely and accurately for through cracks that were present in build up shell structures. The development also addressed several modeling issues that arose in this particular branch of analysis.

* The National Aerospace Laboratory, Amsterdam, The Netherlands

One of the very first additions concerned the implementation of the contour integral method for Mode I stress intensity factors for cracks in shells⁵. This feature was later replaced by a much simpler approach that extracted the K-factors from the determination of the energy release rate during crack extension⁶.

The energy release rate method is based on the concept of releasing the crack tip master and slave nodes whereby during decoupling process the energy that is freed is computed by integration. This integration method makes it possible to distinguish between the various modes of cracking, thus enabling the user to obtain five independent stress intensity factors. In spite of its simplicity, the accuracy of the method turned out to be quite satisfactory as long as the mesh of the discretization of the domain in which the crack resided was chosen sufficiently dense^{6,7}.

Once its usefulness was verified, the release method immediately led to another feature that enabled the user to conduct crack growth simulation. Because master and slave nodes along a string of double nodes could be released sequentially, a mechanism for a growing crack was established that was simple, but nevertheless very useful in many practical applications.

In this period of development some incidents in the world of aviation – in particular the extraordinary Aloha accident in 24 April 1988 - prompted the US government to start an investigation into the early detection and prevention of potentially dangerous structural problems in the existing (aging) fleet of airliners; in particular, problems that could be attributed to fatigue. As is well known, the structures group of NASA under Jim's Starnes guidance got involved in this activity in a major way⁹⁻¹⁴. We also observe that the STAGS code played an important role in these investigations and that during this period more and more additional capabilities were added to the code.

Indeed, Jim's interest, encouragement and support for our attempts to improve the code at that time became much more focused. What we particularly remember and value about his involvement is the un-relented confidence he showed in our abilities to further the code in a direction we all considered to be useful and important. It is safe to say that without his support and encouragement the features described in the sequel would not have been in the code today.

Contents of the paper

The aim of the present discussion is to give an overview of STAGS capabilities with respect to the problem of the evaluation of the residual strength of cracked shells under various loading conditions. We will describe the code's potential, and its limitations in this particular area of analysis.

The organization of the paper is as follows. First a short overview is given of the typical mechanical aspects of the behavior of a through crack in a pressurized shell. After that the various features for the modeling and solution phase are described. The paper is closed by a discussion of residual strength calculations involving two cylindrical shell models that contain one and two longitudinal cracks.

2. Basic Conceptual Aspects of the Cracked Cylinder Problem

The bulge effect

The stress distribution in a thin-walled infinitely long cylindrical shell under internal pressure is given by:

$$\sigma_x = pR/2t; \quad \sigma_y = pR/t \quad (1)$$

In this formula p is the internal pressure, R is the radius of the shell and t its thickness.

In this first approximation of the actual situation in a fuselage shell, the largest of the two principal stresses, - the hoop stress σ_y - is twice as large as the axial stress σ_x . In the case the shell is reinforced with stiffeners as it is done in airplane fuselages, the stress distribution is no longer uniform and the peak values of the stress components σ_x and σ_y are reduced as compared to the situation in the un-stiffened case (at the same value of the pressure p). But for the hoop stress σ_y this reduction is only marginal; the order of magnitude of it is about 12%, except in the neighborhood of the bulkheads of the shell where the reduction can be larger. Thus if the loading of the shell is restricted to internal pressure, the hoop stress remains – approximately - the principal and maximal stress

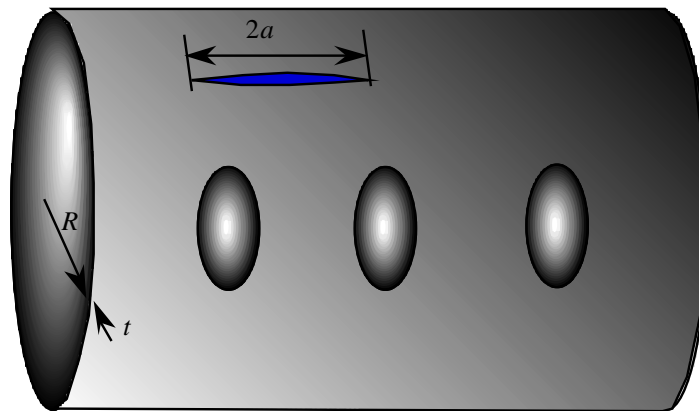


Figure 1 Fuselage crack

component in the shell. It is this stress state that causes cracks in a fuselage loaded by internal pressure to grow longitudinally rather than tangentially (Figure 1).

It is well known that cracks in curved thin walled shells under internal pressure not only open up in the plane tangential to the shell at the crack but also bulge out; i.e., they show a deformation accompanied by normal (outward) displacements of the crack faces (Figure 2). At first sight, one may be tempted to conclude that - because the direction of this load agrees with the outward bulging displacements - it is the internal pressure that causes the bulging deformation. It turns out however, that this supposition is not correct. A metal sheet pulled around a cylindrical mandrill containing a crack will also show a bulging of the crack faces as can easily be demonstrated by experiment. The cause of the bulging must therefore be explained by the curvature of the shell

in the plane that cuts the shell perpendicularly to the crack. It is the redistribution of the internal stress field in the neighborhood of the crack that must satisfy the zero hoop stress condition along the crack faces that causes this “out of the plane” deformation.

As compared to an identical crack in an a flat plate of the same thickness loaded in such a way that the state of stress (1) holds in the far field, the crack tip stress intensity of the crack in the cylindrical panel is larger. This holds particularly for the mode I stress intensity factor K_I defined by:

$$K_I : \sigma_y = K_I \frac{1}{\sqrt{r}} \Phi_y(r, \varphi) + O(\sqrt{r}) \quad (2)$$

where r, φ are the coordinates of a polar coordinate system with origin at the crack tip, and Φ depicts the distribution of the hoop stress σ_y in the immediate neighborhood of the crack tip. The amplification can be expressed by the ratio:

$$\beta = \frac{K_{I_{cyl}}}{K_{I_{plate}}} > 1 \quad (3)$$

The factor β is called the bulge factor. In the case (1) discussed here this factor is always larger than zero.

Geometrical nonlinear effect

In elasticity it was probably Folias¹⁵ who first obtained the solution of the stress intensity factor K_I for a longitudinal crack in an infinitely long cylinder under internal pressure. This solution was obtained within the framework of linear elastic shell theory. As it turned out, it can be relied upon only for relatively small cracks. For larger cracks, a geometrically nonlinear effect comes into play that substantially reduces the bulge effect with respect to the value obtained by linear theory. Please note that by large cracks, we mean - without claiming rigor - that the characteristic parameter α satisfies the inequality $\alpha > 2$, where α is defined by¹⁵.

$$\alpha = 2\sqrt[4]{12(1-\nu^2)} \sqrt{\frac{a^2}{Rt}} \quad (4)$$

In this expression, $2a$ is the crack length, t and R are the thickness and radius of the shell respectively - as before - while it is further supposed that $R \gg t$.

It is noted that this particular effect is due to the same type of mechanism that can cause thin walled panels to buckle if they are loaded in compression. But, in contrast to the buckling problem, for the crack problem featured in this example, the nonlinear mechanism works as a *stiffening effect*.

When the crack opens under increasing load (figure 2), the emerging bulge requires the fibers along the crack faces to elongate and this stretching is met with considerable resistance. In other

words the more the crack opens the more resistance it generates against this deformation. This stiffening effect is proportional to the square of the displacement in normal direction and thus increases super- linearly with the amplitude of the bulge.

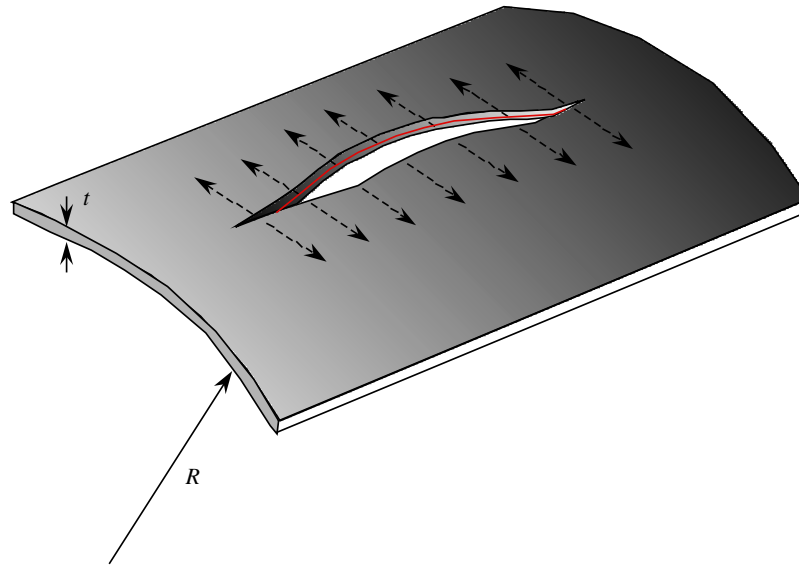


Figure 2 Bulge - and nonlinear - effect

Under the conditions sketched here, the difference between the linear theory and the geometric non-linear theory can be of the order of magnitude (2-4) in the sense that the linear theory over estimates the linear theory substantially. This explains why - for thin shells - geometrically linear theory is not sufficient to describe the conditions at the crack tip adequately^{3, 4, 5}.

Plasticity at the crack tip

In ductile materials a plastic zone develops around the crack tip when the loading is applied. This plastic zone grows under increasing load and moves when the crack advances (Figure 3).

The yielding process thus absorbs part of the energy that is supplied to the structure by the external load. Similarly, when the crack advances, the energy release that is available to create the new fracture surface in the growth process is partly absorbed by the yielding of initially elastic material immediately ahead of the crack. This energy absorption and the accompanying accumulation of plastic strains is the reason why ductile materials can exhibit stable crack growth under increasing load.

3. Modeling Features

The shell model

The shell elements that are available in STAGS are all based on small strain - large displacement/rotation theory -, a theory that was finalized in ^{16, 17}. They are capable to model a large class of engineering structures including structures that suffer from small scale (strain) yielding. The basic restriction that may influence the results of the crack models adversely in the present case is the condition that the state of stress in the shell is approximately two-dimensional. More precisely, the theory assumes that a plane state of stress exists throughout the shell, which is an

assumption that is clearly violated in the immediate surrounding of a crack tip. In what way this restriction can be overcome in STAGS is discussed later.

Stiffeners

Stiffeners can be modeled in various ways in the code¹ but the best way is by means of the same shell elements that are used for the fuselage shell. In many applications this is the only way to guarantee sufficient accuracy. This fact is related to the circumstance that stiffeners in aircraft structures are usually very slender and made of extrusions with wall thicknesses comparable to - or smaller than - that of the fuselage skin.

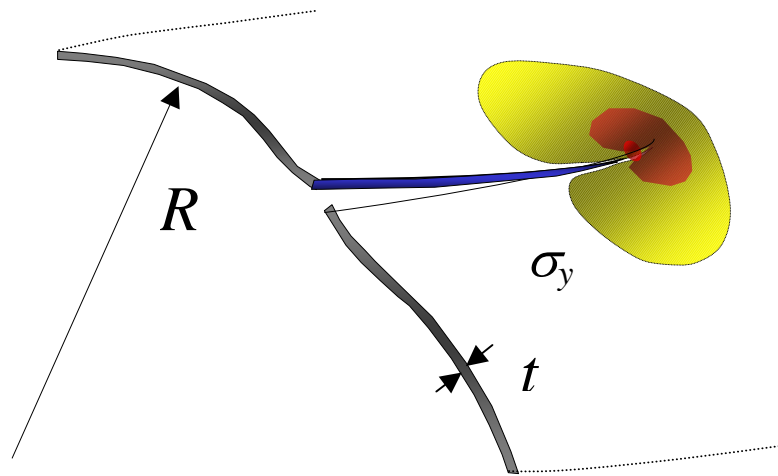


Figure 3 Plasticity effect

The Plasticity Model

The STAGS code is equipped with the fraction model that was originally proposed by Besseling¹⁸. In this model, the state of stress of a material point of the body under investigation can be subdivided in components (called fractions), each of which possesses its own yield function and flow rule. The fractions all undergo the same strain; this is the state of strain of the material point under consideration. In the STAGS code, the individual fractions are treated as elastic-perfectly plastic whereby each fraction has its own yield stress and corresponding strain.

The number of fractions is open to choice of the user. It determines the accuracy of the discrete analog of the experimentally determined stress strain curve of the material in question (see also figure 6). The discrete form of the stress strain curve determines the parameters that govern the behavior of each fraction and, in fact, the behavior of the integrated model. One of the attractive features of Besseling model is its capability to represent cyclic loading and unloading.

To integrate the plastic stress for the computation of the nodal force residuals, STAGS uses the well-known radial return method. A comprehensive description of this method and its implemen-

tation can be found in¹⁹ (although in STAGS this method has been applied with some minor adaptations).

The Crack model

The cracks discussed here are defined along predetermined paths drawn along the shell reference surface. In the un-deformed state, the fracture surfaces of these cracks (only through cracks are considered) are cut by the normals to the reference surface along the fracture path. The curves that define the cracks in this way always coincide with parts of the mesh distribution in the sense that they pass through a string of twin nodes belonging to two sets of elements that reside on either side of the string. The mechanism by which the crack advances consists of releasing the slave node from its master at the crack tip into the direction of growth.

The cracks therefore, cannot be chosen independently of the mesh and, what was already mentioned, they must grow along the paths initially determined by the discretization scheme. The simulation of a crack growing process whereby the crack will seek its progress on the basis of an autonomous criterion, i.e. a criterion that determines the size and direction of the crack tip advance, is outside the scope of the present capabilities.¹ Notwithstanding this restriction, we claim that the crack growth models along predetermined paths are very useful in many engineering applications, in particular, in residual strength calculations. The reason for this is that even in this constrained set of possibilities it is still possible to enact simulations that reveal great deal of the potential danger or - absence thereof - of the damaged structure under investigation.

4. Solution Methods

Crack tip stress intensity parameters

Although the simulations do not necessarily depend on the crack tip parameters that are called stress-intensity factors, STAGS compute these factors routinely at any step of the crack advancing process. For the shell model, five independent intensity parameters are identified⁶. They are associated with two in-plane modes of deformation, one transverse shearing mode and two bending modes. The standard way these intensity factors are computed is by computing the energy release during crack advance, a method that has been proved to be dependable and very easy to apply.

Crack growth simulation

The initial crack at the start of the computations is defined along a string of master and slave nodes that represents at the same time the boundary between two sets of elements. By decoupling the master and slave nodes along a certain stretch of this string the through crack in the shell model is created. Growth of the crack is accomplished by successively releasing the master and slave nodes at the crack tip and beyond. The instant at which the release is carried out depends on the crack growth criterion applied. At present only the “crack opening angle”(CTOA) crite-

¹ There are two ways to address the problem of a self-seeking crack growth simulation. One makes use of a re-meshing scheme after each step of the growth process the other uses special elements that makes it possible for a crack to grow through the element across element boundaries. These refinements are complicated however and come at a price.

tion is implemented in STAGS. The example calculations discussed in chapter 5 are all obtained by using this criterion.

The path following procedure for the residual strength problem

In principle, the cracked structure under load can display three distinct forms of behavior (see Figure 4, where this behavior is sketched in the crack-length versus load domain). Phase I: Initially, the structure deforms but the crack does not change its length (no growth situation) when the load is applied. Phase II: The crack grows under variation of the load but stably, i.e., whenever the load variation is arrested the crack remains stationary in length and the same can be said about the overall deformation of the damaged structure. Phase III: The load (and with it the deformation and crack length) reaches a value (λ_c , μ_c) beyond which the crack becomes unstable; i.e., the growth of the crack becomes uncontrollable under fixed load and an explosive extension of the crack occurs. This corresponds to a jump in the structures state of deformation to IV. The last process (III) may or may not end in destruction of the structure. If crack arrest occurs after the transient process (ending at branch IV, figure 4) the structure may again be loaded in a stable, quasi-static fashion. Continued loading is then again of the type I or II (we mean here that IV is equivalent to I or II because these branches are all stable).

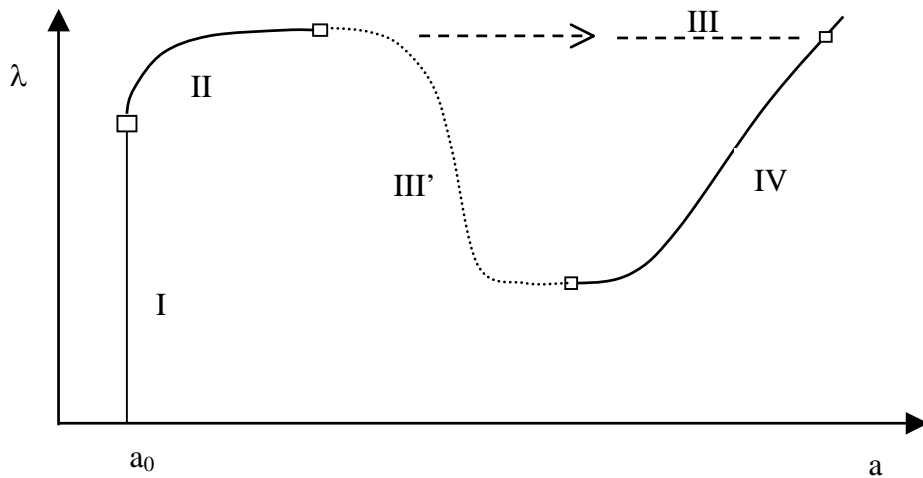


Figure 4 Types of behavior

The solution procedure in STAGS selected for this problem computes the stable branches (I and II) of the equilibrium states of the damaged structure until collapse occurs. Once the crack becomes unstable, this process is automatically followed by the computation of an approximation of the transient jump III (by successive load relaxation) until the crack becomes stable again). It is noted that there is an alternative procedure⁷ available that enables the user to compute the unstable equilibrium states (for descending values of the load) beyond the unstable limit point (λ_c , μ_c) but this strategy was not used here because it is presently only applicable to a single crack.

5. Examples and Conclusion

Cylindrical fuselage panel

In earlier reports we presented results of residual strength calculations for a center cracked plate for which extensive test data were available. In this paper we will discuss an example problem that has a more direct bearing with the problem of a longitudinal crack in a fuselage. It concerns a computational model the concept of which is borrowed from the model discussed in ^{3, 4}.

Consider a cylindrical shell, infinitely long, equipped by equidistant ring stiffeners, which is damaged by cracks periodically distributed over the domain of the shell. The distribution of the cracks is fixed by the following stipulation. The cracks are longitudinal and their positions are symmetrically positioned with respect to the middle of the bays. The arrangement above is repeated evenly, $n = 16$ times over the circumference of the shell.

In this model, the presence of the ring stiffeners is approximated by enforcing the kinematical condition that at their locations $x = \pm k \times 1/2L$, the normal displacement $w = 0$. (This condition is far too severe in comparison with the actual situation in stiffened fuselage but good enough for this model). The loading of the shell is internal pressure with the nominal value taken from what appears to be the standard in airliners at cruising altitude.

The periodic model defined above allows us to focus on a segment of the shell pictured in figure 5; which has a length of $L/2 = 24$ inch and covers a sector along the circumference of $\varphi = 22.50^\circ$. The boundary conditions are dictated by the various symmetry conditions that then apply. The loading is introduced in such a way that if there were no stiffeners and no cracks, the state of stress conforms to that of the state of stress in the infinitely long cylinder in compression, i.e., that what is given by equation (1). Although the precision of the description given here is not particularly important for the demonstration we want to present, it is included here to provide insight to the background of the given formulation.

With this model we attempt to simulate the behavior of longitudinal cracks in a shell segment that could be taken from a bay of a typical fuselage shell, a bay that is bordered by two ring stiffeners and two stringers. We believe that this model presents the most important mechanical aspects of the centrally cracked bay panel in a stiffened shell.

Specification of the model

The dimensions, physical properties and loading of the panel are given by:

Geometry

Bay length	L (only half of it is taken in our model)	24.	inch
Arc-length sector	φL	28.67	inch
Radius	R	73.	inch
Wall-thickness		0.04	inch

Material properties

Notation: E is modulus of Elasticity, ν is Poisson's ration, ρ is weight density, $\varepsilon(i)$, $\sigma(i)$; $i = 1, 2, \dots, 5$ are points in the (uni-axial) stress strain diagram of the material representing the discrete form of the actual stress strain relation of the material (Besseling-model input, Figure 6).

$E = 10.351967E+6$ psi, $\nu = 0.3$, $\rho = 2.59E-5$ lbs/inch³ (material initially isotropic).

$\varepsilon(i), \sigma(i) = (0.00483, 50000.0), (0.015, 56600.0), (0.04, 62400.0), (0.1, 68200.0), (0.16, 71100.0)$.

Internal pressure p

$p = 8.35$ psi (nominal value at cruise altitude)

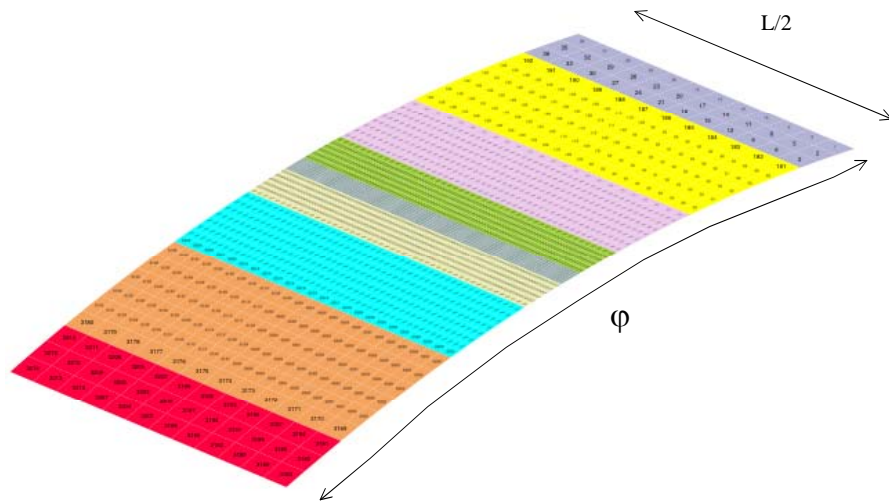


Figure 5 Part of the cylindrical shell modeled

Crack-lengths and location

Two cases are considered. In case *I* there is one longitudinal crack along $y = 0$ symmetrically placed with respect to $x = 0$, with initial length $2a = 8$ inch,. In case *II* there are three cracks, all three along $y = 0$, one central crack of length $2a = 8$ inch and two cracks symmetrically placed with respect to $x = 0$ that are of length $2a_2 = 2.125$ inch. The centers of the two smaller cracks are located at $x = \pm 6.5625$ inch.

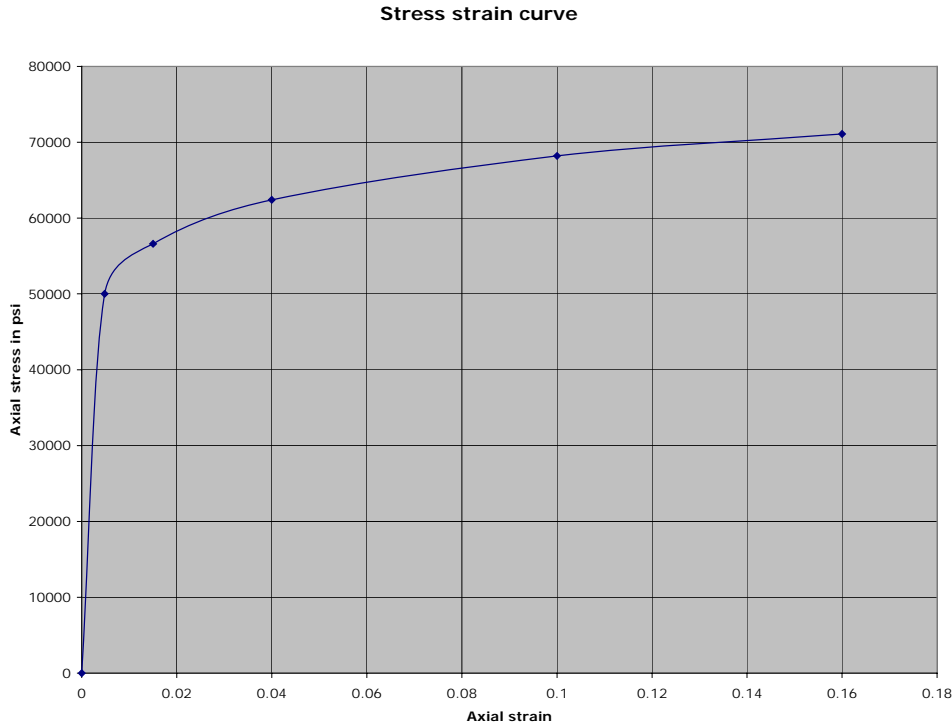


Figure 6 Elastic – Plastic behavior shell material

As mentioned we intend to simulate an experiment where a cylindrical panel is tested under conditions similar to those experienced by a cylindrical panel in a fuselage. In this scenario it is assumed that the cracks present in the test articles are artificially created before the actual test program is launched. The (residual strength) tests are then carried out by slowly increasing the load until the total length of the growing crack(s) reach a preset value. At this point the loading process is reversed until the unloaded state is reached.

CTOA condition

The critical opening angle in these examples is: 4.5° .

Results

The basic results for the two cases are represented in Figures 7 and 8. Use is here made of the load versus central crack-bulge-opening displacement; the normal displacement at the node $x = 0, y = 0$ location. This diagram adequately represents the successive events that occur during the loading cycle (except that it is not possible to see here which crack tip advances at a particular step).

In case I, the (central) crack gradually propagates in small steps at distinct but increasing values of the load. The result suggests that the damaged panel exhibits considerable resistance requiring an overload of $\lambda = 2.41$ to reach the final crack length of $a_f = 8.625$ inch. An image of the hoop stress distribution at that point is given in Figure 9.

In case II, the initial response is like that in the previous case. The central crack starts to grow at about the same load level as in the previous case while the smaller crack first remains stationary. Crack advance continues in steps as before until at $\lambda = 1.04$ this process becomes unstable. What then follows, the merging of the two cracks, corresponds to a change (a jump) in configuration between two equilibrium states that in reality occurs in a transient way, but is here computed with the pseudo static load relaxation method mentioned earlier.

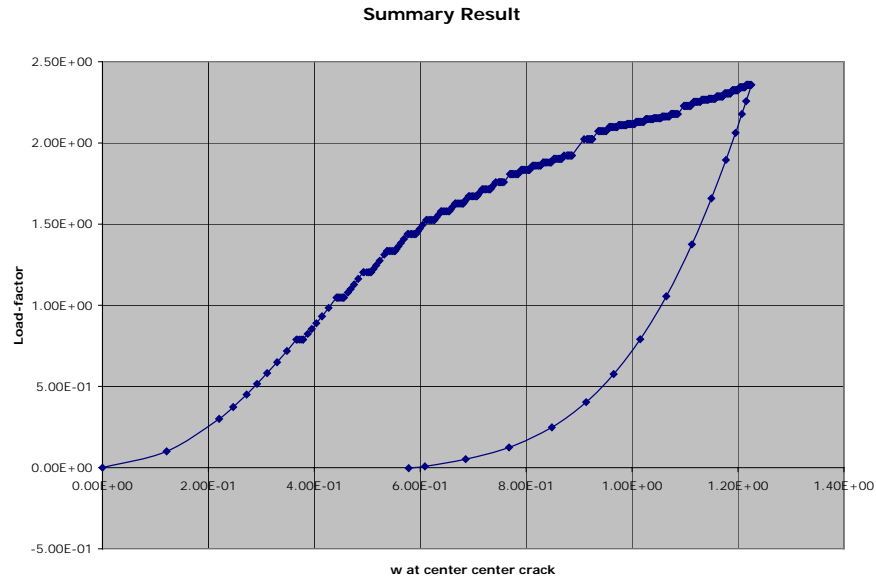


Figure 7 Residual strength; Case I: One crack

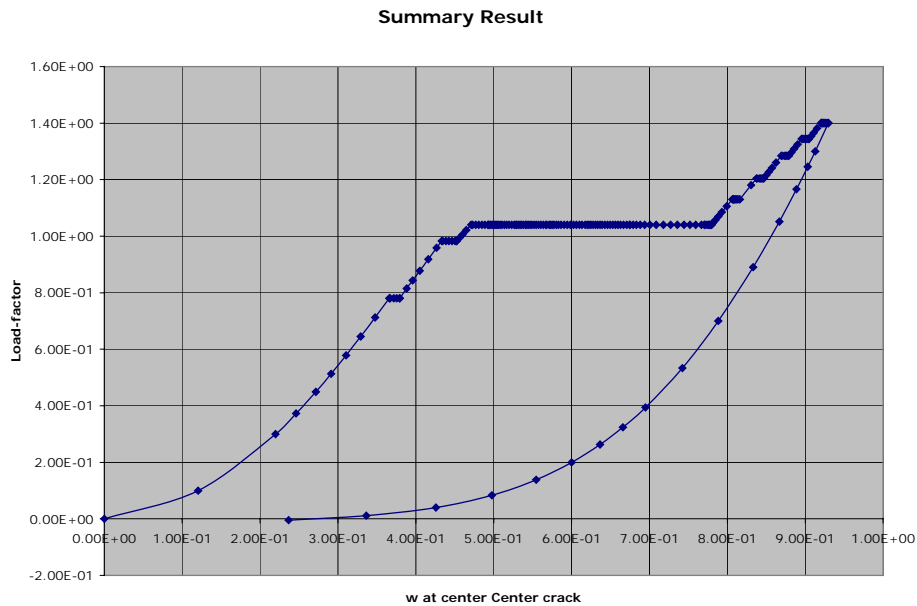


Figure 8 Residual strength; Case II: Two cracks

Crack arrest marks the end of the jump at which point the total length of the merged crack is $a = 7.875$. At this point the load can further be increased. Crack growth then continues in a stable fashion but the final crack length of $a_f = 8.625$ inch is reached at much lower load intensity than in Case I. The hoop stress distribution in the final state (Crack length $a_f = 8.625$) of this case is displayed in Figure 10.

Discussion

The simulations presented here contain several elements that are to some extent speculative. Although it is true, that in a previous comparison of crack growth simulations on a centrally cracked plate²⁰ a satisfactory agreement between computation and experiment could be obtained, this does not automatically mean that for the present test case a similar result can be expected. For example, the assumption that the transient jump that occurs when the two cracks finally merge can be computed by a pseudo static method is clearly heuristic. Moreover, there exists some uncertainty about the accuracy by which the moving plastic zone around the crack tip is calculated and the influence the error has on the resulting residual strength diagram.

From the results reported in²⁰, we know that the shell model used here, overestimates the residual strength somewhat due to the principal characteristic of shell elements that maintains a plane stress condition throughout the model (including the surface surrounding the crack). Of course, it is possible to remove this restriction by using volume elements as a refinement in the crack zone as was demonstrated in²⁰, but we do not pursue this refinement here because it does not add much extra value to the qualitative aspects of the present demonstration.

According to the computations presented here the panel in the second case shows a reduced resilience against overload as one could and would expect intuitively. Why is the load at the crack length $a_f = 8.625$ lower in case II as compared to Case II? We believe that the answer must be sought in

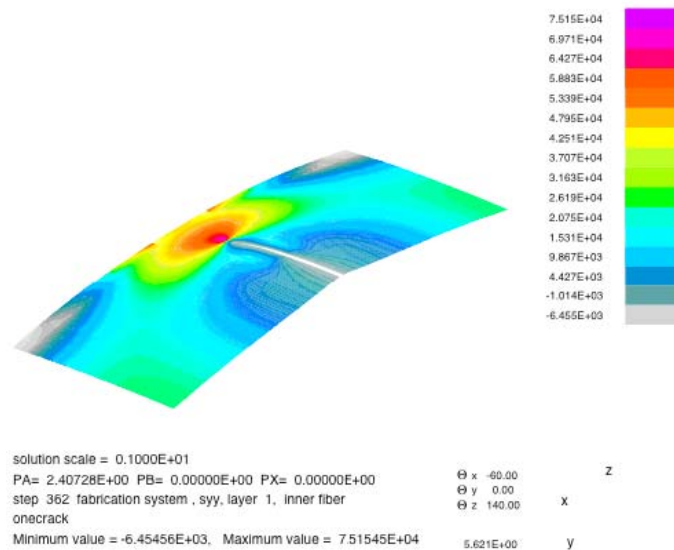


Figure 9 Case I at crack length a_f

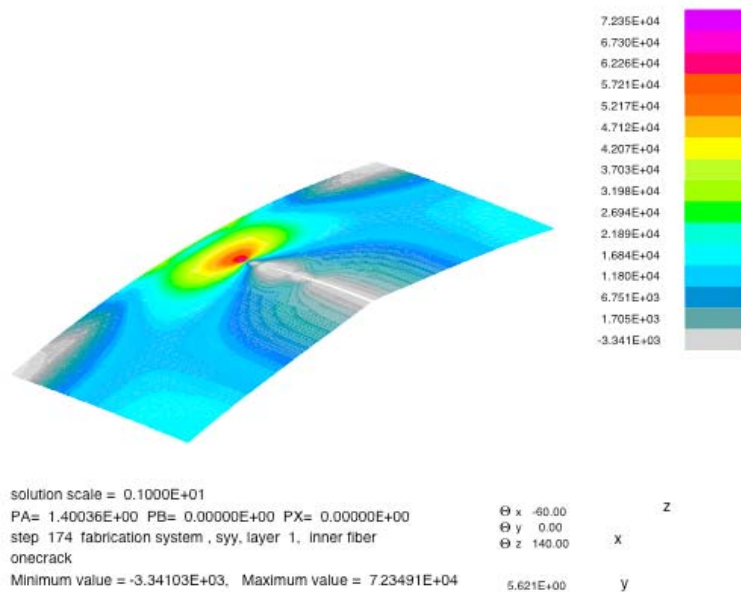


Figure 10 Case II at crack length a_f

the difference between the size of the plastic zone around the crack tips (accumulated in the final step) which is much larger in case I than in case II (Note also the permanent deformation at the end of the loading cycles in both cases, Figures 7, 8). It shows the importance of the role that plasticity plays residual strength problems of this type.

Final remarks

In this report we did not describe in what manner - during the crack growth computations - the algorithm deals with the case of multiple cracks, in particular, the situation that one or more cracks become unstable at the same time, because a clarifying discussion of this particular aspect would take too much space and go beyond the scope of this paper.

Another issue that we left out of the discussion is the alternative of the computational strategy to compute the unstable jumps in crack growth by a transient method. This possibility belongs definitely to the STAGS capabilities. It is our intention to cover this topic at another occasion.

References

- [1] Rankin C. C., Brogan F. A., Loden W. and Cabiness H., **Structural Analysis of General Shells**, STAGS, User Manual, version 3.0, LMMS P032594, Advanced Technology Center, Lockheed Martin, Febr. 1998. Palo Alto, California.
- [2] Almroth B.O., Brogan F. A., Miller E., Zele F. and Peterson H.T., (1973) "Collapse Analysis for Shells of General Shape; II. User's Manual for the STAGS-A Computer Code", Technical Report AFFDL-TR-71-8, Air Force Flight Dynamics Laboratory, Wright-Patterson Air Force Base, Ohio.

- [3] Riks.E , P.J. den Reijer, (1987) "A Finite Element Analysis of Cracks in a Thin Walled Cylinder under Internal Pressure", NLR TR 87021 U, National Aerospace Laboratory, the Netherlands, 1987.
- [4] Riks E. (1987), "Bulge Factors in the Fokker 100 Fuselage: Computational Results", NLR TR 87008C, National Aerospace Laboratory, the Netherlands, December 1987.
- [5] Riks E., Brogan F.A., & Rankin C.C. (1989), "Bulging Cracks in Pressurized Fuselages: A Procedure for Computation", December Meeting ASME, San Francisco, .In: Analytical and Computational Models of Shells, Proceedings Winter Annual Meeting ASME (A.K. Noor, T. Belytschko, J.C. Simo eds.), C.E.D. Volume 3, The American Society of Mechanical Engineers.
- [6] Rankin C.C, Brogan F. A. and Riks E.(1993), "Some Computational Tools for the Analysis of Through Cracks in Stiffened Fuselage Shells", The Journal of Computational Mechanics, Vol. 13, Nr. 3, pp. 143-156.
- [7] Rankin C.C. and Riks E., (2000) On the Simulation of Crack Propagation in Pressurized Fuselages, AIAA/ASME/ASH/ASC 41th Structures, Structural Dynamics and Materials Conference, Atlanta, AIAA Paper No. 2000-1594.
- [8]..Starnes J.H. Jr. and Rose C. A. (1997), Nonlinear Response of Thin Cylindrical Shells with Longitudinal Cracks and Subjected to Internal Pressure and Axial Compression", Paper AIAA-97, 1144, 38th AIAA/ASME/ASCE-/AHS/ASC, Structural Dynamics and Materials Conference, Kissimmee, Florida, April 7-10.
- [9] .Starnes J.H. Jr., Rose C. A., Young R. D., and Rankin C. C. (1997), "Effects of Combined Loads on the Nonlinear Response of Stiffened Shells with Long Cracks", Int. Committee on Aeronautical Fatigue Symposium, June 18-20, Edinburgh, Scotland UK.
- [10] Starnes J.H. Jr. and Rose C. A.(1998), Buckling and Stable Tearing Responses of Unstiffened Aluminum Shells with Long Cracks, AIAA/ASME/ASH/ASC 39th Structures, Structural Dynamics and Materials Conference, AIAA Paper No. 98-1991. (Also presented at: DoD/FAA/NASA Conference on Aging Aircraft Williamsburg, September 1 - 4, VA, USA).
- [11] Young R. D., Rouse M, Ambur D. R., and Starnes J. H. Jr., (1998), Residual Strength Pressure Tests and Nonlinear Analysis of Stringer and Frame-Stiffened Aluminum Fuselage Panels with Longitudinal Cracks, second DoD/FAA/NASA Conference on Aging Aircraft, Williamsburg, September 1 - 4, VA, USA.
- [12] Rose C. A., Young R. D., and Starnes J. H. Jr., (1999), Nonlinear Local Bending Response and Bulging Factors for Longitudinal Cracks in Pressurized Cylindrical Shells, AIAA/ASME/ASH/ASC 40th Structures, Structural Dynamics and Materials Conference, AIAA Paper No. 99-1412.
- [13] Young R. D., Rose C. A., and Starnes J. H. Jr., (2000), Nonlinear Bulging Factors for Longitudinal and Circumferential Cracks in Cylindrical Shells Sublected to Combined Loads, AIAA/ASME/ASH/ASC 41th Structures, Structural Dynamics and Materials Conference, Atlanta, AIAA Paper No. 2000-1514.
- [14] Cowen Amy L., Dávila C. G., Johnsonn E. R. and Starnes J.H. Jr., (2000), Crack Path Bifurcation at a Tear Strap in a Pressurized Shell, AIAA/ASME/ASH/ASC 41th Structures, Structural Dynamics and Materials Conference, Atlanta, AIAA, Paper No. 2000-1517.
- [15] Folias E. S., (1965) An Axial Crack in a Pressurized Cylindrical Shell, Int. J. of Fract. Mech., Vol.1, pp.104-

- [16] Rankin C.C., Brogan F. A. (1984), An Element Independent Corotational Procedure for the Treatment of Large Rotations, in : L/H Sobel and K.Thomas, eds. Collapse Analysis of Structures, ASME, New York.
- [17] Rankin C.C. and Nour Omid B.(1988). The Use of Projectors to Improve Finite Element Performance, Comp. & Structures, Vol. 10, No 1/2,pp. 257-267.
- [18] Besseling J. F., & van der Giessen E., "Mathematical Modeling of Inelastic Deformation, Chapman & Hall, 2-6 Boundary Row, London SE1 8HN, UK, 1994.
- [19] Crisfield, M.A., Nonlinear Finite Element Analysis of Solids and Structures, John Wiley & Sons, 1991.
- [20] Rankin C.C. and Riks E., (2001), Tools for the Evaluation of the Residual Strength of Cracked Pressurized Fuselage Shells, Proceedings The 5th Joint NASA/FAA/DoD Conference on Aging Aircraft, September 10-13, 2001, Orlando, Florida.

This page left blank intentionally.

This page left blank intentionally.

This page left blank intentionally.

Failure Analysis of Large Stiffened Metallic Fuselage Panels Subjected to Compression Loading

Vicki O. Britt* and Frank Simmons, III†

Gulfstream Aerospace Corporation, Savannah, Georgia, 31402

In order to further validate analytical methodologies, a series of tests were performed at the National Aerospace Laboratory in Amsterdam, the Netherlands. Tests were conducted on metallic curved stiffened panels representative of four general structural configurations on the Gulfstream V business jet fuselage. A total of eight panels, two of each configuration, were tested in compression. The panels had both axial and circumferential stiffeners. The axial stiffeners in the test panels were open or closed hat sections, and the circumferential stiffeners were 'C' channels resting on top of the axial stiffeners and connected to the skin with angle shear ties. Finite element analyses were performed for each of the four panel configurations using the STAGS finite element code. The purpose of this paper is to present the method and level of modeling fidelity necessary to accurately predict both the initial buckling and the ultimate failure load of the panels. All finite element analyses included geometric and material nonlinearities. Assumed initial imperfections were used to progress the finite element model past limit points encountered as each of the skin bays buckled. The finite element models predicted the onset of initial buckling with great accuracy. The accuracy of the models for predicting the ultimate failure of the panel varied depending on the mode of failure. Failure predictions were most accurate for panels that failed due to Euler column buckling of the stringers. The ultimate failure of panels experiencing local buckling of the stringers was less accurate. This paper will present the test results for each of the four panel configurations and discuss in detail the modeling approach necessary to obtain the most accurate failure prediction for each configuration.

Nomenclature

t_s	=	stringer thickness
df	=	frame doubler half-width
ds	=	stringer doubler width
$s1, s2, s3$	=	stringer geometry parameters

I. Introduction

The majority of all conventional aircraft structures are made using stiffened panel construction. For most aviation applications, there is an acceptable level of buckling that is allowed to occur at some point prior to ultimate load. Therefore, accurate analyses are required to analyze the stiffened panels in the postbuckling regime.

Solutions for the postbuckling and failure analyses of curved panels have only recently been explored. In 1987 Arnold and Parekh (Ref. 1) presented results for the buckling, postbuckling, and failure of edge-stiffened composite shallow-curved panels subject to axial compression and shear loading. Failure modes included stiffener disbonding and panel crippling due to exceeding fiber strain allowables. In 1992 Minnetyan, Rivers, and Murthy (Ref. 2) predicted ply damage leading to failure of stiffened composite shells subject to axial loads, shear, and internal pressure. Collier, Yarrington, and Van West (Ref. 3) presented a postbuckling analysis for grid-stiffened curved panels subject to axial loads, shear, and bending moments using the Hypersizer optimization code. Several failure modes were analyzed such as stiffener local buckling and crippling, web buckling, and exceedance of maximum strain allowables. Similar optimization results were presented by Lamberti, Venkataraman, Haftka, and Johnson (Ref. 4) using the PANDA2 code to optimize the propellant tank of a reusable launch vehicle. Several configurations were considered including metallic and composite materials, honeycomb sandwich construction, stringer-ring configurations, orthogrid and isogrid-stiffened, and corrugated panels. Given the continued use of metallic

* Technical Specialist III, Preliminary Design, P. O. Box 2206, M/S ABC-105

† Staff Scientist, Structures, P. O. Box 2206, M/S ABC-105, AIAA Associate Fellow.

Copyright 2005 by Vicki Britt. Printed by NASA with permission.

structures in the aerospace industry, more research is necessary in the area of postbuckled behavior and ultimate failure of stiffened metallic structure.

The purpose of the current paper is to examine the level of modeling fidelity necessary not only to predict the buckling load of a metallic stiffened panel, but also to accurately predict the ultimate failure load of the panel. A series of compression tests were conducted on metallic curved stiffened panels representative of four general structural configurations on the Gulfstream V business jet fuselage. Results of the panel tests and the model fidelity necessary to accurately capture the ultimate failure modes of the panels will be presented.

II. Panel Geometry

The general panel configuration is shown in Figure 1. All of the panels have four frames and five hat-section stringers. They have an overall length of 43 inches, an arclength of 38 inches (46 degrees), and a radius of 47 inches. The frame spacing is 12 inches and the stringer spacing is 7.55 inches.

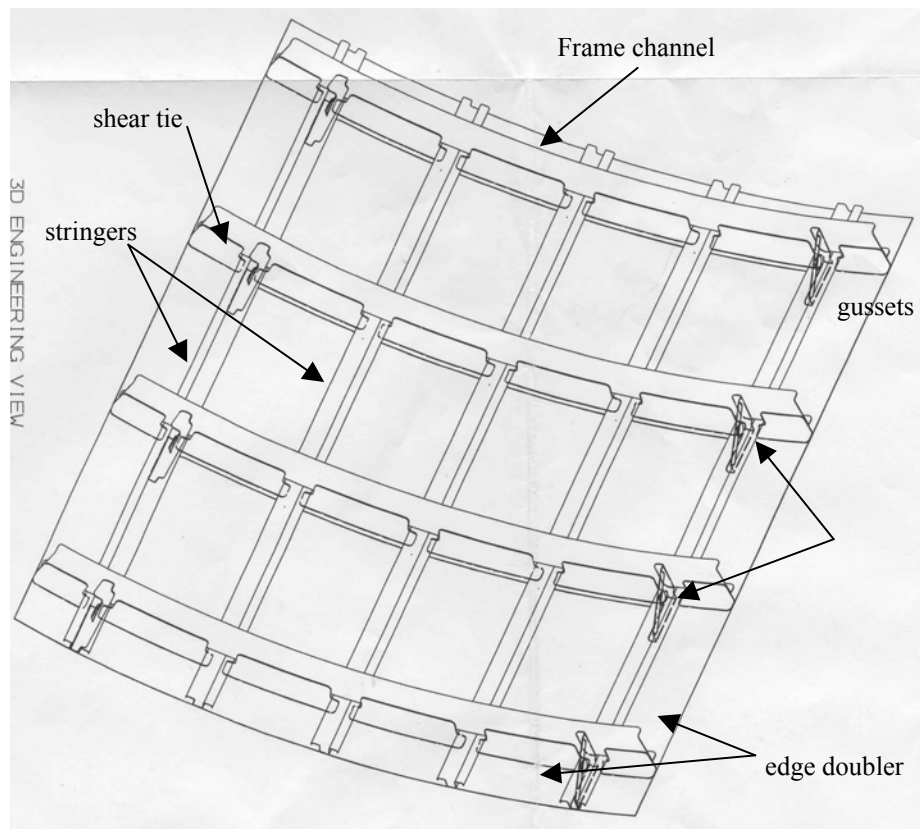


Figure 1. General panel configuration.

The frames and stringers are riveted together at each frame/stringer intersection. The rivets have a diameter of 0.125 in. and are spaced 0.625 in. apart. On each side of the panel there is an .032-inch-thick 2024-T3 skin doubler extending from the edge of the panel underneath the first stringer in the axial direction and underneath the first frame in the circumferential direction. The doubler stops at the inside edge of the stringer or frame shear tie. The height of the two outside stringers is reduced by the thickness of the doubler. Gussets are located at each frame/stringer intersection along the axial edges of the panel giving a total of eight gussets.

The four panel configurations, numbered 614, 615, 616, and 617, differ in their skin and stiffener material thicknesses, skin-doubler configuration, and orientation and attachment of the hat-section stringers. Panel 614 has a skin thickness of .04 inches, includes a doubler under the frames only, and has open hat stringers. Panel 615 has a skin thickness of .04 inches, has a waffle doubler that lies beneath the frames and stringers, and has open hat stringers. Panel 616 has a skin thickness of .04 inches, includes a doubler over the entire skin, and has open hat

stringers. Panel 617 has a skin thickness of .063 inches, does not have a doubler on the skin except at the panel edges, has inverted hat stringers, and has gussets at each frame/stringer intersection for a total of 20 gussets. A summary of the four panel configurations is shown in Table 1.

Table 1. Panel Configuration Definition.

	Test Panel Configuration			
	614	615	616	617
Skin thickness (in.)	0.04	0.04	0.04	0.063
Stringer thickness (in.)	0.025	0.025	0.063	0.025
Stringer orientation	open hat	open hat	open hat	inverted hat
Doubler location	under frames	under frames and stringers	over entire skin	none
Gussets	edges only	edges only	edges only	all frame/stringer intersections

The frame geometry, as shown in Figure 2, is the same for each panel. The frame consists of a channel connected to the panel skin by an angle shear tie. The values of the geometric properties for the frames, stringers, and doublers are shown in Figure 2 for each panel configuration and tabulated in Table 2. The doubler widths are also given in Table 2. For the case where the width of the doubler is equal to the frame or stringer spacing, the doubler is over the entire skin. For each panel, the skin and doublers are made from 2024-T3 clad aluminum. The stringers, frames, and shear ties connecting the frame to the skin are made from 7075-T62 clad aluminum. The cross-section of the hat stiffeners is defined using five parameters: s_1 , s_2 , s_3 , s_4 , and t_s . The doubler widths for the frames and stringers are defined by df and ds , respectively. All values are given in Table 2.

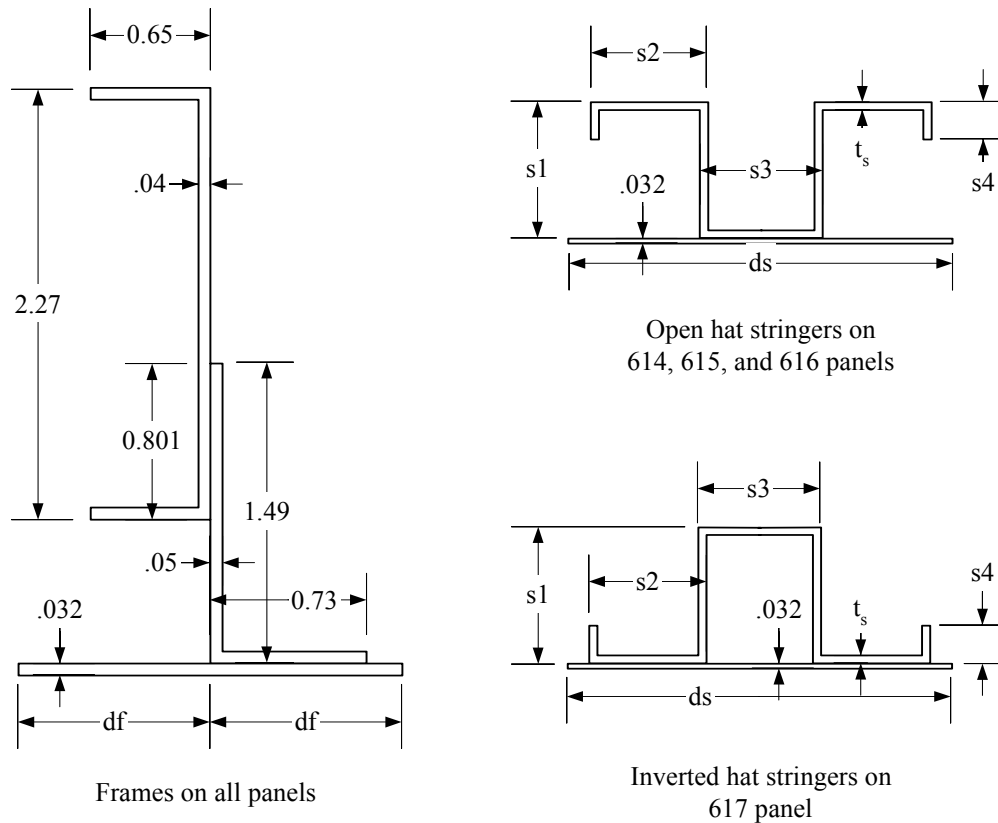


Figure 2. Frame and stringer geometries for the panels.

Table 2. Frame and stringer property values.

Panel	df*	ds [†]	s1	s2	s3	s4	t _s
614	1.0	0.0	.689	.52	.58	.188	.025
615	1.0	2.0	.657	.52	.58	.188	.025
616	6.0	7.55	.657	.51	.67	0.0	.063
617	0.0	0.0	.689	.52	.58	.188	.025

*value of 6.0 indicates doubler over entire panel

[†]value of 7.55 indicates doubler over entire panel

III. Experimental Procedure and Results

The top and bottom edges of the test panels were molded in resin and then milled flat and parallel to each other to provide even load introduction. The panels were supported along the straight edges with a clamping device to create near simply supported boundary conditions. To prevent the simple support clamping device from carrying axial load, teflon tape was bonded on the test panel at the location where the clamping device contacted the panel thus creating a sliding connection. Each of the four frames were supported at their right and left edges to prevent frame translation without restraining frame rotation using a rod attached to the end of the frame with a clevis and pin arrangement. The test set up is shown in Figure 3.



Figure 3. Compression Test Fixture.

A summary of the test buckling and failure loads and failure modes is shown in Table 3. For comparison purposes the cross-sectional area of a single stringer bay midway between two frames is also shown in Table 3.

Table 3. Test panel failure summary.

Panel #	Single bay cross-sectional area	Buckling load, lb.	Failure load, lb.	Failure mode
614-1	0.3826	8318	28821	stringer crippling, inter-rivet buckling
614-2		7868	28551	
615-1	0.4450	13039	29787	stringer crippling
615-2		12365	29563	
616-1	0.7090	31473	78684	Euler column buckling
616-2		39342	82730	
617-1	0.5563	27427	55640	Euler column buckling, stringer crippling
617-2		28326	54764	

In general the failure load increases as the cross-sectional area increases. The two panel configurations having the smallest cross-sectional area and lightweight open hat stringers (614 and 615) failed due to stringer crippling. The crippled stringers are visible in Figure 4 for the 614-2 panel, and the crippled stringers and sharp skin buckles are visible in Figure 5 for the 615-1 test panel. The panel with the largest cross-sectional area and the heavyweight stringers (616) failed due to Euler column buckling as shown for the failed 616-1 panel in Figure 6. The 617 panel that has lightweight open hat stringers experienced both stringer crippling and Euler column failures. Both failure modes are shown in center section of the failed 617-1 panel in Figure 7.

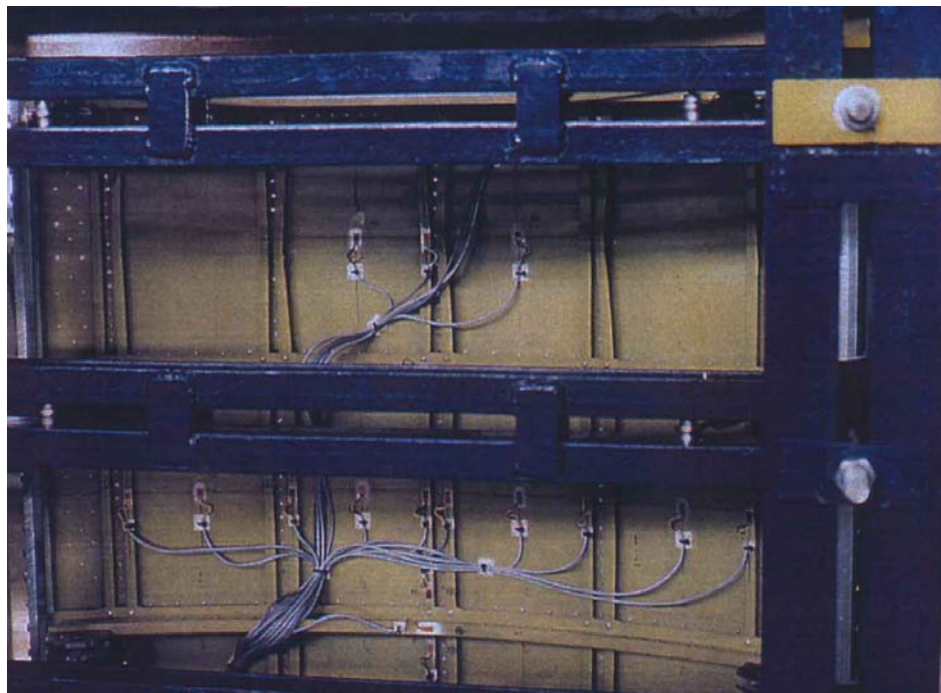


Figure 4. Interior view of failed section of panel 614-2.

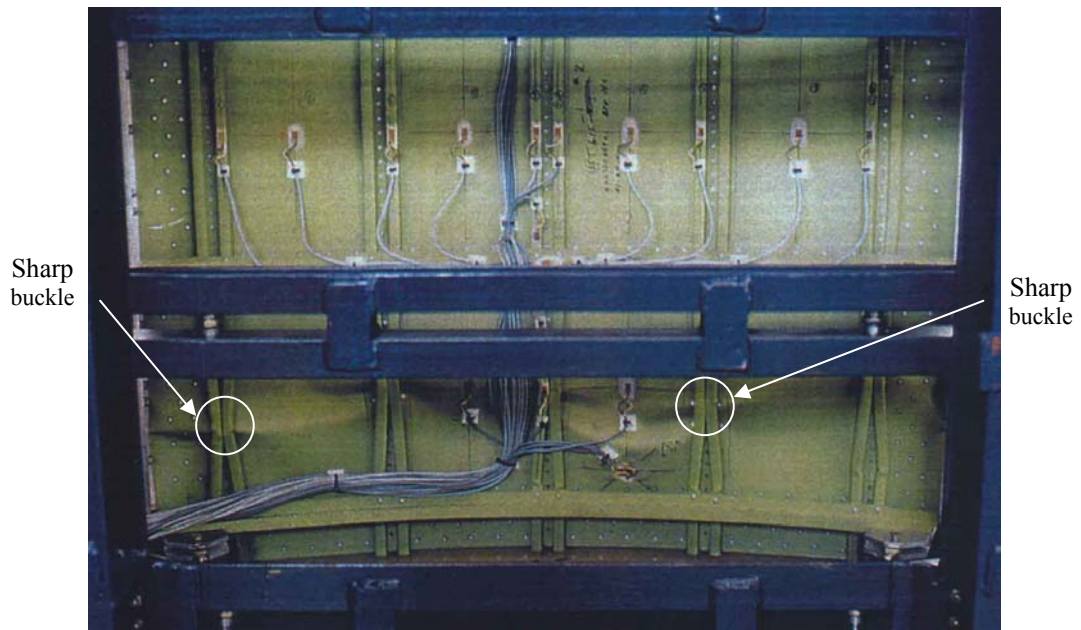


Figure 5. Interior view of failed section of panel 615-1.

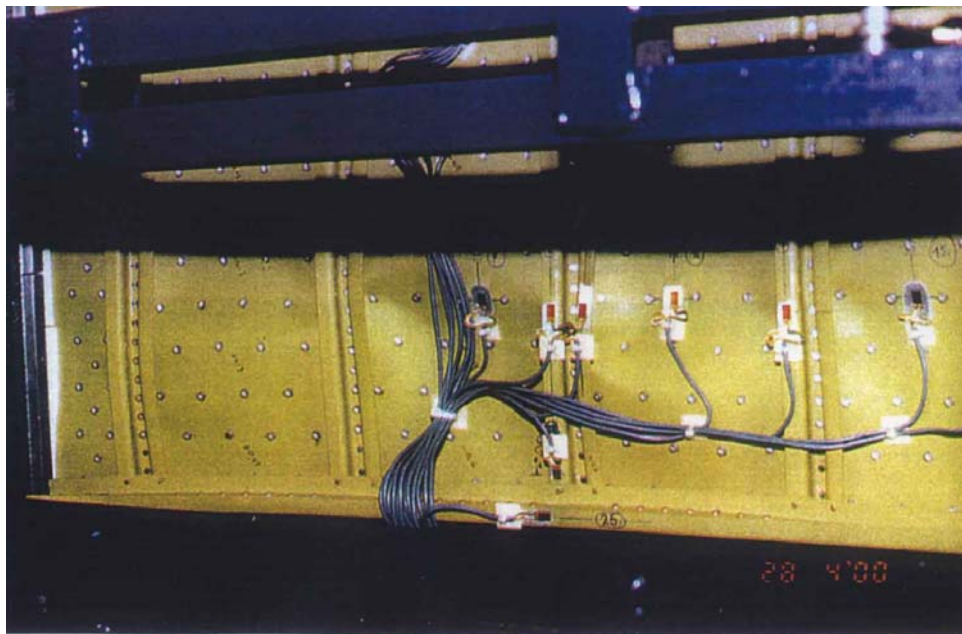


Figure 6. Interior view of failed section of panel 616-1.



Figure 7. Interior view of failed section of panel 617-1.

All of the panels had significant postbuckling strength, and none experienced any rivet failures or fastener pullout. Although the 615 panels that include a waffle doubler have a cross-sectional area 16% greater than the 614 panels, they did not exhibit a significant increase in failure load. The waffle doubler does however support the skin bay and delays the onset of buckling in the panel. For one panel of each configuration, the end-deflection is plotted against the applied load in Figure 8.

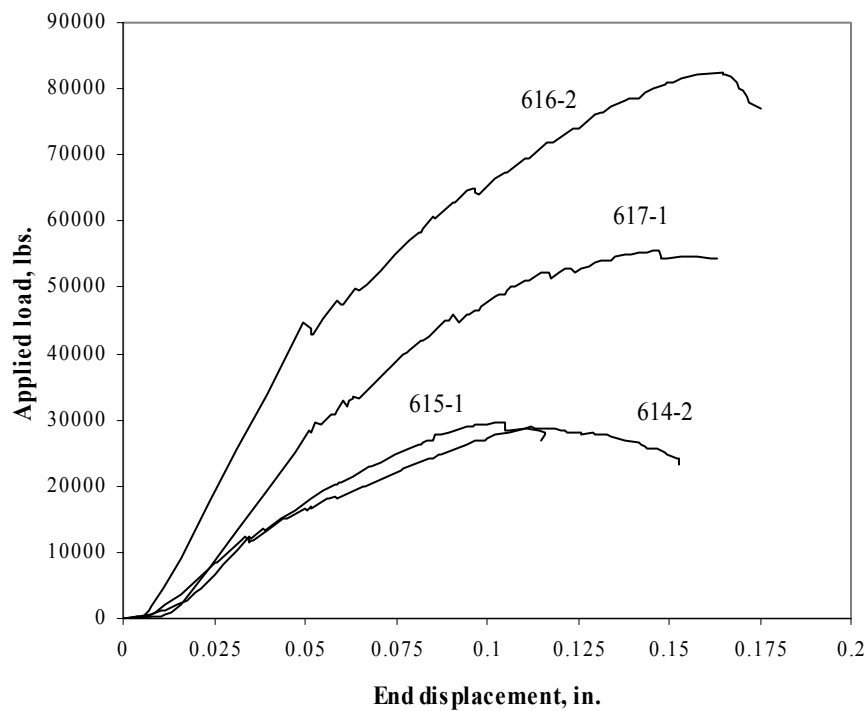


Figure 8. Normalized load-displacement curves for all test panels.

IV. Finite Element Results

Finite element analyses of the four test panel configurations are performed using STAGS (Ref. 5), a nonlinear finite element program for the analysis of general shell-type structures. The same level of refinement was originally used for all four configurations. All skin, stringer, and frame connections are assumed to be bonded. The frames, shear clips, stringers, and gussets are modeled explicitly, and constraints are used to connect these components to one another and to the skin. All models include geometric and material nonlinearity (elasto-plastic response permitted). A higher level of refinement is added to the 614 and 615 panels in order to capture the stringer crippling failures. Smaller study models are created for all four panel configurations to assess the effect of the riveted versus bonded stringer/skin connections on the ultimate failure of the panel. These smaller study models also have a higher level of refinement in addition to modeling the rivet connections as point constraints. Based on the study models, a factor is applied to the ultimate failure load of the panels obtained from the full scale finite element models. These failure loads are compared to the test panel failure loads.

A. Panel 614

The original model of the 614 panel configuration is shown in Figure 9(a). This model consists of 11,840 STAGS E410 4-node, C1 quadrilateral shell elements, 1,424 STAGS 210 Beam elements, 19,274 nodes, and 93,888 active degrees of freedom. The frame caps and stringer lips (dimension s4, Fig.2) are modeled as beams. This model grossly overpredicts the failure mode due to the fact that the failure mode predicted by the model is Euler column buckling instead of stringer crippling as was seen in the test. Therefore, a second model is made of the 614 panel that includes a higher mesh refinement and more detail in the stringer cross-section as shown in Figure 9(b). This model consists of 20,340 STAGS E410 4-node, C1 quadrilateral shell elements, 664 STAGS 210 Beam elements, 34,414 nodes, and 163,848 active degrees of freedom. In this model, the stringer lips are modeled with shell elements.

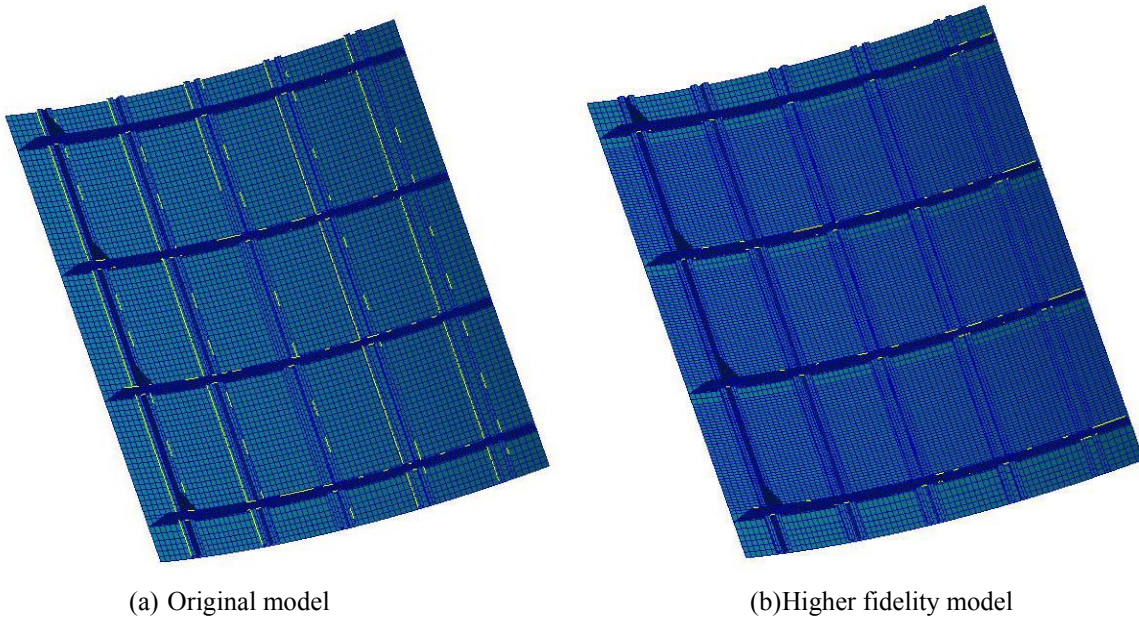


Figure 9. Finite element models for 614 panel configuration.

A linear buckling analysis is performed using the model in Figure 9(b). The linear finite element analysis predicts a first buckling load of 13,506 lbs corresponding to a skin buckling mode. The predicted buckling load is considerably higher than the lowest test panel skin buckling loads of 7868 lbs and 8318 lbs. However, skin buckling in other bays of the test panels continues up to 19,783 lbs. This indicates the presence of significant geometric imperfections in some of the panel skin bays.

A nonlinear analysis of the 614 panel configuration is conducted including both geometric nonlinearity and material nonlinearity. Initial geometric imperfections in the skin and stringers derived from eigenmodes calculated

at varying nonlinear equilibrium states are included in the model to help push the model past limit points associated with local buckling modes. The highest load value achieved with the nonlinear analysis is 43,471lbs. The deformed shape of the panel from the elasto-plastic failure analyses is shown in Figure 10. Both local stringer crippling and Euler column type buckling as seen in the test panel (Fig. 4) are visible.

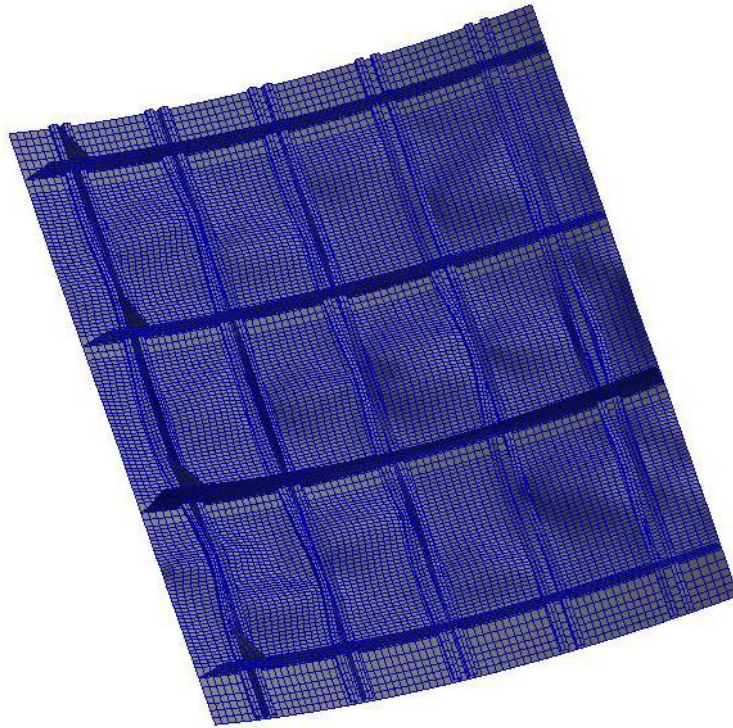
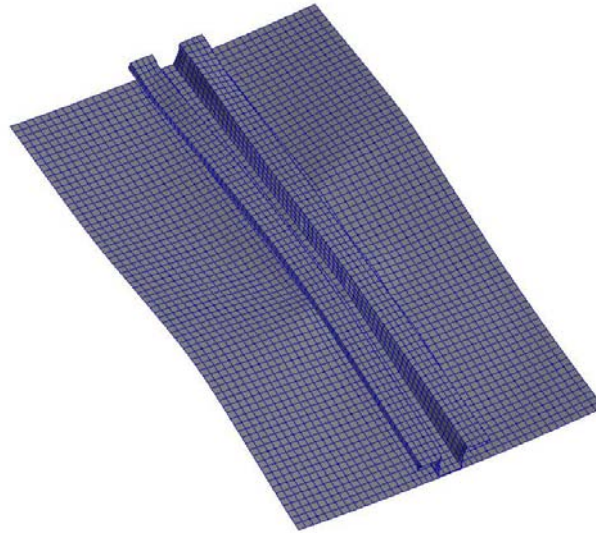
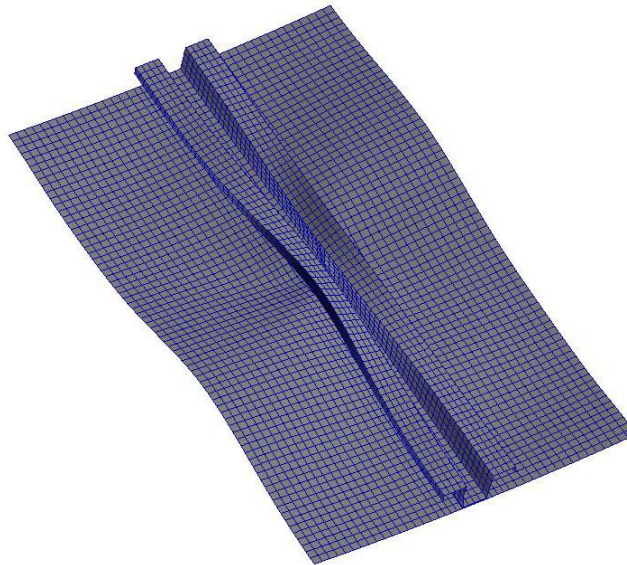


Figure 10. Deformed shape of 614 panel configuration at failure.

The maximum load obtained by the finite element model is 51 percent higher than the highest test panel failure load of 28,821 lbs. To assess the reduction in failure load for a riveted panel of this configuration versus a bonded panel of the same construction, two smaller models are created with and without riveted skin/stringer connections. The failed single bay models are shown in Figure 11. The reduction in failure load predicted by the single-bay models is 20 percent. Applying this reduction factor to the full panel model gives an estimated failure load of 34,777 lbs or 21 percent higher than the test panel failure load.



a) Bonded stiffener failure



b) Riveted stiffener failure

Figure 11. Single bay model failures for 614 panel configuration.

B. Panel 615

The 615 panel fails due to stringer crippling, therefore a higher fidelity model similar to the 614 panel configuration shown in Figure 9(b) is necessary to model the 615 configuration. The 614 panel model is modified to include the doublers under the stringers. The 615 panel configuration model consists of 20,340 STAGS E410 4-node, C1 quadrilateral shell elements, 664 STAGS 210 Beam elements, 32,446 nodes, and 167,484 active degrees of freedom.

A linear buckling analysis is performed and predicts a first buckling load of 16,211 lbs corresponding to a skin buckling mode. The predicted buckling load is higher than the lowest test panel skin buckling loads of 13,039 lbs and 12,365 lbs. However, skin buckling in other bays of the test panels continues up to 15,737 lbs. As with the 614 panels this indicates the presence of geometric imperfections in some of the panel skin bays.

A nonlinear analysis of the 615 panel configuration is conducted including both geometric nonlinearity and material nonlinearity. Initial geometric imperfections derived from eigenmodes calculated at varying nonlinear equilibrium states are included in the model to help push the model past limit points associated with local buckling modes. The highest load value achieved with the nonlinear analysis is 45,621 lb. The deformed shape of the panel from the elasto-plastic failure analyses is shown in Figure 12. The stringer crippling failures as seen in the test panel (Fig. 5) are visible.

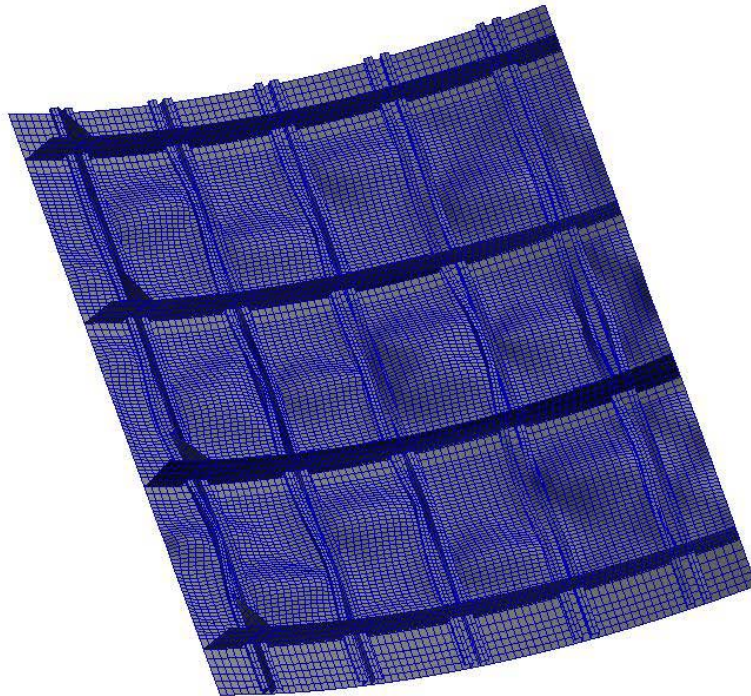
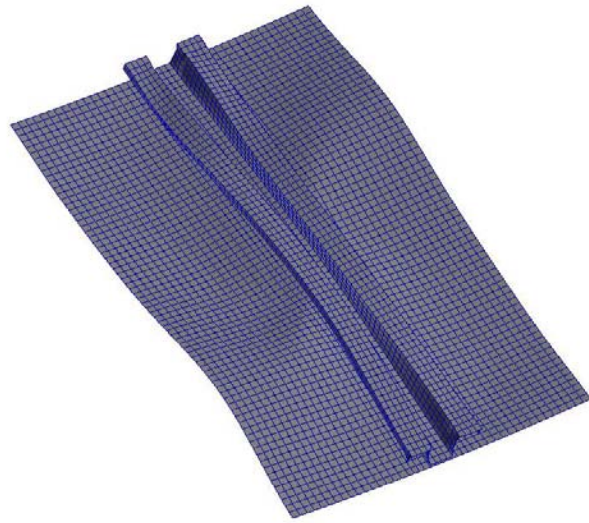
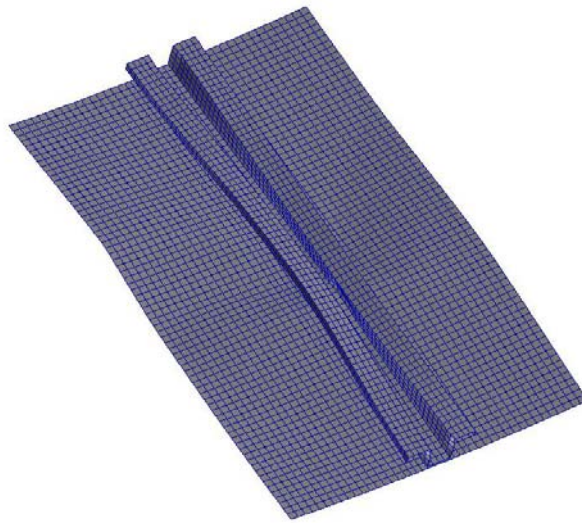


Figure 12. Deformed shape of 615 panel configuration at failure.

The maximum load obtained by the finite element model is 53 percent higher than the highest test panel failure load of 29,787 lbs. To assess the reduction in failure load for a riveted panel of this configuration versus a bonded panel of the same construction, two smaller models are created with and without riveted skin/stringer connections. The failed single bay models are shown in Figure 13. The reduction in failure load predicted by the single-bay models is 16 percent. Applying this reduction factor to the full panel model gives an estimated failure load of 38,321 lbs or 29 percent higher than the test panel failure load.



(b) Bonded stiffener failure



(b) Riveted stiffener failure

Figure 13. Single bay model failures for 615 panel configuration.

C. Panel 616

The original less-refined panel model similar to Figure 9(a) is used for the 616 panel configuration. This model consists of 11,820 STAGS E410 4-node, C1 quadrilateral shell elements, 584 STAGS 210 Beam elements, 19,274 nodes, and 93,888 active degrees of freedom.

A linear buckling analysis is performed and predicts a first buckling load of 45,314 lbs corresponding to a skin buckling mode. The predicted buckling load is higher than the lowest test panel skin buckling loads of 31473 lbs and 39342 lbs. However, skin buckling in other bays of the test panels continues past 48,000 lbs. As with the 614 panels this indicates the presence of geometric imperfections in some of the panel skin bays.

A nonlinear analysis of the 616 panel configuration is conducted including both geometric nonlinearity and material nonlinearity. Initial geometric imperfections in the skin panels derived from eigenmodes calculated at varying nonlinear equilibrium states are included in the model to help push the model past limit points associated with local buckling modes. The highest load value achieved with the nonlinear analysis is 95,188. The deformed

shape of the panel from the elasto-plastic failure analyses is shown in Figure 14. The Euler column failures as seen in the test panel (Fig. 6) are visible in the center section of the model.

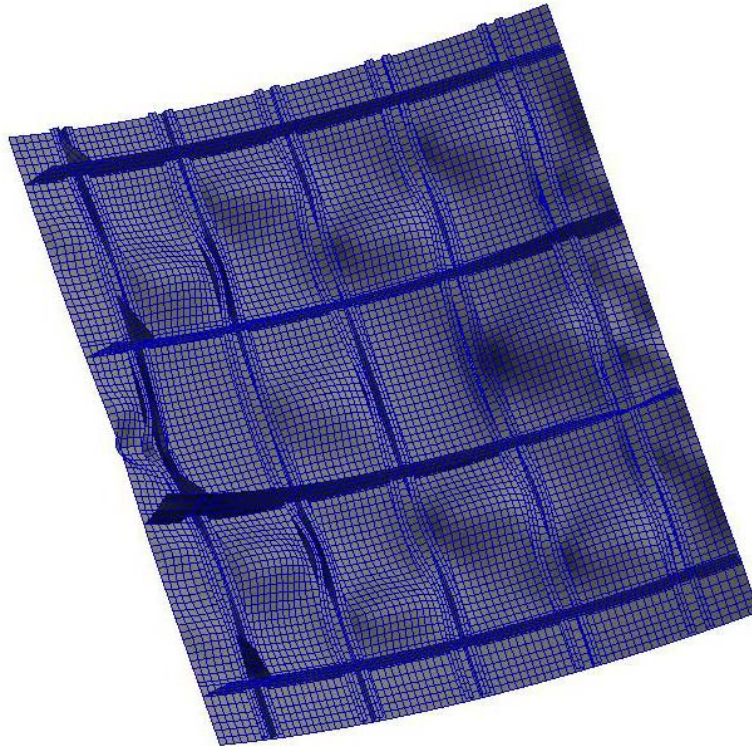
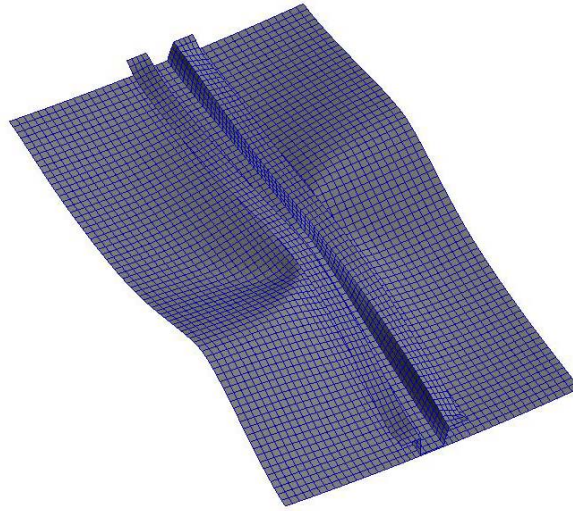
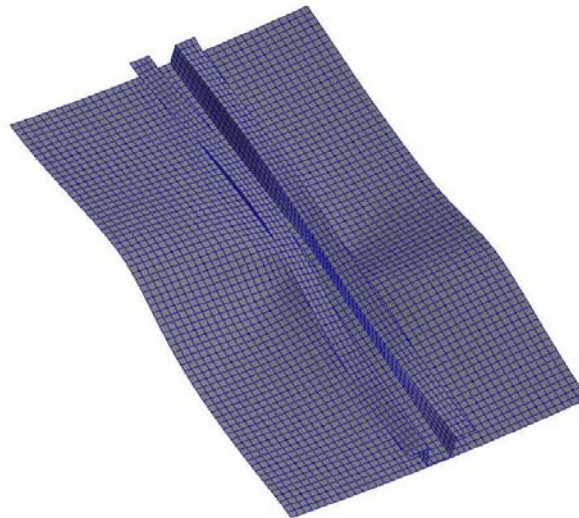


Figure 14. Deformed shape of 616 panel configuration at failure.

The maximum load obtained by the finite element model is 15 percent higher than the highest test panel failure load of 82,730 lbs. To assess the reduction in failure load for a riveted panel of this configuration versus a bonded panel of the same construction, the two smaller models are created with and without riveted skin/stringer connections. The failed single bay models are shown in Figure 15. The reduction in failure load predicted by the single-bay models is 9 percent. Applying this reduction factor to the full panel model gives an estimated failure load of 86,621 lbs or 5 percent higher than the test panel failure load.



a) Bonded stiffener failure



b) Riveted stiffener failure

Figure 15. Single bay model failures for 616 panel configuration.

D. Panel 617

The model of the 617 panel configuration is shown in Figure 15. The model consists of 10,404 STAGS E410 4-node, C1 quadrilateral shell elements, 1,424 STAGS 210 Beam elements, 17,934 nodes, and 86,568 active degrees of freedom.

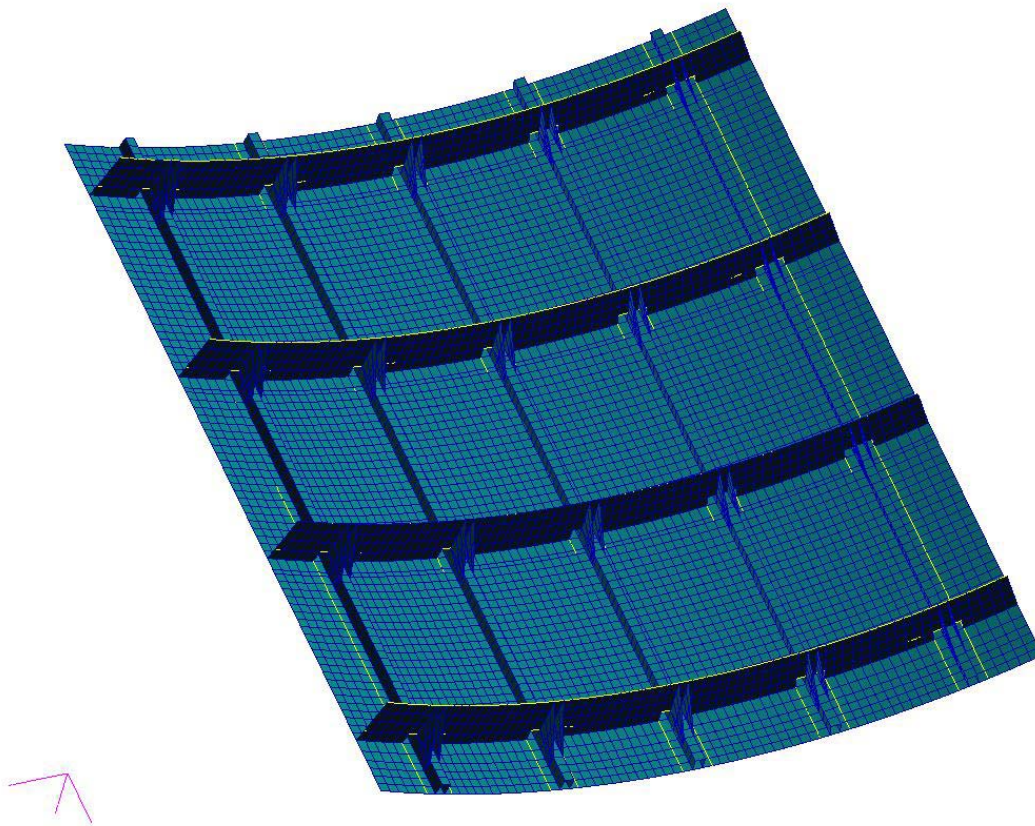


Figure 15. Panel 617 configuration finite element model.

First a linear buckling analysis is performed using the model in Figure 15. The linear finite element analysis predicts a buckling load of 29,530 lbs corresponding to a skin buckling mode. This buckling load is slightly higher than the test panel skin buckling loads of 27,427 lbs and 28,326 lbs.

Secondly a nonlinear analysis of the 617 panel configuration is conducted including both geometric nonlinearity and material nonlinearity. Initial geometric imperfections in the skin panels derived from eigenmodes calculated at varying nonlinear equilibrium states are included in the model to help push the model past limit points associated with local buckling modes. The highest load value achieved with the nonlinear analysis is 59,046 lbs. The deformed shape of the panel from the elasto-plastic failure analyses is shown in Figure 16. Euler column type buckling as seen in the test panel is visible in the outside stringers of the center section of the panel.

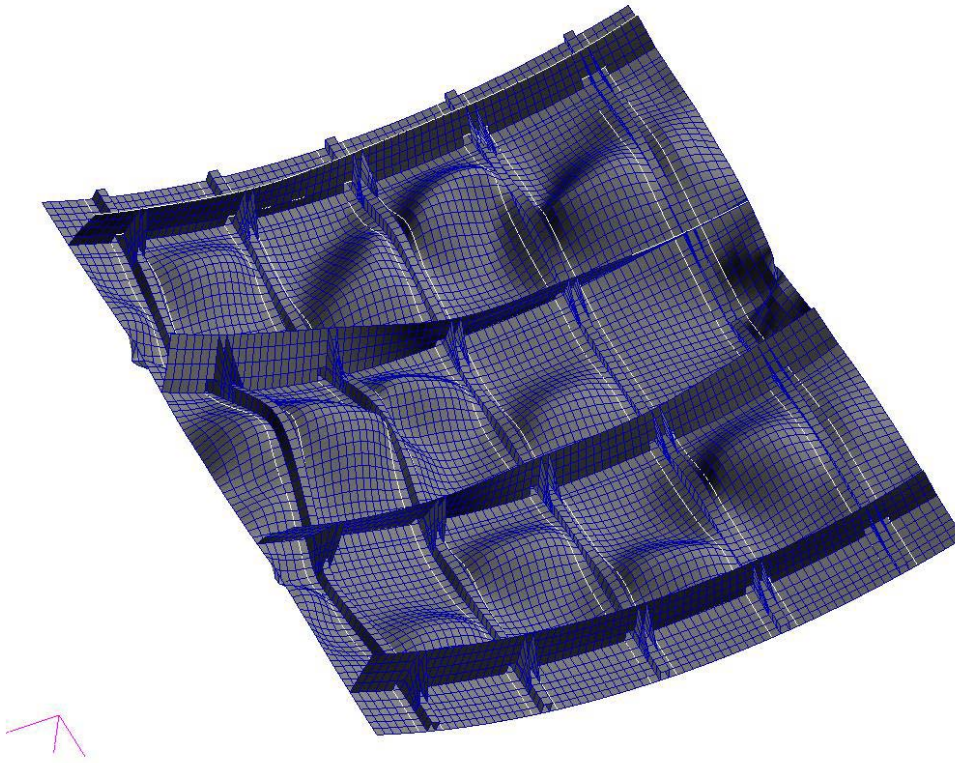
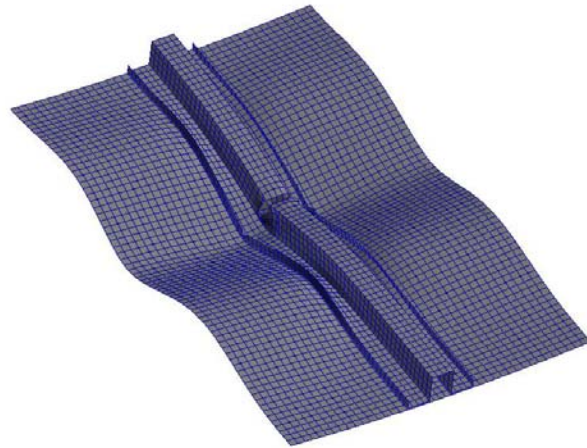
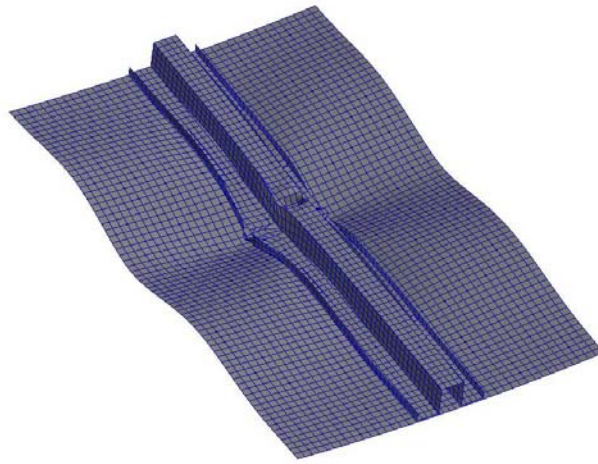


Figure 16. Deformed shape of 617 panel configuration at failure.

The maximum load obtained by the finite element model is 6.5 percent higher than the highest test panel failure load of 55,460 lbs. To assess the reduction in failure load for a riveted panel of this configuration versus a bonded panel of the same construction, two smaller models are created with and without riveted skin/stringer connections. The failed single bay models are shown in Figure 17. The reduction in failure load predicted by the single-bay models is 13 percent. Applying this reduction factor to the full panel model gives an estimated failure load of 51,370 lbs or 7.4 percent lower than the test panel failure.



(a) Bonded stiffener failure



(b) Riveted stiffener failure

Figure 17. Single bay model failures for 617 panel configuration.

V. Summary

A summary of the finite element and experimental results is presented in Table 4. The initial buckling of the panels is driven by the skin thickness and stringer doubler width. The 614 and 615 panel configurations which have an .04 in. skin thickness and no doubler and a 2 in. wide doubler, respectively, have the lowest initial buckling loads. The 616 panel configuration which has a doubler over the entire .04 in. skin has the highest buckling load, and the 617 panel configuration that does not have a doubler but has a 0.063 in. skin has initial buckling loads close to the 616 panel configuration. Finite element initial buckling predictions are from a linear eigenvalue analysis that assumes a perfect shell structure. Imperfection measurements of the skin panels indicate that for the .04 skin panels (614, 615, and 616 configurations) the imperfection magnitude is greater than the skin thickness along the arclength of the panels. For the panel with the thicker skin (617), the skin imperfections along the arclength of the panel are less than the skin thickness. For this reason, the initial buckling predictions for the 617 panel are more accurate than for the other panel configurations. However for each panel, buckling of subsequent bays does occur in the range of the predicted buckling load.

Table 4. Experimental and Analytical Buckling and Failure Loads.

Panel Configuration	Buckling Load, lbs			Failure Load, lbs			
	FEM	Test	% diff	FEM	Factored FEM	Test	% diff
614	13506	8318	-62	43471	34777	28821	-21
		7868	-72			28551	-22
615	16726	13039	-28	45621	38321	29787	-29
		12365	-35			29563	-30
616	45314	31473	-44	95188	86621	78684	-10
		39342	-15			82730	-5
617	29530	27427	-8	59046	51370	55640	8
		28326	-4			54764	6

The ultimate failure of the panels is driven by the stiffness of the stringers. The 614 and 615 panel configurations both have .025 in. thick open-hat stringers that fail due to stringer crippling. The 616 panel configuration has an .063 in. thick open-hat stringer, and the 617 panel configuration has an .025 in. closed-hat stringer. Both the 616 and 617 panel configurations experience Euler column failures of the stringers. Therefore, the original less-refined finite element models for these two configurations predict failure with reasonable accuracy when the effect of the riveted connection is taken into consideration. In addition only skin imperfections are included in the 616 and 617 panel analyses. Because the 614 and 615 panel configurations fail due to local stringer crippling, more refinement is needed in the finite element models. A higher mesh density, a greater cross-section fidelity, and the inclusion of stringer imperfections are all necessary to predict the failure of the 614 and 615 panels. Failure predictions for these two panel configurations are the least accurate most likely due to imperfections in the stringers that were not measured before testing.

References

- ¹ Arnold, R. R., and Parekh, J. C., "Buckling, Postbuckling, and Failure of Stiffened Panels Under Shear and Compression," *Journal of Aircraft*, Vol. 24, No. 11, November 1987, pp. 803-811.
- ² Minnetyan, L., Rivers, J. M., Murthy, P. L. N., and Chamis, C.C., "Structural Durability of Stiffened Composite Shells," *Proceedings of the AIAA 33rd Structures, Structural Dynamics, and Materials Conference*, AIAA paper 92-2244, April 1992, pp. 2879-2886.
- ³ Collier, C., Yarrington, P., and Van West, B., "Composite, Grid-Stiffened Panel Design for Post Buckling Using Hypersizer," *Proceedings of the AIAA 43rd Structures, Structural Dynamics, and Materials Conference*, No. AIAA-2002-1222, April 2002.
- ⁴ C Lamberti, L., Venkataraman, S., Haftka, R. T., and Johnson, T. F., "Preliminary Design Optimization of Stiffened Panels Using Approximate Analysis Models," *International Journal of Numerical Methods in Engineering*, Vol. 57, July 2003, pp. 1351-1380.
- ⁵ Brogan, F. A., Rankin, C. C., and Cabiness, H. D., "STAGS User Manual", Lockheed Martin Missiles and Space Co., Rept. LMSC P032594, Palo Alto, CA, June 1994.

Failure Analysis of Discrete Damaged Tailored Extension-Shear-Coupled Stiffened Composite Panels

Donald J. Baker*

Vehicle Technology Directorate – ARL, NASA Langley Research Center, Hampton, VA 23681

The results of an analytical and experimental investigation of the failure of composite I-stiffener panels with extension-shear coupling are presented. This tailored concept, when used in the cover skins of a tiltrotor aircraft wing has the potential for increasing the aeroelastic stability margins and improving the aircraft productivity. The extension-shear coupling is achieved by using unbalanced $\pm 45^\circ$ plies in the skin. The failure analysis of two tailored panel configurations that have the center stringer and adjacent skin severed is presented. Finite element analysis of the damaged panels was conducted using STAGS (S_{TR}uctural Analysis of General Shells) general purpose finite element program that includes a progressive failure capability for laminated composite structures that is based on point-stress analysis, traditional failure criteria, and ply discounting for material degradation. The progressive failure predicted the path of the failure and maximum load capability. There is less than 12 percent difference between the predicted failure load and experimental failure load. There is a good match of the panel stiffness and strength between the progressive failure analysis and the experimental results. The results indicate that the tailored concept would be feasible to use in the wing skin of a tiltrotor aircraft.

I. Introduction

One of the principal design challenges for high-speed tiltrotor transport aircraft is achieving acceptable proprotor aeroelastic stability margins, which can restrict the operating airspeed of the tiltrotor aircraft in the high-speed airplane mode. The primary mechanism responsible for the proprotor stability problems is discussed by Popelka, et al¹ and will be briefly reviewed here. Historically, the most critical modes affecting the proprotor stability are the symmetric wing beamwise bending (SWB) mode and the symmetric wing chordwise (SWC) bending mode. For these modes, the proprotor can create destabilizing in-plane hub forces, which can overcome the structural and aerodynamic damping of the wing at high speed and resulting in instability. The in-plane shear forces are generated by the proprotor in response to the pylon pitch angle perturbation and pitch rate. The wing SWB mode, SWC mode and symmetric wing torsion (SWT) mode dictate the pylon pitch rate and pitch angle. Proprotor stability can be influenced by changing the frequency placement of the wing modes and by modifying the mode shapes to alter the pylon dynamic response and reduce the destabilizing in-plane hub forces.

In a typical tiltrotor wing design, the rotor pylon pitches up as the wing bends upward in the SWB mode. To increase the stability boundary it is necessary to minimize the pylon pitch motion (θ) in the fundamental wing mode to increase the proprotor stability by reducing the rotor destabilizing forces as shown in Fig. 1. For a conventional tiltrotor composite wing design with structurally balanced skin laminates, the wing provides no structural pitch/bending coupling to resist the nose up pitch due to pylon mass offsets. Unbalanced composite skins, on the other hand, can create nose down structural twist as the wing bends upward to offset the pitch up tendency from the pylon mass offsets. The net effect is reduced pitch/bending (θ/z) coupling and improved stability. The preceding discussion applies to the SWB mode only.

The effects of structural tailoring can be simply shown by considering the cantilever boxbeam shown as the model in Fig. 2. The direction of the -45° plies are shown on Fig. 2. The forward and aft spar web is a balanced $\pm 45^\circ$ laminate. The upward bending from the pylon produces a compression load in the upper skin and a tension load in the lower skin as shown in Fig. 2. The compression load in the upper skin produces an in-plane deflection in the forward direction. The tension load in the lower skin produces an in-plane deflection in aft direction. These in-

* Aerospace Engineer, Mechanics of Structures and Materials Branch, MS 150, Langley Research Center.

plane deflections in the skins combine to produce a couple that results in a nose down pitch as shown in the deformed model in Fig. 2.

The feasibility of a composite tailored wing for a high-speed civil tiltrotor transport aircraft has been addressed by Popelka,² et al, using current analytical methods to design a tailored composite wing for a tiltrotor transport aircraft. Parametric studies indicate that the overall stability gains from composite tailoring can be limited because of conflicting structural design requirements imposed by the two critical modes of instability, SWB and SWC, and the necessity to balance the stability boundaries for both modes. The SWC mode stability can be improved by increasing the chordwise bending stiffness of the wing. The final tailored transport wing configuration from Reference [3] was a three-stringer configuration with a 70/30 blend ratio of $-45^\circ/+45^\circ$ plies for the skin laminate along with stringer cap and spar cap tailoring to improve the SWC mode.

A 1/5-scale wing model was designed to have the same elastic characteristics as the full-scale tailored wing and was tested in a semi-span aeroelastic model to demonstrate that composite tailoring techniques can be used to improve prop rotor stability³. A direct comparison between the baseline and tailored composite wing stability boundaries indicates an increase over baseline of approximately 30 knots in the scaled model or 58 knots in the full-scale design. For a full-scale design, the 58 knot increase in the stability boundary represents a significant improvement.

Recent work has assessed the detailed structural response of tailored panels with and without damage. Specifically, this work addressed: a) development of a test method for testing elastically coupled specimens and b) demonstration of the coupled response of the full-scale wing panel subcomponents with and without impact and discrete source damage. The analytical and experimental results of the study are presented in Reference [4] and illustrate the predictive capability for stiffened, anisotropic panels.

The present paper will summarize the failure analysis of the two panels configurations reported in Reference [4] that have discrete source damage. Specifically, this research addresses: a) utilization of a progressive failure analysis method, and b) comparison of the predicted failure mode with the actual test results. A method of recording the full field displacements at timed intervals during the testing is utilized and will be verified using standard measurement techniques. The analytical and experimental results of the study are presented and compared to illustrate the predictive capability for stiffened, anisotropic panels.

II. Test Specimens and Test Method

The panels to be evaluated were designed by Bell Helicopter, Textron, using the results of the study by Popelka,² et, al and are shown in Fig. 3a. A cross-section of the stiffener and skin is shown in Fig. 3b. The skin is 21 plies increasing to 47 plies under the I-stiffener using Grade 190 IM6-3501-6 carbon-epoxy tape material. The skin orientation is $[45/90/-45_3/45/-45_3/45/\bar{0}]_s$, where 67% of the 45° plies are oriented at the negative angle. The ply orientation for the reinforced area under the stiffener is $[45/90/-45_3/45/a/0_3/a/-45_2/a/0_4/a/-45/45/0/45/-45/a/0_4/a/-45_2/a/0_3/a/45/-45_3/90/45/a/45^I/-45^I/a]$. Where “a” identifies a 0.008-inch-thick layer of FM300 adhesive. The I-stiffener is fabricated from back-to-back C-channels which have the following layup: $[-45/90_2/45/0_4/-45/0_4/45/0_4/45/0_2]$. The cap of the I-stiffener has a layup of $[0_2/-45/0_4/-45/0_4/45/0_4/-45/90_2/45]$. The material for the stiffener and cap is Grade 95 IM6-3501-6 carbon-epoxy material. The stringer spacing is 7.5 inches, which gives an overall panel width of approximately 19 inches.

Four 4-foot-long panels, as shown in Fig. 3a, were manufactured at two different times. These panels were cut into 23-inch-long test specimens, potted and ground flat and parallel for testing. Panels TP-1 through TP-4 were manufactured from the first fabrication run and panels TP-5 through TP-8 were manufacture from the second manufacturing run. Panels TP-4 and TP-7 were selected to have discrete damage by machining a slot through the center stiffener and adjacent skin. The slot extends from the center of each skin panel and is 0.38-inch-wide in the center of the specimen tapering to 0.18-inch-wide at the ends with a tip radius of 0.09-inch. These panels will be identified as *Horizontal cut* panels. Panel TP-5 also had the center stiffener cut similar to the *Horizontal cut* panels except the cut was rotated 15° from the horizontal and will be identified as an *Inclined cut* panel. Photographs of the test specimens are shown in Fig.4.

All specimen tests were performed at room temperature, with no prior environmental conditioning. The specimens were placed between the platens of a 600 kip or 1200 kip hydraulic test machine and loaded at 5 kips/min in compression until failure. The load, strain, out-of-plane and head displacements were recorded with a computer-controlled data acquisition system for each test. The VIC-3D system is also computer controlled for acquiring the images and load at timed intervals.

III. Instrumentation

Three measurement techniques were utilized to determine the response of these panels:

Strain gages – Common off the shelf strain gages were used on the panels. Both the panel configurations contained the same number of gages. Five axial gages (numbers 1, 2, 3, 13 and 14) were located on the stringer caps – one gage was located on each stringer at the quarter point of the panel length and one gage was located on the outside stringers at the panel midpoint. One rosette gage was located on each skin panel centerline and at the quarter point length, on the stringer side. Three axial gages (numbers 4, 5 and 6) were located on the skin side at the quarter point length opposite the axial gages on the stringer caps. One strip gage with 10 gages was located at each end of the slot. The strip gage was located horizontally, on the stringer side, on each panel configuration. Most of the strain gages can be seen in Fig.4.

Displacement transducers – Two Linear Variable Displacement Transducers (LVDT) were located between the test machine platens to measure the panel end shortening. Six LVDT's were utilized to measure the out-of-plane displacements at panel centerline. Four LVDT's were located on the stringers and two LVDT's were located at the skin panel centerline.

Three-dimensional Video Correlation System (VIC-3D) - This system is a full-field-displacement measurement technique [5] that utilizes a camera-based stereo-vision system. VIC-3D[†] is a non-intrusive system that uses a contrasting speckle pattern (e.g., black and white paint) applied to the specimen to provide dense features that can accurately be tracked between different cameras and during deformation. Images of the changing pattern on the test specimen surface are recorded on a computer with the stereo-vision system at user specified time intervals. It is also possible to take data in a local area, e.g., in the vicinity of a notch, with a second camera based system while taking data on a global area. This will give higher resolution to the displacements in the local area of interest.

The strain gages were located on the back side of the damaged panels to allow approximately 60 percent of the skin surface free for the application of a 0.004-inch-thick white vinyl contact paper that has been printed with a random black spackle pattern. A 4.0-inch by 4.0-inch area was selected at one tip of the slot for the local area of interest. The first step in panel preparation was to prepare an area larger than the selected local area with white paint and black spackles. Then the vinyl paper was applied to the global area of interest on the panel. Finally the vinyl paper was removed from the local area of interest.

To determine the geometry of the test specimen just prior to testing, an image of the unloaded specimen is taken as the reference. The specimen shape is determined by the analysis software from the image, and a best fit plane is fit to the image data using 8,000 to 10,000 data points. The best-fit plane is then used as the x-y plane of a new coordinate system, and the data can be plotted as a three-dimensional color-coded contour plot, which permits visual identification of defects.

The VIC-3D analysis software converts the image data taken during a test to the full field u, v, and w displacements. Since the displacements are known, the strains can also be computed. The results can be displayed as displacement or strain contours in 2D or 3-D projections on the deformed or reference surface. Two-dimensional contour plots can also be developed. Options exist that allow extraction of displacement and/or strain results at a point in the image or along a line on the image. Selecting a line on the surface will give the profile of the panel cross-section or all displacements and strains at a pre-selected load. The line location is approximated by selecting two points on the screen. At the present it is not possible to select this line location or any point in direct relation to the specimen reference frame. Selecting a point on the screen is the only method.

For test specimens that have a curvature in a single direction, this software has an option for conversion to a cylindrical coordinate system.

IV. Analysis

Finite element analysis of the panels was conducted using STAGS nonlinear analysis code⁶ to determine the test specimen response. STAGS (STructural Analysis of General Shells) is a general-purpose finite element analysis code for the analysis of shell structures of arbitrary shape and complexity. The STAGS finite element code has unique capabilities related to postbuckling analysis, crack bulging, and damage progression for metallic and laminated composite structures. STAGS also includes a progressive failure capability for laminated composite structures that is based on a point-stress analysis, traditional failure criteria, and ply discounting for material degradation. For the analysis of these panels the maximum strain failure criteria was used at the ply level. Details of the analysis of each panel configuration are given in the following sections.

[†]VIC-3D system supplied by Correlated Solutions, Inc., W. Columbia, SC

A. Horizontal cut panel

The STAGS finite element model for the *Horizontal cut* panels is shown in Fig. 5. The model contains 12,771 quad elements (element 410 in the STAGS element library) and 12,494 nodes. A progressive failure analysis of the *Horizontal cut* panel was performed with the STAGS finite element model by applying an incremental axial displacement to load the specimen to simulate the loading in a test machine. The material properties used in the analysis are typical IM6/3501 carbon-epoxy properties and are shown in Table 1. The material property values shown in Table 1 are typical vendor supplied data and the property distributions were unknown. It was necessary to estimate some of the properties not available in the literature. The predicted initial failure occurred at a load of $N_y = 4.84$ kips/in. The initial failure, shown in Fig. 6, started at each end of the machined slot and started to turn to the right in the top detail and to the left in the bottom detail. The elements that failed indicate that 30 percent to 80 percent of the plies have failed. Increasing the axial displacement until a maximum load was achieved resulted in the predicted failure load for the specimen to be $N_y = 7.87$ kips/in. The progression of failure to the maximum load is shown in Fig. 7. The predicted failure progressed from the initial failure down across the skin at a 35° angle to the panel centerline and stops at the edge of the skin. More than 60% of the plies have failed in the elements that indicated failure. The predicted failure progressed up at a 35° angle to the centerline and has turned into the transition to the stringer pad up. The predicted in-plane (v) and out-of-plane displacements (w) at the maximum load are shown in Fig. 8. The out-of-plane displacements (Fig. 8) predict a skewed pattern resulting from the anisotropic properties of the skin. An increased area of out-of-plane displacement is predicted at the skin failure area. The slot in the central stringer and skin combined with the skin fractures eliminate most of the in-plane coupling. By increasing the axial displacement, the resulting load carrying capacity of the specimen is reduced and the failure line can be predicted. After approximately 100 displacements steps, the failure progresses across one stringer as shown in Fig. 9 and the load carrying capacity is reduced to $N_y = 5.78$ kips/in. As indicated in Fig. 9, the stringer is predicted to be completely severed. Increasing the displacement steps completes the failure line across the entire panel as shown Fig.10 and the load capacity has fallen to $N_y = 2.74$ kips/in. The predicted panel end shortening and transverse in-plane displacement as a function of load are shown in Fig.11. A least squares best fit to the axial displacement between 0 and 5 kips/in. of load is also shown as a dashed line in Fig. 11. The slope of the line is 111.92 kips/in/in. At an applied load of 4.84 kips/in. the predicted in-plane displacement is 15.8 percent of the axial displacement. The axial displacement curve is linear until over 5 kips/in (past the initial failure) and then slightly nonlinear to failure. The remainder of the curve reflects the load reduction indicated previously as different elements of the panel fail.

B. Inclined cut panel

The STAGS finite element model of the specimen with the inclined cut is shown in Figure 12. This model contains 12,702 quad elements and 12,429 nodes. A progressive failure analysis of the *Inclined cut* panel was performed with the STAGS finite element model by applying an incremental axial displacement to load the specimen to simulate the loading in a test machine. The material properties used in the analysis are typical IM6/3501 carbon-epoxy properties and are shown in Table 1. The predicted initial failure occurred at $N_y = 3.8$ kips/in. as shown in Fig. 13 and started at each end of the slot. The failed element at the bottom of the slot as shown in Fig. 13 indicated approximately 25 percent of the plies had failed while the failed element at the top of the slot indicated approximately 40 percent of the plies had failed. Increasing the axial displacement until a maximum load was achieved resulted in the predicted failure load for the specimen to be $N_y = 8.53$ kips/in. The failure progressed down and to the left at a 50° angle from the panel centerline with increasing load as shown in Fig. 14. The failure progressed into the edge of the transition area on the lower side of Fig. 14 while only a few elements indicate damage on the upper side of the slot. Information shown in Figures 14 and 15 are at a load of $N_y = 8.43$ kips/in which is on the unload phase after the maximum load has been achieved. The out-of-plane displacements shown in Fig. 15a predicts a positive 'w' displacement at the top end of the slot while a negative out-of-plane displacement is predicted along the lower part of the slot but not at the tip of the slot. The skin failure can be seen in the in-plane displacements (Fig. 15b). The load continues to drop as the displacement of the test machine platens is increased. The failure progresses to the edge of the panel as shown in Fig 16. At this point only the skin has failed. The stringer cap and web has not failed. A very few additional elements indicated failure at the top of the slot. Increasing the axial displacement for approximately 20 steps the load is maintained at approximately $N_y = 5.7$ kips/in. Then the loads increased as the axial displacement increases resulting in more elements failing and the lower stringer failing in the web and started to fail in the cap. The predicted axial strains in the skin for $N_y = 6.31$ kips/in are shown in Fig. 17. Strain in the bottom of the panel as shown in Fig. 17 is nearly zero. The fracture area is indicated by the strain in excess of 3 percent. Most of the strain is in the top of the panel where the stringer is still

intact. The small strain concentration in the skin on the bottom of the panel is over the stringer that is not completely failed. The load reverses again with increasing the axial displacements. A few more elements fail at the upper end of the slot. Failures are occurring at other locations such as along the web and flange intersection. The predicted panel end shortening and transverse in-plane displacement as a function of load are shown in Fig.18. A least squares best fit to the axial displacement between 0 and 5 kips/in. of load and has a slope of 111.2 kips/in/in. The axial displacement curve is linear until over 5 kips/in (past the initial failure) and then slightly nonlinear to failure. The remainder of the curve reflects the load reduction indicated previously.

V. Test Results and Discussion

Each panel configuration will be discussed individually in the following section

C. Horizontal cut panels

The profile of both *Horizontal cut* panels was determined using the VIC-3D system and most of the surface of panels TP-4 and TP-7 varying ± 0.010 -inches from the theoretical plane with local areas near the edges varying up to 0.06-inch from the theoretical plane⁴. The *Horizontal cut* panels were loaded in compression until failure. The average failure load for the two *Horizontal cut* panels (TP-4 & TP-7) is 7.65 kips/in. Panel TP-4 failed at 7.80 kips/in. while panel TP-7 failed at 7.51 kips/in. This average failure load of 7.65 kips is 97 percent of the predicted failure load of 7.87 kips/in. The average residual strength of the *Horizontal cut* panels is 37 percent of the average strength of undamaged panels⁴. A plot of the *Horizontal cut* panels axial end shortening as a function of load is shown in Figure 19 as solid lines with a filled circle (TP-4) or a filled triangle (TP-7). The transverse in-plane displacements are also shown in Fig. 19 as dashed lines and the same symbols as previously noted. The predicted end displacements are also shown in Fig. 19 as lines (solid or dashed) with a filled square symbol. The average panel axial stiffness of 100.2 kips/in/in. is approximately 10 percent below the computed stiffness of 111.9 kips/in/in. Specimen TP-4 transverse in-plane displacement matches the analysis predictions until a step in the displacement at approximately 5.5 kips/in. The analysis predicted the in-plane transverse displacement to be 15.8 percent of axial displacement. Specimen TP-7 does not show any in-plane displacement until 5.5 kips/in.

An obvious advantage of the VIC-3D system is the recording of events at timed intervals through out the test is that phenomena that occur temporarily have a good chance of being recorded. An intermediate result from the VIC-3D system is shown in Fig. 20 for panel TP-7 where the global view indicates that the panel is bulging in the middle as determined by the concentric out-of-plane contours around the slot. These *Horizontal cut* panels also had a second VIC-3D system recording the response at a local area as defined at the left end of the slot as shown in Fig. 20. This local area, shown in Fig. 20, indicated a delamination was in progress at the corner of the slot for panel TP-7. The delamination shown is for a load of $N_y = 5.1$ kips/in. and is near the end of the slot. The appearance of the delamination started at approximately $N_y = 4.6$ kips/in. and continued to grow until $N_y = 5.61$ kips/in. The delamination could have started at a lower load but would be missed due to a strip of image data on all edges that is lost in the analysis process. There could also have been a delamination on the right end of the slot as it was not be monitored with a local set of cameras. Up to a load of $N_y = 5.61$ kips/in the delamination was only visible in the local area images. At $N_y = 5.76$ kips/in the delaminations/damage grew in size and was visible in the global view image on the L/H side of the slot as shown in Fig. 21a and the delamination/damage does not appear on the R/H side of the slot until $N_y = 5.82$ kips/in. as shown in Fig. 21b. Increasing the axial displacement until failure the damage progresses up and to the left and down and to the right as shown in Fig. 22, which is the last image frame before failure. The damage progressed to the edge of the skin, adjacent to the thickness transition to the stiffener padup as shown in Fig. 22. This damage/delamination growth compares well with the predicted damage growth shown in Fig. 7 where the damage grew to the stiffeners at reaching the maximum load. Panel TP-4 did not exhibit the local delamination as was seen in panel TP-7. Panel TP-4 appeared to fail in the skin from the corner of the slot to the edge of the skin as shown Fig. 23. The first appearance of any out-of-plane displacement in the local images is shown in Fig 23a. At the same time the out-of-plane displacements appeared in the global image as shown in Fig. 23b indicating failure from the end of the slot to the edge of the skin. Panel TP-4 reacts the same as TP-7 and the progressive failure analysis predictions that of the skin failing to the stiffeners as the load increases to the maximum load. Increasing the load resulted in the damage to grow into the padup area of the stringer on the right hand side as shown in Fig. 24.

As indicated previously in this paper, strain can be computed from the u, v, and w displacements determined from the VIC-3D images. The axial strain (ϵ_{yy}) profile for the panel TP-4 image area, which covers approximately 60 % of the skin surface is shown in Fig. 25a for an applied load of $N_y = 5.6$ kips/in. which is the load just prior to

initial failure. This load was selected to have a flat surface to compute the strain in lieu of a load after initial failure where the surface is not flat due to the outer layers delaminating and buckling away from the surface. A non-flat surface would not allow a good strain computation. The anisotropic skin appears to have an effect on the shape of the strain contours at the end of the slot. Two points located at 0.38-inches and 1.0-inches from the left end of the slot have been selected to determine the strain as a function of load. The strain, at these selected points, has been extracted from the VIC-3D images and is shown in Fig. 25b. Strains from gages 28 and 34 which are on the opposite side to the selected points on panel TP-4 are also shown in Fig. 25b. The VIC-3D strain, shown in Fig. 25b, from the point at 0.38-inches from the slot would not be reliable above the load of $N_y = 5.6$ kips/in due to the delamination and buckling from the initial failure. The strain at the point at 1.0-inch from the slot would be more reliable since this location is on the edge of the buckled lamina. There is a good correlation between the strains up to a load of 5.6 kips/in. Strain results from panel TP-7 are shown in Fig. 26 which is plotted to the same scale as Fig. 25. Comparing the Fig. 25 and Fig. 26 indicates that the response of panel TP-7 is similar to the response of panel TP-4. The predicted axial strains (ϵ_{yy}) contours for the *Horizontal cut* panels is shown in Fig. 27 for an applied load of 5.58 kips/in. Comparing Figures 27, 26 and 25 the following can be observed: a) all figures have an area through the center of the panel of near zero axial strain, b) the shape of the strain distributions at the end of the slots are very similar, c) the magnitude of the strains along the side of the panels are similar.

A photograph of the stringer side of a failed *Horizontal cut* specimen is shown in Figure 28a. As indicated in the figure, the failure progressed from each end of the slot up or down across the skin. A view of the skin side of the specimen is shown in Figure 28b. This figure indicates how the failure progressed from the right end of the slot down at approximately a 35° angle until it intersected the stringer then turned and crossed perpendicular to the stringer. Likewise, failure started at the left end of the slot and progressed up at approximately 35° until it approached the stringer, the damage turned parallel to the stringer for a short distance, then turned and crossed perpendicular to the stringer. The progressive failure analysis noted earlier, predicted that the failures would be at 35° to the specimen centerline then turn and cross perpendicular to the stringer which is a very good match with the experimental results. Both of the *Horizontal cut* panels (TP-4 and TP-7) failed in a similar manner and indicates that the fabrication sequence did not contribute to the failure where the panels were manufactured at different times.

In summary, the results shown for the *Horizontal cut* panels indicate a very good correlation between the predicted failure mode and actual failure mode. The predicted failure load of 7.87 kips/in. was less than 3% higher than the average failure load of the two *Horizontal cut* specimens. The average panel stiffness is approximately 90 % of the computed panel stiffness. This is a good strength and stiffness correlation since the exact properties of the material used in the panel was unknown.

D. *Inclined cut* panel

The profile of the *Inclined cut* panel (Fig. 4) indicates that the panel is curved across the panel width as shown in Fig. 29. The panel curvature varies up to 0.025-inches from being flat between the stringers and curves to 0.050-inches from the reference plane between the stringers and panel edges. There is no noticeable curvature in the lengthwise direction. The local area can be seen in Fig. 29 and is where a second VIC-3D system recorded the images of a small area at the end of the slot. The 0.004-inch step can be observed around the edge of the local area in Fig. 29. A defect of unknown origin, shown in Fig. 29, could be an air bubble trapped under the vinyl or a foreign object under the vinyl. The ripple in the contours as shown in Fig. 29 indicates the edge of the painted area under the vinyl for the local area images. The error (noise) in the results can be determined from the VIC-3D analysis and is less than 0.0003-inch for the *Inclined cut* panel. The panel was loaded in compression until failure occurred at 7.54 kips/in. The residual strength of the *Inclined cut* panel is 37 percent of the average strength of the undamaged panels⁴. A plot of the axial end shortening as a function of the axial load is shown in Fig. 30 as a solid line with a filled circle symbol. The transverse in-plane displacements are also shown in Fig. 30 as dashed lines with a filled circle symbol. The panel end shortening shown in Fig. 30 is a uniform function of the load until 6.1 kips/in. where the slope of the curve changes due to a local failure. The initial specimen stiffness is 103.6 kips/in./in⁴. The predicted panel end shortening and in-plane displacement is also shown in Fig. 30 as lines (solid and dashed) with a filled square symbol. The predicted panel end shortening is a linear function of the applied load until a load of 6.6 kips/in. The predicted stiffness of the panel is 111.2 kips/in/in.

An intermediate result from the VIC-3D system at $N_y = 6.32$ kips/in is shown in Fig. 31 and indicates that the panel is bulging as indicated by the concentric displacement contours around the slot. This out-of-plane deflections is different from the predicted displacement shown in Fig. 15 where one end of the slot deflects in one direction with the opposite slot end deflecting in the opposite direction. The local area image indicates a delamination at the corner of the slot. The delamination shown in Fig. 31 first appeared at $N_y = 5.32$ kips/in. and increased in size until $N_y = 6.32$ kips/in. Damage started to show up in both ends of the slot as shown in Fig. 32 after a very small perturbation

in the load. Increasing the axial displacement resulted in the damage progressing to and into the stiffeners as shown in Fig. 33 which is the last image before panel failure. Comparing Fig. 33 with the predicted failure direction shown in Fig. 14 indicates the failure direction is the same, down to the right for one end of the slot.

The VIC-3D axial strain (ϵ_{yy}) profile for the *Inclined cut* panel is shown in Fig. 34a for $N_y = 6.03$ kips/in. Two points located at 0.38-inches and 1.0-inches from the left end of the slot have been selected to determine the strain as a function of load. The strains at these selected points has been extracted from the VIC-3D images and are shown in Fig. 34b. Strains from gages 28 and 34 which are on the opposite side to the selected points on the *Inclined cut* panel are also shown in Fig. 34b. There is good correlation between the strain gages and strain extracted from the VIC-3D images until the skin started to deflect out-of-plane or approximately 4.0 kips/in. The predicted axial strains (ϵ_{yy}) contours for the *Inclined cut* panel is shown in Fig. 35 for an applied load of 6.07 kips/in. The anisotropic skin appears to have an effect on the shape of the strain contours at the end of the slot. Comparing Figures 34 and 35 the following can be observed: a) both figures have an area through the center of the panel of near zero axial strain, b) the shape of the strain distribution at the left end of the slot is similar while the right end of the slot is different, the magnitudes of the strain along the sides of the panel are similar.

A photograph of the failed *Inclined cut* panel is shown in Fig. 36. As indicated in Fig. 36a the failure in the skin progressed up from the L/H end of the slot at approximately a 50° angle and then turned to cross the stringer. Failure progresses in the skin from the right hand end of the slot at a 30° angle from the horizontal and then turned to cross the stringer. The progressive failure analysis predicted that failure would progress from the slot end at a 50° angle to the edge of the skin and turn to cross the stringer which matches the experimental results. Failure from the opposite slot end was not predicted by the analysis.

In summary, the results shown for the *Inclined cut* panel indicate a very good correlation between the predicted failure mode and the actual failure mode. The failure load of $N_y = 7.54$ kips/in is 88 % of the predicted failure load of the inclined panel and the actual stiffness is 93 % of the predicted panel stiffness. This is a good strength and stiffness correlation since the actual properties of the material used in the panel was unknown.

The *Horizontal cut* and *Inclined cut* panels response while under a compression load was recorded with strain gages, displacement transducers and 3D Vision Correlation System (VIC-3D) and there was good correlation between the three methods used in the investigation. The VIC-3D method has several advantages over contemporary strain gages and displacement transducers such as being noninvasive to structure, the equipment is not damaged when structural failure occurs, and preparation time is significantly reduced. One of the main advantages that VIC-3D has over other methods is the ability to detect different events during the loading phase while recording at the global level and not at local or micro level. This means that the need to know high strain locations on the panel before attaching strain gages or displacement transducers is eliminated. The VIC-3D system allowed the tracking of damage progression to the edge of the skin as the load increased which followed the same path as predicted by the STAGS analysis.

VI. Concluding Remarks

Progressive failure analysis has been applied to discrete damaged tailored extension-shear-coupled I-stiffened composite compression panels. The center stringer and adjacent skin on a 3-I stiffener extension-shear coupled panels was cut for the discrete damage. The panels were analyzed with STAGS finite element program using the progressive failure analysis option. The STAGS results compared very well with the experimental results in failure load, stiffness prediction and failure direction. STAGS over predicted the failure load by less than 12 % and the panel stiffness by less than 10 %. The STAGS analysis matched the experimental failure location and direction.

There was a good match of the panel stiffness and strength between the progressive failure analysis and the experimental results. The results indicate that the tailored concept would be feasible to use in the wing skin of a tiltrotor aircraft.

References

- ¹ Popelka, D., Sheffler, M., and Bilger, J. "Correlation of Test and Analysis for the 1/5th Scale V-22 Aeroelastic Model." Journal of the American Helicopter Society, Vol 32, (2), April 1997.
- ² Popelka, D., Lindsay, D., Parham, T., Jr., Berry, V., and Baker, D., "Results of an Aeroelastic Tailoring Study for a Composite Tiltrotor Wing," Presented at the 51st Annual American Helicopter Society Forum, Fort Worth, TX, May 1995.
- ³ Corso, L. M., Popelka, D. A., Nixon, M. W., "Design, Analysis, and Test of a Composite Tailored Tiltrotor Wing." Presented at the 53rd annual American Helicopter Society Forum, Virginia Beach, VA, April 1997.
- ⁴ Baker, Donald J., "Response of Damaged and Undamaged Tailored Extension-Shear-Coupled Composite Panels," AIAA-2003-1461, presented at the 44th Structures, Structural Dynamics, and Materials Conference, Norfolk, VA, April 7-10, 2003.
- ⁵ Helm, J. D., McNeil, S. R., Sutton, M. A., "Improved Three-Dimensional Image Correlation for Surface Displacement Measurement," Optical Engineering, Vol. 35, No 7, July 1996, pp1911-1920.
- ⁶ Brogan, F. A., Rankin, C. C., and Cabiness, H. D., "STAGS Users Manual," Lockheed Palo Alto Research Laboratory, Report LNSC P032594, 1994.

Table 1

		Material	
	IM6-3501-6 tape material.	Carbon fabric interlayer.	FM 300 Adhesive.
$E_1 \times 10^5$ psi.	210	90.	1.32
$E_2 \times 10^5$ psi.	120	85.	1.32
$E_3 \times 10^5$ psi.	120	12.	1.32
$G_{12} \times 10^5$ psi.	8.7	8.0	1.30
$G_{13} \times 10^5$ psi.	8.7	4.0	1.30
$G_{23} \times 10^5$ psi.	2.58	4.0	1.30
μ_{12}	0.3	0.3	0.3
μ_{13}	0.3	0.3	0.3
μ_{23}	0.3	0.3	0.3
X_c , psi.	190,000.	70,000.	10,000.
X_t , psi.	232,750.	110,000.	7,000.
Y_c , psi.	28,700	70,000.	10,000.
Y_t , psi.	14,700.	100,000.	7,000.
S_{xy} , psi.	29,750.	13,000.	7,000.
Z_c , psi.	28,700.	28,700.	10,000.
Z_t , psi.	14,700.	14,700.	7,000.
S_{yz} , psi.	29,750.	13,000.	7,000.
S_{xz} , psi.	29,750.	13,000.	7,000.

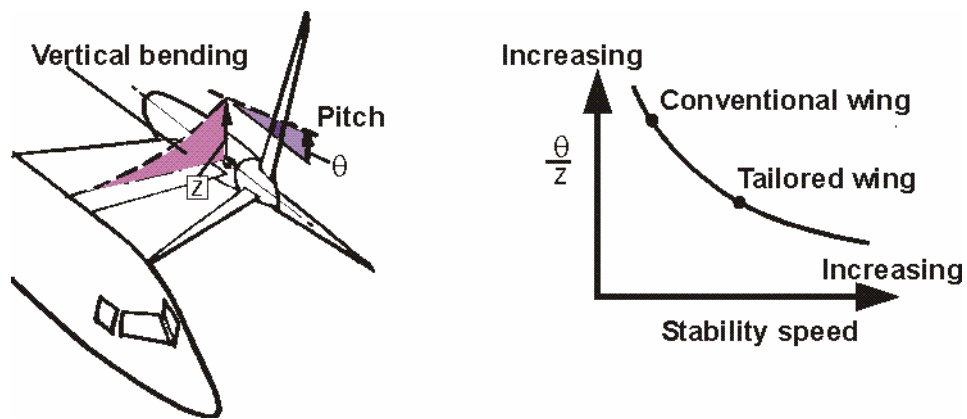


Figure 1. Influence of structural tailoring on wing aeroelastic stability.

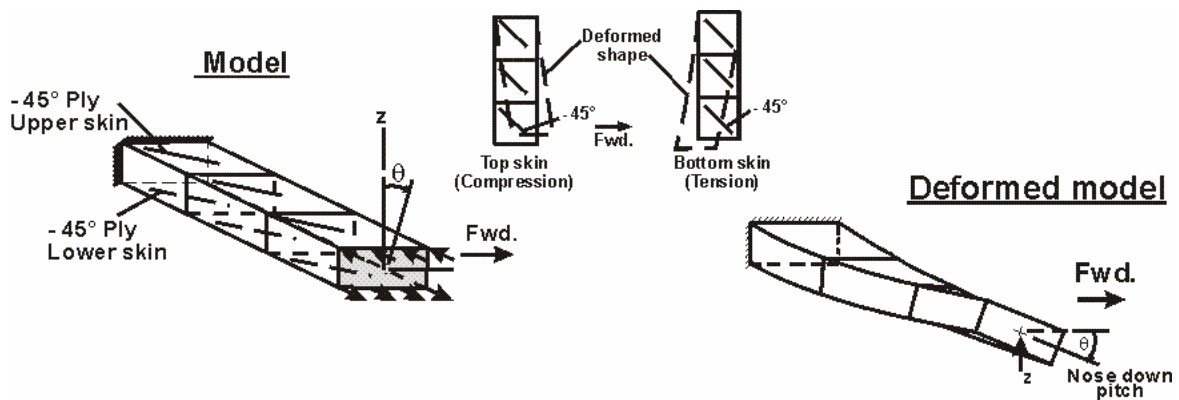


Figure 2. Simple boxbeam model.

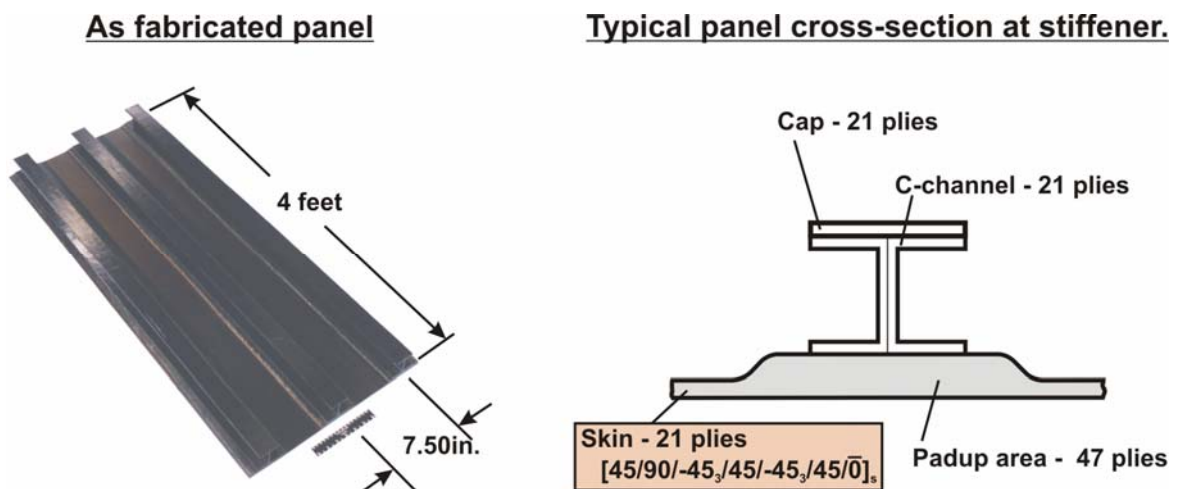


Figure 3. Specimen configuration

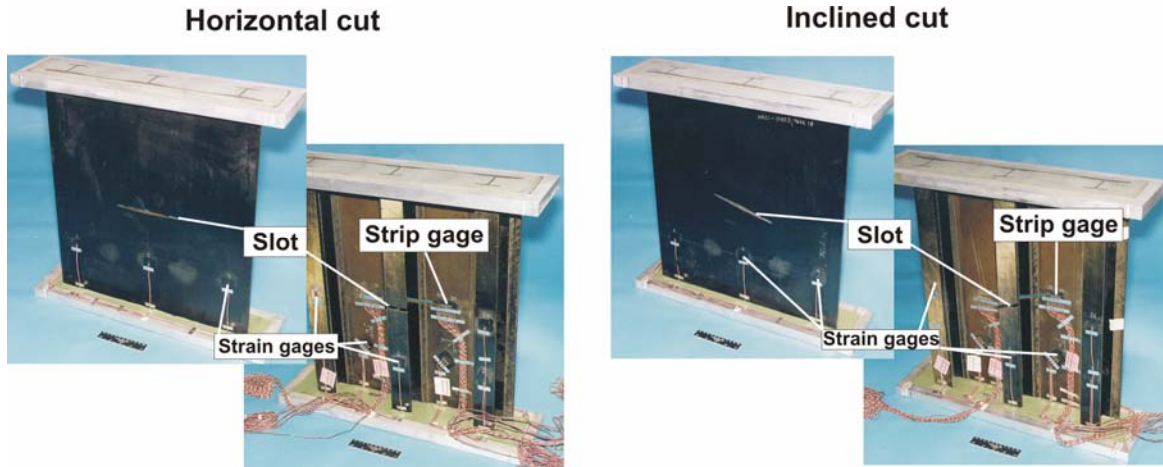


Figure 4. *Horizontal cut* and *Inclined cut* test panels.

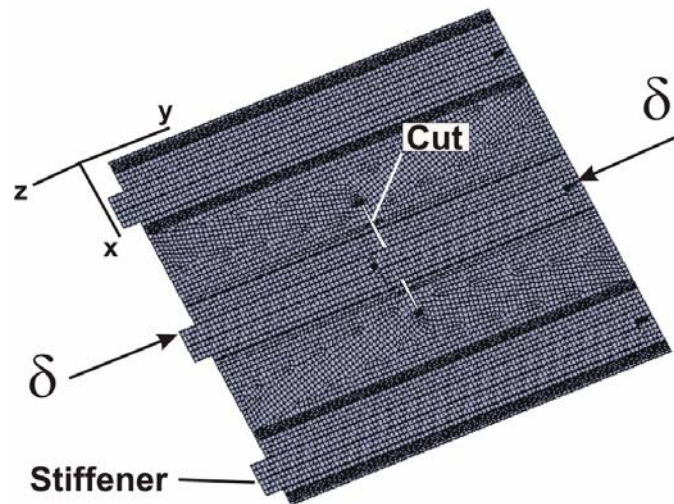


Figure 5. Finite element model of *Horizontal cut* panel.

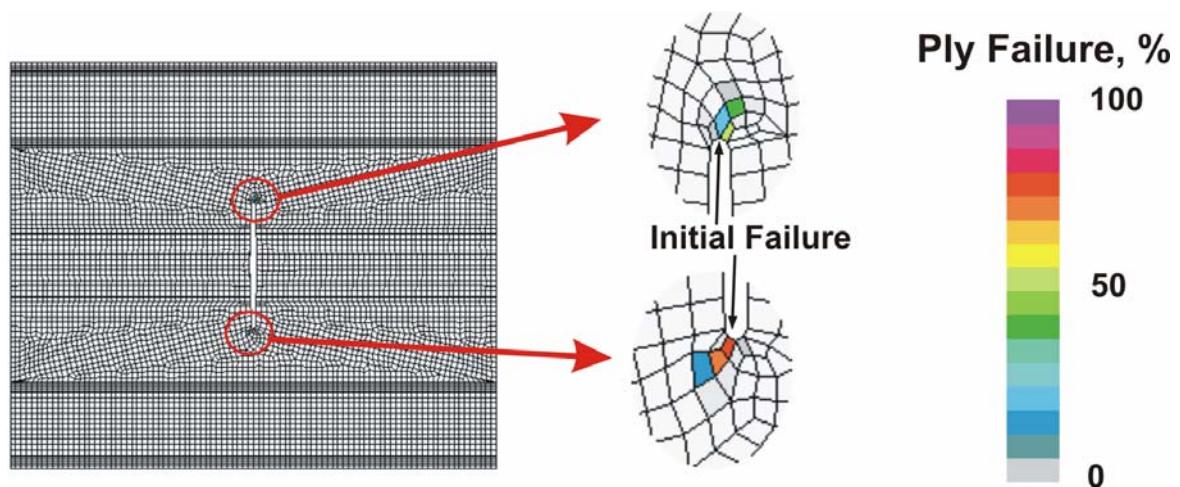


Figure 6. Initial failure in *Horizontal cut* panel, $N_y = 4.84$ kips/in.

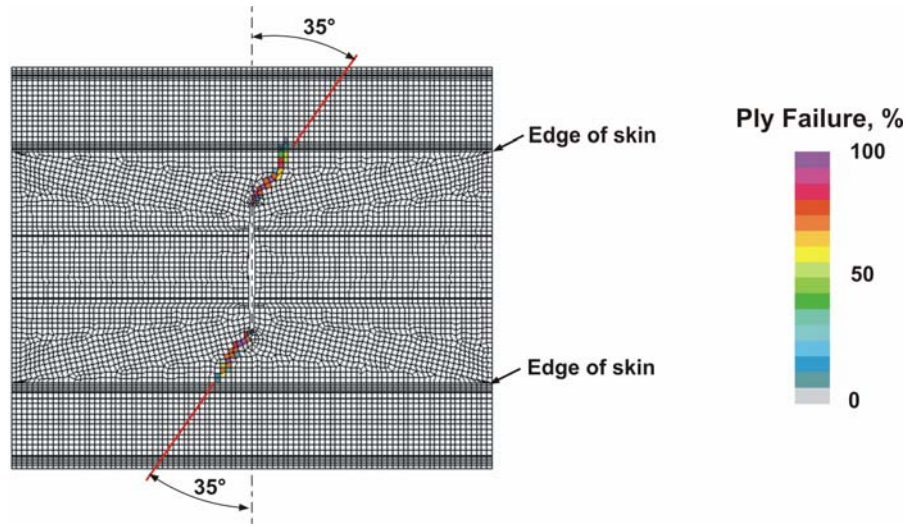


Figure 7. Predicted failure in *Horizontal cut* panel at maximum load, $N_y = 7.87$ kips/in.

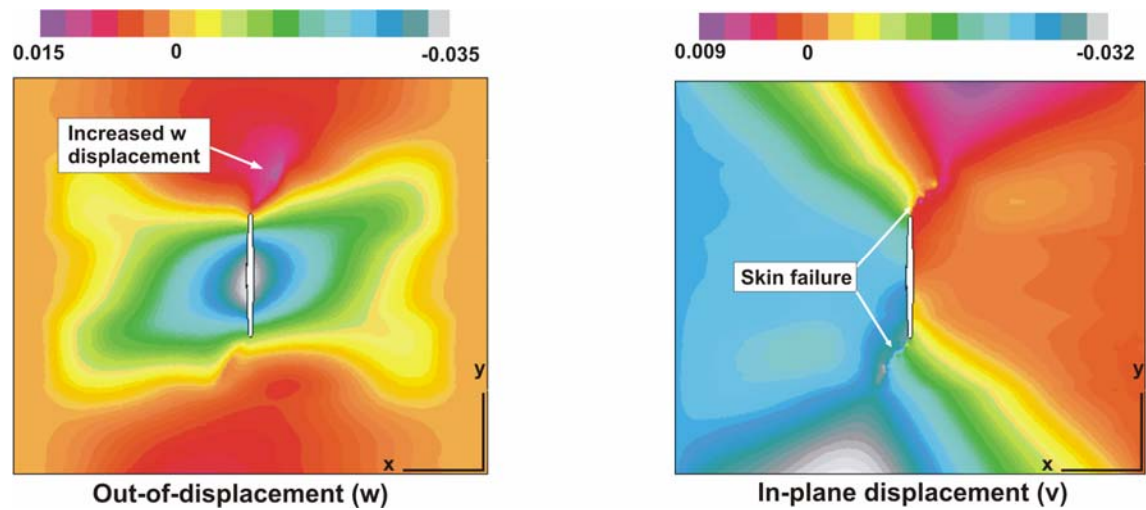


Figure 8. Predicted in-plane and out-of-plane displacements in *Horizontal cut* panel at $N_y = 7.87$

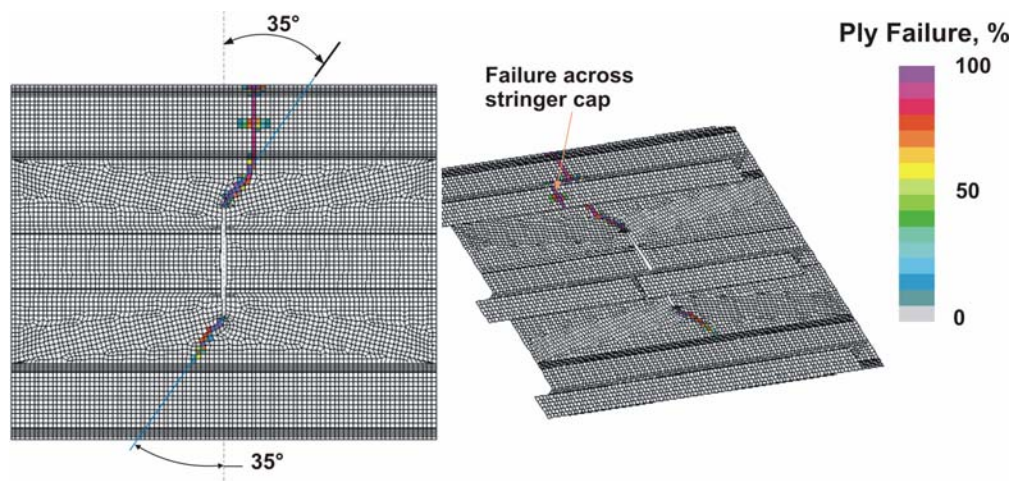


Figure 9. Predicted failure path in *Horizontal cut* panel at $N_y = 5.78$ kips/in.

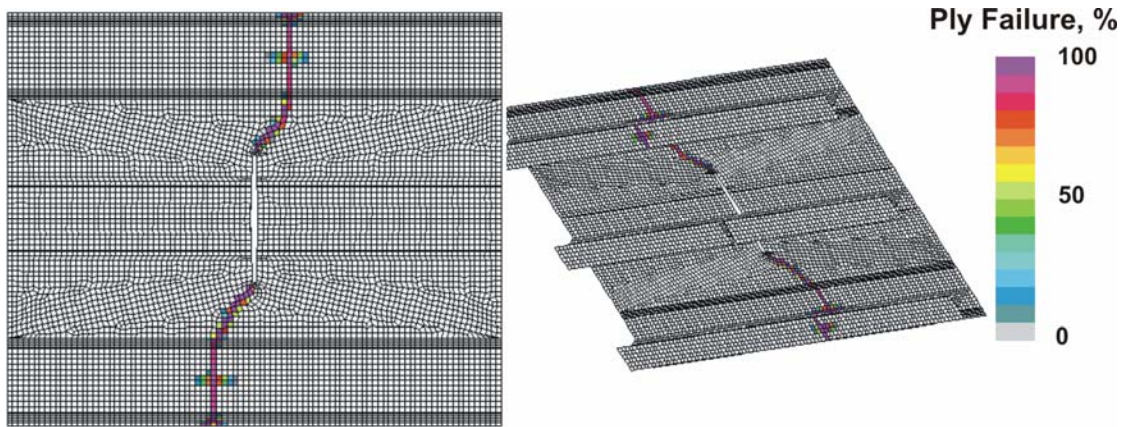


Figure 10. Predicted panel failure in *Horizontal cut* panel at $N_y = 2.74$ kips/in.

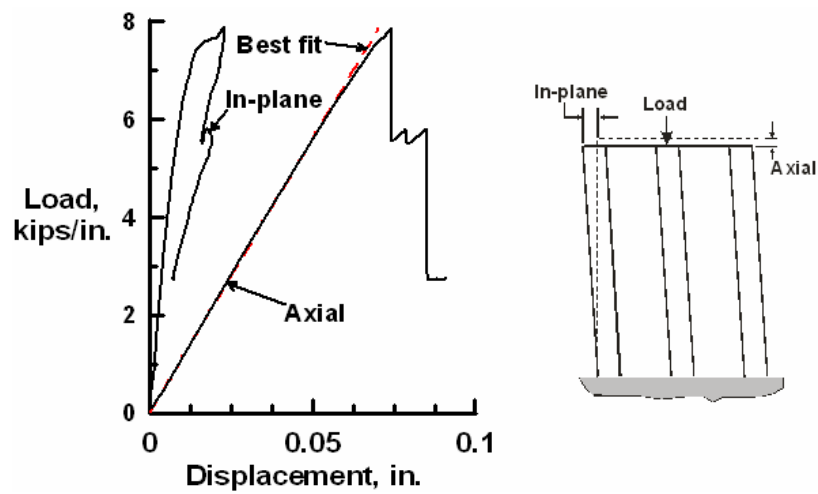


Figure 11. Predicted axial and transverse in-plane displacements in *Horizontal cut* panel as a function of load.

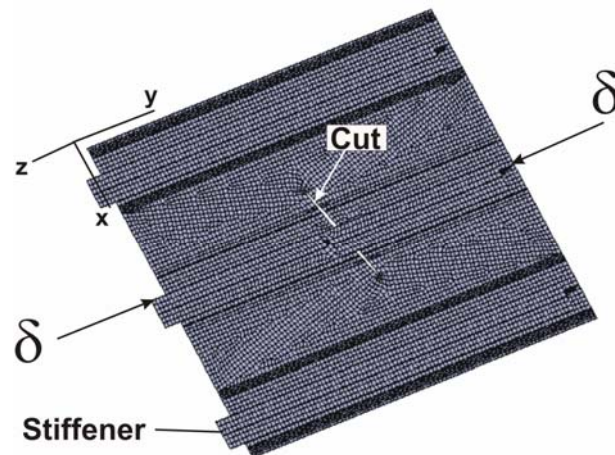


Figure 12. Finite element model of *Inclined cut* panel.

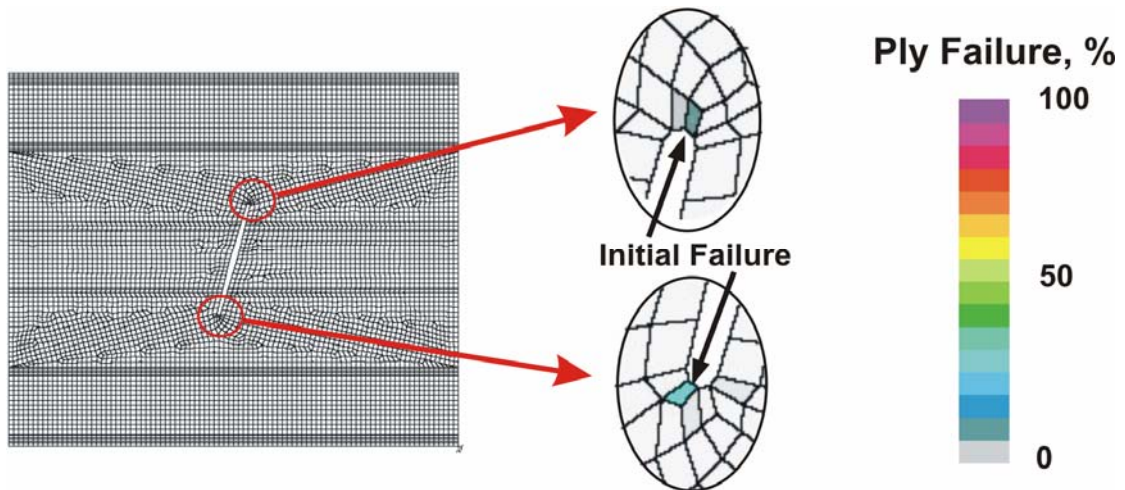


Figure 13. Predicted initial failure in the *Inclined cut* panel, $N_y = 3.8$ kips/in.

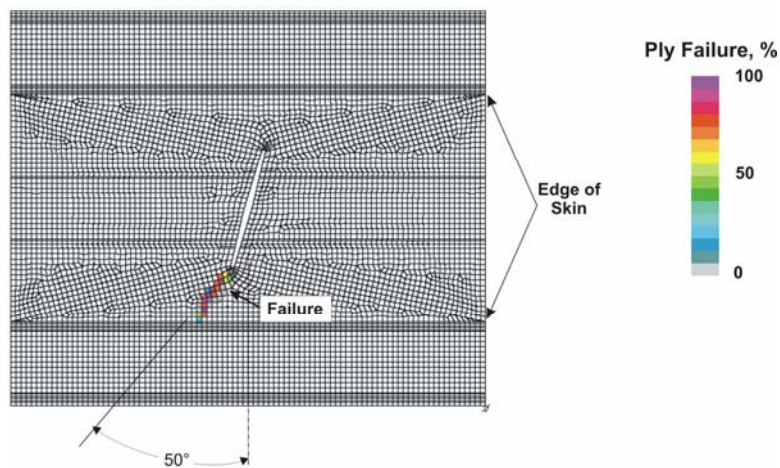


Figure 14. Predicted failure in *Inclined cut* panel $N_y = 8.43$ kips/in.

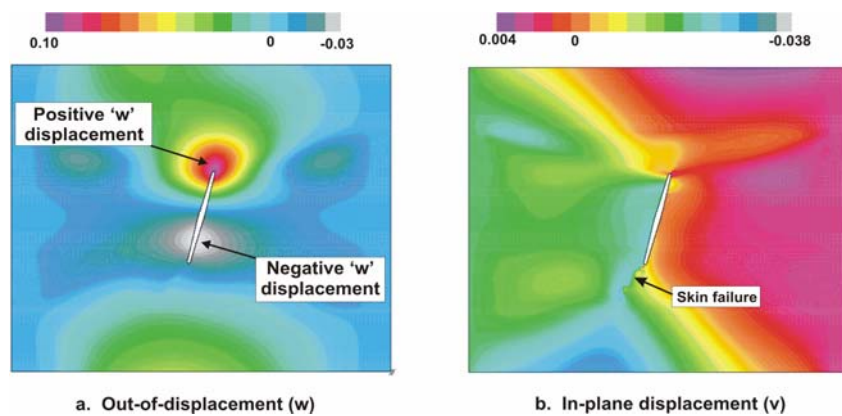


Figure 15. Predicted in-plane and out-of-plane displacements in *Inclined cut* panel, $N_y = 8.43$ kips/in.

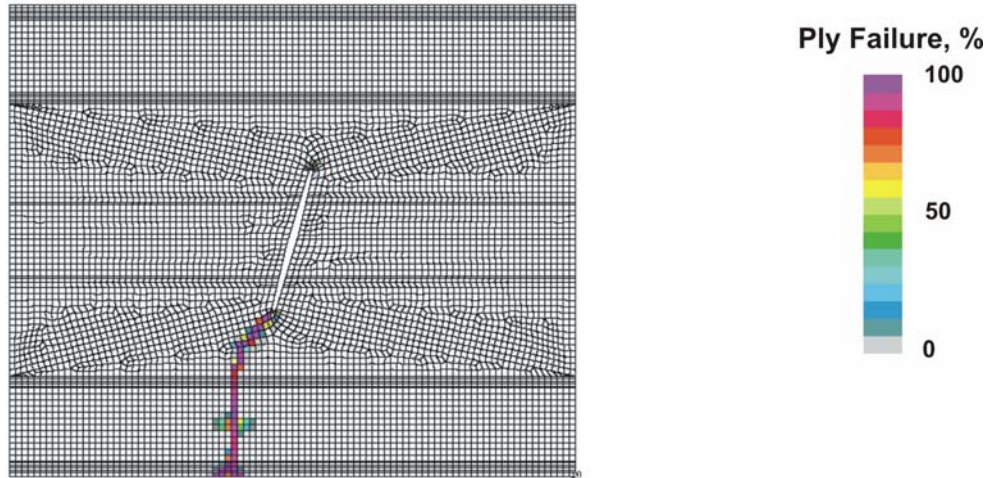


Figure 16. Progression of failure in *Inclined* cut panel at $N_y = 5.69$ kips/in.

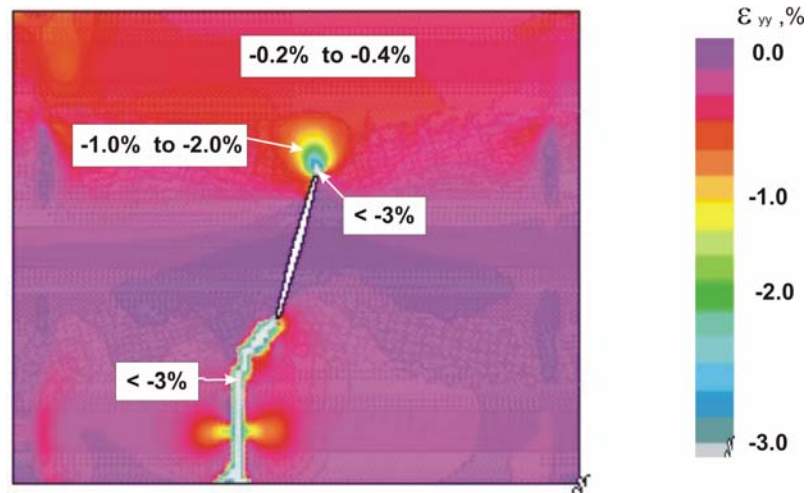


Figure 17. Predicted axial strains in the skin of *Inclined cut* panel at $N_y = 6.31$ kips/in.

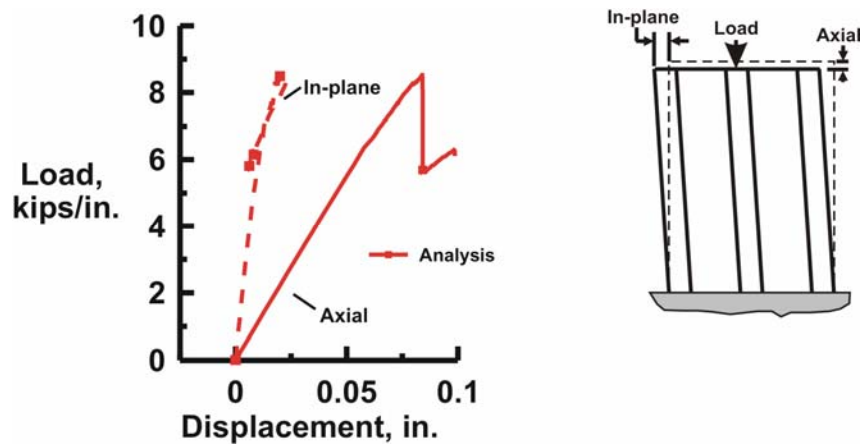


Figure 18. Predicted axial and transverse in-plane displacements as a function of load for the *Inclined cut* panel.

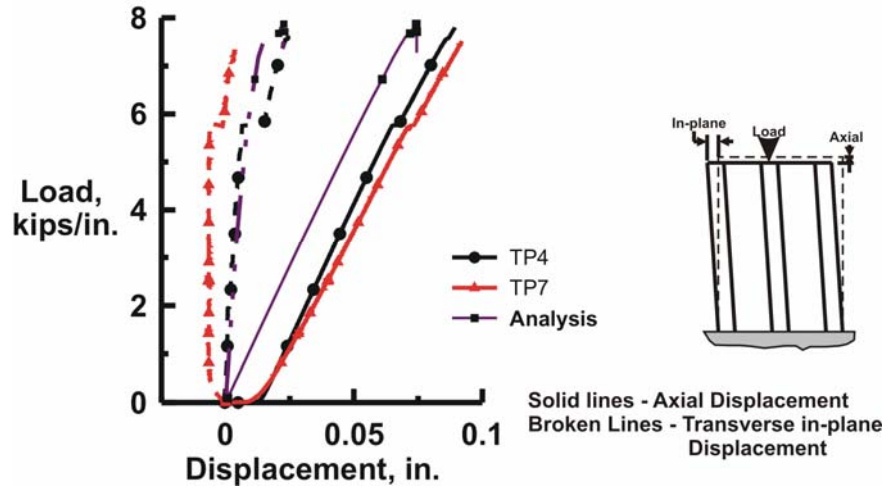


Figure 19. Axial and transverse in-plane displacements as a function of applied load.

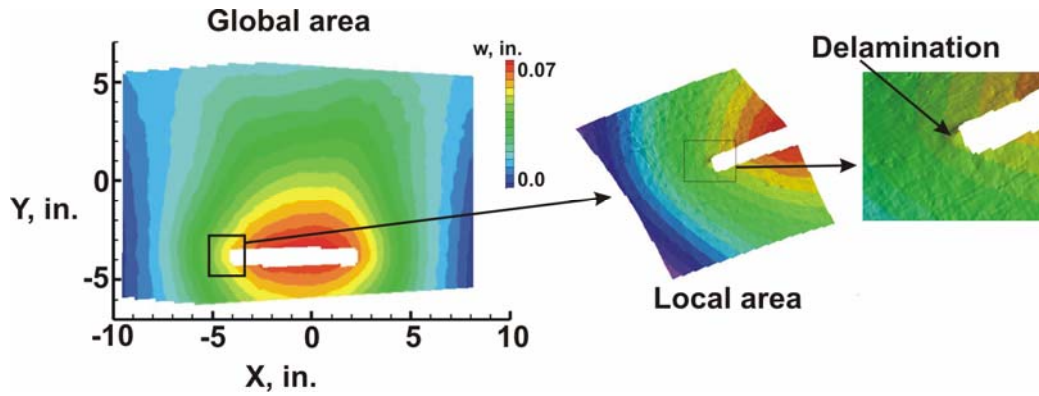


Figure 20. Measured delamination at end of slot in panel TP-7 at a load of $N_y = 5.1$ kips/in.

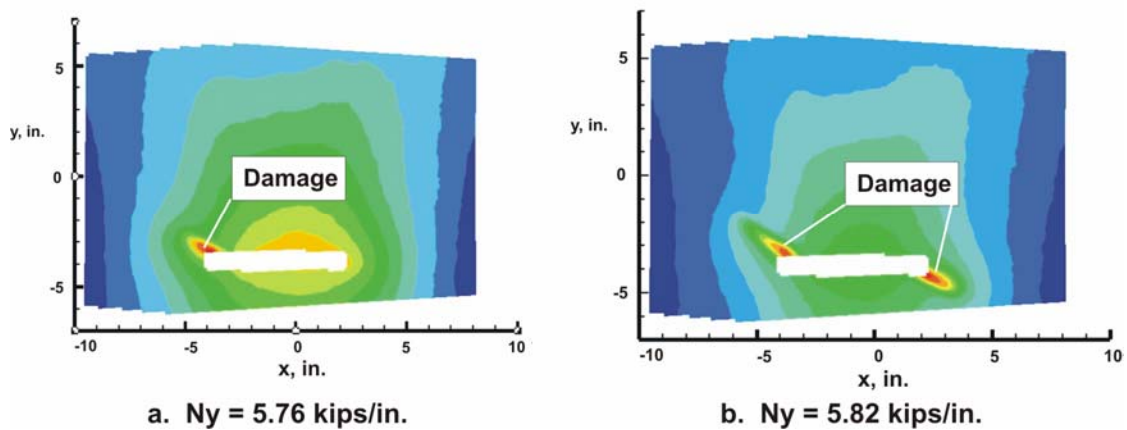


Figure 21. Measured delamination/damage at end of slot at loads shown.

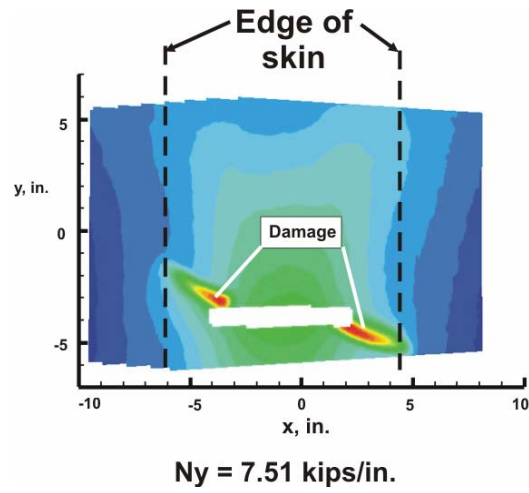


Figure 22. Measured damage propagation in panel TP-7 prior to failure.

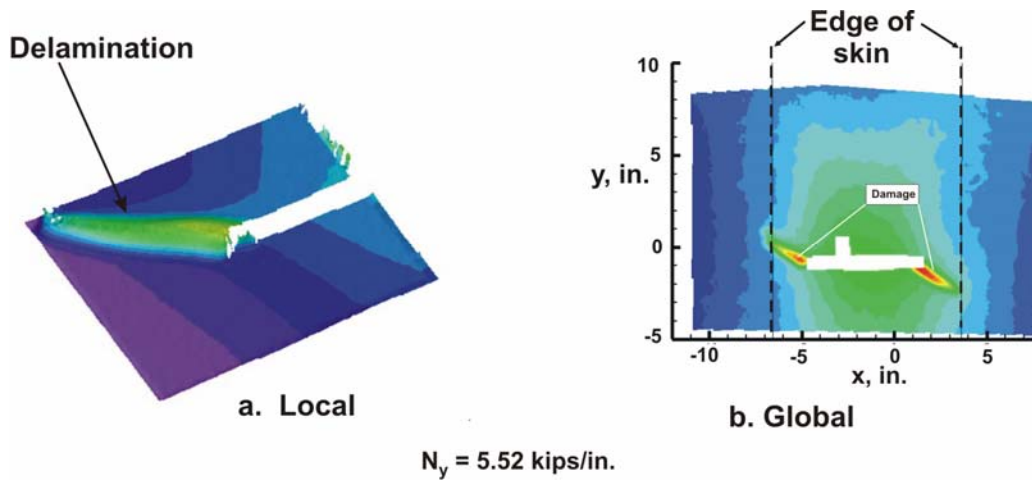


Figure 23. Local and global view of measured delamination on TP-4 at $N_y = 5.52 \text{ kips/in.}$

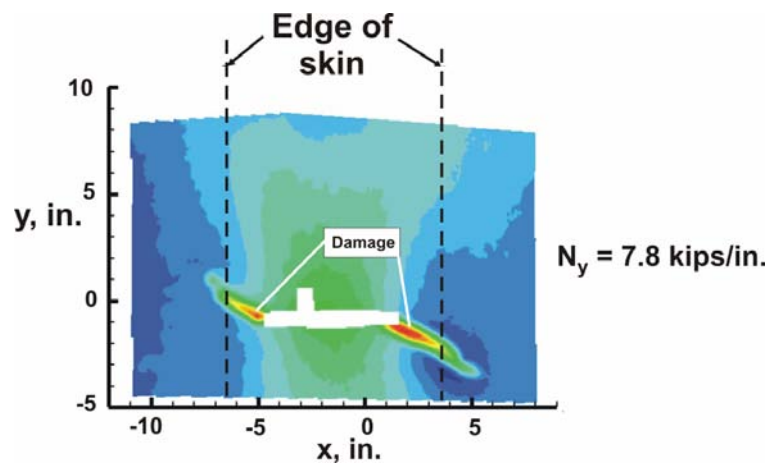


Figure 24. Measured out-of-plane displacements of TP-4 at near failure.

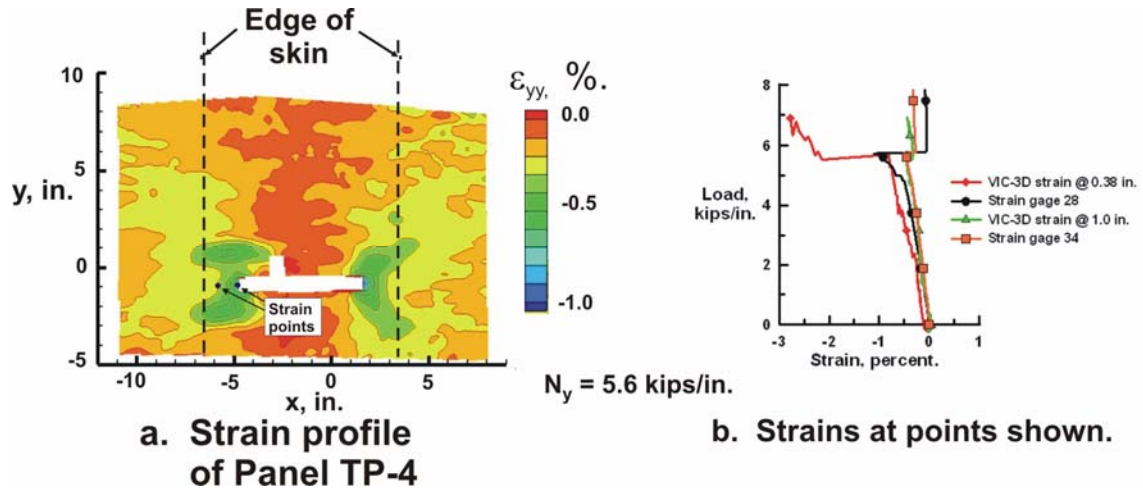


Figure 25. Measured axial strains (ϵ_{yy}) on panel TP-4..

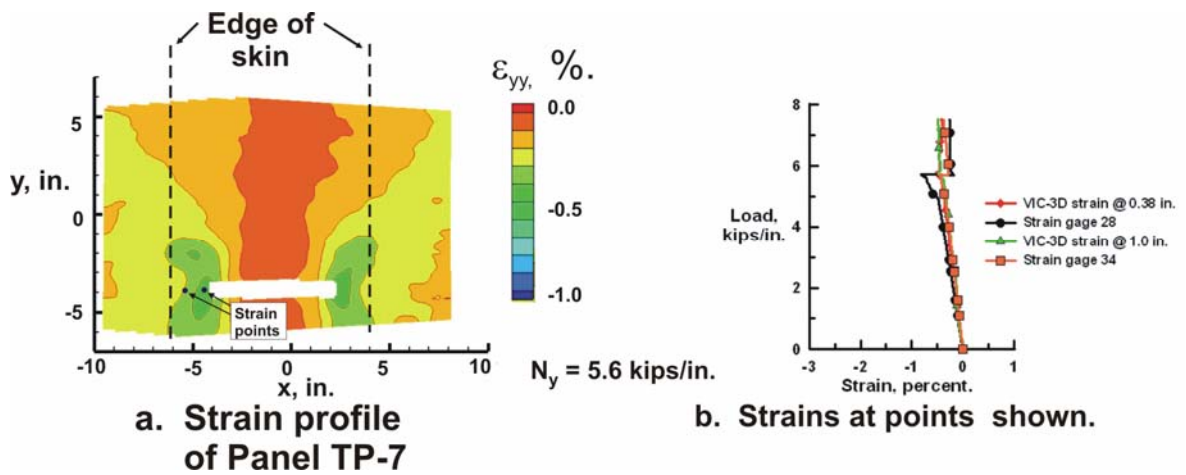


Figure 26. Measured axial strains (ϵ_{yy}) in the skin of panel TP-7.

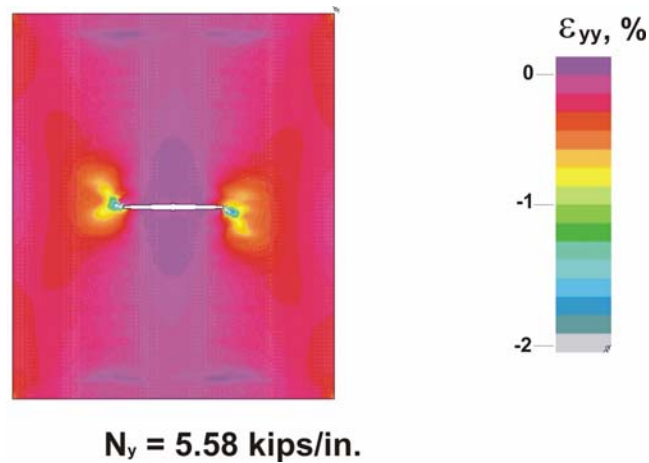


Figure 27. Predicted axial strains in Horizontal cut panel at a load of $N_y = 5.59$ kips/in.

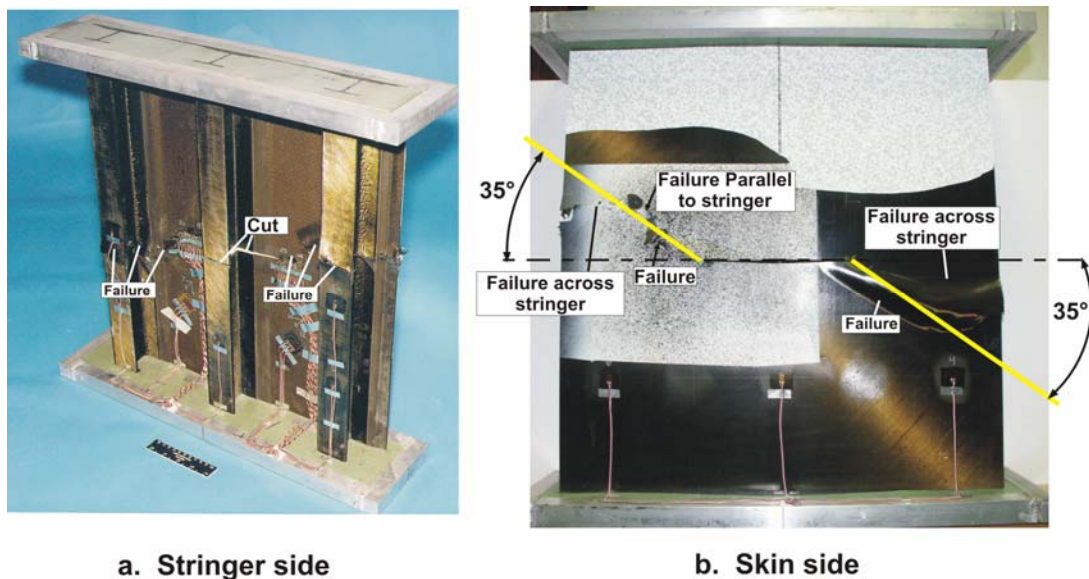


Figure 28. Failed *Horizontal cut* panel.

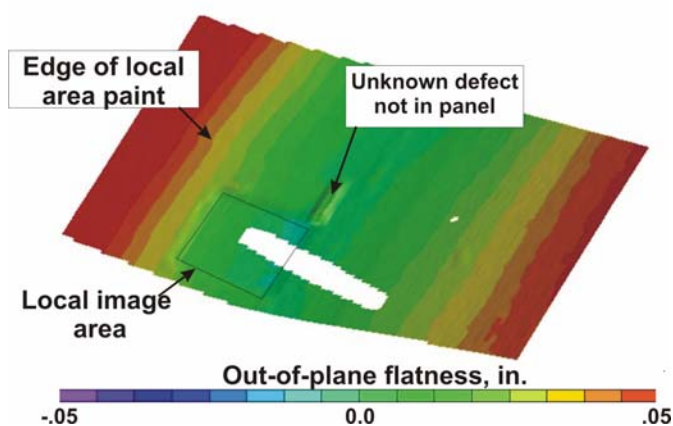


Figure 29. Profile of panel TP-5.

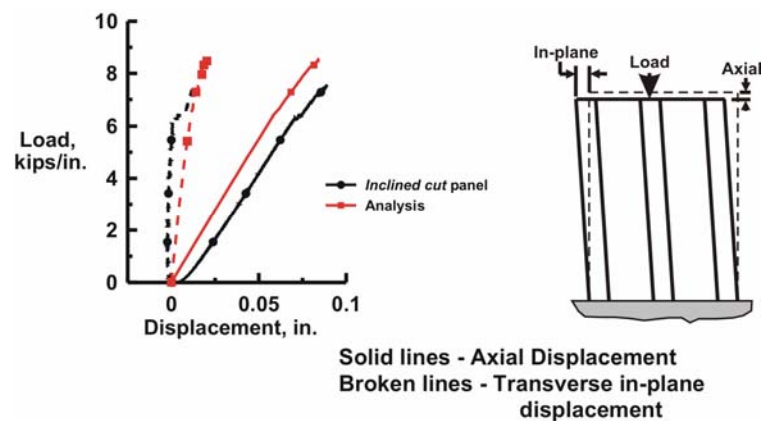


Figure 30. Axial and transverse in-plane displacements as a function of applied load.

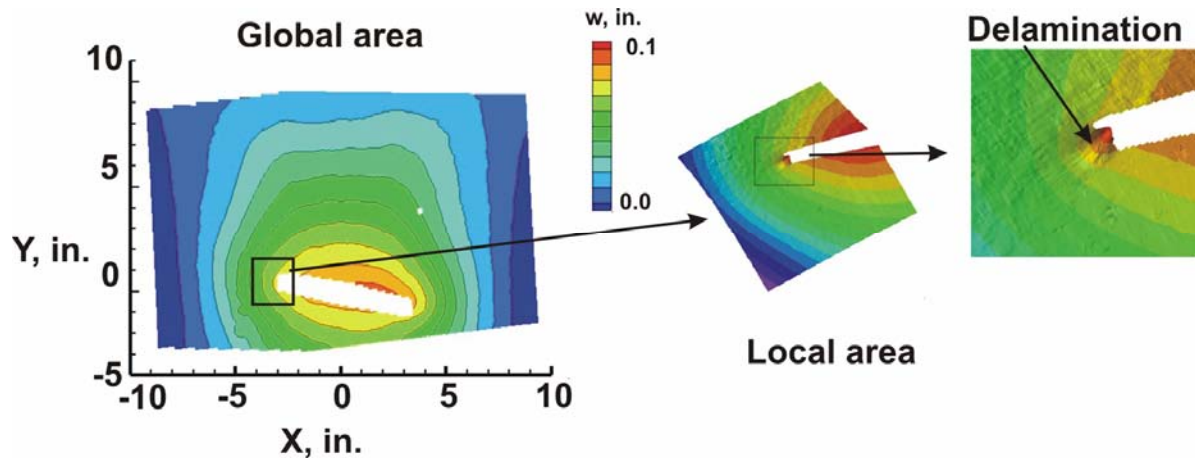


Figure 31. Measured delamination at end of slot in *Inclined cut* panel at a load of $N_y = 6.32$ kips./in.

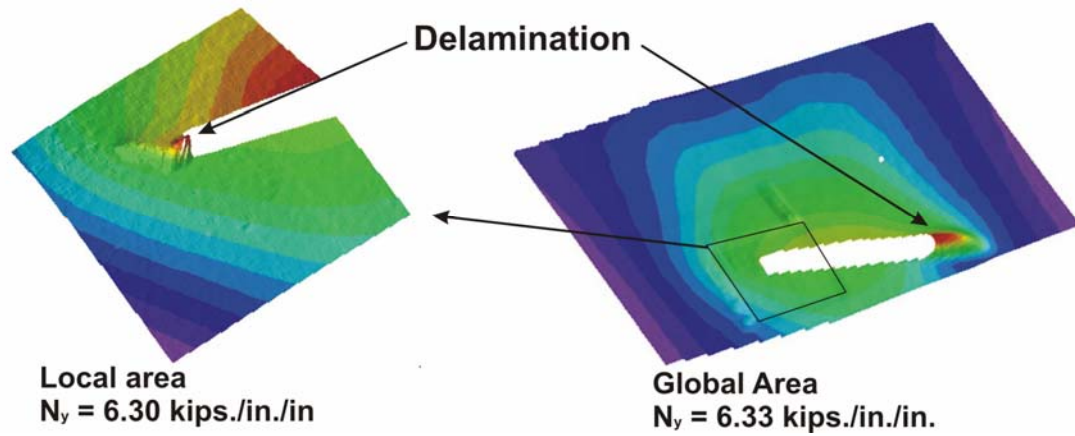


Figure 32. Measured initial failures of *Inclined cut* panel.

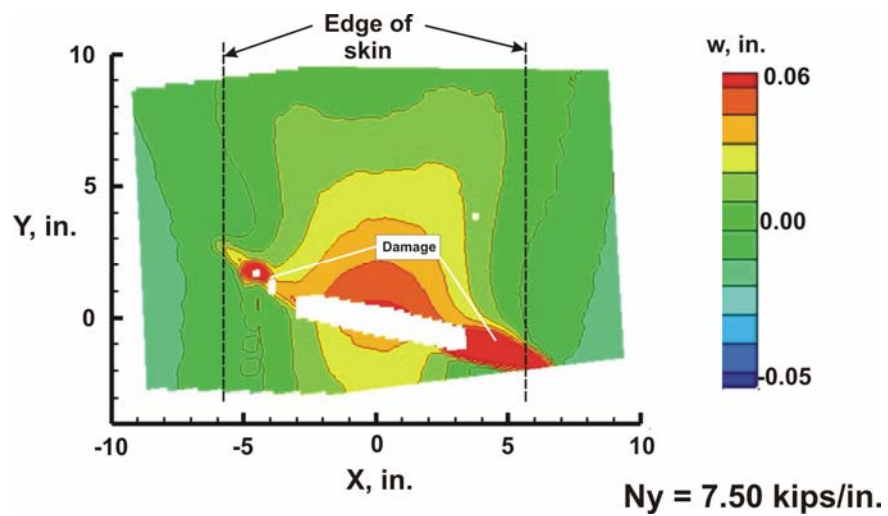


Figure 33. Measured out-of-plane displacements of *Inclined cut* panel at near failure.

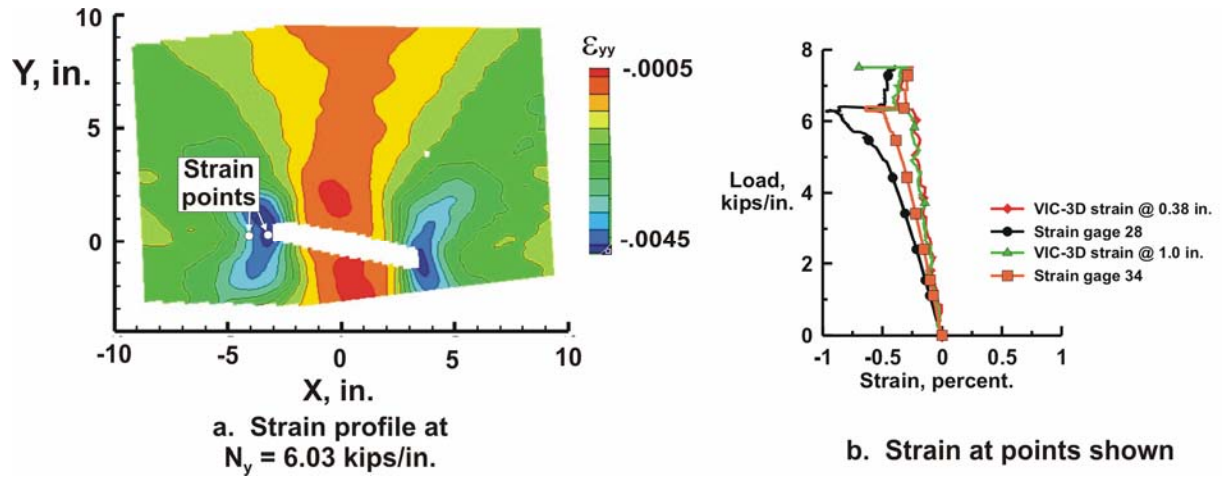


Figure 34, Axial strains in *Inclined cut* panel as determined by VIC-3D and strain gages.

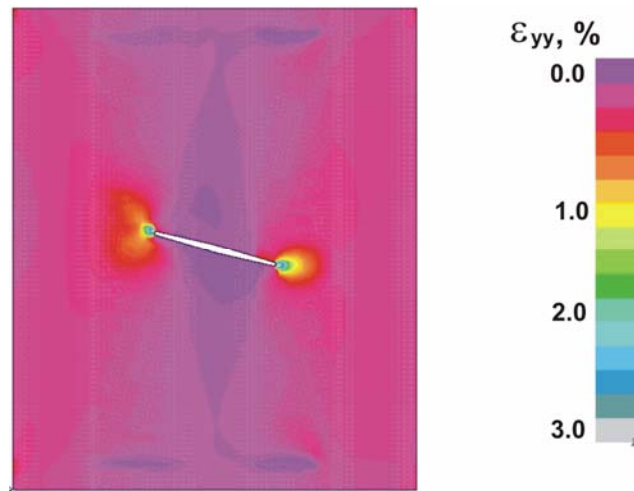


Figure 35. Predicted axial strains in *Inclined cut* panel at a load of 6.07 kips/in.

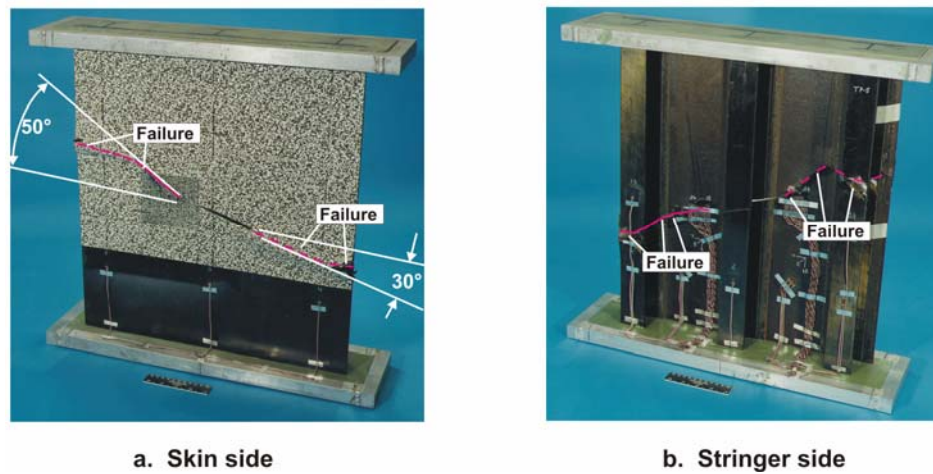


Figure 36. Failed *Inclined cut* panel.

Mechanical Behavior of Inplane-Loaded Unsymmetrically Laminated Plates

Majed A. Majeed* and Michael W. Hyer†

This study focuses on the response of flat rectangular unsymmetric cross-ply laminates to a uniaxial inplane compressive edge displacement that for symmetric laminates are of sufficient magnitude to cause bifurcation buckling, postbuckling, and secondary buckling behavior. One objective of this study is to investigate whether or not the concept of bifurcation buckling is applicable to flat unsymmetric laminates. Past work by other researchers has suggested that such a concept is applicable for certain boundary conditions. The study also has as an objective the determination of the response of flat unsymmetric laminates if bifurcation buckling does not occur. The finite-element program ABAQUS is used to obtain results. Newton-Raphson and Riks static solution schemes for loading and unloading, as well as transient dynamic analyses when instability is an issue, are employed to understand laminate behavior. Two specific laminates, an eight-layer $[0_2/90_2]_S$ symmetric cross-ply laminate and a counterpart eight-layer $[0_4/90_4]_T$ anti-symmetric cross-ply laminate are studied. The symmetric laminate is included to provide a familiar baseline case for comparison. Of course the $[0_2/90_2]_S$ laminate exhibits symmetric bifurcation and postbuckling behavior. In addition, when all four edges are clamped and the tangential displacement on the loaded edges and the normal displacement on the unloaded edges are restrained, secondary buckling behavior occurs. For the $[0_4/90_4]_T$ laminate, bifurcation buckling behavior occurs when all four edges are clamped, and either the tangential displacements on the loaded edges and the normal displacements on the unloaded edges are restrained, or these displacements are unrestrained. If either of these inplane boundary conditions is not satisfied, then the all-clamped $[0_4/90_4]_T$ laminate exhibits what could be termed 'near-bifurcation' behavior. In all the cases, rather complex behavior occurs for levels of compressive edge displacement beyond bifurcation, including asymmetric postbuckling and secondary buckling behavior. For clamped loaded edges and simply-supported unloaded edges, bifurcation buckling behavior does not occur unless the tangential displacements on the loaded edges and the normal displacements on the unloaded edges are restrained. For this case, rather unusual asymmetric bifurcation and associated limit point behavior occur, as well as asymmetric postbuckling and secondary buckling. This is a very interesting boundary condition case and it is studied further for other unsymmetric cross-ply laminates by using a Rayleigh-Ritz-based solution to reveal the problem parameters responsible for the asymmetric response near bifurcation. The overall results of the study have led to an increased understanding of the role of laminate asymmetry and boundary conditions on the potential for bifurcation behavior, and on the response of the laminate for edge-displacements beyond the bifurcation level.

*Department of Mechanical Engineering, Kuwait University, P.O. Box 5969, Safat, Kuwait 13060

†Department of Engineering Science and Mechanics, Virginia Tech, Blacksburg, VA 24061

Copyright©2005 M. A. Majeed and M. W. Hyer, printed by NASA with permission

I. Introduction

THE existence of bending-stretching material coupling in unsymmetric laminates has often been cited as an interesting and unique characteristic of fiber-reinforced composite materials. However, rarely is a composite structure manufactured that takes advantage of this characteristic, if it can indeed be considered an advantage. Bending-stretching coupling effects and the associated thermally-induced bending moments within a cooled laminate due to the elevated-temperature cure of polymer-matrix fiber-reinforced composite materials are often considered a disadvantage. Cooling an unsymmetric laminate from the elevated curing temperature to a lower service temperature leads to thermal deformations that result in a laminate that is warped, to put it into a negative context, relative to the intended shape. Dano and Hyer¹ found that unsymmetric laminates that are flat at their curing temperature may have one of several possible shapes after they are cooled to their service temperature. If multiple shapes exist, the cooled laminates can be made to snap from one shape to another by applying forces and moments.^{2,3,4} Analyses to study these characteristics involve geometric nonlinearities and stability considerations. One application where bending-stretching coupling and the associated thermally-induced bending moments have been used to advantage is in the area of pre-stressed piezoceramic actuators, where the thermally-induced residual curvatures result in larger actuated displacements than if the actuator had been manufactured to be flat.^{5,6} In general, however, it is not clear that residual curvatures are useful, but it is clear that with currently-available composite materials, special manufacturing methods must be used to produce flat unsymmetric laminates. Bonding together two previously-cured flat symmetric laminates at room temperature is an example of such an approach.^{7,8} It is also clear that due to the presence of bending-stretching effects, which are represented by the well-known B matrix in classical lamination theory, the analysis of unsymmetric laminates is more difficult and involved than the analysis of symmetric laminates. Even for a geometrically linear analysis, and not including residual thermally-induced deformations, the three governing differential equilibrium equations written in terms of the three components of displacement involve odd-powered derivatives of the displacements due to the presence of material bending-stretching coupling terms from the B matrix. These odd-powered terms complicate any closed-form and semi-closed-form analysis. If the effects of bending-stretching coupling due to geometric nonlinearities are considered in addition, then the governing equations become even more complex. Obviously the use of finite elements eliminates these problems, but isolating and identifying important parameters becomes more difficult, and the presence of the initial thermally-induced deformations must be accounted for in the analyses, which can make even the finite-element approach involved. In summary, unsymmetric laminates suffer from unwanted thermally-induced deformations, and they are difficult to analyze. However, with the advances in material science, it will someday be possible to manufacture flat, or curved, unsymmetric laminates, or their counterpart in some other advanced material form, that maintain their initial shape during the manufacturing process, so unwanted residual deformations will not be an issue. Then the question becomes one of determining the value of bending-stretching material coupling, determining what can be accomplished with it that cannot be accomplished otherwise, or more fundamentally, just what are the response characteristics of, say, flat plates which exhibit bending-stretching material coupling. It is this latter question that is the motivation for the present paper.

Based on geometrically linear analyses, Leissa⁹ and Qatu and Leissa¹⁰ studied the response of initially flat unsymmetrically laminated plates subjected to inplane loadings. Leissa⁹ formulated the conditions required for the plate to remain flat. Under these conditions, then, a flat unsymmetrically laminated plate could presumably experience bifurcation buckling, like a symmetrically laminated or isotropic plate. The prebuckling deformations of the plate would not involve out-of-plane displacements, so a classic flat-plate bifurcation buckling analyses would make sense. If the conditions were not satisfied, a bifurcation buckling analysis would not make sense and, in fact, would be in error. Qatu and Leissa¹⁰ cited a number of papers that were not correct because so-called buckling analyses had been conducted assuming the plate remained flat under inplane compression, when in fact, the particular plates did not. The focus of the present paper is a study of the response of initially, and perfectly, flat unsymmetrically laminated square cross-ply plates subjected to inplane compression. Leissa⁹ stated that if such a plate is clamped on all four edges, it will

remain flat. For the case of unsymmetric cross-ply laminates, only the B_{11} and B_{22} terms of the B matrix exist. These terms lead to bending moments within the plate when the laminate is compressed inplane, but the clamped boundaries produce the necessary moments to overcome the induced bending effects and the plate will remain flat. An important additional condition is that the inplane strains - i.e., using the nomenclature of classical lamination theory, ϵ_x^o , ϵ_y^o , and γ_{xy}^o - must be spatially uniform. This uniformity can be difficult to achieve in the laboratory, as contacting a plate to compress it produces inplane forces on the loaded edges that could lead to non-uniform inplane strains. For clarity here, by a clamped edge is meant that the displacement and rotation are restrained to be zero. Of course at any edge two more boundary conditions must be specified that address inplane displacements or stress resultants. The specific objectives of this paper are to: (1) examine the predicted response of unsymmetrically laminated cross-ply plates which satisfy Leissa's⁹ required conditions, but consider a geometrically nonlinear analysis, and (2) investigate the response of unsymmetrically laminate cross-ply plates when the inplane boundary conditions on the four edges are other than those which allow the inplane strains to be spatially uniform. The second objective is of value when considering experiments, as it is important to determine the influence of the lack of a uniform strain state on the potential for bifurcation buckling, in particular, and on the overall response in general. The first objective is important as the past work has considered only geometrically linear response, and inclusion of geometric nonlinearities provides for the opportunity to study the bifurcation and consider inplane loading levels greater than the bifurcation level.

The paper begins by describing the specific problem considered: the loading, geometry, nomenclature, and boundary conditions. The finite-element code ABAQUS¹¹ is used to obtain a majority of the results, and the finite-element model is briefly described. Numerical results are then presented for one specific unsymmetric cross-ply laminate, namely a $[0_4/90_4]_T$ graphite-epoxy laminate, and several boundary conditions. The restriction to study only one specific unsymmetric cross-ply stacking sequence is imposed so attention can focus on the influence of boundary conditions, which turn out to be fairly significant. One specific set of boundary conditions leads to particularly interesting results, so the effect of these boundary conditions on other unsymmetric cross-ply laminates is considered. A Rayleigh-Ritz technique is used, to a limited extent, to compare with finite-element results for this particular boundary condition case, and to develop relations that provide insight into the problem. As a baseline for comparison, the responses of a symmetric $[0_2/90_2]_S$ laminates are presented.

II. Problem Studied and Finite Element Model

The specific problem being considered is illustrated on Figure 1. The analysis coordinate system, which is located at the geometric center of the plate, is illustrated in Figure 1(a). The plate has dimension a in the x -direction, b in the y -direction, and is of thickness H . Typical composites nomenclature is used, and the 1-, 2-, and 3-directions are principal material directions, with the +1-direction being oriented at an angle θ relative the $+x$ axis. The displacement of the plate's geometric midsurface in the x -, y -, and z -direction, as represented by the nodal displacements in the finite-element analysis, are denoted as u^o , v^o , and w^o , respectively, whereas nodal rotations about these axes are denoted as ϕ_x^o , ϕ_y^o , and ϕ_z^o , respectively. The boundary conditions considered are shown in Figure 1(b). Note that some of the boundary conditions have an either-or specification. As shown, the plate is compressed in the x -direction by a known displacement Δ at the edge at $x = +a/2$. This displacement is uniform along the edge. The load required to effect this edge displacement will be later identified as P . The edge at $x = -a/2$ has no displacement in the x -direction, so it reacts the load due to displacement Δ . These two edges will be referred to as the loaded edges. The other two edges will be referred to as the unloaded edges. As can be seen, $w^o = 0$ on all four edges. On the loaded edges either the rotation about the y -axis, ϕ_y^o , is additionally specified to be zero (a clamped edge) or the moment M_x is specified to be zero (a simply-supported edge). Regarding the inplane boundary conditions on the loaded edges, the tangential displacement v^o can be restrained ($v^o = 0$), as is most likely the case when the edges are clamped in any experiment, or N_{xy} is specified to be zero (the edges are free to move tangentially). Specifications for the other degrees of freedom are shown and do not vary in this study. The

unloaded edges, $y = +b/2$ and $y = -b/2$, can be clamped or simply supported by specifying ϕ_x^o or M_y to be zero, respectively. Regarding the inplane conditions, the unloaded edges can be free to move normally due to Poisson expansion effects ($N_y = 0$), or Poisson expansion effects can be resisted by restraining the normal displacement ($v^o = 0$), the latter representing, perhaps, the effects of a surrounding stiffer structure, or an intentional restraint in an experiment to induce secondary buckling.¹² Herein, the notation CC-CC will be used for the cases where all edges are clamped, and CC-SS will be used when the loaded edges are clamped and the unloaded edges are simply supported. Specification of the inplane conditions that accompany the clamped or simple-support conditions will be stated on a case-by-case basis, as described next.

The specific boundary condition cases studied are illustrated in Figure 2. The cases are arranged in 'matrix' form. The out-of-plane boundary conditions are constant within a column, and the inplane boundary conditions are constant within a row. As can be seen, the first column considers CC-CC eight-layer symmetric $[0_2/90_2]_S$ cross-ply plates and the other two columns, which are separated from the first column by a vertical line, consider unsymmetric $[0_4/90_4]_T$ cross-ply plates. Though the behavior of symmetric laminates is familiar to most, it is important to illustrate the influence of the inplane boundary conditions considered here on more familiar problems before the studying their influence on unsymmetric laminates.

The first case in the first column considers the situation where the v^o -displacement is unrestrained on all edges. There are a number of issues that make this case difficult to achieve in practice, but it is often the subject of theoretical studies and it does lead to a spatially uniform inplane strain field. The second case in the column considers restraints on the v^o -displacement on the loaded edges, while the third case considers restraints on the v^o -displacement on all four edges. The latter case also leads to a uniform strain field. In particular, the inplane strains are zero. The second case is considered so the effects of a nonuniform inplane strain field can be evaluated, and to serve as an intermediate step between the cases of v^o -displacement being free on all edges and the v^o -displacement being restrained on all edges, the first and third cases. Also, the first and second cases in the first column do not exhibit secondary buckling, while the third case does. The influence of inplane boundary conditions on secondary buckling are more clearly demonstrated by having the intermediate boundary condition case available to consider. Finally, it is this intermediate inplane boundary condition case that is most likely to be considered in the laboratory when the unloaded edges are simply-supported, as in the case with the unsymmetric laminate in the third column. Proceeding to the second column, it is seen the first, second, and third cases are analogs of the first, second, and third cases in the first column as far as the boundary conditions are concerned. However, four of the eight layers in the laminates have their fiber orientations changed to yield unsymmetric $[0_4/90_4]_T$ cross-ply plates. For the unsymmetric laminate, the intermediate boundary condition case will be quite interesting. The third column is the same as the second column, with the exception being that the unloaded edges are simply supported rather than clamped. In this column the consequences of relaxing the clamping effects on the unloaded edges are examined. As mentioned, the second case in the third column represents the boundary conditions that are often used in the laboratory when testing symmetric laminates. This point will be elaborated upon later when this case is discussed in detail.

The various cases in Figure 2 were modeled with S9R5 shell elements in ABAQUS. The elements degenerate to Kirchhoff-type elements when the element is thin, as is the case here, though material properties in a three-dimensional sense are required for input. Only square plates were considered ($b = a$ in Figure 1) with 20 elements in both the x - and y -directions. Meshes with 40 elements in both directions were investigated, but displacement, bifurcation, and stability calculations for the 20 by 20 mesh practically coincided with the results for the 40 by 40 mesh. The responses are computed with a variety of techniques available in ABAQUS. These include starting, stopping, and restarting static analyses using the standard Newton-Raphson solution method, the Riks solution method, both loading and unloading the plate, and a dynamic approach. The dynamic approach was used when the message file from ABAQUS reported that at a particular value of Δ the system stiffness matrix had negative eigenvalues. When this occurred, the plate configuration was considered statically unstable. A dynamic analysis was then started from this configuration, holding the value of Δ fixed, for the purpose of finding a statically stable configuration. In theory, simply starting the dynamic analysis would have allowed the plate to move toward another stable equilibrium configuration.

However, this could have taken considerable amount of integration time, so instead, the plate was given a small disturbance in the form of a small-amplitude short-duration pressure load (i.e., a pressure pulse) perpendicular to the plate surface. A small amount of damping was artificially added to the material and the plate moved rapidly toward another statically stable equilibrium configuration. The plate oscillated around this configuration but the small amount of damping suppressed these oscillations to the point a static restart could be initiated. The analyses quickly converged to the new static equilibrium configuration. For completeness, the pressure pulse was applied in both the positive and negative z -directions, for different lengths of time, and for different pulse amplitudes, but it was always generally clear that the plate intended to move to a particular configuration. In this new configuration, both increasing and decreasing values of Δ were pursued using both Newton-Raphson and Riks solution schemes. The graphite-epoxy properties given in Table 1 were used to compute the results. The properties in Table 1 represent a medium-modulus graphite-epoxy material such as AS4/3501-6.

III. NUMERICAL RESULTS

In the figures to follow, the response of the plate to inplane compressive edge displacement is characterized by way of plots of two relations. First, the relation between the out-of-plane deflection at the center of the plate $w^o(0,0)$ and the inplane compressive edge displacement Δ is illustrated. Both of these deformations are normalized by the plate thickness H , and insets in the figures illustrate the out-of-plane deflections of the entire plate. As all plates discussed herein have the same thickness, a comparison of deflection levels between the cases illustrated in different figures is possible. Second, the relation between the inplane load P associated with the edge displacement and the normalized edge displacement - i.e., often referred to as the load-endshortening relationship - is illustrated. The load is normalized by $A_{11}H$, and again, since all cases considered in Figure 2 have the same value of A_{11} , a comparison of inplane load levels between cases is possible.

Before discussing the cases in Figure 2 in detail, it is useful provide a quick overview of the out-of-plane displacement characteristics for each case. Similarities, differences, and distinctive features become immediately apparent with this overview. Details will be considered in the expanded discussion to be presented shortly. The overview is illustrated in Figure 3. Plotted in each sub-figure in Figure 3 is the out-of-plane deflection at the center of the plate $w^o(0,0)$, on the vertical axis, as a function of the inplane compressive displacement Δ , both normalized by H . These are miniaturizations of the figures to be discussed later. The sub-figures are arranged in the same order as in Figure 2, so the influence of the boundary conditions, particularly the inplane boundary conditions, is obvious. The branches of the relations that represent unstable configurations are identified by the use of dashed line types. A quick examination of Figure 3 shows that bifurcation buckling occurs for all three CC-CC symmetric cross-ply laminate cases, the first column, with secondary buckling occurring for the third case. Secondary buckling is evident in the third case by the vertical line near $\Delta/H = 0.06$ indicating the displacement in the center of the plate goes to zero as the plate snaps to a configuration with two-half waves in the loading direction. All three CC-CC unsymmetric $[0_4/90_4]_T$ cross-ply plates, the second column, appear to bifurcate, like the symmetric cases do, though as will be seen, the postbuckling behavior among the cases is considerably different, and is, in fact, asymmetric. A closer examination of the second case in the second column however, will reveal that the plate does not bifurcate. The first two CC-SS unsymmetric $[0_4/90_4]_T$ cross-ply plates, the third column, exhibit no bifurcation-then-postbuckling behavior, but rather exhibit out-of-plane deformations immediately upon loading. The third CC-SS case in that column exhibits bifurcation-then-postbuckling behavior. As will be seen, the bifurcation is asymmetric, unlike the bifurcations in the first and second columns, which are symmetric. These nine cases will now be discussed in more detail. (Again for clarity; by symmetric is meant that the negative out-of-plane displacement branch is a reflection about the horizontal axis of the positive out-of-plane displacement branch. If this reflection, or mirror image, symmetry does not exist, then the terminology asymmetric is used.)

A. CC-CC $[0_2/90_2]_S$ Symmetric Cross-Ply Cases (First Column in Figure 2)

The out-of-plane deflection and load relations for a $[0_2/90_2]_S$ symmetrically laminated plate clamped on all four edges but with the v^o displacement free everywhere are illustrated Figures 4 and 5. Referring to Figure 4, as the plate is loaded from the no-load condition, toward point A , there is no out-of-plane deflection at the center of the plate. The plate remains flat. At point A , the relation bifurcates symmetrically into positive and negative branches that represent nonzero out-of-plane deflection. The zero deflection branch extends to the right of point A to point A' . The flat plate condition on branch AA' is unstable. Branches AB and $A\bar{B}$, which are symmetric, are stable. On these branches the plate deforms out of plane with a half-wave in both the x - and y -directions. Like an isotropic plate, symmetric bifurcation and stable postbuckling behavior are to be expected.

The load vs. edge displacement relation of Figure 5 shows that the inplane stiffness of the plate (i.e., the slope of the relation) drops sharply when the plate begins to deflect out of plane at bifurcation point A . The load vs. edge displacement relation is the same for negative out-of-plane deflections as it is for positive out-of-plane deflections, and, of course, the slope of the relation when the plate is flat and unstable (branch AA') is the same as when it is flat and stable (branch OA). It should be pointed out that the arrows from the insets to a branch mean the insets are identified with a general region of a branch. Often two insets that depict equal but opposite out-of-plane deflection patterns are directed to the same general region of a branch. This essentially means that either of the deflection patterns is possible in the general region of the branch.

Referring to Figure 6, it is seen that when the v^o -displacement on the clamped loaded edges is restrained to be zero, but the clamped unloaded edges remain free to move in the y -direction, the qualitative character of the out-of-plane deflection vs. edge displacement remains unchanged relative to the previous case. The load vs. edge displacement relations in Figure 7 reflect this.

As the final case in the first column of Figure 2, Figures 8 and 9 illustrate the response of a $[0_2/90_2]_S$ symmetrically laminated plate clamped on all four edges and with the v^o -displacement restricted to be zero on all of these edges. With the v^o -displacement restricted on the unloaded edges, inplane deformations induced by the Poisson effect are restricted, and the plate is subjected to a state of biaxial compression. The response of the plate in this situation is quite different than in the previous two cases. Referring to Figure 8, as the plate is loaded from the no-load condition, the out-of-plane deflection relation bifurcates symmetrically at point A , as with the previous two cases. However, as the edge displacement is increased in the postbuckling range, the plate configuration becomes unstable again, as it did at bifurcation point A . The point of instability is identified as point B or \bar{B} , depending on whether the positive or negative out-of-plane deflection branch is being considered. At points B and \bar{B} the plate snaps to either of two new configurations, each with two half-waves in the loading direction, and one half-wave perpendicular to the loading direction, as shown with the insets. The snapping event is a dynamic one, and was triggered in the analysis by giving the configuration at B the aforementioned small pressure pulse. The ensuing oscillations centered around the configuration of point B' , but subsided due to the artificially induced damping. With the two half-wave configuration, the out-of-plane deflection of the center of the plate is exactly zero, as denoted by points B' and \bar{B}' . The plate can snap into either of the two half-wave configurations. With increased edge displacement to point C (an arbitrary inplane displacement level), the plate remains in the two half-wave configuration, the out-of-plane deflections simply becoming deeper. Upon unloading from point C , the out-of-plane deflections decrease, but the two-half-wave configuration continues with decreased edge displacement to point D . At point D , the two-half-wave configuration becomes unstable, and the plate snaps to the configurations given by points D or \bar{D}' , configurations very similar to those associated with points B and \bar{B} . With a further decrease in edge displacement to point A the plate returns to a flat configuration. The snap from the configuration at point B to that at point B' (or points \bar{B} and \bar{B}') is often referred to as secondary buckling.¹²

The load vs. edge displacement relation is shown in Figure 9, and it is seen that a sudden drop in load accompanies the snap through from points B to B' and \bar{B} to \bar{B}' . The load again increases as the edge

displacement increases to point C , but the slope of the relation is less than for postbuckling branch AB (or $A\bar{B}$) or prebuckling branch $0A$, the decreased slope representing a loss of inplane stiffness due to the increased number of half-waves in the loading direction. Upon unloading to point D , the load suddenly increases as the plate snaps back to having one half-wave in the loading direction, point D' or \bar{D}' . In a rather restricted range of edge displacement, four stable equilibrium configurations exist, two with a single half-wave in the loading direction, and two with two half-waves in the loading direction. Referring to Figure 8, this range is between $0.0565 \leq \Delta/H \leq 0.0575$.

B. CC-CC $[0_4/90_4]_T$ Unsymmetric Cross-Ply Cases (Second Column in Figure 2)

The response of an unsymmetric $[0_4/90_4]_T$ laminate with the same three boundary condition cases discussed above for the symmetric laminate are now considered. All conditions are identical, except the laminate has the directions of four of the eight layers changed. Considering the case where all edges are clamped but the v^o -displacement is free on all edges, the out-of-plane deflection vs. edge displacement and load vs. edge displacement relations are illustrated in Figures 10 through 12, Figure 12 being an enlarged portion of the Figure 11. A quick comparison of the out-of-plane deflection vs. edge displacement relation for this case with that of the counterpart case for the symmetric laminate, Figure 4, shows there are differences. However, there is one important similarity. As the plate is loaded from the no-load condition, the plate remains flat, despite the fact that it is unsymmetrically laminated. The clamped boundaries supply whatever moments are necessary to overcome the moment induced within the plate due to the lack of symmetry of the laminate reflected in the B_{11} term. (For this laminate $B_{22} = -B_{11}$.) With a continued increase in edge displacement, the relation bifurcates at point A , deflecting out of plane in either the positive or negative direction past the bifurcation level of edge displacement. This is exactly what happens with the symmetric laminate of Figure 4. The positive and negative branches of the relation, branches AB and $A\bar{B}$, however, are not mirror images of each other, as they were for the symmetric laminate case. Slightly larger edge displacements are possible on branch AB than on branch $A\bar{B}$, as evidenced by the larger value of Δ/H associated with point B than with point \bar{B} . Also, for a given value of Δ/H , e.g., 0.02, the magnitude of the out-of-plane deflections are slightly greater for the positive branch. It should be noted that the edge displacement that causes bifurcation of this unsymmetric plate is about half the value to cause bifurcation of the counterpart symmetric plate. This is because the four 0° layers are clustered together within the $[0_4/90_4]_T$ laminate, whereas within the $[0_2/90_2]_S$ laminate the four 0° layers are spread out, resulting in a greater resistance to instability. When the edge displacement reaches point B on the positive branch, the plate becomes unstable and the configuration snaps to one of those associated with point B' , configurations that can be approximated by two half-waves in the loading direction, as shown by the inset. However, and an important point, the out-of-plane deflection at the center of the plate is not zero, as it is with the symmetric laminate, rather it is slightly positive, so the half waves are not actually of equal length in the loading direction. This nonzero value of the out-of-plane deflection at the center of the plate is due to the influence of B_{11} , despite the fact it had no influence along branch $0A$. Either of two approximate half-wave configurations is possible, as shown by the insets. On the negative branch, when the edge displacement reaches point \bar{B} , the plate also becomes unstable and the configuration snaps to either of those of point \bar{B}' , which are similar to those of point B' . With increased edge displacement to point C , the configuration remains the same. With decreasing edge displacement from point C , the relation retraces the path to point D , a point of vertical tangency, or limit point. As the relation approaches point D from point C , the two possible approximate two half-wave configurations continue. With a further decrease in edge displacement below point D , the plate snaps to either point D' or to point \bar{D}' . There is a branch from point D to point B , but the branch represents unstable configurations. Like the symmetric laminate, there is a range of Δ/H , specifically $0.017 \leq \Delta/H \leq 0.028$, where there are multiple stable configurations. An applied force or moment could cause the plate to move from one of these configurations to another.

The load vs. edge displacement relation of Figure 11 is complicated by the lack of mirror image symmetry of the positive and negative out-of-plane deflection responses. For increasing edge displacements beyond

bifurcation point A , as might be expected in light of Figure 10, the load vs. edge displacement relation for the positive branch is not the same as the load vs. edge displacement relation for the negative branch, as it was for the symmetric laminate. This is better seen in the enlargement of a specific region of the load vs. edge displacement relation illustrated in Figure 12, where the relations for the two branches are separated slightly. The stiffness on branch $A\bar{B}$ is slightly greater than the stiffness on branch AB . A drop in load accompanies the transition from points B to B' and from points \bar{B} to \bar{B}' , the inplane stiffness of plate decreasing after snap through. An increase in load and stiffness accompanies the transition from point D to either D' or \bar{D}' .

When the v^o -displacement on the clamped loaded edges of the unsymmetric $[0_4/90_4]_T$ laminated plate is restrained to be zero, the out-of-plane deflection and load vs. edge displacement relations illustrated in Figures 13 through 17 result. As seen in Figure 13, the out-of-plane deflection relation looks somewhat like the case for which there are no restraints on the v^o -displacements, Figure 10. However, there are some interesting differences. As the edge-displacement increases from zero, the plate remains almost flat, but it exhibits a small magnitude negative out-of-plane deformation slightly before point A . Then, a noticeable negative out-of-plane deformation, consisting of one half-wave in both the x - and y -directions, builds, causing the noticeable out-of-plane deflection beyond point A . The details of the out-of-plane deflection surrounding point A are shown Figure 14. There is no bifurcation or adjoining positive branch. However, with an increased edge displacement slightly greater than point A , past point E' , a positive out-of-plane deformation consisting of one half-wave in both directions, beginning at point E , a limit point, is possible. Considering the negative branch, at point \bar{B} , in Figures 13, the single half-wave configuration with a negative out-of-plane deflection becomes unstable and the plate snaps to either of two approximate two half-wave configurations at point \bar{B}' . With increasing and then decreasing edge displacement toward and then away from point C , a point of vertical tangency occurs at point D . At point D the plate snaps to a single half-wave configuration at either D' or \bar{D}' . With a continued decrease in edge displacement from point D' , the relation moves to point E . As seen in Figure 14, with a decrease in edge displacement from point E , the plate snaps from a one half-wave configuration with positive out-of-plane deflection to a one half-wave configuration with negative out-of-plane deflection given by point E' . With a further decrease in edge displacement, the plate becomes flatter at point A . For increases in edge displacement from point E , a branch extends to points F and G , but branch EFG represents unstable configurations. On the other hand, with increased edge displacement from point D' , the plate becomes unstable at point B and snaps to either of two approximate two half-wave configurations at point B' .

The relations between load and edge displacement in Figure 15 show changes in inplane stiffness and step changes in the load from points B and \bar{B} to points B' and \bar{B}' , and from D to D' or \bar{D}' . There is also a step change between points E and E' . These features can be better seen in the enlarge views of Figures 16 and 17. The lack of connection of the positive and negative single half-wave branches $AE'\bar{D}'\bar{B}$ and $ED'B$ at point A in Figure 13 aside, it can be seen from the load relation that these two branches have slightly different characteristics and are distinct.

The subtle change of restraining the v^o -displacement on the clamped loaded edges, while allowing the v^o -displacement to remain free on the clamped unloaded edges, had minimal effect on the symmetric laminate, as Figures 4-7 illustrate. For the unsymmetric laminate of the second column, however, this change in inplane boundary conditions prevented the plate from remaining flat and bifurcating. To further consider this issue, the predicted out-of-plane deflection vs. edge displacement relations for the previous case, the present case, and the next case to be discussed, i.e., the first, second, and third cases in the second column of Figure 2, are illustrated in Figure 18 using both a geometrically linear and geometrically nonlinear analyses and considering small edge displacement levels. As seen, when v^o is either free on all edges or restrained on all edges, both linear and nonlinear analyses predict the CC-CC $[0_4/90_4]_T$ laminate will remain perfectly flat upon loading. The case with v^o restrained on the clamped loaded edges but free on the clamped unloaded edges exhibits out-of-plane deflections. Since the linear analysis predicts out-of-plane deflections, the phenomenon is due to material coupling effects as opposed to geometrically nonlinear coupling effects, though geometrically nonlinear effects amplify the out-of-plane deflections. Considering the geometrically linear case, the first two equilibrium equations for the unsymmetric cross-ply laminate, i.e., summation of

forces in the x -direction and summation of forces in the y -direction, in terms of the midsurface strains and curvatures are

$$A_{11} \frac{\partial \epsilon_x^o}{\partial x} + A_{12} \frac{\partial \epsilon_y^o}{\partial x} + A_{66} \frac{\partial \gamma_{xy}^o}{\partial y} + B_{11} \frac{\partial \kappa_x^o}{\partial x} = 0 \quad (1)$$

$$A_{12} \frac{\partial \epsilon_x^o}{\partial y} + A_{22} \frac{\partial \epsilon_y^o}{\partial y} + A_{66} \frac{\partial \gamma_{xy}^o}{\partial x} - B_{11} \frac{\partial \kappa_y^o}{\partial y} = 0 \quad (2)$$

If any of the strains vary with either coordinate, then the curvature gradient term must be nonzero so the terms all sum to zero. Restraining v^o to be zero along the line representing the clamped loaded edges, but allowing v^o to be free elsewhere leads to gradients in ϵ_y^o and γ_{xy}^o . Curvature, and hence out-of-plane displacements, then develop.

Finally, if the v^o -displacements on both the loaded and unloaded clamped edges of an unsymmetric $[0_4/90_4]_T$ laminate are restrained to be zero, then the relations of Figures 19 through 22 result. Referring to Figure 19, as the edge displacement of the plate is increased from zero, the plate remains flat, then bifurcates to have positive and negative postbuckling branches that are not mirror images of each other. The half-wave configuration of the both the positive and negative branches becomes unstable at points B or \bar{B} , respectively, the configurations transitioning to points B' and \bar{B}' , respectively, which can be either of two configurations with approximately two half-waves in the loading direction. With the configurations at B' and \bar{B}' , there are a slight negative out-of-plane deflections at the center of the plate, which is in contrast with the slight positive deflection that occurs with the two cases just discussed. With decreased edge displacement from point C , the out-of-plane deflection relation moves to limit point D , the details which are illustrated in Figure 20. From the insets in Figure 20, it can be seen that near point D one half-wave actually encompasses up about two-thirds of the dimension of the plate in the loading direction, while the other half-wave encompasses up the remaining one-third, so the out-of-plane deflection at the center of the plate is substantial. At point D , the plate loses stability and its configuration snaps to either that of point D' or that of point \bar{D}' , configurations with one half-wave in the loading direction. Segment $D\bar{B}$ represents unstable equilibrium configurations of the plate.

The load vs. edge displacement relation is illustrated in Figure 21, with details near limit point D enlarged in Figure 22. In these figures it is possible to see that the character of branches AB and $A\bar{B}$ are not identical, and that the inplane stiffness of the plate decreases when it snaps from points B or \bar{B} to B' or \bar{B}' .

C. $[0_4/90_4]_T$ CC-SS Laminates (Third Column in Figure 2)

When the boundary conditions on the unloaded edges are relaxed from clamped to simply supported, the response of the unsymmetrically laminated plate changes considerably. The lack of ability to resist moments along those edges allows unsymmetric effects in the laminate to influence the response as soon as the compressive edge displacement is applied. The response of a $[0_4/90_4]_T$ laminate simply-supported along the unloaded edges, clamped along the loaded edges, and with no restraints on the v^o -displacement along any of the edges is illustrated in Figures 23 and 24. The conditions of the plate are identical to those of the plate described in Figures 10 through 12 (the first case in the second column) except for the lack of a moment reaction along the unloaded edges. The out-of-plane deflection vs. edge displacement relation shown in Figure 23 illustrates that the plate deflects out-of-plane in a configuration with a single half-wave in the both directions as the edge displacement is increased from zero. The out-of-plane deflections are small for low levels of edge displacement, but at point A the out-of-plane deflections increase rapidly with increasing edge displacement. This rapid increase is due to geometric nonlinearities. For the range of edge displacement considered, only this configuration occurs. As seen in Figure 24, the load vs. edge displacement relation, the plate abruptly loses stiffness at point A , and continues to do so with increasing edge displacement due to the increased out-of-plane deflection.

Many laboratory experiments focused on compressive loading of flat plates are conducted by compressing one edge of the plate using the movable platen of a load frame and restricting the motion of the opposite

edge by virtue of the fixed platen. The unloaded edges are supported by knife edges that restrict out-of-plane deflection by resisting the development of curvature, but allowing motion in the loading direction, motion perpendicular to the loading direction, and rotation. As mentioned, because the edges of composite plates broom and subsequently fail when subjected to compression, the fixtures designed to apply the compressive edge displacement and support the opposite edge usually clamp the plate in the thickness direction. The clamping action on those two edges generally restricts the v^o -displacement. The second case in the third column simulates these conditions exactly, and therefore represents a realistic set of boundary conditions. This case is identical to the first case in the third column except for the v^o -displacement restraint on the clamped loaded edges. The response of the $[0_4/90_4]_T$ laminate with these more realistic boundary conditions is shown in Figures 25 and 26. It is seen that relative to the first case in the third column, Figures 23 and 24, there are few differences, qualitatively or quantitatively. The plate simply deflects out of plate at the initiation of edge compression, the deflection increasing more rapidly at point A.

If it is further assumed that the v^o -displacement along the unloaded edges is restrained to be zero (the third case in the third column), asymmetric bifurcation is predicted to occur, as illustrated in Figure 27 and the enlargement in Figure 28. As the edge displacement is increased to point A (see the expanded view in Figure 28), the plate becomes unstable and the out-of-plane deflection can suddenly jump to point \bar{A}' , which represents a stable plate configuration with negative out-of-plane deflections and a single half-wave in both directions. With increased edge displacement, as Figure 27 shows, the out-of-plane deflection vs. edge displacement relation moves to point \bar{B} . The relation then changes abruptly to follow branch $\bar{B}C$. As this branch is traversed, the plate configuration changes to one with two half-waves in the loading direction as point C is approached. If the edge displacement is decreased from a value corresponding point C to a value somewhat less than represented by point \bar{A}' , the relation reaches a limit point at point D. The relation then jumps to point D' , the plate returning to a flat configuration. Branch AD represents unstable configurations.

Returning to point A, and referring to Figure 27 and the detail in Figure 28, it is seen that at point A it is possible that increasing edge displacement can be accompanied by a positive out-of-plane deflection at the center of the plate, as represented by branch AB. Referring to the insets, it is seen that the configuration on this branch has a single half-wave in both directions. This configuration becomes unstable when the edge displacement reaches the value corresponding to point B on Figure 27. At point B the plate suddenly changes configuration to that of point B' on branch $D\bar{A}'\bar{B}$. In going from point B to point B' , the plate snaps from having all-positive out-of-plane deflections to having all-negative out-of-plane deflections.

The load vs. edge displacement relation in Figure 29, and the expanded view in Figure 30, reveal a drop in load when the plate configuration changes from that at point A to that at point \bar{A}' , and with a change of configuration from that at point B to that at point B' . The asymmetry in the out-of-plane deflection vs. edge displacement relation, wherein the deflections on the positive branch AB are less than the deflections on the negative branch $D\bar{A}'\bar{B}$, is reflected in the lower load and stiffness for branch $D\bar{A}'\bar{B}$. The stiffness is even less on branch $\bar{B}C$, a reflection of the two half-wave configuration.

D. Rayleigh-Ritz Solution For Other Laminates

The asymmetric bifurcation of the last case discussed has the potential for interesting plate behavior in the laboratory. As the edge displacement is increased from zero, it is not possible to have a smooth transition from the flat configuration to a configuration with a negative out-of-plane deflection. Referring to Figure 28, the plate must snap, or jump, from the flat configuration of point A to the non-flat configuration of point \bar{A}' . To further study this case, a simple five-term Rayleigh-Ritz solution to the problem was developed based on the total potential energy. The solution was based on the assumptions of classical lamination theory and the von Kármán approximations to the geometrically nonlinear strain-displacement relations. The first variation

of the total potential energy is given by

$$\begin{aligned} \delta\Pi = \int_{-b/2}^{+b/2} \int_{-a/2}^{+a/2} & \left\{ N_x \left(\frac{\partial \delta u^o}{\partial x} + \beta_x^o \delta \beta_x^o \right) + N_y \left(\frac{\partial \delta v^o}{\partial y} + \beta_y^o \delta \beta_y^o \right) \right. \\ & + N_{xy} \left(\frac{\partial \delta u^o}{\partial y} + \frac{\partial \delta v^o}{\partial x} + \beta_x^o \delta \beta_y^o + \beta_y^o \delta \beta_x^o \right) \\ & \left. + M_x \frac{\partial \delta \beta_x^o}{\partial x} + M_y \frac{\partial \delta \beta_y^o}{\partial y} + M_{xy} \left(\frac{\partial \delta \beta_x^o}{\partial y} + \frac{\partial \delta \beta_y^o}{\partial x} \right) \right\} dx dy \end{aligned} \quad (3)$$

where N_x , N_y , and N_{xy} and M_x , M_y , and M_{xy} are the force and moment resultants, respectively, which are related to the midplane strains and curvatures through the well-known *ABD* constitutive relations given by

$$\begin{Bmatrix} N_x \\ N_y \\ N_{xy} \\ M_x \\ M_y \\ M_{xy} \end{Bmatrix} = \begin{bmatrix} A_{11} & A_{12} & A_{16} & B_{11} & B_{12} & B_{16} \\ A_{12} & A_{22} & A_{26} & B_{12} & B_{22} & B_{26} \\ A_{16} & A_{26} & A_{66} & B_{16} & B_{26} & B_{66} \\ B_{11} & B_{12} & B_{16} & D_{11} & D_{12} & D_{16} \\ B_{12} & B_{22} & B_{26} & D_{12} & D_{22} & D_{26} \\ B_{16} & B_{26} & B_{66} & D_{16} & D_{26} & D_{66} \end{bmatrix} \begin{Bmatrix} \epsilon_x^o \\ \epsilon_y^o \\ \gamma_{xy}^o \\ \kappa_x^o \\ \kappa_y^o \\ \kappa_{xy}^o \end{Bmatrix} \quad (4)$$

The strains-displacement relations are

$$\begin{aligned} \epsilon_x^o &= \frac{\partial u^o}{\partial x} + \frac{1}{2} \beta_x^{o^2} \\ \epsilon_y^o &= \frac{\partial v^o}{\partial y} + \frac{1}{2} \beta_y^{o^2} \\ \gamma_{xy}^o &= \frac{\partial u^o}{\partial y} + \frac{\partial v^o}{\partial x} + \beta_x^o \beta_y^o \end{aligned} \quad (5)$$

where β_x^o and β_y^o are cross-sectional rotations defined as

$$\beta_x^o = -\frac{\partial w^o}{\partial x} \quad \text{and} \quad \beta_y^o = -\frac{\partial w^o}{\partial y} \quad (6)$$

and the curvatures are given by

$$\begin{aligned} \kappa_x^o &= \frac{\partial \beta_x^o}{\partial x} = -\frac{\partial^2 w^o}{\partial x^2} \\ \kappa_y^o &= \frac{\partial \beta_y^o}{\partial y} = -\frac{\partial^2 w^o}{\partial y^2} \\ \kappa_{xy}^o &= \frac{\partial \beta_x^o}{\partial y} + \frac{\partial \beta_y^o}{\partial x} = -2 \frac{\partial^2 w^o}{\partial x \partial y} \end{aligned} \quad (7)$$

For the Rayleigh-Ritz formulation two functional forms for the assumed displacement field are considered. One form is based on reduced polynomials and is given by

$$\begin{aligned} u^o(x, y) &= \frac{\Delta}{a} x + a_{11} \left[\left(\frac{x}{a} \right) - 3 \left(\frac{x}{a} \right)^2 + 2 \left(\frac{x}{a} \right)^3 \right] \left[\left(\frac{y}{b} \right) - \left(\frac{y}{b} \right)^2 \right] \\ &+ a_{12} \left[\left(\frac{x}{a} \right) - 3 \left(\frac{x}{a} \right)^2 + 2 \left(\frac{x}{a} \right)^3 \right] \left[\left(\frac{y}{b} \right) - \left(\frac{y}{b} \right)^2 \right]^2 \end{aligned}$$

$$\begin{aligned}
v^o(x, y) &= b_{11} \left[\left(\frac{x}{a} \right) - \left(\frac{x}{a} \right)^2 \right] \left[\left(\frac{y}{b} \right) - 3 \left(\frac{y}{b} \right)^2 + 2 \left(\frac{y}{b} \right)^3 \right] \\
&\quad + b_{21} \left[\left(\frac{x}{a} \right) - \left(\frac{x}{a} \right)^2 \right]^2 \left[\left(\frac{y}{b} \right) - 3 \left(\frac{y}{b} \right)^2 + 2 \left(\frac{y}{b} \right)^3 \right] \\
w^o(x, y) &= c_{11} \left[\left(\frac{x}{a} \right)^2 - 2 \left(\frac{x}{a} \right)^3 + \left(\frac{x}{a} \right)^4 \right] \left[\left(\frac{y}{b} \right) - \left(\frac{y}{b} \right)^2 \right]
\end{aligned} \tag{8}$$

and the other form is based on trigonometric functions and is given by

$$\begin{aligned}
u^o(x, y) &= \frac{\Delta}{a} x + a_{11} \sin \left(\frac{2\pi x}{a} \right) \sin \left(\frac{\pi y}{b} \right) + a_{21} \sin \left(\frac{4\pi x}{a} \right) \sin \left(\frac{\pi y}{b} \right) \\
v^o(x, y) &= b_{11} \sin \left(\frac{\pi x}{a} \right) \sin \left(\frac{2\pi y}{b} \right) + b_{12} \sin \left(\frac{\pi x}{a} \right) \sin \left(\frac{4\pi y}{b} \right) \\
w^o(x, y) &= c_{11} \left[1 - \cos \left(\frac{2\pi x}{a} \right) \right] \sin \left(\frac{\pi y}{b} \right)
\end{aligned} \tag{9}$$

In each case there are five unknown coefficients to be determined through the Rayleigh-Ritz approach. The origin of the analysis coordinate system for this Rayleigh-Ritz analysis is the lower left hand corner of the plate in Figure 1. Either of these assumed displacement fields are substituted into the strain-displacement and curvature-displacement relations, these in turn into the constitutive relations, and finally all of these expanded relations into the expression for the first variation of the total potential energy, Equation (3). Integration with respect to coordinates x and y can be carried out. The result is an algebraic expression for the first variation of the total potential energy which leads to five nonlinear algebraic equations for the unknown coefficients. These five equations can be reduced to a single equation of the form

$$c_{11} (f_1(A_{ij}) c_{11}^2 + B_{11} f_2(A_{ij}) c_{11} + f_3(A_{ij}) \Delta + f_4(A_{ij}, B_{11}, D_{ij})) = 0 \tag{10}$$

where, referring to Equations (8) and (9), c_{11} is the amplitude of the out-of-plane displacement and $f_1(A_{ij})$, $f_2(A_{ij})$, $f_3(A_{ij})$, and $f_4(A_{ij}, B_{11}, D_{ij})$ are functions of material constants and are not written in detail here. The form of Equation (10) is quite interesting. First, the material property B_{11} appears in just two components of the expression. Second, the form admits $c_{11} = 0$ as a solution, independent of the value of Δ . Therefore, a solution, at least for this Rayleigh-Ritz approach, is that the plate can remain flat. Third, the expression in the parenthesis equated to zero is another solution to the overall equation. This parenthetical equation can be solved for c_{11} as a function of Δ . There are two solutions, as the expression is a quadratic in c_{11} . These two solutions constitute positive and negative branches of a relation between out-of-plane deflection and edge displacement. Finally the expression in parenthesis in Equation (10) can be solved directly for $d\Delta/dc_{11}$, namely

$$\frac{d\Delta}{dc_{11}} = -\frac{2 f_1(A_{ij}) c_{11} + B_{11} f_2(A_{ij})}{f_3(A_{ij})} \tag{11}$$

This expression can be inverted to give $dc_{11}/d\Delta$, and the slope at the bifurcation point, where $c_{11} = 0$, can be computed, namely

$$\frac{dc_{11}}{d\Delta} = -\frac{f_3(A_{ij})}{B_{11} f_2(A_{ij})} \tag{12}$$

Note that when $B_{11} = 0$, i.e., the laminate is symmetric, the slope at the bifurcation point is infinite, as is the case for symmetric bifurcation. The point of vertical tangency, i.e., the limit point, is given by $dc_{11}/d\Delta = \infty$, which translates to $d\Delta/dc_{11} = 0$. The value of $w^o(0, 0)$ associated with the point of vertical tangency, w_p^o , can be solved for in closed-form by solving for c_{11} from the numerator of Equation (11) set to zero, namely,

$$c_{11} = -B_{11} \frac{f_2(A_{ij})}{2 f_1(A_{ij})} \tag{13}$$

and using this value in Equations (8) and (9). Note again, when $B_{11} = 0$, from equation (13) $c_{11} = 0$, which is interpreted to mean that the point of vertical tangency is associated with $c_{11} = 0$. This is certainly the case. It is clear from Equations (11) through (13) that the value of w_p^o and the slope $dc_{11}/d\Delta$ are directly related to B_{11} .

The out-of-plane deflection vs. edge displacement relations near the bifurcation point for six eight-layer unsymmetric cross-ply laminates, including the $[0_4/90_4]_T$ case, are illustrated in Figures 31 and 32 using both the five-term reduced polynomial Rayleigh-Ritz solution, as an example, and the ABAQUS calculations. These six laminates represent the six unique double-layer unsymmetric laminates that can be constructed from eight layers. (There is actually another set of six, but they differ only in the sign of B_{11} , and therefore the sign of the out-of-plane deflection.) There are differences between the ABAQUS and Rayleigh-Ritz relations, but the five-term Rayleigh-Ritz approach captures the important features. Stability analyses were not carried out with the Rayleigh-Ritz solutions. Table 2 provides a comparison of these calculated values of w_p^o using ABAQUS and the two Rayleigh-Ritz solutions. These are arranged in order of increasing value of $|w_p^o|$. Though the predicted trends of increasing value of $|w_p^o|$ as a function of the stacking sequence for both Rayleigh-Ritz solutions follows the trend predicted by ABAQUS, the maximum deviation for the trigonometric solution is about 14% relative to the ABAQUS prediction (for the $[0_2/0_2/0_2/90_2]_T$ laminate), while the maximum deviation for the reduced polynomial solution is about twice that (for the $[90_2/0_2/90_2/90_2]_T$ and $[0_2/0_2/0_2/90_2]_T$ laminates). Considering the number of degrees of freedom in the ABAQUS solution, the comparisons are good and reinforce the fact that these boundary conditions result in asymmetric bifurcation behavior. While in many such problems the asymmetric bifurcation behavior is due to geometric asymmetry, here the behavior is due to material asymmetry.

It should be mentioned before closing that when the loaded edges are simply supported (SS), the plate response is similar to that shown in Figures 23-26, namely, the plate deforms out of plane immediately upon application of a compressive edge displacement.

IV. Concluding Remarks

This paper has presented interesting results for inplane loaded unsymmetric laminates. A quick review of the response for the cases in the second and third columns of Figure 3 clearly illustrates this point. The specific boundary conditions studied could be considered quite specific, and therefore the results presented could be considered of limited value. On the contrary, it is believed the results presented are broad in scope and have a wider impact. The CC-CC case with the v^o -displacement free everywhere (first case in second column in Figure 3) was chosen as a starting point because, based on the past geometrically linear results of Leissa⁹ and Qatu and Leissa,¹⁰ they argued that the potential for classical bifurcation buckling behavior existed. This, despite the fact that the laminate was unsymmetric and some sort of asymmetric response might be expected right from the onset of loading. However, bifurcation buckling was shown to occur, and then, since the analysis here was based on geometrically-nonlinear analyses, the postbuckling behavior was examined, including secondary buckling. It was found that the asymmetries in response expected at the lower load level did exist at this higher level of loading. With a slight change of boundary conditions to those of the second case in the second column, a change which had minimal influence on the counterpart symmetric laminate in the first column, the bifurcation behavior disappeared and asymmetric response developed from the onset of loading, as shown in Figure 18. The disappearance of the bifurcation was subtle, and might even be missed in an experiment. However, since inplane and out-of-plane deformations are coupled in unsymmetric laminates, perhaps it should not be surprising that inplane boundary conditions play an important role in the out-of-plane response. However, the dependence on inplane boundary conditions seems so sensitive that it might be impossible to successfully conduct experiments to verify any particular findings. Further changing the boundary conditions to those of the third case in the second column again resulted in bifurcation behavior and asymmetric postbuckling response, like the first case in the column, but the sign of the secondary buckling response changed. Then, releasing the clamped unloaded edges so they were simply supported, the third case in the third column, did not cause the bifurcation behavior

to disappear, as expected. Rather, the bifurcation became asymmetric. The findings of this study, then, illustrate that attention to inplane boundary conditions is very important when considering the response of unsymmetric laminates, much more so than for symmetric laminates. The findings also indicate bifurcation behavior of flat unsymmetric cross-ply laminates is possible for a variety of conditions. Before closing, it should be noted that Johnson and Haftka¹³ studied the response of composite laminates loaded inplane by compressive loads acting eccentrically relative to the geometric midsurface so as to produce edge moments that countered the effects of bending-stretching coupling. The authors reported an asymmetric bifurcation.

Acknowledgements

The first author would like to thank the Department of Mechanical Engineering at Kuwait University for the financial support provided during the course of this investigation.

References

- ¹Dano, M.-L. and Hyer, M., "Thermally-Induced Deformation Behavior of Unsymmetric Laminates," *International Journal of Solids & Structures*, Vol. 35, No. 17, June 1998, pp. 2101–2120.
- ²Dano, M.-L. and Hyer, M., "The Response of Unsymmetric Laminates to Simple Applied Forces," *Mechanics of Composite Materials & Structures*, Vol. 3, No. 1, March 1996, pp. 65–80.
- ³Dano, M.-L. and Hyer, M., "Snap Through Behavior of Unsymmetric Composite Laminates," *International Journal of Solids & Structures*, Vol. 39, No. 1, June 2002, pp. 2101–2120.
- ⁴Dano, M.-L. and Hyer, M., "SMA-Induced Snap-Through of Unsymmetric Fiber-Reinforced Composite Plates," *International Journal of Solids & Structures*, Vol. 40, June 2003, pp. 5949–72.
- ⁵Yoon, K., Park, K., Lee, S., Goo, N., and Park, H., "Analytical Design Model for a Piezo-Composite Unimorph Actuator and its Verification using Lightweight Piezo-Composite Curved Actuators," *Smart Materials and Structures*, Vol. 13, June 2004, pp. 457–67.
- ⁶Aimmanee, S. and Hyer, M. W., "Analysis of the Manufactured Shape of Rectangular Thunder-T type Actuators," *Smart Materials & Structures*, Vol. 13, No. 6, December 2004, pp. 1389–1406.
- ⁷Lagace, P. A., Jensen, D. W., and Finch, D. C., "Buckling of Unsymmetric Composite Laminates," *Composite Structures*, Vol. 5, No. 2, 1986, pp. 100–123.
- ⁸Jensen, D. W. and Lagace, P. A., "Influence of Mechanical Couplings on the Buckling and Postbuckling of Anisotropic Plates," *AIAA Journal*, Vol. 26, No. 10, October 1988, pp. 1269–1277.
- ⁹Leissa, A. W., "Conditions for Laminated Plates to Remain Flat Under Inplane Loading," *Composite Structures*, Vol. 6, No. 4, 1986, pp. 261–270.
- ¹⁰Qatu, M. S. and Leissa, A. W., "Buckling and Transverse Deflections of Unsymmetrically Laminated Plates Subjected to In-Plane Loads," *AIAA Journal*, Vol. 31, No. 1, January 1993, pp. 189–194.
- ¹¹*ABAQUS/STANDARD User's Manual*, Hibbitt Karlsson & Sorensen Inc, Pawtucket, Rhode Island, 6.3 Edition 1998.
- ¹²Tiwari, N. and Hyer, M. W., "Secondary Buckling of Compression-Loaded Composite Plates," *AIAA Journal*, Vol. 40, No. 10, October 2002, pp. 2120–2126.
- ¹³Johnson, E. R. and Haftka, R. T., "Initial Postbuckling Response of Anisotropic Laminated Rectangular Plates," *33rd AIAA/ASME/ASCE/AHS/ASC Structures, Structural Dynamics, and Materials Conference*, AIAA Paper No. 92-2284, Dallas, TX, April 1992.

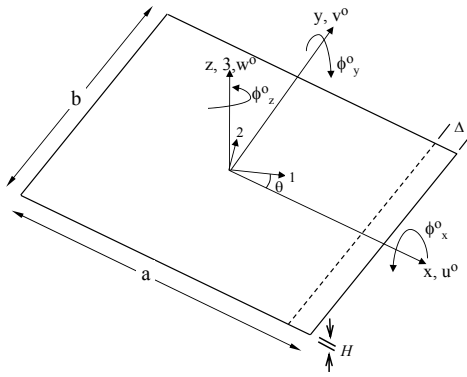
Table 1: Graphite Layer Material Properties

Property	Value
E_1 (Msi)	18.85
E_2 (Msi)	1.407
E_3 (Msi)	1.407
G_{23} (Msi)	0.725
G_{13} (Msi)	0.725
G_{12} (Msi)	0.725
ν_{23}	0.3
ν_{13}	0.3
ν_{12}	0.3

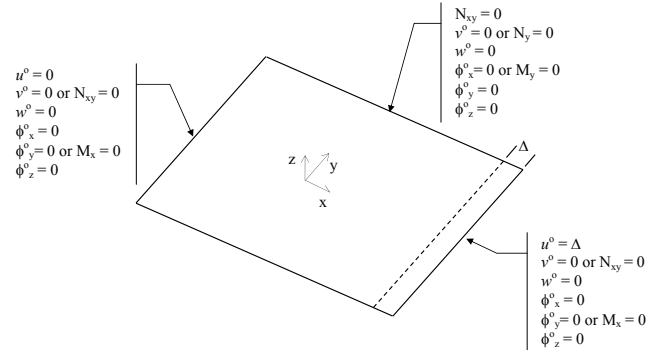
Table 2: w^o -location of the limit point, ABAQUS and Rayleigh-Ritz predictions

Fig.	Stacking Sequence	$(w_p^o/H)^a$	$(w_p^o/H)^b$	$(w_p^o/H)^c$
31a,b	$[0_2/0_2/90_2/0_2]_T$	-0.0438	-0.0470	-0.0415
32a,b	$[90_2/0_2/90_2/90_2]_T$	-0.0465	-0.0598	-0.0467
31c,d	$[0_2/90_2/0_2/90_2]_T$	-0.0962	-0.1047	-0.0881
31e,f	$[0_2/0_2/0_2/90_2]_T$	-0.1092	-0.1410	-0.1248
32e,f	$[0_2/90_2/90_2/90_2]_T$	-0.1570	-0.1796	-0.1402
32c,d	$[0_2/0_2/90_2/90_2]_T$	-0.1680	-0.2095	-0.1762

^aABAQUS, estimate of location of $dw^o(0,0)/d\Delta = \infty$ ^bFive-term Rayleigh-Ritz reduced polynomials, computed using solution for $d\Delta/dc_{11} = 0$ ^cFive-term Rayleigh-Ritz trigonometric functions, computed using solution for $d\Delta/dc_{11} = 0$



(a) Plate geometry and analysis coordinate system



(b) Possible boundary condition

Figure 1: Plate geometry, analyses and coordinate system, and boundary conditions

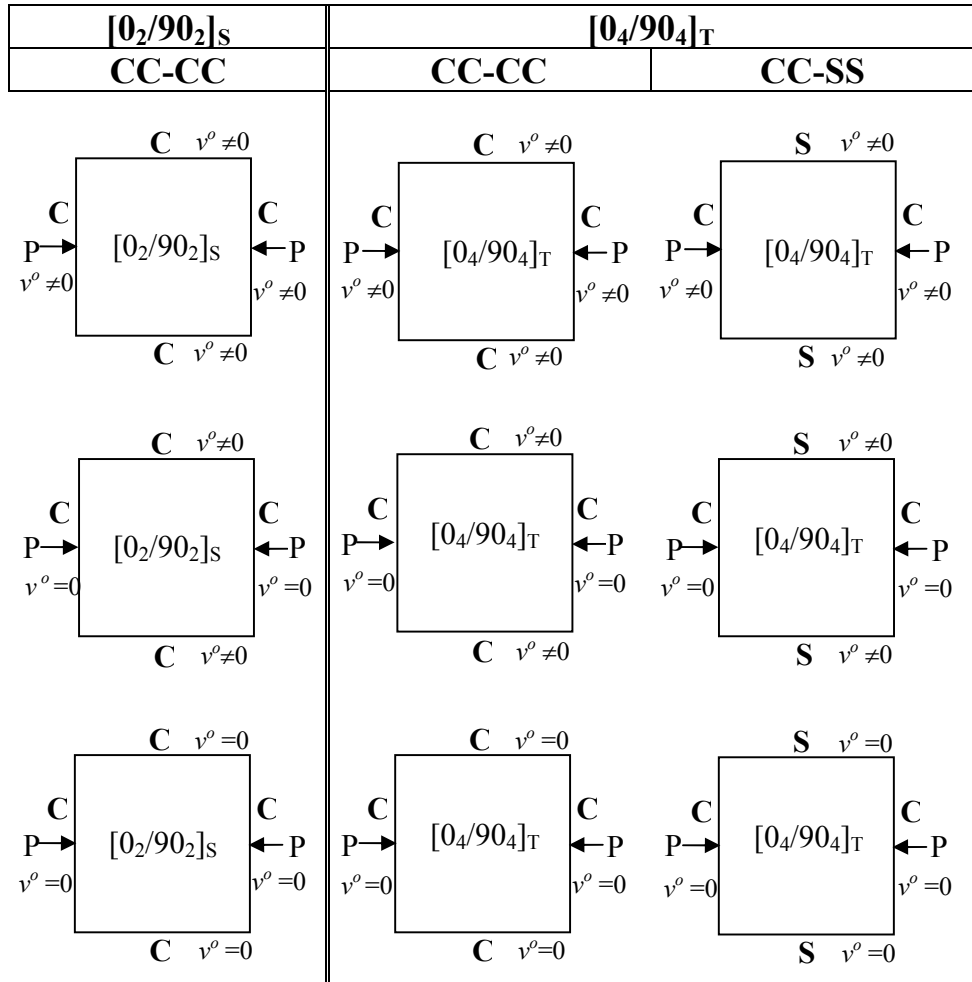


Figure 2: Cross-ply laminates and boundary conditions studied

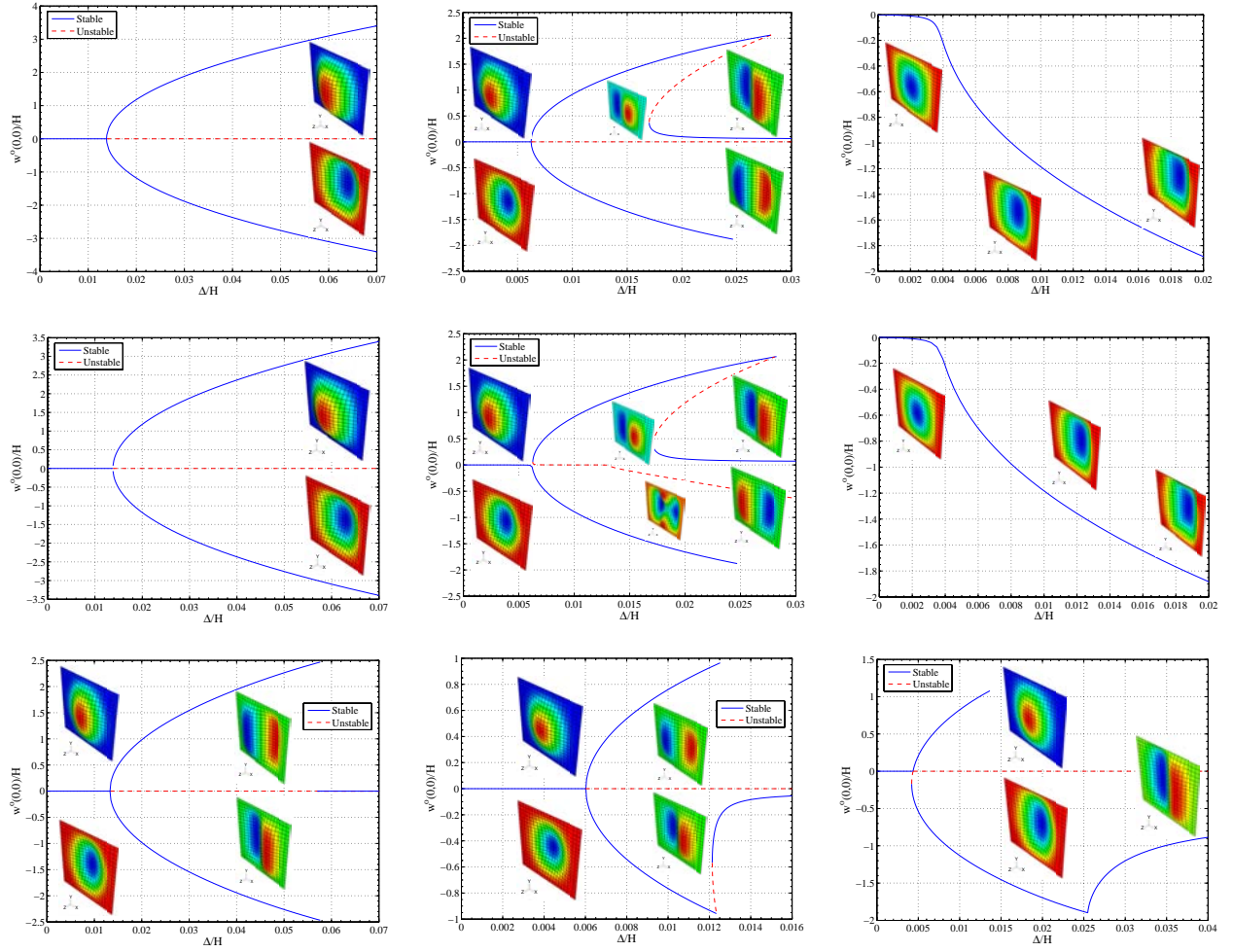


Figure 3: Overview of out-of-plane deflection characteristics of cases in Figure 2

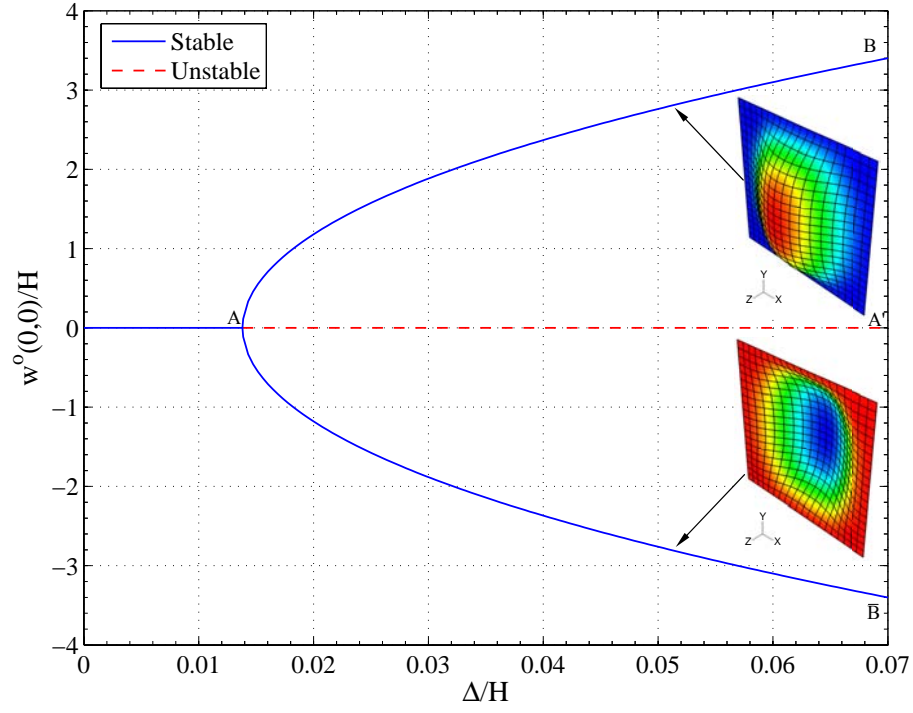


Figure 4: Out-of-plane deflection vs. edge displacement for CC-CC $[0_2/90_2]_s$ square plate with v^o free on all edges

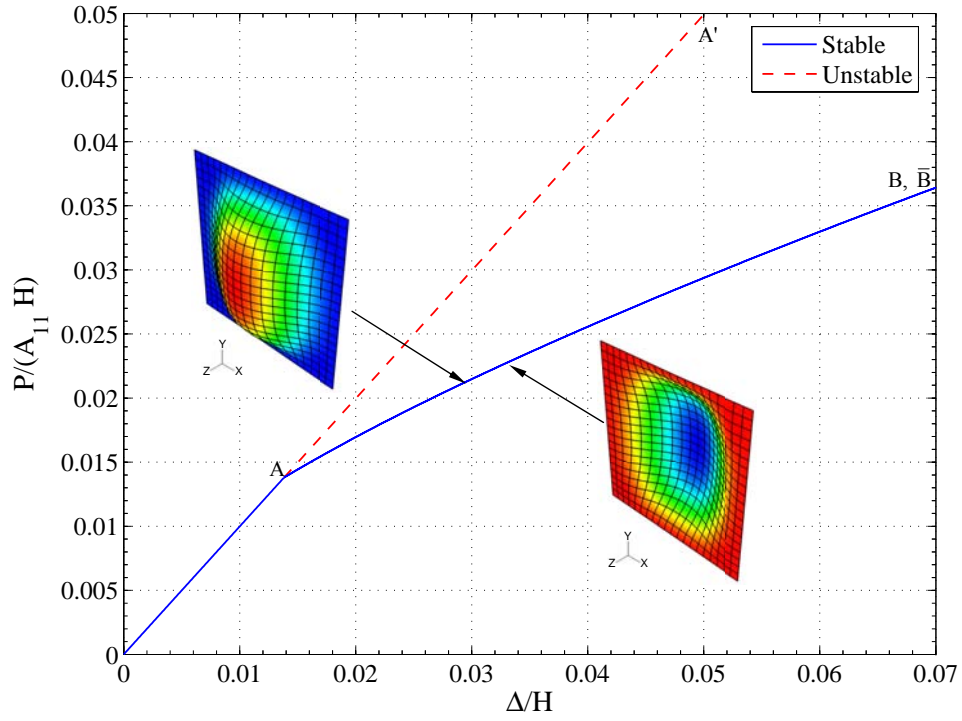


Figure 5: Load vs. edge displacement for CC-CC $[0_2/90_2]_s$ square plate with v^o free on all edges

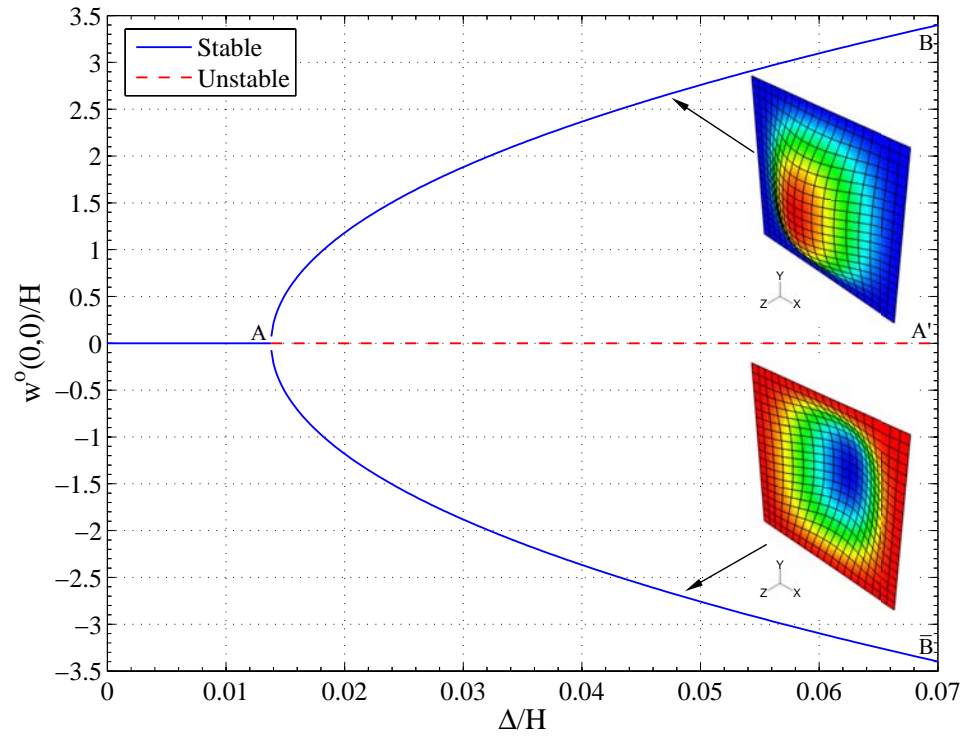


Figure 6: Out-of-plane deflection vs. edge displacement for CC-CC $[0_2/90_2]_S$ square plate with v^o restrained on loaded edges, free on unloaded edges

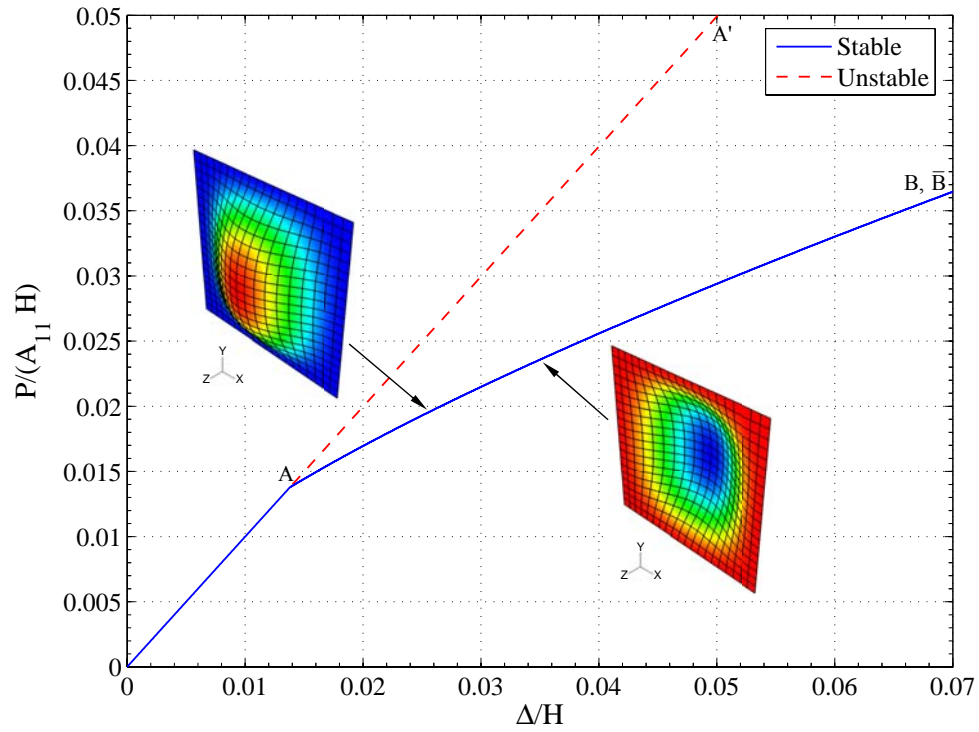


Figure 7: Load vs. edge displacement for CC-CC $[0_2/90_2]_S$ square plate with v^o restrained on loaded edges, free on unloaded edges

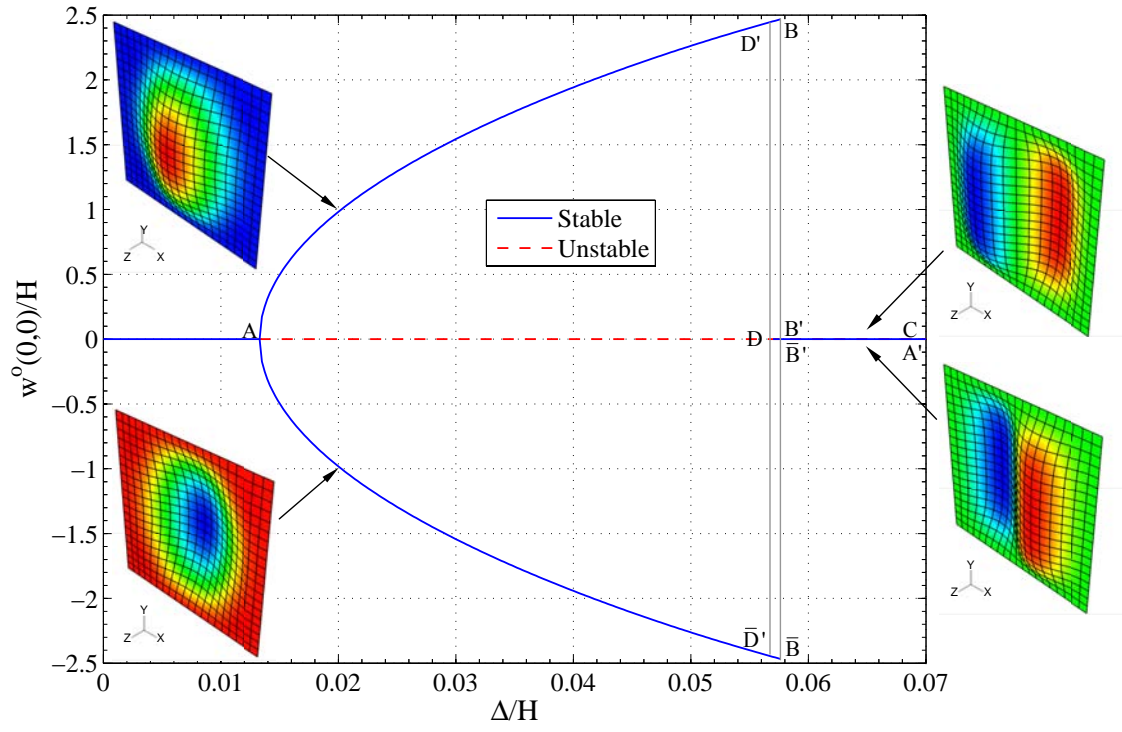


Figure 8: Out-of-plane deflection vs. edge displacement for CC-CC $[0_2/90_2]_S$ square plate with v^o restrained on all edges

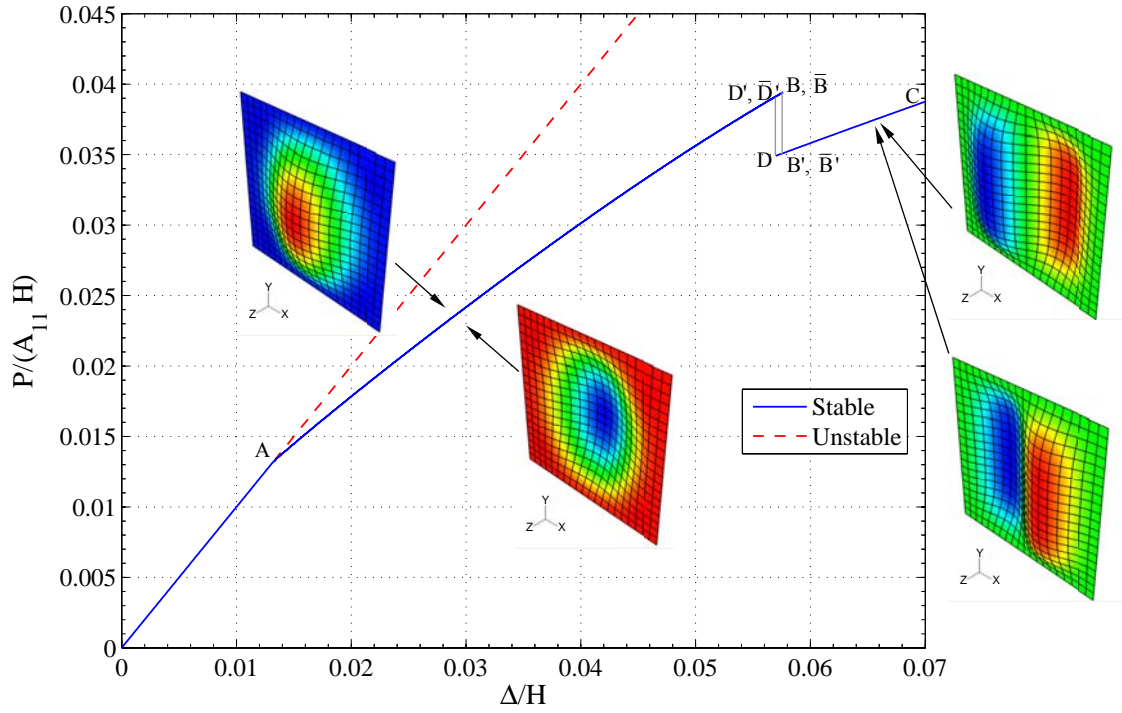


Figure 9: Load vs. edge displacement for CC-CC $[0_2/90_2]_S$ square plate with v^o restrained on all edges

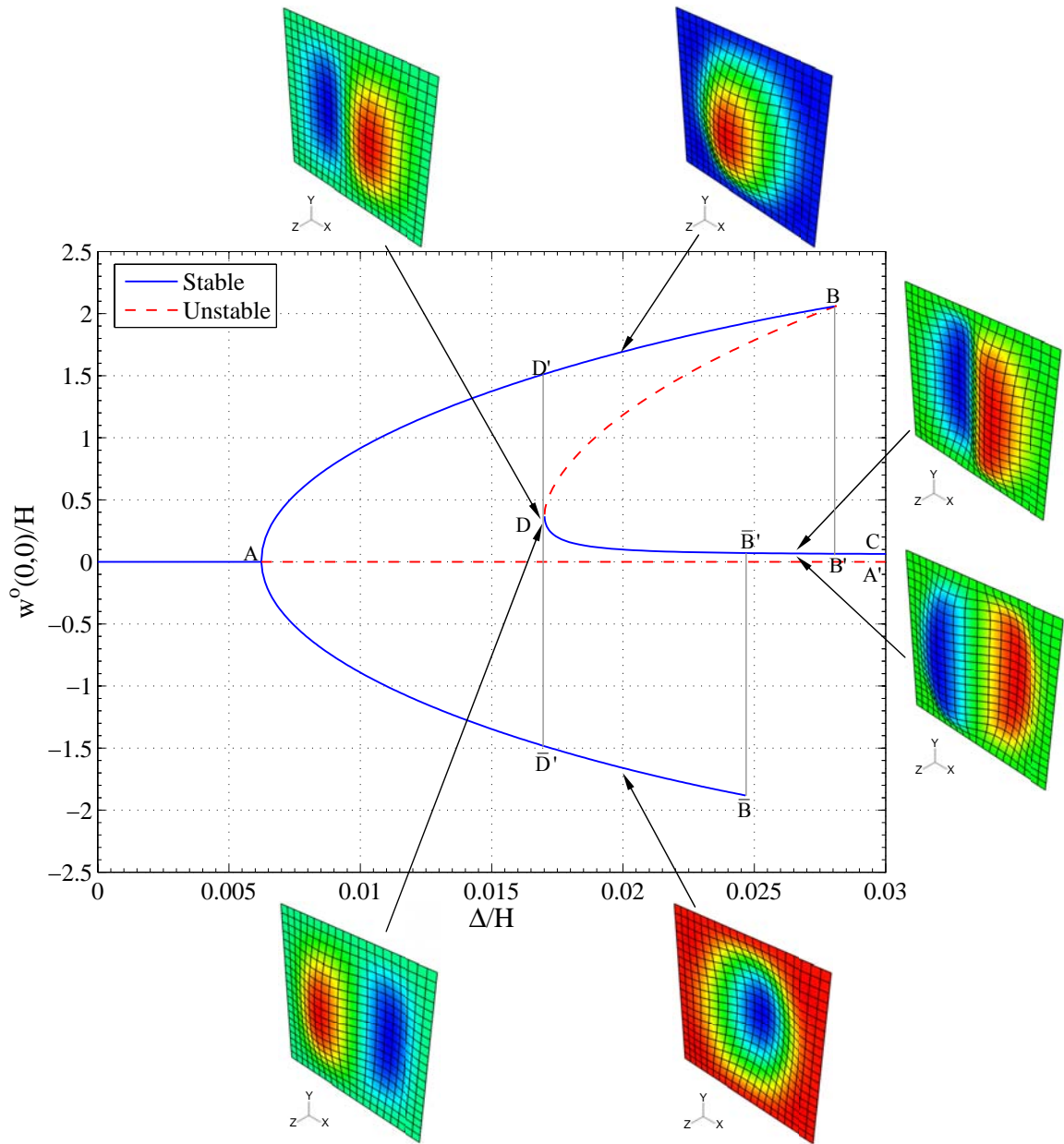


Figure 10: Out-of-plane deflection vs. edge displacement for CC-CC $[0_4/90_4]_T$ square plate with v^o free on all edges

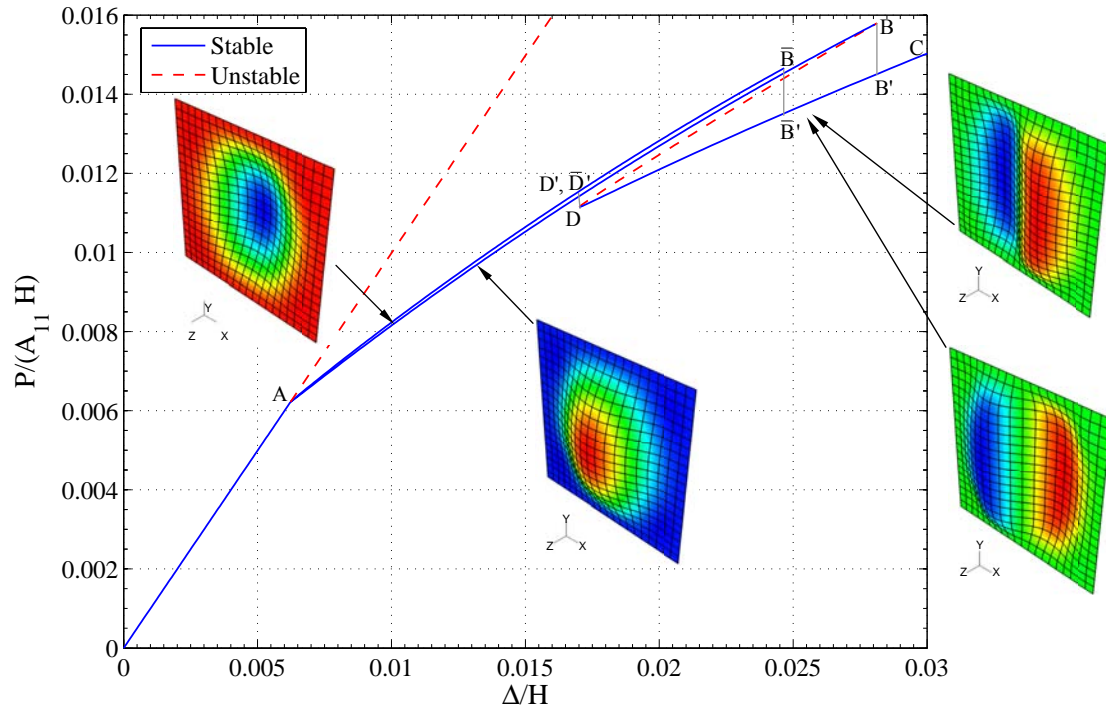


Figure 11: Load vs. edge displacement for CC-CC $[0_4/90_4]_T$ square plate with v^o free on all edges

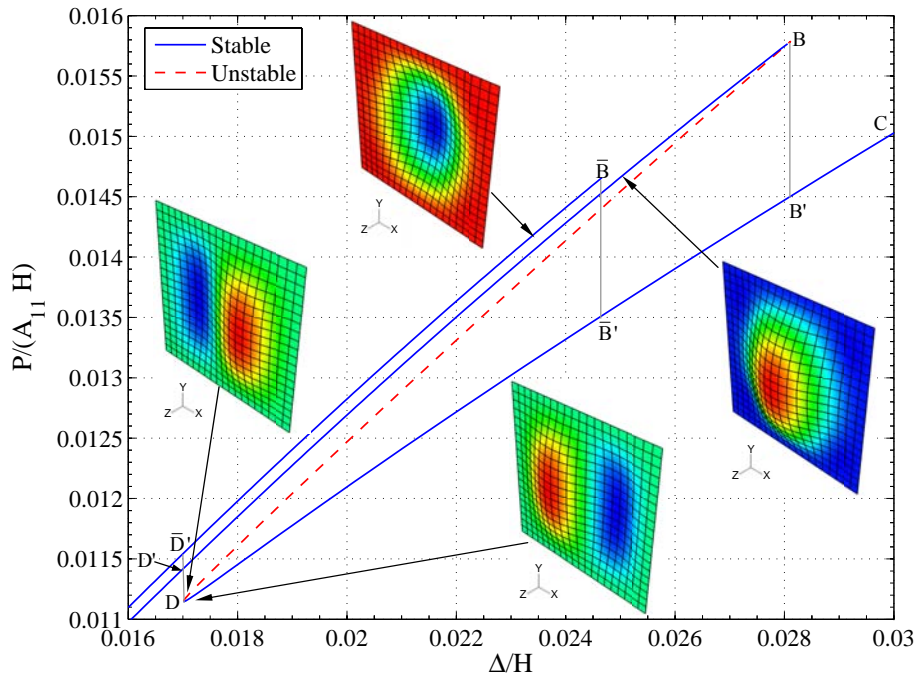


Figure 12: Details of load vs. edge displacement for CC-CC $[0_4/90_4]_T$ plate with v^o free on all edges

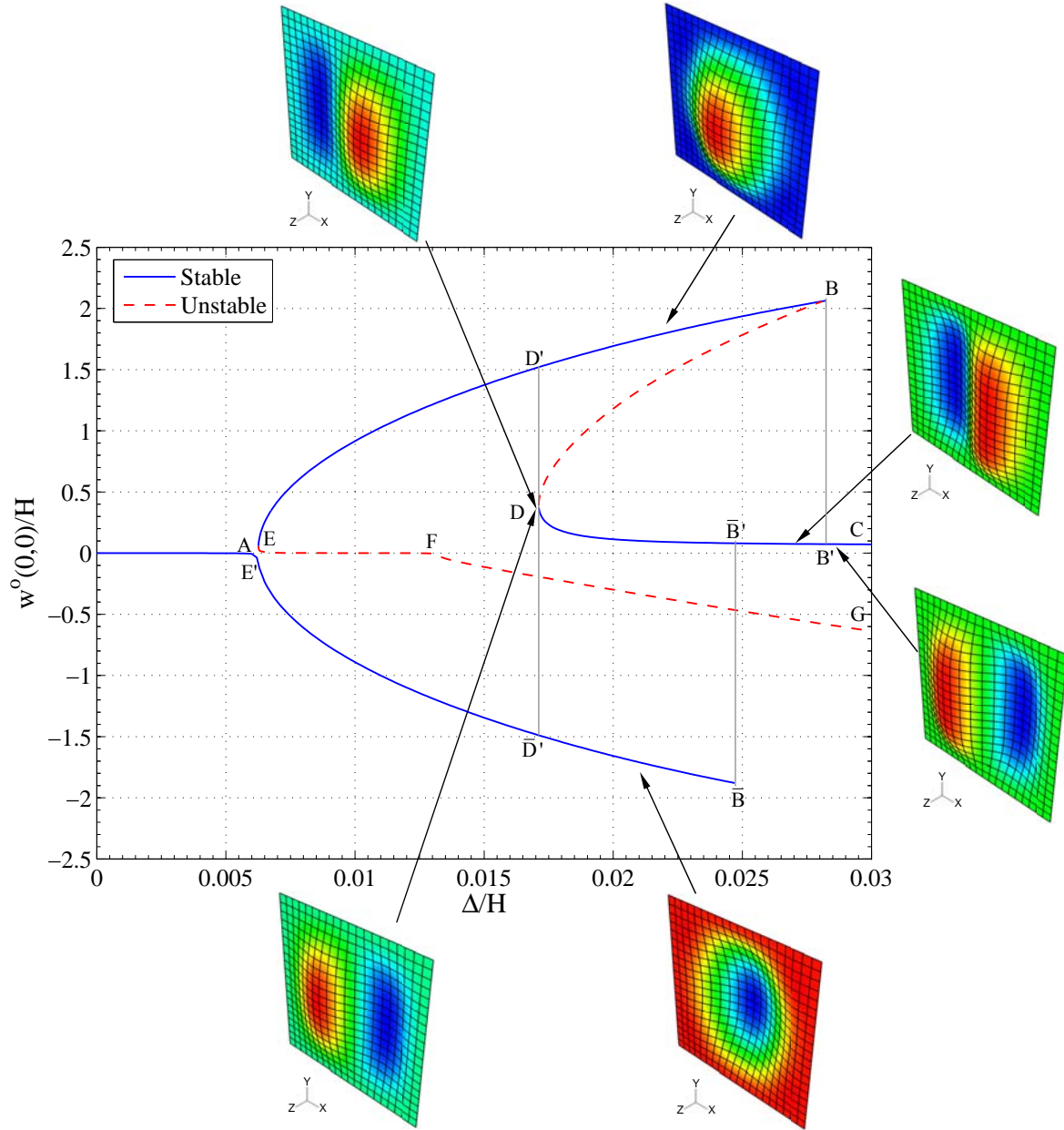


Figure 13: Out-of-plane deflection vs. edge displacement for CC-CC $[0_4/90_4]_T$ square plate with v^o restrained on loaded edges, free on unloaded edges

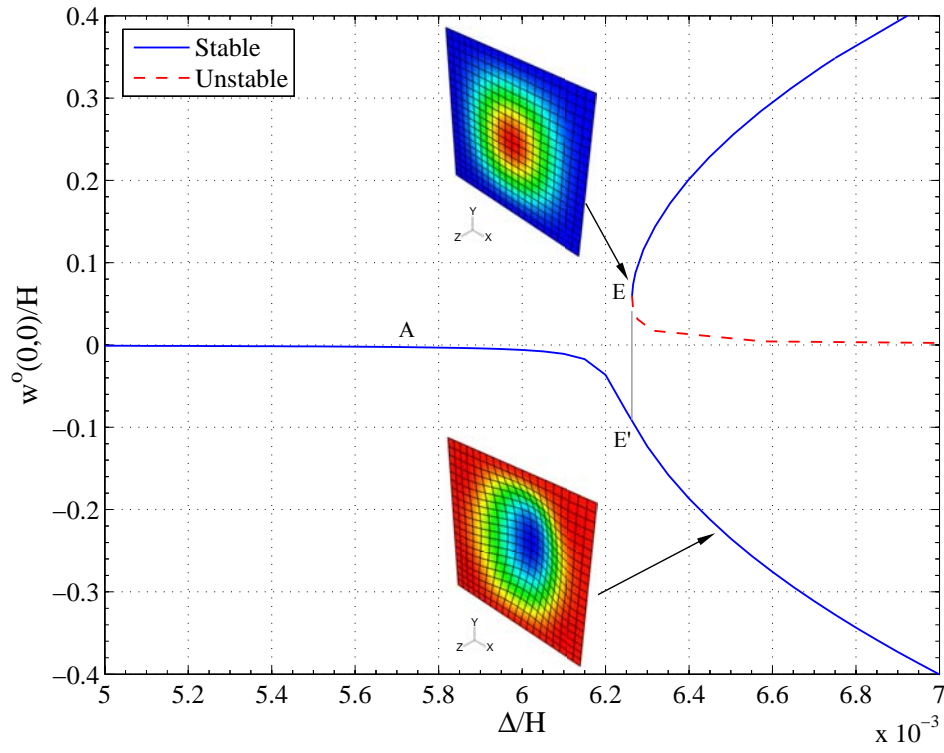


Figure 14: Details of deflection vs. edge displacement for CC-CC $[0_4/90_4]_T$ square plate with v^o restrained on loaded edges, free on unloaded edges

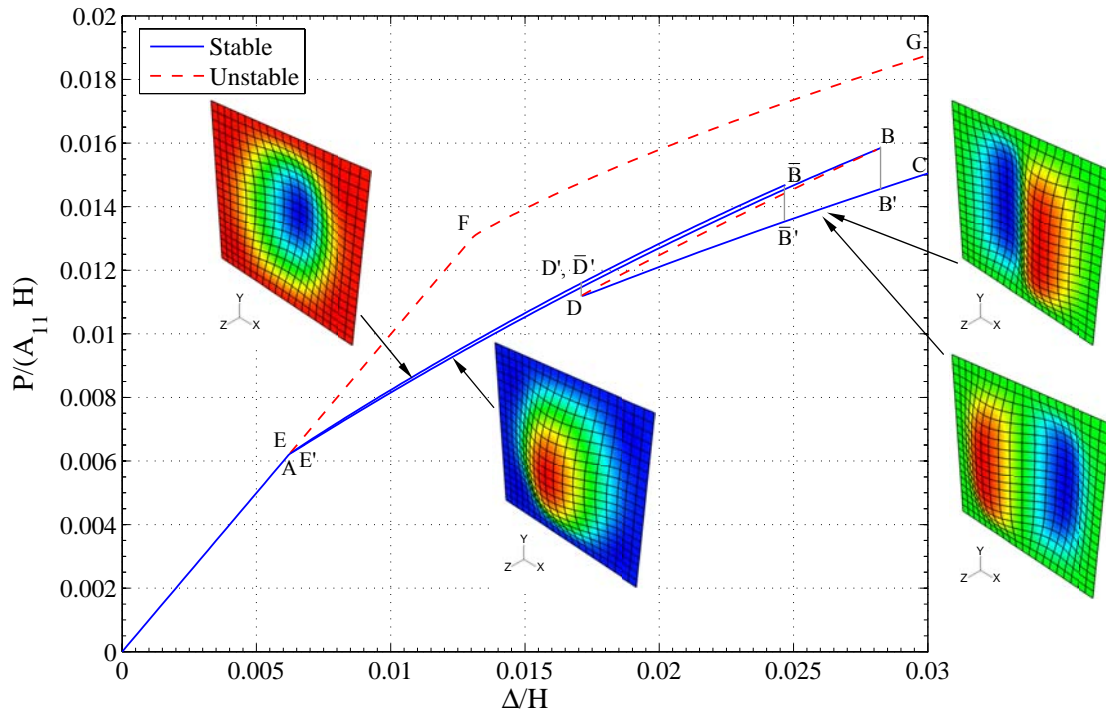


Figure 15: Load vs. edge displacement for CC-CC $[0_4/90_4]_T$ plate with v^o restrained on loaded edges, free on unloaded edges

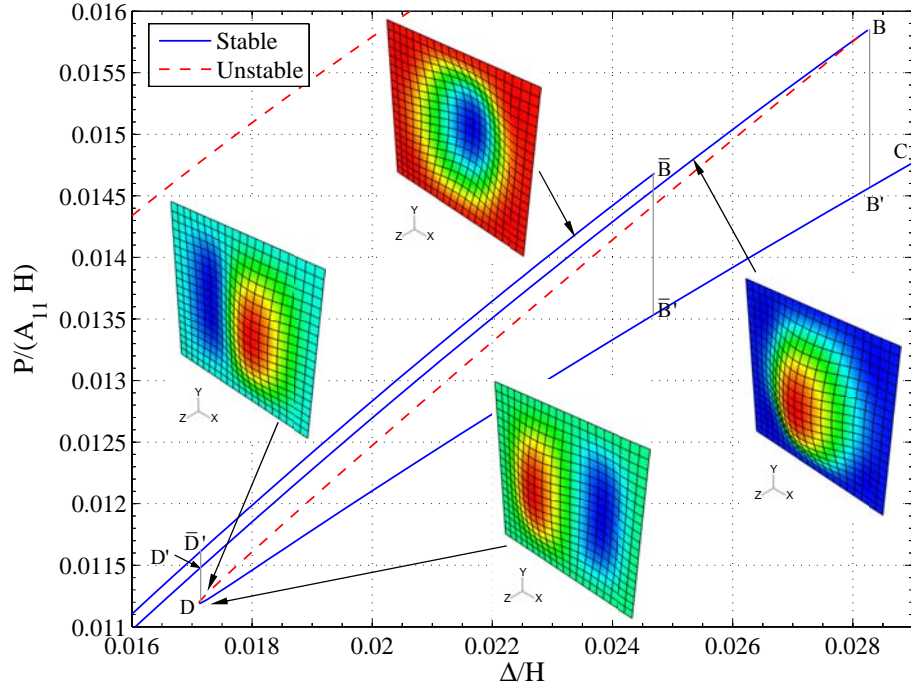


Figure 16: Details of load vs. edge displacement for CC-CC $[0_4/90_4]_T$ plate with v^o restrained on loaded edges, free on unloaded edges

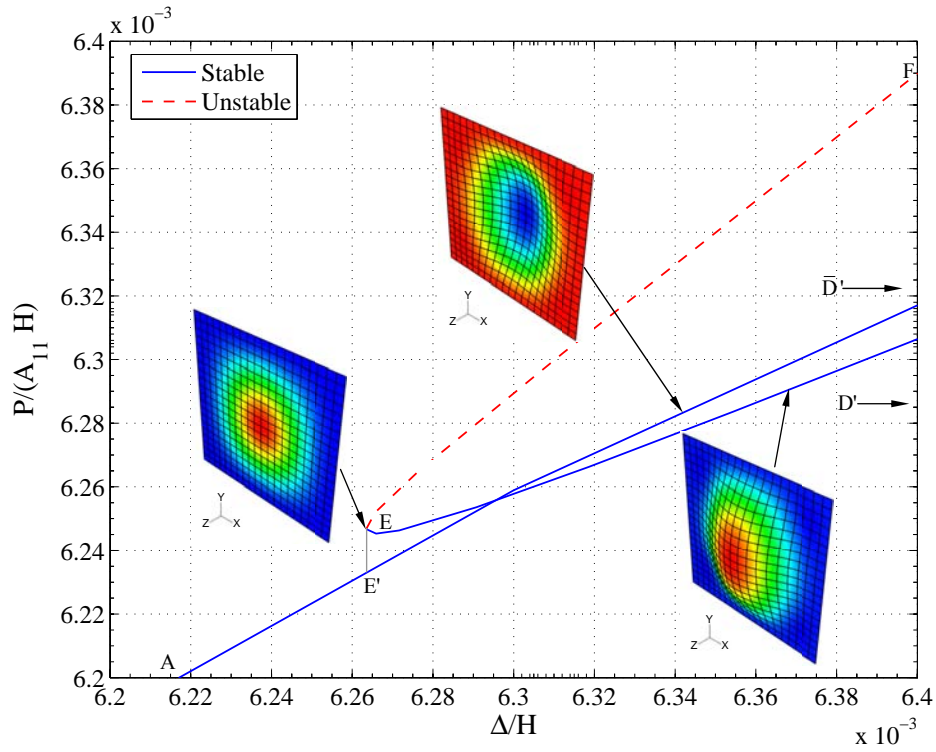


Figure 17: More details of load vs. edge displacement for CC-CC $[0_4/90_4]_T$ plate with v^o restrained on loaded edges, free on unloaded edges

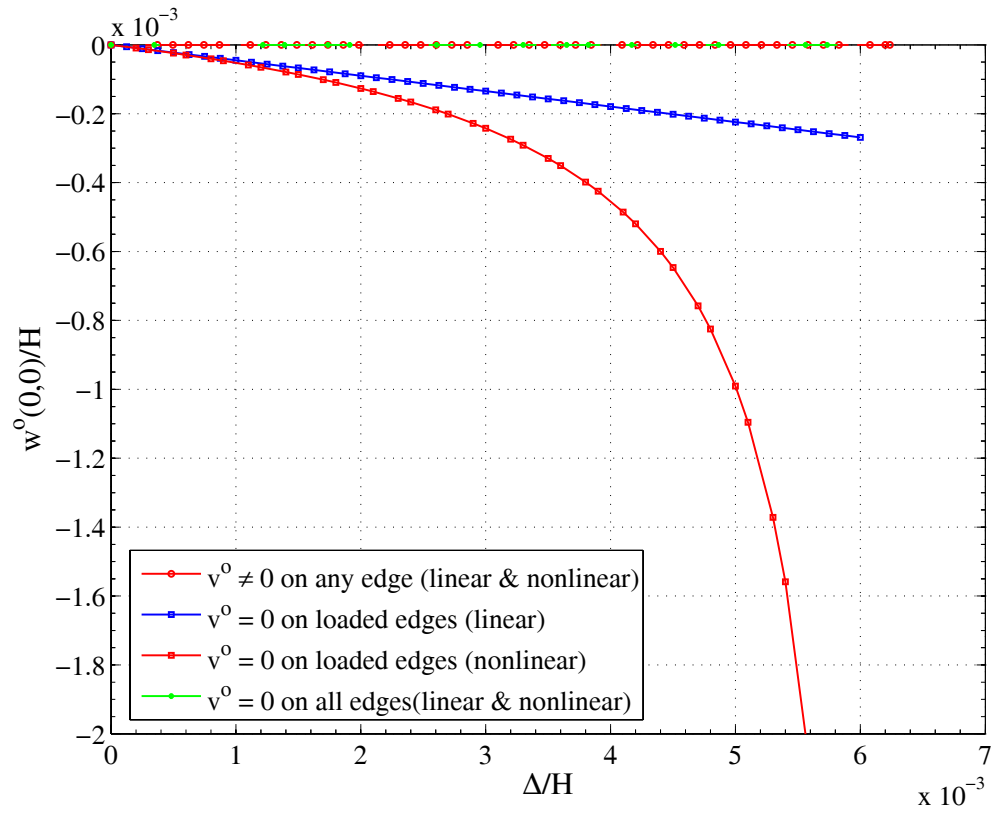


Figure 18: Out-of-plane deflection vs. edge displacement of CC-CC $[0_4/90_4]_T$ square plates, three different restraint conditions on v^o

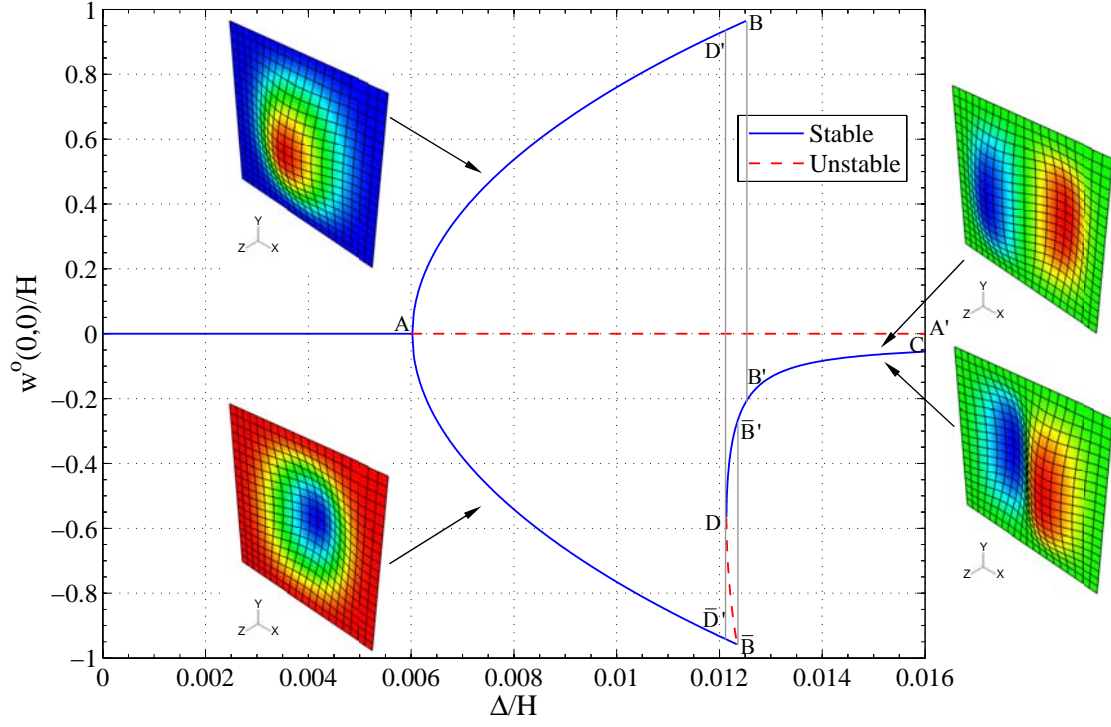


Figure 19: Out-of-plane deflection at the center vs. edge displacement for CC-CC $[0_4/90_4]_T$ plate with v^o restrained on all edges

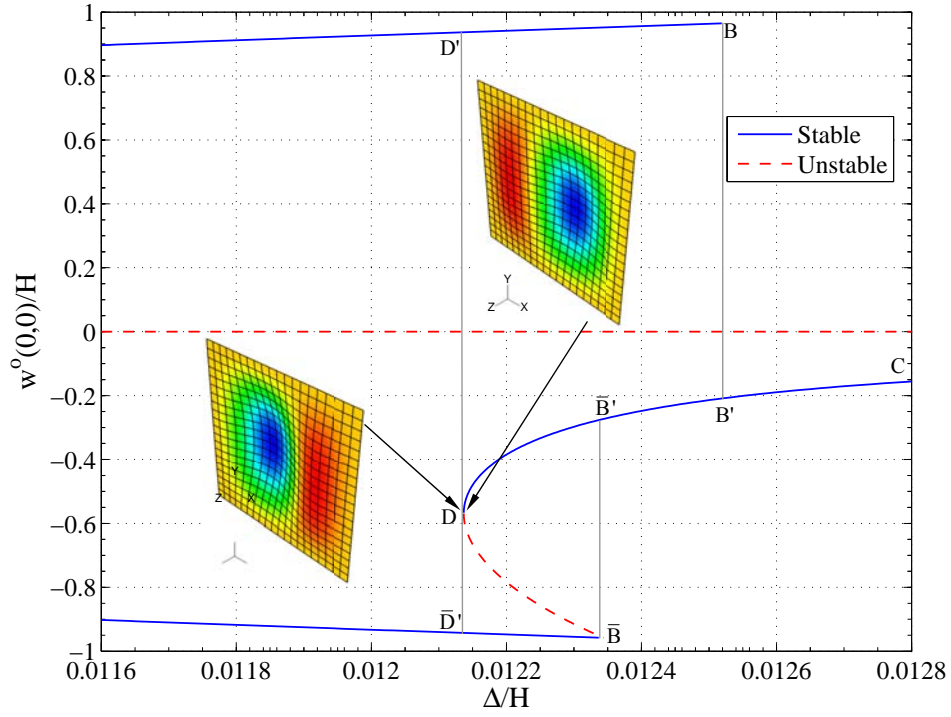


Figure 20: Details of out-of-plane deflection vs. edge displacement for CC-CC $[0_4/90_4]_T$ plate with v^o restrained on all edges

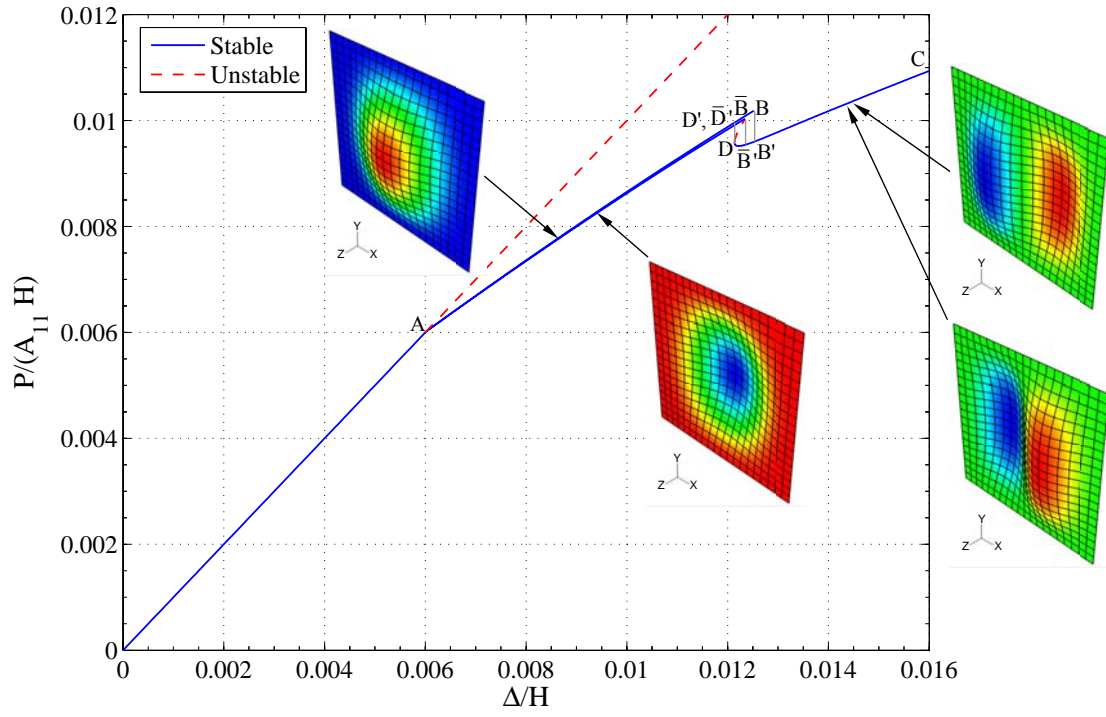


Figure 21: Load vs. edge displacement for CC-CC $[0_4/90_4]_T$ square plate with v^o restrained on all edges

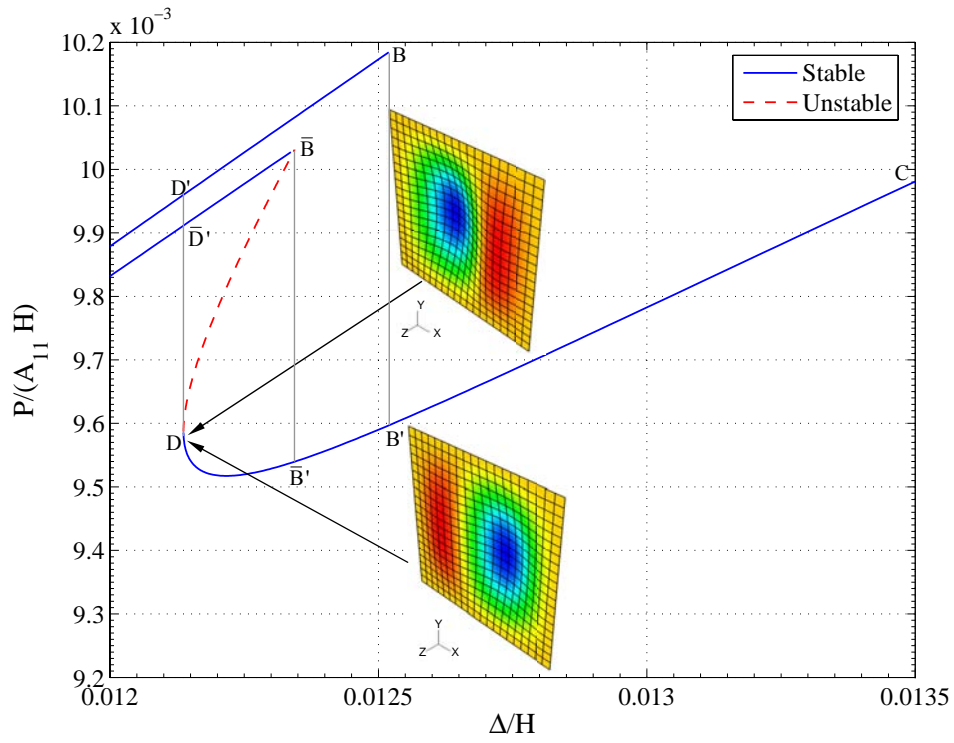


Figure 22: Details of load vs. edge displacement for CC-CC $[0_4/90_4]_T$ square plate with v^o restrained on all edges

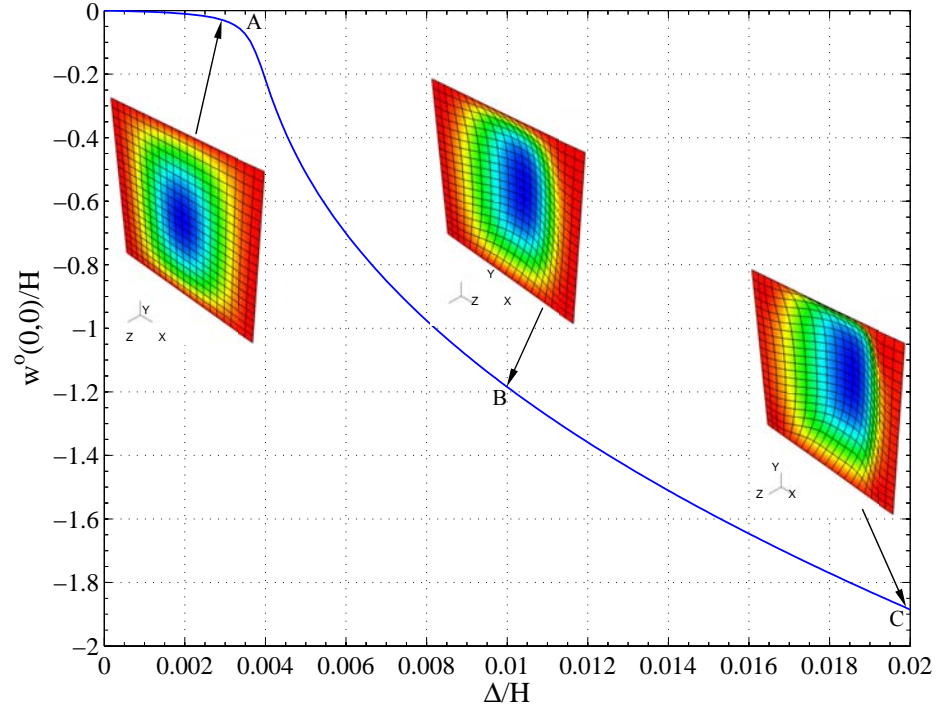


Figure 23: Out-of-plane deflection vs. edge displacement for CC-SS $[0_4/90_4]_T$ square plate with v^o free on all edges

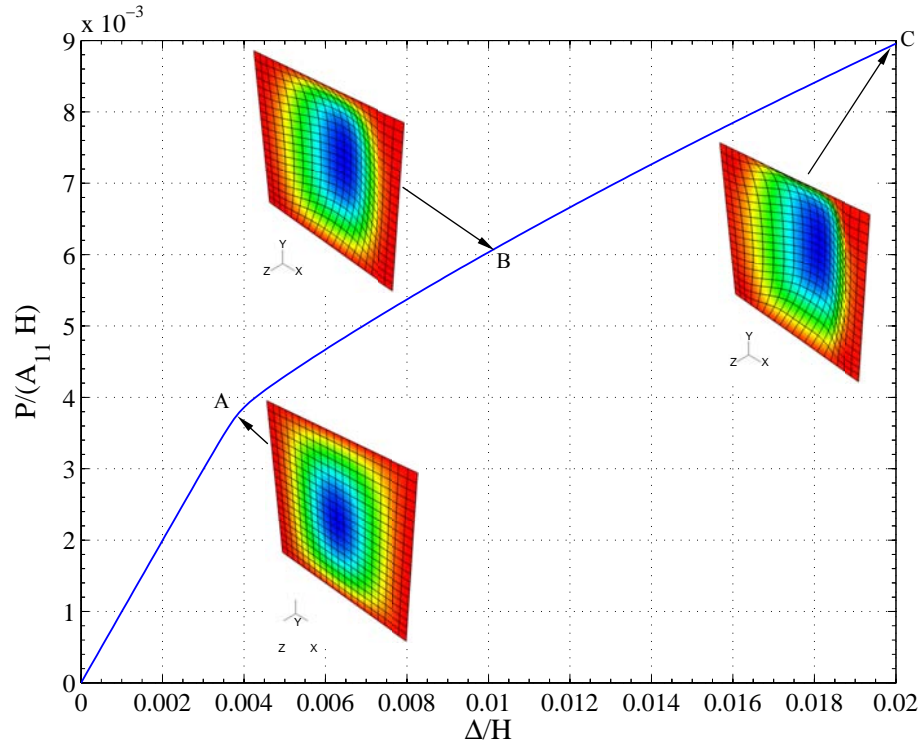


Figure 24: Load vs. edge displacement for CC-SS $[0_4/90_4]_T$ square plate with v^o free on all edges

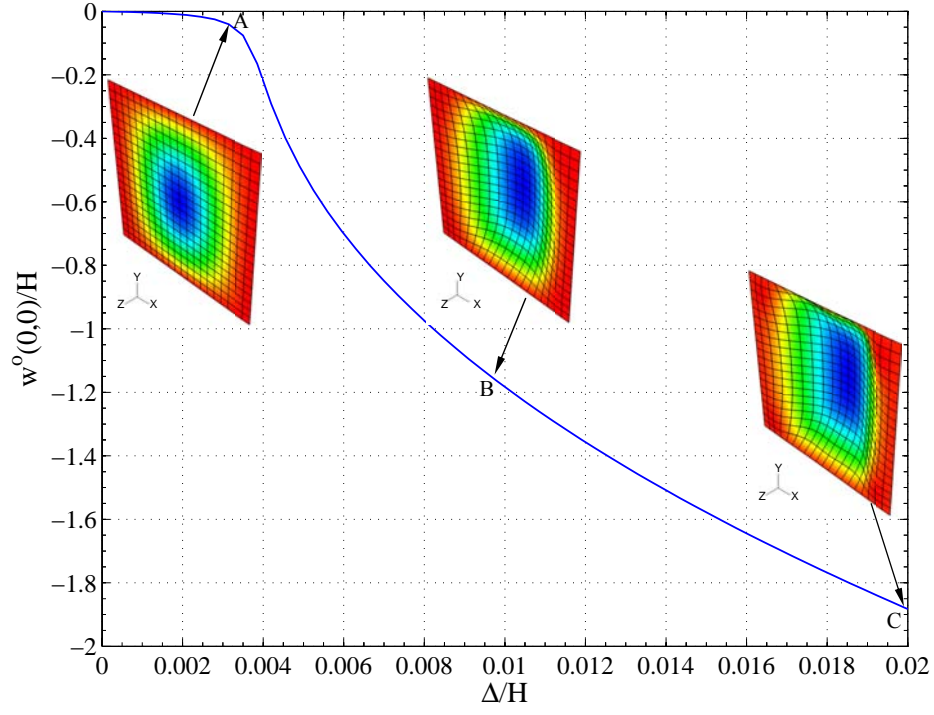


Figure 25: Out-of-plane deflection vs. edge displacement for CC-SS $[0_4/90_4]_T$ square plate with v^o restrained on loaded edges, free on unloaded edges

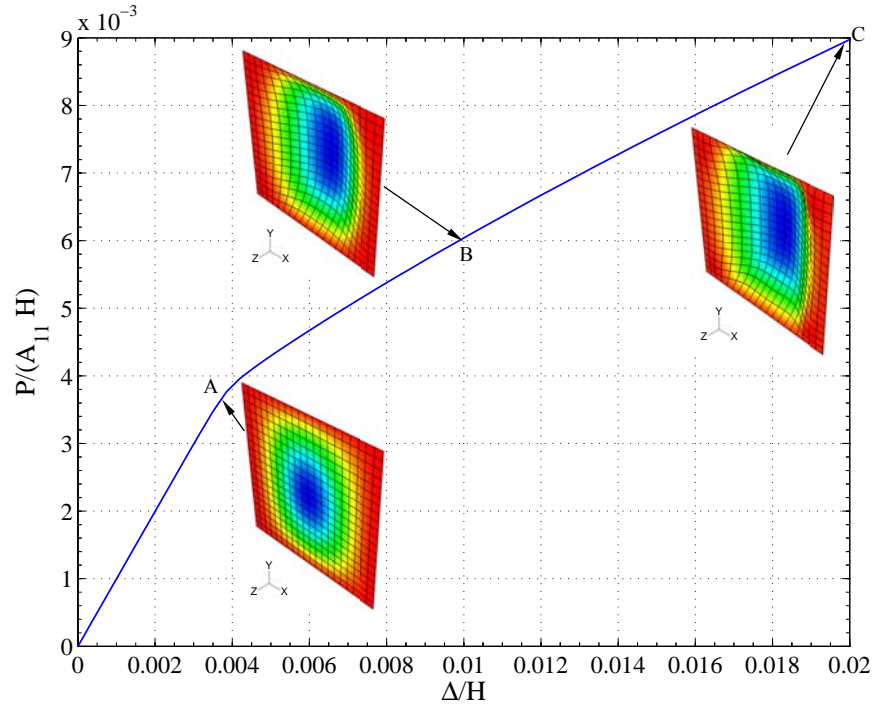


Figure 26: Load vs. edge displacement for CC-SS $[0_4/90_4]_T$ square plate with v^o restrained on loaded edges, free on unloaded edges

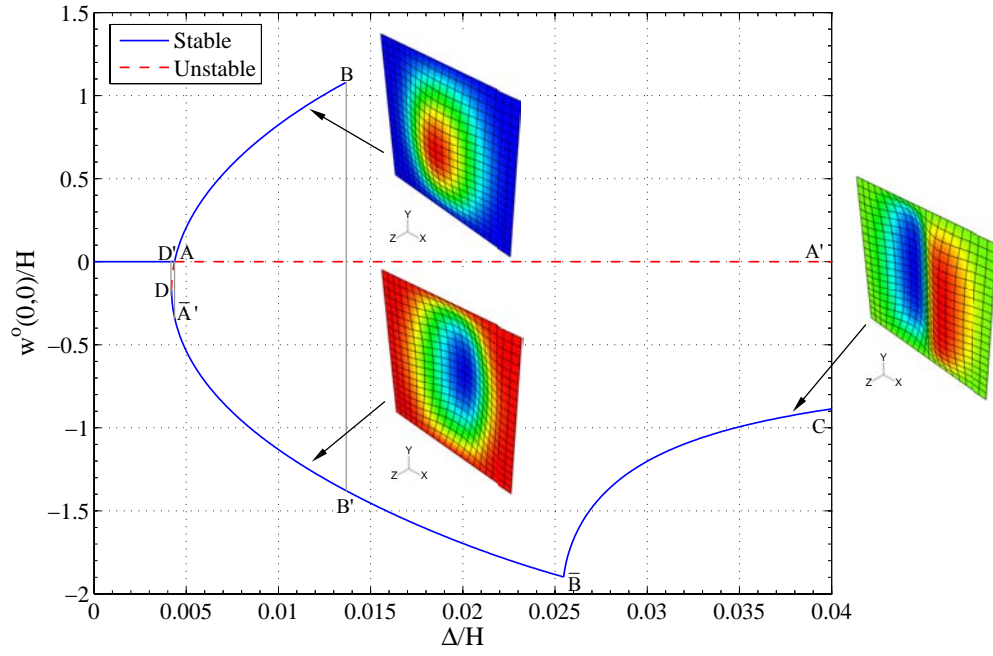


Figure 27: Out-of-plane deflection vs. edge displacement for CC-SS $[0_4/90_4]_T$ square plate with v^o restrained on all edges

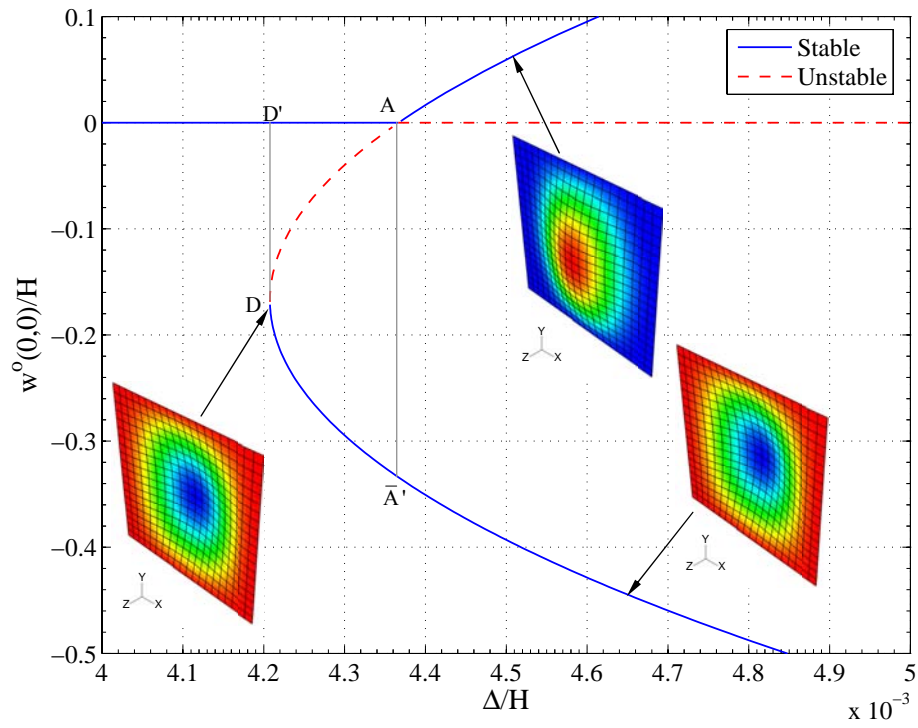


Figure 28: Details of out-of-plane out-of-plane deflection vs. edge displacement for CC-SS $[0_4/90_4]_T$ square plate with v^o restrained on all edges

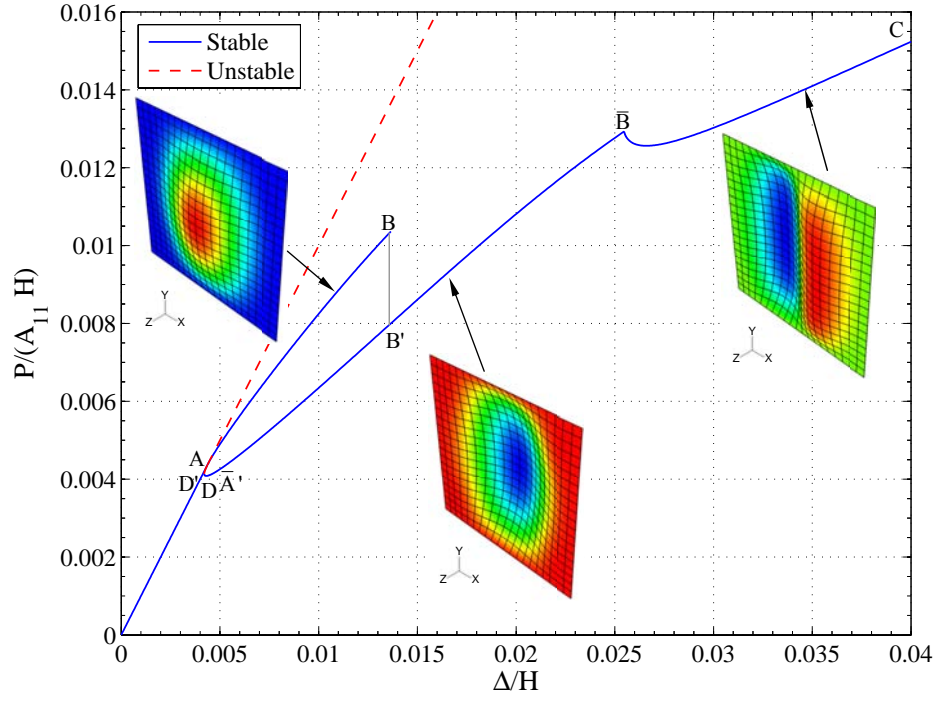


Figure 29: Load vs. edge displacement for CC-SS $[0_4/90_4]_T$ square plate with v^o restrained on all edges

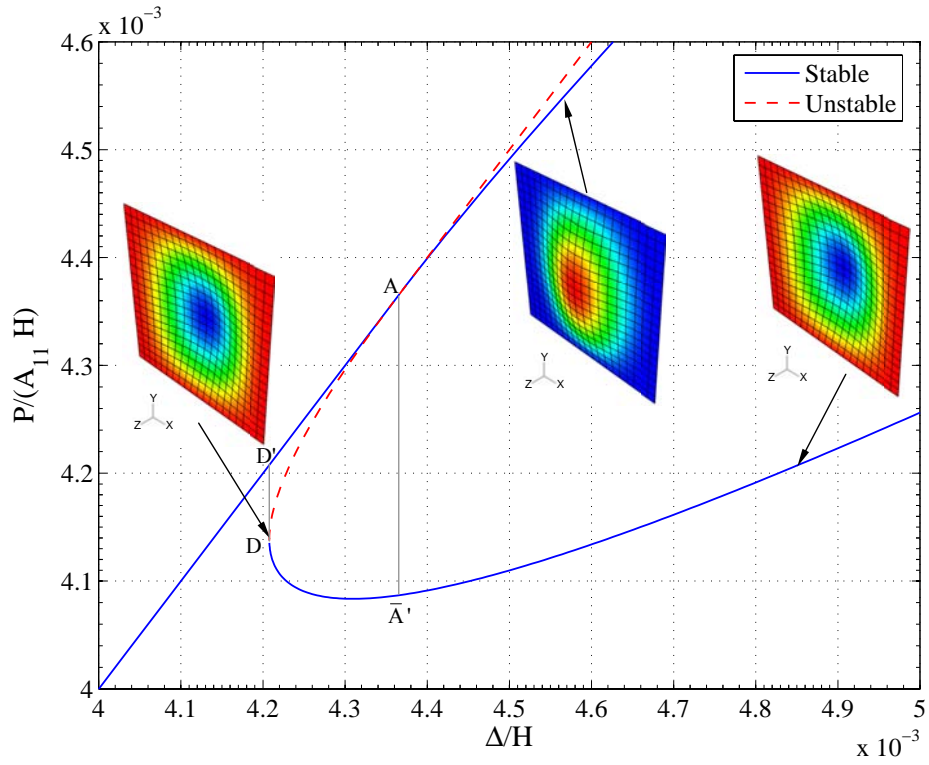
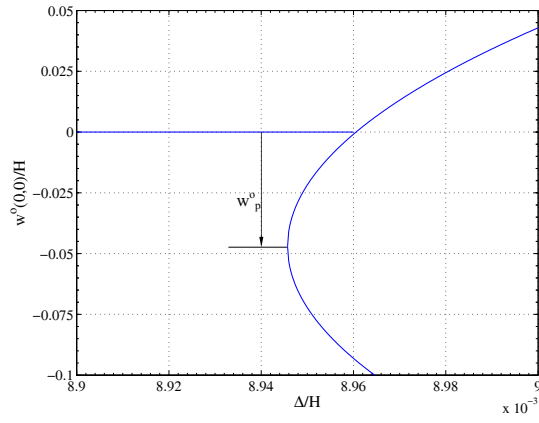
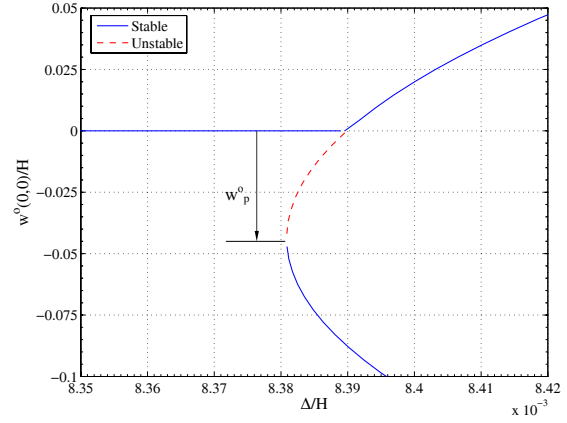


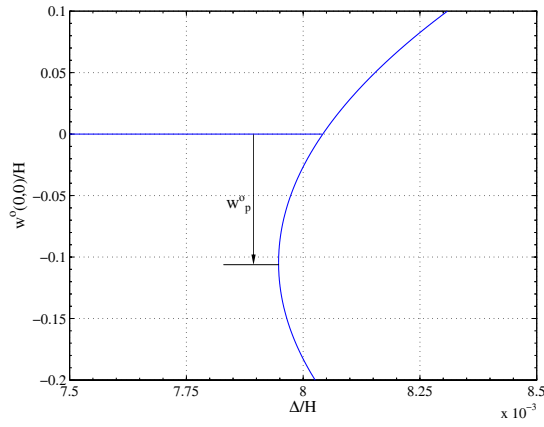
Figure 30: Details of load vs. edge displacement for CC-SS $[0_4/90_4]_T$ square plate with v^o restrained on all edges



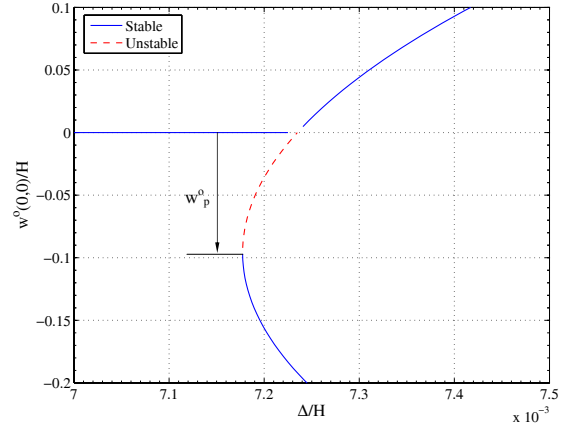
(a) $[0_2/0_2/90_2/0_2]_T$, 5-Term Reduced Polynomials



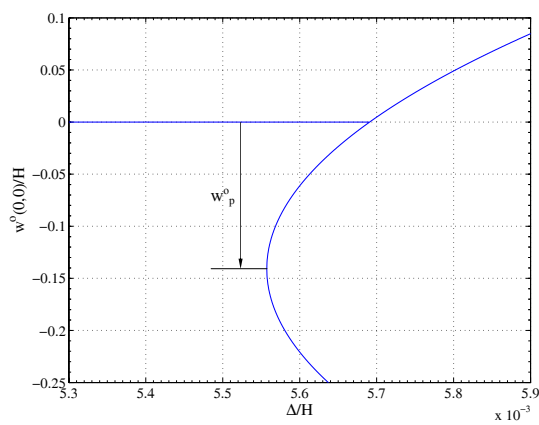
(b) $[0_2/0_2/90_2/0_2]_T$, ABAQUS



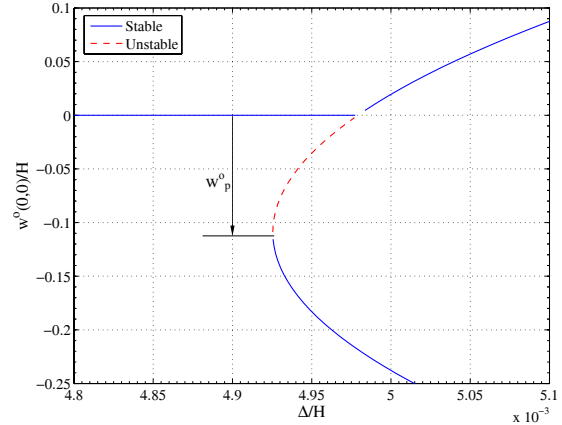
(c) $[0_2/90_2/0_2/90_2]_T$, 5-Term Reduced Polynomials



(d) $[0_2/90_2/0_2/90_2]_T$, ABAQUS

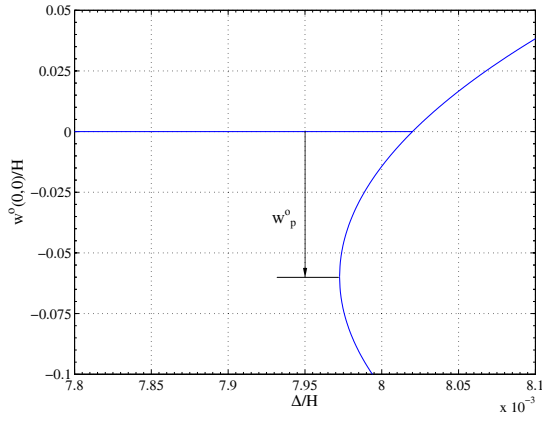


(e) $[0_2/0_2/0_2/90_2]_T$, 5-Term Reduced Polynomials

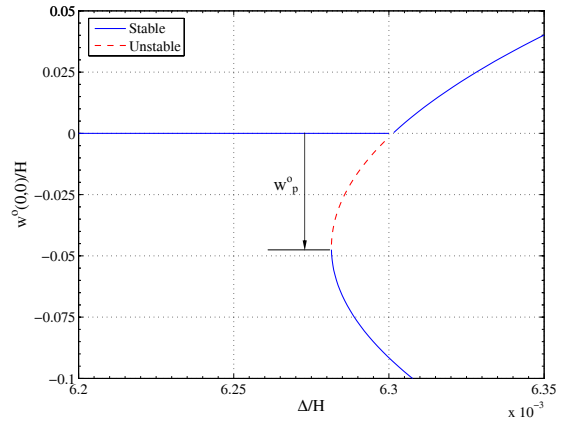


(f) $[0_2/0_2/0_2/90_2]_T$, ABAQUS

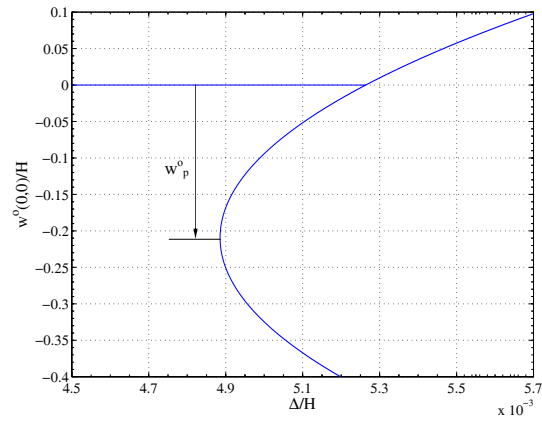
Figure 31: Initial postbuckling deflections for CC-SS cross-ply plates with v^o restrained on all edges, Rayleigh-Ritz and ABAQUS predictions



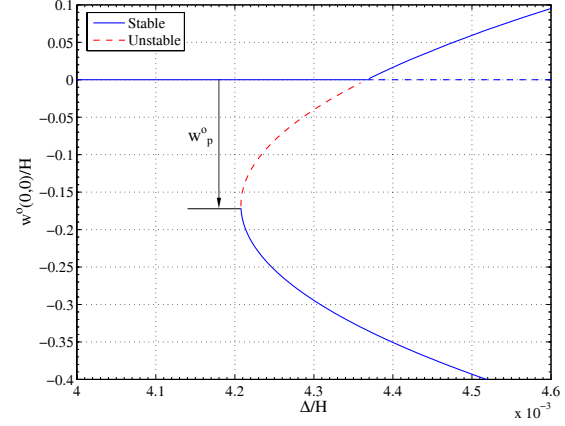
(a) $[90_2/0_2/90_2/90_2]_T$, 5-Term Reduced Polynomials



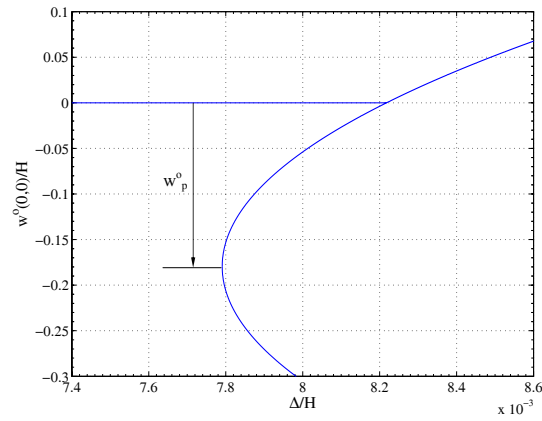
(b) $[90_2/0_2/90_2/90_2]_T$, ABAQUS



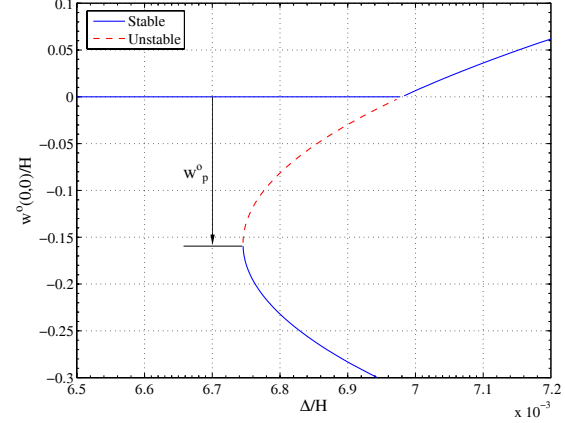
(c) $[0_2/0_2/90_2/90_2]_T$, 5-Term Reduced Polynomials



(d) $[0_2/0_2/90_2/90_2]_T$, ABAQUS



(e) $[0_2/90_2/90_2/90_2]_T$, 5-Term Reduced Polynomials



(f) $[0_2/90_2/90_2/90_2]_T$, ABAQUS

Figure 32: Initial postbuckling deflections for CC-SS cross-ply plates with v^o restrained on all edges, Rayleigh-Ritz and ABAQUS predictions

This page left blank intentionally.

Simulation of Progressive Failure in Multidirectional Composite Laminated Panels *

Shiladitya Basu[†] and Anthony M. Waas[‡]

University of Michigan, Ann Arbor, Michigan, 48109

Damodar R. Ambur[§]

NASA Glenn Research Center, Cleveland, OH 44135

A mechanism-based progressive failure analyses (PFA) approach is developed for fiber reinforced composite laminates. Each ply of the laminate is modeled as a nonlinear elastic degrading lamina in a state of plane stress according to Schapery theory. In this theory, each lamina degrades as characterized through laboratory scale experiments. In the fiber direction, elastic behavior prevails, however, in the present work, the phenomenon of fiber microbuckling, which is responsible for the sudden degradation of the axial lamina properties under compression, is explicitly accounted for by allowing the fiber rotation at a material point to be a variable in the problem. The latter is motivated by experimental and numerical simulations that show that local fiber rotations in conjunction with a continuously degrading matrix are responsible for the onset of fiber microbuckling leading to kink banding. These features are built into a user defined material subroutine that is implemented through the commercial finite element (FE) software ABAQUS. The present model, thus, disbands the notion of a fixed compressive strength of a lamina and instead uses the mechanics of the failure process to provide the in-situ compression strength of a material point in a lamina, the latter being dictated strongly by the current local stress state, the current state of the lamina transverse material properties and the local fiber rotation. The inputs to the present work are laboratory scale, coupon level test data that provide information on the lamina transverse property degradation (i.e. appropriate, measured, strain-stress relations of the lamina transverse properties), the elastic lamina orthotropic properties, the ultimate tensile strength of the lamina in the fiber direction and the geometry of the structural panel. The validity of the approach advocated is demonstrated through numerical simulations of the response of two composite structural panels that are loaded to complete failure. A flat, 24-ply unstiffened panel with a cutout subjected to in-plane shear loading, and a double notched 70 ply unstiffened stitched panel subjected to axial compression are selected for study. The predictions of the simulations are compared against experimental data. Good agreement between the present PFA and the experimental data are reported.

I. Introduction

Development of computational methodologies for the prediction of damage accumulation and growth in continuous fiber composite laminates is presently an active area of research. A large body of literature devoted to progressive failure analysis (PFA) of composite laminated structures is now present. Many of the PFA schemes introduced and available today have relied on the phenomenological approach of defining strength criteria for a single lamina when subjected to different single component stress states. These methods define the onset of failure through specific indices that are expressed as functions of the current stress state. When any of these indices exceeds a predefined critical value, the material at that point is said to have failed.^{1,2} When a material point has failed, for subsequent loading, it is assumed to have

*This paper is dedicated to the memory of Dr. James H. Starnes, Jr., for sustained and life long contributions to composite structural mechanics and especially for his contributions to the subject of structural stability.

[†]Doctoral candidate, University of Michigan, member, AIAA.

[‡]Professor, author to whom all correspondence should be addressed. (dcw@umich.edu, Tel:734-764-8227, Fax:734-763-0578), Associate Fellow, AIAA.

[§]Chief, Structures Division, NASA Glenn Research Center, Cleveland, OH. Associate Fellow, AIAA.

Copyright © 2005 by Anthony M. Waas. Published by NASA with permission.

a reduced stiffness that is predetermined in an empirical manner. Depending on the type of failure (for instance, fiber breaking and/or matrix cracking due to tension along the fibers, fiber kink-banding due to compression along the fibers, fiber/matrix debonding due to in-plane shear), different elastic moduli are set to zero. In addition, linear elastic material behavior is assumed throughout the analysis. In a laminated composite plate, the stiffness at a material point is determined by the current local stress state and the local ‘state’ of the material. The local stress state, in general, is multi-axial and a material point at the current state may have accumulated damage, dictated by the loading history. Thus, ‘strength’ at a material point is influenced to a great extent by the current stress and strain state and is predicated on the mechanism of failure. Schemes that abruptly change material properties and rely on a linear elastic analysis may be unable to realistically account for features associated with the mechanisms of failure. Furthermore, these approaches lack an appropriate definition of the material state beyond first failure. For progressive failure modeling, a framework that accounts for the continued degradation of the material is needed. Schapery³ introduced a thermodynamically based theory (referred to as ST) that uses internal state variables (ISVs) to analyze damage evolution in composite laminates. These ISVs are related to mechanical aspects of damage mechanisms. The ISVs are related to the energy required for the evolution of the damaged states. Different damage mechanisms can have distinct ISVs to track the damage evolution. For instance, matrix microcracking can be expressed via one ISV, while transverse cracking can be represented by another ISV.⁴ The evolution of these ISVs with global loading is determined at each material point and as functions of load history through the satisfaction of a thermodynamic criterion (an evolution equation), throughout the loading history. Various experimental⁵ and analytical⁶ studies show that the maximum load sustained by a lamina in the axial direction (σ_{11}^{cr}), in compression, depends greatly on the presence of the other in-plane stress components such as σ_{22} and τ_{12} . Experimental, analytical and micromechanical studies show that the main physical event occurring during kinking is the rotation of fibers within a degrading matrix. The rotation of fibers gives rise to high localized shear strains which drives the shear degradation of the local matrix. The shear degradation in turn drives the rotation of the fibers creating a positive feedback loop. The simultaneous presence of both these phenomena results in a limit load situation for a lamina under axial compression. This limiting load, which is dictated by the local stress state and the state of the transverse lamina properties, can be relieved (increased) by the presence of other stress components or, in certain cases, can be elevated (reduced). The present approach captures these two phenomena in a numerical setting and is able to reproduce the broad micromechanical observations associated with compressive failure at a macro-level (lamina level, instead of at the individual fiber/matrix level). Two structural panel configurations, for which a set of laboratory data is available, are studied using the present PFA approach. A thick (70-ply), stitched double notched carbon fiber reinforced laminated panel subjected to axial compression loading and a relatively thin (24-ply) flat unstiffened laminated shear panel (FSP) with a cutout, loaded deep into the postbuckling regime are analyzed. Double notched panels (DNPs), with notch tip radii equal to the laminate thickness are cut from a master laminate (Figure 1). The notches act as stress concentrators and create a high stress zone, making it easier to observe damage initiation and progression. The use of a stitched laminate eliminates delamination among adjacent plies of a multidirectional laminate making it possible to isolate matrix dominated failure events in an uncomplicated manner. The unnotched sides of the DNPs are subjected to remote uniaxial displacement control compression loading. The notched sides are placed in anti-buckling guides to prevent premature global buckling. Figure 2 shows the loading scheme and boundary conditions. Global load-deflection data and damage initiation and progression data are obtained from the laboratory experiments, through strain gages, load cells, LVDT’s and post-experiment microscopic studies. The experiments show that fiber kinking in the zero plies (plies parallel to the loading direction) is the dominant mode of failure and is seen to occur at the vicinity of the notch tip within the zero plies. The kinking zone subsequently grows towards the center of the panel resulting in global catastrophic failure. For the flat unstiffened, 24-ply panel, experimental results and related PFA modeling has been reported earlier⁷⁻⁹. These panels are loaded in shear using a picture frame test set-up. Back to back strain gage data and load and load point displacement data from the panel tests are used to validate the present PFA approach.

The main objective of the present paper is to introduce a new PFA approach for composite laminates that is based on capturing features associated with failure mechanisms and embedding these in a numerical scheme that can model the laminate as a collection of degrading lamina. The selected examples account for both material degradation in a nonlinear manner (DNP), and the interaction of these nonlinearities with geometrical nonlinearities (FSP) which dominate the response of thin-gage structures that are loaded in compression.

II. Progressive Failure Analysis using Schapery Theory (ST)

A. Elements of the PFA approach

1. Non-linear Constitutive Formulation

Schapery¹⁰ developed nonlinear elastic constitutive relations for an orthotropic lamina using a work potential approach which accounted for the effect of microdamage. The lamina stress-strain relations are,

$$\begin{aligned}\sigma_{11} &= Q_{11}\epsilon_{11} + Q_{12}\epsilon_{22} \\ \sigma_{22} &= Q_{12}\epsilon_{11} + Q_{22}\epsilon_{22} \\ \tau_{12} &= Q_{66}\gamma_{12}\end{aligned}\tag{1}$$

where,

$$\begin{aligned}Q_{11} &= \frac{E_{11}}{1 - \nu_{12}\nu_{21}} \quad ; \quad Q_{22} = \frac{E_{22}}{1 - \nu_{12}\nu_{21}} \\ Q_{12} &= \nu_{12}Q_{22} \quad ; \quad Q_{66} = G_{12} \\ \nu_{21} &= \frac{\nu_{12}E_{22}}{E_{11}}\end{aligned}\tag{2}$$

In the existing literature on damage mechanics as applied to continuous fiber laminated composite materials, the effect of damage is incorporated through the change in transverse Young's modulus E_{22} and in plane shear modulus G_{12} . For instance, Sun and Chen¹¹ proposed a one parameter plastic potential in conjunction with orthotropic incremental plasticity theory to study the evolution of E_{22} and G_{12} in tension. Schapery and Sicking,⁴ used ST to study the evolution of E_{22} and G_{12} . These previous studies were not concerned with the state of the lamina beyond first failure in the fiber direction. Yet, it is recognized¹² that such damage is dominant for compression loaded composite structures. Lamina level coupon tests in tension have shown that fiber direction modulus, E_{11} and Poissons ratio, ν_{12} can be assumed to be independent of microdamage that influence E_{22} and G_{12} .¹³ This situation is also true for compression until the onset of kinking (the axial compression load reaches a maximum limit load at the point in which a kink band starts to form, for example, as shown in Lee and Waas¹⁴). During kink band formation and propagation, it is likely that microdamage mechanisms do influence E_{11} , ν_{12} , E_{22} and G_{12} . Subsequent to kink banding, other failure mechanisms such as delamination can occur. These mechanisms are not accounted for here, but have received attention recently in the context of PFA.⁹

2. Elements of Schapery Theory

In Schapery and Sicking,⁴ ISVs are used to incorporate *inelastic* behavior in the material response. Earlier, Schapery,³ introduced a more general thermodynamic framework to study materials that undergo damage. In these developments, the total work done, W_T , in a mechanical process is composed of the inelastic work, W_s and the work of deformation W .

$$W_T = W + W_s\tag{3}$$

The irrecoverable portion of total energy (W_s) can be determined from the material stress-strain response as shown in Figure 3. *ISVs* are described through S_i 's. Each S_i is associated with a particular damage mechanism. To satisfy the path independence of total work, these *ISVs* have to satisfy the following relation,

$$f_i = \frac{\partial W_s}{\partial S_i}\tag{4}$$

The left hand side of Eq. (4) is referred to as the *thermodynamic force* related to the i^{th} *ISV*. If the i^{th} *driving force*, which is the available thermodynamic force, given by Eq. (5), exceeds $\frac{\partial W_s}{\partial S_i}$, then the material undergoes a structural change that is associated with S_i .

$$f_i \equiv -\frac{\partial W}{\partial S_i}\tag{5}$$

Stated another way,

$$\dot{S}_i > 0 \quad (6)$$

However, as pointed out by Schapery,³ it is to be noted that if the available thermodynamic force, $(-\frac{\partial W}{\partial S_i})$ is less than the required thermodynamic force $(\frac{\partial W}{\partial S_i})$ then,

$$\dot{S}_i = 0 \quad (7)$$

Furthermore, S_i need not change continuously with the loading.

Schapery considered two *ISVs*. They were the energies associated with matrix microcracks (S) and of the transverse intra-ply cracks (S_c), respectively. Inelastic work is described as,

$$W_s = S + S_c \quad (8)$$

These ISVs affect the moduli E_{22} and G_{12} through Eq. (9)

$$\begin{aligned} E_{22} &= E_{22_0} e_s(S) e_c(S_c) \\ G_{12} &= G_{12_0} g_s(S) g_c(S_c) \end{aligned} \quad (9)$$

Here, E_{22_0} and G_{12_0} are transverse and shear moduli of the virgin material, i.e., at zero strain and zero damage; $e_s(S)$ and $g_s(S)$ are functions relating these two moduli to microdamage ISV, S and $e_c(S_c)$ and $g_c(S_c)$ are functions relating E_{22} and G_{12} to the transverse cracking ISV, S_c . The functions e_s , e_c , g_s and g_c are expressed as polynomial relations in the respective ISVs.⁴

The strain energy density (or work of deformation) can be written as

$$W = \frac{1}{2} (Q_{11} \epsilon_{11}^2 + Q_{22} \epsilon_{22}^2) + \nu_{12} Q_{22} \epsilon_{11} \epsilon_{22} + \frac{G_{12} \gamma_{12}^2}{2} \quad (10)$$

To incorporate geometric nonlinearities, Green's strains and the second Piola Kirchhoff stresses need to be used in the expression for W . For small strains, Eq. (10), would contain only the first order terms in the strain-displacement relations. Schapery and Sicking⁴ have shown that material non-linearities as incorporated in Eq. (10) are still significant for fiber reinforced composites even when inclusion of geometric nonlinearities are not called for.¹⁵

Using Eqs (1)-(5), the evolution equations for S and S_c are as follows,

$$\begin{aligned} \frac{1}{2} \epsilon_{11}^2 \frac{\partial Q_{11}}{\partial S} + \left(\frac{1}{2} \epsilon_{22}^2 + \nu_{12} \epsilon_{11} \epsilon_{22} \right) \frac{\partial Q_{22}}{\partial S} + \frac{\gamma_{12}^2}{2} \frac{\partial G_{12}}{\partial S} &= -1 \\ \frac{1}{2} \epsilon_{11}^2 \frac{\partial Q_{11}}{\partial S_c} + \left(\frac{1}{2} \epsilon_{22}^2 + \nu_{12} \epsilon_{11} \epsilon_{22} \right) \frac{\partial Q_{22}}{\partial S_c} + \frac{\gamma_{12}^2}{2} \frac{\partial G_{12}}{\partial S_c} &= -1 \end{aligned} \quad (11)$$

In the present work, it is assumed that the fiber direction stiffnesses are unaffected by S and S_c . Thus, the first terms in these equations can be neglected. Also, $\nu_{12} \nu_{21} \ll 1$. Thus, the above equations reduce to,

$$\begin{aligned} \left(\frac{1}{2} \epsilon_{22}^2 + \nu_{12} \epsilon_{11} \epsilon_{22} \right) \frac{\partial E_{22}}{\partial S} + \frac{\gamma_{12}^2}{2} \frac{\partial G_{12}}{\partial S} &= -1 \\ \left(\frac{1}{2} \epsilon_{22}^2 + \nu_{12} \epsilon_{11} \epsilon_{22} \right) \frac{\partial E_{22}}{\partial S_c} + \frac{\gamma_{12}^2}{2} \frac{\partial G_{12}}{\partial S_c} &= -1 \end{aligned} \quad (12)$$

For an inelastic process, the entropy production rate is non-negative. Hence,

$$\dot{S} + \dot{S}_c \geq 0 \quad (13)$$

The overdots represent temporal derivatives. Physically, \dot{S} and \dot{S}_c are both non-negative because healing (or reversible damage) is not allowed for in the damage mechanisms considered. Thus the ISVs individually satisfy Eq. (13), as well.

From experiments,⁴ it has been observed that for small strains, S behaves as ϵ^3 . This is based on the fact that moduli are constant for small strains. Thus to express the moduli, E_{22} and G_{12} in terms of a polynomial of S , a reduced variable S_r can be used,

$$S_r \equiv S^{1/3} \quad (14)$$

The evolution equation for S_r now becomes,

$$\left(\frac{1}{2}\epsilon_{22}^2 + \nu_{12}\epsilon_{11}\epsilon_{22}\right)\frac{\partial E_{22}}{\partial S_r} + \frac{\gamma_{12}^2}{2}\frac{\partial G_{12}}{\partial S_r} = -3S_r^2 \quad (15)$$

The effect of transverse inter-ply cracking is not as easily measurable as the effect of microdamage due to matrix microcracking. An estimate can be obtained using Eq. (15) to approximate S_r , and then using the following relation,

$$S_c = W_T - W - S \quad (16)$$

In the present study, it is assumed that matrix microcracking is the only responsible mechanism for transverse property degradation. Consequently, Eq. (15) is the only relevant evolution equation. A detailed discussion of obtaining S_c is provided by Schapery and Sicking.⁴ It should be noted that it is possible to include other softening damage mechanisms such as local fiber-matrix debonding and shear banding through S as has been discussed by Schapery.³

3. Fiber rotation under axial compression

Results from previous experimental, analytical and numerical studies have shown that the main feature of laminate failure under predominantly compression loading is fiber kinking. The presence of initial fiber misalignment in a lamina that experiences compression along the fibers gives rise to local shear strain in the matrix adjacent to the misaligned fibers. These shear strains accelerate degradation of the local matrix shear stiffness. Imperfect fiber systems are prone to rotate under axial compression. That is, the fibers within a lamina that are subjected to axial compression have the propensity to *change* their alignment. This change is dictated by the local multiaxial stress state and the local shear stiffness of the matrix. As the local shear strains degrade the matrix shear stiffness, the resistance to fiber rotation diminishes and slowly the fiber rotation begins to build up which in turn creates more local imperfection and local shear strain. Thus a positive feedback loop is established between these two competing events. A point is reached when the in-situ shear stiffness is not sufficient to prevent the additional fiber rotation. This point usually coincides with the peak load in an axial material response curve. Beyond this point, the matrix is unable to resist any fiber rotation and the fibers rotate aligning themselves in localized deformed bands, commonly described as ‘kink bands’¹⁶ (Figure 4(a)).

Consider a fiber reinforced lamina under a generalized load state as indicated in Figure 4(c). A band of misaligned fibers is shown sandwiched between two regions where the fibers are nominally straight and aligned. This equilibrium configuration is conceptualized from images of kink bands captured experimentally (Figure 4(a)). In these real kink bands, there is a conical region where fiber bending is dominant and this region is sandwiched between the regions where there is dominant shearing (inside the band) and the far-field aligned region where there is uniform deformation (Figure 4(b)). Owing to the fiber bending dominant region, the kink band boundary inclination ($\beta + \beta_0$) has the flexibility of changing during the loading, i.e., there is continuous exchange of material between the fiber bending dominant region and the shearing dominant region. In the idealization presented here, the fiber bending dominant region is disregarded and the shearing dominant region is assumed to be held in equilibrium between the two nominally aligned regions.

A reference frame $x-y$ can be defined such that the x -direction is parallel to the nominal fiber direction in the lamina and the y -direction is normal to it. In subsequent discussions, the $x-y$ reference frame will be termed as the ‘global’ frame. The misaligned band of fibers, in the current configuration, is defined through two angles, $\hat{\phi} = \phi + \phi_0$ and $\hat{\beta} = \beta + \beta_0$. The angles (ϕ_0, β_0) are constants and the angles ϕ and β are variables that may change as a function of current far-field stress state. The reference frame, 1-2, is defined in the unstressed initial configuration of the misaligned lamina. Fibers inside the misaligned band are parallel to the ‘1’ direction in the initial state. A current reference frame 1’-2’ is defined where ‘1’ is always parallel to the current fiber direction inside the band, thus the 1-axis rotates to 1’-axis during loading. The ‘2’ and ‘2’ directions are always orthogonal to the ‘1’ and ‘1’ directions respectively. The 1-2 frame will be defined as the ‘local’ frame and the 1’-2’ system will be termed the instantaneous frame. Initially, when the matrix retains most of its in-situ shear stiffness, the 1-2 and 1’-2’ axes systems will be nearly co-incident. As the matrix loses its in-situ shear stiffness, local shear strain, γ_{12} , will start to rise rapidly. It can be shown that the angle between the 1-axis and the 1’-axis, given by ϕ and γ_{12} , for small strains, are related by

$$\gamma_{12} = \gamma_{12}^\infty + \phi - \beta \quad (17)$$

Here, γ_{12}^∞ is the contribution from the externally applied shear loading, if any. For a uniaxial compression loading and assuming $\beta = \beta_0 = 0$, we arrive at,

$$\gamma_{12} \approx \phi \quad (18)$$

B. Numerical Implementation via the Finite Element (FE) Method

The material behavior outlined in the previous subsection is modeled in the numerical domain using the commercially available FE package ABAQUS. ABAQUS has the capability of integrating user defined material behavior with its existing element library through user defined material subroutine, UMAT.¹⁷ This subroutine is called at each material point for which the constitutive law is defined through the user defined option. A UMAT receives from the solver in ABAQUS, the stresses and strains from the previous loading step, the increment of strain in the current loading step and various other parameters. After calculations, the UMAT returns to the solver the updated stresses and internal state variables, if any, and the incremental tangent stiffness matrix, $\partial\sigma_{ij}/\partial\epsilon_{ij}$. Here it is pertinent to relate the three reference frames described in the previous subsection to the finite element solver reference systems. The $x-y$ reference frame is the ‘global’ or ‘laminate’ frame. The master geometry of the numerical domain is defined in this system. We will also use this frame to define external loading. The 1-2 reference frame coincides with the ‘local’ lamina orientation, without any loss in its significance. For the present problem, 0° , 90° and $\pm 45^\circ$ are the angles (denoted by θ in this subsection) associated for both panels studied. The solver in ABAQUS passes variables to a UMAT in this coordinate frame. The 1’-2’ reference frame is the ‘instantaneous’ frame, with the 1’ direction coincident with the current fiber direction, and is used for computations within the UMAT. A description of the computation steps performed within the UMAT (which is also presented in Figure 5) is now given. In the n -th loading increment, the solver sends in the stresses σ_{ij}^{n-1} in the 1-2 coordinate frame which are related to the stresses in the $x-y$ frame via the transformation relation,

$$\begin{aligned} \sigma_{11}^{n-1} &= \cos^2 \theta \sigma_{xx}^{n-1} + \sin^2 \theta \sigma_{yy}^{n-1} + 2 \cos \theta \sin \theta \tau_{xy}^{n-1} \\ \sigma_{22}^{n-1} &= \sin^2 \theta \sigma_{xx}^{n-1} + \cos^2 \theta \sigma_{yy}^{n-1} - 2 \cos \theta \sin \theta \tau_{xy}^{n-1} \\ \tau_{12}^{n-1} &= \cos \theta \sin \theta (\sigma_{xx}^{n-1} - \sigma_{yy}^{n-1}) + (\cos^2 \theta - \sin^2 \theta) \tau_{xy}^{n-1} \end{aligned} \quad (19)$$

The strains ϵ_{ij}^{n-1} and strain increments $d\epsilon_{ij}^n$ in the local coordinate system are also passed in from the solver. Within the UMAT, these local strain increments are added to the total strains to obtain the total strains ϵ_{ij}^n . These strains, ϵ_{ij}^n are then transformed to the 1’-2’ system using the angle between the local and the instantaneous frames, ϕ^{n-1} to obtain total strains in the instantaneous direction, $\epsilon_{i'j'}^n$. These strains, $\epsilon_{i'j'}^n$ are used in Eq. (15) to solve for the thermodynamic damage variable S_r . If the S_r value thus obtained satisfies Eq. (13), then the material point accumulates damage and the lamina *in situ* moduli E_{22} and G_{12} are degraded according to the input data provided. If S_r does not satisfy Eq. (13), then the *in situ* moduli are not changed from their previous values. This ensures that the material point never ‘heals’ and the moduli always degrade monotonically. Subsequently, the material secant constitutive matrix, $Q_{i'j'}^n$ is computed using the *in situ* moduli, E_{11} , ν_{12} , E_{22} and G_{12} . According to the present modeling scheme, E_{11} and ν_{12} are not affected by S_r . Thus they retain their values at the undamaged state throughout the analysis. Next, the stresses $\sigma_{i'j'}^n$ and the material incremental constitutive matrix, $\partial\sigma_{i'j'}/\partial\epsilon_{i'j'}$ are computed. When the increment of shear strain is small, then the instantaneous fiber rotation can be equated to the change in shear strain $d\gamma_{1'2'}^n$.¹³ From the constitutive relation one can also write,

$$\gamma_{1'2'}^n = S_{66}^n \tau_{1'2'}^n \quad (20)$$

where, $S_{66} = 1/G_{12}$. Taking differentials on both sides of Eq. 20,

$$d\gamma_{1'2'}^n = S_{66}^n d\tau_{1'2'}^n + dS_{66}^n \tau_{1'2'}^n \quad (21)$$

Equation (21) provides an expression for the change in angle $d\phi^n$. This change is added to the fiber angle value of the previous step to obtain the current fiber angle ϕ^n .

$$\phi^n = \phi^{n-1} + d\phi^n \quad (22)$$

This angle is used in the current increment, to transform the stresses and the material incremental constitutive matrix computed in the 1’-2’ frame to the 1-2 frame, to return to the solver in ABAQUS. In the absence of damage (or when the damage is small) the angle ϕ^n will be small. But with the accumulation of damage, ϕ^n starts to increase leading to local fiber direction instability.

The steps outlined in this section are repeated at each loading increment until the analyses are completed.

III. Details of the Experimental Studies

A. Stitched Double Notched Panels (DNPs)

Multidirectional composite laminated specimens used in the present experimental study are cut from a master laminate which was obtained from NASA Langley Research Center and is similar to the panels used by McGowan et al.¹⁸ The master laminate is fabricated from Hercules Inc. AS4/3501-6 graphite-epoxy materials. It is stitched through the thickness and parallel to the principal fiber direction using E.I. Dupont de Nemours Inc. *Kevlar*^(R) thread. The master laminate is made of ten prefabricated ‘stacks’ of dry preknitted lamina each of which is 1.397 mm thick and has seven layers of unidirectional plies with a stacking sequence of $[\pm 45/0/90/0/\mp 45]$. The 0° layers are parallel to the stitching direction. The resulting laminate is then infused with resin by using resin film infusion technique. Cured thicknesses of individual ± 45 , 0 , and 90 -deg layers are given in Table 1.

Schematics of an experimental specimen is shown in Figure 2. Each specimen has overall dimensions of 210 mm x 210 mm x 15 mm. Two 52.5 mm deep notches with a notch tip radius of 15 mm are cut on opposite side of each specimen. These notches create a localized high stress region which induces failure initiation and provides a predefined location for probing and obtaining diagnostics of damage initiation. Multiple DNPs have been studied. For convenience, the specimen face with thicker visible stitches is marked as the ‘top’ surface. Figure 1 shows the top surface of a typical specimen. A water-jet cutting procedure is used to cut the specimens from the master laminate. All four sides of each specimen are ground with a fine grit grinding wheel after cutting to ensure parallelism between opposite sides.

The unnotched sides of the specimens are used as loading edges. Each loading edge is slotted in end supports and puttied using Devcon steel putty to end caps that are made from hardened steel. This way, a ‘clamped’ boundary condition is obtained at each loading edge. Notched sides are slotted into anti-buckling guides. A schematic of the boundary conditions is shown in Figure 2. Experiments are carried out in an MTS machine with a crosshead displacement rate of 0.01 mm/s and an axial load capacity of 500 KN (110,000 lbf). Back to back strain gages are used at the center of each test specimen to check for specimen bending. Six quarter bridge strain gages are placed along the line joining the notch tips on the ‘top’ surface of each specimen to monitor strains during loading. These locations are shown in Figure 1. Figure 6 shows a typical specimen just prior to an experiment. The bottom surface of the specimen is visible with two strain-gages which check for out-of-plane bending during the experiment. A 500 KN capacity load-cell placed in the MTS actuator is used to measure the compressive load throughout the loading history.

B. Flat Shear Panel (FSP)

Rouse⁷ performed experimental studies on flat unstiffened shear panels with and without a cutout. The effects of the material system and the laminate lay-up on the failure characteristics of the panels were studied. Figure 7 shows a typical experimental specimen from his study with a cut-out. In the present work, experimental results of a graphite-epoxy material system will be compared with simulations. The graphite/epoxy specimens were made from unidirectional tapes of Hercules Inc AS4 graphite fibers and thermosetting resin 3502. The specimens had a lay-up of $[\pm 45/0_2]_{3S}$ with 24 plies. Nominal thickness of each ply was 0.1397 mm. Overall dimensions of the specimens were, 445 mm x 445 mm x 3.3528 mm. Edges of the specimen were stiffened with steel reinforcements bonded to the specimen with room temperature adhesives which produced a gage section of 305 mm square. A circular cut-out of 25.4 mm diameter was drilled at the center using diamond impregnated core drills. Tensile loading was applied to the specimen using a picture frame loading apparatus in a 1.33 MN hydraulic test machine as shown in Figure 7. Figure 8 describes the schematic of the applied load and the axis system used in testing. The global X-axis is perpendicular to the applied loading direction and the global Y-axis is parallel to the loading direction. The 45° layers on the top surface were parallel to the applied loading. Strain gage readings from the top and bottom surfaces of the panel were recorded at a location 12.7 mm below the cutout along the loading diagonal (location X). Linear variable displacement transducers were used to measure the out of plane displacement at the edge of the cut-out and Moiré-fringe techniques were used to measure the complete out-of-plane deformation field of the specimen.

IV. Numerical Simulations

The predictive capabilities of the present PFA methodology is assessed by simulating the experimental results of the panels described in the previous section. Test sections of the experimental geometries (both the

DNP and the FSP) were discretized using the shear deformable three noded (S3) and four noded (S4/S4R) shell elements available in ABAQUS (Figure 9). Truss elements (T3D2) were used to simulate the picture frame loading frame of the FSP. A summary of the nodal and elemental data are presented in Table 2. For both the panels, static analyses were performed using displacement control loading. Linear eigenvalue buckling analyses were also performed to generate perturbations in the form of the linear eigen modes to be used in subsequent response analyses. Geometric nonlinearity is included in the response analysis through the RIKS¹⁹ option available in ABAQUS.

Elastic material properties for the AS4/3501-6²⁰ and AS4/3502⁷ material systems are described in Table 1 and Table 3 respectively. Nonlinear shear stress-strain curves for these material systems are shown in Figure 10. A material point is denoted as ‘damaged’ when it reaches the end of the input stress-strain curve. For the present analysis, this refers to a 55% degradation in the *in situ* shear modulus, G_{12} . Complete material constitutive behaviors are modeled via the user material subroutine option of ABAQUS. Section lay-up of the laminates are defined using the *SHELL SECTION, COMPOSITE option available for shell elements. Thickness effects are incorporated by using multiple integration points through the thickness.

Boundary conditions for the panels are applied at nodal positions. For the DNPs, nodes corresponding to the top grip location are constrained from having any motion. Nodes occupying the bottom grip location are constrained to move only in the 1-2 plane. Rows of nodes corresponding to the knife edge support locations are constrained from moving out-of-plane. Loading applied by the MTS cross-head is simulated by specifying displacement in the 2-direction for nodes at the bottom grip location. For the flat shear panel with a cutout, effects of the steel reinforcements were modeled via rigid truss elements at the edges of the specimen. Tensile loading is simulated by specifying displacements in X- and Y- direction at point C. Equal displacements are specified such that the resultant motion is along the diagonal AC.

Geometric and material perturbations are both used in the DNP analysis. An out-of-plane perturbation equal to 0.001% of the laminate thickness is provided using the lowermost global buckling mode (obtained from a linear eigenvalue buckling analysis). In-plane geometric perturbation is provided using a negative shear loading on the bottom grip such that the bottom grip is offset by a predetermined amount with respect to the vertical (Y-direction). An offset angle of 2^0 was used in the analysis. Material axis system of the axial layers (90^0 layers) are offset from the Y-direction by 2^0 in addition to the in-plane geometric perturbation. The geometric and the material axis perturbations are defined such that they act in harmony. For the FSP, only an out-of-plane geometric perturbation is used. The lowermost global buckling mode shape, obtained from a linear eigen value buckling analysis, is used for this purpose. Magnitude of the largest perturbation is 0.3% of the total laminate thickness. It is to be noted that material imperfections (misalignment of fibers within a layer) are usually on the order of $1^0 - 2^0$ for pre-preg based laminates.

A. Results for the Stitched Panel

Results from the DNP tests and the FE simulation are presented and salient features of compressive damage diagnostics obtained from the specimens are discussed in the present section. Experimental results are discussed first followed by the comparison with the FE simulation results. Strain readings from the back to back gages at the center of the specimen showed insignificant amount of bending being present. This was true for all three specimens examined. However, it is likely that the panels had initial geometric imperfection shapes unlike that of the lowest eigenmode shapes assumed here in the analysis to follow. This is evident in the back to back strain gage readings from the right and left notch tip areas that show differences between them suggesting that the panel deformation also shows a ‘skewed x-wise’ bending, unlike the first elastic eigenmode shape.

A linear elastic FE study predicted that the notch tip compressive strain in the loading direction will exceed 0.01 (10000 micro-strain) at a global reaction force of 220 KN (Table 4). This value of axial strain is typical for fiber kinking for the present class of materials.^{14, 21} Figure 11 presents the membrane strains (obtained from the back-to-back center gages shown in Figure 1) plotted against the reaction forces. Comparison with the finite element analysis prediction shows that the overall panel response remains largely linear during loading. Nonlinearity in the global response sets in beyond 200 KN which is near the predicted load level for fiber kinking near the notch tip. The resultant load - displacement ($P - \Delta$) data from the DNP tests are plotted in Figure 12. The responses show a bilinear behavior with a distinct knee around a load of 220 KN. A slight ‘kink’ in the $P - \Delta$ responses near 340 KN is also observed. There was no audible or visible indication of damage prior to this load level and the DNP specimens failed catastrophically at an external load of 370 KN. The specimens separated in two halves during their removal from the end supports. Comparison of the catastrophic failure loads of the DNP specimens (Table 5) with the predicted linear buckling load (Table 4)

shows that specimen failure did not occur due to global buckling. Instead, progressive damage accumulation in all the layers in the vicinity of each notch tip leads to a zone of ‘degraded’ material. These zones grow towards each other just prior to catastrophic failure and the panel undergoes an out-of-plane shear failure separating into two halves as shown in the post-experiment image of Figure 13.

Figure 13 shows the top surface of the first DNP specimen (Test-1) after it was removed from the fixture. As it can be seen, damage which initiated near the notches grew suddenly across the specimen above the center stitch. On the bottom surface, a damage zone propagated across the specimen below the center stitch (Figure 14(a)). Presence of the center stitch seems to prevent damage initiation exactly at the notch tip. It is also seen that a view of the through thickness damage is inclined at an angle to the loading axis rather than being perpendicular to it (Figure 14(b)).

In view of these observations from the panels studied, a third DNP specimen was tested such that damage would initiate in the vicinity of the notch tips but would not progress towards catastrophic failure. This specimen was loaded up to 340 KN and subsequently unloaded. Strain gage readings from the gages near the notch tips showed nonlinearity at this load level indicating the presence of internal damage. The unloaded specimen was taken off the grips and cut along the center line of the left notch tip gage (section AA’, Figure 1). Post-experiment damage diagnostics were performed using optical microscopy and Scanning Electron Microscopy (SEM). Figure 15 shows the AA’ sectional view of the notch tip looking from inside the laminate. Multiple damage locations on this section are indicated with ‘ABCD’ close-up markers and studied with the aid of an SEM. Fiber kinking in the vicinity of the notch tip is the main source of damage (Figure 16 and Figure 17).

Load-displacement comparison

Load-vs.-load point displacement data for the DNP test specimens are compared with the FE result in Figure 12. The experimental data show regions of ‘settling’ in the initial stages. The FE simulation results are plotted after accounting for the settling of laboratory specimens. The overall behavior of the FE simulation is similar to the experimental observations. Initial slopes of the curves presented match quite well. Beyond 220 KN, the FE result does not show the pronounced ‘knee’ as seen in the experimental curves. Instead it remains bounded by the experimental responses. The FE analysis predicts a peak load of 386 KN which is within 3% of the experimentally observed maximum load.

Strain-gage measurements

The strain readings recorded from the DNP panels are shown in Figure 18. The locations of the gages are indicated in Figure 1 and tabulated in Table 6. All strains initially are linear with the applied load, but a careful examination shows a softening behavior as loading proceeds. This nonlinearity is progressive and is indicative of damage accumulation in the panel. As expected, the gages closest to the notch tips record the highest values and the intensity decreases with distance away from the notch tips. The back to back notch tip gages show bending and also differ between the right notch and left notch (Figure 18(a),(c) and Figure 18(b),(d)), suggesting a width wise skewed (in the x-direction) bending during the deformation. An acceleration of the notch tip strain nonlinearity is observed at 300 KN (gage 6 in Figure 18(d)) and the gage is rendered malfunctioning at about 310 KN. The FE results, because they are based on a panel with a very slight out-of-plane geometric imperfection in the form of the smallest elastic eigen mode, does not show any differences in the back to back notch tip readings. The FE data is also ‘stiffer’ as expected, indicating that the panel properties are most likely underestimated. However, the trends in all the strains captured by the FE simulation are correct with respect to softening nonlinearity and with respect to the acceleration of the non-linearity as loading proceeds. Indeed, all the FE strain readings become near vertical at approximately 384 KN, indicative of the softening induced localized instability experienced by the panel. An examination of the strain readings appears to indicate that the strain predictions of the FE simulations are slightly shifted. That is, if all the panel strain readings are correlated with the FE strains at locations that are further away from the notch, then the readings show a remarkable agreement. This suggests that a ‘scaling’ of the material properties and proper accounting for the initial geometric imperfections should bring agreement much closer. It must be noted that the FE simulations are based on classical lamination theory ideas (strictly 2D) which neglect possible 3D effects that can also contribute to the discrepancies. A study that examines the effects of material property uncertainty was carried out in a limited sense for the FSP (see later). A similar study for the DNP is currently under progress.

Damage contours at various load levels

Contours of the damage variable S_r are presented at increasing load levels in Figure 19 through Figure 21. Results are presented for the top four layers, $\pm 45^\circ$, 0° and 90° layers, where the layer orientation is given with respect to the x-direction. A color closer to red indicates a higher level of degradation compared to a color closer to blue which indicates zero or minimal damage. The dark areas in these maps correspond to

shear stiffness loss of 55% or more. In the following discussion, damage state or level of degradation is used interchangeably with the loss of shear stiffness. It is readily observable that different layers are at different levels of degradation at a given global reaction force. It is also noticeable that the 90° layer which is under global axial compression, shows the least amount of damage whereas the $\pm 45^\circ$ layers show the most damage. The axial layer damage, suddenly starts to accelerate and grow near and beyond the peak load. The $\pm 45^\circ$ layers make up nearly 60% of the laminate, thus the global stiffness of the system is greatly affected by the degradation of these layers. In a through-thickness view at the notch tips, at a load of 350 KN load, only 14% of the layers have substantial shear stiffness remaining and the rest have lost 55% or more of their shear stiffnesses. Thus the laminate weakens in both inplane and out-of-plane directions. Damage zones grow a little offset from the notch tips in the 90° layer and converges towards the notch tips with increasing load. In the $\pm 45^\circ$ layers, damage nucleates from the notch tips in a small region. Then the two separate damage zones propagate towards each other along the center line of the specimen, finally establishing a region of uniformly damaged material between the two notches (the continuous red band in Figure 21). Evidence of this phenomenon is readily visible in the damage contours of the 0° layer. The contours do not appear to change much between the peak load (386 KN) and the 384 KN load levels. Under closer inspection, the distance between the fronts of the advancing damage zones are smaller at 384 KN compared to 386 KN indicating continuous damage growth. This damage growth coupled with the strain gage readings becoming near vertical signals the onset of catastrophic failure.

B. Results for the flat unstiffened shear panel

Simulation results for the FSP are compared with the experimental results obtained by Rouse.⁷ Experimental observations for the FSP reported that the panel failed deep into the post-buckling regime. Delamination zones and tension cracks developed at the edges of the cut-out and lead to the failure of the specimen. Two types of data are reported from the experiment, namely load-vs.-load point displacement and load-vs.-surface strain variation. Similar data sets are generated from FE simulations and compared with the experimentally reported data.

Three different FE cases are reported in the following discussions. Finite element analysis results with the elastic properties as reported by Rouse⁷ are denoted as ‘case 1’. Case 2 corresponds to analyses with elastic moduli values 110% of those reported by Rouse.⁷ A third analysis, using an explicit tensile failure criterion was performed and those results are reported under ‘case 3’.

Load-displacement comparison

Load (P) and load point displacement (Δ) data from the experiment and the simulations are plotted in Figure 22. The experimental buckling load for the specimen was reported to be 112 KN. A linear eigenvalue buckling analysis of the FSP geometry produced a buckling load of 113 KN. Results from the case 3 analysis, shows a peak load of 186 KN which is within 3% of the experimental peak load of 191 KN.

Strain-gage measurements

Figure 23 shows the variation of reaction force P with strains ϵ_{22} (perpendicular to the fiber direction) measured on the top and bottom surfaces of the panel at a station 12.7 mm below the cutout edge along the loading diagonal (Figure 8). It can be seen that the present analysis is able to capture the experimentally observed phenomena of bifurcation and subsequent strain evolutions on the top and bottom surfaces. The simulation results also show a softer behavior compared to the experimental observation, which is due to the incorporation of continuous material damage. Experimental data for the stiffness degradation of the AS4/3502 system used in the FSP experiments were not available. Hence, experimental data that provide the degradation behavior (i.e., the S_r -vs.-normalized stiffness relations) of the AS4/3501-6 system was used as an approximation. The results show that such a degradation behavior provides a ‘lower’ bound for the FSP panel (FE, case 1 in the figures). The ‘FE, case 2’ analysis was performed by increasing the elastic constants of the FSP material by 10% and keeping the degradation behavior unchanged. This approach led to an ‘upper’ bound of the FSP material. The actual specimen material properties lie somewhere in between these two limits. The ϵ_{22} -P behavior suggests that the degradation law (form of the S_r -vs.-normalized G_{12} curve) has a lesser effect on the system response of these FSPs than the initial undamaged moduli.

Damage maps of various layers

Various locations are marked on Figure 22 which correspond to the various damage events occurring in the laminate. Table 7 shows the loads associated with these events. Contours of damage variable S_r for each of these events are shown for the top three layers ($\pm 45^\circ$ and 0° layers) and the bottom layer (45° layer) in Figure 24 through Figure 28. The first set of contours (Figure 24) show the material state just prior to global buckling. It can be seen that damage occurs in limited areas in various plies. Global FSP

buckling coupled with other failure events accelerates material degradation (Figure 25- Figure 28). The damage is seen to nucleate in areas surrounding the edge of the cut-out. Propagation of the damage zones are mainly perpendicular (-45° and 0° plies) and parallel (bottom 45° ply) to the loading direction. Beyond the global buckling event, damage accelerates in the bottom 45° ply compared to the other layers. At a global load of 124 KN, the contours of damage in various layers are shown in Figure 25. During subsequent loading, degradation accelerates in other layers also and at 140 KN (event B) tensile failure nucleates in the top 45° layer. Figure 29 shows the contours of the damage variable S_r near the cut-out at event B. It is readily observable that the -45° layer and the 0° layer near the cut-out (at locations perpendicular to the external loading) are at a higher level of damage compared to the outermost layers. Thus these locations subsequently loose support for the outermost layers and other damage modes appear. Results from 'FE, case 3' incorporates contours of a variable which is monitored during the analysis to indicate when the local tensile axial stress exceeds the tensile strength of the material (1378 KN).⁸ The initiation of tensile failure occurs in the topmost layer followed by the tensile failure in the bottom layer (event C) and coincides with the inner layers losing 55% of their *in situ* shear stiffness at those locations. Figure 30 shows the growth of tensile damage in the topmost layer which is perpendicular to start with but propagates at an angle with the loading direction. As the tensile failure zone extends from its nucleation site, the strain in the topmost layer is seen to deviate from the 'FE, case 2' results (Figure 23). In the laboratory experiment, the tensile failure could have propagated abruptly leading to a sudden catastrophic failure of the panel. The contours of damage variables clearly show that the present analysis is able to capture the different rates of damage progression in the top and the bottom layers.

Out-of-plane displacement data

Figure 31 shows the out-of-plane displacement(w) at the cut-out boundary along the loading diagonal (Figure 8) plotted against the global reaction force P. Experimental data of w-vs.-P for the experimental FSP specimen analyzed here are not available (these results are available for FSP specimens with different material systems and laminate lay-ups). But the trends shown are similar to the experimental results reported by Rouse.⁷

V. Concluding Remarks

In this paper, a failure mechanism based progressive failure analysis methodology is developed and validated against experimental data for two types of structural panels. The methodology uses the complete non-linear stress-strain relations for the lamina in shear and in transverse tension/compression as input, along with readily available lamina level elastic properties. Using only these (a minimum number) as inputs, progressive failure and damage growth in two types of structural panels, loaded under a pre-dominantly compression loading have been simulated. In particular by modeling the physics of the kink banding process responsible for limiting the lamina axial compression strength, the maximum load sustained by the panels and the subsequent damage evolution have been captured accurately. The notion of a fixed compression strength has been disbanded, instead the *in-situ* compression strength of a lamina is determined as a part of the solution process, and as a function of loading history. The success of the present PFA methodology is encouraging and points the way for extending the methodology to analyze other structural configurations.

Acknowledgements

The authors are grateful for financial sponsorship through NASA Langley research grant NCC-1-03013.

References

- ¹Hashin, Z., "Failure Criteria for Unidirectional Fiber Composites," *Journal of Applied Mechanics*, Vol. 47, June 1980, pp. 329-334.
- ²Chang, F.-K. and Lessard, L. B., "Damage Tolerance of Laminated Composites Containing an Open Hole and Subjected to Compressive Loadings: Part I-Analysis," *Journal of Composite Materials*, Vol. 25, January 1991, pp. 2-43.
- ³Schapery, R. A., "A Theory of Mechanical Behavior of Elastic Media with Growing Damage and other Changes in Structure," *J. Mech. Phys. Solids*, Vol. 38, No. 2, June 1990, pp. 215-253.
- ⁴Schapery, R. A. and Sicking, D. L., "On Nonlinear Constitutive Equations for Elastic and Viscoelastic Composites with Growing Damage," *Mechanical Behavior of Materials*, Vol. 47, June 1995, pp. 45-76.
- ⁵Oguni, K., Tan, C. Y., and Ravichandran, G., "Failure Mode Transition in Unidirectional E-Glass/Vinylester Composites under Multiaxial Compression," *Journal of Composite Materials*, Vol. 34, No. 24, 2000, pp. 2081-2097.
- ⁶Basu, S., Waas, A. M., and Ambur, D. R., "Compressive Failure of Fiber Composites under Multiaxial Loading," *in*

review, 2005.

⁷Rouse, M., "Effect of Cutouts or Low-speed Impact Damages on the Postbuckling Behavior of Composite Plates Loaded in Shear," 31st SDM Conference, AIAA, , No. AIAA-90-0966-CP, 1990, pp. 877–891.

⁸Ambur, D., Jaunky, N., Dávila, C., and Hillburger, M., "Progressive Failure Studies of Composite Panels with and without Cutouts," 42nd SDM Conference, AIAA, Seattle, , No. AIAA-2001-1182-CP, April 2001, pp. 1–11.

⁹Goyal, V. K., Jaunky, N., Johnson, E. R., and Ambur, D., "Intralaminar and Interlaminar Progressive Failure Analysis of Composite Panels with Circular Cutouts," 43rd SDM Conference, AIAA, Denver, , No. AIAA 2002-1745, 2002, pp. 1–12.

¹⁰Schapery, R. A., "Mechanical Characterization and Analysis of Inelastic Composite Laminates with Growing Damage," *Mechanics of Composite Materials and Structures*, Vol. AMD-100, June 1989, pp. 1–9.

¹¹Sun, C. T. and Chen, J. L., "A Simple Flow Rule for Characterizing Nonlinear Behavior of Fiber Composites," *Journal of Composite Materials*, Vol. 23, October 1989, pp. 1009–1020.

¹²Dávila, C. G., Ambur, D. R., and McGowan, D. M., "Analytical Prediction of Damage Growth in Notched Composite Panels Loaded in Compression," *Journal of Aircraft*, Vol. 37, No. 5, September–October 2000, pp. 898–905.

¹³Schapery, R. A., "Prediction of Compressive Strength and Kink Bands in Composites using a Work Potential," *International Journal of Solids and Structures*, Vol. 32, No. 6/7, 1995, pp. 739–765.

¹⁴Lee, S. H. and Waas, A. M., "Compressive Response and Failure of Fiber Reinforced Unidirectional Composites," *International Journal of Fracture*, Vol. 100, No. 3, December 1999, pp. 275–306.

¹⁵Schapery, R. A., "Private communication," 2002.

¹⁶Evans, A. G. and Adler, W. F., "Kinking as a Mode of Structural Degradation in Carbon Fiber Composites," *Acta Metallurgica*, Vol. 26, 1978, pp. 725–738.

¹⁷Anon., *ABAQUS User's Manual, Ver. 6.3-1*, Hibbit, Karlson and Sorenson, Pawtucket, RI, 2003.

¹⁸McGowan, D. M., Dávila, C. G., and Ambur, D. R., "Damage Progression in Buckle-Resistant Notched Composite Plates Loaded in Uniaxial Compression," 42nd SDM Conference, AIAA, Seattle, April 2001.

¹⁹Riks, E., "The Application of Newton's Method to the Problem of Elastic Stability," *Journal of Applied Mechanics-Transactions of the ASME*, Vol. 39, No. 4, December 1972, pp. 1060–1065.

²⁰Soden, P., Hinton, M. J., and Kaddour, A. S., "Lamina Properties, Lay-up Configurations and Loading Conditions for a Range of Fiber-Reinforced Composite Laminates," *Composite Science and Technology*, Vol. 58, 1998, pp. 1011–1022.

²¹Kyriakides, S., Arseculeratne, R., Perry, E. J., and Liechti, K. M., "On the Compressive Failure of Fiber Reinforced Composites," *International Journal of Solids and Structures*, Vol. 32, No. 6/7, 1995, pp. 689–738.

²²Yerramalli, C., *A Mechanism based Modeling Approach to Failure in Fiber Reinforced Composites*, Ph.D. thesis, Aerospace Engineering Department, University of Michigan, Ann Arbor, 2003.

Table 1. Properties of the different prefabricated ply orientations.¹⁸

Properties	Layer Orientation		
	$\pm 45^0$	0^0	90^0
thickness (mm)	0.14986	0.15697	0.16967
E_{11} (GPa)	111.0	113.0	110.0
E_{22} (GPa)	11.0	11.0	11.0
G_{12} (GPa)	5.5	5.5	5.5
G_{13} (GPa)	5.5	5.5	5.5
G_{23} (GPa)	2.8	2.8	2.8
ν_{12}	0.34	0.34	0.34

Table 2. Summary of nodal and elemental data for the FE analyses

Elements	11713	2699
S3/S4	11713	2635
T3D2	-	64
Nodes	11951	2697
Degrees of Freedom	71706	16182

Table 3. Properties of the different prefabricated ply orientations.⁷

Properties	
thickness (mm)	0.1397
E_{11} (GPa)	131.0
E_{22} (GPa)	13.0
G_{12} (GPa)	6.4
G_{13} (GPa)	6.4
G_{23} (GPa)	1.8
ν_{12}	0.38

Table 4. Predictions from a linear elastic FE analysis of the DNP geometry. Negative strains indicate compression.

Event	Global Load (KN)
Notch tip axial strain -0.010	220
Notch tip axial strain -0.015	330
Global buckling	1300

Table 5. Summary of experimental observation of the DNP specimens. Negative strains indicate compression.

	Ultimate failure load (UFL) (KN)	Axial strain at UFL (μ -strain)
Test-1	372	-6110
Test-2	375	-5943

Table 6. Summary of the experimental strain measurement stations for the DNP panel.

Distance from the left notch tip	Test-1	Test-2
Gage 1	5 mm	2 mm
Gage 1 back	-	3 mm
Gage 2	12 mm	10 mm
Gage 3	25 mm	25 mm
Distance from the right notch tip		
Gage 4	24 mm	25 mm
Gage 5	12 mm	11 mm
Gage 6	6 mm	3 mm
Gage 6 back	-	3 mm

Table 7. Summary of various failure events and corresponding loads for the FSP panel.

Event	Load
Global Buckling	107 KN
(A) Bottom ply G_{12} degrades 55%	124 KN
(B) Top ply tensile failure	140 KN
(C) Bottom ply tensile failure	156 KN
(D) Peak load	186 KN

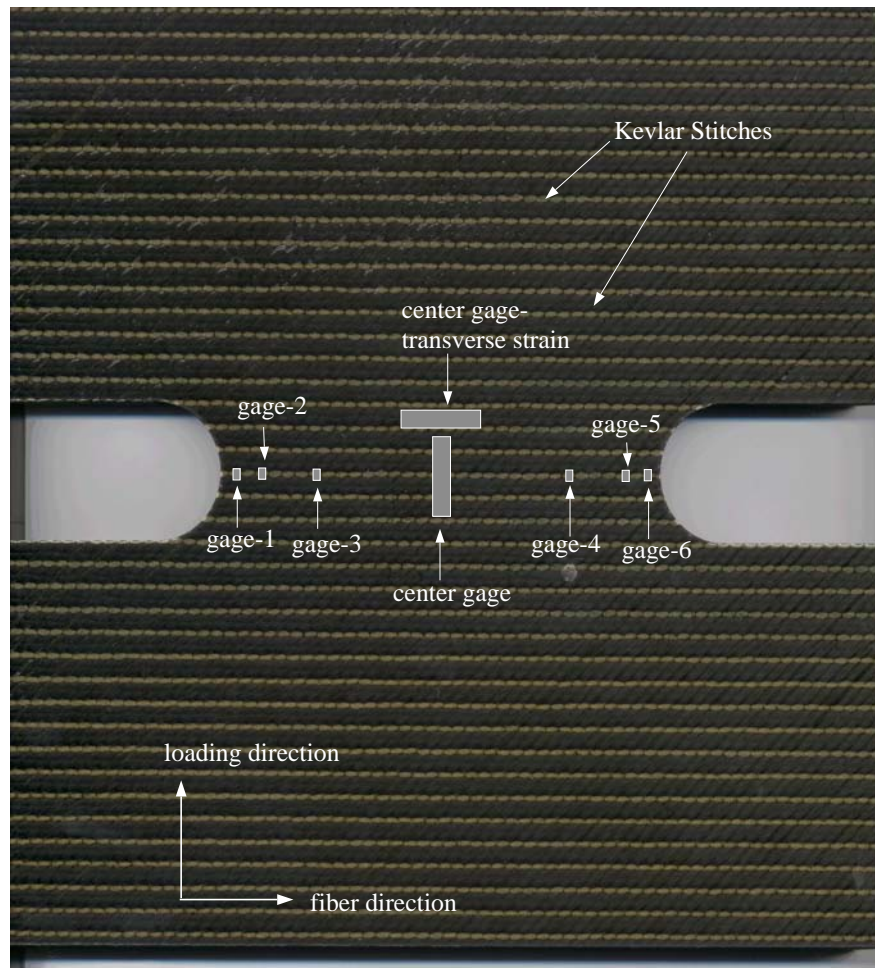
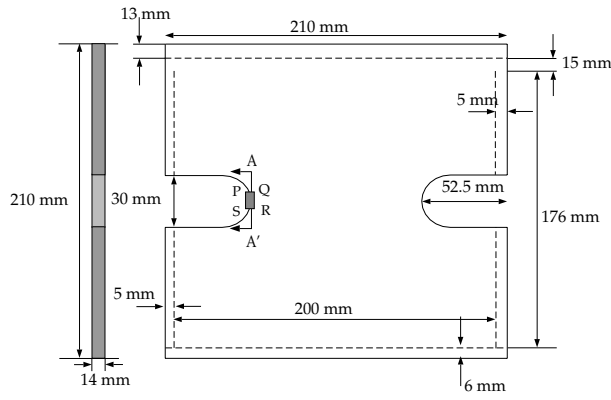
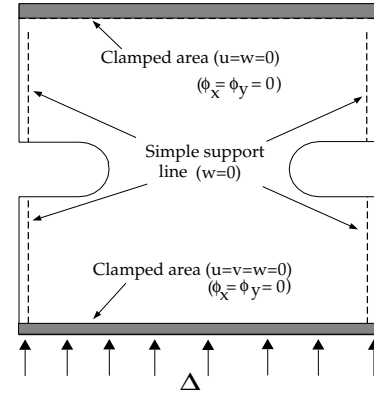


Figure 1. Top surface of a DNP specimen. Strain gage locations are shown with white boxes.



(a) Dimensions of the DNP



(b) Boundary conditions of the DNP

Figure 2. Schematics of the specimens and test conditions used in the present study. Section AA' is used to cut Test-3 specimen for damage diagnostics. The kinked zero-ply viewed as PQRS is shown in Figure 17.

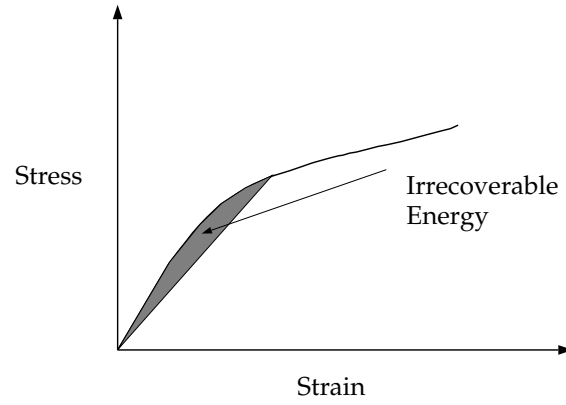
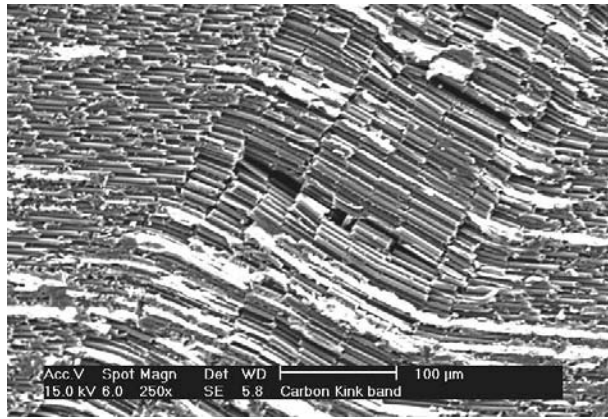
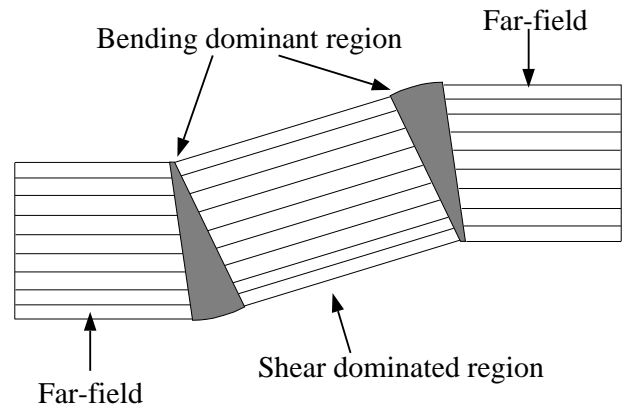


Figure 3. Definition of irrecoverable energy using a generic stress-strain curve.



(a) Developing kink band



(b) Schematic of a lamina

Figure 4. The developing kink band in Carbon composites²² and the schematic representation of such within a lamina.

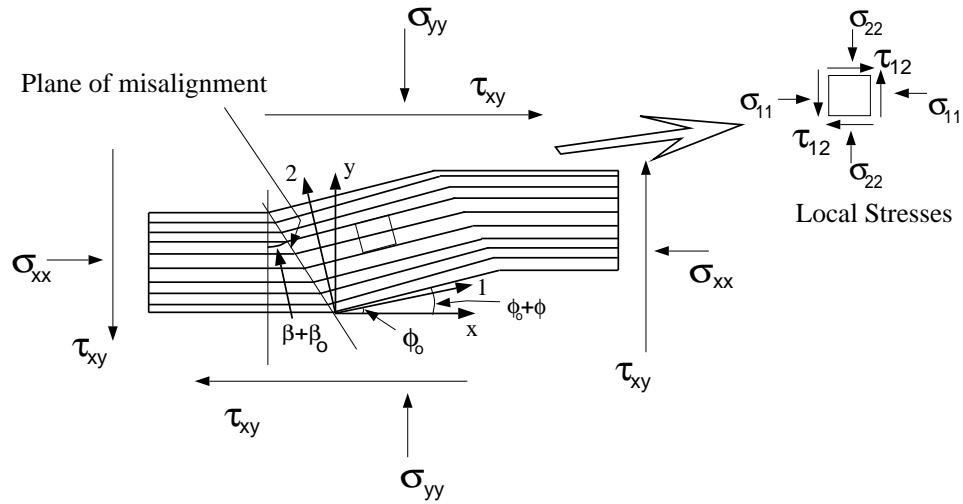


Figure 4.(c) A unidirectional lamina with a band of misaligned fibers in equilibrium under a multiaxial stress state. Inset shows the stress state inside the misaligned band.

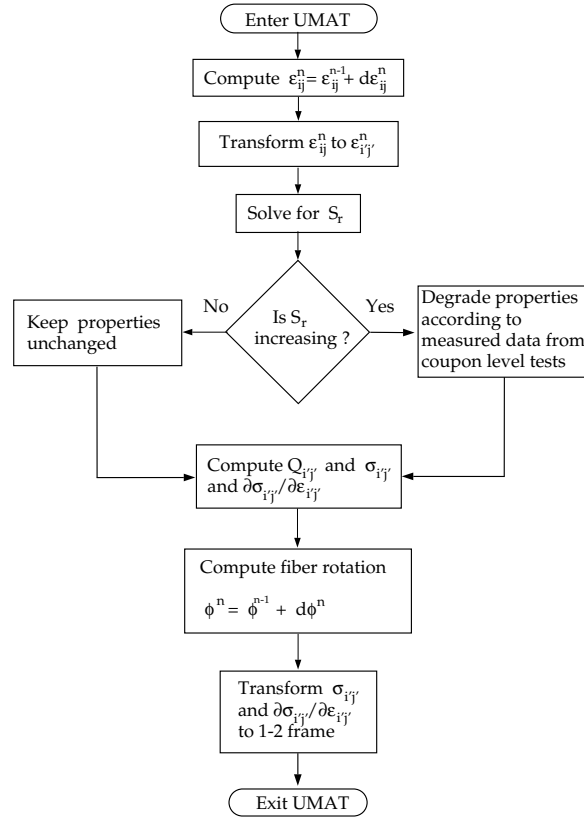


Figure 5. Flow chart of the operations performed inside a UMAT for implementing the fiber rotation and Schapery Theory ideas.

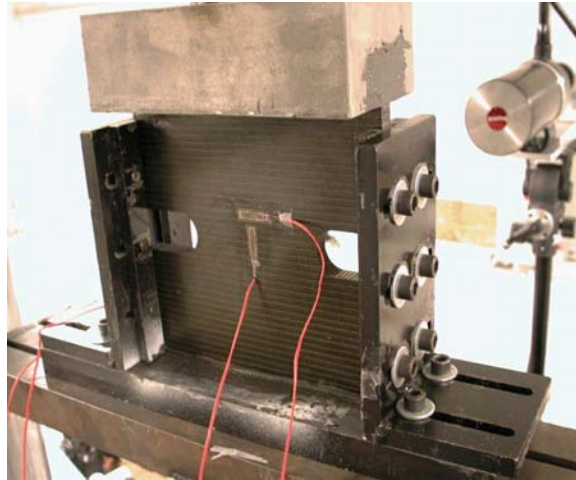


Figure 6. A DNP specimen is shown with supports and bottom surface strain gages prior to an experiment.

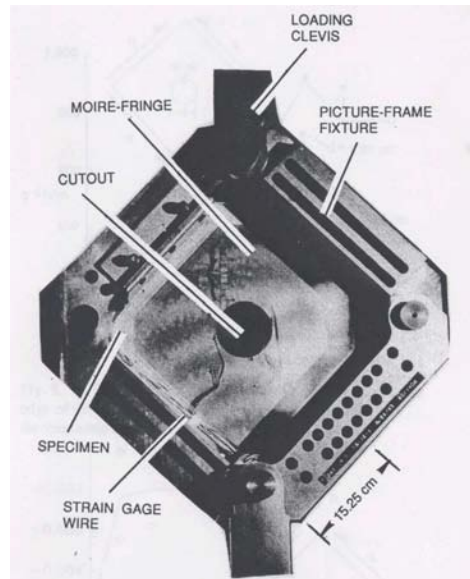


Figure 7. Typical experimental set-up for FSPs.⁷

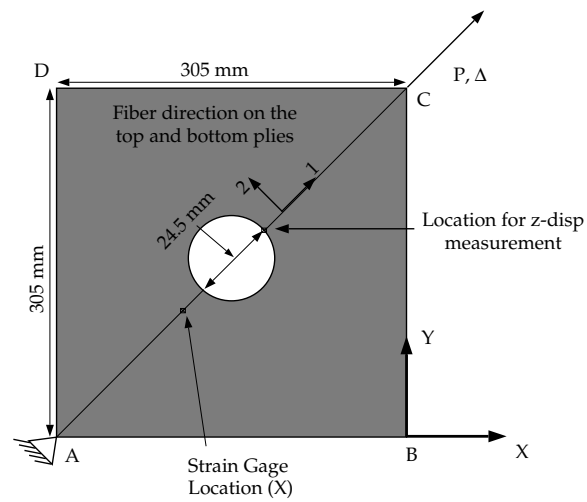


Figure 8. Schematic geometry of the FSP specimen.

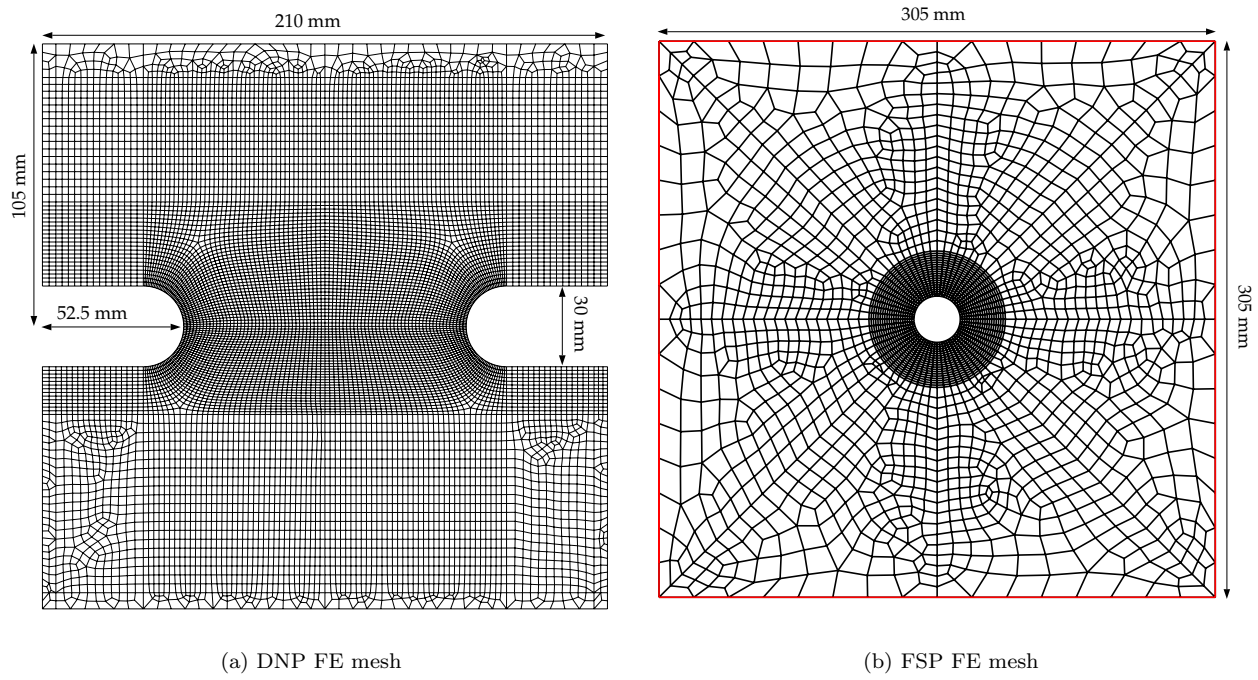


Figure 9. Finite element meshes used in the present study.

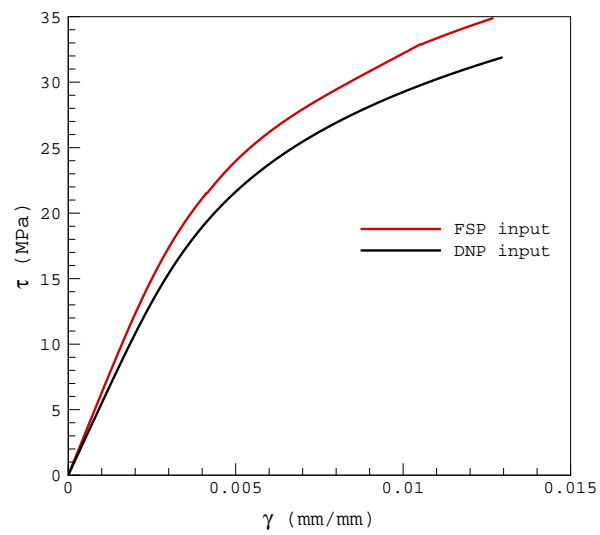


Figure 10. Material inelastic input curves used in the present study.

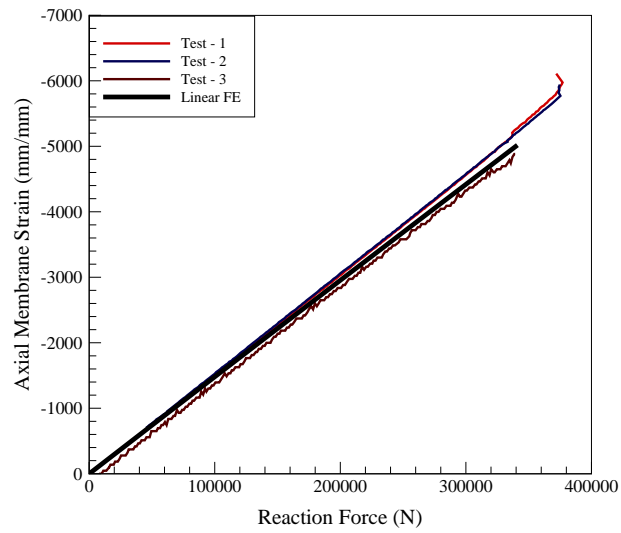


Figure 11. Membrane strain plotted against reaction force from three DNP specimens and the FE analysis. Notice the repeatability of the test results and agreement with the FE prediction.

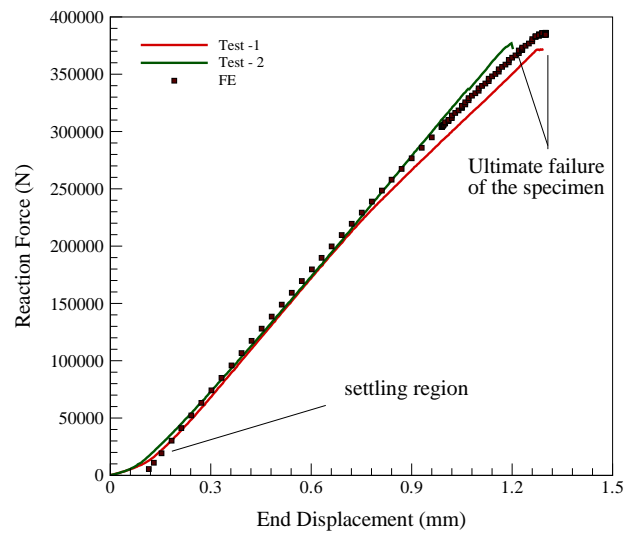


Figure 12. Load-vs.-displacement data comparison of the DNP experiments and the numerical simulation.

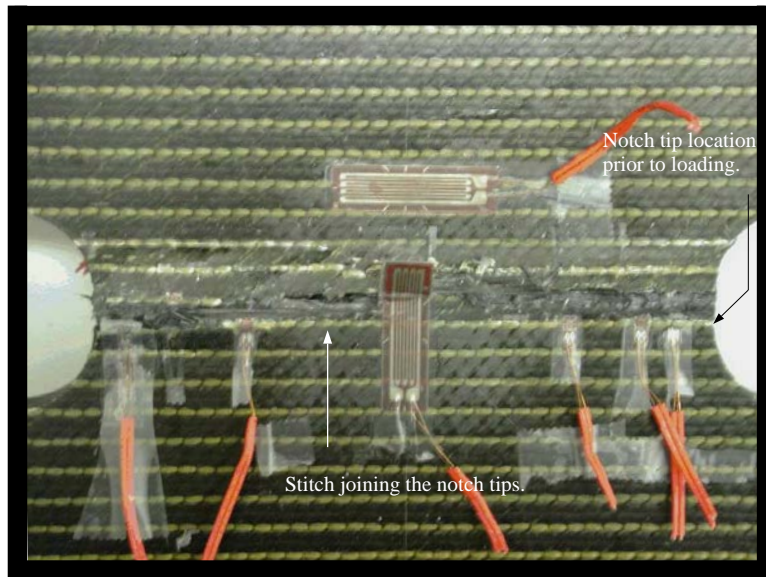
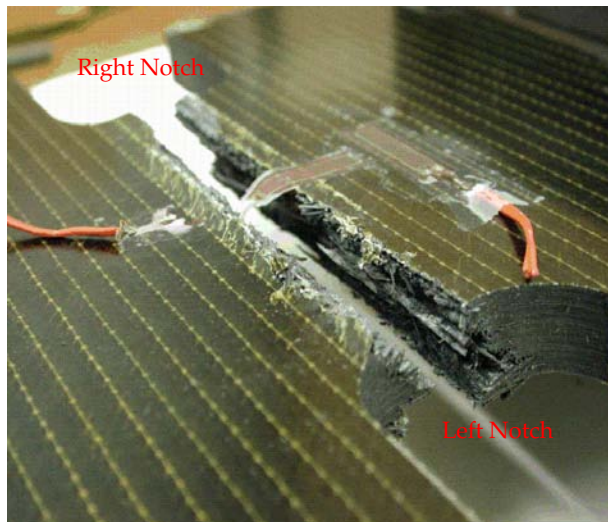
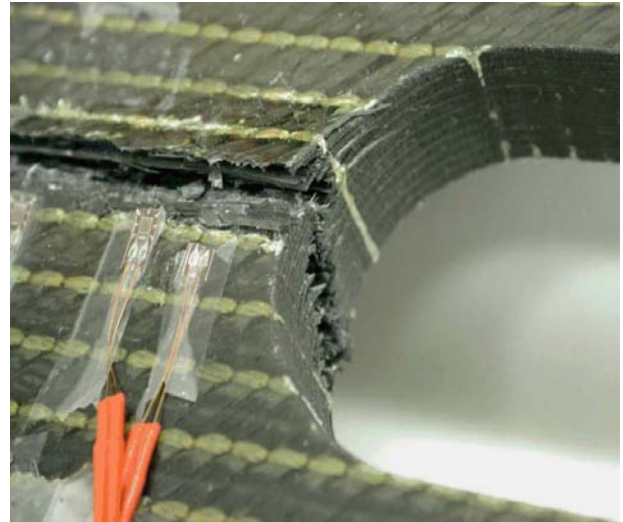


Figure 13. Top surface of a DNP specimen is shown after being loaded beyond catastrophic failure.



(a) Left Notch



(b) Right Notch

Figure 14. Close-ups of the notches of the specimen shown in Figure 13 after experiment.

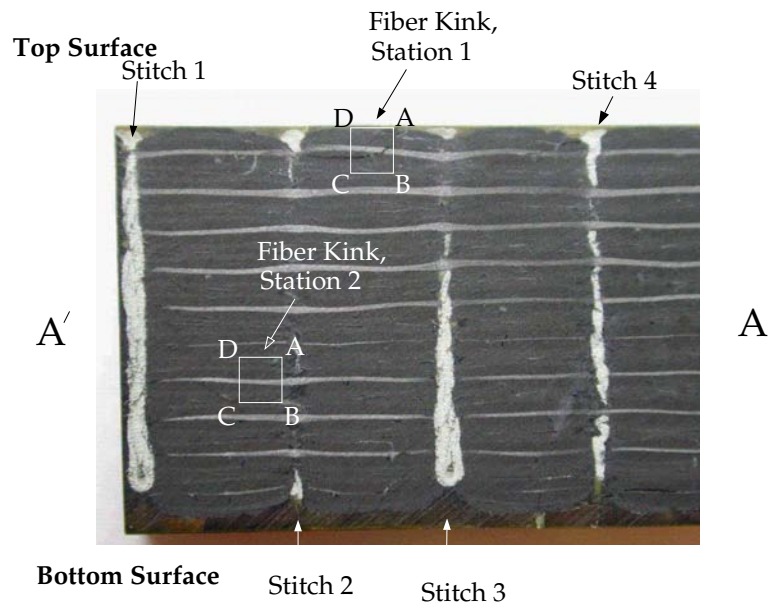


Figure 15. Cross-section view AA' (Figure 2) behind the left notch tip. Prominent damage locations are marked and the corresponding SEM pictures are shown in subsequent figures. Global loading is applied along the vertical.

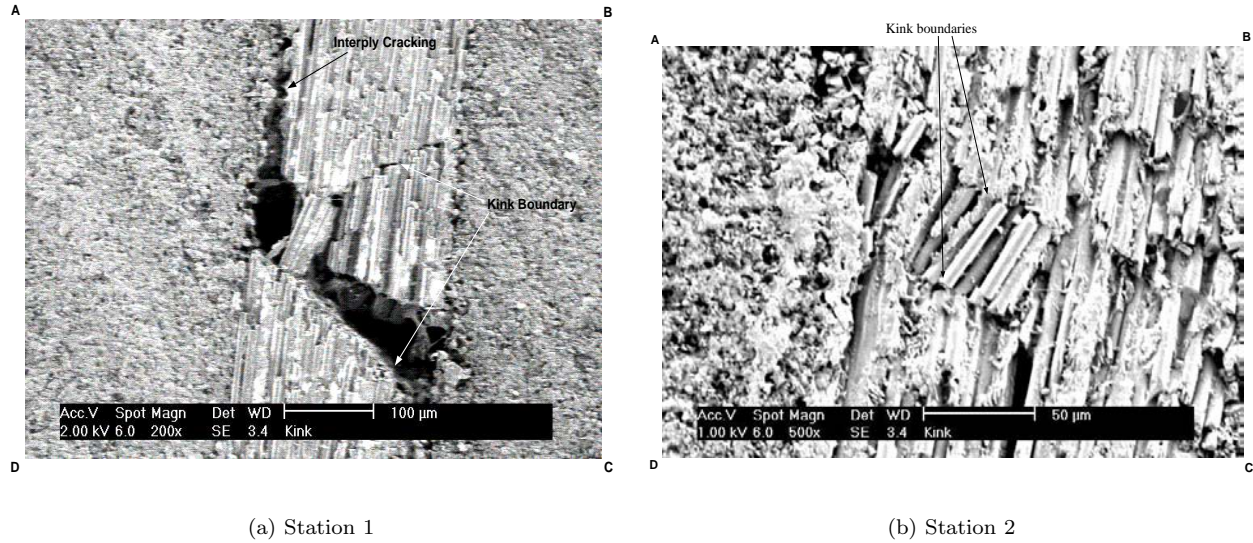


Figure 16. Fiber kinking followed by fiber breakage at an axial layer near the top surface. Subsequent interply cracking can also be observed. Notice that the kink band width is about $50 \mu\text{m}$.

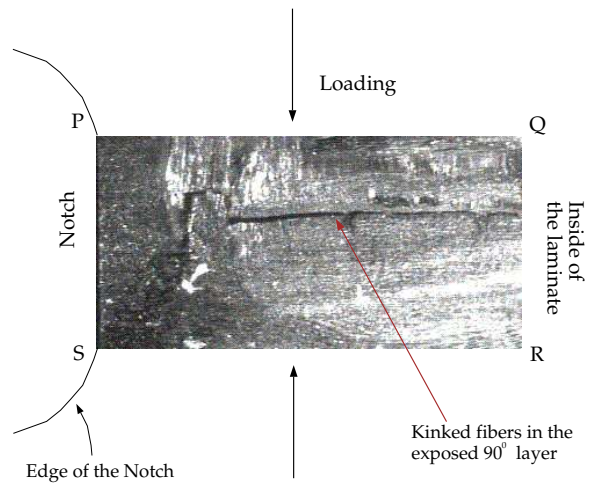
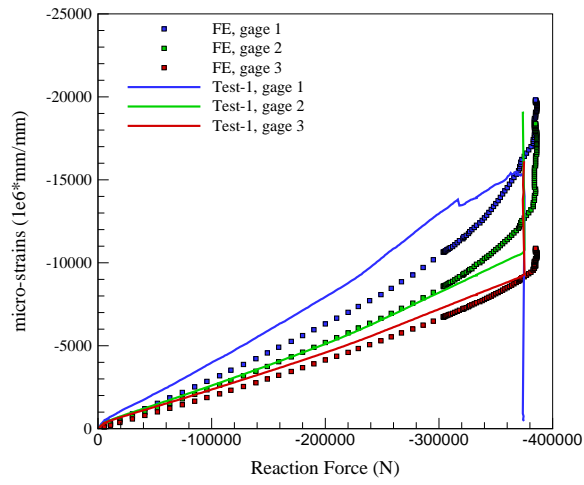
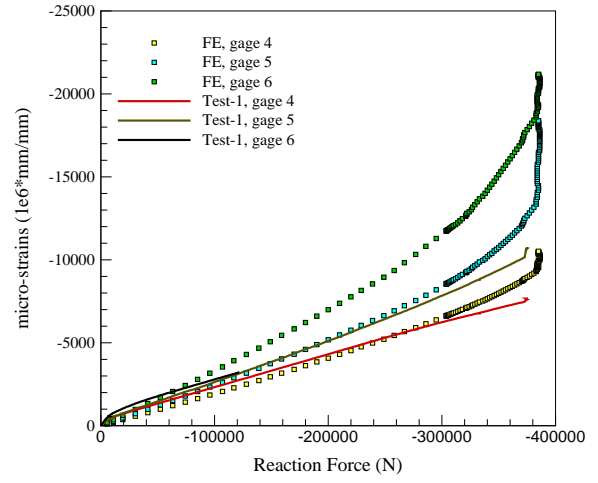


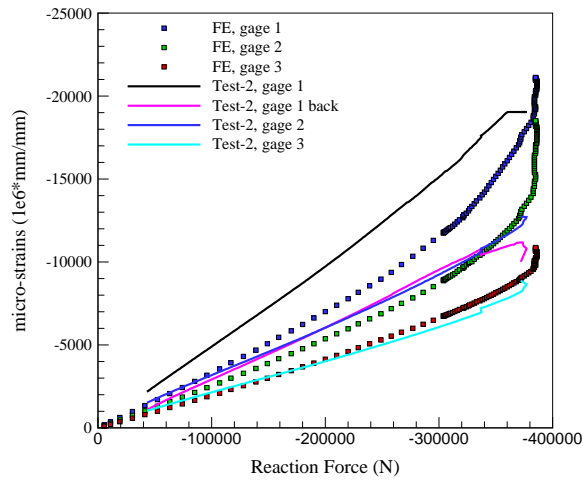
Figure 17. Top view of the kink site PQRS shown in Figure 2. See Figure 16 for the side view - from inside of the laminate.



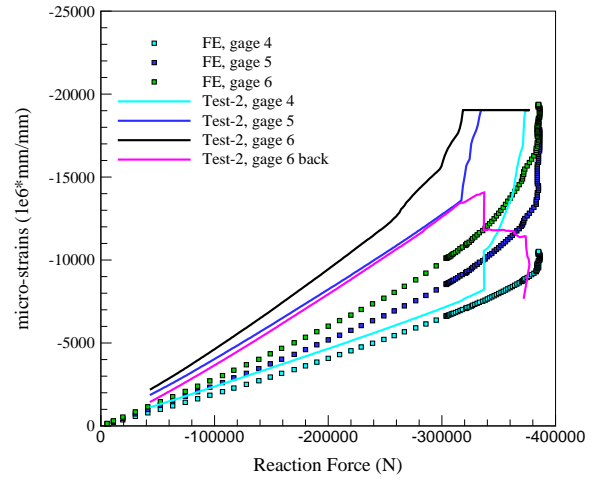
(a) Test-1, left gages



(b) Test-1, right gages

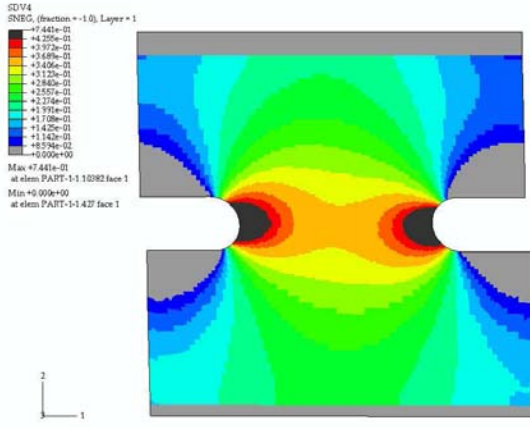


(c) Test-2, left gages

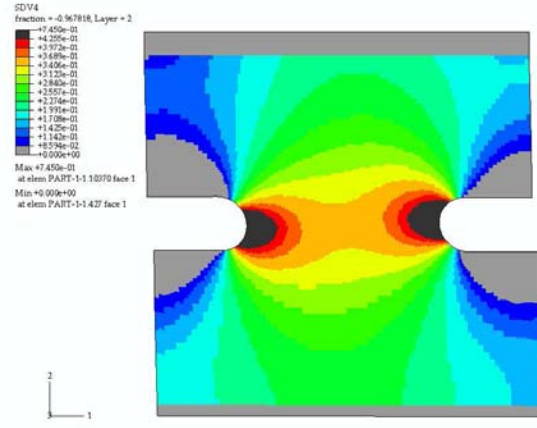


(d) Test-2, right gages

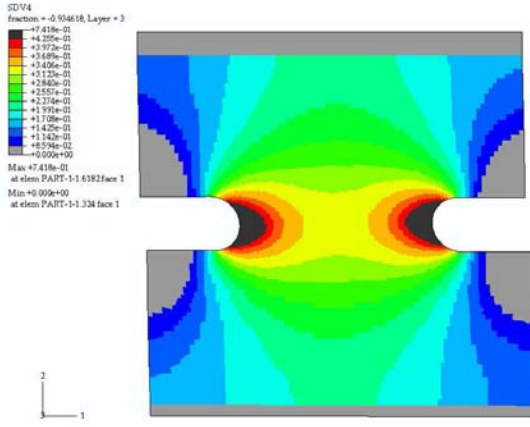
Figure 18. Comparison of measured strain data from experiments with the FE results. Locations of the strain measurement stations on the experimental specimen are given in Table 6.



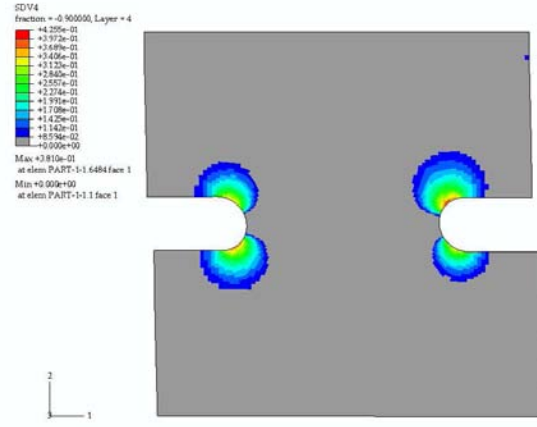
(a) 45^0 Layer



(b) -45^0 Layer

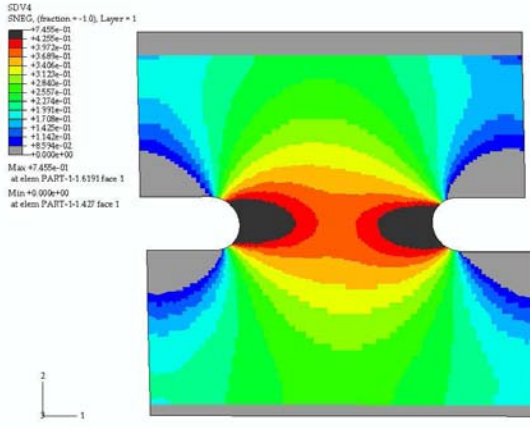


(c) 0^0 Layer

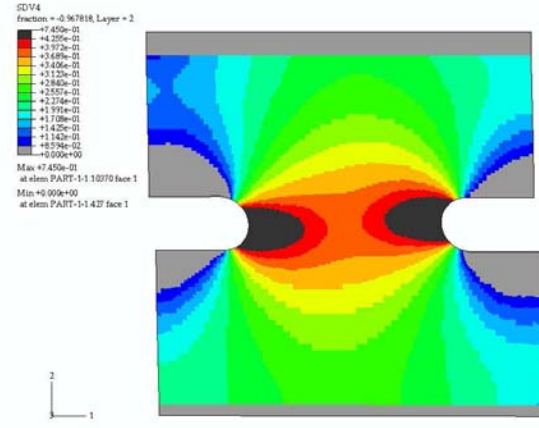


(d) 90^0 Layer

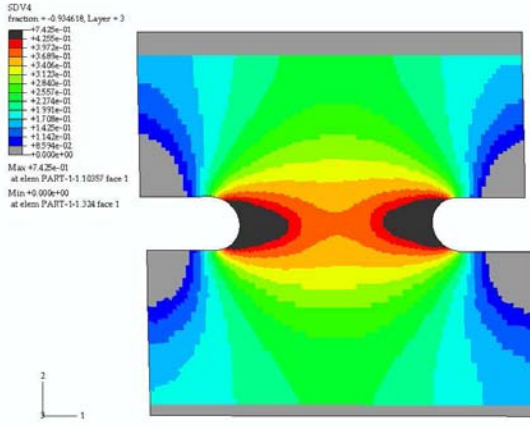
Figure 19. Contours of the damage variable S_r shown at a global load of 350 KN. The contours are shown for the top four layers. Orientation of the layers are given with respect to the global x-direction. The dark areas in these contours correspond to 55% or higher degradation in shear stiffness.



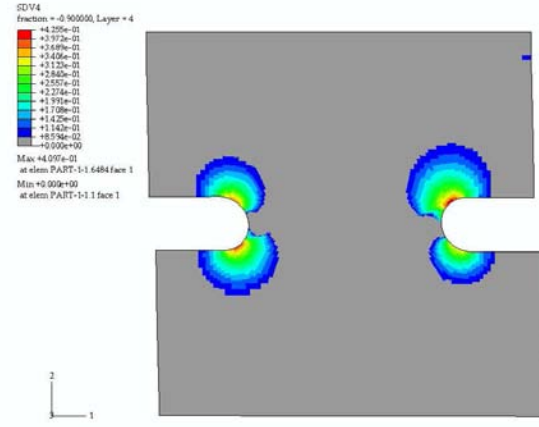
(a) 45^0 Layer



(b) -45^0 Layer

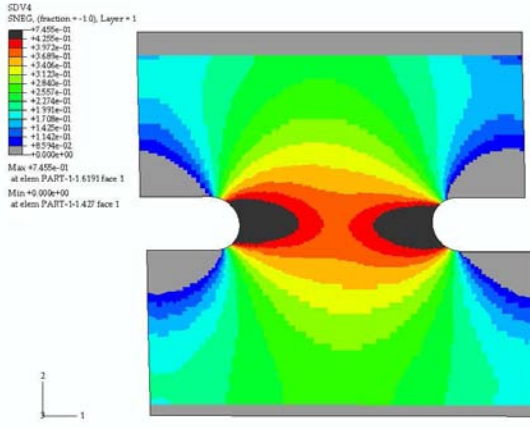


(c) 0^0 Layer

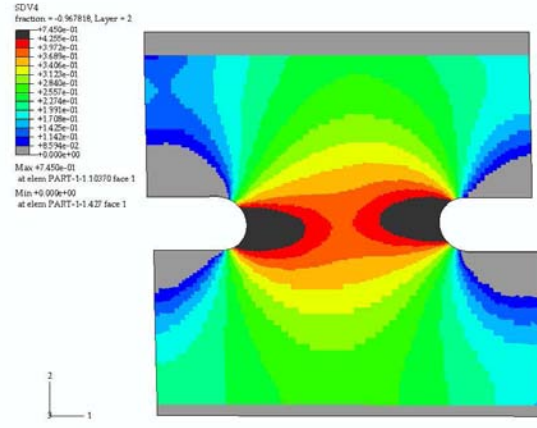


(d) 90^0 Layer

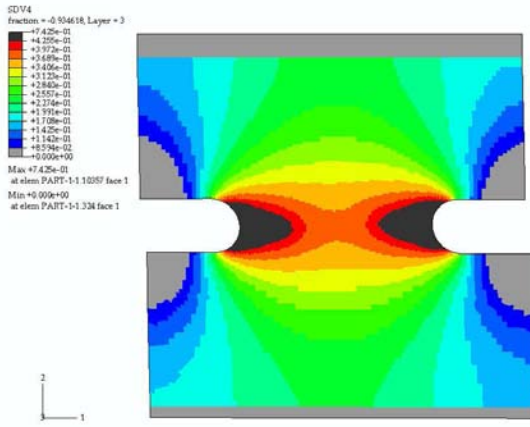
Figure 20. Contours of damage variable S_r at the peak load of 386 KN. The *in situ* shear modulus of the band of material between the two notch tips is 50% of their undamaged value.



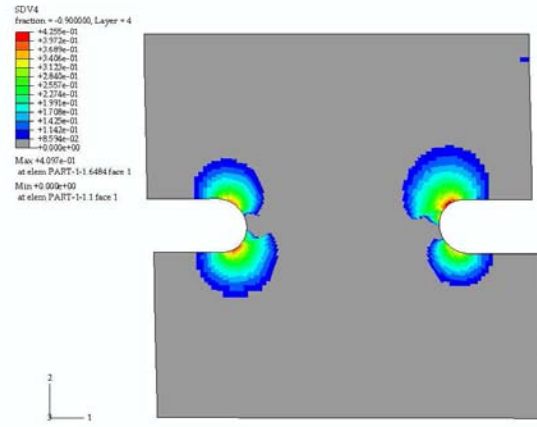
(a) 45^0 Layer



(b) -45^0 Layer



(c) 0^0 Layer



(d) 90^0 Layer

Figure 21. Contours of damage variable S_r at a global load of 384 kN (the final point of the FE P- Δ response curve).

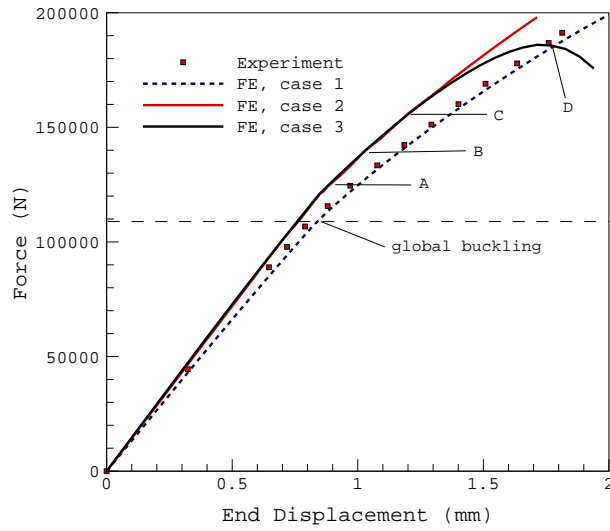


Figure 22. Load-vs.-load point displacement data for the FSP specimen. Locations A, B, C and D represent various damage events occurring in the laminate and are explained in Table 7.

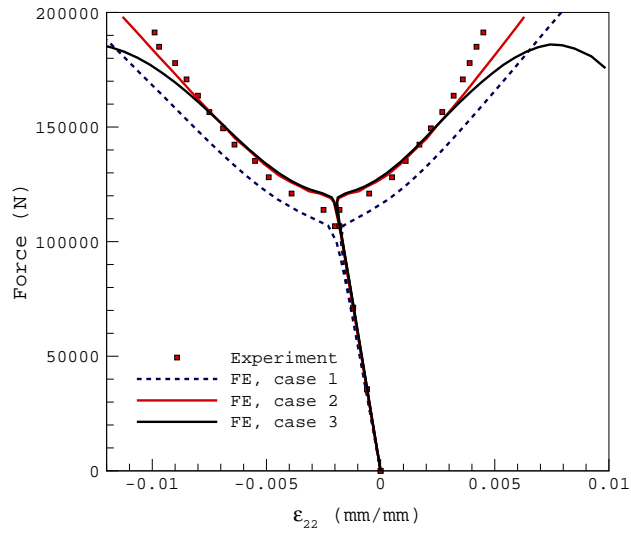
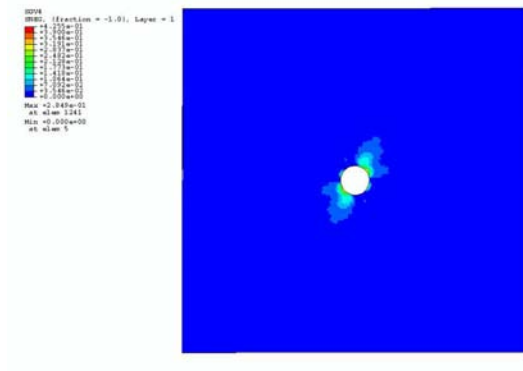
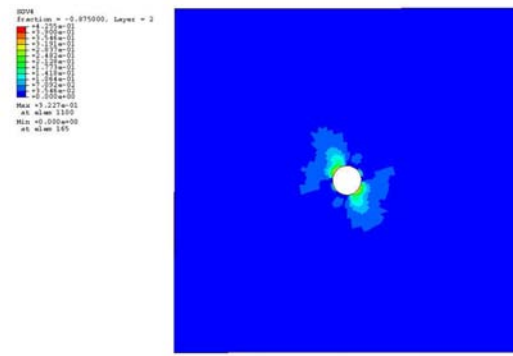


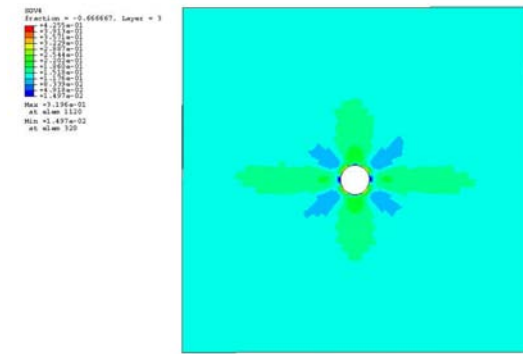
Figure 23. Transverse Strain (ϵ_{22}) data at location X (Figure 8) plotted against global load for the FSP specimen.



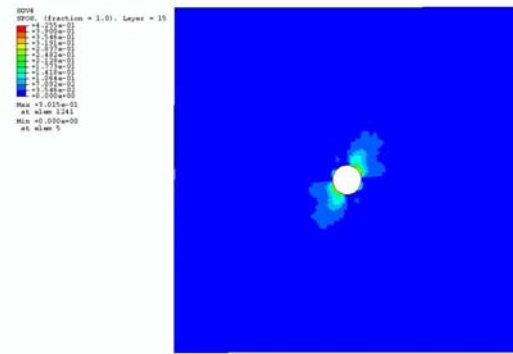
(a) Top 45⁰ Layer



(b) -45⁰ Layer

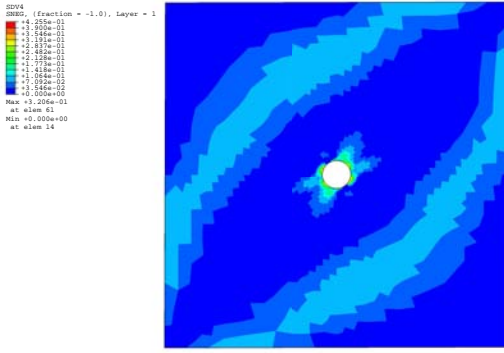


(c) 0⁰ Layer

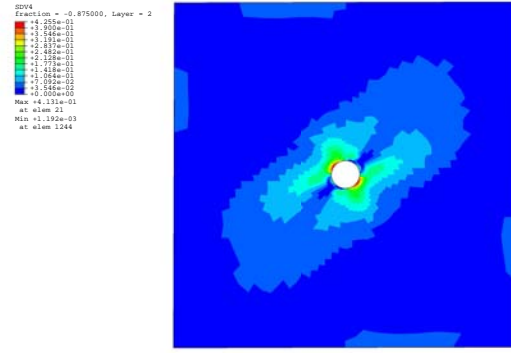


(d) Bottom 45⁰ Layer

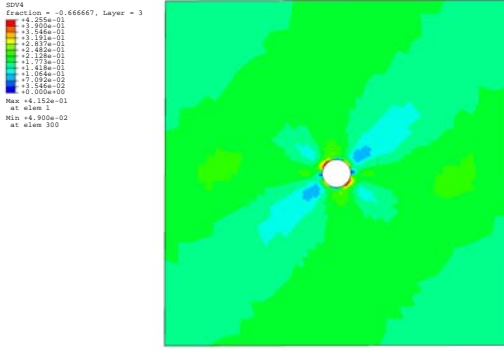
Figure 24. Contours of the damage variable S_r shown at a global load of 100 KN. The contours are shown for the top three layers and the bottom layer. Orientation of the layers are given with respect to the global x-direction. The grey areas in these contours correspond to a shear stiffness loss of 55% or higher.



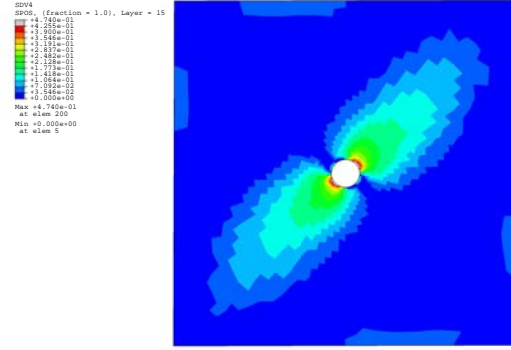
(a) Top 45° Layer



(b) -45° Layer

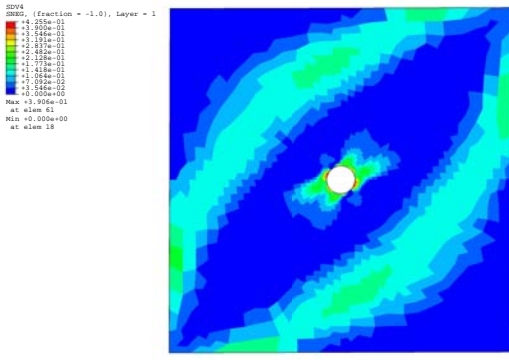


(c) 0° Layer

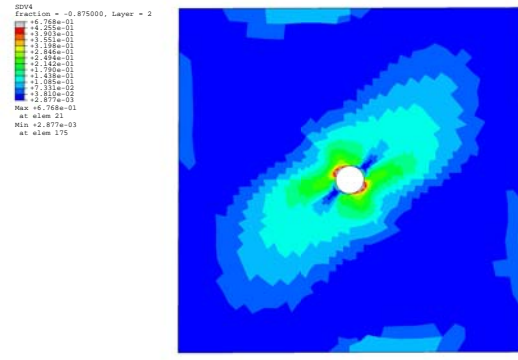


(d) Bottom 45° Layer

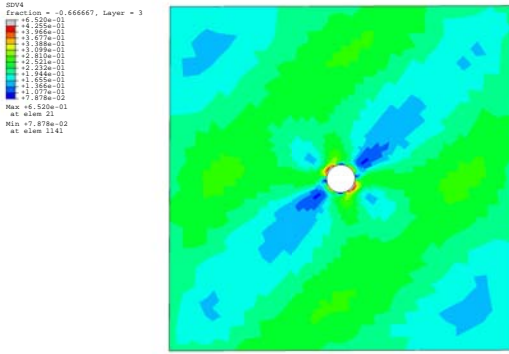
Figure 25. Contours of damage variable S_r at event A ($P = 124$ KN).



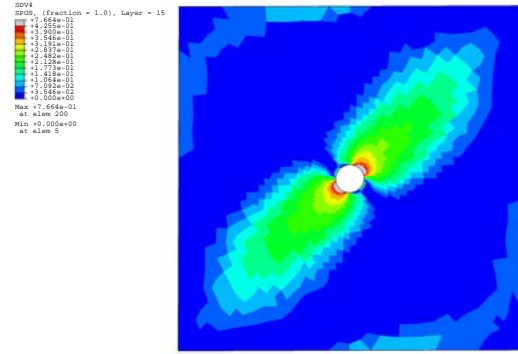
(a) Top 45° Layer



(b) -45° Layer

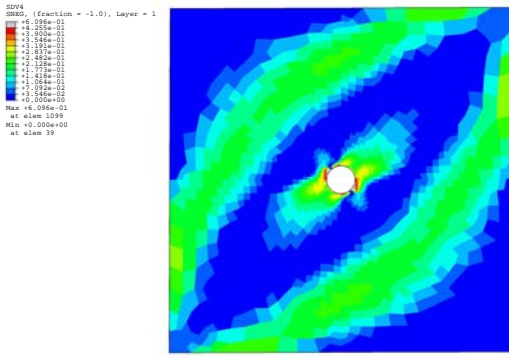


(c) 0° Layer

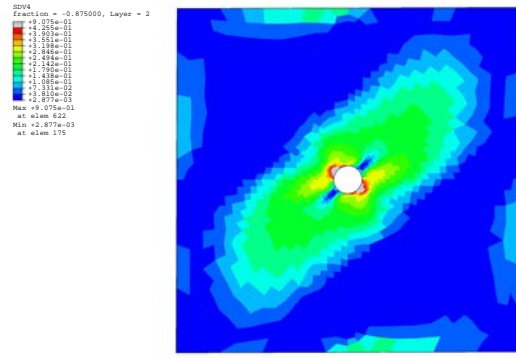


(d) Bottom 45° Layer

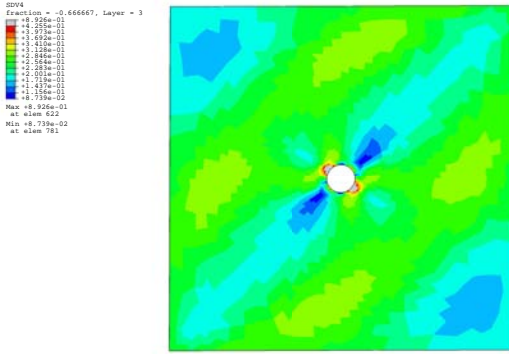
Figure 26. Contours of damage variable S_r at event B ($P = 140$ KN). Tensile failure initiates in the topmost layer.



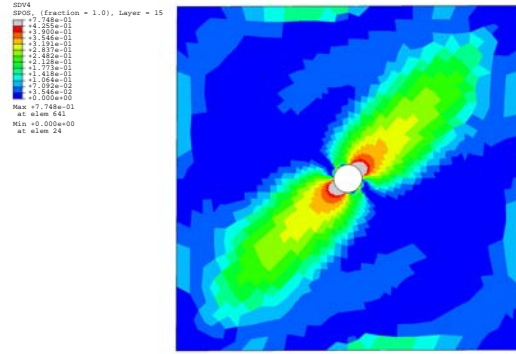
(a) Top 45° Layer



(b) -45° Layer

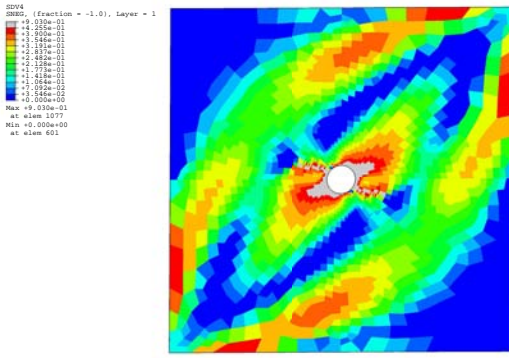


(c) 0° Layer

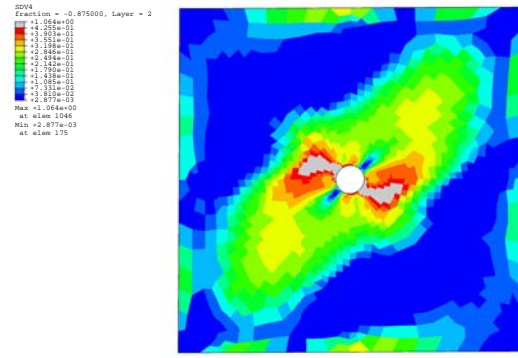


(d) Bottom 45° Layer

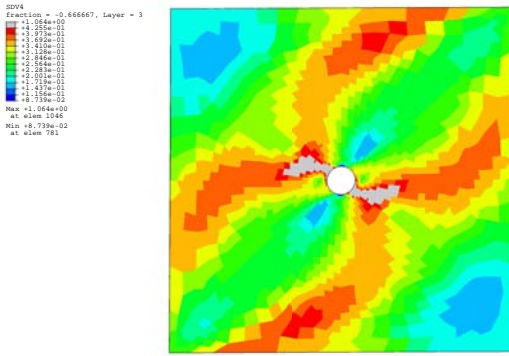
Figure 27. Contours of damage variable S_r at event C ($P = 156$ KN). Tensile failure initiates in the bottommost layer.



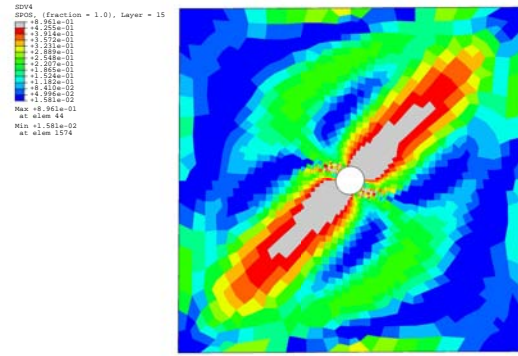
(a) Top 45° Layer



(b) -45° Layer

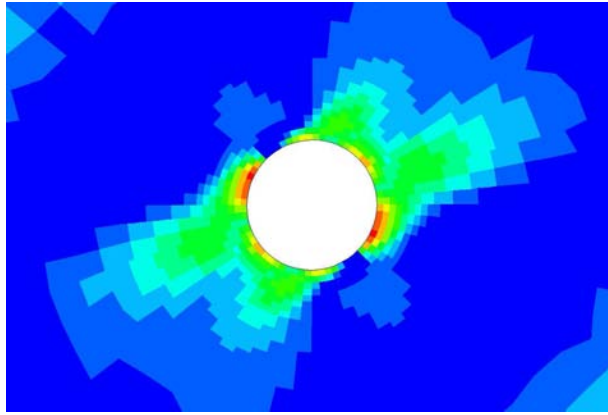


(c) 0° Layer

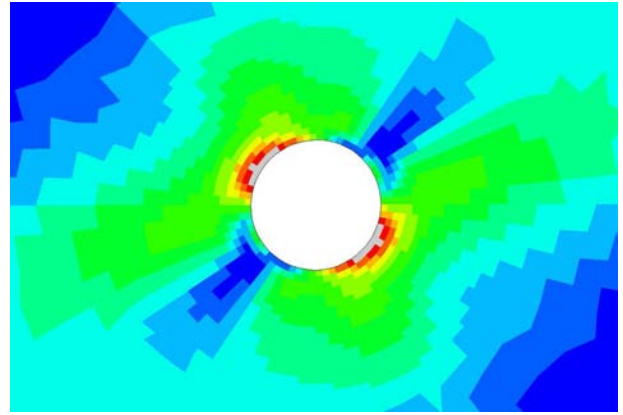


(d) Bottom 45° Layer

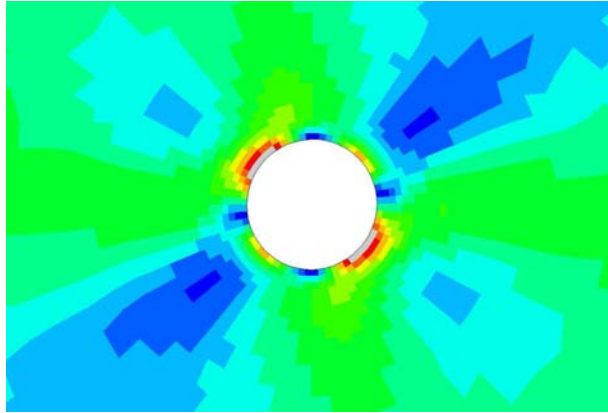
Figure 28. Contours of damage variable S_r at event D ($P = 186$ KN). Peak load is obtained in the system.



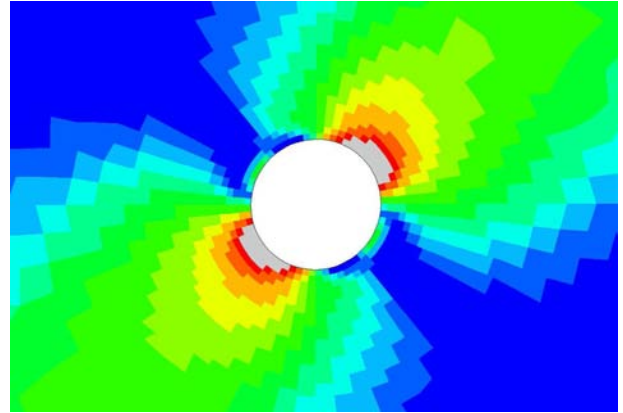
(a) Top 45° Layer



(b) -45° Layer

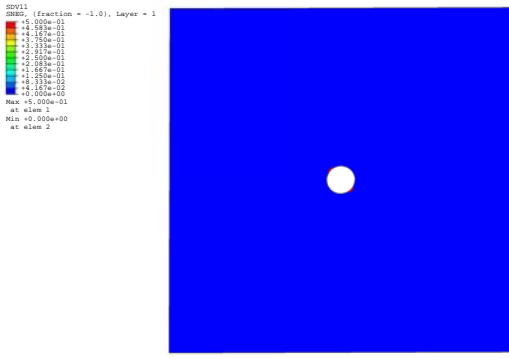


(c) 0° Layer

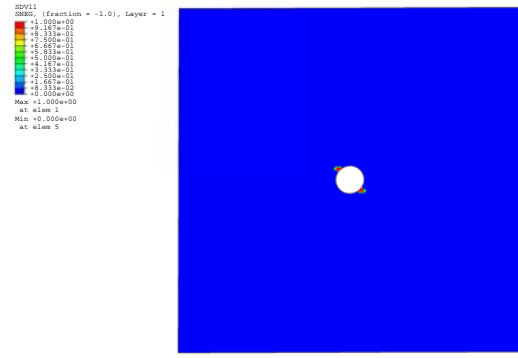


(d) Bottom 45° Layer

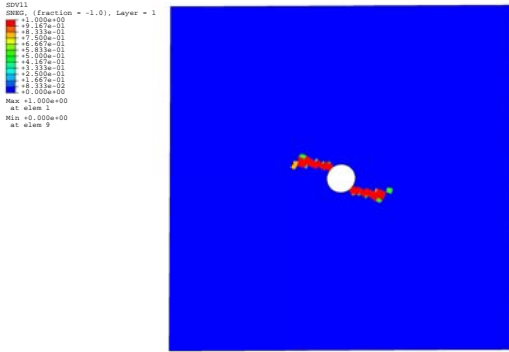
Figure 29. Close ups of contours of the damage variable S_r at event B. The contours show that the inner layers are at a higher level of damage compared to the top layers at the location of tensile failure. The bottom most layer is overall at a higher level of damage compared to the top layer



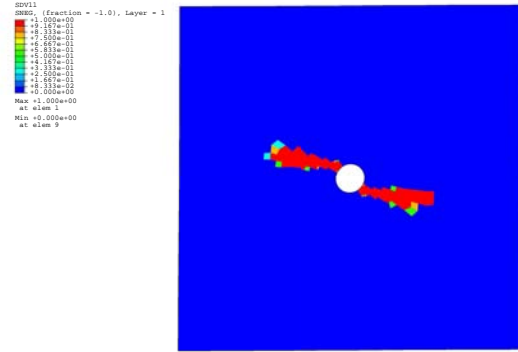
(a) $P = 140$ KN



(b) $P = 156$ KN



(c) $P = 186$ KN



(d) $P = 176$ KN

Figure 30. Contours of tensile failure in the topmost layer at various points during loading. Tensile failure coupled with off-axis layer shear damage will lead to ultimate failure at the locations indicated.

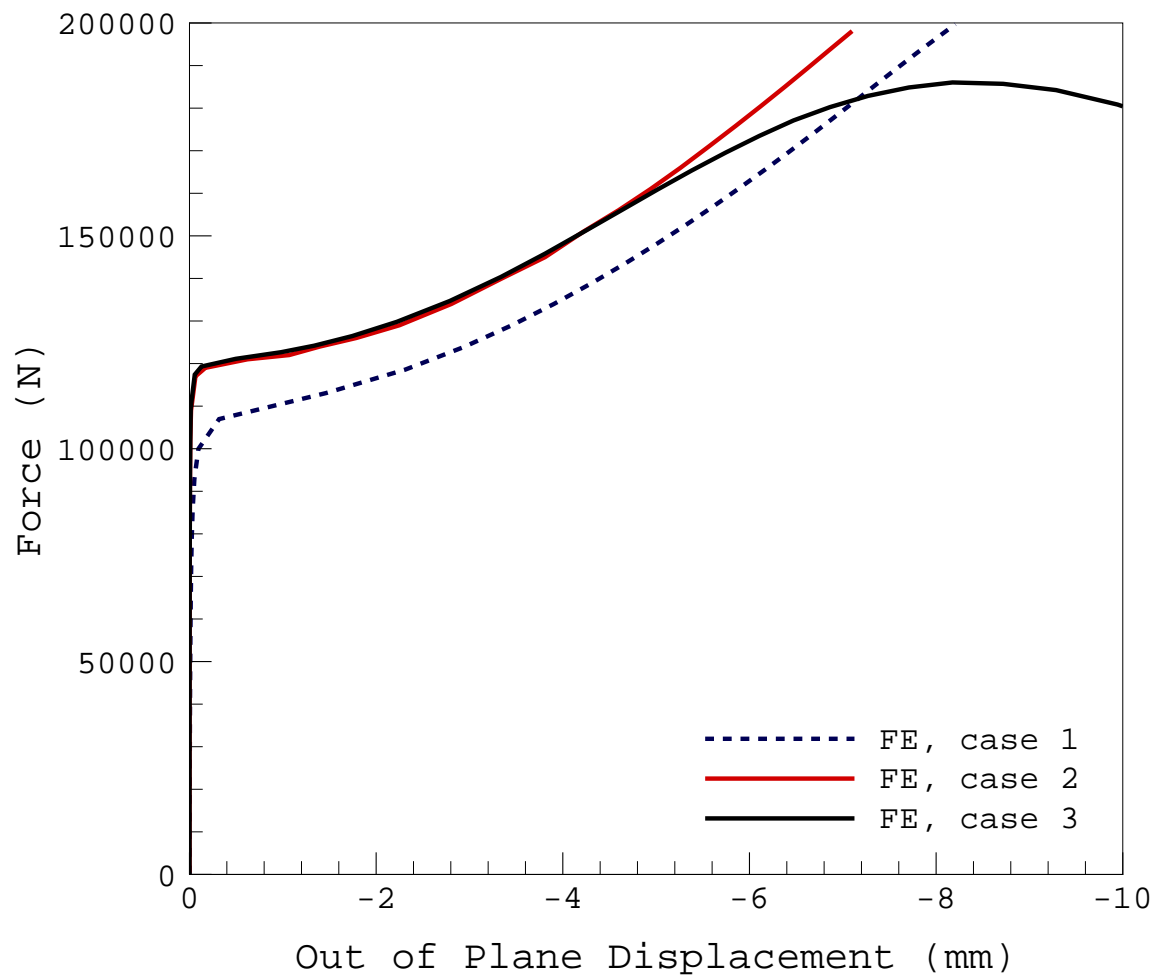


Figure 31. Out-of-plane displacement(w) at the cut-out boundary (Figure 8).

This page left blank intentionally.

Buckling and Failure of Compression-loaded Composite Cylindrical Shells with Reinforced Cutouts

Mark W. Hilburger* and Michael P. Nemeth*

NASA Langley Research Center, Hampton Virginia 23681-2199

Results from a numerical and experimental study that illustrate the effects of selected cutout reinforcement configurations on the buckling and failure response of compression-loaded composite cylindrical shells with a cutout are presented. The effects of reinforcement size, thickness, and orthotropy on the overall response of compression-loaded shells are described. In general, reinforcement around a cutout in a compression-loaded shell can retard or eliminate the local buckling response and material failure near the cutout and increase the buckling load of the shell. However, some results show that certain reinforcement configurations can cause a significant increase in the local interlaminar failures that can accumulate near the free edges of a cutout during a local buckling event.

I. Introduction

Thin-walled shell structures are a fundamental component found in aircraft, spacecraft, and launch vehicles. In many applications, these structural components contain cutouts or openings that serve as doors, windows, or access ports, or are used to reduce weight. Often, some type of reinforcement is used around a cutout to eliminate local deformations and stress concentrations that can cause local buckling or premature material failures. Thus, it is important to understand how a cutout affects the baseline performance of a shell structure without a cutout, how loads are redistributed by cutout reinforcement, and how cutout reinforcement can be tailored to enhance performance and reduce weight. In addition, it is important to understand performance enhancements that can be obtained by using lightweight fiber-reinforced composite materials. Furthermore, these structures usually experience compression loads during vehicle operation and, as a result, their buckling response and failure characteristics must be understood and accurately predicted in order to develop efficient, safe designs.

Many numerical and experimental studies of the buckling behavior of cylindrical shells have been conducted since the early 1900s. It took nearly 100 years to reach the point where robust, high-fidelity analysis tools and measurement technologies were available that could be used to conduct test-analysis correlations that include the effects of initial geometric, material, and manufacturing imperfections and the effects of load introduction and support conditions. Two noteworthy studies conducted at the NASA Langley Research Center that document these advanced capabilities are given in Refs. 1 and 2. It is worth pointing out that these two studies show that differences as small as 5% between corresponding analytical and experimental results can be obtained for buckling and postbuckling of compression-loaded, laminated-composite, circular cylindrical shells. This small difference is on the same order as the error that inherently exists in the use of nominal material properties. Thus, technology and physical insight now exists that can be used to develop greatly improved buckling design criteria, such as that presented in Ref. 3. An important part of such an effort would, of course, need to include the effects of cutouts on the buckling performance.

In contrast to the body of work that exists for complete cylindrical shells and curved panels, studies that address the effects of a cutout on the buckling performance of cylindrical shells didn't appear until 1968.⁴ Since 1968, only about 20 studies have appeared that address the effects of unreinforced cutouts and that focus on the buckling behavior of compression-loaded isotropic and laminated-composite circular cylindrical shells and curved panels.⁵⁻²⁵ Some of the general lessons learned from these studies are as follows. The presence of a cutout in an isotropic circular cylindrical shell can cause a localized response to occur near the cutout when the shell is loaded. This localized response typically consists of large out-of-plane deformations, large-magnitude stress concentrations, and rapidly varying stress gradients near the cutout. In a compression-loaded circular cylindrical shell, the cutout may cause a local buckling response to occur in the shell, near the cutout, at applied loads lower than the general instability load of the corresponding shell without a cutout. For some cases, this localized buckling is followed by a

* Senior Research Engineer, Mechanics of Structures and Materials Branch.

stable postbuckling response near the cutout, which is indicated by the fact that additional load can be applied to the shell before it exhibits overall collapse. However, other cases have shown that a local response in the shell can occur that causes a disturbance with enough kinetic energy to cause overall collapse to occur immediately after the local buckling occurs. Starnes^{6, 11} suggested that the buckling of compression-loaded isotropic shells with a cutout is governed by the nondimensional geometric parameter $\tilde{a} = a^2/Rt$, where a is the characteristic cutout dimension and R and t are the shell radius and thickness, respectively. In addition, Starnes identified approximate ranges of the \tilde{a} parameter that corresponded to the various behavioral trends described above.

For shallow, isotropic curved panels with a central circular cutout and subjected to compression loads, it has been found that cutout size greatly affects the nonlinear behavior. For example, it has been shown that curved panels with relatively small cutouts exhibit a linear prebuckling state followed by an unstable global buckling response and those with somewhat larger cutouts exhibit a nonlinear prebuckling state followed by an unstable global buckling response. As the cutout size gets even larger, the panels exhibit a monotonically increasing load–end-shortening response. These results suggest that traditional linear bifurcation buckling analyses may misrepresent the physics of the response for a certain range of cutout sizes because of significant nonlinear behavior and should not be used for design.

Numerical and experimental studies of the response of compression-loaded, laminated-composite, circular cylindrical shells with unreinforced rectangular cutouts indicate similar response characteristics to those exhibited by the corresponding isotropic shells. In addition, results have shown that localized regions of biaxial membrane compression stresses form in the shell near the cutout and that these regions of biaxial stresses couple with radial deformations of the shell wall, causing an unstable local buckling response to occur near the cutout. Hilburger et al.^{19, 20} has shown that the buckling of compression-loaded anisotropic shells with a cutout is governed by a stiffness-weighted nondimensional geometric parameter, similar to that proposed by Starnes, and a stiffness-weighted cutout aspect ratio. In addition, the initial local buckling and postbuckling response near the cutout are characterized by large-magnitude deformations and stresses that cause material failure. Furthermore, laminate orthotropy and initial shell imperfections have been shown to have a significant effect on the nonlinear response and buckling behavior of a laminated-composite, circular cylindrical shell with a cutout.

Results for shallow, laminated-composite, curved panels with a central circular cutout and subjected to compression loads indicate similar trends to those exhibited by the corresponding isotropic shells. However, whether the panel exhibits an unstable snap-through-type buckling response or a monotonically increasing load-end-shortening response, depends significantly on the panel orthotropy and anisotropy. Furthermore, numerical and experimental studies have identified cases where panels exhibited large-magnitude radial prebuckling deformations and buckling loads that exceeded the classical linear bifurcation buckling load. This behavior is contrary to previously known behavioral characteristics of compression-loaded shallow curved panels. It was determined that these response characteristics are caused by circumferential edge restraint on the loaded boundaries of the panels and indicated a high degree of boundary condition sensitivity.

Very few studies of the response of compression-loaded circular cylindrical shells and curved panels with reinforced cutouts have been conducted, and the majority of results that do exist are limited to isotropic shells (e.g., Refs. 13, 26). However, a recent numerical study of the response of compression-loaded, laminated-composite shells with reinforced cutouts was presented by Hilburger and Starnes.^{27, 28} This work predicts that reinforcement can be placed around a cutout in a compression-loaded shell that will affect the local deformations and stresses near the cutout such that the onset of local buckling near the cut is retarded or suppressed, compared to the corresponding shell without cutout reinforcement. For some reinforcement configurations, the local buckling response is followed by a stable, local postbuckling response near the cutout and additional load can be applied to the shell before it undergoes a global collapse. For other configurations, the analyses predict that the local buckling response causes a disturbance with enough kinetic energy to cause the global collapse immediately after local buckling occurs. For still other configurations, the results predict that the reinforcement suppresses local buckling near the cutout and causes overall buckling to initiate in the bending boundary-layer regions near the ends of the shell.

Review of the literature cited herein indicates that the response of a compression-loaded cylindrical shell with an unreinforced cutout is becoming better understood. In addition, studies have been conducted that address numerical simulation of progressive failure in compression-loaded, laminated-composite, curved panels with a central circular cutout.^{29, 30} However, the effects of cutout reinforcement on the buckling and failure of compression-loaded composite cylindrical shells, is not well understood. Therefore, the objective of the present study is to present numerical and experimental results that will identify typical buckling and failure response characteristics and trends for a compression-loaded, thin-walled, quasi-isotropic, laminated-composite, circular cylindrical shell with a square cutout and several cutout reinforcement configurations. This shell configuration represents a generic example of a typical aerospace shell structure with a cutout subjected to a destabilizing load. To accomplish this objective,

selected experimental and numerical results that illustrate the buckling response of compression-loaded shells with unreinforced cutouts are presented first. Then, similar numerical and experimental results that show the effects of several different reinforcement configurations on the response of these shell structures are presented. The various cutout reinforcement configurations considered were used to study the effects of reinforcement orthotropy, thickness, and size on the response of the shell. Results obtained from an advanced high-fidelity nonlinear analysis procedure that includes the effects of initial geometric imperfections, thickness variations, and nonuniform load introduction is used in the study and offers the opportunity to provide insight into the effects of various cutout reinforcement concepts on the buckling and failure response of compression-loaded shell structures. In addition, preliminary results from a progressive failure analysis of selected shells are presented and include intralaminar and interlaminar failure modes in the failure analysis. The results include load-shortening response curves, out-of-plane displacement response curves and displacement contours, and descriptions of the observed shell buckling and failure responses.

II. Test Specimens, Imperfection Measurements, and Tests

A. Test Specimens

Fifteen test specimens were fabricated and tested in this investigation and include three cylinders with an unreinforced square-shaped cutout, referred to herein as specimens C1-C3, and twelve cylinders with reinforced square-shaped cutouts, referred to herein as specimens C4-C15. The specimens were fabricated from 12-in-wide, 0.005-in.-thick AS4/3502 unidirectional graphite-epoxy tape material. The nominal unidirectional lamina properties of a typical 0.005-in-thick ply with a fiber volume fraction of 0.62 are as follows: longitudinal modulus $E_1 = 18.5$ Msi, transverse modulus $E_2 = 1.64$ Msi, in-plane shear modulus $G_{12} = 0.87$ Msi, and major Poisson's ratio $\nu_{12} = 0.30$. The material was laid up by hand on a 15.75-in-diameter mandrel and vacuum bagged and cured in an autoclave to form shells with different 8-ply shell-wall laminates. These laminates include an axially stiff $[\mp 45/0_2]_s$ laminate, a quasi-isotropic $[\mp 45/0/90]_s$ laminate, and a circumferentially stiff $[\mp 45/90_2]_s$ laminate (a 0° lamina ply and a 90° lamina correspond to plies with fibers aligned along the length of the cylinder and around its circumference, respectively). A 1.0-in by 1.0-in square cutout with 0.05-in-radius reentrant corners was machined in each cylinder at the shells mid-length. Twelve quasi-isotropic specimens were manufactured to include reinforcement around the cutout (specimens C4-C15). The addition of the reinforcement in the shell was achieved by including additional square-shaped pieces of unidirectional graphite-epoxy tape at the mid-surface of the laminate, aligned concentrically with the position of the square cutout. After curing, the cutout was carefully machined in the center of the reinforced region of the specimen thus creating a cutout with an annular region of reinforcement around its perimeter. Six reinforcement stacking sequences were considered in the present study that include 0 , 0_2 , 0_4 , 90 , 90_2 , and 90_4 lay-ups. Three reinforcement sizes were also considered that include 2.4-in by 2.4-in square, 4.4-in by 4.4-in square, and 8.0-in by 8.0-in square reinforcements. A list of shell identification codes and the corresponding reinforcements are given in Table 1. It is important to note that because the specimens were laid up on a uniform-diameter cylindrical mandrel, the shell-wall mid-surface in the region of the reinforcement had a radial eccentricity with respect to the nominal shell-wall mid-surface. The specimens had a nominal length L equal to 16.0 in., a nominal radius R equal to 8.0 in, and a nominal shell-wall thickness t_{nom} equal to 0.04 in. Both ends of the specimens were potted in an aluminum-filled epoxy resin to ensure that the ends of the specimen did not fail prematurely during the test. The potting material extended approximately 1.0 inch along the length of the specimens at each end, resulting in a test section that is approximately 14.0 in long. The ends of the specimens were machined flat and parallel to a tolerance of ± 0.001 in. to facilitate uniform load introduction during the tests. A typical cylinder specimen with a centrally located square cutout is shown in Fig. 1.

B. Imperfection Measurements

Three-dimensional surveys of the inner and outer shell-wall surfaces of the specimens were made prior to testing to determine the initial geometric shell-wall imperfection shape and the shell-wall thickness distribution. Measurements were taken over a uniform grid with increments of 0.125 in. in the axial direction and 0.139 in. (approximately 1° of arc) in the circumferential direction over the exposed surfaces of each specimen. The inner surface measurement was used to determine the initial shell-wall geometric imperfection shape and the difference between the outer and inner surface measurements was used to determine the shell-wall thickness distribution. A plot of a typical nondimensionalized initial shell-wall geometric imperfection is shown in Fig. 2. The measured shell-wall imperfection w_0 is nondimensionalized by the nominal shell-wall thickness $t_{nom} = 0.04$ inches of the

unreinforced region of the shell. These results indicate that the initial geometric imperfection is periodic in the circumferential direction and has slight variations in the axial direction. The amplitude of the normalized shell-wall geometric imperfections of the specimens range from $-1.33t_{nom}$ to $2.0t_{nom}$. A plot of a typical shell-wall thickness variation is shown in Fig. 3. The measured shell-wall thickness t_o is nondimensionalized by the nominal shell-wall thickness t_{nom} . These results indicate that the shell-wall thickness in the unreinforced region of the shell typically varies within each specimen from 0.93 to 1.3 times t_{nom} . The square-shaped reinforced region in this shell is clearly visible in the plot and indicates a thickness that ranges from 1.45 to 1.6 times t_{nom} and is typical for a four-ply-thick reinforcement that is nominally 1.5 times t_{nom} . Most of the thickness variation throughout the specimen is attributed to local variations in the resin content of the laminate and outer-surface texture that results from the laminate fabrication process. However, gaps between adjacent pieces of graphite-epoxy tape in some of the laminate plies are generated during the lay-up and curing process. Such a region is referred to as a ply-gap. These locally thin regions of the shell wall have, associated with them, a significant mid-surface eccentricity and a reduced stiffness. The observed ply-gaps in the specimens have widths as large as 0.1 in. Similarly, local thick regions, other than the reinforcement, are attributed to ply overlaps.

To help characterized nonuniform load introduction effects, measurements of the top and bottom loading surfaces of the specimens were made at one-degree increments around the circumference of the specimen to determine the variation in the shell-end or loading-surface geometry. A typical top and bottom shell-end imperfection are denoted by δ_{top} and δ_{bot} , respectively, and are shown in Fig. 4. The average maximum amplitude of this shell-end or loading-surface variation is approximately ± 0.0005 in., and corresponds to less than 0.01% of the nominal specimen length.

C. Test Apparatus and Instrumentation

The specimens were instrumented with electrical-resistance strain gages. In particular, sixteen back-to-back pairs of uniaxial strain gages were positioned around the perimeter of the cutout edge to characterize the rapidly varying strain gradients that develop during loading. These gages were aligned tangent to the cutout edge at the four corners and at the mid-length of each of the four sides, as shown in Fig. 5. In addition, far-field strain gages were positioned at several locations around the specimen to characterize the prebuckling load introduction into the specimen and load redistribution after local and global buckling occurs.

Direct-current differential transducers (DCDTs) were used to measure displacements. In particular, several DCDTs were positioned in the interior of the specimen to measure radial displacements near the cutout, as shown in Fig. 5a. In addition, three non-collinear DCDTs were positioned at three corners of the upper loading platen and used to measure the end-shortening displacement and the loading platen rotations, as shown in Fig. 1. Typical measured upper loading platen rotations r_y and r_z for a compression-loaded cylinder with a cutout are shown in Fig. 6, where r_y and r_z denote dextral rotations about the y and z axis, respectively. These results indicate that significant loading platen rotation occurs from the onset of loading up to a load level of approximately $P/P_{cr} = 0.1$. These rotations are attributed to initial misalignments between the specimen and the loading platen. The loading platen reaches an equilibrium position at approximately $P/P_{cr} = 0.1$, and the loading of the specimen, for the most part, continues with out appreciable additional rotations until buckling occurs.

A shadow moiré interferometry technique was used to observe the shell-wall prebuckling, buckling, and postbuckling radial deformation patterns. All data were recorded with a data acquisition system, and the moiré patterns were recorded photographically, on videotape, and with a high-speed digital video camera. The high-speed digital video camera recorded images at a rate of 2000 Hz.

The specimens were loaded in compression with a 120-Kip hydraulic universal-testing machine by applying an end-shortening displacement to the shell ends (loading surfaces) of a specimen. To control the load introduction into the specimen, the upper loading platen was aligned with the loading surface of the specimen before the test by adjusting leveling bolts in the corners of the upper loading platen until strains measured by selected far-field strain gages on the specimens indicated a uniform axial strain distribution around the circumference of the shell. The specimens were loaded until global collapse and failure of the shells occurred.

III. Finite-element Models and Analysis Methods

A. Finite-Element Models

All the shells considered in this study were analyzed with the STAGS (Structural Analysis of General Shells) nonlinear shell analysis code.³¹ STAGS is a finite-element code designed for the static and dynamic analysis of general shells, and includes the effects of geometric and material nonuniformities and progressive interlaminar and intralaminar material failure. The cylinders were modeled using the standard 410 quadrilateral elements from the

STAGS element library. This element is a flat facet-type element based on Kirchhoff-Love thin shell theory and the nonlinear Lagrangian strain tensor. Geometrically imperfect shells were analyzed in the present investigation and the finite-element models used herein are based on similar high-fidelity cylinder models developed previously for predicting the elastic buckling response of geometrically perfect and imperfect compression-loaded cylinders.^{1,2} The geometrically imperfect models include the effects of the measured shell imperfections to more closely simulate the response of the specimens. The imperfection considered include, initial shell-wall geometric imperfections, shell-wall thickness variations, thickness-adjusted lamina properties, and nonuniform load introduction effects. A more thorough explanation of model development and validation procedures for high-fidelity modeling of imperfect compression-loaded composite laminated shells with and without cutouts is presented in Refs. 1 and 2. In addition, selected models were modified to include the effects of progressive intralaminar and interlaminar material failures and preliminary results from these analyses are presented herein. The progressive failure methodology is described next.

B. Progressive Failure Methodology

Intralaminar material failures were predicted by using the Hashin³² failure criteria. The progressive failure theory and implementation are discussed in Ref. 29 and 30. Some relevant details are presented subsequently.

The intralaminar failure modes considered include matrix cracking, fiber-matrix shear failure, and fiber failure. To apply the failure criterion, the stress state is analyzed at each material point in the finite element model for a given solution step in the analysis. If the failure criteria is met (i.e., if the Hashin failure index exceeds a value of 1.0) then it is assumed that the material at point has failed and the material stiffnesses at that point are then degraded according to the Chang and Lessard degradation model.³³ Material allowables used in the present study for AS4/3502 material are as follows: in-plane shear stress allowable $S_{I2} = 25.5$ ksi, longitudinal tension and compression stress allowables $X_t = 200.0$ ksi and $X_c = 180.0$ ksi, respectively, and transverse tension and compression stress allowables $Y_t = 12.6$ ksi and $Y_c = 24.6$ ksi, respectively.

The initiation and progression of interlaminar, delamination failures are predicted by using a decohesion element that is positioned between composite laminae in potential delamination locations. A material-softening constitutive law developed by Goyal et al.³⁰ is used in the formulation of the decohesion element. This constitutive law governs the initiation of a delamination and the subsequent delamination growth. The initiation of a delamination is specified to occur when the maximum interfacial strength between plies is exceeded and subsequent propagation of the delamination occurs when the fracture energy release rate is exceeded. The interfacial material failure properties used in the present study for AS4/3502 are as follows: the critical energy release rates $G_{Ic} = 1.13$ lb/in., and $G_{IIc} = G_{IIIc} = 3.3$ lb/in. The maximum interfacial strengths $T_1^c = 9.0$ ksi, and $T_2^c = T_3^c = 10.5$ ksi. The decohesion element was implemented in the STAGS finite-element code as a user-defined element.

IV. Results and Discussion

Numerically predicted and experimentally measured results for fifteen compression-loaded composite cylindrical shells with unreinforced and reinforced cutouts are presented in this section. The predicted results were obtained from finite-element analyses of geometrically imperfect shells that include the effects of initial shell-wall geometric imperfections, shell-wall thickness variations, thickness-adjusted lamina properties, and nonuniform load introduction effects. First, results are presented for three cylinders with different laminate stacking sequences and with unreinforced cutouts to illustrate the effects of laminate orthotropy on the buckling and failure response of the shells and to provide a baseline for comparison with the corresponding shells with reinforced cutouts. Then, similar results are presented for selected quasi-isotropic shells with reinforced cutouts to illustrate the effects of reinforcement orthotropy, size and thickness on the buckling and failure response of the shells. Finally, overall response trends are identified and discussed. The results include load-shortening response curves, load versus out-of-plane displacement response curves, load-strain response curves, and observed and predicted radial deformation patterns and material failures. The values of axial load P , presented herein, are normalized with respect to the linear bifurcation buckling load of a geometrically perfect, quasi-isotropic cylinder without a cutout, $P_{cr}^0 = 42,590$ lb. Radial displacements are normalized by the nominal shell-wall thickness $t_{nom} = 0.04$ in. and end-shortening displacements are normalized by the specimen length $L = 16.0$ in., respectively.

A. Shells with an Unreinforced Cutout

Measured load-end-shortening response curves for the three cylinders with unreinforced cutouts, C1 ($[-\mp 45/0/90]_s$), C2 ($[\mp 45/0_2]_s$), and C3 ($[\mp 45/90_2]_s$), considered in this study, are shown in Fig. 7. Buckling loads are indicated by filled circles and global collapse loads are indicated by an **X**. The cylinders exhibit a linear prebuckling

load-shortening response up to buckling (note: the initial nonlinearity in the prebuckling response is attributed to the usual initial misalignment between the specimen and the loading platen). Cylinders C1 and C2 exhibit a local buckling response at normalized load levels of 0.48 and 0.39, respectively. The buckling response is characterized by a localized, unstable dynamic buckling event in the cylinder and includes the formation of large-magnitude radial deformations and rapidly varying strains near the cutout. It has been shown by Hilburger et al.^{19, 20} that this local buckling response is caused by nonlinear coupling between the compressive membrane biaxial stresses and the radial deformations that occur near the cutout. A stable post-local-buckling response is exhibited by specimens C1 and C2 and additional load is carried by these shells until global collapse occurs at load levels of 0.52 and 0.41, respectively. As loading continues in the post-local-buckling region of the response, these shells exhibit a slight reduction in the effective axial stiffness. This reduction in axial stiffness, manifested by a change in slope of the response curves, is caused by increasingly large out-of-plane deformations that develop in the shell and cause a redistribution of load away from the cutout, thereby reducing the effective load-carrying cross-section of the shell. The global collapse response is characterized by a significant reduction in axial load and the development of the general instability deformation pattern. Specimens C1 and C2 obtain stable post-collapse equilibrium at load levels of 0.32 and 0.23, respectively and can sustain additional loading until complete failure of the cylinders occurs due to significant accumulation of material failures in the shell wall. In contrast, shell C3 exhibits an unstable local buckling response, at a load of 0.51, that caused a catastrophic failure of the specimen and, as a result, there was no residual post-buckling strength for this specimen.

The results in Fig. 7 and results in Ref. 1 also indicate that the measured initial buckling load of specimens with a cutout are an average of 37.3% less than the measured buckling loads of the corresponding specimens without a cutout. However, there are no noticeable differences in the prebuckling stiffnesses of the specimens with the same laminate, regardless of whether there is a cutout or not. Moreover, the measured post-buckling loads for specimens C1 and C2 after global collapse are 2.1 and 1.4% greater than the corresponding buckling loads for the shells without cutouts and indicates that, in some cases, the cutout can have a relatively small effect on the post-buckling strength of these specimens.

Measured out-of-plane displacements for specimens C1, C2, and C3 are shown in Fig. 8 and selected observed local buckling and global collapse radial deformation patterns for specimens C1 and C2 are shown in Figs. 9 and 10, respectively. The displacement measurements were taken at the upper right corner of the cutout. Positive displacement values correspond to inward radial deformations of the shell wall. The results in Fig. 8 indicate that the specimens exhibit small radial pre-buckling deformations. During the local buckling response, cylinders C1 and C2 exhibit radial displacements at the corner of the cutout equal to approximately -1.0 and +1.5 times the nominal shell-wall thickness, respectively. After global collapse, the specimens exhibit displacements of approximately +3.0 and +2.0 times the shell-wall thickness. Specimen C2 exhibits inward deformations throughout the local buckling and global collapse response at this corner of the cutout. The local-buckling deformation response consists of large ellipse-like buckles on either side of the cutout and are aligned in a helical or skew direction (see Fig. 10a). After additional load is applied, the specimen collapses into a general instability buckling pattern in which the local buckles near the cutout increase in size and magnitude, and additional buckles develop around the circumference of the specimen (see Fig. 10b). In contrast, specimen C1 buckles into an asymmetric local buckling deformation pattern with an outward displacement of the upper right corner of the shell, but then exhibits a snap-through response upon global collapse, as indicated in Fig. 8. The asymmetric local buckling deformations are shown in Fig. 9a and the global collapse deformations are shown in Fig. 9b. The apparent snap-through behavior in specimen C1 is associated with a significant increase in the size and magnitude of the local inward buckle located at the right side of the cutout. This response causes the appearance of a local snap-through response in the measured displacements near the upper right corner of the cutout. The asymmetry in the deformation response is attributed to initial geometric imperfections in the specimen. Post-buckling displacement data for shell C3 has been omitted because the DCDT lost contact with specimen as a result of the buckling and failure event.

Typical measured strain results for specimens C1, C2, and C3 are shown in Fig. 11. The figure includes data from three axially aligned back-to-back strain gage pairs located at the right edge of the cutout in specimens C1-C3. The solid and dashed lines denote measured strain data from gages located on the outer shell-wall surface and the inner shell-wall surface, respectively. In general, the results indicate that specimens C1 and C2 exhibit some local bending during the prebuckling response, as indicated by the divergence of the back-to-back strain gage curves, and have maximum strains that approach 0.6% strain. The strains near the cutout in specimens C1 and C2 increase significantly when local buckling and global collapse occur and can exceed 2.0% strain. Once local buckling occurs, these large-magnitude bending strains near the cutout activate an interlaminar shear failure mechanism in specimens C1 and C2, as shown in Fig. 12 for specimen C1. The local interlaminar shear failures that developed in specimens C1 and C2 typically propagate approximately 0.5 in. beyond the free edge of the cutout around the

circumference of the shell. In contrast, specimen C3 exhibits significant bending from the onset of loading and these large-magnitude bending strains activate an interlaminar shear failure mechanism prior to buckling. The initial local failures that occur near the cutout in shell C3 propagated around the circumference of the specimen very rapidly and, as a result, this specimen had no post-buckling strength, as shown in Fig 13.

Predicted results were obtained for the three shell specimens with unreinforced cutouts and include load–end-shortening response curves; pre-buckling, buckling, and post-buckling deformations; and selected results that illustrate the progressive interlaminar and intralaminar failure response of these shells. Some of these results have been presented in Refs. 27 and 28, and thus, only highlights are presented here along with new results from a progressive failure analysis. In particular, predicted normalized buckling loads for shells C1, C2, and C3 that include the effects of initial imperfections and loading nonuniformities are 0.51, 0.40, and 0.56, respectively, and are approximately 6.0%, 2.5%, and 9.8% greater than the corresponding measured results. A summary of these measured and predicted buckling loads is presented in Table 1. In addition, results from a previous study presented in Ref. 1 indicate that the initial geometric imperfections and thickness variations cause a 13.9%, 2.6%, and 1.3% reduction in the buckling loads for shells C1, C2, and C3, respectively, with respect to the predicted linear bifurcation buckling loads for the corresponding geometrically perfect shells. The results suggest a relatively small degree of imperfection sensitivity for these shells. Similarly, nonuniform loading caused by shell-end imperfections and loading platen rotations caused a 12.2%, 31.2%, and 1.3% reduction in the buckling loads of shells C1, C2, and C3, respectively. In particular, the significant reduction in the buckling load exhibited by shell C2 is attributed to a relatively large magnitude shell-end imperfection that causes nonuniform end loading. The magnitude of this shell-end imperfection was approximately 60% of the magnitude of the end-shortening displacement of the shell at buckling. In addition, the predicted local buckling displacements and general instability displacements agree well with the observed displacements from the tests (see Figs. 9 and 10, for shells C1 and C2, respectively). For example, typical predicted initial local buckling deformations are shown for shell C1 in Fig. 14a and indicate an asymmetric buckling response in the shell near the cutout similar to that exhibited by specimen C1 shown in Fig 9. The asymmetry in the local response is attributed to an initial geometric imperfection in the shell wall near the cutout that appears to have a greater influence over the local deformations in shell than the cutout. Predicted intralaminar and interlaminar material failures incipient to global collapse for shell C1 are shown in Figs. 14b and 14c, respectively. The results indicate some intralaminar failures in the upper and lower right corners of the cutout in the form of matrix tension failures and fiber compression failures. However, the analysis also predicts the initiation and propagation of significant interlaminar shear-type failures near the free-edge of the cutout (see Fig 14c). The location and the extent of the damage in the shell appears to agree well with the observed damage shown in Fig. 12. Similar failure predictions were obtained for shell C2 and C3. Predicted delamination type failures in shell C2 are less pronounced than those predicted for shell C1 and agree well with the observed failure response in the shell. Preliminary failure predictions obtained for shell C3 indicate an increased potential for the initiation of interlaminar failures at the edges of the cutout and the rapid propagation of these delaminations around the circumference of the shell, as observed in the test (see Fig. 13). This increased potential for interlaminar shear failures is due to relatively large-magnitude bending strains ($> 1\%$ strain) and deformations near the cutout, as compared to the strains exhibited by shells C1 and C2. In addition, it is well established that delamination-type failures will initiate and propagate more easily in a structure where the lamina fibers are oriented parallel to the direction of propagation. However, convergence difficulties in the numerical solution associated with a rapid reduction in local shell wall stiffness during the quasi-static progressive failure analysis did not permit the analysis to predict the full extent of the catastrophic failure observed in the test. It may be possible to overcome these convergence difficulties by using a transient analysis capability in STAGS coupled with the progressive failure analysis capability, however, this analysis option is not currently available.

B. Shells with a Reinforced Cutout

The measured results for the compression loaded shells C1, C2, and C3 with unreinforced cutouts, presented in the previous section, and predicted results presented herein and in previous work¹, identified several features of the behavior that are associated with the local buckling and failure response of the shells. In particular, the nonlinear interaction between the local radial deformations and destabilizing biaxial stresses near the cutout cause the local buckling response to occur. The magnitude of the deformations and strains near the cutout, as indicated by DCDT and back-to-back strain gage measurements and verified by analysis, are affected by laminate orthotropy. Furthermore, local interlaminar shear failures develop near the cutout in the post-local-buckling region of loading and the extent to which these failures occur is affected by the local deformations and laminate orthotropy. These fundamental behavioral characteristics suggest that it may be possible to retard or eliminate the onset of the local

buckling and failure response near the cutout if a cutout reinforcement configuration can be identified that reduces the local deformations or the local stresses near the cutout.

Prior to conducting the test presented herein, a numerical parametric study was conducted to identify the effects of selected cutout reinforcement configurations on the response of similar compression-loaded shells with a cutout.^{27, 28} The reinforcements investigated consisted of square-shaped, concentrically aligned lamina plies added to the shell-wall mid-surface. Three reinforcement sizes and three reinforcement thicknesses, including 1-ply-thick, 2-ply-thick, and 4-ply-thick reinforcements, were studied to identify the effects of reinforcement size and thickness on the deformation response and stress distribution in the shell. In addition, two reinforcement ply orientations of 0° and 90° were investigated to study the effects of reinforcement orthotropy on the response. Some of the general trends identified in the study that are relevant to the tests presented herein are as follows. The reinforcement can retard or suppress the onset of local buckling in the shell near the cutout. For some cases, the local buckling response near the cutout results in a stable post-local-buckling response near the cutout and additional load can be applied to shell before global collapse. For other cases, the local response near the cutout in the shell causes a disturbance with enough kinetic energy to cause the overall collapse of the shell immediately following the local instability. The results indicate, for the most part, that the buckling load of a shell with a 90°-ply cutout reinforcement is greater than the buckling load of the corresponding shell with a 0°-ply cutout reinforcement.

Based on the results of the numerical study, described above, a similar set of twelve [F45/0/90]_s quasi-isotropic shells with reinforced cutouts were fabricated and tested to verify the predicted response trends (see Table 1). Selected measured results from these twelve compression-loaded shells, C4-C15, with 1.0-in-square reinforced cutouts are presented in this section to identify the potential for using cutout reinforcements to enhance the buckling and failure response of the shells with cutouts. The results for these shells are compared to results for the corresponding shell C1 with an unreinforced cutout. First, experimentally measured results that illustrate the effects of cutout reinforcement thickness and orthotropy on the typical buckling and failure response characteristics for compression-loaded shells with a 4.4-in.-square cutout reinforcement are presented. Then, results summarizing the effects of cutout reinforcement size, thickness, and orthotropy on the buckling and failure of a shell with a reinforced cutout are presented. Selected predicted results that were obtained from finite-element analyses of imperfect shells are also presented to illustrate the effects of initial imperfections on the buckling response of the shells.

1. 4.4-in. Square Reinforcement

Results for shells C4-C9 are presented in this section. The cutout reinforcements for shells C4 through C6 consist of 4.4-in square-shaped 0° lamina plies and the cutout reinforcements for shells C7-C9 consist of 4.4-in square-shaped 90° lamina plies. Measured load-shortening response curves for shells C1 (no reinforcement), and C4-C6 are presented in Fig. 15. The results show that the increasing the amount of reinforcement has a significant effect on the overall character of the shell response. In particular, the normalized buckling loads increase by as much as 56% as the thickness of the reinforcement increases. Specifically, the normalized buckling loads for shells C4, C5, and C6, with 0°-ply reinforcement are equal to 0.67, 0.74, and 0.75, respectively. The normalized buckling load for the corresponding unreinforced shell C1 is 0.48. In addition, the results indicate that the shells with the reinforcement do not exhibit stable post-local-buckling responses. For these shells, the local-buckling response causes a disturbance with enough kinetic energy to cause global collapse of the shell. After global collapse occurs, each shell has a stable post-collapse configuration, accompanied by a significant reduction in the axial load. The normalized post-collapse loads range from 0.26 and 0.27 for shells C4 and C5, respectively, to 0.34 and 0.35 for shells C1 and C6, respectively. In general, these response trends agree well with the corresponding numerically predicted results for geometrically perfect shells presented in Refs. 27 and 28 and the predicted buckling loads for imperfect shells presented in Table 1. In particular, the predicted buckling loads are 1.4%, 5.4%, and 6.7% greater than the experimentally measured results for specimens C4- C6, respectively.

Measured radial displacements for shells C1 and C4 through C6 are presented in Fig. 16, and observed out-of-plane deformations patterns of the local buckling and collapse response of shells C4-C6 are shown in Figs. 17-19, respectively. The displacement measurements were taken at the upper right corner of the cutout. Positive displacement values correspond to inward deformations of the shell wall. The moiré fringe patterns shown in Figs. 17-19 were obtained by using a high-speed digital video camera with a frame rate of 2000Hz. The dashed lines in Figs. 17-19 outline the edges of the cutout reinforcement. The results in Figs. 16-19 indicate that the shells pre-buckling and buckling deformation response near the cutout can change significantly with an increase in the reinforcement thickness. In particular, local buckling in shell C4 initiates near the cutout and is characterized by a rapid increase in local out-of-plane deformations, as indicated by the displacements incipient to and during the initial local buckling response, as shown in Fig. 16. At the onset of buckling, a local unstable response occurs in the shell

and is characterized by the development of localized ellipse-shaped buckles near the cutout, as shown in Figs. 17a (time = 0.0 seconds) and 17b (time = 0.001 seconds). This local buckling response in the shell triggers the global collapse of the shell, as indicated in Figs. 17c (time = 0.002 seconds) and 17d (time = 0.004 seconds), and is accompanied by a significant increase in the local displacements near the cutout. The density of the fringes in the moiré patterns is indicative of the shell-wall bending gradients. The post-collapse displacements near the corner of cutout are approximately +2.4 times the nominal shell-wall thickness. In contrast, the buckling response for shells C5 and C6 is characterized by a single, small-magnitude, ellipse-shaped buckle that forms at the edge of the cutout reinforcement, as shown in Figs 18a (time = 0.0005 seconds) and 19a (time = 0.0005 seconds), respectively. The local buckles are marked with an **X** symbol in the figures. At the onset of buckling, a local unstable response occurs in shell C5 and C6 that is characterized by a significant increase in the size and magnitude of the ellipse-shaped buckle, as shown in Figs 18b (time = 0.001 seconds) and 19b (time = 0.001 seconds), respectively. The lack of symmetry in the response is attributed to the effects of initial geometric imperfections in the shell wall. As the buckling process continues, the local buckles in the deformation pattern rapidly increase in number and become distributed around the circumference of the shell and are associated with the overall collapse of the shell, as shown in Figs 18c (time = 0.002 seconds) and 18d (time = 0.004 seconds) for shell C5, and Figs. 19c (time = 0.002 seconds) and 19d (time = 0.004 seconds) for shell C6. The post-collapse displacements near the corner of cutout in shell C5 are approximately +2.4 times the nominal shell-wall thickness and the overall character of the deformation pattern is similar to that exhibited by shell C4 shown in Fig. 17d. However, the post-collapse displacements and bending gradients near the cutout in shell C6 (see Figs. 19c and 19d) are reduced significantly, compared to shells C4 and C5 shown in Figs. 17d and 18d, respectively. Specifically, the moiré fringe patterns in Figs 19c and 19d indicate a marked reduction in local bending near the cutout as compared to the corresponding fringe patterns observed for shells C5 and C6.

Typical measured strain results for specimens C1, C4- C6 are shown in Fig. 20. The figure includes data from four back-to-back strain gage pairs at the upper right corner of the cutout, aligned tangent to the edge. The solid and dashed lines denote measured strain data from gages located on the outer shell-wall surface and on the inner shell-wall surface, respectively. The results show that the local pre-buckling and post-buckling bending strains near the cutout, indicated by the divergence of the curves for the back-to-back strains, are significantly reduced with an increase in the thickness of the reinforcement, as expected. In particular, local pre-buckling strains in shell C1 (unreinforced cutout) approach 5000 microstrain and rapidly increase to over $\pm 15,000$ microstrain (1.5% strain) during global collapse. In contrast, shell C6 exhibits relatively low-magnitude prebuckling strains of -1500 and -2500 microstrain on the inner and outer surface of the shell, respectively. At buckling, the bending strains in the corner of the cutout in shell C6 increase, but not to the extent exhibited by the other three shells. For the most part, the largest-magnitude strains develop in the corners of the shell and correspond to the locations where the majority of the material failures were observed. Observed failures for the unreinforced shell C1 are shown in Fig 12 and indicate significant delamination along the entire free edge of the cutout. The damage in shells C4 and C5 is generally much less severe, as indicated in Fig. 21a, and is characterized by delaminations in the upper left and lower right corners of the cutout. In contrast, no damage was evident near the cutout in shell C6 during the test, rather, interlaminar and intralaminar material failures developed away from the cutout in regions of the shell that exhibited large-magnitude bending gradients associated with the nodal lines between adjacent buckles in the general instability deformation response, as shown in Fig. 21b.

In general, the corresponding experimental results for shells C7- C9 with 90° ply reinforcements exhibit very similar response trends as those for shells C4- C6 with 0° ply reinforcements, presented previously. However, more extensive delamination failures develop near the cutouts in shells C7 and C8, shells with 1-ply-thick and 2-ply-thick 90° ply reinforcements, respectively, than the failures exhibited by the corresponding shells C4 and C5 with 0° ply reinforcements. This failure trend is similar to that exhibited by the unreinforced shells, in which shell C3 ($[\mp 45/90_2]_s$) developed catastrophic delamination failures near the cutout, compared to shells C1 and C2 which exhibited relatively small amounts of failure near the cutout in the post buckling region of the response.

2. Response Trends

Buckling and failure trends for the fifteen shells tested in this study are presented in this section. In addition, selected predicted results are presented to illustrate the effects of initial imperfections on the buckling response of shells with reinforced cutouts and to verify some the behavioral characteristics observed in the tests.

Measured and predicted buckling loads for all fifteen specimens considered in the present study have been summarized in Table 1. These results indicate that, for the most part, the buckling load of the quasi-isotropic shell increases as the reinforcement size and thickness increases. In addition, the results indicate that the buckling load of the shell with the 90°-ply reinforcement configuration is slightly greater (on average 4.5% greater) than the buckling

load of the corresponding shell with the 0°-ply reinforcement. These buckling-load trends agree well with the predicted trends presented in Refs. 27 and 28 for similar geometrically perfect shells with reinforced cutouts. However, the experimentally measured results and predicted results for imperfect shells indicate an average increase in the shell buckling load of only 2.9% when the reinforcement thickness is increased from a 2-ply-thick reinforcement configuration to a 4-ply-thick reinforcement configuration, for the same reinforcement size and ply orientation. In contrast, the predicted results for geometrically perfect shells presented in Refs. 27 and 28 indicate an average increase in the shell-buckling load of approximately of 18.1%. These results suggests that, as the reinforcement thickness increases, the shell may be becoming more imperfection sensitive, and this imperfection sensitivity is negating any additional improvements in the buckling load of the shell. Similarly, the specimen reinforcement configurations tested in this study include a slight outward shell-wall mid-surface eccentricity that results from the manufacturing process. This eccentricity detail was included in the analysis models of the imperfect shells presented herein, but was not included in the geometrically perfect shell analysis models reported in Refs 27 and 28. Thus, it is also likely that local bending is occurring in the specimens near the edges of the reinforcement region due to the discontinuity in the mid-surface geometry at this location, and that this bending response is triggering a local buckling response in the shell at lower applied load levels.

Shells with unreinforced cutouts (C1-C3) and shells with relatively thin reinforcements (C4, C7, and C8) exhibit a local buckling response near the cutout (see initial buckling deformations in Fig 17a for shell C4). Shells with thicker reinforcement, however, exhibit initial buckling just outside the reinforced region of the shell, i.e., shells C5, C6, and C9-C15 (see initial buckling deformations in Fig 18a for shell C5). In addition, the initial buckling event in these shells with thicker reinforcement are typically characterized by a single, small-magnitude, ellipse-shaped buckle that forms at the edge of the reinforcement region. This lack of symmetry in the initial buckling deformations is attributed to the effects of initial geometric imperfections, and this response agrees well with the corresponding predicted results. For example, predicted initial buckling displacements contours are shown in Fig. 22a, 22b, and 22c, for imperfect shells C13, C9, and C15, with 2.4-in.-square, 4.4-in.-square, and 8.0-in.-square, 90° reinforcement configurations, respectively. For all cases, the results indicate a localized buckling response that occurs near the edge of the reinforcement region in the shell. Shells with unreinforced cutouts can exhibit a stable post-local buckling equilibrium and can sustain additional axial load until global collapse occurs in the shell (e.g., see shells C1 and C2 in Fig. 7). The results indicated that, in all shells with reinforced cutouts, the local buckling response in the shell caused a disturbance in the shell with enough kinetic energy to cause the immediate global collapse to occur in the shell. The results also indicate that unreinforced shells and shells with 1-ply-thick and 2-ply-thick reinforcements exhibit interlaminar shear failures at the free edge of the cutout that are caused by large-magnitude bending gradients that develop near the cutout in the postbuckling range of loading. The shells with 90°-ply reinforcements always exhibited more local damage near the cutout, as compared to the corresponding shell with 0°-ply reinforcement. In contrast, the shells with 4-ply-thick reinforcements do not sustain damage near the cutout because the reinforcement significantly reduces the magnitude of the local bending deformations near the cutout that typically activate the interlaminar failures seen in the other shells. Rather, damage occurs in these shells along nodal lines between each of the inward buckles associated with the general instability deformation pattern.

V. □ Concluding Remarks

Results from a numerical and experimental study of the response of compression-loaded, laminated-composite, cylindrical shells with either reinforced or unreinforced cutouts have been presented. The numerical results were obtained by using high-fidelity nonlinear finite-element analyses. The analysis accounted for the effects of initial geometric imperfections, shell-wall thickness variations, material property variations, and nonuniform load introduction effects. In addition, preliminary results from a progressive failure analysis for predicting intralaminar and interlaminar material failures are presented. The results identify some of the effects of cutout-reinforcement orthotropy, size, and thickness on the buckling and failure response of the shells.

In general, the addition of reinforcement around a cutout in a compression-loaded shell can have a significant effect on the shell response. Results have been presented that indicate that the reinforcement can affect the local shell-wall deformations and strains near the cutout and retard or suppress the onset of local buckling and failure in the shell near the cutout. For some cases, the local buckling response near the cutout in the shell results in a stable post-local-buckling response near the cutout and additional load can be applied to the shell before it undergoes global collapse. For other cases, the local response near the cutout in the shell cause a disturbance in the shell with enough kinetic energy to cause the global collapse of the shell immediately following the local instability. For still other cases, the reinforcement suppresses the local buckling response near the cutout and causes buckling to occur at the edge of the reinforcement region in the shell. In general, the buckling load of the shell increases as the size and

the thickness of the reinforcement increases. The results also indicate that shells with 90°-ply cutout reinforcement generally have higher buckling loads than the corresponding shells with 0°-ply reinforcements. The results indicate that the shells with unreinforced, and some with reinforced, cutouts exhibit large-magnitude displacements and bending strains near the cutout and that these deformations and strains activate an interlaminar shear failure mechanism in the shell. Furthermore, shells with 90°-ply cutout reinforcement typically exhibit significantly larger amounts of interlaminar damage accumulation near the cutout than the corresponding shells with 0°-ply reinforcements.

The selected results presented herein suggest that tailoring the orthotropy, thickness, and size of the cutout reinforcement in a compression-loaded shell can result in significant increases in the buckling load of the shell, and can reduce the local deformations, strains, and damage accumulation near the cutout. The robust validated high-fidelity nonlinear analysis procedure used in this study offers the opportunity to provide insight into various cutout reinforcement concepts on the buckling and failure response of compression-loaded shell structures. Moreover, results from such a high-fidelity analysis procedure can improve some of the engineering approximations and methods that are used in the design of composite shell structures with cutouts.

Acknowledgment

The authors would like to dedicate this paper to the memory of the late Dr. James H. Starnes, Jr. of the NASA Langley Research Center. Dr. Starnes was an internationally recognized expert in structural mechanics and aerospace structures technology. He was also a renowned technical leader and a dedicated public servant. He is greatly remembered at NASA Langley for his exemplary service, positive attitude, and friendly interactions with colleagues. Dr. Starnes was particularly recognized by his employees as an exceptional supervisor, mentor, and technical leader. He routinely demonstrated great technical breadth and depth, enthusiasm, and a willingness to listen to other views. In addition, he was masterful at motivating his employees to make contributions that far exceeded their own expectations. He gained the respect of everyone whose life he touched and he profoundly influenced the careers and lives of many, including the authors'.

References

1. Starnes, J. H., Jr., Hilburger, M. W., and Nemeth, M. P., "The Effects of Initial Imperfections on the Buckling of Composite Shells," *Composite Structures: Theory and Practice*, ASTM STP 1383, P. Grant and C. Q. Rousseau, Eds., American Society for Testing and Materials, 2000, pp. 529-550.
2. Hilburger, M. H., and Starnes, J. H., Jr., "Effects of Imperfections on the Buckling Response of Compression-loaded Composite Shells," *International Journal of Non-linear Mechanics*, Vol. 37, 2002, pp. 623-643.
3. Hilburger, M. W., and Nemeth, M. P., and Starnes, J. H., Jr., "Shell Buckling Design Criteria Based on Manufacturing Imperfection Signatures," NASA/TM-2004-212659, May, 2004.
4. Tennyson, R. C., "The Effects of Unreinforced Circular Cutouts on the Buckling of Circular Cylindrical Shells," *Journal of Engineering for Industry*, Transactions of the American Society of Mechanical Engineers, Vol. 90, November 1968, pp. 541-546.
5. Brogan, F. A. and Almroth, B. O., "Buckling of Cylinders with Cutouts," *AIAA Journal*, Vol. 8, No. 2, February 1970, pp. 236-240.
6. Starnes, J. H., Jr., "The Effect of a Circular Hole on the Buckling of Cylindrical Shells," Ph. D. Dissertation, California Institute of Technology, Pasadena, California, 1970.
7. Jenkins, W. C., "Buckling of Cylinders with Cutouts under Combined Loading," MDC Report G2476, October 1971, McDonnell-Douglas Astronautics Co.
8. Almroth, B. O. and Holmes, A. M. C., "Buckling of Shells with Cutouts, Experiment and Analysis," *International Journal of Solids and Structures*, Vol. 8, 1972, pp. 1057-1071.
9. Starnes, J. H., Jr., "Effect of a Slot on the Buckling Load of a Cylindrical Shell with a Circular Cutout," *AIAA Journal*, Vol. 10, No. 2, February 1972, pp. 227-229.
10. Almroth, B. O., Brogan, F. A., and Marlowe, M. B., "Stability Analysis of Cylinders with Circular Cutouts," *AIAA Journal*, Vol. 11, No. 11, 1973, pp. 1582-1584.
11. Starnes, J. H., Jr., "The Effects of Cutouts on the Buckling of Thin Shells," *Thin-Shell Structures: Theory, Experiment, and Design*, edited by Y. C. Fung and E. E. Sechler, Prentice-Hall, Inc., Englewood Cliffs, New Jersey, 1974, pp. 289-304.
12. Almroth, B. O., Meller, E., and Brogan, F. A., "Computer Solutions for Static and Dynamic Buckling of Shells," *Buckling of Structures*, edited by B. Budiansky, IUTAM Symposium, Cambridge, Massachusetts, 1974, pp. 52-66.
13. Toda, S., "Buckling of Cylinders with Cutouts Under Axial Compression," *Experimental Mechanics*, Vol. 3, 1983, pp. 414-417.
14. Janisse, T. C. and Palazotto, A. N., "Collapse Analysis of Composite Panels With Cutouts," Proceedings of the AIAA/ASME/ASCE/AHS 24th Structures, Structural Dynamics, and Materials Conference, AIAA paper 83-0875, 1983.

15. Knight, N. F. and Starnes, J. H., Jr., "Postbuckling Behavior of Selected Graphite-Epoxy Cylindrical Panel Loaded in Compression," Proceedings of the AIAA/ASME/ASCE/AHS 27th Structures, Structural Dynamics, and Materials Conference, AIAA paper 86-0881-CP, 1986.
16. Knight, N. F. and Starnes, J. H., Jr., "Postbuckling Behavior of Axially Compressed Graphite-Epoxy Cylindrical Panels with Circular Holes," Proceedings of the 1984 ASME Joint Pressure Vessels and Piping/Applied Mechanics Conference, 1984.
17. Lee, C. E. and Palazotto, A. N., "Nonlinear Collapse Analysis of Composite Cylindrical Panels With Small Cutouts or Notches," Proceedings of the AIAA/ASME/ASCE/AHS 25th Structures, Structural Dynamics, and Materials Conference, AIAA paper 84-0889, 1984.
18. Madenci, E. and Barut, A., "Pre- and Postbuckling Response of Curved, Thin, Composite Panels with Cutouts Under Compression," *International Journal for Numerical Methods in Engineering*, Vol. 37, 1994, pp. 1499-1510.
19. Hilburger, M. W., "Numerical and Experimental Study of the Compression Response of Composite Cylindrical Shells with Cutouts," Ph. D. Dissertation, University of Michigan, Ann Arbor, Michigan, 1998.
20. Hilburger, M. W., Waas, A. M., and Starnes, J. H., Jr., "Response of Composite Shells with Cutouts Subjected to Internal Pressure and Compression Loads," *AIAA Journal*, Vol. 32, No. 2, 1999, pp. 232-237.
21. Hilburger, M. W., Starnes, J. H., Jr., and Waas, A. M. "A Numerical and Experimental Study of the Response of Selected Compression-loaded Composite Shells with Cutouts," Proceedings of the 39th AIAA/ASME/ASCE/AHS/ASC Structures, Structural Dynamics, and Materials Conference, Long Beach, CA, AIAA Paper No. 98-1768, 1998.
22. Jullien, J. F. and Limam, A., "Effects of Openings on the Buckling of Cylindrical Shells Subjected to Axial Compression," *Thin-Walled Structures*, Vol. 31, 1998, pp. 187-202.
22. Nemeth, M. P. and Starnes, J. H., Jr., "The NASA Monographs on Shell Stability Design Recommendations: A Review and Suggested Improvements, NASA/TP-1998-206290, January 1998.
23. Hilburger, M. W., Britt, V. O., and Nemeth, M. P., "Buckling Behavior of Compression-Loaded Quasi-Isotropic Curved Panels with a Circular Cutout," *International Journal of Solids and Structures*, Vol. 38, 2001, pp. 1495-1522.
24. Tafreshi, A., "Buckling and Post-buckling Analysis of Composite Cylindrical Shells with Cutouts Subjected to Internal Pressure and Axial Compression Loads," *International Journal of Pressure Vessels and Piping*, Vol. 79, 2002, pp. 351-359.
25. Madenci, E. and Barut, A., "The Influence of Geometric Irregularities on the Linear Buckling of Cylindrical Shells with an Elliptical Cutout," Proceedings of the 44th AIAA/ASME/ASCE/AHS/ASC Structures, Structural Dynamics, and Materials Conference, Norfolk, VA. AIAA Paper No. 2003-1929, 2003.
26. Cervantes, J. A. and Palazotto, A. N., "Cutout Reinforcement of Stiffened Cylindrical Shells," *Journal of Aircraft*, Vol. 16, No. 3, 1979, pp. 203-208.
27. Hilburger, M. W., and Starnes, J. H., Jr., "Buckling of Compression-loaded Composite Cylindrical Shells with Reinforced Cutouts," Proceedings of the AIAA/ASME/ASCE/AHS/ASC 43rd Structures, Structural Dynamics, and Materials Conference, Denver, CO. AIAA Paper No. 2002-1516, 2002.
28. Hilburger, M. W., and Starnes, J. H., Jr., "Buckling of Compression-loaded Composite Cylindrical Shells with Reinforced Cutouts," NASA/TM-2004-212656, September 2004.
29. Jaunky, N., Ambur, D. R., Davila, C. G., and Hilburger, M. W., "Progressive Failure Studies of Composite Panels with and without Cutouts," NASA/CR-2001-211223, September 2001.
30. Vinay, K. G., Jaunky, N., Johnson, E. R., and Ambur, D. R., "Intralaminar and Interlaminar Progressive Failure Analyses of Composite Panels with Circular Cutouts," Proceedings of the AIAA/ASME/ASCE/AHS/ASC 43rd Structures, Structural Dynamics, and Materials Conference, Denver, CO. AIAA Paper No. 2002-1745, 2002.
31. Rankin, C. C., Brogan, F. A., Loden, W. A., and Cabiness, H. D., "STAGS Users Manual, Version 5.0," Lockheed Martin Missiles & Space Co., Inc., Advance Technology Center, Report LMSC P032594, 2005.
32. Hashin, Z., "Failure Criteria for Unidirectional Fiber Composites," *Journal of Applied Mechanics*, 47, 1980, pp. 329-334.
33. Chang, F. K., and Lessard, L., "Damage Tolerance of Laminated Composites Containing an Open Hole and Subjected to Compressive Loadings: Part I – Analysis," *Journal of Composite Materials*, 25, 1991, pp. 2-43.

Table 1: Predicted and measured normalized buckling loads ($P_{cr}^o = 42,590$ lb is the corresponding linear bifurcation buckling load of a geometrically perfect quasi-isotropic cylinder).

Specimen number	Shell-wall laminate / reinforcement size (in.) / reinforcement lay-up	Predicted buckling load (imperfect shell), P_{cr}^{imp}/P_{cr}^o	Measured buckling load, P_{cr}/P_{cr}^o	Difference between measured and predicted buckling loads, %
C1	$[\mp 45/0/90]_s$ / none	0.51	0.48	6.3
C2	$[\mp 45/0_2]_s$ / none	0.40	0.40	2.6
C3	$[\mp 45/90_2]_s$ / none	0.50	0.51	9.8
C4	$[\mp 45/0/90]_s$ / 4.4 / 0_1	0.68	0.67	1.5
C5	$[\mp 45/0/90]_s$ / 4.4 / 0_2	0.78	0.74	5.4
C6	$[\mp 45/0/90]_s$ / 4.4 / 0_4	0.80	0.75	6.7
C7	$[\mp 45/0/90]_s$ / 4.4 / 90_1	0.76	0.75	1.3
C8	$[\mp 45/0/90]_s$ / 4.4 / 90_2	0.76	0.76	0.0
C9	$[\mp 45/0/90]_s$ / 4.4 / 90_4	0.80	0.75	6.7
C10	$[\mp 45/0/90]_s$ / 2.4 / 0_2	0.72	0.71	1.4
C11	$[\mp 45/0/90]_s$ / 2.4 / 0_4	0.76	0.73	4.1
C12	$[\mp 45/0/90]_s$ / 2.4 / 90_2	0.72	0.72	0.0
C13	$[\mp 45/0/90]_s$ / 2.4 / 90_4	0.73	0.76	3.9
C14	$[\mp 45/0/90]_s$ / 8.0 / 0_4	0.73	0.71	2.8
C15	$[\mp 45/0/90]_s$ / 8.0 / 90_4	0.79	0.75	5.3

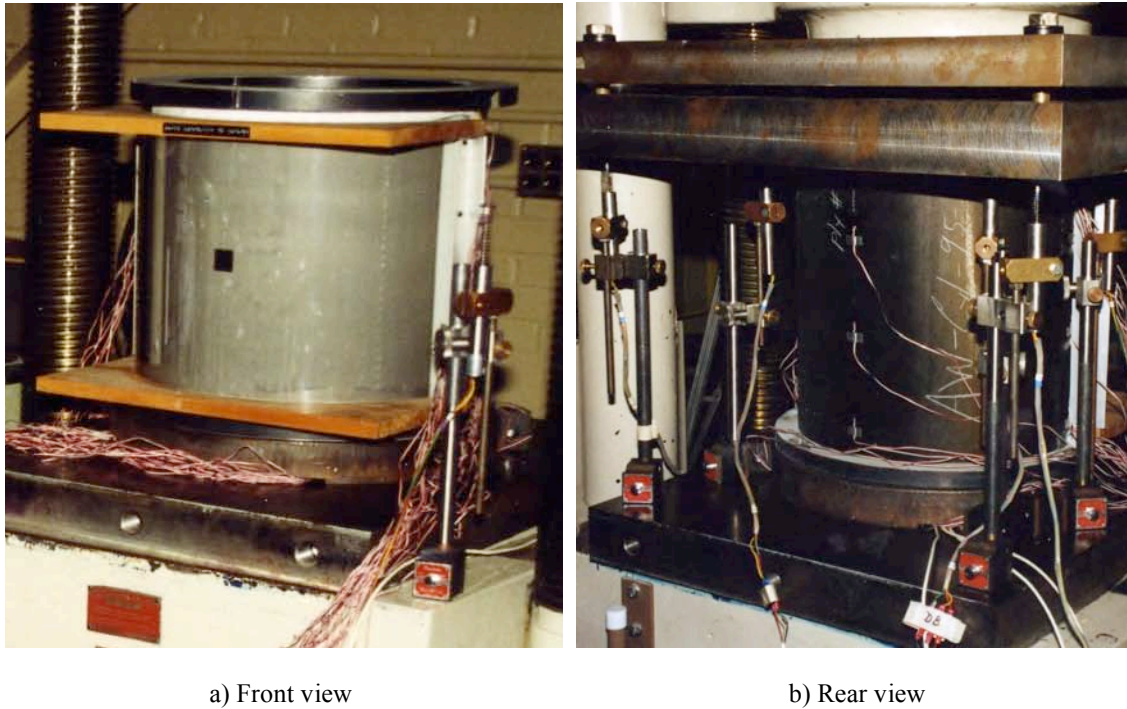


Fig. 1 Typical test set-up for a compression-loaded composite cylinder with a cutout.

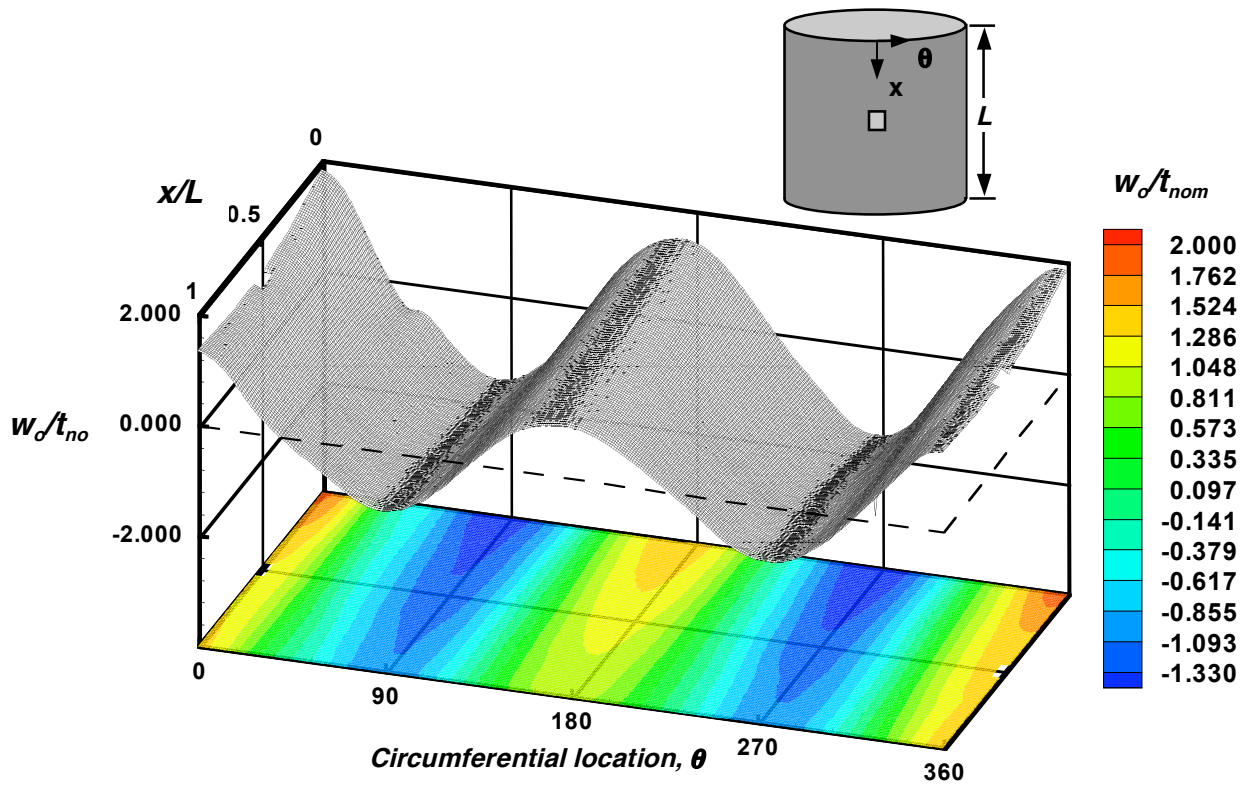


Fig. 2 Typical measured initial geometric imperfection for a composite cylinder with a cutout.

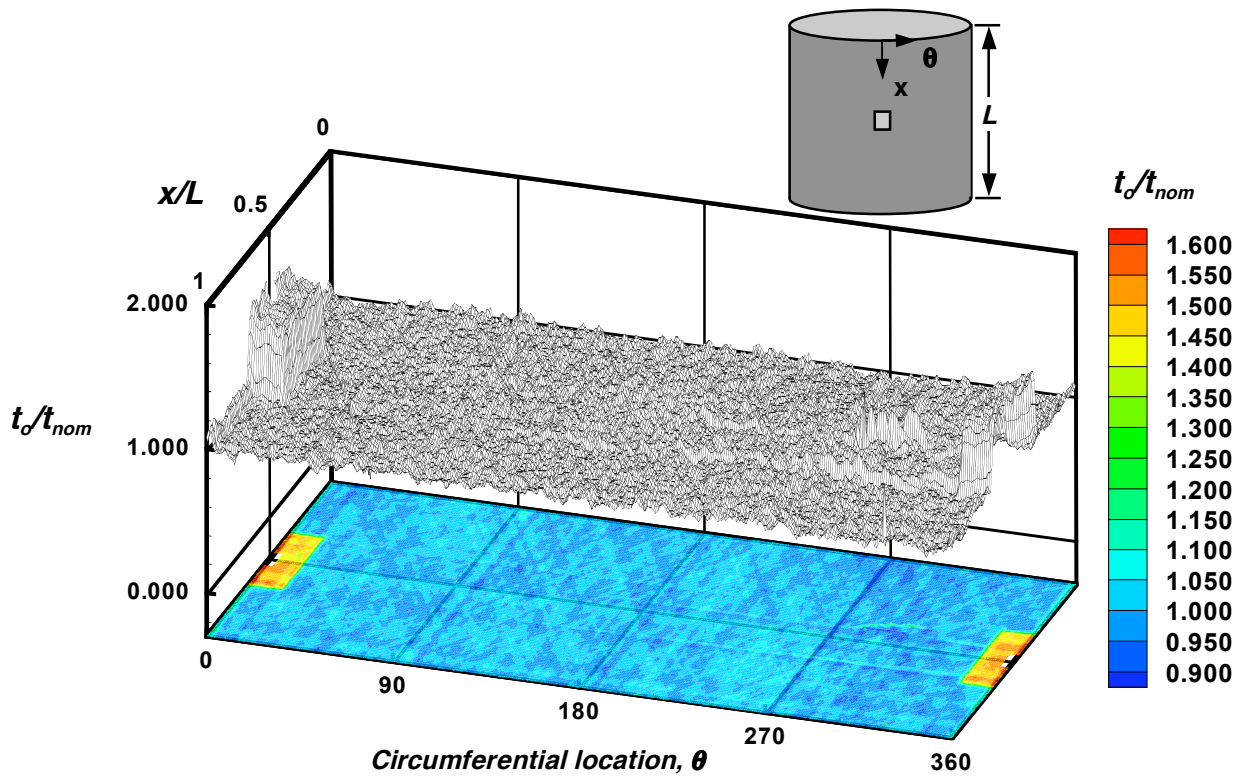


Fig. 3 Typical measured shell-wall thickness variation for a composite cylinder with a reinforced cutout.

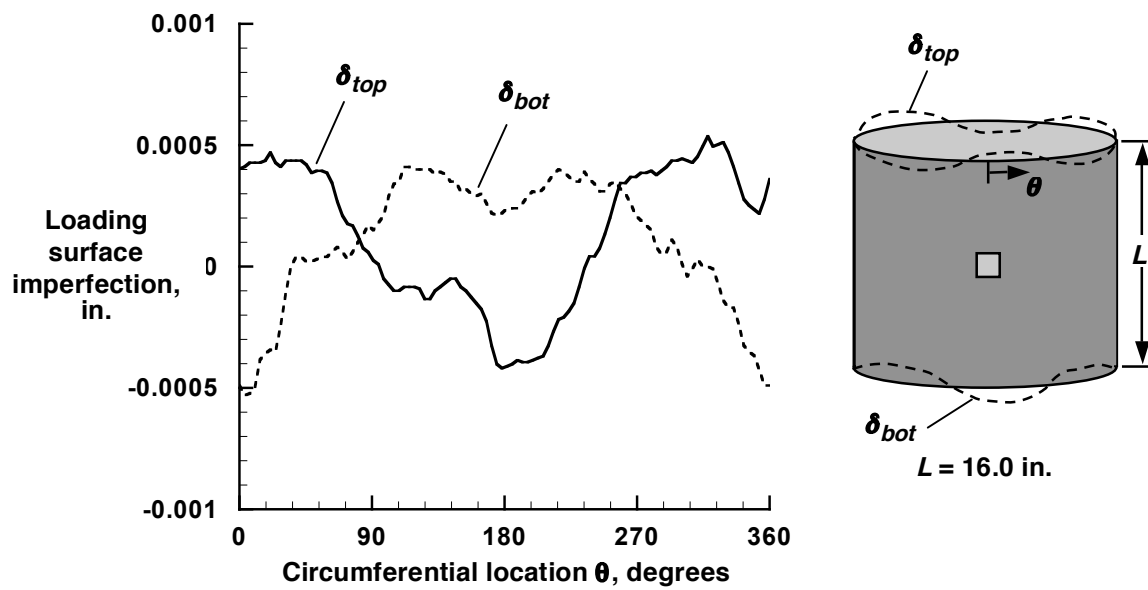
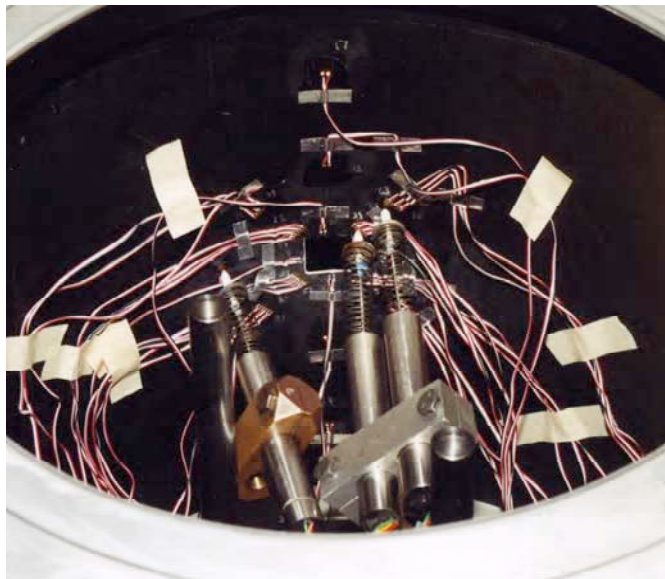
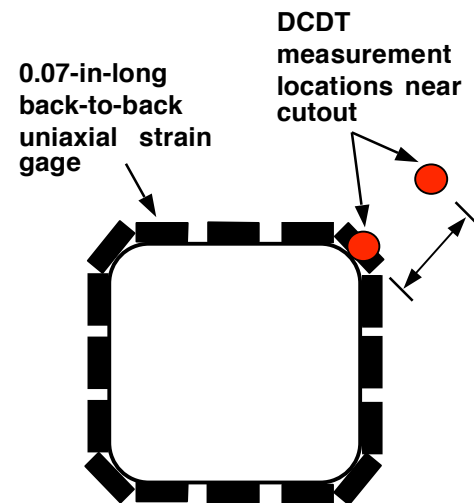


Fig. 4 Typical measured shell-end or loading-surface imperfections for a composite cylinder specimen.



a) Internal strain gages and DCDTs



b) Instrumentation pattern near cutout

Fig. 5 Typical DCDT and strain gage instrumentation near the cutout.

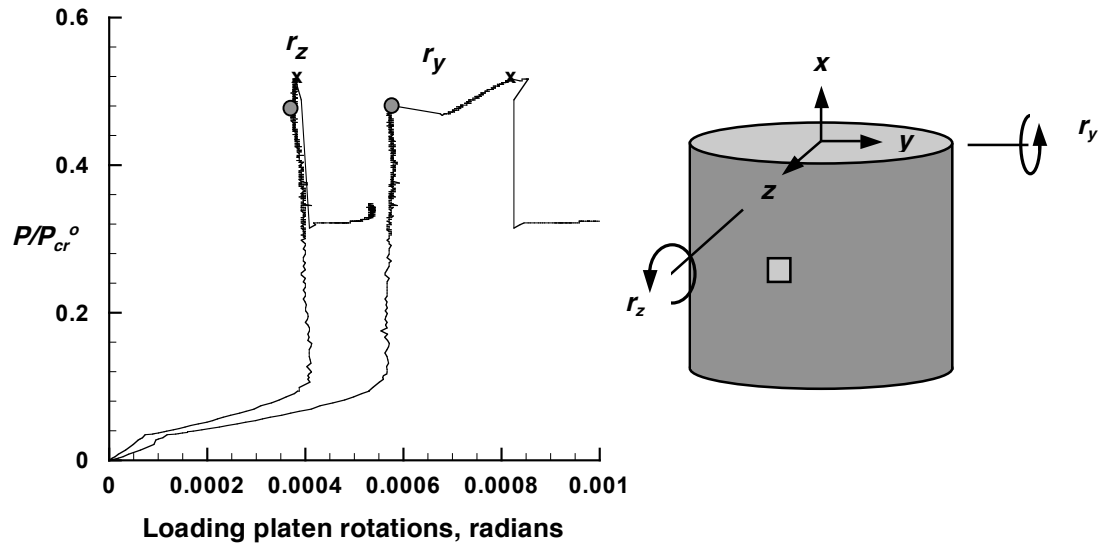


Fig. 6 Measured loading platen rotations for a compression-loaded composite cylinder with a 1-in. by 1-in. square cutout ($P_{cr}^o = 42,590$ lb is the predicted linear bifurcation buckling load of the corresponding geometrically perfect quasi-isotropic shell without a cutout).

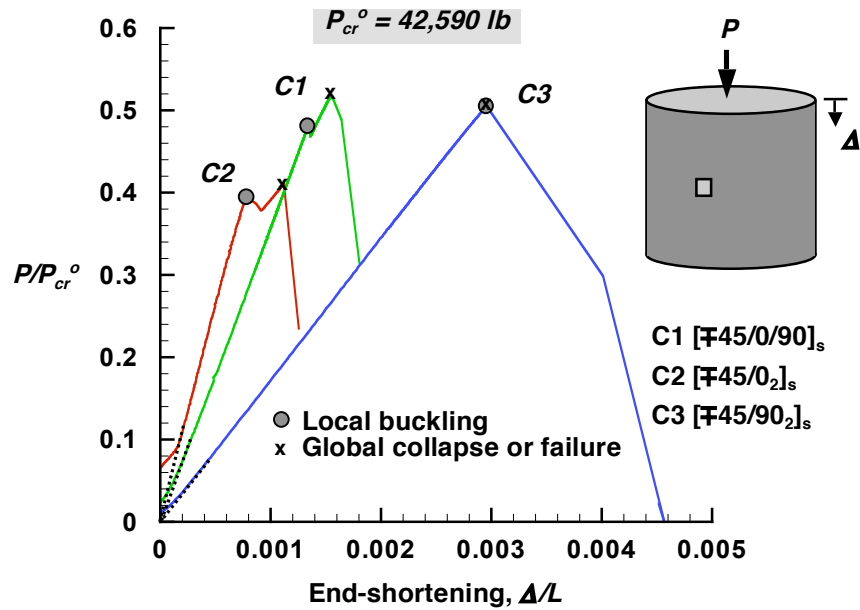


Fig. 7 Load-shortening response curves for compression-loaded composite cylinders with unreinforced 1-in. by 1-in. square-shaped cutouts ($P_{cr}^o = 42,590$ lb is the linear bifurcation buckling load of the corresponding geometrically perfect quasi-isotropic shell without a cutout).

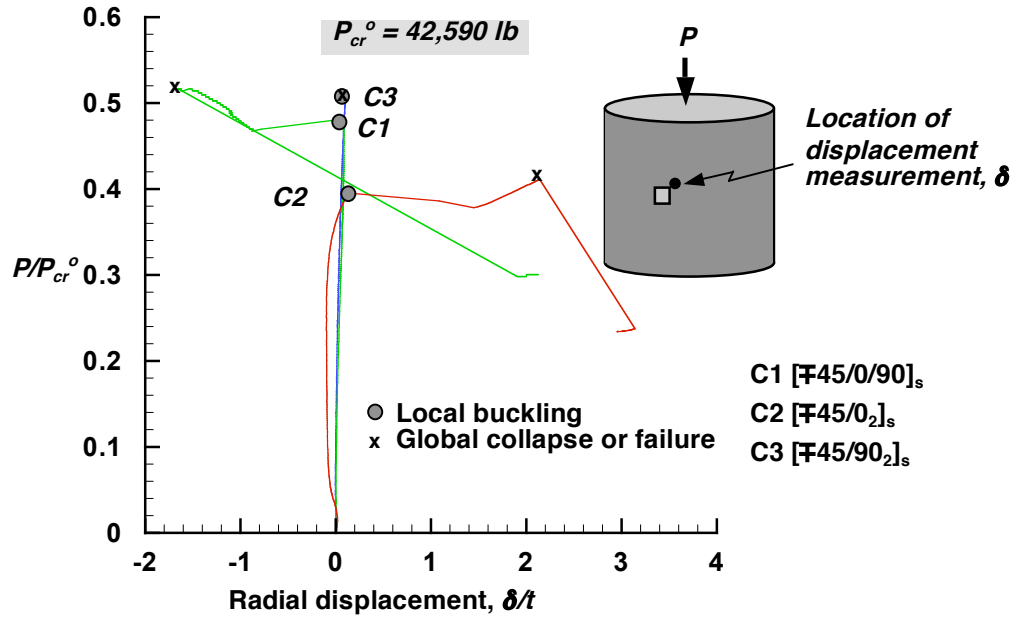


Fig. 8 Radial displacement response curves for compression-loaded composite cylinders with unreinforced 1-in. by 1-in. square-shaped cutouts ($P_{cr}^o = 42,590 \text{ lb}$ is the linear bifurcation buckling load of the corresponding geometrically perfect quasi-isotropic shell without a cutout).

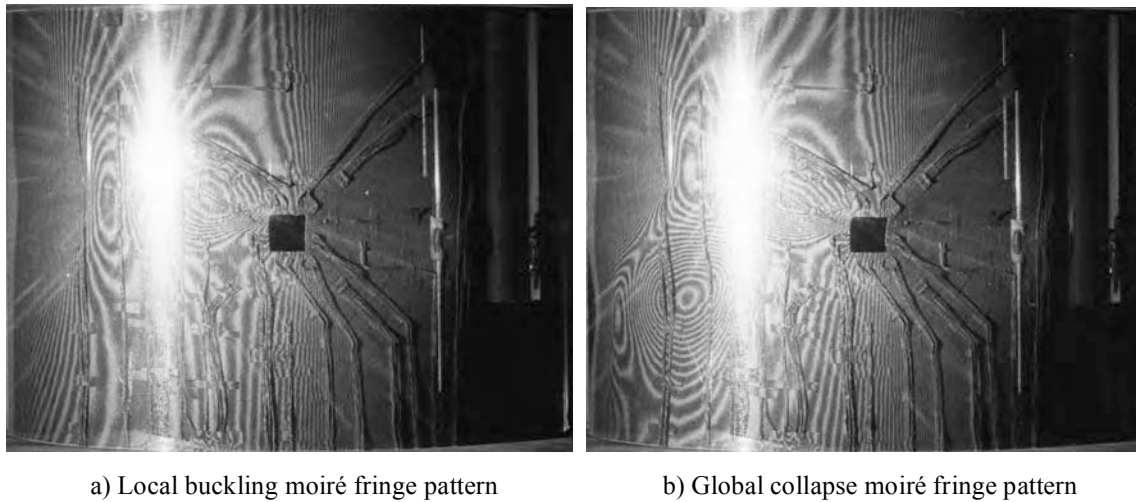


Fig. 9 Observed radial deformation patterns near a cutout for specimen C1.

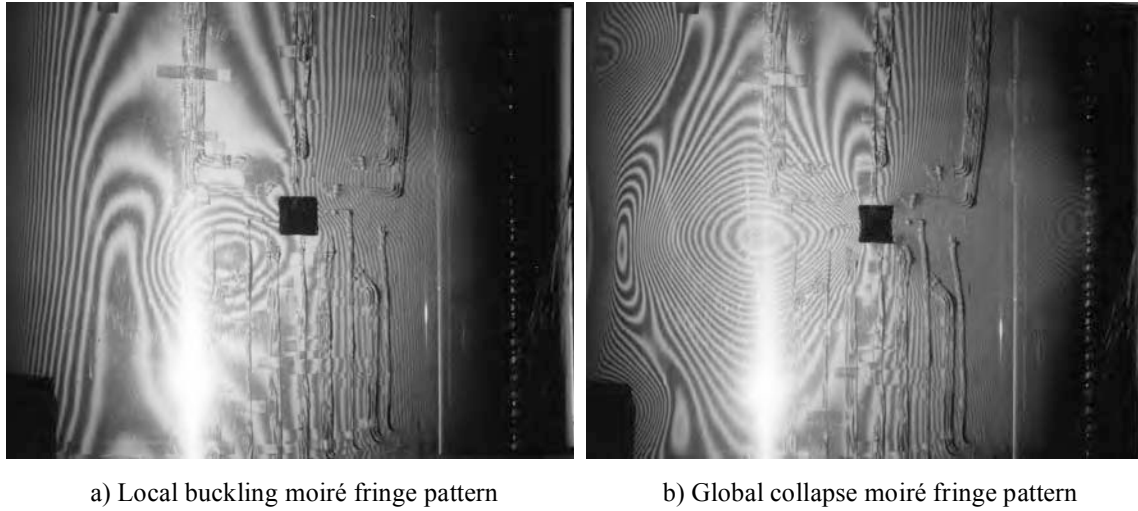


Fig. 10 Observed radial deformation patterns near a cutout for specimen C2.

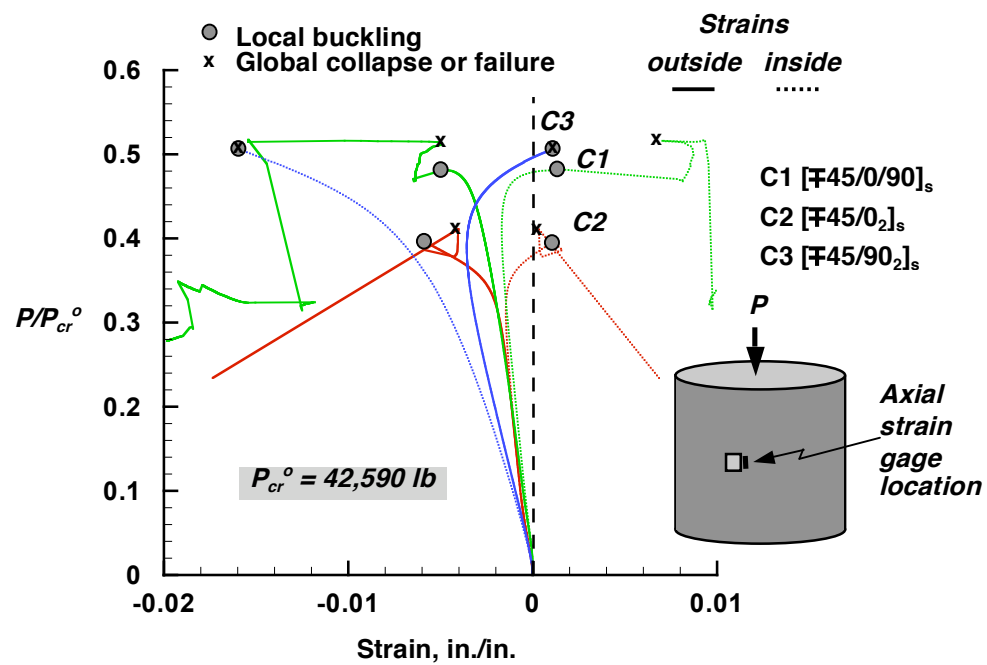
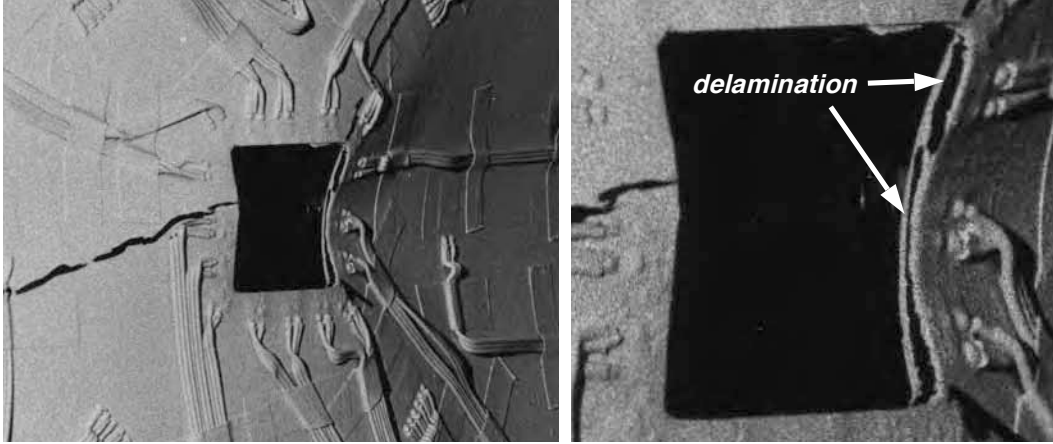
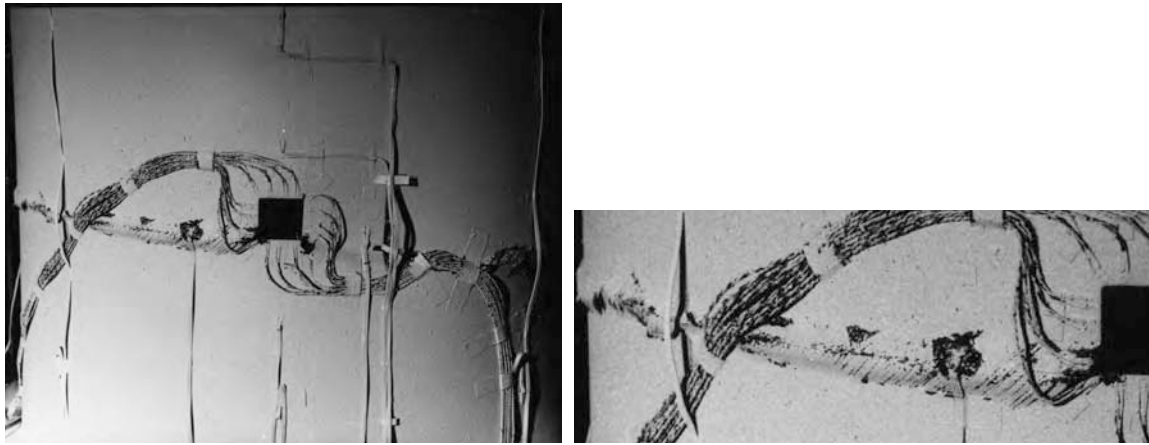


Fig. 11 Load-strain response near unreinforced 1-in. by 1-in. square-shaped cutouts in compression-loaded composite cylinders ($P_{cr}^o = 42,590 \text{ lb}$ is the linear bifurcation buckling load of the corresponding geometrically perfect quasi-isotropic shell without a cutout).



a) delamination at the right edge of the cutout b) magnified view of cutout delamination

Fig. 12 Observed local delamination failures in specimen C1.



a) global view of failed specimen b) magnified view of delamination on left side

Fig. 13 Observed catastrophic delamination failures in specimen C3.

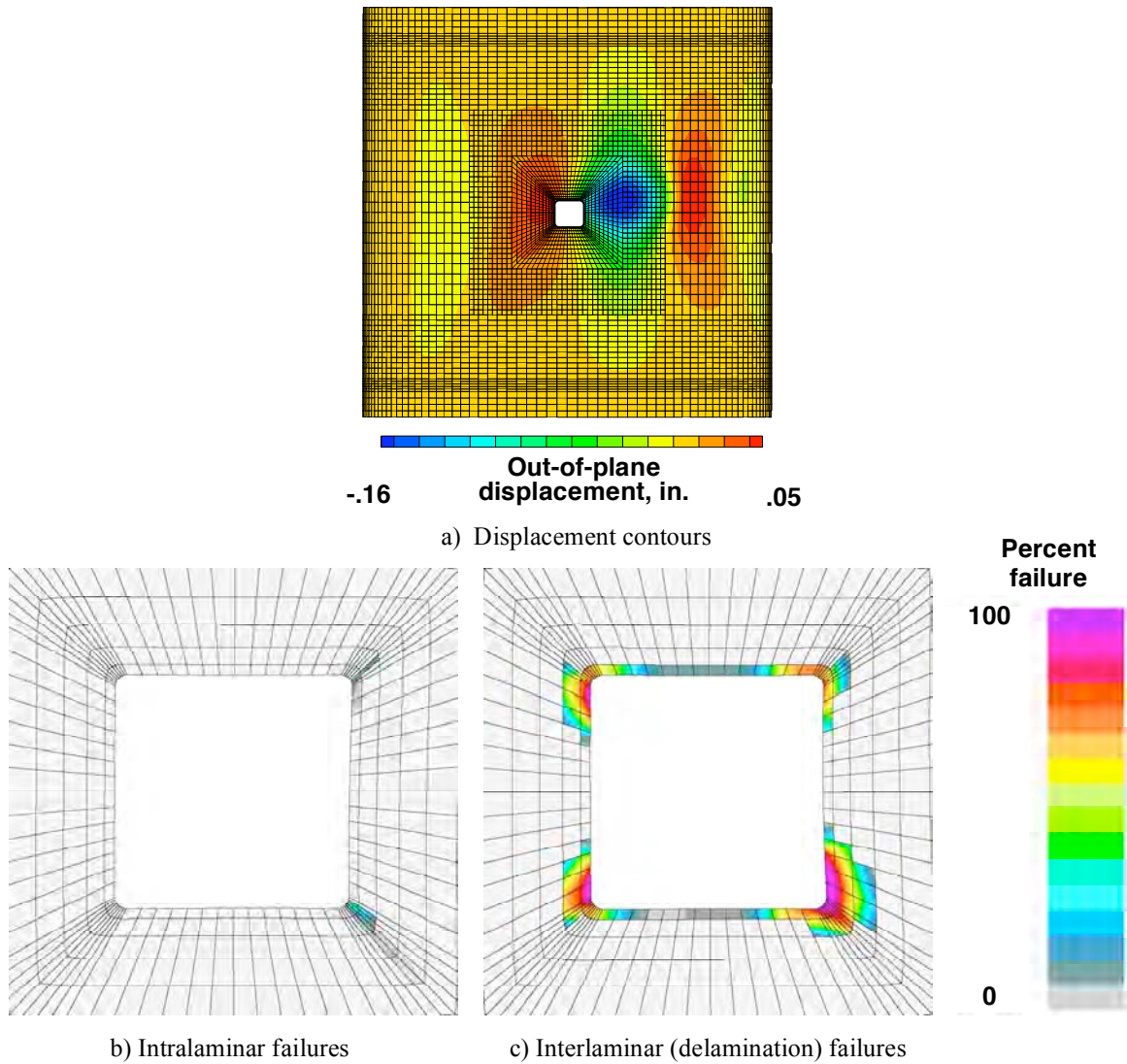


Fig. 14 Predicted local buckling displacements and material failures for specimen C1.

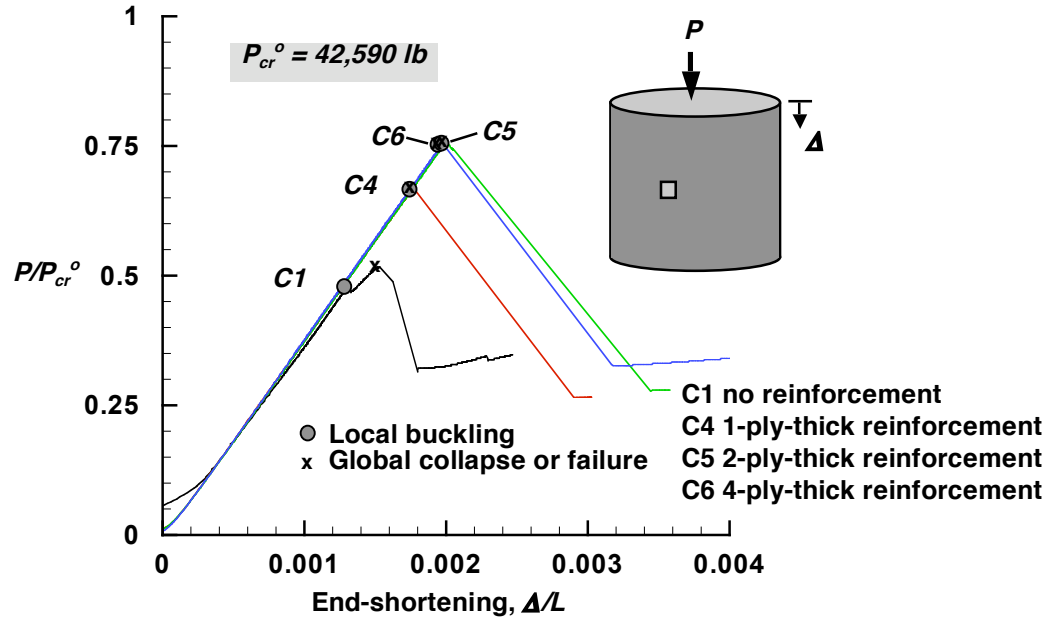


Fig. 15 Load-shortening response curves for compression-loaded quasi-isotropic cylinders with unreinforced and reinforced 1-in. by 1-in. square-shaped cutouts ($P_{cr}^o = 42,590 \text{ lb}$ is the linear bifurcation buckling load of the corresponding geometrically perfect shell without a cutout).

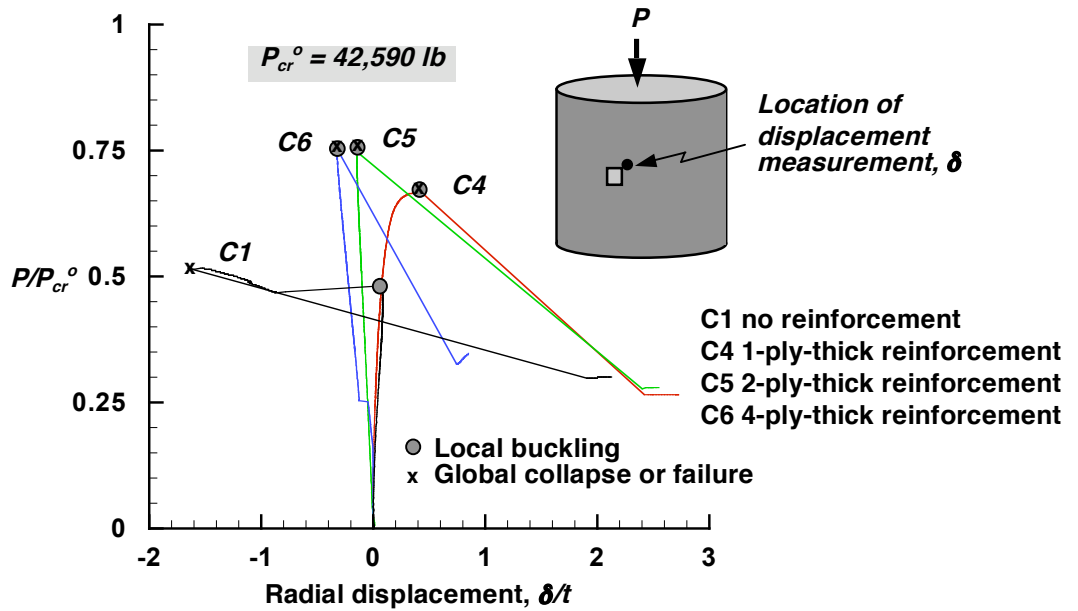
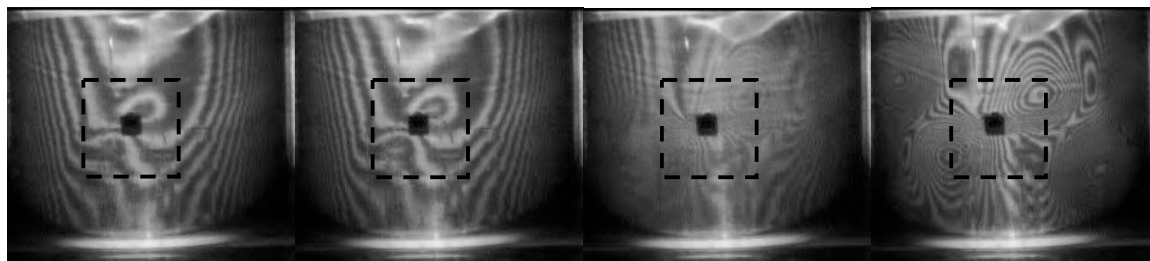
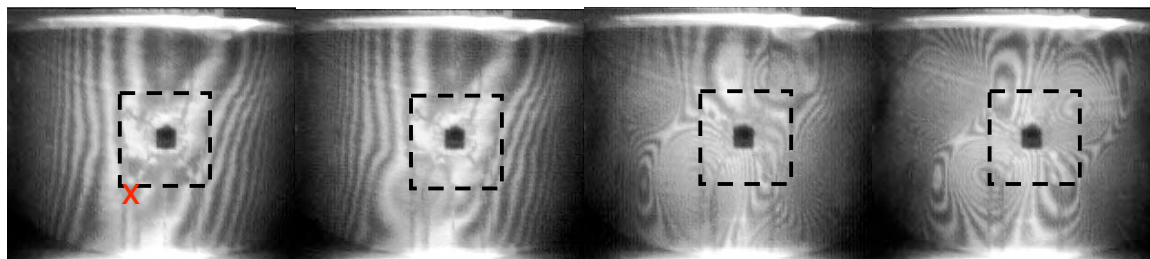


Fig. 16 Radial displacements response curves for compression-loaded quasi-isotropic cylinders with unreinforced and reinforced 1-in. by 1-in. square-shaped cutouts ($P_{cr}^o = 42,590 \text{ lb}$ is the linear bifurcation buckling load of the corresponding geometrically perfect shell without a cutout).



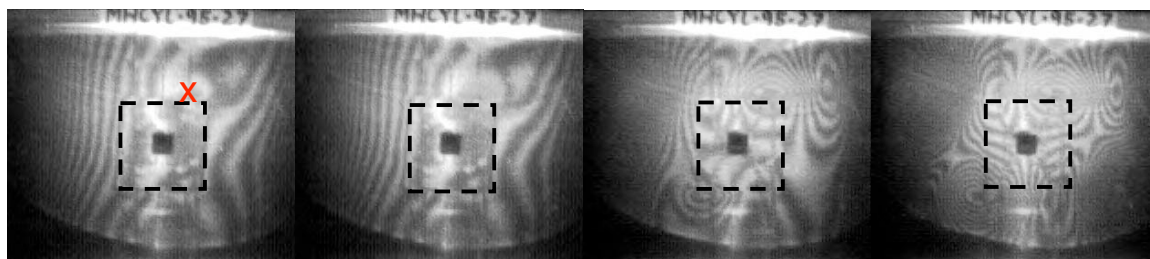
a) initial local buckling time = 0.0 sec b) local buckling time = 0.001 sec c) Global buckling time = 0.002 sec d) Postbuckling time = 0.004 sec

Fig. 17 Observed buckling and postbuckling out-of-plane deformation patterns for specimen C4, quasi-isotropic shell with 1-in square cutout and 4.4-in square, 1-ply-thick, 0° reinforcement.



a) initial local buckling time = 0.0005 sec b) local buckling time = 0.001 sec c) Global buckling time = 0.002 sec d) Postbuckling time = 0.004 sec

Fig. 18 Observed buckling and postbuckling out-of-plane deformation patterns for specimen C5, quasi-isotropic shell with 1-in square cutout and 4.4-in square, 2-ply-thick, 0° reinforcement.



a) initial local buckling time = 0.0005 sec b) local buckling time = 0.001 sec c) Global buckling time = 0.002 sec d) Postbuckling time = 0.004 sec

Fig. 19 Observed buckling and postbuckling out-of-plane deformation patterns for specimen C6, quasi-isotropic shell with 1-in square cutout and 4.4-in square, 4-ply-thick, 0° reinforcement.

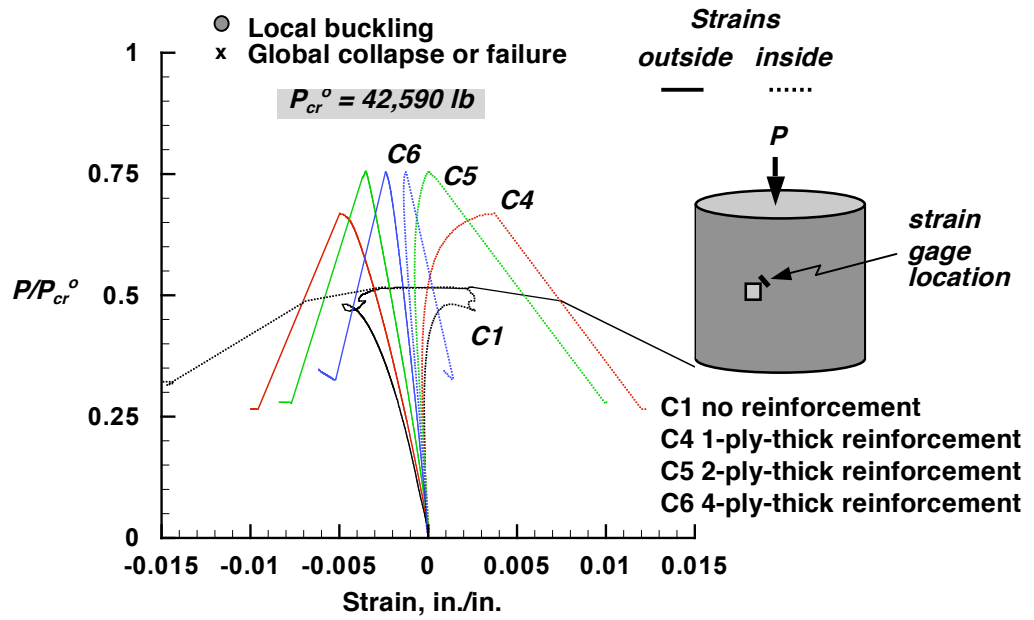
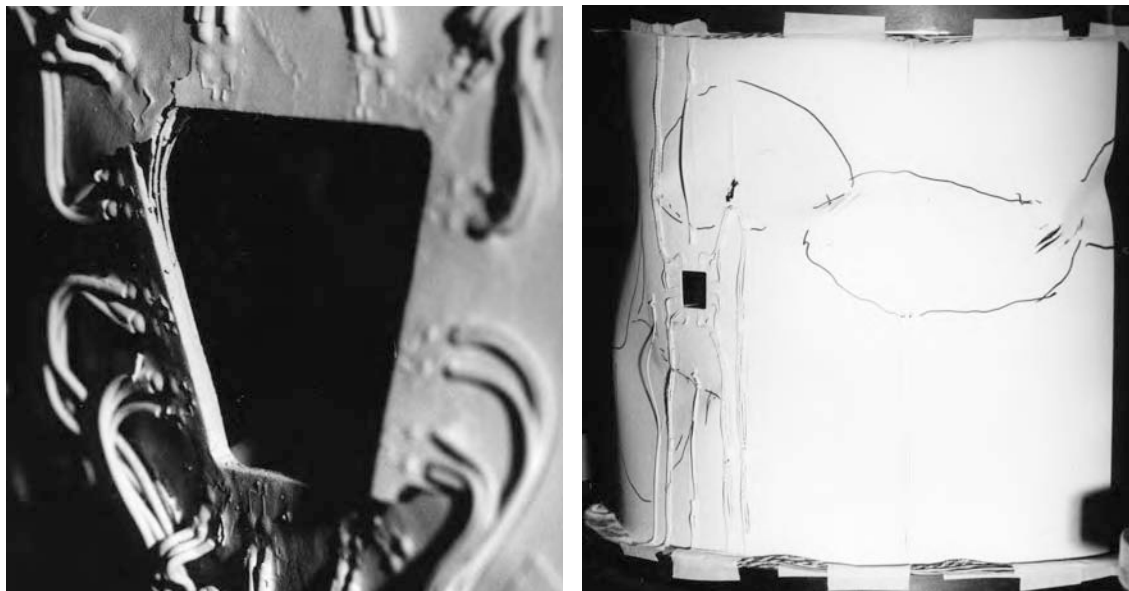


Fig. 20 Load-strain response near 1-in. by 1-in. square-shaped cutouts compression-loaded quasi-isotropic cylinders ($P_{cr}^0 = 42,590 \text{ lb}$ is the linear bifurcation buckling load of the corresponding geometrically perfect shell without a cutout).



a) Local delamination failures in specimen C5

b) Failures in specimen C6

Fig. 21 Observed material failures for specimens C5 and C6.

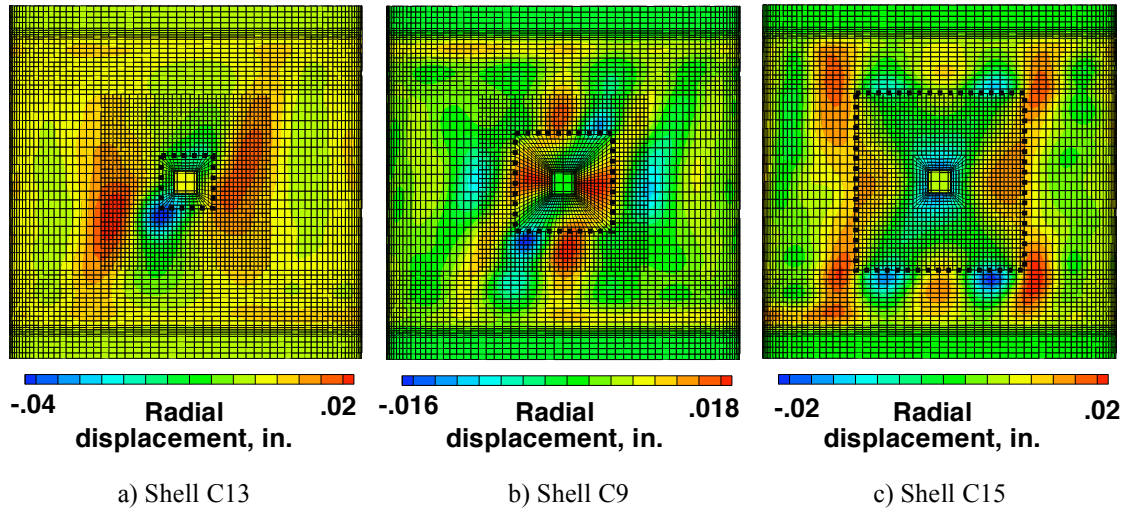


Fig. 22 Observed buckling and postbuckling radial deformation patterns for specimen C13, C9, and C15, quasi-isotropic shell with 1-in square cutout and 2.4-in.-square, 4.4-in.-square, and 8.0-in square, 4-ply-thick, 90° reinforcement, respectively.

STRESS ANALYSIS OF COMPOSITE CYLINDRICAL SHELLS WITH AN ELLIPTICAL CUTOUT

E. Oterkus,[†] E. Madenci[‡]

The University of Arizona, Tucson, AZ 85721

M. P. Nemeth[§]

NASA Langley Research Center, Hampton, VA 23681

Abstract

A special-purpose, semi-analytical solution method for determining the stress and deformation fields in a thin laminated-composite cylindrical shell with an elliptical cutout is presented. The analysis includes the effects of cutout size, shape, and orientation; non-uniform wall thickness; oval-cross-section eccentricity; and loading conditions. The loading conditions include uniform tension, uniform torsion, and pure bending. The analysis approach is based on the principle of stationary potential energy and uses Lagrange multipliers to relax the kinematic admissibility requirements on the displacement representations through the use of idealized elastic edge restraints. Specifying appropriate stiffness values for the elastic extensional and rotational edge restraints (springs) allows the imposition of the kinematic boundary conditions in an indirect manner, which enables the use of a broader set of functions for representing the displacement fields. Selected results of parametric studies are presented for several geometric parameters that demonstrate that analysis approach is a powerful means for developing design criteria for laminated-composite shells.

Introduction

Cutouts in cylindrical shell-type components are unavoidable in the construction of aerospace structures. This fact is significant because the structural failure of these components usually begins near the cutout because of high stress concentrations that initiate the formation of cracks. Hence, a cutout can trigger a local failure at a load level lower than the global failure load of a corresponding shell without a cutout. As a result, preliminary-design sizing of a cylindrical shell with a cutout is often based on the magnitude of the stress

concentrations near the cutout. Therefore, an accurate assessment of the stress concentrations in a given shell subjected to various types of loading and support conditions is essential to the development of safe and reliable designs. Moreover, validated special-purpose analysis tools that enable rapid parametric studies would be very valuable to structural designers and for the development of new design criteria and design concepts.

Several analytical, numerical and experimental studies have been conducted during the past sixty years to determine stress distributions in cylindrical shells with a cutout and subjected to various types of loadings; such as, axial tension and compression, torsion, and internal and external pressure. Pioneering analytical work was conducted by Lurie^{1,2} to investigate the effect of axial tension and internal pressure, and shell curvature, on the stress concentrations around a circular cutout in the 1940s. Many years later, analytical studies were presented by Lekkerkerker,³ Van Dyke,⁴ Ashmarin,⁵ Murthy et al.,⁶ Guz et al.,⁷ and Van Tooren et al.⁸ that further investigated the effects of various factors on the stress concentrations around a cutout in a cylindrical shell. Similarly, experimental investigations have been conducted by Tennyson,⁹ Starnes,¹⁰ Pierce and Chou,¹¹ Bull,¹² and Zirka and Chernopiskii,¹³ and numerical studies have been conducted by Liang et al.,¹⁴ and Shnerenko and Godzula.¹⁵ In 1964 and 1972, respectively, Hicks¹⁶ and Ebner and Jung¹⁷ summarized the results obtained from several of these previous studies and provided extensive lists of references related to this problem. Most of these previous studies are for isotropic cylindrical shells with a circular cutout. Only a few of these studies, such as those presented by Pierce and Chou¹¹ and by Murthy et al.,⁶ address the effects of cutout shape (elliptical cutouts) on the stress concentrations.

Mitigation of high stress concentrations by tailoring shell-wall thickness, material orthotropy and anisotropy, and cutout reinforcement are also important considerations in the design of aerospace structures made of lightweight composite materials. Likewise, the potential for using shells of non-circular cross section are relevant to fuselage-like structures. However, only a few studies have considered these effects. For

[†]Graduate Research Assistant, Department of Aerospace and Mechanical Engineering.

[‡]Professor, Department of Aerospace and Mechanical Engineering.

[§]Senior Research Engineer, Mechanics of Structures and Materials Branch.

Copyright 2005 by Erdogan Madenci. Printed by NASA with permission.

example, the influence of wall-thickness variation on the stresses in axially loaded composite cylindrical shells, without a cutout, has been investigated by Li et al.¹⁸ Although numerous analyses exist in the literature on the analysis of shells with circular cross sections, only a few include non-circular cross sections. Sheinman and Firer¹⁹ provided an analytical investigation of stresses in laminated cylindrical shells with arbitrary non-circular cross sections. More recently, Hyer and Wolford^{20,21} studied the effect of non-circular cross sections on damage initiation and progressive failure in composite cylinders by employing the finite element method.

The objective of the present study is to present a special-purpose analysis for a laminated-composite cylindrical shell with an elliptical cutout that can be used to rapidly, and parametrically, investigate the effects of shell curvature; cutout size, shape, and orientation; and ply lay-up on stress-resultant concentrations near the cutout. The analysis is applicable to thin-walled cylindrical shells with non-uniform wall thickness, a non-circular (e.g., oval) cross section, and subjected to tension, torsion, and bending loads as illustrated in Fig. 1.

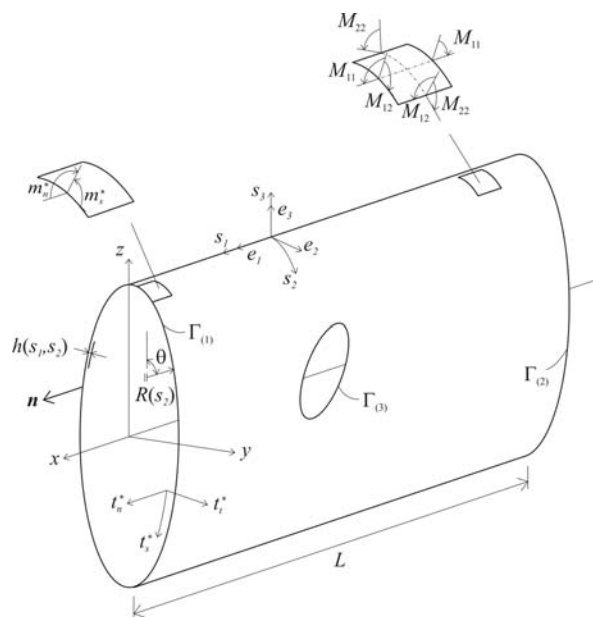


Fig. 1 Geometry, coordinates systems, and applied edge tractions for an oval cylindrical shell with an elliptical cutout and non-uniform wall thickness.

To accomplish this objective, an overview of the analysis is presented first. Next, the boundary value problem is defined along with the kinematics and stress-strain relations used in the analysis. Then, the derivation of the equations governing the response and numerical procedure are described. Finally, selected numerical results for oval and circular cylindrical shells

with either circular or elliptical cutouts and subjected to either tension, torsion, or pure-bending loads are presented.

Analysis Overview

The analytical approach used herein permits the determination of the pointwise variation of displacement and stress components. It is based on the principle of stationary potential energy, but utilizes local and global functions that are not required to satisfy the kinematic boundary conditions directly. Thus, the choice of local and global functions is not limited by a particular type of kinematic boundary condition. The kinematic boundary conditions are imposed by employing the Lagrange multiplier method. Both local and global functions are used, in contrast to the traditional approach, to enhance the robustness of the analysis method. In particular, the local functions are used to capture rapidly varying stress and strain gradients and local deformations near a cutout. Toward that goal, Laurent series are used for the local functions and are expressed in terms of the mapping functions introduced by Lekhnitskii.²² Fourier series are used for the global functions and are used to capture the overall deformation and stress fields. The kinematic admissibility requirements on the local and global functions are relaxed by defining that the edges of the shell are supported by extensional and rotational springs. Zero-valued displacement and rotation kinematic boundary conditions are enforced in an indirect manner by specifying values for the spring stiffnesses that are large compared to the corresponding shell stiffnesses. This approach effectively yields a prescribed kinematic boundary condition in the limit as the relative stiffness of the spring becomes much greater than the corresponding shell stiffness. Similarly, values for the spring stiffnesses can be selected that correspond to a given uniform elastic restraint along an edge, similar to that provided by an end-ring. This capability is important, and useful, because in some test fixtures or actual structures the edge supports may not be stiff enough to simulate a fully clamped boundary condition or flexible enough to simulate a simply supported boundary condition.

As suggested by Li et al.¹⁸ and Sheinman and Firer,¹⁹ nonuniform wall-thickness variations of a shell, which lead to non-uniform laminate stiffnesses, are represented by using trigonometric series. Specifically, nonuniform shell-wall thickness is represented in the present study by perturbing the ply thicknesses with a function that is periodic in either the longitudinal or the circumferential direction. The variation in wall thickness is accounted for by adjusting the lamina properties, resulting in nonhomogeneous in-plane and bending stiffness matrices. The nonuniform shell curvature associated with a noncircular cross section is

represented by using trigonometric series for the coordinates of an oval-cross-section shell reference surface.²³ The aspect ratio, or out-of-roundness, of the cross-section is represented in the analysis by using an eccentricity parameter.

In the derivation of the equations governing the response, the total potential energy consists of the elastic strain energy of the shell, the elastic edge restraints and the potential energy of the applied loads. The conditions that may arise from the choice of displacement approximations without any kinematic restrictions are treated as constraint equations, and the potential energy arising from constraint reactions is invoked into the total potential energy through the use of Lagrange multipliers. The equations governing the shell response are obtained by enforcing the requirement that the first variation of the total potential energy vanish. The evaluation of the area integrals appearing in the potential energy are achieved numerically by using a basic quadrature method in conjunction with standard triangulation of the entire domain described by Shewchuk.²⁴ Solution to the equations governing the response are obtained by using a standard Gaussian elimination procedure, which yields the generalized displacement coefficients and, thus, the stress and strain fields. The accuracy of the analysis depends on the number of terms used for the functional representation of the displacement fields. As the number of terms increases, the results converge to the exact solution.

Representation of Shell Geometry

The geometry of a thin-walled, noncircular, cylindrical shell of length L and with an elliptical cutout located at the shell mid-length is shown in Fig. 1. The origin of the global Cartesian coordinate system, (x, y, z) is located at an end point of the longitudinal axis of the shell. As shown in Fig. 1, the x -axis coincides with the longitudinal axis of the shell. The y and z coordinates span the cross-sectional plane. A curvilinear coordinate system is also attached to the mid-surface of the cylindrical shell. The coordinates of points in the longitudinal, circumferential (tangential), and normal-to-the-surface (transverse) directions of the shell are denoted by (s_1, s_2, s_3) , and the corresponding unit base vectors are $\{\mathbf{e}_1, \mathbf{e}_2, \mathbf{e}_3\}$.

Following Romano and Kempner,²³ the non-circular cross-section of the cylindrical shell is defined as an oval with the coordinates, y and z expressed as

$$y = R_0 \sum_{m=1,3,5,7,\dots} a_m(\xi) \sin \frac{ms_2}{R_0} \quad (1a)$$

and

$$z = R_0 \sum_{m=1,3,5,7,\dots} b_m(\xi) \cos \frac{ms_2}{R_0} \quad (1b)$$

where ξ represents the eccentricity of the oval cross section and R_0 is the equivalent radius of a circular cylindrical shell that has the same circumference as that of the oval cylindrical shell. The circumferential coordinate, s_2 varies between 0 and $2\pi R_0$. The derivation of Eqs. (1) along with the explicit forms of the coefficients $a_m(\xi)$ and $b_m(\xi)$ are given by Madenci and Barut.²⁵

As derived by Romano and Kempner,²³ the coordinates y and z in Eqs. (1a) and (1b) can be related to the radius of curvature of an oval-cross-section cylindrical shell, $R(s_2, \xi)$, by

$$R(s_2, \xi) = \frac{R_0}{1 + \xi \cos(2s_2/R_0)} \quad (2)$$

Therefore, $\xi = 0$ implies no eccentricity and corresponds to a circular cross section with radius R_0 . For positive values of the eccentricity parameter, ξ , the z -coordinate becomes the major axis and the y -coordinate becomes the minor axis. For negative values of ξ , the major and minor axes switch to the y - and z -axes, respectively. The range of values of the eccentricity parameter, ξ , is bounded by $-1 < \xi < 1$.

As shown in Fig. 1, the cylindrical shell contains a cutout. The shape of this cutout is defined such that if the shell is cut along a generator and flattened into a plane, the cutout becomes an ellipse with major and minor axes denoted by a and b , respectively. For simplicity and convenience, the cutout is referred to herein as an "elliptical" cutout. Because the domain of the analysis shown in Fig. 2 corresponds to a similar flat region, a subsequent mapping of the ellipse to a unit circle is possible, which enables the use of Laurent series expansions for the local functions. Note that the special case of a "circular" cutout is given by $a = b$.

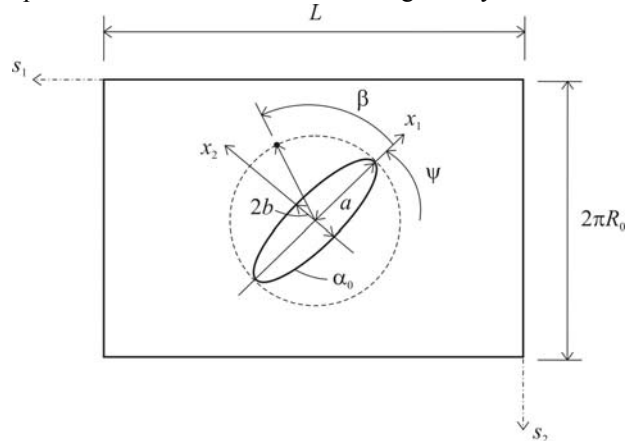


Fig. 2 Computational domain of a cylindrical shell with an elliptical cutout.

In the flat analysis domain, the minor and major axes of the ellipse are aligned with a local coordinate system, (x_1, x_2) , whose origin is located at the center of the cutout and coincides with the origin of the parameter grid, given by constant values of s_1 and s_2 , that forms the curvilinear coordinates (s_1, s_2) on the cylindrical shell mid-surface. The orientation of the elliptical cutout is arbitrary with respect to the longitudinal shell axis. Hence, the orientation of the local x_1 -axis (major axis) of the cutout and the longitudinal s_1 -axis of the cylindrical shell is denoted by the angle, ψ . The elliptical coordinates, α and β , representing a family of confocal ellipses and hyperbolas, respectively, are utilized in order to obtain the stress-resultant distribution in the direction tangent to the cutout boundary. The coordinate α is equal to $\alpha_0 = \tanh^{-1}(b/a)$ on the particular ellipse that corresponds to the elliptical cutout. The other coordinate, β , varying from 0 to 2π , is known as the eccentric angle and is related to the (x_1, x_2) coordinate system by $x_1 = a \cos \beta$ and $x_2 = b \sin \beta$. The eccentric angle β is similar to the angle used for polar coordinates.

The symmetrically laminated cylindrical shells considered herein are made of K specially orthotropic layers, and each layer has an orientation angle, θ_k , that is defined with respect to the s_1 -axis. Each layer also has elastic moduli E_L and E_T , shear modulus, G_{LT} and Poisson's ratio ν_{LT} , where the subscripts L and T represent the longitudinal (fiber) and transverse principal material directions, respectively.

As for the shell thickness variation, the non-uniform wall thickness of the shell is denoted by $h(s_1, s_2)$, and its variation is included by assuming that the thickness of each ply, t_k , varies as a function of the curvilinear coordinates in the form

$$t_k(s_1, s_2) = t_{k0} \left(1 - \varepsilon_1 \cos\left(\frac{2\pi m_1 s_1}{L}\right) - \varepsilon_2 \cos\left(\frac{m_2 s_2}{R_0}\right) \right) \quad (3)$$

where t_{k0} denotes the nominal thickness of the k^{th} layer in the laminate, and the parameters (m_1, m_2) and $(\varepsilon_1, \varepsilon_2)$ respectively, denote the wave numbers and the amplitudes of the periodic thickness variation in the longitudinal and circumferential directions. While the wall thickness of the shell is allowed to vary across the shell surface, the aspect ratio of the plies through the thickness is maintained, thus making the thickness variation of each ply to remain conformable to each other throughout the shell surface. A periodic thickness variation in the longitudinal direction is obtained by

setting $\varepsilon_1 \neq 0$ and $\varepsilon_2 = 0$, and in the circumferential direction by $\varepsilon_1 = 0$ and $\varepsilon_2 \neq 0$. A shell with uniform thickness, $t_k = t_{k0}$, is obtained by setting $\varepsilon_1 = 0$ and $\varepsilon_2 = 0$.

Boundary Conditions and External Loads

To facilitate a general imposition of prescribed boundary tractions, displacements, or rotations; the external as well as the internal edge boundary Γ of the shell is decomposed into

$$\Gamma = \Gamma_{(1)} + \Gamma_{(2)} + \Gamma_{(3)} \quad (4)$$

As shown in Fig. 1, $\Gamma_{(1)}$ and $\Gamma_{(2)}$ denote the external edge boundary of the cylindrical shell and $\Gamma_{(3)}$ represents the traction-free internal edge boundary around the cutout. The unit vector normal to an edge is represented by \mathbf{n} . Throughout this paper, a variable with the superscript “*” is treated as a *known quantity*, arising from the externally applied loads or from prescribed displacements and rotations. Also, the subscripts n , s , and t denote the directions normal, tangent, and transverse (through-the-thickness) to the boundary, respectively. The details of how prescribed edge loads and displacements are imposed in the analysis are presented subsequently.

Prescribed edge loads

External loads are applied to a shell by specifying values for the positive-valued stress resultants shown in Fig. 1. More precisely, the membrane loads applied to the ℓ^{th} boundary segment, $\Gamma_{(\ell)}$, are given by

$$N_{11} = t_n^* \quad (5a)$$

$$N_{12} = t_s^* \quad (5b)$$

where N_{11} and N_{12} are the axial and shear stress resultants, respectively, defined in the cylindrical coordinate system. Likewise, shell-wall bending loads that are applied to the ℓ^{th} boundary segment are given by

$$M_{11} = -m_n^* \quad (6a)$$

$$M_{11,1} + 2M_{12,2} = t_t^* - 2m_{s,2}^* \quad (6b)$$

where M_{11} and M_{12} are the pure-bending and twisting stress resultants, respectively, defined in the cylindrical coordinate system. Moreover, the left-hand side of Eq. (6b) is the Kirchhoff shear stress resultant of classical shell theory.

As a matter of convenience, the analysis is formulated to also permit the specification of concentrated forces and moments that are transmitted to the ends of the shell as if through a rigid end-ring, as shown in Fig. 3. Presently, the concentrated force P_n^* and the concentrated axial torque P_s^* are included in the

analysis. The force P_n^* is simulated in the analysis by specifying a uniform distribution of the axial displacement, with the unknown magnitude Δ_n , such that

$$\int_{\Gamma^{(\ell)}} N_{11} d\Gamma = P_n^* \quad (7a)$$

Likewise, the torque P_s^* is simulated by specifying a uniform distribution of the tangential displacement, with the unknown magnitude Δ_s , such that

$$\int_{\Gamma^{(\ell)}} N_{12} d\Gamma = P_s^* \quad (7b)$$

The analytical process that is used to ensure that the magnitudes of Δ_n and Δ_s correspond to the specified values of P_n^* and P_s^* , respectively, is described in the following section and in Appendix A.

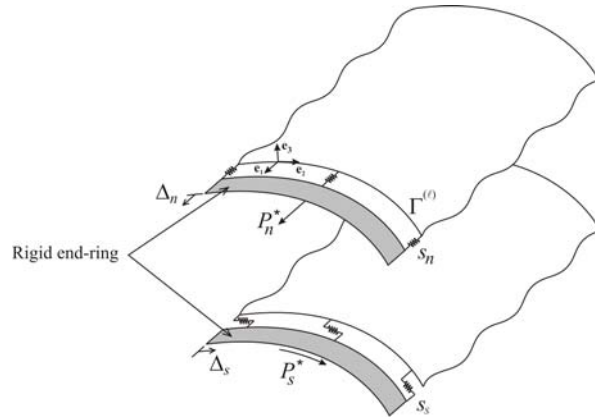


Fig. 3 Application of a concentrated force through a rigid end-ring by using elastic springs along a shell edge

Prescribed edge displacements and rotations

Edge displacements and rotations are applied to a shell by specifying values for the displacements and rotations shown in Fig. 4 that correspond to the positive-valued stress resultants shown in Fig. 1. In particular, the axial and tangential displacements, u_n^* and u_s^* , respectively, that are applied to the ℓ^{th} boundary segment, $\Gamma^{(\ell)}$, are given by

$$u_1(\mathbf{n} \cdot \mathbf{e}_1) = u_n^* \quad (8a)$$

$$u_2[(\mathbf{e}_3 \times \mathbf{n}) \cdot \mathbf{e}_2] = u_s^* \quad (8b)$$

Similarly, the transverse displacement u_3^* and the rotation about an axis tangent to an edge \mathcal{G}_n^* that are applied to the ℓ^{th} boundary segment are defined by

$$u_3 = u_3^* \quad (9a)$$

$$u_{3,1}(\mathbf{n} \cdot \mathbf{e}_1) = \mathcal{G}_n^* \quad (9b)$$

As mentioned previously, these prescribed displacements are enforced through the use of elastic edge restraints (springs) to relax kinematic admissibility requirements on the functions that are used to represent the displacement fields. The uniformly distributed extensional and rotational springs that are attached to the shell edges in the normal, tangential, and transverse directions and used to enforce the kinematic boundary conditions are depicted in Fig. 4.

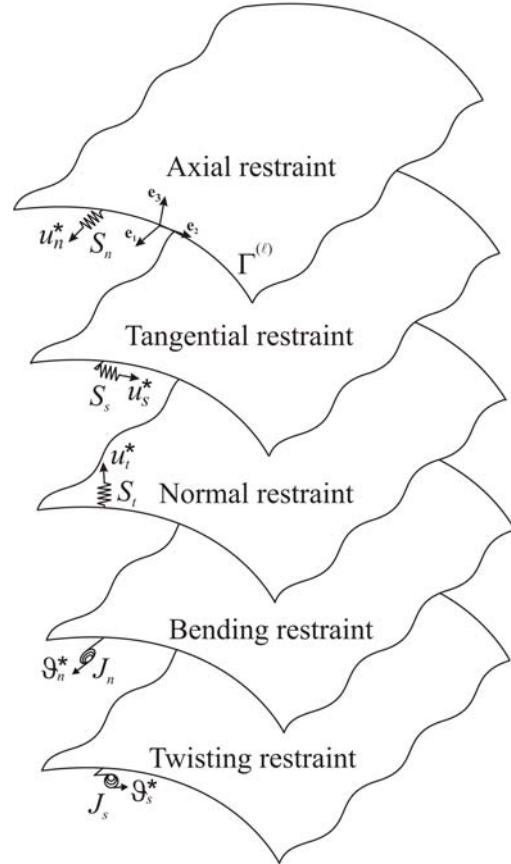


Fig. 4 Types of uniformly distributed elastic spring supports that can be prescribed along the edge of a cylindrical shell.

Specifying appropriate stiffness values for the springs results in full or partial restraints along the shell edges. A zero value of the spring stiffness corresponds to a traction-free-edge condition. In contrast, a value of the spring stiffness that is large compared to the corresponding shell stiffness effectively corresponds to a prescribed zero-valued boundary displacement or rotation. This approach effectively yields a prescribed kinematic boundary condition in the limit as the relative stiffness of the spring becomes much greater than the corresponding shell stiffness. Similarly, values for the spring stiffness can be selected that correspond to a specified uniform elastic restraint along an edge, similar

to that provided by a rigid end-ring. This capability is important, and useful, because in some test fixtures or actual structures the edge supports may not be stiff enough to simulate a fully clamped boundary condition or flexible enough to simulate a simply supported boundary condition.

As depicted in Fig. 4, the membrane displacements, u_n and u_s , and the transverse displacement, $u_t = u_3$ along the ℓ^{th} boundary segment are restrained by extensional springs with stiffness values of S_n , S_s , and S_t in the directions normal, tangent, and transverse to the boundary, respectively. In addition to the extensional springs, the edge rotations, \mathcal{G}_n and \mathcal{G}_s , along the ℓ^{th} boundary segment are restrained by rotational springs with stiffness values of J_n and J_s that correspond to rotation about axes tangent and normal to the edge, respectively.

Extensional springs in the directions normal and tangent to the shell edge, with stiffness values of s_n and s_s , are also used to simulate load introduction through a rigid end-ring, as shown in Fig. 3. Specifying values for the spring stiffnesses s_n and s_s that are relatively large compared to the corresponding shell stiffnesses causes the shell edge to behave as if a rigid end-ring is attached that produces the uniformly distributed displacements with the corresponding magnitudes Δ_n and Δ_s . The values for Δ_n and Δ_s that correspond to the specified concentrated loads are determined by using a penalty parameter approach. This approach enforces the difference between the edge displacements of the shell and the unknown uniform rigid end-ring displacements, $(u_n - \Delta_n)$ and $(u_s - \Delta_s)$ to vanish, while retaining the corresponding potential energy of the applied concentrated loads P_n^* and P_s^* .

Kinematics and Stress-Strain Relations

The kinematic equations used in the present study are based, to a large extent, on the assumptions of Love-Kirchhoff classical thin-shell theory. Specifically, the axial, circumferential (tangential), and normal (normal to the mid-surface) displacements of a generic point of the shell are denoted by $U_1(s_1, s_2, s_3)$, $U_2(s_1, s_2, s_3)$ and $U_3(s_1, s_2, s_3)$, respectively. The corresponding displacements of a generic point of the shell mid-surface that share the same unit vector normal to the mid-surface are denoted by $u_1(s_1, s_2)$, $u_2(s_1, s_2)$ and $u_3(s_1, s_2)$, respectively. In classical shell theory, these displacements are related by

$$U_1(s_1, s_2, s_3) = u_1(s_1, s_2) - s_3 \beta_1(s_1, s_2) \quad (10a)$$

$$U_2(s_1, s_2, s_3) = u_2(s_1, s_2) - s_3 \beta_2(s_1, s_2) \quad (10b)$$

$$U_3(s_1, s_2, s_3) = u_3(s_1, s_2) \quad (10c)$$

where $\beta_1(s_1, s_2)$ and $\beta_2(s_1, s_2)$ are the mid-surface rotations about the s_2 and s_1 axes, respectively, that are given by

$$\beta_1(s_1, s_2) = u_{3,1}(s_1, s_2) \quad (11a)$$

$$\beta_2(s_1, s_2) = u_{3,2}(s_1, s_2) - \frac{1}{R(s_2)} u_2(s_1, s_2) \quad (11b)$$

in which a subscript after a comma denotes partial differentiation. The corresponding linear membrane-strain-displacement relations are given by

$$\boldsymbol{\varepsilon} = \begin{Bmatrix} \varepsilon_{11} \\ \varepsilon_{22} \\ \gamma_{12} \end{Bmatrix} = \begin{Bmatrix} u_{1,1} \\ u_{2,2} + \frac{1}{R} u_3 \\ u_{1,2} + u_{2,1} \end{Bmatrix} \quad (12a)$$

and the bending-strain-displacement relations are given by

$$\boldsymbol{\kappa} = \begin{Bmatrix} \kappa_{11} \\ \kappa_{22} \\ \kappa_{12} \end{Bmatrix} = \begin{Bmatrix} -u_{3,11} \\ -\left(u_{3,22} - \left(\frac{u_2}{R} \right)_{,2} \right) \\ -2 \left(u_{3,12} - \frac{1}{R} u_{2,1} \right) \end{Bmatrix} \quad (12b)$$

It is important to point out that the expression given for the change in surface twist due to deformation, κ_{12} , is that originally published by Love^{26, 27} in 1888 for general shells, in terms of lines of principal-curvature coordinates, and derived in the book by Timoshenko and Woinowsky-Krieger²⁸ for circular cylindrical shells. As indicated by Bushnell,²⁹ the expression for κ_{12} vanishes for rigid-body motions in contrast to the corresponding expression presented in Reissner's version of Love's first-approximation shell theory (see Reissner,³⁰ Kraus,³¹ and Naghdi³²). Equations (12a) and (12b), and the more general forms presented by Bushnell,²⁹ are sometimes referred to as the Love-Timoshenko strain-displacement equations. Justification for this terminology is given by Chaudhuri.³³

The stress-strain relations used in the present study are those of the classical theory of laminated plates and shells,³⁴ which are based on a linear through-the-thickness distribution of the strain fields. For a thin, symmetrically laminated cylindrical shell, with variable wall thickness, the relationship between the membrane and bending stress resultants and the membrane and bending strains is expressed conveniently in matrix notation by

$$\mathbf{N} = \mathbf{A}(s_1, s_2) \boldsymbol{\varepsilon} \quad (13a)$$

and

$$\mathbf{M} = \mathbf{D}(s_1, s_2) \boldsymbol{\kappa} \quad (13b)$$

The membrane and bending stress resultants in Eqs. (13a) and (13b) are defined as

$$\mathbf{N}^T = \{N_{11}, N_{22}, N_{12}\} \quad (14a)$$

and

$$\mathbf{M}^T = \{M_{11}, M_{22}, M_{12}\} \quad (14b)$$

It is important to reiterate that when shell-wall thickness variations are present, the membrane and bending stiffness matrices, $\mathbf{A}(s_1, s_2)$ and $\mathbf{D}(s_1, s_2)$, are dependent on the curvilinear surface coordinates s_1 and s_2 .

It is convenient, in the present study, to combine the relations given in Eqs. (13a) and (13b) into the matrix form

$$\mathbf{s} = \mathbf{C} \mathbf{e} \quad (15)$$

in which \mathbf{s} , \mathbf{e} and \mathbf{C} are defined as follows:

$$\mathbf{s}^T = \{\mathbf{N}^T, \mathbf{M}^T\} \quad (16a)$$

$$\mathbf{e}^T = \{\boldsymbol{\varepsilon}^T, \boldsymbol{\kappa}^T\} \quad (16b)$$

$$\mathbf{C} = \mathbf{C}(s_1, s_2) = \begin{bmatrix} \mathbf{A}(s_1, s_2) & \mathbf{0} \\ \mathbf{0} & \mathbf{D}(s_1, s_2) \end{bmatrix} \quad (16c)$$

Equations Governing the Response

A general analytical approach for the exact solution of the equilibrium equations for a laminated-composite cylindrical shell with variable curvature is not mathematically tractable. Therefore, a semi-analytic variational approach that is based on the principle of stationary potential energy is used in the present study to obtain numerical results. Because elastic edge restraints are used as a means to relax the kinematic admissibility conditions on the assumed displacement functions, and because a rigid-end-ring capability is used to impose shell-end force resultants, the potential energy consists of the elastic strain energy of the shell and the elastic edge restraints and the potential energy of the applied loads. In particular, the potential energy is expressed symbolically by

$$\pi(\mathbf{q}, \Delta) = U(\mathbf{q}) + \Omega(\mathbf{q}, \Delta) + V(\mathbf{q}, \Delta) \quad (17)$$

in which U and Ω represent the strain energy of the laminate and the elastic edge supports (springs), and V represents the potential energy due to external boundary loads. Their explicit forms are presented in Appendix A. The symbol \mathbf{q} is the vector of unknown, generalized displacement coefficients that arises from the mathematical representation of the mid-surface displacement fields that is used in the variational solution process. In particular, the mid-surface

displacement fields are given symbolically by $u_1(\mathbf{q})$, $u_2(\mathbf{q})$, and $u_3(\mathbf{q})$. The symbol Δ represents the vector of unknown edge displacements that arise from prescribing end loads.

Subjected to the constraint equations that arise from the use of Lagrange multipliers, the equations governing the shell response are obtained by enforcing the requirement that the first variation of the total potential energy vanish. As discussed by McFarland et al.,³⁵ because the constraint equations are not functionally dependent on spatial coordinates, s_1 and s_2 , the equations governing the response may be generated by modifying the total potential energy into the form

$$\pi^*(\mathbf{q}, \Delta, \boldsymbol{\lambda}) = \pi(\mathbf{q}, \Delta) + W(\mathbf{q}, \boldsymbol{\lambda}) \quad (18)$$

in which W is viewed as the potential energy arising from constraint reactions. In particular,

$$W(\mathbf{q}, \boldsymbol{\lambda}) = \boldsymbol{\lambda}^T \mathbf{G} \mathbf{q} = 0 \quad (19)$$

where $\boldsymbol{\lambda}$ is the unknown vector of Lagrange multipliers and \mathbf{G} is the known constraint coefficient matrix.

Substituting the specific expressions for $U(\mathbf{q})$, $\Omega(\mathbf{q}, \Delta)$, $V(\mathbf{q}, \Delta)$, and $W(\mathbf{q}, \boldsymbol{\lambda})$ that arise from approximation of the surface-displacement field and enforcing the first variation of the modified form of the total potential energy to vanish lead to

$$\begin{aligned} \delta \pi^* = \delta \mathbf{q}^T & \left[\mathbf{k}_{qq} \mathbf{q} + \mathbf{S}_{qq} \mathbf{q} - \mathbf{s}_{q\Delta} \Delta - \mathbf{f}^* - \mathbf{T}^* + \mathbf{G}^T \boldsymbol{\lambda} \right] \\ & + \delta \Delta^T \left[\mathbf{s}_{\Delta\Delta} \Delta - \mathbf{s}_{q\Delta}^T \mathbf{q} - \mathbf{P}^* \right] + \delta \boldsymbol{\lambda}^T \mathbf{G} \mathbf{q} = 0 \end{aligned} \quad (20)$$

in which the matrix, \mathbf{k}_{qq} represents the stiffness matrix of the shell and requires evaluation of the corresponding integrand over a doubly connected region (see Appendix A for details). The spring-stiffness matrices, \mathbf{S}_{qq} and $\mathbf{s}_{\Delta\Delta}$, are associated with the deformation of the shell edges and displacement of the rigid end-ring, respectively. The spring-stiffness matrix, $\mathbf{s}_{q\Delta}$, captures the coupling between the displacement of the shell edges and the rigid end-ring. The vectors \mathbf{f}^* , \mathbf{T}^* , and \mathbf{P}^* arise from the prescribed boundary displacements, external tractions and moments, and the concentrated forces applied to a rigid end-ring, respectively. For the arbitrary variations ($\delta \mathbf{q}$, $\delta \Delta$, and $\delta \boldsymbol{\lambda}$), the stationary condition requires that the following equations must be satisfied:

$$\left[(\mathbf{k}_{qq} + \mathbf{S}_{qq}) \mathbf{q} - \mathbf{s}_{q\Delta} \Delta - \mathbf{f}^* - \mathbf{T}^* + \mathbf{G}^T \boldsymbol{\lambda} \right] = \mathbf{0} \quad (21a)$$

$$\left[\mathbf{s}_{\Delta\Delta} \Delta - \mathbf{s}_{q\Delta}^T \mathbf{q} - \mathbf{P}^* \right] = \mathbf{0} \quad (21b)$$

$$\mathbf{G} \mathbf{q} = \mathbf{0} \quad (21c)$$

It is convenient, to express Eqs. (21a) - (21c) into the single matrix equation

$$\mathbf{K} \mathbf{Q} = \mathbf{F} \quad (22)$$

where \mathbf{K} and \mathbf{F} represent the overall, system stiffness matrix and the overall load vector, respectively. These matrices have the general, expanded form

$$\mathbf{K} = \begin{bmatrix} \mathbf{K}_{qq} & -\mathbf{s}_{q\Delta} & \mathbf{G}^T \\ -\mathbf{s}_{q\Delta}^T & \mathbf{s}_{\Delta\Delta} & \mathbf{0}^T \\ \mathbf{G} & \mathbf{0} & \mathbf{0} \end{bmatrix} \quad \text{and} \quad \mathbf{F} = \begin{bmatrix} \mathbf{F}^* \\ \mathbf{P}^* \\ 0 \end{bmatrix} \quad (23a,b)$$

in which

$$\mathbf{K}_{qq} = \mathbf{k}_{qq} + \mathbf{S}_{qq} \quad \text{and} \quad \mathbf{F}^* = \mathbf{f}^* + \mathbf{T}^* \quad (23c,d)$$

The vector of unknowns, \mathbf{Q} , that appears in Eq. (22) is defined as

$$\mathbf{Q} = \begin{bmatrix} \mathbf{q} \\ \Delta \\ \lambda \end{bmatrix} \quad (24)$$

Solving for the vector of unknowns in Eq. (22) yields all the information needed to obtain a complete variational solution to a specific problem. The accuracy of a solution depends on the number of terms included in the expressions for the local and global functions representing the displacement fields and converges to the corresponding exact solution as the number of terms increases.

Displacement-field representation

Representation of the mid-surface displacement field is a critical step in the variational solution to the problem. By relaxing the requirements for kinematic admissibility, the mid-surface displacement fields are represented in the present study by a combination of rigid-body modes, u_{Ri} , and global and local functions, denoted by \bar{u}_i and $\bar{\bar{u}}_i$, respectively; that is,

$$u_i = u_{Ri} + \bar{u}_i + \bar{\bar{u}}_i \quad (25)$$

where the values of the index are given by $i = 1, 2$, and 3 . The rigid-body modes account for the overall or global translation and rotation of the shell, and are selected so that they produce neither membrane strain nor changes in shell curvature and twist. These terms are included for the completeness of the kinematics of the cylindrical shell. The presence of the appropriate displacement boundary conditions inherently eliminates the rigid-body motion. However, for cases where an insufficient number of kinematic boundary conditions are imposed, these rigid-body terms need to be eliminated, as discussed in detail in Appendix C. Following the complex-variable solution techniques used in the theory of elasticity, the local functions are expressed in terms of robust, uniformly convergent Laurent series (used for doubly connected regions) to enhance capturing steep stress gradients and

deformations near the cutout. Complete sets of trigonometric expansions are used to primarily capture the overall global response of the shell. Here, completeness means that all the fundamental waveforms needed to construct the typical overall deformations of a shell are included in the set.

For convenience, the displacement representations are rewritten in matrix form as

$$u_i = \mathbf{V}_{Ri}^T \mathbf{a}_R + \bar{\mathbf{V}}_i^T \mathbf{c}_i + \bar{\bar{\mathbf{V}}}_i^T \mathbf{a} \quad (i = 1, 2) \quad (26a)$$

$$u_3 = \mathbf{V}_{R3}^T \mathbf{a}_R + \bar{\mathbf{V}}_3^T \mathbf{c}_3 + \bar{\bar{\mathbf{V}}}_3^T \boldsymbol{\beta} \quad (26b)$$

An even more useful, compact form is given by

$$u_i = \mathbf{V}_i^T \mathbf{q} \quad \text{with } i = 1, 2, 3 \quad (27)$$

where the vector of unknown displacement coefficients, \mathbf{q} , is defined by

$$\mathbf{q}^T = \{ \mathbf{a}_R^T, \mathbf{c}_1^T, \mathbf{c}_2^T, \mathbf{c}_3^T, \mathbf{a}^T, \boldsymbol{\beta}^T \} \quad (28)$$

In Eq. (28), the vector \mathbf{a}_R contains the unknown coefficients for the rigid-body motion of the shell, and the vectors \mathbf{a} and $\boldsymbol{\beta}$ contain the real and imaginary parts of the unknown coefficients α_{nm} and β_{nm} , respectively, that are associated with the local functions. The vectors \mathbf{c}_i , where $i = 1, 2, 3$, contain the real-valued unknown coefficients, $c_{i(mn)}$ that are associated with the global functions. The explicit forms used herein for the unknown coefficient vectors \mathbf{a}_R , \mathbf{c}_i , \mathbf{a} , and $\boldsymbol{\beta}$ that appear in Eqs. (26a) and (26b) along with the vector functions \mathbf{V}_i (and the corresponding subvectors \mathbf{V}_{Ri} , $\bar{\mathbf{V}}_i$, and $\bar{\bar{\mathbf{V}}}_i$) are given in Appendix B.

In addition to the general representation of the shell surface-displacement fields, similar matrix expressions are needed for the displacements and rotations of points on the shell boundary. In the present study, the boundary displacement vector \mathbf{u}_r is introduced that consists of the mid-surface boundary displacements in the directions normal, tangent, and transverse to a shell edge, and the mid-surface rotations about axes that are normal and tangent to a shell edge. The boundary displacements in the directions normal, tangent, and transverse to a shell edge are denoted herein by u_n , u_s , and u_t , respectively. Similarly, the mid-surface rotations about axes that are tangent and normal to a shell edge are denoted by ϑ_n and ϑ_s , respectively. In terms of the vector of unknowns defined by Eq. (28), the boundary displacements and rotations are expressed in matrix form by

$$\mathbf{u}_r = \mathbf{B} \mathbf{q} \quad (29)$$

in which the boundary displacement vector, \mathbf{u}_Γ is defined by

$$\mathbf{u}_\Gamma^T = \{u_n, u_s, u_t, \theta_n\} \quad (30)$$

The matrix \mathbf{B} is a known matrix of coefficients that is defined as

$$\mathbf{B} = \begin{bmatrix} \mathbf{u}_n^T \\ \mathbf{u}_s^T \\ \mathbf{u}_t^T \\ \boldsymbol{\theta}_n^T \end{bmatrix} \quad (31)$$

in which the sub-vectors, \mathbf{u}_n^T , \mathbf{u}_s^T , \mathbf{u}_t^T and $\boldsymbol{\theta}_n^T$ are known and defined by

$$\mathbf{u}_n^T = (\mathbf{n} \cdot \mathbf{e}_1) \mathbf{V}_1 \quad (32a)$$

$$\mathbf{u}_s^T = [(\mathbf{e}_3 \times \mathbf{n}) \cdot \mathbf{e}_2] \mathbf{V}_2 \quad (32b)$$

$$\mathbf{u}_t^T = \mathbf{V}_3^T \quad (32c)$$

and

$$\boldsymbol{\theta}_n^T = (\mathbf{n} \cdot \mathbf{e}_1) \mathbf{V}_{3,1}^T \quad (32d)$$

Strain- and stress-resultant-field representation

After defining the shell mid-surface displacement field in terms of the generalized coordinate \mathbf{q} , the corresponding representation of the strains is obtained by substituting Eq. (27) into the strain-displacement relations given in vector form by Eqs. (12a) and (12b). This substitution yields

$$\boldsymbol{\varepsilon} = \mathbf{L}_\varepsilon \mathbf{q} \quad (33a)$$

and

$$\boldsymbol{\kappa} = \mathbf{L}_\kappa \mathbf{q} \quad (33b)$$

where the strain-coefficient matrices \mathbf{L}_ε and \mathbf{L}_κ are defined as

$$\mathbf{L}_\varepsilon = \begin{bmatrix} \mathbf{V}_{1,1}^T \\ \mathbf{V}_{2,2}^T + \frac{1}{R} \mathbf{V}_3^T \\ \mathbf{V}_{1,2}^T + \mathbf{V}_{2,1}^T \end{bmatrix} \quad (34a)$$

$$\mathbf{L}_\kappa = \begin{bmatrix} -\mathbf{V}_{3,11}^T \\ -\mathbf{V}_{3,22}^T + \frac{1}{R} \mathbf{V}_{2,2}^T + \frac{R_{,2}}{R^2} \mathbf{V}_2^T \\ -2\mathbf{V}_{3,12}^T + \frac{2}{R} \mathbf{V}_{2,1}^T \end{bmatrix} \quad (34b)$$

Next, the representations for $\boldsymbol{\varepsilon}$ and $\boldsymbol{\kappa}$ are substituted into Eq. (15b) to obtain

$$\mathbf{e} = \mathbf{L} \mathbf{q} \quad (35)$$

where the overall strain-coefficient matrix \mathbf{L} is defined as

$$\mathbf{L}^T = [\mathbf{L}_\varepsilon^T \quad \mathbf{L}_\kappa^T] \quad (36)$$

Finally, the corresponding matrix representation of the stress resultants in terms of the generalized coordinates is obtained by substituting Eq. (35) into constitutive Eq. (15). The resulting vector of stress resultants is given by

$$\mathbf{s} = \mathbf{C} \mathbf{L} \mathbf{q} \quad (37)$$

Constraint Equations

In the generalized-coordinate representations for u_1 and u_2 , the coefficients $c_{1(00)}$ and $c_{2(00)}$ associated with the global functions, \bar{u}_1 and \bar{u}_2 , also correspond to rigid-body translation in the s_1 direction and rigid-body rotation about the s_1 axis, respectively. These two redundant rigid-body modes are eliminated by introducing constraint conditions using Lagrange multipliers. In particular, the unknown Lagrange multipliers $\lambda_{RRB(1)}$ and $\lambda_{RRB(2)}$ are associated with the redundant rigid-body modes. Also, multi-valuedness of the normal-direction displacement $u_3(s_1, s_2)$ that arises from the presence of logarithmic terms in the Laurent-series-expansion for the local function—must be eliminated. The unknown Lagrange multipliers $\lambda_{SV(r)}$ and $\lambda_{SV(s)}$ are used herein to eliminate this multi-valuedness. Likewise, the rigid-body modes of the cylindrical shell must be eliminated by the Lagrange multipliers $\lambda_{RB(j)}$ ($j = 1, \dots, 6$) if the specified kinematic boundary conditions are not sufficient enough to prevent them. In other words, the non-vanishing rigid body modes must be eliminated by introducing constraint conditions prior to the stress analysis in order for the overall system stiffness matrix \mathbf{K} , given in Eq (22), to be nonsingular.

These requirements on the representation of the shell displacement field are enforced by using constraint equations that use Lagrange multipliers. These constraint equations are functionally independent, forming a set of linearly independent equations equal in number to the total number of Lagrange multipliers. The Lagrange multipliers can be viewed as the reactions that are needed to enforce the corresponding constraints. In the present study, all of these constraint conditions are included in the matrix equation given in Eq. (19). The explicit form of the vector of unknown Lagrange multipliers, $\boldsymbol{\lambda}$, and the known coefficient matrix, \mathbf{G} , are given in Appendix C.

Overview of Validation Studies

A limited series of validation studies were conducted in the present study to determine the accuracy of results obtained by using analysis method presented herein. Specifically, the studies included circular and non-

circular cylindrical shells with either a circular or an elliptical cutout under uniform tension. The stress resultants around the circular and elliptical cutout for varying aspect ratios and orientations in a circular cylinder as well as the stress concentrations arising from a circular cutout in a non-circular cylindrical shell were computed. Comparisons of the stress-resultant distributions and magnitudes in the shells were made with the corresponding results obtained by using an in-house finite element program developed earlier by Madenci and Barut.³⁶ This finite element program has been validated, to a large extent, against previously published experimental and numerical results for stress, buckling, and post-buckling of thin-shell structures (see Madenci and Barut^{37,38}). Therefore, this finite element program is expected to serve as a reliable indicator of the accuracy of the analysis methods and results presented herein. Overall, the comparisons indicate very good agreement (less than 1% difference) between the corresponding results produced by the two analysis methods. For shells with high-aspect-ratio cutouts, differences of approximately 5% were obtained and found to be the result of insufficient mesh refinement in the finite element models.

Selected Numerical Results

Selected numerical results are presented in this section to demonstrate the utility of the analysis method presented herein and the potential for its use in developing design technology. These results elucidate the effects of loading condition, non-circular cross-section geometry, wall-thickness variation, cutout shape, cutout size, and cutout orientation on the intensity of stress-resultant concentrations near a cutout. Specifically, tension, torsion, and pure-bending loads are considered for $[45^\circ / -45^\circ / 90^\circ / 0^\circ / 90^\circ / -45^\circ / 45^\circ]_s$ quasi-isotropic shells with length $L = 356$ mm and made of graphite-epoxy plies. The nominal ply thickness is $t_{k0} = 0.14$ mm, resulting in the total thickness of the shell given by $h = 2.24$ mm, and the ply orientation angles are measured with respect to the longitudinal shell axis. The Young's moduli of each ply in the longitudinal, fiber direction and in the direction transverse to the fibers are specified as $E_L = 135.0$ GPa and $E_T = 13.0$ GPa, respectively. The in-plane shear modulus and Poisson's ratio of each ply are given by $G_{LT} = 6.4$ GPa and $\nu_{LT} = 0.38$.

The effects of varying the radius of curvature R_0 on the stress-resultant concentration along the contour of a circular cutout with radius $a = 25.5$ mm are shown in Fig. 5 for a circular cylindrical shell subjected to a uniform axial tension load. Four curves that correspond

to values of $R_0/L = 0.5, 0.75, 1$, and 1.25 are presented that show the tangential stress resultant, $N_{\phi\phi}$, normalized by the far-field applied uniform stress resultant N_0 , as a function of position around the cutout (indicated by the "cutout angle", ϕ). As shown in Fig. 5, the stress-resultant concentration is a maximum at $\phi = 90^\circ$ and 270° (at the net section of the shell) for each case and reduces from a maximum value of approximately 4.0 to a minimum value of 3.4 at the net section as the radius of curvature increases. In addition, the results show that the $N_{\phi\phi}(a, 90^\circ)$ stress-resultant concentration approaches the well-known value of three for an isotropic plate as the shell radius increases. Away from the net section, changes in the radius of curvature have a relatively small effect on the stress-resultant concentration.

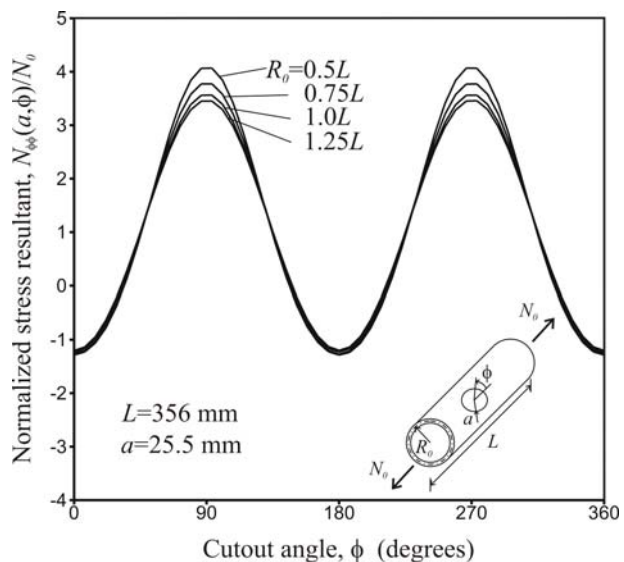


Fig 5 The effect of varying shell radius on the tangential stress resultants around a circular cutout in a quasi-isotropic circular cylindrical shell subjected to a uniform tension load.

The effects of varying the circular-cutout radius on the stress-resultant concentration along the contour of a circular cutout is shown in Fig. 6 for a circular cylindrical shell with radius $R_0 = 381$ mm and subjected to a uniform axial tension load. Five curves that correspond to values of the cutout radius $a = 15, 25.5, 30, 40$, and 50 mm are presented that also show the tangential stress resultant $N_{\phi\phi}(a, \phi)$, normalized by the far-field applied uniform stress resultant, N_0 , as a function of the cutout angle ϕ . The results in Fig. 6 show that the stress-resultant concentration is a maximum at the net section of the shell for each case,

as expected, and changes significantly from a minimum value of approximately 3.1 to a maximum value of 5.1 at the net section as the cutout radius increases - an increase of approximately 65%. The results also show that the $N_{\phi\phi}(a, 90^\circ)$ stress-resultant concentration approaches the well-known value of three for an isotropic plate as the cutout radius decreases. Away from the net section, changes in the cutout radius have a much smaller effect on the stress-resultant concentration.

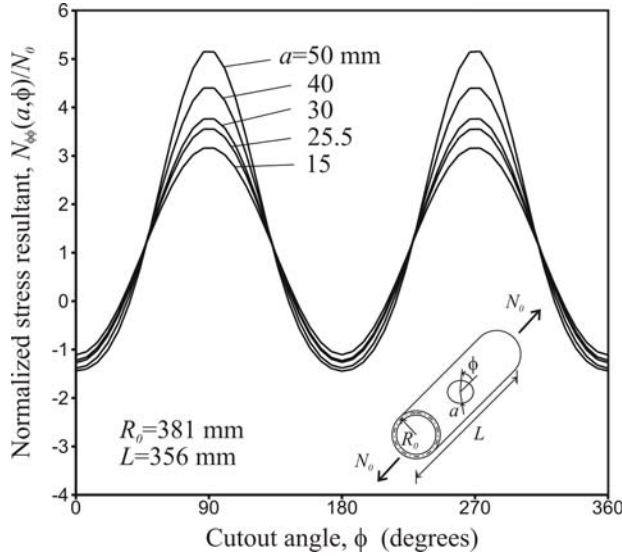


Fig 6 The effect of varying circular-cutout radius on the tangential stress resultants around a circular cutout in a quasi-isotropic circular cylindrical shell subjected to a uniform tension load.

The effect of varying the elliptical-cutout aspect ratio, a/b , on the tangential stress-resultant distribution around the edge of a cutout in a cylindrical shell with radius $R_0 = 178$ mm, and subjected to uniform tension is presented in Fig. 7. The orientation of the elliptical cutout is specified by $\psi = 0^\circ$. Two curves that correspond to the locations $\phi = 0^\circ$ and 90° are presented that show the tangential stress resultant, $N_{\beta\beta}(\alpha_0, \beta)$ normalized by the far-field applied uniform stress resultant N_0 , as a function of the cutout aspect ratio. As expected, the normalized stress-resultant concentration, $N_{\beta\beta}(\alpha_0, \beta)/N_0$, remains negative for all aspect ratios at $\phi = 0^\circ$, consistent with the expected Poisson effect, and the magnitudes are relatively insignificant at this location. In contrast, large stress-resultant concentrations are indicated at the net section ($\phi = 90^\circ$) that diminish from a maximum value of approximately 17.0 for a widthwise, slot-like cutout

with ($a = 5$ mm and $b = 30$ mm) or ($a/b = 1/6$) to a minimum value of 1.4 for a lengthwise, slot-like cutout ($a = 30$ mm and $b = 5$ mm) or ($a/b = 6$).

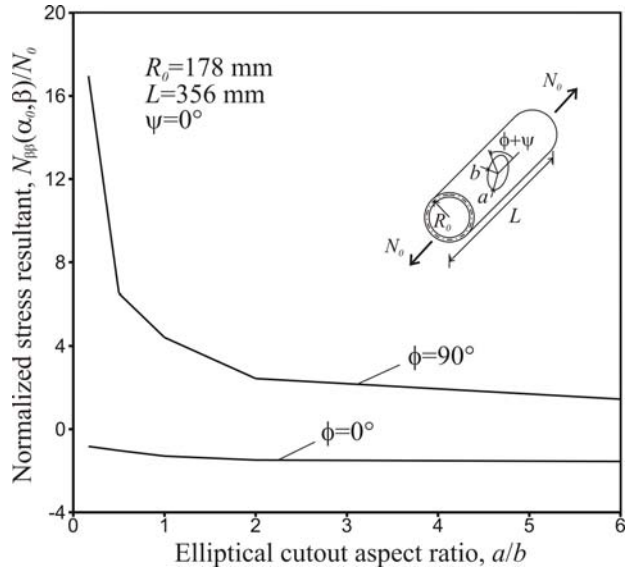


Fig 7 The effect of varying elliptical-cutout aspect ratio on the tangential stress resultants around a cutout in a quasi-isotropic cylindrical shell subjected to a uniform tension load.

The effects of varying the orientation of a high-aspect-ratio, slot-like elliptical cutout on the stress-resultant concentration along the cutout contour is shown in Fig. 8 for a circular cylindrical shell with radius $R_0 = 178$ mm and subjected to a uniform axial tension load. The major and minor axes of the cutout are given by $a = 30$ mm and $b = 5$ mm, respectively. The orientation of the elliptical cutout, with respect to the longitudinal shell axis, is measured by the angle, ψ . Three curves that correspond to values of $\psi = 0^\circ, 45^\circ$, and 90° are presented that show the tangential stress resultant at the cutout edge, $N_{\beta\beta}$ normalized by the far-field applied uniform stress resultant, N_0 as a function of the cutout angle ϕ .

The results in Fig. 8 show that the stress-resultant concentration is the least pronounced for the case of $\psi = 0^\circ$. For this case, the cutout major axis is aligned lengthwise with the shell axis and the net section of the shell is the largest. The location on the cutout edge defined by $\phi = 0^\circ$ corresponds to where the edge of the cutout intersects the major axis. At this location, the edge of the cutout is in tangential compression ($N_{\beta\beta}/N_0 = -1.6$), consistent with a Poisson effect. The location defined by $\phi = 90^\circ$ corresponds to where

the edge of the cutout intersects the minor axis; that is, at the net section of the shell. At this location, the edge of the cutout is in tangential tension ($N_{\beta\beta}/N_0 = 1.4$). Between approximately $\phi = 10^\circ$ and 170° and between $\phi = 190^\circ$ and 350° , the cutout width (and hence net section width) does not vary greatly. This attribute accounts for the corresponding flat regions in the $\psi = 0^\circ$ curve shown in Fig. 8.

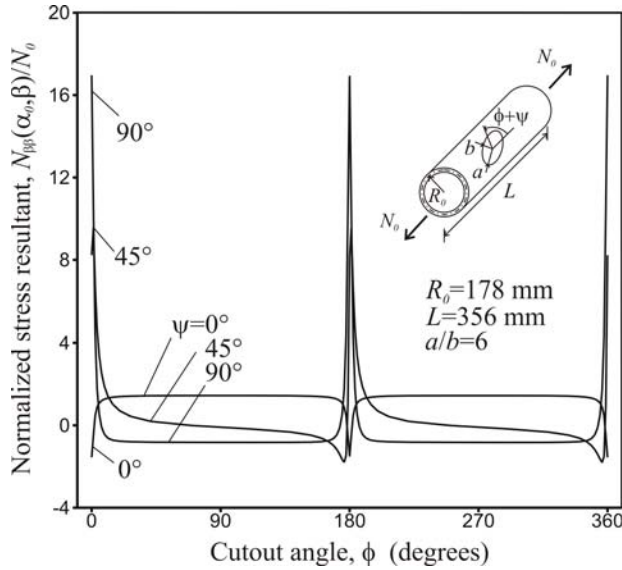


Fig 8 The effect of varying elliptical-cutout orientation on the tangential stresses around the cutout in a quasi-isotropic cylindrical shell subjected to a uniform tension load.

For the case of $\psi = 90^\circ$, the cutout major axis is perpendicular to the shell axis and the net section of the shell is the smallest. As before, the locations defined by $\phi = 0^\circ$ and 180° correspond to where the edge of the cutout intersects the major axis; that is, at the net section of the shell. The results in Fig. 9 show that the edge of this high-aspect-ratio cutout has extremely high stress-resultant concentrations at these locations ($N_{\beta\beta}/N_0 = 17.$) that have very steep gradients. Between approximately $\phi = 5^\circ$ and 175° and between $\phi = 185^\circ$ and 355° , the analysis predicts relatively benign variations in the stress-resultant concentration. The case of $\psi = 45^\circ$, exhibits stress-resultant concentrations that are, for the most part, bounded by the corresponding results for $\psi = 0^\circ$ and 90° . The analysis also predicts very high stress-resultant concentrations where the cutout edge intersects the major principal cutout axis ($N_{\beta\beta}/N_0 = 8.2$).

The effects of varying the cross-section eccentricity (see Eq. (2)) of a tension-loaded oval shell with a circular cutout are shown in Fig. 9. The results in this figure correspond to the equivalent shell radius $R_0 = 381$ mm and a circular-cutout radius given by $a = 25.5$ mm. Moreover, the tangential stress-resultant concentration at the shell net section, $N_{\phi\phi}(a, 90^\circ)$, normalized by the applied load N_0 , is shown as a function of the eccentricity parameter for the range of $-0.15 \leq \xi \leq 0.15$. As indicated in the figure, negative and positive values of ξ correspond to cylindrical shells with the largest cross-sectional width oriented parallel and perpendicular to the tangent plane that passes through the two points of the cutout edge that are on the surface generator that passes through the center of the cutout, respectively. A value of $\xi = 0$ corresponds to a circular cross-section and a value of $\xi = 0.15$ corresponds to cross-sectional aspect ratio of 0.9.

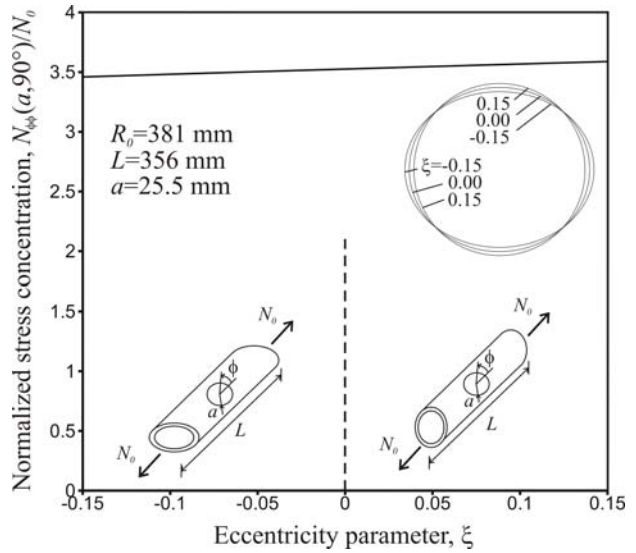


Fig 9 The effect of shell cross-section eccentricity on the stress-resultant concentration in an oval quasiisotropic cylindrical shell with a circular cutout and subjected to a uniform tension load.

The results presented in Fig. 9 show that the stress-resultant concentration is affected benignly by the cross-sectional eccentricity. In particular, the stress-resultant concentration increases almost linearly with increases in the eccentricity parameter from $N_{\phi\phi}(a, 90^\circ)/N_0 = 3.5$ to 3.6, which is slightly less than a 3% variation. This trend is understood by noting that the shells that correspond to negative values of ξ are flatter near the cutout than those that correspond to

positive values of ξ and, as indicated by the results in Fig. 5, are expected to have the lower values for the stress-resultant concentrations.

The effects of longitudinal and circumferential periodic wall-thickness variations on the stress-resultant concentration at the net section of circular cylindrical shell with radius $R_0 = 178$ mm, circular cutout radius $a = 25.5$ mm, and subjected to uniform axial tension load are shown in Fig. 10. Two monotonically increasing curves that correspond to values of ε_1 (with $\varepsilon_2 = 0$) and ε_2 (with $\varepsilon_1 = 0$) are presented that show the tangential stress resultant $N_{\phi\phi}(a, 90^\circ)$, normalized by the far-field applied uniform stress resultant N_0 , as a function of thickness-variation amplitudes (see Eq.(3)) that range from 0 to 0.2. For the longitudinal thickness variation, the wave numbers used in Eq. (3) are $m_1 = 1$ and $m_2 = 0$. Similarly, for the circumferential thickness variation, the wave numbers used in Eq. (3) are $m_1 = 0$ and $m_2 = 1$.

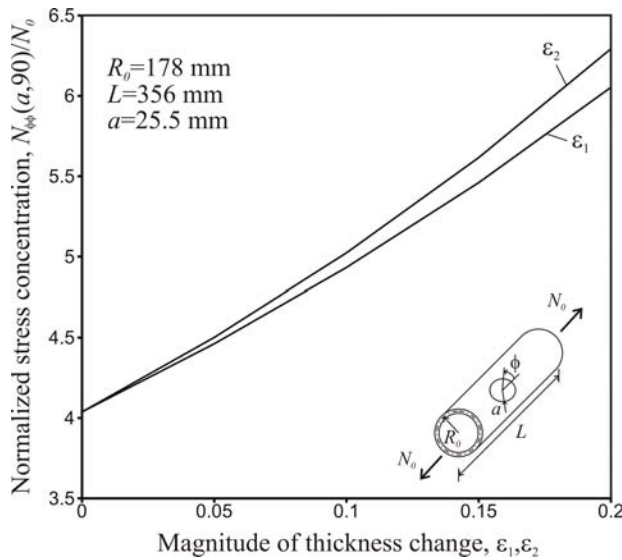


Fig 10 The effects of longitudinal ($\varepsilon_1 \neq 0$ and $\varepsilon_2 = 0$) and circumferential ($\varepsilon_1 \neq 0$ and $\varepsilon_2 = 0$) wall thickness variations on the tangential stress-resultant concentration around a circular cutout in a quasi-isotropic circular cylindrical shell subjected to a uniform tension load.

The results shown in Fig. 10 indicate that the stress-resultant concentration at the shell net section increases as the magnitude of the thickness variation increases, for variations in either the longitudinal or circumferential direction. The maximum variation in the results is approximately 56%. Furthermore, the change in the stress-resultant concentration is slightly

more pronounced for the circumferential thickness variation than for the longitudinal thickness variation. These increases are primarily due to a drastic loss of bending stiffness near the net section of the shell, as indicated by the wave numbers $m_1 = 0$ and $m_2 = 1$, where the thickness of the shell near the center of the cutout is smaller.

The effects of varying the radius of curvature R_0 on the stress-resultant concentration along the contour of a circular cutout with radius $a = 25.5$ mm is shown in Figs. 11 and 12 for a circular cylindrical shell subjected to a uniform torsion load and a pure-bending load, respectively. The pure-bending load corresponds to using $t_n^* = M_0 \cos(\pi/s_2)$ in Eq. (5a). Four curves that correspond to values of $R_0/L = 0.5, 0.75, 1$, and 1.25 are presented that show the normalized values of the tangential stress resultant $N_{\phi\phi}$ as a function of position around the cutout. In Fig. 11, $N_{\phi\phi}$ is normalized by the far-field applied uniform shear stress resultant, T_0 . In Fig. 12, $N_{\phi\phi}$ is normalized by the far-field applied uniform bending stress resultant, M_0 .

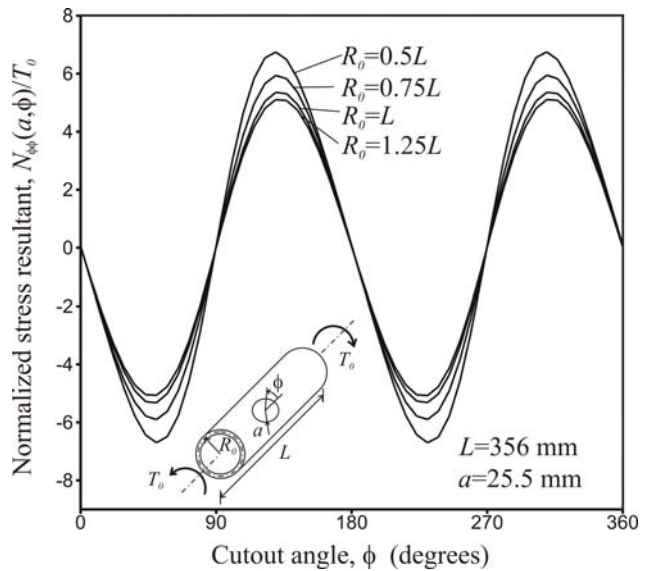


Fig 11 The effect of varying shell radius on the tangential stresses around a circular cutout in a quasi-isotropic circular cylindrical shell subjected to a uniform torsion load.

The results in Fig. 11 indicate that the stress-resultant concentration has identical maximum magnitudes at $\phi = 45^\circ, 135^\circ, 225^\circ$, and 315° (at the net section of the shell) for each case, which corresponds to maximum diagonal tension and compression stress resultants associated with the shear stress resultants near the cutout. The magnitudes of the stress-resultant

concentration for these four locations reduces from a maximum value of 6.8 to a minimum value of 5.1 as the radius of curvature increases (33% variation). Away from these four locations, changes in the radius of curvature have a smaller effect on the stress-resultant concentration. The results in Fig. 12 indicate that the stress-resultant concentration for the shell subjected to the pure-bending load is quite similar to that presented in Fig. 5 for the corresponding tension-loaded shell.

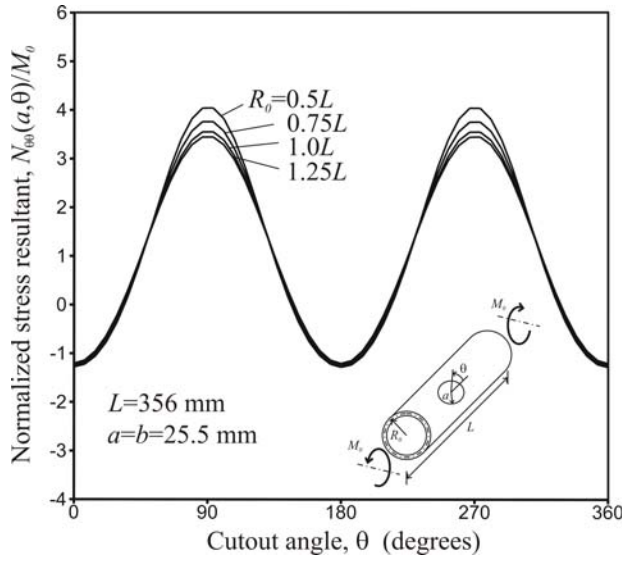


Fig 12 The effect of varying shell radius on the tangential stresses around a circular cutout in a quasi-isotropic circular cylindrical shell subjected to a pure-bending load.

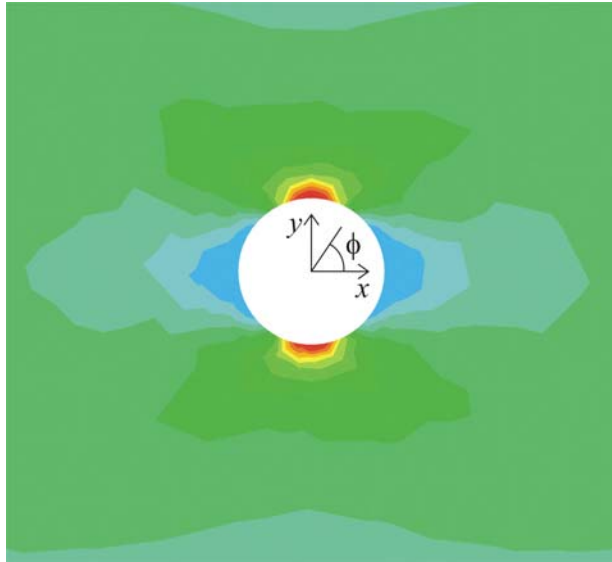


Fig 13 Stress resultant distribution near the cutout in a quasi-isotropic circular cylindrical shell subjected to a pure-bending load.

Specifically, the stress-resultant concentration is a maximum at $\phi = 90^\circ$ and 270° (at the net section of the shell) for each case and reduces from a maximum value of 4.0 to a minimum value of 3.5 at the net section as the radius of curvature increases (14% variation). In addition, $N_{\phi\phi}/M_0$ approaches the well-known value of three for an isotropic plate as the shell radius increases, and away from the net section, changes in the radius of curvature have a relatively small effect on the stress-resultant concentration. For the case of $R_0/L = 0.5$ shown in Fig. 12, a contour plot of $N_{\phi\phi}/M_0$ near the cutout is shown in Fig. 13. The extent of the stress concentration at the shell net section ($\phi = 90^\circ$ and 270°) is clearly captured by the analysis method presented herein. The highest stress-resultant concentration is $N_{\phi\phi}(a, 90^\circ)/M_0 = 4$ and it attenuates to the value of 1.01 at a radius of about 80 mm (approximately three times the cutout radius), measured from the center of the cutout.

Concluding Remarks

A special-purpose, semi-analytical approach based on complex potential functions has been presented that can be used to investigate the behavior of thin, noncircular cross-section cylindrical shells made of laminated-composite materials and with a cutout, efficiently and parametrically. In particular, the effects of radius of curvature; elliptical cutout size, aspect ratio, and orientation; oval cross-section eccentricity; wall-thickness variations; and loading conditions on the stress-resultant concentration near the cutout have been presented for a quasi-isotropic shell subjected to uniform tension, uniform torsion and pure bending. In addition, studies that were conducted to validate the analysis method have been described.

A key finding of the results obtained with this analysis method is that the maximum tangential stress-resultant concentration near a circular cutout in a tension-loaded, circular, quasi-isotropic shell increases by approximately 18% as the shell radius-to-length ratio decreases from 1.25 to 0.5. Likewise, increases in the maximum tangential stress-resultant concentration as large as 65% have been found to occur with a five-fold increase in cutout radius. Results have also been presented that show extremely high tangential stress-resultant concentrations can occur for high aspect ratio elliptical cutouts whose principal axes are not aligned with the longitudinal axis of a tension-loaded shell.

Additionally, results have been presented that show tension-loaded oval shells with a circular cutout on one of the flatter sides exhibit slightly lower tangential stress-resultant concentrations than the corresponding shell with the cutout on one of the more highly curved sides. Results have also been presented that show that

wall-thickness variations in either the longitudinal or circumferential directions significantly affect the stress concentration, with respect to that for the corresponding shell with a nominal thickness. The analysis also predicts that a quasi-isotropic shell with a circular cutout and subjected to pure bending that yields the maximum tensile stress resultant at the longitudinal axis of the cutout behaves similarly to the corresponding tension-loaded shell. The corresponding shell subjected to torsion was found to exhibit the maximum tangential stress-resultant concentrations at locations consistent with the maximum diagonal tension and compression near the cutout. Overall, the results demonstrate that the analysis approach is a powerful means for developing design criteria for laminated-composite shells.

Acknowledgement

The authors wish to dedicate this paper to the memory of Dr. James H. Starnes, Jr. of the NASA Langley Research Center. Dr. Starnes was an internationally recognized expert in aerospace structures technology and a proponent of the development of special-purpose, design-oriented analysis methods such as that presented herein.

References

- ¹Lurie, A. I., "Concentration of Stresses in the Vicinity of an Aperture in the Surface of a Circular Cylinder," *Prikl. Mat. Mekh.*, Vol. 10, 1946, pp. 397-406.
- ²Lurie, A. I., *Statics of Thin-Walled Elastic Shells*, State Publishing House of Technical and Theoretical Literature, Moscow, 1947.
- ³Lekkerkerker, J. G., "Stress Concentration Around Circular Holes in Cylindrical Shells," *AIAA Journal*, Vol. 10, 1964, pp. 1466-1472.
- ⁴Van Dyke, P., "Stresses about a Circular Hole in a Cylindrical Shell," *AIAA Journal*, Vol. 3, 1965, pp. 1733-1742.
- ⁵Ashmarin, I. A., "Stress Concentration Around a Circular Opening in an Orthotropic Cylindrical Shell," *Prikladnaya Mekhanika*, Vol. 2, 1966, pp. 44-48.
- ⁶Murthy, M. V. V., Rao, K. P. and Rao, A. K., "On the Stress Problem of Large Elliptical Cutouts and Cracks in Circular Cylindrical Shells," *International Journal of Solids and Structures*, Vol. 10, 1974, pp. 1243-1269.
- ⁷Guz, A. N., Chernyshenko, I. S. and Shnerenko, K. I., "Stress Concentration Near Openings in Composite Shells," *International Applied Mechanics*, Vol. 37, 2001, pp. 139-181.
- ⁸Van Tooren, M. J. L., Van Stijn, I. P. M. and Beukers, A., "Curvature Effects on the Stress Distribution in Sandwich Cylinders with a Circular Cut-out," *Composites: Part A*, Vol. 3, 2002, pp. 1557-1572.
- ⁹Tennyson, R.C., "The Effects of Unreinforced Circular Cutouts on the Buckling of Circular Cylindrical Shells under Axial Compression," *ASME Journal of Engineering Industry*, Vol. 90, 1968, pp. 541-546.
- ¹⁰Starnes, J. H., Jr., "Effect of a Circular Hole on the Buckling of Cylindrical Shells Loaded by Axial Compression," *AIAA Journal*, Vol. 10, 1972, pp. 1466-1472.
- ¹¹Pierce, D. N. and Chou, S. I., "Stresses Around Elliptical Holes in Circular Cylindrical Shells," *Experimental Mechanics*, Vol. 13, 1973, pp. 487-492.
- ¹²Bull, J. W., "Stresses Around Large Circular Holes in Uniform Circular Cylindrical Shells," *Journal of Strain Analysis*, Vol. 17, 1982, pp. 9-12.
- ¹³Zirka, A. I. and Chernopiskii, "Stress Concentration in an Axially Compressed Cylindrical Shell of Medium Thickness with an Elliptic Opening," *International Applied Mechanics*, Vol. 10, 2003, pp. 1466-1472.
- ¹⁴Liang, C., Hsu C. and Chen W., "Curvature Effect on Stress Concentrations Around Circular Hole in Opened Shallow Cylindrical Shell Under External Pressure," *International Journal of Pressure Vessels and Piping*, Vol. 75, 1998, pp. 749-763.
- ¹⁵Shnerenko, K. I. and Godzula, V. F., "Stress Distribution in a Composite Cylindrical Shell with a Large Circular Opening," *International Applied Mechanics*, Vol. 39, 2003, pp. 1323-1327.
- ¹⁶Hicks, R., "Stress Concentrations Around Holes in Plates and Shells," *Proceedings of the Applied Mechanics Conference*, New Castle Upon Tyne, 1964, pp. 3-12.
- ¹⁷Ebner, H. and Jung, O., 1972, "Stress Concentration Around Holes in Plates and Shells," *Contributions to the Theory of Aircraft Structures*, Delft University Press, Rotterdam.
- ¹⁸Li, Y. W., Elishakoff, I., and Starnes, J.H., Jr., "Axial Buckling of Composite Cylindrical Shells with Periodic Thickness Variation," *Computers and Structures*, Vol. 56, 1995, pp. 65-74.
- ¹⁹Sheinman, I. and Firer, M., "Buckling Analysis of Laminated Cylindrical Shells with Arbitrary Noncircular Cross Sections," *AIAA Journal*, Vol. 32, 1994, pp. 648-654.
- ²⁰Hyer, M. W. and Woldford, G. F., "Progressive Failure Analysis of Internally Pressurized Noncircular Composite Cylinders," ^{43rd} *AIAA/ASME/ASCE/AHS/ASC Structures, Structural Dynamics, and Materials Conference*, Denver, Colorado, Paper No. 2002-1403, 2002.
- ²¹Hyer, M. W. and Woldford, G. F., "Damage Initiation and Progression in Internally Pressurized Noncircular Composite Cylinders," ^{44rd} *AIAA/ASME/ASCE/AHS/ASC Structures, Structural*

Dynamics, and Materials Conference, Norfolk, Virginia, Paper No. 2003-1594, 2003.

²²Lekhnitskii, S. G., *Anisotropic Plates*, Gordon and Breach Science Publishers, Inc., New York, 1968.

²³Romano, F. and Kempner, J., "Stress and Displacement Analysis of a Simply Supported Non-circular Cylindrical Shells under Lateral Pressure," PIBAL Report No. 415, Polytechnic Institute of Brooklyn, New York, 1958.

²⁴Shewchuk, J. R., "Triangle: Engineering a 2D Quality Mesh Generator and Delaunay Triangulator," *First Workshop on Applied Computational Geometry*, Philadelphia, Pennsylvania, pp. 124-133, 1996.

²⁵Madenci, E. and Barut, A., "Influence of an Elliptical Cutout on Buckling Response of Composite Cylindrical Shells with Non-uniform Wall-Thickness and Non-Circular Cross-Section," *44th AIAA/ASME/ASCE/AHS/ASC Structures, Structural Dynamics, and Materials Conference*, Norfolk, Virginia, Paper No. 2003-1929, 2003.

²⁶Love, A. E. H., "The Small Free Vibrations and Deformation of a Thin Elastic Shell," *Philosophical Transactions of the Royal Society of London*, Vol. 179, A, 1888.

²⁷Love, A. E. H., *A Treatise on the Mathematical Theory of Elasticity*, 4th ed., Dover Publications, New York, 1944.

²⁸Timoshenko, S. and Woinowsky-Krieger, S., *Theory of Plates and Shells*, 2nd ed., McGraw-Hill Book Company, New York, 1959.

²⁹Bushnell, D., "Computerized Analysis of Shells - Governing Equations," *Computers & Structures*, Vol. 18, No. 3, 1984, pp. 471-536.

³⁰Reissner, E., "A New Derivation of the Equations for the Deformation of elastic Shells," *American Journal of Mathematics*, Vol. 63, 1941, pp. 177-184.

³¹Kraus, H., *Thin Elastic Shells - An Introduction to the Theoretical Foundations and the Analysis of Their Static and Dynamic Behavior*, John Wiley and Sons, Inc., 1967.

³²Naghdi, P. M., "Foundations of Elastic Shell Theory," Office of Naval Research, Technical Report No. 15, January 1962.

³³Chaudhuri, R. A., Balaraman, K., and Kunukasseril, V. X., "Arbitrarily Laminated, Anisotropic Cylindrical Shell Under Internal Pressure," *AIAA Journal*, Vol. 24, No. 11, 1986, pp. 1851-1858.

³⁴Jones, R. M., *Mechanics of Composite Materials*, 2nd ed., Taylor & Francis, Inc. Philadelphia, Pennsylvania, 1999.

³⁵McFarland, D., Bert L. Smith, B. L. and Walter D. Bernhart, W. D., *Analysis of Plates*, Spartan Books, New York, 1972.

³⁶Madenci, E. and Barut, A., "A Free-Formulation Based Flat Shell Element for Non-Linear Analysis of Thin Composite Structures," *International Journal for*

Numerical Methods in Engineering, Vol. 37, 1994, pp. 3825-3842.

³⁷Madenci, E. and Barut, A., "Pre- and Postbuckling Response of Curved, Thin Composite Panels with Cutouts under Compression," *International Journal for Numerical Methods in Engineering*, Vol. 37, 1994, pp. 1499-1510.

³⁸Madenci, E. and Barut, A., "Thermal Postbuckling Analysis of Cylindrically Curved Composite Laminates with a Hole," *International Journal for Numerical Methods in Engineering*, Vol. 37, 1994, pp. 2073-2091.

Appendix A

Strain Energy of shell

Based on classical laminated shell theory, the strain energy of the shell can be expressed as

$$U = \frac{1}{2} \int_A \mathbf{s}^T \mathbf{e} \, dA \quad (38)$$

in which A is the planform area of the shell mid-surface. Substituting the expressions for the resultant stress and strains, given in terms of the vector of unknown displacement coefficients, \mathbf{q} , by Eqs. (35) and (37), leads to

$$U(\mathbf{q}) = \frac{1}{2} \int_A \mathbf{q}^T (\mathbf{L}^T \mathbf{C} \mathbf{L}) \mathbf{q} \, dA \quad (39)$$

The matrix \mathbf{L} involves the derivatives of the assumed, functional displacement representations, and \mathbf{C} is the overall constitutive matrix defined by Eq. (16c). The expression for the strain energy is rewritten into the final form used herein as

$$U(\mathbf{q}) = \frac{1}{2} \mathbf{q}^T \mathbf{k}_{qq} \mathbf{q} \quad (40)$$

where

$$\mathbf{k}_{qq} = \int_A (\mathbf{L}^T \mathbf{C} \mathbf{L}) \, dA \quad (41)$$

The evaluation of this area integral is performed numerically by employing basic quadrature techniques. In this analysis, the quadrature points are pre-determined by employing standard triangulation of the entire domain as described by Shewchuk.²⁴

Strain energy of elastic restraints

The strain energy of the elastic edge restraints (springs), Ω , is expressed as

$$\begin{aligned}\Omega = & \frac{1}{2} \sum_{\ell=1}^2 \sum_{\alpha=n,s,t} \int_{\Gamma_{(\ell)}} S_{\alpha} (u_{\alpha} - u_{\alpha}^*)^2 d\Gamma \\ & + \frac{1}{2} \sum_{\ell=1}^2 \sum_{\alpha=n,s} \int_{\Gamma_{(\ell)}} J_{\alpha} (\vartheta_{\alpha} - \vartheta_{\alpha}^*)^2 d\Gamma \\ & + \frac{1}{2} \sum_{\ell=1}^2 \sum_{\alpha=n,s} \int_{\Gamma_{(\ell)}} s_{\alpha} (u_{\alpha} - \Delta_{\alpha})^2 d\Gamma +\end{aligned}\quad (42)$$

As depicted in Fig. 4, the boundary displacements u_n, u_s , and u_t along the ℓ^{th} boundary segment are restrained by extensional springs with the stiffness values S_n , S_s , and S_t , respectively. Likewise, the boundary rotations ϑ_n and ϑ_s are restrained by rotational springs with the stiffness values J_n and J_s , respectively.

In order to apply concentrated forces along the edge of a shell and introduce edge displacements that are similar to those introduced by a rigid end-ring or by the loading platens of a testing machine, additional springs are used to simulate the load-introduction effects of a rigid end-ring. In particular, rigid-end-ring loads are introduced into the shell by using extensional springs in the directions normal and tangent to the boundary with corresponding stiffness values of s_n and s_s , as shown in Fig. 3. By specifying relatively large values for the spring stiffnesses s_n and s_s , the laminate edge behaves as if a rigid end-ring is attached that produces the uniform displacements Δ_n and Δ_s . In contrast, a relatively small spring stiffness between the shell edge and the rigid end-ring eliminates the presence of a rigid end-ring.

The desired form of the elastic-restraint strain energy is obtained in terms of the unknown vector \mathbf{q} by substituting expressions for the boundary displacements and rotations, given collectively by Eq. (29), into Eq. (42). This step yields

$$\begin{aligned}\Omega = & \frac{1}{2} \sum_{\ell=1}^2 \sum_{\alpha=n,s,t} \left(\mathbf{q}^T \mathbf{S}_{\alpha\alpha}^{(\ell)} \mathbf{q} + \Omega_{u(\alpha)}^{(\ell)*} - 2\mathbf{q}^T \mathbf{f}_{\alpha}^{(\ell)*} \right) \\ & + \frac{1}{2} \sum_{\ell=1}^2 \sum_{\alpha=n,s} \left(\mathbf{q}^T \mathbf{J}_{\alpha\alpha}^{(\ell)} \mathbf{q} + \Omega_{\vartheta(\alpha)}^{(\ell)*} - 2\mathbf{q}^T \mathbf{r}_{\alpha}^{(\ell)*} \right) \\ & + \frac{1}{2} \sum_{\ell=1}^2 \sum_{\alpha=n,s} \left(\mathbf{q}^T \mathbf{s}_{\alpha\alpha}^{(\ell)} \mathbf{q} + \int_{\Gamma_{(\ell)}} s_{\alpha} \Delta_{\alpha}^2 d\Gamma - 2\mathbf{q}^T \mathbf{s}_{\alpha}^{(\ell)} \Delta_{\alpha} \right)\end{aligned}\quad (43)$$

where the matrices $\mathbf{S}_{\alpha\alpha}^{(\ell)}$ and $\mathbf{J}_{\alpha\alpha}^{(\ell)}$ represent the stiffness contribution of the extensional and rotational springs attached to the ℓ^{th} segment of the boundary. These matrices are defined as

$$\mathbf{S}_{\alpha\alpha}^{(\ell)} = \int_{\Gamma_{(\ell)}} S_{\alpha} \mathbf{u}_{\alpha} \mathbf{u}_{\alpha}^T d\Gamma \quad (\alpha = n, s, t) \quad (44a)$$

and

$$\mathbf{J}_{\alpha\alpha}^{(\ell)} = \int_{\Gamma_{(\ell)}} J_{\alpha} \boldsymbol{\theta}_{\alpha} \boldsymbol{\theta}_{\alpha}^T d\Gamma \quad (\alpha = n, s) \quad (44b)$$

The matrix $\mathbf{s}_{\alpha\alpha}^{(\ell)}$, representing the stiffness of the springs attached to the rigid end-ring, is defined as

$$\mathbf{s}_{\alpha\alpha}^{(\ell)} = \int_{\Gamma_{(\ell)}} s_{\alpha} \mathbf{u}_{\alpha} \mathbf{u}_{\alpha}^T d\Gamma \quad (\alpha = n, s) \quad (45)$$

The load vectors, $\mathbf{f}_{\alpha}^{(\ell)*}$ and $\mathbf{r}_{\alpha}^{(\ell)*}$, are associated with the prescribed boundary displacements and rotations and are defined as

$$\mathbf{f}_{\alpha}^{(\ell)*} = \int_{\Gamma_{(\ell)}} S_{\alpha} u_{\alpha}^* \mathbf{u}_{\alpha} d\Gamma \quad (\alpha = n, s, t) \quad (46a)$$

and

$$\mathbf{r}_{\alpha}^{(\ell)*} = \int_{\Gamma_{(\ell)}} J_{\alpha} \vartheta_{\alpha}^* \boldsymbol{\theta}_{\alpha} d\Gamma \quad (\alpha = n, s) \quad (46b)$$

The vector, $\mathbf{s}_{\alpha}^{(\ell)}$, is associated with the unknown end-displacements that correspond to a given concentrated load and is defined as

$$\mathbf{s}_{\alpha}^{(\ell)} = \int_{\Gamma_{(\ell)}} s_{\alpha} \mathbf{u}_{\alpha} d\Gamma \quad (\alpha = n, s) \quad (47)$$

The strain energies in the springs that arises from the known prescribed displacements (u_n^* , u_s^* and u_t^*) and rotations (ϑ_n^* and ϑ_s^*) are defined as

$$\Omega_{u(\alpha)}^{(\ell)*} = \int_{\Gamma_{(\ell)}} S_{\alpha} u_{\alpha}^{*2} d\Gamma \quad (\alpha = n, s, t) \quad (48a)$$

and

$$\Omega_{\vartheta(\alpha)}^{(\ell)*} = \int_{\Gamma_{(\ell)}} J_{\alpha} \vartheta_{\alpha}^{*2} d\Gamma \quad (\alpha = n, s) \quad (48b)$$

For convenience, the expression for the strain energy in the springs is recast in matrix form as

$$\begin{aligned}\Omega(\mathbf{q}, \Delta) = & \frac{1}{2} \mathbf{q}^T \mathbf{S}_{qq} \mathbf{q} + \frac{1}{2} \Delta^T \mathbf{s}_{\Delta\Delta} \Delta \\ & - \mathbf{q}^T \mathbf{s}_{q\Delta} \Delta - \mathbf{q}^T \mathbf{f}^* + \Omega^*\end{aligned}\quad (49)$$

in which the matrices, \mathbf{S}_{qq} , $\mathbf{s}_{\Delta\Delta}$ and $\mathbf{s}_{q\Delta}$ represent the stiffness of the springs associated with the deformation of the laminate, the end-displacements and their coupling, respectively. These matrices are defined by

$$\mathbf{S}_{qq} = \sum_{\ell=1}^2 \sum_{\alpha=n,s,t} \mathbf{S}_{\alpha\alpha}^{(\ell)} + \sum_{\ell=1}^2 \sum_{\alpha=n,s} \mathbf{J}_{\alpha\alpha}^{(\ell)} + \sum_{\ell=1}^2 \sum_{\alpha=n,s} \mathbf{s}_{\alpha\alpha}^{(\ell)} \quad (50a)$$

$$\mathbf{s}_{\Delta\Delta} = \text{Diag}[s_n^{(1)}, s_n^{(2)}, s_s^{(1)}, s_s^{(2)}] \times 2\pi R_0 \quad (50b)$$

$$\mathbf{s}_{q\Delta} = [s_n^{(1)} \quad s_n^{(2)} \quad s_s^{(1)} \quad s_s^{(2)}] \quad (50c)$$

The vector of unknown end-displacements, Δ , is defined by

$$\Delta^T = \{\Delta_n^{(1)}, \Delta_n^{(2)}, \Delta_s^{(1)}, \Delta_s^{(2)}\} \quad (51)$$

The load vectors arising from all prescribed boundary displacements and rotations, \mathbf{f}^* , is defined as

$$\mathbf{f}^* = \frac{1}{2} \sum_{\ell=1}^2 \sum_{\alpha=n,s,t} \mathbf{f}_\alpha^{*(\ell)} + \frac{1}{2} \sum_{\ell=1}^2 \sum_{\alpha=n,s} \mathbf{r}_\alpha^{*(\ell)} \quad (52)$$

and the strain energy of all the springs due to prescribed displacements and rotations is

$$\Omega^* = \frac{1}{2} \sum_{\ell=1}^2 \sum_{\alpha=n,s,t} \Omega_{u(\alpha)}^{(\ell)*} + \frac{1}{2} \sum_{\ell=1}^2 \sum_{\alpha=n,s} \Omega_{g(\alpha)}^{(\ell)*} \quad (53)$$

Potential of external loads

The potential energy of the external tractions (t_n^* , t_s^* and t_t^*) and moments (m_n^* and m_s^*) acting along the ℓ^{th} boundary segment, and the concentrated loads (P_n^* and P_s^*) acting on the rigid end rings, is given in terms of the corresponding boundary displacements and rotations by

$$V = - \sum_{\ell=1}^2 \sum_{\alpha=n,s,t} \int_{\Gamma(\ell)} t_\alpha^* u_\alpha d\Gamma - \sum_{\ell=1}^2 \sum_{\alpha=n,s} \int_{\Gamma(\ell)} m_\alpha^* g_\alpha d\Gamma - \sum_{\ell=1}^2 \sum_{\alpha=n,s} P_\alpha^* \Delta_\alpha \quad (54)$$

Substituting the expressions for the boundary displacements and rotations, given in terms of the vector \mathbf{q} , and combining terms in Eq. (55) yields

$$V(\mathbf{q}, \Delta) = -\mathbf{q}^T \mathbf{T}^* - \Delta^T \mathbf{P}^* \quad (55)$$

where the vector Δ , containing the uniform end-displacements Δ_n and Δ_s of the ℓ^{th} boundary segment, is defined by

$$\Delta^T = \{ \Delta_n^{(1)}, \Delta_n^{(2)}, \Delta_s^{(1)}, \Delta_s^{(2)} \} \quad (56)$$

The load vectors, \mathbf{T}^* and \mathbf{P}^* are defined by

$$\mathbf{T}^{*T} = \sum_{\ell=1}^2 \sum_{\alpha=n,s,t} \int_{\Gamma(\ell)} t_\alpha^* \mathbf{u}_\alpha^T d\Gamma + \sum_{\ell=1}^2 \sum_{\alpha=n,s} \int_{\Gamma(\ell)} g_\alpha^* \boldsymbol{\theta}_\alpha^T d\Gamma \quad (57a)$$

and

$$\mathbf{P}^{*T} = \{ P_n^{*(1)}, P_n^{*(2)}, P_s^{*(1)}, P_s^{*(2)} \} \quad (57b)$$

in which $^{(\ell)}P_\alpha^*$, with $(\alpha = n, s)$, represents the membrane forces applied on the ℓ^{th} boundary segment through a rigid end-ring.

Appendix B

Rigid-body modes

As given by Madenci and Barut²⁴, the rigid-body displacements (u_{R1} , u_{R2} and u_{R3}) of a cylindrical shell, defined with respect to the curvilinear coordinates, (s_1, s_2, s_3) , are expressed herein as

$$u_{R1} = \alpha_1 - \alpha_6 y + \alpha_5 z \quad (58a)$$

$$u_{R2} = \alpha_2 \cos \theta - \alpha_3 \sin \theta - \alpha_4 (y \sin \theta + z \cos \theta) + \alpha_5 x \sin \theta + \alpha_6 x \cos \theta \quad (58b)$$

$$u_{R3} = \alpha_2 \sin \theta + \alpha_3 \cos \theta + \alpha_4 (y \cos \theta - z \sin \theta) - \alpha_5 x \cos \theta + \alpha_6 x \sin \theta \quad (58c)$$

where θ denotes the angle between the radius of curvature at a point on the shell surface and z -axis as shown in Fig. 1.

Global functions

The global functions \bar{u}_i that are used to capture the overall deformations away from the cutout are expressed in terms of a series expansion of orthogonal functions of the form

$$\bar{u}_i(s_1, s_2) = \sum_{m=0}^M \sum_{n=0}^m c_{i(mm)} T_m(s_1) W_n(s_2) \quad (59)$$

The symbols $c_{i(mm)}$ are the unknown real-valued coefficients, and $T_m(s_1)$ and $W_n(s_2)$ are defined as

$$T_m(s_1) = \begin{cases} 1 & m=0 \\ \zeta & m=1 \\ \sin \left[\frac{(m-1)}{2} (\zeta+1) \right] & m>1 \end{cases} \quad (60a)$$

and

$$W_n(s_2(\theta)) = \begin{cases} \cos(n\theta/2) & n=0,2,4,6,8,\dots \\ \sin((n+1)\theta/2) & n=1,3,5,7,9,\dots \end{cases} \quad (60b)$$

in which $-1 \leq \zeta \leq 1$ and s_1 is related to ζ as $s_1 = \zeta L/2$, with L being the length of the cylinder.

Note that W_n is periodical. These particular functions were chosen because they form a complete set of functions when used with Eq. (59). Hence, they are desirable for employing in energy based semi-analytic solution techniques such as the total potential energy principal that is used in this study.

Local functions

The local functions are expressed in terms of mapping functions that transform the contour of an elliptical cutout to a unit circle. These mapping functions are used permit the use of Laurent series expansions as local functions, which is desirable because Laurent series are analytic and uniformly convergent in domains with a circular hole. As a result, the use of mapping functions reduces the number of terms in the Laurent series significantly that are needed to adequately capture steep stress and strain gradients and local deformations near a cutout. In accordance with the principle of minimum potential energy, the local local functions are not required to satisfy the traction boundary conditions at the cutout boundary. Thus, the local functions, $\bar{\bar{u}}_i$, are expressed in the form of Laurent series, in terms of complex functions, as

$$\bar{u}_1 = 2 \operatorname{Re} \left[\sum_{m=1}^2 u_m^{(1)} \sum_{\substack{n=-N \\ n \neq 0}}^N \alpha_{nm} \Phi_{nm}^*(z_{\varepsilon m}) \right] H(\rho) \quad (61a)$$

$$\bar{u}_2 = 2 \operatorname{Re} \left[\sum_{m=1}^2 u_m^{(2)} \sum_{\substack{n=-N \\ n \neq 0}}^N \alpha_{nm} \Phi_{nm}^*(z_{\varepsilon m}) \right] H(\rho) \quad (61b)$$

$$\bar{u}_3 = 2 \operatorname{Re} \left[\sum_{m=1}^2 \sum_{\substack{n=-N \\ n \neq 0}}^N \beta_{nm} F_{nm}^*(z_{\kappa m}) \right] H(\rho) \quad (61c)$$

with

$$\rho = \sqrt{x_1^2 + x_2^2} \quad (62)$$

where the parameter N defines the extent of the complex series. In these series, α_{nm} and β_{nm} are the unknown complex coefficients that appear in Eqs. (26)-(28). The auxiliary function $H(\rho)$ that defines the domain of influence of the local functions is expressed in a polynomial form as

$$H(\rho) = \begin{cases} 1 - 10 \left(\frac{\rho}{\rho_o} \right)^3 + 15 \left(\frac{\rho}{\rho_o} \right)^4 - 6 \left(\frac{\rho}{\rho_o} \right)^5 & 0 \leq \rho \leq \rho_o \\ 0 & \rho > \rho_o \end{cases} \quad (63a)$$

with

$$H(\rho_o) = H'(\rho_o) = H''(\rho_o) = 0 \quad (63b)$$

where the prime marks denotes differentiation with respect to the variable ρ and the parameter ρ_o denotes the radius of the region in which the local functions are effective. The purpose of choosing the auxiliary function is to prevent any possible linear dependency between the local and global functions and to restrict the influence of the local functions to a limited domain around the cutout.

The complex functions $u_m^{(1)}(z_{\varepsilon m})$ and $u_m^{(2)}(z_{\varepsilon m})$ that appear in Eqs. (61a) and (61b) are defined as

$$u_m^{(1)}(z_{\varepsilon m}) = \cos \psi \quad p_m(z_{\varepsilon m}) - \sin \psi \quad q_m(z_{\varepsilon m}) \quad (64a)$$

$$u_m^{(2)}(z_{\varepsilon m}) = \sin \psi \quad p_m(z_{\varepsilon m}) + \cos \psi \quad q_m(z_{\varepsilon m}) \quad (64b)$$

where the complex constants p_m and q_m are given by

$$p_m = a_{11} \mu_{\varepsilon m}^2 + a_{12} - a_{16} \mu_{\varepsilon m} \quad (65a)$$

$$q_m = a_{12} \mu_{\varepsilon m} + a_{22} / \mu_{\varepsilon m} - a_{26} \quad (65b)$$

In Eqs. (65a) and (65b), the unknown complex constants, $\mu_{\varepsilon m}$, are the roots to the characteristic equation associated with membrane deformation, i.e.,

$$a_{11} \mu_{\varepsilon m}^4 - 2a_{16} \mu_{\varepsilon m}^3 + (2a_{26} + a_{66}) \mu_{\varepsilon m}^2 - 2a_{26} \mu_{\varepsilon m} + a_{22} = 0 \quad (66)$$

in which the coefficients a_{ij} are the coefficients of the flexibility matrix \mathbf{a} , which is the inverse of the stiffness matrix \mathbf{A} defined by Eq. (13a). Both the flexibility and

the stiffness matrices, \mathbf{a} and \mathbf{A} , are measured with respect to the local coordinate system (x_1, x_2) . The angle, ψ represents the orientation of the local coordinate system with respect to the global coordinate system, (s_1, s_2) .

The complex potential function, $\Phi_{nm}^*(z_{\varepsilon m})$, appearing in Eqs. (61a) and (61b) is defined as

$$\Phi_{nm}^*(z_{\varepsilon m}) = \xi_{\varepsilon m}^n \quad (67)$$

in which the mapping functions, $\xi_{\varepsilon m}$, map a cutout onto a unit circle. The mapping functions for an elliptical cutout, introduced by Lekhnitskii²², are given by

$$\xi_{\varepsilon m} = \frac{z_{\varepsilon m} \pm \sqrt{z_{\varepsilon m}^2 - a^2 - \mu_{\varepsilon m}^2 b^2}}{a - i \mu_{\varepsilon m}^2 b} \quad (m=1,2) \quad (68)$$

where $z_{\varepsilon m} = x_1 + \mu_{\varepsilon m} x_2$, a and b are the major and minor axes of the elliptical cutout, and $i = \sqrt{-1}$. The sign of the square-root term is chosen so that $|\xi_{\varepsilon m}| \geq 1$ (i.e., the mapped point is guaranteed to be on or outside the unit circle).

Inverting the mapping function provides $\omega_{\varepsilon m}(\xi_{\varepsilon m})$ as

$$z_{\varepsilon m} = \omega_{\varepsilon m}(\xi_{\varepsilon m}) = r_{\varepsilon m} \xi_{\varepsilon m} - \frac{s_{\varepsilon m}}{\xi_{\varepsilon m}} \quad (69)$$

in which

$$r_{\varepsilon m} = \frac{1}{2}(a - i \mu_{\varepsilon m} b), \quad s_{\varepsilon m} = \frac{1}{2}(a + i \mu_{\varepsilon m} b) \quad (70a,b)$$

The unknown complex constants $\mu_{\varepsilon 1}$ and $\mu_{\varepsilon 2}$, and their complex conjugates, i.e., $\mu_{\varepsilon 3} = \bar{\mu}_{\varepsilon 1}$ and $\mu_{\varepsilon 4} = \bar{\mu}_{\varepsilon 2}$, are the roots obtained from the characteristic equation associated with membrane deformation

The complex potential functions, $F_{nm}^*(z_{\kappa m})$ in E. (61c) are defined as

$$F_{nm}^*(z_{\kappa m}) = \begin{cases} \frac{r_{\kappa m}}{n+1} \xi_{\kappa m}^n - \frac{s_{\kappa m}}{n-1} \xi_{\kappa m}^{n-2}, & |n| > 1 \\ \frac{r_{\kappa m}}{2} \xi_{\kappa m}^2 - s_{\kappa m} \ln \xi_{\kappa m}, & n = 1 \\ r_{\kappa m} \ln \xi_{\kappa m} + \frac{s_{\kappa m}}{2} \xi_{\kappa m}^{-2}, & n = -1 \end{cases} \quad (71)$$

in which the expressions for the mapping function $\xi_{\kappa m}$ and the constants $r_{\kappa m}$ and $s_{\kappa m}$ have the same form as the corresponding expressions for $\xi_{\varepsilon m}$, $r_{\varepsilon m}$, and $s_{\varepsilon m}$ given by Eqs. (68) - (70a,b), except that the subscript ε is replaced by κ .

The complex variables $z_{\kappa m}$ are defined by

$$z_{\kappa m} = x_1 + \mu_{\kappa m} x_2 \quad (72)$$

in which the unknown complex constants μ_{k1} and μ_{k2} and their conjugates, i.e., $\mu_{k3} = \bar{\mu}_{k1}$ and $\mu_{k4} = \bar{\mu}_{k2}$, are the roots obtained from the characteristic equation associated with the bending equilibrium equation

$$D_{22}\mu_{km}^4 + 4D_{26}\mu_{km}^3 + (2D_{12} + 4D_{66})\mu_{km}^2 + 4D_{16}\mu_{km} + D_{11} = 0 \quad (73)$$

where D_{ij} are the components of the bending stiffness matrix \mathbf{D} (see Eq. (13b), which is defined with respect to the local coordinate system, (x_1, x_2)).

It is important to note that the local functions in Eq. (61) satisfy the in-plane and bending equilibrium equations of a homogeneous, flat laminate of uniform thickness, not a cylindrical shell. Therefore, the roots to the characteristic equations, Eqs. (66) and (73) serve as approximation to their exact values which are not mathematically tractable. Because the solution procedure is based on the principle of minimum potential, their exact values are not necessarily required. However, they capture the stress concentration and local deformation near the cutout in cylindrical shells because these functions possess the inherent solution characteristics. They satisfy the equilibrium equations exactly as the radius of curvature approaches infinity and are uniformly convergent in a doubly connected region.

In the displacement representations defined by Eqs. (26a) and (26b), the vectors, \mathbf{a}_R , \mathbf{c}_i , \mathbf{a} , and $\mathbf{\beta}$ are defined as

$$\mathbf{a}_R^T = \{\alpha_{R1}, \alpha_{R2}, \alpha_{R3}, \alpha_{R4}, \alpha_{R5}, \alpha_{R6}\} \quad (74a)$$

$$\mathbf{c}_i^T = \{c_{i(00)}, c_{i(10)}, c_{i(01)}, \dots, c_{i(M0)}, \dots, c_{i((M-1)1)}, \dots, c_{i(1(M-1))}, c_{i(0M)}\} \quad (74b)$$

$$\mathbf{a}^T = \{\mathbf{a}_{-N}^T, \mathbf{a}_{-N+1}^T, \dots, \mathbf{a}_{-1}^T, \mathbf{a}_1^T, \dots, \mathbf{a}_{N-1}^T, \mathbf{a}_N^T\} \quad (74c)$$

in which

$$\mathbf{a}_n^T = \{\mathbf{a}_{n1}^T, \mathbf{a}_{n2}^T\} \quad (75)$$

with

$$\mathbf{a}_{nj}^T = \{\text{Re}[\alpha_{nj}], \text{Im}[\alpha_{nj}]\} \quad (76a)$$

and

$$\mathbf{\beta}^T = \{\mathbf{\beta}_{-N}^T, \mathbf{\beta}_{-N+1}^T, \dots, \mathbf{\beta}_{-1}^T, \mathbf{\beta}_1^T, \dots, \mathbf{\beta}_{N-1}^T, \mathbf{\beta}_N^T\} \quad (76b)$$

in which

$$\mathbf{\beta}_n^T = \{\mathbf{\beta}_{n1}^T, \mathbf{\beta}_{n2}^T\} \quad (77)$$

with

$$\mathbf{\beta}_{nj}^T = \{\text{Re}[\beta_{nj}^T], \text{Im}[\beta_{nj}^T]\} \quad (78)$$

The vector functions, \mathbf{V}_i , with $i = 1, 2, 3$ associated with the unknown generalized coordinates \mathbf{q} appearing in Eq. (27) are defined as

$$\mathbf{V}_1^T = \{\mathbf{V}_{R1}^T, \bar{\mathbf{V}}_1^T, \bar{\mathbf{0}}^T, \bar{\mathbf{0}}^T, \bar{\bar{\mathbf{V}}}_1^T, \bar{\bar{\mathbf{0}}}^T\} \quad (79a)$$

$$\mathbf{V}_2^T = \{\mathbf{V}_{R2}^T, \bar{\mathbf{0}}^T, \bar{\mathbf{V}}_2^T, \bar{\mathbf{0}}^T, \bar{\bar{\mathbf{V}}}_2^T, \bar{\bar{\mathbf{0}}}^T\} \quad (79b)$$

$$\mathbf{V}_3^T = \{\mathbf{V}_{R3}^T, \bar{\mathbf{0}}^T, \bar{\mathbf{0}}^T, \bar{\mathbf{V}}_3^T, \bar{\bar{\mathbf{0}}}^T, \bar{\bar{\mathbf{V}}}_3^T\} \quad (79c)$$

where

$$\bar{\mathbf{0}}^T = \{0, 0, 0, \dots, 0\} \text{ of order } [(M+1)(M+2)/2] \quad (80a)$$

$$\bar{\bar{\mathbf{0}}}^T = \{0, 0, \dots, 0\} \text{ of order } 8N \quad (80b)$$

The vectors associated with rigid body motion are

$$\mathbf{V}_{R1}^T = \{1, 0, 0, 0, z, -y\} \quad (81a)$$

$$\mathbf{V}_{R2}^T = \left\{0, \frac{dy}{ds_2}, \frac{dz}{ds_2}, \left(y \frac{dz}{ds_2} - z \frac{dy}{ds_2}\right), -x \frac{dz}{ds_2}, -x \frac{dy}{ds_2}\right\} \quad (81b)$$

$$\mathbf{V}_{R3}^T = \left\{0, -\frac{dz}{ds_2}, \frac{dy}{ds_2}, \left(y \frac{dy}{ds_2} + z \frac{dz}{ds_2}\right), -x \frac{dy}{ds_2}, -x \frac{dz}{ds_2}\right\} \quad (81c)$$

Similarly, the vectors associated with the global functions are

$$\begin{aligned} \bar{\mathbf{V}}_i^T = & \{T_0(s_1)W_0(s_2), T_1(s_1)W_0(s_2), \\ & T_0(s_1)W_1(s_2), T_2(s_1)W_0(s_2), \\ & T_1(s_1)W_1(s_2), T_0(s_1)W_2(s_2), \dots \\ & \dots, T_M(s_1)W_0(s_2), T_{M-1}(s_1)W_1(s_2), \dots \\ & \dots, T_1(s_1)W_{M-1}(s_2), T_0(s_1)W_M(s_2)\} \end{aligned} \quad (82)$$

in which the expressions for $T_i(s_1)$ and $W_i(s_2)$ are given by Eq. (60), and

$$\bar{\bar{\mathbf{V}}}_i^T = \{\bar{\bar{\mathbf{V}}}_{i(-N)}^T, \bar{\bar{\mathbf{V}}}_{i(-N+1)}^T, \dots, \bar{\bar{\mathbf{V}}}_{i(-1)}^T, \bar{\bar{\mathbf{V}}}_{i(1)}^T, \dots, \bar{\bar{\mathbf{V}}}_{i(N-1)}^T, \bar{\bar{\mathbf{V}}}_{i(N)}^T\} \quad (83)$$

with

$$\bar{\bar{\mathbf{V}}}_{i(n)}^T = \{\bar{\bar{\mathbf{V}}}_{i(n1)}^T, \bar{\bar{\mathbf{V}}}_{i(n2)}^T\} \quad (84)$$

in which

$$\bar{\bar{\mathbf{V}}}_{i(nj)}^T = \{2 \text{Re}[u_j^{(i)} \Phi_{nj}^*], -2 \text{Im}[u_j^{(i)} \Phi_{nj}^*]\} \quad (85)$$

where $i, j = 1, 2$ and

$$\bar{\bar{\mathbf{V}}}_3^T = \{\bar{\bar{\mathbf{V}}}_{3(-N)}^T, \bar{\bar{\mathbf{V}}}_{3(-N+1)}^T, \dots, \bar{\bar{\mathbf{V}}}_{3(-1)}^T, \bar{\bar{\mathbf{V}}}_{3(1)}^T, \dots, \bar{\bar{\mathbf{V}}}_{3(N-1)}^T, \bar{\bar{\mathbf{V}}}_{3(N)}^T\} \quad (86)$$

with

$$\bar{\bar{\mathbf{V}}}_{3(n)}^T = \{\bar{\bar{\mathbf{V}}}_{3(n1)}^T, \bar{\bar{\mathbf{V}}}_{3(n2)}^T\} \quad (87)$$

in which

$$\bar{\mathbf{V}}_{3(nj)}^T = \left\{ 2\text{Re}[F_{nj}^*], -2\text{Im}[F_{nj}^*] \right\}, (j=1,2) \quad (88)$$

Appendix C

Constraint Equations

The unknown vector of Lagrange multipliers, λ and the known coefficient matrix, \mathbf{G} , in Eq. (19) are defined by

$$\lambda^T = \left\{ \lambda_{RRB(1)}, \lambda_{RRB(2)}, \lambda_{SV(r)}, \lambda_{SV(s)}, \lambda_{RB(1)}, \dots, \lambda_{RB(6)} \right\} \quad (89a)$$

and

$$\mathbf{G} = \begin{bmatrix} \mathbf{0}_R^T & \mathbf{g}_{RRB(1)}^T & \bar{\mathbf{0}}^T & \bar{\mathbf{0}}^T & \bar{\bar{\mathbf{0}}}^T & \bar{\bar{\mathbf{0}}}^T \\ \mathbf{0}_R^T & \bar{\mathbf{0}}^T & \mathbf{g}_{RRB(2)}^T & \bar{\mathbf{0}}^T & \bar{\bar{\mathbf{0}}}^T & \bar{\bar{\mathbf{0}}}^T \\ \mathbf{0}_R^T & \bar{\mathbf{0}}^T & \bar{\mathbf{0}}^T & \bar{\mathbf{0}}^T & \bar{\bar{\mathbf{0}}}^T & \mathbf{g}_{SV(s)}^T \\ \mathbf{0}_R^T & \mathbf{0}_L^T & \bar{\mathbf{0}}^T & \bar{\mathbf{0}}^T & \bar{\bar{\mathbf{0}}}^T & \mathbf{g}_{SV(r)}^T \\ \mathbf{g}_{RB(1)}^T & \bar{\mathbf{0}}^T & \bar{\mathbf{0}}^T & \bar{\mathbf{0}}^T & \bar{\bar{\mathbf{0}}}^T & \bar{\bar{\mathbf{0}}}^T \\ \mathbf{g}_{RB(2)}^T & \bar{\mathbf{0}}^T & \bar{\mathbf{0}}^T & \bar{\mathbf{0}}^T & \bar{\bar{\mathbf{0}}}^T & \bar{\bar{\mathbf{0}}}^T \\ \mathbf{g}_{RB(3)}^T & \bar{\mathbf{0}}^T & \bar{\mathbf{0}}^T & \bar{\mathbf{0}}^T & \bar{\bar{\mathbf{0}}}^T & \bar{\bar{\mathbf{0}}}^T \\ \mathbf{g}_{RB(4)}^T & \bar{\mathbf{0}}^T & \bar{\mathbf{0}}^T & \bar{\mathbf{0}}^T & \bar{\bar{\mathbf{0}}}^T & \bar{\bar{\mathbf{0}}}^T \\ \mathbf{g}_{RB(5)}^T & \bar{\mathbf{0}}^T & \bar{\mathbf{0}}^T & \bar{\mathbf{0}}^T & \bar{\bar{\mathbf{0}}}^T & \bar{\bar{\mathbf{0}}}^T \\ \mathbf{g}_{RB(6)}^T & \bar{\mathbf{0}}^T & \bar{\mathbf{0}}^T & \bar{\mathbf{0}}^T & \bar{\bar{\mathbf{0}}}^T & \bar{\bar{\mathbf{0}}}^T \end{bmatrix} \quad (89b)$$

in which the constant coefficient vectors, $\mathbf{g}_{RRB(1)}$ and $\mathbf{g}_{RRB(2)}$ are associated with redundant rigid-body modes, $\mathbf{g}_{SV(r)}$ and $\mathbf{g}_{SV(s)}$ with single valuedness of the radial displacement component, and $\mathbf{g}_{RB(j)}$ with the rigid-body modes introduced by the global functions defined in Eq. (59). The rigid-body modes must be eliminated in the absence of a sufficient number of specified kinematic boundary conditions. These terms, as well as, the vectors with zeros are defined in the following subsections.

Redundant rigid-body modes

The coefficients, $c_{1(00)}$ and $c_{2(00)}$ in Eq. (59) for the global displacement functions produce additional rigid-body translation in the s_1 direction and rigid body rotation about the s_1 axis, respectively. Because these rigid-body modes are already represented by α_{R1} and α_{R6} in Eq. (58), the redundant rigid-body motion arising from the presence of $c_{1(00)}$ and $c_{2(00)}$, must be eliminated in order to obtain a unique representation of the displacements. These redundant rigid-body modes are eliminated by using the constraint conditions

$$\lambda_{RRB(1)} c_{1(00)} = 0 \quad (90a)$$

$$\lambda_{RRB(2)} c_{2(00)} = 0 \quad (90b)$$

in which the unknown Lagrange multipliers are denoted by $\lambda_{RRB(1)}$ and $\lambda_{RRB(2)}$. In terms of the vector of unknowns, \mathbf{q} , these constraints are rewritten in vector form as

$$\lambda_{RRB(1)} \left\{ \mathbf{0}_R^T, \mathbf{g}_{RRB}^T, \bar{\mathbf{0}}^T, \bar{\mathbf{0}}^T, \bar{\bar{\mathbf{0}}}^T, \bar{\bar{\mathbf{0}}}^T \right\} \begin{Bmatrix} \mathbf{a}_R \\ \mathbf{c}_1 \\ \mathbf{c}_2 \\ \mathbf{c}_3 \\ \mathbf{a} \\ \mathbf{\beta} \end{Bmatrix} = 0 \quad (91a)$$

$$\lambda_{RRB(2)} \left\{ \mathbf{0}_R^T, \bar{\mathbf{0}}^T, \mathbf{g}_{RRB}^T, \bar{\mathbf{0}}^T, \bar{\bar{\mathbf{0}}}^T, \bar{\bar{\mathbf{0}}}^T \right\} \begin{Bmatrix} \mathbf{a}_R \\ \mathbf{c}_1 \\ \mathbf{c}_2 \\ \mathbf{c}_3 \\ \mathbf{a} \\ \mathbf{\beta} \end{Bmatrix} = 0 \quad (91b)$$

in which the vectors of zeros, $\mathbf{0}_R^T$, $\bar{\mathbf{0}}_R^T$ and $\bar{\bar{\mathbf{0}}}_R^T$ are defined as

$$\mathbf{0}_R^T = \{0, 0, 0, 0, 0, 0\} \quad (92a)$$

$$\bar{\mathbf{0}}^T = \{0, 0, 0, \dots, 0\} \text{ of order } [(M+1)(M+2)/2] \quad (92b)$$

$$\bar{\bar{\mathbf{0}}}^T = \{0, 0, 0, \dots, 0\} \text{ of order } 8N \quad (92c)$$

The constant coefficient vector, \mathbf{g}_{RRB} is defined as

$$\mathbf{g}_{RRB}^T = \{1, 0, 0, \dots, 0\} \text{ of order } [(M+1)(M+2)/2] \quad (93)$$

Single-valuedness of the radial displacement component

The multi-valuedness of the normal displacement component that arises from the presence of logarithmic terms in the local expression for the radial displacement component in Eq. (61c) must be rendered single valued in order to obtain a unique solution. The logarithmic terms associated with complex constants, β_{-1m} and β_{1m} , with $(m=1,2)$, in Eq. (71) result in two real constants. Representing the complex variable of the Laurent series, $\xi_m = \rho_m e^{i\theta_m}$, the single-valuedness requirement is enforced as

$$u_z(\xi_m = \rho_m e^{i\theta_m}) - u_z(\xi_m = \rho_m e^{i(\theta_m+2\pi)}) = 0 \quad (94)$$

Associated with the complex constants, β_{-1m} and β_{1m} with $(m=1,2)$, in Eq. (71), this condition yields

$$2\text{Re} \left\{ \sum_{m=1}^2 \left\{ F_{-1m}^* (\xi_m = \rho_m e^{i\theta_m}) - F_{-1m}^* (\xi_m = \rho_m e^{i(\theta_m+2\pi)}) \right\} \beta_{-1m} \right\} = 0 \quad (95a)$$

or

$$\text{Im} \sum_{m=1}^2 [r_m \beta_{-1m}] = 0 \quad (95b)$$

and

$$2 \text{Re} \left\{ \sum_{m=1}^2 \left\{ F_{1m}^* (\xi_m = \rho_m e^{i\theta_m}) - F_{1m}^* (\xi_m = \rho_m e^{i(\theta_m + 2\pi)}) \right\} \beta_{1m} \right\} = 0 \quad (96a)$$

or

$$\text{Im} \sum_{m=1}^2 [s_{km} \beta_{1m}] = 0 \quad (96b)$$

In order to ensure single-valuedness, these constraints are enforced as

$$\lambda_{SV(r)} \text{Im} \left[\sum_{m=1}^2 [r_{km} \beta_{-1m}] \right] = 0 \quad (97a)$$

and

$$\lambda_{SV(s)} \text{Im} \left[\sum_{m=1}^2 [s_{km} \beta_{1m}] \right] = 0 \quad (97b)$$

in which the unknown Lagrange multipliers are denoted by $\lambda_{SV(r)}$ and $\lambda_{SV(s)}$.

In terms of the vector of unknowns, \mathbf{q} , these constraint conditions can be recast in matrix form as

$$\lambda_{SV(r)} \left\{ \begin{matrix} \mathbf{a}_R \\ \mathbf{c}_1 \\ \mathbf{c}_2 \\ \mathbf{c}_3 \\ \mathbf{a} \\ \mathbf{\beta} \end{matrix} \right\} = 0 \quad (98a)$$

$$\lambda_{SV(s)} \left\{ \begin{matrix} \mathbf{a}_R \\ \mathbf{c}_1 \\ \mathbf{c}_2 \\ \mathbf{c}_3 \\ \mathbf{a} \\ \mathbf{\beta} \end{matrix} \right\} = 0 \quad (98b)$$

where the constant coefficient vectors $\mathbf{g}_{SV(r)}$ and $\mathbf{g}_{SV(s)}$ are given by

$$\mathbf{g}_{SV(j)}^T = \left\{ \mathbf{g}_{SV(j)(-N)}^T, \mathbf{g}_{SV(j)(-N+1)}^T, \dots, \mathbf{g}_{SV(j)(-1)}^T, \mathbf{g}_{SV(j)(1)}^T, \dots, \mathbf{g}_{SV(j)(N-1)}^T, \mathbf{g}_{SV(j)(N)}^T \right\} \quad (99)$$

in which

$$\mathbf{g}_{SV(r)(1)}^T = \{ \text{Im}[r_1], \text{Re}[r_1], \text{Im}[r_2], \text{Re}[r_2] \} \quad (100a)$$

$$\mathbf{g}_{SV(r)(n)}^T = \{0, 0, 0, 0\} \quad \text{if } n \neq 1 \quad (100b)$$

and

$$\mathbf{g}_{SV(s)(1)}^T = \{ \text{Im}[s_1], \text{Re}[s_1], \text{Im}[s_2], \text{Re}[s_2] \} \quad (100c)$$

$$\mathbf{g}_{SV(s)(n)}^T = \{0, 0, 0, 0\} \quad \text{if } n \neq 1 \quad (100d)$$

with $-N \leq n \leq N$.

Rigid-body modes

In the absence of kinematic boundary conditions, the rigid-body modes of the displacement field are eliminated by enforcing the constraint conditions in the form

$$\lambda_{RB(j)} \alpha_{R(j)} = 0 \quad (101)$$

where $j = 1, 2, 3, 4, 5, 6$, and the unknown Lagrange multipliers are denoted by $\lambda_{RB(j)}$. In terms of the vector of unknowns, \mathbf{q} , these constraints are rewritten in vector form as

$$\lambda_{RB(j)} \left\{ \begin{matrix} \mathbf{a}_R \\ \mathbf{c}_1 \\ \mathbf{c}_2 \\ \mathbf{c}_3 \\ \mathbf{a} \\ \mathbf{\beta} \end{matrix} \right\} = 0 \quad (102)$$

where the constant coefficient vectors, $\mathbf{g}_{RB(j)}$ are defined as

$$\mathbf{g}_{RB(j)}^T = \{ \delta_{1j}, \delta_{2j}, \delta_{3j}, \delta_{4j}, \delta_{5j}, \delta_{6j} \} \quad (103)$$

in which δ_{ij} is the Kronecker delta.

Global Buckling and Face Wrinkling Response of Sandwich Panels under Transient Loads

Jörg Hohe*

Fraunhofer Institut für Werkstoffmechanik, 79108 Freiburg/Brsg., Germany

Liviu Librescu^{† ‡} and Sang Yong Oh[§]

Virginia Polytechnic Institute and State University, Blacksburg, VA, 24061-0219, USA

The present study is concerned with the transient dynamic response of sandwich panels subjected to rapidly applied loads. Special interest is directed to the effect of the transverse compressibility of sandwich structures with weak core. For the analysis, a previously presented higher-order sandwich shell theory of the v. Kármán type is utilized. The structural problem is solved by means of an extended Galerkin procedure in conjunction with an explicit, variable step Runge-Kutta scheme for the transient problem. In a number of examples dealing with the transient dynamic response of sandwich structures under rapid loading conditions, it is observed that the transverse core compressibility has distinct effects even on the overall response, if face wrinkling occurs during the loading history.

Nomenclature

$\delta(\dots)$	variational symbol
γ_{ij}	components of the Green-Lagrange strain tensor
λ, μ	buckling mode parameters
Ω_α	warping functions
τ_{ij}	components of the second Piola-Kirchhoff stress tensor
h	layer thickness
l	panel edge length
m	integrated mass density
M, N	stress resultants
m, n	number of modal waves of global instability mode
p, q	number of modal waves of face wrinkling instability mode
q	distributed load
$r_\alpha, r_{\alpha\beta}$	radii of curvature, matrix of the radii of curvature
T	kinetic energy
t	time
U	strain energy
u_i	two-dimensional midsurface displacements
v_i	three-dimensional displacements
W	work done by external forces
w	modal amplitude
x_i	components of the spatial vector

Subscripts

i, j	variable number ($i, j = 1, 2, 3$)
--------	--------------------------------------

*Scientist, Department of Components Structural Integrity.

†Professor, Department of Engineering Science and Mechanics.

‡Copyright by L. Librescu. Printed by NASA with permission.

§Scientist, Department of Engineering Science and Mechanics.

n, t normal and tangential direction on external boundaries
 α, β variable number ($\alpha, \beta = 1, 2$)

Superscripts

a, d average of face sheet quantities, half difference of face sheet quantities
 b, c, t bottom face sheet, core, top face sheet, core

I. Introduction

STRUCTURAL sandwich panels are important elements found in many areas of modern lightweight construction. The main advantage of the sandwich construction principle is the combination of a rather high bending stiffness with an extremely low specific weight. The standard sandwich panel is a layered structure according to Fig. 1 consisting of two high-density face sheets which are adhesively bonded to a low density core mostly consisting of a two-dimensional cellular or foamed material. Within the sandwich principle, the face sheets carry the tangential and bending loads whereas the core keeps the face sheets at their desired distance and transmits the transverse normal and shear loads. The classical technological field for sandwich construction is the field of aerospace engineering. Nevertheless, today sandwich structures can be found in many other areas as well. Especially in the naval industry, strong trends can be observed for using sandwich plates as structural members in ship construction (see e.g. Mouritz et al¹).

Due to the presence of a thick core layer made from a weak material, the structural response of sandwich plates is essentially different from the corresponding response of classical laminae consisting solely of thin layers and monolayer structures. Especially in buckling and post-buckling, distinct differences in the structural response can be observed since the presence of the weak core enables an additional local instability mode – the face wrinkling instability – where the face sheets buckle into the core region whereas the entire structure might remain globally stable. Due to the geometrically nonlinear nature of buckling phenomena, interaction effects between the local and the standard overall buckling mode might occur as it has been pointed out, among others, by Frostig et al.,² Starlinger and Rammerstorfer³ or the two of the present authors (Hohe and Librescu,^{4,5} Other theoretical and numerical studies concerning interaction effects between overall and local buckling of sandwich structures have recently been provided e.g. by da Silva and Santos⁶ or Wadee and Hunt.⁷

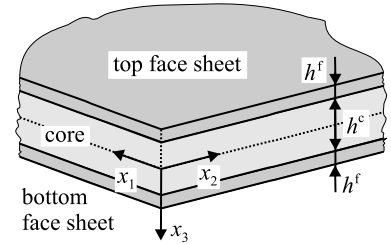


Figure 1. Structural sandwich panel.

The specific deformation behavior of structural sandwich panels with transversely incompressible core requires a specialized mechanical model for sandwich structures accounting for the effect of transverse core compressibility. In this context, Frostig et al.,²⁸ have provided a model which is based on the Kirchhoff-Love model for the face sheets and an assumed stress distribution for the core layer. Pure displacement based models have been provided by Dawe and Yuan,⁹ by Pai and Palazotto¹⁰ as well as in a previous study by the present authors (Hohe and Librescu,⁴⁵). The latter model also includes the effect of geometrical nonlinearity and thus enables a postbuckling analysis. An alternative effective single-layer approach, which accounts for interface stress equilibrium has recently been proposed by Barut et al.¹¹ Overviews can be found e.g. in the review articles by Noor et al.¹² or Vinson.¹³

The transient dynamic response of structural sandwich panels subject to time-dependent excitation has been studied in a one-dimensional sense by Mäkinen.¹⁴ Other recent work on the response of structural sandwich panels subject to pressure pulses includes the work by Xue and Hutchinson¹⁵ as well as a contribution by the present authors (Hohe et al.¹⁶).

The present study is directed to a theoretical and numerical analysis of the time-dependent response of structural sandwich panels subjected to rapidly applied in-plane edge loads and transverse pressure pulses. The study utilizes the structural model for sandwich plates with transversely compressible core presented Hohe and Librescu,^{4,5} The model is applied to a transient analysis of a rectangular, simply supported sandwich plate under time-dependent excitation. The structural problem is solved analytically by means of an extended Galerkin procedure. The time-dependent solution is obtained by means of an explicit fourth-order Runge-Kutta method. In a number of examples concerning both in-plane and transverse loads, it is observed that the transverse compressibility of the core and the local face wrinkling instability mode enabled by this feature can have distinct effects even in the overall response of sandwich structures and therefore

should not be neglected. The trends observed in the simulations coincide with earlier observations by other authors (Budiansky and Hutchinson¹⁷).

II. Structural model for sandwich plates with compressible core

THE present study utilizes the structural model for sandwich shells with transversely compressible core presented by Hohe and Librescu,^{4,5} In the current section, the model is briefly outlined in order to be concise. Full details can be found in the original papers.

The sandwich structure under consideration is a sandwich shell according to Fig. 1. The structure is symmetric with respect to the global midsurface which is employed as the structure's reference surface. The thicknesses of the core and the face sheets are denoted by h^c and h^f respectively. The core thickness is assumed to be much larger than the face sheet thickness. For the analysis, a local Cartesian reference system x_i ($i = 1, 2, 3$) is introduced, where x_α ($\alpha = 1, 2$) are the tangential directions whereas x_3 denotes the downward normal direction.

The displacements $v_i(x_j)$ for the three principal layers of the sandwich plate are expanded into power series with respect to the transverse (x_3 -) direction. For the face sheets, the standard Kirchhoff-Love hypothesis is adopted. Hence, the three-dimensional displacement fields $v_i^t(x_j)$ and $v_i^b(x_j)$ for the top and bottom face sheets, respectively, are given by

$$v_\alpha^t = u_\alpha^a + u_\alpha^d - \left(x_3 + \frac{h^c + h^f}{2}\right) u_{3,\alpha}^a - \left(x_3 + \frac{h^c + h^f}{2}\right) u_{3,\alpha}^d \quad (1)$$

$$v_\alpha^b = u_\alpha^a - u_\alpha^d - \left(x_3 - \frac{h^c + h^f}{2}\right) u_{3,\alpha}^a + \left(x_3 - \frac{h^c + h^f}{2}\right) u_{3,\alpha}^d \quad (2)$$

$$v_3^t = u_3^a + u_3^d \quad (3)$$

$$v_3^b = u_3^a - u_3^d \quad (4)$$

where

$$u_i^a = \frac{1}{2} (u_i^t + u_i^b) \quad (5)$$

$$u_i^d = \frac{1}{2} (u_i^t - u_i^b) \quad (6)$$

In order to include the transverse compressibility of the core, a higher-order displacement expansion has to be employed for the central layer which is at least of the first order for the transverse displacements. Thus, the first and second order power series expansion

$$v_\alpha^c = u_\alpha^a - \frac{h^f}{2} u_{3,\alpha}^d - \frac{2x_3}{h^c} u_\alpha^d + \frac{h^f}{h^c} x_3 u_{3,\alpha}^a + \left(\frac{4(x_3)^2}{(h^c)^2} - 1\right) \Omega_\alpha^c \quad (7)$$

$$v_3^c = u_3^a - \frac{2x_3}{h^c} u_3^d \quad (8)$$

is employed which satisfies the interface displacement continuity requirements at the core and face sheet interfaces. In Eq. (7), the displacement function Ω_α^c denotes an additional displacement function describing the warping of the core. It is implicitly understood, that all unknown displacement functions u_i^a , u_i^d and Ω_α^c depend only on the tangential directions x_α as well as on time t .

The deformation of the sandwich plate is expressed in terms of the nonlinear Green-Lagrange strain tensor. In case of an orthogonal coordinate system, the strain components are given by

$$\gamma_{ij} = \frac{1}{2} (v_{i|j} + v_{j|i} + v_{k|i} v_{k|j}) \quad (9)$$

where the vertical bar denotes the covariant derivative. Eq. (9) is evaluated individually for each of the three principal layers. In the v. Kármán sense, only the nonlinear terms related to the transverse (x_3 -) direction

are kept whereas all other nonlinear terms are discarded. Thus, a sandwich plate model for small strains and moderately large rotations is obtained.

The equations of motion and the boundary conditions are derived by means of Hamilton's principle

$$\int_{t^0}^{t^1} (\delta U - \delta W - \delta T) dt = 0 \quad (10)$$

where δU , δW and δT are the variation of the strain energy, of the work done by the external loads and of the kinetic energy, respectively, in case of a virtual displacement of the sandwich structure during the time interval $[t^0, t^1]$. The variations δU , δW and δT of the energy components are expressed in terms of the virtual displacements and the components τ_{ij} of the second Piola-Kirchhoff stress tensor for all three principal layers. The core warping functions are eliminated by the condition that no antisymmetric distribution of the transverse shear strain and thus the transverse shear stress components should occur. All tangential distributed loads as well as all tangential inertia effects are neglected. The stress components and the integration with respect to the panel thickness are eliminated by introduction of the tangential and bending stress resultants

$$\{N_{\alpha\beta}^t, M_{\alpha\beta}^t\} = \int_{-h^f - \frac{h^c}{2}}^{-\frac{h^c}{2}} \tau_{\alpha\beta}^t \left\{ 1, \left(x_3 + \frac{h^c + h^f}{2} \right) \right\} dx_3 \quad (11)$$

$$\{N_{\alpha\beta}^b, M_{\alpha\beta}^b\} = \int_{\frac{h^c}{2}}^{h^f + \frac{h^c}{2}} \tau_{\alpha\beta}^t \left\{ 1, \left(x_3 - \frac{h^c + h^f}{2} \right) \right\} dx_3 \quad (12)$$

$$\{N_{i3}^c, M_{i3}^c\} = \int_{-\frac{h^c}{2}}^{\frac{h^c}{2}} \tau_{i3}^t \{1, x_3\} dx_3 \quad (13)$$

where

$$\{N_{\alpha\beta}^a, M_{\alpha\beta}^a\} = \frac{1}{2} \{ (N_{\alpha\beta}^t + N_{\alpha\beta}^b), (M_{\alpha\beta}^t + M_{\alpha\beta}^b) \} \quad (14)$$

$$\{N_{\alpha\beta}^d, M_{\alpha\beta}^d\} = \frac{1}{2} \{ (N_{\alpha\beta}^t - N_{\alpha\beta}^b), (M_{\alpha\beta}^t - M_{\alpha\beta}^b) \} \quad (15)$$

The resulting expression is integrated by parts wherever possible. As a result, a single homogeneous linear equation for the virtual displacements δu_i^a and δu_i^d is obtained. Since the virtual displacements are arbitrary and independent from each other, the corresponding coefficients must vanish independently. From the area integrals, the equations of motion

$$0 = N_{\alpha\beta,\beta}^a \quad (16)$$

$$0 = N_{\alpha\beta,\beta}^d + \frac{1}{h^c} N_{\alpha 3}^c \quad (17)$$

$$0 = \left(u_{3,\alpha\beta}^a + \overset{\circ}{u}_{3,\alpha\beta}^a - \frac{1}{r_{\alpha\beta}} \right) N_{\alpha\beta}^a + M_{\alpha\beta,\alpha\beta}^a + \left(u_{3,\alpha\beta}^d + \overset{\circ}{u}_{3,\alpha\beta}^d \right) N_{\alpha\beta}^d + \frac{1}{h^c} \left(\frac{h^c + h^f}{2} - u_3^d - \overset{\circ}{u}_3^d \right) N_{\alpha 3,\alpha}^c - \frac{2}{h^c} \left(u_{3,\alpha}^d + \overset{\circ}{u}_{3,\alpha}^d \right) N_{\alpha 3}^c + \hat{q}_3^a - \left(m^f + \frac{1}{2} m^c \right) \ddot{u}_3^a \quad (18)$$

$$0 = \left(u_{3,\alpha\beta}^d + \overset{\circ}{u}_{3,\alpha\beta}^d - \frac{1}{r_{\alpha\beta}} \right) N_{\alpha\beta}^d + M_{\alpha\beta,\alpha\beta}^d + \left(u_{3,\alpha\beta}^d + \overset{\circ}{u}_{3,\alpha\beta}^d \right) N_{\alpha\beta}^a + \frac{2}{h^c} \left(\frac{h^c}{2} - u_3^d - \overset{\circ}{u}_3^d \right) N_{33}^c + \hat{q}_3^d - \left(m^f + \frac{1}{6} m^c \right) \ddot{u}_3^d \quad (19)$$

are obtained, where the prescribed transverse normal loads \hat{q}_3^a and \hat{q}_3^d are defined in a similar manner as the stress resultants in Eqns. (14) and (15) as the average and the half difference of the corresponding quantities for the top and bottom face sheet whereas m^c and m^f are the integrated mass densities of the core and the face sheets respectively. The symbols \hat{u}_3^a and \hat{u}_3^d denote small initial geometric imperfections of the sandwich plate. The matrix of the radii of curvature is defined by

$$r_{\alpha\beta} = \begin{pmatrix} r_1 & 0 \\ 0 & r_2 \end{pmatrix} \quad (20)$$

where r_α are the radii of curvature within the x_α - x_3 -planes. The boundary conditions are obtained in a similar manner as the equations of motion from the coefficients in the boundary integrals:

$$u_\alpha^a = \hat{u}_\alpha^a \quad \text{or:} \quad N_{n\alpha}^a = \hat{N}_{n\alpha}^a, \quad \alpha = n, t \quad (21)$$

$$u_{3,n}^a = \hat{u}_{3,n}^a \quad \text{or:} \quad M_{nn}^a = \hat{M}_{nn}^a \quad (22)$$

$$u_\alpha^d = \hat{u}_\alpha^d \quad \text{or:} \quad N_{n\alpha}^d = \hat{N}_{n\alpha}^d, \quad \alpha = n, t \quad (23)$$

$$u_{3,n}^d = \hat{u}_{3,n}^d \quad \text{or:} \quad M_{nn}^d = \hat{M}_{nn}^d \quad (24)$$

$$u_3^a = \hat{u}_3^a \quad \text{or:} \quad \left(u_{3,\alpha}^a + \hat{u}_{3,\alpha}^a \right) N_{n\alpha}^a + \left(u_{3,\alpha}^d + \hat{u}_{3,\alpha}^d \right) N_{n\alpha}^d + M_{nn,n}^a + 2M_{nt,t}^a \quad (25)$$

$$+ \frac{1}{h^c} \left(\frac{h^c + h^f}{2} - u_3^d - \hat{u}_3^d \right) N_{n3}^c = \hat{M}_{nt,t}^a + \frac{1}{2} \hat{N}_{n3}^c, \quad \alpha = n, t$$

$$u_3^d = \hat{u}_3^d \quad \text{or:} \quad \left(u_{3,\alpha}^a + \hat{u}_{3,\alpha}^a \right) N_{n\alpha}^d + \left(u_{3,\alpha}^d + \hat{u}_{3,\alpha}^d \right) N_{n\alpha}^a + M_{nn,n}^d + 2M_{nt,t}^d = \hat{M}_{nt,t}^d - \frac{1}{h^c} \hat{M}_{n3}^c \quad (26)$$

where x_n and x_t are the normal and tangential directions of the external edges. Prescribed quantities are denoted by (\dots) .

III. Solution for simply supported panels under transient loads

THE general sandwich plate model derived in Section II is applied to the analysis of the transient response of rectangular sandwich plates subject to time-dependent dynamic loading conditions. The sandwich plate under consideration has the edge lengths l_α with respect to the x_α -axes respectively and is assumed to be simply supported along all four external edges. An appropriate form for the transverse normal displacements for this type of problem is given by

$$u_3^a = w_{mn}^a \sin(\lambda_m^a x_1) \sin(\mu_n^a x_2), \quad \lambda_m^a = \frac{m\pi}{l_1}, \quad \mu_n^a = \frac{n\pi}{l_2} \quad (27)$$

$$u_3^d = w_{pq}^d \sin(\lambda_p^d x_1) \sin(\mu_q^d x_2), \quad \lambda_p^d = \frac{p\pi}{l_1}, \quad \mu_q^d = \frac{q\pi}{l_2} \quad (28)$$

where m , n , p and q are the number of modal waves with respect to the x_1 - and x_2 -directions of the overall deformation and the local face wrinkling deformation respectively. The corresponding modal amplitudes w_{mn}^a and w_{pq}^d remain unknown at this stage. The initial geometric imperfections \hat{u}_3^a and \hat{u}_3^d are assumed in the same form as the load-dependent transverse displacements u_3^a and u_3^d according to Eqns.(27) and (28) with the identical number of modal waves but with constant prescribed modal amplitudes \hat{w}_{mn}^a and \hat{w}_{pq}^d .

For the in-plane displacements u_α^a and u_α^d , a consistent solution can be obtained, if the analysis is restricted to the special case of orthotropic linear elasticity. In this case, the in-plane and bending stress resultants $N_{\alpha\beta}^a$, $N_{\alpha\beta}^d$, $M_{\alpha\beta}^a$ and $M_{\alpha\beta}^d$ can directly be expressed in terms of the unknown displacement functions. Subsequently, the expressions for the face sheet stress resultants are substituted into the first two sets (16) and (17) of the equations of motion, resulting in a set of differential equations for the in-plane displacement functions u_α^a and u_α^d . An analytical solution for this system has been derived by Hohe and Librescu.⁴ By virtue of this solution, the complete displacement field $u_i^a(x_\alpha)$ and $u_i^d(x_\alpha)$ is described in terms of the unknown modal amplitudes w_{mn}^a and w_{pq}^d . The displacement field in the obtained form satisfies the first two sets (16) and (17) as well as all boundary conditions with respect to the transverse direction – (22), (24), (25) and

(26) – identically. The remaining two sets (21) and (23) are satisfied in an integral average sense along the respective edges.

For determination of the remaining unknowns w_{mn}^a and w_{pq}^d , an extended Galerkin procedure is employed (see e.g. Hohe and Librescu⁴). Therefore, the previously determined consistent solution for the displacement field is substituted into the variational equation (10). All stress resultants are expressed in terms of the displacement functions and their derivatives using the constitutive equations for the core and face sheet material. Subsequently, the virtual displacements δu_i^a and δu_i^d are expressed in terms of the variations δw_{mn}^a and δw_{pq}^d of the modal amplitudes and the coefficients are collected. The result is a single homogeneous linear equation for the δw_{mn}^a and δw_{pq}^d . Since the virtual modal amplitudes are arbitrary and independent from each other, the corresponding coefficients must vanish independently, resulting in a system of two differential equations for the unknown modal amplitudes w_{mn}^a and w_{pq}^d .

The system is linear in terms of the accelerations \ddot{w}_{mn}^a and \ddot{w}_{pq}^d of the modal amplitudes. Hence, the system can easily be solved numerically using a fourth-order Runge-Kutta scheme with piecewise constant time increments.

IV. Results

A. Plane sandwich plate under rapidly applied in-plane compression

THE first example considered in the present study is directed to the dynamic buckling response of a square sandwich plate loaded by a prescribed rapid displacement of one of its external edges. The plate has the in-plane edge lengths $l_1 = l_2 = 500$ mm, a core thickness of $h^c = 18$ mm and a face sheet thickness of $h^f = 1$ mm resulting in a total thickness $h^{\text{tot}} = 20$ mm of the entire structure. The face sheets are made of aluminum with a Young's modulus of $E^f = 70$ GPa, a Poisson's ratio of $\nu^f = 0.3$ and a mass density of $\rho^f = 3700$ kg/m³. For the core layer, a low density material with $E^c = 0.7$ MPa, $\nu^c = 0.3$ and $\rho^c = 37$ kg/m³ is assumed. A buckling mode with $m = 1$, $n = 1$, $p = 55$ and $q = 1$ are assumed, which proves to be the globally stable mode involving the minimum total strain energy under static loading conditions. For regularization of the bifurcations, initial geometric imperfections with $\dot{w}_{mn}^a = 0.25$ mm and $\dot{w}_{pq}^d = 0.001$ mm are applied.

During the loading history, the edges at $x_1 = 0$ and $x_2 = 0$ are kept fixed with respect to the in-plane directions x_α . The x_2 -parallel edge at $x_1 = l_1$ is subject to a prescribed displacement of $\hat{u}_1 = -20$ mm, which is applied linearly during the interval $t \in [0, t^{\text{load}}]$. For $t \geq t^{\text{load}}$, the prescribed edge deflection is kept constant. With a moderately high loading rate with $t^{\text{load}} = 4$ ms and a rather high loading rate with $t^{\text{load}} = 2$ ms, two different loading rates are considered. The x_1 -parallel edge at $x_2 = l_2$ is assumed to be freely movable within the x_1 - x_2 -plane. The results are presented in Fig. 2, where the first row consisting of Figs. 2a, c, e and g is directed to the transient response in terms of the overall deflection w_{mn}^a , the face wrinkling deflection w_{pq}^d , the resulting edge load N_{11}^a of the edge with the prescribed edge deflection and the resulting deflection u_2^a of the movable edge in case of the moderately high loading rate. The second row consisting of Figs. 2b, d, f and h is directed to the corresponding results for the extremely high loading rate. In order to study the effect of the transverse compressibility of the core, results are added which are obtained by means of a simplified model with transversely incompressible core under the constraint $w_{pq}^d(t) = 0$.

As it can be observed in Fig. 2, the structure remains stable in the first part of the loading history. In this period, the overall transverse deflection w_{mn}^a vanishes (Figs. 2a and b) whereas both, the level $-N_{11}^a$ of the resulting edge load (see Figs. 2e and f) and the resulting deflection u_2^a of the freely movable edge (see Figs. 2g and h) increase linearly. Once the resulting edge load reaches the overall buckling load, a global buckling mode with an oscillating modal amplitude w_{mn}^a develops. At the moderately high loading rate with $t^{\text{load}} = 4$ ms, the results based on the standard model with incompressible core and the results based on the refined model including the transverse core compressibility are identical during the first 2 ms of the loading history. At $t \approx 2$ ms, the resulting edge load N_{11}^a along the edge with the prescribed deflection first exceeds the buckling load for development of a face wrinkling instability with non-zero modal amplitude w_{pq}^d (see Fig. 2c). Since soon afterwards, the level $-N_{11}^a$ of the resulting edge load drops due to the actual rapid increase in the overall deflection w_{mn}^a , the face wrinkling vanishes and re-develops during the following high-compression period from $t \approx 3.1$ ms till $t \approx 3.9$ ms when the oscillating transverse deflection w_{mn}^a reaches low levels near its minimum during the following free vibration and thus the level $-N_{11}^a$ of the resulting compressive in-plane load reaches levels in the vicinity of its maximum.

Since the development of a face wrinkling instability mode results in an weakening of the structure re-

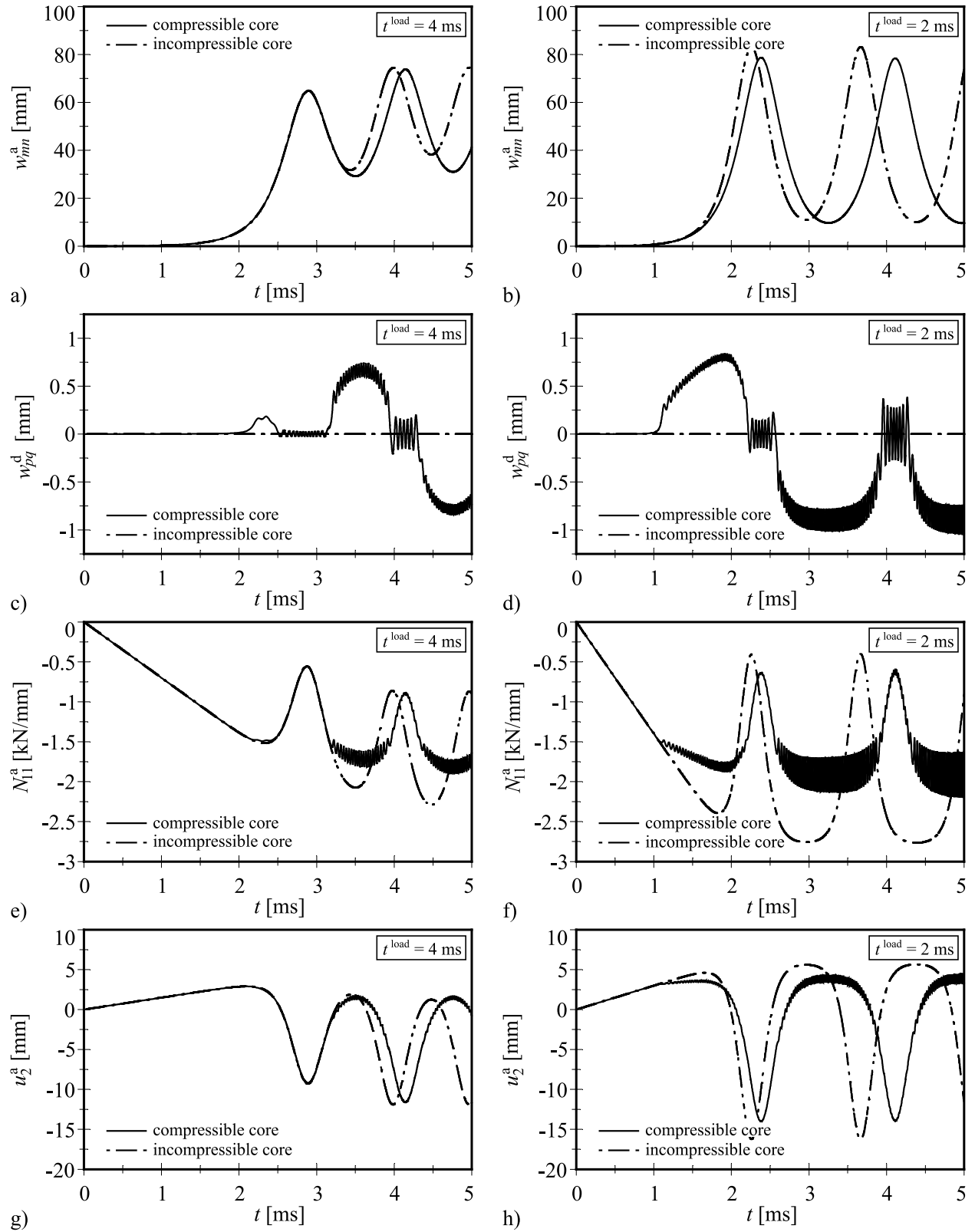


Figure 2. Transient response of sandwich plate to rapidly applied in-plane compression

garding its in-plane stiffness, the level $-N_{11}^a$ of the resulting edge load reaches higher values in the case of the model, where the transverse compressibility of the core is not considered compared to the present refined model including this effect. The lower in-plane stress levels in case of the refined model with transversely compressible core result in a delay in the development of the transient overall transverse deflection w_{mn}^a compared to the case of the standard incompressible plate model. Hence, the eigenfrequency of the overall vibration $w_{mn}^a(t)$ decreases, if a face wrinkling instability with non-zero modal amplitude develops. Thus, in the case of dynamic buckling, the standard sandwich plate models under the assumption of a transversely incompressible core might underestimate the natural frequency of the structure under the additional application of additional tangential loads or deflections.

Regarding the extremely high loading rate with $t^{\text{load}} = 2$ ms (see Figs. 2b, d, f and g), the observations are qualitatively similar as in case of the moderately high loading rate. Nevertheless, due to the higher loading rate, an overall vibration $w_{mn}^a(t)$ with larger amplitudes develops. Notice that in both cases, the oscillations are nonlinear and thus are not of the sinusoidal type.

B. Cylindrical sandwich shell under rapidly applied axial load

As a second example, the transient dynamic response of a cylindrical sandwich shell under rapidly applied axial compression is considered. The face sheets are assumed to consist of aluminum with $E^f = 70$ GPa, $\nu^f = 0.3$, $\rho^f = 3700$ kg/m³ and a thickness of $t^f = 1$ mm. The core consists of a low density material with $E^c = 0.7$ GPa, $\nu^c = 0.3$, $\rho^c = 37$ kg/m³ and a thickness of $t^c = 18$ mm. The panel is curved within the x_2 - x_3 -plane with $r_2 = 1000$ mm and has a square projection with $l_1 = l_2 = 500$ mm. The x_1 -parallel edges are assumed to be immovable with respect to the x_2 -direction. The prescribed load on the edge at $x_1 = 500$ mm is increased linearly from zero level to $\hat{N}_{11} = -2500$ N/mm during the time interval $t \in [0, 5]$ ms. A buckling mode with $m = n = q = 1$ and $q = 55$ is assumed, which involves the lowest amount of strain energy in the corresponding static buckling problem. For the face wrinkling instability, a geometric imperfection with $\hat{w}_{pq}^d = 0.001$ mm is assumed whereas two different geometric imperfections with $\hat{w}_{mn}^a = 9.4$ mm and 9.5 mm respectively are considered for the overall buckling mode. The geometry with the first overall imperfection features a smooth behavior in corresponding static buckling problem in the vicinity of the bifurcation load whereas geometry with the latter global imperfection features a distinct snap through jump.

The results are presented in Fig. 3 where the subfigures in the first column (Figs. 3a, 3c, 3e and 3g) belong to the geometry with the smaller geometric imperfection whereas the subfigures in the second column (Figs. 3b, 3d, 3f and 3h) belong to the geometry with the slightly larger overall imperfection. In both cases, the structures remain stable during the first 1.4 ms of the loading history until the applied edge load reaches the critical load for the face wrinkling instability. Subsequently, a face wrinkling mode with oscillating modal amplitude w_{pq}^d develops. The buckling load for development of an overall instability mode is reached at $t \approx 2$ ms. From this point onwards, distinct differences between the results based on the present transversely compressible sandwich model and the results based on the classical sandwich model assuming a transversely incompressible core are observed. In case of the geometry with the lower geometric imperfection ($\hat{w}_{mn}^a = 9.4$ mm, see Fig. 3a), the consideration of the transverse compressibility of the core results in the development of a snap-through jump with a positive transverse deflection w_{mn}^a which is not observed, if - as in the classical approaches - the simplified transversely incompressible model is used for the analysis. Furthermore, the development of a face wrinkling instability due to the transverse compressibility of the core results in an additional end shortening of the compressed sandwich structure and thus an increased compressive deflection $-u_1^a$ compared to the classical approach (see Fig. 3g). In case of the resulting edge load N_{22}^a perpendicular to the loading direction (see Fig. 3e), the development of a face wrinkling instability results in an increase of the stiffness and thus in an increase in the level $-N_{22}^a$ of the compressive edge load at the time when the face wrinkling instability starts to develop. In the subsequent vibration, the model with the transversely compressible core features an increased amplitude of the resulting edge load N_{22}^a compared to the classical approach. Even the peak values in the tensile (positive) range are increased. Thus, the classical sandwich shell models under the assumption of transversely incompressible cores might underestimate the resulting stresses.

For the geometry with the slightly larger initial geometric imperfection ($\hat{w}_{mn}^a = 9.5$ mm, see Figs. 3b, d, f and h), the effect of the transverse core compressibility is not as severe as in the previous case since - in contrast to the previous example - no transition from a structural response without a snap-through jump to a response with a snap-through jump occurs. Nevertheless, even in this example, the consideration of

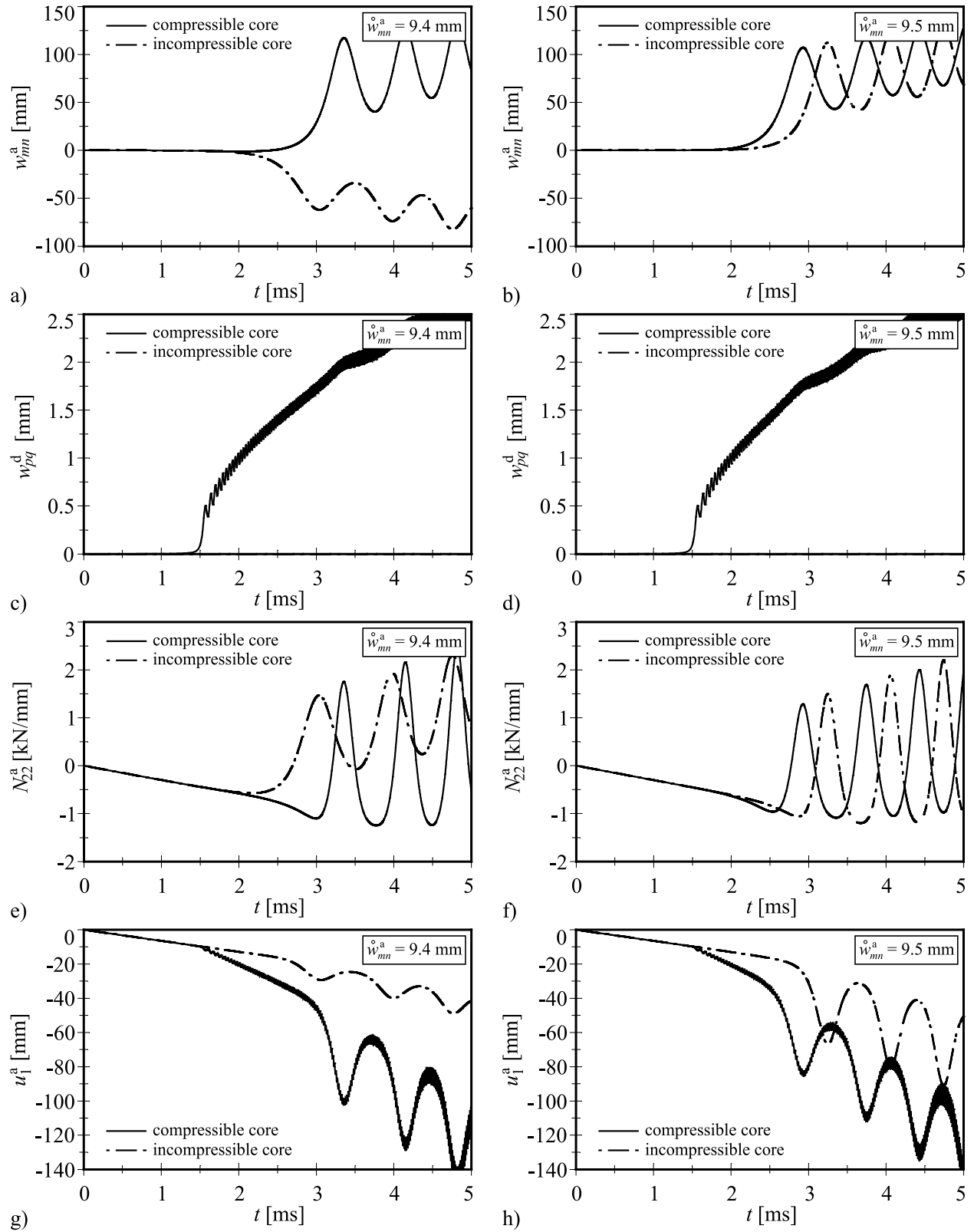


Figure 3. Transient response of cylindrical sandwich shell to rapidly applied axial compression

the core compressibility results in a distinct increase in the resulting deflection u_1^a of the loaded edge (see Fig. 3h). Furthermore, both, the frequency and the phase angle of the resulting vibration are affected.

V. Conclusions

OBJECTIVE of the present study is the analysis of the effect of the transverse compressibility of weak sandwich cores on the structural response of sandwich plates and shells under transient loading conditions. The analysis is based on an enhanced sandwich shell model using a higher-order power-series expansion for the core displacements, which accounts for the geometrical nonlinearity in the v. Kármán sense. Consistent equations of motion and boundary conditions are derived by means of Hamilton's principle. For the special case of simply supported sandwich plates and shells with square projection, an analytical solution is derived using an extended Galerkin procedure with a double sine representation of the transverse displacements in a postbuckling state. The transient problem is solved numerically by means of a variable step Runge-Kutta scheme of the fourth order.

The enhanced sandwich shell model is applied to the dynamic buckling and postbuckling analysis of plane and cylindrical sandwich panels under rapidly applied edge loads. In both cases it is observed that the transverse compressibility of the core layer can have distinct effects even on the global response of soft-core sandwich structures. Depending on the loading conditions, the development of the local face wrinkling instability mode, which is suppressed in the classical sandwich models due to the assumption of an incompressible core, might result in an increased amplitude of the free vibration following after the rapid loading process. In general, increased amplitudes will result in increased resulting local stresses. Thus, the neglect of the transverse compressibility of the core layer in the classical sandwich plate and shell models can result in an underestimation of the resulting stresses.

Furthermore, the development of a face wrinkling mode affects the eigenfrequency of the free vibration following after the loading process. Due to the geometrically nonlinear nature of buckling phenomena, the resulting local and overall vibrations can exchange energy. Due to this feature, a chaotic vibration with unpredictable model amplitudes for the individual degrees of freedom - especially for the face wrinkling mode - is encountered. Therefore, the integrity assessment of sandwich structures under dynamic buckling conditions might be a crucial problem.

Acknowledgement

THIS work has been financially supported by the Office of Naval Research (Composites Program) under Grant No. N00014-02-1-0594. The financial support and the interest and encouragement of the Grant Monitor, Dr. Y.D.S. Rajapakse, are gratefully acknowledged.

References

- ¹Mouritz, A. P., Gellert, E., Burchill, P., and Challis, K., "Review of advanced composite structures for naval ships and submarines," *Composite Structures*, Vol. 53, 2001, pp. 21–41.
- ²Frostig, Y., Baruch, M., Vilnay, O., and Sheiman, I., "High-order buckling theory for sandwich-beam behavior with transversely flexible core," *Journal of Engineering Science*, Vol. 118, 1992, pp. 1026–1043.
- ³Starlinger, A. and Rammerstorfer, F. G., "A finite element formulation for sandwich shells accounting for local failure phenomena," *Proceedings of the Second International Conference on Sandwich Construction*, EMAS Publishing, London, 1992, pp. 161–179.
- ⁴Hohe, J. and Librescu, L., "A nonlinear theory for doubly curved anisotropic sandwich shells with transversely compressible core," *International Journal of Solids and Structures*, Vol. 40, 2003, pp. 1059–1088.
- ⁵Hohe, J. and Librescu, L., "Core and face sheet anisotropy in deformation and buckling of sandwich panels," *AIAA Journal*, Vol. 42, 2004, pp. 149–158.
- ⁶da Silva, L. A. P. S. and Santos, J. M. C., "Localised formulations for thick "sandwich" laminated and composite structures," *Computational Mechanics*, Vol. 22, 1998, pp. 211–224.
- ⁷Wadee, M. A. and Hunt, G. W., "Interactively induced localized buckling in sandwich structures with core orthotropy," *Journal of Applied Mechanics*, Vol. 65, 1998, pp. 523–528.
- ⁸Frostig, Y., "Buckling of sandwich panels with a flexible core-high-order theory," *International Journal of Solids and Structures*, Vol. 35, 1998, pp. 183–204.
- ⁹Dawe, D. J. and Yuan, W. X., "Overall and local buckling of sandwich plates with laminated faceplates, Part I: Analysis," *Computer Methods in Applied Mechanics and Engineering*, Vol. 190, 2001, pp. 5197–5213.

- ¹⁰Pai, P. F. and Palazotto, A., "A higher-order sandwich plate theory accounting for 3-D stresses," *International Journal of Solids and Structures*, Vol. 38, 2001, pp. 5045–5062.
- ¹¹Barut, A., Madenci, E., Heinrich, J., and Tessler, A., "Analysis of thick sandwich construction by a {3, 2}-order theory," *International Journal of Solids and Structures*, Vol. 38, 2001, pp. 6063–6077.
- ¹²Noor, A. K., Burton, W. S., and Bert, C. W., "Computational models for sandwich panels and shells," *Applied Mechanics Reviews*, Vol. 49, 1996, pp. 155–199.
- ¹³Vinson, J. R., "Sandwich Structures," *Applied Mechanics Reviews*, Vol. 54, 2001, pp. 201–214.
- ¹⁴Mäkinen, K., "The transverse response of sandwich panels to an underwater shock wave," *Journal of Fluids and Structures*, Vol. 13, 1999, pp. 631–646.
- ¹⁵Xue, Z. and Hutchinson, J. W., "Preliminary assessment of sandwich plates subject to blast loads," *International Journal of Mechanical Sciences*, Vol. 45, 2003, pp. 687–705.
- ¹⁶Hohe, J., Librescu, L., and Oh, S. Y., "Dynamic buckling of flat and curved sandwich panels with transversely compressible core," *Composite Structures*, 2005, pp. (in press).
- ¹⁷Budiansky, B. and Hutchinson, J. W., "Dynamic buckling of imperfection-sensitive structures," *Proceedings of the Eleventh International Congress on Applied Mechanics*, Springer-Verlag, Berlin, 1966, pp. 636–651.

This page left blank intentionally.

Plastic Thermal Buckling of Uniformly Heated Rectangular Plates with Temperature-Dependent Material Properties

by Robert M. Jones*

Virginia Tech, Blacksburg, Virginia 24061-0219

Geometrically perfect plates that are restrained from in-plane expansion when slowly and uniformly heated throughout their volume generally develop compressive stresses and then buckle at a specific temperature. However, the temperature at which buckling occurs can be high enough to render inapplicable the room-temperature material properties that are typically used to calculate the buckling temperature. Moreover, the stresses generated in the plate can exceed the yield stress of the material thus exciting nonlinear stress-strain behavior. Finally, the nonlinear stress-strain behavior of the material varies significantly with temperature, as does the thermal expansion behavior. These temperature- and stress-dependent material properties are taken into account in the calculation of the plastic thermal buckling temperature of simply supported rectangular plates that cannot expand in their plane in one direction. Shanley's concept of no strain reversal during buckling and the J_2 deformation theory of plasticity are employed along with a variable Poisson's ratio after yielding of the material. The highly nonlinear stress-strain behavior characteristic of aluminum alloys is represented with the Nadai-Jones stress-strain curve model and interpolated at temperatures needed that are intermediate to the necessarily discrete temperatures at which measured data stress-strain curves are available. Finally, the two-level transcendental buckling problem in temperature and position on the stress-strain curve is solved by the equivalent mechanical load concept with an interval-halving technique. Examples of thermal buckling of uniaxially in-plane restrained 7075-T6 aluminum plates with thermo-physical properties ranging from room temperature to 600°F (316°C) are used to illustrate the theory. The effect of temperature-dependent material properties on thermal buckling of uniformly heated plates is readily apparent and can be quite strong. Thus, in a robust thermal environment, the actual mechanical behavior of a material with temperature must be considered when evaluating structural behavior.

Tribute

To the memory of Dr. James H. Starnes, Jr. who was long associated with NASA Langley Research Center. He informed, inspired, motivated, and led by example two generations of engineers and scientists in the pursuit of buckling problems in particular and aerospace structural mechanics problems in general.

1. Introduction

The advent of supersonic aircraft, missiles, and reentry vehicles in the mid-1900s quite naturally led to heating of the portions of their structures exposed to high-speed air flow. That structural heating can cause thermal buckling of various structural elements such as bars, plates, and shells as noted by Hoff¹. The history of the development of theories for plastic thermal buckling of plates is irretrievably linked to, and based on, concepts developed for plastic thermal buckling of bars. The inherently two-dimensional nature of heated, plastically deforming plates, as contrasted with the one-dimensional nature of bars, leads to far more involved equations the solution of which is much less obvious than for bars. Bryan² was the first to solve the elastic plate buckling problem, and his solution can be extended to the elastic portion of the present thermal buckling problem by use of the equivalent mechanical load concept described by Jones³. Thermal buckling of uniformly heated plates results are shown in abbreviated form for square plates by Parkes⁴ and for rectangular plates by Boley and Weiner⁵. The time-dependent form of thermal buckling, i.e., buckling of a structural element under a constant load after some lapse of time, is called creep buckling (creep is the deformation of a material under constant stress with time during which the material properties decrease). The time to creep buckling depends strongly on temperature level and generally decreases rapidly with increasing temperature. Creep buckling was measured for 7075-T6 aluminum bars under temperatures ranging from room temperature to 600°F (316°C) by Mathauser and Brooks⁶. They made creep buckling lifetime predictions with Libove's theory⁷ and found good correlation with their experimental results even without consideration of initial geometric imperfections. The time-independent form of buckling under thermal loading is simply called thermal buckling.

*Professor Emeritus of Engineering Science and Mechanics. Fellow ASME and ASC. Associate Fellow AIAA. rmjones@vt.edu
Copyright © 2005 by Robert M. Jones. Printed by NASA with permission.

Bert addressed dependence of the thermal expansion coefficient on the stress level for thermal buckling of plates⁸. He found that a relatively small decrease in modulus [10% in 180°F (100°C)] for a thin steel plate leads to a disproportionately larger decrease in buckling temperature (23%, i.e., about a factor of two) when the associated change in thermal expansion coefficient is considered. Hilton used linear elastic temperature-dependent material properties to analyze thermal stresses in bodies⁹. Many thermal buckling analyses have been performed with room-temperature material properties (both stress-strain behavior and thermal expansion characteristics). However, the buckling temperatures predicted are often well above room temperature, and the buckling stresses are often well above yielding even when temperature-dependent (but elastic) material properties are considered.

The classical elastic bar buckling problem solved by Euler¹⁰ was properly extended to plastic buckling by Shanley¹¹ in 1947 after nearly a century of lively controversy over the modulus to be used. Shanley argued that the tangent modulus (E_{tangent} hereafter abbreviated as E_{tan}) of the nonlinear stress-strain curve must be used instead of previous arguments in favor of some form of reduced modulus such as that forwarded by von Kármán¹². The reduced modulus is approximately an average of the tangent and Young's moduli. Shanley's approach brought theory into agreement with experiment in a logical manner so that even von Kármán¹¹ agreed nearly forty years after his own proposed approach. Shanley's contribution to, or clarification of, plastic buckling is often thought of as stating that E_{tan} is to be used as E in $\pi^2 EI/L^2$ for the bar buckling load instead of von Kármán's E_{reduced} . Actually, the *reason* for the use of E_{tan} is Shanley's real contribution, namely that no 'strain reversal' occurs at the instant of plastic buckling. That is, the strains in the bar continue to increase upon buckling and do not decrease on the side of the bar that changes from straight to having convex curvature. Thus, there is no unloading of any part of the bar which would lead to an elastic unloading modulus, E , combined with a plastic loading modulus, E_{tan} , as in the reduced modulus theory proposed by von Kármán¹². Shanley's justification for the 'no strain reversal' concept was that initial geometric imperfections probably exist in every actual bar and cause slight bending of the bar prior to buckling resulting in continuous loading and never any unloading that would certainly occur if the bar were perfectly straight. All previous theories had the premise that the bar was perfectly straight and therefore had to have unloading on one side of the bar at the instant of buckling, hence 'strain reversal'.

The logical extension of the 'no strain reversal' plastic buckling concept for bars to plates and shells involves only the plastic moduli of loading, E_{tan} and E_{secant} (hereafter abbreviated as E_{sec}), and never the modulus of unloading, namely E . For the two-dimensional stress states of plates and shells, that concept 'translates' as variations in stresses are accompanied by moduli and variations in moduli that include both E_{tan} and E_{sec} (but of course not E). However, reduction of the biaxial stress state to a uniaxial stress state leads to the sole modulus E_{tan} . Shanley's fundamental approach to plastic buckling of 'no strain reversal' was extended to plates by Stowell¹³ and to stiffened plates and shells by Gerard¹⁴ and Jones¹⁵. Various plasticity formulations have been used, although the J_2 deformation theory¹⁶ (also called maximum octahedral shear stress theory, maximum energy of distortion theory, etc.) is utilized in spite of the fact that an incremental theory is probably more valid for general loading histories. Cogent reasons, however, are given by Budiansky¹⁷ as to why a deformation theory cannot be summarily rejected in favor of incremental theory for problems involving other than proportional loading. Moreover, Hutchinson¹⁸ thoroughly discusses the merits and deficiencies of both flow theory (also called incremental theory) and deformation theory for bifurcation buckling and concludes that deformation theory predictions are always closer to experimental results than flow theory predictions. Deformation theory buckling predictions agree with measured response even at high temperatures as shown for bars by Jones¹⁹. That flow theory always gives predicted buckling loads well above measured buckling loads has frustrated proponents of flow theory in their search for the perfect plasticity theory. That deformation theory gives good agreement with experimental results is further frustration and even irritation. However, the clear indication is that deformation theory is more suitable for predicting plastic buckling loads than flow theory, so we will confine our attention to deformation theory. Along with the J_2 deformation theory, a Poisson's ratio is used that varies continuously from the elastic value during elastic behavior to the plastic value in the fully plastic flow state in accordance with Gerard and Wildhorn's results²⁰. The nonlinear stress-strain behavior of aluminum alloys has been represented with several stress-strain curve models, including the Ramberg-Osgood model²¹ and the Nadai model²². For the highly nonlinear stress-strain behavior with two distinctly different regions of behavior characteristic of aluminum alloys at high temperatures, the recent extension of the Nadai model by Jones¹⁹ is required.

The objective of this paper is to analyze thermal buckling of simply supported rectangular plates with due consideration of temperature-dependent nonlinear stress-strain behavior and thermal expansion characteristics as an extension of Jones' work on bars¹⁹. The plates are regarded as 'perfect', i.e., without

any geometric or material imperfections. Thermal loading is restricted to slow, uniform heating throughout the volume of the in-plane-restrained plate. Although creep buckling is possible at elevated temperatures, that behavior is not treated in this paper. The plates are restrained from in-plane free thermal expansion in one direction, so they develop stresses that can exceed the yield stress. Moreover, the temperatures that cause buckling can be far in excess of room temperature, so the room-temperature material properties that are typically used are no longer valid. Thus, elevated-temperature nonlinear stress-strain behavior and thermal expansion behavior must be considered. The plates are uniaxially restrained in their plane as in Figure 1, and a schematic illustration of the specific manner of achieving in-plane restraint is shown using Almroth's notation²³ for the four possible types of simply supported edges, i.e., edges with no rotational restraint and zero deflection transverse to the plate surface, but with four types of in-plane support conditions. The equilibrium boundary conditions that all can be called simply supported edges are shown in Figure 2. Analogous buckling boundary conditions are obtained by putting the variational symbol, δ , in front of each equilibrium boundary condition in Figure 2, e.g., $w = 0$ goes to $\delta w = 0$. The objective is achieved in the steps described in the following paragraphs.

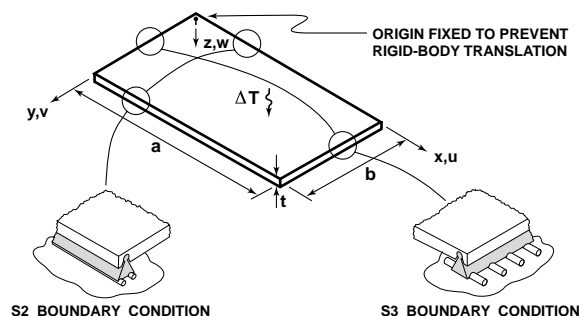


Figure 1 A Uniaxially In-Plane Restrained Simply Supported Rectangular Plate Subjected to Uniform Temperature Change

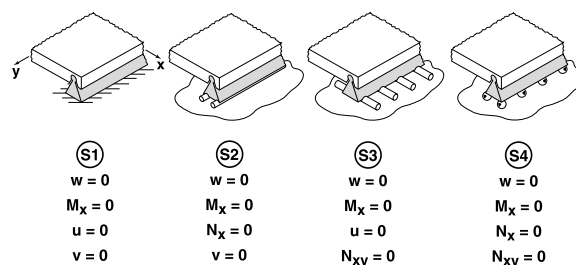


Figure 2 Equilibrium Boundary Conditions for Plates with Simply Supported Edges

In the second section, the equivalent mechanical load concept³ is used to find the thermal buckling temperature for a statically indeterminate restrained structural element such as a bar or plate. With that concept, the thermal restraining force is identified and then equated to the mechanical force that causes buckling in order to find the buckling temperature. The thermal restraining force can be found by application of the boundary conditions on the restrained plate or by equating the deformations of the free-thermal-expansion problem to the deformations of the thermal-restraining-force-caused-contraction problem. Both problems can be linear or nonlinear, but must satisfy the fundamental deformation conditions associated with the actual plate restraint. The temperature is increased until the thermal-restraining force reaches the mechanical buckling load. That buckling load is determined from the mechanical buckling load of a uniaxially loaded plate with temperature-dependent nonlinear material properties. Next, the variation with temperature of thermal expansion is used to assess the thermal restraining forces and hence the temperature that causes buckling. The plastic plate buckling problem for both temperature-independent and temperature-dependent material properties leads to a transcendental equation, i.e., the unknown buckling temperature and buckling stress is a function of nonlinear material properties that are themselves dependent on the buckling temperature and buckling stress.

The third section of this paper is a description of the strategy for solving the transcendental equation resulting from equating the two deformations by searching for the self-consistent combination of temperature and position on the nonlinear stress-strain curve for that temperature. Those two elements are brought together in a two-level transcendental search procedure with an interval-halving technique. Solution of the two-level transcendental equations involves searching for the buckling temperature and buckling stress at which the material properties are consistent with the temperature and stress. Thus, a solution strategy is developed for how to treat the stress-strain curve nonlinearities simultaneously with the temperature-dependent material properties to find the thermal buckling load in a computerized search procedure for the two-level transcendental equation. The temperature- and stress-dependent search procedure is an extension of Jones' nonlinear stress-strain behavior search procedure²⁴.

The objective of the fourth section is to represent the highly nonlinear stress-strain behavior in equation form at each temperature for which stress-strain curves are available by use of the Nadai-Jones stress-strain curve model. Those models for a set of stress-strain curves at various measured temper-

atures are then interpolated in the search procedure at temperatures intermediate to the known measured stress-strain curves. Accordingly, the Nadai stress-strain curve equation concept has been extended to a new form to be able to represent measured stress-strain behavior at higher stress levels than possible with the Nadai equation and at various temperatures, including the ability to realistically interpolate between stress-strain curves at different temperatures. The resulting Nadai-Jones model and a single level of the numerical search procedure has been validated by calculating buckling stresses for static mechanical loading of bars at constant elevated temperatures (see Jones¹⁹). Those predicted mechanical buckling stresses are in very good agreement with Mathauser and Brooks' experimental results⁶ for uniformly heated, 7075-T6 aluminum pinned-end bars at 300°F (149°C), 400°F (204°C), 500°F (260°C), and 600°F (316°C), an essential prerequisite to any procedure to treat plastic thermal buckling.

Finally, in the fifth section, to illustrate the two-level numerical search procedure, numerical examples of thermal buckling temperatures and stresses are calculated for uniformly heated uniaxially in-plane restrained simply supported rectangular plates made of 7075-T6 aluminum with measured thermophysical properties ranging from room temperature to 600°F (316°C). Those results are studied to determine the reductions in buckling temperatures caused by plastic effects as well as the reductions caused by temperature-dependent material properties including variable thermal expansion with temperature.

2. Analysis

This section has three steps: (1) elastic thermal buckling, (2) plastic thermal buckling, and (3) plastic thermal buckling with temperature-dependent material properties. The difficulties encountered in each successive step are clarified on the way to the most difficult formulation. The key factor for development of restraining thermal forces is the boundary conditions on each of the four edges including the in-plane restraint provided in addition to the obvious influence of the edge rotational restraint for a clamped-edge plate or lack thereof for a simply supported plate.

The equivalent mechanical load concept³ is the process of identifying the thermal restraining force caused by the thermal load acting on the structural element and then equating that thermal restraining force to the mechanical force that causes buckling in order to determine the buckling temperature. That is, the thermal restraining force is the equivalent mechanical load. The thermal restraining force can be identified (1) by superimposing deformation conditions to ensure that the deformation caused by the free thermal expansion is equal to the deformation (contraction) caused by the thermal restraining force or (2) by applying the boundary conditions prior to buckling. The force can be the force, P , in a bar or the force per unit width, N_x , in a plate or shell. To illustrate the concept of required compatibility between the deformation caused by the free thermal expansion and the deformation caused by the thermal restraining force, consider a perfectly straight, axially loaded, simply supported bar, i.e., pinned at both ends, as in Figure 3. If the bar is restrained from thermal growth in the axial direction while being heated uniformly (still pinned at each end, but the pins cannot move in the axial direction of the bar as in Figure 3a), then the problem can be thought of as the superposition of two problems: (1) the free thermal expansion problem and (2) the thermal restraining force problem. We first allow free thermal expansion of the bar in Figure 3b and then push the bar back to its original position with the thermal restraining force in Figure 3c so that no net movement occurs. Thus, the free thermal expansion, Δ_{FTE} , must be precisely equal to the thermal restraining force compression, Δ_{TRF} , i.e., we must satisfy the fundamental deformation condition

$$\Delta_{FTE} = \Delta_{TRF} \quad (1)$$

The free thermal expansion of a bar that is both unrestrained and uniformly heated is

$$\Delta_{FTE} = \alpha \Delta T L \quad (2)$$

in which α is the (constant) coefficient of thermal expansion and ΔT is the temperature change from the initially unstressed and unrestrained state. The axial compression of a bar loaded with a thermal restraining force, P , is

$$\Delta_{TRF} = \frac{PL}{AE} \quad (3)$$

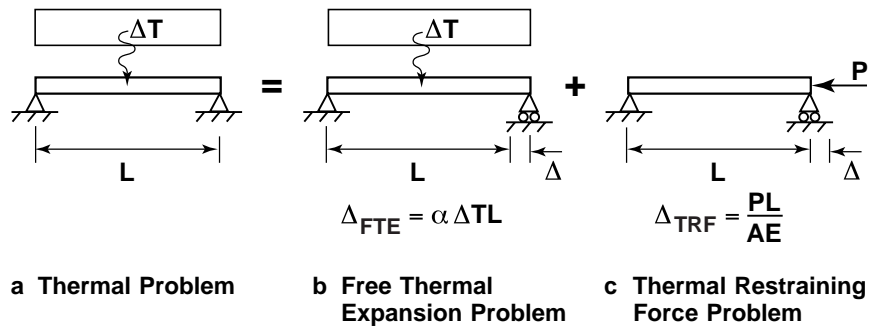


Figure 3 Superposition of Loading Cases for a Statically Indeterminate Restrained Bar

in which L is the bar length, A is the cross-sectional area of the bar, and E is the elastic modulus of the bar material. Then, because of the deformation condition in Equation (1), along with the deformations in Equations (2) and (3), the compressive thermal restraining force has magnitude

$$P_{\text{restraining}} = E \alpha \Delta T A \quad (4)$$

For an elastic bar, the thermal buckling load, $\bar{\Delta T}$, occurs when the thermal restraining force grows to equal the classical Euler buckling load¹⁰:

$$\bar{P} = \pi^2 \frac{EI}{L^2} \quad (5)$$

(in which the buckling load is denoted by P with an overbar and I is the second moment of the bar cross-sectional area) if the bar is elastic which is usually true if the bar is slender enough. Thus, upon equating the loads in Equations (4) and (5), the thermal buckling load, $\bar{\Delta T}$, is

$$\bar{\Delta T} = \frac{1}{E \alpha A} \pi^2 \frac{EI}{L^2} = \pi^2 \frac{1}{\alpha} \frac{1}{(L/r)^2} \quad (6)$$

after substitution of the radius of gyration, r , for $\sqrt{I/A}$. We observe from Equation (6) that elastic thermal buckling is independent of the bar material's modulus of elasticity, E , a fact that is somewhat misleading when we later consider inelastic material behavior. Moreover, the bar result depends on the single geometric parameter of the slenderness ratio, L/r . The equivalent mechanical load concept will now be described for buckling of a simply supported plate under in-plane restraint in the x -direction in Figure 1.

2.1 Elastic Thermal Buckling

Consider a rectangular plate that is simply supported on all four edges, but in different manners as in Figure 1. There, restraint of in-plane movement exists only in the x -direction with S3 boundary conditions on edges $x = 0$ and $x = a$. Thus, a compressive thermal force is developed in the x -direction when heat is applied. However, the plate is supported with S2 boundary conditions on edges $y = 0$ and $y = b$. Thus, the plate is free to move in the y -direction on all four edges. No mechanical force, N_x , can be applied (unless by deformation-type loading followed by heating) nor can any thermal force develop in the y -direction from heating. Although N^T appears in the equation for N_y , no force can develop in the y -direction. Also, N_{xy} does not exist. Another, perhaps more direct, yet incomplete, manner of perceiving the in-plane plate support conditions is depicted in Figure 4 where the permissible in-plane movements are shown (and will be used in figures to remind the reader of the present boundary conditions). Thus, ΔT causes force but no displacement in the x -direction and displacement but no force in the y -direction. A plate with fixed edges C3 and C2 on the respective sides has the same in-plane movement as the present simply supported plate and, thus, the same prebuckling force distributions, but a higher ΔT at buckling because of the rotational restraint.

First, find the linear prebuckling (equilibrium) force state.

The force-strain and force-displacement relations are

$$\begin{aligned} N_x &= A(\epsilon_x + \nu \epsilon_y) - N^T = A(u_x + \nu v_y) - N^T \\ N_y &= A(\epsilon_y + \nu \epsilon_x) - N^T = A(v_y + \nu u_x) - N^T \end{aligned} \quad (7)$$

in which N_x and N_y are positive in tension and

$$N^T = \frac{E}{1-\nu} \int \alpha \Delta T dz = \frac{E}{1-\nu} \alpha \Delta T t \quad (8)$$

for the case of a uniform temperature change through the plate thickness (positive ΔT for heating leading to compressive N_x and N_y). Moreover, ΔT and hence N^T are constant over the plate area. The boundary conditions are $u = 0$ at $x = 0$ and $x = a$, as well as for all x (and y), in addition to $v = 0$ at $y = 0$, but v is unrestrained (and a function of ΔT) at $y = b$. Thus, $N_y = 0$ at $y = 0$ and $y = b$. Then, the force-strain relations become

$$N_x = A \nu v_y - N^T \quad (9)$$

$$0 = A v_y - N^T \quad (10)$$

so that, from Equation (10),

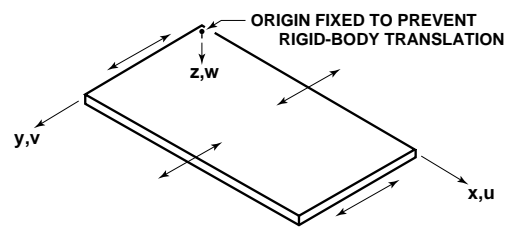


Figure 4 Possible In-Plane Movement of a Uniaxially In-Plane Restrained Simply Supported Rectangular Plate

$$v_y = \frac{N^T}{A} \quad (11)$$

Thus, with substitution of Equation (8) in Equation (9), the prebuckling in-plane forces are

$$\begin{aligned} N_x &= A v \frac{N^T}{A} - N^T = -(1 - v)N^T = -E\alpha\Delta T t \\ N_y &= 0 \end{aligned} \quad (12)$$

so the condition of zero force in the y-direction coexists with a compressive force for a positive ΔT (heating) in the x-direction plus no displacement in the x-direction and some expansion in the y-direction. Note that N_x is reduced by the factor $1 - v$ from the nominal thermal force N^T .

For a constant uniaxial mechanical prebuckling load throughout the plate, the buckling load is the well-known solution of Bryan²:

$$\bar{N}_x = \frac{Et^3}{12(1 - v^2)} \frac{\pi^2}{b^2} \left[m \frac{b}{a} + \frac{1}{m} \frac{a}{b} \right]^2 \quad (13)$$

in which the plate buckling load is denoted by \bar{N}_x with an overbar, m is the number of buckle half-sine waves in the x-direction, and the plate always buckles with only one half-sine wave in the y-direction.

By the equivalent mechanical load concept, we merely identify the thermal prebuckling force from Equation (12) that is in the same form as the mechanical prebuckling force, i.e., constant throughout the plate, of magnitude

$$\bar{N}_x = E \alpha t \bar{\Delta T} \quad (14)$$

which is positive in compression. Thus, upon substitution of the prebuckling thermal force, Equation (14), in the buckling equation, Equation (13), we find the thermal buckling change in temperature:

$$\bar{\Delta T} = \frac{\pi^2}{12} \frac{1}{\alpha} \frac{1}{(1 - v^2)} \frac{1}{(b/t)^2} \left[m \frac{b}{a} + \frac{1}{m} \frac{a}{b} \right]^2 \quad (15)$$

which can be rearranged to read

$$k_T = \frac{12}{\pi^2} (1 - v^2) \alpha \bar{\Delta T} \left[\frac{b}{t} \right]^2 = \left[m \frac{b}{a} + \frac{1}{m} \frac{a}{b} \right]^2 \quad (16)$$

We observe from Equation (15) that elastic thermal buckling is independent of the plate material's modulus of elasticity, E , a fact that is somewhat misleading when we later consider inelastic material behavior. However, elastic thermal buckling in Equation (15) does depend on the Poisson's ratio. These results are shown in abbreviated form for square plates by Parkes⁴ and for rectangular plates by Boley and Weiner⁵. The results for Equation (16) are plotted in Figure 5 as a function of the plate aspect ratio, a/b . Obviously, from the left-hand side of Equation (16), the higher the coefficient of thermal expansion

for a material, the lower the change in temperature to cause thermal buckling. Also, as the plate gets thinner, the thermal buckling load decreases. These conclusions are in agreement with our intuition. Figure 5 is identical to the standard mechanical buckling load result for \bar{N}_x in Figure 9-2 on page 353 of Timoshenko and Gere²⁵ if $k = \bar{N}_x b^2 / \pi^2 D$ is replaced by k_T . That is, the same festooned curves exist for various values of m . The lower limit of both behaviors is $k_T = 4$ and $k = 4$ at integer values of a/b . Both $k_T = 4$ and $k = 4$ are reasonable lower bounds to use for $a/b > 1$ in design situations.

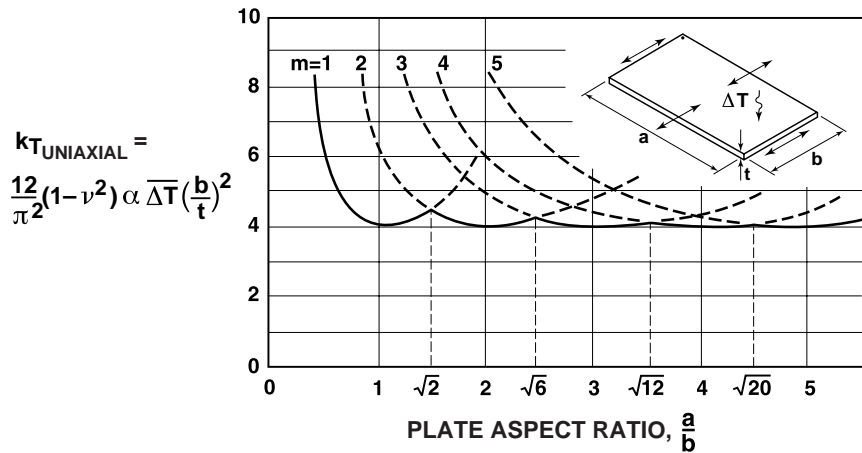


Figure 5 Thermal Buckling of a Uniformly Heated Elastic Uniaxially In-Plane Restrained Simply Supported Rectangular Plate with Variable Plate Aspect Ratio, a/b

The ordinate of Figure 5 [the left side of Equation (16)], k_T , is four [from the right-hand side of Equation (16)] when the plate aspect ratio, a/b , is any integer (including infinity) and $m = a/b$. As a numerical example, we solve for ΔT from Equation (16) for integer a/b for a 6061-T6 aluminum plate with material properties $E = 10 \times 10^6$ psi (70 GPa), $\alpha = 13.1 \times 10^{-6}/^\circ\text{F}$ ($23.6 \times 10^{-6}/^\circ\text{C}$), $\nu_e = .32$, and $\sigma_y = 35 \times 10^3$ psi (240 MPa) (note that σ_y is the yield stress of the material, not the stress in the y-direction). For these room-temperature material properties, we get

$$\Delta T = \frac{4\pi^2}{12(1 - \nu^2) \alpha \left[\frac{b}{t} \right]^2} = 2.80 \times 10^5 \text{ } ^\circ\text{F} \text{ (} 1.55 \times 10^5 \text{ } ^\circ\text{C)} \left[\frac{t}{b} \right]^2 \quad (17)$$

Nemeth's results²⁶ for infinitely long, laminated composite plates with thermal restraint only in the x-direction can be shown to reduce to this solution, i.e., Equation (17). The resulting variation of ΔT with plate side-length-to-thickness ratio, b/t , for integer a/b is shown in Figure 6. For $b/t = 100$, the ΔT for buckling is 28.0°F (15.6°C). However, it is unlikely that a plate that thin would be truly flat before thermal loading, so the plate would probably have an imperfection that would mean the plate is bent prior to any heating. Thus, the plate would behave in a manner similar to a nonuniformly heated bar, i.e., the plate would immediately bend, bow, or curl with the imposition of any heat whatsoever. For $b/t = 50$, the ΔT for buckling is 112°F (62°C). Finally, for $b/t = 10$, the ΔT for buckling is 2800°F (1550°C). Such a thick plate would certainly require a very significant correction for the influence of material property degradation with elevated temperature and for the influence of extensive plastic deformation, not to mention the fact that the plate has long since melted with such a large ΔT (so some correction must be made)! The compressive stress in the x-direction corresponding to ΔT is $\sigma_x = -E \alpha \Delta T$ with no stress in the y-direction. Thus, at yielding, ΔT takes on the value

$$\Delta T_y = \frac{\sigma_y}{E \alpha} = 267^\circ\text{F} \text{ (} 148^\circ\text{C)} \quad (18)$$

at $b/t = 32.4$. Above this value of ΔT , the thermal buckling results must be modified to account for plastic deformation and to account for decreasing E with increasing temperature, not to mention changing ν and α . Below ΔT_y , the elastic behavior is nearly valid. For example, for a plate with $b/t = 60$, $\Delta T = 77.7^\circ\text{F}$ (43.2°C). However, the buckling temperature changes of several hundred degrees below yielding are affected by material property variation with temperature as we will see in Section 5.

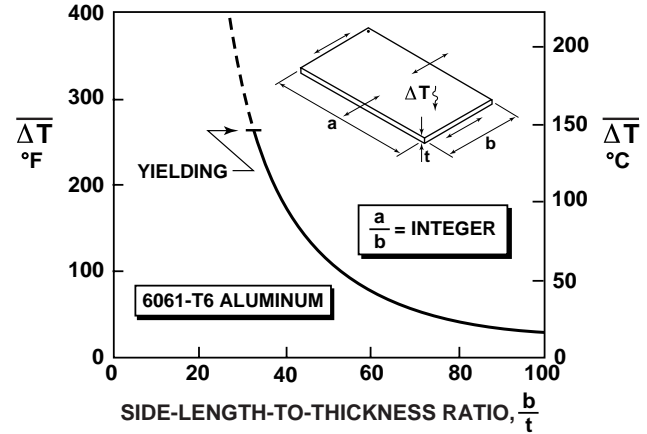


Figure 6 Thermal Buckling of a Uniformly Heated Simply Supported Rectangular Plate with Uniaxial In-Plane Restraint and Variable Side-Length-to-Thickness Ratio, b/t

2.2 Plastic Thermal Buckling

Often buckling occurs above the yield stress, σ_y , (proportional limit, i.e., limit of linear elastic behavior and the start of yielding) as distinguished from the offset yield stress, σ_{oy} , located where the line at slope E from the plastic permanent set, ϵ_{oy}^p , crosses the stress-strain curve in Figure 7. The offset yield stress has no physical significance whatsoever, but is often mistakenly called the yield stress. Actually, yielding occurs at σ_y which is well below σ_{oy} . The secant modulus, E_{sec} to a generic point on the stress-strain curve is shown in Figure 7. At that point, the tangent modulus, E_{tan} , is also identified. The following plate plastic buckling criterion can be adapted from the shell plastic buckling criterion in Jones¹⁵ or seen directly for plates in Jones³. Both are obtained using J_2 deformation theory with no strain reversal for an elastic-plastic compressible material with Poisson's ratio that varies continuously from the elastic value, ν_e , to the plastic value, $1/2$. That is, Poisson's ratio, ν , is a variable throughout the elasto-plastic range of stress from the end of elastic behavior at yielding through fully plastic behavior,

$$\nu = \frac{1}{2} - \left(\frac{1}{2} - \nu_e \right) \frac{E_{sec}}{E} \quad (19)$$

as shown by Gerard and Wildhorn²⁰.

The basic premise of Jones' derivation of the plate buckling criterion is that all stresses are varied from their prebuckling values with resulting expressions involving the moduli, E_{\tan} and E_{\sec} . If his approach is applied to the uniaxial stress case of an axially loaded bar, the resulting stress variation is $\delta\sigma_x = E_{\tan}\delta\epsilon_x$ which is consistent with Shanley's result in which no strain reversal occurs¹¹. In contrast, Ilyushin²⁷ assumes that strain reversal occurs at buckling whereas Stowell¹³ assumes that no strain reversal occurs. Both use a constant Poisson's ratio, $\nu = 1/2$, despite the fact that buckling occurs in the knee of the stress-strain curve well below the plastic flow condition for which $\nu = 1/2$.

For the plate buckling problem with uniaxial load, N_x , and hence σ_x , the variations in biaxial stresses during buckling from a uniaxial stress state involving σ_x are

$$\begin{aligned}\delta\sigma_x &= \frac{E_{\sec}}{1-\nu^2} (K_{11}\delta\epsilon_x + \nu K_{12}\delta\epsilon_y) \\ \delta\sigma_y &= \frac{E_{\sec}}{1-\nu^2} (\nu K_{12}\delta\epsilon_x + K_{22}\delta\epsilon_y) \\ \delta\tau_{xy} &= \frac{E_{\sec}}{1-\nu^2} K_{33}\delta\gamma_{xy}\end{aligned}\quad (20)$$

in which for the uniaxial stress state

$$\begin{aligned}K_{11} &= 1 - \frac{(2-\nu)^2}{4(1-\nu^2)H} \left[1 - \frac{E_{\tan}}{E_{\sec}} \right] & K_{22} &= 1 - \frac{(1-2\nu)^2}{4(1-\nu^2)H} \left[1 - \frac{E_{\tan}}{E_{\sec}} \right] \\ K_{12} &= 1 + \frac{(1-2\nu)(2-\nu)}{4\nu(1-\nu^2)H} \left[1 - \frac{E_{\tan}}{E_{\sec}} \right] & K_{33} &= (1-\nu)/2\end{aligned}\quad (21)$$

in which

$$H = 1 + \frac{(1-2\nu)^2}{4(1-\nu^2)} \left[1 - \frac{E_{\tan}}{E_{\sec}} \right] \quad (22)$$

Thus, the plate variations in stresses during buckling in Equation (20) involve only the loading plastic moduli, E_{\tan} and E_{\sec} . Moreover, those relations are quite a bit more complicated than the bar relation, $\delta\sigma_x = E_{\tan}\delta\epsilon_x$, and less obviously the plate analog of the bar relation.

For uniaxial loading N_x only, the lowest buckling load always occurs for $n = 1$, so the plate plastic buckling criterion derived by Jones³ reduces to

$$\bar{N}_x = \frac{\pi^2}{b^2} \frac{E_{\sec} t^3}{12(1-\nu^2)} \left[K_{11} m^2 (b/a)^2 + 2(\nu K_{12} + 2K_{33}) + K_{22} \frac{1}{m^2} (a/b)^2 \right] \quad (23)$$

The K_{ij} are plasticity coefficients, Equation (21), on the plate bending stiffnesses, $D_{ij} = K_{ij}D$, in which $D = E_{\sec} t^3 / 12(1-\nu^2)$ (no longer the same as for isotropic materials because $K_{11} \neq K_{22} \neq 1$ and $K_{12} \neq 0$ thereby effectively creating an orthotropic material when plastic deformation occurs). The K_{ij} on the right-hand side of Equation (23) are a function of the buckling load on the left-hand side, so Equation (23) is a transcendental relationship that must be solved by trial and error or by searching in a logical manner for the plastic buckling load. Because of the many parameters involved, the need to examine a large range of buckling modes (values of m) to find the mode for the lowest buckling load, and the search procedure for the transcendental equation, a computer is essential for practical numerical work (see Jones²⁸). The solution represented by Equation (23) reduces to Stowell's plastic plate buckling solution¹³ if $\nu = 1/2$ and to the classical Euler load for elastic plates by Bryan².

For the thermal buckling problem, the fundamental deformation condition, $\Delta_{FTE} = \Delta_{TRF}$ in Equation (1) is valid irrespective of any material nonlinearities. Superposition of the two loading conditions is not the addition of two linear problems to achieve the solution to a third linear problem, but the addition of two physically nonlinear deformation events to achieve their result, namely a plate that does not expand against the restraints when heated. That is, we are not restricted by linearity, but can address both as-

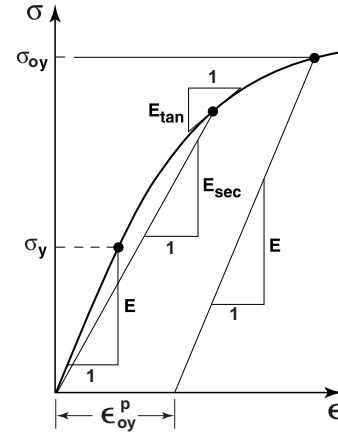


Figure 7 Nonlinear Stress-Strain Curve for Aluminum Alloys

pects of the overall problem, free thermal expansion and plate compression, as independent linear or nonlinear problems. The free thermal expansion of the plate with uniaxial restraint in the x-direction in Figure 1 is

$$\Delta_{FTE} = \alpha \Delta T a \quad (24)$$

if α is constant over the change in temperature, ΔT , as well as throughout the plate volume. The axial compression of the plate caused by the thermal restraining force is

$$\Delta_{TRF_x} = \epsilon a \quad (25)$$

but from Figure 7, the strain to any generic point on the stress-strain curve is $\epsilon = \sigma_x / E_{sec}$ and the stress is $\sigma_x = P/A = N_x b / bt = N_x / t$, so

$$\Delta_{TRF_x} = \frac{N_x / t}{E_{sec}(\sigma)} a = \frac{N_x a}{t E_{sec}(\sigma)} \quad (26)$$

Upon application of the fundamental deformation condition in Equation (1), $\Delta_{FTE_x} = \Delta_{TRF_x}$,

$$\Delta_{FTE} = \alpha \Delta T a = \Delta_{TRF} = \frac{N_x a}{t E_{sec}(\sigma)} \quad (27)$$

Thus, when the thermal stress exceeds the yield stress, the thermal restraining force is

$$N_{restraining_x} = E_{sec}(\sigma) \alpha \Delta T t \quad (28)$$

Plastic thermal buckling occurs when the thermal restraining force, $N_{restraining}$, in Equation (28) grows to equal the plastic buckling load, \bar{N}_x in Equation (23), i.e.,

$$E_{sec}(\sigma) \alpha \Delta T t = \frac{\pi^2}{b^2} \frac{E_{sec} t^3}{12(1 - \nu^2)} \left[K_{11} m^2 (b/a)^2 + 2(\nu K_{12} + 2K_{33}) + K_{22} \frac{1}{m^2} (a/b)^2 \right] \quad (29)$$

Thus, the resulting plastic thermal buckling temperature change, $\bar{\Delta T}$, is

$$\bar{\Delta T} = \frac{\pi^2}{12(1 - \nu^2)} \frac{1}{\alpha} \left[\frac{t}{b} \right]^2 \left[K_{11} m^2 (b/a)^2 + 2(\nu K_{12} + 2K_{33}) + K_{22} \frac{1}{m^2} (a/b)^2 \right] \quad (30)$$

for α constant over the range ΔT and throughout the plate volume. This thermal plastic buckling temperature change, unlike the elastic thermal buckling temperature change, obviously depends on the stress-dependent moduli of the stress-strain curve through the coefficients K_{ij} (which depend on the ratio E_{tan}/E_{sec} and both the elastic and plastic buckling temperature changes depend on the variable Poisson's ratio). Thus, the problem is transcendental as is any plastic buckling problem, namely the buckling temperature change depends on the material properties which, in turn, depend on the load, and hence the temperature. In fact, we cannot solve Equation (30) directly. We must first calculate the plastic buckling load of a plate from Equation (23), finding E_{tan} and E_{sec} in the process. Then, we solve for $\bar{\Delta T}$ from Equation (30) because we know E_{sec} from the work in solving Equation (23). The solution to Equation (30) is the temperature and stress level at which $E_{sec}(\sigma)$ and $E_{tan}(\sigma)$ have consistent (identical) values of $\sigma = \bar{\sigma} = \sigma_{final}$ at room temperature or some constant elevated temperature.

2.3 Plastic Thermal Buckling with Temperature-Dependent Material Properties

The major difficulty with the thermal buckling problem is that not only are the nonlinear stress-strain curve properties a function of stress level, but they are also a fairly strong function of temperature over the usual range of ΔT values encountered. In addition, the coefficient of thermal expansion is a function of temperature, and that fact causes a pronounced change in the calculation of Δ_{FTE} , i.e.,

$$\Delta_{FTE} = \begin{cases} \alpha \Delta T a, & \text{if } \alpha \text{ is constant} \\ \int \alpha dT a, & \text{if } \alpha \text{ varies with } T \end{cases} \quad (31)$$

Thus, the plastic thermal buckling temperature change is not merely Equation (30) with temperature dependence and stress-level dependence of nearly every variable therein, but some more complicated form. The plate plastic buckling load depends only on the nonlinear stress-strain curve properties at the buckling temperature, i.e., the *instantaneous material properties*. In contrast, Δ_{FTE} depends on the manner in which the coefficient of thermal expansion varies throughout the entire range of ΔT from the reference stress-free temperature up through the buckling temperature, i.e., the *cumulative behavior* of α . That cumulative behavior is best expressed in terms of the manner in which the thermal expansion characteristics are actually measured for a material. The fundamental measurement of thermal expansion of a material is to heat a bar of original length, L_o (measured at room temperature) and determine its change in length, ΔL . Thus, the *free thermal expansion* of the sample bar is ΔL , and the *free thermal strain* is $\Delta L/L_o$ (an engineering strain based on the original length) as shown for 7075-T6 aluminum in Figure 8 in which $\Delta L/L_o$ is in percentage form.

If $\Delta L/L_o$ increases linearly with increase in temperature, then at any temperature T_{final} ,

$$\frac{\Delta L}{L_o}(T_{final}) = \alpha(T_{final} - T_{initial}) = \alpha \Delta T \quad (32)$$

in which the *coefficient of linear thermal expansion*, α , is the (constant) slope of the (linear) $\Delta L/L_o$ versus temperature curve (the dashed $\alpha_{RT}\Delta T$ curve in Figure 8 in which α_{RT} is the room-temperature coefficient of thermal expansion). However, $\Delta L/L_o$ typically does not increase linearly with increase in temperature. Then, the local slope of the $\Delta L/L_o$ versus temperature curve is α , the *instantaneous coefficient of thermal expansion*. For aluminum alloys, that curve is concave upward as the solid curve in Figure 8, so α increases with increase in temperature. However, we need not be concerned with the instantaneous α because curves and tables of $\Delta L/L_o$ at various temperatures as can be found in the TPRC Data Series²⁹ are information directly useful in a thermal buckling analysis. Then, $(\Delta L/L_o)L$ is precisely Δ_{FTE} of our plate in Equation (24). Those discrete tabular values are perfectly parallel to the nonlinear stress-strain behavior expressed as stress-strain curves at discrete temperatures.

We therefore recast the thermal buckling problem into one with (cumulative) free thermal expansion as a function of temperature. The free thermal expansion of a plate at any temperature is

$$\Delta_{FTE}(T) = \left[\frac{\Delta L}{L_o}(T) \right] a \quad (33)$$

The axial compression caused by the thermal restraining force for nonlinear stress-strain behavior is

$$\Delta_{TRF} = \frac{\sigma}{E_{sec}(T, \sigma)} a = \frac{N_{restraining} a}{tE_{sec}(T, \sigma)} \quad (34)$$

Then, the fundamental deformation condition of $\Delta_{TRF} = \Delta_{FTE}$ leads to

$$\Delta_{TRF}(T) = \frac{N_{restraining} a}{tE_{sec}(T, \sigma)} = \Delta_{FTE}(T) = \left[\frac{\Delta L}{L_o}(T) \right] a \quad (35)$$

so that

$$N_{restraining} = tE_{sec}(T, \sigma) \left[\frac{\Delta L}{L_o}(T) \right] \quad (36)$$

The plate buckles when $N_{restraining}$ in Equation (36) reaches \bar{N}_x , the buckling load in Equation (23), so

$$tE_{sec}(T, \sigma) \overline{\frac{\Delta L}{L_o}}(T) = \frac{\pi^2}{b^2} \frac{E_{sec} t^3}{12(1 - \nu^2)} \left[K_{11} m^2 (b/a)^2 + 2(\nu K_{12} + 2K_{33}) + K_{22} \frac{1}{m^2} (a/b)^2 \right] \quad (37)$$

(in which the overbar signifies a value at buckling) or the free thermal strain at buckling is

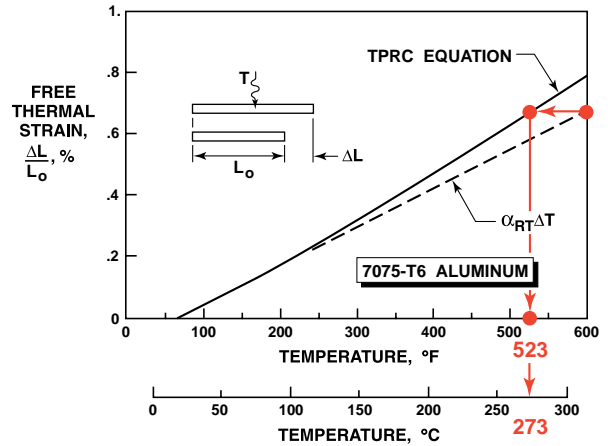


Figure 8 Thermal Expansion of 7075-T6 Aluminum

$$\frac{\Delta L}{L_0}(T) = \frac{\pi^2}{12(1-\nu^2)} \left[\frac{t}{b} \right]^2 \left[K_{11}m^2(b/a)^2 + 2(\nu K_{12} + 2K_{33}) + K_{22} \frac{1}{m^2} (a/b)^2 \right] \quad (38)$$

in which the K_{ij} are a strong function of stress level, E_{\tan} , and E_{\sec} .
If the thermal expansion has a constant rate, α , at all temperatures,

$$\frac{\Delta L}{L_0}(T) = \int \alpha dT = \alpha(T_{\text{final}} - T_{\text{initial}}) = \alpha \Delta T \quad (39)$$

in which α is the linear coefficient of thermal expansion, then

$$\frac{\Delta L}{L_0}(T) = \alpha \Delta T = \frac{\pi^2}{12(1-\nu^2)} \left[\frac{t}{b} \right]^2 \left[K_{11}m^2(b/a)^2 + 2(\nu K_{12} + 2K_{33}) + K_{22} \frac{1}{m^2} (a/b)^2 \right] \quad (40)$$

or the change in temperature at buckling is

$$\Delta T = \frac{1}{\alpha} \frac{\pi^2}{12(1-\nu^2)} \left[\frac{t}{b} \right]^2 \left[K_{11}m^2(b/a)^2 + 2(\nu K_{12} + 2K_{33}) + K_{22} \frac{1}{m^2} (a/b)^2 \right] \quad (41)$$

which is identical to Equation (30) for plastic thermal buckling with temperature-independent material properties and which reduces to Equation (15) for elastic thermal buckling with temperature-independent material properties because then the moduli are equal, i.e., $E_{\tan} = E_{\sec} = E$.

However, for temperature-dependent material properties, the concept of a linear coefficient of thermal expansion is not valid because the expansion behavior is generally not linear. Thus, we must solve Equation (38), a two-level transcendental equation because the stress-strain behavior is a function of both temperature and stress level. In fact, temperature is only implicit in the formulation of Equation (38) whereas the temperature change at buckling, ΔT , is explicit in Equations (15) and (30) for elastic and plastic plate buckling with temperature-independent material properties, respectively. Unlike for elastic buckling in Equation (15), we cannot solve Equation (38) directly for ΔT or even T_{final} at which buckling occurs. Also, Equation (38) is transcendental in terms of stress level. Moreover, because of temperature-dependent material properties, Equation (38) is transcendental to a higher level, namely in terms of temperature, than Equation (30). To solve the problem, we must search for both a temperature and a stress level at which the left-hand side equals the right-hand side of Equation (38). Thus, two levels of searching are required: (1) a search for the correct plastic buckling load for specific nonlinear stress-strain curve properties at an estimated temperature and (2) a search for the correct temperature at which Equation (38) is satisfied. The solution to Equation (38) is the temperature and stress level at which $E_{\sec}(T, \sigma)$, $E_{\tan}(T, \sigma)$, and $\Delta L/L_0(T)$ have consistent (identical) values of $T = \bar{T} = T_{\text{final}}$ and $\sigma = \bar{\sigma} = \sigma_{\text{final}}$. For an estimated right-hand side of Equation (38), the calculated $\Delta L/L_0(T)$ can be back-interpolated from tabulated values to find the implied temperature. That is, instead of given the temperature, what is $\Delta L/L_0(T)$, we must ask: given a $\Delta L/L_0(T)$, what is the corresponding temperature? Alternatively to back-interpolation, we can solve for the buckling temperature from the cubic equation for the free thermal strain, $\Delta L/L_0(T)$, for 7075-T6 aluminum in the TPRC Data Series²⁹:

$$\frac{\Delta L}{L_0}(T) = -.478 + 9.368 \times 10^{-4} T + 2.688 \times 10^{-6} T^2 - 1.082 \times 10^{-9} T^3 \quad (42)$$

in which T is the *number of °K*, i.e., without units. Equation (42) is the summary of many data sources and is claimed to be accurate to $\pm 7\%$. The cubic equation can either be solved directly or by searching with the interval-halving numerical search technique discussed in the following section. The driver for thermal buckling problems is the free thermal strain that must be balanced by the deformation caused by the thermal restraining force. In Figure 8, we see that the temperature to cause a specific free thermal strain is lower for the TPRC curve than for the $\alpha_{RT}\Delta T$ line. For example, the temperature to cause the same free thermal strain as that predicted with α_{RT} at 600°F (316°C) is 523°F (273°C) from the TPRC equation or 13% less. Such a difference translates directly into a similar percentage difference in predicted thermal stresses. Thus, we simply interpolate or back-calculate the fundamental $\Delta L/L_0(T)$ data and the parameters of the equations representing the nonlinear stress-strain behavior at an estimated temperature in the numerical search procedure. We address the numerical search procedure for the estimated temperature and its convergence to the final buckling temperature in the next section.

3. Solution Strategy

The solution strategy has two calculation or logic loops: (1) find the plastic plate buckling stress for specified nonlinear material properties corresponding to an estimated thermal buckling temperature and (2) find the actual thermal buckling temperature at which plastic plate buckling occurs by changing the estimated temperature until the plate buckles at a stress with material properties at a calculated temperature equal to the estimated temperature.

3.1 Mechanical Plastic Plate Buckling Stress for Estimated ΔT

The solution of the transcendental equation for the plastic plate buckling stress involves the following searching procedure. Note that the load-deformation curve coincides with the stress-strain curve in Figure 9 for this uniaxial loading case. First, estimate a buckling stress, $\sigma_{\text{estimated}}$. Then, find the plastic moduli, E_{tan} and E_{sec} , for that stress level. Next, calculate the buckling stress, $\sigma_{\text{calculated}}$, from Equation (23) corresponding to the material properties implied in the first step. Now compare the calculated buckling stress with the estimated buckling stress. If the calculated buckling stress is bigger than the estimated buckling stress, then the estimated buckling stress was too low. This conclusion is easily reached when you recognize that the plastic moduli, E_{tan} and E_{sec} *always decrease* as stress increases for concave-downward stress-strain curves. Moreover, from Equation (23), if $\sigma_{\text{estimated}}$ is too low and thus the estimated properties are too high, then $\sigma_{\text{calculated}}$ will be too high. Conversely, if $\sigma_{\text{estimated}}$ is too high and therefore the estimated properties are too low, then $\sigma_{\text{calculated}}$ will be too low. This relationship will be referred to as the *special relationship* between the estimated and calculated buckling stresses. For example, if the elastic Young's modulus is selected, then the first estimated buckling stress, σ_{1e} , is, by implication, the stress at yielding or lower. However, buckling does not necessarily take place at yielding. In fact, the material can yield but not buckle until a considerably higher stress level is reached. Thus, buckling and yielding are two *totally independent* physical events. Buckling can occur at stresses below yielding, and, in that case, the buckling is elastic. In contrast, yielding can occur at stresses below buckling, and, in that case, the buckling is called plastic buckling or inelastic buckling or elastic-plastic buckling.

If the plate buckles plastically, then the first estimated buckling stress σ_{1e} is less than the corresponding calculated buckling stress σ_{1c} in Figure 9. Because of the basic concave-downward nature of the stress-strain curve for most materials, the same relation exists between all estimated and calculated buckling stresses. The estimated buckling stress is less than the actual buckling stress for the first three estimated buckling stresses in Figure 9. The fourth estimated buckling stress leads to a calculated stress that is below the estimated buckling stress because the estimate is above the actual buckling stress. Only when the estimated buckling stress is precisely the actual buckling stress do the estimated, the calculated, and the actual buckling stresses coincide. The *special relationship* between the estimated, the calculated, and the actual buckling stresses is the fundamental basis for a simple strategy to determine the actual buckling stress of a plate. Thus, if a buckling stress is estimated and a buckling stress calculated, then we know whether to increase or decrease the next estimate to get closer to the actual buckling stress, i.e., we know which way to go on the stress-strain curve.

The next question is *how much* to increase the second estimated buckling stress above the first estimated buckling stress, if the buckling is plastic. The known special relationship between estimated, calculated, and actual buckling stresses does not, however, help to determine the *magnitude* of the next estimated buckling stress. Thus, we must resort to simply guessing in an educated manner, and then we can rely upon the known special relationship to determine the sign, but not the amount, of the next adjustment. Thus, we simply march up the stress-strain curve or the load-deformation curve as in Figure 9 until the known special relationship dictates that we have increased the estimated buckling stress to too

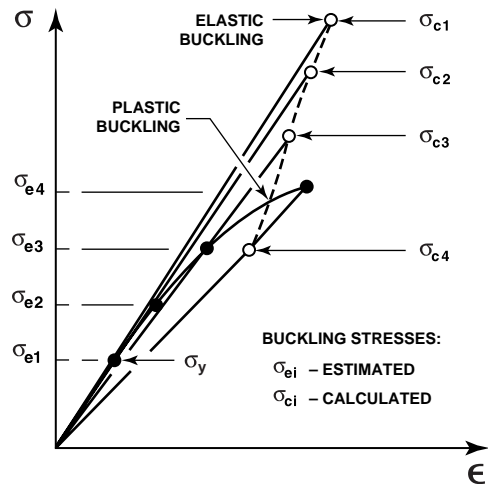


Figure 9 Estimated vs. Calculated Buckling Stress

high a level. Then, we know two estimated stresses that bracket the actual buckling stress. For example, σ_{3e} is too low and σ_{4e} is too high. Thus, σ_{actual} must lie between σ_{3e} and σ_{4e} .

Now that we have bracketed the actual buckling stress, how do we find that stress? Again, we have no quantitative way of choosing the next estimated buckling stress. Thus, we must again rely upon the known *special relationship* and adopt a special searching strategy. That special searching strategy could take several forms. The strategy could be to drop back to the estimated buckling stress that is below the actual buckling stress and march up the load-deformation curve at increments of, say, one-tenth the stress difference between σ_{3e} and σ_{4e} . That is, split the bracket into ten parts (i.e., interval tenting) and find which of the ten segments is a closer bracket on the actual buckling stress than the original bracket. That closer bracket can subsequently be split into ten parts to get an even closer bracket. The splitting and searching procedure is repeated until a bracket with sufficient accuracy is found. That is, the upper bound and lower bound on the bracket can be averaged to obtain an estimate of the actual buckling stress. The error in that estimate is related to the deviation of the bounds on the bracket from the average of the bounds. Thus, the smaller the bracket, the higher the accuracy of the calculated buckling stress.

Another useful numerical technique for searching for the solution of a transcendental equation is the *interval-halving* or *binomial-search* procedure. Instead of dividing the segment between the upper and lower bounds into ten parts as in the preceding method, we merely halve the segment. The ends of each half segment are examined to find new upper and lower bounds to the solution (one is actually an old bound). Then, the half segment that provides the new upper and lower bounds is investigated. Its half that gives yet another more refined set of upper and lower bounds is split in two, and so on. This interval-halving technique is far more efficient, i.e., has fewer calculations, than the interval-tenting procedure. Thus, interval halving will be applied in the solution of the present transcendental equations.

3.2 Determination of $\overline{\Delta T}$ from $\overline{\Delta T}_{\text{estimated}}$ and $\overline{\Delta T}_{\text{calculated}}$

Although the plastic plate buckling stress has been found in the previous search procedure for an estimated temperature, $\overline{\Delta T}_{\text{estimated}}$, that $\overline{\Delta T}_{\text{estimated}}$ will not correspond to the $\overline{\Delta T}_{\text{calculated}}$ (unless we made an incredibly lucky estimate). Thus, we simply search for the correct $\overline{\Delta T}$ by use of a special relationship similar to that in Section 3.1. That is, if $\overline{\Delta T}_{\text{estimated}}$ is too low, then $\overline{\Delta T}_{\text{calculated}}$ will always be too high, and conversely, if $\overline{\Delta T}_{\text{estimated}}$ is too high, then $\overline{\Delta T}_{\text{calculated}}$ will always be too low. This special relationship is easily reached when you recognize that the plastic moduli, E_{tan} and E_{sec} , *always decrease* as stress increases for concave-downward stress-strain curves. Moreover, E_{tan} decreases more rapidly than E_{sec} . In addition, $\Delta L/L_0$ always increases with temperature causing a larger ΔF_{TE} , but not necessarily a larger thermal restraining force nevertheless leading to a higher $\overline{\Delta T}$. We will see that much of the heating goes into softening the material (just as increased stress goes into softening the material in Section 3.1). We increase the $\overline{\Delta T}_{\text{estimated}}$ from some initial estimate until we find a $\overline{\Delta T}_{\text{estimated}}$ that leads to $\overline{\Delta T}_{\text{calculated}}$ less than $\overline{\Delta T}_{\text{estimated}}$. Having bracketed the true $\overline{\Delta T}$, we proceed with the interval-halving procedure until we find $\overline{\Delta T}$ to the desired accuracy. Note that $\Delta L/L_0(T)$ is actually calculated in Equation (38), so $\overline{\Delta T}$ (actually \overline{T}) must be back-interpolated from tabular values of $\Delta L/L_0(T)$ or back-calculated from the $\Delta L/L_0(T)$ expression in Equation (42).

3.3 Summary of Solution Strategy

The sheer mass of data necessary to define the parameters of the material models at the various temperatures and the implementation of the searching strategy for (1) finding E_{sec} , E_{tan} , and ν on an interpolated nonlinear stress-strain curve and $\Delta L/L_0$ for an estimated temperature and (2) finding the temperature at which the material properties, E_{sec} , E_{tan} , and ν as well as $\Delta L/L_0$, are consistent such that $\overline{\Delta T}_{\text{estimated}} = \overline{\Delta T}_{\text{calculated}}$ to the desired accuracy require a computer program. This two-level numerical search procedure will be used in the following sections. At each of the estimated temperatures and each of the estimated stresses, the corresponding material properties must be determined and the buckling stress calculated for those properties and temperatures. Fortunately, the calculation of the plate buckling stress from Equation (38) in each of those steps is trivial, so this process takes virtually no perceptible computer time. Graphical solution techniques often used for plastic buckling problems cannot be used in plastic thermal buckling problems because the stress-strain curves and hence tangent modulus, secant modulus, and ν versus stress curves essential at all temperatures simply do not exist!

4. Nonlinear Temperature-Dependent Material Model

4.1 Introduction

The procedure for searching for the plastic buckling temperature requires that we know the nonlinear stress-strain curve at every estimated temperature in the search procedure along with the thermal expansion character to that temperature. Obviously, that specific information is simply not available, nor will it ever be, at every °F (or °C) or fraction thereof that is encountered in a numerical search procedure. Instead, only a few stress-strain curves are available over a range of temperatures in which bars are expected to buckle, and a few thermal expansion measurements are available over the same range. Thus, to solve our thermal buckling problem, we must be able to meaningfully interpolate the available data at every temperature encountered in the search procedure. Knowing the stress-strain curves and the thermal expansion data at a few temperatures is not enough. We must be able to represent those curves and data in some appropriate equation form so that we have something definitive to interpolate. We could also desire to extrapolate beyond the available data, e.g., above the highest temperature at which a stress-strain curve is available or above the highest stress defined on a measured stress-strain curve. However, extrapolation is speculation, so it must be done with suitable caution and reservations.

We use the stress-strain curves as a function of temperature measured by Mathauser and Brooks⁶ for 7075-T6 (called 75S-T6 in their day) aluminum alloy in Figure 10. There, the yield stress, σ_y , decreases by a factor of about ten over the temperature range of 70°F (20°C) to 600°F (316°C). Over that range, the Young's modulus, E , decreases by only a factor of two, but the stress-strain curves become considerably more nonlinear because their maximum strains are all .012. The free thermal strain data are obtained from a Thermophysical Properties Research Center reference book²⁹. Over the same temperature range, the instantaneous coefficient of thermal expansion increases by about one-sixth. However, as argued in Section 2.3, it is more appropriate to use the TPRC free thermal strain expression, Equation (42), in the analysis. These attributes of the 7075-T6 aluminum material property data constitute a formidable modeling challenge, especially because the stress-strain curves are not very closely spaced in temperature.

The concept of the Nadai stress-strain curve equation²² is used as the basic modeling tool, but only after its nature is significantly extended in order to properly represent the high-temperature material behavior at high stress relative to the yield stress with considerable nonlinearity in Figure 10. Then, interpolation procedures must be developed to enable determination of stress-strain curves at temperatures intermediate to those in Figure 10. Finally, the data for description of the extended Nadai-Jones stress-strain curves¹⁹ and the thermal expansion characteristics are summarized in tabular and equation form suitable for use in the numerical search procedure for the thermal buckling temperature. The variation of all material properties with temperature will be interpolated linearly as a first approximation when results at a temperature not on Figure 10 are required in the thermal buckling search procedure. The exception is the thermal expansion behavior for which the actual TPRC expression, Equation (42), for the smooth variation of the free thermal strain as a function of temperature is addressed²⁹. Also, there is a large gap between the 400°F (204°C) and the 500°F (260°C) stress-strain curves followed by a smaller gap between the 500°F (260°C) and the 600°F (316°C) curves. That first increasing, then decreasing, gap between curves with the same temperature difference will be seen to have an effect later.

4.2 Nadai Stress-Strain Curve Model

Consider elastic-plastic material behavior with a linear elastic region ended by a yield stress and then a gradual 'bending over' of the concave-downward stress-strain curve as the material becomes more and more plastic, such as is typical of aluminum and its alloys at room temperature and is represented in

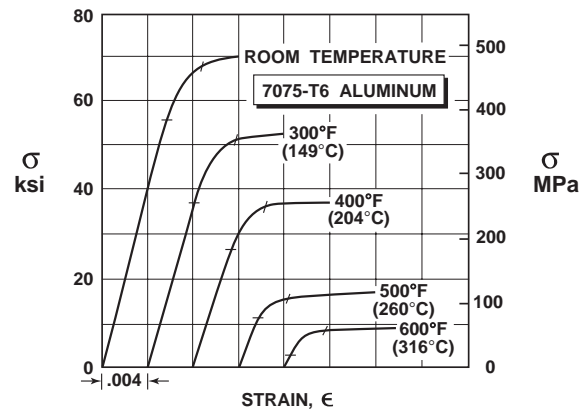


Figure 10 Compressive Stress-Strain Curves for 7075-T6 Aluminum as a Function of Temperature
(After Mathauser and Brooks⁶)

Figure 7. Often, that nonlinear stress-strain behavior can be described with the Nadai* stress-strain curve model²² which was originally developed for alloy steel oil-well casings and which has two parts:

$$\epsilon = \frac{\sigma}{E} \quad \sigma \leq \sigma_y \quad (43)$$

$$\epsilon = \frac{\sigma}{E} + \epsilon_{oy}^p \left[\frac{\sigma - \sigma_y}{\sigma_{oy} - \sigma_y} \right]^n \quad \sigma \geq \sigma_y \quad (44)$$

in which σ_{oy} is the offset yield stress at a specific permanent strain ϵ_{oy}^p in Figure 11, σ_y is the yield stress (the end of linear elastic behavior which is, of course, the beginning of yielding) and n is an exponent that need not be an integer. We can see in Equation (44) that the strain above yielding is separated into elastic strain plus plastic strain. Thus, ϵ_{oy} is easily shown to be the plastic strain at σ_{oy} , i.e., the permanent strain used to determine σ_{oy} shown in Figure 11. A common value used for ϵ_{oy}^p is .002 for both steel and aluminum. Osgood³⁰ suggested that Equation (44) be written as

$$\epsilon = \frac{\sigma}{E} + K(\sigma - \sigma_y)^n \quad \sigma > \sigma_y \quad (45)$$

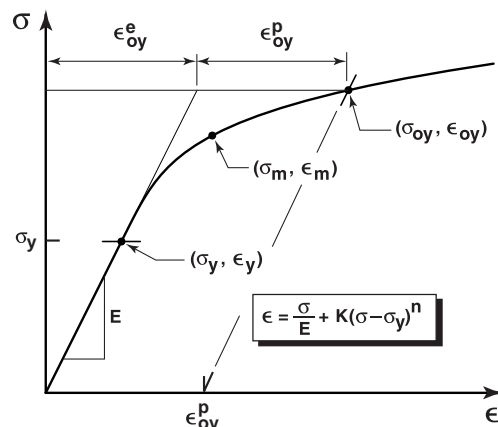


Figure 11 Nadai Stress-Strain Curve Model

which is called the generalized Nadai model in which some constant terms are gathered as

$$K = \epsilon_{oy}^p (\sigma_{oy} - \sigma_y)^{-n} \quad (46)$$

The strain in Equation (45) at each stress level, just as in Equation (44), is the sum of an elastic component (σ/E) and a plastic component as shown for the offset yield stress in Figure 11. The plastic component is the deviation from the linear elastic component. The units of K are ksi^{-n} (or MPa^{-n}) and vary as n changes. Moreover, because n is generally not an integer, the units of K are rather unusual, although valid. Expressions for E_{\tan} and E_{\sec} needed in the buckling and thermal buckling analyses are readily obtained from Equation (45) as

$$E_{\tan} = \frac{d\sigma}{d\epsilon} = 1 / \frac{d\epsilon}{d\sigma} = \frac{E}{1 + KEn(\sigma - \sigma_y)^{n-1}} \quad E_{\sec} = \frac{\sigma}{\epsilon} = \frac{E\sigma}{\sigma + KE(\sigma - \sigma_y)^n} \quad (47)$$

Nadai's approach was to force the curve to pass through the offset yield point (σ_{oy} , ϵ_{oy}) with varying integer powers of n , so there were two assigned variables in addition to σ_y . Instead, it is possible to force the curve to pass through two points (in addition to the yield point) and accept the resulting noninteger value of the associated n and achieve more effective material models than with Nadai's approach.

The parameters for a curve of the form in Equation (45) are determined by requiring the curve to pass through three points, called *pass-through points*, on the measured stress-strain curve. The first pass-through point must be (σ_y , ϵ_y) in order to properly start the nonlinear portion of the curve from the linear portion (to model E and the extent of the linear portion). The value of n is determined by requiring the curve to have the same value of n for the two arbitrarily chosen pass-through points, (σ_2 , ϵ_2) and (σ_3 , ϵ_3) which are the two pass-through points [other than the required point (σ_y , ϵ_y)]. That is, we require the curve to pass through both points 2 and 3. Thus,

$$\epsilon_2 = \sigma_2/E + K(\sigma_2 - \sigma_y)^n \quad \epsilon_3 = \sigma_3/E + K(\sigma_3 - \sigma_y)^n \quad (48)$$

which can be solved for n after eliminating K (K , like n , must have the same value at both pass-through points) to get (after recognizing that $\log a^n = n \log a$)

$$n = \log \frac{\epsilon_2 - \sigma_2/E}{\epsilon_3 - \sigma_3/E} \div \log \frac{(\sigma_2 - \sigma_y)}{(\sigma_3 - \sigma_y)} \quad (49)$$

Then, K is found from

$$K = \epsilon_2^p (\sigma_2 - \sigma_y)^{-n} = \epsilon_3^p (\sigma_3 - \sigma_y)^{-n} \quad (50)$$

*Although Holmquist and Nadai co-authored the paper, Nadai was stated as responsible for the stress-strain curve modeling and presented that part of the paper; hence, the name Nadai on the stress-strain curve model without the name Holmquist.

in which $\epsilon_2^p = \epsilon_2 - \sigma_2/E$ and $\epsilon_3^p = \epsilon_3 - \sigma_3/E$ are the plastic strains at the pass-through points as seen for $\sigma_3 = \sigma_{oy}$ in Figure 11. That is, either of the two arbitrarily chosen pass-through points can be used to calculate K . In the original Nadai formulation²², $(\sigma_{oy}, \epsilon_{oy})$ was always one of the pass-through points, although Nadai did not use the simple concept of pass-through points (he only displayed curves for integer values of n). If neither of the two pass-through points is $(\sigma_{oy}, \epsilon_{oy})$, then σ_{oy} and ϵ_{oy}^p do *not* appear in the Nadai equation, and the curve does not necessarily (and probably does not) pass through $(\sigma_{oy}, \epsilon_{oy})$.

The offset yield stress, σ_{oy} , is simply a conventional parameter often used in reporting measured stress-strain behavior, but otherwise is merely a perfectly arbitrary point on the stress-strain curve, i.e., without any notable physical significance whatsoever, unlike the yield stress, σ_y . Thus, there is no reason why one of the two arbitrarily chosen pass-through points cannot be located at some stress above or below σ_{oy} . In addition, there is no reason why one of the pass-through points need be $(\sigma_{oy}, \epsilon_{oy})$. After all, we're simply trying to model a nonlinear stress-strain curve, i.e., approximate the measured stress-strain curve with a convenient equation, in a simple, yet undeniably *approximate* manner.

The preceding stress-strain curve equation formulation can be generalized to better enable fitting the Nadai stress-strain curve to measured behavior that changes above σ_{oy} from what it is below σ_{oy} . The stress-strain curve equation is modified with

$$K = \epsilon_o^p (\sigma_o - \sigma_y)^{-n} \quad (51)$$

so that the curve is passed through some 'other' point (σ_o, ϵ_o) in which the subscript 'o' stands for 'other'. That is, the pass-through points must now include a point above $(\sigma_{oy}, \epsilon_{oy})$ unlike Nadai's originally stated form. The two pass-through points can be used to specify the range of stress and strain over which the Nadai equation fits the measured data. However, *compromises in quality of fit occur* if the curve of the actual data changes character 'too much' as stress increases. For example, it is difficult to fit any equation to a curve that first bends over gradually and gracefully just above σ_y and then dramatically bends over in the region of $(\sigma_{oy}, \epsilon_{oy})$ as do the curves at high temperature in Figure 10.

The Nadai stress-strain curve formulation is limited to passing through three specified points, namely two arbitrarily chosen pass-through points in addition to the yield point, (σ_y, ϵ_y) (at which point the Nadai nonlinear curve begins because yielding occurs). Usually, the offset yield stress $(\sigma_{oy}, \epsilon_{oy})$ is one of those two points. That leaves only one point to choose to represent the shape of the measured stress-strain curve. If the third point is chosen to be the mid-point (σ_m, ϵ_m) midway between (σ_y, ϵ_y) and $(\sigma_{oy}, \epsilon_{oy})$, then the behavior between the later two points is fairly well represented at the expense of the behavior above $(\sigma_{oy}, \epsilon_{oy})$ as seen with the long-dashed curve in Figure 12. There, the solid curve is the measured stress-strain behavior that we are trying to model. In contrast, if the point (σ_h, ϵ_h) which is above $(\sigma_{oy}, \epsilon_{oy})$ is used as a pass-through point, then the behavior between $(\sigma_{oy}, \epsilon_{oy})$ and (σ_h, ϵ_h) is well represented at the expense of the behavior between (σ_y, ϵ_y) and $(\sigma_{oy}, \epsilon_{oy})$ as seen with the short-dashed curve in Figure 12. The choice of (σ_h, ϵ_h) leads to a higher than actual buckling stress if the buckling stress falls in the range of (σ_y, ϵ_y) to $(\sigma_{oy}, \epsilon_{oy})$, but the buckling stress is properly limited above $(\sigma_{oy}, \epsilon_{oy})$, i.e., the stress cannot grow above the measured behavior. Somewhat better modeling might be achieved if a point between (σ_m, ϵ_m) and $(\sigma_{oy}, \epsilon_{oy})$, say $(\sigma_{3/4}, \epsilon_{3/4})$, were selected in addition to (σ_h, ϵ_h) . However, then the Nadai stress-strain curve would not be required to pass through $(\sigma_{oy}, \epsilon_{oy})$, but that pass-through is not an inherent requirement of the modeling process, although it might be an apparent (but artificial and hence false) desire.

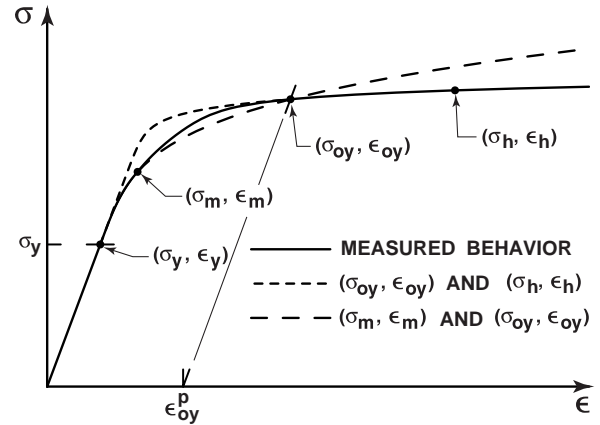


Figure 12 Approximation of Measured Behavior with Nadai Stress-Strain Curve Models

The behaviors in Figure 12 are representative of the Nadai stress-strain curve modeling of 7075-T6 aluminum at 600°F (316°C) from Figure 10. For lower temperatures, the contrast between the two approximations and the measured behavior is less pronounced, although still present.

We must be careful about the fit of the Nadai curve above $(\sigma_{oy}, \epsilon_{oy})$ because in analysis we automatically extend or extrapolate the stress-strain curve to the level at which buckling supposedly occurs. If that extension is not reasonable, the predicted results will be inaccurate in some manner. Note that the point (σ_h, ϵ_h) does not necessarily correspond to a plastic flow region of behavior, but merely the largest

stress and strain in the available measured behavior. As the stress and strain increase from $(\sigma_{oy}, \epsilon_{oy})$ to (σ_h, ϵ_h) , E_{tan} approaches zero and E_{sec} decreases substantially. Thus, the bar buckling load more rapidly approaches zero than the thermal restraining force decreases toward zero, leading to an increasing ΔT . The point (σ_h, ϵ_h) is the best-available high point on the stress-strain curve and is therefore better representative of stress-strain behavior at high stresses than $(\sigma_{oy}, \epsilon_{oy})$. Using (σ_h, ϵ_h) ensures that we do not overestimate E_{tan} for a specified E_{sec} at high stresses. Thus, (σ_h, ϵ_h) must be used to model the stress-strain behavior for bars and probably for plates.

With only three pass-through points, the ability to model stress-strain behavior with the Nadai curve is somewhat limited. In particular, if the stress-strain curve is first fairly stiff and then considerably more flexible, as is typical for aluminum above room temperature, the Nadai curve can be used only with serious consequences of being stiffer than the measured behavior in one range of stresses and less stiff in other ranges. In this buckling problem with its natural sensitivity to E_{tan} and E_{sec} , such approximations lead to inaccurate and uncertain thermal and mechanical buckling predictions. The fundamental problem that we face is that the actual stress-strain behavior changes character as stress and strain increase more than can be represented with the single exponential form of the generalized Nadai stress-strain curve. Fortunately, a stress-strain curve equation can be devised to accurately characterize the behavior of aluminum over a wide range of stresses, e.g., the Mathauser and Brooks curves⁶. However, the new equation is a little more complicated than the Nadai equation, involving three regions of applicability with five pass-through points instead of two regions and three pass-through points. Most importantly, there are two regions of modeling above σ_y as opposed to only one for the Nadai model.

4.3 Nadai-Jones Stress-Strain Curve Model

The Nadai stress-strain curve model must be extended to properly represent the two distinctly different regions of nonlinear behavior for the aluminum stress-strain curves of Figure 10. The generalized Nadai equation with a single nonlinear term is used to model the first portion of the mildly nonlinear region from σ_y up to some stress, σ_3 . Then, a second nonlinear term is added to the Nadai formulation to create a new stress-strain curve equation to represent the upper portion of the highly nonlinear region from σ_3 to some high stress, σ_h (see Jones¹⁹):

$$\begin{aligned} \sigma \leq \sigma_y: \quad \epsilon &= \frac{\sigma}{E} \\ \sigma_3 \geq \sigma \geq \sigma_y: \quad \epsilon &= \frac{\sigma}{E} + K(\sigma - \sigma_y)^n \\ \sigma \geq \sigma_3: \quad \epsilon &= \frac{\sigma}{E} + K(\sigma - \sigma_y)^n + J(\sigma - \sigma_3)^m \end{aligned} \quad (52)$$

in which the constants are determined by forcing the curves to pass through five pass-through points.

$$K = \epsilon_2^p (\sigma_2 - \sigma_y)^{-n} = \epsilon_3^p (\sigma_3 - \sigma_y)^{-n} \quad (53)$$

$$J = \epsilon_4^{p2} (\sigma_4 - \sigma_3)^{-m} = \epsilon_5^{p2} (\sigma_5 - \sigma_3)^{-m} \quad (54)$$

in which ϵ_4^{p2} and ϵ_5^{p2} are two portions of the plastic strain in excess of the plastic strains, ϵ_4^{p1} and ϵ_5^{p1} , respectively, from the Nadai curve as shown for pass-through point 5 in Figure 13. The units of K and J are ksi^{-n} (or MPa^{-n}) and ksi^{-m} (or MPa^{-m}), respectively, and vary as n and m change. Moreover, because n and m are generally not integers, the units of K and J are rather unusual, although still perfectly valid.

The two regions of behavior collectively represented with the two nonlinear formulations in Equation (52) and Figure 13 require three pass-through points each, but have in common the point at the boundary between the two regions. Thus, only five pass-through points are required to determine the parameters in Equation (52). The first point must be the yield point where the nonlinear deformation starts. The first, second, and third points are used to define the Nadai curve used for small nonlinear stresses in the manner of Section 4.2. The third, fourth, and fifth points are used to define the Nadai-Jones curve used for higher nonlinear stresses. The third point must be the end of the Nadai curve range and, simultaneously, the beginning of the Nadai-Jones range. The fourth and fifth points are used to determine m by requiring m to have the same value for the two points, i.e., by requiring the curve to pass through both points 4 and 5:

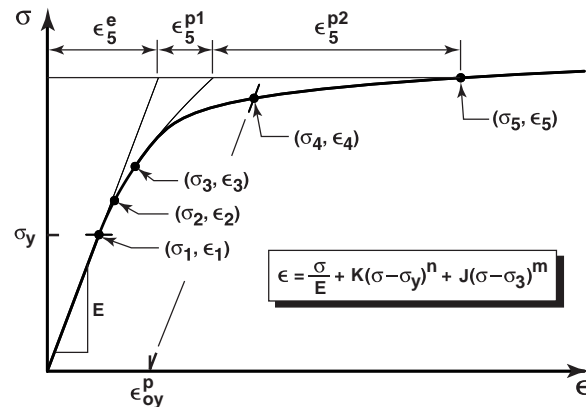


Figure 13 Nadai-Jones Stress-Strain Curve Model

$$\begin{aligned}
\varepsilon_4 &= \sigma_4/E + K(\sigma_4 - \sigma_y)^n + J(\sigma_4 - \sigma_3)^m \\
&= \varepsilon_4^e + \varepsilon_4^{p1} + J(\sigma_4 - \sigma_3)^m \\
\varepsilon_5 &= \sigma_5/E + K(\sigma_5 - \sigma_y)^n + J(\sigma_5 - \sigma_3)^m \\
&= \varepsilon_5^e + \varepsilon_5^{p1} + J(\sigma_5 - \sigma_3)^m
\end{aligned} \tag{55}$$

in which K and n are already known from the Nadai phase of modeling. Equation (55) can be solved for m after eliminating J (J , like m , must have the same value at both pass-through points) to get (after recognizing that $\log a^n = n \log a$)

$$m = \log \left[\varepsilon_4^{p2} / \varepsilon_5^{p2} \right] \div \log [(\sigma_4 - \sigma_3) / (\sigma_5 - \sigma_3)] \tag{56}$$

and then J is calculated from Equation (54). Alternatively, m can be obtained from Equation (54). The fourth pass-through point can be the offset yield stress, and the fifth point is typically the highest point on the measured stress-strain curve, although it need not be.

Expressions for E_{\tan} and E_{\sec} in the third region are readily obtained from Equation (52) as

$$\begin{aligned}
E_{\tan} &= \frac{E}{1 + KEn(\sigma - \sigma_y)^{n-1} + JEm(\sigma - \sigma_3)^{m-1}} \\
E_{\sec} &= \frac{E\sigma}{\sigma + KE(\sigma - \sigma_y)^n + JE(\sigma - \sigma_3)^m}
\end{aligned} \tag{57}$$

and the plastic moduli are plotted for all three regions in Figure 14. The secant modulus decreases in a seemingly monotonic manner as stress increases. However, the tangent modulus decreases in a non-monotonic fashion as stress increases. The nature of the tangent modulus decrease is somewhat like a roller coaster track with a drop-off, then a relative rise (relative to the slope prior to the rise) near the bottom of the slope, and next another drop-off followed by the absolute rise at the bottom. The relative rise (a segment of downward curvature in Figure 14) is caused by the third portion of the stress-strain curve model being activated in the same manner as the second portion becomes activated just above σ_y with an associated initial downward curvature from the Nadai curve. The measure of the relative rise near the bottom of the 'roller coaster track' is the amplitude of the deviation, Δ , from a linear slope of the 'track' (a linear decrease of E_{\tan} with increasing stress) as shown in Figure 14. Although it might be desirable to have a monotonically decreasing E_{\tan} , that desire is not necessarily met with the present Nadai-Jones stress-strain curve model. This non-monotonic behavior has some non-serious implications for the accuracy of the buckling stresses and the buckling temperatures for the bar problem¹⁹, but none are observed for the plate problem.

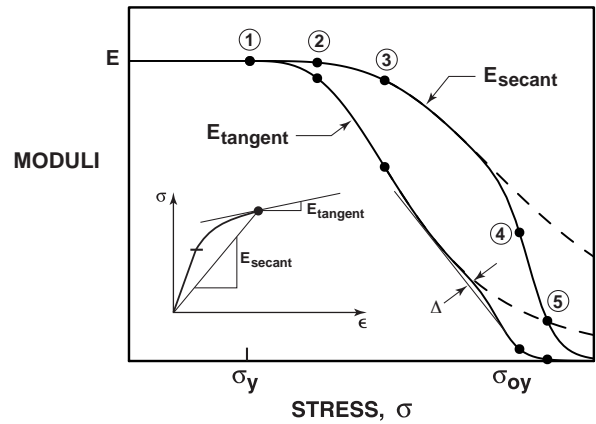


Figure 14 Plastic Moduli Variation with Stress Level

4.4 Nadai-Jones Stress-Strain Curves for 7075-T6 Aluminum

The Nadai-Jones stress-strain curve equation is used to model Mathauser and Brooks' stress-strain curves⁶ for 7075-T6 aluminum alloy over the measured temperature range from room temperature to 600°F (316°C). The modeling process involves estimating the location of the five pass-through points from plotted data, but that step is not as simple as it might seem because it is hard to measure the co-ordinates of points on a small-scale plot. If the plot is enlarged, the curve width increases, so interpretation of the location of a specific point is made somewhat ambiguous. Small changes to the stress and strain coordinates of the estimated location of each pass-through point lead to decidedly different stress-strain curves at higher stress levels than in the region of the pass-through points. Repeated adjustments to the 'measured data' are needed to force the model curves (1) to 'look like' the measured curves and simultaneously (2) to minimize the 'roller-coaster rise' effect in the tangent modulus in Figure 14.

Mathematica^{®31} was used to calculate and plot each adjustment to the 'measured data' (actually, data *interpreted* by the author from small-scale plots) for comparison to the measured curve on a light

table and to measure the magnitude of the relative rise in the tangent modulus curve in order to select a set of points that satisfy the two 'goodness of fit' criteria. A 'nice-looking' stress-strain curve might have a 'largish' Δ , so we must keep 'adjusting the input data' (but only within a reasonable interpretation of the measured data!) until we find a 'nice-looking' stress-strain curve with a 'small' Δ . Perhaps surprisingly, the number of combinations of points investigated before that success is achieved (i.e., the two 'goodness of fit' criteria are met) can easily exceed fifty per temperature.

The reason for this difficulty is that the shapes of both the stress-strain curve and the tangent modulus versus stress curve are very sensitive to the specific locations of the pass-through points used. The human eye simply cannot perceive the location of a point on a plotted curve to the accuracy required (especially one at a small scale in an old report). That is, very small changes in the values of the input pass-through points produce changes elsewhere on the stress-strain curves and plastic modulus versus stress curves. For example, the behavior above the first three pass-through points can change dramatically with changes in the fourth significant figure in the input strains. Also, the value of σ_y is usually well below what you might judge with your eye; the lowness is necessary to achieve a concave-downward nature of E_{tan} at σ_y . Moreover, how the slope of the stress-strain curve changes is virtually imperceptible to the human eye.

The coordinates of the five pass-through points are essential to establish the three-region Nadai-Jones stress-strain curves. To model the various Mathauser and Brooks curves in a consistent manner (to enable interpolation between curves), σ_3 is always chosen to be the average of σ_1 and σ_4 , i.e., halfway between σ_1 and σ_4 , and, in turn, σ_2 is always chosen to be the average of σ_1 and σ_3 . Moreover, the strains are $\epsilon_4 = .002 + \sigma_4/E$ and $\epsilon_5 = .0120$ for each of the curves (ϵ_5 is the highest strain measured for each of the curves). The final set of model curves are shown in Figure 15 as solid curves which are virtually indistinguishable from the measured curves in Figure 10 when superimposed at the same scale. In addition, the five pass-through points are shown.

4.5 Interpolation of Nadai-Jones Stress-Strain Curves for 7075-T6 Aluminum

The parameters of the Nadai-Jones stress-strain curves for two adjacent measured temperatures can be interpolated to predict a hopefully representative curve at an intermediate temperature. Successfully accomplishing that goal depends on the group of measured stress-strain curves being 'similar enough' that interpolation of the parameters describes representative curves. In contrast to a family of stress-strain curves that are 'similar enough', curves that have different shapes at different temperatures are difficult, if not impossible, to interpolate between.

The family of curves obtained by Mathauser and Brooks⁶ meets that somewhat vague similarity criterion, although the curves do not have a uniformly progressive change from 70°F (20°C) to 600°F (316°C). The 400°F (204°C) and 500°F (260°C) curves are further apart than the 300°F (149°C) and 400°F (204°C) curves, and the 500°F (260°C) and 600°F (316°C) curves are closer than the 400°F (204°C) and 500°F (260°C) curves, thus reversing the trend as temperature increases. Accordingly, the Mathauser and Brooks curves do not have a monotonic progression of shape with temperature. The reason for this non-monotonic progression (or different rate of softening as temperature increases) is related to the behavior of the zinc in the 7075-T6 aluminum alloy of aluminum, zinc, magnesium, and traces of other elements [Al + (4-6) Zn + 2.5 Mg + trace] as shown by Nadai³² (Figure 1-16, p. 27). When the temperature 788°F (420°C) is reached, the zinc has melted, but the remaining aluminum and magnesium combination softens at a slower rate than the original combination of aluminum, magnesium, and zinc. This change in softening rate influence begins well below the melting point of zinc and influences the shape and the spacing of the stress-strain curves with temperature. Note that the Young's modulus, E , does not decrease to zero at the melting temperature for aluminum, but still has some small positive value.

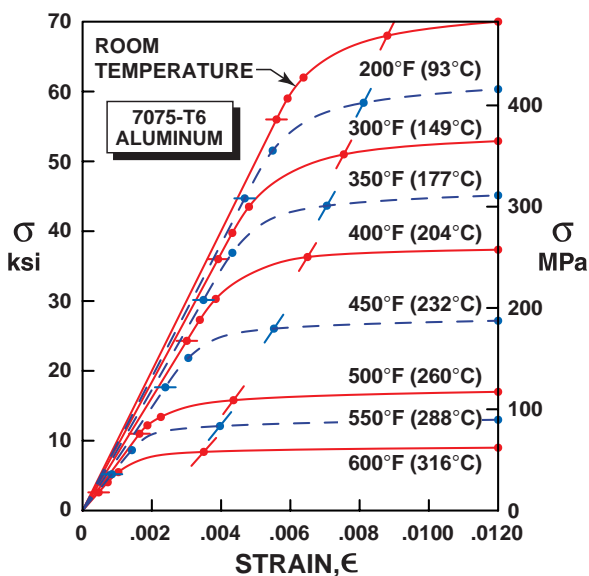


Figure 15 Modeled and Interpolated Families of Stress-Strain Curves for 7075-T6 Aluminum

It might seem logical to simply interpolate the parameters σ_y , E , K , J , n , and m to obtain the stress-strain curves at temperatures intermediate to those for the measured stress-strain curves. However, the values of K and J differ so much between adjacent measured curves (sometimes by several orders of magnitude) that the interpolated curves at temperatures intermediate to the available data do not appear to be reasonable members of the measured family of curves. Moreover, the values of K and J depend on n and m , respectively, so independent interpolation for all four values is self-contradictory. For example, a curve so obtained for 350°F (177°C) can be calculated, but is much lower than reasonable when viewed among the original curves at 70°F (20°C), 300°F (149°C), 400°F (204°C), 500°F (260°C), and 600°F (316°C). That is, the new curve does not look like part of a reasonable progression of behavior.

We cannot interpolate the yield point, (σ_y, ϵ_y) , between stress-strain curves at two temperatures using the three quantities, σ_y , E , and ϵ_y , because only two are independent. That interpolation is redundant (we can interpolate two and calculate the third, but we cannot interpolate three) and typically leads to an interpolated E that is too low. Thus, we interpolate σ_y and ϵ_y and accept the resulting E calculated from the interpolated σ_y and ϵ_y . Analogous to this situation, we sometimes have difficulty interpolating the pass-through points 2 and 3. In fact, interpolating (σ_2, ϵ_2) between 500°F (260°C) and 600°F (316°C) leads to a point with less strain than the elastic strain, not more as required for a concave-downward stress-strain curve. Accordingly, the numerical stress-strain equation procedure blows up. However, we interpolate ϵ_3 (σ_3 is calculated from interpolated values of σ_y and σ_{oy}), and σ_3 and ϵ_3 are assumed (hopefully) to constitute a representative viable point. Nevertheless, because an interpolated ϵ_2 is too low, we must realize that the interpolated ϵ_3 is probably also lower than a measurement would reveal. If the stress-strain curves are 'too far apart' and have somewhat different degrees of nonlinearity, even interpolation of ϵ_3 can fail.

The solution to this interpolation dilemma is to interpolate the stress-strain curve models for a combination of the pass-through points and n . Specifically, the values to be interpolated are E , $\sigma_1 (= \sigma_y)$, ϵ_3 , $\sigma_4 (= \sigma_{oy})$, σ_5 , and n . All other values are calculated from those values, namely $\sigma_3 = (\sigma_1 + \sigma_4)/2$, $\sigma_2 = (\sigma_1 + \sigma_3)/2$, K from Equation (53), m from Equation (56), J from Equation (54), and $\epsilon_5 = .0120$ for all curves. The value of ϵ_2 is not used because of the previously mentioned difficulty interpolating strains near σ_y . Linear interpolation of those data result in the dashed curves for 200°F (93°C), 350°F (177°C), 450°F (232°C), and 550°F (288°C) in Figure 10 that appear to be quite reasonable members of the family of curves obtained by Mathauser and Brooks⁶. That is, the two families of curves have a 'fairly nice' progression of shape with increasing temperature. Interpolation of the curves at other intermediate temperatures is presumed to be similarly reasonable and hopefully accurate (hence representative).

4.6 Nadai-Jones Model for 7075-T6 Aluminum

The material properties vary with temperature and obviously the temperature at which buckling occurs is sought, so some form of table look-up of material properties must be included in the numerical search procedure. That is, the numerical analysis must have the material properties as a function of temperature in a useable form so that calculations can be made. In accordance with the foregoing comments, the following properties must be available as a function of temperature: E , $\sigma_1 (= \sigma_y)$, $\sigma_4 (= \sigma_{oy})$, σ_5 , and $\Delta L/L_0$ plus ϵ_2 , ϵ_3 , and ϵ_5 (σ_3 is always midway between σ_y and σ_4 , σ_2 is always midway between σ_y and σ_3 , and $\epsilon_4 = .002 + \sigma_4/E$). Alternatively, n can be used in place of ϵ_2 with better results because interpolation of ϵ_2 sometimes does not work.

The mechanical properties in Table I are obtained by modeling the stress-strain curves measured by Mathauser and Brooks⁶ with the Nadai-Jones stress-strain curve in the manner just described. The stress-strain data are scaled from enlargements of their curves and subsequently 'adjusted' to meet the two criteria for 'goodness of fit'. The free thermal strain expression versus temperature from the TPRC Data Series²⁹ in Equation (42) can be back-interpolated to find the temperature quite accurately. The quantities K , J , n , and m are included in Table 1 because they are part of the precise model for each temperature at which data are available, although they could be calculated from the other values in the table. Note that m and n , although dimensionless, are different in the two sets of units. Also, the results in SI units have an additional significant figure (to ensure accuracy in units conversion) because of the sensitivity of the Nadai-Jones equation to input values.

As temperature increases, Heimerl and Roberts³³ believed that Poisson's ratio also increases although they had no data and no way to measure the change. They claimed that "a consistent lack of correlation was found at elevated temperatures in the elastic range when μ [ν] was taken as .33, the room-temperature value for 75S-T6 aluminum alloy. When μ [ν] was arbitrarily increased with temperature, however, a satisfactory correlation was obtained in the elastic range." No change in Poisson's ratio with temperature was attempted in the present study.

5. Numerical Results and Observations

First, elastic and plastic buckling stresses for plates mechanically loaded at room temperature are predicted in order to enable comparison of the present plastic buckling prediction procedures with available experimental data. Next, elastic and plastic thermal buckling of uniformly heated pinned-end and fixed-end bars with temperature-dependent material properties is reviewed to set the stage for the plates problem. Then, the more difficult problems of elastic and plastic thermal buckling of uniformly heated simply supported rectangular plates with temperature-dependent material properties are addressed. For bars, the only geometric parameter necessary is the bar slenderness ratio, L/r . For plates, the essential geometric parameters are the plate aspect ratio, a/b , and the plate width-to-thickness ratio, b/t .

5.1 Buckling of Plates under Mechanical Loading at Room Temperature

To establish confidence in the plastic buckling of plates portion of the present plastic thermal buckling analysis, we examine predicted and measured stresses for uniaxial mechanical loading. Definitive plastic versus elastic buckling experiments are quite difficult to perform with plates. Actually creating the simply supported edge boundary conditions on all four edges of a plate to which the present theory applies is quite difficult, if not nearly impossible, to precisely accomplish under conditions of in-plane loading. For a plate with flat edges under axial compression between the platens of a loading frame, the real boundary conditions are somewhere between simply supported and fixed (clamped) because the flat edges cannot rotate freely against the platens. The principal problem is loading the plate and simultaneously permitting both the loaded edges and the non-loaded edges to freely rotate. Certainly, in any practical loading condition, the theoretical approximations to the actual boundary conditions can be quite crude.

Pride and Heimerl³⁴ measured buckling stresses for uniaxially loaded simply supported rectangular plates of 14S-T6 aluminum (now known as 2014-T6) at room temperature. Simply supporting all four edges and also applying load up to the buckling load is a very difficult experimental problem, as just discussed. Pride and Heimerl largely avoided that difficulty by employing the technique suggested by Timoshenko²⁵ (Figure 9-3, p. 356). Timoshenko observed that it is possible to reduce the influence of boundary conditions along the two non-loaded lateral edges of a plate by axially loading thin-walled square-cross-section tubes and interpreting each side or wall of the tube as a simply supported plate as in Figure 16. There, each adjacent side or wall of the tube rotates at the adjoining edges such that no restraining moment occurs. Hence, the four sides or walls of the tube are effectively four simply supported plates *if the loaded edges of the tube are simply supported*.

Use of thin-walled square-cross-section tubes is not the perfect solution to the simply supported edge boundary condition problem because the loaded edges at each end of the tube are certainly not simply supported. Instead, each tube end was machined flat so that it mounted evenly against each platen of a load frame. Thus, the edges at each end are somewhere between fixed and simply supported. However, the longer the tube, the lower the influence the end conditions have on the buckling load. If the tube is too short, each tube wall (plate) is affected by end effects as if it were partially clamped on at least one end edge, so the buckling stress exceeds that of a simply supported plate. In addition, the tube must be short enough that local buckling of the tube walls as plates as in Figure 16 occurs before buckling of the long tube as a column or bar. Pride and Heimerl determined that the tube length must be at least four times the tube width,

i.e., $a/b > 4$, before a minimum buckling load is achieved in order to avoid the influence of end effects. In contrast, the theoretical results for a simply supported elastic plate have equal minima of the buckling stresses at all integer values of a/b , including low values of $a/b = 1, 2, 3, \dots$, as shown in Figure 5.

Pride and Heimerl varied the plate aspect ratio, a/b , and the plate width-to-thickness ratio, b/t , by using different lengths and cross sections of commercially available drawn tubes. They observed that the material properties changed somewhat from specimen to specimen as did the thicknesses as well as other dimensions. They presented their results in the form of various stress-strain curves as in Figure 17 by plotting the plastic buckling stress at the elastic buckling strain because the latter is easily calculated. That is, *they implicitly assumed that the strain at plastic buckling was equal to the strain at elastic buckling*. Various deformation theories of plastic buckling lead to curves similar to, but somewhat above, the short-dashed curve in Figure 17. The incremental or flow theory results of Handleman and Prager³⁵ are the medium-dashed curve in Figure 17 and are obviously outrageously higher than measured plastic buckling results. Thus, buckling predictions with flow theory are very unconservative.

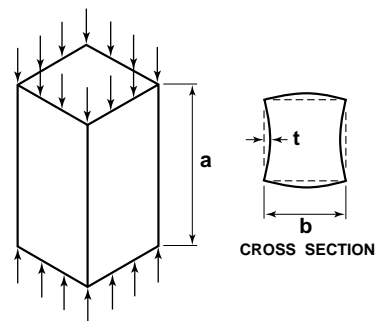


**Figure 16 Timoshenko's
Tube-as-Four-Plates Experiment**

The problem with the manner of presentation in Figure 17 is that Pride and Heimerl's implicit assumption that $\bar{\epsilon}_P = \bar{\epsilon}_E$ is simply wrong! In fact, $\bar{\epsilon}_P \neq \bar{\epsilon}_E$ and, more importantly, $\bar{\epsilon}_E > \bar{\epsilon}_P$. That is, complete plastic buckling analysis (calculation of both the buckling stress and strain including all stresses and strains prior to buckling) leads to a lower plastic buckling stress and lower plastic buckling strain than the respective elastic results. Thus, the artificial points $(\bar{\sigma}_P, \bar{\epsilon}_E)$ automatically fall to the right of the stress-strain curve as seen in Figure 17. There is no basis to guarantee that alignment of a theory prediction of $(\bar{\sigma}_P, \bar{\epsilon}_E)$ with the data means the theory is correct, i.e., no guarantee that the point $(\bar{\sigma}_P, \bar{\epsilon}_E)$ means anything at all. Accordingly, the stress-strain curve is not a rational or valid basis for comparison of measured and predicted plastic buckling results. In fact, the stress-strain curve manner of presentation is erroneous and misleading. All behavior of a uniaxially loaded member must result in measured and predicted behavior with points that are precisely on the stress-strain curve. After all, every uniaxial loading experiment before buckling is simply another way to determine the uniaxial stress-strain curve! Pride and Heimerl did not measure the plastic buckling strain in their experiments. Had they done so, they probably would have realized the fallacy in their use of the stress-strain curve in Figure 17 as the basis for comparison of theoretical and experimental results. The two measured buckling results plotted above the stress-strain curve just above $\epsilon = .004$ in Figure 17 further highlight the inadequacy of this manner of comparing predicted and measured plastic buckling results. However, those two results are for small a/b for which the tube approach is not suitable because of end effects. The important geometric parameters a/b and b/t are ignored, and the variables σ_P and ϵ_E that are emphasized are, in fact, violated by the manner of presentation in Figure 17.

We now make a valid comparison of predicted and measured buckling stresses on the basis of the important plate geometric parameters width-to-thickness ratio, b/t , and aspect ratio, a/b . Pride and Heimerl's results³⁴ for $a/b = 4.5$ (long enough that end effects are small) and various b/t are shown as circles in Figure 18. There, two experimental results are shown for each of four b/t ratios. The two measured elastic buckling results are in excellent agreement with the predicted elastic buckling curve (with the usual hyperbolic shape) obtained with use of the Nadai stress-strain curve model²² [the behavior of 14S-T6 (2014-T6) aluminum at room temperature is not nonlinear enough to warrant use of the Nadai-Jones model¹⁹]. Also, the six measured plastic buckling results agree very well with the predicted plastic buckling curve. If the somewhat lower material properties of the two specimens at $b/t = 22.5$ were adjusted as if they were made of the same material as for the other data points (as is suggested by Pride and Heimerl), those two points would raise by about 1 ksi making the agreement between the measured and predicted buckling stresses excellent. Pride and Heimerl reported other buckling results that were primarily elastic, but all were at a/b values other than 4.5, so they are not comparable to results for $a/b = 4.5$ in Figure 18. Other plastic buckling stresses measured earlier by Kollbrunner³⁶ and later by Teodosiadis, Lang-

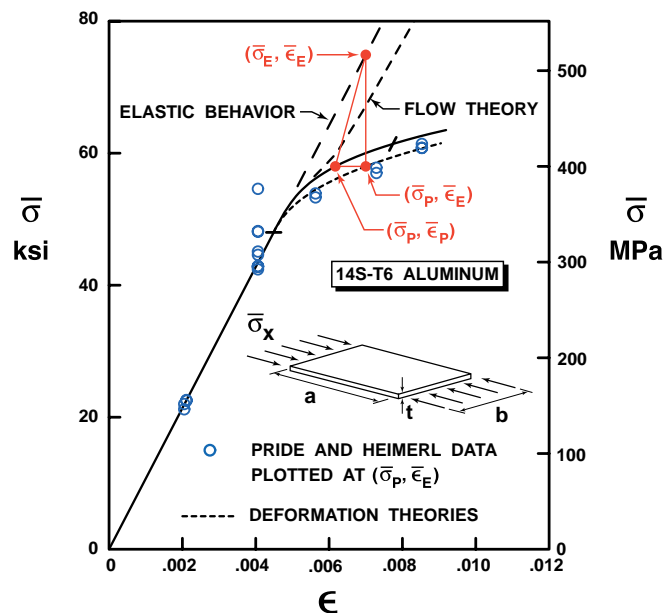


Figure 17 Stress-Strain Curve Presentation of Plastic Buckling Results

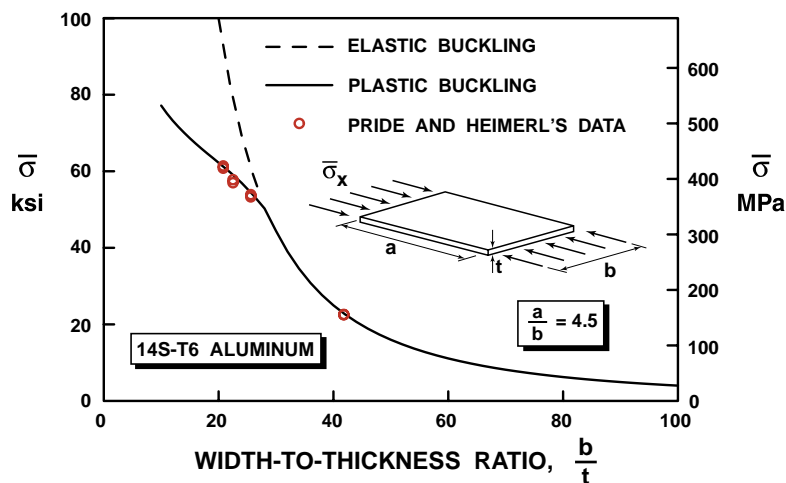


Figure 18 Buckling of Uniaxially Loaded Simply Supported Plates

haar, and Smith³⁷ were not compared with the present theory. The agreement between measured and predicted results in Figure 18 gives us confidence that the present plastic buckling analysis is essentially correct, so we can proceed to the plastic thermal buckling problem.

Plastic buckling stresses for mechanical loading generally can also be plotted as a function of the plate aspect ratio, a/b , as for the elastic results in Figure 5, so we can learn even more about the transition from elastic buckling to plastic buckling. Pride and Heimerl's results could not be effectively plotted against a/b because the tube a/b had to be four or greater to avoid the influence of end effects. Moreover, each plot of $\bar{\sigma}$ versus a/b must be for a specific plate-width-to-thickness ratio, b/t . Only one group of their measured results could be plotted, namely at $a/b = 4.5$ with variable b/t after their use of the stress-strain curve as a basis for comparing theoretical and experimental results is rejected. Of course, if the data agree well with the theory for constant a/b and variable b/t as in Figure 18, then we would certainly expect them to also agree for constant b/t and variable a/b (except any tube data for $a/b < 4$).

Other plastic buckling predictions under mechanical loading are obtained from implementation of the present buckling criterion embedded in the solution strategy of Section 3 for a specified range of buckle mode values. For a 7075-T6 aluminum plate of thickness $t = .40$ in (1.02 cm), width $b = 10$ in (25.4 cm) ($b/t = 25$), and variable length, the elastic and plastic buckling stresses are shown in Figure 19 as the usual festooned curves with various buckling mode shapes that change at cusps. The yield stress is 55 ksi (379 MPa). The plate always buckles into one lateral half-sine wave, i.e., $n = 1$, with a variable number of axial half-sine waves, m . Below $a/b = .8$, very large reductions from elastic to plastic buckling stress are observed. On Figure 19, dots are located at cusps at low values of a/b , and arrows go from the cusps for the elastic results to the cusps for the plastic results. Note in Figure 19 that buckle mode shape changes (the cusps) occur at lower values of a/b for plastic buckling than for elastic buckling. The cusps in the plastic buckling results migrate from coincidence with the cusps in the elastic buckling results for thin plates toward lower values of a/b than for the elastic buckling results as the plate thickness increases. Thus, the plate that buckles plastically behaves as if it were longer than the elastic plate. This shift in minimum $\bar{\sigma}_x$ is a characteristic of plastic buckling and will also be observed later in plastic thermal buckling. For a slightly thinner plate of thickness $t = .37$ in (.94 cm) and width 10 in (25.4 cm) ($b/t = 27$) in the intermediate range of a/b from .8 to 1.5, sometimes the buckling is elastic and sometimes plastic. For an even thinner plate ($b/t > 27$), all buckling is elastic except at very low plate aspect ratios. Only in the vicinity of $t = .37$ in (.94 cm) is a transition from elastic to plastic buckling observed with varying plate aspect ratio, a/b .

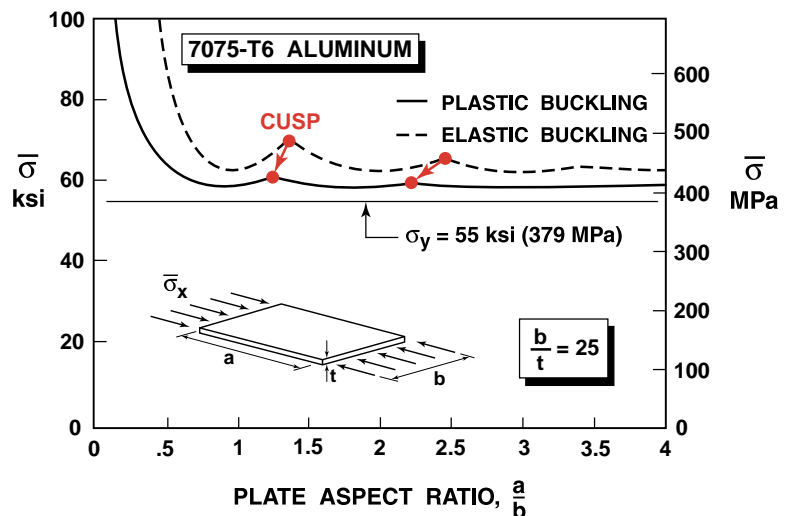


Figure 19 Plastic Buckling of a Simply Supported Plate

5.2 Thermal Buckling of Pinned-End and Fixed-End Bars with Temperature-Dependent Material Properties

Thermal buckling results by Jones¹⁹ for simply supported bars with temperature-dependent material properties are shown as a function of the bar slenderness ratio, L/r , in Figure 20. The results are plotted as the buckling temperature, \bar{T} , instead of the eigenvalue, i.e., the *change in temperature at buckling*, $\Delta\bar{T}$, from room temperature. Plotting \bar{T} instead of $\Delta\bar{T}$ enables a direct correlation between behavior and the corresponding material properties that strongly affect the behavior. Thus, we do not always have to add 70°F (20°C) to ΔT to know the temperature and hence the corresponding material properties that play such a big role in the thermal buckling problem. We can therefore readily perceive when the \bar{T} behavior curve passes from the influence of a stress-strain curve at one temperature to the influence at another temperature. Zones of temperature influence (horizontal bands) could be drawn on Figure 20 for each of the stress-strain curves in Figure 10, but would have to be drawn for either °F or °C values (not both!). We naturally refer to \bar{T} as a buckling temperature because the calculated $\Delta\bar{T}$ is always measured relative to the stress-free state at room temperature in the present results. With proper attention to (nonlinear)

deformation conditions such as Equation (1), ΔT can be measured relative to any other desired temperature.

If all properties are presumed to be elastic and are measured only at room temperature [actually, the coefficient of thermal expansion, α , alone leads to the elastic ΔT], the highest (long-dashed) curve in Figure 20, *Room-Temperature Properties*, results. The bar with room-temperature properties yields at about $\bar{T} = 500^\circ\text{F}$ (260°C) (from $\sigma_y = -E\alpha\Delta T$), obviously far above any temperature at which room-temperature properties could be even approximately applicable. Thus, the variation in material properties with temperature must be taken into account. If only free thermal strain properties are considered, i.e., if

$\Delta L/L_0$ is a function of temperature, then the second highest (short-dashed) curve, *Linear Properties (T)*, results which is always lower than the *Room-Temperature Properties* curve. The free thermal strain to cause buckling is the same for both curves, but corresponds to different temperatures in Figure 8. For example, if $L/r = 38.45$, the *Room-Temperature Properties* curve is precisely at 600°F (316°C) in Figure 20, and the horizontal distance in Figure 8 at the same free thermal strain is 77°F (43°C) leading to T of 523°F (273°C), the value of the *Linear Properties (T)* curve at $L/r = 38.45$ in Figure 20, a difference of 13%. Smaller percentage differences between the *Room-Temperature Properties* curve and the *Linear Properties (T)* curve occur as L/r increases in Figure 20. If the inherent nonlinearity of the stress-strain behavior is considered in addition to temperature dependence of all material properties, the lowest (solid) curve, *Nonlinear Properties (T)*, is obtained. The reduction in predicted plastic thermal buckling temperature, *Nonlinear Properties (T)*, from both the *Room-Temperature Properties* curve and the *Linear Properties (T)* curve is quite large. The *Room-Temperature Properties* curve is too high by 50% at $L/r = 40$ and by 137% at $L/r = 30$. The *Linear Properties (T)* curve is too high by 33% at $L/r = 40$ and by 98% at $L/r = 30$. Both curves for elastic properties are even more inaccurate below $L/r = 30$, although those results need not be shown because they exceed the validity limit of the applicable material property data.

Similar thermal buckling results were obtained for fixed-end bars, i.e., bars with both rotational and axial restraint at their ends. These results are easily obtained by merely substituting the known fixed-end bar buckling load solution, $\bar{P} = 4\pi^2 EI/L^2$, in place of $\bar{P} = \pi^2 EI/L^2$ in the appropriate places in the analysis and proceeding to solve for ΔT (or \bar{T}). As would be expected, the predicted plastic \bar{T} are higher for fixed-end bars than for pinned-end bars in Figure 20. However, the magnitude of the increased \bar{T} in the nonlinear range of behavior is much less than might have been expected. The fixed-end condition forces higher stresses to exist before buckling than occur with pinned-end bars, so a higher \bar{T} results. All elastic results for room-temperature properties have fixed-end buckling temperature changes four times those for pinned-end bars, as they must be because of the factor of four difference in the two equations governing buckling. However, at stresses above σ_y , the increase in \bar{T} or ΔT because of the end-fixity condition is far less than a factor of four because the implicit higher stress level in fixed-end bars leads to extensive yielding that reduces the difference between the *Nonlinear Properties (T)* curves for pinned-end and fixed-end bars in Figure 20. The difference varies from a factor of four at $L/r = 105$ (elastic buckling) and above to about 15% at $L/r = 50$ and below (bars with both support conditions have yielded). Moreover, the transition from elastic to plastic buckling as L/r decreases takes place at higher L/r for fixed-end bars than for pinned-end bars (105 versus 50, respectively). Note that the plastic thermal buckling results, including the temperatures and stresses, are identical, for example, for (1) fixed-end bars with $L/r = 60$ and (2) pinned-end bars with $L/r = 30$ because the factor of four in the fixed-end results combined with 60^{-2} precisely equals 30^{-2} in the pinned-end results.

No measured thermal buckling loads for bars appear to be available. However, confidence in the pinned-end bar results (and by implication the fixed-end bar results) was increased by verifying that the predicted mechanical buckling loads at various constant elevated temperatures were in very good agreement with the mechanical buckling portion of the analysis with the corresponding material properties¹⁹.

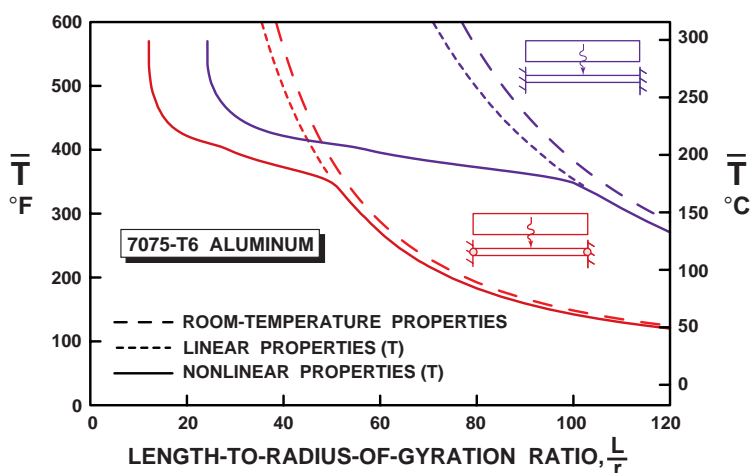


Figure 20 Plastic Thermal Buckling of Pinned-End and Fixed-End 7075-T6 Aluminum Bars

5.3 Thermal Buckling of Simply Supported Plates with Temperature-Dependent Material Properties

The change in temperature needed to cause thermal buckling of a uniformly heated, unidirectionally restrained elastic plate with room-temperature material properties is, from Equation (15), the minimum of

$$\overline{\Delta T} = \frac{\pi^2}{12} \frac{1}{\alpha} \frac{1}{(1 - \nu^2)} \frac{1}{(b/t)^2} \left[m \frac{b}{a} + \frac{1}{m} \frac{a}{b} \right]^2 \quad (58)$$

for an integer number of buckling half-sine waves, m . This expression depends simultaneously on two geometric parameters, the plate width-to-thickness ratio, b/t , and the plate aspect ratio, a/b . Conceptually, we could create a three-dimensional plot with vertical axis, $z = \overline{\Delta T}$ and with two horizontal axes, $x = a/b$ and $y = b/t$ to elegantly and compactly display all the buckling results. However, those comprehensive results would be difficult to present and even harder to interpret. Thus, we settle for a few simple slices through the three-dimensional plot parallel to each of the two horizontal axes in the following manner:

- (1) If a/b is constant, then m is correspondingly fixed at some integer value [i.e., constrained to achieve a minimum of Equation (58)]. Accordingly, for a constant a/b , $\overline{\Delta T}$ depends on the inverse of $(b/t)^2$ which is a hyperbolic relationship just like the $\overline{\Delta T}$ of bars depends on the bar slenderness ratio, L/r , in Equation (6) and Figure 20. That is, $\overline{\Delta T}$ rapidly approaches zero as b/t increases. Thus, $\overline{\Delta T}$ for a plate is a strong function of b/t as in Figure 6.
- (2) If b/t is constant, then $\overline{\Delta T}$ depends on the term in brackets in Equation (58) which results in the scalloped behavior as a function of a/b in Figure 5 for integer values of m , a behavior with no bar analogy. Note that the term in brackets always approaches a non-zero minimum as a/b increases. The term in brackets is the plate effect of support on all four edges [as opposed to the bar effect of supports at two ends in (1)] that does not permit buckling simply as a/b increases except at the minimum of the term in brackets. Thus, $\overline{\Delta T}$ for a plate is a fairly weak function of a/b except for $a/b < 1$ as in Figure 5.

The product of the two functions, $1/(b/t)^2$ and the bracketed term involving a/b , as represented by Equation (58), must approach zero in a nearly hyperbolic manner as b/t increases, but approaches some minimum for a constant b/t as a/b increases. Two material properties, α and ν , affect Equation (58). The coefficient of thermal expansion, α , has a wide range of possible values for engineering materials, but appears in a simple form in Equation (58), namely the higher the α , the lower the $\overline{\Delta T}$. The Poisson's ratio, ν , plays a relatively modest role in Equation (58) because ν varies over a relatively narrow range of values for any isotropic material, i.e., most engineering materials have ν in a tight band around some fraction between 0 and .5. Note that no data are available from which to determine how ν varies with temperature. Thus, only the variation of ν with stress is treated, and that occurs only when nonlinear properties are addressed. If $\nu(T)$ data were available, then that variation with temperature would be relatively mild in comparison to other effects.

The equivalent of the change in temperature expression in Equation (58) for plates with stress-dependent material properties is Equation (30) and for plates with stress-dependent and temperature-dependent material properties is Equation (38). Both Equations (30) and (38) are far too complicated to attempt to break down the stress and temperature dependencies into as simple a situation as just presented for elastic, room-temperature behavior. Instead, we will observe those dependencies in the light of various numerical examples.

We now investigate the effect of the various stress-dependent and temperature-dependent material properties on the $\overline{\Delta T}$ in two manners: (1) dependence on a/b and (2) dependence on b/t . Three types of results for temperature-dependent material properties are presented: (1) \overline{T} versus a/b ; $\overline{\sigma}$ versus a/b , and \overline{T} versus b/t . In all cases, the results are plotted as the buckling temperature, \overline{T} , instead of the eigenvalue, i.e., the *change in temperature at buckling*, $\overline{\Delta T}$, from room temperature. Plotting \overline{T} instead of $\overline{\Delta T}$ enables a direct correlation between the response and the corresponding material properties that strongly affect the response. Thus, we do not always have to add 70°F (20°C) to $\overline{\Delta T}$ to know the temperature and hence the corresponding material properties that play such a big role in the thermal buckling problem. We can therefore readily perceive when the \overline{T} response curve passes from the influence of a stress-strain curve at one temperature to the influence at another temperature. We naturally refer to \overline{T} as a buckling temperature because the calculated $\overline{\Delta T}$ is always measured relative to the stress-free state at room temperature in the present results. With proper attention to the (nonlinear) deformation conditions such as Equation (1), $\overline{\Delta T}$ can be measured relative to any other desired temperature.

Three types of analysis approximations to material property dependence on stress and temperature are studied, i.e., \bar{T} is calculated for three different sets of material properties with various stress and temperature dependencies:

- (1) *Room-Temperature Properties*, i.e., $\bar{T}(\alpha, \nu)$ (all properties constant)
- (2) *Linear Properties (T)*, i.e., $\bar{T}[\frac{\Delta L}{L_0}(T), \nu]$ (free thermal strain is a function of temperature)
- (3) *Nonlinear Properties (T)*, i.e., $\bar{T}[\frac{\Delta L}{L_0}(T), E_{\text{sec}}(\sigma, T), E_{\text{tan}}(\sigma, T), \nu(\sigma)]$ (free thermal strain is a function of temperature plus mechanical properties are a function of temperature and stress)

5.3.1 \bar{T} versus a/b The buckling temperature, \bar{T} , is plotted against the plate aspect ratio, a/b, for plate width-to-thickness ratio b/t = 25 for the three material property dependencies, *Room-Temperature Properties*, *Linear Properties (T)*, and *Nonlinear Properties (T)*, in Figure 21. The three festooned buckling-mode-shape-dependent curves are roughly 'parallel' to one another in a generalized sense of the term parallel and each rapidly approaches a different minimum as a/b increases. Thus, \bar{T} is not a strong function of a/b. The essentially 'parallel' nature of the three material property approximations is caused by the fact that the term in brackets in Equation (58) or its highly modified equivalent in Equations (30) and (38) achieves a constant minimum as a/b increases. The value of \bar{T} for *Room-Temperature Properties* is about 110°F (60°C) above the \bar{T} for *Nonlinear Properties (T)*. Also, \bar{T} for *Room-Temperature Properties* is about 65°F (36°C) above \bar{T} for *Linear Properties (T)*. Those numbers are for the minima of each curve, e.g., at integer values of a/b for *Room-Temperature Properties* and *Linear Properties (T)*, and at somewhat lower values of a/b for *Nonlinear Properties (T)*. The lowest buckling temperature, \bar{T} , with elastic material properties always occurs at integer values of a/b, i.e., 1,2,3,..., as in Figure 5. In contrast, for plastic material properties, the values of a/b for the minimum buckling temperature shift to the left from the values for elastic buckling (as noted previously for the plastic versus elastic buckling under mechanical loading results in Figure 19). In addition, the plastic buckling curve 'flattens out' (approaches its minimum) at a much lower a/b than does the elastic buckling curve. That is, the plastic buckling results are effectively for a longer plate (higher a/b) than the elastic buckling results.

The \bar{T} values predicted with room-temperature properties are unrealistically high as would be expected. At the minima, the *Linear Properties (T)* curve is about 13% below the *Room-Temperature Properties* curve. That magnitude is about what we expect given that the only difference between the two curves is the actual variation of the free thermal strain, $\Delta L/L_0$, as a function of \bar{T} curve for the *Linear Properties (T)* curve as opposed to the constant α of the *Room-Temperature Properties* curve. That different approach lowers the temperature to achieve the same free thermal strain by about 13% at 600°F (316°C) with lesser decreases in the temperature range from room temperature to 600°F (316°C) than the 13% at 600°F (316°C). Of course, an even better approach is to use the material properties as a function of both temperature and stress as in the *Nonlinear Properties (T)* curve.

Thermal buckling for a plate as thick as b/t = 25 excites both material properties as a function of temperature and material properties as a function of stress level. Thinner plates (higher b/t than the present 25) exhibit less plastic behavior and less temperature effect than that shown in Figure 21 because the buckling temperatures are much closer to room temperature. Thicker plates (lower b/t than the present 25) buckle nearly at 600°F or above which is beyond the applicability of the present material property data, so the thermal buckling predictions cannot be relied upon. Of course, the minimum buckling temperatures are always the highest for *Room-Temperature Properties*, intermediate for *Linear Properties (T)*, and the lowest for *Nonlinear Properties (T)* irrespective of the plate thickness.

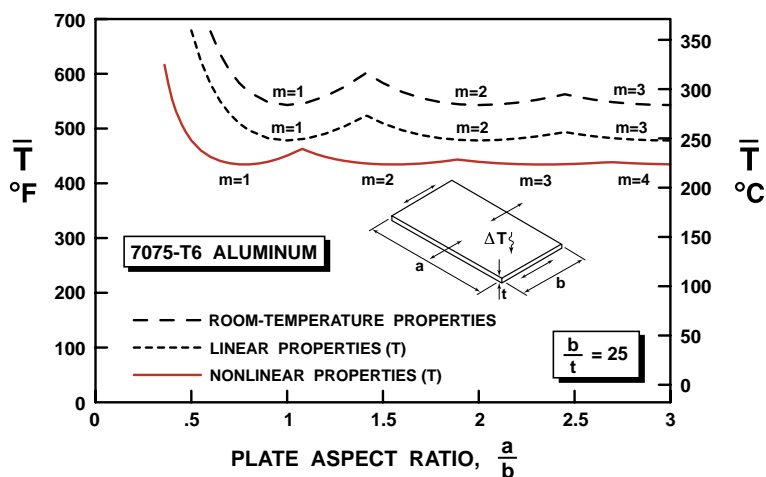


Figure 21 Thermal Buckling Temperature versus Aspect Ratio

5.3.2 $\bar{\sigma}$ versus a/b The stresses at thermal buckling corresponding to the \bar{T} values in Figure 21 are interesting to observe in Figure 22. There, the elastic buckling stress for *Room-Temperature Properties* increases very rapidly in the usual manner corresponding to the buckling temperature as the plate aspect ratio, a/b , decreases below one. In contrast, the predicted plastic buckling stress in the *Nonlinear Properties (T)* curve in Figure 22 actually decreases as a/b decreases below one because the stress-strain curves at high temperatures are lower than at room temperature in Figure 10. Similarly, the predicted elastic stresses for *Linear Properties (T)* also decrease as a/b decreases below one because the

modulus decreases with increasing temperature (however, the predicted elastic stresses are invalid because they exceed the yield stress at the respective temperatures by a large amount). Moreover, the *Nonlinear Properties (T)* curve is *upside down* relative to the *Room-Temperature Properties* curve, but the reason is quite simple. The higher the \bar{T} , the lower the material properties because the stress-strain curves decrease dramatically with increasing temperature in Figure 10 and hence the *lower* the corresponding buckling stress, $\bar{\sigma}$, which is highly affected by the high temperature and the corresponding low stress-strain curves. In contrast, for the *Room-Temperature Properties* curve, the properties are constant, so the higher the \bar{T} , the higher the corresponding buckling stress, $\bar{\sigma}$. The *Linear Properties (T)* curve has some of both attributes, although it is decreasing only at very high temperatures. The values of the plastic thermal buckling stresses are, of course, all above yielding, but below the maximum stresses in Figure 10, i.e., well within the range of applicability of the measured stress-strain curves. The differences between the three types of stresses in Figure 22 increase as b/t decreases from 25 to thicker plates (with corresponding increased room-temperature stresses) and decrease as b/t increases from 25 to thinner plates (with corresponding decreased room-temperature stresses). Quantitative comparison of the stresses is not useful because of yielding and temperature effects that render the stresses in the *Room-Temperature Properties* and *Nonlinear Properties (T)* approaches inherently inaccurate.

The two cusps in the *Nonlinear Properties (T)* curve below $a/b = .5$ in Figure 22 (one at $a/b = .36$ is difficult to see at this scale except as a small dash) are *not buckling mode shape changes like the other cusps*. Instead, those two cusps are caused by the fact that the material properties change very differently above the temperature at the cusp than below that temperature. This observation is solidified by examining the expanded crucial region of the buckling stress, $\bar{\sigma}$, versus a/b plot in Figure 23. There, the buckling temperatures at specific values of a/b are labeled. The two cusp-like deviations in the behavior, one at $a/b = .36$ and the other at $a/b = .46$, coincide precisely with $\bar{T} = 600^\circ\text{F}$ (316°C) and $\bar{T} = 500^\circ\text{F}$ (260°C), respectively. Thus, although the \bar{T} versus a/b behavior is smooth, the $\bar{\sigma}$ versus a/b behavior is not. The behavior below $\bar{T} = 500^\circ\text{F}$ (260°C) [above $\bar{\sigma} = 17$ ksi (110 MPa)] is quite smooth and progresses as might be expected (except for being 'upside down'). At the 'top' of the curve, i.e., at $a/b = .7$, $\bar{T} = 435^\circ\text{F}$ (224°C); at $a/b = .6$, $\bar{T} = 450^\circ\text{F}$ (232°C); and at $a/b = .5$, $\bar{T} = 478^\circ\text{F}$ (248°C). At $\bar{T} = 500^\circ\text{F}$ (260°C) [$\bar{\sigma} = 17$

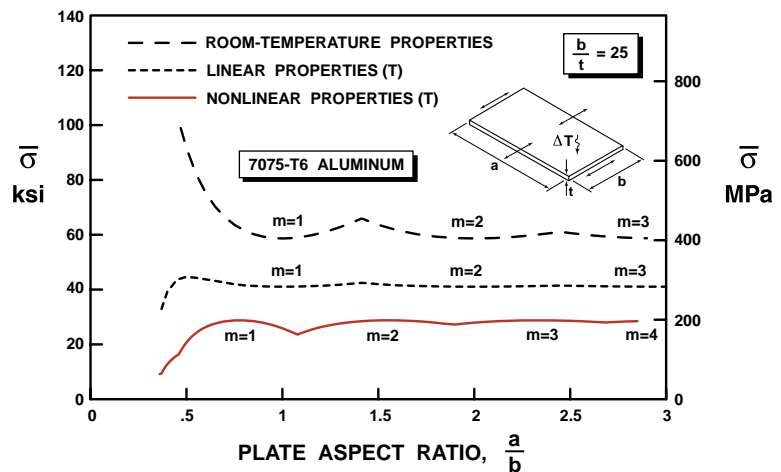


Figure 22 Plastic Thermal Buckling Stresses versus Aspect Ratio

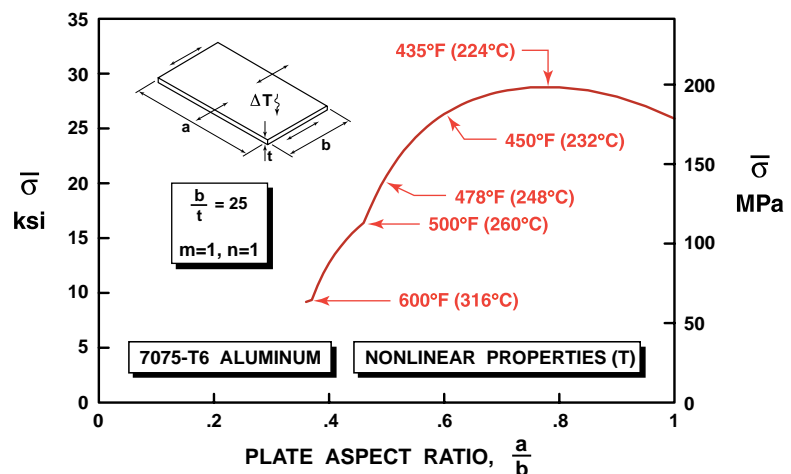


Figure 23 Expanded View of Plastic Thermal Buckling Stresses

Thus, although the \bar{T} versus a/b behavior is smooth, the $\bar{\sigma}$ versus a/b behavior is not. The behavior below $\bar{T} = 500^\circ\text{F}$ (260°C) [above $\bar{\sigma} = 17$ ksi (110 MPa)] is quite smooth and progresses as might be expected (except for being 'upside down'). At the 'top' of the curve, i.e., at $a/b = .7$, $\bar{T} = 435^\circ\text{F}$ (224°C); at $a/b = .6$, $\bar{T} = 450^\circ\text{F}$ (232°C); and at $a/b = .5$, $\bar{T} = 478^\circ\text{F}$ (248°C). At $\bar{T} = 500^\circ\text{F}$ (260°C) [$\bar{\sigma} = 17$

ksi (110 MPa)], the material property linear interpolation scheme changes from involving the stress-strain curves at 400°F (204°C) and 500°F (260°C) to involving the stress-strain curves at 500°F (260°C) and 600°F (316°C). Such a change naturally causes quite different behavior on each side of the point where $\bar{T} = 500^\circ\text{F}$ (260°C) [$\bar{\sigma} = 17$ ksi (110 MPa)], although, of course, the two behaviors match there (in value, but not in slope). If the measured stress-strain curves were more closely spaced than the present 100°F (55°C) difference between the Mathauser and Brooks stress-strain curves, this cusp-like behavior would be reduced, if not eliminated. Or, if the linear interpolation between two adjacent stress-strain curves were replaced with interpolation that involves three stress-strain curves in the neighborhood of the estimated temperature, then the cusps might be smoothed out. However, such an enhanced interpolation scheme might not be possible to implement because of the interpolation difficulties mentioned in Section 4.5. No similar temperature-related cusp exists in the *Linear Properties (T)* curve in Figure 22 because the pertinent free thermal strain expression, the TPRC equation in Equation (42), is continuous with continuous derivatives throughout the range presented.

5.3.3 \bar{T} versus b/t For a plate aspect ratio, a/b , that is low enough that significant plastic effects can occur, the plate width-to-thickness ratio, b/t , is varied over a wide range to obtain the thermal buckling curves for the three material property approximations in Figure 24. There, the elastic room-temperature response is hyperbolic as shown with the long-dashed curve (*Room-Temperature Properties*). The behavior of \bar{T} with b/t for linear (elastic) material properties that are a function of temperature, *Linear Properties (T)* is also hyperbolic, but with a modifying effect that the instantaneous α always rises as \bar{T} increases. At $b/t = 29.5$, the comparison between the three curves is particularly convenient because the *Room-Temperature Properties* curve is precisely at 600°F (316°C) which is the upper limit of the range of applicability of the Mathauser and Brooks stress-strain curve data⁶. Also at $b/t = 29.5$, the *Linear Properties (T)* curve is at 523°F (273°C) and the *Nonlinear Properties (T)* curve is at 406°F (208°C). Thus, the *Room-Temperature Properties* curve value at $b/t = 29.5$ is 13% above the *Nonlinear Properties (T)* curve because of the difference in temperature for the same free thermal strain between the $\alpha_{RT}\Delta T$ and $\Delta L/L_0$ curves in Figure 8 as previously noted. The \bar{T} for nonlinear properties that are a function of stress and temperature, *Nonlinear Properties (T)*, departs markedly from the \bar{T} for *Linear Properties (T)* starting below $b/t = 37$ as b/t decreases. That behavior is quite similar to, but much less dramatic than, the behavior of \bar{T} versus L/r for a bar in Figure 20 because of the moderating influence of the bracketed term involving a/b in Equation (58) that slows the approach of \bar{T} to zero. The *Nonlinear Properties (T)* curve is about 50°F below the *Room-Temperature Properties* curve at $a/b = 37$ and about 180°F below at $a/b = 30$. The *Nonlinear Properties (T)* curve departs from the *Linear Properties (T)* curve at $a/b = 37$ and, at $a/b = 30$, is about 100°F below the *Linear Properties (T)* curve. The \bar{T} for *Room-Temperature Properties* and the \bar{T} for *Linear Properties (T)* approach each other as b/t increases. However, they never actually meet (except for practical purposes at $\bar{T} = 70^\circ\text{F}$). The effects of nonlinear material behavior as a function of temperature shown for $a/b = .5$ in Figure 24 diminish somewhat as a/b increases as can be inferred by comparison with the variable a/b results in Figure 21. In contrast, the results in Figure 24 would be even farther apart if a/b were to decrease from the value .5.

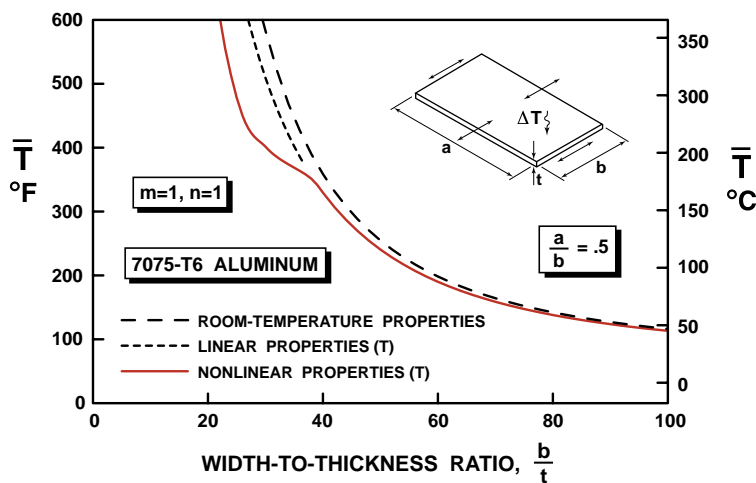


Figure 24 Buckling Temperature versus Width-to-Thickness Ratio

5.3.4 Summary There is less difference between the results for the *Nonlinear Properties (T)* approximation and the two elastic material property approximations for plates in Figures 21 and 24 than exists for bars in Figure 20. The reason for the smaller differences is related to the additional factor of the bracketed term in Equation (58) which depends on a/b and which exists for plates, but not for bars. The bracketed term is caused by the presence of four edges on a plate as contrasted with the two ends of a bars and is responsible for the considerable difference between the elastic and plastic behavior of the two

structural elements. As expected, \bar{T} is a fairly strong function of b/t in Figure 24 and a fairly weak function of a/b in Figure 21 except for $a/b < 1$.

The nature of results for different a/b or b/t than displayed is alluded to as much as possible in the preceding sub-sections in an effort to generalize the present few slices through the three-dimensional world of plastic thermal buckling of plates. As part of that effort, the character of the plate plastic thermal buckling results from Equation (30) are investigated in a somewhat crude fashion. The expressions for the plasticity coefficients K_{ij} and H in Equations (21) and (22) are such complicated functions of ν that they are difficult to understand. Moreover, ν is a function of stress level, i.e., position on the stress-strain curve. Thus, to cut through the maize of various complexities, two special cases of constant ν are examined: (1) $\nu = 1/2$ and (2) $\nu = 0$. In both cases, the complicated expressions simplify enormously (with certain approximations being necessary for the $\nu = 0$ case). Only a square plate is treated for further simplification and more focus on plasticity factors alone, but with no reduction in generality of the results. For $\nu = 1/2$, the ΔT expression in Equation (30) simplifies for a square plate to

$$\bar{\Delta T}_{\nu=1/2} = \frac{\pi^2}{36} \frac{1}{\alpha} \frac{1}{(b/t)^2} \left[\left[1 + 3 \frac{E_{\tan}}{E_{\sec}} \right] m^2 + 8 + 4 \frac{1}{m^2} \right] \quad (59)$$

for which the minimum $\bar{\Delta T}$ always occurs for $m = 1$. Thus,

$$\bar{\Delta T}_{\nu=1/2} = \frac{\pi^2}{36} \frac{1}{\alpha} \frac{1}{(b/t)^2} \left[13 + 3 \frac{E_{\tan}}{E_{\sec}} \right] \quad (60)$$

For $\nu = 0$, the $\bar{\Delta T}$ expression in Equation (30) simplifies for a square plate to *approximately* (in some terms, E_{\tan}/E_{\sec} has been neglected in comparison to five, but not in comparison to one)

$$\bar{\Delta T}_{\nu=0} = \frac{\pi^2}{60} \frac{1}{\alpha} \frac{1}{(b/t)^2} \left[\left[1 + 4 \frac{E_{\tan}}{E_{\sec}} \right] m^2 + 10 + \left[4 + \frac{E_{\tan}}{E_{\sec}} \right] \frac{1}{m^2} \right] \quad (61)$$

for which the minimum $\bar{\Delta T}$ always occurs for $m = 1$. Thus, in parallel to Equation (60),

$$\bar{\Delta T}_{\nu=0} = \frac{\pi^2}{36} \frac{1}{\alpha} \frac{1}{(b/t)^2} \left[9 + 3 \frac{E_{\tan}}{E_{\sec}} \right] \quad (62)$$

Therefore, E_{\tan}/E_{\sec} has more influence in the $\nu = 0$ expression than in the $\nu = 1/2$ expression. The plastic thermal buckling temperature change for a bar is shown by Jones¹⁹ to be

$$\bar{\Delta T} = \pi^2 \frac{1}{\alpha} \frac{E_{\tan}}{E_{\sec}} \frac{1}{(L/r)^2} \quad (63)$$

For a concave-downward stress-strain curve as in Figure 7, as the stress increases, both E_{\tan} and E_{\sec} decrease from the value E for elastic behavior. However, E_{\tan} decreases much more rapidly than E_{\sec} . Thus, E_{\tan}/E_{\sec} decreases from one and rapidly approaches zero as stress increases. This behavior is a measure of the sensitivity to plasticity effects to position on the stress-strain curve. As E_{\tan}/E_{\sec} decreases, a few simple numerical substitutions will readily reveal that the bar ΔT expression in Equation (63) decreases far more rapidly than the plate ΔT expressions in Equations (60) and (62). Furthermore, the bar ΔT rapidly goes to zero whereas the two approximate plate ΔT expressions for $\nu = 1/2$ in Equation (60) and for $\nu = 0$ in Equation (62) slowly approach different limiting minima as E_{\tan}/E_{\sec} goes from one to zero. Thus, for plates, $\bar{\Delta T}$ is a much weaker function of E_{\tan}/E_{\sec} than for bars because the effect of E_{\tan}/E_{\sec} is diminished by the term in brackets in Equation (60) going from 16 to 13 as E_{\tan}/E_{\sec} goes from one to zero and in Equation (62) going from 12 to 9. Thus, we have proved why the plastic thermal buckling results for plates in Figure 24 have so much smaller effect of plasticity than the bar results in Figure 20. The further dependence of plate thermal buckling on temperature-dependent material properties does not need to be investigated in any approximate manner because we know that, although all moduli decrease with increasing temperature, the behavior of the moduli ratio, E_{\tan}/E_{\sec} , has the same character, but with the complications of temperature dependence. Thus, no fundamental conclusions are changed if temperature is introduced in the approximate analysis.

6. Concluding Remarks

The concluding remarks are first a summary of what is accomplished in the present reported research, including the physical significance of the present results. Then, possible direct extensions of the present problem to other in-plane restraint and loading conditions (such as combined thermal and mechanical loading) are described. Finally, more complex problems involving other plate edge support boundary conditions and nonuniform heating situations are discussed relative to the difficulties encountered including the computational effort required in comparison to the present research. The latter two sub-sections are an attempt to put the present study into the perspective of the general plate thermal buckling problem.

6.1 The General Plate Thermal Buckling Problem

Geometrically perfect plates that are restrained from in-plane expansion when slowly heated symmetrically about the plate middle surface generally develop compressive stresses and then buckle at some specific amplitude of the temperature distribution in the plate. Some temperature distributions cause compressive stresses even when the plate is not restrained in its plane. However, the temperature at which buckling occurs can be high enough to render inapplicable the room-temperature material properties that are typically used to calculate the buckling temperature. Moreover, the stresses generated in the plate can exceed the yield stress of the material thus exciting nonlinear stress-strain behavior. Finally, the nonlinear stress-strain behavior of the material varies significantly with temperature, as does the free-thermal-expansion behavior. Thus, these temperature-dependent and stress-dependent material properties must be taken into account in the calculation of the plastic thermal buckling temperature of rectangular plates that develop compressive thermal stresses.

6.2 The Present Problem

Thermal buckling under slow, uniform heating of simply supported, geometrically perfect rectangular plates with temperature-dependent nonlinear stress-strain behavior is addressed in this paper. Creep buckling, i.e., buckling under constant load after some time during which the material properties decrease, is not treated. The plates are restrained from free thermal expansion in one direction in their plane as in Figure 1, so they develop stresses that can exceed the yield stress, and they attain temperatures that can be well above room temperature. Thus, the elevated-temperature nonlinear stress-strain behavior and free-thermal expansion behavior are considered. The specific manner of achieving prebuckling in-plane restraint is schematically shown in Figure 1 using Almroth's notation²³ for the four possible types of simply supported edges, i.e., edges with no rotational restraint and zero deflection, but with four types of in-plane support conditions. The equilibrium boundary conditions that all can be called simply supported edges are shown in Figure 2. Analogous buckling boundary conditions are obtained by putting the variational symbol, δ , in front of each prebuckling equilibrium boundary condition, e.g., $w = 0$ before buckling goes to $\delta w = 0$ during buckling. The plates are regarded as 'perfect', i.e., without any geometric or material imperfections. However, Shanley's 'no strain reversal' approach to plastic buckling¹¹ is used in which the inherent imperfections of a real structural element are recognized implicitly. The J_2 deformation theory of plasticity¹⁶ is employed along with a variable Poisson's ratio²⁰ after the material yields. The equivalent mechanical load concept³ is used to solve the plastic thermal buckling problem in a very straightforward manner. The highly nonlinear stress-strain behavior characteristic of aluminum alloys at high temperature is represented with the Nadai-Jones stress-strain curve model¹⁹ and interpolated at temperatures that are intermediate to the discrete temperatures at which Mathauser and Brooks⁶ measured stress-strain curves. Finally, the two-level transcendental buckling problem in temperature and stress level on the stress-strain curve is solved with an interval-halving technique. Examples of plastic thermal buckling of uniaxially in-plane restrained 7075-T6 aluminum plates are used to illustrate the theory.

Two ancillary efforts are undertaken: (1) thermal buckling of bars with temperature-dependent nonlinear stress-strain behavior is reviewed to set the stage for the plate thermal buckling problem and to provide a basis for comparison with plate response, and (2) plastic buckling stresses of plates under mechanical loading predicted with the present theory are shown to be in excellent agreement with buckling stresses measured by Pride and Heimerl³⁴. Thus, because of that favorable comparison with experimental results, we have at least one measure of confidence in the present approach, although not under actual *thermal* buckling conditions. Pride and Heimerl's use of the uniaxial stress-strain curve as the basis for comparison of theoretical and experimental results is demonstrated to be incorrect and misleading.

Thermal buckling temperatures of uniformly heated, simply supported 7075-T6 aluminum plates with temperature-dependent nonlinear material properties using the Nadai-Jones model and the two-level numerical search procedure are predicted as a function of the two plate geometric variables, the plate aspect ratio, a/b , and the plate width-to-thickness ratio, b/t . Three types of analysis approximations to material property dependence on stress and temperature are studied, i.e., $\bar{\Delta T}$, the change in temperature from room temperature at buckling, is calculated for three different sets of material properties with various stress and temperature dependencies:

- (1) *Room-Temperature Properties*, i.e., $\bar{\Delta T}(\alpha, \nu)$ (all properties constant)
- (2) *Linear Properties (T)*, i.e., $\bar{\Delta T}[\frac{\Delta L}{L_0}(T), \nu]$ (free thermal strain is a function of temperature)
- (3) *Nonlinear Properties (T)*, i.e., $\bar{\Delta T}[\frac{\Delta L}{L_0}(T), E_{\text{sec}}(\sigma, T), E_{\text{tan}}(\sigma, T), \nu(\sigma)]$ (free thermal strain is a function of temperature plus mechanical properties are a function of temperature and stress)

Actually, \bar{T} is calculated and is $\bar{\Delta T}$, the eigenvalue, plus room temperature to enable direct comparison with the temperatures at which the nonlinear stress-strain curves are measured. Three numerical results are obtained: \bar{T} versus a/b , $\bar{\sigma}$ versus a/b , and \bar{T} versus b/t .

The highest buckling temperatures and stresses are obtained with the *Room-Temperature Properties* approximation, intermediate values with the *Linear Properties (T)* approximation, and the lowest values with the *Nonlinear Properties (T)* approximation, as expected. The *Room-Temperature Properties* results differ from the *Linear Properties (T)* results by at most 13% in the range of temperatures from room temperature to 600°F (316°C) because only the difference between the free thermal strain as a function of temperature for the *Linear Properties (T)* approximation and the $\alpha_{RT}\Delta T$ for the *Room-Temperature Properties* approximation affects the two results. If the more important, inherently nonlinear stress-strain behavior is considered in addition to temperature dependence of all material properties, the lowest prediction for plate buckling temperatures and stresses is obtained. Because of the very good agreement between the predicted and measured plastic buckling stresses under mechanical loading, the *Nonlinear Properties (T)* results for thermal buckling are believed to be relatively accurate. However, the author is not aware of any relevant measured plate thermal buckling temperatures or stresses to verify that claim.

The *Room-Temperature Properties* and *Linear Properties (T)* curves for a thin plate with variable a/b and $b/t = 25$ in Figure 21 are 25% and 10% too high, respectively, relative to the *Nonlinear Properties (T)* results. For a very short plate of $a/b = .5$, at $b/t = 29.5$, the *Room-Temperature Properties* buckling temperature is 48% higher than the *Nonlinear Properties (T)* result, and the *Linear Properties (T)* buckling temperature is 29% higher than the *Nonlinear Properties (T)* result. Those percentage differences are larger for thicker plates and smaller for thinner plates. Also, those percentage differences are larger for shorter plates and smaller for longer plates with the caveat that the percentage differences approach a constant difference for long plates.

There is less difference between the results for the *Nonlinear Properties (T)* approximation and the two elastic material property approximations for plates with variable a/b in Figure 21 and with variable b/t in Figure 24 than exists for bars with variable L/r (the only bar geometric variable) in Figure 20. The reason for the smaller differences is related to the additional factor of the bracketed term for the elastic results in Equation (58) which depends on a/b and which exists for plates, but not for bars. That term results from the fact that plates are (simply) supported on all four edges, including those in the restraint direction, as opposed to bars being supported only at their two (pinned) ends (and not along their axial sides). Two very approximate expressions are developed for $\nu = 0$ and $\nu = 1/2$, respectively, to represent the crude effects of plasticity for plates as contrasted with bars. From those approximate expressions, we easily see that plates have much lower plasticity effects on buckling loads than bars because of less demonstrated effect of the plastic moduli ratio, $E_{\text{tan}}/E_{\text{sec}}$. In general, from the present numerical results, \bar{T} is a fairly strong function of b/t and a fairly weak function of a/b except for $a/b < 1$, as expected. Moreover, plates are clearly much less sensitive to plasticity effects than are bars. The present procedure can be readily applied to plates with other boundary (edge) conditions if the buckling stress solution for those boundary conditions is known.

No measured thermal buckling temperatures for uniformly heated simply supported rectangular plates appear to be available. However, confidence in the present results was increased by verifying that the plastic buckling stresses for mechanical loading at room temperature predicted with the plastic buckling portion of the plastic thermal buckling analysis with the appropriate material properties are in very good agreement with measured stresses. Many difficulties are identified with creating actual simply supported

edge boundary conditions on all plate edges. Loading an edge and simultaneously requiring and enabling it to freely rotate is the biggest challenge. Moreover, application of uniform heating throughout the plate volume is also quite difficult to implement. Note especially that the edge supports must not be a heat sink to locally disturb the plate temperature distribution, but that objective is also very difficult to achieve.

One case of measured buckling behavior of uniformly heated plates with other than simply supported edges is known. Murphy and Ferreira³⁸ analyzed and almost uniformly heated very thin elastic rectangular plates with clamped edges (which they defined as zero edge rotation and zero in-plane movement, i.e., C1 boundary conditions in Almroth's notation²³). The difference between the actual heating and uniform heating occurs near the plate edges where the boundary insulation interferes with the plate fixity condition and was therefore removed to ensure the proper support boundary condition at the expense of developing nonuniform heating because the heating boundary condition is violated. The presence of initial geometric imperfections in the thin plates leads to a nonlinear relation of temperature versus deflection perpendicular to the plate surface (w in Figure 1). That is, bending, bowing, or curling takes place from the very onset of temperature application. In contrast, without initial geometric imperfections, the deflection perpendicular to the plate surface is zero until bifurcation buckling at a specific load followed by nonlinear behavior. The behavior prior to bifurcation buckling is nonlinear in the present analysis because of the nonlinear material properties. In Murphy and Ferreira's problem, bifurcation buckling does not occur because of imperfections, but buckling (mode-shape change at a specific temperature) does occur at temperatures above the buckling temperature that corresponds to a geometrically perfect plate. The clamped-edge plate does not, of course, have a closed-form solution for the buckling load or buckling temperature, so it would be computationally expensive to implement their plate in the present plastic thermal buckling analysis procedure. Moreover, their plates were so thin ($b/t = 100$ to 200) that they buckled at very low temperature changes of only about 30°F (15°C). Thus, they were concerned with only temperature-independent linear elastic room-temperature material properties. Accordingly, their study is not amenable to simple analysis or to inclusion in the present study of temperature-dependent nonlinear material properties. Moreover, their experimental results are not comparable to the present analysis predictions in any range of behavior because of both initial geometric imperfections and the large differences in boundary conditions.

6.3 Practical Significance of the Present Results

The calculated plate buckling load or buckling temperature must be put into the perspective of general plate behavior to determine its practical significance. The buckling load for a linear elastic plate is typically the end of one straight segment of the load-deformation curve and the beginning of another straight segment with a significantly lower stiffness as described by Jones³. Thus, buckling of a plate does not constitute the end of its useful load-carrying capability as is buckling of a bar. More load (in this case, temperature) can be applied to a plate and readily carried if the resulting additional deformation is acceptable in the design application. Such concepts of operating a structure in the post-buckling regime are not uncommon, e.g., some high-performance military aircraft have such operating characteristics. However, structural elements in a commercial jetliner would probably not be designed to operate in the post-buckling regime. Nonlinear stress-strain behavior (as opposed to linear elastic behavior) leads to curved load-deformation plot segments, still with a lesser initial slope of the second segment than the final slope of the first segment. Other segments develop as higher buckling modes are encountered. With initial geometric imperfections, the present results are an upper bound on the buckling behavior in the following sense. An imperfect plate would continuously deform out of plane as it is heated (instead of suddenly at the buckling temperature as in the present problem), and the magnitude of that deformation at a specific temperature is larger for larger initial imperfections. Thus, the behavior of the imperfect plate always lies below and to the right of the present behavior on a load-deformation plot.

6.4 Possible Direct Extensions of the Present Problem

The present approach could readily be extended to plastic thermal buckling of biaxially in-plane restrained plates with temperature-dependent nonlinear stress-strain behavior. Then, the plasticity coefficients for the bending stiffnesses during buckling in Equation (21) would need to be modified because of the biaxial state of stress as opposed to the present uniaxial state of stress. Several efforts have been made toward parts of that goal, except with temperature-independent material properties. Wang, Xiang, and Chakrabarty³⁹ studied buckling under mechanical loading of thick plates with temperature-independent material properties by use of Mindlin's approach and found that flow theory results are even higher than deformation theory results for thick plates than the usual discrepancy that occurs for thin plates.

They comprehensively addressed rectangular plates with uniaxial and equal biaxial loading and boundary conditions with two opposite edges simply supported and the other two various combinations of free, clamped, and simply supported with various types of Ramburg-Osgood material model parameters²¹. They similarly addressed simply supported and clamped circular plates with uniform in-plane load.

The present approach could also be extended to uniaxial restraint of a plate under thermal loading plus mechanical loading perpendicular to the uniaxial restraint. In such a situation except with only temperature-independent elastic material properties, Jones⁴⁰ showed that transverse tension (transverse to the uniaxial restraint) can raise the thermal buckling load (temperature) just as transverse compression decreases the thermal buckling load. Similarly, cooling raises the mechanical buckling load perpendicular to the uniaxial restraint, and heating, of course, lowers that mechanical buckling load. Durban and Zuckerman⁴¹ showed for temperature-independent material properties that biaxial mechanical loading in which tension in one direction normally increases the buckling load in the compression direction has a diminished effect with plastic deformation, irrespective of whether flow theory or deformation theory is used. Analogously, the effect of tension in one direction would be expected to have a diminished effect on the buckling temperature of a plate with restraint in the perpendicular direction.

6.5 Other Plate Edge Support Boundary Conditions

Thermal buckling loads for uniformly heated plates with boundary conditions other than simply supported edges are much more complicated to determine than in the case of the present focus on uniformly heated simply supported plates. That is, plates with boundary conditions other than simply supported edges generally do not have exact solutions for the buckling load (with a few exceptions) as does the present problem. One of the exceptions is the class of elastic plates with two opposite edges that are loaded and simply supported with the other two edges unloaded and either clamped, simply supported, or free²⁵. Such combinations as clamped and free on the other two edges are possible and are representative of the flanges of beams. The separation of variables approach to the differential equations results in transcendental equations that are trivially easy to solve with current techniques. For plates with support boundary conditions that do not have an exact solution, approximate solution techniques, such as Rayleigh-Ritz or finite elements, must be employed at each step of a very large number of steps in the two-level transcendental search procedure to find the corresponding buckling load. Accordingly, computational demands are very significantly higher than with the present simple closed-form buckling solution.

6.6 Nonuniform Heating

Thermal buckling loads (temperatures) for nonuniformly heated plates have several complicating factors over those of uniformly heated plates. Uniform heating of a plate results in uniform material properties and stresses throughout the plate, so the differential equation governing thermal buckling has constant coefficients, and is readily solved in an exact manner for plates with simply supported edges as demonstrated in this paper. In contrast, with nonuniform heating, the material properties and stresses change over the surface of the plate and perhaps as well through the thickness of the plate. Such inhomogeneity of material properties results in a differential equation governing the buckling load that has nonconstant coefficients and is not easily solved even if the plate edges are simply supported. Accordingly, the solution must be approached numerically with finite element techniques being the probable preferred method of solution. However, the computational expense of repetitively determining the buckling load at each step of a very large number of steps in the two-level search procedure is quite significant, yet perhaps no higher than if the edges were not simply supported. That is, if the plate has both non-simply-supported edges plus nonuniform heating, then the problem is no more complicated from a computational expense standpoint than either case separately because both involve idealization of the entire plate with finite elements over the surface (so both aspects require a very similar computational outlay). One factor that might require additional finite elements for the nonuniform heating problem than for the different boundary conditions problem is the number of elements needed to represent the nonuniform temperature distribution with the associated material property variability, *especially if the temperature varies through the plate thickness*. Of course, any nonuniform heating must be such that the plate has a continuously increasing amplitude of some characteristic facet of the nonuniform heating distribution without any moment being induced in the plate. Such moments would cause immediate bending, bowing, or curling of the plate thereby eliminating the possibility of thermal buckling and reducing the problem from an eigenvalue problem to a nonlinear equilibrium problem. That is, thermal buckling is an instantaneous action of the plate (a sudden change of deformation mode at a specific load or temperature) rather than a gradually developing deformation such as bending, bowing, or curling. All the issues of actual

plates buckling under heating are clouded by the realities of geometric imperfections of the plate as well as inevitable variabilities in the heating distribution. The heating distribution is heavily influenced by the realities of the plate support conditions such as how well the edge and surface boundaries either 'carry off' (act as a heat sink) or help retain the heating of the interior of the plate.

A few nonuniform heating distributions for rectangular plates have been treated, although all seemingly are for temperature-independent material properties and usually for linear stress-strain curves. To simulate the heating condition on aircraft wing panels in supersonic flight, Heldenfels and Roberts⁴³ developed the heating apparatus to apply a tent-shaped distribution to an aluminum plate that is not restrained at its edges. Then, for that same tent-shaped temperature distribution, Gossard, Seide, and Roberts⁴⁴ developed both a thermal buckling solution with a postbuckling behavior analysis for a geometrically perfect plate and a large-deflection equilibrium solution for the deformation of a plate with initial geometric imperfections. Indeed, *buckling can be caused without the presence of edge restraint* if the temperature varies over the plate surface and causes regions of compressive stress with self-equilibrating tensile stress in other regions. The measured and predicted plate center deflections agreed with each other and approached that of the geometrically perfect plate analysis with postbuckling behavior accounted for as temperature increased. Klosner and Forray⁴² applied a double Fourier sine series to address an arbitrary, but symmetric, temperature distribution with a parabolic distribution as an example. However, their specific procedure was not clear, and their references were either missing or not accurate. Of course, neither of the two nonuniform temperature distributions could be addressed with the present plastic thermal buckling analysis procedure without very significant computational expense.

6.7 Summary

The effect of temperature-dependent nonlinear stress-strain behavior on thermal plastic buckling of uniformly heated, simply supported, uniaxially restrained rectangular plates is readily apparent from the present results and can be quite strong. Thus, in a robust thermal environment, the actual nonlinear stress-strain behavior of a material as a function of temperature must be considered when evaluating structural response of plates, as was previously shown by Jones¹⁹ for bars. Other types of in-plane restraint and combined thermal and mechanical loading of uniformly heated, simply supported plates should be assessed. The response of plates with other edge support boundary conditions and other types of heating distributions as well as other structural elements such as shells, and even complete structures, should be similarly affected and modeled.

References

- ¹ N. J. Hoff, 'Buckling at High Temperature', *Journal of the Royal Aeronautical Society*, Volume 61, Number 563, November 1957, pp. 756-774.
- ² G. H. Bryan, 'On the Stability of a Plane Plate under Thrusts in Its own Plane, with Applications to the "Buckling" of the Sides of a Ship', *Proceedings of the London Mathematical Society*, Volume 22, from November 1890 to November 1891 (read 11 December 1890), pp. 54-67.
- ³ Robert M. Jones, *Buckling of Bars, Plates, and Shells*, Bull Ridge Publishing, Blacksburg, Virginia, to be published.
- ⁴ E. W. Parkes, 'Panels under Thermal Stress, The Behavior of a Panel Restrained against Expansion in one Direction and Loaded in the other Direction when Subjected to Kinetic Heating', *Aircraft Engineering*, Volume 28, Number 328, June 1956, pp. 180-186.
- ⁵ Bruno A. Boley and Jerome H. Weiner, *Theory of Thermal Stresses*, Wiley, New York, 1960.
- ⁶ Eldon E. Mathauser and William A. Brooks, Jr., *An Investigation of the Creep Lifetime of 75S-T6 Aluminum-Alloy Columns*, NACA Technical Note 3204, National Advisory Committee for Aeronautics, Washington, D. C., July 1954.
- ⁷ Charles Libove, *Creep Buckling Analysis of Rectangular-Section Columns*, NACA Technical Note 2956, National Advisory Committee for Aeronautics, Washington, D. C., June 1953.
- ⁸ Charles W. Bert, 'Thermal Buckling of Thin Plates with Stress-Dependent Thermal Expansion Coefficient', *Proceedings of the 5th International Congress on Thermal Stresses and Related Topics*, TS2003, Blacksburg, Virginia, 8-11 June 2003, pp. TM-5-2-1 through TM-5-2-4.
- ⁹ H. H. Hilton, 'Thermal Stresses in Bodies Exhibiting Temperature-Dependent Elastic Properties', *Journal of Applied Mechanics*, Volume 19, Number 3, September 1952, pp. 350-354.
- ¹⁰ Leonhard Euler, 'On the Strength of Columns', *Academie Royale des Sciences et Belle Lettres Memoires*, Volume 13, p. 252, 1759. English translation by A. J. Van den Broek, Euler's Classic Paper 'On the Strength of Columns', *American Journal of Physics*, Volume 15, Number 4, July-August 1947, pp. 309-318.
- ¹¹ F. R. Shanley, 'Inelastic Column Theory', *Journal of the Aeronautical Sciences*, Volume 14, Number 5, May 1947, pp. 261-268, including discussion by Theodore von Kármán.

- 12 Theodore von Kármán, 'Untersuchungen über Knickfestigkeit', *Mitteilungen über Forschungsarbeiten, Verein Deutscher Ingenieure*, Heft 81, Berlin, 1910, pp. 1–44. Reprinted in *Collected Works of Theodore von Kármán*, Butterworths, London, 1956, Volume I, 1902–1913, pp. 90–140.
- 13 Elbridge Z. Stowell, *A Unified Theory of Plastic Buckling of Columns and Plates*, NACA Report 898, National Advisory Committee on Aeronautics, Washington, D.C., 1948.
- 14 George Gerard, 'Plastic Stability Theory of Geometrically Orthotropic Plates and Cylindrical Shells', *Journal of the Aeronautical Sciences*, Volume 29, Number 8, August 1962, pp. 956–962.
- 15 Robert M. Jones, 'Plastic Buckling of Eccentrically Stiffened Circular Cylindrical Shells', *AIAA Journal*, Volume 5, Number 6, June 1967, pp. 1147–1152. See also *Plastic Buckling of Axially Compressed Stiffened Cylinders*, NASA Technical Note TN D-3769, National Aeronautics and Space Administration, Washington, D.C., January 1967.
- 16 A. Nadai, *Theory of Flow and Fracture of Solids*, Volume I, McGraw-Hill, New York, 1950.
- 17 Bernard Budiansky, 'A Reassessment of Deformation Theories of Plasticity', *Journal of Applied Mechanics*, Volume 26, Number 2, June 1959, pp. 259–264.
- 18 John W. Hutchinson, 'Plastic Buckling', *Advances in Applied Mechanics*, Edited by Chia-Shun Yih, Volume 14, Academic Press, 1974, pp. 67–144.
- 19 Robert M. Jones, 'Plastic Thermal Buckling of Uniformly Heated Bars with Temperature-Dependent Material Properties', *Proceedings of the AIAA/ASME/ASCE/AHS/ASC Structures, Structural Dynamics, and Materials Conference*, Palm Springs, California, 19–22 April 2004, AIAA Paper 2004-1709, AIAA, Reston, Virginia.
- 20 George Gerard and Sorrel Wildhorn, *A Study of Poisson's Ratio in the Yield Region*, NACA Technical Note 2561, National Advisory Committee on Aeronautics, Washington, D.C., January 1952.
- 21 Walter Ramberg and William R. Osgood, *Description of Stress-Strain Curves by Three Parameters*, NACA Technical Note 902, National Advisory Committee on Aeronautics, Washington, D.C., July 1943.
- 22 J. L. Holmquist and A. Nadai, 'A Theoretical and Experimental Approach to the Problem of Deep-Well Casing', *Drilling Production Practice*, 1939, American Petroleum Institute, 1940, pp. 392–420.
- 23 B. O. Almroth, 'Influence of Edge Conditions on the Stability of Axially Compressed Cylindrical Shells', *AIAA Journal*, Volume 4, Number 1, January 1966, pp. 134–140.
- 24 Robert M. Jones, 'Plastic Buckling of Eccentrically Stiffened Multilayered Circular Cylindrical Shells', *AIAA Journal*, Volume 8, Number 2, February 1970, pp. 262–270.
- 25 S. P. Timoshenko and James M. Gere, *Theory of Elastic Stability*, 2nd Edition, McGraw-Hill, New York, 1961.
- 26 Michael P. Nemeth, 'Buckling Behavior of Long Anisotropic Plates Subjected to Restrained Thermal Expansion and Mechanical Loads', *Proceedings of the 40th AIAA/ASME/ASCE/AHS/ASC Structures, Structural Dynamics and Materials Conference*, 12–15 April 1999, St. Louis, Missouri, AIAA Paper 99-1229, AIAA, Reston, Virginia. Also *Journal of Thermal Stresses*, Volume 23, Number 9, December 2000, pp. 873–916.
- 27 A. A. Ilyushin, *The Elasto-Plastic Stability of Plates*, NACA Technical Memorandum 1188, National Advisory Committee on Aeronautics, Washington, D.C., December 1947. Originally published as 'Uprugo-Plasticheskaya Ustoichivost Plasteen', *Prikladnaya Matematika i Mekhanika*, Volume 10, 1946, pp. 623–638.
- 28 Robert M. Jones, *Plastic Buckling of Eccentrically Stiffened Circular Cylindrical Shells*, Aerospace Corporation Report Number TR-0158(S3816-72)-1, San Bernardino, California, December 1967. Available only from the Clearinghouse CFSTI, United States Department of Commerce.
- 29 Y. S. Touloukian, R. K. Kirby, R. E. Taylor, and P. D. Desai, *Thermophysical Properties of Matter, The TPRC Data Series, Volume 12, Thermal Expansion – Metallic Elements and Alloys*, IFI/Plenum, New York - Washington, 1975.
- 30 William R. Osgood, 'Stress-Strain Formulas', *Journal of the Aeronautical Sciences*, Volume 13, Number 1, January 1946, pp. 45–48.
- 31 *Mathematica*, Version 5.0, Wolfram Research, Inc., Champaign, Illinois, 2004.
- 32 A. Nadai, *Theory of Flow and Fracture of Solids*, Volume II, McGraw-Hill, New York, 1963.
- 33 George J. Heimerl and William M. Roberts, *Determination of Plate Compressive Strengths at Elevated Temperatures*, NACA Technical Report 960, National Advisory Committee for Aeronautics, Washington, D. C., 1950.
- 34 Richard A. Pride and George J. Heimerl, *Plastic Buckling of Simply Supported Compressed Plates*, NACA Technical Note 1817, National Advisory Committee for Aeronautics, Washington, D. C., April 1949.
- 35 G. H. Handelman and W. Prager, *Plastic Buckling of a Rectangular Plate under Edge Thrusts*, NACA Technical Note 1530, National Advisory Committee for Aeronautics, Washington, D. C., August 1948.
- 36 C. F. Kollbrunner, *Das Ausbeulen der auf einseitigen, gleichmässig verteilten Druck beanspruchten Platten im elastischen und plastischen Bereich*, Mitteilungen aus dem Institut für Baustatik an der Eidgenössischen Technischen Hochschule in Zürich, No. 17, 1946.
- 37 R. Teodosiadis, H. L. Langhaar, and J. O. Smith, 'Inelastic Buckling of Flat Plates', *Proceedings of the First Mid-western Conference on Solid Mechanics*, 24–5 April 1953, Urbana, Illinois, pp. 105–111.
- 38 Kevin D. Murphy and David Ferreira, 'Thermal Buckling of Rectangular Plates', *International Journal of Solids and Structures*, Vol. 38, No. 22–23, May–June 2001, pp. 3979–3994.
- 39 C. M. Wang, Y. Xiang, and J. Chakrabarty, 'Elastic/Plastic Buckling of Thick Plates', *International Journal of Solids and Structures*, Vol. 38, No. 48–49, November–December 2001, pp. 8617–8640.
- 40 Robert M. Jones, 'Buckling of Simply Supported Rectangular Plates under Uniform Thermal and Mechanical Loading', pp. 178–194 in *Problems of Mechanics of Thin Deformable Bodies, Devoted to the 80th Anniversary of Academician NAS RA S. A. Ambartsumian*, Institute of Mechanics, National Academy of Sciences of Armenia, Yerevan, 2002. Also in abbreviated form as pp. TM-5-4-1 to TM-5-4-4 in *Proceedings of the 5th International*

Congress on Thermal Stresses and Related Problems, TS2003, 8–11 June 2003, Virginia Polytechnic Institute and State University, Blacksburg, Virginia.

⁴¹ David Durban and Zvi Zuckerman, 'Elastoplastic Buckling of Rectangular Plates in Biaxial Compression/Tension', *International Journal of Mechanical Sciences*, Vol. 41, No. 7, July 1999, pp. 751–765.

⁴² J. M. Klosner and M. J. Forray, 'Buckling of Simply Supported Plates Under Arbitrary Symmetrical Temperature Distributions', *Journal of the Aeronautical Sciences*, Volume 25, Number 3, March 1958, pp. 181–184.

⁴³ Richard R. Heldenfels and William M. Roberts, *Experimental and Theoretical Determination of Thermal Stresses in a Flat Plate*, NACA Technical Note 2769, National Advisory Committee for Aeronautics, Washington, D. C., August 1952.

⁴⁴ Myron L. Gossard, Paul Seide, and William M. Roberts, *Thermal Buckling of Plates*, NACA Technical Note 2771, National Advisory Committee for Aeronautics, Washington, D. C., August 1952.

Table 1 Nadai-Jones Stress-Strain Curve Parameters as a Function of Temperature

Temperature °F	$\sigma_y = \sigma_1$ ksi	$\sigma_{oy} = \sigma_4$ ksi	ϵ_3	$\sigma_h = \sigma_5$ ksi	K ksi ⁻ⁿ	n	J ksi ^{-m}	m	E ksi	$\Delta L/L_o$
70	56.0	68.0	.006380	70.	6.146×10^{-7}	3.170	4.374×10^{-9}	6.347	10000.	.00000
300	36.0	51.0	.004805	52.9	8.529×10^{-9}	4.519	2.079×10^{-14}	11.501	9200.	.00314
400	24.3	36.3	.003845	37.35	5.397×10^{-8}	4.157	4.284×10^{-17}	16.588	8075.	.00464
500	11.0	15.8	.002260	17.0	3.331×10^{-5}	2.347	4.077×10^{-6}	5.840	6700.	.00621
600	2.60	8.40	.001034	9.00	5.811×10^{-7}	4.218	5.187×10^{-9}	11.462	5600.	.00784

Temperature °C	$\sigma_y = \sigma_1$ MPa	$\sigma_{oy} = \sigma_4$ MPa	ϵ_3	$\sigma_h = \sigma_5$ MPa	K MPa ⁻ⁿ	n	J MPa ^{-m}	m	E GPa	$\Delta L/L_o$
20	386.1	468.8	.006380	482.6	1.3108×10^{-9}	3.1779	1.6632×10^{-25}	11.8963	68.95	.00000
149	248.2	351.6	.004805	364.7	1.2898×10^{-12}	4.5372	8.9444×10^{-14}	11.501	63.43	.00314
204	167.5	250.3	.003845	257.5	1.7379×10^{-11}	4.1612	3.5864×10^{-31}	16.6869	55.68	.00464
260	75.84	108.9	.002260	117.2	3.5415×10^{-7}	2.3513	4.9266×10^{-11}	5.8547	46.20	.00621
316	17.93	57.92	.001034	62.05	1.6853×10^{-10}	4.2187	1.2635×10^{-18}	11.4634	38.61	.00784

* σ_3 is calculated from σ_y and σ_{oy} (their average), and ϵ_h is .01200 for all temperatures

Nonlinear Dynamic Buckling of a Composite Shell

Christos C. Chamis^a
NASA Glenn Research Center
Cleveland, OH 44135

Galib H. Abumeri^b
QSS Group, Inc.
Cleveland, OH 44135

A computationally effective method is described to evaluate the nonlinear dynamic buckling of thin composite shells. The method is a judicious combination of available computer codes for finite element, composite mechanics and incremental structural analysis. The solution method is an incrementally updated Lagrangian. It is illustrated by applying it to a thin composite cylindrical shell subjected to dynamic loads. Buckling loads are evaluated to demonstrate the effectiveness of the method. A universal plot is obtained for the specific shell that can be used to approximate buckling loads for different dynamic loading rates. Results from this plot show that the faster the rate, the higher the buckling load and the shorter the time. Results also show that the updated solution can be carried out in the post buckling regime until the shell collapses completely.

I. Introduction

Thin shell structures are in general very efficient structural components for resisting combined loading conditions. Examples of their use are aircraft fuselages, submarine hulls and space launch vehicles and many others for transportation and storage. Cylindrical shells made from composites utilize composites most effectively. Thin shells are susceptible to buckling when subjected to compressive static loads. In more aggressive loading environments, they may also be subjected to dynamic or time dependent loads. Predicting the buckling resistance of thin shells is not difficult because the simplifying assumptions that are made in order to obtain results that may be representative of the physical situation. The advent of the finite element method has overcome many of the difficulties associated with the shell boundary conditions, loadings and geometric configuration. The finite element method has also made possible the evaluation of the buckling load of thin composite shell under dynamic loading. Dynamic Buckling of imperfect cylindrical shell has been investigated in Ref. 1, where relevant references are also cited. However, nonlinear evaluation of the dynamic buckling of composite shells has not been performed as of this writing. Therefore, the objective of this investigation is to describe one approach that has been successfully used to perform nonlinear dynamic buckling of composite shells. A secondary objective specific and centerpiece to the approach was to use conventional finite elements, available composite mechanics and incremental structural analysis methods. In essence, the approach may be considered an updated nonlinear Lagrangian solution method. The emphasis of the investigation was on developing the method and demonstrating its effectiveness by using a cylindrical composite thin shell. The authors recognize that the how part of the solutions is not unique and that other methods could be used. The authors' objective was to develop a method that is generic and not restrictive to any class of problems or conditions. The authors believe that the method described meets and perhaps exceeds those objectives.

II. Fundamental Considerations

The governing equation for dynamic structural response in matrix form is

$$[M]\{\ddot{u}\} + [C]\{\dot{u}\} + [K]\{u\} = \{F(t)\} \quad (1)$$

where M is the mass; C is the damping; K is the stiffness and F is the forcing function; \ddot{u} is the acceleration, \dot{u} is the velocity and u is the displacement. Equation (1) is of generic form and represents the single or multi-degrees of freedom structures. Dynamic buckling is obtained by solving Equation (1) as a linear eigen value problem or as a large displacement amplitude problem by using the updated Lagrangian method. Available structural analysis finite element computer codes/programs have both options.² The linear eigen value approach is usually referred to as the frequency domain. The large amplitude is usually referred to as the time domain. The approach (method) used

^aSenior Aerospace Scientist

^bSenior Engineer, Work Performed Under the GESS Contract

expresses the displacements in Equation (1) in finite difference form and then solve the equation by incrementing the time. In this approach, updates for material properties, temperature changes, geometric deformations and structural damage are readily incorporated as they occur in time. This approach is often referred to as the updated Lagrangian, as was mentioned earlier. A combined capability of at least multidisciplinary composite mechanics, dynamic structural analysis and incremental simulation methods are needed to evaluate nonlinear dynamic buckling of composite shell structures. The multidisciplinary computer code used in this investigation is called EST/BEST for Engine Structures Technology/Benefits ESTimator depicted schematically in Figure 1.³ It is noted that the modules in EST/BEST are integrated stand-alone computer programs that are connected and communicate with the executive module by soft (loose) coupling. Those that were used to evaluate the nonlinear dynamic buckling of composite shells are: Engine Component Structural and Fluid Modeling, ICAN (PMC)⁴ in the Materials Library, and CODSTRAN^{5,6} for Progressive Damage in Composite Structures. More details will be described as each of these modules is used in the evaluation.

III. Nonlinear Dynamic Buckling

The specific shell evaluated is depicted schematically in Figure 2 where the material and loading conditions are also shown. The corresponding constituent material properties are listed in Table 1. The undamped version of Equation (1) can be expressed in finite difference and in the time domain as follows by assuming that at relatively very small time increments the Equation (1) can be decomposed:

$$\begin{aligned} \{\ddot{u}\} &= [M]^{-1} \{F(t)\} \\ \{\dot{u}\} &= \Delta T \{\ddot{u}\} \quad ; \quad \{u\} = \Delta T^2 \{\ddot{u}\} \end{aligned} \quad (2)$$

The acceleration is solved first, then the velocity and then displacement. The results obtained from solving the undamped version of Equation (1) by direct time integration are shown in Figure 3 for loaded-end axial acceleration; in Figure 4 for the corresponding velocity; and in Figure 5 for the corresponding incremental displacement. It is instructive to examine the results shown in Figures 3-5. There is considerable fluctuation in the acceleration from about 357,000 to 750,000 cm/sec² (150,000 to 300,000 in/sec²) initially and decreases monotonically with time to near zero. The only explanation at this time about the intermediate fluctuations is interactions with either radial or circumferential acceleration responses. The velocity plotted in Figure 4 is also oscillatory varying from about 12.7 to 127 cm/sec (5 to <50 in/sec) initially. The velocity is smooth compared to the acceleration and appears to approach a value of 62.5 cm/sec (25 in/sec). The incremental end displacement (axial shell shortening) plotted in Figure 5 is also oscillating from 0.01 to 0.25 cm (0.004 to 0.01 in). The oscillatory behavior is more predominant at early times as can be seen in Figure 6 where it decays very rapidly approaching a value of about 0.0178 cm (0.007 in). The effects of the total time for the same total load are evident in Figure 6 where the two rates differ by one decade.

The nonlinear dynamic buckling load is obtained at each time step by first satisfying Equation (1), including iteration for convergence when necessary, and then solving for the buckling load from the equation

$$([K] - [F(t)]\{u\}) = \mathbf{I}^2 \{u\} \quad (3)$$

Equation (3) is solved by available eigen value extraction routines in conventional structural analysis computer codes by using the differential stiffness method, such as MSC NASTRAN.³ The step-by-step procedure is outlined in the Appendix. The nonlinear dynamic buckling load predicted by using Equation (3) versus incremented dynamic load is shown in Figure 7. As can be seen, the dynamic buckling load decreases monotonically approaching asymptotically a value that is about 50% of the static value (at t=0). The corresponding buckled shapes of the shell are shown in Figure 8a for static load, and in Figure 8b for the dynamic load prior to ply failures. Ply failure is determined by the combined-stress failure criterion.⁵ It is interesting to observe that the buckled shape of the shells is about the same, relative to the number of waves especially around the circumferences. The amplitudes are different, as would be expected. The other notable observation in Figure 8 is that most of the buckled activity dominates the middle part of the shell. It is seen from Equation (3) that a shell-buckling load exists for any dynamic load magnitude greater than zero. The graph in Figure 7 suggests that superimposing the increasing dynamic load in the same graph with the nonlinear dynamic buckling load, the dynamic buckling load can be determined from the intersection of the two curves, which is the innovation of this investigation. This is illustrated graphically in Figure

9. The authors consider the results in Figure 9 as demonstration of a straightforward procedure to evaluate nonlinear dynamic buckling loads of composite shell structures by using available general purpose structural analysis finite element with updated Lagrangian and composite mechanics computer codes. The approach is not limited to linearly incremented dynamic loads, although the authors have not checked it for nonlinearly incremented loads or for “suddenly applied” ($t \sim 0$) loads.

IV. Nonlinear Dynamic Buckling and Snap-Through Results and Discussion

The nonlinear part of the loaded end displacement is shown in Figure 10 at a time of 0.052 sec. It is observed in Figure 10 (left scale) that the nonlinear end-displacement grows exponentially as the dynamic load increases. The corresponding shell deformation is shown in Figure 11. It is seen in Figure 11 that the nonlinear deformation is concentrated at the loaded end and at the supported end. The deformed nonlinear buckled shape for 0.05225 seconds is illustrated in Figure 12. Note that the nonlinear displacement activity has become greater at the loaded end.

At this point it is important to see whether the shell is operating near a snap through and post buckling positions. This aspect of the shell status is illustrated in Figure 13, where the snap through is displayed by a large decrease in the nonlinear buckling load curve at about 0.050 sec. Expanding the time scale shows the snap through more graphically as is illustrated in Figure 14 for the radial displacement. The corresponding structured shape of the shell is shown in Figure 15 for the two times just before and after snap through. The initial circular section of the shell deforms into Figure 8. The results in Figure 15 demonstrate the flexibility of the updated Lagrangian method. It is possible to capture the entire behavior of the dynamic nonlinear response with one simulation

It is instructive to evaluate the nonlinear response of the shell under a static load. A graphical illustration of the post buckling nonlinear behavior is shown in Figure 16. In this figure deformed shapes of the shell are indicated for three different static loading conditions. The top part of the figure shows the changes in frequency as the nonlinear deformation progresses from a static load of 12,746N (3044 kips) to 15,220N (5000 kips). At the 15,220N (5000 kips) case the shell has collapsed completely. The corresponding frequencies changed from 268.5 cps for the pristine shell to 124.7 cps for the collapsed position.

The afore-discussion leads to the conclusion that nonlinear dynamic buckling of composite shell structures can be evaluated by a capability that integrates (1) dynamic structural simulation, (2) composite mechanics and (3) updated structural analysis. As was demonstrated in the evaluation for the dynamic buckling of a composite shell, that capability appears to be sufficient and efficient since it relies on proven and readily available methods.

V. Summary of Results

The salient results of an investigation to develop an effective method for the nonlinear dynamic buckling of thin composite shells are as follows: (1) The method was developed and consists of the judicious combination of conventional finite element method, available composite mechanics, and incrementally updated Lagrangian solution algorithm. (2) The method is generic and it is not restricted to any special class of shells and/or loading conditions. (3) The effectiveness of the method is demonstrated by evaluating the nonlinear dynamic buckling load of a specific thin composite shell. (4) Typical results obtained include nonlinear dynamic buckling, buckling modes shapes. (5) A universal plot is developed which shows the nonlinear dynamic buckling load at the intersection of the dynamic load versus time. (6) The authors consider the method easy to apply and to their knowledge the first of its kind.

APPENDIX

Procedure to Perform Nonlinear Dynamic Buckling Evaluation of Structures

The following steps are suggested to perform a nonlinear buckling analysis of composite shells:

1. Generate finite element model for the structure in consideration.
2. Make appropriate material selection.
3. Impose proper structural boundary conditions.
4. Choose a total time for dynamic analysis.
5. Select time step Δt .
6. Define time dependent (dynamic) load $F(t)$.
7. For each time step Δt :
 - 7.1 Perform dynamic analysis of the structure.
 - 7.2 Save the structural displacements in X, Y, and Z directions $\Delta X(t)$, $\Delta Y(t)$,

and $\Delta Z(t)$ for use in the next step.

- 7.3 Generate a time dependent static buckling input file based on updated geometry as follows:

$$X(t) = X(t-1) + \Delta X(t)$$

$$Y(t) = Y(t-1) + \Delta Y(t)$$

$$Z(t) = Z(t-1) + \Delta Z(t)$$

- 7.4 Carry out static buckling analysis using updated geometry from 7.3 and calculate the critical load for the structure $F_{cr}(t)$.

8. The dynamic buckling load F_{db} is determined graphically by plotting the $F_{cr}(t)$ and $F(t)$ as a function of time. Note that the plot must use the same scale for the two time dependent loads $F_{cr}(t)$ and $F(t)$. The magnitude of F_{db} is determined by the ordinate of the intersection of the curves from the two loads $F_{cr}(t)$ and $F(t)$.
9. Time of occurrence of dynamic buckling $TIME_{db}$ is determined from the abscissa of the plot generated in the current step. When the two loads $F_{cr}(t)$ and $F(t)$ intersect, that would be the time of occurrence of dynamic buckling: point of intersection ordinate – dynamic buckling load, abscissa – time of occurrence.

References

- ¹X. Huyan and G. J. Simites, Dynamic Buckling of Imperfect Cylindrical Shells Under Axial Compression and Bending Moment. *AIAA Journal*. Vol. 35, No. 8, August 1997.
- ²MSC NASTRAN 2001-Quick Reference Guide. MSC Software Corporation, Los Angeles, CA, 2001.
- ³G.H. Abumeri and C.C. Chamis, EST/BEST A Computer Code for Assessing the Benefits of Advanced Aerospace Technologies. *Elsevier, Advances in Engineering Software*. Vol. 28, No. 4, June 1997.
- ⁴P.L.N. Murthy and C.C. Chamis, “Integrated Composites Analyzer (ICAN) User’s and Programmer’s Manual,” NASA TP 2515, March 1986.
- ⁵C.C. Chamis, “Computational Simulation of Progressive Fracture in Fiber Composites.” NASA TM 87341, May 1986.
- ⁶L. Minnetyan, C.C. Chamis and P.L.N. Murthy, “Damage and Fracture in Composite Thin Shells.” NASA TM 105289, October 1991.

Table 1: Graphite/Epoxy Constituents Material Properties

Constituents	Value
Fiber:	
Normal Modulus E_{f11}	32 mpsi
Normal Modulus E_{f22}	3 mpsi
Poisson’s Ratio ν_{12}	0.23
Poisson’s Ratio ν_{23}	0.25
Shear Modulus G_{f12}	2.5 mpsi
Shear Modulus G_{f23}	2.5 mpsi
Tensile Strength S_{fT}	400 ksi
Compressive Strength S_{fC}	400 ksi
Matrix:	
Normal Modulus E_m	0.45 mpsi
Poisson’s Ratio ν_m	0.41
Tensile Strength S_{mT}	6.7 ksi
Compressive Strength S_{mS}	39 ksi
Shear Strength S_{mS}	8.9 ksi
Fabrication Variables:	
Fiber volume ratio (fvr)	60%
Void volume ratio (vvr)	0.01%
Ply thickness	0.005 in.
Ply misalignment	0

(1 mpsi = 6890 GPa; 1 ki = 6.89 MPa; 1 in = 25 mm)

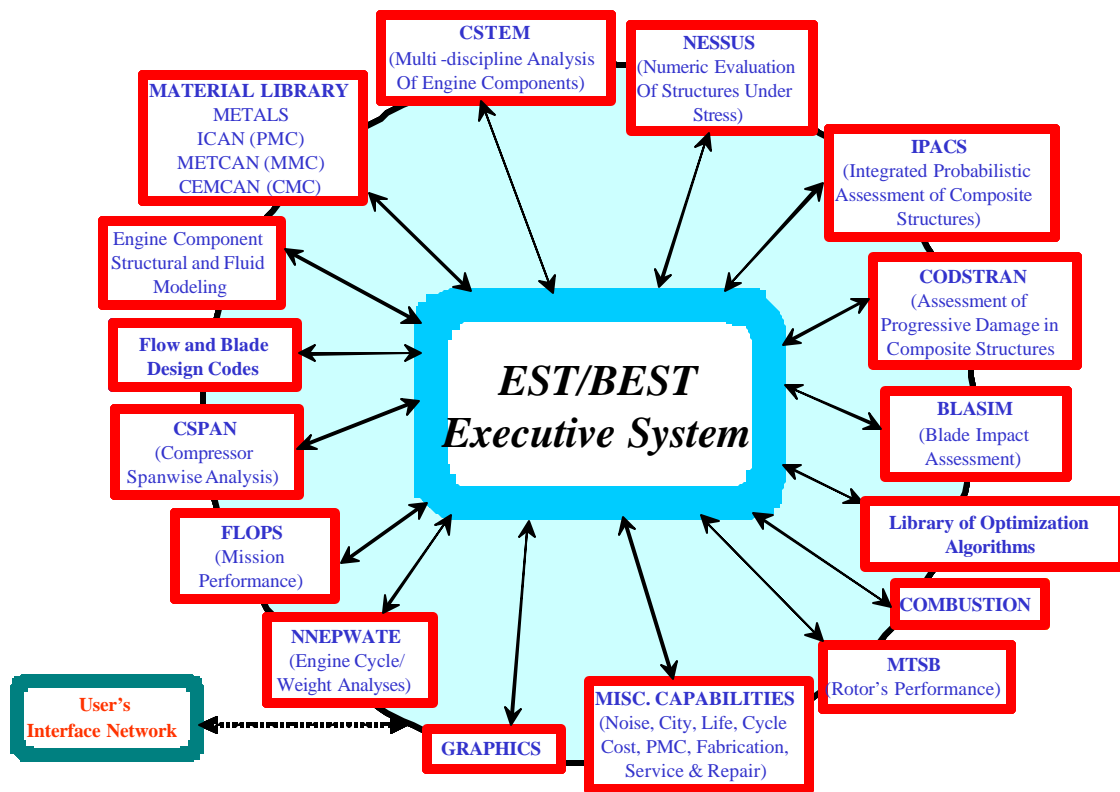
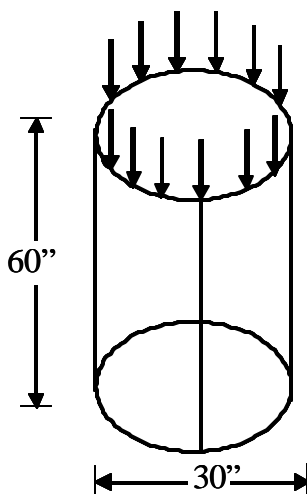


Figure 1: EST/BEST Engine Structures Technology Benefit Estimator



Material and Loading Configurations

- Graphite Epoxy: $[(45, -45, 0, 90)]_{4s}$
- Ply thickness: 0.005"
- Total thickness: 0.16"
- Fiber volume ratio: 0.65
- Void volume ratio: 0.05
- Time step for dynamic analysis: 0.00025 sec
- Total time considered for dynamic analysis: 0.05 sec
- 20 Kips dynamic load is applied in equal increment.
- Buckling analysis is performed at the end of each time step using updated deformed geometry.

Converting Factors: 1 kip = 4.45 N; 1 in = 2.54 cm

Figure 2: Buckling of a Clamped-Clamped Composite Shell
(With Static and Dynamic Compressive Axial Loads)

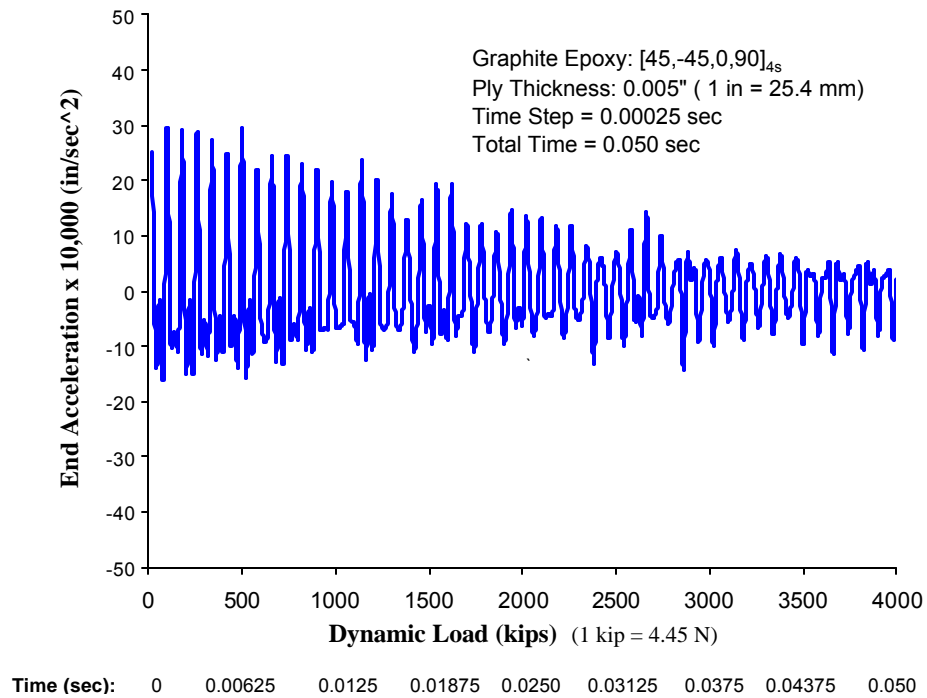


Figure 3: Incremental End Acceleration of a Composite Shell Due to Compressive Axial Loading

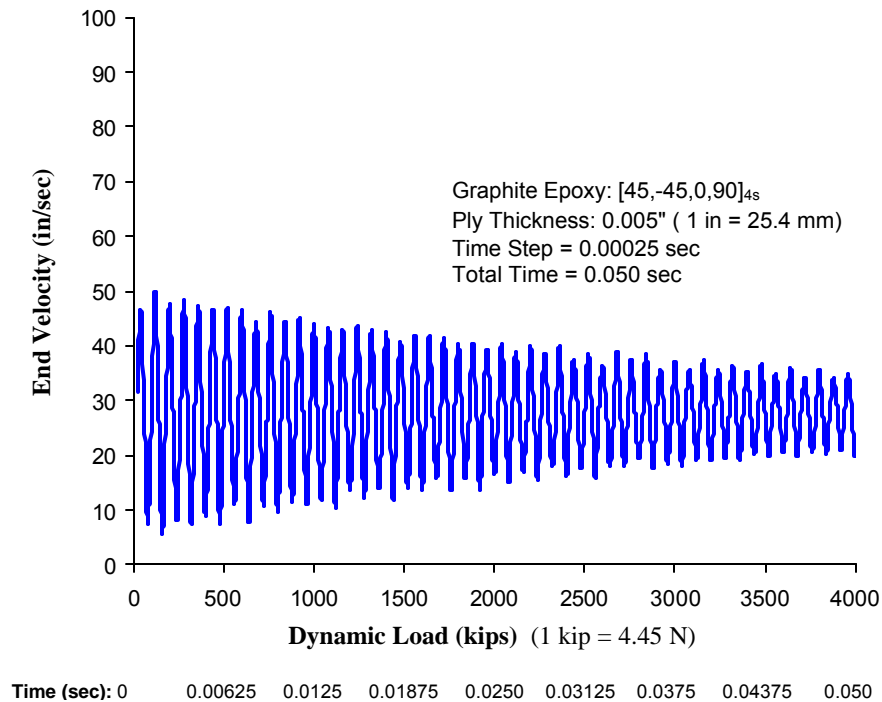


Figure 4: Incremental End Velocity of a Composite Shell Due to Compressive Axial Loading

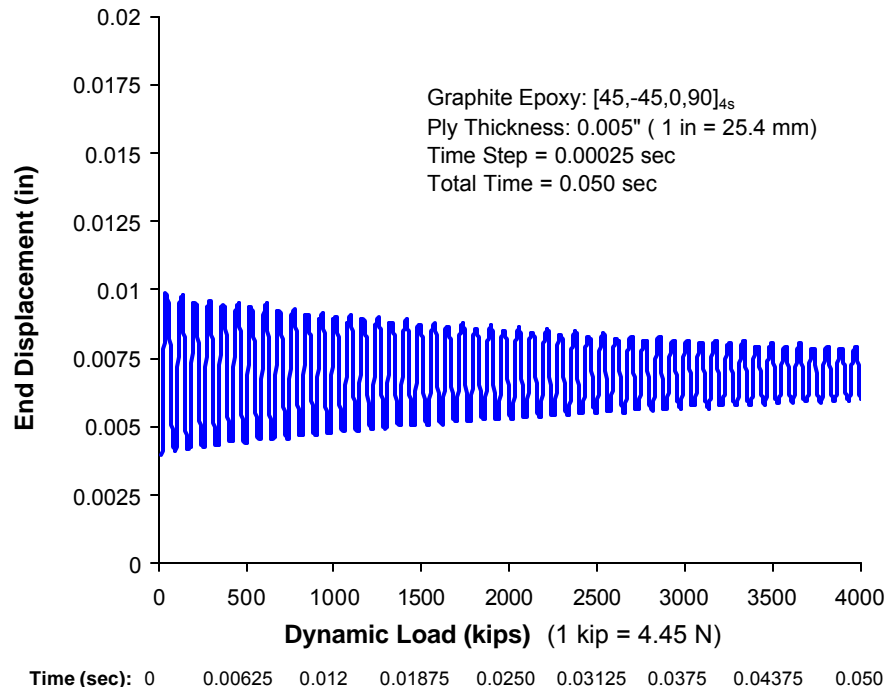


Figure 5: Incremental End Displacement of a Composite Shell Due to Compressive Axial Loading

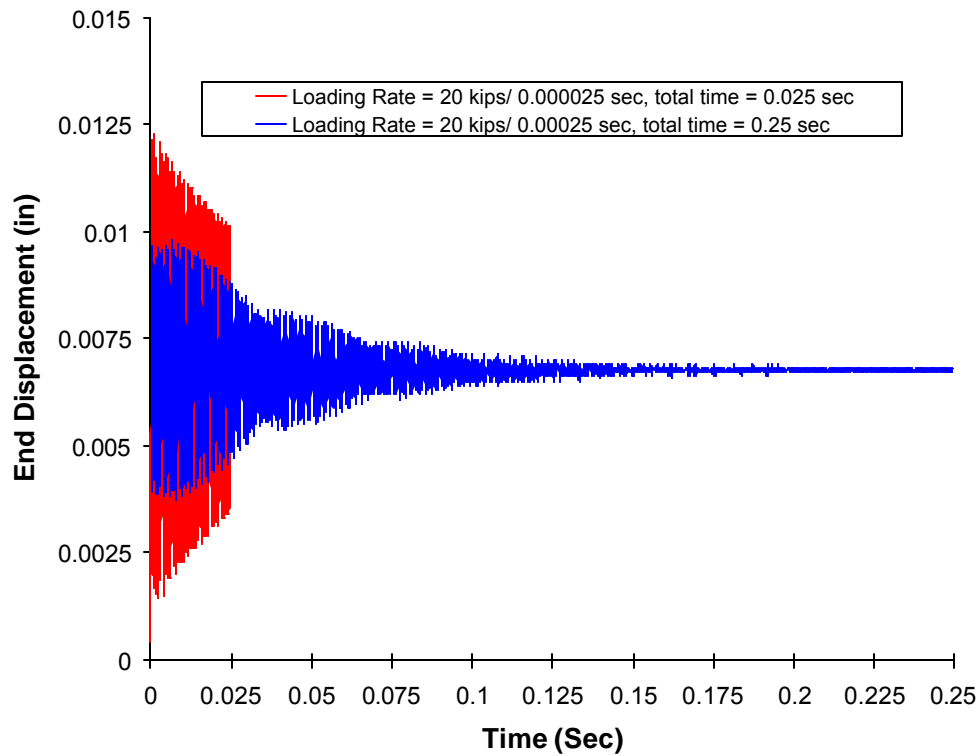


Figure 6: Effect of Loading Rate on the Incremental End Displacement of a Compressive Shell (With Dynamic Compressive Axial Loading (1 kip = 4.45 N))

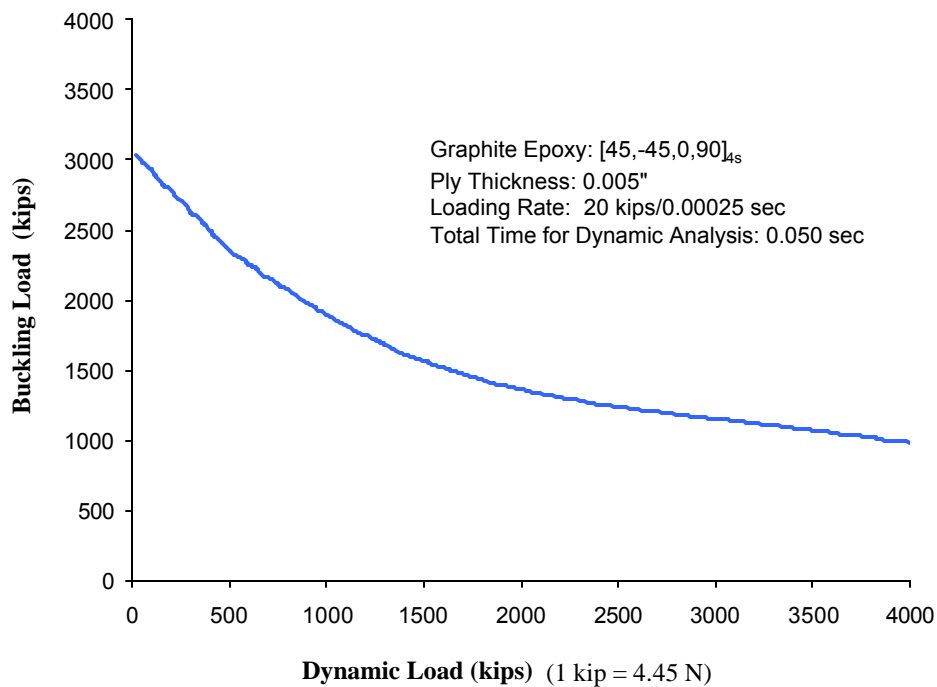


Figure 7: Effect of Dynamic Load on the Buckling Load of a Composite Shell

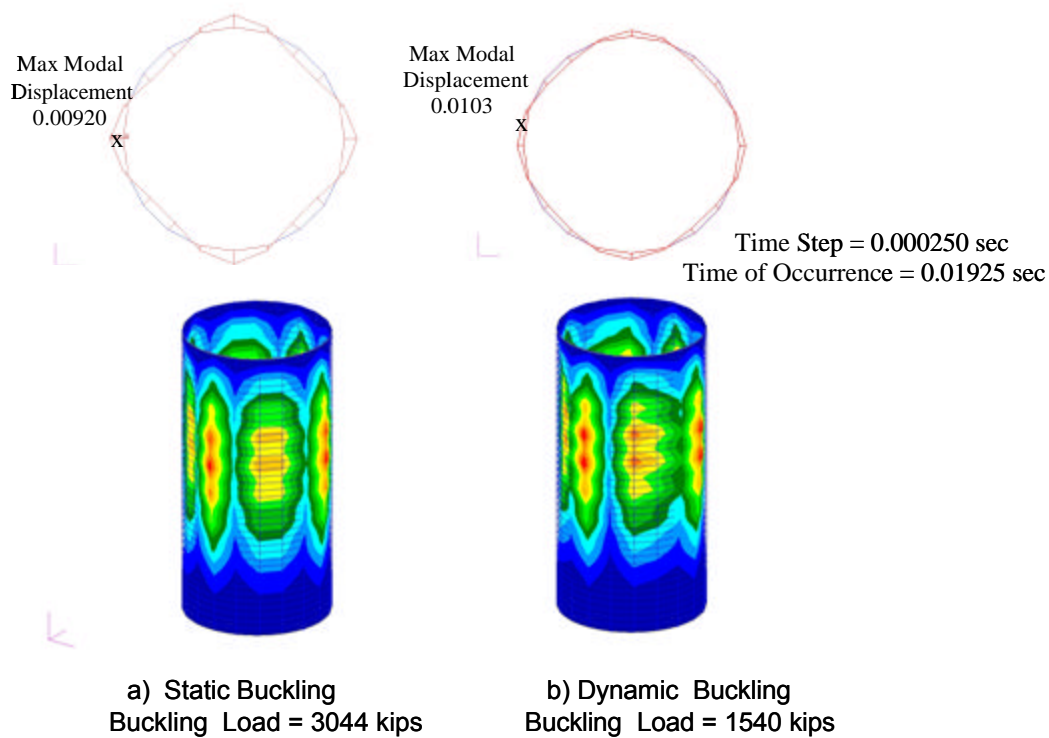


Figure 8: First Buckling Mode Shape of a Composite Shell – Static and Dynamic (With Compressive Axial Loading (1 kip = 4.45 N))

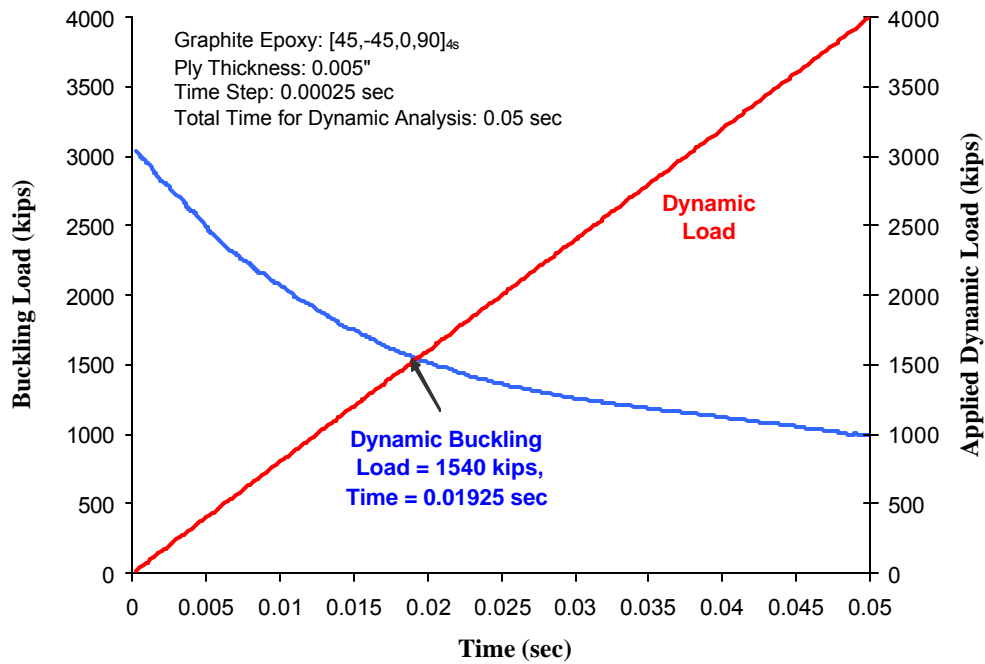


Figure 9: Effect of Time on the Buckling Load and Applied Dynamic Load
 (Composite Shell with Compressive Axial Loading (1 kip = 4.45 N; 1 in = 25.4 mm))

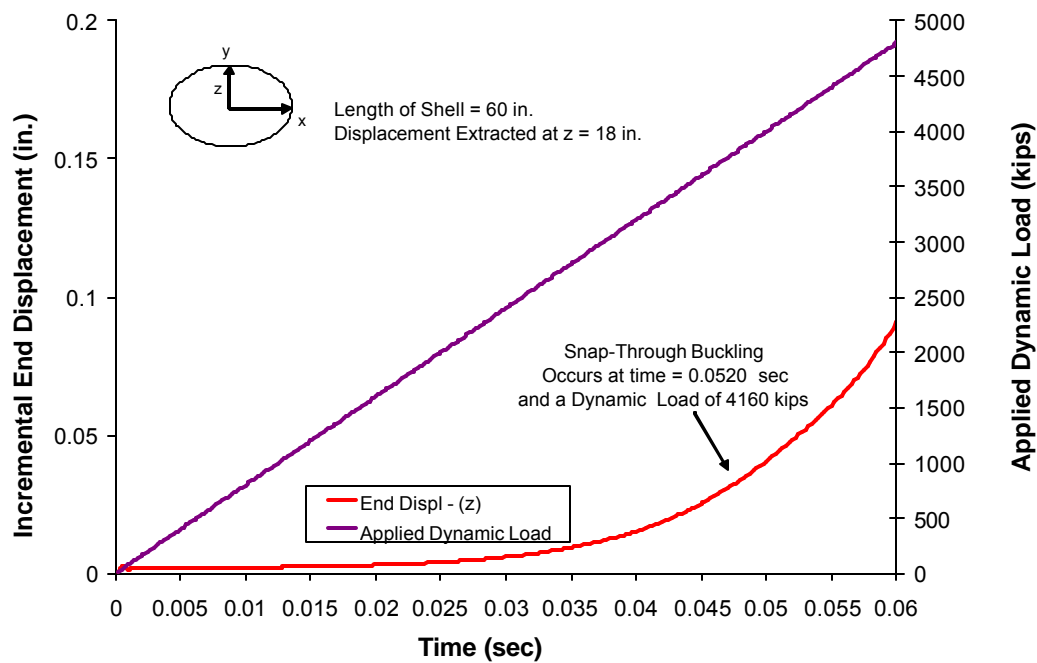


Figure 10: Incremental End Displacement of a Composite Shell Based on Non-Linear Dynamic Analysis
 (With Dynamic Compressive Axial Loading (1 kip = 4.45 N; 1 in = 25.4 mm))

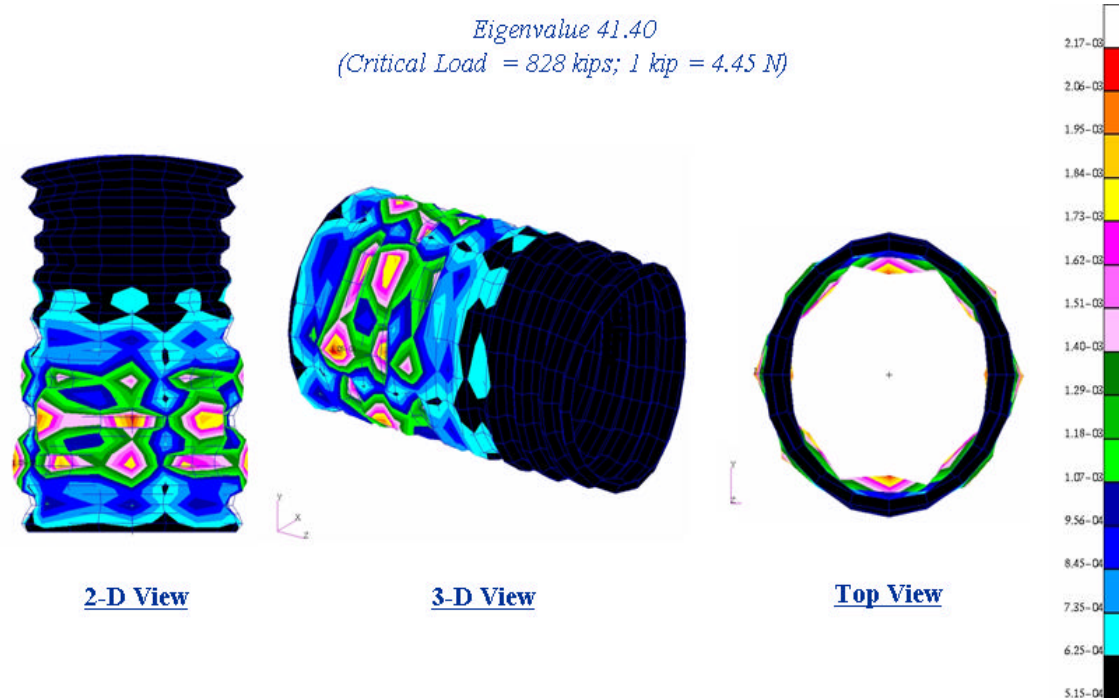


Figure 11: Nonlinear Dynamic Buckling of a Composite Shell
(1st Buckling Mode Shape at 0.052 sec)

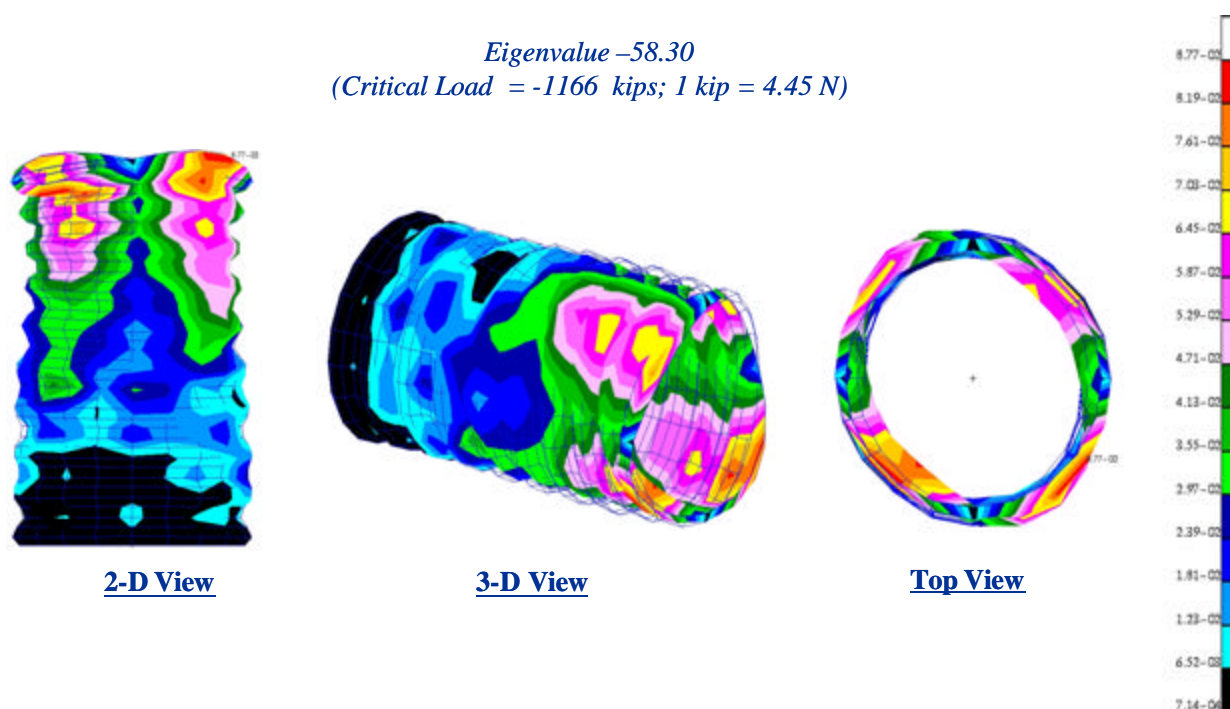


Figure 12: Nonlinear Dynamic Buckling of a Composite Shell
(1st Buckling Mode Shape at 0.05225 sec)

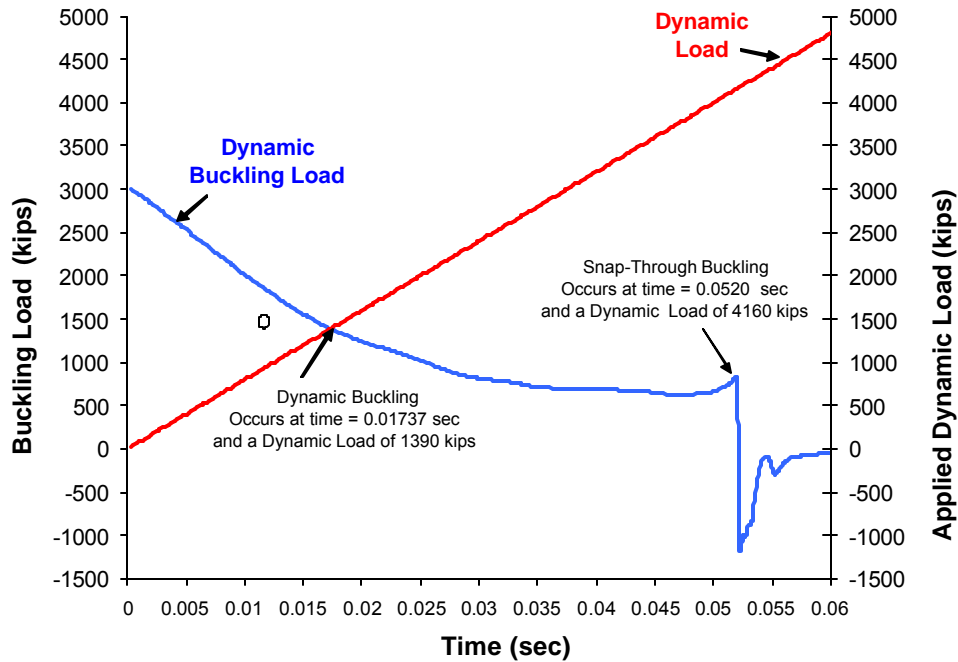


Figure 13: Dynamic Buckling Load of a Composite Shell Based on Nonlinear Dynamic Analysis
(With Dynamic Compressive Axial Loading ; 1 kip = 4.45 N; 1 in = 25.4 mm)

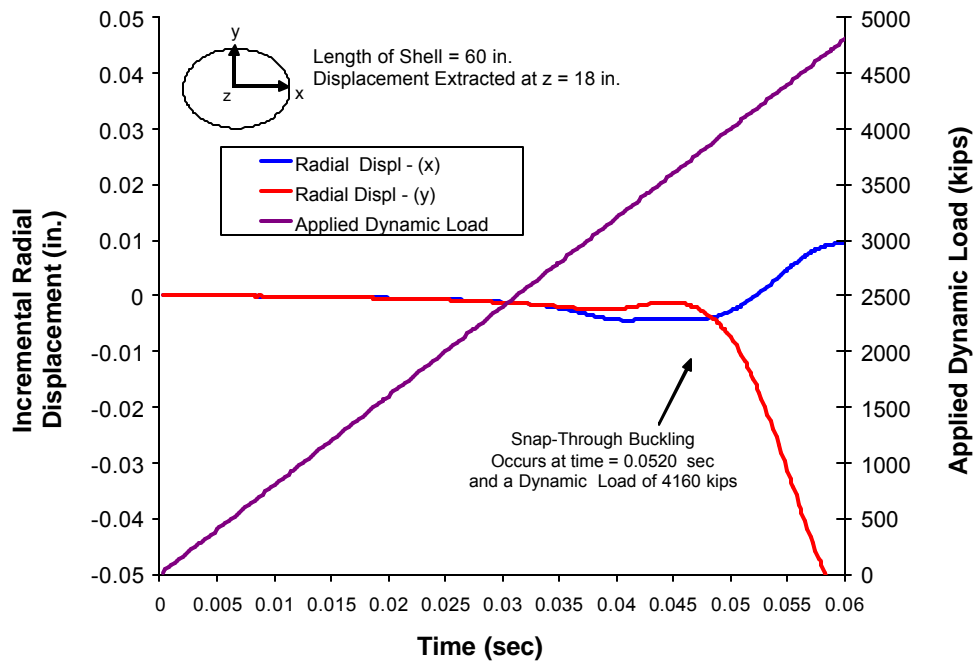


Figure 14: Incremental Radial Displacement of a Composite Shell Based on Non-Linear Dynamic Analysis
(With Dynamic Compressive Axial Loading ; 1 kip = 4.45 N; 1 in = 25.4 mm)

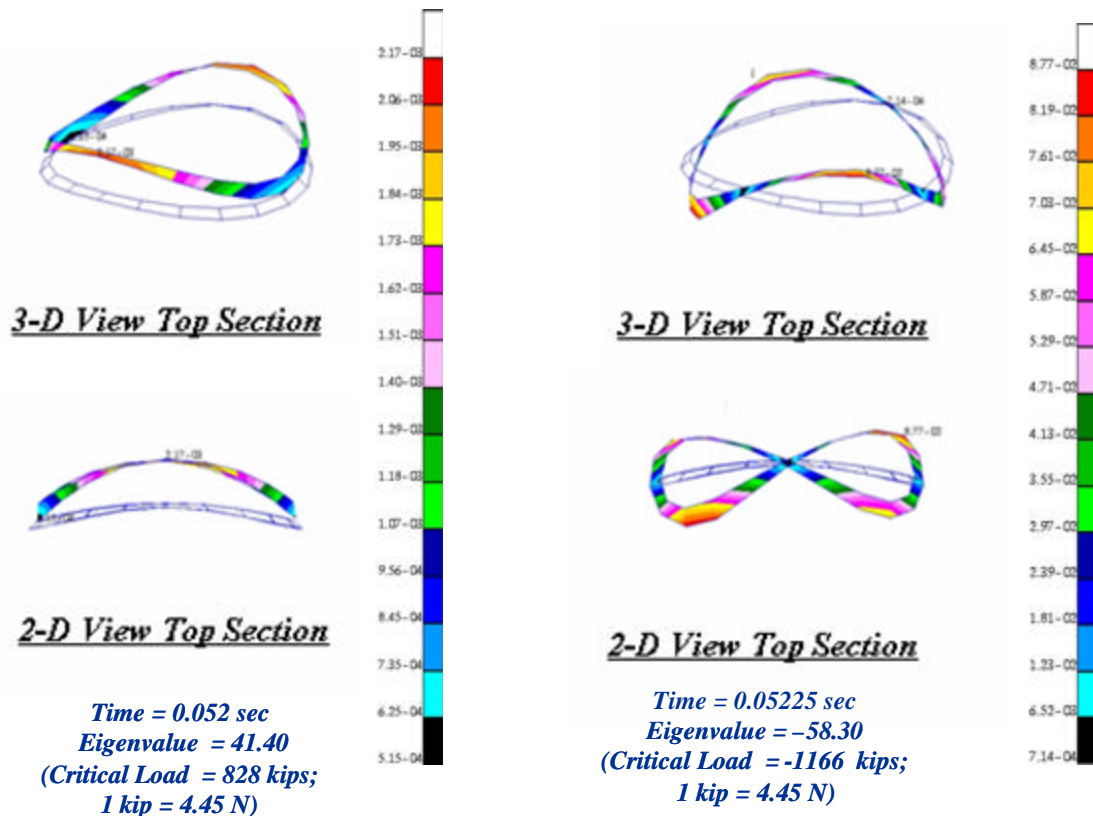


Figure 15: Nonlinear Dynamic Buckling of a Composite Shell – Mode Switch
1st Buckling Mode Shape at 0.052 and 0.05225 sec

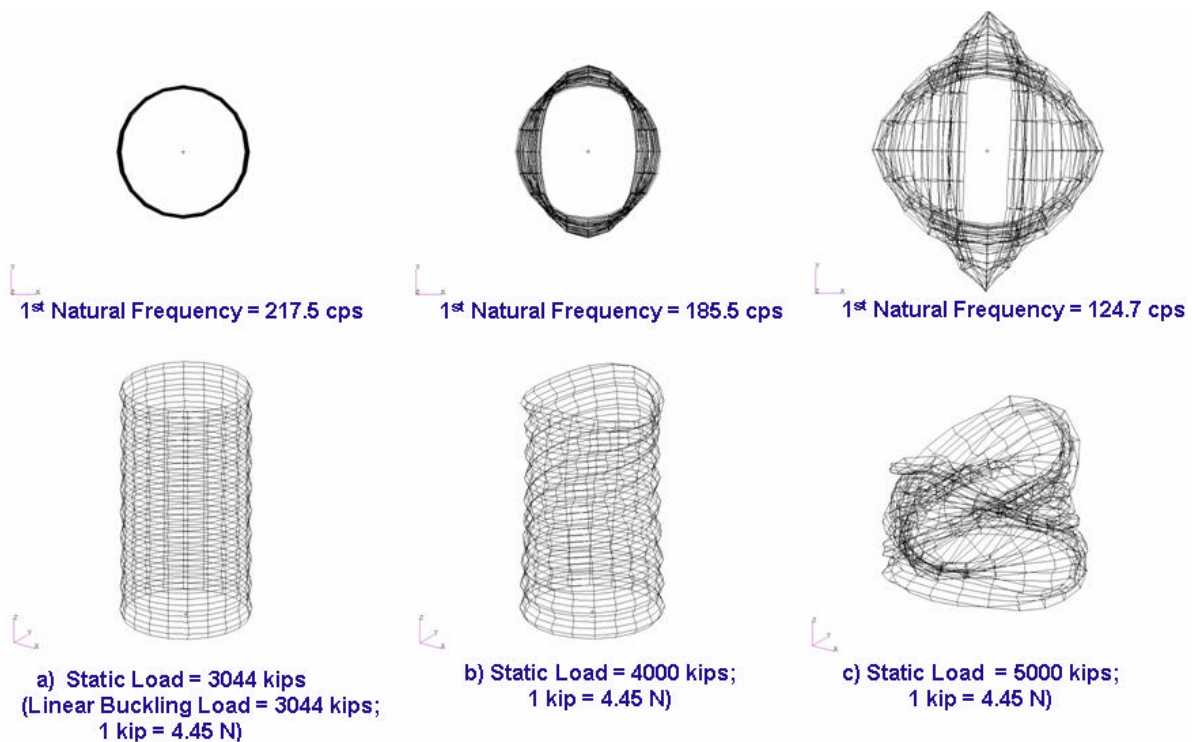


Figure 16: Nonlinear Static Analysis of a Composite Shell – Deformed Body Plot

DYNAMIC THERMAL STRESS CREEP BUCKLING, PROBABILISTIC FAILURES AND SURVIVAL TIMES OF VISCOELASTIC COLUMNS WITH FOLLOWER LOADS¹

Harry H. Hilton²

Aerospace Engineering Department
National Center for Supercomputing Applications
University of Illinois at Urbana-Champaign
104 South Wright Street, MC-236
Urbana, IL 61801-2935 U.S.A.

ABSTRACT

The influence of temperatures on viscoelastic energy dissipation is investigated. While dissipation may help retard creep buckling the associated presence of thermal stresses can be detrimental to material failures and thus shorten column lifetimes. Analytical results indicate that large deflection linearly viscoelastic columns with quasi-static follower and thermal loads under quasi-static conditions exhibit smaller deflections, smaller probabilities of failure and longer survival times than identical columns under the same loads but with dynamic effects caused solely by viscoelastic creep. Column end shortening due to both curvature, and external and thermal loads is also taken into account and the governing coupled nonlinear differential equations are solved numerically. The effects of end shortening on elastic and viscoelastic columns are discussed. Probabilistic column survivability due to creep buckling and material failure (delamination) are examined in detail.

Key words: buckling, columns, creep, delamination, failure probabilities, follower loads, large deformations, material damping, thermal stresses, survival times, and viscoelasticity.

DEDICATION

This paper is dedicated to Dr. James H. Starnes Jr. whose tremendous contributions in solid mechanics and flight structures led us all into the 21st century.

INTRODUCTION

Previous investigations of quasi-static creep buckling due to follower loads (Hilton *et al.*, 1994a, 1996) indicate the significant contributions follower loads play. Equally important effects have been observed in non-follower load linear viscoelastic columns due to inertia loads (Hilton 2002a, b). In the present paper the effects of inertia are examined for large deformation non-homogeneous columns with linear viscoelastic responses, large deformations, initial imperfections

¹Copyright 2005© by the author. Printed by NASA with permission.

²Professor Emeritus of Aerospace Engineering and Senior Academic Lead for Computational Structural/Solid Mechanics at NCSA. AIAA Fellow. Voice: 217-333-2653 or 217-840-1116 FAX: 217-244-0720 Email: h-hilton @ uiuc.edu

and follower loads. The additional nonlinear contributions due to column end shortening due to both curvature and compressive loads are taken into account. Galerkin's method is used to eliminate spatial variations and the resulting nonlinear temporal governing relations are solved numerically using a fourth order Runge-Kutta approach. The effects of end shortening on elastic and viscoelastic follower load columns are discussed. Column probabilities of failure and survival times due to creep buckling and/or material failure (delamination) are examined in detail including the influence of temperature.

Previously developed deterministic and stochastic combined load invariant failure criteria (Hilton & Ariaratnam 1994) are used to determine the onset of delamination in viscoelastic columns. The analysis includes the effects of initial imperfections as well as offset column loads and transverse shear contributions. The delamination predictions are found to be sensitive to the magnitude of applied loads and of initial imperfections. Illustrative numerical examples are presented for elastic and viscoelastic columns with random combined failure stresses in bending, shear, compression and with normal interlaminar stresses. Probabilities of delamination onset are established for various axial loads and initial imperfections and in the viscoelastic columns additionally as a function of lifetime. Since the failure theories consider the combined effects of bending, shear, compression and normal interlaminar stresses, delamination onset is predicted at smaller axial loads than the critical buckling loads in the elastic case and at shorter viscoelastic lifetimes compared to equivalent columns with no delamination effects.

Polymer matrix composites are rapidly becoming the structural materials of choice because of their lightweight and relatively high failure stresses which produce very attractive strength to weight ratios. Even though their initial behavior is elastic, composites require viscoelastic stress-strain and failure analyses at higher than room temperatures. At these conditions elastic analyses are inadequate because they fail to take into account material property degradation time dependencies of polymer matrix composites. However, for some forms of loading and for some conditions, elastic solutions may be considered as first order design" approximations and they always form the initial conditions for viscoelastic composite problems. For example, Ashby & Jones (1986) used a general form of the elastic modulus to approximate the behavior of fiber reinforced composites. Additional comprehensive treatments of composite structural analyses have been presented by Vinson & Sierakowski (1987).

Failure mechanisms observed in composites are substantially different from those observed in metals (Hiel *et al.* 1991). Delamination, a phenomenon unique to laminated composites, is frequently characterized by rapid crack propagation resulting in eventual catastrophic structural failures (Chai *et al.* 1983). From a design analysis point of view one needs only to consider delamination onset because at that stage the structure has for all practical purposes failed, particularly if it is a lightweight flight structure. Dillard & Brinson (1983) have formulated an expression for the temperature, moisture and time dependency of uniaxial composite failure stresses and Hilton & Yi (1993) have presented an extensive review of available experimental composite failure data.

The buckling of elastic columns, which are not subject to delamination, is a purely geometric phenomenon described by the classical Euler theory (Timoshenko 1936, Bleich 1952, Elishakoff

et al. 2001). However, polymer matrix composites at moderately elevated temperatures exhibit general viscoelastic behavior, i. e. they are a class of materials exhibiting creep and relaxation properties and, consequently, cause viscoelastic columns to buckle in time at loads smaller than the Euler loads of corresponding elastic columns (Bažant & Cedolin (1991), Hilton (1952), Jahsman & Field (1962), Libove (1952), Wilson & Vinson (1984, 1985). Polymer composites suffer from additional problems such as degradation of material properties (modulus and failure stresses with time.

Deterministic elastic and single Maxwell model viscoelastic delamination buckling has been studied by Kachanov (1988). Kim *et al.* (1992) have found that elastic and viscoelastic plates will propagate cracks only after the buckling stress has been reached, however it must be remembered that the plate stability problem is quite distinct from column buckling. The viscoelastic laminated plate problem has also been treated extensively by Wilson & Vinson (1984). Another interesting problem is the investigation by Suemasu (1992) into the effects of through the width delaminations using a Rayleigh-Ritz approximation and Timoshenko type shear effects.

Furthermore, viscoelastic material property and failure condition data are generally very scattered and may require stochastic analyses (Hilton *et al.* 1991) including the possibility of independently random loads. Stochastic failure criteria under combined random loads have been formulated by Hilton & Feigen (1960) and by Hilton & Ariaratnam (1994). Multidimensional deterministic and stochastic delamination of plates has been considered respectively by Yi (1991) and by Hilton & Yi (1993). In the latter paper relationships of delamination onset probabilities to times of occurrence were predicted.

The phenomenon of stochastic delamination buckling combines the consequences of creep buckling, delamination, random material properties and temperatures, moistures and loads, and of failure (Hilton & Yi 1996). In the present paper, the effects of random failure criteria on delamination buckling are studied under deterministic loads, geometries, moduli, temperatures and moisture contents. This allows for an investigation, which focuses on random delamination failure criterion effects under otherwise deterministic conditions.

Viscoelastic failure stresses and moduli decrease in time, while column bending stresses, strains and deformations increase with time. Using the experimentally determined delamination probability distributions reported by Hiel *et al.* (1994) in conjunction with the combined load invariant stochastic failure criterion of Hilton & Ariaratnam (1994), probabilities of delamination onset occurrence as time functions are formulated and evaluated.

The expressed purpose of this investigation is to conduct a sensitivity analysis of deterministic and stochastic delamination onset conditions in composite columns. In order to isolate this phenomenon only the failure stresses will be considered random, while all other parameters such as geometry, temperature, moisture, applied loads, material properties (moduli) are deterministic. This approach, as will be seen subsequently, reduces the usual two failure conditions (Hilton 1952, Hilton & Ariaratnam 1994) to a single expression. The composite column no longer presents a simple homogeneous and isotropic Euler type stability problem, since it is subject to delamination failures in addition to instability. Furthermore, because its various ply orientations make up the

cross section, the composite column becomes non-homogeneous as well as anisotropic. The delamination onset criterion must account for the combined effects of bending, shear, compressive and normal interlaminar stress conditions of the column.

Large deformations and nonlinearities due the presence of follower loads combined with viscoelastic constitutive relations are considered in the present analysis and computer simulations. Fig. 1 illustrates the deflected column indicating the extent of the lateral deflections, end shortening and load rotations. Galerkins method is used for spatial considerations and the temporal solutions are based on a Runge-Kutta approach as well as a step-by-step time evaluation of the constitutive integrals. During the time that the column creeps and lateral deflections and consequently applied bending moments are increasing, material strength is decreasing.

Temperature effects manifest themselves in terms of (1) additional axial loads due to thermal expansions, (2) thermal stresses due to in-plane and/or longitudinal temperature gradients and (3) decreases in relaxation moduli with increasing temperatures. The first two conditions increase applied bending moments and, therefore, increase failure probabilities and decrease column survival times. Condition (3) further exacerbates the situation by increasing creep rates and, consequently, shortening columns life times and increasing failure probabilities.

Column failure will occur either through creep buckling or by exceeding in time the ever-decreasing failure stresses, thus introducing the additional concept and restraint of column life or survival time. Results show that large deflection linearly viscoelastic columns with quasi-static follower loads under quasi-static conditions exhibit smaller deflections, smaller probabilities of failure and longer survival times than identical columns under the same loads but with dynamic effects caused solely by creep included.

COLUMN BENDING ANALYSIS

Consider a linear isotropic viscoelastic prismatic column with large deflections subjected to external follower loads and thermal expansions due to temperatures $T(x_2, t)$. The reference system consists of Cartesian coordinates, $x = \{x_i\}, (i = 1, 2, 3)$ and an embedded coordinate $s(x_1, t)$ tangent to the deformed column mid-surface (Fig. 1). The Bernoulli-Euler prescriptions of plane sections remaining plane apply. Bending, compressive, tension, thermal and shear stresses will arise from the deformations. The column constitutive relations are

$$\begin{Bmatrix} \sigma_b(x, t) \\ \sigma_c(x, t) \\ \sigma_s(x, t) \end{Bmatrix} = \int_{-\infty}^t \left\{ E_b(\Xi) \ E_c(\Xi) \ E_s(\Xi) \right\} \begin{Bmatrix} \epsilon_b(x, t') \\ \epsilon_c(x, t') \\ \epsilon_s(x, t') \end{Bmatrix} dt' \quad (1)$$

where

$$\Xi = \Xi(x, t, t') = \Xi \left[x, t, t', T(x, t') \right] \quad (2)$$

and the relaxation moduli are

$$E_\beta(x, t) = E_{\infty\beta} + \sum_{n=1}^N E_{n\beta} \exp \left\{ \int_0^t \frac{-dt'}{\tau_{n\beta} [x, t', T(x, t')]} \right\} \quad \text{and} \quad E_{\infty\beta} + \sum_{n=1}^N E_{n\beta} = E_{0\beta} \quad (3)$$

with $(\beta = b, c, s)$ and where $E_{0\beta}$ are the corresponding elastic moduli.

The follower loads $F(t)$ are taken as normal to the column cross section of area A . This is essentially a 1-D spatial problem and the governing relations are

$$\underbrace{m \frac{\partial^2 w(s, t)}{\partial t^2}}_{\text{inertia force}} + \underbrace{\frac{\partial^2}{\partial s^2} \int_{-\infty}^t \int_A \overbrace{E_b [x_2, t, t', T(x_2, t')]}^{EI_{eff}(t, t')} x_2^2 dA \frac{\partial [\theta(s, t') - \theta_0(s)]}{\partial s} dt'}_{\text{internal viscoelastic resisting moment}} + \underbrace{[F(t) + N_T(t)] \frac{\partial^2 \{\cos [\theta(s, t)] w(s, t)\}}{\partial s^2}}_{\text{applied \& thermal load moment}} = - \underbrace{\frac{\partial^2 M_T}{\partial s^2}}_{\text{thermal moment}} \quad (4)$$

$$\frac{\partial w(s, t)}{\partial s} = \sin [\theta(s, t)] \quad \text{and} \quad \frac{dw_0(s)}{ds} = \sin [\theta_0(s)] \quad (5)$$

$$\frac{\partial x_1(s, t)}{\partial s} = \cos [\theta(s, t)] \quad (6)$$

Fig. 2 depicts temperature influences on relaxation moduli.

The initial imperfection $w_0(x_1)$ or $w_0(s)$ is prescribed *a priori* and with its associated angle θ_0 can both be expressed in terms of Fourier series as

$$w_0(s) = \sum_{m=1}^{\infty} w_{0m} \sin \frac{m \pi s}{L_0} \quad \theta_0(s) = \sum_{m=1}^{\infty} \theta_{0m} \sin \frac{m \pi s}{L_0} \quad (7)$$

whereas the actual deflection $w(s, t)$ and angle $\theta(s, t)$ are expressible by similar but more complicated series with sets of unknown coefficients and with the original length L_0 replaced by the instantaneous length $L_s^c(t)$ given by

$$L_s^c(t) = \int_0^t \int_0^{L_s^c(t')} \frac{F(t') + N_T(t')}{A} \cos [\theta(s', t')] J[s', t, t', T(0, t')] ds' dt' \quad \text{with} \quad \Delta L_s^c(t) \leq 0 \quad (8)$$

The length change $L_s^c(t)$ is due to compressive/tension loads and represents the distance along the column between its ends at the neutral axis. There is an additional component due to bending given by

$$\int_0^{L_1(t)} dx_1 = \int_0^{L_s^b(t)} \sqrt{1 - \left[\frac{dw(s,t)}{ds} \right]^2} ds \quad \text{with} \quad \Delta L_s^b(t) > 0 \quad (9)$$

The unloaded length due to the initial imperfection $w_0(s)$ is similarly given by

$$\int_0^{L_1^0} dx_1 = \int_0^{L_s^0} \sqrt{1 - \left[\frac{dw_0(s)}{ds} \right]^2} ds \quad \text{with} \quad \Delta L_s^0 > 0 \quad (10)$$

The thermal contributions are

$$N_T(t) = \int_{-\infty}^t \int_A E_c [x_2, t, t', T(x_2, t')] \alpha T(x_2, t') dA dt' \quad (11)$$

$$M_T(t) = \int_{-\infty}^t \int_A E_b [x_2, t, t', T(x_2, t')] \alpha T(x_2, t') x_2 dA dt' \quad (12)$$

If one column end is free to move in the x_1 -direction, then $N_T(t) = 0$. The thermal bending moment $M_T(t)$ is non zero only if the kernel of its integral is an odd function.

In order to keep the beam prismatic, the temperature distribution cannot vary in its axial x_1 -direction as material properties are considered temperature dependent. Since the expressed purpose of this study is to focus on the influence of viscoelastic material damping properties on dynamic column responses, the follower load and the temperature distribution are prescribed as time independent. This conditions effectively changes all integrals involving moduli or compliances to time convolution ones, such that

$$\int_{-\infty}^t E_\beta [x, t, t', T(x, t')] f_2(t') dt' = \int_{-\infty}^t E_\beta(x, \xi - \xi') f_2(\xi') d\xi' \quad (13)$$

with

$$\xi(x, t) = \int_0^t a_T [T(x, t')] dt' \quad (14)$$

where a_T is the temperature shift function and is a material property.

While this permits expressing viscoelastic material behavior in terms of master relaxation or compliance curves, it does not, however, allow the use of integral transforms (Laplace, Fourier, etc.) due to the nonlinear nature of the governing Eqs. (4) – (6).

Viscoelastic initial conditions (IC) correspond to elastic solutions $w^e(x_1, t)$ at $t = 0$ of equivalent problems with identical $F(t)$, $T(x, t)$ and boundary conditions at $s = 0, L_s$, but with time

independent elastic Young's moduli E^e . All elastic relations are then obtained from modification of all above ones by the removal of all time integrals.

FAILURE ANALYSIS

The classical creep buckling definition is

$$\lim_{t \rightarrow t_{cr}} \{w(x, t)\} \rightarrow \infty \quad \text{or} \quad \lim_{t \rightarrow t_{cr}^*} \left\{ \frac{\partial w(x, t)}{\partial t} \right\} \rightarrow \infty \quad (15)$$

However, Hilton (1952, 1961) and Kempner & Pohle (1953) have shown that small deflection linear viscoelasticity analysis results in finite deflections for $0 < t_{cr}, t_{cr}^* < \infty$. Consequently, alternate creep buckling definitions based on material failure criteria must be sought.

Viscoelastic failure criteria, such as ultimate stresses, degrade in time independently of relaxation moduli and failures may occur before or after any creep buckling instabilities manifest themselves. These are material failures which are independent of creep buckling and define the life time of the structure designated as t_{LF} . Consequently, t_{cr} or t_{cr}^* may be greater, smaller or equal than t_{LF} . Indeed, Gerard (1962), Hilton (1952) and Steinbacker & Gerard (1952) have used the Shanley & Ryder's (1937) interaction curve approach to estimate failures under combined inelastic deterministic stresses.

Some failure mechanisms observed in composites are substantially different from those observed in metals (Dillard & Brinson 1983, Hiel *et al.* 1991, Lifshitz & Rotem 1970, Phoenix 1979, Phoenix & Tierney 1982, Watson & Smith 1985). For example, delamination is a phenomenon unique to composites. From a design analysis point of view, one needs only to consider delamination onset because at that stage a structure has for all practical purposes failed, particularly if it is a light weight flight structure. Dillard & Brinson (1983) have formulated an expression for the temperature, moisture and time dependency of uniaxial composite failure stresses and Hilton & Yi (1993) have presented an extensive review of available experimental composite failure data. Using such data, they have formulated deterministic and stochastic delamination failure analyses. Experimental results indicate that uniaxial deterministic delamination onset stresses in tension and shear obey laws of the type

$$\sigma_{ij}^F(t) = \begin{cases} \sigma_{ij0}^F & -\infty \leq t \leq t_2^F \\ \sigma_{ij0}^F - D_{ij} \log(t/t_4^F) & t_2^F \leq t \leq t_3^F \\ 0 & t \geq t_3^F \end{cases} \quad (16)$$

where all parameters are material, temperature, moisture and load (tension, shear, etc.) dependent (Fig. 3).

Hilton & Ariaratnam (1994) developed deterministic and stochastic invariant combined load failure criteria in terms of two relations

$$\frac{1}{3} \sum_{i=1}^q \left[\frac{\tilde{J}_i(x, t)}{\mathcal{J}_i(x, t)} \right]^{c_i} = \tilde{V}(x, t) \quad (17)$$

$$\frac{1}{3} \sum_{i=1}^q \left[\frac{\tilde{\mathcal{J}}_i(x, t)}{\mathcal{J}_i(x, t)} \right]^{c_i} = \tilde{v}(x, t) \quad (18)$$

where $\tilde{\mathcal{J}}_i$, \mathcal{J}_i and c_i are mean values and random variables are indicated with a \sim . The upper summation limit q is the number uniaxial loads. Typical deterministic failure stress surfaces may be found in Hilton & Ariaratnam (1994), Hilton *et al.* (1997a). The applied and failure stress invariants are defined by

$$\tilde{\mathcal{J}}_1 = \tilde{\sigma}_{ii} \quad \tilde{\mathcal{J}}_2 = \tilde{\sigma}_{ij} \tilde{\sigma}_{ij} \quad \tilde{\mathcal{J}}_3 = \tilde{\sigma}_{ij} \tilde{\sigma}_{ik} \tilde{\sigma}_{kj} \quad (19)$$

$$\tilde{\mathcal{J}}_1 = \tilde{\mathcal{F}}_{ii} \quad \tilde{\mathcal{J}}_2 = \tilde{\mathcal{F}}_{ij} \tilde{\mathcal{F}}_{ij} \quad \tilde{\mathcal{J}}_3 = \tilde{\mathcal{F}}_{ij} \tilde{\mathcal{F}}_{ik} \tilde{\mathcal{F}}_{kj} \quad (20)$$

where \mathcal{F}_{ij} are uniaxial failure stresses.

Failure occurs whenever

$$\tilde{U}(x, t) = \tilde{V}(x, t) - \tilde{v}(x, t) \leq 0 \quad (21)$$

For deterministic applied loads and random failure stresses, or vice versa, one needs only to apply one probability density function (PDF) to either Eq. (17) or (18). Hiel *et al.* (1991) have reported experimental delamination data which can be represented by a Weibull type probability density function (PDF) (Weibull 1951). Upon integrating this PDF, one obtains the failure probability \tilde{P}_F as

$$\tilde{P}_F(x, t) = 1 - \exp \left\{ - \left[\frac{\tilde{U}(x, t)}{\kappa} \right]^\gamma \right\} \quad (22)$$

where the material property parameters γ and κ and their values were discussed in detail by Hiel *et al.* (1991) and Hilton and Yi (1993). Since for column problems the stresses σ_b , σ_n and σ_s are functions of x and t , it follows that the failure probabilities \tilde{P}_F are also dependent on position within the column and on time.

The time t_{LF} corresponding to the largest value of \tilde{P} at a point $x_i = c_i$ in a structure is the life time or survival time. It is defined by

$$\tilde{P}(c, t_{LF}) = \max \left\{ \tilde{P}(x, t) \right\} \leq 1 \quad (23)$$

In stochastic probabilistic structural failure analysis, one seeks similar points or regions where $\tilde{P}_F(x, t_{LF}) = 1$ or alternately the maximum probability value $\tilde{P}_F(x, t_{LF}) < 1$ to indicate column survival probabilities under a prescribed load $F(t) < F_E$, the Euler load, and a given initial imperfection $w_o(x_1)$. A similar but distinct class of problems arises from the imposition of the specification of design survival times t_{LFD} each corresponding to a design failure probability $\tilde{P}_{FD}(t_{LFD}) \leq 1$, or conversely the prescription of a t_{LFD} with an attendant $\tilde{P}_{FD}(t_{LFD})$.

It must, of course, be remembered that the four distinct times of Eqs. (15) and (23), namely t_{cr} , t_{cr}^* , t_{LF} and t_{LFD} , are unrelated and each represent distinct definitions of instability or failure conditions.

COMPUTATIONAL ISSUES

The viscoelastic governing relations (4) – (6), even in quasi-static or solely elastic configurations, are too complicated due to their nonlinear geometric nature to be reducible to analytical solutions and numerical protocols need to be applied. They consist of

- Reduction of spatial dependence through the application of collocation, Rayleigh-Ritz, Timoshenko, Galerkin or like methods (Hoff 1956).
- Subsequent solution of the time integral-differential relations by Runge-Kutta approaches.
- Alternately, finite element methods with numerical evaluation of the material property time integrals can be undertaken.
- The use of the elastic-viscoelastic analogy as described in Hilton (2002b) is prohibited due to the nonlinear nature of the governing relations.

The simultaneous solution of Eqs. (4) – (6) presents special difficulties, in particular due to the presence of the time integral in (4) which does not allow an analytical solution as is the case for the nonlinear viscoelastic column. A direct formal numerical approach necessitates the storage of all function values at all s points for all preceding times. This is obviously uneconomical in terms of computer storage as well as computational real time usage and other approaches must be sought.

In connection with viscoelastic finite element analyses, a number of step by step time approximations for the evaluation of convolution and of non-convolution integrals have been proposed by Taylor *et al.* (1970), Yi *et al.* (1993, 1994, 1999) and Zak (1968). These methods are summarized and compared by Hilton & Yi (1993). The advantage of these approaches is that only the previous time step needs to be retained for each time interval, thereby drastically reducing the needed computer memory and required computational time. The disadvantage lies in the close relation between accuracy and time step size. The accuracy can only be determined by varying the time step sizes and comparing results until “convergence” takes place. Yi & Hilton (1993, 1994) have developed recurrence relations which involve only the two previous time steps and yield solutions which are markedly more accurate than other methods.

Solution by Galerkin's method

Galerkin's method (Hoff 1956) consist of assuming expressions for the unknown functions with arbitrary coefficients where each term independently satisfies prescribed boundary conditions, such as for example

$$\theta(s, t) = \sum_{m=0}^M \Theta_m(t) F_m^\theta(s) \quad (24)$$

$$\frac{\partial w(s, t)}{\partial s} = \sin[\theta(s, t)] = \sum_{m=0}^M W_m(t) F_m^w(s) \quad (25)$$

$$\frac{\partial x(s, t)}{\partial s} = \cos[\theta(s, t)] = \sum_{m=0}^M X_m(t) F_m^x(s) \quad (26)$$

Each function $F_m^i(s)$ satisfies all BCs identically for all m without constraining any of the amplitude functions $\Theta_m(t)$, $W_m(t)$ and $X_m(t)$.

Introducing expressions (24) – (26) into Eqs. (4) – (6) and integrating each w.r.t. s over the length of the column according to the Galerkin or other aforementioned protocols eliminates the variable s and reduces the system of governing PDE relations to $3M$ simultaneous second order ordinary integral-differential relations in the unknown functions $\Theta_m(t)$, $W_m(t)$ and $X(t)$ which are amenable to solutions by finite difference approaches or Runge-Kutta methods.

Note from the discussion in the previous Section that the column lengths $L_s^c(t)$ and $L_1(t)$ of Eqs. (8) and (9) are part of the solution and are, of course, heavily influenced by the BCs.

DISCUSSION

In order to isolate dynamic effects solely due to viscoelastic material time responses, simulations studies were carried out on prismatic columns subjected to time independent follower loads³ and temperature distributions, i.e. $F = F_0$ and $T = T(x_2)$. Under such thermal conditions, the relaxation modulus is reduced to a non-homogenous material property function and the time integrals become convolution types, since now

$$E_b \left[x, t, t', T(x, t') \right] = E_b \left[x, t - t', T(x) \right] \quad (27)$$

Shear stresses due to bending produced by external and thermal moments but not by twist, given by

$$\sigma_s(x_1, x_2, t) = \int_{x_2}^c \frac{\partial \sigma_b(x_1, x'_2, t)}{\partial x_1} dx'_2 \quad (28)$$

are included. Previously, Beldica *et al.* (2004) have classified the types of temperature distributions producing thermal moments, and the relationship between thermal expansions and column end conditions in non-follower load columns. These relations apply equally here, except that the axial thermal loads, if present, are now considered as normal to the cross section and not parallel to the longitudinal x_1 -axis. (See Eq. (4).)

Material nonlinearity could also be added to problem definition through the relaxation time dependence on displacement or strain velocity, such that the relaxation moduli of Eqs. (3) become

³Note that by their very nature even though the follower end loads F_0 have time independent magnitudes, their directions normal to cross sectional column areas and hence tangent to $s(x_1, t)$ are time dependent as measured by the angle $\theta(x_1, t)$.

$$E_{\beta} = E_{\infty\beta} + \sum_{n=1}^N E_{n\beta} \exp \left\{ \int_0^t \frac{-dt'}{\tau_n \left[x, t', T(x, t'), \frac{\partial w(x, t')}{\partial t} \right]} \right\} \quad (29)$$

This would require an interactive solution protocol with instantaneous updating of material properties as deformations and their velocities change with time. In this paper, however, linear viscoelastic properties are considered and nonlinearities are introduced only through large deformations, follower loads and column length changes.

The time dependent relaxation moduli and hereditary constitutive relations (1) lead to creep and energy dissipation through changes in phase angles between stresses and strains which are distinct from their elastic counterparts. This phenomenon is readily discernible if one takes a Fourier transform (FT) of Eqs. (1) with $T(x)$ only, leading to

$$\begin{Bmatrix} \bar{\bar{\sigma}}_b(x, \omega) \\ \bar{\bar{\sigma}}_c(x, \omega) \\ \bar{\bar{\sigma}}_s(x, \omega) \end{Bmatrix} = \left\{ \bar{\bar{E}}_b(x, \omega) \bar{\bar{E}}_c(x, \omega) \bar{\bar{E}}_s(x, \omega) \right\} \begin{Bmatrix} \bar{\bar{\epsilon}}_b(x, \omega) \\ \bar{\bar{\epsilon}}_c(x, \omega) \\ \bar{\bar{\epsilon}}_s(x, \omega) \end{Bmatrix} \quad (30)$$

and compares them to the equivalent FT elastic ones

$$\begin{Bmatrix} \bar{\bar{\sigma}}_b^e(x, \omega) \\ \bar{\bar{\sigma}}_c^e(x, \omega) \\ \bar{\bar{\sigma}}_s^e(x, \omega) \end{Bmatrix} = \left\{ E_b^e(x) E_c^e(x) E_s^e(x) \right\} \begin{Bmatrix} \bar{\bar{\epsilon}}_b^e(x, \omega) \\ \bar{\bar{\epsilon}}_c^e(x, \omega) \\ \bar{\bar{\epsilon}}_s^e(x, \omega) \end{Bmatrix} \quad (31)$$

where

$$\bar{\bar{E}}_{\beta}(x, \omega) = E_{\infty\beta} + \sum_{n=1}^N \frac{E_{n\beta}}{i\omega + 1/\tau_{n\beta}(x)} \quad (32)$$

It is clearly seen in the above that elastic moduli, being time and frequency independent, do not cause stresses and strains to be out of phase *per se*. In the elastic case, only inertia terms will cause out of phase responses. In viscoelastic materials, on the other hand, stresses and strains will always be out of phase with each other because of the time variations of relaxation moduli, regardless whether the system is exposed to inertia forces.

Fig. 4 represents an extreme situation where dynamic deformation contributions are severe when compared to equivalent quasi-static ones. The oscillatory deformations are only due to material contributions and inertia effects, as loads and temperatures are time invariant. It must be remembered that the external energy supplied to the column and given by

$$\mathcal{E}_{ext}(t) = \int_0^t \int_0^{L^c(t')} F(t') \dot{w}(s, t') ds dt' \quad (33)$$

is essentially unlimited and produces an ever increasing column creep deflection due to the applied bending moment $M(s, t) = F(t) \cos[\theta(s, t)]w(s, t) > 0$, including when oscillatory amplitudes diminish in time. This leads to $\dot{w}(s, t) > 0$ for $0 \leq t \leq t_{cr}$. It is, of course, possible to impose prescribed temperature distributions such that resulting thermal moments $M_T(s, t)$ are of opposite sign to $M_{ext}(s, t)$, which helps to delay creep buckling by increasing t_{cr} . Additionally in order to maintain the same trend, the thermal load moment due to N_T must also be of opposite sign to M . However, during all this time the column continues to creep.

Independently of these creep buckling phenomena, viscoelastic failure properties degrade with time as seen in Fig. 3. This leads to the possibility that material failures may precede creep buckling as seen in Fig. 5 where $t_{ult} < t_{cr}$, as these two times bear no relations to each other. Once the column is loaded and the creep process is initiated, then it is a race to instability or failure to see which will occur first. With either event as long as the load F remains in place at some compressive magnitude, the viscoelastic column is doomed and its lifetime or survival time is finite.

Figs. 6 and 7 provide a measure of comparison between quasi-static and dynamic conditions at a number of operating temperatures. The results are based on the invariant failure criteria discussed in a previous Section and derived in detail in Hilton & Ariaratnam (1994). Probability of failure results are presented based on Weibull (1951) distribution of failure stresses with all other variables as deterministic. The first set of graphs indicates that when dynamic effects (inertia) are included in the column analysis, survival times are shortened and failure probabilities are increased when compared to equivalent quasi-static conditions. This should not be unexpected due to the oscillatory motion seen in Fig. 4.

The consequence of rising temperatures is the appearance of creep effects at earlier times and thus shorten the duration during which elastic moduli prevail ($E(t) = E_0$) as shown in Fig. 2. The result is to shorten lifetimes and increase failure probabilities, since relaxation moduli degrade sooner.

The severity of thermal stresses leading to bending generated by temperature distributions $T(x_2) = T_0 f(x_2)$ depends primarily on df/dx_2 with T_0 acting as an amplitude multiplier. However, independently additional follower thermal loads N_T are proportional to αT_0 , under proper boundary conditions. Consequently, thermal distributions affect column lifetimes in two distinct modes.

CONCLUSIONS

The following observations emerge from this study

- Increasing temperatures reduce column lifetimes and augment failure probabilities.
- Higher temperatures degrade relaxation moduli and failure properties earlier.

- Steady state temperature distributions with their attendant thermal stresses and longitudinal expansions are detrimental to column life.
- Time dependent temperatures may delay dynamic column lifetimes provided phase relationships are properly altered to dissipate additional energy.
- Viscoelastic columns with materials which are less sensitive to property degradations under combined loads will survive longer at lower failure probabilities.

REFERENCES

- Ashby, M. F., & Jones, D. H. (1986) *Engineering Materials*. Pergamon Press, New York.
- Bažant, Z. P., & Cedolin, L. (1991) *Stability of Structures – Elastic, Inelastic, Fracture and Damage Theories*. 584–632. Oxford University Press, New York.
- Beldica, C. E., Hilton, H. H., & Lobdell, T. (2004) “Thermal creep buckling of linear viscoelastic columns under piezoelectric control – probabilistic failures and survival times,” *Proceedings 45th AIAA/ASME/ASCE/AHS Structures, Structural Dynamics and Materials Conference, AIAA 2004-1746*, Palm Springs, CA.
- Bleich, F. (1952) *Buckling Strength of Metal Structures*. McGraw-Hill Book Co., New York.
- Chai, H., Knauss, W. G., & Babcock, C. D. (1983) “Observation of damage growth in compressively loaded laminates,” *Experimental Mechanics* **30**:329–337.
- Dillard, D. A., & Brinson, H. F. (1983) “A numerical procedure for predicting creep and delayed failures in laminated composites,” *Long Term Behavior of Composites, ASTM STP 813* (T. K. O’Brien, ed.), 23–37.
- Elishakoff, I., Li, Y., & Starnes, Jr., J. H. (2001) *Non-Classical Problems in the Theory of Elastic Stability*. Cambridge University Press, New York.
- Gerard, George (1962) *Introduction to Structural Stability Theory*. McGraw-Hill, New York.
- Hiel, C. C., Sumich, M., & Chappell, D. P. (1991) “A curved beam test specimen for determining the interlaminar tensile strength of a laminated composite,” *Journal of Composite Materials* **25**:854–868.
- Hilton, H. H. (1952) “Creep collapse of viscoelastic columns with initial curvature,” *Journal of the Aeronautical Sciences* **19**:844–846.
- Hilton, H. H., & Feigen, M. (1960) “Minimum weight analysis based on structural reliability,” *Journal of the Aero/Space Sciences* **27**:641–652.
- Hilton, H. H., Hsu, J. & Kirby, J. S. (1991) “Linear viscoelastic analysis with random material properties,” *Journal of Probabilistic Engineering Mechanics* **6**:57–69.

- Hilton, H. H., & Yi, S. (1993) Stochastic viscoelastic delamination onset failure analysis of composites, *Journal of Composite Materials* **27**:1097–1113.
- Hilton, H. H., & Ariaratnam, S. T. (1994) “Invariant anisotropic large deformation deterministic and stochastic combined load failure criteria,” *International Journal of Solids and Structures* **31**:3285–3293.
- Hilton, H. H., Yi, S. & Ruijun, T. (1994a) “Large deflections of linearly elastic and viscoelastic columns with follower loads,” *Recent Advances in Engineering Science, Proceedings of 31st Annual Technical Conference Society of Engineering Science*, (D. H. Allen and D. C. Lagoudas, eds.) 168, Texas A&M University, College Station.
- Hilton, H. H., & Yi, S. (1996) Stochastic delamination onset of large deformation elastic and viscoelastic columns with follower loads, *Proceedings Seventh International Conference on Applications of Statistics and Probability* (M. Lemaire, J. L. Favre and A. Mébarki, Eds.) **3**:1491–1495, A. A. Balkema, Rotterdam.
- Hilton, H. H., Yi, S., & Danyluk, M. J. (1997) “Probabilistic analysis of delamination onset in linear anisotropic elastic and viscoelastic composite columns,” *International Journal of Reliability Engineering & System Safety* **56**:237–248.
- Hilton, H. H. (2002a) “Dynamic creep buckling of linear viscoelastic columns including failure probabilities and survival times,” submitted to *AIAA Journal*. *Technical Report UILU-ENG 02-0503*, 58 pp. University of Illinois at Urbana-Champaign.
- Hilton, H. H. (2002b) “Probabilistic delamination onset analysis of nonlinear viscoelastic composite columns with large deformations,” *Proceedings 43rd AIAA/ASME/ASCE/AHS/ASC Structures. Structural Dynamics and Materials Conference, AIAA Paper 2002 – 1713*, AIAA, Renton, VA.
- Hoff, N. J. (1956) *The Analysis of Structures*. John Wiley & Sons, New York.
- Jahsman, W. E., & Field, F. A. (1962) “Comparison of theoretical and experimental creep buckling times of initially straight, centrally loaded columns,” *Journal of the Aerospace Sciences* **29**:431–433, 467.
- Jones, D. I. G. (2001) *Handbook of Viscoelastic Vibration Damping*. John Wiley & Sons, New York.
- Kachanov, L. M. (1988) *Delamination Buckling of Composite Materials*. Kluwer, Boston.
- Kim, W. C., Miller, T. C. & Dharan, C. K. (1992) “Strength of composite sandwich panels containing debonds,” *International Journal of Solids and Structures* **30**:211–223.
- Koiter, W. T. (1970) *Translation of the Stability of Elastic Equilibrium*. Management Information Services, Detroit.
- Libove, C. (1952) “Creep buckling of columns,” *Journal of the Aeronautical Sciences* **19**:459–467.

- Lifshitz, J. M., & Rotem, A. (1970) "Time-dependent longitudinal strength of unidirectional fibrous composites," *Fibre Science and Technology* **3**:1–20.
- Phoenix, S. L. (1979) "Statistical aspects of failure of fibrous materials," *Composite Materials: Testing and Design, ASTM STP 674*, (S. W. Tsai, Ed.), 455–483.
- Phoenix, S. L., & Tierney, L-J. (1982) "A statistical model for the time dependent failure of unidirectional composite materials under local elastic load-sharing among fibers," *Engineering Fracture Mechanics* **18**:193–215.
- Shanley, F. R., & Ryder, E. I. (1937) "Stress Ratios: The Answer to the Combined Loading Problem," *Aviation* **36**:28–29, 43, 66, 69–70.
- Shanley, F. R. (1946) "Inelastic column buckling," *Journal of the Aeronautical Sciences* **14**:261–268.
- Shanley, F. R. (1952) *Weight–Strength Analysis of Aircraft Structures*. McGraw-Hill, New York.
- Steinbacker, F. R., & Gerard, G. (1952) *Aircraft Structural Mechanics*. Pitman Publishing Co., New York.
- Suemasu, H. (1992) "Effects of multiple delaminations on compressive buckling behaviors of composite panels," *Journal of Composite Materials* **27**:1172–1193.
- Taylor, R. L., Pister, K. L., & Goudreau, G. L. (1970) "Thermomechanical analysis of viscoelastic solids," *International Journal for Numerical Methods in Engineering* **2**:45–59.
- Timoshenko, S. P. (1936) *Theory of Elastic Stability*. McGraw-Hill, New York.
- Vinson, J. R., & Sierakowski, R. T. (1987) *The Behavior of Structures Composed of Composite Materials*. Martinus Nijhoff Publishers, Boston.
- Watson, A. S. & Smith, R. L. (1985) "An examination of statistical theories for fibrous materials in the light of experimental data," *Journal of Materials Science* **20**:3260–3270.
- Weibull, W. (1951) "A statistical distribution function of wide applicability," *ASME Journal of Applied Mechanics*, **18**:293–297.
- Wilson, D. W., & Vinson, J. R. (1984) "Viscoelastic analysis of laminated plate buckling," *AIAA Journal* **22**:982–988.
- Wilson, D. W., & Vinson, J. R. (1985) "Viscoelastic buckling analysis of laminated composite columns," *Recent Advances in Composites in the United States and Japan, ASTM STP 864* (J. R. Vinson and M. Taya, Eds.), 368–383, ASTM, Philadelphia.
- Yi, S. (1991) "Thermoviscoelastic analysis of delamination onset and free edge response in epoxy matrix composite laminates," *AIAA-91-0962-CP*. (1993) *AIAA Journal* **32**:2320–2328.
- Yi, S., & Hilton, H. H. (1994) "Dynamic finite element analysis of viscoelastic composite plates in the time domain," *International Journal for Numerical Methods in Engineering*, **37**:4081–4096.

Yi, S., Ling, S. F., Ying, M., Hilton, H. H., & Vinson, J. R. (1999) "Finite element formulation for anisotropic coupled piezo-hygro-thermo-viscoelasto dynamic problems," *International Journal of Numerical Methods in Engineering*, **45**:1531–1546.

Zak, A. R. (1967) "Structural analysis of realistic solid propellant materials," *Journal of Spacecraft and Rockets* **5**:270–275.

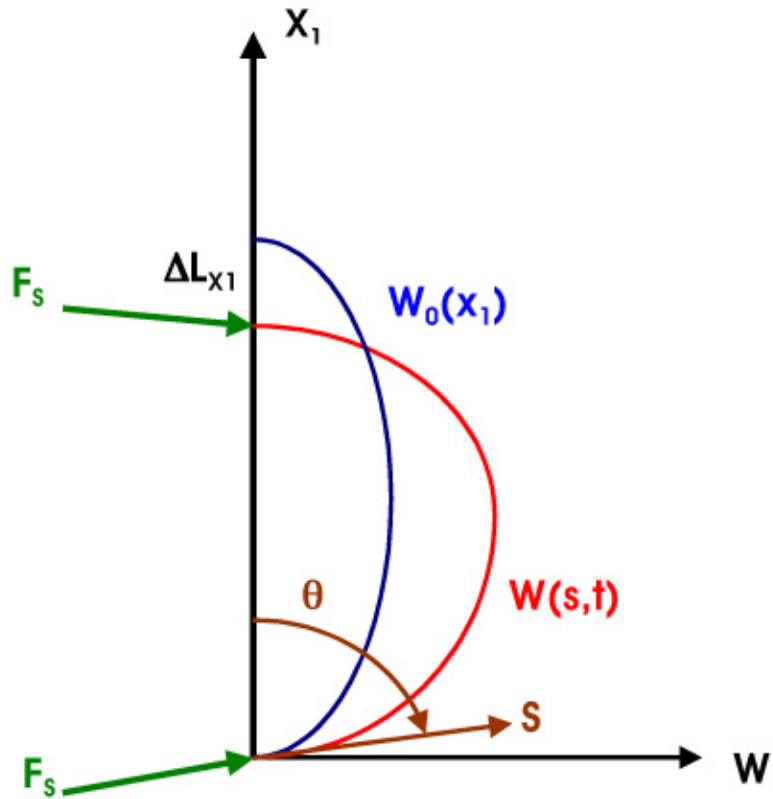


Fig. 1 - Column Deflection

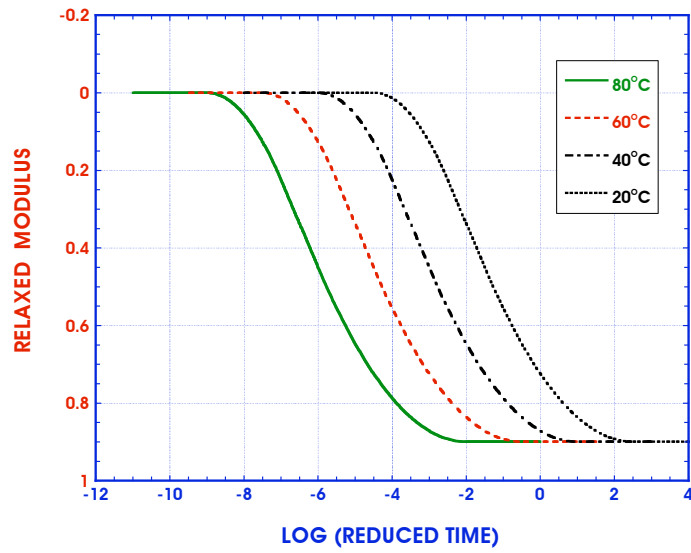
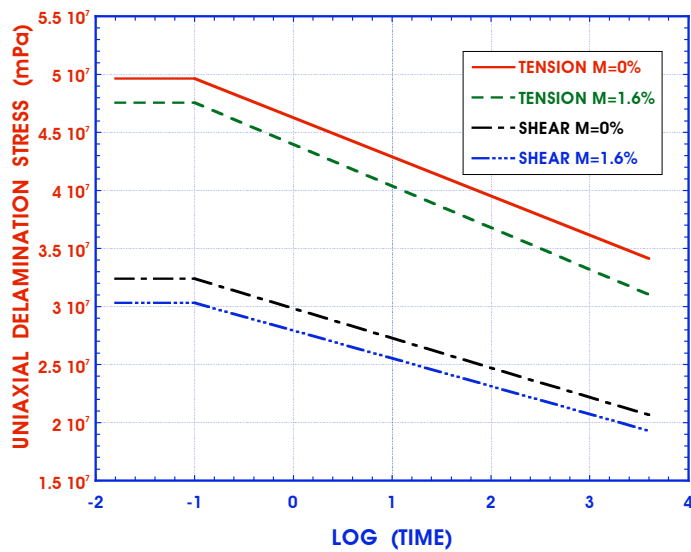


Fig. 2 - Relaxation Modulus and Temperature



**Fig. 3 - Uniaxial Delamination Strengths
(Dillard & Brinson 1983)**

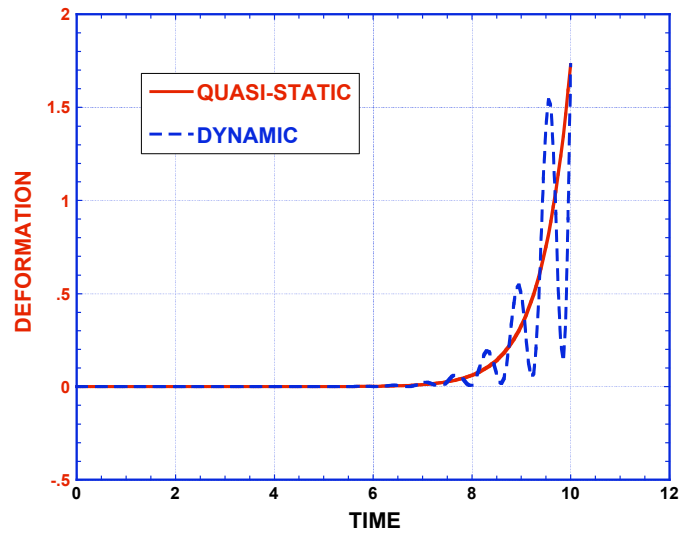


Fig. 4 - Column Deformation

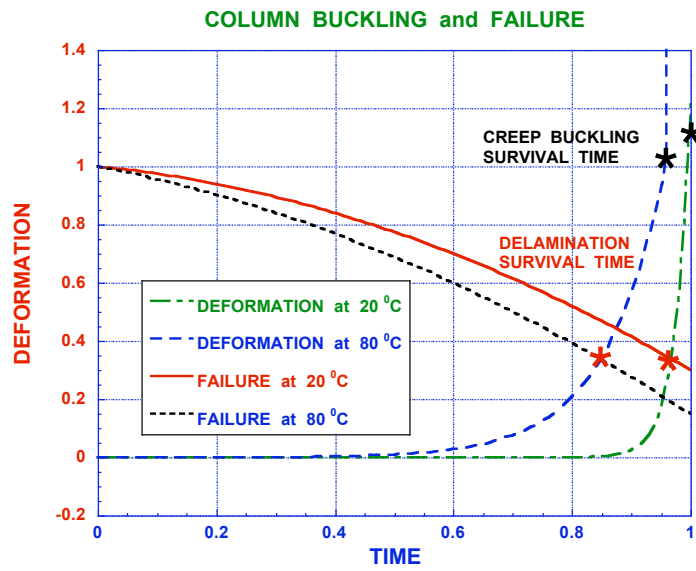


Fig. 5 - Creep Buckling and Failure

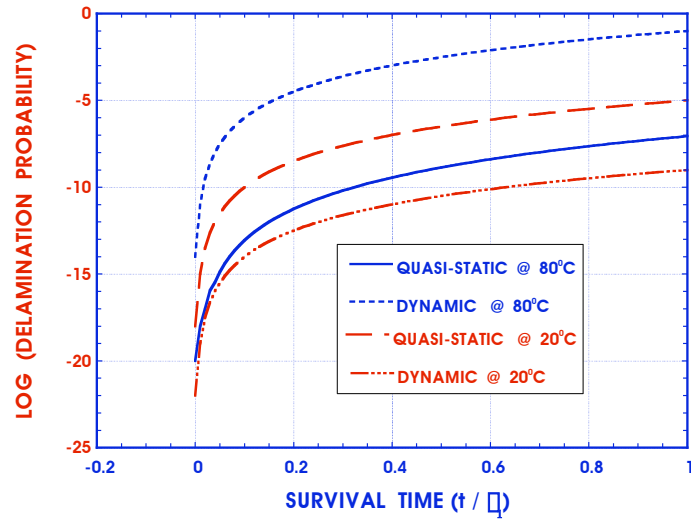


Fig. 6 - Delamination Probability for Quasi-Static and Dynamic Conditions

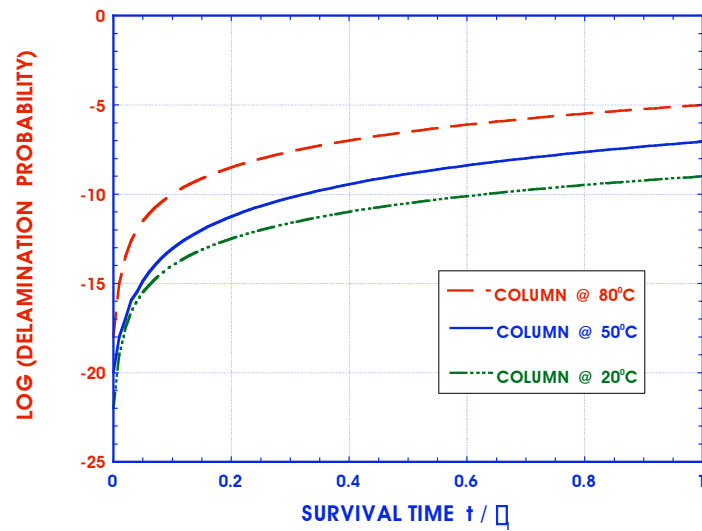


Fig. 7 - Delamination Probability and Survival Times

This page left blank intentionally.

Behavior of Composite Laminates and Sandwich Panels Subject to Compression and Fire

Victor Birman¹, George A. Kardomateas² and George J. Simitses²

Abstract

The problem of failure and residual properties of laminated composite structures subject to fire is of critical importance in aircraft and naval applications as well as in civil engineering. The effects of fire are multifaceted, including the heat transfer problem, a degradation of properties of the constituent phases, and structural strength and/or stability. All these problems are coupled making a comprehensive analysis particularly difficult. In the present paper, we analyze the response of cross-ply composite and sandwich panels subject to compression and fire applied at one of the surfaces. Two problems are considered and solved exactly, i.e. bending of a large aspect-ratio thin panel where geometrically nonlinear effects are present and bending of a shear-deformable finite aspect ratio panel where geometric nonlinearity can be disregarded. While the solution of the former problem is based on a quasi-static formulation neglecting time-dependent effects, the approach to the latter problem includes dynamic effects into the formulation. The solutions obtained in the paper present both deformations and stresses throughout the panels.

Introduction

In the present paper, we analyze the response of composite and sandwich panels subject to a simultaneous action of fire that occurs on one side of the panel and compressive stresses. The dynamic formulation of the heat transfer problem and the resin decomposition problem modeled by the Arrhenius equation has previously been developed (Gibson et al., 2004; Krysl et al., 2004). The solution of these coupled problems has to account both for the influence of resin decomposition on the thermal properties of the composite material as well as for the effect of the instantaneous local temperature on thermal properties. The outcome from the solution of this inherently nonlinear thermal problem includes a distribution of temperature as a function of time

¹ Engineering Education Center, University of Missouri-Rolla, One University Blvd., St. Louis, MO 63121; ² School of Aerospace Engineering, Georgia Institute of Technology, Atlanta, Georgia 30332-0150.

and position within the structure and a map of progressive decomposition of the matrix and core materials. Subsequently, a micromechanical theory can be employed to evaluate the instantaneous values of the matrices of extensional, coupling and bending stiffnesses i.e. $[A]$ $[B]$ and $[D]$.

A large number of studies of the behavior of composite structures subjected to an elevated temperature has been published since the seventieth, including the papers by Whitney and Ashton (1971), Chang and Allen (1988), Hamamoto and Hyer (1987), Meyers and Hyer (2002), Librescu et al. (1993), Nemeth (2001), Birman, (2004, 2005) and Birman et al. (2005). The problems considered in the present paper eliminate some of the simplifying assumptions employed in the previous studies and incorporate the boundary conditions that are rather typical in applications where in-plane displacements of the panel are not constrained by adjacent structures.

In the first problem considered in the paper, a large aspect ratio cross-ply panel was subject to compression along the short edges. The panel being symmetrically laminated about its middle plane, such compression does not cause bending and it is not sufficient to result in buckling or wrinkling instabilities. When elevated temperature due to fire is applied on one side of the panel, both the presence of thermally induced bending moments as well as the non-zero coupling stiffness generated as a result of a nonuniform through the thickness degradation of material properties cause bending. While the heat transfer problem is dynamic, the variations of temperature and resin content are assumed relatively slow compared to the period of vibrations of a typical composite or sandwich structure warranting the formulation of a quasi-static structural problem.

In the case of a thin laminated plate or a slender sandwich panel, the technical (thin-plate) geometrically nonlinear theory is sufficient for the analysis of large deformations and stresses. The solution of the nonlinear problem for a panel bending into the cylindrical surface is obtained exactly. The solution shown in this paper could also be generalized accounting for transverse shear deformations.

The second problem analyzed in the paper refers to a relatively thick finite aspect ratio composite or sandwich panel where transverse shear deformations have to be incorporated in the analysis. The solution is obtained using a geometrically linear formulation.

Analysis: Part 1. Thin large aspect ratio cross-ply composite or sandwich panels

Consider a large aspect ratio cross-ply composite or sandwich panel subjected to compression along short edges and fire (Fig. 1). The long edges $x = \pm \frac{a}{2}$ are assumed free to move in the x-direction, transmitting the applied compressive stress resultant N to the sandwich or composite structure (the solution for the case of edges immovable in the x-direction was considered by Birman, 2005). Temperature is uniformly distributed over the surface (it is independent of x and y coordinates), but it is nonuniform through the thickness of the plate resulting in thermally-induced property variations through the thickness. Accordingly, even if the panel was symmetrically laminated prior fire, it becomes asymmetric as a result of heating (and also, as a result of material decomposition). The distribution of temperature and properties through the thickness are assumed known.

As a result of combined effects of temperature, degradation of properties and compression, the panel bends in both xz and yz planes, contrary to the case of symmetrically laminated structures that form a cylindrical surface at a sufficient distance from the short edges. However, bending in the xz-plane is dominant, i.e. strains in the yz-plane can often be neglected. In this case, the formulation is simplified, i.e. the central sections of the panel deform similarly to a composite beam, although the stresses in the y-direction are present.

According to the previous discussion, the solution is obtained neglecting strains in the y-direction. The strain in the composite panel or in the facings of a sandwich panel that are assumed to be in the state of plane stress is composed of the contributions of the strain of the middle plane of the panel and the change of its curvature (both of them in the xz-plane):

$$\varepsilon_x = \varepsilon'_x + z\kappa_x \quad (1)$$

where

$$\varepsilon'_x = u^0_{,x} + \frac{1}{2} w_{,x}^2 \quad (2)$$

$$\kappa_x = -w_{,xx}$$

In these equations, u^0 is a displacement of the middle plane in the x-direction, w is a deflection of the panel, and $(\dots)_x = d(\dots)/dx$.

The stresses in the i -th specially laminated layer are given by

$$\begin{Bmatrix} \sigma_x \\ \sigma_y \end{Bmatrix}_i = \begin{bmatrix} Q_{11}(T_i) & Q_{12}(T_i) \\ Q_{12}(T_i) & Q_{22}(T_i) \end{bmatrix} \begin{Bmatrix} \varepsilon_x - \alpha_x(T_i) \\ -\alpha_y(T_i) \end{Bmatrix} \quad (3)$$

where $Q_{mn}(T_i)$ and $\alpha_p(T_i)$ are transformed reduced stiffnesses and the coefficients of thermal expansion, respectively, evaluated at the temperature of the layer.

The stress resultant and stress couple acting in the xz-plane are

$$\begin{aligned} N_x &= A_{11}\varepsilon'_x + B_{11}\kappa_x - N_x^T \\ M_x &= B_{11}\varepsilon'_x + D_{11}\kappa_x - M_x^T \end{aligned} \quad (4)$$

In these equations, A_{11} , B_{11} , D_{11} are the extensional, coupling, and bending stiffnesses introduced according to the standard definition (the engineering constants employed to evaluate these stiffnesses are affected by temperature). The thermally induced stress resultant and stress couple in (4) are

$$\{N_x^T, M_x^T\} = \int_{-h/2}^{h/2} [Q_{11}(T(z))\alpha_x(T(z)) + Q_{12}(T(z))\alpha_y(T(z))] (z) \{1, z\} dz \quad (5)$$

where h is the total thickness of the panel.

The equations of equilibrium of a panel bent into the cylindrical surface are

$$\begin{aligned} N_{x,x} &= 0 \\ M_{x,xx} + N_x w_{,xx} &= 0 \end{aligned} \quad (6)$$

The substitution of (2) and (4) into (6) yields

$$\begin{aligned} A_{11}(u^0_{,xx} + w_{,x} w_{,xx}) - B_{11} w_{,xxx} &= 0 \\ D_{11} w_{,xxxx} - B_{11}(u^0_{,xxx} + (w_{,x} w_{,xx})_{,x}) - N_x w_{,xx} &= 0 \end{aligned} \quad (7)$$

The substitution of the axial displacement from the first equation into the second equation (7) yields a linear differential equation

$$\left(D_{11} - \frac{B_{11}^2}{A_{11}} \right) w_{,xxxx} - N_x w_{,xx} = 0 \quad (8)$$

The solution of this equation is

$$w = K_0 + K_1 x + K_2 \sin \eta x + K_3 \cos \eta x \quad (9)$$

where K_i are constants of integration and

$$\eta = \sqrt{\frac{|N|}{D_{11} - B_{11}^2 / A_{11}}} \quad (10)$$

The requirement that deflections must be symmetric with respect to $x = 0$ yields $K_1 = K_2 = 0$. Subsequently, applying the requirement that deflections are zero at the edges, we obtain

$$w = K_3 \left(\cos \eta x - \cos \frac{\eta a}{2} \right) \quad (11)$$

This result is substituted into the first equation (7) yielding

$$u = K_4 + K_5 x - \frac{B_{11}}{A_{11}} K_3 \eta \sin \eta x + \frac{K_3 \eta}{8} \sin 2\eta x \quad (12)$$

The antisymmetry requirement for axial displacements implies that $K_4 = 0$.

It remains to determine two constants of integration, i.e. K_3, K_5 . They can be found from the conditions

$$\begin{aligned} M_x \left(\frac{a}{2} \right) &= 0 \\ N_x \left(\frac{a}{2} \right) &= N \end{aligned} \quad (13)$$

In case where the long edges of the panel are prevented from axial displacements, the stress resultant N_x is not known in advance and the second boundary condition in (13) is replaced with $u \left(\frac{a}{2} \right) = 0$. An additional condition has to be satisfied, implying that the axial stress resultant, while remaining independent of the x-coordinate, is defined by a degree of stretching of the middle plane, i.e. for a thin panel,

$$N_x = N_x^T - \frac{1}{a} \left(A_{11} \int_0^a (u^0_{,x} + \frac{1}{2} w_{,x}^2) dx - B_{11} \int_0^a w_{,xx} dx \right) \quad (14)$$

Details of this solution are presented for geometrically nonlinear in the recent paper (Birman, et al., 2005). As is shown in this paper, it is also possible to account for transverse shear deformations. The corresponding solution incorporating both transverse shear deformation and the effect of geometric nonlinearity yields the following results for axial and transverse displacements and for the rotation in the xz-plane:

$$u^0 = C'_5 + C'_6 x + \frac{B_{11}}{A_{11}} \left(1 + \frac{N_x}{A_{55}} \right) \left(C'_2 \sqrt{\lambda} \cosh \sqrt{\lambda} x + C'_3 \sqrt{\lambda} \sinh \sqrt{\lambda} x - \frac{\eta}{\lambda} C'_4 \right) - F(C'_2, C'_3, C'_4)$$

$$w = C'_1 + C'_2 \sinh \sqrt{\lambda} x + C'_3 \cosh \sqrt{\lambda} x - \frac{\eta C'_4}{\lambda} x \quad (15)$$

$$\psi = - \left(1 + \frac{N_x}{A_{55}} \right) w_{,x} + C'_4$$

where $F(C'_2, C'_3, C'_4)$ is a nonlinear function of constants of integration. The constants of integration are related to the axial stress resultant by a counterpart of (14):

$$N_x = N_x^T - \frac{1}{a} \left(A_{11} \int_0^a (u^0_{,x} + \frac{1}{2} w_{,x}^2) dx + B_{11} \int_0^a \psi_{,x} dx \right) \quad (16)$$

Six boundary conditions employed to evaluate the constants of integration in case of immovable edges are:

$$x = \pm \frac{a}{2} :$$

$$u^0 = w = 0$$

$$M_x = B_{11} (u^0_{,x} + \frac{1}{2} w_{,x}^2) + D_{11} \psi_{,x} - M_x^T = 0 \quad (17)$$

Analysis: Part 2. Dynamic problem for a finite aspect ratio shear deformable geometrically linear composite or sandwich panel subject to compression and fire

The analysis is conducted by the first-order shear deformation theory that was shown accurate in the problems of global deformations of composite and sandwich structures. The solution shown here for a sandwich panel employs standard assumptions of the technical theory for such structures, neglecting transverse shear in thin facings that

are in the state of plane stress, while assuming that the core is capable of resisting transverse shear stresses only. In the case of a shear deformable composite panel, the following solution is also applicable and the constitutive relations have to employ engineering constants of the layers of the panel. Contrary to the previous section, in the case of a finite aspect ratio panel, the strains in both xz and yz planes have to be considered. The panel and the coordinate system employed in the analysis are shown in Fig. 1.

The strain-displacement relations in an arbitrary laminated layer of the facings is

$$\begin{aligned}\varepsilon_x &= u^0_{,x} + z\varphi_{x,x} \\ \varepsilon_y &= v^0_{,y} + z\varphi_{y,y} \\ \gamma_{xy} &= u^0_{,y} + v^0_{,x} + z(\varphi_{x,y} + \varphi_{y,x})\end{aligned}\quad (18)$$

where u^0 and φ_x are the displacement at the middle plane in the x-direction and the rotation of the normal to the middle plane in the xz-plane, respectively, while v^0 and φ_y are the displacement at the middle plane in the y-direction and the rotation of the normal to the middle plane in the yz-plane, respectively.

Transverse shear strains in the core are

$$\begin{aligned}\gamma_{xz} &= w_{,x} + \varphi_x \\ \gamma_{yz} &= w_{,y} + \varphi_y\end{aligned}\quad (19)$$

The stresses in the i-th layer of the facings are

$$\begin{Bmatrix} \sigma_x \\ \sigma_y \\ \tau_{xy} \end{Bmatrix}_i = \begin{bmatrix} Q_{11}(t) & Q_{12}(t) & Q_{16}(t) \\ Q_{12}(t) & Q_{22}(t) & Q_{26}(t) \\ Q_{16}(t) & Q_{26}(t) & Q_{66}(t) \end{bmatrix}_i \begin{Bmatrix} \varepsilon_x - \alpha_x(t)T(t) \\ \varepsilon_y - \alpha_y(t)T(t) \\ \gamma_{xy} - \alpha_{xy}(t)T(t) \end{Bmatrix}_i \quad (20)$$

where Q_{kl} are transformed reduced stiffnesses of the layer that vary with time reflecting gradual degradation of material exposed to the effect of fire, α_k are the coefficients of thermal expansion that may be affected by temperature (therefore, they are functions of time), and T is an increase of temperature over the reference value. Note that in cross-ply facings, $Q_{16} = Q_{26} = \alpha_{xy} = 0$.

The stresses in the core can be determined as

$$\begin{Bmatrix} \tau_{yz} \\ \tau_{xz} \end{Bmatrix} = \begin{bmatrix} Q_{44}(t) & Q_{45}(t) \\ Q_{45}(t) & Q_{55}(t) \end{bmatrix} \begin{Bmatrix} \gamma_{yz} \\ \gamma_{xz} \end{Bmatrix} \quad (21)$$

where $Q_{45} = 0$ if the core is isotropic.

The stress resultants and stress couples can now be evaluated. Notably, even if the sandwich structure was symmetric relative to the middle plane prior to fire, the symmetry is lost as a result of nonuniform property degradation during fire. Accordingly, all terms must be retained in the matrices of extensional $[A]$, coupling $[B]$, and bending $[D]$ stiffnesses. The stress resultants and couples are

$$\begin{aligned} \begin{Bmatrix} N_x(t) \\ N_y(t) \\ N_{xy}(t) \end{Bmatrix} &= \begin{bmatrix} A_{11}(t) & A_{12}(t) & A_{16}(t) \\ A_{12}(t) & A_{22}(t) & A_{26}(t) \\ A_{16}(t) & A_{26}(t) & A_{66}(t) \end{bmatrix} \begin{Bmatrix} u^0_{,x} \\ v^0_{,y} \\ u^0_{,y} + v^0_{,x} \end{Bmatrix} + \\ &\begin{bmatrix} B_{11}(t) & B_{12}(t) & B_{16}(t) \\ B_{12}(t) & B_{22}(t) & B_{26}(t) \\ B_{16}(t) & B_{26}(t) & B_{66}(t) \end{bmatrix} \begin{Bmatrix} \varphi_{x,x} \\ \varphi_{y,y} \\ \varphi_{x,y} + \varphi_{y,x} \end{Bmatrix} - \begin{Bmatrix} N_x^T(t) \\ N_y^T(t) \\ N_{xy}^T(t) \end{Bmatrix} \\ \begin{Bmatrix} M_x(t) \\ M_y(t) \\ M_{xy}(t) \end{Bmatrix} &= \begin{bmatrix} B_{11}(t) & B_{12}(t) & B_{16}(t) \\ B_{12}(t) & B_{22}(t) & B_{26}(t) \\ B_{16}(t) & B_{26}(t) & B_{66}(t) \end{bmatrix} \begin{Bmatrix} u^0_{,x} \\ v^0_{,y} \\ u^0_{,y} + v^0_{,x} \end{Bmatrix} + \\ &\begin{bmatrix} D_{11}(t) & D_{12}(t) & D_{16}(t) \\ D_{12}(t) & D_{22}(t) & D_{26}(t) \\ D_{16}(t) & D_{26}(t) & D_{66}(t) \end{bmatrix} \begin{Bmatrix} \varphi_{x,x} \\ \varphi_{y,y} \\ \varphi_{x,y} + \varphi_{y,x} \end{Bmatrix} - \begin{Bmatrix} M_x^T(t) \\ M_y^T(t) \\ M_{xy}^T(t) \end{Bmatrix} \\ \begin{Bmatrix} Q_y(t) \\ Q_x(t) \end{Bmatrix} &= k \begin{bmatrix} A_{44}(t) & A_{45}(t) \\ A_{45}(t) & A_{55}(t) \end{bmatrix} \begin{Bmatrix} w_{,y} + \varphi_y \\ w_{,x} + \varphi_x \end{Bmatrix} \end{aligned} \quad (22)$$

where k is the shear correction factor. Although equations (22) are well known, the difference from the typical form of such equations is related to the fact that the elements of the stiffness matrices and thermally induced contributions to stress resultants and stress couples are functions of time. Accordingly, the vectors in the left side of these equations are also time-dependent. The elements of the matrices of extensional, coupling and bending stiffnesses are defined by standard equations.

Thermal contributions to stress resultants and stress couples are

$$\begin{aligned}
\begin{Bmatrix} N_x^T(t) \\ N_y^T(t) \\ N_{xy}^T(t) \end{Bmatrix} &= \int_z \begin{bmatrix} Q_{11}(t) & Q_{12}(t) & Q_{16}(t) \\ Q_{16}(t) & Q_{22}(t) & Q_{26}(t) \\ Q_{16}(t) & Q_{26}(t) & Q_{66}(t) \end{bmatrix} \begin{Bmatrix} \alpha_x(t) \\ \alpha_y(t) \\ \alpha_{xy}(t) \end{Bmatrix} T(t) dz \\
\begin{Bmatrix} M_x^T(t) \\ M_y^T(t) \\ M_{xy}^T(t) \end{Bmatrix} &= \int_z \begin{bmatrix} Q_{11}(t) & Q_{12}(t) & Q_{16}(t) \\ Q_{16}(t) & Q_{22}(t) & Q_{26}(t) \\ Q_{16}(t) & Q_{26}(t) & Q_{66}(t) \end{bmatrix} \begin{Bmatrix} \alpha_x(t) \\ \alpha_y(t) \\ \alpha_{xy}(t) \end{Bmatrix} zT(t) dz
\end{aligned} \tag{23}$$

where the integration is carried out through the thickness of the facings.

The equations of motion can now be formulated. For the first-order shear deformation theory utilized in this study such equations are well known (see for example, Reddy, 2004):

$$\begin{aligned}
N_x(t)_{,x} + N_{xy}(t)_{,y} &= I_0 \ddot{u}^0 + I_1(t) \ddot{\varphi}_x \\
N_{xy}(t)_{,x} + N_y(t)_{,y} &= I_0 \ddot{v}^0 + I_1(t) \ddot{\varphi}_y \\
Q_x(t)_{,x} + Q_y(t)_{,y} + N_{w,xx} &= I_0(t) \ddot{w} \\
M_x(t)_{,x} + M_{xy}(t)_{,y} - Q_x(t) &= I_1 \ddot{u}^0 + I_2(t) \ddot{\varphi}_x \\
M_{xy}(t)_{,x} + M_y(t)_{,y} - Q_y(t) &= I_1 \ddot{v}^0 + I_2(t) \ddot{\varphi}_y
\end{aligned} \tag{24}$$

The coefficients at the inertial terms are $I_i(t) = \int_z \rho(t) z^i dz$ where ρ is a mass density.

Naturally, the dependence of the inertial coefficients on time reflects the process of material degradation and its conversion into char in the case of fire.

The substitution of constitutive equations (22) yields the system of equations of motion in terms of displacements. This system usually cannot be integrated analytically, even if the problem is static. However, an important practical case is found in cross-ply composite panels and in sandwich panels with cross-ply facings. It is easy to show that in this case

$$A_{16}(t) = A_{26}(t) = A_{45}(t) = B_{16}(t) = B_{26}(t) = D_{16}(t) = D_{26}(t) = 0, \quad N_{xy}^T(t) = M_{xy}^T(t) = 0 \tag{25}$$

If the conditions (25) are satisfied, the equations of motion in terms of displacements can be written as an expansion of the corresponding equations for a laminate with constant stiffness matrices (Reddy, 2004). For simplicity, the stiffness, thermal and inertial terms are shown in the following equations without a reference to their dependence on time, i.e. $A_{ij}(t) \rightarrow A_{ij}$, $N_i^T(t) \rightarrow N_i^T$, $I_i(t) \rightarrow I_i$, etc. Accordingly,

$$\begin{aligned}
& A_{11}u^0_{,xx} + A_{12}v^0_{,xy} + A_{66}(u^0_{,yy} + v^0_{,xy}) + B_{11}\varphi_{x,xx} + B_{12}\varphi_{y,xy} + B_{66}(\varphi_{x,yy} + \varphi_{y,xy}) - N^T_{x,x} = \\
& I_0\ddot{u}^0 + I_1\ddot{\varphi}_x \\
& A_{22}v^0_{,yy} + A_{12}u^0_{,xy} + A_{66}(u^0_{,xy} + v^0_{,xx}) + B_{22}\varphi_{y,yy} + B_{12}\varphi_{x,xy} + B_{66}(\varphi_{x,xy} + \varphi_{y,xx}) - N^T_{y,y} = \\
& I_0\ddot{v}^0 + I_1\ddot{\varphi}_y \\
& kA_{55}(w_{,xx} + \varphi_{x,x}) + kA_{44}(w_{,yy} + \varphi_{y,y}) + Nw_{,xx} = I_0\ddot{w} \\
& B_{11}u^0_{,xx} + B_{12}v^0_{,xy} + B_{66}(u^0_{,yy} + v^0_{,xy}) + D_{11}\varphi_{x,xx} + D_{12}\varphi_{y,xy} + D_{66}(\varphi_{x,yy} + \varphi_{y,xy}) - \\
& kA_{55}(w_{,x} + \varphi_x) - M^T_{x,x} = I_1\ddot{u}^0 + I_2\ddot{\varphi}_x \\
& B_{22}v^0_{,yy} + B_{12}u^0_{,xy} + B_{66}(u^0_{,xy} + v^0_{,xx}) + D_{22}\varphi_{y,yy} + D_{12}\varphi_{x,xy} + D_{66}(\varphi_{x,xy} + \varphi_{y,xx}) - \\
& kA_{44}(w_{,y} + \varphi_y) - M^T_{y,y} = I_1\ddot{v}^0 + I_2\ddot{\varphi}_y
\end{aligned} \tag{26}$$

The analytical solution can be obtained by specifying the boundary conditions. In the present problem, the panel is assumed simply supported along all boundaries. The boundaries do not constrain in-plane displacements in the direction perpendicular to the corresponding edge. Such conditions are often found in applications where the panel is not supported by adjacent panels in the same plane. Mathematically, the conditions outlined above imply:

$$\begin{aligned}
x = 0, x = a : \quad & w = N_x = M_x = 0 \\
y = 0, y = b : \quad & w = N_y = M_y = 0
\end{aligned} \tag{27}$$

The solution can be obtained by representing the distribution of temperature within the panel in double Fourier series, i.e.

$$T(x, y, z, t) = \sum_{m,n} T_{mn}(z, t) \sin \frac{m\pi x}{a} \sin \frac{n\pi y}{b} \tag{28}$$

Using temperature given by (28), it is now possible to represent thermal loading terms in the form of double Fourier series, i.e.

$$\begin{aligned}
N^T_x &= \sum_{m,n} N_{xmn}(t) \sin \frac{m\pi x}{a} \sin \frac{n\pi y}{b} \\
N^T_y &= \sum_{m,n} N_{ymn}(t) \sin \frac{m\pi x}{a} \sin \frac{n\pi y}{b} \\
M^T_x &= \sum_{m,n} M_{xmn}(t) \sin \frac{m\pi x}{a} \sin \frac{n\pi y}{b} \\
M^T_y &= \sum_{m,n} M_{ymn}(t) \sin \frac{m\pi x}{a} \sin \frac{n\pi y}{b}
\end{aligned} \tag{29}$$

Displacements and rotations that can be sought in the form

$$\begin{aligned}
 u &= \sum_{m,n} U_{mn}(t) \cos \frac{m\pi x}{a} \sin \frac{n\pi y}{b} & v &= \sum_{m,n} V_{mn}(t) \sin \frac{m\pi x}{a} \cos \frac{n\pi y}{b} \\
 w &= \sum_{m,n} W_{mn}(t) \sin \frac{m\pi x}{a} \sin \frac{n\pi y}{b} & \varphi_x &= \sum_{m,n} P_{mn}(t) \cos \frac{m\pi x}{a} \sin \frac{n\pi y}{b} \\
 \varphi_y &= \sum_{m,n} R_{mn}(t) \sin \frac{m\pi x}{a} \cos \frac{n\pi y}{b}
 \end{aligned} \tag{30}$$

It is easy to check by substitution that thermal loads and displacements given by (29) and (30) satisfy all boundary conditions of the problem.

The substitution of (29) and (30) into equations of motion (26) yields a system of five equations with respect to time-dependent amplitudes for each harmonic of motion:

$$[I(t)] \{f_{mn}(t)\}_{tt} + [K(t)]_{mn} \{f_{mn}(t)\} = \{F_{mn}(t)\} \tag{31}$$

where the vector of displacements is

$$\{f_{mn}(t)\} = \{U_{mn}(t), V_{mn}(t), W_{mn}(t), P_{mn}(t), R_{mn}(t)\}^T \tag{32}$$

The matrix of inertial coefficients is

$$I(t) = \begin{bmatrix} I_0(t) & 0 & 0 & I_1(t) & 0 \\ 0 & I_0(t) & 0 & 0 & I_1(t) \\ 0 & 0 & I_0(t) & 0 & 0 \\ I_1(t) & 0 & 0 & I_2(t) & 0 \\ 0 & I_1(t) & 0 & 0 & I_2(t) \end{bmatrix} \tag{33}$$

The symmetric matrix of the time-dependent stiffness coefficients $[K(t)]_{mn}$ is omitted for brevity.

The vector of loading thermal terms in the right side of (28) is

$$\{F_{mn}(t)\} = -\{n'N_{xmn}(t), n'N_{ymn}(t), 0, m'M_{xmn}(t), n'M_{ymn}(t)\}^T \tag{34}$$

where $m' = \frac{m\pi}{a}$, $n' = \frac{n\pi}{b}$.

The integration of the system of five equations of motion (31) should be conducted by one of the initial value methods, such as the Runge-Kutta method, using zero initial conditions.

Numerical results and discussion

Numerical results for large aspect ratio panels with long edges restrained against displacements in the x-direction were obtained both for thin and for shear deformable sandwich structures. The properties of cross-ply graphite/epoxy facings and two grades of the 20mm thick core (Divinycell H45 and H60) are presented in the paper by Birman et al. (2005). Two facing thicknesses were considered in examples, i.e. $h_f = 2.5mm$ and $h_f = 5.0mm$. The temperature of air on the colder surface of the panel was assumed to be 20°C. The results obtained accounting for a degradation of the properties of the facing and core material reported in literature (Kulkarni and Gibson, 2004; Elkin, 2004) reflect the effect of stretching of the middle plane of the panel as it experiences increasing thermally-induced deformations. As a result of this stretching, the in-plane axial reaction of the immovable edges decreases with a higher surface temperature (Fig. 2 and Table 1). It is interesting to note that the stiffness of the panel has a relatively small effect on the axial restraint at the immovable edge.

A typical panel experienced a reversal of deformations and stresses as temperature of the exposed surface increased. This situation is depicted in Fig. 3 illustrating maximum deflections of a representative panel with long edges completely restrained against in-plane displacements as a function of the exposed surface temperature. Note that the phenomenon of the reversal of deformations as the exposed surface temperature increases was also reported by Meyers and Hyer (1992) who analyzed deflections of a composite panel subject to a linearly distributed through the thickness temperature. A recent experimental paper of Lattimer et al. (2004) who considered deformations of sandwich panels subjected to fire also supports the observations in the present paper. The reversal of deflections occurs even before temperature reaches the glass transition value for the matrix material of the facings.

The results shown in Figs. 4 and 5 refer to deformations and stresses in a square plain-woven glass/polyester panel with the boundaries that are not constrained against in-plane displacements (Part 2 of the analysis shown above). The material data has been adopted from the paper of Gibson et al. (2004). The plates were subject to a compressive load along the x-axis equal to 20% of the static buckling value (Fig. 4) or increasing in increments to 95% of this value (Fig. 5). It is interesting to consider the results shown in

Fig. 5 that illustrate a small change in stresses, even as the compressive load increases from zero to 95% of the buckling value. The factors contributing to the stress include bending due to fire, a degradation of material properties associated with the exposure to fire, and directly applied compressive stresses. As a result of the combination of these factors there is a relatively small increase in compressive stresses on the surface exposed to fire as the compressive load increases. On the colder surface, the stresses remain tensile, reflecting a dominant bending effect.

It is emphasized that the loss of strength is only one possible failure mode for sandwich panels subjected to a combination of compressive and thermal loads (the latter loads include those generated by fire). Another possible mode of failure is wrinkling of one of the facings. This phenomenon has to be analyzed, accounting for temperature-induced property degradation of the facings and the core. Accordingly, it is often impossible to predict in advance which of two facings will actually wrinkle first. An example of the analysis illustrating the wrinkling stress in a quasi-isotropic E-glass vinyl-ester facing supported by Divinycell H60 is shown in Fig. 6 (Birman, 2005). As follows from this figure, the analysis neglecting the effect of temperature on the properties of the facings and core produces inadequate and unconservative predictions of the wrinkling stress. Moreover, as a result of the loss of stiffness due to elevated temperatures, wrinkling may become the dominant mode of failure in sandwich panels where it does not represent danger at room temperature.

Conclusions

The paper presents a comprehensive methodology of the structural analysis of composite and sandwich panels subject to compression and fire, accounting for geometrically nonlinear deformations, a degradation of the properties due to an elevated temperature, and the effect of the resin decomposition. The solutions for real-time deformations and stresses shown in the paper can be effortlessly introduced into design of composite and sandwich panels. The ultimate outcomes from the solution are a predicted life for the structure subjected to compression and elevated temperature or fire and/or real-time and residual strength and stiffness of such structure.

One of the important conclusions from the analysis is the necessity to account for a degradation of material properties in composite and sandwich structures as a result of their exposure to fire. This may result in a rather unexpected behavior of the structure, affecting both deformations and stresses. Therefore, “conventional” wisdom should not be applied to predicting the effect of fire on composite structures.

Acknowledgement: The financial support of the Office of Naval Research, Grant N00014-03-1-0189, and the interest and encouragement of the Grant monitor, Dr. Luise Couchman, is gratefully acknowledged. The authors would also like to acknowledge Mr. Renfu Li who generated some of the numerical results.

References

Birman, V., 2004. “Thermomechanical Wrinkling in Sandwich Composite Structures,” AIAA Journal, Vol. 42, pp. 1474-1479, 2004.

Birman, V., 2005. “Thermally-Induced Bending and Wrinkling in Large Aspect Ratio Sandwich Panels,” Composites Part A. In Press.

Birman, V., Kardomateas, G.A., Simites, G.J. and Li, R. 2005. “Response of a Sandwich Panel Subject to Compression and Elevated Temperature on One of the Surfaces,” Composites Part A: Engineering. In press.

Chang, H.T. and Allen, D.H., 1988. “Analysis of Viscoelastic Plates Subjected to Rapid External Heating,” AIAA Paper, AIAA 88-2422.

Elkin, R. 2004. Personal communication.

Gibson, A.G., Wright, P.N.H., Wu, Y.-S. and Evans, J.T. 2004. “Laminate Theory Analysis of Composites under Load in Fire,” Proceedings of the SAMPE 2004 meeting, Long Beach, CA, May 16-20, 2004.

Hamamoto, A. and Hyer, M.W., 1987. “Non-Linear Temperature-Curvature Relationships for Unsymmetric Graphite-Epoxy Laminates,” International Journal of Solids and Structures, Vol. 23, pp. 919-935.

Krysl, P., Ramroth, W. and Asaro, R.J. 2004. “FE Modeling of FRP Sandwich Panels Exposed to Heat: Uncertainty Analysis,” Proceedings of the SAMPE 2004 Meeting, Long Beach, CA, May 16-20, 2004.

Kulkarni, A.P. and Gibson, R.F. 2003. “Nondestructive Characterization of Effects of Temperature and Moisture on Elastic Moduli of Vinyl Ester Resin and E-glass/vinylester

Composite,” Proceedings of the American Society for Composites 18th Annual Technical Conference, CD-ROM, Paper #122, Eds. Sankar BV, Ifju PG, Gates TS, Gainesville, Florida. 2003.

Lattimer, B.Y., Ouellette, J. and Sorathia, U. 2004. “Large-Scale Fire Resistance Tests on Sandwich Composites,” Proceedings of the SAMPE 2004 Meeting, Long Beach, CA, May 16-20, 2004.

Librescu, L., Lin, W., Nemeth, M.P. and Starnes, J.H., 1993. “Classical Versus Non-Classical Postbuckling Behavior of Laminated Composite Panels Under Complex Conditions,” In: Non-Classical Problems of the Theory and Behavior of Structures Exposed to Complex Environmental Conditions, Ed. Librescu, L., ASME Press, Volume AMD-Vol. 164., New York, pp. 169-182.

Meyers, C.A. and Hyer, M.W., 1992. “Thermally-Induced Geometrically Nonlinear Response of Symmetrically Laminated Composite Plates,” AIAA Paper, AIAA-92-2539-CP.

Meyers, C.A. and Hyer, M.W. 1992. “Thermally-Induced Geometrically Nonlinear Response of Symmetrically Laminated Composite Plates,” AIAA Paper AIAA-92-2539-CP.

Nemeth, M.P., 2001. “Buckling Behavior of Long Anisotropic Plates Subjected to Fully Restrained Thermal Expansion,” AIAA Paper, AIAA-2001-1330.

Reddy, J.N., 2004, Mechanics of Laminated Composite Plates and Shells. Theory and Analysis. 2nd edition, CRC Press, Boca Raton.

Whitney, J.M. and Ashton, J.E., 1971. “Effect of Environment on the Elastic Response of Layered Composite Plates,” AIAA Journal, Vol. 9, pp. 1708-1713.

TABLE 1. Axial edge restraint stress resultant of a large aspect ratio sandwich panel ($MN * m$) as a function of the exposed surface temperature T_0

$T(^{\circ}C)$	50.0	75.0	100.0	125.0
H45 ($h_f=2.5mm$)	0.340791	0.326334	0.304722	0.247510
H60 ($h_f=2.5mm$)	0.416041	0.398344	0.371917	0.302148
H45 ($h_f=5.0mm$)	0.341365	0.327056	0.305511	0.248027
H60 ($h_f=5.0mm$)	0.417263	0.399664	0.373288	0.303093

Note: The properties of facings and two grades of core (H45 and H60) are presented in the paper by Birman et al. (2005). The core is 20mm thick. Two facing thicknesses considered are $h_f = 2.5mm$ and $h_f = 5.0mm$.

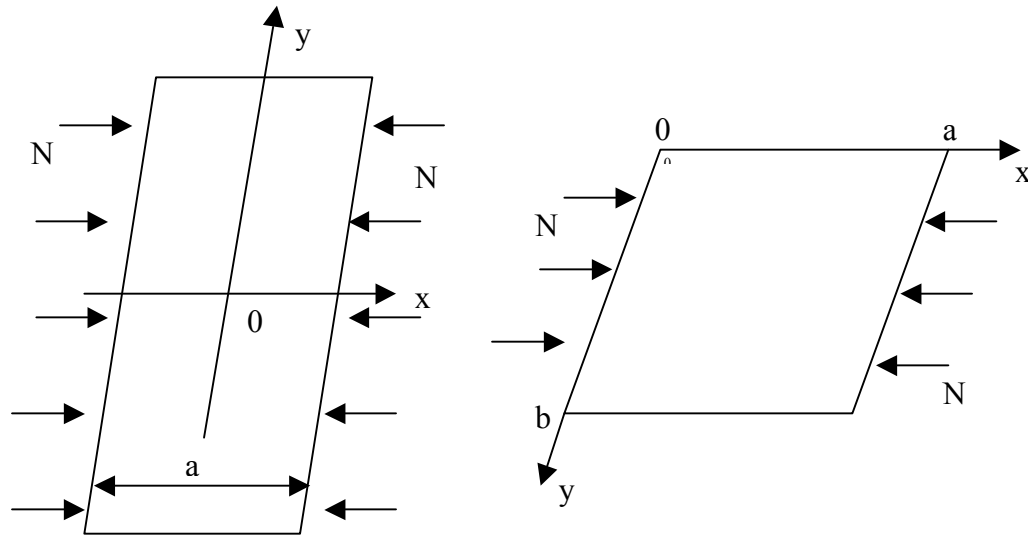


Fig. 1. Geometry and coordinate axes of panels considered in the analysis (large aspect ratio panel is on the left and finite aspect ratio panel is on the right). The z-axis that is oriented perpendicular to the plane of the panel is not shown.

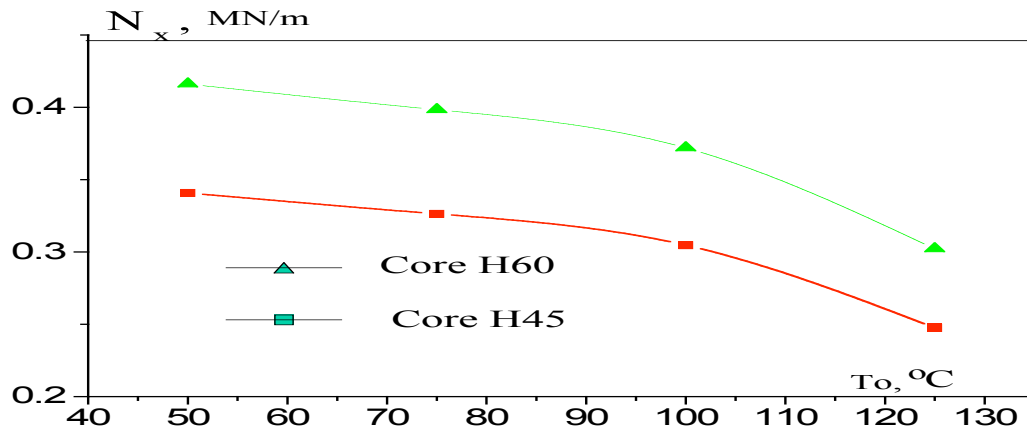


Fig. 2. Axial edge restraint stress resultant of a large aspect ratio sandwich panel ($MN \cdot m$) as a function of the exposed surface temperature T_0 . The facings are 2.5mm thick.

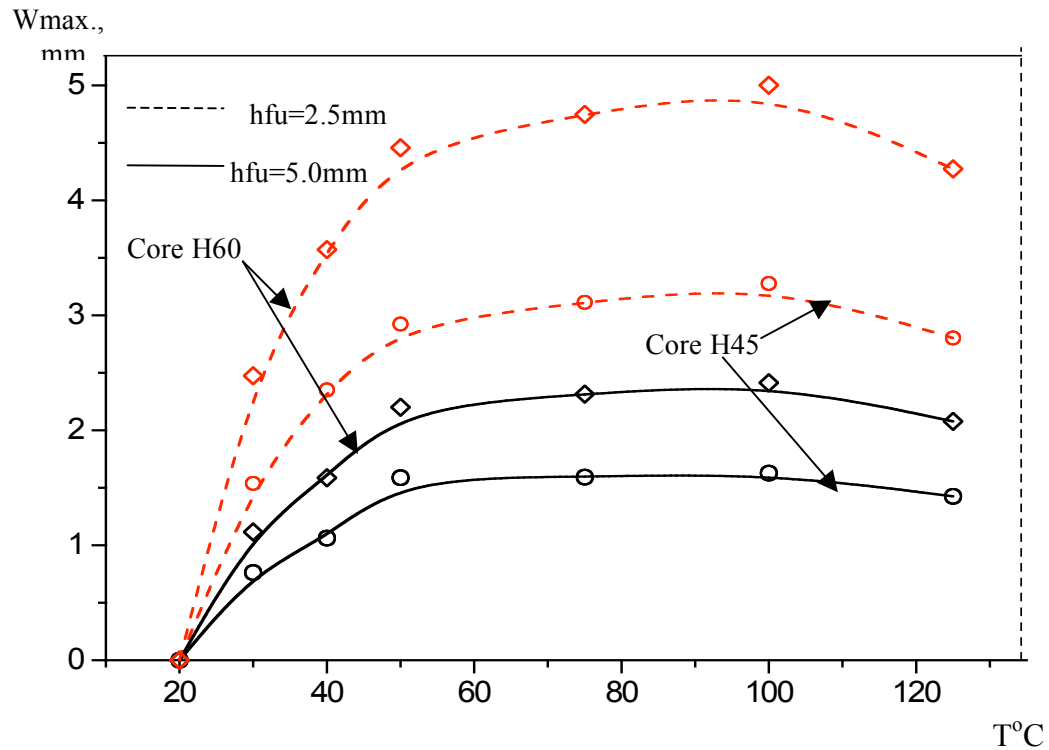


Fig. 3. Maximum deflections of a large aspect ratio sandwich panels as a function of the exposed surface temperature. The length of the short edge of the panels is equal to 101.6mm.

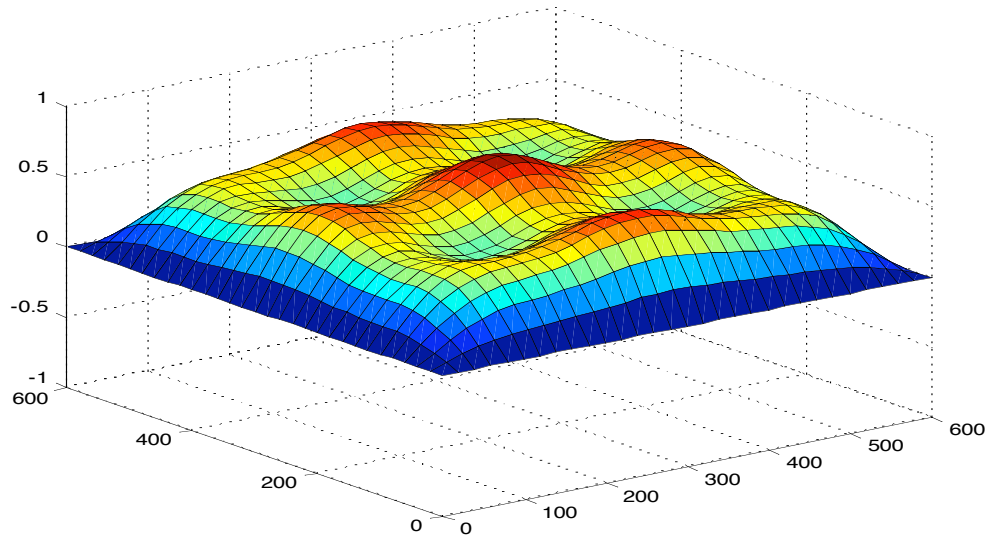


Fig. 4. The shape of a square 12-mm thick glass/polyester plate subjected to heat flux of 75 kW/m^2 for 60 seconds. The compressive load is equal to 20% of the buckling value. The in-plane dimensions of the plate are 600 mm. Time elapsed since the ignition is 60 seconds.

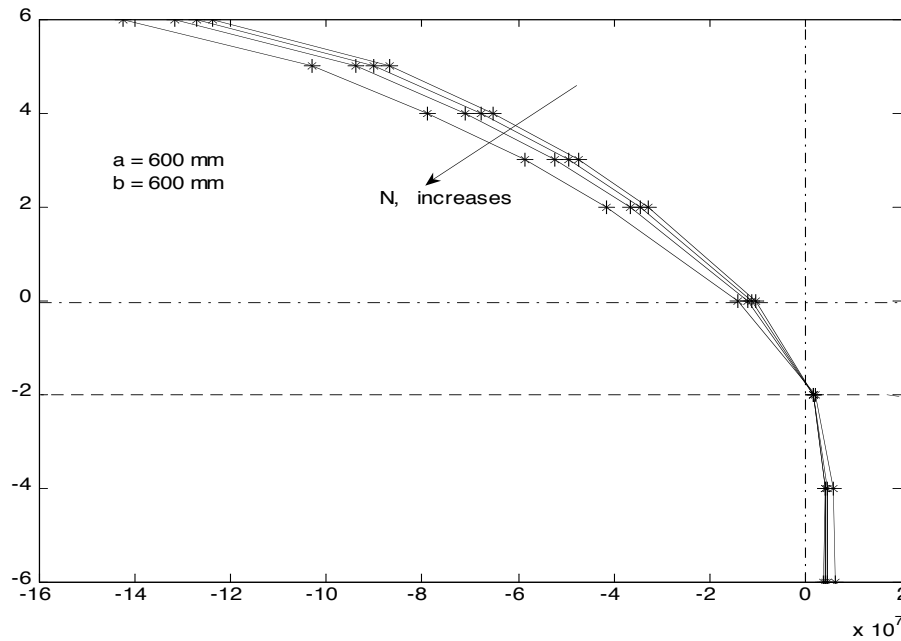


Fig. 5. A distribution of the stresses σ_x at the center of a square plate (600*600mm) through the thickness under different loads. The plate is subjected to a compressive load directed along the x-axis and heat flux of 75 kW/m^2 applied for 60 seconds.

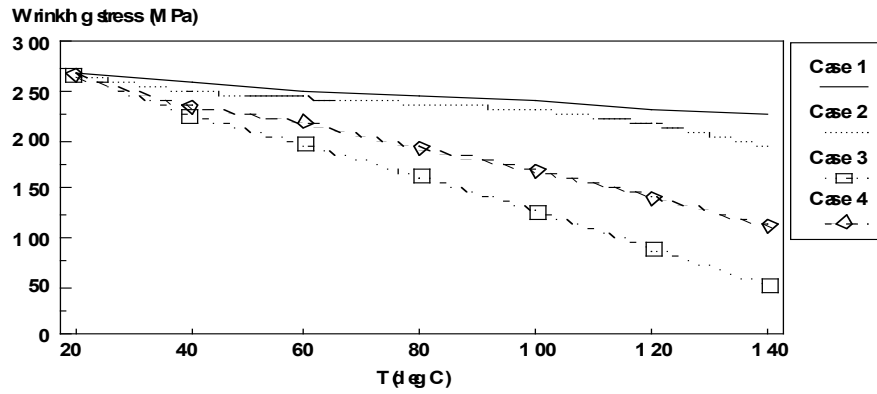


Fig. 6. Wrinkling stress of a quasi-isotropic E-glass vinyl ester facing supported by a Divinycell H60 core. Case 1: Thermal stresses are accounted for, while the effect of temperature on properties of the facing and core is neglected. Case 2: Thermal stresses and the effect of temperature on the properties of the facing are accounted for. Cases 3 and 4: Thermal stresses and the effect of temperature on the properties of the facing and core are accounted for (20% and 50% of the stiffness of the core is retained at 140°C in cases 3 and 4, respectively).

This page left blank intentionally.

Preliminary Design of Piezo-activated Composite Sandwich Fins for Projectile Maneuverability*

James T. Arters[†] and Jack R. Vinson[‡]

*Center for Composite Materials and the Department of Mechanical Engineering, University of Delaware,
Newark, Delaware, 19716*

Travis A. Bogetti[‡], Paul Weinacht[§] and William H. Drysdale[¶]
U.S. Army Research Laboratory, Aberdeen Proving Ground, Maryland, 21005

Moti Leibowitz[#]
RAFAEL, Haifa, Israel

and

Oded Rabinovitch^{**}
Technion Israel Institute of Technology, Haifa, Israel

More than two years ago a research project was initiated to design a smart fin utilizing a piezoelectric actuator in order to alter the ballistic trajectory of a surface-to-surface projectile to a maneuverable flight path. This activation would involve developing an angle of attack to provide lift for any desired maneuver. Thus a capability would be developed to better track a moving target, change targets in midcourse flight, and/or move around an obstacle such as a mountain or building. The original design involved piezoelectric ceramics bonded onto the upper and lower surfaces of composite cantilevered beams that were the spars of the fin. With the forward beam bending in one direction and the aft beam bending in the opposite direction, an angle of attack was created. Practical application of smart fins requires that the piezoelectric material being bonded onto the host composite can withstand rough handling. Piezoelectric ceramics are not capable of meeting this requirement since they are extremely brittle. The piezoelectric material that was found to be sufficient for the requirement is Macro Fiber Composites (MFC). As a result of using this new piezoelectric material, the overall design was modified to one involving a steel tube as the spar located at approximately the quarter chord of the rectangular fin. It includes a slot to pot in the piezoelectric actuator, which is cantilevered aft from the spar. An MFC is adhesively bonded to each side of the host plate. Thus, when one MFC is activated in tension and the other in compression, an angle of attack is achieved. Bench top tests as well as wind tunnel tests were conducted on the smart fins. The primary objective of the wind tunnel tests was to analyze the performance of the smart fins in a practical application. The smart fin performance was based on the amount of flutter experienced by the smart fin and the maximum angle of attack/rotation achieved by the smart fin when applying the maximum allowable voltage.

* Copyright 2005 by James Arters. Printed by NASA with permission.

[†] Graduate Student, Mechanical Engineering, 126 Spencer Lab, University of Delaware, Newark, DE 19716, U.S.A., AIAA Member.

[‡] H. Fletcher Brown Professor, Mechanical Engineering, 126 Spencer Lab, University of Delaware, Newark, DE 19716, U.S.A., Fellow, AIAA.

[§] Mechanical Engineer, U.S. Army Research Laboratory, Building 4600, Aberdeen Proving Ground, MD.

[¶] Aerospace Engineer, Aerodynamics Branch, BWCD, WMRD, Associate Fellow, AIAA.

[#] Research Engineer, U.S. Army Research Laboratory, Building 4600, Aberdeen Proving Ground, MD, 21005.

^{**} Principal Systems Engineer, RAFAEL, P.O. Box 2250, Haifa, 31021, Israel.

^{**} Senior Lecturer, Civil and Environmental Engineering, Technion City, Haifa, 32000, Israel, AIAA Member.

Nomenclature

ϕ	=	smart fin angle of attack
L	=	length from middle of spar to tip of outer shell
δ	=	tip deflection

I. Introduction

THIS research project investigates the feasibility of designing an active fin structure, referred to as a smart fin, which utilizes piezoelectric materials to activate the fin. The piezoelectric actuation rotates the fin, which alters the ballistic trajectory of a small-scale surface-to-surface projectile to a maneuverable flight path. Thus, the steering of the flight trajectory can be controlled using the global positioning satellite guidance system. Control of the small scale projectile will be provided by sending electrical signals to the piezoelectric materials in the smart fin. The electrical signals will generate a fin rotation thus developing an angle of attack to provide lift for a desired maneuver. The possible capabilities of this active fin structure would be to better track a moving target, change targets in midcourse flight, and/or move around an obstacle such as a mountain or building.

A. Original Smart Fin Design

The original design shown in Figure 1 was developed by Oded Rabinovitch and Jack R. Vinson¹. This design uses piezoelectric ceramics to actuate composite cantilevered beams that were used as spars of the smart fin. A piezoelectric ceramic was bonded to the top and bottom surfaces of the composite cantilevered beams. In order to activate a composite cantilevered beam a voltage of positive or negative polarity is applied to the top surface piezoelectric ceramic and a voltage with a polarity opposite to that of the voltage sent to the top surface piezoelectric ceramic is applied to the bottom piezoelectric ceramic. The piezoelectric ceramics would expand or contract depending on the polarity of the voltage thus causing the composite cantilevered beam to bend. With the forward composite cantilevered beam bending in one direction and the aft composite cantilevered beam bending in the opposite direction, an angle of attack is produced.

The design approach by Oded Rabinovitch and Jack R. Vinson¹ uses analytical and computational tools that are based on a high-order beam theory in order to predict the optimized design of the smart fin. Design curves were generated from their analysis which determined the optimized design for each parameter of the smart fin. The design parameters that were investigated included the properties and geometries of both the host composite beam and adhesive layers, the number of active piezoelectric layers, the distance between the piezoelectric composite beam benders, and the effects of various applied voltages. Their analysis also provided the capability to compare the structural analyses with the aerodynamic analyses.

B. Macro Fiber Composites

Practical application of smart fins requires that the piezoelectric material being bonded onto the host composite can withstand rough handling and harsh environments. Piezoelectric ceramics are not capable of meeting this requirement since they are extremely brittle and fragile. Due to this requirement a search for different and new types of piezoelectric materials began. The piezoelectric material that was found to be sufficient for the requirement

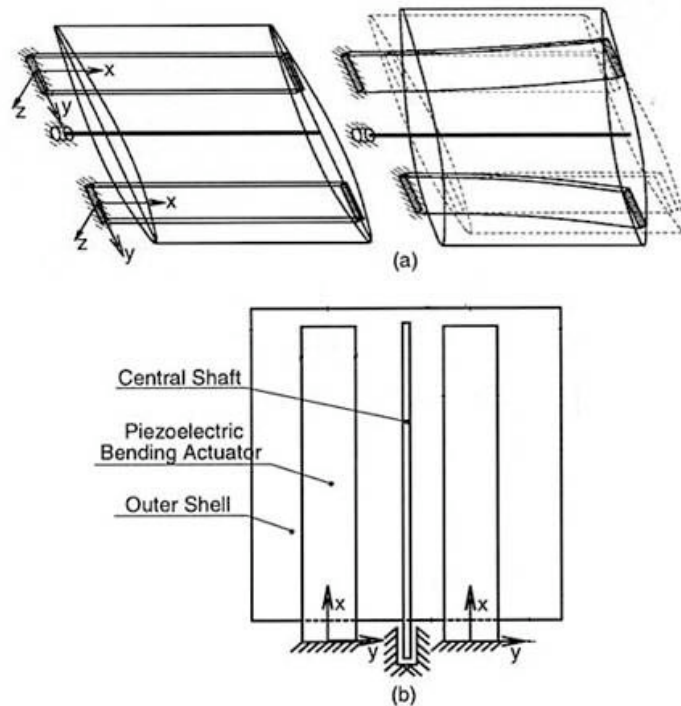


Figure 1. Original smart fin design: a) undeformed and deformed shapes, b) the overall configuration (reprinted from Ref. (1)).

is Macro Fiber Composites (MFC). The robustness of MFC makes them ideal for the smart fins application. The main advantage that MFC have over piezoelectric ceramics is that they are very flexible and durable. A schematic of Macro Fiber Composites is seen in Figure 2. According to R. Brett Williams and Daniel J. Inman² Macro Fiber Composites combine piezoelectric and composite material technologies that use interdigitated electrodes to apply voltage to the piezoelectric fibers. They also stated that MFC are designed to have uniaxially aligned fibers surrounded by a polymeric matrix as well as an interdigitated electrode pattern that is used to deliver an applied electric field along the length of the fibers, as illustrated in Figure 2.

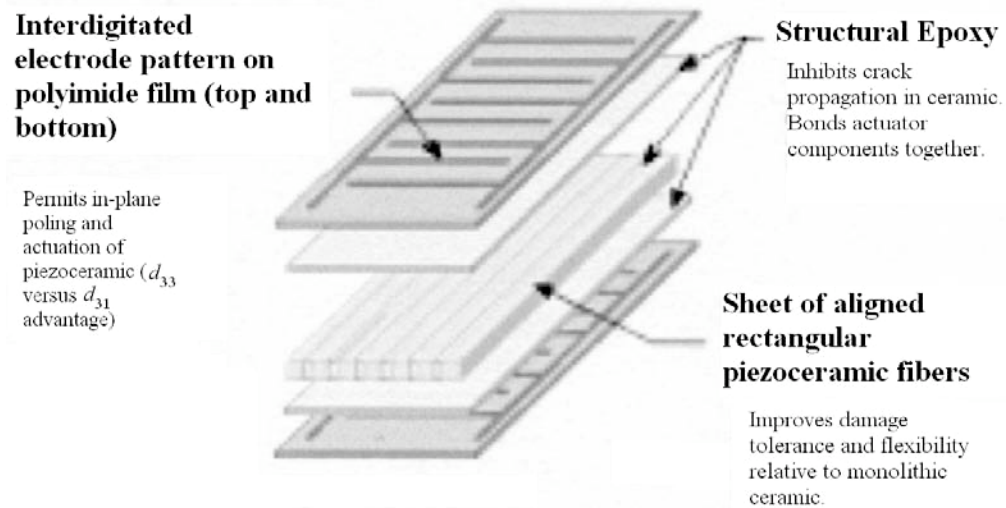


Figure 2. Macro Fiber Composite Schematic (reprinted from Ref (2)).

C. New Smart Fin Design

As a result of using this new piezoelectric material, a new smart fin design was adopted. The new design is approximately six inches in width and four inches in length. A steel hollow circular shaft is used as the spar which is located at approximately the quarter chord of the rectangular fin. A composite rectangular plate, referred to as the actuator, is cantilevered from the steel hollow circular shaft. Bonded to the top and bottom surfaces of the composite rectangular plate are MFC patches. Thus when one MFC is activated in tension and the other in compression, an angle of attack is achieved. Figure 3 (a) shows the assembled view of the smart fin where the black and white checkered region indicates the active MFC patch area. Figure 3 (b) describes the angle of attack, ϕ , that is generated from the actuator inside the fin.

Design decisions were made using parametric studies so that the newly designed smart fins could be manufactured. Two complete smart fins have been assembled and tests have been conducted to characterize their performance. Deflection tests conducted to date have been mostly statically measured by a laser and a rotary encoder, as the actuator and

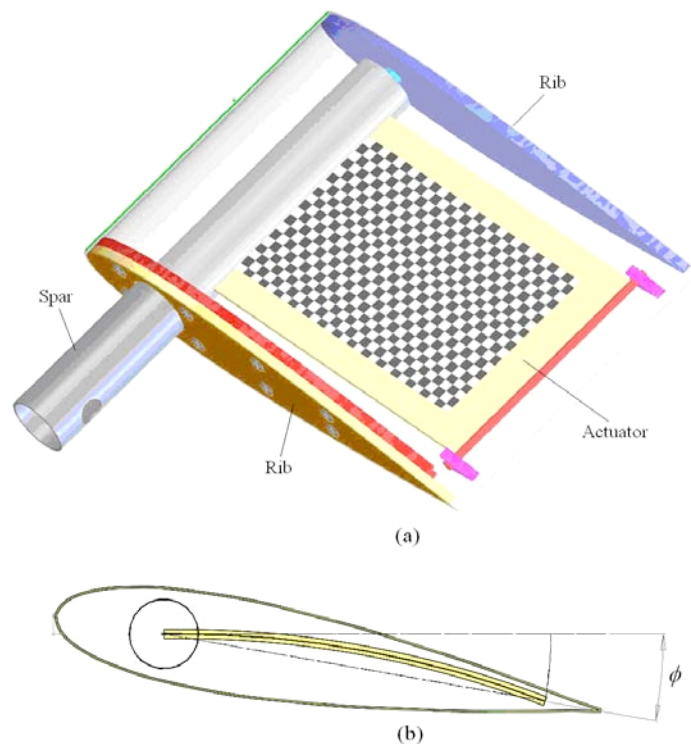


Figure 3. a) Assembled view of new smart fin design, b) Angle of attack generated from piezoelectric actuation.

smart fin are subjected to various mechanical loads, various voltages applied to the MFC patches, and the combination of both.

Wind tunnel tests have been conducted on the newly designed smart fins at the Glenn L. Martin (GLM) wind tunnel located at the University of Maryland. During these tests the smart fins were subjected to aerodynamic loads as well as a combination of piezoelectric actuation and aerodynamic loads. The wind tunnel test facility provided velocities of up to 200 mph. The maximum angles of attack obtained from the wind tunnel tests will be presented to show the feasibility of using piezoelectric actuators in smart fins.

II. □ Research Objective

A. Design and Fabrication Objective

The main objective of this research is to develop and fabricate a smart fin design to a point where the performance capabilities of a smart fin can be characterized. This characterization will help in determining the feasibility of using piezoelectric materials in smart fins. The design must involve using a piezoelectric actuator. The fabrication of the piezoelectric actuators starts with having an analytical model to help determine the actuator's optimized design. This analytical model was developed by Oded Rabinovitch and Jack R. Vinson¹ which determined the design objectives for this project. The design objectives are to manufacture a thin and flexible composite host panel to which the piezoelectric material can be bonded and to manufacture an actuator with a thin adhesive layer. Another design objective is to use a piezoelectric material which is flexible and durable. Meeting these design objectives will provide an optimized smart fin.

A fabrication goal was set to manufacture three actuators using three different types of adhesives. Different fabrication techniques were used in manufacturing each of the actuators. The techniques involved using an autoclave, a vacuum bag, and weights. The three objectives in designing the spar, ribs, and other internal components of the smart fin included: ease of assembly, ease of testing in a wind tunnel facilities, and minimization of mechanical losses due to friction from internal connections in the smart fin.

B. Experimental Objective

The performance capabilities of a smart fin are defined as follows: the angle of attack which is generated by applying voltage to the piezoelectric actuators, the angle of attack which is generated by applying various mechanical loads to the smart fin, and the behavior of the smart fin in a wind tunnel. When applying voltage to the piezoelectric actuators, a larger angle of attack translates to better actuator performance. When applying a mechanical load, a stiffer actuator that does not lose voltage actuation performance translates into better actuator performance. In addition, a minimal amount of smart fin flutter during the wind tunnel tests can be interpreted as good behavioral performance.

In order to determine these performance capabilities, an experimental data acquisition technique was developed. This technique was to position a laser over the tip of the smart fin. Next, the maximum tip deflections for various test scenarios were measured using this laser. A LabVIEW data acquisition program was used to measure the tip deflections over time. These tip deflections were then converted into angles of attack. After the actuator was attached inside the outer shell of the fin, a rotary encoder was fixed on the smart fin which measured the angle of attack directly. Results from different smart fins were compared to determine which performed the best.

C. Wind Tunnel Test Objective

Wind tunnel tests were conducted on the smart fins at the GLM wind tunnel at the University of Maryland. The primary objective of these tests was to determine the feasibility of using piezoelectric actuators in smart fins by analyzing their performance in a practical application. The smart fin performance was based on the amount of flutter experienced by the smart fin and the maximum angle of attack/rotation achieved by the smart fin when applying the maximum allowable voltage. Using the rotary encoder, measurements of the angle of attack were taken while the fin was subjected to a range of air velocities. The maximum wind velocity in the tunnel was 200mph. The angles of attack measured from the wind tunnel tests were compared with the angles of attack measured from the static tests. Other objectives of the wind tunnel tests include backing out the aerodynamic torques and finding the center of pressure on the smart fin in order to optimize the location of the hinge placement.

III. □ Component Design and Fabrication

A. Assembled Actuator

The actuators were assembled by bonding MFC patches to both surfaces of a thin and flexible composite host panel. The material selected to manufacture the host panel was unidirectional E-Glass epoxy prepregs. Figure 4 shows a diagram of the piezoelectric actuator. Regions 1 and 3 are inactive regions that consist of a host layer and two adhesive layers. The actuator is activated by the piezoelectric layers in region 2. The prepregs were cured in an autoclave with a pressure of 50psi at 250 °F for one hour and 350 °F for two hours.

Three different adhesives were used in the manufacturing of the actuators. The first was a

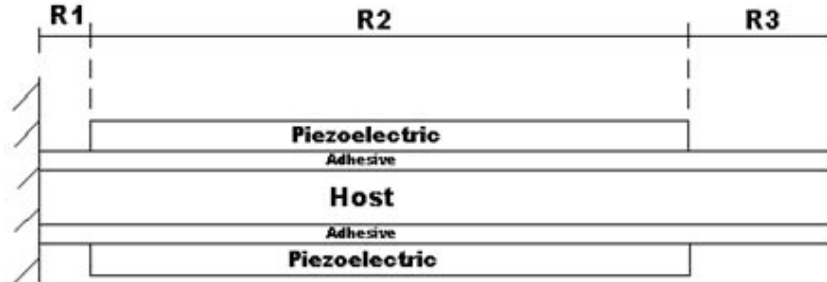


Figure 4. Diagram of piezoelectric actuator.

structural film adhesive that was cured in an autoclave with a cure cycle of 250 °F at 30psi for one hour. A Loctite E-120HP epoxy adhesive was used to manufacture the second actuator. This was a room temperature two part epoxy which was cured overnight in a vacuum bag.

Figure 5 shows the actuator manufactured with the Loctite E-120HP epoxy adhesive along with a drawing of the actuator with dimensions. The active, piezoelectric region of the actuator is the darker region with dimensions of 2.20 inches x 3.40 inches. The entire dimension of the actuator including the inactive region is 2.90 inches x 4.30 inches. Wiring soldered to the connections of the MFC patch can be seen at the bottom of the photograph of the actuator.

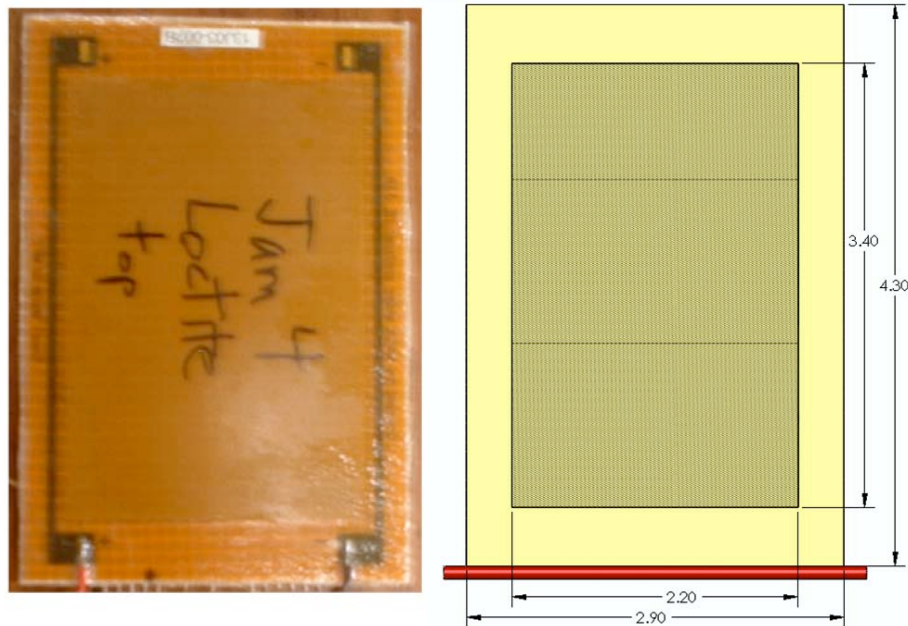


Figure 5. Photograph of Actuator (left) and Drawing of Actuator with Dimensions in Inches (right).

B. Smart Fin Component Design and Assembly Process

The objectives in designing the spar, ribs and other internal components of the smart fin were ease of assembly, ease of testing in a wind tunnel facility, and minimization of mechanical losses due to friction from internal connections in the smart fin. The smart fin assembly consists of bonding together and connecting several different components. These components include the actuator, a spar, a shaft insert, ribs, a base plate, and an outer shell. The

entire assembly was designed to meet the dimensional requirements of the actuator so that there would be no interference with the motion of the actuator.

1. Spar

The spar, shown in Figure 6, was manufactured from a steel hollow circular shaft. Several features were machined into the spar. The first feature was a slot cut 3.2 inches along the length of the spar and approximately 0.065 inches wide. The length of the slot was chosen in order to meet the dimensional requirements of the actuator and connector at the end of the spar. The overall thickness of the actuator assembly determined the width of the slot. Assembly of the smart fin required the actuator to slide into this slot. The next feature was a rounded, rectangular opening 0.64 inches long and 0.38 inches wide. This opening was needed to fasten the ribs to the hinge connection inside the spar, and to run the lead wires from the actuators, through the spar, to the power supplies. The last feature was a 0.313 inch diameter hole through the spar. The purpose of this hole was to attach the spar to a fixture used during the wind tunnel tests.

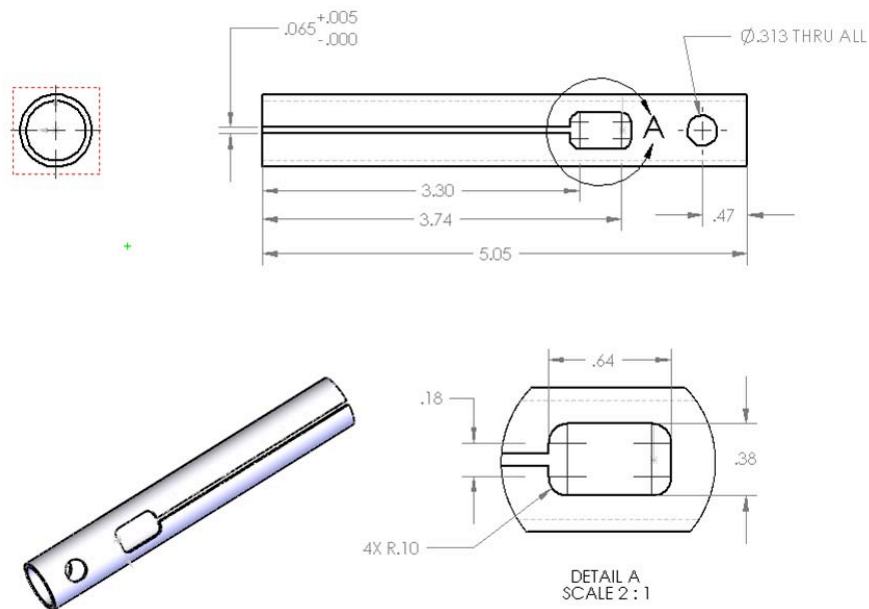


Figure 6. Drawing of Spar with Dimensions in Inches.

2. Shaft Insert

The shaft insert, shown in Figure 7, was machined out of a 0.6 inch diameter aluminum rod. This diameter was chosen in order for the shaft insert to loosely slide into the spar. A length of 3 inches was chosen for the shaft insert, which is approximately the same width as the actuator. A slot with a depth of 0.46 inches was machined into the shaft insert. The width of the slot was the same as the slot machined out of the spar. Again, the overall thickness of the actuator assembly determined the width of this slot.

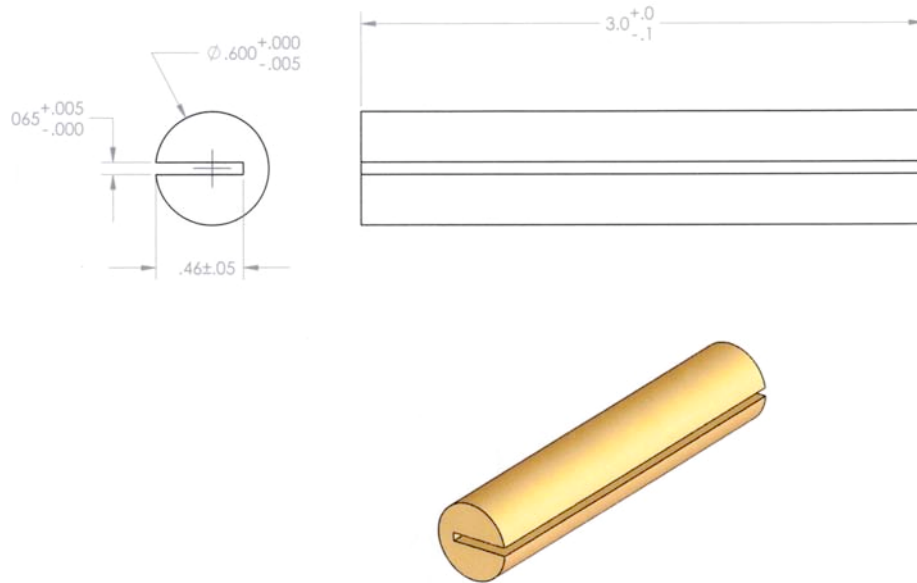


Figure 7. Drawing of Shaft Insert with Dimensions in Inches.

3. Base Plate

The base plate, shown in Figure 8, was machined out of a block of aluminum. This piece was specifically designed to meet attachment requirements at a wind tunnel facility. The overall dimensions of the base plate were 1.8 inches long, 1.6 inches wide and 1.25 inches thick. The tube section of the base plate has an inner diameter of 0.755 inches. This section also has a 0.31 inch diameter hole through it. The purpose of this hole is to attach the smart fin to the base plate using a bolt. Holes were drilled in each corner of the base plate with diameters of 0.25 inches. These holes are used to attach the base plate and smart fin assembly to other fixtures.

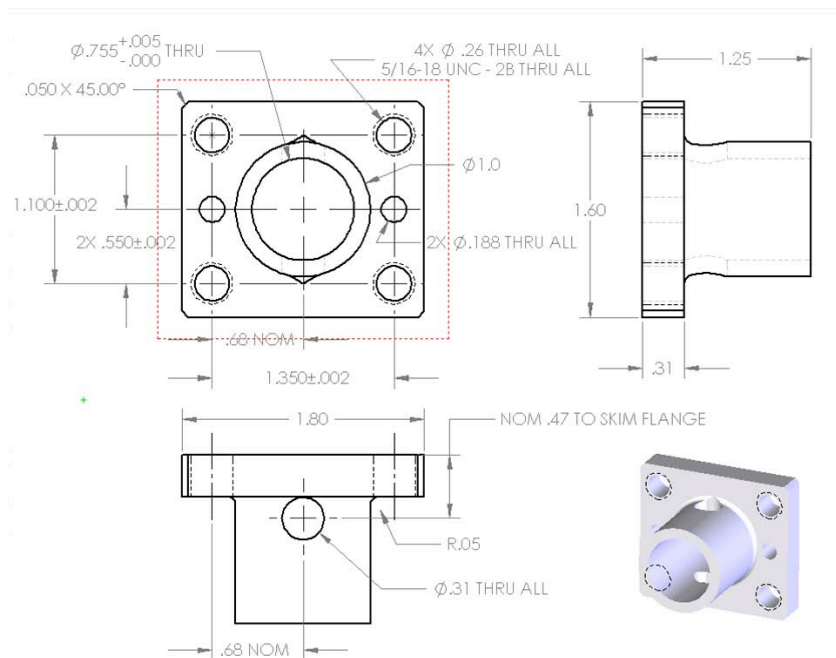


Figure 8. Drawing of Base Plate with Dimensions in Inches.

4. Outer Shell

The outer shell was manufactured from 3K, Plain Weave Graphite Fabric which is commonly used for lightweight aerodynamic parts. Three plies of plain weave graphite fabric were wrapped around a Styrofoam mold of an airfoil. The Styrofoam airfoil mold was designed using one of the NACA standard airfoil cross-sections. The outer shell was wet laminated with System 2000 Epoxy Resin from FiberGlast and was cured at room temperature under vacuum. The airfoil mold was designed to allow room for the internal parts of the smart fin. It was also designed so that there would be no interference with the motion of the actuator shown in Figure 3 (b). The outer shell, shown in Figure 9, was cut into 4 inch x 6 inch sections.



Figure 9. Picture of Outer Shell.

5. Ribs

The ribs, shown in Figure 10, were water jet cut from aluminum pieces. The far side rib of the smart fin assembly, better shown in Figure 13, was bonded to the outer shell. A hole was water jet cut out of this rib in order for the hinge connection, located at the far end of the spar, to be attached into the rib. The near side rib, seen at the top of Figure 10, was also bonded to the outer shell and had a larger hole and slot water jet cut out of it to allow for the spar and actuator assembly to slide into the outer shell. This near side rib was used as an attachment for a third rib. The third rib, seen at the bottom of Figure 10, was screwed into the near side rib. The purpose of this third rib was to provide another hole for the second hinge connection between the spar and outer shell.



Figure 10. Pictures of Ribs.

6. Spar and Actuator Bonding Process

The smart fin assembly process started with bonding the actuator into the slot of the shaft insert. This slot was designed to be thick enough to allow the actuator to firmly slide into it. The bonding process consisted of filling the slot with Loctite E-120HP epoxy adhesive, which is the same aerospace grade adhesive used in manufacturing one of the actuators. The actuator was then slid into the slot and the excess epoxy was wiped off. The same epoxy adhesive was liberally applied on the inner surface of the hollow spar. The shaft insert and actuator were then slid into the spar slot. Excess epoxy was wiped off. The spar, shaft insert, and actuator assembly were allowed to bond together overnight at room temperature. The overall assembly can be seen in Figure 11 (a) where the black and white checkered region shows the active, piezoelectric region of the actuator. The placement of the actuator and shaft insert inside the spar is shown in Figure 11 (b). An actual picture of the actuator bonded into the spar can be seen in Figure 12.

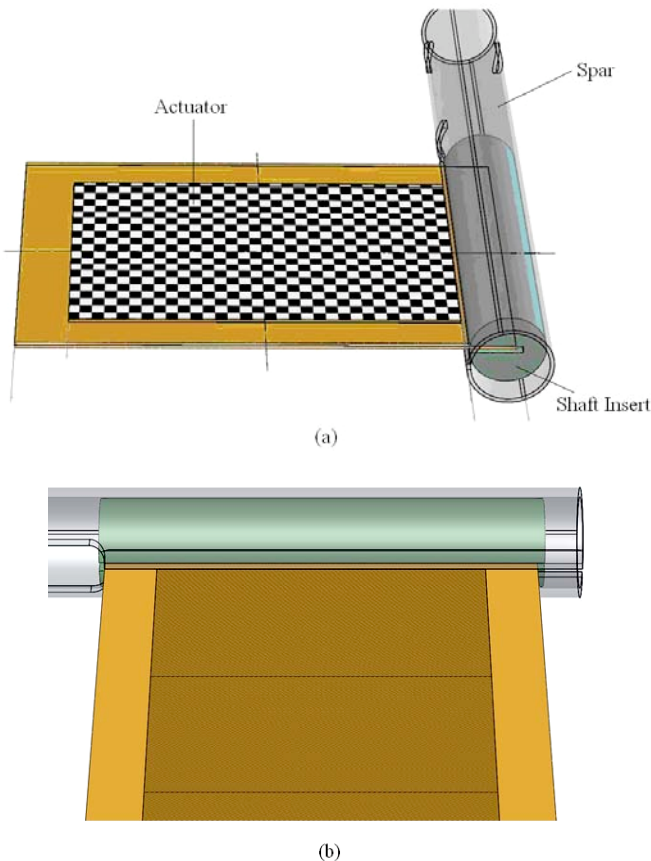


Figure 11. a) Overall Assembly Drawing, b) Drawing of Actuator and Shaft Insert Placement.

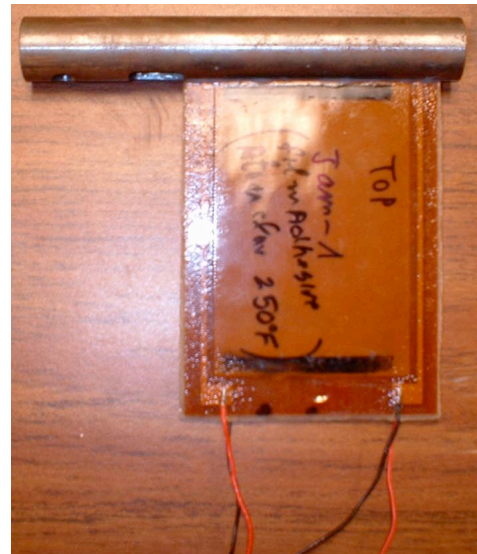


Figure 12. Photograph of Prototype Actuator Bonded into Spar.

7. Final Smart Fin Assembly

The final smart fin assembly process included sliding the spar and actuator assembly in the outer shell and rib assembly, then securing the actuator and spar assembly into the outer shell. In order to do this, hinge connections were used. The hinge connections between the spar and the ribs are silicon bronze bearings on nylon bushings. This combination of hinge materials allows for minimization of mechanical losses due to friction. The bearing bonded inside the far end of the spar was slid into the hole of the far side rib shown in Figure 13. A nylon bushing was bonded to the inside of this hole. The second bearing was fastened inside the hole of the third rib using a bolt and nut. Teflon inserts 0.020 inches thick were placed inside the tip of the outer shell to assure a tight fit between the actuator and outer shell at the end of the fin and to provide a low friction contact surface for the tip of the

actuator. Side and top views of the final smart fin assembly can be seen in Figures 13 and 14, respectively. Approximate dimensions of the entire smart fin assembly are shown in Figure 15.

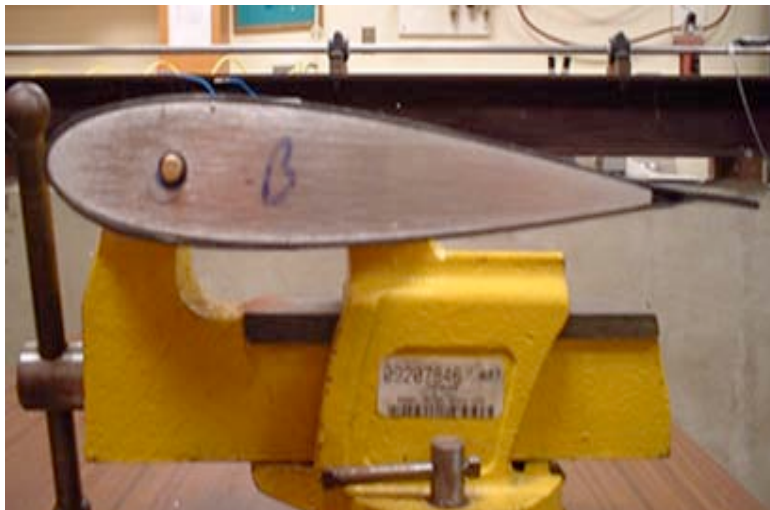


Figure 13. Side View of Smart Fin.

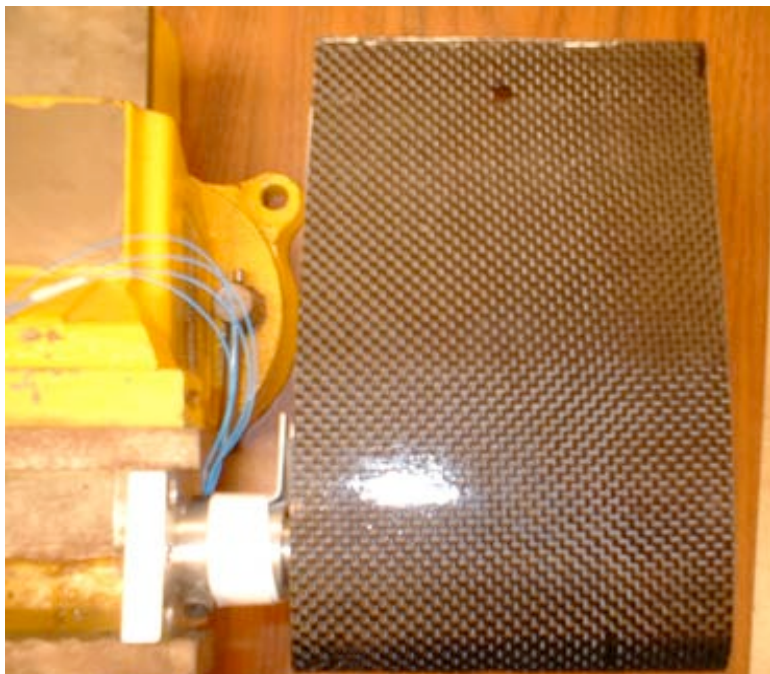


Figure 14. Top View of Smart Fin.

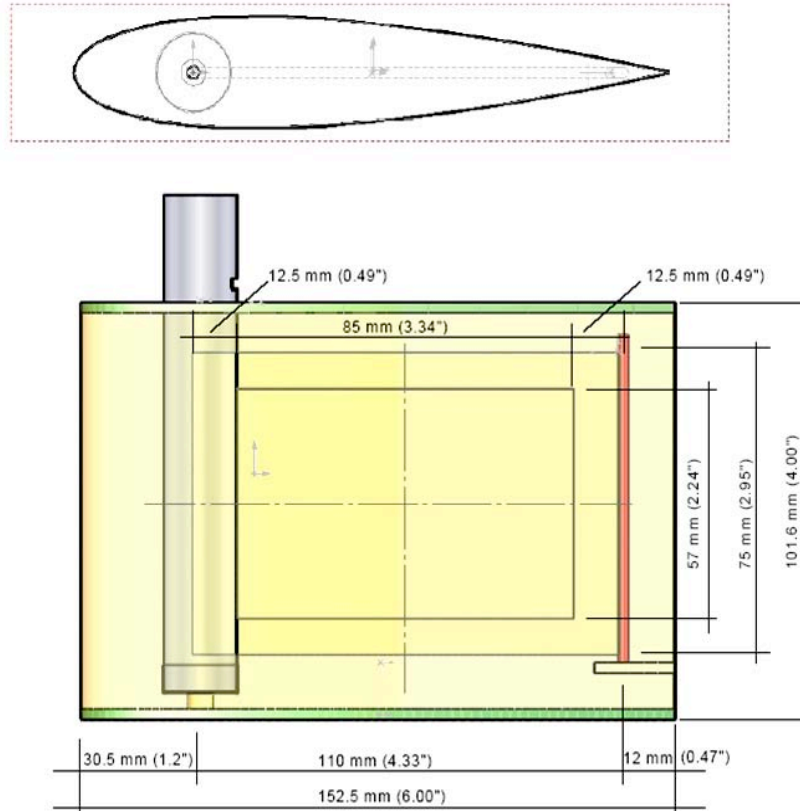


Figure 15. Drawing of Smart Fin Assembly with Approximated Dimensions.

IV. Experimental Setup

A. Introduction

This section discusses the experimental equipment and process for the bench top tests that were conducted on the smart fins. An overview of the experimental equipment will be given. This equipment consisted of a laser, a laser displacement meter, power supplies, a rotary encoder, and a laptop.

B. Laser and Laser Displacement Meter

In order to measure the tip deflection of the smart fins a class 2 type diffuse-reflective laser model LC-2450 from Keyence Corporation, shown at the top of Figure 16, was used. This laser had a measuring range of $\pm 8\text{mm}$ with a response time of $100\text{ }\mu\text{s}$. Connected to the laser was a Keyence LC-2400A laser displacement meter with a 50 kHz sampling rate. The displacement meter, seen at the bottom of Figure 16, displays the tip deflection in millimeters. A laptop was connected to the laser displacement meter and a LabVIEW program was used to record the tip deflection at 100 measurements/second.

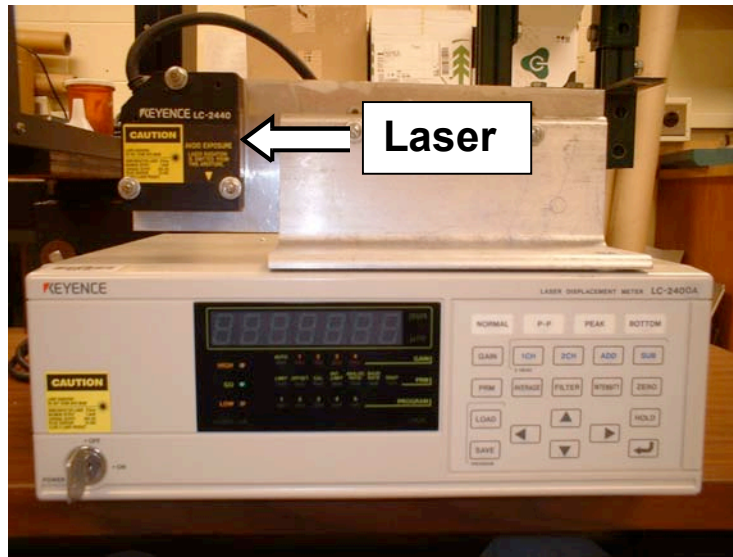


Figure 16. Keyence LC-2450 Laser (top). Keyence LC-2400A Laser Displacement Meter (bottom).

C. Power Supplies

Three power supplies were needed in order to achieve the maximum voltage output of 1500V to one MFC and -500V to the other MFC. Two identical high voltage power supplies were purchased from Smart Material, the same company from which the MFC's were ordered. These power supplies, shown in Figure 17, were capable of providing approximately -1000V to 1000V. They also had a manual dial for offset and amplitude, an internal frequency generator 1Hz to 1kHz manual dial, and a BNC input for external AM modulation. These power supplies

were controlled using an external power supply through the BNC input for external AM modulation. A laptop was used to externally input the 0-5V needed to control these power supplies. For example, when 0V was input from the laptop the high voltage power supply output -1000V and when 5V was input from the laptop the high voltage power supply output 1000V. The high voltage power supply did not output any voltage when the laptop input 2.5V. The third power supply was provided from the Army Research Laboratory (ARL). Shown in Figure 18, this power supply was a Stanford Research Systems, Inc. high voltage power supply model PS325 which was capable of providing ± 2500 V. The extra 500V needed to reach 1500V was provided from this power supply. This power supply was



Figure 17. Power Supply from Smart Material.

connected in series with the other two power supplies. The circuit diagram of the power supply configuration is shown in Figure 19. Since the Smart Material power supplies were wired in series with the ARL power supply when one of the Smart Material power supplies output 1000V and the other output -1000V the additional 500V from the ARL power supply thus provided the maximum 1500V and -500V that were required to be applied to the MFC's.



Figure 18. ARL Power Supply.

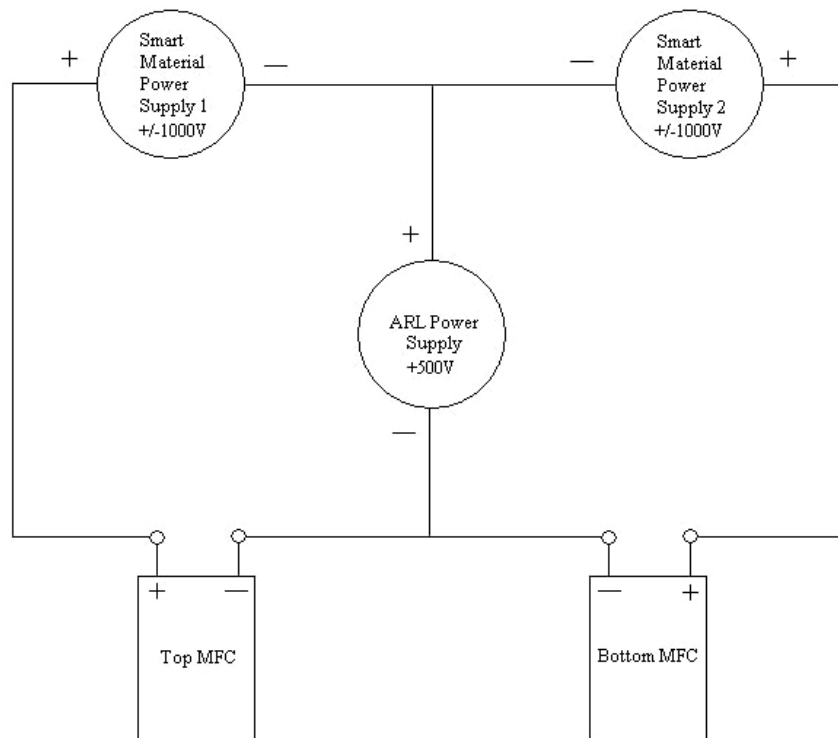


Figure 19. Circuit Diagram.

D. Rotary Encoder

A MicroE Systems rotary encoder was used to measure the angle of attack that was produced by the piezoelectric actuator. This device was used only after the smart fin had been completely assembled. The rotary encoder was connected to a laptop and SmartSignal encoder software was used to display the achieved angles of attack. This software was also used to calibrate the signal strength of the rotary encoder. Superglue was used to attach the rotary encoder to a metal bracket that was bonded to the base plate as seen in Figure 20. The rotary encoder faced the rib nearest to the base plate. A glass disc was bonded on this rib also using superglue. The glass disc contained a metal strip which was used by the rotary encoder to measure the change in angle.

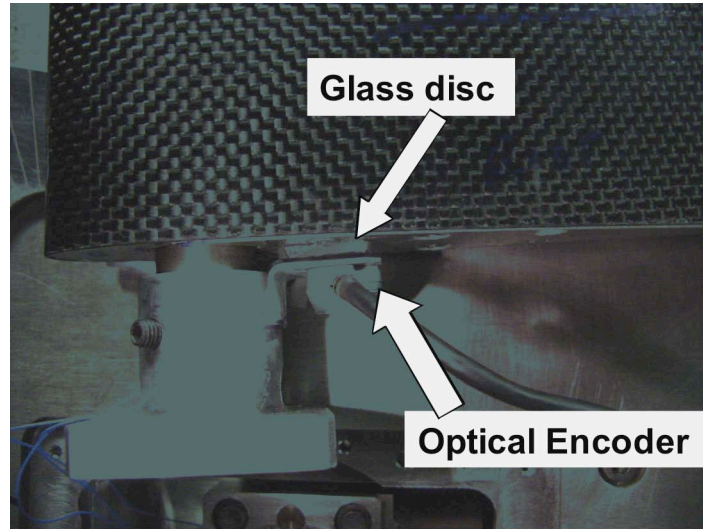


Figure 20. Rotary encoder attachment.

V. □ Experimental Results

A. Smart Fin Assembly Test Results

When testing the smart fin assemblies the maximum allowable voltages were applied to the piezoelectric actuators inside the outer shell. This actuation caused the outer shell to rotate about the spar. The tip deflection, δ , that was measured using the laser was translated into an angle of rotation/attack, ϕ ,

using $\tan\phi = \frac{\delta}{L}$. Figure 21

describes the laser placement over the smart fin. In later experiments a rotary encoder was used to directly measure the angle of rotation which eliminated the need for measuring the length, L , and translating the fin tip deflection into an angle of rotation.

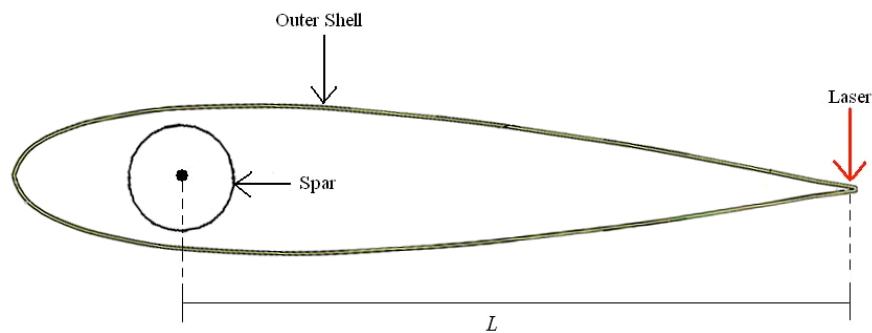


Figure 21. Description of Laser Placement.

1. Laser Measurements

The smart fin assembly with the 250 ° F cure structural film adhesive piezoelectric actuator was statically tested using the maximum allowable voltages of +1500V and -500V. Tests 1-5 consisted of applying +1500V to the top MFC and -500V to the bottom MFC. The voltages were switched for tests 6-10 and switched once again for test 11. The maximum voltages were held for 30 seconds for each test and then the deflection measurements were recorded

manually from the laser displacement meter. The angles of rotation for the smart fin assembly with the 250 ° F cure structural film adhesive piezoelectric actuator were calculated using $L = 117.29\text{mm}$.

The testing procedures involved applying the maximum allowable positive voltage of +1500V to both MFC for a certain amount of time. This process was termed “reconditioning”. “Reconditioning” was done before tests 3 and 8 for one minute. Seen in Figure 22, test 3 resulted in an increase of angle of rotation but test 8 did not. When comparing tests 6-10 the largest angle of rotation was achieved right after the voltages were switched. The overall largest angle of rotation was achieved during test 11 after the voltages were switched a second time.

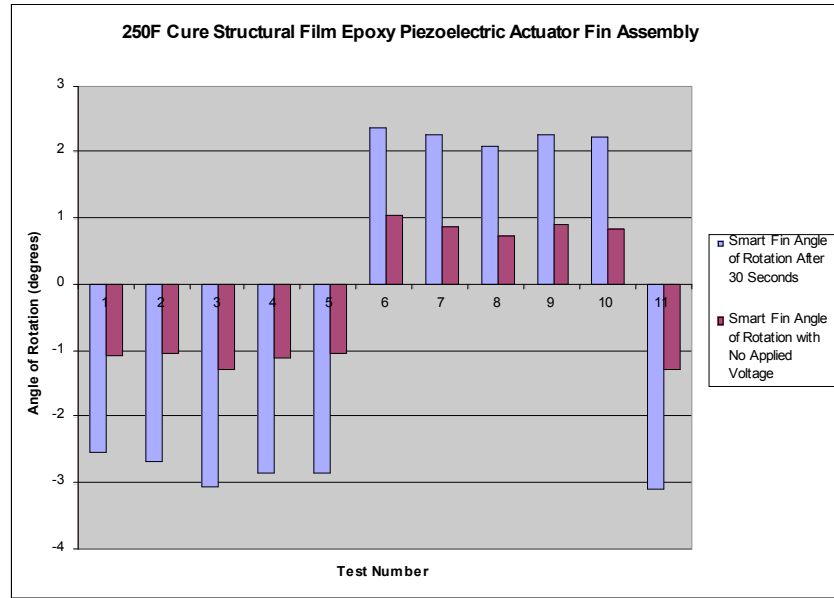


Figure 22. Results of Smart Fin Assembly Tests with the 250 °F Cure Structural Film Adhesive Piezoelectric Actuator.

Table 1 provides the summary of the angles of rotation achieved for the 250 °F cure structural film adhesive piezoelectric actuator fin assembly. When compared to tests 1, 2, 4, and 5, “reconditioning” the MFC’s before test 3 resulted in an average increase in angle of rotation of -0.335 degrees. “Reconditioning” the MFC’s before test 8 did not result in an increase in angle of rotation. This may be due to interference from the smart fin assembly during testing. Switching the applied voltages to -500V to the top MFC and +1500V to the bottom MFC resulted in an average increase in angle of rotation of 0.1648 degrees. Similarly, switching the applied voltages a second time resulted in another increase in angle of rotation of -0.307 degrees.

Table 1. Summary of Angles of Rotation for 250 °F Cure Structural Film Adhesive Piezoelectric Actuator Smart Fin Assembly.

Test Number	Angle of Rotation for Maximum Allowable Voltages (degrees)	Angle of Rotation for No Applied Voltage (degrees)
1	-2.5238	-1.0599
2	-2.6506	-1.0355
3	-3.0502	-1.2650
4	-2.8553	-1.1087
5	-2.8309	-1.0355
6	2.3922	1.0501
7	2.2605	0.8987
8	2.0947	0.7375
9	2.2703	0.9036
10	2.2410	0.8645
11	-3.0891	-1.2796

The Loctite epoxy adhesive piezoelectric actuator smart fin was also tested using the laser. The test procedures were the same as for the 250 °F cure structural film adhesive piezoelectric actuator smart fin except the measurements were recorded over time with a laptop and switching the applied voltages a second time was not done. The length, L , for this actuator was measured to be 121.9mm. “Reconditioning” the MFC’s was done before tests 3 and 8 were conducted. Figures 23 and 24 provide the Loctite epoxy adhesive piezoelectric actuator smart fin

assembly experimental data for the angles of rotation over time. Again, it can be seen that test 6, which was conducted after switching the applied voltages, provides the overall largest angle of rotation of 3.3626 degrees. Also, it can be seen from the figures that the angles of attack slowly increased over time.

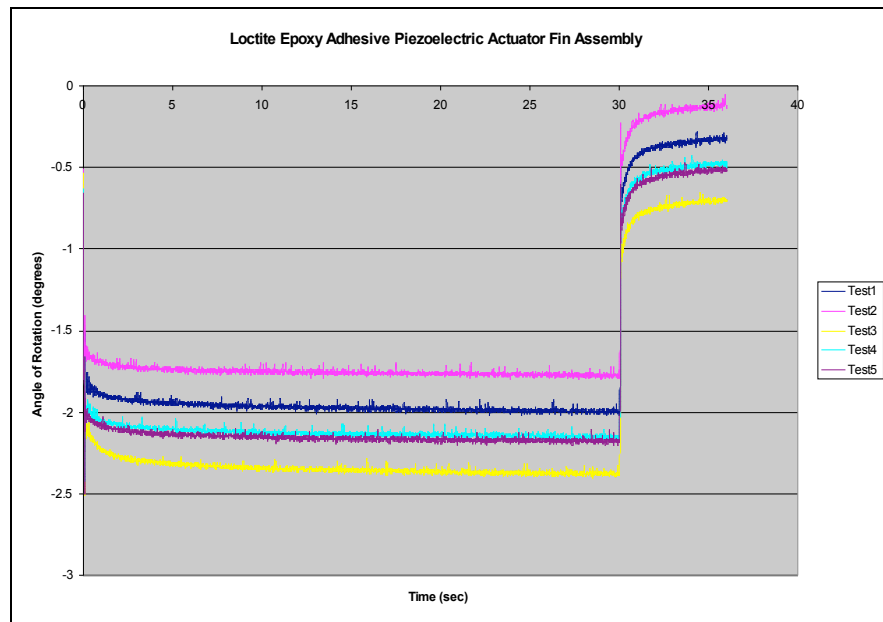


Figure 23. +1500V/-500V Loctite Epoxy Adhesive Piezoelectric Actuator Smart Fin Assembly Tests.

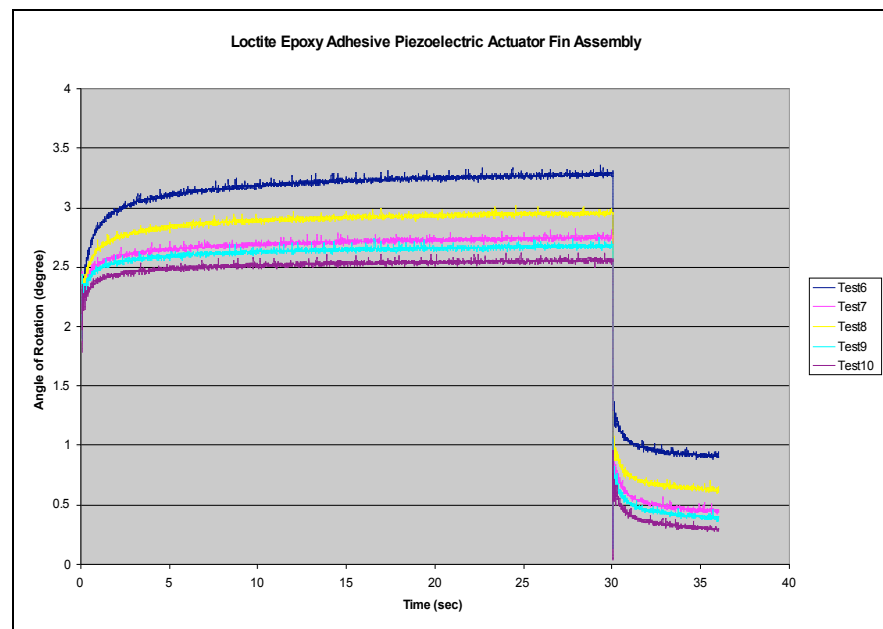


Figure 24. -500V/+1500V Loctite Epoxy Adhesive Piezoelectric Actuator Smart Fin Assembly Tests.

A summary of the average maximum angles of rotation before and after “reconditioning” is given in Table 2. There is an average increase in angle of rotation of 0.31785 degrees after “reconditioning”.

Table 2. Summary of Average Maximum Angles of Rotation for Loctite Epoxy Adhesive Piezoelectric Actuator Smart Fin Assembly.

Voltage	Average Maximum Angles of Rotation (degrees)	Maximum Angle of Rotation after “reconditioning” (degrees)
+1500V/ -500V	-2.0443	-2.3969
-500V/ +1500V	2.7365	3.0196
0V	-0.2584	-0.5714

2. Rotary Encoder Measurements

The test procedures when testing the Loctite epoxy adhesive piezoelectric actuator smart fin with the rotary encoder consisted of applying +1500V to the top MFC and -500V to the bottom MFC. The voltages were switched for tests 6-10 and then switched back for test 11. After 10 seconds of applied voltage the angle of rotation measurements were recorded manually from a laptop with the results given in Figure 25. Before tests 3 and 8 were conducted both MFC’s were “reconditioned” for one minute. Once again, switching the voltages to the MFC’s before tests 6 and 11 produced the overall largest angles of rotation.

It can be seen from Table 3 that the rotary encoder measurements are in close agreement with the angles of rotation measured by the laser for the Loctite epoxy adhesive piezoelectric actuator smart fin given in Table 2. The average angle of rotation without “reconditioning” was -1.79 degrees for tests 1-5 and 2.40 degrees for tests 6-10. Also, switching the applied voltages to the MFC’s the first time resulted in an angle of rotation of 3.72 degrees and switching the applied voltages again produced an angle of rotation of -3.14 degrees.

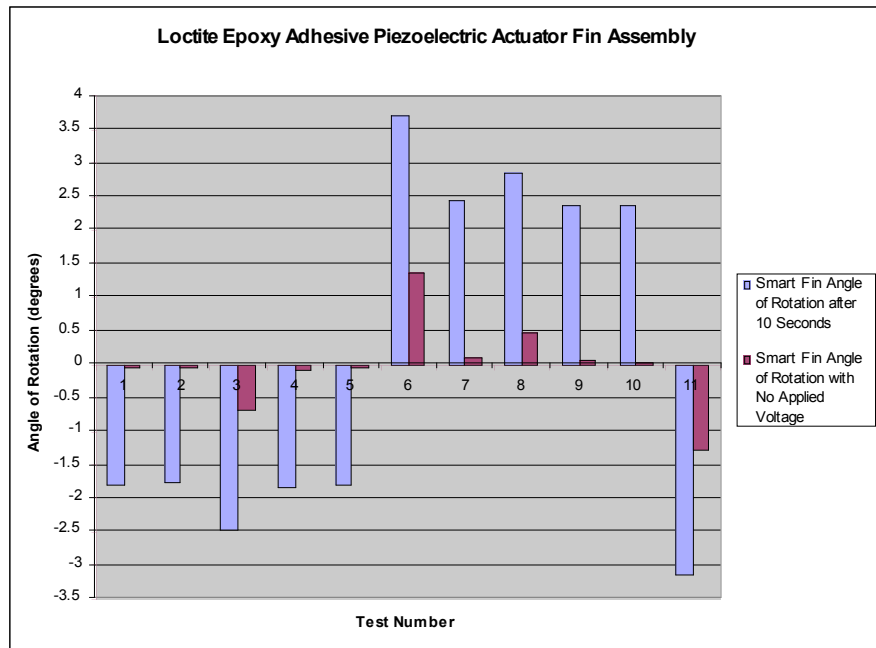


Figure 25. Rotary Encoder Measurements for the Loctite Epoxy Adhesive.

Table 3. Summary of Rotary Encoder Measurements for the Loctite Epoxy Adhesive Piezoelectric Actuator Smart Fin.

Test Number	Angle of Rotation for Maximum Allowable Voltages (degrees)	Angle of Rotation for No Applied Voltage (degrees)
1	-1.79	-0.05
2	-1.76	-0.03
3	-2.45	-0.69
4	-1.82	-0.09
5	-1.79	-0.05
6	3.72	1.37
7	2.45	0.1
8	2.86	0.47
9	2.39	0.05
10	2.37	0.04
11	-3.14	-1.26

VI. □ Wind Tunnel Tests

A. Setup

The majority of the wind tunnel test setup, which was done by the personnel at the wind tunnel facility, consisted of attaching the smart fin and base plate assembly to the balance of the wind tunnel and running the wires from the piezoelectric actuator to the control room. The wind tunnel balance was the circular metal plate seen in Figure 26. It was used to measure the aerodynamic forces on the smart fin and to rotate the smart fin to predetermined, fixed angles of attack seen in Figure 26 (a). This predetermined, fixed angle of attack will be referred to as the balance angle. Also, Figure 26 (a), (b), and (c) show different views of the missile half body which was machined out of a six inch diameter wood log. The missile half body was screwed to the wind tunnel floor. The spar and base plate were fixed inside the missile half body in order to minimize perturbations on the air flow that would otherwise be caused by the drag of the spar and base plate.

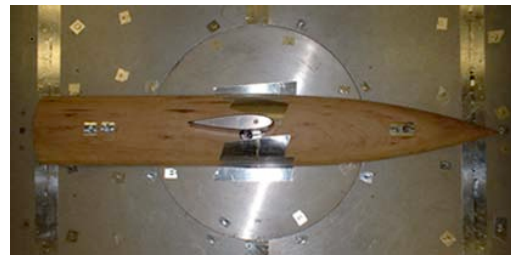
B. Procedures and Results

The wind tunnel test consisted of 12 tests. The first two tests were used to calibrate the wind tunnel balance. No data was recorded during these tests. Tests 3-7 were performed using the 250 °F cure structural film adhesive piezoelectric actuator smart fin and the Loctite E-120HP room temperature epoxy adhesive piezoelectric actuator smart fin was tested during tests 9-12. For Tests 4-12, the maximum allowable voltage was applied for 30 seconds and then the maximum angle of rotation was recorded from the rotary encoder. Another angle of rotation measurement was recorded at 60 seconds to determine the time dependent response of the piezoelectric actuators.

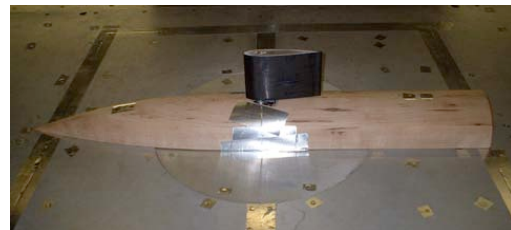
Test 3 was a preliminary test done at 60mph with the smart fin sweeping through various balance angles. No voltage was applied to the piezoelectric actuator for this test. Table 4 provides the angle of rotation seen by the rotary encoder at the various balance angles. These angles of rotation were



(a)



(b)



(c)

Figure 26. a) Smart Fin Rotated at a Predetermined, Fixed Angle of Attack, b) Top View of Wind Tunnel Setup, c) Side View of Wind Tunnel Setup.

produced only by the aerodynamic forces acting on the smart fin.

Table 4. Wind Tunnel Test 3 Results.

Balance Angle (degrees)	Smart Fin Angle of Rotation (degrees)
0	-0.05
5	-0.02
0	-0.05
-5	-0.04
-10	-0.05

After test 3, the wind was turned off and a maximum allowable voltage test was performed on the smart fin where initially +1500V was applied to the top MFC and -500V was applied to the bottom MFC. The voltages were then turned off and then switched. The results from this test are seen in Table 5. These angles of rotation are similar to the initial experimental results of Table 1.

Table 5. Maximum Voltage Test with No Wind Following Test 3.

Voltage	Smart Fin Angle of Rotation (degrees)
+1500V/-500V	-2.87
0V	-0.62
-500V/+1500V	2.89

The rotary encoder was zeroed then test 4 was conducted at 100mph with the smart fin sweeping through positive balance angles. The maximum allowable voltage was applied to the piezoelectric actuator and switched continuously at each balance angle. It can be seen from the results presented in Table 6 that when the balance angle was increased, the angle of rotation of smart fin against the wind decreased and the angle of rotation of the smart fin with the wind increased.

Table 6. Wind Tunnel Test 4 Results.

Balance Angle (degrees)	Smart Fin Angle of Rotation after 30 sec. (degrees)	Smart Fin Angle of Rotation after 60 sec. (degrees)
0	-3	-3
0	3.26	3.44
0	-2.92	-2.99
0	3.34	3.43
5.01	-2.74	-2.83
5.01	3.31	3.42
5.01	-2.75	-2.81
5.01	3.35	3.44
10.02	-2.52	-2.59
10.02	3.45	3.55
10.02	-2.6	-2.7
10.02	3.48	3.5

Following test 4, the wind was turned off and another maximum allowable voltage test was performed on the smart fin. The results from this test are seen in Table 7. When compared with the zero balance angle results of Table 6 it can be seen that the angles of rotation generated by the smart fin were larger when the wind was turned on.

Table 7. Maximum Voltage Test with No Wind Following Test 4.

Voltage	Smart Fin Angle of Rotation after 30 sec. (degrees)	Smart Fin Angle of Rotation after 60 sec. (degrees)
+1500V/-500V	-2.68	-2.74
-500V/+1500V	2.86	2.93
+1500V/-500V	-2.68	-2.74
-500V/+1500V	2.84	2.91

Table 8 shows the results from Test 5 where the wind velocity was increased to 150mph. The balance angle was set at zero and the maximum allowable voltage was applied to the piezoelectric actuator and switched continuously. Once again, at a balance angle of zero, the angles of rotation generated by the smart fin with the wind turned on were larger then the angles of rotation seen for the maximum allowable voltage test with no wind.

Table 8. Wind Tunnel Test 5 Results.

Balance Angle (degrees)	Smart Fin Angle of Rotation after 30 sec. (degrees)	Smart Fin Angle of Rotation after 60 sec. (degrees)
0	-2.8	-2.88
0	3.59	3.76
0	-2.78	-2.88
0	3.65	3.8

During Test 6 the wind velocity was increased to 200mph and the smart fin was swept through various balance angles. At each balance angle, the maximum allowable voltage was applied to the piezoelectric actuator and switched continuously. The results are given in Table 9. When comparing these results with those of Table 6 it can be seen that the for the five and ten degree balance angles, the smart fin angles of rotation into the wind were decreased but increased in the direction of the wind due to the increased wind velocity. Also included in this table are the average sweep angles which are calculated by adding the absolute value of the negative smart fin angle of rotation to the positive smart fin angle of rotation. As the balance angle increases, so do the aerodynamic forces subjected on the smart fin; this therefore decreases the range of the sweep angle.

Table 9. Wind Tunnel Test 6 Results.

Balance Angle (degrees)	Smart Fin Angle of Rotation after 30 sec. (degrees)	Smart Fin Angle of Rotation after 60 sec. (degrees)	Average Sweep Angle (degrees)
0	-2.95	-3.05	7.02
0	3.99	4.14	
0	-2.9	-2.99	
0	3.96	4.1	
4.93	-2.43	-2.5	6.26
4.93	3.52	3.65	
4.93	-2.78	-2.88	
4.93	3.55	3.71	
9.92	-1.7	-1.88	5.65
9.92	3.88	3.97	
9.92	-1.59	-1.72	
9.92	3.88	3.98	
-9.96	-2.55	-2.65	5.3
-9.96	2.64	2.72	
-9.96	-2.6	-2.69	
-9.96	2.64	2.7	

The last test conducted on the 250 °F cure structural film adhesive piezoelectric actuator smart fin was performed at 200mph, but no voltage was applied to the piezoelectric actuator. The balance angle was swept and angle of rotation measurements, shown in Table 10, were taken at each angle. These angles of rotation were produced only by the aerodynamic forces acting on the smart fin. There were no time dependent measurements taken due to the fact that no voltage was being applied to the actuator.

Table 10. Wind Tunnel Test 7 Results.

Balance Angle (degrees)	Smart Fin Angle of Rotation (degrees)
0	0.2
-9.89	0.3
-4.99	0.55
0	0.25
5.01	0.34
10.02	0.92

The piezoelectric actuators were changed after test 7. The wind tunnel balance had to then be recalibrated during test 8. No data was recorded for this test. After the recalibration test, the wind was turned off and a maximum allowable voltage test was performed on the smart fin where the voltages were switched continuously. The results from this test are given in Table 11.

Table 11. Maximum Voltage Test with No Wind Following Test 7.

Voltage	Smart Fin Angle of Rotation after 30 sec. (degrees)	Smart Fin Angle of Rotation after 60 sec. (degrees)
+1500V/-500V	-2.80	-2.88
-500V/+1500V	3.13	3.22
+1500V/-500V	-2.80	-2.87
-500V/+1500V	3.16	3.26

The balance angle was set at zero with a wind velocity of 150mph for test 9. The maximum allowable voltage was applied to the piezoelectric actuator and switched continuously. Table 12 provides the results for this test.

Table 12. Wind Tunnel Test 9 Results.

Balance Angle (degrees)	Smart Fin Angle of Rotation after 30 sec. (degrees)	Smart Fin Angle of Rotation after 60 sec. (degrees)
0	-3.45	-3.55
0	2.71	2.9
0	-3.49	-3.54
0	2.78	2.85

The wind velocity was increased to 200mph for test 10 with the results given in Table 13. For this test, the maximum allowable voltage was applied to the piezoelectric actuators and switched continuously. The smart fin was swept through positive balance angles only. When compared with the zero balance angle results of Table 12 it can be seen that the negative smart fin angles of rotation were increased with the increase in wind velocity but there was little change in the positive angles of rotation. Similar to the results of Table 9, the range of the sweep angle decreases as the aerodynamic forces subjected on the smart fin increase with balance angle.

Table 13. Wind Tunnel Test 10 Results.

Balance Angle (degrees)	Smart Fin Angle of Rotation after 30 sec. (degrees)	Smart Fin Angle of Rotation after 60 sec. (degrees)	Average Sweep Angle (degrees)
0	-3.9	-3.99	6.77
0	2.7	2.88	
0	-3.95	-4.05	
0	2.72	2.9	
2.4	-3.96	-4.01	6.89
2.4	2.8	3	
2.4	-3.98	-4.02	
2.4	2.85	2.95	
4.9	-3.77	-3.85	6.28
4.9	2.38	2.5	
4.9	-3.75	-3.85	
4.9	2.45	2.55	
7.41	-3.5	-3.59	5.83
7.41	2.2	2.35	
7.41	-3.5	-3.58	
7.41	2.25	2.35	
9.9	-3.1	-3.15	5.62
9.9	2.45	2.45	
9.9	-3.05	-3.2	
9.9	2.48	2.6	

Test 11 was performed at 200mph with the balance angle being swept to large negative angles. The maximum allowable voltage was once again applied to the piezoelectric actuators and switched continuously. More often than not, the results, presented in Table 14, are similar to the results for the positive balance angle test given in Table 13 implying that the angles of rotation are symmetric.

Table 14. Wind Tunnel Test 11 Results.

Balance Angle (degrees)	Smart Fin Angle of Rotation after 30 sec. (degrees)	Smart Fin Angle of Rotation after 60 sec. (degrees)
0	-3.9	-3.91
0	2.92	3.01
-2.51	2.75	2.88
-2.51	-3.8	-3.91
-5.01	-3.62	-3.68
-5.01	2.42	2.5
-7.5	-3.6	-3.65
-7.5	2.1	2.19
-10	-3.82	-3.89
-10	1.6	1.65
-12.49	-4.01	-4.15
-12.49	1.15	1.22
-14.89	-4.44	-4.48
-14.89	0.65	0.75
-17.39	-4.8	-4.88
-17.39	0.17	0.28

Lastly, test 12 was conducted with no applied voltage. The balance angle was continuously swept from -9.92 degrees to 12.47 degrees. No time dependent angle of rotation measurements were taken since no voltage was being applied. The results, given below in Table 15, show the range of the smart fin rotation generated by the aerodynamic forces only.

Table 15. Wind Tunnel Test 12 Results.

Balance Angle (degrees)	Smart Fin Angle of Rotation (degrees)
-9.92	-1.2
-7.52	-0.92
-5.01	-0.72
-2.51	-0.5
-0.02	-0.5
2.48	-0.84
4.97	-0.85
7.48	-0.7
9.98	-0.41
12.47	-0.05

VII. □ Conclusion

As seen by the experimental results, designing an active fin for ballistic projectiles using piezoelectric actuators is feasible. The smart fin design consisted of several active and inactive parts. The active part was a piezoelectric actuator designed as a sandwich structure consisting of a thin and flexible host layer along with two thin layers of adhesive that bonded the piezoelectric material to the top and bottom surfaces of the host layer. In order to provide a low modulus structure, the host material was composed of two unidirectional E-Glass epoxy layers. For experimental purposes, two different adhesives were used in fabricating the piezoelectric actuators. These adhesives

were a 250 ° F cure structural film adhesive and a Loctite E-120HP epoxy adhesive. A relatively new piezoelectric material called Macro Fiber Composites was used in manufacturing the actuators. This piezoelectric material was chosen due to its flexibility, durability, damage tolerance and ease of use.

The inactive parts of the smart fin design included the spar, shaft insert, base plate, outer shell, and ribs. The spar was manufactured from a steel hollow circular shaft. The shaft insert and base plate were machined out of an aluminum rod and block, respectively. Three plies of 3K, Plain Weave Graphite Fabric were wet laminated over a Styrofoam airfoil mold and cured at room temperature in order to create the outer shell. Finally, the ribs were water jet cut from pieces of aluminum.

The first assembly process involved bonding/potting the piezoelectric actuators into the shaft insert and then the spar. Loctite E-120HP epoxy adhesive was used in the potting process. The slot machined in the shaft insert, into which the piezoelectric actuator was fitted, was first filled with the epoxy. Epoxy was then applied to the inner diameter of the spar where the shaft insert and piezoelectric actuator assembly was inserted. The final assembly process involved simply inserting the spar and actuator assembly into the outer shell. This was done using the ribs which had holes water jet cut out of them to allow the spar to be attached to the outer shell using hinge connections. The hinge connections consisted of silicon bronze bearings on nylon bushing, which allowed for low friction contact to minimize mechanical losses.

In order to actuate the piezoelectric actuators, power supplies were needed. Three power supplies were used in testing these actuators. Two power supplies of similar make, which provided a voltage range from -1000V to +1000V, were wired in series with the third power supply. The third power supply constantly provided +500V allowing the maximum allowable applied voltages, +1500V and -500V, to be delivered to the MFC's.

The entire smart fin assembly was tested using applied voltages. The smart fin assembly tip deflections were measured using a laser and the angles of attack achieved by the smart fin were measured using a rotary encoder. A LabVIEW program was used to record these measurements.

The angles of rotation that were achieved with applied voltages were graphed over time for the Loctite epoxy piezoelectric actuator fin. Also, three different phenomena were noticed from the test results. The first phenomenon was that the smart fin angles of attack/rotation seemed to slowly increase over time. The second phenomenon was that when both of the MFC's were "reconditioned" or subjected to the maximum allowable voltage in between tests the following test would result in increased performance. A third phenomenon was seen after the applied voltages

had been switched. For example, when testing an actuator with +1500V applied to the top actuator and –500V applied to the bottom actuator a certain angle of rotation was achieved, but after switching the voltages to –500V applied to the top actuator and +1500V applied to the bottom actuator a performance even higher than the increased performance resulting from the second phenomenon was seen.

Lastly, in order to study the performance of the smart fins in a practical application, wind tunnel tests were conducted. The smart fins performed well in the wind tunnel tests. Angles of attack/rotation similar to those seen in the experimental tests were achieved by the smart fin and no flutter was experienced while being subjected to wind velocities of 200mph. These wind tunnel tests encouraged further wind tunnel testing to be performed on the smart fins as well as fabricating additional piezoelectric actuators using different host materials. Manufacturing the piezoelectric actuators with a thinner host layer will be considered since the smart fins did not flutter during the wind tunnel tests. A thinner host layer will result in larger angles of rotation, therefore, increasing the performance of the smart fin.

Acknowledgments

J. T. Arters would like to acknowledge Roderic Don for his large contributions to this research project. Gratitude is given to him for his help in preparing the experimental equipment and procedures and for his help in the manufacturing processes. Also, he is responsible for designing several of the smart fin components as well as creating the 3-D computer automated drawings of the various smart fin components and assemblies.

J. T. Arters would like to thank the Center of Composite Manufacturing at the University of Delaware for the use of their test facilities and the Army Research Laboratory for the sponsorship of this project. The advice and help of Touy Thiravong is also appreciated.

References

¹Rabinovitch, O. and Vinson, J.R., “On the Design of Piezoelectric Smart Fins for Flight Vehicles”, *Smart Materials and Structures*, Vol. 12, 2003, pp. 686-695.

²Williams, R.B. and Inman, D.J. n.d., “An Overview of Composite Actuators with Piezoceramic Fibers”, Center for Intelligent Material Systems and Structures, Department of Mechanical Engineering, Virginia Polytechnic Institute and State University, viewed 10 November 2004, Smart Material Website, http://www.smart-material.com/media/Publications/27_wil.pdf.

Evaluation of Composite Bonded Joint Designs for Space Applications

Keith T. Kedward* , Yuqiao Zhu [†] and Steven H. Kiefer[†]

University of California, Santa Barbara, CA 93106, USA

Acceptable approaches that can be utilized for establishing safe operational loads for adhesively-bonded composite joints invariably adopt an integrated methodology. The methodology selected typically combines theoretical analysis, both numerical and closed-form, supported by a carefully-planned experimental program. Specific details of the approach may range widely with regard to the balance of analysis versus experimental content as dictated by the environmental conditions and the nature of the processing and fabrication methods that are to be adopted.

For the orbiting space instrument platforms of interest in this paper the range of temperature extremes are progressively increasing and consequently major concerns with respect to thermal stress and distortion of composite and metallic assemblies have become particularly challenging. In most instances a combination of analysis techniques are utilized for space hardware designs, e.g. a "macroscopic" finite element analysis to define mechanical and thermal loadings developed in the various structural joints and attachments followed by use of either detailed closed-form analyses or more refined finite element analyses of the individual joint configurations. As an example the complex arrangement of structural joints on the Mars Exploration Rover (MER) Lander Structure was analyzed by using a global finite element model plus a series of theoretical analyses of adhesive bondline stresses based on a combination of Volkersen, shear lag and Beam-on-Elastic-Foundation models. These closed form expressions were used to evaluate the distributions of shear and peel stresses developed in the bonded joint details.

In this paper the acceptability of the above methodology is evaluated using, as background, results of previous UCSB research, directed at general aviation composite aircraft structures for which the mechanical loading conditions are the dominant concern. Acknowledging that most geometrically practicable designs of bonded lap joints exhibit high shear and peel stresses in the end regions of the lap length confined to less than 5% of the total lap length. To illustrate the localized nature of the bondline stress distribution the more critical region at the termination of the outer adherend of a double lap joint where general tensile loading is considered.

Two finite element modeling techniques were also used to predict both the shear and the peel stress distributions also along the adhesive central plane. A simplified finite element model (FEM) utilizes two noded interface elements to represent the adhesive layer, and combines both shear and peel effects where appropriate. The results for this model are illustrated and indicate slightly lower maximum shear stresses but again violates the free edge condition. Finally a more conventional 8-node plane strain quadrilateral FEM is used for both adhesive and adherend regions and is shown to yield the lowest peak shear stresses. It is noted here, however, that by using the relatively high fidelity mesh subdivision indicated that the vanishing free edge shear stress condition is satisfied with this model.

Recommendations will be presented along with expressions for predicting peel stress states developed under mechanical and thermal loadings. The conclusions are intended to serve the design/analyst who is chartered with the task of developing reliable criteria, based on selective experimental evidence, for bonded composite joints.

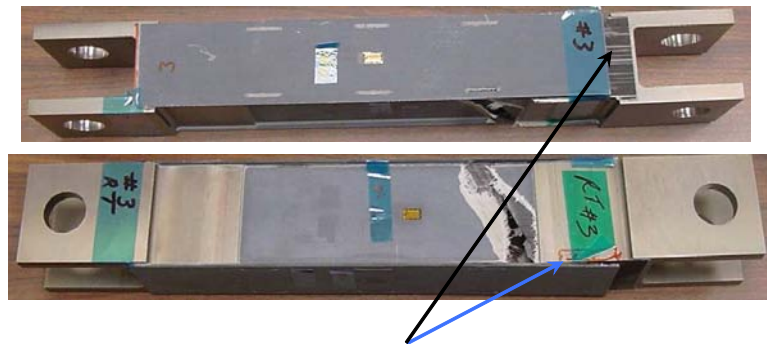
*Professor, Department of Mechanical Engineering, University of California, Santa Barbara, and AIAA Fellow.

[†]Graduate student, Department of Mechanical Engineering, University of California, Santa Barbara.

I. Introduction

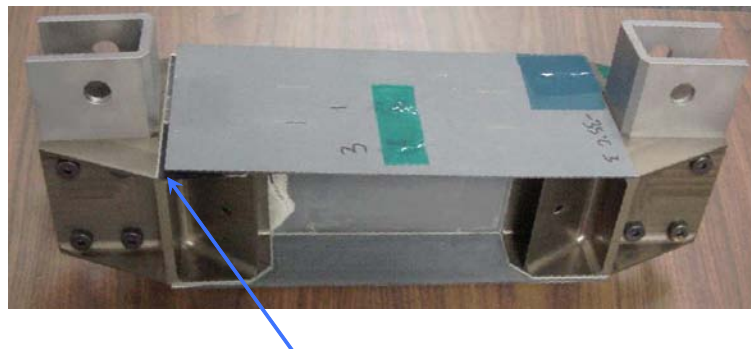
A current perception that there exists throughout the technically-oriented structural composites industry an expanded usage of adhesive-bonded approaches. This situation and the fact that Dr. James Starnes himself had recognized this trend several years ago prompted the motivation for this paper. In concert with this trend is the general acknowledgement that the design analysis functions directed at the stress analysis and failure prediction for adhesively bonded structural joints has represented a special challenge and, indeed, much frustration.

We also make the observation that the expanded application of adhesive bonding has been impacting the space structures community extensively in recent years; a consequence of the need to design for progressively lower temperatures and the attendant growth in differential thermally-induced strains, to the high-altitude autonomous air vehicles applications, for similar reasons, and even to the recreational sports-equipment industry, e.g. golf club heads for largely aesthetic advantages. Specifically, however, we cite an example of hardware development failures experienced in some complex configurations of structural joints associated with the Mass Exploration Rover (MER) Lander structure, see Figure 1, 2. Here, interfacial type failures were observed between the titanium and the carbon fiber-reinforced cyanate-ester matrix composite layers. In this paper, however, we will concentrate on illustrating the potential treatment and complexities to be addressed in a geometrically much simpler configurations, the single and double lap joint, that are used widely to provide experimental data that can support the early stage of the design effort.



Typical Failure Mode
- Primary Failure (Interlaminar Shear) at Single Lap Bond Region

Figure 1. Typical failure surface 1



Typical Failure Mode
- Primary Failure (Interlaminar Shear) at Single Lap Bond Region

Figure 2. Typical failure surface 2

A. Background

As a background to the subject we include our previous research conducted in support of the general aviation industry for which relatively "ductile" adhesives are utilized and considerable variability is generally unavoidable in regard to bondline thickness control for example. In these cases the methods due to Hart-Smith¹ are frequently adopted and, in an effort to assess the general applicability of such simplified approaches, we provide a case study that includes a skin-doubler, splice joint design study. In addition examples of analysis of both linear elastic and nonlinear (elastic-plastic) adhesive phenomena for single and double lap joints are treated and comparisons between finite element analysis and by use of simple shear lag (Volkersen) and Beam-on-Elastic Foundation models are included. The discussion builds on our previous research activity^{2 3 4} and on the predominantly experimental research on surface preparation measured by mode I fracture testing of an adhesively-bonded composite joints.^{5 6}

Further development of some refinements of the aforementioned simplified analysis are also presented and include the approximation of transverse and shear deformation effects contributed by Tsai, Opliger and Morton.⁷

II. Analysis, Development and Results

A. Stress Distribution in a Double Lap Joint Configuration

A typical double lap joint configuration is used for this case study. The half overlap length c is 12.7 mm, the thicknesses of the outer adherend t_o , inner adherend t_i and adhesive t_a are 1.27, 1.27 and 0.127 mm, respectively. Geometrical details are indicated in Figure 3, and a defect-free bond is assumed. The linear-elastic material properties are as follows:

Epoxy Adhesive: Young's modulus $E_a = 4.14 GPa$, Poisson's ratio $\nu_a = 0.43$

Aluminum Adherends: $E = 71.7 GPa$, $\nu = 0.33$

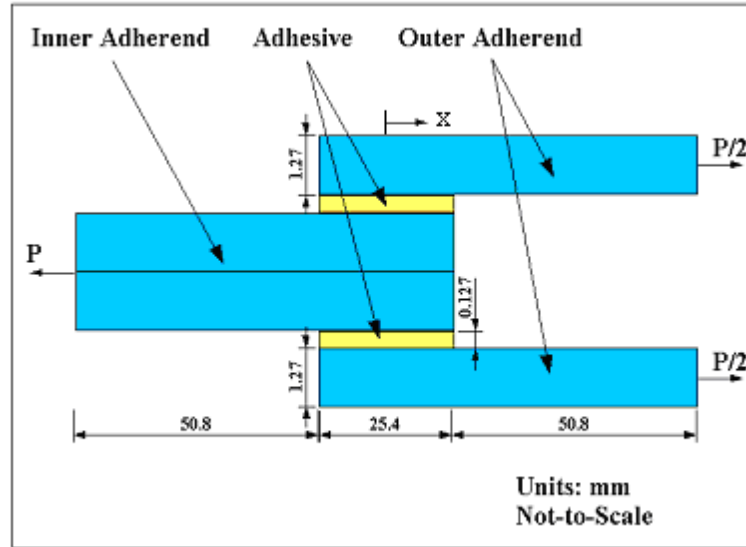


Figure 3. A typical double lap joint configuration

1. Volkersen solution and adaptations by Tsai, Oplinger and Morton

Volkersen⁸ first proposed a simple shear lag model for load transfer from one adherend to another by a simple shearing mechanism alone. In the model, the adherends are assumed to support purely tensile loading and the adhesive is subjected to shear only; the shear stress is assumed to be constant across the thickness of the adhesive layer. The important relationships are given by:

$$\tau(x) = A \sinh \lambda x + B \cosh \lambda x \quad (1)$$

where

$$\lambda^2 = \frac{G_a}{t_a} \left(\frac{1}{E_o t_o} + \frac{2}{E_i t_i} \right)$$

$$A = \frac{\lambda P}{4 \cosh \lambda c} \left(\frac{2E_o t_o - E_i t_i}{2E_o t_o + E_i t_i} \right)$$

$$B = \frac{\lambda P}{4 \sinh \lambda c}$$

In these expressions, the subscripts o , i , and a denote the respective component moduli and thickness pertaining to the outer adherend, inner adherend, and adhesive. The loading parameter P denotes the loading applied at the end of the inner adherend, and the parameter c is half length of the adhesive lap length (12.7 mm in this case). Thus the origin of the x coordinate is the center of joint overlap region.

The Volkersen or shear lag, solution does not reflect the effect of the adherend bending or shear deformation which is potentially significant for composite adherends with a low transverse and thickness-direction moduli and strength. Tsai, Oplinger and Morton⁷ (hereafter referred to as the TOM solution) provided a correction to the shear lag model with the assumption that the shear stress is linear through the adherend thickness at all axial locations. As a result, λ^2 is replaced by β^2 :

$$\beta^2 = \alpha^2 \lambda^2 \quad (2)$$

where

$$\alpha^2 = \left\{ 1 + \frac{G_a}{t_a} \left(\frac{t_o}{3G_o} + \frac{t_i}{6G_i} \right) \right\}^{-1}$$

2. Linear finite element analysis(FEA)

For the above double lap joint, several different modeling schemes with regard to the element type and meshing techniques are discussed in detail as described in the following section. A plane strain condition is assumed throughout this study.

h-method: Due to the symmetry of the loads and structure, only one-half of the joint is considered. Eight-node plane strain elements representing the adherends and the adhesive are used to discretize the joint. Figure 4 shows the finite element model. The mesh density is biased with a ratio of 12 near the ends of the adhesive due to the high stress concentration in that region. Details of this local region are shown in Figure 5. The mesh used here is considered to be suitably refined for the present evaluation. In Figure 4, the lower boundary is symmetric, and the left end is fully constrained in the x-direction. A uniform tensile stress, $p = 6.89 \text{ MPa}$, is applied at the right end of the adherend.

Simplified method: An approximate numerical idealization, two-node spring elements for the adhesive and eight-node elements for the adherend are used. According to Loss and Kedward,⁹ the adhesive can be modeled by a pair of springs. In ANSYS, this can be realized by using eight-node elements, for the adherend, and shear and peel spring elements, for the adhesive. The stiffness coefficients of the peel and shear springs are calculated from:⁹

$$k_{peel} = \frac{A_{el}(E_a)_{eff}}{t_a} \quad (3)$$

$$k_{shear} = \frac{A_{el}G_a}{t_a} \quad (4)$$

where $A = l \times b$; E_a and ν_a are adhesive Young's modulus and Poisson's ratio; l , b , t_a , G_a and $(E_a)_{eff}$ are in-plane distance between nodes, width of the joint being modeled, adhesive thickness, elastic adhesive shear modulus, and effective elastic modulus of adhesive, respectively. For a triaxial stress state, $(E_a)_{eff}$ is defined as below

$$(E_a)_{eff} = \frac{E_a(1 - \nu_a)}{1 - \nu_a - 2\nu_a^2} \quad (5)$$

The effective moduli defined here is representation of the constraints imposed in the central region of the adhesive away from the edges.

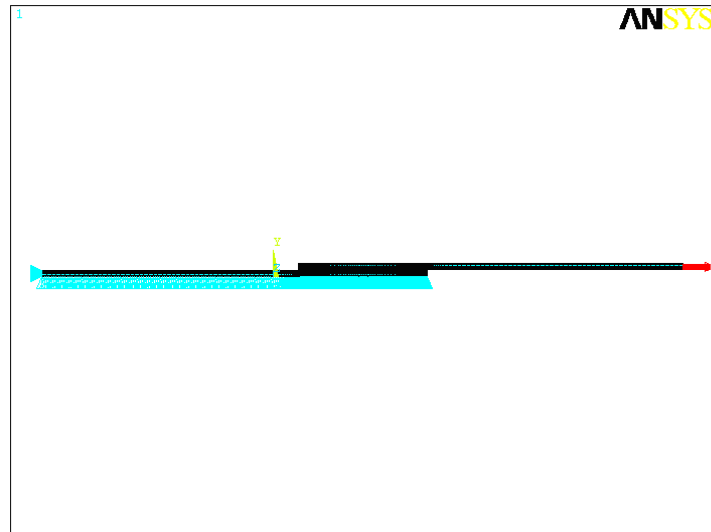


Figure 4. Finite element model using plane82

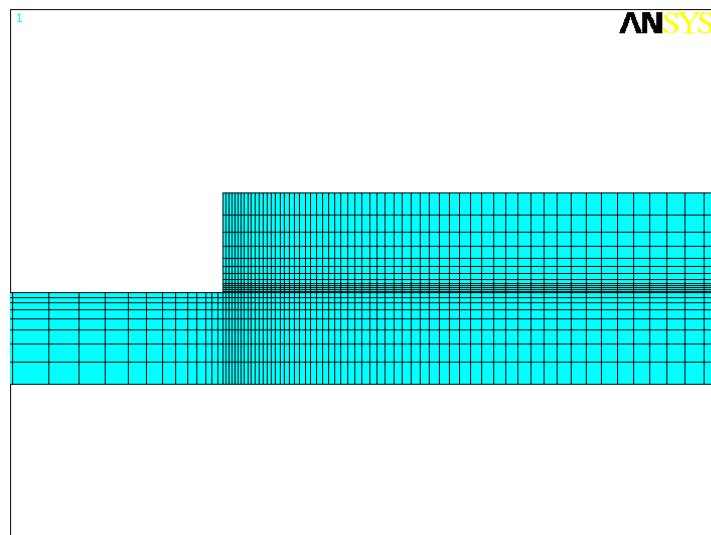


Figure 5. Detail meshes around the termination region of the adhesive

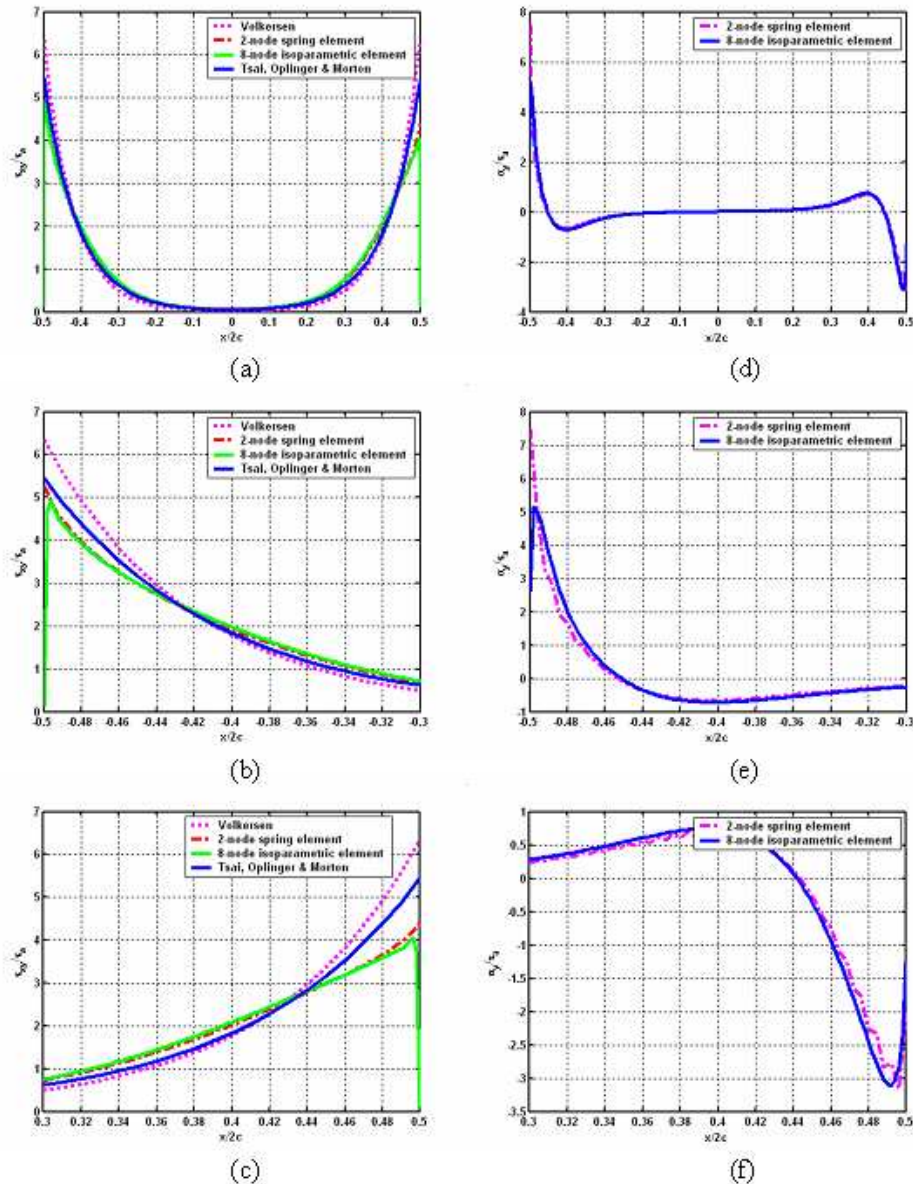


Figure 6. Comparisons of shear and peel stresses along the centerline of the adhesive ((a) and (d) show stress distribution over total overlap region. (b), (e) shows stress distribution in local region at left end of overlap, and (c), (f) in local region at right end of overlap.)

For uniform meshing along the overlap direction of the adhesive, stiffness coefficients for the peel and shear springs at the termination points of the overlap region are one half the stiffness of the internal springs.

All analysis results show that peel and shear stresses near the ends of the lap are the dominant ones among all the stress components. Figure 6 (a)-(f) shows the normalized stress comparison of the spring element and eight-node element results along the centerline of the adhesive with predictions from available closed form solutions. Normalized stress hereafter is referred to as the stress divided by the average bondline shear stress $\tau_a = 0.34MPa$.

The classical Volkersen solution overestimates the maximum shear stress, and the TOM results are closer to the FEA solution (Figure 6 (a)-(c)). This is because Volkersen assumed a one-dimensional model with only shear deformation in the adhesive layer, the effect of the adherend shear deformation being ignored. The TOM accounts for adherend shear deformation by approximating a linear shear stress through the adherends, and thereby predicts that maximum normalized shear stress of 5.45 occurs at both ends of the lap joint overlap. However, the maximum shear stress found by using eight-node elements to represent the adhesive occurs at a small distance from the free edge. Near the left end, the maximum normalized shear stress is 4.91, and near the right edge, it is 4.06.

Figure 6 (d)-(f) shows the comparison of normalized peel stress in the adhesive by using the spring elements and eight-node elements for the adherends. The peel stress prediction by spring element is higher than that obtained by using eight-node elements, and the maximum peel stress is seen to occur at the free edge instead of at a small distance away from the free edge. Near the left end, the peel stress is in tension and near right end, the peel stress is in compression as expected intuitively.

As to the element type used, a high order element is preferred. For the eight-node element analysis, the stress varies within the element and the free surface condition is satisfied. For the "mixed element" modeling, the results are reasonable approximations noting that this is only a relatively coarse mesh (502 spring elements). A finer mesh will involve much manual work in element generation, and it is not convenient to implement. However, this "mixed element" modeling could be very useful for evaluating closed form predictions when the lap joint is simplified as a beam on an elastic foundation considering axial and transverse effects, and it will help understand the mechanism of the adhesive deformation. Furthermore, the idea using spring elements to model the adhesive behavior is also used in the cohesive zone models.^{10 11 12}

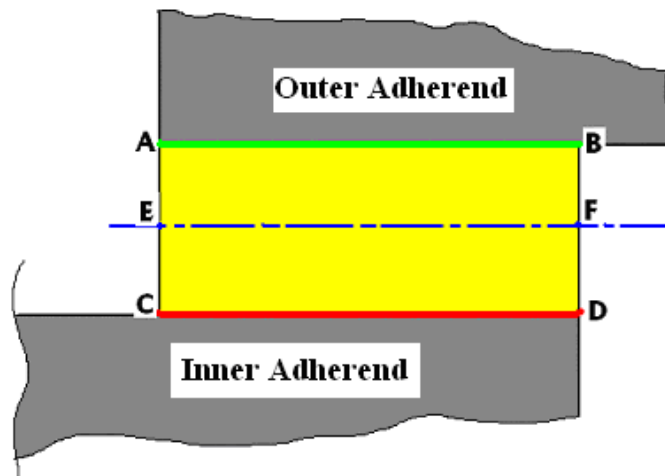


Figure 7. Three different planes along the overlap of the joint

Figure 7 shows three different planes along the overlap region of the joint (AB, CD and EF). Figure 8 (a)-(f) show the stress comparisons along these planes. Considerable stress variation exists near bondline terminations. Apart from that region, stresses can be considered to be close approximation along these three different planes.

p-method: The p-method, in conjunction with the eight-node elements (ANSYS plane145) is used in this

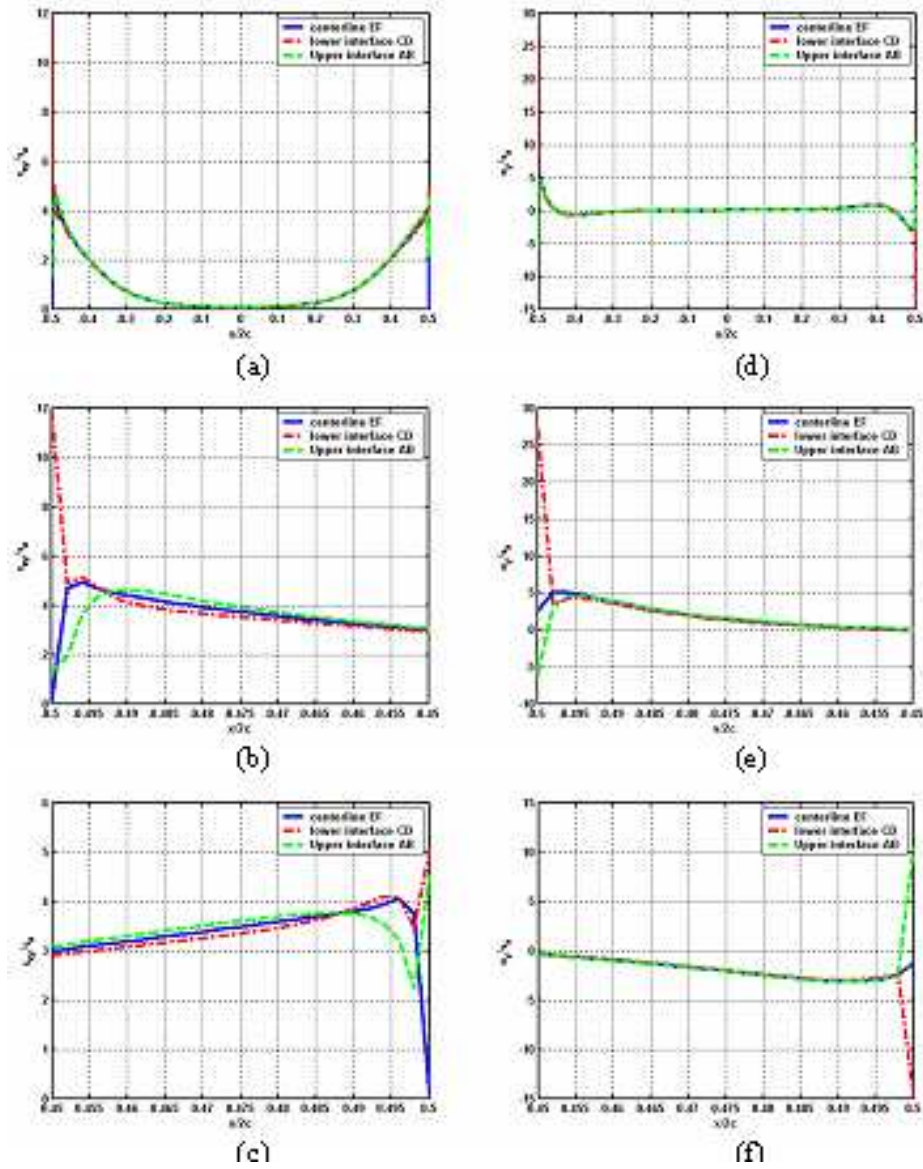


Figure 8. Comparisons of normalized shear and peel stresses along three different planes (AB, CD and EF shown in Figure 7)

section. The mesh subdivision and the total number of the elements and nodes are the same as that used in the h-method. Local convergence criteria at specified locations in the model are used, and it is defined that the tolerance for convergence specifications is 1% based on shear stress τ_{xy} at point A in Figure 9, a distance of 0.038 mm from the free edge along the adhesive centerline.

Peak stresses occurs at the joint corner C (shown in Figure 7), and normalized peak peel stress and shear stress are 51.8 and 20.6 as compared with 27.0 and 11.9 respectively, by h-method. Finally, the p-level which refers to the polynomial level used at the local point A (shown in Figure 9) is shown in Figure 10.

Analysis results show that p-method gives higher peak stresses at the stress singularity point than the h-method using same mesh density. In another words, a finer mesh is needed for the conventional h-method to get the equivalent stress state as in the p-method. Compared with the conventional h-method, a further advantage of using the p-method include the ability of adaptive meshing to obtain good results to a required accuracy, and the error estimate can be made locally and globally except at local points where stress singularity occurs.

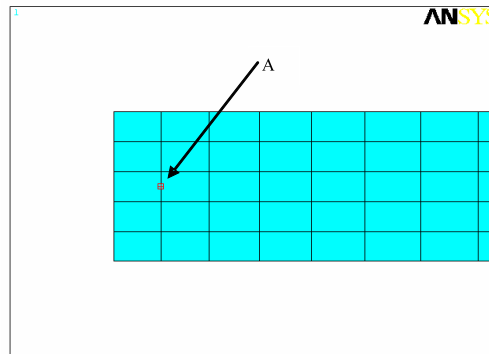


Figure 9. Point A in local adhesive termination region

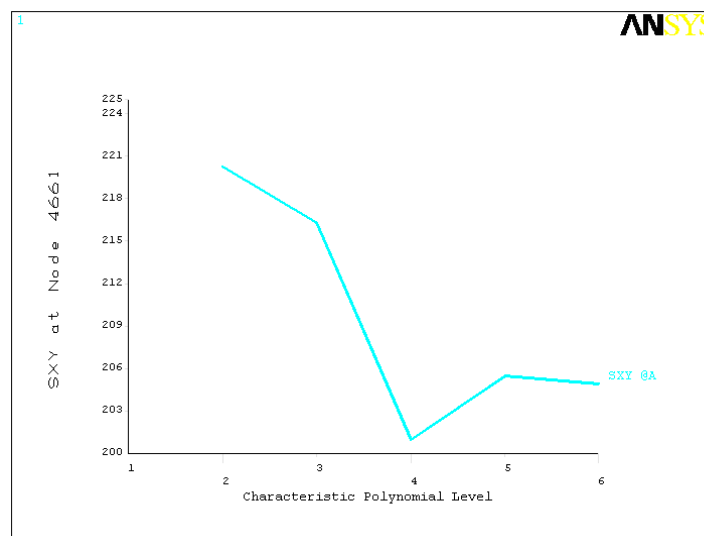


Figure 10. p-level used at point A(shear stress vs. polynomial level)

B. Nonlinear Analysis of a Single Lap Joint Configuration

A single lap joint with Titanium adherends and a ductile adhesive system (Figure 11) is considered. The adherend material is changed to Titanium and the thickness is 0.035 inch (refer to ASTM D1002-99). With one end constrained and at the other end the load is applied gradually until the joint fails unstably due to

large area plastic deformation. Efforts have been made on deciding load control or displacement control to be used for this analysis. As a result, it is found that there is only 0.5% difference in the maximum simulation load in load control and in displacement control.

Analyses for a 0.01 inch and 0.03 inch thickness adhesive yield maximum failure loads of 1870 lb and 1856 lb. Both are less than the test failure load of Titanium single lap joint which varies between 2000 lb to 2200 lb for a range of bondline thickness from 0.01 inch to 0.035 inch. FEA shows that the deformed shape of single lap joint is center symmetric. Von Mises stress contours, at the termination region of the adhesive, under different load levels are shown in Figure 12, 13 and 14 (only the adhesive is shown). It can be seen that the initial yielding starts at the joint corners (stronger singular point), and develops around the joint ends in a certain angle through the thickness of the adhesive, till the whole adhesive yields except a very small region around the weaker singularity point and the free edge.

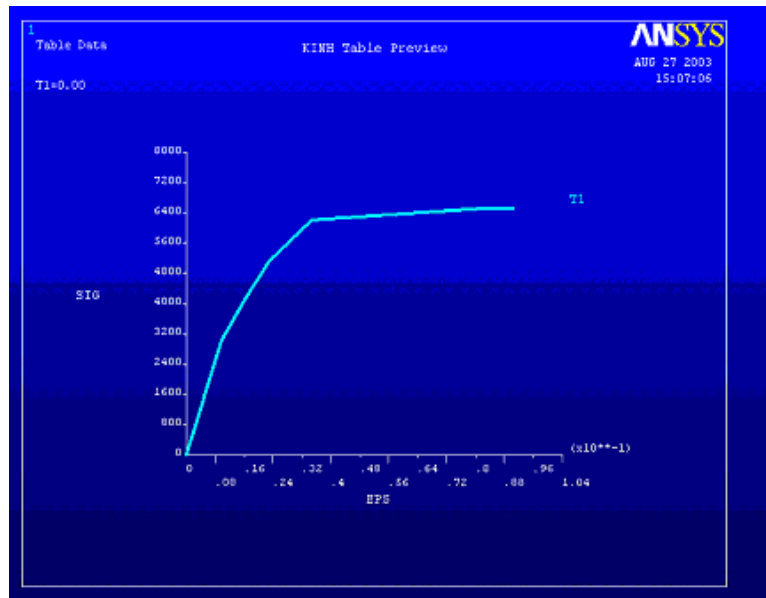


Figure 11. True stress-true strain curve for a ductile adhesive system

Nonlinear analysis of variable bondline thickness from 0.0085 inch to 0.0255 inch ($\bar{t}_a = 0.017inch$) shows that the failure load is 1865 lb., while the test failure load is around 2150 lb. Figure 15 and 16 show the Von Mises stress contours at different load, where a center symmetric characteristic no longer exists, and the yield starts from the left corner. With increasing load, the plastic zone increases until most of the adhesive region has yielded.

It is assumed that the joint is well bonded and the adhesive is representative of the physical condition, the failure load predicted by nonlinear finite element analysis is lower than the test failure load. A possible rationale may be one or more of the following:

- Lower yield strength of the adhesive properties in FEA simulation. Adhesive material properties come from the test results of the adhesive bulk material, in which case, the possibility of more extensive micro-defects increases. From the simple Weibull, statistics viewpoint, the strength of a small volume of adhesive will be higher.
- Spew fillet effects. There is no fillet included in the FEA analysis, whereas in the actual specimen some form of fillet geometry is typically present. It is expected that with such a spew fillet, the maximum predicted load would be higher.
- A different yield criterion may apply. Typically, a polymer material has a higher yield stress in compression than in tension, and unlike the case of the metals, its yielding behavior is pressure dependent.^{13 14 15 16} The following modified Von Mises yield criterion is considered to be appropriate for modeling adhesive yielding:

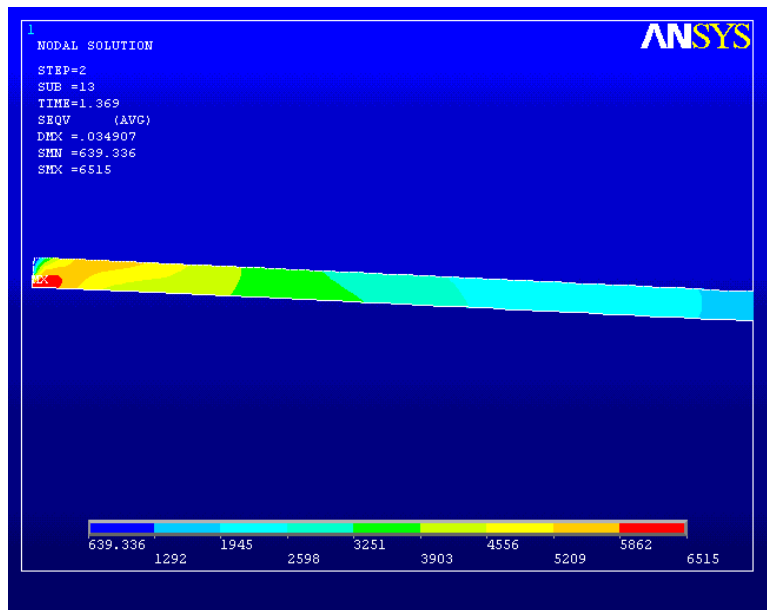


Figure 12. Von Mises stress contours of 0.01 inch thickness joint at $P = 908lb$ ($\bar{\tau} = 1816psi$)

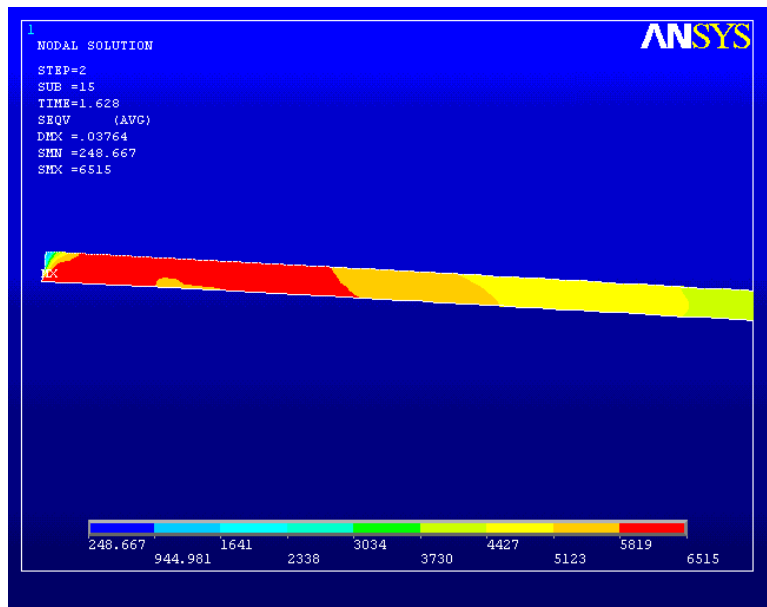


Figure 13. Von Mises stress contours of 0.01 inch thickness joint at $P = 1545lb$ ($\bar{\tau} = 3090psi$)

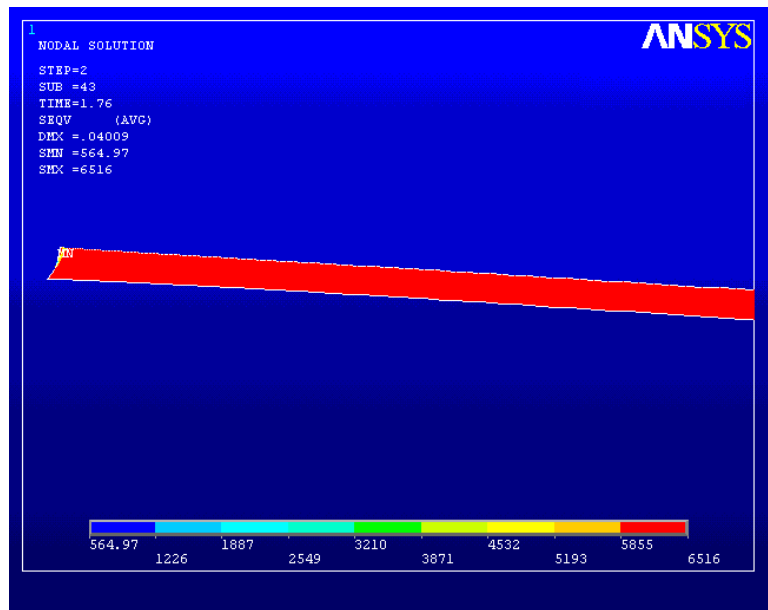


Figure 14. Von Mises stress contours of 0.01 inch thickness joint at $P = 1870lb$ ($\bar{\tau} = 3740psi$)

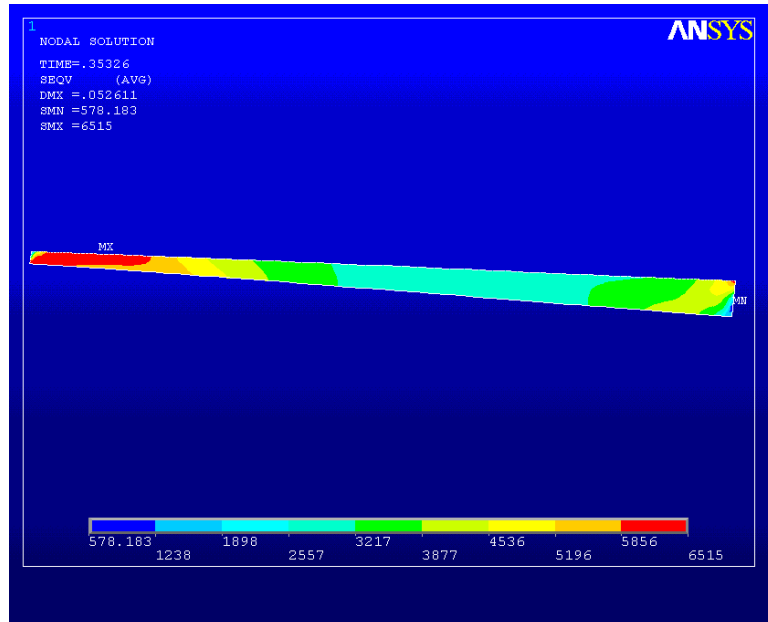


Figure 15. Von Mises stress contours of variable bondline thickness joint at $P = 1122lb$ ($\bar{\tau} = 2244psi$)

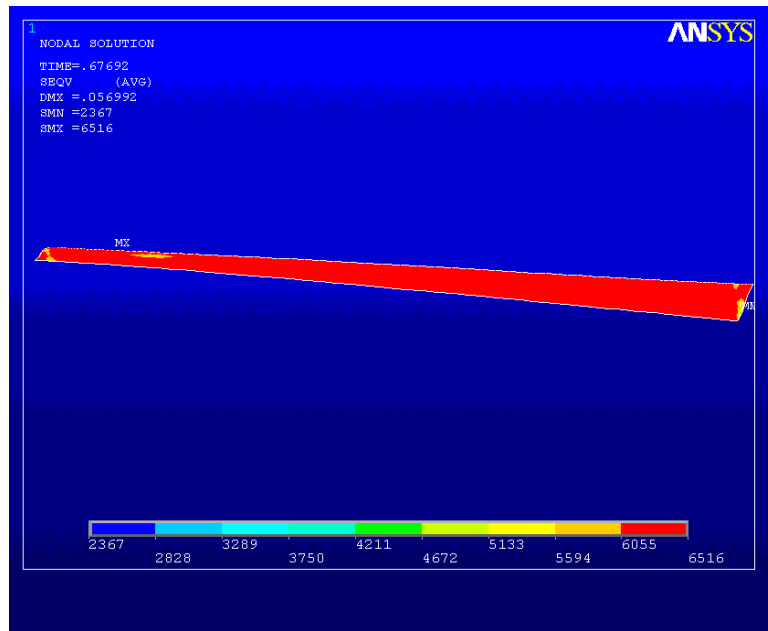


Figure 16. Von Mises stress contours of variable bondline thickness joint at $P = 1865lb$ ($\bar{\tau} = 3730psi$)

$$(\sigma_{vm})^2 - 3(\sigma_{yc} - \sigma_{yt})p = \sigma_{yc}\sigma_{yt} \quad (6)$$

where σ_{vm} , p , σ_{yc} and σ_{yt} are Von Mises stress, hydrostatic stress, yield stresses in compression and in tension, respectively. For the adhesive used, the ratio $\frac{\sigma_{yc}}{\sigma_{yt}}$ is typically assumed to be 1.3.^{13 14 15}

Using the Von Mises yield criterion for the single lap joint studied, a certain point of the adhesive yields when the equivalent stress reaches the yield stress of the adhesive. However, a modified Von Mises yield criterion Eq.(6) might not predict yielding because yielding is also dependent on the level of the hydrostatic stress.

C. On Adhesively Bonded Tubular Assemblies for Space Applications

CFRP composite tubular structures are simple and efficient structural elements incorporated into many space hardware designs. Metallic end fittings are often incorporated in these assemblies due to the complex geometry and load paths existing in these regions. The strict mass requirements imposed on space hardware provide motivation for the use of structural adhesives as the main joining method when attaching the tubular components to the end fittings. While mass efficient, adhesively bonding tubular structures for space applications poses unique challenges that an efficient design must address.

Much of the research in adhesive bonding has focused on simple, flat single lap specimen as general, representative coupons. While many concepts of adhesive bonding gained by studying flat coupons can be applied to tubular joints, the inherent circumferential constraint of tubular adherends adds additional challenges. Concepts such as tapering the adherends near the end of the joint to increase flexibility and reduce peel become less effective with the tubular constraint. Configuration or the relative position of the adherends becomes important due to the differential radial contraction/expansion during thermal loading. Therefore, it is important to evaluate tubular joint designs with tubular specimen relatively early in the design phase.

Adhesively bonded joints for use in space structures are often conditioned by thermal cycling prior to proof testing. Differences in the radial and axial Coefficients of Thermal Expansion (CTE) among the adherends and adhesive itself can initiate damage in the joint during thermal cycling. This damage is often in the form of delamination within the first few plies of the tubular composite adherend and may not be apparent until proof loading. Even when the circumferential CTE of the composite is designed to match the

metallic fitting, the large CTE of the adhesive can cause relative high peel stresses within a tubular joint exposed to low temperatures. See Figure 17.

Fabrication methods and associated design features are more challenging to address for tubular joints. This is mainly due to an often inaccessible internal joint termination region. Controlling the adhesive spew in this region, when injection bonding is employed, is important due to the stress concentrations at regions where the spew fillet makes an angle less than 90 with the adherend. The stress concentrations associated with the spew fillet geometry can be significant and should be controlled. See Figure 18.



Figure 17. Failure surface of CFRP-metal tubular joint. Interlaminar failure occurred within the first ply of the CFRP

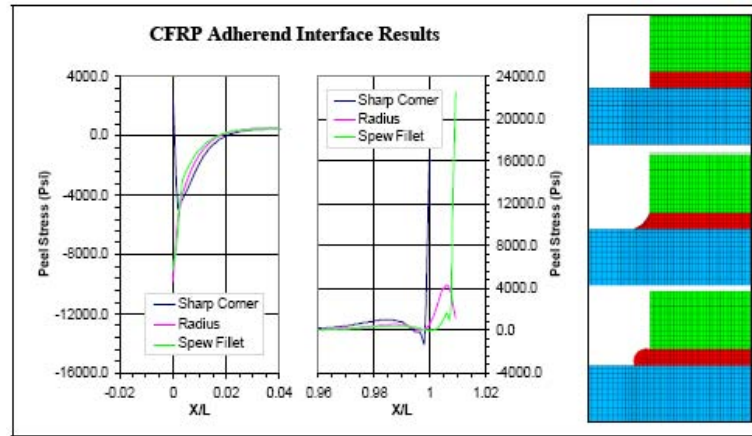


Figure 18. (Left) Stress concentrations near the joint termination regions associated with fillet geometries at the composite to adhesive interface. (Right) Adhesive fillet geometries and finite element model mesh used to develop the stress profiles.

D. Case Study of Doubler Splice Joint Design

We now consider a case study on an adhesively bonded doubler Splice Joint design¹⁷(Figure 19). The overlap length l is 1.46 inch, the free length is taken as 2 inch, and the thicknesses of the outer adherend t_o , inner adherend t_i and the adhesive η are 0.032, 0.05 and 0.005 inch respectively.

The Aluminum adherend properties are as follows: $E = 10.5msi$, $\nu = 0.33$. An elastic perfectly plastic model is assumed with an ultimate stress of $\sigma_{ult} = 65000psi$ and ultimate strain of $\varepsilon_{ult} = 0.15$.

The adhesive is also assumed to be elastic-perfectly plastic material, with $E = 0.105msi$, $\nu = 0.3$, $\sigma_y = 4330psi$ and $\varepsilon_{ult} = 0.10$.

Hart-Smith's design rule shows that the plastic zone size can be obtained using the following formula:

$$l_p = \frac{F_{tu}t_i}{2\tau_p} \quad (7)$$

The finite element model based on plane stress condition and Von Mises yield criterion is used for the analysis. Earlier works^{13 14 15 16} show that a pressure dependent yield criterion is more appropriate for modeling an adhesive, however, due to the limited data available, the basic Von Mises criterion is assumed for the current analysis. For the current model, FEA analysis shows that the joint fails due to yielding of

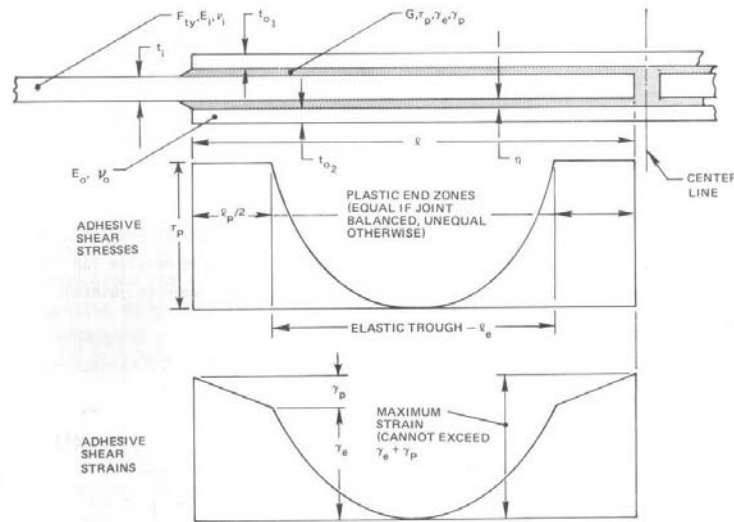


Figure 19. A worked example of a adhesively bonded doubler from Hart-Smith¹⁷

the inner adherend at a failure load of 3270 lb. The Von Mises stress contours at the left and right end of the joint are shown in Figure 20, and plastic shear strain and equivalent plastic strain along the centerline of the adhesive are also shown (Figure 21). At this load, the adhesive partially yields with different plastic zone sizes at each end. The extent of yielding is shown to be significantly lower than that determined by Hart-Smith.¹⁷ This difference results from the over-simplification in the structure of simply shear-induced yielding that is implied by Hart-Smith's design rule.

III. Conclusion

Numerical and analytical methods for adhesively bonded joints were reviewed, applied, and evaluated. The following items serve to summarize the outcomes:

- For bonded joint stress analysis purposes, finite element analysis has been found to be a suitable method of analysis providing that the mesh, boundary condition and the loading are applied appropriately. For FEA modeling using ANSYS, an adequately refined mesh and eight-node element (plane82) are recommended.
- Based on linear analysis, closed form solutions & simplified FEA tend to overestimate the stress levels around the overlap ends, but provide a reasonable estimate of bondline stress distributions at the centerline of the adhesive.
- Along different planes (upper adherend interface, centerline of the adhesive and lower adherend interface), considerable stress variation occurs near bondline terminations. Apart from this region, the differences are small.
- In searching for a workable failure criterion for bonded joints, more extensive studies on testing, post fracture study and nonlinear effects will be performed in the future.
- In the future, the effort will be continued to establish meaningful peel stress prediction (Mechanically and thermally-induced conditions).
- An adequate data base will be developed for temperature-dependent thermo-elastic properties of the adhesive or particularly for low temperature range.
- The methodologies to investigate thermal effects will be extended.

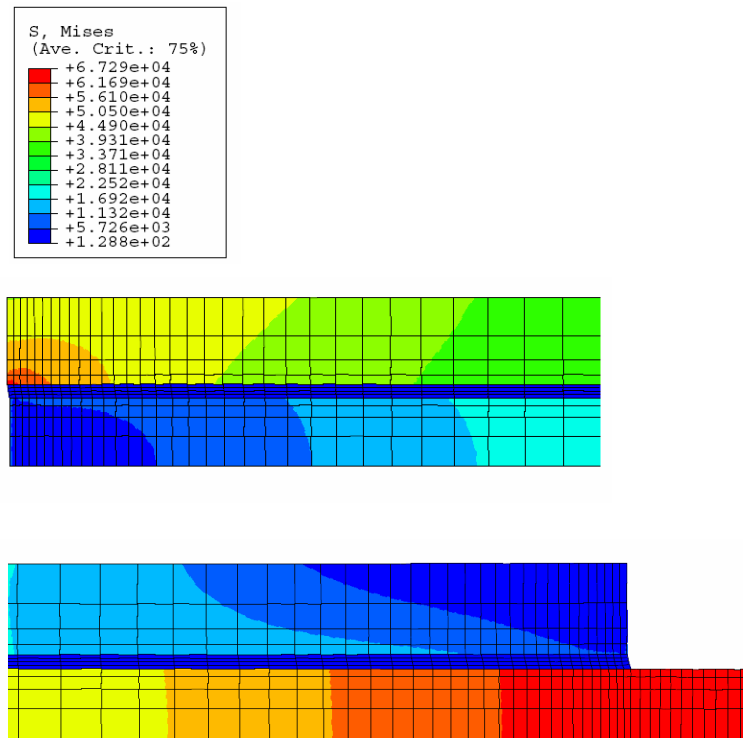


Figure 20. Von Mises stress contours at the ends of the joint (top plot: at the left end; bottom plot: at the right end)

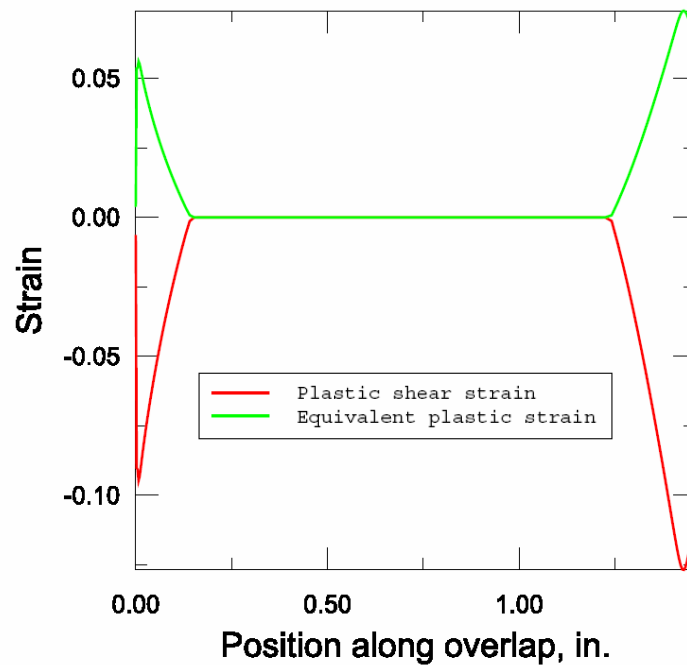


Figure 21. Plastic shear strain and equivalent plastic strain along the centerline of the adhesive

Acknowledgments

The authors wish to acknowledge the support of the Federal Aviation Administration in addition to the guidance of Peter Shyprykevich in particular. The authors would also like to acknowledge the support of Alliant Technologies (ATK) Space Systems, Inc. and valuable insights and discussions with Eddy Derby and Greg Mehle of ATK.

References

- ¹Hart-Smith, L. J., *Adhesive-Bonded Double Lap Joints*. NASA-Langley Contract Report NASA-CR-112235 (1973).
- ²Zhu, Y., Kedward, K. T. and Kim, H., *Methods of Analysis for Adhesively Bonded Joints*, Symposium on 'Joining and Repair of Composite Structures', Kansas city, MO. March, 2003.
- ³Kim, H., and Kedward, K.T., *Stress Analysis of Adhesively-bonded Joints Under In-plane Shear Loading*, J. Adhesion, 2001, Vol. 76, pp.1-36.
- ⁴Kim, H., and Kedward, K.T., *The Design of In-plane Shear and Tension-loaded Bonded Composite Lap Joints*, J. Comp. Tech. & Res., Vol.24, no.2, April 2002, pp45-55.
- ⁵Bardis, J. D. and Kedward, K. T., *Surface Preparation Effects on Mode I Testing of Adhesively-Bonded Composite Joints*, J. Comp. Tech. & Res., Vol.24, 2002, pp.30-37.
- ⁶Bardis, J. D., PhD thesis. *Effect of Surface Preparation on the Long-Term Durability of Adhesively-Bonded Composite Joints*, University of California, Santa Barbara, March, 2002.
- ⁷M. Y. Tsai, D. W. Oplinger, J. Morton, *Improved Theoretical Solutions for Adhesive Lap Joints*. Int. J. Solids structures, Vol.35, No. 13, 1998, pp.1163-1185.
- ⁸Volkersen, O., *Die Niekraftverteilung in Zugbeanspruchten mit Konstanten Laschenquerschnitten*. Luftfahrtforschung 15, pp. 41-47 (1938).
- ⁹K. R. Loss and K. T. Kedward, *Modeling and Analysis of Peel and Shear Stresses in Adhesively Bonded Joints*, Proceedings, 25th AIAA SDM Conference, Palm Springs, CA, May 1984.
- ¹⁰Q. D. Yang and M. D. Thouless, *Mixed-mode Fracture Analyses of Plastically-deforming Adhesive Joints*. International Journal of Fracture, vol.110, no.2, 2001, pp.175-87.
- ¹¹V. Tvergaard and J. W. Hutchinson, *On the toughness of ductile adhesive joints*. Journal of the Mechanics & Physics of Solids, vol.44, no.5, May 1996, pp.789-800.
- ¹²J. W. Hutchinson and Z. Suo, *Mixed Mode Cracking in Layed Materials*. Advances in Applied Mechanics, v29. 1992, pp.63-191.
- ¹³J. A.Harris and R.D.Adams, *Strength Prediction of Bonded Single Lap Joints by Nonlinear Finite Element Methods*. International Journal of Adhesion and Adhesives, Volume 4, Issue 2, April 1984, pp.65-78.
- ¹⁴R.D. Adams, J. Comyn and the late W.C. Wake, *Structural Adhesive Joints in Engineering*, Chapman & Hall, 1997.
- ¹⁵M. N. Charalambides, A. J. Kinloch and F. L. Matthews, *Adhesively-bonded Repairs to Fiber-composite Materials II: Finite Element Modeling*. Composite part A 29A, 1998, pp.1383-1396.
- ¹⁶N. G. McCrum, C. P. Buckley, C. B.Bucknall, *Principles of Polymer Engineering*, Oxford university Press, 1997.
- ¹⁷Potter et. al., *Primary Adhesively-Bonded Structure Technology(PABST)*, AFFDL-TR-79-3129, November 1979.

This page left blank intentionally.

A HIGH FIDELITY COMPOSITE BONDED JOINT ANALYSIS VALIDATION STUDY – PART I: ANALYSIS

S. P. Engelstad^{*}, O.T. Berry[†]
Lockheed Martin Aeronautics Company, Marietta, Georgia

G.D. Renieri[‡], L.R. Deobald[§], G.E. Mabson^{**}, B. Dopker^{††}
The Boeing Company, St. Louis MO & Seattle, WA

E.W. Nottorf^{‡‡}
Bell Helicopter, Ft. Worth, TX

and

S.B. Clay^{§§}
Air Force Research Laboratory, Dayton, Ohio

The analysis/prediction phase of a high fidelity analysis validation activity conducted by the Composites Affordability Initiative (CAI) Program on composite bonded structure is presented in this paper. The CAI program has developed two improved approaches for the analysis of bonded joints, (1) high fidelity stress analysis combined with a new composite strain invariant failure criteria for the prediction of failure initiation, and (2) an interface fracture finite element (IFE) for predicting the delamination propagation, damage tolerance, and residual structural strength. This paper describes a test program that was designed to validate these prediction methodologies, the theory behind the analytical predictions, and the analysis results. The test articles are that of an all composite skin and stiffener run-out geometry with both bonded and co-cured configurations. Due to availability of the test data, a follow-on Part II paper will be written that describes the analysis/test correlation results.

Nomenclature

CAI	=	Composites Affordability Initiative
IFE	=	Interface Fracture Finite Element
CSE	=	Complex Stress Element
Gr	=	Graphite
SIFT	=	Strain Invariant Failure Theory
DaDT	=	Durability and Damage Tolerance
ESRD	=	Engineering Software Research and Development
J1	=	1 st Strain Invariant
$e_{\text{von mises}}$	=	von Mises Strain
ITE	=	Interface Traction Element
VCCT	=	Virtual Crack Closure Technique
G_I	=	Mode I Energy Release Rate

^{*} LM Technical Fellow, Technology Development and Integration, AIAA Associate Fellow.

[†] LM Staff Engineer, Technology Development and Integration, non-member AIAA.

[‡] Boeing Technical Fellow, Composite Processes-Phantom Works, AIAA Member.

[§] Boeing Associate Technical Fellow, IDS MR&D CFAC, non-member AIAA.

^{**} Boeing Structures Analyst, Phantom Works Structures Technology, AIAA Member.

^{††} Boeing Associate Technical Fellow, 787 Fuselage Structural Test and Technology, non-member AIAA.

^{‡‡} Bell Principal Engineer, Xworx., non-member AIAA.

^{§§} USAF Aerospace Engineer, AFRL/VA Structures Division, AIAA Member.

G_{II}	=	Mode II Energy Release Rate
G_{III}	=	Mode III Energy Release Rate
MMB	=	Mixed Mode Bending
DCB	=	Double Cantilever Beam
ENF	=	End Notched Flexure
ERR	=	Energy Release Rate

I. Introduction

The Composites Affordability Initiative (CAI) Program has focused on composite bonded joints as a way to decrease the recurring costs of composite airframe structure, thereby making composites more affordable for tactical aircraft. Participants in the initiative include the Air Force, Navy, Lockheed Martin, Boeing, Bell Helicopter, and Northrop Grumman. A CAI analysis tools team, with members from each of the participants, was created to study improved static strength and damage tolerance analysis capabilities for composite bonded joints, which has motivated the work in this paper. In this paper, an analysis/test validation activity for two new CAI analysis methods is described.

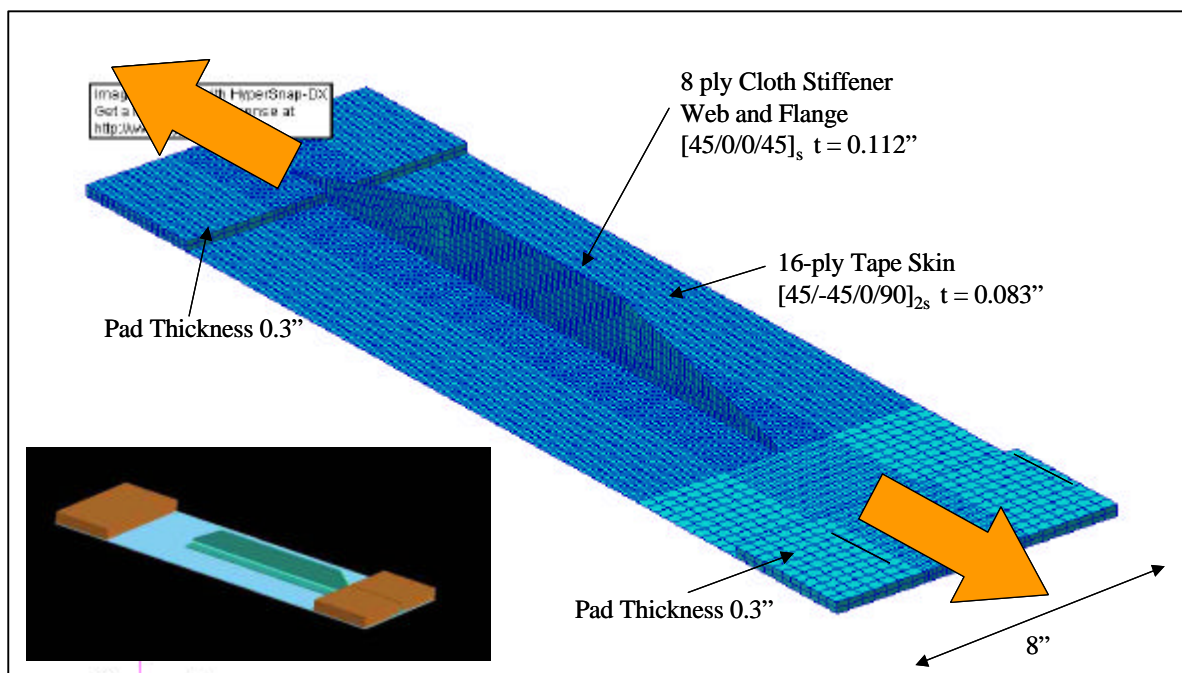


Figure 1. Stiffener Termination Test Article

The CAI program has developed two improved approaches for the analysis of bonded joints, (1) high fidelity stress analysis^{1,2,3} combined with a new composite strain invariant failure criteria² for the prediction of failure initiation, and (2) an interface fracture finite element (IFE)⁴ designed as a user element in *ABAQUS*^{®†} for predicting the delamination propagation, damage tolerance, and residual structural strength. This paper describes a test program that was designed to validate these prediction methodologies, the theory behind the analytical predictions, and the analysis results. Due to the timely availability of the test data, the test results and correlation of the tests with predictions will be discussed in a follow-on Part II paper. The test article was that of an all composite stiffener termination in a composite skin, shown in Figure 1. It was selected to be a compromise between the need for a complex state of stress to test the new analysis capabilities, and a simple composite bonded construction. It will be referred to as the Complex Stress Element (CSE) specimen throughout this paper.

The CAI analysis tools team went through significant efforts to select a test article to use for analysis tools validation. After the CSE test article was selected, the team progressed through the development of a detailed test plan, designing the test article and fixturing, and fabrication of the test articles. This paper will discuss the up-front

[†] *ABAQUS*[®] is a software product from ABAQUS, Inc., Pawtucket, Rhode Island.

predictions related to both initial and final failure of this structure using the CAI tools. At this point in time, the articles will begin testing very soon, and the follow-on paper will summarize the results of the test results and analysis correlation activities. In the following sections, a discussion is presented on the fabrication of the CSE specimen, the test plan, and analysis methodologies, and the analysis predictions.

II. Fabrication

The Complex Stress Element test articles consisted of a baseline stiffener run-out geometry with some basic parameter changes. Both bonded and co-cured specimens were fabricated. The bonded specimens consisted of precured stiffeners secondarily bonded to a precured skin. Non-tapered and tapered flange specimens were fabricated. Co-cured specimens consisted of three non-tapered flange variants: no adhesive between the skin and cap; layer of B-staged FM300 adhesive between the skin and cap; Gr Z-Pins at the skin/T interface. Selected photographs of the bonded specimens are shown in Figure 2.

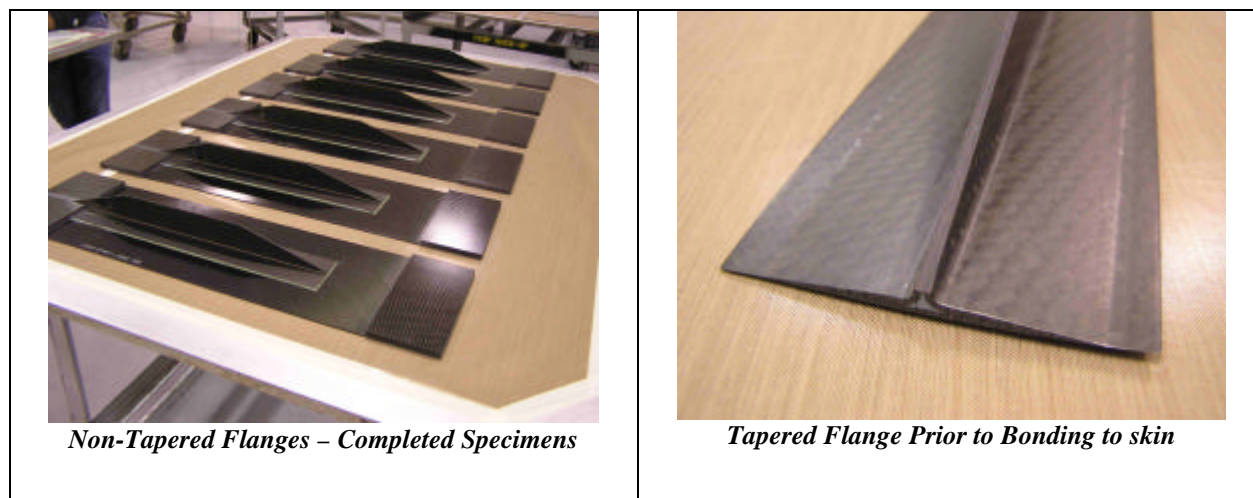


Figure 2. Photographs of the Bonded Complex Stress Elements

III. Test Plan

The test matrix is shown in Table 1. Plans call for testing 10 bonded specimens and 15 co-cured specimens. Both ends of the CSE will be clamped in hydraulic grips and an axial displacement will be applied to the point of catastrophic failure. Two bonded configurations will be tested where one has a square edge of flange and one has a tapered edge of flange. Three co-cured configurations with a square flange will also be tested. One co-cured element will not contain z-pin reinforcements and the other will be reinforced with 2% areal density graphite z-pins. Additionally, one co-cured CSE will have B-staged adhesive, but no z-pins.

Configuration	Quantity	Flange Taper	Interface
Bonded ^β , No taper	6 ^α	No Taper	FM300-2
Bonded, Tapered	5	10:1 Taper	FM300-2
Co-cured ^χ Only	5	No Taper	Co-cured
Co-cured with Adhesive	5	No Taper	FM300-2
Co-cured with Z-pins	5	No Taper	2% Gr Z-pins

^α One “pathfinder” element used to verify instrumentation and test setup.

^β “Bonded” implies precured stiffener and skin assembled in secondary bonding process.

^χ “Co-cured” implies green stiffener and skin cured and assembled in one autoclave cycle.

Table 1. Stiffener Run-Out (CSE) Test Matrix

Extensive instrumentation is planned for the CSE testing. Data gathered will include strain (from strain gauges), elongation, out-of-plane displacement, Moiré Interferometry measured surface displacement (and strain), and delamination growth. Significant efforts will be made to measure the *onset* of damage initiation through crack detection break wires, acoustic emission, and microscopes.

IV. Analysis Methodology

As shown in Figure 3, the analysis methodology encompasses the enhanced analytical tools in a sequence that uses existing finite element codes (*NASTRAN*^{†††} or *ABAQUS*) to produce a global model. With the goal of strength analysis to determine the onset of damage initiation, a global/local strategy is utilized in which tractions or displacements from the global model are imposed on a local *StressCheck*[†] model where the strain invariant failure theory (SIFT)² can be applied. At this point, the IFE tools being developed under the durability and damage tolerance (DaDT) effort are applied to determine overall failure. The IFE tools utilize the *ABAQUS* software combined with fracture-based interface elements for delamination propagation.



Figure 3. Analysis Methodology

StressCheck Global/Local

In the area of failure initiation predictions for bonded joints, the CAI team has looked hard at improvements in the state of the art of prediction of the interlaminar stress/strain state. It has adopted a new modeling strategy for 3-D continuum analysis called “thin-solid” modeling. CAI has worked with Engineering Software Research and Development (ESRD), Inc., the developers of *StressCheck*, to develop and implement this approach, as it can control (reduce) the p-extension in the thin laminate thickness direction, thereby reducing the degrees of freedom required in the solution. As p-elements are also much less sensitive to aspect ratio difficulties, very high aspect ratio elements are allowed in this solution, thereby not constraining the ability of the analyst to transition from high fidelity to low fidelity regions^{2,3}. In other papers, CAI has discussed the Zig-Zag^{5,6} elements, which also have interlaminar prediction and thin solid capabilities, also with insensitivity to aspect ratio. It has been discovered that the Zig-Zag elements due to their lower order interpolation are not quite as efficient in the high gradient stress/strain regions as the p-version, but have other advantages as they work in a general nonlinear code (*ABAQUS*).

CAI has worked with ESRD not only to produce the thin solid capabilities, but also to develop global/local strategies for efficiently importing shell element displacement and rotations, or forces and moments from a global shell model. CAI has also worked with ESRD to efficiently incorporate efficient composite analysis capabilities and failure theories such as SIFT. Each of these new capabilities has been validated through extensive testing and analysis. The CSE validation study will validate the global/local modeling tools, the thin solid composite modeling strategies in *StressCheck*, and the SIFT failure criteria implementation, all working together as a process.

^{†††} *NASTRAN*[®] is a software product from MSC.Software, Santa Ana, California.

[†] *StressCheck*[®] is a software product from Engineering Software Research and Development, Inc., St. Louis, Missouri.

As previously mentioned, a global/local modeling procedure was used to analyze the CSE specimen. Figure 4 shows the global *ABAQUS* shell model that was developed, with the area highlighted in red indicating the region where local *StressCheck* analysis was performed. In order to more accurately transfer loads and/or displacements

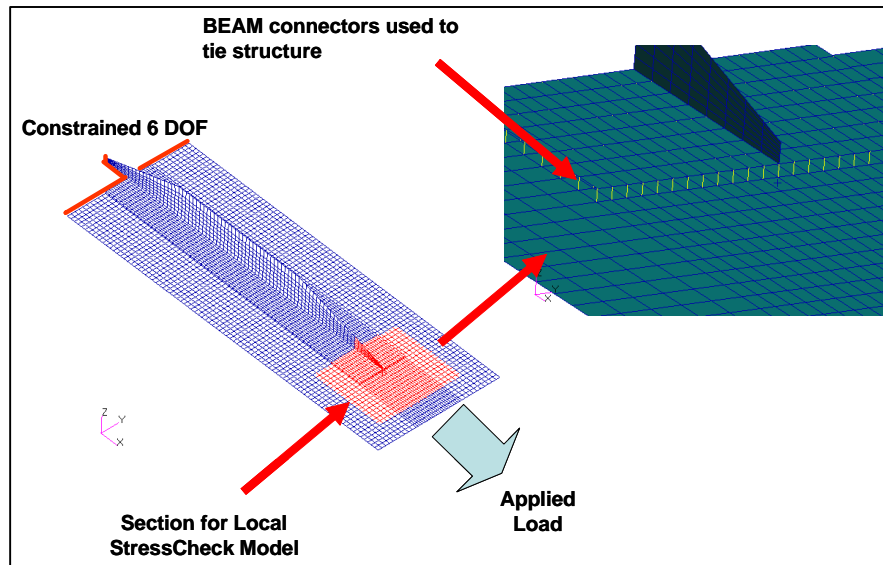


Figure 4. CSE Global ABAQUS Shell Model

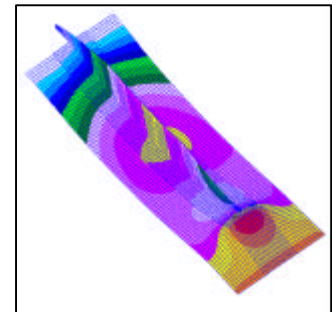


Figure 5. CSE Global ABAQUS Non-Linear Magnitude Displacement Plot

from the global to local models, shells were located at their reference plane or their half thickness location. BEAM (kinematic) connector elements were used to tie the offset structure together. Figure 5 shows the out of plane displacement contour plot of the global model under mechanical loading. Thermal stress analysis was also performed on the global model in order to map the thermal deformation to the local model. The global model with the appropriate thermal load and free-free boundary conditions was run as a separate static solution (from the mechanical solution) to produce displacements to map to the local model.

A detailed 3D *StressCheck* local model was built to perform the stress analysis and failure predictions for both the tapered and untapered configurations. The *StressCheck* model contained appropriate fidelity to perform detailed ply-level analysis in the first 3 plies of the skin, any ply of the cap, any ply of the flange, and the adhesive. Thus the first 3 plies of the skin and all of the plies of the cap and flange and the adhesive were modeled discretely with one element through the thickness of each ply. This is an example of thin solid modeling. The local *StressCheck* model for the untapered specimen is shown in Figure 6.

Global /local analysis was performed between the global *ABAQUS* shell model and the local *StressCheck* solid p-version model. Displacement/rotation boundary conditions were imported from the global *ABAQUS* model and applied to the *StressCheck* model. Figures 7 and 8 show comparisons of the local model displacement field of the *StressCheck* model to the global model

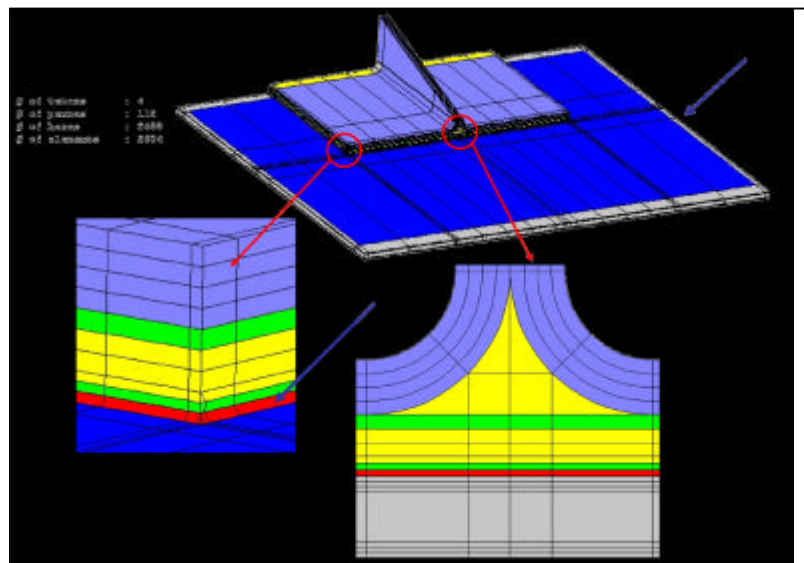


Figure 6. CSE Local *StressCheck* Model

displacement field from the *ABAQUS* model. Separate solutions were run for a mechanical load case and a thermal load case. Each of these solutions were from a different boundary value problem with different boundary conditions. The mechanical load case represented the mechanically applied load with the specimen in its loading fixture. The thermal load case represents a uniform temperature change from the glass transition temperature of the composite to room temperature, with boundary conditions to restrict rigid body motion.

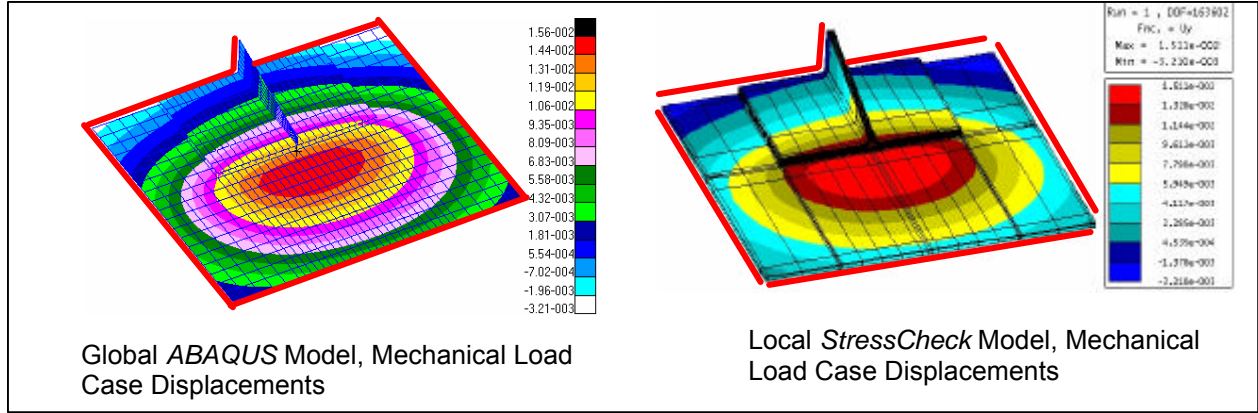


Figure 7. Displacement Contour Comparisons Between Global and Local Models for the Mechanical Load Case

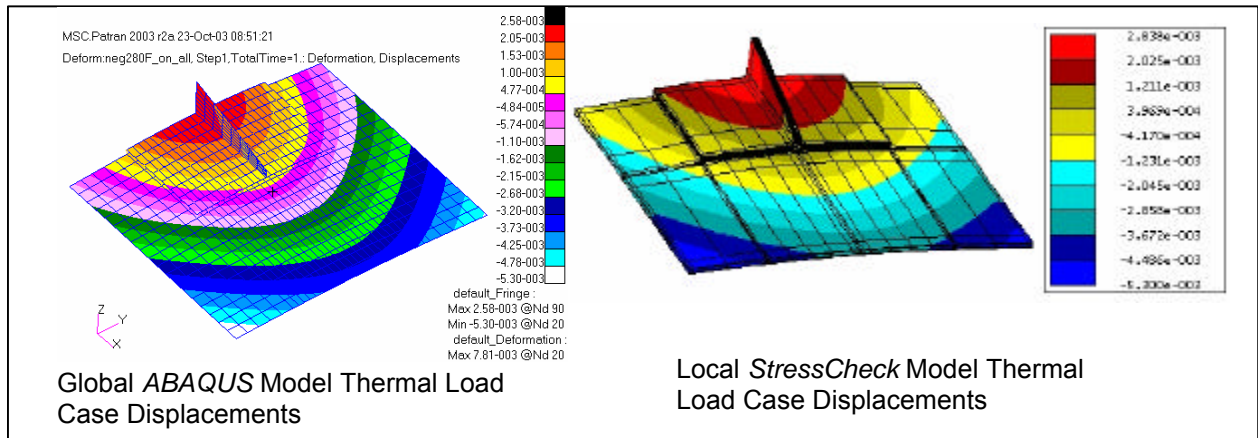


Figure 8. Displacement Contour Comparisons Between Global and Local Models for the Thermal Load Case

Strain Invariant Failure Theory (SIFT)

A relatively new failure theory for damage initiation within composite materials and bonded assemblies, identified as the strain invariant failure theory (SIFT), has received considerable attention recently^{2,7,8}. The theory is based on failure of solid continua through excessive deformation, either dilatational or distortional. Distortional failure theories have been commonly used in metals, the most common being von Mises yielding. SIFT extends this theory through the addition of the dilatational deformation failure mode. As described in Ref. 8, for composite unidirectional tape there are two critical strain invariants for failure initiation within the matrix phase,

$$J_1 = e_1 + e_2 + e_3 = J_1^{\text{critical}} \quad (1)$$

$$e_{\text{von Mises}} = e_{\text{von Mises}}^{\text{critical}} \quad (2)$$

and one critical invariant that represents damage initiation within the fiber phase,

$$e_{\text{von Mises}}^{\text{fiber}} = e_{\text{von Mises}}^{\text{fiber critical}} \quad (3)$$

where $e_{\text{von Mises}} = 1/2[(e_1 - e_2)^2 + (e_1 - e_3)^2 + (e_2 - e_3)^2]^{1/2}$. The developers of this theory have applied micromechanical modification of the homogeneous strain state to compute the constituent strain tensors needed for application of SIFT. Equations 1-3 describe the onset of damage initiation within the polymer and fiber phases of the composite structure. All critical values of the strain invariants are extracted numerically from unnotched tensile lamina coupons. For much more detailed information on this subject, see Refs. 2,7,8.

The CAI program has gone through an extensive validation activity of the SIFT theory for onset of damage initiation only, using increasingly complex building block scales starting with coupons, joint elements, and finally the CSE specimen at the largest scale. One of the goals of the CSE testing is to validate the SIFT damage initiation theory at a complex structural scale.

V. Analysis Predictions – *StressCheck*/SIFT Onset of Damage Initiation

The global/local *StressCheck* modeling procedure, combined with the SIFT failure criteria were used to predict the onset of irreversible damage, or very early initiation. Figure 9 shows the location of failure initiation for the non-tapered bonded and co-cured specimens. Both of these specimens assumed a tangent spew fillet with a radius equal to the adhesive bondline thickness for the bonded specimen, or the 1st ply thickness of the cap for the co-cured specimen. Figure 10 shows a side view of the failure location in the 1st ply of the skin, with failure margins computed using CAI tested critical values of J_1 . Note in the right side of Figure 10, that a characteristic distance was assumed of 1/2 ply thickness penetration into the first ply for the failure margin surface indicated by the gold color to be critical. All critical margins computed in for initiation were critical in the matrix J_1 , and thus other margins for $e_{\text{von Mises}}$ in the matrix are not shown.

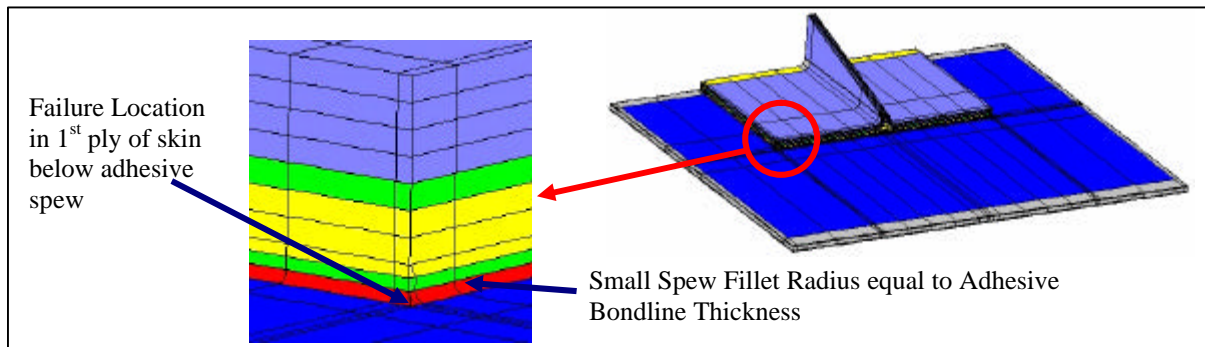


Figure 9. Predicted Failure Location in non-Tapered Bonded and Co-cured Specimen

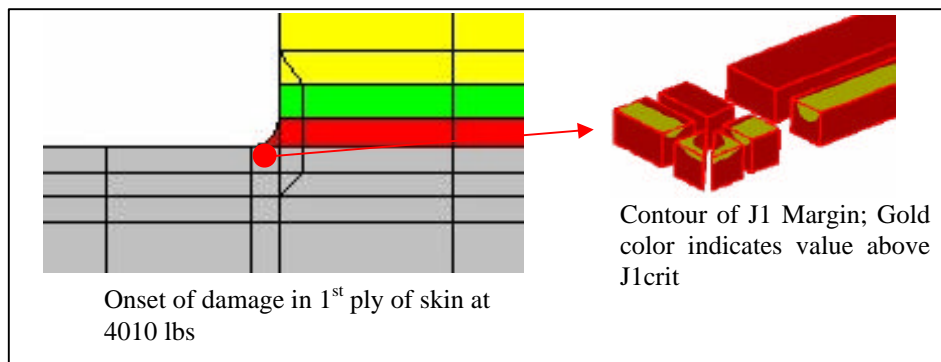


Figure 10. Side View of Predicted Failure Location in non-Tapered Bonded and Co-cured Specimen

Figure 11 shows a comparison of a small spew model of the non-tapered bonded specimen to a very large spew model which is representative of the as-manufactured specimens. The analysis for the large spew model assumes the adhesive properties are consistent and effective throughout the large spew region. In reality this is probably not true in a spew this large. The analysis for this very large spew shows a dramatically increased failure initiation load.

Whereas the small spew predicted failure load was 4010 lbs, the large spew predicted failure load is 11720 lbs (see Figure 12). This dramatic difference is due to the greatly decreased stress concentration effect due to the very large radius spew. It is not expected that the as-manufactured large spew is fully effective.

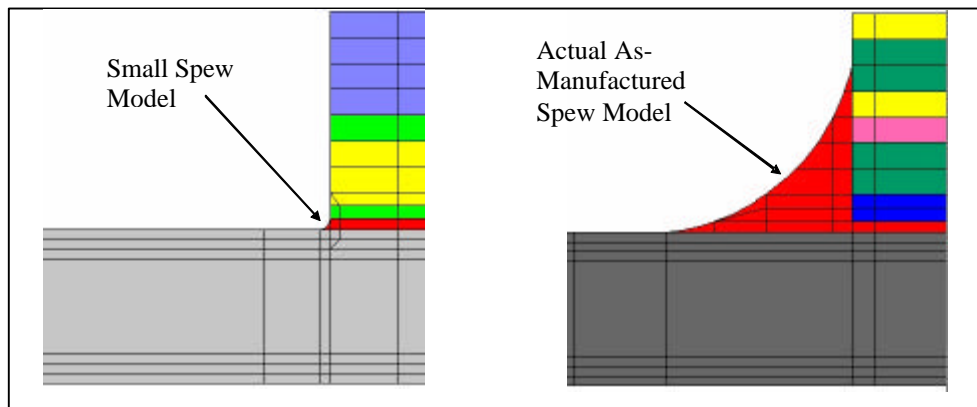


Figure 11. Comparison of Small Adhesive Spew and Large Spew Models

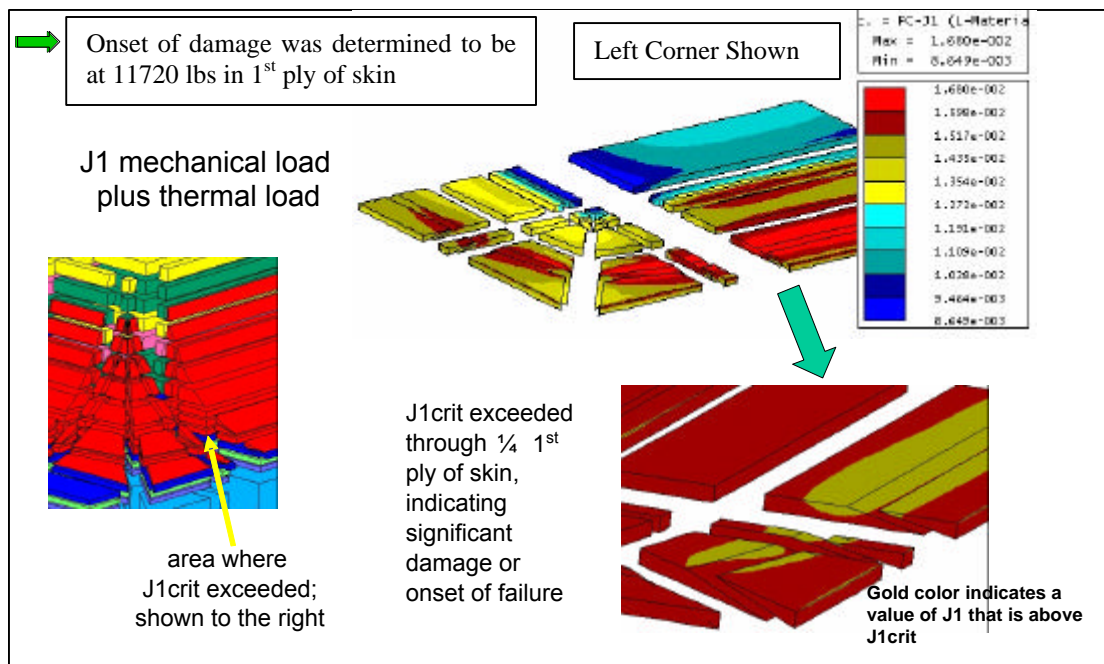


Figure 12. Failure Prediction of Large Spew Model

Figure 13 shows a zoomed-in view of the bonded tapered flange *StressCheck* model. This model also uses the small tangent spew assumption. Figure 14 shows the analysis locations for the tapered flange model. In Figure 15, a summary of the initiation failure loads are shown, with the minimum at the midspan location in the 1st ply of the skin under the spew fillet.

In Table 2, a summary is given of the predicted initiation failure loads for the non-tapered bonded specimen (with both a small spew and a large spew model), the tapered bonded specimen, and the co-cured specimen. Note that the predictions for matrix initiation are very low in load, as compared to the expected final skin fracture load of 65×10^3 lbf. The J_{1crit} value used here is measured from 90 deg tension lamina coupons, which is a very early matrix micro-cracking event for the CSE specimen. No progressive damage simulation has been performed for these predictions.

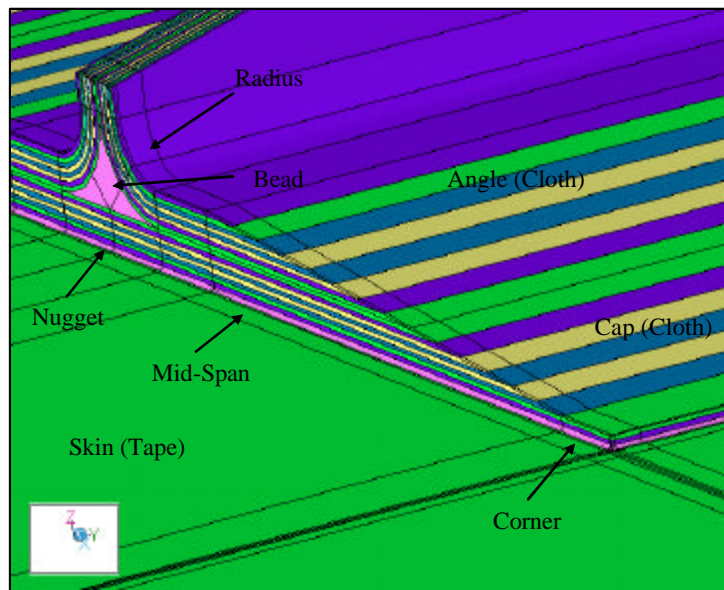


Figure 13. Bonded Tapered Flange StressCheck Model

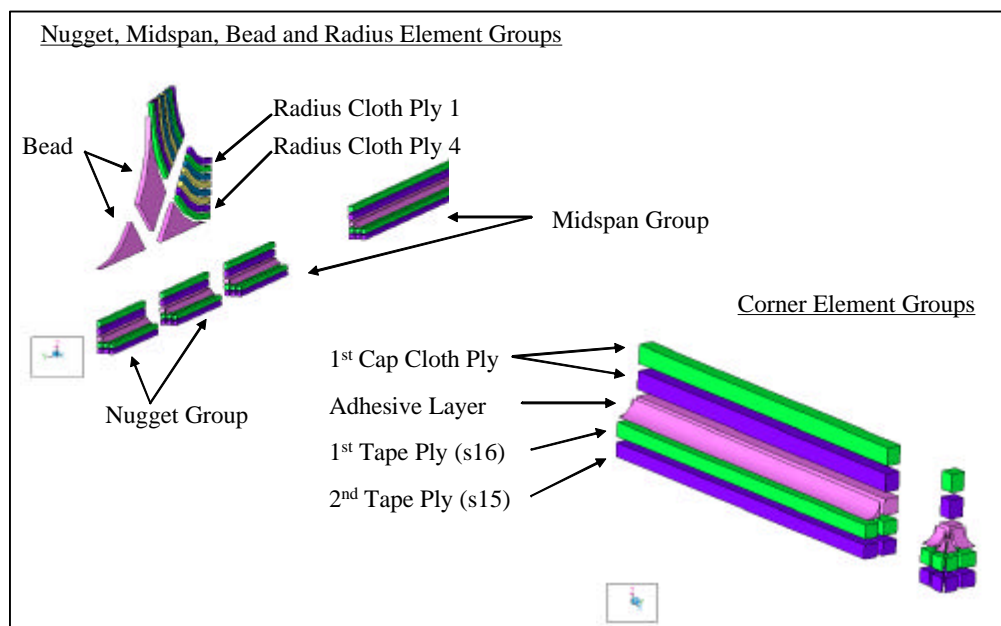


Figure 14. Analysis Locations for Bonded Tapered Flange *StressCheck* Model

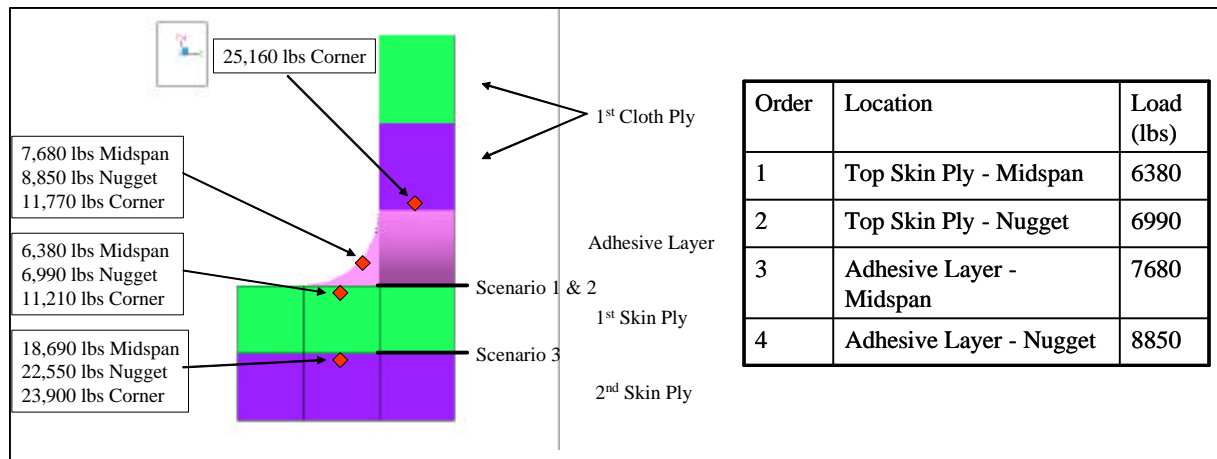


Figure 15. StressCheck/SIFT Failure Analysis Results for Bonded Tapered Flange Configuration

Specimen Type	Initiation Onset Location	Initiation Onset Load (lbs)
Bonded No Taper (Small Spew)	Top Ply Skin Left Corner	4010
Bonded No Taper (Large Spew)	Top Ply Skin Left Corner	11720
Bonded Taper (Small Spew)	Top Ply Skin Midspan	6380
Co-cured	Top Ply Skin Left Corner	4010

Table 2. Onset of Failure Prediction Results

VI. Analysis Predictions – Interface Element for Modeling Composite Delamination Growth

CAI Durability and Damage Tolerance (DaDT) analysis tool development has focused on the development of 2D and 3D Interface Fracture Elements (IFE) and 2D and 3D Interface Traction Elements (ITE) for predicting the behavior of delaminations with and without z-pin reinforcements. This section concerns the application of the 3D IFE and ITEs to predict the delamination onset load and peak load of the CSE blade-stiffener run-out detail.

The element suite was developed under the CAI program as an *ABAQUS* user element where an analysis is accomplished in a single nonlinear *ABAQUS* run. The 2D and 3D fracture element implements the widely accepted Virtual Crack Closure Technique (VCCT) incorporated into the novel interface element. In regards to the Interface Fracture Elements, a number of past works^{9, 10, 11} have recognized the advantage of performing delamination analysis using various interface element approaches. Unfortunately, the onset of node release was based on unreliable local stress/stain fields near the crack tip. Concurrent and independent works by the authors⁴ and by Xie¹² have resulted in interface elements where the onset of delamination growth is controlled by VCCT based failure criteria. Figure 16 represents the 3D IFE and ITE. The center nodes are initially constrained together and the four (4) mid-side node pairs act as antennae to sense an

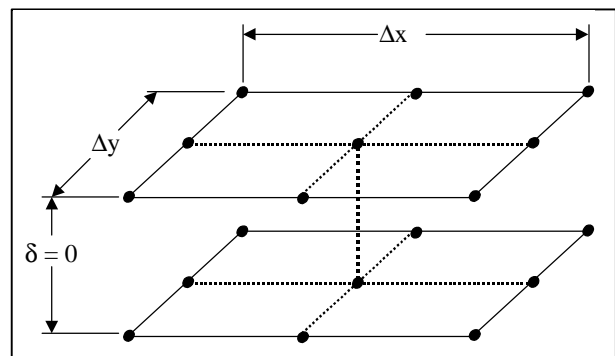


Figure 16. 3D Interface Fracture Element (IFE) Based on VCCT

approaching crack front. The remaining corner node pair locations are necessary to account for the element area in the energy calculations. The element senses an approaching crack front by the onset of a relative displacement between the nodes of one or more of the antennae node pairs. Elements are overlapped in both directions to constrain each node pair from co-located solid surfaces. Once the element becomes active, the constraining forces between the center node pair and the periphery crack opening displacement are used in a fracture mechanics based failure criteria that uses G_{IC} , G_{IIC} and G_{IIIC} to determine if the center node should begin to release. A number of failure criteria are available to evaluate mixed-mode interlaminar fracture. Dr. James Reeder recommended a modification to the Benzeggagh and Kenane failure criteria to permit evaluation of G_{III} independent of G_{II} in a 3D mixed mode criterion as shown in Equation (4)¹³. The parameter, m , in the “BKR” criteria quantifies mode interaction in the realm between pure mode I and pure mode II, and is measured using the MMB test¹⁴. Once the fracture mechanics based failure criteria is satisfied, the constraining forces between the center node pair will be released. Ideally, the residual force between the released nodes will follow a linear strain softening law such that the area under the force-displacement curve satisfies the fracture mechanics failure criteria. This precise analysis may converge very slowly and is more prone to divergence in the nonlinear solution (caused by a negative tangential stiffness in a Newton’s solution). The IFE code may be flagged to perform an “approximate” solution where each element that satisfies the failure criterion is released fully on the next iteration. This mode of operation provides good results when the crack advances across several elements for each time increment. This was the mode of operation for the analyses presented here.

All tested configurations were evaluated using the 3D IFEs and ITEs in nonlinear *ABAQUS* finite element analyses (FEA). The 3D IFE and ITEs were incorporated into an *ABAQUS* model of the stiffener termination (Figure 17) such that a layer of shells that represents the cap of the stiffener were constrained to a layer of shells that represents the “skin panel”. A row of node pairs at the termination were not constrained to represent a small initial delamination. Node spacing in the vicinity of the termination was about 0.015 inch square. Input values of G_{IC} and G_{IIC} were acquired through DCB and ENF testing and G_{IIIC} was assumed based on G_{IIC} . Specific material fracture toughness properties for the unreinforced interface are given in Figure 18. The apparent R-curve behavior from DCB testing was programmed as a function of crack length in the 0-degree direction to provide a prediction of peak load that is not overly conservative. Fiber bridging, ply bridging and collateral matrix cracking will all tend to absorb additional energy as the crack front moves forward. One would anticipate that this approach to accommodate R-curve is only approximate since increasing toughness as a function of crack length is expected to be stiffness dependent in a composite laminate. However, experimental correlations with small structural coupons, thus far, have demonstrated reasonable correlation. Separate analyses were not completed for CSEs containing FM300-2 at the interface between the skin and stiffener. The adhesive layer certainly demonstrates a higher toughness than the composite substrate. However, a composite layer is only one ply thickness away and this analysis has no way to predict if the delamination will jump to the composite matrix layer. A prudent approach is to use the lowest fracture toughness properties in the vicinity of the interface to make conservative predictions of the structural loads.

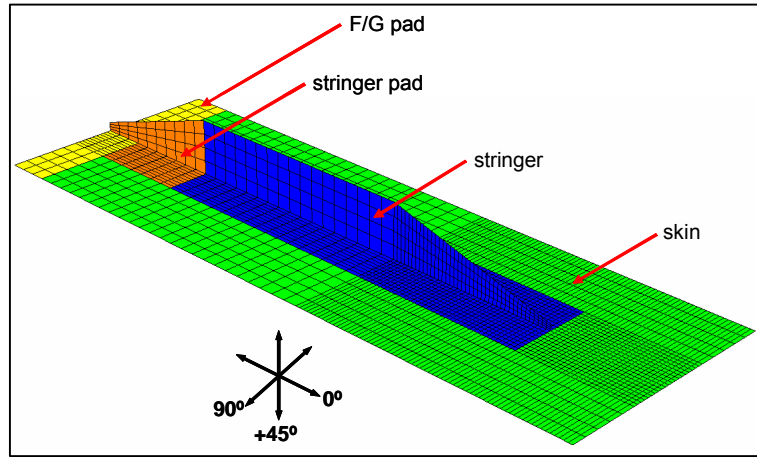


Figure 17. 3D Overview of the Stiffener Termination FEA Model

$$G_{com} = G_T / \left(G_{IC} + ((G_{IIIC} - G_{IIC}) \cdot G_{3R} + (G_{IIC} - G_{IC}) \cdot (G_{2R} + G_{3R})) \cdot (G_{2R} + G_{3R})^{m-1} \right) \geq 1 \quad (4)$$

$$\text{where } G_T = G_I + G_{II} + G_{III}, \quad G_{IR} = G_I / G_T, \quad G_{2R} = G_{II} / G_T, \quad G_{3R} = G_{III} / G_T$$

The ITEs are a type of decohesion element similar to the new *ABAQUS* decohesion element in version 6.5. The characteristic of a decohesion element is that initial release is typically based on a pressure or strain, and the residual force during element release follows a strain softening curve that extends over multiple element lengths. Consequently,

the initial release is inherently mesh size dependent and analysis with a decohesion element with gradual release tends to be more stable than analyses incorporating interface fracture elements. In general, composites reinforced with z-pins will not exhibit improvement in the onset of delamination growth, but may greatly improve the peak load at which a structural element is expected to delaminate. The analysis of a z-pin reinforced composite structure follows a strategy revealed by the physics of the problem whereby the toughness characteristics of the interface is divorced from the process zone characteristics of the z-pins. The VCCT based IFEs simulate the material interface with precisely the same properties used in the analysis of the unreinforced CSE. The ITEs are used to simulate the traction forces imparted by the z-pins once the delamination progresses into the z-pin field. Onset of delamination depends only on the IFEs, but the ITEs will dominate the structural response once the crack front has moved down the stiffener by several inches. Figure 19 provides simplistic z-pin response curves that were extracted from test data of z-pinned DCBs and ENFs. Considering a z-pin that has a length that extends across the prospective plane of delamination, the smallest embedded depth of the z-pin is the most dominant feature for controlling the capability of z-pin reinforcements and is represented by the abscissa in Figure 19.

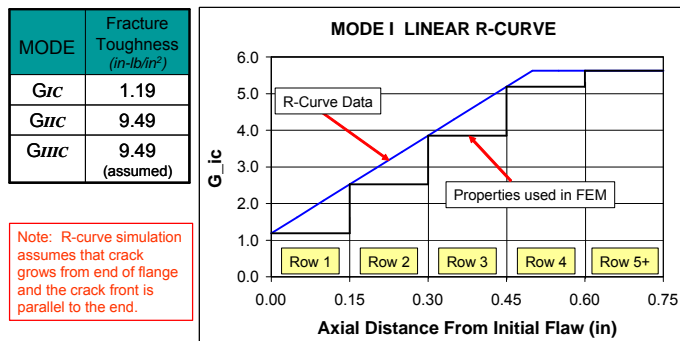


Figure 18. Material property inputs and mode I R-curve.

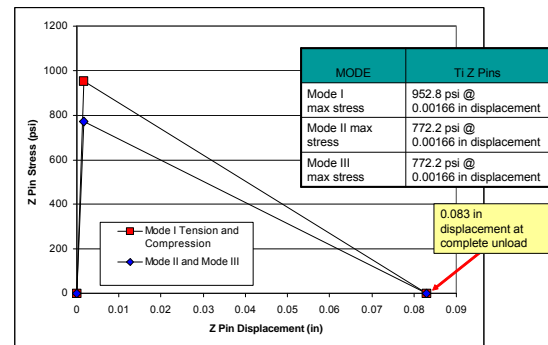


Figure 19. Z-pin traction characteristics

Figure 20 compares the load displacement graphs from each of the three configurations evaluated. Configuration 1 is the unreinforced CSE with the square-edge flange, configuration 2 is the same geometry except the edges of the flange are tapered, and configuration 5 is the same as 1 except 2% graphite z-pins have been embedded in 1-inch wide strips along either flange and extending six inches from the termination. Skin strains are expected to fracture the skin at a load around 65×10^3 lbf. The two configurations with the square-edge flange were predicted to initiate delamination at the corner of the flange at a very low load of 10.8×10^3 lbf. Figure 21 shows the deformed plots and critical load levels for the co-cured structure with a square edge of flange. The first image shows onset of delamination growth from the corner of the flange. This bonded corner feature creates a sharp rise in the Energy Release Rate (ERR) in a manner similar to the well-known chevron notch. The delamination then grows into a parabolic shape and extends beyond the termination before reaching a point of catastrophic delamination growth at a peak load of 22.8×10^3 lbf for the unreinforced CSE. Analyses were completed for configuration 2 that contained the tapered edge of flange. The tapered

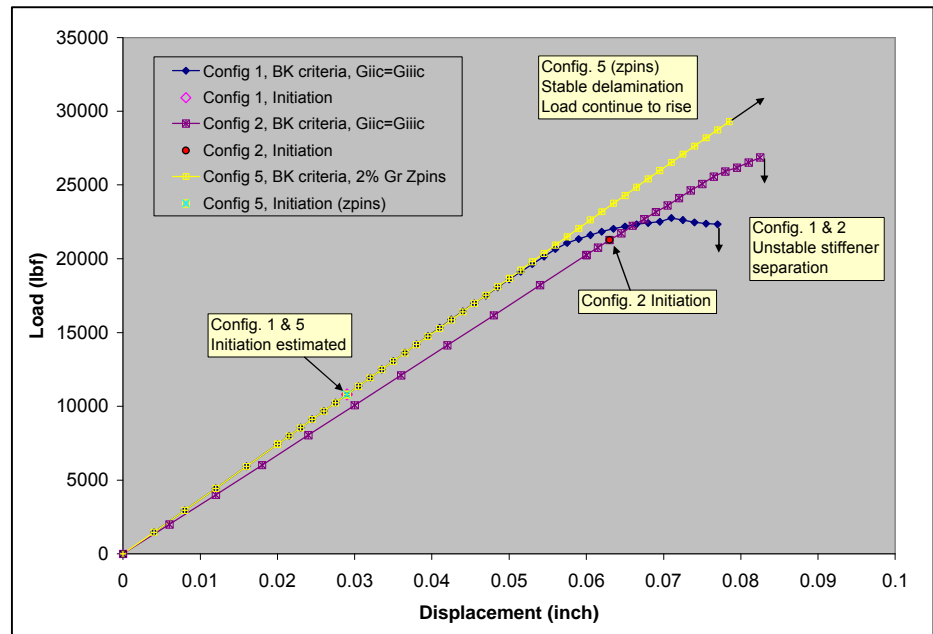


Figure 20. 3D Predicted load-displacement plots from FE analysis.

flange feature increased the onset of delamination critical load by nearly a factor of two and provided a modest (20%) improvement in peak load capability. Z-pins in a squared flange design provided no improvement in the onset load, however the peak load was greatly improved. The predicted critical loads are summarized in Table 3.

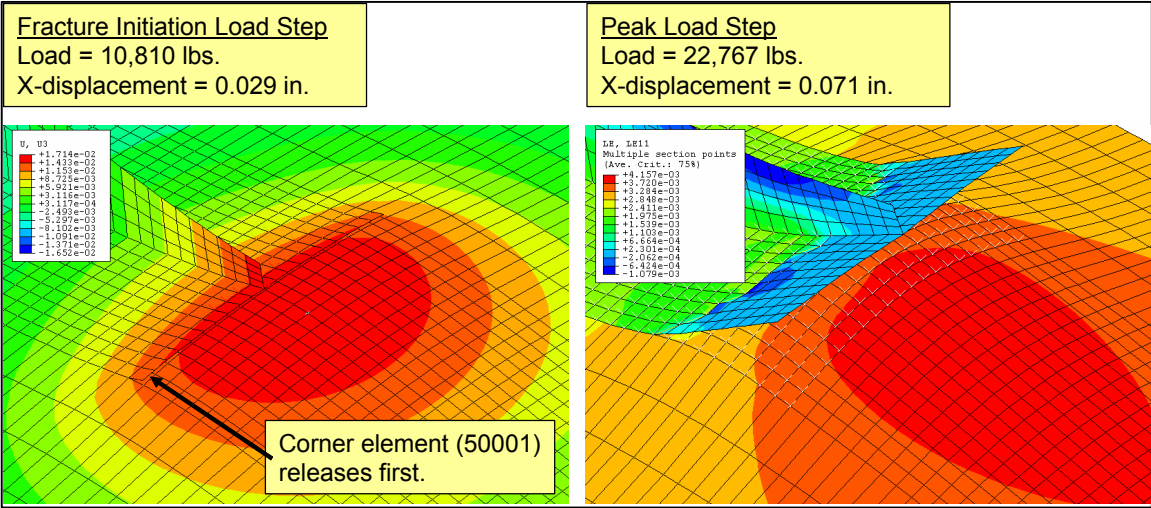


Figure 21. Early Delamination Onset and Peak Loads Predicted

Note that prediction for initial growth from the corner of the flange is only an estimate. Delamination from this corner feature is not self-similar and violates a fundamental assumption in the VCCT calculation. Numerical studies were conducted comparing the predicted onset load for a 0.05 inch versus a 0.15 inch mesh. The predicted critical load decreased with decreasing mesh size.

Considerable insight into proper design practice is gained by examining the deformed plots in Figure 21, 22 and 23. Viewing Figure 21, the stiffener separation apparently has significant mode I contribution. Onset of delamination from the corner of the flange is controlled by the relative stiffness of the flange to skin. An increase in critical load would be expected by increasing the skin thickness or softening the flange corner. In this case, the softer tapered flange in Figure 22 followed the skin during deformation. A more surprising result was the increase in peak load provided by the tapered flange. The squared-edge flange had a delamination front that was only slightly curved across the width of the stringer where as the tapered stiffener was parabolic in shape with the edges trailing the delamination under the web. The three-dimensional crack front apparently had a reinforcing effect to

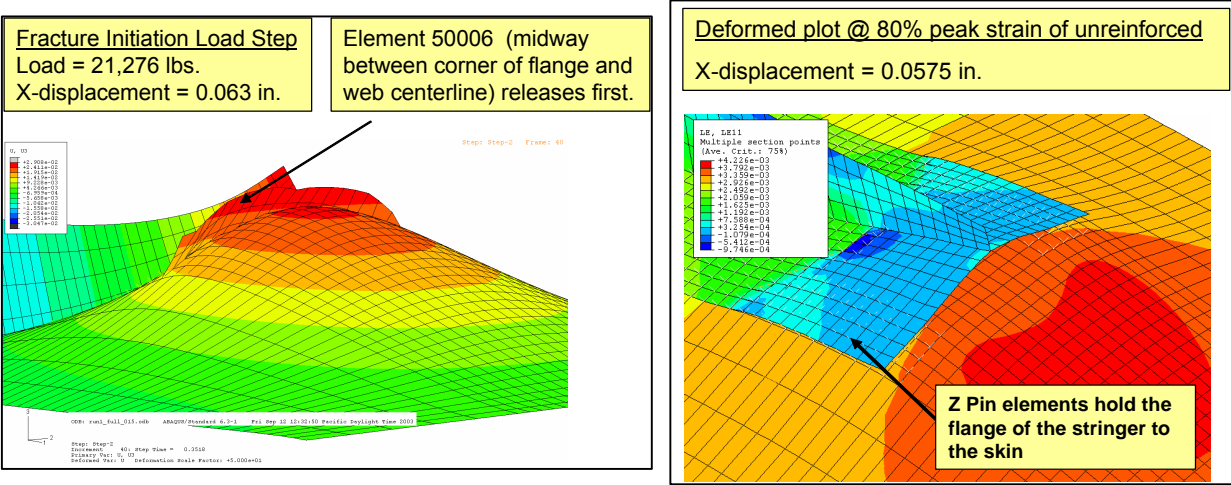


Figure 22. Deformed plot of tapered flange.

Figure 23. Z-pins resisting delamination in Config 5.

better resist the delamination. Figure 23 shows how the z-pins caused the flange to follow deformations in the skin and to minimize the loading at the crack front. This shielding effect translated to increased peak loads suitable for damage tolerant design.

Configuration	Onset of Failure (10 ³ lbf)	Peak Load (10 ³ lbf)	Location of 1 st Failure
(1) Shell Model, Square-Edge Flange	10.8	22.8	Corner of Flange
(2) Shell Model, Tapered Flange	21.3	26.5	Termination near web
(5) Shell Model Square-Edge Flange and 2% Gr Z-pins	10.8	>40	Corner of Flange

Table 3. Summary for Stiffener Delamination

VII. Initial Test Results

An initial test of a bonded stiffener pathfinder specimen with the Flange Taper 1 configuration has been tested. The specimen was instrumented with both strain gauges and crack gauges, and shadow moiré was utilized to monitor the displacement field. The specimen configuration and shadow moiré results are illustrated in Figures 24 and 25. In addition to the displacement instrumentation, both accelerometer and acoustic emission sensors were utilized to capture any responses that might indicate initial failure events. The purpose of the pathfinder test was to verify the instrumentation concepts and to identify the behavior of the specimen so that the test procedure for the remainder of the specimens could be established. Initial results indicate that the damage initiation location is consistent with predictions. Once the testing is completed, the theoretical and experimental damage initiation loads will be compared.

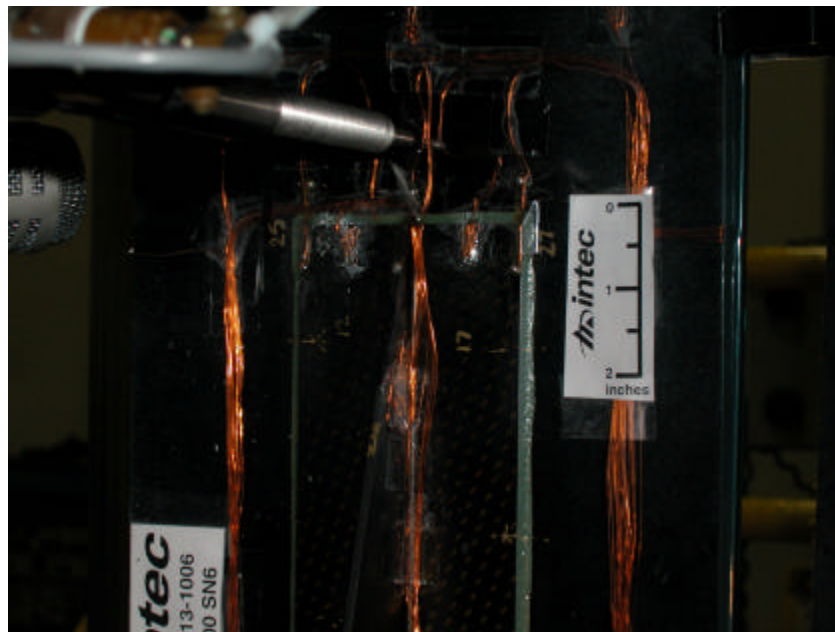


Figure 24. Pathfinder Specimen Test Configuration

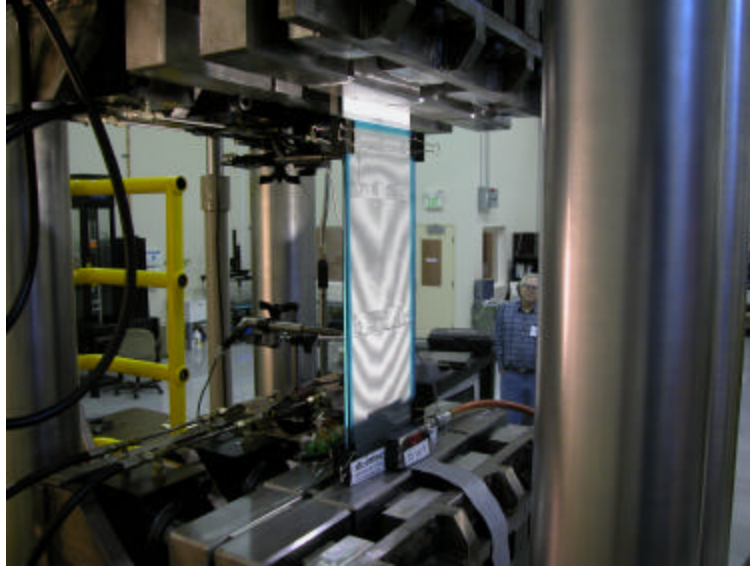


Figure 25. Pathfinder Shadow Moiré Results

VIII. Summary

This paper has presented the analysis results of a study to validate two new high fidelity analysis techniques for bonded composite structure through very detailed testing of an all-composite stiffener-termination element. Details of the analysis methods, pre-test predictions, and test plans have been presented and discussed. The correlation of the tests to analysis will be presented in a follow-on Part II paper.

In Table 4, all predictions have been summarized. Note the large difference in predicted initiation loads for the *StressCheck*/SIFT and IFE/Shell models. For the square-edge flange, the *StressCheck*/SIFT models showed sensitivity to the assumed adhesive spew size, whereas the IFE/shell model does not account for the spew shape. All predictions are in agreement as to failure location/mode for initiation. No predictions were made for failure initiation using the *StressCheck*/SIFT model for the Z-pinned specimen. Also, only the IFE/Shell models made predictions for peak failure load.

Configuration	StressCheck Initiation Onset (10 ³ lbf)	IFE Prediction Onset of Failure (10 ³ lbf)	IFE Prediction Peak Load (10 ³ lbf)	IFE Prediction Location of 1 st Failure
Bonded No Taper (square-edge flange), No Z-pins	4.01 (Small Spew) 11.72 (Large Spew)	10.8	22.8	Corner of Flange 1 st ply skin
Bonded Tapered Flange, No Z-pins	6.38 (Small Spew)	21.3	26.5	Termination near web 1 st ply skin
Co-cured, No Taper, No Z-pins	4.01	10.8	22.8	Corner of Flange 1 st ply skin
Square-Edge Flange and 2% Gr Z-pins	N/A	10.8	>40	Corner of Flange 1 st ply skin

Table 4. Summary of All Model Predictions

References

1. Mollenhauer, D., Engelstad, S., Berry, O., Iarve, E., Colleary, A., "Comparisons of Measured Moire' Fringe Surface Strains and Model Predictions for a Co-Bonded Pi-Preform Composite Tee Joint", Presented at the 45th AIAA/ASME/ASCE/AHS/ASC Structures, Structural Dynamics, and Materials Conference, 19-22 April 2004, Palm Springs, CA.
2. Wollschlager, J.A., Gosse, J.H., Christensen, S., Engelstad, S. P., "Current Developments in Composite Analysis and Failure Advocating an Advanced Composite Design Methodology", Presented at SAMPE 2002, in Long Beach, CA, May 2002.
3. Engelstad, S.P., Actis, R.L., "Development of p-version Handbook Solutions For Analysis of Composite Bonded Joints", Published in Journal: Computers and Mathematics with Applications, Volume 46, 2003, pp 81-94; Also presented at the P-FEM 2000, St. Louis MO, 5/31-6/2, 2000.
4. G. Mabson, "Fracture Interface Elements", Mil Handbook 17 Committee Mtg, Charleston, SC, October 2003.
5. Cho, Y.B. and Averill, R.C., "First Order Zig-Zag Sublaminar Plate Theory and Finite Element Model for Laminated Composite and Sandwich Panels," Composite Structures, Vol. 50, 2000, pp. 1-15.
6. Engelstad, S.P., Averill, R.C., Berry, O.T., Eby, D.J., "Implementation and Application of Zig-Zag Finite Elements for Composite Bonded Tee-Joint Modeling", May 2001, Presented at the 42nd AIAA Structures, Structural Dynamics, and Materials Conference, Seattle WA.
7. Gosse, J.H., "A Damage Functional Methodology for Assessing Post-Damage Initiation Environments in Composite Structure", Presented at the 45th AIAA/ASME/ASCE/AHS/ASC Structures, Structural Dynamics, and Materials Conference, 19-22 April 2004, Palm Springs, CA, AIAA Paper #1788.
8. Gosse, J.H., Christensen, S., Wollschlager, J.A., Llanos, A.S., "A Strain Invariant Failure Theory (SIFT) for Composite Materials", Submitted for publication in *J. Composite Materials*.
9. O.Allix, P. Ladeveze, and A. Corigliano, "Damage Analysis of Interlaminar Fracture Specimens," Composite Structures, Vol. 31, 1995, pp. 61-74
10. Weicheng Cui, and M.R. Wisnom, "A Combined Stress-Based and Fracture-Mechanics-Based Model for Predicting Delamination in Composites," Composites, Vol. 24, Number 6, 1993, pp. 467-474
11. Y. Mi, M.A. Crisfield, G.A. O. Davies, and H.B. Hellweg, "Progressive Delamination Using Interface Elements," Journal of Composite Materials, Vol. 32, No. 14/1998, pp. 1246-1272
12. D. Xi, Damage Progression in Tailored Laminated Panels with a Cutout and Delamination Growth in Sandwich Panels with Tailored Face Sheets, Dissertation, Clemson University, December 2002, UMI Number 3071576.
13. J. Reeder, NASA Langley Research Center, Private communication, June 2004.
14. ASTM D6671-01, "Standard Test Method for Mixed Mode I-Mode II Interlaminar Fracture Toughness of Unidirectional Fiber Reinforced Polymer Matrix Composites," Copyright ASTM International, West Conshohocken, PA, USA.

Validation and Certification of Aircraft Structures

Michael Mohaghegh, Ph.D., S.E.
Engineering Technology Development
Boeing Commercial Airplanes

Nomenclature

BVID	Barely Visible Impact Damage	JAR	Joint Aviation Requirements
CAA	Civil Aviation Authority	LCPT	Life Cycle Product Team
CATIA	Computer-Aided Three-Dimensional Interactive Application	LOV	Limit of Validity
CDR	Critical Design Review	M&PT	Material and Process Technology
CFD	Computational Fluid Dynamic	NASA	National Aeronautics and Space Administration
CFRP	Carbon Fiber Reinforced Plastic	NDI	Nondestructive Inspection
CIPR	Critical Integrated Product Review	ODA	Organization Designation Authorization
DPA	Digital Preassembly	PDR	Preliminary Design Review
DSO	Design Service Objective	PIN	Part Identification Number
DTR	Damage Tolerance Rating	PIPR	Preliminary Integrated Product Review
DUL	Design Ultimate Loads	PRR	Production Revision Record
EDI	Electronic Deflection Indicator	PSE	Principal Structural Element
FAA	Federal Aviation Administration	SCN	Strength Check Notes
FAR	Federal Aviation Regulation	SIPD	Structural Inspection Planning Data
FEA	Finite Element Analysis	TDPA	Transparent Digital Preassembly
FEM	Finite Element Method	TIA	Type Inspection Authorization
FRF	Fatigue Reliability Factor	VID	Visible Impact Damage
JAA	Joint Aviation Authorities	WFD	Widespread Fatigue Damage

I. Introduction

Validation of aircraft structures is critical to the design process in that it provides assurance that the structure will perform as intended in all respects: form, fit, function, producibility, durability, and, above all, safety and reliability. Structures design and analysis is substantiated by extensive testing. Although the validation process is essential for certification to regulatory requirements, in total it is much more far reaching. It is the process by which we gain confidence that the structure will deliver all the reliable performance our customers expect and demand.

The materials and design features of any new or derivative airframe structure will generally be a mixture of existing proven elements and new features being used for the first time. In each case, it is essential to validate that the structure will perform as intended as early as possible in the design process, preferably before the design has been committed to production and while any necessary changes can be made without major impact to the program. When existing materials and design concepts are extended to a new or derivative design, the validation process should be relatively straightforward. The primary effort will be to ensure that the available database justifies the proposed design. One must vigorously examine subtle changes from established materials and concepts that could affect performance and require unique substantiation.

For new materials and design features, the available database may well be limited or nonexistent. In this case, the need for validation is more imperative and is more difficult to achieve. Therefore, selection of new materials/concepts should always be made early enough in the airplane program to permit a reasonable level of validation through preliminary analysis and testing prior to commitment. Some risk will always remain until full-

scale test and service experience has fully validated the new concepts. Consequently, wherever possible, such designs should be amenable to relatively simple corrective modification if the need arises.

II. The Building-Block Approach

The validation and certification approach is primarily analytical, supported by test evidence at the coupon, element, subcomponent, and component levels and full-scale limit or ultimate load test at ambient environment as shown in Figure 1. The environmental effects on the structure are characterized at the coupon, element, and subcomponent levels and are accounted for in the structural analysis. Supporting evidence includes testing through the traditional building-block approach that obtains material characterization, allowable and analysis methods development, design concept verification, and final proof of structure. The effects of temperature and moisture are accounted for in design values and strength properties. Thermal and moisture strains may be calculated using finite element model for each critical condition. Structural testing is described in sections V – VIII.

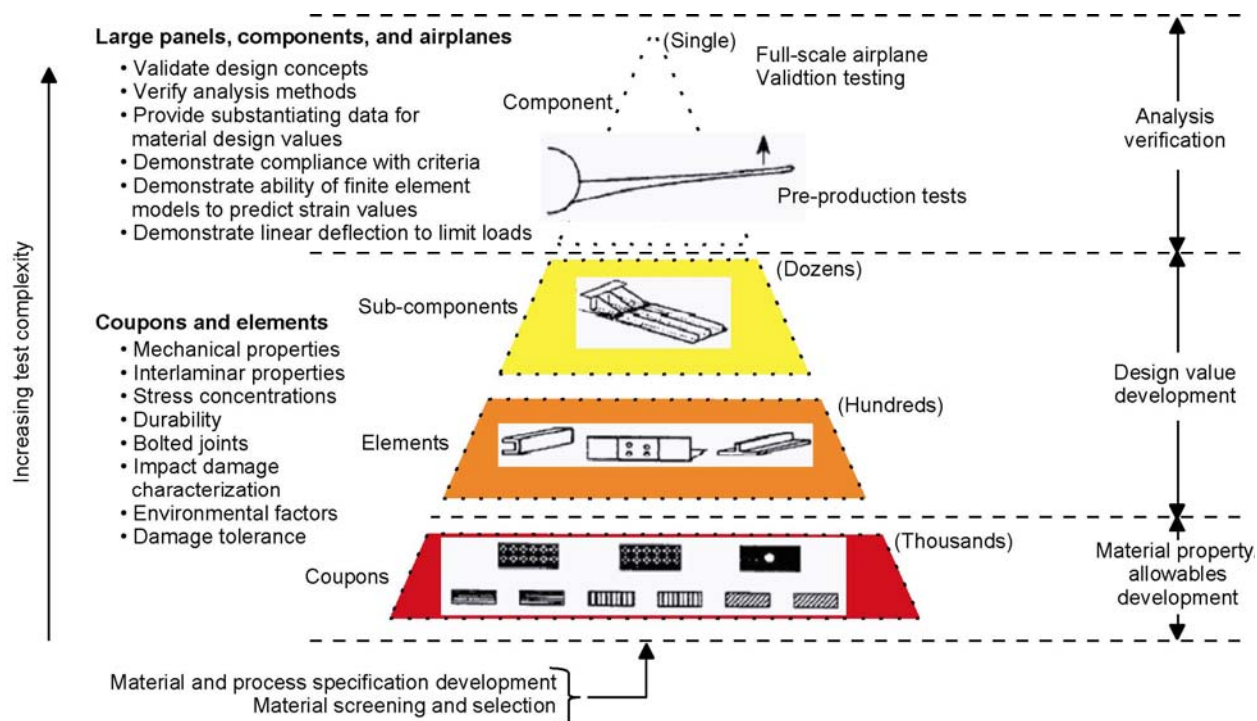


Figure 1. Building-block approach

III. Design Criteria

It is important to understand all the design requirements and how they are each validated. The principal structural design requirements consist of ten core elements shown in Figure 2. This figure also acts as a roadmap to the next level of detail in the structures design requirements and criteria. It can be used as a checklist by the designer to make sure that all requirements for a given design have been met. Each design requirement is typically verified by analysis and further validated by test using the building block approach.

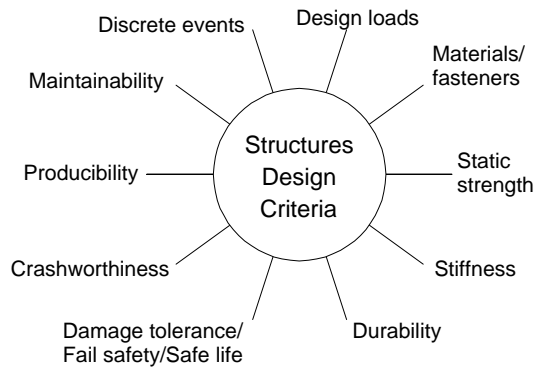


Figure 2. Principal structural design requirements

A. Design Loads

Boeing design loads requirements are derived from both internal criteria and from the regulatory agency standards. Early design requirements were more straightforward than today. They had their roots in a philosophy that mandated criteria that had historically been shown to provide a level of passenger safety. These requirements were continually augmented by additional criteria that were found to be necessary due to accidents, incidents, or new features on the airplanes. Today's trend is toward an increasing reliance on a more probabilistic approach, where fleet statistics are utilized to derive criteria that will produce expected load levels, such as limit load, the maximum load expected in service. An example of this is evident in the recent development of new gust regulations, where new gust intensities have been derived from thousands of hours of in-service airline data.

Improvements in methodologies for loads predictions have evolved simultaneously with the increases in knowledge and computing capabilities. From simple beam models using strip theory for an aeroelastic solution, to highly complex, total airplane finite element models and Computational Fluid Dynamics (CFD) applications, increased computer power has allowed for dramatic advances in how loads are calculated (see Fig. 3). The improvements in the accuracy of the tools, the ability to solve more complex problems, and a better understanding of the important parameters have allowed for optimized structural solutions for performance, while maintaining or improving stringent safety levels. Aerodynamics, mass properties, and structural representations have all been improved. Input data such as aerodynamics, which used to be taken strictly from wind tunnel testing, have been augmented by running CFD models, allowing for greater accuracy in the final results. The tools and methods have been validated using data collected during flight testing on the new airplane programs. These new methods, which allow for better, more accurate loads analysis, are also being used to develop advanced airfoil designs to further benefit aircraft performance. The increase in requirements and the complexity of the analysis have caused a large increase in work required and computing power and have fed downstream customers with increased numbers and variety of load conditions they have to consider in structural design. The number of design conditions has escalated from less than 100 on early Boeing models to numbers in the thousands on more recent projects.

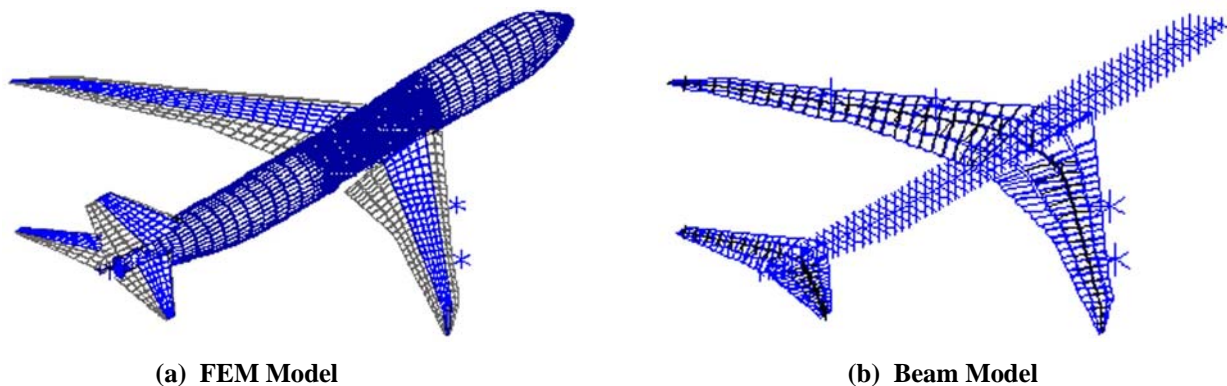


Figure 3. External loads model

B. Internal Loads and Stresses

In today's structural design environment, major, highly complex components and mechanisms can be more accurately modeled in order to determine detailed stresses for ultimate, fatigue or damage tolerance requirements, often eliminating what previously had to be done by expensive structural tests. Furthermore, much of the pre- and post-processing of the analytical models has become increasingly automated and in the future will be tied more closely to the design tools than today (see Fig. 4).

Over time, computing capacity has increased, finite element tools have been enhanced, structural idealizations have improved, and increasing acreage of the airplane structure has been covered. These trends have allowed Boeing not only to optimize structure for improved performance and safety, but also to eliminate some expensive testing.

Credibility in using the FEM for major structural analysis was developed by validating analysis results with test data such as shown in Figure 5.

C. Stiffness/Flutter

Flutter characteristics of airplanes are validated during the design phase by wind tunnel testing. Ground vibration tests and flight tests are conducted to validate the structural stiffness, as described by mode shapes and frequencies and demonstrate that the airplane is free from flutter within the design speed envelope. Flight tests up to the airplane dive speed are conducted to validate that the airplane is free of flutter.

D. Static Strength

Validation testing is conducted where sufficient confidence does not exist for the analysis or if specific validation testing is required for certification (FAR 25.307). One requirement is to validate that the airplane test that airplane remains elastic up to the design limit loads. Static failure of metallic airplane structures has been predicted by an increasingly high level of accuracy (see Figure 12).

E. Durability/Fatigue Performance

Extensive fatigue testing including a minimum of two lifetime testing is conducted to validate airplane fatigue performance in service. Historically, fatigue testing has been conducted to find any problem areas and correct the design to minimize fatigue problems experienced by the customer. There is a new FAA requirement to run full-scale fatigue tests to demonstrate that Widespread Fatigue Damage (WFD) does not occur during the airplane design service objective (see Table 1). Full-scale fatigue tests to multiple anticipated service lifetimes may either pinpoint the anticipated onset of WFD, or, if none occurs on test, a conservative threshold can be reasonably predicted. Likewise, special intense in-service inspections of high time airplanes can be conducted as well as tear down inspections of high time out-of-service airplanes. Ultimately, however, it may be that safety can only be guaranteed by structural modifications or even retirement from service. One of the new requirements is a concept called Limit of Validity (LOV). The LOV is a point in the structural life of an airplane where there are significantly increased uncertainties in structural performance and increased probability of development of WFD. Additional fatigue test evidence and validation of the maintenance program for effectiveness against WFD is required to extend an established LOV.

F. Damage Tolerance

The evolution of FAR 25.571 (see Table 1) shows how design requirements for fail safety and damage tolerance emerged as a result of the service experience described in Reference 2. These additional requirements profoundly influence airframe design today. Damage tolerance testing is conducted with various size specimens including built-up panels and full-scale fuselage sections. There is a Boeing requirement that airplane structures must have limit load capability with large damage. This is a critical design requirement, and sizeable tests to validate this residual strength are often run early in the airplane design phase.

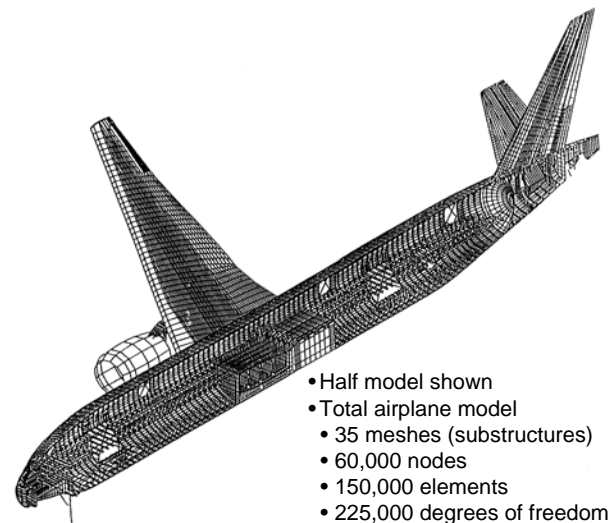


Figure 4. FEM model for internal loads/stresses

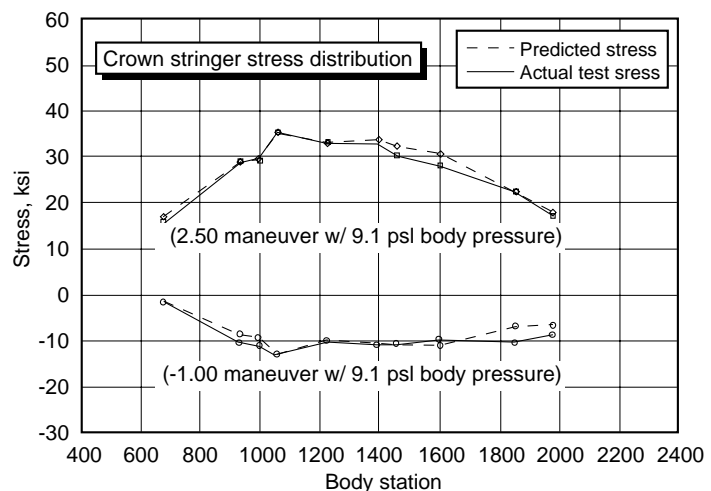


Figure 5. Crown stringer stress distribution

Table 1. FAR 25.571 Amendments related to fail safety and damage tolerance

Amendment Level & Date	Title	Summary of Changes to FAR 25.571
25-0 (12/24/64)	Fatigue evaluation of flight structure.	(c) Fail safe strength. “It must be shown by analysis, tests, or both, that catastrophic failure or excessive deformation, that could adversely affect the flight characteristics of the airplane, are not probable after fatigue or obvious partial failure of a single PSE.
25-45 (12/1/78)	Damage-tolerance and fatigue evaluation of structure.	(b) Damage-tolerance (fail-safe) evaluation. “The evaluation must include a determination of the probable locations and modes of damage due to fatigue, corrosion, or accidental damage. The residual strength evaluation must show that the remaining structure is able to withstand loads corresponding to ...”
25-96 (4/30/98)	Damage-tolerance and fatigue evaluation of structure.	(b) Damage-tolerance evaluation, for WFD Initial flaw of maximum probable size from manufacturing defect or service induced damage used to set inspection thresholds; sufficient full scale fatigue test evidence must demonstrate that WFD will not occur within DSO (no airplane may be operated beyond cycles equal to ½ the cycles on fatigue test article until testing is completed).

G. Composite Structures

FAA issued AC 20-107A, Composite Aircraft Structure, in 1984. The certification of composite primary structures has followed the guidelines contained in AC 20-107A. For damage tolerance, composite structure certification has been based on demonstrating the “no-growth” of damage of sizes up to the damage limit. Environmental degradation caused by temperature, humidity, and so on must be considered. The residual strength versus damage size criteria is shown in Figure 6. The airplane is designed to maintain ultimate strength with barely visible impact damage, limit strength with visible impact damage, and 70% of limit strength with large accidental damage.

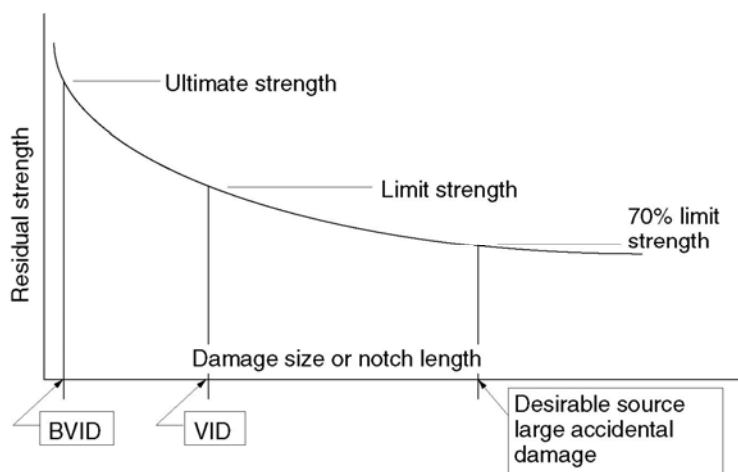


Figure 6. Residual strength versus damage size or notch length

IV. Design Validation

Design validation is the process of ensuring that all of the design requirements are met. This should happen continually from conceptual design through drawing release. This section discusses the methods used to validate that the design requirements have been met by applying the appropriate processes and tools. Figure 7 shows some of the methods used for design validation.

The designer has the responsibility for design validation. There is no single method or process to ensure design validation; it is a combination of methods. This section will elaborate on some of these. There is no optimal cookbook method, but if this validation does not happen concurrently in the process, there is a high risk of either not meeting all the design requirements or driving up costs.

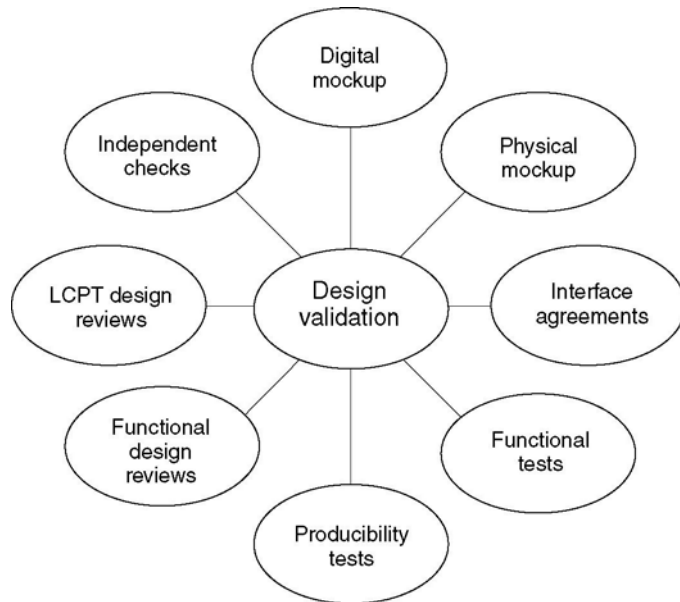


Figure 7. Design Validation Methods

H. Structural Integration

A design process that utilizes built-in checks and balances will help ensure well integrated structure that meets all the design requirements. Here are a few methods to validate the integration of the design:

Interface Agreements. Agreements need to be negotiated between groups for each part-to-part interface. There are many different ways to document these agreements based on the program or team. The documented agreement makes validation easier and more visible. Some interfaces are simply agreements between engineers with no official documentation, and the validation happens within the digital mockup.

Digital Mockup. DPA (digital preassembly) in CATIA is the cornerstone of the current design process, allowing the designer to create a digital mockup to integrate the design. With this mockup we can validate part-to-part interferences using Fly Thrus, TDPA (transparent digital preassembly), fit check, 4D navigator, or any of the functionality of CATIA. Part interference is only one area we need to validate. Part function includes gaps, clearances, maintenance access, producibility, tooling, electrical grounding, and a host of other requirements that need to be checked. Unfortunately, this validation is not automated like part interferences, so it must be analyzed using the digital mockup.

Physical Mockup. The digital mockup has some limitations for validating the design. To reduce the risk of these limitations, sometimes a physical mockup is appropriate. These mockups could be in a variety of forms, such as a foam core mockup built by the designer, a wood or metal mockup built by the mockup shop, or a mockup built by stereolithography. Stereolithography is particularly well suited for small parts and assemblies. An example of the mockup purpose is validation of assembly sequence, tool clearance, and ergonomics. A more indirect purpose would be to get the product team/mechanic buy-in to a design before it is committed; sometimes this is difficult to do with only digital mockups.

I. Design Reviews

Design reviews help validate the design by allowing a diverse population to critique a design concept. Requirements are identified and scrutinized with a free-form flow of potential solutions. During all reviews, some engineering requirements are not negotiable and should not be compromised; it is the responsibility of engineering to identify these to the team. Some of the reviews that take place are:

- Functional reviews
- PDRs (preliminary design review)
- CDRs (critical design review)
- LCPTs (Life cycle product team) reviews
- PIPR (preliminary integrated product review)
- CIPRs (critical integrated product review)

Some reviews can be made by a few people around a CATIA terminal or drafting board. Structured meetings are not always the best method for information exchange, but getting the right people to review the design is critical. There is no right answer as to how many reviews are required; judgment on how much risk is involved by delaying validation will dictate the frequency.

J. Reliability Based Design and Validation

There is considerable effort being applied to probabilistic methods for structures similar to those used for systems design (see Figure 8). The incentive is to better understand and quantify the uncertainties in structural design so that some worst-case conservatism can be avoided while designing to a desirable safety level, especially with new materials. The quantifiable risk or safety level can be treated as a measurement of structural performance and used as a design and maintenance metric to ensure consistent safety throughout the life cycle. The core of this approach is the ability to characterize the uncertainties needed in the design analyses. Availability of data needed for uncertainty characterization so far has been the biggest challenge, especially for new materials and applications. However, it has much to do with the lack of processes and requirement for such data in the past because of the current mostly deterministic design approach. More research is still required in several areas to develop an adequate level of maturity before its full implementation by the industry. One imminent example is how to support certification with the probabilistic design approach. Although there have been some successes, more collaboration between government agencies and manufacturers will be critical to the success of making this revolutionary change of design and certification approach. If validated, this approach may lead to structures that are both lighter and safer at the same time. The use of this approach is expanded to include effects like the environment on the allowables of composite structures.

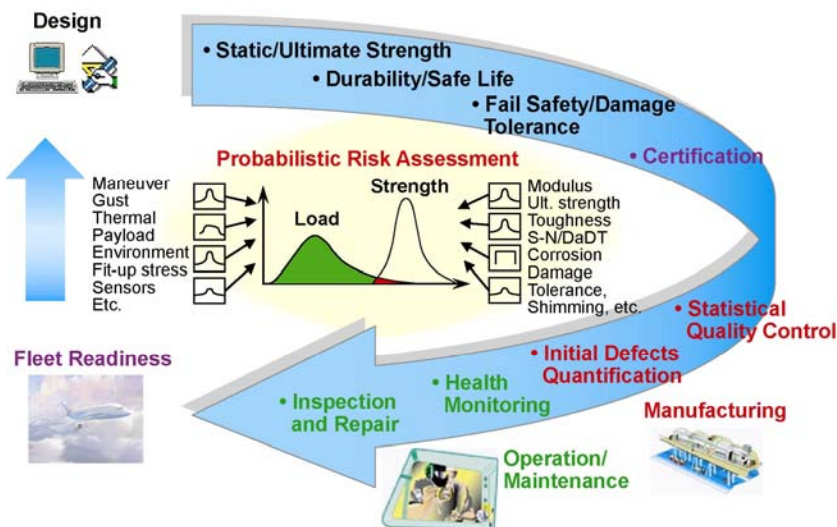


Figure 8. Probabilistic life cycle management

V. Structural Testing

The amount of validation testing on a new airplane depends on the amount of change that exists in the new design. Testing can include ultimate strength, fatigue, crack growth, residual strength, material properties and corrosion resistance, fastener shear and tension strength, and joint strength.

Testing begins with small coupons, then panel tests, followed by component tests and then full-scale airplane static and fatigue tests as shown in Figure 9. If aerodynamic heating is involved, the above tests usually are repeated at various temperatures. To account for the effects of engine or thrust reverser noise, sonic fatigue tests may be necessary. If boundary layer noise or shock wave effects are appreciable high, cabin noise transmission tests may be conducted.

Windshield and passenger window strength tests must typically be conducted, including bird strike tests on a windshield, mounted in a representative cab structure that has the correct sill and post stiffnesses.

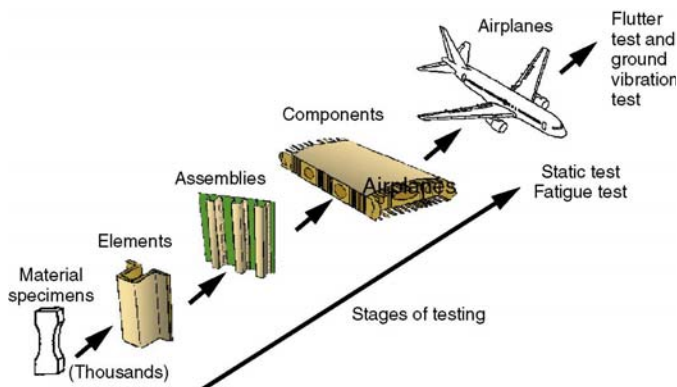


Figure 9. Levels of structural testing

Full-scale static tests are required to demonstrate the validity of both internal loads and design allowables. Fatigue full-scale tests are conducted to validate the fatigue performance of the structure and make any design changes that might be needed if problems are discovered during the test. They also validate that the new design has accounted for any forced deflections that occur at the wing/body joint, stabilizer/body joint, and fin/body joint.

The full-scale test is also needed to demonstrate that thermal strain compatibility has been accounted for when a graphic epoxy component is fastened to an aluminum component, or any other combination of materials having different modulus of elasticity and coefficient of thermal expansion.

K. Requirements for Testing

One of the most important reasons for testing is to evaluate structural behavior when reliable analysis methods are not available or when the assumptions needed to make use of these methods are open to some question. In fact, part 25 of the Federal Aviation Regulations, *Airworthiness Standards*, makes testing mandatory in such cases.

When new materials are being considered for use, testing of coupon samples must be undertaken to determine such properties as F_{tu} , F_{ty} , F_{cy} , and E . Depending upon the anticipated environment, such properties may have to be obtained over a wide range of temperatures. Such testing is usually performed on relatively small but numerous specimens of standard configurations. This type of testing is generally conducted under the direction of the Allowables Group. Such testing is directed toward finding the actual properties of materials tested as a step toward using the test results to calculate standard material properties.

Components are also tested to verify the applicability of analysis methods to new materials. For example, a series of compression tests have been performed on skin-stiffener panels in 7075-T6, 7150-T6, 7150-T6, Ti 6Al-4V, and Ti 8Al-Mo-IV to determine the applicability of the Johnson-Euler formula to aluminum and titanium structures.

Testing of a complete airplane to destruction is customarily done on all new models at Boeing. This is done to establish growth potential and also to substantiate the analysis methods employed.

Fatigue testing of a complete airplane has become more common and has become a requirement in recent years. This type of "accelerated life" testing makes possible the discovery of potential trouble areas that would be encountered in service. Thus, if alterations to structure become necessary, they can be made either in advance of the airplane's entry into service or when an in-service airplane is scheduled for major inspection or maintenance.

L. Types of Testing

There are several valid reasons for performing the various types of tests to validate the design. The guidelines to help in determining the requirement for new testing are based on the following reasons for testing. These are divided into larger categories and summarized as follows:

1. Material Property/Allowables Development

- Testing of standard coupons to establish material properties and allowables is required whenever a new material is introduced. This paper will include details on the testing required to establish static, durability, and damage tolerance allowables.
- The basis of a static allowable provides the user the statistical basis of the values published. FAR 25 defines the type of structure for which an allowable is applicable by the basis of that value. The required basis may also impact the number of tests required to obtain the value. Table 2 provides descriptions of the three classifications.

Table 2. Design allowables descriptions

Basis	Description	Typical Use
A	A value which 99% of the measured values will exceed associated with a 95% confidence level.	Single loadpath structures
B	A value which 90% of the measured values will exceed associated with a 95% confidence level.	Multiple loadpath structures
S	A value associated with specification acceptance values. No statistical significance may be assumed.	Initial designs, or when properties will be verified on a part-by-part basis

2. Design Value Development

- Develops design values for a specific detail (e.g., crippling values for a particular stringer cross-section).
- Small specimen tests or sub-component tests are required to establish design values only if analytical methods for predicting the design values are not available and design values are not available from

testing of comparable designs on earlier airplane models. The use of analytical methods validated by test data is preferred because the analytical methods can cover a range of configurations and sizing.

3. Development Testing

- Development tests are used to evaluate alternative new designs that offer substantial savings in cost or weight, and for which there are substantial unknowns compared to previous designs that can be quantified only by testing. Development testing typically involves small-scale test articles but may include sub-component size articles or larger.
- Compares relative efficiencies of alternative designs.
- Obtains information concerning modes of failure, or secondary effects, and so on that can be used to refine existing analysis methods or to develop new analysis methods, if required.

4. Analysis Verification

- Verification testing is required when design configurations requirements, or materials, are used that differ significantly from those used to verify existing analysis methods. New tests, which generally involve small specimen or sub-component test articles, should be designed to fill in the primary unknowns, building on the previous knowledge base. Note that information obtained from verification tests, including full-scale tests, can contribute to the analysis verification.
- Obtains information to ensure that the analysis methods used to predict failure modes, loads, deflections, and so on are adequate and sufficient to cover the various designs and sizing ranges used on a particular airplane model.
- Generally, only the most critical locations are selected for representation in sub-component or component tests.

5. Qualification Testing (for reliability of processes, tools and techniques)

- Qualification tests are required when equipment, such as riveting, bolting, and so on, is new, undergoes major maintenance, or exceeds previous limitations. This type of qualification testing is primarily composed of small-scale test specimens.
- New equipment or new applications of equipment is typically qualification tested to ensure engineering standards are met (e.g., Gemcor machine riveting).

6. Functional Tests

- These tests are used to validate the ability of the design to meet functional requirements. For example, tests are conducted to validate requirements such as electrical bonding, corrosion resistance, impact resistance, and sealing. Boeing Materials & Processes Technology conducts many of these tests for the designer's benefit, and the information is reflected in design guides and documents.

7. Producibility Tests

- These tests are used to validate the ability of the design to meet producibility requirements. For example, test parts prove machine capability relating to a wide array of tolerance requirements, and Manufacturing gains experience working with new alloys or processes. Producibility tests may also be used in trade studies either for cost data or for make/buy decisions. The object is to obtain data prior to committing the design, thereby validating the design as early in the design process as possible.

VI. Airplane Static Test

The full-scale static test program is typically part of the certification requirements of a new airplane model. A structurally complete airplane is built solely for test purposes, which subject the structurally significant items to design limit load levels. The static test program is used to show compliance with the following regulatory agency requirements:

FAR 25.305 and JAR 25.305 *Strength and Deformation*

- Deformations do not interfere with safe operation at any load up to Design Limit Load.
- No detrimental *permanent* deformation at Design Limit Load.

FAR 25.307 and JAR 25.307 *Proof of Structure*

- Compliance for each critical load condition shown by analysis.
- Analytical prediction of *internal* loads/stresses *validated by testing* at up to Design Limit or Ultimate Load.

The number of individual test conditions, amount of structure tested to limit loads, test schedule, and sequence must be presented to and concurred with by the regulatory agencies as part of the overall certification plan. Additionally, several unit load conditions are applied to the airplane to verify analytical predictions and look for potential highly stressed areas. To determine inherent wing growth capability for derivative models, the last test of the program typically takes the wing to ultimate load levels and beyond, until failure occurs.

Static testing to limit load is mainly of value validating the methods used to determine external deflections and internal load distributions (i.e., finite element analyses). Where the stress variation up to limit load is linear or well understood, this validation can be accomplished at load levels less than limit.

Static testing to ultimate load validates the use of component panel testing to establish allowable stresses. When the methods of establishing allowables from component panel testing are understood and proven by the prior static test results, testing to ultimate load is normally of little value because the test is really only applicable at one location under one specific design condition. The only value is if there has been some error made in design/analysis of the structure, or taking advantage of any growth due to failure being significantly above DUL (i.e., > 5%). The latter is unlikely to occur using current analysis methods and materials.

M. Past Models

A static test program has been completed on every major commercial jet airplane model, since the Boeing 707. The number of limit and discrete unit load applications is varied for each model, depending on test load combination potential and amount of data that is required. Figure 10 compares the limit load tests performed for the Boeing 777 airplane. The 777 major tests will be used as an example to provide detail information on test methods.

N. Configuration

The static test airplane is structurally complete with no payload or systems installations except for the brackets that tie to the primary structure. The passenger floor installation is complete, primarily for ease of access. All potential cargo floor load carrying members, such as roller trays and shear decks, are installed. All wing control surfaces were installed on the left wing; the right wing consisted only of the wingbox and fixed leading edge. The horizontal stabilizer has typically been tested separately, as its three-point attach system (hinge fittings and jackscrew) allows for a simplified and more efficient separate test program. Separate static testing was performed on the nose and main landing gears, the horizontal stabilizer, Rolls-Royce strut, and inboard flap.

FAA conformity inspections for production hardware and test hardware installations that attach directly to the airplane are required, because this is a certification test. These inspections must be defined early in the program in order to be included into the airplane manufacturing plan.

O. Applied Loads

The 777 limit load static test program was composed of 14 major airplane load conditions, and two conditions run on the separate horizontal stabilizer. Test loads were established to produce shears, moments, and torsions that closely approximated the airplane design values. For certain test cases, several areas of the airplane were tested beyond limit load to meet or exceed shear and bending moment envelopes and still provide a balanced airplane condition. This allowed for a reduced number of test conditions. An ELFINI finite element analysis solution, using methods identical to the 777 certification analysis models, was generated for each test condition utilizing the load applied by test hardware fittings. This solution was used to generate stress, strain, load, and deflection predictions for the instrumentation setup chosen for each particular test condition.

Pressure	Case 1 – 13.0 psi
Positive maneuver	Case 2/3 – 2.5g
	Positive envelope
Negative maneuver	Case 5 – (-1g)
Lateral loads	Case 6 – Max fin bending
	Case 7 – Max fin torsion
	Case 8 – Lateral gust
Section 48	Case 4 – Pitch initiation
	Case 17 – Stall buffet
Ground loads	Case 14A – 2 Pt braked roll
	Case 14B – 2.4 g Taxi
	Case 14C – Dynamic braking
	Case 15 – Unit loads
Strut loads	Case 13 – 10 Conditions/strut
	(gust loads, thrust, etc.)
Control surfaces	Case 12 – Inboard & outboard
	Case 10 – spoilers 4 and 6
	Case 9, 12 – aileron, flap/ron
	Case 11 – slats #2, 5, and 7
Stabilizer	Case S1 – Pitch initiation
(Separate test)	Case S2 – Checkback
	Case S3 – Stall buffet

Figure 10. Static test limit load condition comparisons

P. Schedule

Static testing should be scheduled to allow for test documentation to be submitted prior to initial certification of a model. The critical tests include positive and negative maneuvers, lateral loads, proof pressure, and control surface, strut and stabilizer loads. The tests also satisfied Type Inspection Authorization (TIA) requirements. Issuance of the TIA cleared the way for certification flights to begin.

Q. Wing Destruct Testing

Following the completion of limit load static proof tests, the wing of the test airplane is typically tested beyond ultimate load until failure occurs. This provides data to determine potential wing growth for derivative models, as well as determining any non-linear effects, and verifying material allowable properties. For the 777, failure occurred at 103% of design ultimate load in the upper panels at approximately mid-span. Data from load actuators and strain gauges was monitored continuously at 100 scans per second, in order to pinpoint the exact loads and stresses at the moment of failure. The failure location, mode (compression buckling), and stress levels were as analytically predicted according to the wing finite element stress analysis, component testing, and other analysis. This was confirmed by high-speed video of both wings, as well as a post-test inspection and metallurgical analysis of the fracture area. The largest measured wing tip deflection was more than 24 feet (see Figure 11). In order to ensure a wing failure, forward and aft body moments were reduced to below limit load levels by reacting a large portion of the wing loads near the center section. Some local stringer reinforcements were added in the body center section to prevent potential body damage. All wing control surfaces were removed prior to the test. Wing destruct test results for previous Boeing commercial airplanes are shown in Figure 12.

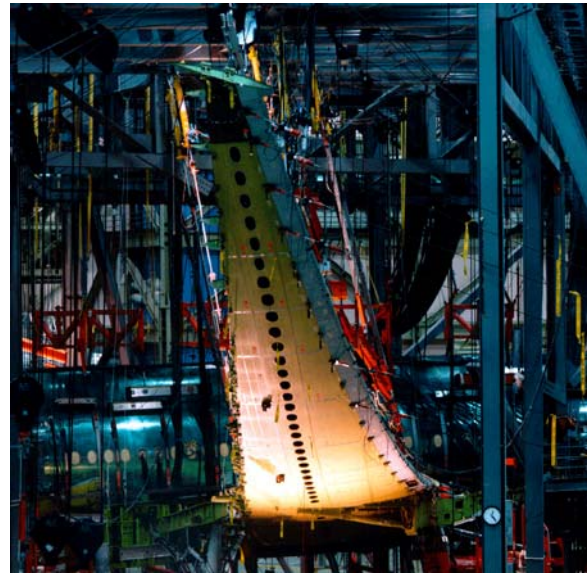


Figure 11. 777 Airplane static test

Airplane model	707 (KC135)	727	737	747	767	757	777
% wing ultimate design load @ failure	110%	110%	106%	115%	99.4% ①	111%	103%
Failure location	Lower panel	Upper panel	Upper panel	Upper panel	No wing failure	Upper failsafe chord	Upper panel

① No wing failure; test terminated due to failure of non-representative body.

Figure 12. Full scale airplane static test results

VII. Airplane Fatigue Test

Full-scale fatigue testing of airplanes is a major part of Boeing structural performance data development. Next to monitoring in-service airplanes, this is the optimum method of obtaining fatigue data as it exposes a full-scale, three-dimensional, structurally complete airplane (Figure 13) to the operating loads that closely approximate those experienced by an airplane fleet. In addition to providing the validation of aircraft design concepts, full-scale fatigue testing is often used to identify any preventive maintenance actions for the fleet, if the fatigue testing is done at the time of certification of a new model of jet transport



Figure 13. 777 Airplane fatigue test

(which has primarily been the case). Full-scale fatigue testing to at least twice the design service objective is required for a new model. Significant test results are shared with the regulatory agencies on an informal basis.

The test objective is to lead the fleet in locating areas that might exhibit early fatigue problems. Fatigue testing also provides opportunities to develop and verify inspection, maintenance, and repair procedures. However, the test is not an alternative to inspections required by the maintenance program to ensure structural integrity over the life on an airplane in service. Separate testing is typically performed on the nose and main landing gears and gear support structure to establish life limits for continued airworthiness in accordance with FAA / JAA requirements. Environmental effects, such as corrosion and climate variables critical for composite structure, are typically accounted for in component rather than full-scale testing.

R. Past Models

Fatigue testing has been performed on every major commercial jet airplane model, starting with the 707, which was tested in a water tank for safety purposes. Figure 14 shows the Boeing airplane models, the minimum design service objective (DSO) in flight cycles, and the number of cycles achieved during full-scale fatigue testing. It may be seen from Figure 2 that full-scale testing is generally accomplished to twice the minimum 20-year DSO, with several exceptions. The first is the model 727, which was originally fatigue tested to its DSO of 60,000 flight cycles. In order to stay ahead of the fleet leaders in terms of flight cycles, an in-service 727 airplane with 47,000 accumulated flight cycles was acquired, and the fuselage was cyclic pressure tested for an additional 76,000 cycles. The second exception is the model 747, which was originally fatigue tested to the DSO of 20,000 flight cycles. As in the case of the 727, Boeing acquired a 747 airplane with 20,000 accumulated flight cycles and cyclic pressure tested the fuselage an additional 20,000 cycles. In addition, the fuselage sections 41 and 42 of the derivative model 747-400 were cyclic pressure tested to 60,000 cycles, representing three DSOs.

Airplane	Minimum design service objectives	Fatigue test cycles	Remarks
707	20,000	50,000	Fuselage Hydro-fatigue test
727	60,000	(a) 60,000 (b) 170,000	Complete airframe Complete fuselage 47,000 cycles in service, plus 123,000 pressure test cycles
737	75,000	(a) 150,000 (b) 129,000	Fuselage section/pressure and shear Complete aft fuselage 59,000 cycles in service, plus 70,000 pressure test cycles
747	20,000	(a) 20,000 (b) 40,000 (c) 60,000	Complete airframe Complete airframe 20,000 cycles in service, plus 20,000 pressure test cycles. 747-400 sections 41 and 42 pressure test cycles
757	50,000	100,000	Complete airframe
767	50,000	100,000	Complete airframe
777	44,000	120,000 plus 20,000 pressure cycles	Complete wing and fuselage airframe

Figure 14. Boeing Airplanes are Fatigue Tested Far Beyond Their Design Service Objectives

The 777 was the first full-scale test to be subjected to twice the airplane's 30-year design service objective, as it completed a total of 120,000 cycles plus 20,000 pressure cycles. This extended testing also provided opportunities to extend the widespread fatigue damage and damage tolerance inspection thresholds, as well as to obtain data to economically operate an aging fleet. The 777 major fatigue test will be used as an example to provide detail information on test methods.

S. Applied Loads

Development of the 777 fatigue test loads spectrum, represented in Figure 15, was based on the concept of applying loads as realistically as possible, while conforming to time and economic constraints and test equipment limitations. Test loads were derived from the 777-200 short flight (1.5 hour) mission because this requires

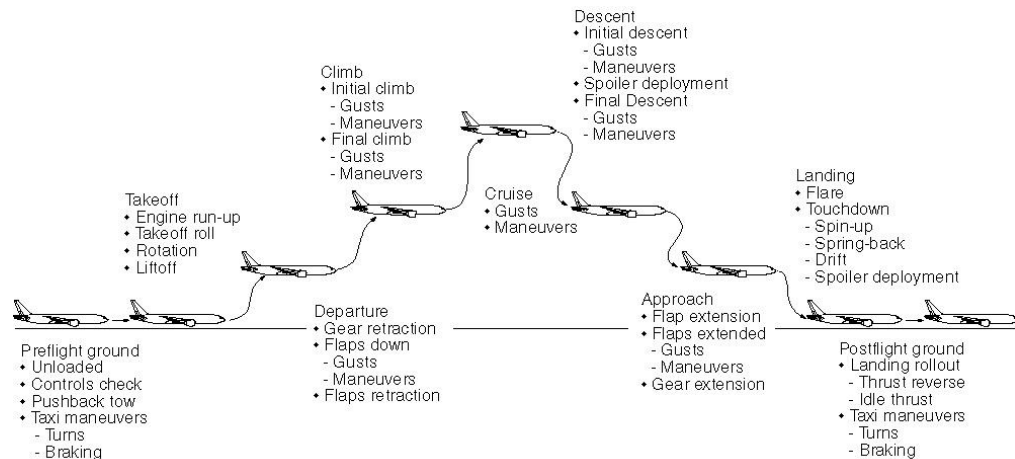


Figure 15. Aircraft fatigue loads overview

the maximum number of flight cycles (44,000 cycles for a 20-year design service objective). Actuator loads were calculated to produce shears, moments, torsions, and point loads equivalent to design values. Fatigue test loads are applied in blocks of 5,000 flights using five different flight types. These five flight types (A, B, C, D, and E) are composed of five alternating load levels (I, II, III, IV, and V) for load conditions simulating gust and maneuver type loadings. The A flight contains the highest loads but is applied only once per 5,000 flight block. The E flight has the smallest loads and is applied most frequently. Figure 16 shows the flight types, their frequencies of occurrence, and typical associated gust and maneuver levels for the 777 cruise segment. Figure 17 demonstrates the wing tip deflections for each of the flights. The combination of all of these applied flights statistically represents the desired

1.5-hour, in-service, short-haul mission. The 777 test consisted of 24 blocks of 5,000 flights. The A and B flights were specified within each block to aid in marker band identification for striation counts. The C, D, and E flights were located randomly in the flight blocks.

Flight type	Flights/block	Control points	Actual time	Final climb gust levels	Cruise maneuver 'g' levels
A	1	1,834	49:02	+/- 27.96 fps	1 g +/- 0.652 g's
B	13	1,534	33:47	+/- 22.49 fps	1 g +/- 0.563 g's
C	215	760	14:33	+/- 13.56 fps	1 g +/- 0.400 g's
D	1,067	432	6:44	+/- 8.37 fps	1 g +/- 0.274 g's
E	3,704	220	2:02	+/- 5.78 fps	1 g +/- 0.186 g's
	5,000 total	292 avg	3:40 avg		

Figure 16. Fatigue test loads 5 x 5 spectrum statistics

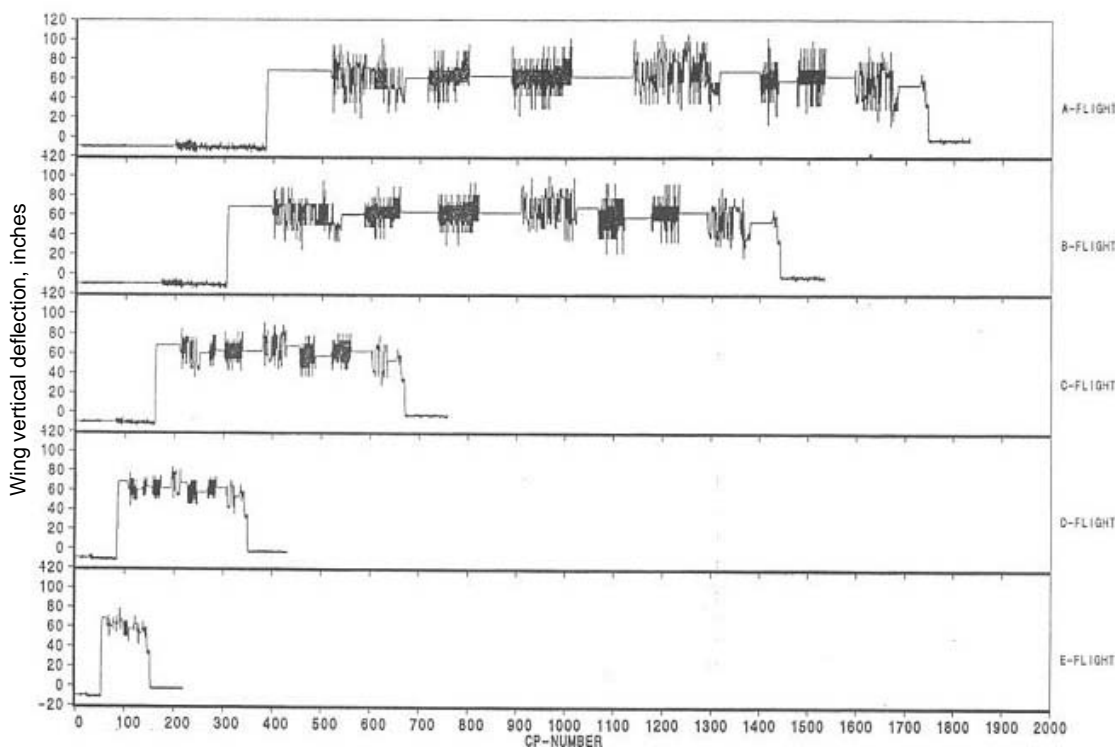


Figure 17. Fatigue test deflections

The procedures for this so-called 5x5 variable amplitude fatigue test spectrum were standardized for the full-scale testing of the 757 and 767. A total of 364 unique balanced airplane load conditions were developed and utilized for the five different flights. An internal loads solution and a special program template were generated to verify that test load damage and loads closely represented those used for design of the structure. In addition to flight loads, fuselage pressurization to 8.6 psi was accomplished for each flight cycle.

T. Instrumentation

Approximately 1,000 strain gauges and calibrated parts were monitored and recorded initially, and at the completion of each design service objective, to help identify any changes in stress levels resulting from potential airplane fatigue damage. Locations for instrumentation consisted primarily of anticipated hot-spots, as well as to verify proper load introductions. Correlation with analysis was done using the static test article, which had more than four times the number of strain gauges installed. Gauges were also added throughout the test in order to obtain detailed stress level information at areas where damage had occurred.

U. Inspection Procedures and Intervals

Inspection requirements for detection of potential fatigue damage were based on the structural inspection plan (SIPD) developed for the 777 fleet with customer airlines and regulatory agencies. The test inspection zones and methods agree with the SIPD. However, the inspection intervals and thresholds were extended and phased to maximize test efficiency. A bi-weekly inspection of critical fatigue areas, and areas where damage had already occurred, was also conducted. Some damage was monitored on a daily basis, to obtain crack growth information and protect the test article as required. Full airplane inspections, including all damage tolerance inspections, took place at the completion of each design service objective. This test provided an opportunity to verify the inspection methods, particularly non-destructive (NDI) methods, prior to them being required by the operators.

V. Data Collection for Damaged Structure

After discovery of damage on the test airplane, a thorough engineering review of the area was accomplished. Included was a review of strain gauge readings, a comparison of test loads versus design loads in the region, inspectability of the structure, consequence of part failure, a check of design loads not incorporated on the test, any special configuration differences to production airplanes, and a review of related problems in the existing Boeing fleet. As applicable, the Materials Technology group performed a lab analysis on the damaged part to verify and determine material properties, geometry, crack origins, and, if possible, striation counts to determine the number of cycles from crack origin to damage discovery.

Several options were available to disposition the damage on the test airplane. The crack could be left unrepaired and monitored at a frequent interval to obtain crack growth information and the effects of damage on the surrounding structure. This was done more frequently toward the end of the test. Strain gauges could be added to enhance the understanding of stress levels in the area. Simpler parts were often removed and replaced, in order to provide additional data. For complex damage, a repair drawing was prepared to specify airplane modifications. Removed parts, or pieces of damaged structure many times were given to the Materials group for evaluation. In some cases, a modified part was installed on the airplane to verify the redesign used for production changes or fleet rework action.

W. Design Change Policy

The process to determine incorporation requirements of production and/or fleet actions following the discovery of structural damage consists of three primary phases. The first is the engineering data collection as described above. Next is a statistical analysis to determine the actual test-demonstrated life of the part, and the anticipated amount of fleet damage. This is dependent on the number of cracked and uncracked similar details and the validity of the test loading in the particular region. Full-scale Boeing test reduction factors are used to accomplish this. Finally, an economic trade study to evaluate the costs of structural changes to the airplane is undertaken. This model determines the net present costs of releasing a design change, releasing a service bulletin, or making no change and repairing the fleet as required, according to the estimated amount of fleet damage. The object of this policy is to provide the Structures engineer with appropriate engineering as well as economic data to make a rational decision regarding rework of structural details that exhibit damage on the 777 major fatigue test.

The number of damage reports for each model, and the subsequent design changes, have decreased for each model (Figure 18), thereby demonstrating the benefit of incorporating lessons learned from the previous full-scale testing.

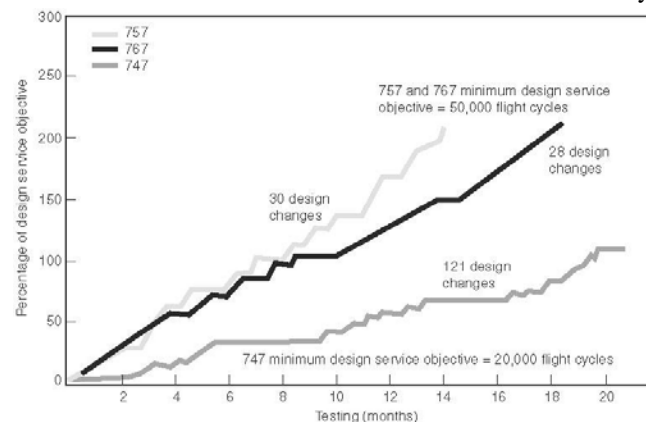


Figure 18. Design changes during full-scale fatigue testing

VIII. Horizontal Stabilizer Tests

Boeing tested the 777 horizontal stabilizer and elevators separately from the airplane because the attachment to the body is determinate. The test specimen was a structurally complete production article (Figure 19). The test plan

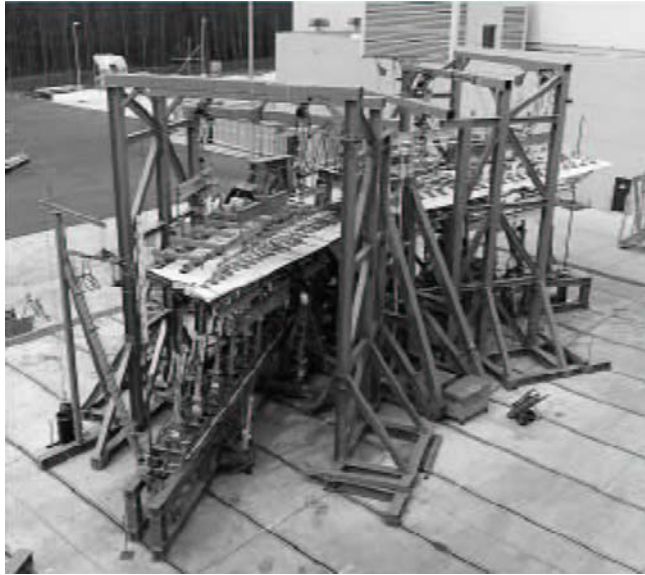


Figure 19. 777 Horizontal stabilizer test setup

deflection indicators (EDI), and calibrated load-cells at selected locations. Instrumentation monitored structural responses and provided data for correlation to analytical predictions during all strain surveys. Testing was conducted outdoors at ambient conditions.

The test included three critical static load conditions: up, down, and unsymmetric bending. Figure 20 depicts the loading sequence. As in the preproduction test box, limit load strain survey results demonstrated the predictive capability of the FEA model. Calculations accurately predicted measured strains (Figure 21). Overall deflection along the span of the stabilizer correlated well (Figure 22). There were no signs of permanent deformation.

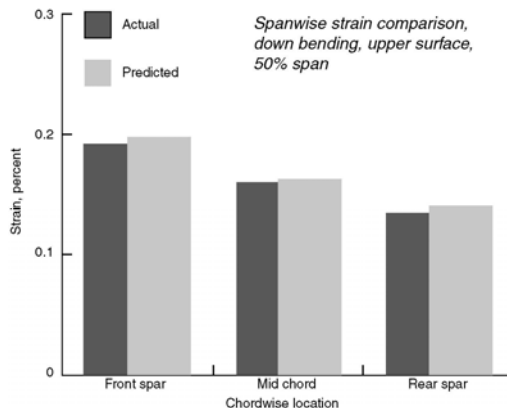
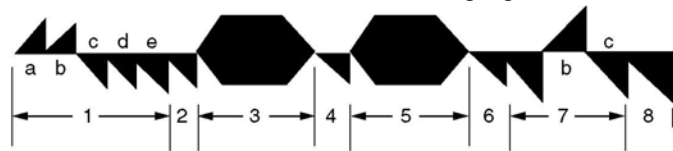


Figure 21. 777 Horizontal stabilizer test, predicted versus actual strains

omitted nonstructural components and systems not essential to the structural performance or induced loading of the stabilizer.

The strakelet and tip fairings were not installed, and the elevator actuators were replaced by rigid links. The test specimen was fabricated by the same construction methods and governed by the same specification requirements as other production structure. Inspectors maintained FAA conformity on a majority of the parts during fabrication. Tests began in April 1994 and were complete in June 1995.

Engineers computed test loads for each static load condition to match the required shear, moment, and torsion values. These test loads were applied to the stabilizer using hydraulic actuators connected to attachment fittings, mounted on the stabilizer structure. The stabilizer was mounted in the test fixture at the pivot and jackscrew fittings, as it would be in an airplane. The test article was instrumented with strain gauges, electronic



Sequence	Load description	Sequence	Load description
1	Limit proof load	4	Strain survey
	a. Up bending	5	Fatigue spectrum
	b. Up bending/unsymmetric	6	Strain survey
	c. Down bending	7	Ultimate load strain survey
	d. Down bending/unsymmetric		a. Stall buffet
	e. Stall buffet (unsymmetric)		b. Up bending
2	Strain survey		c. Down bending
3	Fatigue spectrum	8	Destruction test - down bending

Figure 20. 777 Horizontal stabilizer test sequence

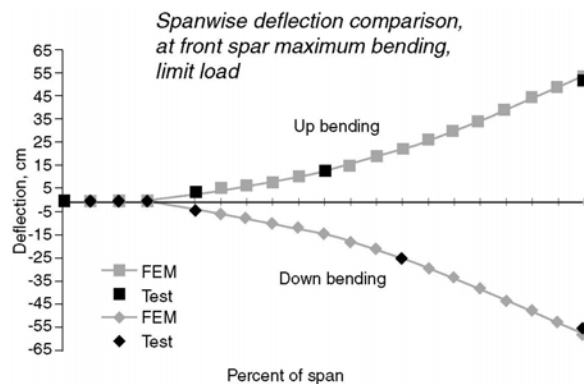


Figure 22. 777 Horizontal stabilizer test, predicted versus actual deflection

Additional testing that was not required for certification included fatigue, ultimate load, and destruct testing. The horizontal stabilizer was subjected to 120,000 flights of spectrum fatigue loading to satisfy the program objectives. This test verified the fatigue characteristics of the metallic portion of the stabilizer. The preproduction test box described earlier verified the composite structure.

Ultimate load and destruct testing supplemented the data that was acquired as part of the certification program. The test team ran three load cases representative of up, down, and unsymmetric bending. The critical down bending load case became the destruct run. The test box was subjected to barely visible impact damage and loaded to failure. Engineers accurately identified the failure location and predicted the failure load within 3%. Final failure occurred above the required load level.

The 777 horizontal stabilizer test program met the following goals:

- Verified compliance with FAR/JAR 25.305 and 25.307. The test article sustained limit load for critical conditions without permanent deformation.

- Verified predictive capability of analysis methods coupled with subcomponent tests. Strains and deflections closely matched the analysis.

- Verified the design service goals of the 777 horizontal stabilizer.

- Verified the absence of widespread damage due to fatigue.

IX. Vertical Stabilizer Test

Boeing tested the 777 vertical stabilizer, including the rudder, as part of the airplane full-scale test (Figure 23). Again, the purpose was to show limit load capability and verify the accuracy of analytically calculated strains and deflections. Tests began in June 1994 as part of the full-scale airplane test and were completed in April 1995. Boeing used a second airplane with vertical stabilizer and rudder in the major fatigue test, which began in January 1995.

The static test article was the second production airplane built. The aft portion of the aircraft was structurally complete except for nonstructural components and systems; the horizontal stabilizer was replaced by a load fixture attached at the pivot bulkhead and jackscrew attachment. The leading edge and tip were not installed on the vertical stabilizer, and the rudder actuators were replaced by rigid links.

As described for the horizontal stabilizer test, engineers computed loads for critical cases, based on the external load conditions, and applied them through a series of actuators, fixtures, and pads. The test article contained a full set of instrumentation to monitor behavior and collect data for comparison with the analysis. Testing was conducted indoors at ambient conditions.

Three critical conditions tested included maximum bending (engine-out), maximum torsion (hinge moment), and maximum shear (lateral gust). Technicians applied other test conditions as part of the overall airplane test sequence, which were not critical for the vertical stabilizer. In comparison with the analysis, measured strains were accurately predicted (Figure 24).

A completely separate test using another production airframe verified the fatigue behavior of the 777. This test subjected the vertical stabilizer and rudder to 120,000 flights of spectrum fatigue loading. The 777 vertical stabilizer test program exceeded the same goals as described for the horizontal stabilizer test.



Figure 23. 777 Vertical stabilizer test setup

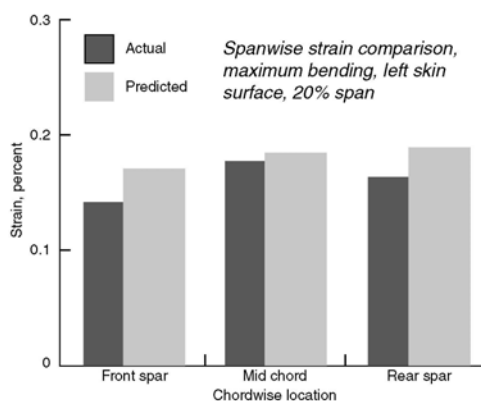


Figure 24. Vertical Stabilizer Test, Predicted Versus Actual Strains

X. Distributed Certification

The plan for partner/supplier engagement in new airplane development, such as the 787 Dreamliner, will result in more delegated authority for those partners and suppliers than historical programs. The new airplane plan will have partners and suppliers engaged earlier than previous programs. These partners and suppliers will be a combination of domestic and international companies and have access to certification offices and agencies potentially far removed from the Seattle office. These partners and suppliers will be engaged in and have responsibility for necessary technology development and subsequently be responsible for design definition and hardware production of their particular component. Boeing will provide for proper integration and consistency across the airframe by the requirements that are defined and levied on the partners. Depending on the degree of delegation, the partners will then execute their work statement with a greater degree of autonomy and authority than granted on previous programs. For example, a partner that has previously displayed a high degree of expertise and competence in a design development and engineering release process might be controlled by requirements defined at a relatively high level. These requirements would ensure that the partner component would integrate properly and be consistent with the rest of the airframe but would not control the details of execution. That partner could define requirements in addition to the FARs that they deem appropriate; use their own design criteria, tools, and processes; select materials from their knowledge and experience base; release and approve the engineering through their own local system; maintain the engineering data; and sustain the product. The ultimate vision of delegation would have that partner certify that hardware through the most proximate (domestic or foreign) certification agency or office. A partner with less delegation authority would have a more complete requirement set to meet. The future airplane models will have a large diversified partner and supplier base that will have many and varying levels of delegation authority. The details and processes of an efficient, integrated certification plan must be defined to enable this global engineering and certification working model. These details and processes must also recognize and account for Boeing working toward receiving Organization Designated Authorization (ODA).

XI. Summary

Design and analysis of structure must be validated per Boeing and regulatory requirements. All requirements are satisfied by analysis, and tests are run to validate the analysis of new or modified structure with different material or geometry. Considerable experience and judgment are required to determine the number and types of tests on a new or derivative program. Analytical structural models are generally based on those methods previously validated on successful existing aircraft, including correlation with static test and flight loads or strain surveys. Aspects of the models are further verified by ground vibration tests, engine blade-loss tests, and component structural tests. In the event that new analytical methods are introduced on a program, validation can be achieved through their application on a previous airplane and the subsequent correlation of results with those achieved earlier by using the original analysis method. Certification agencies, on the basis of FAR/JAR 25.307, 25.301, and 25.305, often require that analytical predictions be corroborated by comparison with static test and/or flight test results.

XII. References

1. Al Fawcett, Jess Trostle, and Steve Ward, "777 Empennage Certification Approach," presented at the 11th International Conference on Composite Materials, Gold Coast, Queensland, Australia, July 14-18, 1997.
2. Michael Mohaghegh, "Evolution of Design Philosophy and Criteria," presented at the 45th Annual SDM Conference, Palm Springs, California, April 19-22, 2004.
3. FAA Advisory Circular 20-107A, "Composite Aircraft Structure," 1984; and companion document by the JAA, ACJ 25.603, "Composite Aircraft Structure (Acceptable Means of Compliance)," 1986.
4. Code of Federal Regulations, Aeronautics and Space, Part 25, "Airworthiness Standards: Transport Category Airplanes."
5. Joint Aviation Requirements, JAR-25, "Large Aeroplanes."
6. MIL-Handbook 17, "Composite Materials Handbook."

Consistent Structural Integrity in Preliminary Design Using Experimentally Validated Analysis

Craig Collier¹ and Phil Yarrington²
craig.collier@hypersizer.com
Collier Research Corp., Hampton, VA 23666

Coupling analytical methods to experimental results forms the basis of consistent structural integrity by analysis. By establishing repeatable statistical variance from building block test data for unique failure modes, it is possible to identify correlation factors (CFs) that account not only for analysis inaccuracy, but also observed scatter in test results. Industry accepted failure analysis predictions then can be used to design more robustly and to avoid unanticipated design flaws discovered in final design, or worse yet lead to part failure. The CFs can be used to adjust the individual margins-of-safety to produce more consistent structural integrity in the design and dependability in weight predictions of an aerospace vehicle. Such a capability is most useful during preliminary design where 80% of the design decisions carry forward, including the uninformed ones that bring with them undesirable difficulties of meeting weight goals, passing structural testing on the first try, and costly certification. The presented approach has been implemented in the HyperSizer® automated design tool that results in significant design cycle time reduction with the ability to analyze orders of magnitude more design configurations. Substantial risk reduction in final design is achieved from the integration and use of correlated, higher fidelity tools earlier in the design process. Presented are summary results from a recent Long Range Strike Aircraft preliminary design that compares the traditional, zero-margin for all failure modes approach, vs. the presented approach that achieves the same % reliability for all potential failure modes. Included are identified areas of the vehicle sized the traditional zero-margin method that results in an unexpected and unacceptable low reliability even though it is 9% heavier than reliability based sizing.

1 Introduction

Full scale airframe testing costs and schedule delays prohibit experimental validation of all but a few potential failure modes for a limited number of load cases. For this reason industry relies more on analysis for cost effectively identifying potential failure modes for all load cases. As a result, most structural integrity supporting evidence is provided not by test data, but rather by extensive “strength calculation”, or “stress analysis,” terms that are synonymous with analytical modeling. Analytical modeling of structures means the capability to predict 1) internal load distributions 2) the resulting detail stresses and strains, and 3) failure. Qualification of structural integrity requires all three of these analytical capabilities. However, this paper maintains that current aircraft designs are suffering from inconsistent structural integrity that is prevalent throughout a project’s analysis maturity. Four primary inconsistencies practiced in aerospace structural analysis are identified. Presented are proposed solutions for these inconsistencies and results from software implementation and application to a real world example.

© 2005 Collier Research Corporation. Published by NASA with permission.

¹ Senior Research Engineer, Hampton, VA

² Senior Research Engineer, Hampton, VA

In contrast to full scale production airframe testing, tests of individual airframe features are more cost effective, particularly when their costs can be shared by reuse of the resulting non-restricted data for many aircraft programs. In fact, the data found to be most useful is indeed for small structural components such as material coupons, panels, and joints that are tested individually in well controlled environments of precise loadings and boundary conditions and that are setup to investigate a particular failure response. Additionally, these types of tests can be affordably repeated to generate multiple, statistical relevant test data and produce valuable “building-block” data.

By establishing repeatability from building-block test data for unique failure modes, it is possible to identify correlation factors (CFs) that account not only for analysis inaccuracy, but also observed scatter in test results. Correlating analytical methods to experimental building block test data forms the basis of consistent structural integrity by analysis. Therefore, industry accepted failure analysis methods then can be used to design more robustly and to avoid unanticipated design flaws discovered in final design, or worse yet lead to in-service part failure. The CFs can be used to adjust individual margins-of-safety to produce more consistent structural integrity in the design and dependability in analysis of an aerospace vehicle. Such a capability is most useful during preliminary design where 80% of the design decisions carry forward, including the uninformed ones that bring with them undesirable difficulties of meeting weight goals, passing structural testing on the first try, and costly certification.

The presented test data CF approach has been implemented in the HyperSizer® commercial automated analysis and design tool that results in significant design cycle time reduction with the ability to analyze orders of magnitude more design configurations. Substantial risk reduction in final design is achieved from the integration and use of correlated, higher fidelity analyses earlier in the design process. Correlation factors are established based on available, non-proprietary test data, from sources such as NASA. Presented are summary results from a recent Air Force, Long Range Strike Aircraft preliminary design that compares the traditional, zero margin-of-safety for all failure modes approach, vs. the presented ‘test data driven’ approach that achieves higher reliability for all potential failure modes. Included are identified areas of the vehicle sized using the traditional zero-margin method that results in an unexpected and unacceptable low reliability, even though it is 9% heavier than the new reliability sized design. The presented ‘test data driven’ reliability approach as implemented in HyperSizer conclusively provides: 1) substantial weight savings, 2) consistent structural integrity, 3) higher reliability/safety, and 4) convincing rational to certification authorities of airframe structural airworthiness.

2 Consistent Structural Integrity

2.1 Problem: More test failures in last 25 years than in previous 50 years

Fig. 1 provides a relative score of how well aerospace is doing at predicting structural integrity [1]. The blue curve represents test predictions performed with modern analytical modeling approaches such as FEA. As compared to the red line, which represents pre 1976 aircraft test failures, this implies more erroneous predictions than in the past. Added to the original plot are green and purple curves. The green vertical line at 150% represents a perceived desired result. But considering statistics, we know this is not obtainable. Therefore, if failures are not to occur before 150%, then the necessary percent failures would follow a statistical distribution similar to that represented with the purple dotted curve.

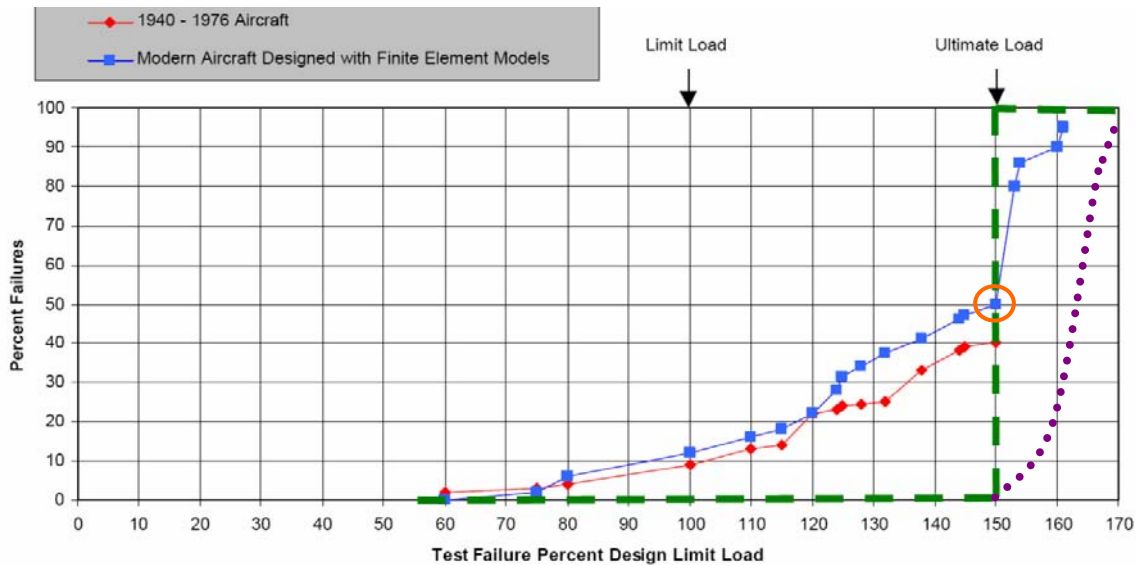


Fig. 1, Red and Blue curves are percent test failures of wing, fuselage, vertical tail, horizontal tail, landing gear and unique major components before reaching required ultimate load of 1.5 Design Limit Load. The green vertical line at 150% represents a perceived desired result, but the purple curve represents the expected statistical distribution.

The obvious question Fig. 1 poses is why structural integrity has not improved in modern times since computing hardware and analytical modeling techniques have improved and are available and applied on a production basis. There are several plausible reasons for this increase in aircraft failure before reaching required ultimate load. The first may appear due to FEA in general in that the FEM is not more accurately capturing structural response of airframe structures. However, though improvements are necessary and will occur over time, it is held that state of the art FEA used in industry is accurately computing running “load paths” throughout the skin panels and internal substructure of airframes. The cause for less accurate pretest predictions may be attributed to three reasons. The first is improperly applied failure analysis predictions. The observed analytical modeling downfall is likely due to over reliance on FEA modeling for detail analysis where specialized analysis tools are more robustly suited for failure prediction. Specialized analysis tools perform better than detailed FEA for failure prediction because they are designed specifically to represent a given phenomena including its innate boundary conditions and also because they are correlated to extensive testing to achieve required validation.

A second possible reason more test failures have occurred in the last quarter century is because the FEA computed internal loads though far more accurate, are also less conservative in their magnitudes. As a result, there is less room for error in failure predictions in a test environment where the applied load is explicitly known, and therefore the internal loads predicted are very accurately quantified without built-in conservatism. It is statistically meaningful to note that with the more accurate internal load predictions of the last quarter century, there are 50% failures at the ultimate design load of 150% limit load, noted with the orange circle in Fig. 1. This is expected when industry designs to 150% limit load (DLL), which is analogous to a 50/50 chance of a coin flip. If our goal is to avoid test failure at 150% DLL then we must design considering a statistical distribution as indicated with the purple curve of Fig. 1.

The application of validated tools by the aerospace engineering community is based on the traditional zero-margin-of-safety analysis approach, which relies on the use of an historical 1.5 ultimate load factor for necessary conservatism and confidence. In other words, airframe structure is designed to fictitious ultimate loads which are simply the actual worse case expected loads (called limit loads) increased by

50%. The third and most important reason test failures occur is that *one constant load factor, applied to all potential failure modes, is not possible to raise all deterministic failure analyses to the same level of safety.* Though providing substantial margin for analysis error, some failures to certain load combinations are not predictable to within 50%. Meaning that 150% DLL is not sufficient for some failure modes, and too conservative for others.

Described in this paper is a design sizing and analysis process, based on building-block test data that brings all applied failure mode analyses to the same reliability. Incorporating this recommended approach, as implemented in HyperSizer, will lead to more consistent structural integrity in airframes and thus contribute to more successful test programs in the future.

2.1.1 Inconsistency of deterministic failure analyses

An aerospace stress analyst spends more time and effort in predicting failure and writing the margin-of-safety stress report than any other activity. This is because failure prediction is the area of most uncertainty and much effort is expended in trying to definitively quantify it. The problem is: failure cannot be deterministically predicted, because failure is not deterministic. The issue is how to handle scatter in experimental testing of observed failure while assigning a deterministic margin to it.

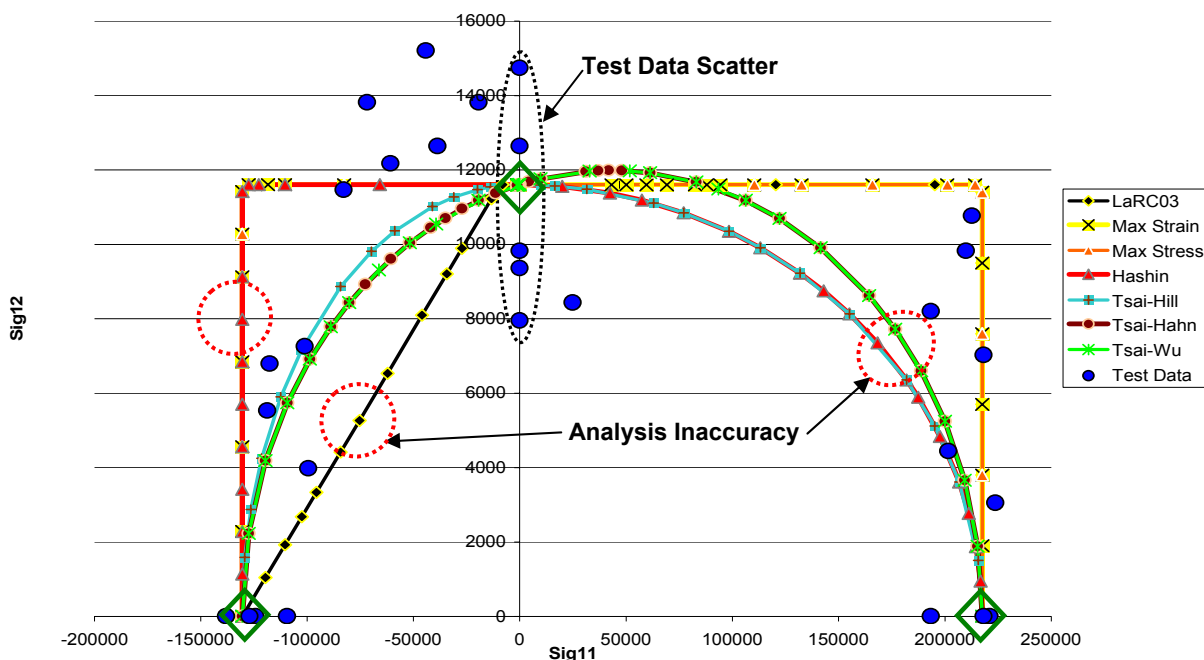


Fig. 2, Top half of a composite material failure envelope from the World Wide Failure Exercises (WWFE) Case #2. The vertical axis of pure shear shows approximately a 90% difference in test data scatter for failure stress. Analysis inaccuracy is worst for quadratic failure theory Tsai-Wu for the ply tension quadrant, and worse for max strain, max stress, and LaRC03 for ply compression failure quadrant. All failure criteria are calibrated to the three anchor points (noted as green diamond symbol) of pure tension, shear, and compression.

As an example, Fig. 2 illustrates scatter for test results from the World Wide Failure Exercises (WWFE) Case #2 [2,3]. The test is for a composite laminate material subjected to a combination of tension/compression membrane and in-plane shear loads. Only the top half of the composite material

failure envelope is shown, meaning tests were assumed not necessary for negative values of shear. This laminate is unidirectional exhibiting no progressive post 1st ply failure strength. The computed failure envelopes of seven composite failure theories are superimposed on the test data. All seven failure criteria are calibrated to the three anchor points of pure fiber tension, fiber compression, and ply shear. Even still, for combined bi-axial loads, large variations in predicted strengths are computed with the different theories, with none of them matching all test data. And the test data itself exhibits substantial scatter at all three anchor points, particularly for pure shear (σ_{12}), where approximately a 90% difference is reported.

The typical way to address analysis inaccuracy and test failure scatter is to define a **knockdown** to theoretical load. However, the knockdown is a single value that does not provide insight into each failure theories' intrinsic level of uncertainty, as illustrated again for buckling shown next.

2.1.2 Inconsistency of the typical one knockdown approach

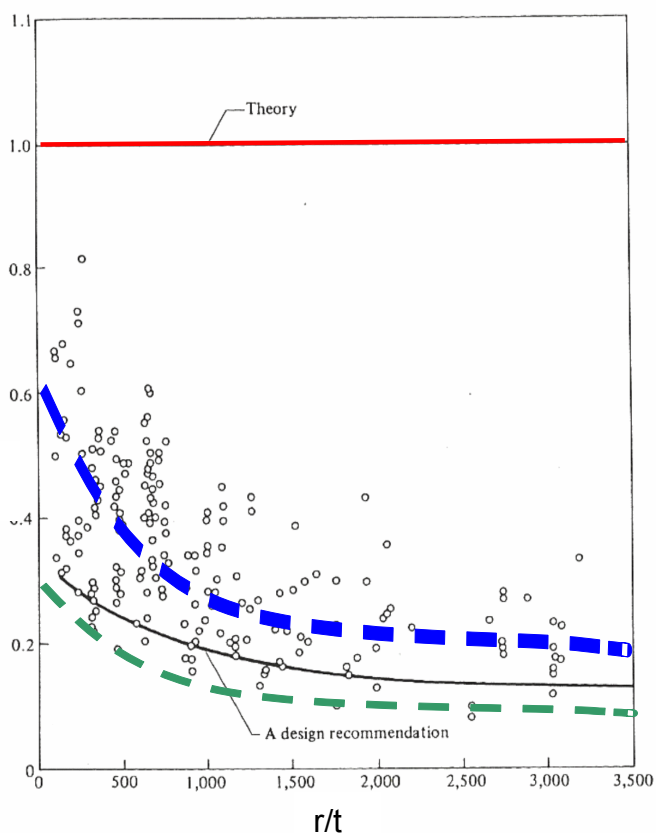


Fig. 3, Traditional one knockdown approach to cylindrical panel buckling, noted as a design recommendation. The black curve is the original NASA SP-8007 knockdown, the green curve, a possible more conservative knockdown, and the blue curve, the average (typical) failure. The original, one constant knockdown equation doesn't give insight into the average test data, nor does it allow the engineer to choose his level of reliability, such as the green curve.

Fig. 3 shows cylindrical panel buckling test data as points. Each test data point is normalized against its theoretical value (vertical axis). The horizontal axis represents decreasing theoretical accuracy as the radius/shell thickness (r/t) ratio increases. Fig. 3 is related to the NASA SP8007 report [4]. Note the large discrepancy between theory (red line) and test results, i.e. inaccuracy of theoretical. The design recommendation is an established knockdown defined as an equation that includes the r/t ratio. So regardless if the knockdown is expressed as a single value or as a curve fit equation, the NASA one knockdown approach defines a once-and-for-all acceptable limit of risk.

Other curve fit equations, such as the blue and green curves can be defined based on a function of selected parameters. Even though the knockdown (black curve) is somewhat dynamic based on changing variables, in this case the r/t ratio, the first shortcoming with this traditional approach is that the acceptable level of risk (black curve) is "cast-in-stone" when first defined, and for the most part unchanging as more test data becomes available. In fact, the actual comparison is rarely known by the practicing engineer.

A second shortcoming is the acceptable level of risk defined originally may not meet the reliability requirement of your particular design (shown as green

dashed-curve). A program manager should be able to choose required knockdown/reliability for each design project. Furthermore, insight and flexibility should be provided to bring each analysis failure mode to a consistent value.

The third shortcoming, which also relates directly to the goal of efficient structural certification using analysis, is that with a single knockdown that takes the theoretical value (shown as red line) down to an allowable design-to value, does not provide nor expose any knowledge of an average or expected typical failure load, represented with a blue curve. So unlike being able to use “typical” material properties for test predictions, the user is left to perform test correlations using a “design-to” failure analysis allowable, which should for almost all cases significantly under predict, and be very conservative to test results.

As a note, the NASA knockdown, black curve, is approximately a 90% reliability against failure and is combined with a 1.5 ultimate load factor to achieve considerable conservatism (safety).

2.1.3 Inconsistency of the zero margin-of-safety approach

It is not possible to achieve consistent structural integrity simply by requiring all failure modes to have a positive (but close to zero) margin-of-safety as in the current industry process of design and analysis. This is because there are different levels of inaccuracy for different failure modes. Additionally, different failure modes exhibit different levels of measured scatter in test results. For example, Classical Lamination Theory (CLT) is very reliable in predicting in-plane strains, but less reliable for predicting failure for off axis laminates. Predicting the post-buckled response of a large shear web and the internal strains is a bit less accurate. If one then extracts edge forces to compute bolted joint margins then the reliability is further eroded. Finally, if one desires to predict the post-impact damage response, the confidence in the prediction is almost zero. Clearly if each of these analysis types quantify a zero margin, then there is a veritable safety inconsistency of the structural integrity. For this reason, each failure mode should be targeted to a different required margin based on its unique uncertainty. Such an approach is the first phase of implementing consistency in analysis accuracy. Industry movement in this direction, which has been slow, can be acknowledged with just a few examples. For instance, it is customary for aircraft programs to specify a required $MS=.25$ for joint strength analysis, especially when the joint is bonded composite [5, 6].

Fig. 4 portrays this concept graphically. If we performed many analyses with high fidelity analysis codes, we would expect some analyses to closely match test results, in terms of this analogy, the analysis predictions fall tightly within the target circle. However, even high fidelity analyses are likely to miss the target all together for some cases, and perhaps even outside the larger diameter dashed circle which represents the safety of an additional 1.5 ultimate load factor.

By including probabilistic methods (PM), analysis predictions can reliably be centered together. By the use of correlation factors (CF) these predictions can then be accurately calibrated to test results. Such an approach would neither target a zero margin-of-safety nor use a 1.5 ultimate load factor.

2.1.4 Inconsistency of the 1.5 ultimate load approach to safety

It is not possible to achieve consistent structural integrity simply by using a constant load amplification factor to all of the failure mode analyses. The misconception is that all failure analyses are raised to the same level of safety. Each failure mode has its own unique uncertainty, so that by designing to a 50% higher load, 1.5 Design Limit Load (1.5 DLL), many failure predictions are extremely conservative while others don't meet the level of safety required. This line of reasoning suggests that since the design-to load is 1.5 DLL (a 1.5 ultimate load factor), test articles, statistically speaking, should rarely fail at loads close to 1.5 DLL. If they did, then contrary to expectation, it should indicate less confidence in the analysis.

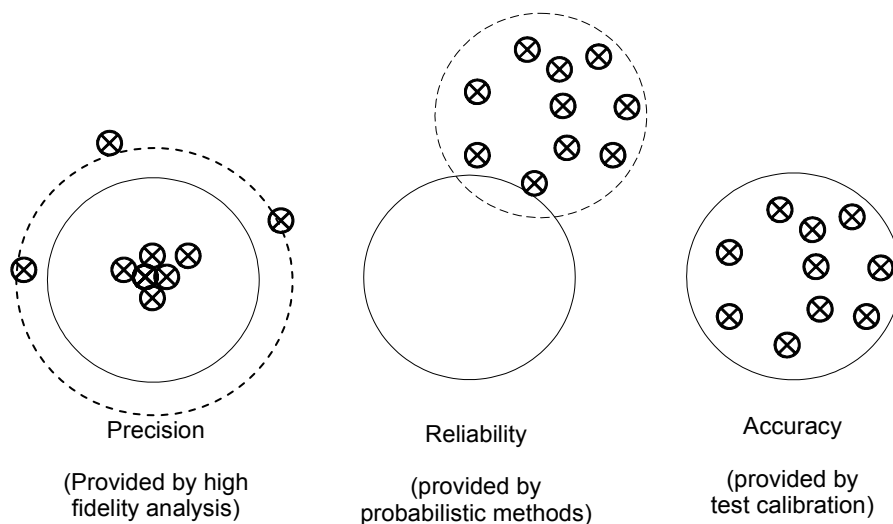


Fig. 4, High fidelity analyses provide precision, defined as an ability to hit a bull's eye but not ensuring that all results fall within the target. Therefore, even with a 1.5 ultimate load factor, which in essence expands the circle to a dashed circle, some analyses for structure designed to a zero margin may still fall outside. Conversely, probabilistic methods reliably bring the scatter into a circle, and physical test calibration then accurately moves the circle onto the target, and a larger diameter target (1.5 load factor) is not necessary.

Over the years industry has adopted in a limited way, the use of other load factors for particular strength checks. It has been a long standing requirement that pressure vessels be designed to a burst proof pressure test load of 2.0 times the operating in-service pressure. [5]

The solution to the first four inconsistencies is addressed with a new “test data driven reliability” approach. [7,8,9] covers this subject in detail. As depicted in Fig. 4, essentially two correlation factors are defined to first bring the analysis predictions within a circle, and second to calibrate them to test values.

2.2 Specific Recommendation: Implement higher fidelity analysis tools and reliability in preliminary design

Over the years as vehicle performance expectations and mission demands increase, aircraft designs tend to be lighter and do more with less material. Additionally, due to economic drivers, the industry attempts to accomplish more analyses per engineer, perhaps causing important details to be overlooked. To better prepare for these possibilities, this recommendation is to implement the use of more accurate and comprehensive analyses during the conceptual and **preliminary design** (PD) phases [9]. The purpose of which is to design-in reliability and robustness, instead of trying to analyze-in margin with extremely advanced analyses after the design is set. Fig. 5 illustrates a cause and effect diagram which identifies a way this could be accomplished in three areas. These areas are described next.

Reliability Determined Statistically for FEA Computed Design-To Loads. Red items in Fig. 5 address the generation of FEA computed internal loads. The issue is related to what are the “design-to” loads? The answer is to adopt a statistically based approach for determining their values from the thousands of load cases.

Reliability Designed-In Using Robust Optimization. Yellow items address sizing optimization of the structure. A primary concept is to use nearly all of the available analyses during sizing optimization so

that no new failure mode surprises will occur when going to the final analysis. Another primary concept is to minimize design variable sensitivities and find commonality in optimum design variables from multiple optimized solutions.

Reliability Quantified Using Probabilistic Methods. Blue items cover the final analysis and margin-of-safety reporting. A key objective is achieving a building block validation and verification (V&V) documented process for analytical modeling. Without such documentation the product customer will not have the basis available for certifying the methods used. To address human error, checks would be applied to each input value that would define an envelope of applicable lower and upper bounds for given analysis methods. Such checks would also catch and filter out inappropriate variable combinations generated by automated optimization.

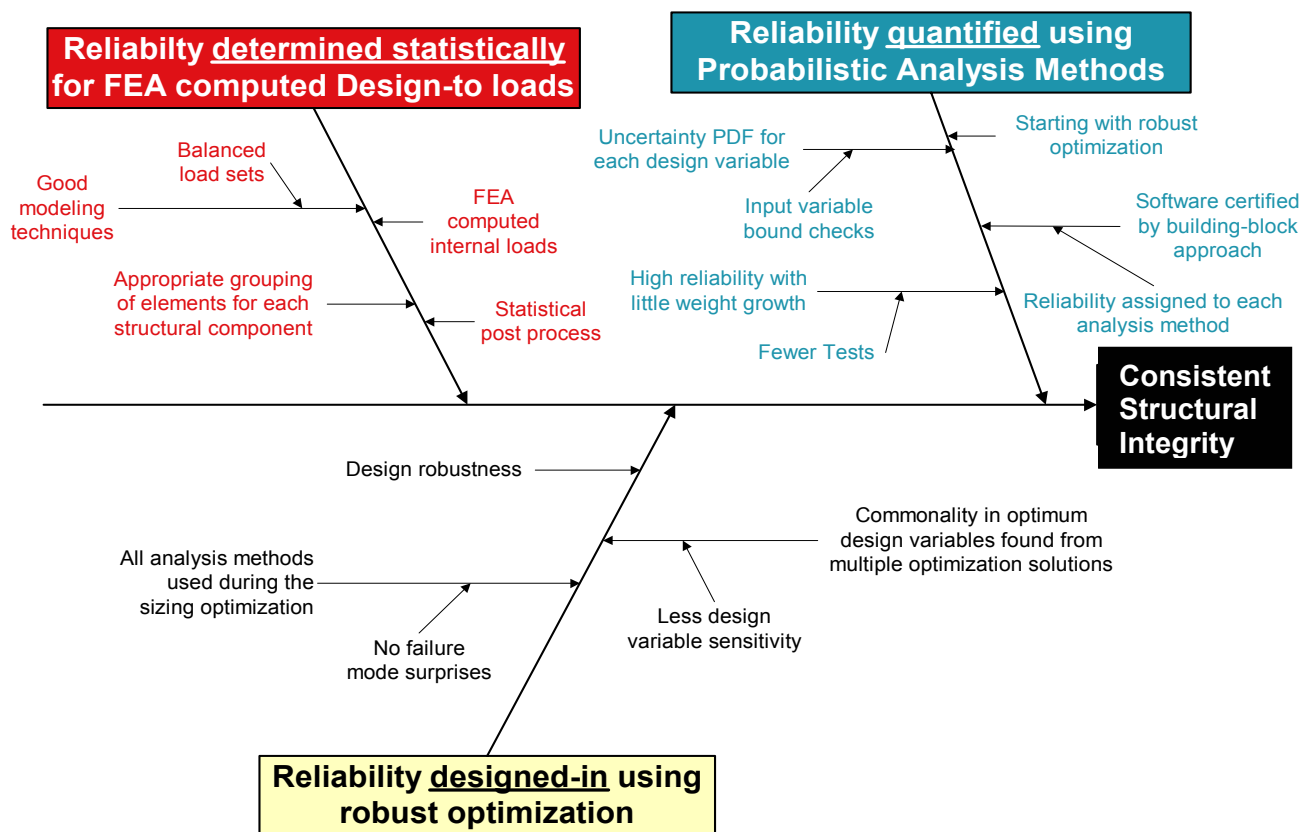


Fig. 5, Cause and effect of using building-block, test data correlated analyses early in design. An important concept of this process is consistent structural integrity starts with design-by-analysis, where reliability is designed-in, and not attempted to be analyzed-in.

3 Use two correlation factors for each failure mode to analyze to the same level of reliability

Test data can be presented in the form of an histogram, Fig. 6, where the height of the vertical bars quantify the frequency of occurrence of test scatter. This histogram is normalized by the **mean** of the test data collection. The horizontal distance of a vertical bar from the mean is noted in terms of the statistical standard deviation, σ . Therefore, a normal distribution has the highest frequency near the mean with the left and right halves dropping off into tails forming a “bell shaped curve.” Such a curve is also known statistically as a probability density function (PDF). The equation for the graph of a normal distribution is:

$$f(x) = \frac{e^{-(x-\mu)^2/(2\sigma^2)}}{\sigma\sqrt{2\pi}} \quad (9.1)$$

where the equation is defined with two inputs, the mean (μ) and the standard deviation, (σ). This equation is used by HyperSizer to superimpose the curve on top of interactive histogram plots that follow. The benefit of representing test results as a histogram, or PDF, is that it provides a universal way to compare the relative accuracies of different failure analyses and associated test results that are graphed using various parameters.

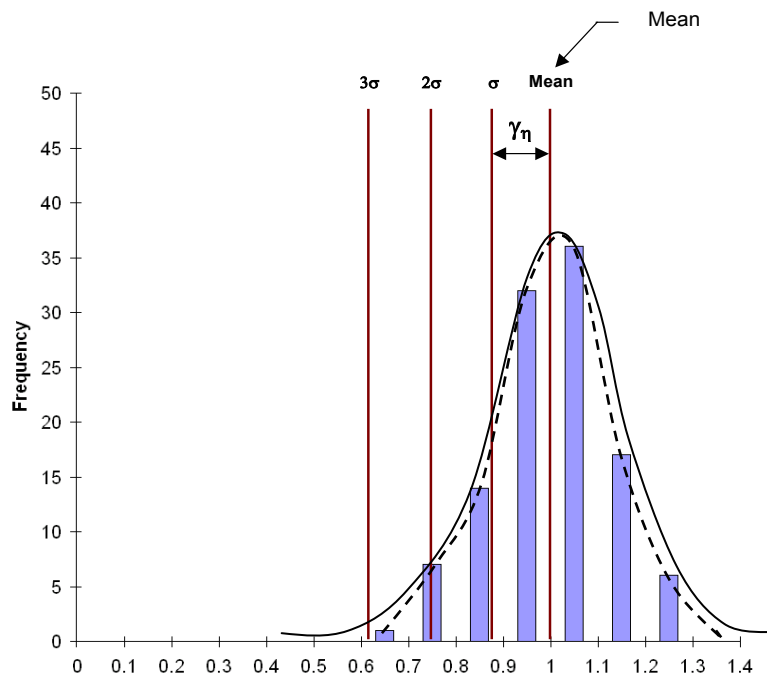


Fig. 6, The frequency of failure from test data, illustrated as a histogram with a statistical normal distribution (dotted curve on top of vertical bars) used to quantify load carrying confidence. The solid curve represents a statistical PDF. The histogram is normalized to the mean (average test result).

A PDF signature derived from test data can be used for accurate prediction of mean (μ) failure load, and choosing the level of risk. This is accomplished with two factors. The first factor mentioned above, γ_μ (abbreviated to μ) for analysis uncertainties is used to calibrate theoretical solutions to typical measured test values. The calibration is usually a reduction of the theoretical as indicated by the arrow moving to the left. The second factor, coefficient of experimental failure load variation, γ_η (abbreviated to η) for

specific failure mode test data scatter repeatability is a measure of the variance (statistical deviation) of the test results. The coefficient of variation, η , is defined as

$$\eta = \frac{\sigma}{\mu}$$

which is a normalized standard deviation. As shown in Fig. 6, the theoretical value (red line) can be scaled by γ_{μ} to establish a **predicted** failure load (blue dashed line), then the user selects a desired level of reliability. The “K” value, from Table 4, represents a specific reliability percentage (i.e. 99.9%) and is used to scale γ_{η} , the coefficient of experimental failure load variation to define an appropriate design-to allowable load (green line). Thus, a specific PDF signature for a given structure and loading type permits more reliable prediction of both expected failure load and allowable load.

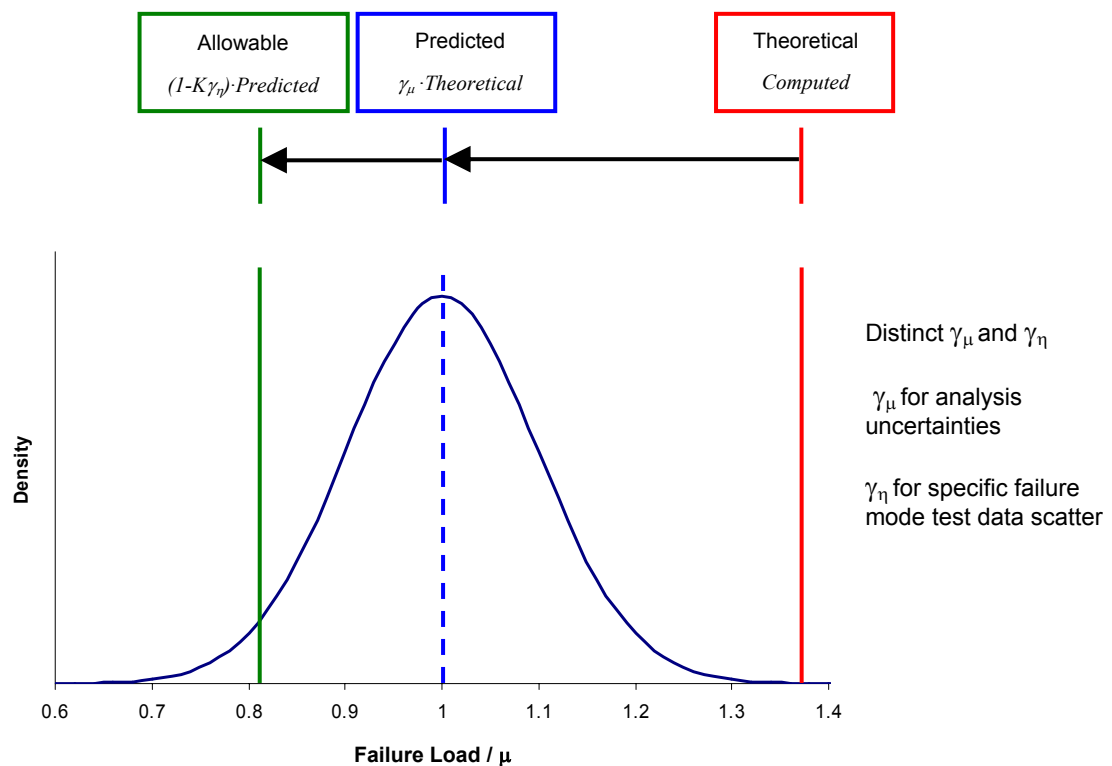


Fig. 6, Application of the probability density function (PDF) for determining desired reliability (allowable load).

There are many specific benefits derived from implementing two correlation factors per failure mode.

- Each failure mode, after individually being correlated to test data, can now be adjusted “on-the-fly” to provide across the board consistent reliability and safety
- Predicted failure load can be distinguished from design allowable load at any given time and made available to the engineering community at large
- The PDF is a universal way to be able to represent all failure mode test correlations
- Comparison to test data is widely available or known by the practicing engineer
- As more data becomes available, there is a readily available means to reevaluate correlations and to assign risk appropriately to meet missions and customers preferences

4 An Example Failure Analysis represented with correlation factors

4.1 WWFE Case 1 with 19 test data

A typical failure envelope for a composite material has four quadrants representing the four possibilities of compression-tension biaxial loading. As a way of introduction, however, we start with Case 1 of the WWFE that only shows two quadrants of the failure envelope - meaning no distinction between positive/negative shear. The calculated failure envelopes generated for that material system and loading is illustrated in Fig. 7, along with test data shown as blue circles. The discrepancy between the test data and the failure envelopes shows the analysis inaccuracies of many leading composite failure theories. We see that the Max Strain and Max Stress failure theories do not appear to be capturing the measured biaxial loading strength behavior. Both Tsai-Hahn and LaRC03 appear to do quite well, particularly in the first

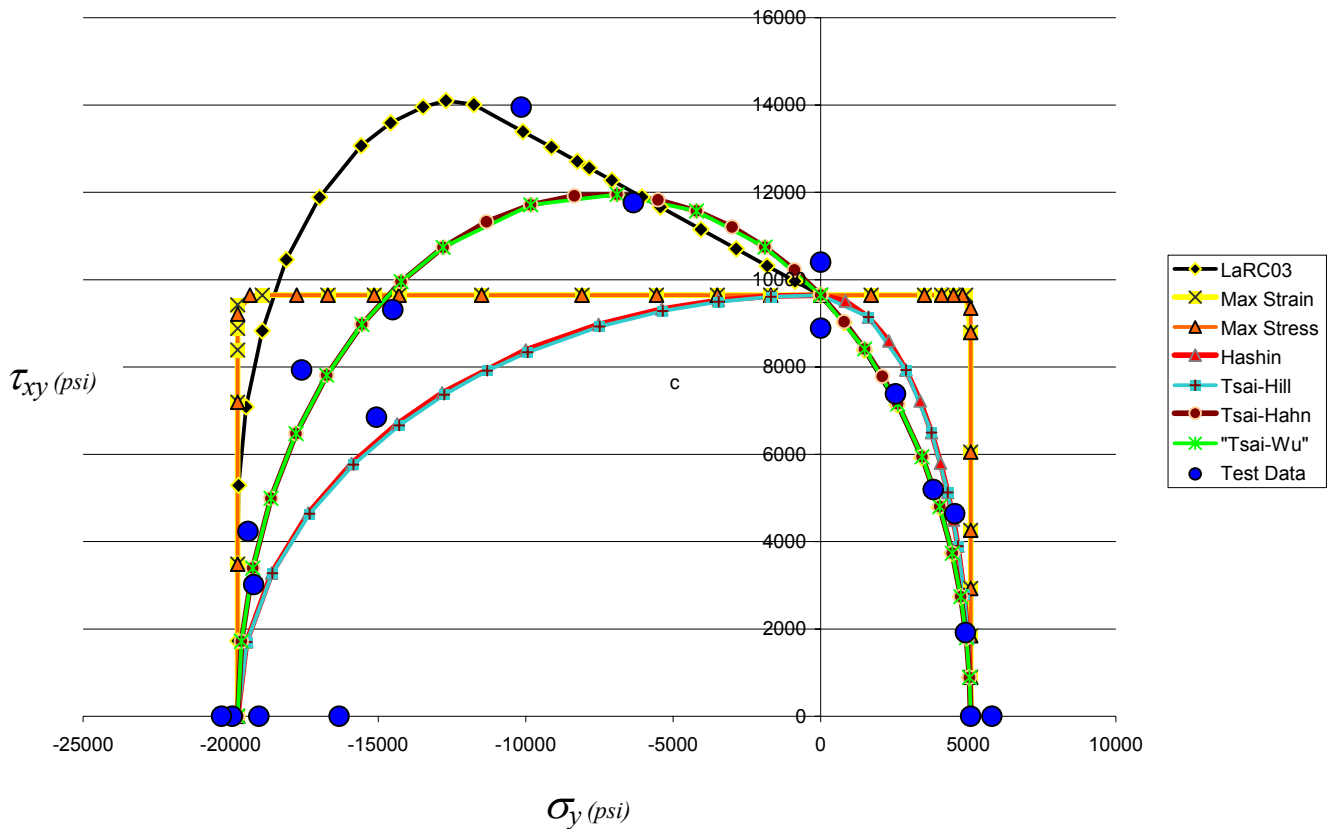


Fig. 7, HyperSizer generated failure envelopes for WWFE Case 1, biaxial σ_y - τ_{xy} of 0° E-glass/LY556 lamina. 19 Test data shown as filled blue circles. These plots use unidirectional strengths based on test results.

quadrant of tension transverse stress combined with in-plane shear stress. LaRC03 failure theory seems to be tracking well an apparent linear relationship in the compressive/in-plane shear quadrant. However, by doing so, it appears to be overshooting failures that are best captured with Tsai-Hahn interaction criteria. However the one data point not being predicted by Tsai-Hahn is captured by LaRC03.

While some criteria match test data better than others, all failure theories exhibit inaccuracies, as illustrated by their calculated failure envelopes. Even if there was a perfect criterion, there always exists natural scatter in observed strengths. Referring back to Figs 2 and 7, as indicated with the blue filled circles, there exist large variations in test measured strengths for pristine laminates. All of the reported test cases of WWFE and those collected by the authors show a great amount of test data scatter in

measured strengths. It is for this reason that the CF approach provides significant benefit to establishing consistent structural integrity and the means to move toward more consistent structural integrity.

Test data entered, and histograms and PDFs generated

Fig. 8 and Fig. 9 show histograms for the 19 test values of WWFE Case 1. Three different failure theories are included: Tsai-Hahn, LaRC03, and Max Strain since it is the most frequently used in industry. Tsai-Hahn and LaRC03 show the 19 values in one histogram, where as for Max Strain, two histograms are shown: one for the condition where strain 2 (transverse to the fiber) controls and one for the condition where max strain 12 (in-plane shear) controls. For these combinations of stresses, a matrix cracking criteria controls for LaRC03 in all 19 tests.

Failure theories compared for case 1

The four histograms, displayed side-by-side, give a statistical indication of the relative accuracy of the different failure theories. In general we see that Tsai-Hahn and LaRC03 do considerably better than Max Strain. Also note that **Tsai-Hahn** does exceptionally well for Case 1, as it also did for the entire collection of test data. Again, its histogram illustrates the ratio of failure load to failure prediction = **1.012** which is very close to 1.0 and its standard deviation is small ($1.012 - 0.933 = \mathbf{0.079}$) meaning the test data is relatively tight without much scatter. Each dashed vertical bar, starting from left to right represents 3σ , 2σ , and 1σ standard deviations. In contrast to the accuracy of Tsai-Hahn, Max Strain is less accurate. For instance, **Max Strain 12** shows a ratio of failure load to failure prediction = **1.072** which is not that bad, however more importantly, its standard deviation is quite large ($1.072 - 0.829 = \mathbf{0.243}$). This will cause this failure theory's theoretical prediction to be heavily knocked down to achieve equal reliability as other failure theories. Finally, since the ratio of failure load to failure prediction, and standard deviation are slightly smaller for Tsai-Hahn, the histograms quantify what is observed in the graphical failure envelopes of Fig. 7, and that is it matches test data slightly better than LaRC03.

Two step process for defining correlations factors

After statistically quantifying analysis inaccuracy and scatter in measured tests, the next step is to establish proper CFs for a particular correlation category. The entire process is performed in two steps. The first step is to collect test data and make comparisons directly between theoretical and test data. In fact, Fig. 8 and Fig. 9 are histograms of this first step. They are untouched theoretical failure predictions against experimentally measured failure loads.

The second step is to define the CFs and then rerun HyperSizer (using the new reliability analysis) for all the components that comprise the 19 test data points. The CFs are established by using the inaccuracy of the theoretical and standard deviation of the test scatter. Using max strain 2 as an example, from Fig. 9 we see that $T=P=0.9422$. The horizontal axis (failure load/HyperSizer predicted) means that HyperSizer is theoretically over predicting failure. We need to knockdown the theoretical by 0.9422. This value is placed into the user input box for μ , Fig. 11. The CF η is entered into the user input box as well. η is calculated as:

$$\eta = \frac{\sigma}{\mu} = \frac{(0.9422 - 0.616)}{3} \left(\frac{1}{0.9422} \right) = 0.115$$

Fig. 10 and Fig. 11 are histograms made after the second step. They show us how well HyperSizer is now predicting average failure. After running HyperSizer with the CFs for the 19 tests, the histograms of Figs. 10 and 11 should show $P=1.0$, or very close due to round off. A $P=1.0$ means that we can now predict average failure load. Fig. 11 for Max Strain 2 now shows theoretical to be 1.061 higher than the calibrated predicted failure load ($T=1.061=1/0.942$). Since this is one material system, the material characterization and calibration of correlation factors is based on in-situ properties from the tests. One of the more important in-situ data is for the shear allowable, F_{su} . These issues are covered in detail in [9, Volume III].

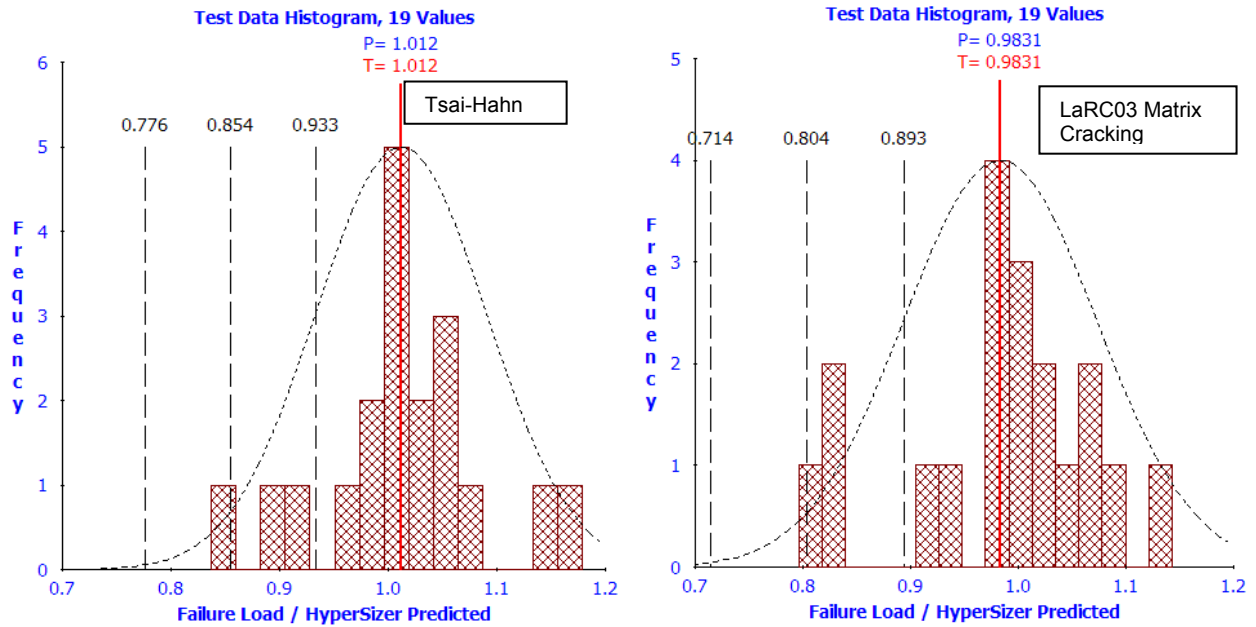


Fig. 8, For WWFE Case 1, biaxial σ_y - τ_{xy} failure envelopes of 0° E-glass/LY556 lamina. Composite Failure Theories: Tsai-Hahn on the left, LaRC03 Matrix Cracking on the right.

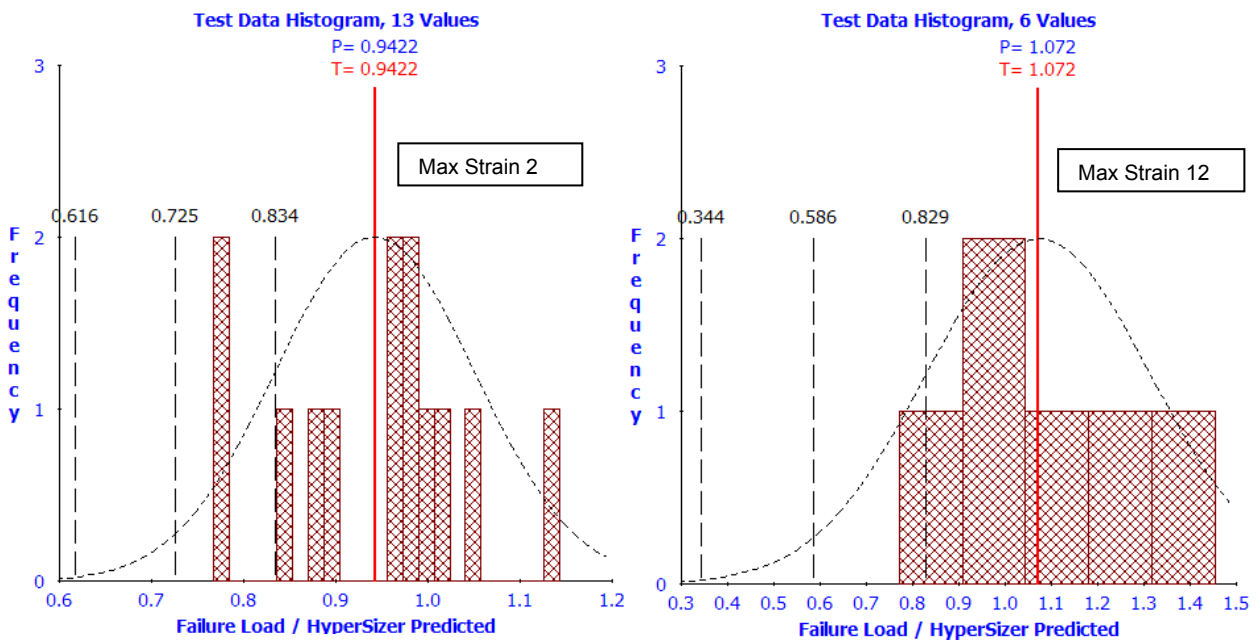


Fig. 9, For WWFE Case 1, biaxial σ_y - τ_{xy} failure envelopes. Max Strain Failure Theory: Max strain 2 direction on the left, Max strain 12 direction on the right.

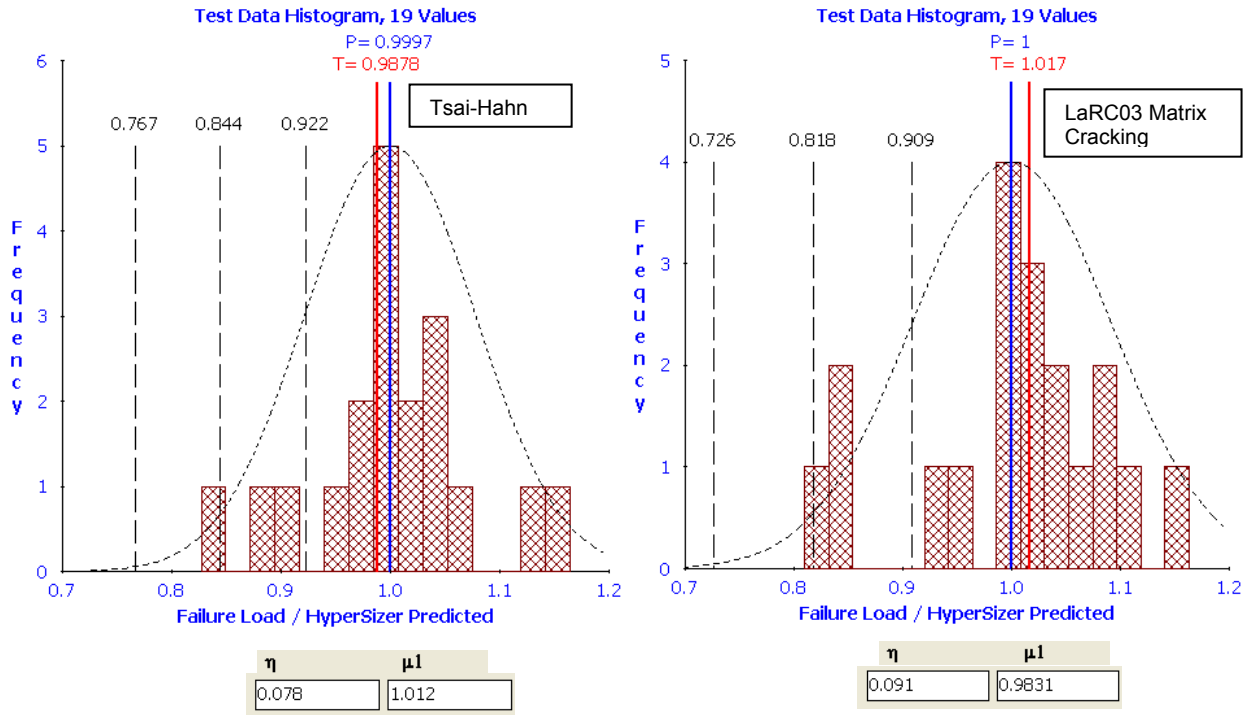


Fig. 10, After applying correlation factors for WWFE Case 1, biaxial σ_y - τ_{xy} failure envelopes of 0° E-glass/LY556 lamina. Tsai-Hahn on the left, LaRC03 Matrix Cracking on the right.

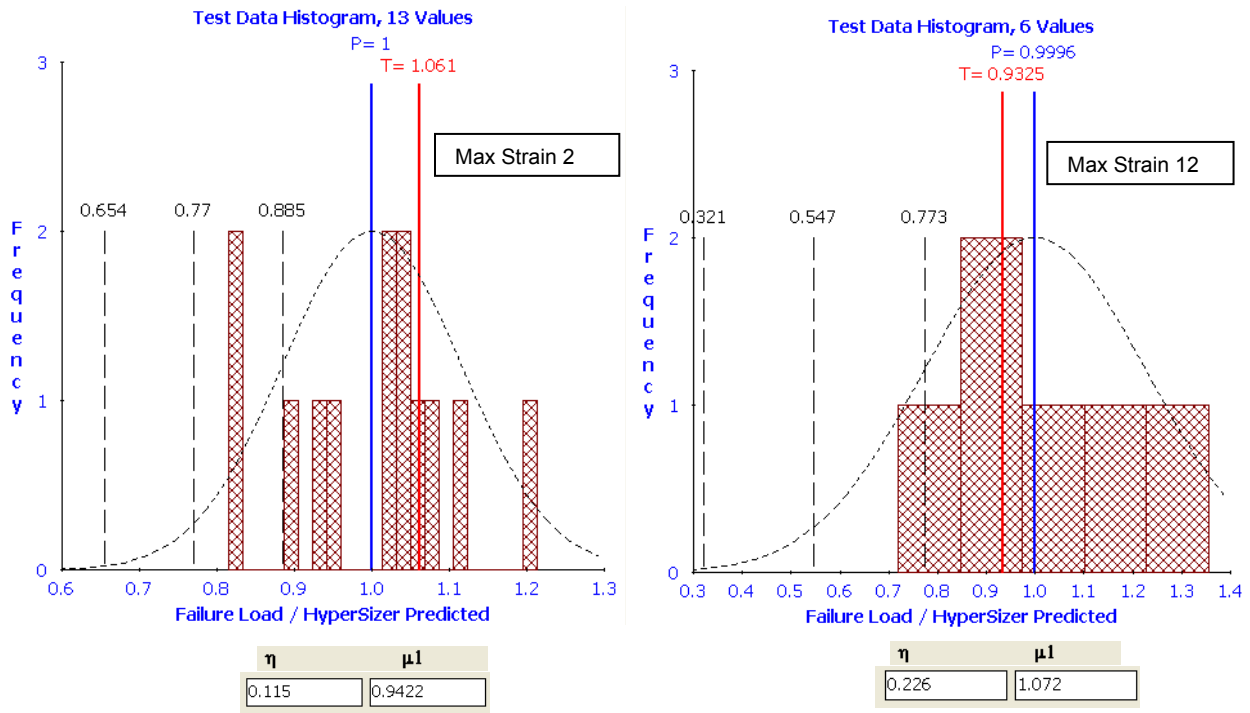


Fig. 11, After applying correlation factors for WWFE Case 1, biaxial σ_y - τ_{xy} failure envelopes. Max Strain Failure Theory: Max strain 2 direction on the left, Max strain 12 direction on the right.

4.2 As an example, actual Tsai-Hahn correlations to 130 tests

Above we described the process for inputting test data and displaying it as a histogram. Here we continue discussion of that process by giving more detail into the source of the data and by showing the final histogram generated after running HyperSizer on all 130 applicable tests with the Tsai-Hahn specific CFs.

Included in the 130 test correlations for composite laminate strength are all of the unidirectional and $[\pm\theta]$ failure envelope test cases (cases 1, 2, and 3) from the World Wide Failure Exercises (WWFE), two additional failure envelope unidirectional cases (cases 8 and 9) from other publications, and case 10, a $\pm\theta$ layup case of AS4/3502 material reported by [10,11]. Failure of a laminate comprised of unidirectional or $[\pm\theta]$ layups occurs at first ply failure. Strength allowables presented here are based on damage initiation and not ultimate laminate strength which can be predicted using progressive failure techniques. The cases not included from WWFE involve progressive failure. Correlations to these progressive failure test data will come later. As a final point, the composite strengths are for pristine laminates, that is without damage. For an airframe design, damage tolerance and survivability allowables would be established and used as additional limiting strength requirements.

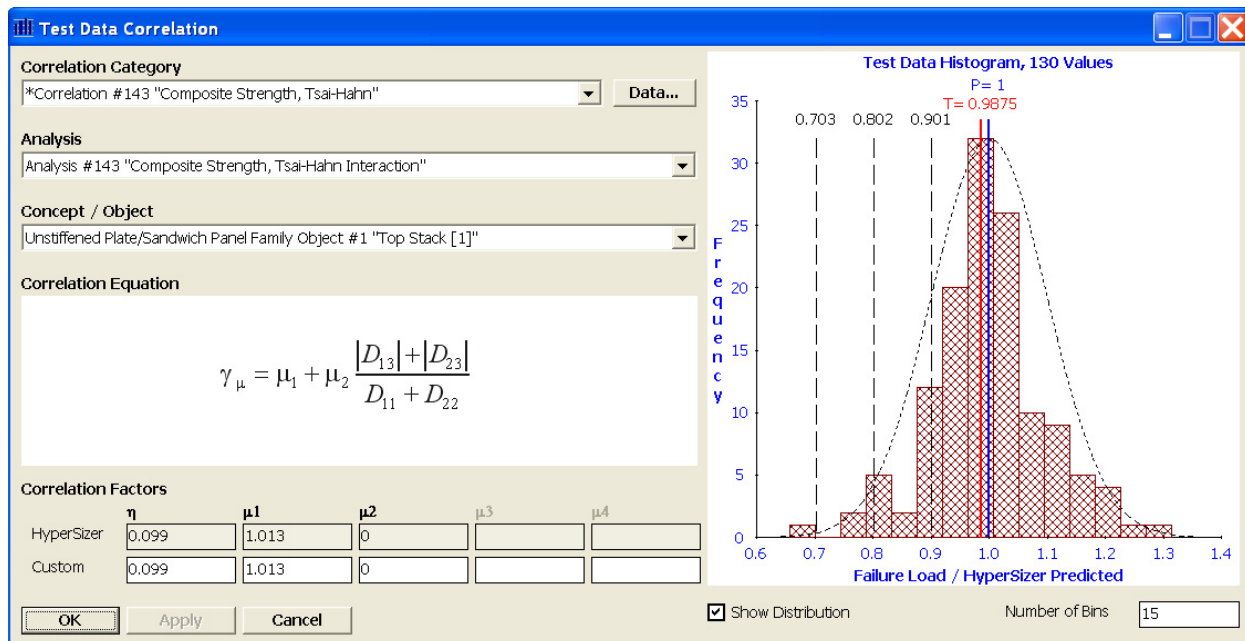


Fig. 12, A HyperSizer representative histogram plot of 130 test data points, before correlation. These are untouched, theoretical comparisons to tests. Tsai-Hahn theory matches test very well.

Shown in Fig. 12 is a histogram generated by HyperSizer that plots the statistical distribution of the 130 test failures normalized by predicted failures. The histogram is used to determine the proper correlation factors (CFs) for a given correlation category: in this case "Composite Strength, Tsai-Hahn." The height of the vertical bars indicates frequency of occurrence and to some degree a normal distribution. More importantly, the histogram illustrates the ratio of failure load to failure prediction is very close to 1.0 for the Tsai-Hahn failure theory and the standard deviation is small meaning the data is relatively tight without much scatter.

5 Two correlation factor values established from test for each failure analysis mode

The previous sections introduced concepts that form the basis of test data driven reliability. This section defines the actual PDF's and CF's defined from all available test data for the following general failure

modes: composite material strength, composite panel buckling, composite bonded linear and non-linear joint strength, and honeycomb sandwich composite facesheet wrinkling.

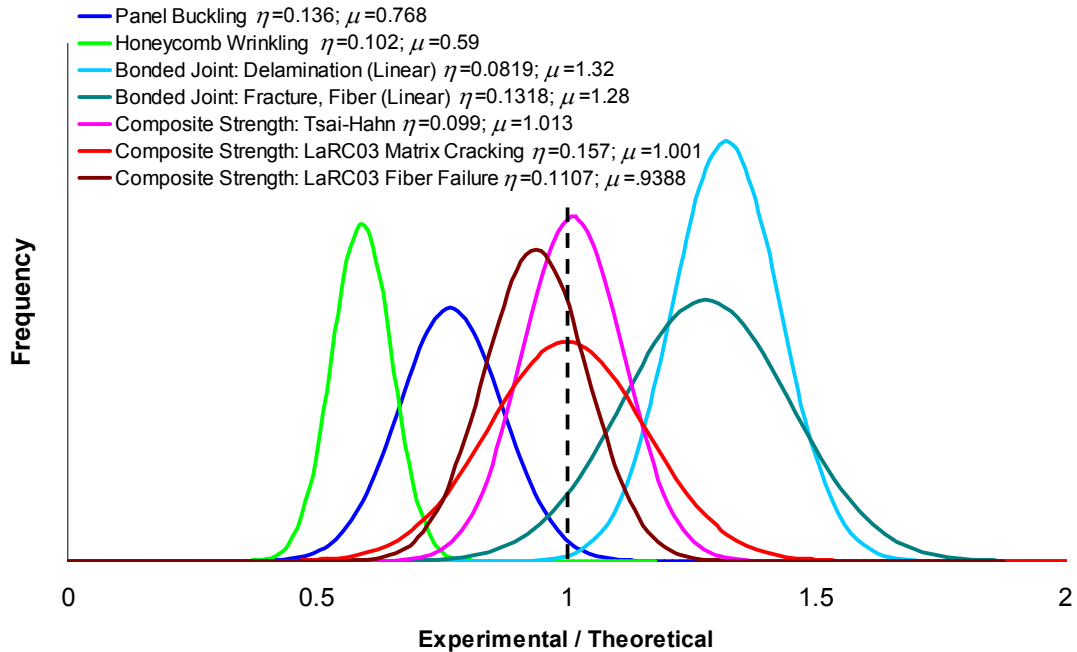


Fig. 13, Normalizing to theoretical. The relative inaccuracies of the theoretical analysis and their relative scatter from experimental measurements. Wrinkling has the worst inaccuracy and Tsai-Hahn the best accuracy. Tsai-Hahn and surprisingly Bonded Joint Delamination can be more confidently used due to its narrower PDF and therefore will have less knockdown for a given reliability.

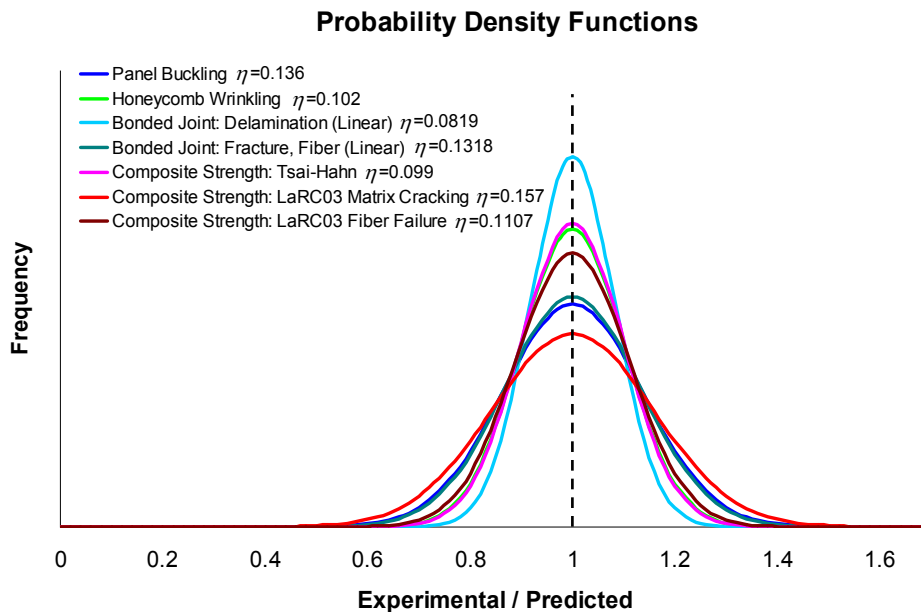


Fig. 14, Normalization to predicted. The PDF signatures of the five different specific failure modes. Only the relative shape (flat vs. narrow) of the PDF curve will change results when using different % reliabilities.

Fig. 13 graphically depicts the PDF curves and their relative inaccuracies and test data scatter normalized by (experiment data/theoretical calculation) which is depicted as a dashed (experimental/theoretical) line. Analysis PDFs that fall left of the dashed line unconservatively predict failure loads higher than experiments. These methods include panel buckling (blue curve) and honeycomb wrinkling (green curve). These theoretical analysis predictions need to be knocked down before using as design allowables. Wrinkling, shown in green has the worst inaccuracy (noted with the smallest μ value) as it is the farthest away from the vertical dashed line. Since the wrinkling PDF is left of the vertical dashed line, it over predicts strength by a ratio of $1/.59 = 1.695$.

Fig. 14 graphically depicts the same PDF curves but normalized this time by (experiment data/predicted) by use of the analysis inaccuracy correlation factor, μ . Once the analysis inaccuracy is accounted, then the natural scatter in failure load is quantified with the correlation factor, η . Failure modes that fall within a tighter, narrower band can be more confidently used with a smaller knockdown to obtain the same given reliability.

For bonded composite joints, there are two primary strength failures: delamination and fracture. For both of these failures, two types of analyses are performed: linear and non-linear, Fig 15.

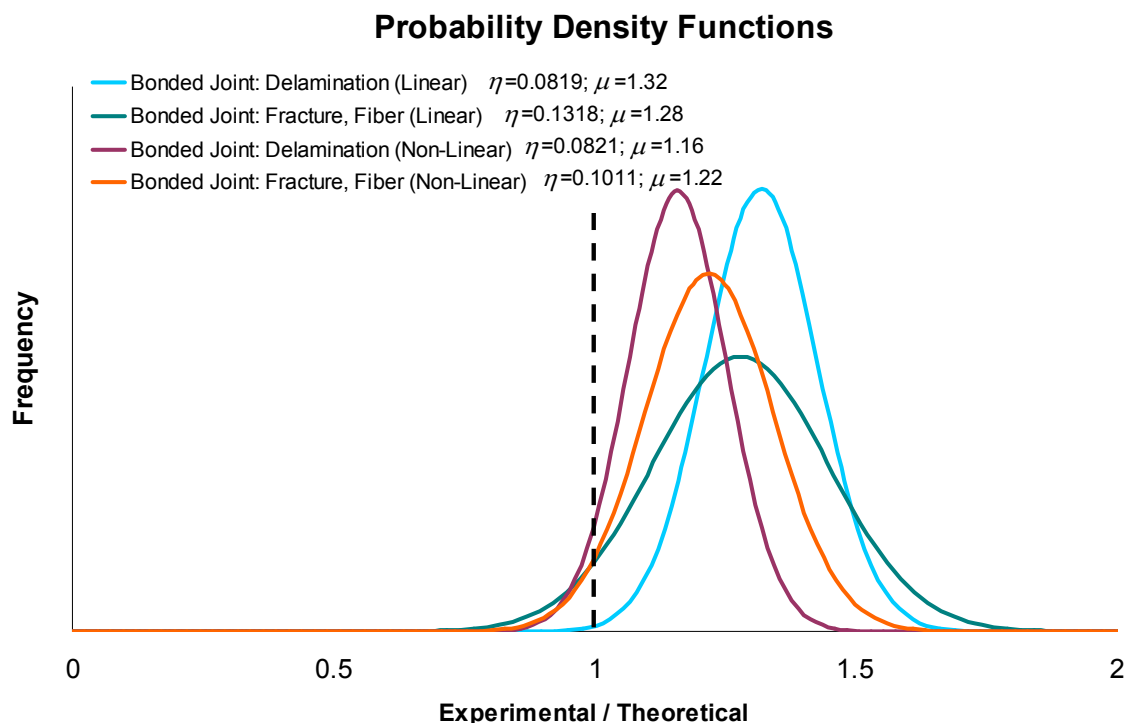


Fig. 15, Application of the (PDF) for determining desired reliability for composite bonded joints (allowable load). As expected, the theoretical predictions are more accurate when non-linear analyses are used, as indicated by the PDF's being closer centered to the test mean.

Figs 16 and 17 display all PDFs for all failure analyses that are derived from test data.

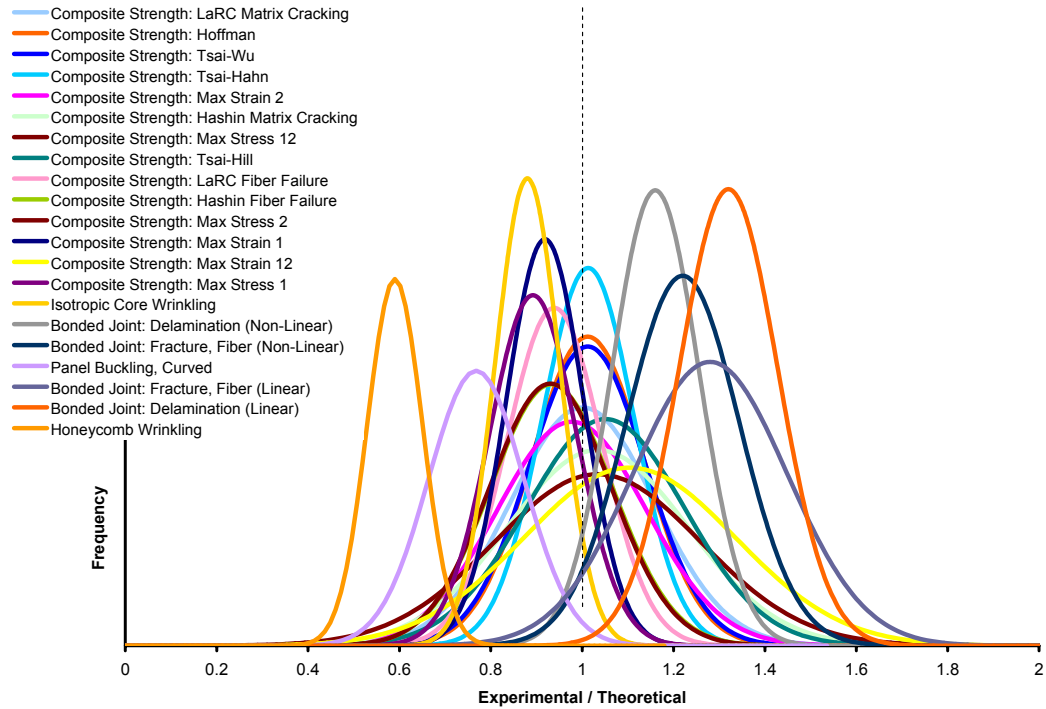


Fig. 16, *HyperSizer* current analysis PDFs that have test data. (normalized to predicted)

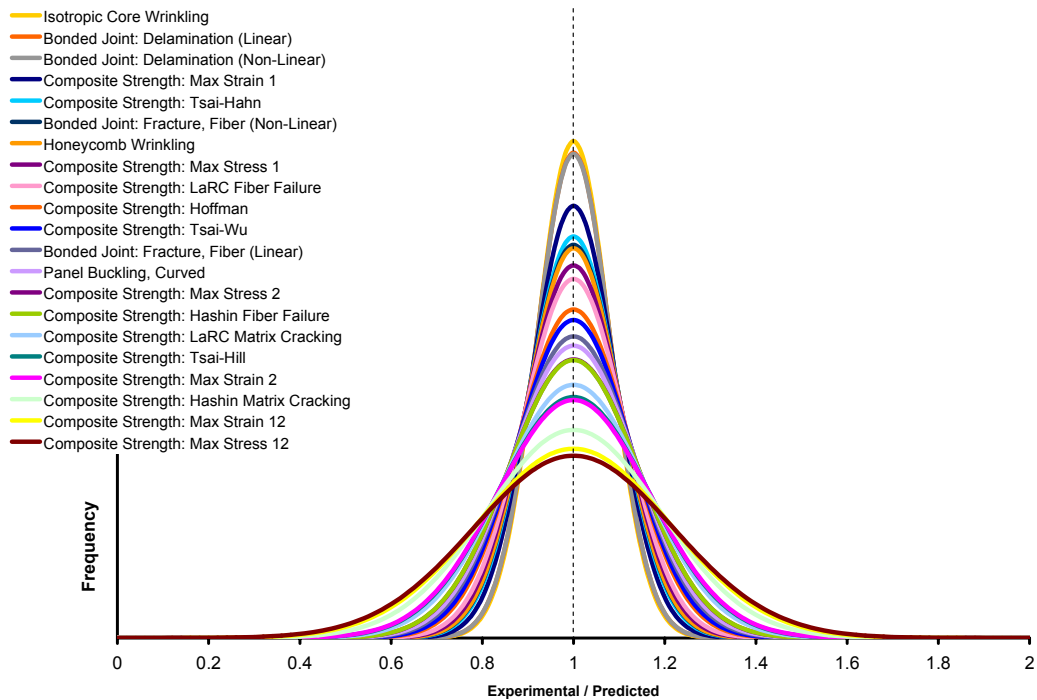


Fig. 17, *HyperSizer* current analysis PDFs that have test data. (normalized to theoretical)

6 Airframe Preliminary Design Example; Air Force Long Range Strike Aircraft (LRSA)

In this example of an actual preliminary design performed in 2003, [9], the relative difference in predicted weights and controlling failure modes is quantified between two approaches: the traditional zero-margin approach, and the % reliability approach. Thus this full vehicle example is presented to bridge the traditional approach to the new. The traditional approach is based on a limit load factor of 1.0, an ultimate load factor of 1.5, and with all of the failure modes being analyzed deterministically to the same 0.0 margin-of-safety. To be considered passing, the new approach assigns, in effect, a different required margin-of-safety for each failure mode. Each failure mode's required margin is based on achieving the same % reliability against failure. In this way, consistency is achieved in that all failure modes are targeted to the same chosen level of structural integrity.

First, a study is presented that shows the weight increase as the chosen % reliability goes up from 1σ (84.1%), 2σ (97.7%), 3σ (99.9%). Second, a study is presented that identifies areas of the vehicle sized the traditional zero-margin method that results in an unexpected and unacceptable low reliability. In this study, it is also shown that the traditional zero-margin approach sizes the vehicle weight to be 11% heavier than the reliability approach using 2σ (97.7%), and 8% heavier at 99.0%.

6.1 An Automated Analysis and Sizing Tool

The HyperSizer automated structural analysis and sizing optimization commercial software was used to perform the analysis and preliminary design. There are four primary steps followed in this process.

1. Couple to FEA for Internal Loads
2. Generate Well Defined Equivalent Stiffness Terms for FEM Update
3. Perform Traditional Closed Form and Modern Numerical Analyses
4. Size for Optimum Light Weight Structure Based on Positive Margins for all Failure Modes

6.1.1 Failure Analyses Performed

For this airframe example, the four failure modes are used: 1) composite stiffened and sandwich panel buckling, 2) honeycomb sandwich composite facesheet wrinkling, and 3) composite laminate strength, and 4) composite bonded joint strength. For composite strength, three failure criteria are toggled on: Tsai-Hahn, LaRC03 fiber failure, and LaRC03 matrix cracking. Two CFs per each analyses are used, Table 1.

Table 1, Correlation Factors per Analysis

Failure mode	η	μ_1	μ_2	μ_3	μ
<i>Cylindrical Panel Buckling</i>	.136	.3956	-.1144	.8751	.768*
<i>Wrinkling</i>	.102	.59		1,000,000	
<i>Tsai-Hahn</i>	.099	1.013			
<i>LaRC03 Fiber Failure</i>	.1107	.9388			
<i>LaRC03 Matrix Cracking</i>	.157	1.001			
<i>Bonded Joint Delamination, Linear</i>	0.0819	1.32			
<i>Bonded Joint Fracture, Linear</i>	0.132	1.28			

* an average value

6.2 Vehicle Description

The vehicle chosen as an example application is a Mach 3.5 long range strike aircraft designed by LM Aero in Fort Worth and sponsored by Air Force Research Lab (AFRL) Air Vehicles Directorate. A subset of the FEM, defined as an assembly, consisting of external surface panels is analyzed. This assembly includes 4 groups and 84 components. For these groups, honeycomb sandwich panels and thick laminate

skins are used. The AS4/3502 graphite epoxy facesheets have 42 different layups to choose from and the Nomex honeycomb core considers 27 different thicknesses ranging from .05” to 2”. The optimization used AS4/3502 graphite epoxy (typical properties) with 29 different layups. Stiffened panels along with bonded composite joint analysis are also included.

6.2.1 Load Cases

Seven different load cases are defined, as shown in Table 2. For each external load case, the airframe loads were balanced with the integrated flight pressures equal to and opposite to the resulting loads from inertial accelerations of its mass. Internal fuel pressures were applied on the relatively flat panels and their resulting secondary panel bending moments, out-of-plane shears, and deflection were computed by HyperSizer offline from FEA. These secondary panel loads are then superimposed with the global FEA computed internal running loads. Heating was mapped to the exterior skin with 1D thermal analysis performed to produce structural temperatures resulting in proper temperature dependent material properties and thermally induced stresses.

Table 2, Vehicle Load Cases

Load Set	Description
#1	3G Begin Cruise
#2	3G Before Weapon Drop
#3	3G End Cruise
#4	2G Begin Cruise
#5	-1G TOGW
#6	Taxi Bump
#7	Vertical Tail Loads

6.2.2 FEM

A coarse NASTRAN FEM was constructed with shell and beam elements: CQUAD4, CSHEAR, and CBAR. Of particular modeling significance is only one element spans the internal substructure.

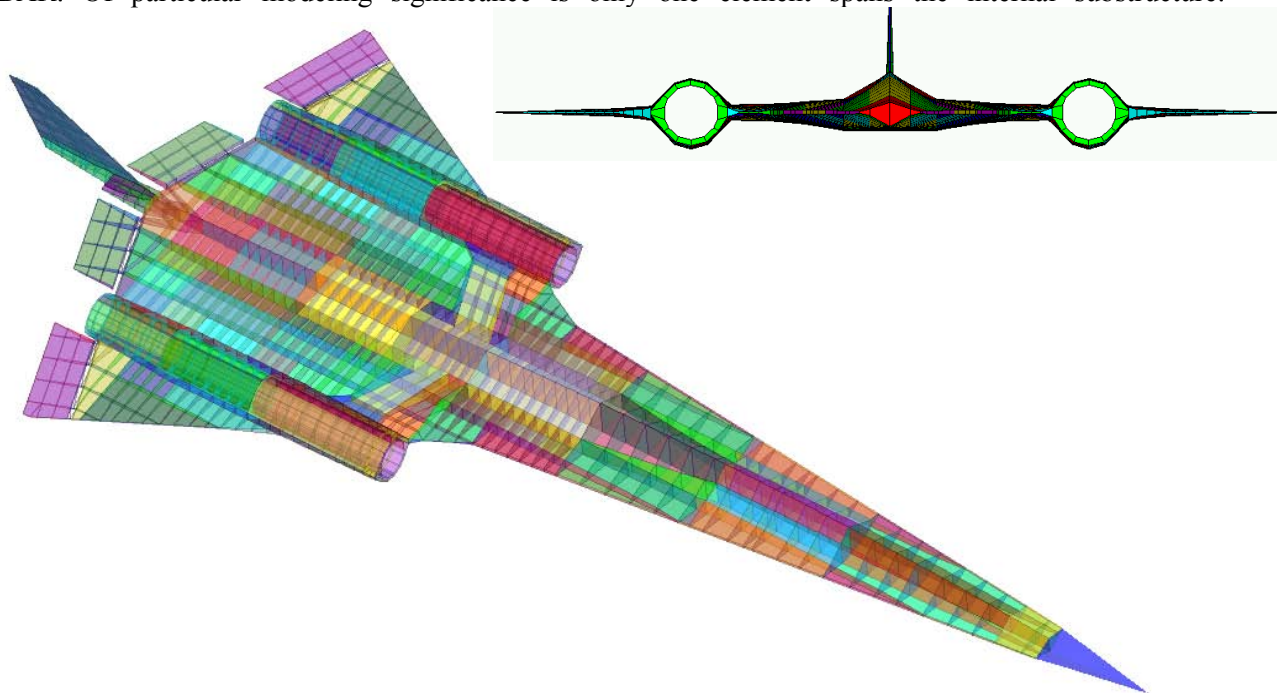


Fig. 18, HyperSizer used for weight estimation, analysis and sizing trade studies of external skin panel structure and internal rib and spar substructure displayed in this transparent view of the AFRL Long Range Strike (LRS).

6.3 Comparison to 85.1%, 97.7% and 99.86% Reliability Sizing

Fig. 19 illustrates an interesting result. As the reliability criteria is increased, the controlling failure modes change. Failure modes which have the highest observed scatter in test results (a higher statistical standard deviation) will control more as reliability is increased. Therefore the relative width of the PDF as shown in Fig. 14, and quantified with the CF γ_η (also noted simply as η), has a larger affect for higher reliabilities because of their greater uncertainty (less confidence). As shown in Table 1, wrinkling, Tsai Hahn, and LaRC03 fiber failure criteria all have η values close to 0.1. Panel buckling has a $\eta = 0.136$ and LaRC03 matrix cracking composite strength has a $\eta = 0.157$. Therefore, as depicted in Fig. 19, as the reliability increases, the controlling failure mode goes toward panel buckling (blue) and LaRC03 matrix cracking (red) which have higher η factors and away from honeycomb facesheet wrinkling (green), Tsai-Hahn interaction (yellow), and LaRC03 fiber breakage (brown) failures.

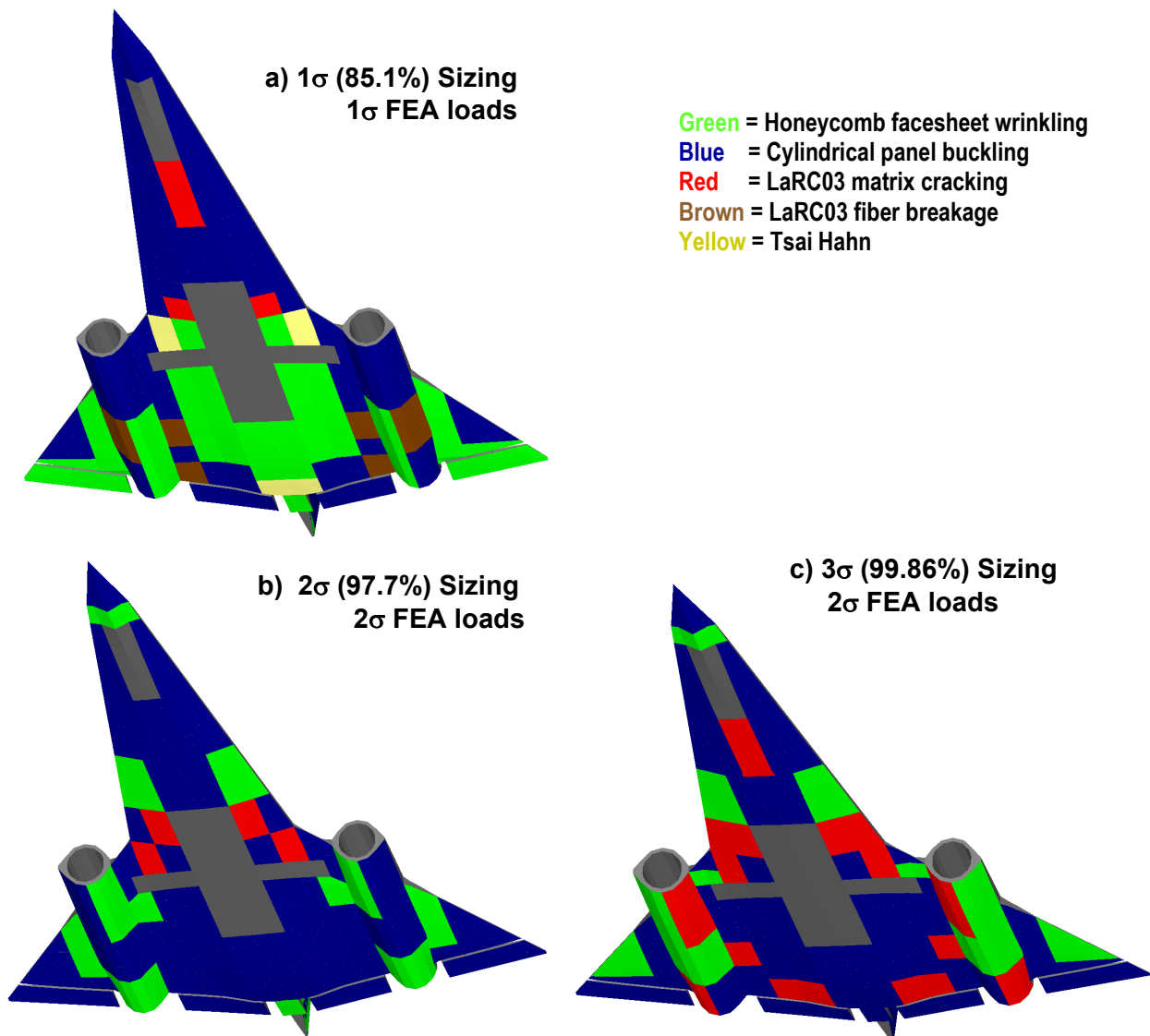


Fig. 19, Effect of varying reliability on controlling failure mode. As the specified reliability increases, the controlling failure modes change. At the lowest reliability (1σ or 85.1%), all activated failure modes are controlling some location of the vehicle, with most of the bottom surface controlled by honeycomb wrinkling. The gray areas represent structure not sized in this study such as the main landing gear doors.

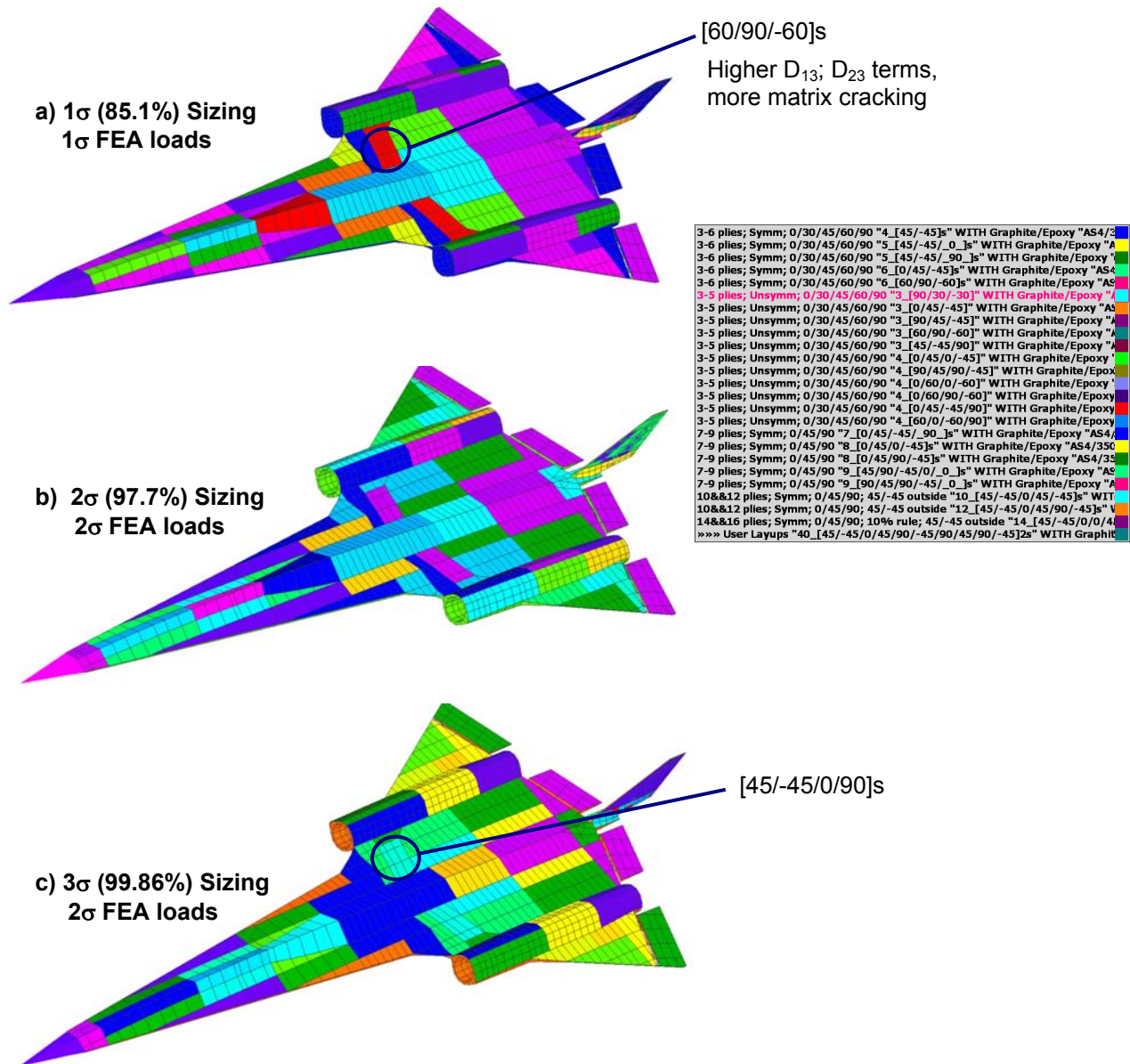


Fig. 20, Effect of varying reliability on controlling optimum layup. As the specified reliability increases, the best suited layup varies as indicated by the change in color pattern. Certain layups for a given load of a vehicle location are more efficient and selected by HyperSizer as optimum. However some of those layups may be less confidently used because of their measured variability in strength and as a result not optimum at higher reliabilities.

The test data driven reliability is integrated into the fundamental HyperSizer strength analysis, and as such is automatically influencing the sizing optimizations. Results for several different reliability percentages show not only the weight going up, but also another interesting transition in the optimum layup design, Fig. 20. As the optimization attempts to use layups that are dominated by failure modes that exhibit more test data scatter, say for material matrix cracking strength, they will effectively be penalized more and not chosen at higher reliabilities. Therefore, for different required reliabilities the optimization finds different materials and design variables. Each unique combination of variables provides different levels of reliability. Fig. 20a shows a [60/90/-60]s is suitable for 85% reliability, but Fig 20c shows [45/-45/0/90]s is selected for 99.9% reliability.

6.4 Comparing Analysis Approaches: Traditional Zero Margin-of-Safety vs. New Test Data Driven Reliability

6.4.1 Comparison of load factors and material allowables.

The traditional zero-margin sizing is based on the author's experience of current industry practice with structural analysis margin-of-safety reporting. Essentially, the key aspects in contrast to the new reliability approach are summarized in Table 3.

Table 3, Contrasting Approaches for the LRS Airframe Analysis.

Issue	Traditional Zero-Margin Analysis	New Reliability Analysis
Load Factor	1.0 limit* 1.5 ultimate**	1.0 limit* only
FEA Computed Design-to Loads	2 Sigma statistical loading method	2 Sigma statistical loading method
Material Allowable	A or B basis "Design-to" from Mil Handbook 5 or 17	"Typical test" properties (average) from Mil Handbook 5 or 17. Two Correlation Factors that dynamically change with layup optimization.
Panel Buckling	Constant knockdown of 0.85 for all panels and laminates	All panels and laminates have two Correlation Factors that dynamically change with panel spans, radius of curvature, and with thickness and layup sequence.
Sandwich Wrinkling	A required MS of 0.695 was used that is equivalent to the test average knockdown of .59 as described in section 4.	All panels and laminates have two Correlation Factors that dynamically change with core thickness and facesheet layup sequence.

* Limit loads are load values that are estimated to occur only once in five vehicle lifetimes.

** 1.5 ultimate loads are limit loads increased by 50%. They have no physical basis.

6.4.2 Panel Buckling

Both sandwich panels and solid "plank" laminates are used in the airframe. The vast majority of the sized assembly is honeycomb sandwich. For the 'stiffened' sandwich panels, the industry practice is to use a constant knockdown factor of anywhere between 0.75 and 0.9 as is recommended in [4]. The authors experience is that a 0.85 knockdown is more frequently used during Preliminary Design. So for the traditional zero MS analysis of the sandwich panels, a constant 0.85 is used, and for the reliability analysis, the knockdown of the sandwich is a dynamic function of the panels core thickness, facesheet layups, panel span lengths, and radius of curvature.

6.4.3 Sandwich Wrinkling

The traditional analysis is not based on theoretically wrinkling allowables, but instead on the same knocked-down allowable (predicted failure loads) as used in the reliability analysis. This provides a more realistic comparison. An average knockdown of 0.59 equals an equivalent required MS = 0.695. Refer to [9, Vol 2, Ch 2] that summarizes the test data collected and derivation for the relevant CFs.

6.4.4 Material Strength

For the traditional analysis, Mil Handbook 17 data was used for the AS4/3502 “B” basis design-to-allowables. The *design-to* allowables were used for the traditional zero margin analysis and the *typical* material properties used with the reliability analysis.

6.5 Process for calculating reliability for traditional analysis

The process used to reveal the reliability of the traditional zero-margin design is: 1) Perform traditional sizing optimization, 2) send that design (optimum variables) to the reliability project, 3) perform a reliability analysis with those optimization variables frozen. This process is defined in five steps.

6.5.1 1st step, size airframe to zero margins

The Long Range Strike preliminary design is based on achieving positive near zero MS for each structural component of the external surface assembly. This was accomplished by finely adjusting each sizing variable’s bounds. Using this resulting design as a basis of comparison, this design was ‘frozen’ and passed to the new reliability analysis. HyperSizer was used to perform both the automated failure analyses and sizing optimization. The sizing process generates candidate designs and computes MS for the many potential failures. If a particular MS analysis was negative, then another candidate design is attempted. This process continues until all vehicle components have positive MS. A goal is to achieve only the amount of margin required. The assumption is that the lightest possible design will have close to zero MS for all failure modes. Therefore, the 1st step is to achieve the lowest obtainable weight (as the comparative benchmark) using the traditional zero-margin approach.

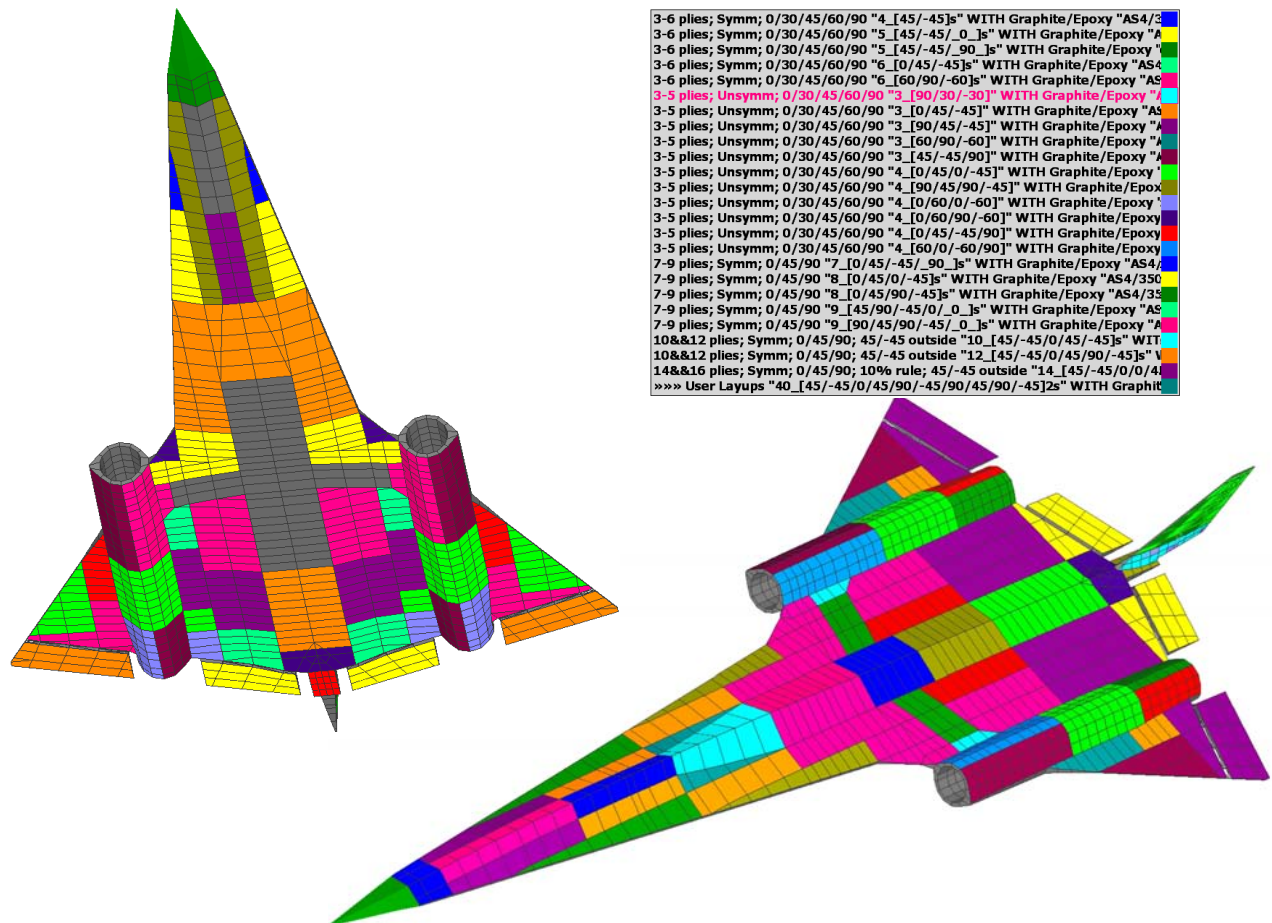


Fig. 21, Optimum layup from the traditional zero-margin sizing. This design is sent to reliability analysis.

6.5.2 2nd step, pass the traditional optimum variables to the reliability analysis

Once the optimum LRS preliminary design has been established, the next step is to pass the state of the design to the reliability analysis. In essence, the sizing variable optimum values are sent to the reliability analysis and the reliability analyses treats them as “frozen”, where no further sizing optimization is performed. Fig. 21 illustrates the optimum layups that are frozen.

6.5.3 3rd step, perform reliability analysis on the traditional design and compute true margins

After the traditional design is passed into the reliability analysis, the next step is to compute true MS. In this definition, true MS are those that are based on specific test data derived CF's. Even though the same variables from the traditional design were used in the reliability analysis, including the same FEA computed internal loads, different MS are established.

6.5.4 4th step, back out reliability for each airframe component

This section presents the reliability of each structural component. Identified are areas of the vehicle sized the traditional way that result in an unexpected and unacceptable low reliability. The margins of the traditional design were consistently near the desired value of zero but were determined by the developed

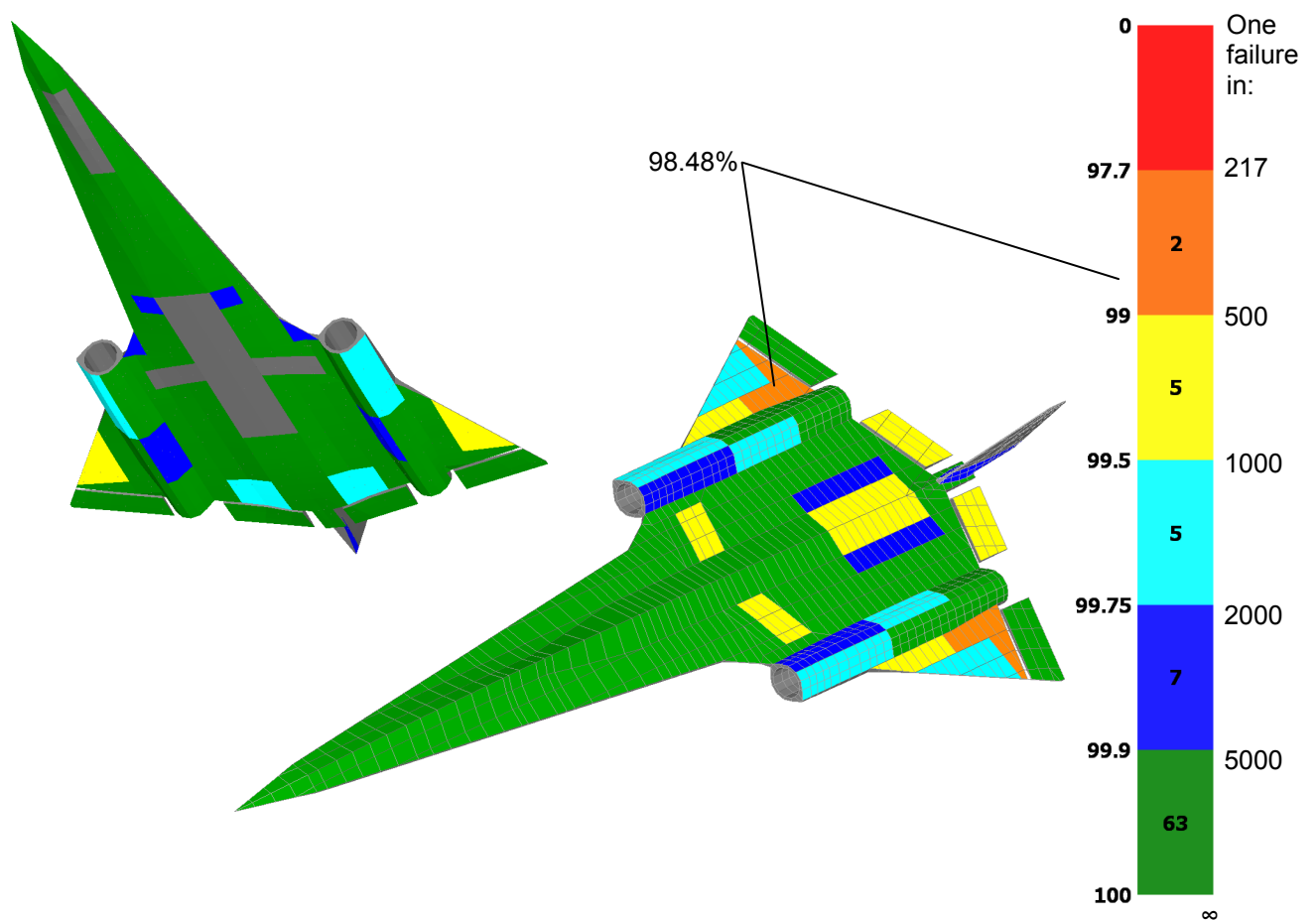


Fig. 22, The traditional zero-margin sizing approach cannot produce consistent structural integrity. The major concern is the areas of the vehicle identified in orange. These two structural components have less than 99% reliability.

reliability analysis to be inconsistent. Fig. 22 identifies the reliability of each structural component to the seven loadcases. The inconsistency of the traditional design is obvious. 65 out of 82 structural components have a reliability > 99.9% causing the weight of the airframe to be heavier than necessary.

Using the lowest margin of any failure mode, for any component, the airframe reliability was backed out of the HyperSizer analysis to equal **98.5%**. This equates to $(1 / (1 - 0.985)) = 66.6$, which implies 1 in 66.6 vehicles will fail due to the design limit loading. However, DLL is statistically predicted to occur once in five (1 in 5) vehicle lifetimes. Therefore, the probability of failure for this approach is 1 in 333, $(5 * 66.6) = 333$. (See Table 4). Based on the few known actual in-service structural failures, this appears to be low. We postulate that the magnitudes of the limit loads are also likely conservative, meaning airframes likely experience limit loads less than predicted by the loads group. Therefore, in-service operation loads using the traditional zero-margin approach likely provides more than 1 in 333 lifetime airframe failures.

As a summary, shown in Fig. 23 are four LRSA images where red color identifies areas of the airframe that have unacceptable safety based on two different lifetime criteria. As the criteria goes from 1 in 1000 failures to 1 in 2000 failures, as expected, more area shows up red.

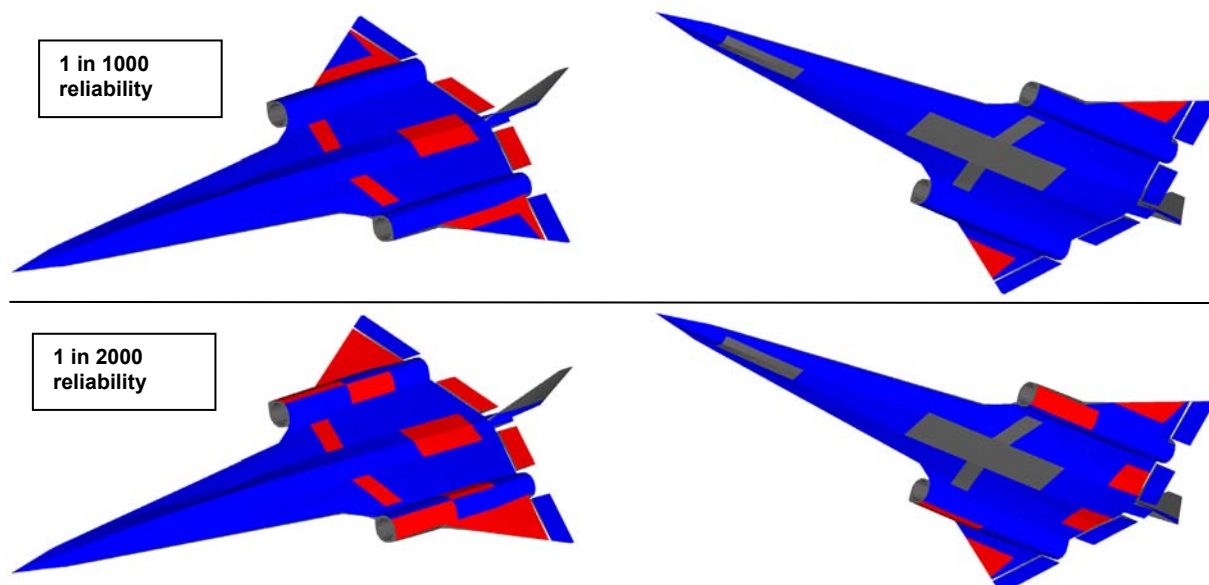


Fig. 23, The traditional zero-margin sizing approach cannot produce consistent structural integrity. The major concern is the areas of the vehicle identified in red. These are panel components that have less than 99.5% (1 in 1000) reliability top images and 99.75% (1 in 2000) reliability bottom images. The left images are the top of the LRS aircraft and the right images are the bottom. Gray color are unsized areas.

6.5.5 5th step, compare controlling failure analyses and load cases

The last step is informational and useful for a more in-depth understanding. Fig. 24 shows how the controlling failure analyses differ between the traditional and reliability analyses. Even though the same variables from the traditional design were used in the reliability analysis, including the same FEA computed internal loads, a different set of controlling failure modes are identified. Note primarily how the composite strength criteria for matrix cracking (an analysis with relatively high uncertainty) controls for the reliability analysis while Tsia-Hahn and fiber breakage (analyses with relatively high confidence) controls for the traditional.

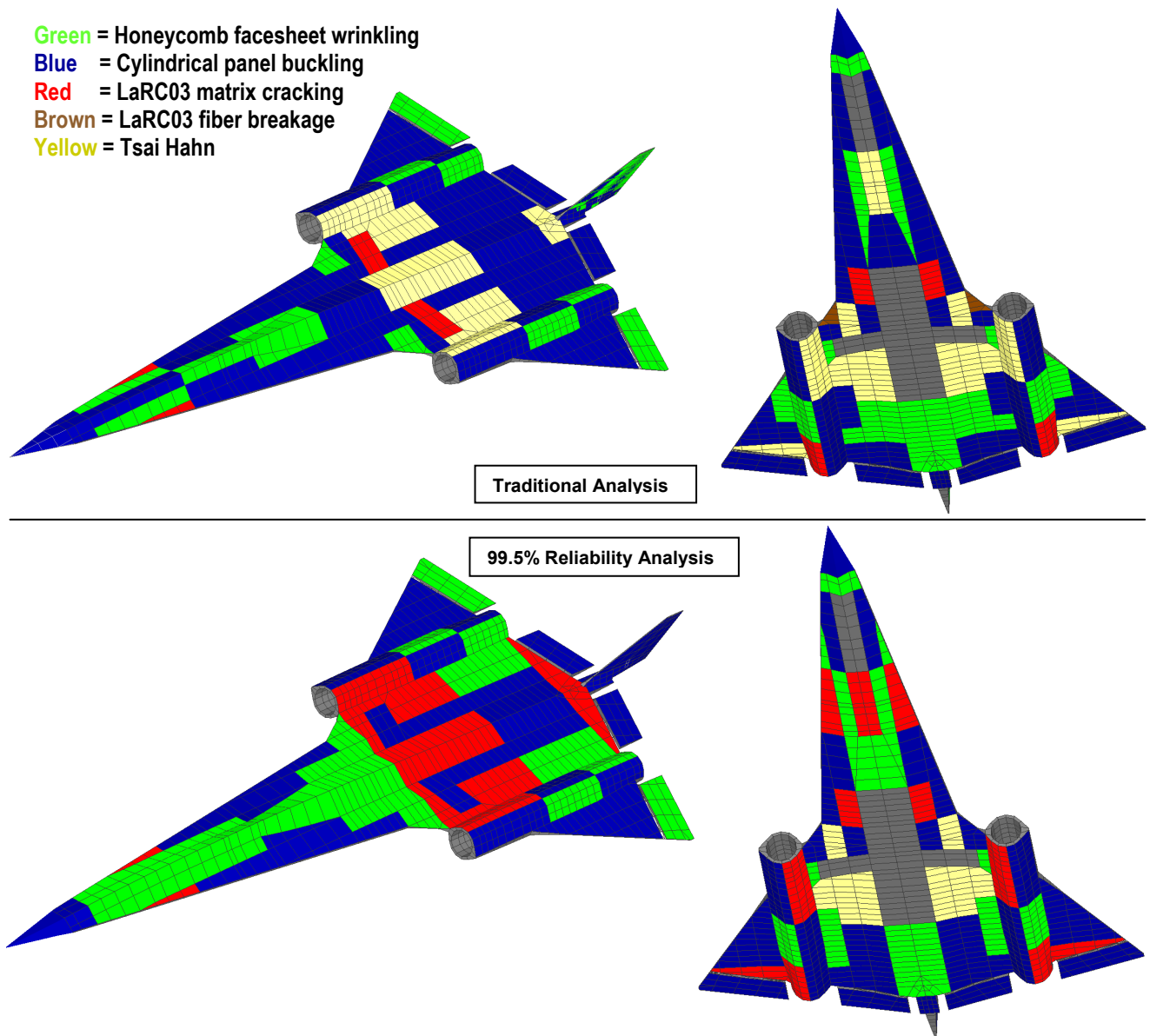


Fig. 24, Compared are the controlling failure modes between the traditional zero-margin approach vs. a 99.5% reliability analysis using the same design. Traditional design on top, reliability on bottom.

In this preliminary design example, it is shown that the traditional zero-margin approach sizes the vehicle weight to be about 9% heavier than the reliability approach if the lifetime airframe failures are the same. By allowing airframe weight to increase, but still be less than the traditional approach, 10 times more airframe lifetimes is achievable. This relationship is depicted in Fig. 25 where the blue diamond is the lowest weight achievable using the current aerospace industry structural analysis approach of attempting to bring all failure modes to a zero margin-of-safety and by obtaining conservatism with a uniformly applied 1.5 ultimate load factor to all potential failure modes. Table 4 lists data normalized against the traditional zero-margin result.

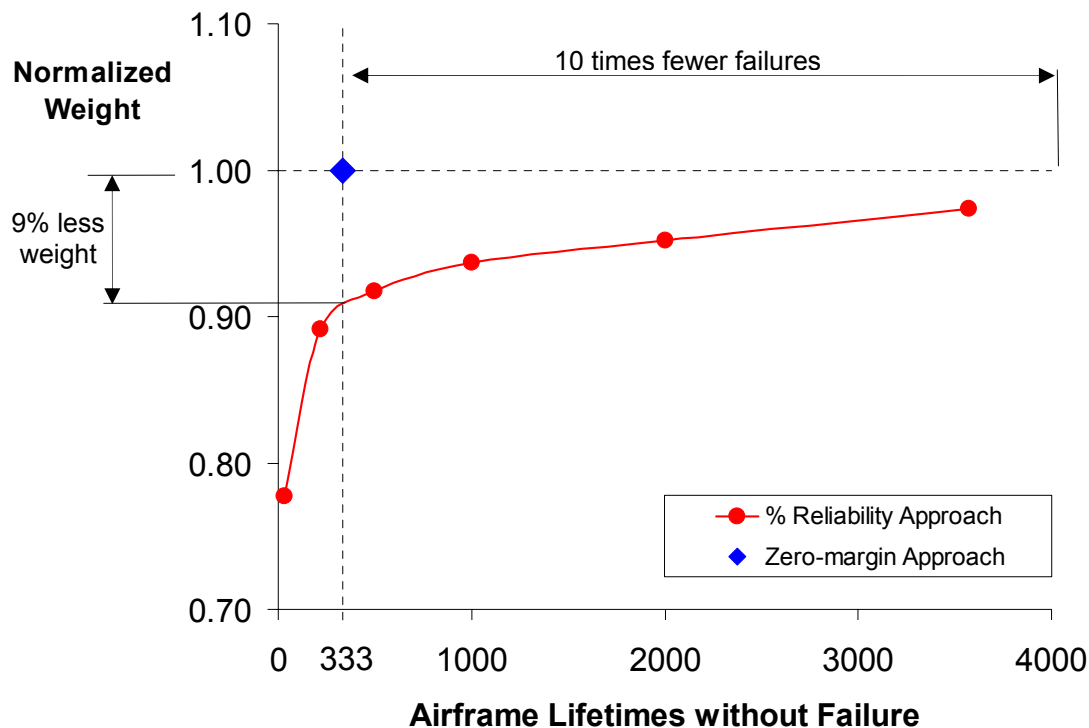


Fig. 25, An example airframe structural weight vs. lifetime failures. Note that significant reliability can be achieved with moderate weight growth. Note also that the traditional zero-margin analysis (blue diamond) currently practiced in aerospace provides neither acceptable structural integrity nor minimum weight. This data is normalized to the traditional analysis.

Table 4, The New Test Data Driven Reliability Provides Less Airframe Weight and More Structural Integrity

PDF Standard Deviation (K value)	Reliability	Lifetime Airframe Failures	Normalized Weight	Weight Savings
1 σ	85.1%	1 in 34	.773	22.7%
2 σ	97.7%	1 in 217	.887	11.3%
2.33 σ	99.0%	1 in 500	.912	8.8%
2.58 σ	99.5%	1 in 1000	.932	6.8%
2.81 σ	99.75%	1 in 2000	.947	5.3%
3 σ	99.86%	1 in 3571	.969	3.1%
Traditional	98.5%	1 in 333	1	0%

7 Conclusions

The new reliability analysis approach is grounded on building block test data and will produce robust designs that are less susceptible to problems that get revealed in final design phases. The uniform reliability approach to all failure analyses was made possible by implementation in existing sizing automation software. This makes it practical to bring into PD many higher fidelity analyses that are performed for all identified external load cases and for all airframe locations (no spot checking of parts). This capability resolves the most important reason for inconsistent structural integrity which is one constant load factor, applied to all potential failure modes, is not possible to raise all deterministic failure analyses to the same level of safety. Some failures, under certain load combinations are not predictable to within 50%. Meaning that aerospace industry's use of designing to 150% Design Limit Load, DLL, (a 1.5 load safety factor) is not sufficient for some failure modes, and far too conservative for others. With the test data driven reliability approach, all potential failure modes can be accurately assessed at the same level of confidence in a rapid manner that will not delay schedule nor require increase project funding. Achieving consistent structural integrity was demonstrated in a practical way on a complete airframe PD.

The reliability of material strength (both metallic and composite damage initiation) is very high. The use of 'A' or 'B' Basis allowables from MIL HNBK 5 and 17 provide substantial conservatism, especially when combined with the 1.5 ultimate load factor. So a material strength failure is not likely to occur in-service, at least not for pristine (undamaged) material. The concern to structural integrity is achieving consistency, and contrast to material strength, other failures such as instability and honeycomb wrinkling, or more likely to occur. The same level of conservatism is not built-in to the analysis process for all failure modes.

Achieving consistent structural integrity was demonstrated in a practical way on a complete airframe PD of a recent AFRL Long Range Strike aircraft. Presented are summary results that compare the traditional, zero margin-of-safety for all failure modes approach, vs. the presented approach that achieves consistent reliability for all potential failure modes. Included are identified areas of the vehicle sized using the traditional zero-margin method that results in an unexpected and unacceptable low reliability, even though it is 9% heavier than 'test data driven' reliability analysis and design. Alternatively, for the same weight as that provided by the traditional sizing, the vehicle can be sized to provide 10 additional lifetimes of reliability, Fig. 25. Test data driven reliability provides: 1) substantial weight savings, 2) consistent structural integrity, and 3) rationale to certification authorities of airframe structural airworthiness.

8 Acknowledgments

This material is based upon work partially supported by the United States Air Force under Contract.

1. AFRL VA SBIR Phase I contract # F33615-01-M-3125
2. AFRL VA SBIR Phase II contract # F33615-02-C-3216
3. LM Aero LRSA Contract/PO # 7067581
- 4.

9 References

1. Jennewine, Tim, (Air Force ASC/ENFS, Dayton, OH) "Uninhabited Air Vehicle (UAV) Certification," ASIP 2002, Special Session on Certification, Savannah GA, 11 Dec 2002
2. Soden, P.D., Hinton, M.J., and Kaddour, A.S., "A Comparison of the Predictive Capabilities of Current Failure Theories for Composite Laminates," Composites Science and Technology, Vol. 58, No. 7, 1998, pp.1225-1254.

3. Hinton, M.J., Kaddour, A.S., and Soden, P.D., "A Comparison of the Predictive Capabilities of Current Failure Theories for Composite Laminates, Judged against Experimental Evidence," *Composites Science and Technology*, Vol. 62, No. 12-13, 2002, pp. 1725-1797.
4. NASA SP-8007, Buckling of Thin-Walled Circular Cylinders, NASA Space Vehicle Design Criteria (Structures), August 1968
5. NASA SP-8108, Advanced Composite Structures, NASA Space Vehicle Design Criteria (Structures), December 1974 (of particular interest pp 74-81))
6. Niu, M. C. Y., Airframe stress analysis and sizing, 1997, Hong Kong Conmilit Press Limited.
7. Phase I Final Report for Air Force Research Lab (AFRL) SBIR AF01-239, Certification of Aerospace Structures by Analysis, Collier Research Corporation December 2001
8. Collier, Craig, Velej, Duane, and Owens, Steve, "Virtual Testing with Validated Analysis Tools," NATO AVT symposium in Paris, France, April 2002
9. Collier Research Corporation, SBIR Final Report: Consistent Structural Integrity and Efficient Certification with Analysis, Air Force Research Lab (AFRL) SBIR Phase II contract # F33615-02-C-3216 Volumes 1, 2, and 3, October 2004
10. Shuart, M.J., "Failure of Compression-Loaded Multidirectional Composite Laminates," *AIAA Journal*, Vol.27, No. 9, 1989, pp. 1274-1279.
11. Davila, C. G. and Camanho, P. P., "Failure criteria for FRP laminates in plane stress," NASA/TM-2003-212663.

A Perspective on Design and Certification

Duane E. Velez and Christopher L. Clay
Air Force Research Laboratory, Wright-Patterson AFB, Ohio 45433

Jim Starnes and the authors were involved in several activities which focused on improving the process of designing and certifying new airframes. This paper summarizes the current state of the art in design and certification of airframes and looks at the future of airframe design and certification as gleaned from the authors' experience in those activities.

I. Introduction

Since the advent of modern computers, there has been the dream of design of air vehicles by the push of a button. Simply enter the performance requirements and out pops the plans to manufacture the ultimate vehicle for those specifications. While this dream is far from reality, many people even question the prudence of such a venture: it eliminates the flexibility of human ingenuity, defies the ability to capture innovative technologies in a robust fashion, and many other excuses are given as to why such a dream should not be pursued. Yet it remains a plumb line by which we can judge our progress in capturing knowledge, thought and wisdom necessary to design air vehicles.

If we examine this dream a little closer, we do notice three things: it is exclusively based in analysis, it does not depend on testing that has not already been performed, and it significantly reduces the work load of the engineers. These three things, while expressed in extremes, provide guidance for future development that is more palatable to the engineers and managers of today. This guidance is to enhance our analytical capabilities with the goals of developing new weapon systems with 1) fewer costly tests, 2) fewer redesigns due to unanticipated test results, and 3) a shorter design cycle all through using analytical methods more thoroughly, consistently and reliably. It is for these goals that our hearts beat with enthusiasm and the anticipation of discovering an excellence in system development that was heretofore unobtainable.

The authors had the opportunity to work with Jim Starnes in pushing forth this concept of improving the way that analysis methods are used in the certification process in several groups. This paper addresses some of the issues surrounding the issues of improving reliance on analytical methods in the certification process.

II. Certification and Design

There has been much confusion in the term certification by analysis and in similar terms. Thus, the purpose of this section is to clarify what is meant in this document by the term certification, and what is meant when it is coupled with the phrase "by analysis."

The terminology used here is based in the certification process used by the US Air Force. This concept may differ from other countries, and from civil applications since the US Air Force is both customer and regulatory (certifying) agency. For example, the EuroFighter community defines certification as meeting the requirements of the regulatory agency and qualification as meeting the performance requirements of the customer. In this paper, those two distinct concepts are combined into the single concept of certification.

A. Certification

A system is certified when it meets regulatory (safety) requirements in a rigorous manner. Thus certification is the process by which those requirements are met. While many may view certification simply as the regulatory agency signing off on the system, it is really more complex. Certification is the process by which risk is identified and managed.

In certifying a system for regulatory requirements, the performance of the air vehicle must be taken into consideration. Performance parameters include range, payload, cruise speed and specific fuel consumption. The performance of the vehicle is related to the safety of the vehicle. As the performance changes, so change the loads on the vehicle. As the loads change, so change the stresses in the vehicle. As the stresses

change, so change the safety margins. So when an air vehicle is certified, it is certified for a specified performance envelope.

B. Certification by Analysis

The term “certification by analysis” can be viewed in essentially three ways 1) the push button dream described in the introduction (or something close to that), 2) the goals of developing new weapon systems stated in the introduction, and 3) current practice. Thus the extreme views of the process can be viewed as completely devoid of test, and analytical methods themselves as being grounded in tests. While the authors hold the first as the ideal plumb line for determining if something is certified by analysis, the second option expresses the obtainable reality for certification by analysis within the foreseeable future.

The claim that certification by analysis is captured in current practice misses the essence of a significant reliance on analysis in the certification process. The argument in favor of this option states that current practice uses analysis extensively to arrive at a design and to establish a test to tune the analysis; and the design that is actually built is not necessarily the design that was tested, but a perturbation from that test based on analysis. However, the tests show over and over that the analyses are not what we would like them to be. Thus, even though this concept represents the current state-of-the-art and describes the meaning behind the terms fairly well, its emphasis on current capabilities undermines the cost and time saving potential of increasing dependency on analytical methods even further. To align these terms with current practice removes the hope of achieving new designs faster and at lower cost.

The term “certification by analysis” embodies both the sense of establishing a certified design based on analyses away from test conditions and the sense of the future expectations of analytical capabilities in achieving the goals of fewer tests, fewer unanticipated test results and a significantly shorter design cycle. The term “analytical certification” is synonymous with “certification by analysis”.

C. Design

Intuitively the design process is one in which a system is developed from the concept of how it should perform to the details of how it is manufactured. While the authors do not wish to belabor the issue of what is meant by design, the authors do wish to recognize that the information used to certify a system is extracted from the design process.

In order for a regulatory agency to sign off on a system as suitable for specified use, the regulatory agency must be provided with information demonstrating that the system does perform within that specified use in a way that is consistent with the regulatory requirements. This requires much information which was generated in the design development process. The certifying agency works with the manufacturer during the design process to make sure that any certification questions concerning the system are answered. The design development process is therefore considered to be a part of the certification process, and assumes the role of a risk management process for schedule, performance, cost and safety.

As the design process progresses and design parameters are varied to explore the design space, constraints generated by regulatory requirements work toward mitigating risks in the system. The design process is a key part of the certification process and can aid significantly in reaching toward the goals of certification by analysis: developing new air vehicles with 1) fewer costly tests, 2) fewer redesigns due to unanticipated test results, and 3) a shorter design cycle all through using analytical methods more thoroughly, consistently and reliably.

III. Current Practice

A. Integrated Tools and Processes

One of the groups that Jim Starnes participated in with the primary author considered the integration of tools and processes. It was recognized by a number of people in that group that the integration of tools and processes was a key component in striving toward the goal of certification by analysis. This working group considered the issues of the architecture of integrated tools and processes and the application of such integration in the development of air, land and sea vehicles.

The integration of tools and processes has been attempted to varying degrees of success over the past 30 years. Initial attempts at the integration of tools and processes brought multiple tools into a single computing environment that contains all necessary functionality to model, analyze, and optimize a given structure. This is called a monolithic approach. These tools are usually robust and easy to use, but lack the

flexibility or ease of expanding that is required to reach toward the goal of certification by analysis. A few examples of such systems are MSC NASTRAN, UASF ASTROS, ANSYS, Elfini, and Lagrange.

More recently, a best in class approach to integrating tools and processes has prevailed. Typically a scripting language, such as TCL or Perl, is used to glue the “best” independent applications together. While this approach is generally more flexible than the monolithic approach, it tends to suffer from a lack of robustness. A few examples of such architectures are iSight, Model Center, Model Logics, MDICE and Visual Doc. In developing a framework within these architectures, it is typical to capture the process as it is currently performed. These environments enable rapid iteration over that process, but require significant setup time. These methods typically produce a 50% savings in time over the traditional approach of passing the data from application to application by hand.

The best in class approach can also be implemented from a product based perspective that captures the process as well. This approach is perhaps even more flexible than the process based approaches. One example of this approach is the Adaptive Modeling Language (AML), an object-oriented, knowledge based, programming language. Applications generated in AML have demonstrated time savings in excess of 90% over the traditional approach of passing the data from application to application by hand.

In addition to speeding up the design process, environments generated in these best of class approaches have other desirable features. They bring together disparate data resources with the grand goal of accumulating all relevant data in a comprehensive system making communications between disciplines much easier and they enable the ability to automatically generate appropriate models. A comprehensive system does not necessarily mean a single database, but generally a distributed database with links connecting the various portions. Automatic model generation in this approach promotes certification by analysis in that it removes the variability of human interaction in model generation.

B. Risk Assessment

Risk is the exposure to injury or loss. The primary method for mitigating (reducing the exposure to) risk is to identify the potential risks and establish efforts that target the reduction of those risks. The process of identifying risk is in some sense a pessimistic view of the future as those performing the risk assessment try to answer the questions, “What can possibly go wrong?” and “What is the worst that can happen?” The efforts that target the reduction of the identified risks are discussed in the following subsections.

A process of identifying risks is to gather experts together in a room and allow them to brainstorm on potential risk factors in the system. This process is repeated a number of times and at different levels of detail. It is performed for the system, for the structure and for each of the subsystems.

After an exhaustive list of potential risks has been identified, the experts independently assess each risk subjectively for probability of occurrence and for the impact if failure occurs. Typically the probability of occurrence is broken up into three or five levels of probability, e.g. low, medium and high. The impact of failure is also typically broken up into three to five levels, e.g. negligible – fix at next scheduled maintenance, moderate – it will need to be fixed when it returns, and catastrophic – the system is lost. The individual responses are pulled together and a collective risk assessment of each factor is negotiated. A sample risk assessment plot is shown in Figure 1: Risk is low in the lower left hand corner of the plot and high in the upper right hand corner of the plot. This sample shows potential risks identified by a letter-number code to represent categories and the risk element within the category.

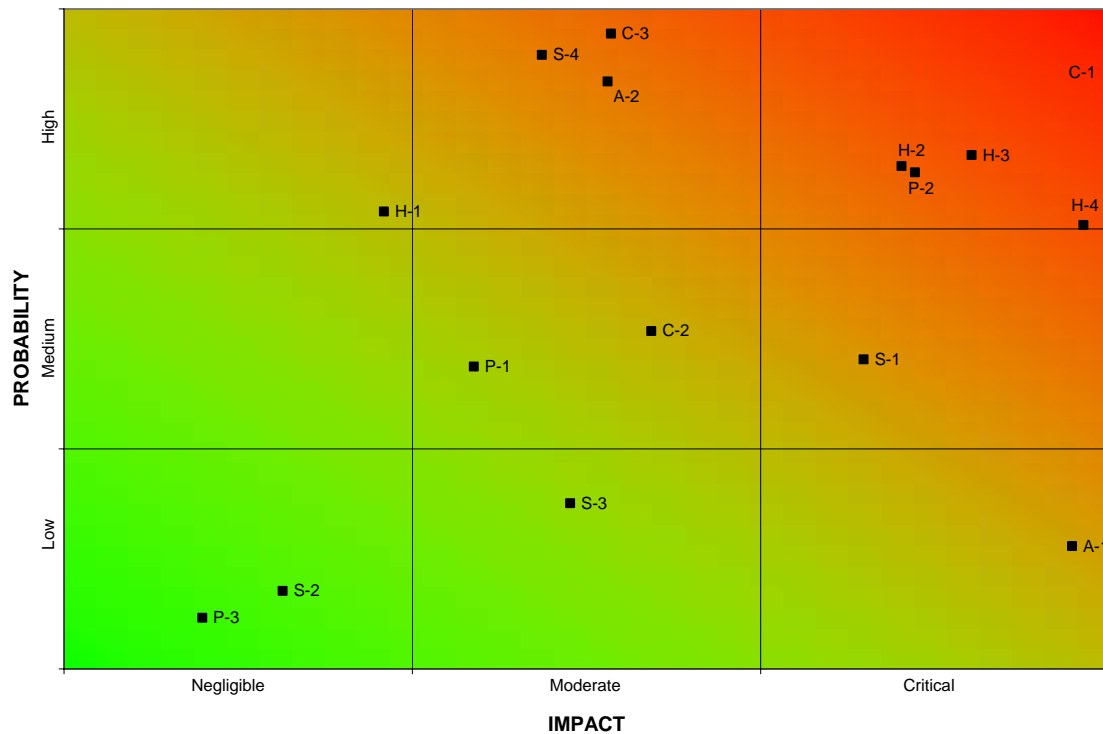


Figure 1: Sample Risk Analysis

While predicting what could go wrong and the worst that can happen, the experts are limited by their experience, which consists of education, experience with test failures and experience with field failures. The experience can either be first hand experience, or learned from others who had the experience. True, the human mind is capable of cross-correlating and extrapolating previous experience to new applications, but that does not enable them to foresee all new failure mechanisms. Thus, an exhaustive list is not truly exhaustive, but it incorporates the knowledge base of the experts performing the risk assessment.

It is apparent from this process that risk assessment is to a large degree subjective. It is a collection of possible events that people perceive as a risk. Oftentimes the effort of mitigating a risk amounts to nothing more than collecting information. The design doesn't change at all to reduce the risk; the experts are simply better informed of the way the system responds so the perceived risk vanishes.

This is not to imply that the effort of subjectively collecting potential failure mechanisms is unmerited. For example, with new materials, the response of that material to all environmental conditions may not be well understood, and until the response of the material in an environmental condition is understood, there is a risk that the material may behave in a way that is not favourable.

Once potential risks have been identified and assessed for probability of occurrence and impact of occurrence, it is necessary to determine how to bring the risks down to an acceptable level. There are essentially four ways to deal with risk: avoid the risk, mitigate the risk, abate the risk, and accept the risk. The first method of dealing with risk is to avoid the risk. This can be accomplished by changing the requirements in a way that the risk is reduced to an acceptable level while still meeting the users' needs. The second method of dealing with risk is to mitigate the risk. Risk can be mitigated by taking active steps to minimize the impact of the risk on the system.

The third method is to abate the risk. Risk is abated by shifting the design requirements to systems that can meet the performance requirements at a lower risk level. For example risk is often abated by reverting back to proven technology.

The final method for dealing with risk is to accept the risk. This is commonly done with low level risks. What is considered a low level risk is subjective and depends to some degree on the cultural attitudes

regarding risk at the time. In today's litigious society, the level of risk that is deemed acceptable is quite low.

In being able to identify how to handle risk, it is normally appropriate to understand the source of risk. Oftentimes, especially early in a development program, the primary source of risk is ignorance, which may be classified as a type of uncertainty. For example, if a new material is being proposed, it is likely that the material has not been fully characterized for all of the environmental conditions that it will undergo. There are also issues associated with manufacturing with the new material and how the large, complex production articles compare with small, simple parts that were developed in a laboratory setting. This type of uncertainty is mitigated through additional research.

In Jim's area of structural strength, risk associated with the uncertainty of structural response has classically been handled with a margin of safety. The margin of safety mitigates the risk by moving the design to a level nominally considered safe. This margin of safety covers a multitude of risks and uncertainties which have a presumed cumulative effect. The presumed cumulative effect is based on years of experience. Designs generated using a margin of safety approach have some parts that are over-designed and some parts that are under-designed. Current research seeks to circumvent this disparity by breaking out the risks and uncertainties into their constitutive parts. This concept of identifying the risks more clearly should enable designers and decision makers to target risk factors with more precision. This topic will be addressed further in "A Glimpse of the Future of Certification."

C. Airframe Certification for Structural Strength

This is not intended to be a complete survey of issues associated with airframe certification by any means. However, it is appropriate to address the issues of concern to Jim Starnes in another working group which focused more directly on issues associated with certification by analysis. Jim's contributions were in the area of static strength.

1. Requirements

The following section is based on US JSSG 2006 [DoD, 1998] requirements, however most other equivalent strength requirements are fundamentally similar, as they have been based upon similar experiences and international collaborative programs have naturally led to some commonality.

"Adequate airframe strength must be provided not only for safety of flight, for landings, and for maintenance functions, but also to permit full operational capability of the air vehicle to perform its required missions. An under-strength airframe impairs the mission potential of the air vehicle, since it must be restricted during its operations." In general the airframe must ensure adequate strength "to provide operational and maintenance capability commensurate with the general [performance, environmental and maintenance] parameters" and with the specific design and construction parameters "without detrimental deformations ... at 115 percent limit or specified loads and without structural failure at ultimate loads." Further explanation on the deformation requirements are given by: "Excessive deflections may not only produce deleterious aerodynamic or aeroelastic effects, but may cause binding interferences between hinge connected and adjacent structures as well. Exterior surface buckles, especially those that are permanent, may produce undesirable aerodynamic characteristics." Individual Nations' requirements differ in detail, but the main principles are similar.

There are also more specific requirements associated with airframe strength. Other typical requirements for airframe strength cover 10 different sub areas: material properties, material processes, internal loads, stresses and strains, fitting factor, bearing factor, castings, high variability structure, static strength, dynamic strength, initial and interim strength flight releases, final strength flight release, modifications and major repairs, rework, refurbishment and remanufacture. Not all these sub-areas are identified in other requirements, for example, in the UK Def Stan 00 970 there are no specific references to fitting factors, bearing factors or castings. The assumption is made that it is preferable to discourage stress analysts from using simple factors to allow for difficult to analyze features; rather these aspects should be taken into account as part of the stress analysis in the case of fitting and bearing factors and by consideration of variability (and quality control) for the case of castings. However, this type of difference is not very significant in practice, since the interpretation of the written requirements by each Nations' regulators/advisors is likely to reduce the apparent differences. A formal discussion on each of these topics is beyond the scope of this effort. The discussion will therefore focus only on the static strength.

2. Current Practice

Metallic airframe structures have been commonplace for many decades now. Aluminium alloys, generally 2000 and 7000 series are used for the majority of aircraft structure, with Titanium alloys normally

employed where their high temperature properties and/or their strength/volume ratio were required. In addition some very high strength steels were and are used where their combination of strength and volume were desirable, for example in landing gears.

As a result of widespread use of the more common alloys, databanks of materials properties were gradually built up in which designers and regulators had confidence. These are contained in references such as Mil Hbk 5(now referred to as DOT/FAA/AR-MMPDS-01 [Rice et al, 2003]

Improved analysis tools and knowledge have gradually increased our ability to analyse the complete structure, but we have not been able to accurately model every feature.

It could be argued that, originally, certification was largely test-based, the successful test demonstrating the quality/accuracy of the analysis used in design. However, static tests have never exercised every part of an airframe to the extremes of their design envelope, so it must be accepted that some features were, and still are, certified by analysis either partially or totally. Among the reasons for this are the following:

1. Practicality of applying a large number of test cases to exercise all features desired.
2. Difficulties of accurately representing ground and flight loads in a test facility. Associated with this is the difficulty of restraining the structure in a representative manner.
3. Some loading inputs are difficult to introduce e.g. thermal loads; this not only compromises the actual loading, but may result in the material not being tested in a representative condition (e.g. material properties can vary with temperature). The temperature aspect may be of significance even for a subsonic aircraft, due to high altitude flight on the one hand, and discreet heating sources on the other (engines, APUs, pumps, generators etc.).

A further complication is that all materials demonstrate some variability in their mechanical properties. The analysis is usually conducted using some form of minimum properties, either “S” values or statistically derived figures (A or B values). The test article is more likely to be constructed of materials nearer the average level of properties; thus a test to Design Ultimate Load (D.U.L.) does not necessarily represent all fleet aircraft.

In some cases, an attempt was made to take into account some of the above points, particularly those concerning variability and temperature effects, by taking the test article above D.U.L. by a “test factor”. However, this practice was, and is, not widespread, and even then perhaps only in one or two load cases. In addition, the actual factor used was to some extent arrived at by engineering judgement rather than a number that could be substantiated analytically. One way of obviating the use of a variability factor, which has been used for modern composite structures, is to inflict BVID damage and state that this is representative of the worst manufactured component.

Nevertheless, the entire certification process, including the value of ultimate factors and many other aspects, resulted in a very safe record for aircraft structures. However, it must be accepted that analysis has always played a major role in static strength certification, with testing not the sole component. A further reason for this conclusion is that the critical test load cases are selected partly on the basis of analysis results. It may not have been considered as such by all parties, but a major role of testing has always been validation of analysis.

A major development in the process came about as a result of advances in technology particularly computing power and testing facilities. Many more loading cases could be derived and this was matched by the ability to analyse them using, for example, the Finite Element Method (FEM). It was also possible to analyse more complex structures with greater accuracy. The drive for increased performance and/or reduced cost of operation led to a drive for lighter, more efficient structures. This helped remove the inherent conservatism built into some parts of the airframe structure, making it more important to have confidence in the analysis. Similar advances in testing techniques and facilities have led to more realistic testing with much more data which could be used to improve analysis validation.

However, probably the most significant effect on the process came about as a result of the introduction of Carbon Fibre Reinforced Plastic (CFRP) Composite Structures. They were found to require increased consideration of environmental degradation of some properties, particularly under hot/wet conditions, and raised the complexity of analysis due to their anisotropic properties and ability to “tailor” their lay-up to produce light weight efficient structures. A further driver for change was the realization that variability in properties required more rigorous treatment to avoid the application of conservative “safety factors”. A great deal of effort was invested into developing a suitable certification method, now universally recognised as the “building block” or “pyramid” approach.. Although some would argue that, in principle, this approach had been used before, the use of CFRP materials led to its adoption as a more formal method illustrated in Figure 2.

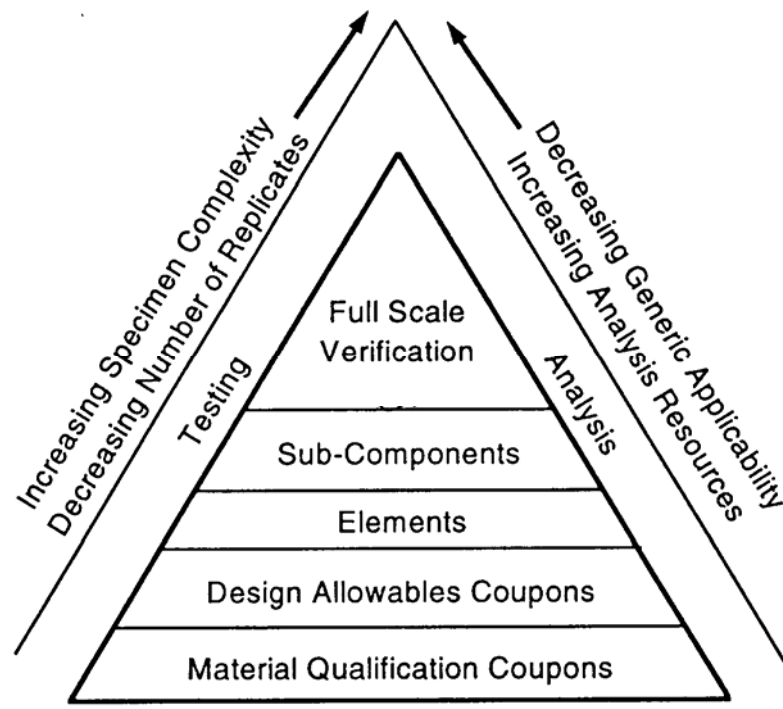


Figure 2: Building-Block Certification Methodology

Examples of typical building block levels for military and commercial airframes are described in MIL-HDBK-17 [DoD, 2002]. This approach combines analysis and testing to assure structural integrity of airframe components constructed from composites. As can be seen from Figure 2, at the lowest levels of the pyramid testing is predominant, but is comprised of small test coupons. Lamination theory analysis at this level is used to reconcile unidirectional or lamina test results with multi-directional test results in terms of stiffness and strength. The design stress/strain levels for unnotched and undamaged structure are established. The test data generated at this level has sufficient replication to be statistically meaningful. Furthermore, composite material performance at the range of applicable service temperatures and moisture levels is assessed. Analysis plays no significant role except for statistical methods to reduce the data.

At the second tier of Figure 2 the complexity level is increased to establish structural performance of simple joints and impacted structure. The test data generated here is at the laminate level loaded uniaxially. Analysis is then used to extend the test data to other laminates and multi-axial loading. The available analysis methods to perform these calculations are semi-empirical but have sound theoretical basis from anisotropic plate theory and fracture mechanics.

Finite Element Analysis (FEA) is used to correlate test data obtained for higher complexity elements, subcomponents and components, either full-scale or scaled. In practice, the FEA of the complete component, such as a wing, is used to obtain loads. Smaller finite element models are then constructed with more detail to model critical areas of the component. The FEA uses the material properties from lower tier testing to formulate the initial model and then correlates the model to the strain-gage data. This is particularly useful and if successful can avoid testing at elevated temperatures with moisture-conditioned structure. A good reference for the current practice can be obtained from [JSSG, 1998]. The major strides in metallic materials and processing technologies have triggered renewed thinking on the certification process, including the testing and analysis question. These developments have in no small way been driven by the need for metallic structures to maintain competitiveness with composite structures, particularly those manufactured from Carbon Fibre Reinforced Plastic (CFRP). Different product forms such as Castings were already being developed before this time, but more recently we have seen, for example, the application of Super Plastically Formed and Diffusion Bonded (SPFDB) Titanium, Powder Metallurgy, Aluminium Lithium Alloys, advanced (and larger) castings and forgings and many others. In addition, metals have entered the composites field as well with Metal Matrix Materials.

Even before the application of CFRP structures, with the associated re-evaluation of the certification process, it was realised that account needed to be taken of material properties that displayed different features compared with conventional aluminium alloys for example. A good example of this was the use of castings, where it was realised that they often display greater variability in strength amongst other issues. This was typically addressed (and still is in some cases) by the application of a “castings factor” which effectively reduces the material property allowables. However, the basis for the factor sometimes seems somewhat arbitrary, and it raises the question of what a test in isolation can actually prove.

For example, it is often very difficult to test a component on its own realistically. If a casting, designed with a casting factor, is tested as part of an airframe assembly, in order to generate the correct loading conditions, then unless the surrounding structure is inefficiently, over designed, a major test cannot exercise the component to fully certify it. This is exactly the same problem which occurs with hybrid CFRP/metal structures where “over testing” is a possible alternative to testing under degraded, hot wet conditions.

There are other examples where the introduction of new materials and manufacturing processes, has led to new problems. An example is the introduction of Aluminium-Lithium (Al-Li) alloys. It was found by several workers, probably always accidentally, that some early forms of Al-Li alloy components could be susceptible to failure as a result of impact damage. This was not expected, as conventional metallic structures are quite tolerant to such threats, the most serious result being perhaps a harmless dent in thinner sheet components. In contrast, CFRP structures must include an assessment of impact damage tolerance in their certification programme, as this aspect is often a major design driver, limiting their potential weight savings.

A conclusion, which may be drawn from the proceeding discussion, is that we should not differentiate between metallic and composite structures in the certification process, but rather should adopt the building block or pyramid approach to ensure that we deal rationally with all aspects of the certification process.

For well-established materials and forms of construction, we can make a rational argument to omit some of the lower levels of the “pyramid” as all the material properties are well established and accepted. A note of caution must be made here that, although a well-known material is being used, it may be in a different form than in previous experience, e.g. machined from a thicker section plate than previously, and some properties, including resistance to corrosion can be changed. The ability to analyse particular features, from previous programmes most likely, would remove the necessity to carry out these stages. The certification process can then concentrate on those aspects where there is insufficient confidence in the design.

It is not being suggested here that this doesn’t happen anyway, but the building block approach does allow a basis for a contractor to plan a route to certification, which can then be presented and debated with the regulatory authorities.

When a new material or manufacturing process is proposed, the principles established by experience in composite materials, can be applied to derive a certification programme which addresses aspects such as property variability, susceptibility to impact damage, confidence in the designers ability to analyse particular features, dealing with temperature effects, susceptibility to environmental degradation and so on.

A further important conclusion that has been reached by many workers, from experience on composite structures, regards the purpose of the major static test. It is a gross simplification to state that early static tests were mainly used in a pass/fail sense, but they have been increasingly viewed as principally a tool to validate analyses. This works in two specific areas:

- Validation of full FEM to provide overall internal load paths and distributions. Arguably, this is the most important aspect of the full scale airframe static test.
- Validation of stressing methods/procedures, including local FEMs, for particular features. This can include ensuring local allowable strains are not exceeded as with composite structure. However, it can be argued that much of this is done in the sub-component and box tests of the building block pyramid.

Of course, the same criteria/conditions apply; in particular the fact that it is the FEM of the actual test loading (including restraint) and environmental conditions that is being validated. This provides confidence in the (different) FEM of the operational aircraft in its operational loading and environmental conditions.

A further related aspect not covered thus far is functionality, i.e. the ability of the control surfaces etc to operate correctly under representative loading, with no fouling or binding. Again, testing, e.g. on the major airframe static test, can be used to validate the analyses, which in this area have also improved greatly in

recent years. It is normally impractical to move a loaded control surface, mounted on a loaded structure, over anything like its full range, e.g. a rudder on a vertical tail/fin. However, the test can validate the analysis of an unloaded control surface on a representatively loaded primary flying surface. The analysis can then be used to certify that there are no problems for the more representative flight cases. Of course, in some cases, the analysis may show that the most critical condition for a particular surface is the unloaded condition; nevertheless, the same principles apply of the test validating the analysis.

3. Future Capabilities

At the composite material characterization stage, a significant amount of testing could be eliminated if standardized materials were available with pedigree and accompanied by materials and process specifications. Coupon testing at each manufacturer would be limited to demonstrations that indeed they can process this material and obtain equivalent material properties to those that are in the original database. FAA has embarked down this path by issuing documents that describe required characteristics of both the processing and materials specifications. This should lead to a common specification as issued by SAE International and a material qualified to that specification would be available to all aircraft manufacturers once they meet data sharing requirements.

A more dramatic increase in the role of analysis in qualification would be the development of methodology to predict composite lamina properties knowing the properties of constituent materials, fiber and matrix. Various attempts through micro-mechanics and meso-mechanics have been made in this area, but no validated approaches exist.

There is a focus of the research community to increase reliance on design and analysis tools and reduce the amount of testing required to qualify/certify airframes. Static strength has been identified as an area that may be sufficiently well understood to proceed in developing improved design and analysis methods, which will enhance the confidence in the analysis.

The new design methodology described in the General Methodology chapter has been implemented to a small degree for static analysis. The expected capability of generating new structural layouts and the corresponding meshes rapidly gives rise to the hope of executing design trades that have heretofore been infeasible. The reliability of this method under the versatility of diverse structural layouts is not yet guaranteed. Much work remains to be accomplished in this area to cover the breadth of static strength analysis alone.

The new analysis methodology developed by Surana has little impact on linear elastic analysis other than to recognize that the element formulation requires consistency with variational principles [Surana 2002]. Current finite element methods for nonlinear analyses do not conform to variational principles and as such are not as reliable as they could be. There is some hope that this method will bring forth soundness to post-yield static analysis.

IV. A Glimpse of the Future Certification

The future of certification of airframes rests in the ability to acquire pertinent information in a timely manner and organized in a manner that is easy to review and assess. This can be accomplished by capturing the issues associated with airframe certification in a product based design environment including risk, cost and schedule assessments.

Today's analytical methods have reached a high level of maturity in many areas: analysis of single components accounting for multiple physical phenomena or reduced size sub-systems for single physical phenomena. They are however not as reliable for predicting the behaviour of sub-systems with multiple physical phenomena or very complex systems.

There are several areas of methods development directed to improving analytical capabilities. The first is focused on integrating multiple disciplines. One approach is to formulate basic principles of physics so that the multiple disciplines can be analyzed by a single solver. Others look at a) simply linking existing analysis programs together through parsing the input and output files, or b) linking individual programs in a more robust computer science manner directly through shared memory. The value of either approach is that industry accepted and validated programs are used in the integrating discipline analyses. Since these integrated methods reduce the amount of human intervention in transferring or exchanging data between various analysis tools, it is anticipated that the amount of error in the design will be reduced, leading to a reduced number of unanticipated test results and reducing the amount of redesign.

To further this goal of reducing unanticipated test results, another major area of development is integrating test data into the analytical design environment. The value of existing test data in developing a robust and reliable analysis capability is described in reference [Collier, 2002]. Two distinct correlation factors can be identified from tests: one for analysis inaccuracy and the other for observed test scatter. When both are implemented for each unique structural failure mode, more reliable structural integrity and analysis confidence can be achieved.

While these efforts must be vigorously pursued, the increasing complexity of weapons systems, the continued expansion of technology, especially new materials, and pressure to reduce development program and systems costs will always force analytical methods to be often used outside of their known applicability domain. This uncertainty makes the goal of further reducing expensive testing a difficult one to achieve universally, but substantial progress toward this goal should be accomplished in the next decade.

V. Summary

Jim was very interested in the certification of aerospace structures and recognized the potential of improving the certification process through an increased reliance on analysis tools and that integrated analysis tools aid in eliminating some of the difficulties associated with running the individual tools separately. This paper asserts that simply combining the tools into a process based environment provides some advantages, but misses the power that can be achieved from a product based environment.

VI. Acknowledgements

The authors would like to acknowledge John Moon of Qinetiq and Peter Shyprykevich of the FAA Technical Center who were partners with Jim Starnes in the international working group and provided much of the material used for the section on "Issues Associated with Airframe Certification."

VII. References

Department of Defense, *Joint Services Specification Guide, Aircraft Structures*, JSSG-2006, 30 October 1998,

Richard C. Rice, Jana L. Jackson, John Bakuckas, and Steven Thompson, "Metallic Materials Properties Development And Standardization (MMPDS)" Jan 2003, NTIS

Department of Defense, *Military Handbook – MIL-HDBK-17*, 2002

Surana, K.S., Ahmadi, A.R., Reddy, J.N., "The K-Version of Finite Element Method for Self-Adjoint Operators in BVP," *International Journal of Computational Engineering Science*, Vol. 3, No. 2, pp 155-218, 2002.

Collier, Craig; Velez, Duane; and Owens, Steve, "Virtual Testing with Validated Analysis Tools," Proceedings of Reduction of Military Vehicle Acquisition Time and Cost through Advanced Modelling and Virtual Simulation, Paris, France, 22-25 April 2002, RTO-MP-089, Paper 23.

Design Tailoring of Laminated Composite Structures

A Tribute to Dr. James H. Starnes, Jr.

Zafer Gürdal*

*Professor, Departments of Aerospace and Ocean Engineering, and
Engineering Science and Mechanics, Virginia Tech, Blacksburg VA 24061
Currently Aerospace Structures Chair,
Delft University of Technology, Delft, The Netherlands*

The primary purpose of this paper is to share the experiences of the author and some of his students in design and optimization of fiber reinforced laminates and laminated composite structures. The experiences are gathered during the past twenty-four years working in close collaboration with the NASA Langley Research Center (LaRC), in particular with Dr. James H. Starnes Jr. who provided encouragement, guidance, and support. As such, it is not intended to be a survey of the literature on the topic, nor is it a complete reflection of the wide range of expertise developed in what used to be the Structural Mechanics branch at LaRC under the leadership of Dr. Starnes. It is a rather limited account of a series of developments in the area of design and optimization of laminated composite structures. As part of the paper, the publications that are authored/co-authored by Dr. Starnes in this particular area are surveyed.

I. Introduction

With the realization of substantial weight savings that can be achieved through the use of fiber-reinforced composite materials, a new era in design of aerospace vehicle structures started. The early efforts in which the existing metal structural components were simply replaced by composite ones with reasonably well understood laminates, such as the commonly used quasi-isotropic lay-up with 0-deg, ± 45 -deg, and 90-deg oriented fibers, proved to fall short of expectations. It became quite clear early on that the high material cost coupled with the inefficient manual touch-labor would result in parts that would not be cost competitive compared to traditional metallic components. In order to bring the use of fiber reinforced composite materials into the mainstream structural engineering applications, research and development in multiple fronts was initiated. At the forefront of this research was, what was then called, the Structural Mechanics Branch of NASA Langley Research Center headed by Dr. James H. Starnes Jr., who early on recognized the futility of building composite structures that looked like aluminum structures. This was the beginning of, the so called, “fight against black aluminum”¹.

A considerable portion of the initiatives that were aimed at achieving increased use of fiber reinforced composites were in the area of improving the cost effectiveness and quality through new and improved fabrication methodologies. Although some of the studies that will be discussed in this paper utilized some of the new manufacturing technologies to fabricate the designs that are studied, and even though some of the designs (especially the ones that we will call “novel” design concepts) were inspired by the new fabrication methods, the present paper does not cover the discussion on development and technical details of fabrication methods. Instead we concentrate on the efforts of structural engineers and designers to demonstrate the advantages that can be achieved through the use of fiber reinforced composite materials.

It was not too long before the researchers recognized the advantages that composite materials offered in structural design in terms of the design problem formulation, particularly in terms of optimal design. As will be discussed shortly, with the introduction of composite materials into a design problem formulation, designers obtained a new flexibility through the use of variables that directly change the properties of the material, and therefore optimal design of structures has acquired a new meaning. In order to improve structural performance and meet the requirements of a specific design situation, it was possible to tailor the properties of the structural material and its distribution in addition to structural dimensions. Therefore, use of the methods and tools of structural

* Copyright 2005 by Zafer Gurdal. Printed by NASA with permission.

optimization became one of the ways in achieving reliable, high-performance, composite structures that will outperform their metallic counterparts. In the following the first part immediately after the introduction will discuss the topic of Laminate Optimization, which was aimed at the development of tools for selection of fiber orientation angles and their relative location in the laminate thickness to provide best material performance characteristics.

It will, however, be misleading if we isolate the developments in composite design concepts from the available fabrication methods. The section following the Laminate Optimization discusses the introduction of Novel Structural Concepts along with the tailoring of the same to achieve high-performance composite structures that will outperform their metallic counterparts in a cost-effective manner. The next section, called by the author “High-Fidelity Optimization”, is an attempt to introduce optimization methodologies that will enable designers of advanced composite structures to use high fidelity analyses in the design optimization environment.

II. Laminate Optimization

One of the immediate solutions in increasing the competitiveness of composite structural components was to improve their performance. It was obvious that by starting to effectively use the directional properties of the fiber reinforced composites, one could improve the performance, such as load carrying capability or vibration characteristics, of a structural component for the same weight. Alternatively, the weight could be reduced even beyond the weight afforded by the favorable specific-stiffness and specific-density offered by composites without degrading the measure of performance under consideration. In order to create laminates with directional properties, the number of layers with specific orientations, their orientation angles, and through-the-thickness location within the laminate of the layers with specific orientations had to be chosen carefully.

A. Laminate Design with Continuous Variables

Mathematical optimization, which deals with either the maximization or minimization of an objective function subject to constraint functions, has already been becoming a favorite tool for structural designers. The use of mathematical optimization for design relieves the designer of the burden of repeated manual iterations and transforms the design process into a systematic well-organized activity. In the case of composite laminate design, the optimization becomes a natural tool because of the increased number of design variables associated with the laminate definition. Rather than having to use a single material type (in earlier aerospace applications only the selection of an aluminum alloy was required), there are more controls to fine-tune the directional material properties of a structure to meet design requirements. It was not too difficult for Jim Starnes at NASA Langley research center, who was already familiar with the use of optimization in structural design through his collaboration with Raphael Haftka,^{2,3} to see the potential of the use of optimization in composite structures design.⁴ The paper by Starnes and Haftka was on the use of a mathematical programming structural optimization procedure for the global level preliminary design of a composite wing with buckling, strength, and displacement constraints. For the wing skin, the design variables used were the thicknesses of 0, ± 45 , and 90-deg layers of a balanced symmetric laminate with specified stacking sequence, $[\pm 45_i / 0_j / 90_k / 0_j / \pm 45_i]$, where the i, j , and k , are used to as continuous variables to control the thickness of the associated orientation angles. The results demonstrated that there was indeed an added benefit in changing the relative percentages of the layers with different orientations rather than changing the total thickness of the laminate. If not the first, this was one of the early applications of optimization in composite structures, and was the beginning of a series of publications that Jim Starnes either actively participated or provided support for their development.

In the years following the initial optimization study mentioned above, Jim Starnes’ attention turned to the much needed studies on, among other things, the mechanics of composite structures, buckling and postbuckling of composite laminates, and in particular to the effects of local stress concentrations such as holes and notches on composite laminate response. Series of articles published during the early 80’s established the ground work for modeling of such effects and their experimental verification. It was in the summer of 1981 the present author worked for Jim Starnes at Langley as a summer intern while he was a graduate student at Illinois Institute of Technology under the guidance of Raphael T. Haftka. The experimental work performed during this period on the effects of slots and notches on the buckling and postbuckling behavior of laminated plates later formed the basis for development of a capability to optimize stiffened plates with damage tolerance constraints.

Optimization of stiffened composite panels with local stress concentration in the form of a crack, Fig. 1, was performed for demonstrating the use of fracture constraint as a damage condition during design.⁵ A linear finite element analysis with special crack tip element was used to compute Stress Intensity Factor (SIF) along with its

sensitivities with respect to the design variables, which were the continuously varying thicknesses of plies with fixed angles. In a similar study, Haftka and Starnes⁶ used optimization method to tailor the stiffness distribution in compression panels with holes utilizing a point stress failure criteria. Optimally tailored panels were fabricated and tested to compare efficiencies obtained compared to the uniform cross-section laminates.⁶ Similar tools were also used for optimal design of laminates for stiffened panels with a damage tolerance

constraint under compressive loads.⁷ The significance of this latter work was the inclusion of a micromechanical failure model that considered the fiber kink formation, see Fig. 1, during the laminate optimization.

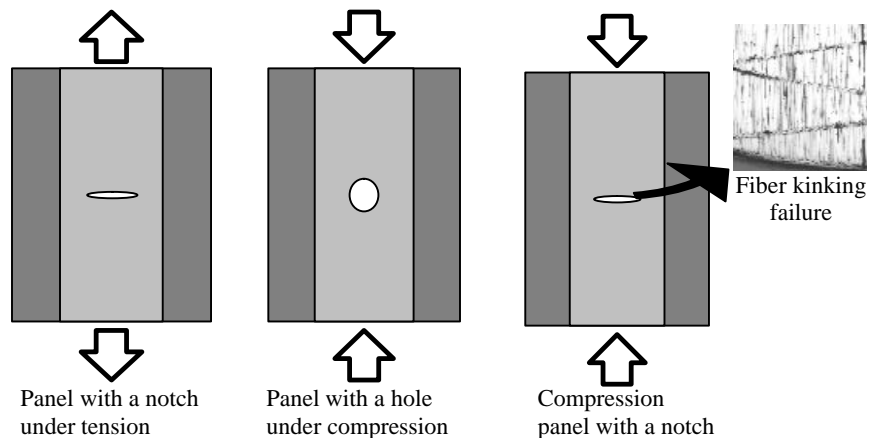


Figure 1. Stiffened panel optimization with stress concentrations.

As the confidence level in using optimization in composite laminate design for structural applications grew and as the more powerful computing was possible for the structural analyses, the complexity of the structural configurations and the analysis approach used for the design became increasingly more sophisticated.⁸⁻¹¹ For example, the simple strength criteria based optimization of stiffened panels with holes performed earlier was amended by adding buckling constraints.⁸ For the panel analyses, a computer code capable of performing buckling and vibration analysis of assemblage of prismatic finite strip components capable of modeling complex stiffened panel configurations, Fig. 2, along with a finite element analysis code for the local stress concentrations was used. The finite strip analysis was imbedded in a computer code called PASCO (Panel Analysis and Sizing Code) which used a constrained minimization algorithm CONMIN. The effect of the hole, which could not be accounted by the buckling analysis code, on the load carrying capability of the panel was taken into account by establishing a linear approximation to the strength constraint via the finite element code. Selected optimized panel configurations were later tested experimentally, comparing the analytical predicted failure loads with the experimental ones.⁹

Computationally more challenging laminate optimization problems were the ones that involved nonlinear analyses for response computations, such as the design of imperfect cylindrical shells and compression panels capable of operating in a post buckled state.^{10,11} For example, for the design of imperfect anisotropic ring-stiffened circular cylindrical shells under combined axial compression, torsion, and internal pressure loads, a branched shell analysis code that assumed a nonlinear axisymmetric prebuckling equilibrium state in the shell wall was used, allowing us to study the effects of imperfections on optimal designs.¹⁰ Minimum weight design for compressively loaded stiffened panel laminates for postbuckling performance were determined in Ref. 11, and the comparison of panel weight and imperfection sensitivity between the linear analysis based designs and nonlinear analysis based designs were made. In general, the designs that were obtained based on the nonlinear analysis were lighter and less imperfection sensitive.¹¹

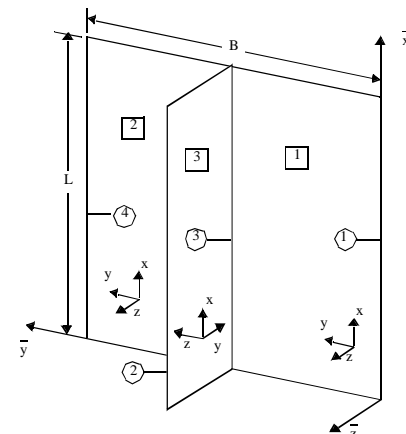


Figure 2. Linked-plate model used for linear and non-linear analyses.

B. Laminate Design with Discrete Variables

Although the traditional optimization schemes with continuous variables have been used successfully for optimization of laminates, the stacking sequence design is a discrete optimization problem and calls for methods that

can handle discrete layer thicknesses and fiber orientations. It is this realization that led to the development of various discrete optimization techniques¹²⁻¹⁷ for the design of fiber reinforced composite laminates.

A straightforward modification of a nonlinear optimization method for continuous variable problems by using a penalty approach was one of the early ways of handling discrete variables.¹² The approach used is very similar to the Sequential Unconstrained Minimization Technique commonly employed to convert constraint minimization problems to unconstrained one. In addition to the penalty terms associated with constraints, the approach appends the augmented objective function with penalty terms to force the design variables to converge to a set of prescribed discrete values. Application of the method to computationally challenging design optimization of rectangular composite plates for postbuckling performance demonstrated the approach for laminate optimization.¹⁴

A more elegant approach was the one introduced by Haftka and Walsh,¹⁵ who posed the laminate design problem as a linear integer programming problem using ply identity 0/1 integers. By using flexural lamination parameters, they have shown that the buckling load of a rectangular laminate can be expressed as a linear function of the ply-identity variables. The approach was then expanded to the design optimization of laminates with buckling and strain constraints, in which the strains that are nonlinear in terms of the ply-identity variables were linearized and the problem is solved sequentially.¹⁶ Among discrete optimization approaches, one of the most versatile one proved to be the Genetic Algorithms (GA)¹³ approach, which is discussed in the following. A somewhat more comprehensive discussion of the discrete optimization of laminated composites, including a graphical procedure originally introduced by Mitsunori Miki for continuous variable designs then adopted by the author for discrete optimization,¹⁸ was provided in a NATO Advanced Science Institute series paper.¹⁷

As stated above, one of the most heavily used optimization tool for laminated composites is the GA. A survey of the international literature on that topic is likely to produce large number of publications, which are beyond the coverage of the present paper. Even the number of publications of our local group on the subject is considerable, and spans a wide range of issues that are designed to improve the performance of the GA's and make them specifically suitable for composite laminate design.¹⁹⁻²⁸ Following the initial application of the GA to a laminate optimization problem by Le Riche¹⁹ a number of additions were implemented to improve the computational efficiency of the algorithm. Despite all the advantages of the GA's, large number of analyses that are typically needed to find a reliable optimal solution is one of its biggest disadvantages. Some of the improvements were, inclusion by Kogiso of a memory using a binary-tree to eliminate repeated analysis of previously analyzed designs,²¹ and a local improvement scheme to implement a local approximation using lamination parameters,²² which are then applied to the design of a stiffened composite panel.²³ Other improvements include the use of derivative based approximations to evaluate the effects of stacking sequence changes,²⁴ and use of generalized elitist scheme to clone multiple high performance individuals from one generation to another.²⁵

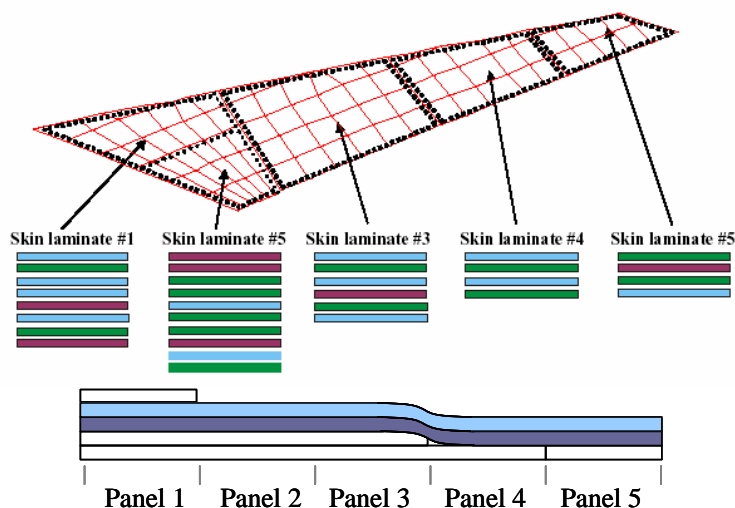


Figure 3. Wing skins laminate with individually optimized laminates and blended panels.

A more significant improvement, however, was the treatment of structures that are composed of multiple laminate segments with different thicknesses. This is a typical situation in designing larger structures in which different parts are designed for different loads. For example, a schematic of a wing skin laminate shown in Figure 3 may have different optimal stacking sequences for the different sections of the wing. From the fabrication perspective, such a situation will be highly unacceptable since there may not be any continuity of the layers from one panel to another. In an ideal situation, one would expect the laminate stacking sequence of the thin sections of the wing to continue and be presents almost unaltered in the thicker sections of the laminate.

Therefore, the extension of the GA based design of blended laminates across multiple sections of a structure has been the topic of recent work.²⁶⁻²⁸ Initially a practical multi-step blending approach was adopted,²⁶ in which in the first step each laminate is optimized to determine the minimum layup thickness distributions. Once the layup with the smallest thickness is determined, a laminate of that thickness whose stacking sequence is to be optimally determined was assigned over the entire structure with additional laminates with unknown stacking sequences added at appropriate thicker sections. A more sophisticated version of the blending process was later developed based on evolution of the individual layups for the different sections of the laminate in different genetic populations with migrating individuals from adjacent populations providing the blending pressure.²⁷ Although the process also made parallelization of the design effort trivial (each population evolving on a different processor of a cluster), the method occasionally converged to local optimum making the method unreliable. A more recent effort is to use a guide laminate that is to be designed, and that applies every panel, with the caveat that each laminate is obtained from the same guide by eliminating plies. During the analysis phase of the GA, a guide design (a single individual from the population) is evaluated to determine the optimal initial sequence for each local panel satisfying loading constraints and minimizing weight. This is accomplished by stripping ply layers from the guide design, starting from the outermost (for outward blending) layers, one layer at a time and analyzing the resulting designs according to the constraints for each local panel.²⁸ The process works well and for the test problems studied produced the lightest design for complicated blending problems.

III. Novel Structural Concepts

High material cost of composites may also be offset by innovative design concepts that lend themselves to cost effective manufacturing. Besides the cost effectiveness, novel concepts often require investigation of the effects of various design features and sizing variables, uniquely defined by the concept in hand, on the performance of the structures. As such, they provide a fertile ground for implementing optimization schemes forming the second important aspect of tailored structures. From the early stages of composite design activities, NASA LaRC has pursued and promoted ideas to come up with innovative and advanced structural concepts that will outperform traditional structural components. Frequently, these advanced concepts and configurations used and relied on unique manufacturing techniques.

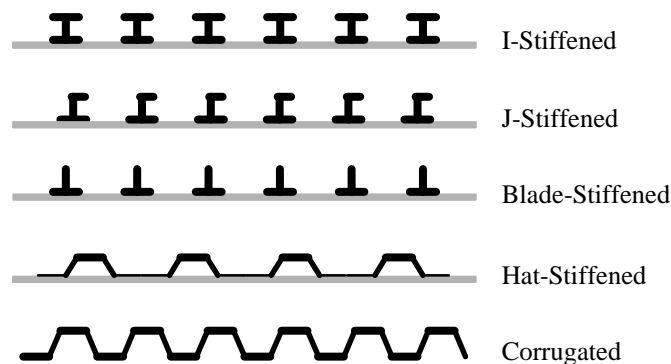


Figure 4. Various panel cross-sectional geometries used for efficiency studies.

It may be argued that advances in manufacturing go hand in hand with the development of advanced structural concepts to accelerate the introduction of composite parts into widespread use. For example, with the development of the thermoforming process efficient stiffened plate concepts, such as corrugated panel and beaded panel concepts have emerged. In early 90's the author and some of his students started looking into the analysis²⁹ and design of various panel configurations, including corrugated panels, and their structural efficiencies under loads.³⁰ Another example is the use of Resin Transfer Molding (RTM) or Resin Film Infusion (RFI) processes, which led to the fabrication of braided integrally stiffened panels to

became possible. For the design of such a configuration, manufacturing considerations have been incorporated into the design optimization of a blade-stiffened composite panel.³¹ For the manufacturing analysis, a one-dimensional resin film infusion model is developed to compute the infiltration time of the resin into a fabric preform of the panel. The structural problem is formulated to minimize the panel mass subject to buckling constraints. A simplified buckling analysis model for the panel is used to compute the critical buckling loads. The objective of the manufacturing problem is to minimize the resin infiltration time. Optimum panel designs for the manufacturing and structures problems alone, as well as for the combined problem, are generated using a genetic algorithm. These results indicate a strong connection between the structural and manufacturing design variables and trade-offs between the two responses.

One of the best examples of a successful transition of a fabrication technique to an innovative design concept is for filament wound shells, where a pressure vessel can be fabricated by winding strands or tows of fibers around a

mandrel in the shape of the vessel itself. By changing the rotational speed of the mandrel, the speed of the filament winding head along the vessel axis of rotation, and the profile of the spherical domes of the ends of the vessel, fiber orientation angles that provide the most efficient reinforcement with respect to the stress states in the shell walls can be achieved. Filament winding has also been successfully extended to stiffened structural components such as grid-stiffened panels and geodesically stiffened shells. Therefore, study of the optimization of grid-stiffened composite structures became a topic that NASA LaRC was interested in.³²⁻³⁴ Initially, structural efficiency of optimally designed grid-stiffened panels were studied.³² Lack of efficient analysis tools that capture the local skin buckling and stiffener buckling modes during design optimization iterations led to the development of a cost effective analysis procedure.³³ The concept was also studied for the optimal design of shells³⁴, Fig. 5.

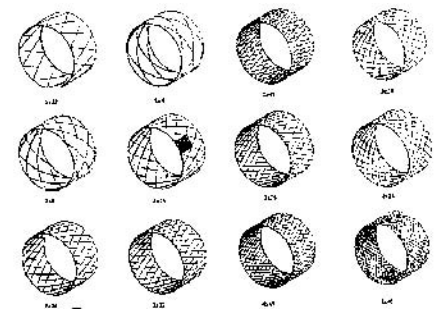


Figure 5. Grid-stiffened shell design.

One of the more intriguing novel structural concepts was the one that has been developed in conjunction with NASA LaRC, called Variable Stiffness (VS) Laminate Concept, shown in Fig. 6. The concept utilizes curvilinear fiber paths yielding structures with spatially varying stiffness properties. Since the stiffness properties, such as the longitudinal and transverse moduli and the Poisson's ratio, depend on the local fiber orientation angle, a curvilinear layer will have variable stiffness properties as opposed to a traditional straight-fiber layer that has constant in-plane stiffness properties. Hence, the laminates constructed of layers of curvilinear fibers were dubbed variable stiffness laminates.³⁵ Such laminates not only have variable in-plane stiffness properties, but in general possess variable bending and coupling stiffness properties as well.

The concept has been under investigation since the early 1990's for thin-walled composite structures under NASA funding.³⁵ In an effort to integrate realistic fabrication techniques into the design of laminates with curvilinear fiber layers, research carried out by Gürdal and Olmedo³⁵ introduced a fiber path definition and formulated closed-form and numerical solutions for simple rectangular plates. Substantial buckling improvements

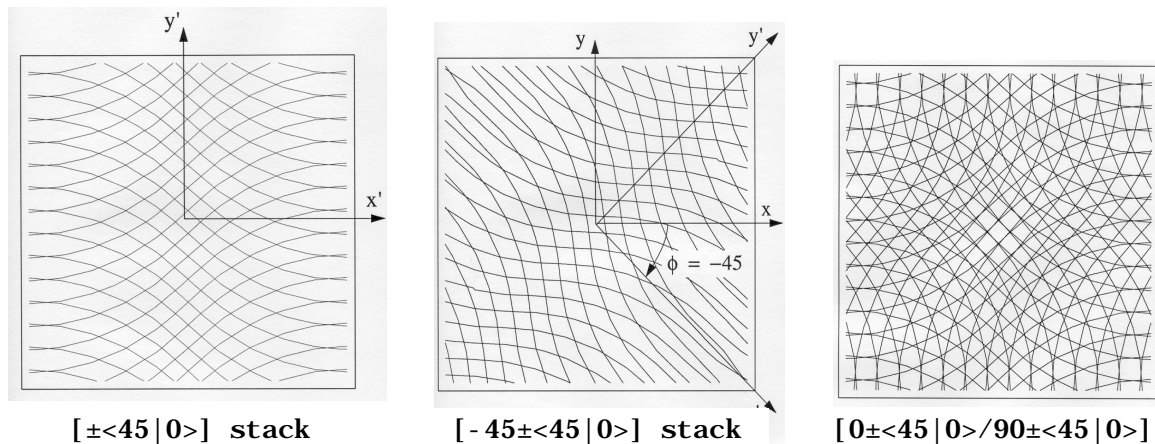


Figure 6. Various variable stiffness composite laminate lay-ups.

for such panels have been numerically shown compared to the constant stiffness laminates.³⁶ The proposed fiber path definition was intended to be used with state of the art manufacturing techniques for composite laminates, such as automated fiber/tow placement machines that allow the fiber orientation angle of a layer to vary as a function of position throughout the structure. Therefore, in a follow-up design study by Waldhart et al.³⁷ a parametric study of the small set of variables used in the fiber path definitions indicated increased buckling performance due to the stiffness variation, which in turn caused favorable re-distribution of the internal stresses. Also, additional mechanisms that help improve the buckling load of panels were also identified. Considerations for the manufacturability of the plies, based on estimates of the limitations of the advanced tow placement system, were also included to ensure the manufacturability of the designs.³⁷

Promising results of the analytical and numerical research mentioned above established the need for experimental validation of the findings. As part of the research carried out by the present authors, manufacturing

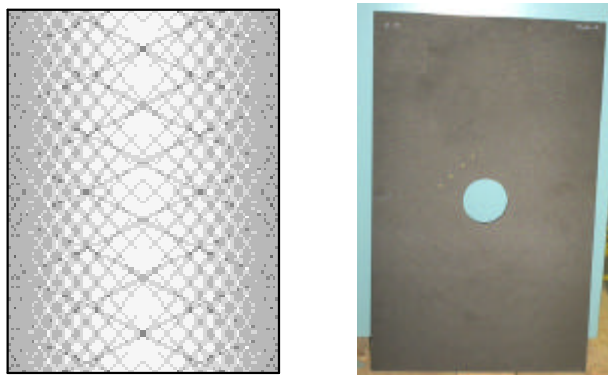


Figure 7. Theoretical Thickness Distribution and Photograph for Manufactured Tow-placed VS Panel.

ongoing research on this topic is to design, tow-placement manufacture, and testing of laminates with curvilinear layers that exhibit improved performance with respect to traditional fiber-reinforced laminates, and also analyze and correlate the predicted results with those of the experimental ones. In a series of programs, analysis of variable stiffness panels for circular holes, and panels under compressive and shear loads have been designed, fabricated, and tested at NASA Langley Research Center. The results of such studies are currently being documented for publication in the near term.

and testing of elastically tailored variable stiffness panels that exhibit improved performance compared to traditional fiber-reinforced laminates commenced³⁸. Several panels were fabricated, see Fig. 7 for example, using the VIPER[®] advanced tow placement machine made by Cincinnati Machine³⁹ to validate the manufacturability of variable stiffness laminates with curvilinear fiber paths through tow-steering. Subsequent testing by Wu et. al.⁴⁰ confirmed the increased load-carrying capability of the variable stiffness panels, with gains of up to 3-5 times the compressive buckling load of a straight-fiber panel.

The underlying goal of the currently

IV. High-Fidelity Analysis Based Optimization

In the present context the term is used not to imply the higher fidelity in final design optimization results, but to indicate the need for using high-fidelity analyses in design optimization. It was well known that one of the aims of the effort of LaRC research team was to develop high fidelity modeling for structural analysis. Early realization of the local nature of failures in composite laminates, such as delaminations, matrix cracking, and fiber kinking/microbuckling, which originate around stress concentrations such as notches and holes, stimulated the use of detailed high fidelity models in the analysis of such configurations. Another area that requires high-fidelity analyses is the geometrically nonlinear postbuckling response of thin walled stiffened panels and imperfection sensitivity of shells.

Such high fidelity analyses are often computationally expensive, and therefore, their use in optimization environment is somewhat limited. However, use of high-fidelity analyses in design optimization is necessary, because of the well known feature of optimization process that often exploits the weaknesses in the formulation and modeling to achieve optimal solutions that are far from being realistic. Recognizing this limitation, research in design tailoring of composite structures often emphasized improving the computational cost of higher fidelity analyses that can become affordable in the design optimization environment. It is for that reason that some of the earlier optimization studies mentioned earlier for structural tailoring included special analysis development to produce cost effective models within the context of design optimization.

Finally more recent research is focused on improvements to and developments of optimization schemes that will yield high quality design results. To account for the effects of local stress concentrations, the author and his collaborators have been working on local/global modeling. Also, a new combined analysis and design scheme based on the Cellular Automata paradigm has been developed. The Cellular Automata approach have been used quite successfully in the last couple of years for tailoring of laminates in terms of both topology and local fiber orientation distribution, and is currently being used for design of tow-place variable stiffness laminates.

Acknowledgments

The author acknowledges the support of NASA Langley Research Center (LaRC) through a series of grants encouraging the research in design and optimization of composite materials and structures. Many individuals both from NASA LaRC (especially individuals from what used to be the Structural Mechanics Branch, more recently called the Mechanics and Durability Branch) and Virginia Tech have contributed to the ideas and research generated over the last 25 years of authors' work. In particular two individuals, namely Dr. James H. Starnes Jr. and Raphael

T. Haftka, provided many valuable discussions that led to development of many of the ideas reviewed in this paper. A number of colleagues who worked under the NASA Virginia Tech Composites Program umbrella grant were also highly instrumental in increasing our collective understanding of the mechanics of composite structures, and the design needs. Of course what I appreciate the most and acknowledge highly is the work of many graduate students who diligently worked with me on their degree programs over the years.

References

- ¹Haftka, R. T., "Reflections on Jim Starnes' Technical Contributions," AIAA Paper No: 2005-1872, Proceedings of the 46th AIAA/ASME/ASCE/AHS/ASC Structures, Structural Dynamics & Materials Conference, 18 - 21 April 2005, Austin, Texas.
- ²Haftka, R. T., **Starnes, J. H., Jr.**, Barton, F. W., and Dixon, S. C., "A comparison of Two Types of Structural Optimization Procedures to Satisfy Flutter Requirements," *AIAA Journal*, Vol. 13, No. 10, 1975, pp. 1333-1339.
- ³Haftka, R. T. and **Starnes, J. H., Jr.**, "Applications of a Quadratic Extended Interior Penalty Function for Structural Optimization," *AIAA Journal*, Vol. 14, No. 6, 1976, pp. 718-724.
- ⁴**Starnes, J. H., Jr.** and Haftka, R. T., "Preliminary Design of Composite Wings for Buckling Strength and Displacement Constraints," *Journal of Aircraft*, Vol. 16, No. 8, 1979, pp. 564-570.
- ⁵Gürdal, Z. and Haftka, R. T., "Design of Stiffened Composite Panels with a Fracture Constraint," *Computers and Structures*, Vol. 20, No. 1-3, 1985, pp. 457-465.
- ⁶Haftka, R. T. and **Starnes, J. H., Jr.**, "Use of Optimum Stiffness Tailoring to Improve the Compressive Strength of Composite Plates with Holes," *AIAA Journal*, Vol. 26, No. 1, 1988, pp. 72-77.
- ⁷Gürdal, Z. and Haftka, R. T., "Automated Design of Composite Plates for Improved Damage Tolerance," *Composite Materials: Testing and Design*, Ed. J. D. Whitcomb, ASTM-STP 972, 1988, pp. 5-22.
- ⁸Nagendra, S., Haftka, R. T., Gürdal, Z., and **Starnes, J. H., Jr.**, "Design of a Blade-Stiffened Composite Panel with a Hole," *Composite Structures*, Vol. 18, 1991, pp. 195-219.
- ⁹Nagendra, S., Gürdal, Z., Haftka, R. T., and **Starnes, J. H., Jr.**, "Buckling and Failure Characteristics of Compression-Loaded Stiffened Composite Panels with a Hole," *Composite Structures*, Vol. 28, 1994, pp. 1-17.
- ¹⁰Ley, R. P., Gürdal, Z., and Johnson, E. R., "Optimal Design of Imperfect Anisotropic Ring-Stiffened Cylinders under Combined Loads," *Structural Optimization*, Vol. 9, No. 3/4, 1995, pp. 160-167.
- ¹¹Perry, A. C., Gürdal, Z., and **Starnes, J. H., Jr.**, "Minimum-Weight Design of Compressively Loaded Stiffened Panels for Postbuckling Response," *Engineering Optimization*, Vol. 28, 1997, pp. 175-197.
- ¹²Shin, D. K., Gürdal, Z., and Griffin, O. H., "A Penalty Approach for Nonlinear Optimization with Discrete Design Variables," *Engineering Optimization*, Vol. 16, 1990, pp. 29-42.
- ¹³Hajela, P., "Genetic Search— An approach to Nonconvex Optimization Problems," *AIAA Journal*, Vol. 28, No. 7, 1990, pp. 1205-1210.
- ¹⁴Shin, D. K., Gürdal, Z., and Griffin, O. H., "Minimum Weight Design of Laminated Composite Plates for Postbuckling Performance," *Applied Mechanics Reviews*, Vol. 44, No. 11, Part 2, 1991, pp. 219-231.
- ¹⁵Haftka, R. T. and Walsh, J. L., "Stacking Sequence Optimization for Buckling of Laminated Plates by Integer Programming," *AIAA Journal*, Vol. 30, No. 3, 1992, pp. 814-892.
- ¹⁶Nagendra, S., Haftka, R. T., and Gürdal, Z., "Stacking Sequence Optimization of Simply Supported Laminates with Stability and Strain Constraints," *AIAA Journal*, Vol. 30, No. 8, 1992, pp. 2132-2137.
- ¹⁷Gürdal, Z. and Haftka, R. T., "Optimization of Composite Laminates," in *Optimization of Large Structural Systems*, NATO ASI Series, Vol. 231, Ed. G. I. N. Rozvany, Kluwer Academic Publishers, 1993, pp. 623-648.
- ¹⁸Gürdal, Z., Haftka, R. T., and Hajela P., "*Design and Optimization of Laminated Composite Materials*," John Wiley & Sons, Inc, New York, NY, 1999, Chapters 4,7, and 8.
- ¹⁹Le Riche, R. and Haftka R. T., "Optimization of Laminate Stacking Sequence for Buckling Load Maximization by Genetic Algorithm," *AIAA Journal*, Vol. 31, No. 5, 1993, pp. 951-956.
- ²⁰Gürdal, Z., Haftka, R. T., and Nagendra, S., "Genetic Algorithms for the Design of Laminated Composite Panels," *SAMPE Journal*, Vol. 30, No. 3, 1994, pp. 29-35.
- ²¹Kogiso, N., Watson, L.T., Gürdal, Z., Haftka, R.T., and Nagendra, S., "Design of Composite Laminates by a Genetic Algorithm with Memory," *Mechanics of Composite Materials and Structures*, Vol. 1, No. 1, 1994, pp. 95-117.
- ²²Kogiso, N., Watson, L. T., Gürdal, Z., and Haftka, R. T., "Genetic Algorithms with Local Improvement for Composite Laminate Design," *Structural Optimization*, Vol. 7, No. 3, 1994, pp. 207-218.
- ²³Nagendra, S., Jestin, D., Gürdal, Z., Haftka, R.T., and Watson, L.T., "Improved genetic Algorithms for the Design of Stiffened Composite Panels," *Computers & Structures*, Vol. 58, No. 3, 1996, pp. 543-555.

- ²⁴Nagendra, S., Haftka, R.T., Gürdal, Z., and Watson, L.T., "Derivative Based Approximation for Predicting the Effect of Changes in Laminate Stacking Sequence," *Structural Optimization*, Vol. 11, No. 3/4, 1996, pp. 235-243.
- ²⁵Soremekun, G., Gürdal, Z., Haftka, R.T., and Watson, L.T., "Composite Laminate Design Optimization by Genetic Algorithm with Generalized Elitist Selection," *Computers & Structures*, Vol. 79, 2001, pp. 131-144.
- ²⁶Soremekun, G., Gürdal, Z., Kassapoglou, C., and Toni, D., "Stacking Sequence Blending of Multiple Composite Laminates Using Genetic Algorithms," *Composite Structures*, Vol. 56, No. 1, April 2002, pp. 53-62.
- ²⁷Adams, D. B., Watson, L. T., and Gürdal, Z., "Optimization and Blending of Composite Laminates Using Genetic Algorithms With Migration," *Mechanics of Advanced Materials and Structures*, Vol. 10, No. 3, 2003, pp. 183-203.
- ²⁸Adams, D. B., Watson, L. T., Gürdal, Z., and Anderson-Cook, C. M., "Genetic Algorithm Optimization and Blending of Composite Laminates by Locally Reducing Laminate Thickness", *Advances in Engineering Software*, Vol. 35, No. 1, 2004, pp. 35-43.
- ²⁹Young, R. D. and Gürdal, Z., "Importance of Anisotropy on Buckling of Compression Loaded Composite Corrugated Panels," *Journal of Aircraft*, Vol. 27, No. 4, 1990, pp. 378-380.
- ³⁰Swanson, G. D., Gürdal, Z., and Starnes, J. H., Jr., "Structural Efficiency Study of Graphite-Epoxy Aircraft Rib Structures," *Journal of Aircraft*, Vol. 27, No. 12, 1990, pp. 1011-1020.
- ³¹Henderson, J. L., Gürdal, Z., and Loos, A., "Combined Structural and Manufacturing Optimization of Stiffened Composite Panels," *Journal of Aircraft*, Vol. 36, No. 1, Jan./Feb. 1999, pp. 246-254.
- ³²Phillips, J. L. and Gürdal, Z., "Analysis and Optimum Design of Geodesically Stiffened Composite Panels," in *Composite Materials Design and Analysis*, Eds. W.P de Wilde and W.R. Blain, 1990, pp. 509-528.
- ³³Gürdal, Z. and Grall, B., "Analysis of Geodesically Stiffened Composite Panels with Discrete Stiffeners," *Journal of Aircraft*, Vol. 31, No. 5, 1994, pp. 1197-1204.
- ³⁴Gürdal, Z. and Gendron, G., "Optimal Design of Geodesically Stiffened Composite Cylindrical Shells," *Composites Engineering*, Vol. 3, No. 12, 1993, pp. 1131-1147.
- ³⁵Gürdal, Z. and Olmedo, R., "Composite Laminates with Spatially Varying Fiber Orientations: Variable Stiffness Panel Concept," *AIAA Journal*, Vol. 31, No. 4, April 1993, pp. 751-758.
- ³⁶Olmedo, R. and Gürdal, Z., "Buckling Response of Laminates with Spatially Varying Fiber Orientations," Proceedings of the 34th AIAA/ASME/ASCE/AHS/ASC Structures, Structural Dynamics and Materials (SDM) Conference, La Jolla, CA, April 1993.
- ³⁷Waldhart, C. J., Gürdal, Z., and Ribbens, C., "Analysis of Tow Placed, Parallel Fiber, Variable Stiffness Laminates," Proceedings of the 37th AIAA/ASME/ASCE/AHS/ASC Structures, Structural Dynamics and Materials (SDM) Conference, Salt Lake City, UT, April 1996.
- ³⁸Tatting, B. F. and Gürdal, Z., "Design and Manufacture of Tow-Placed Variable Stiffness Composite Laminates with Manufacturing Considerations," Proceedings of the 13th U.S. National Congress of Applied Mechanics (USNCAM), Gainesville, FL, 1998.
- ³⁹Wu, K. C., and Gürdal, Z., "Thermal Testing of Tow-Placed Variable Stiffness Panels," Proceedings of the 42nd AIAA/ASME/ASCE/AHS/ASC Structures, Structural Dynamics and Materials (SDM) Conference, Seattle, WA, April 2001, paper no. 1190.
- ⁴⁰Wu, K. C., Gürdal, Z., and Starnes, J. H., "Buckling and Postbuckling of Tow-Placed Variable Stiffness Panels," Proceedings of the 43rd AIAA/ASME/ASCE/AHS/ASC Structures, Structural Dynamics and Materials (SDM) Conference, Denver, CO, April 2002, paper no. 1512.

This page left blank intentionally.

Accelerated Insertion of Materials - Composites

Charles R. Saff*
Technical Fellow
Structures

Gail D. Hahn
Associate Technical Fellow
Materials and Processing
Boeing – Phantom Works
St. Louis, MO

John M. Griffith
Technical Fellow
Manufacturing Tech.

Robert L. Ingle
Senior Manager
Structures
Boeing Phantom Works
St. Louis, MO

Karl M. Nelson
Technical Fellow
Materials and Processing
Boeing Phantom Works
Seattle, WA

Abstract

The benefits of integrated product definition teams to balance requirements from multiple sources have been known for years. Each functional expert has knowledge, analysis, and test techniques that are not readily accessible or understood by others. What would happen if the functions could be optimized simultaneously? What would happen if the materials focal could see the impact of a change on a structural analysis? What would happen if the structural analyst could trade design considerations with manufacturing defect probabilities? What would happen if the uncertainties associated with analytical techniques and test methods were dissected, understood, and tracked?

DARPA devised the Accelerated Insertion of Materials initiative to answer these questions by challenging Materials, Manufacturing, Structures, Math and Computing personnel to integrate the best of the tools and methodologies of their trades. A Boeing led team, along with the U.S. Government, jointly accomplished “Accelerated Insertion of Materials – Composites” under the guidance of NAVAIR as part of the DARPA sponsored Accelerated Insertion of Materials (AIM) initiative.

The Accelerated Insertion of Materials – Composites (AIM-C) program established a methodology to evaluate historical roadblocks to effective implementation of composites materials and to offer a process to eliminate these roadblocks via use of knowledge, analysis, and test to mature the material/process/design knowledge base for successful qualification and certification. Uncertainty is addressed through identification and management of error and

application of statistical and probabilistic approaches.

The AIM-C Program has successfully developed improved methods for four areas that historically have been schedule/cost drivers in past composite insertions:

- *Multi-scale modeling and global and local solid modeling applied along with the Strain Invariant Failure Theory (SIFT):* The AIM-C materials, processing, and structural analysis tools link global parametric design tools with (local) physics based micromechanics models. The micromechanics analyses used a new Strain Invariant Failure Theory (SIFT) that demonstrated first failure and failure propagation within 10% of legacy data.
- *Processing and producibility assessments which keep pace with design development and highlight issues throughout decision-making:* AIM-C processing and producibility methodology/tools have resulted in an order of magnitude reduction in time for developing processing information while eliminating unnecessary trial panel fabrication, and highlighting showstoppers in design concepts, consumable materials, and variability.
- *Durability methodology and tools:* The physics-based Strain Invariant Failure Theory (SIFT) has been integrated with an accelerated environmental test methodology enabling more accurate long term durability predictions at the component level.
- *Methodologies and the tools for uncertainty management:* Using the statistical, probabilistic, and optimizing methods of the Robust Design Computational System in the

* AIAA Fellow

AIM toolset, uncertainty analysis and quantification techniques now can be more efficiently considered in design trades.

Introduction

The objective of the Accelerated Insertion of Materials Program is to provide the concepts, approach, and tools that can accelerate the insertion of composite materials into DoD systems. The primary concepts used to enable accelerated insertion of materials include: the definition of an integrated product team (IPT) made up of both the technology and application development members; the use of a disciplined, orchestrated maturation plan developed by this IPT; the combination of this maturation plan with existing knowledge, analysis tools, and test techniques, that enable accelerated development of a design knowledge base (DKB) from which maturity of the material system is determined; and the incorporation of an early key features fabrication and test article to focus the insertion, qualification, and certification efforts.

In the development of the methodology presented herein, two groups of people were instrumental in helping us define the roadblocks and pitfalls that caused the failure of previous attempts to accelerate insertion of materials into systems. The first of these was the Design Team which included several people who had led IPTs that sought to use composite materials in their systems but had either encountered problems too difficult to overcome, or had spent considerable time and money to overcome the obstacles. It was important to gather their experience before we developed this methodology so that we knew it would address the critical shortcomings of previous attempts. Secondly, we instituted a Certification Team – a group of leading members of the government agencies most responsible for certifying composite structures that could not only give us their experiences, but could also review the methodology we developed and give us feedback on it and guide it toward a process that would lead to certifiable structures when the methodology was applied. Jim Starnes was the Structures person for the NASA team. Jim was a tremendous encourager to the AIM-C team and regularly offered guidance, criticism, and help as needed throughout the development. The AIM-C Team and the aerospace industry as a whole lost two great members of our profession in the loss of Jim Starnes and Jack Lincoln (leader of the Air Force Certification Team). Both were

strong supporters of the efforts being conducted by the AIM-C team.

This paper describes the approach taken to combine these concepts into a cohesive plan to accelerate maturation for successful insertion. During the development of this methodology, several analytical and test tools were developed to aid the IPT in developing their plan and in predicting and assessing the capabilities of the material system being introduced. The methodology described herein, the analysis tools that support it, their generation, validation, and the software that house those tools can be found in the AIM-C Final Report, Vol. 1, Reference 1.

Purpose

– The purpose of this paper is to present the methodology developed during the AIM-C program that can accelerate development of the design knowledge base required for insertion of new materials into DoD systems. To achieve this purpose the AIM-C program evaluated the historical roadblocks to effective implementation of composites; offers a process or protocol to eliminate these roadblocks. The AIM-C program provides a strategy to expand the use of the systems and processes developed to technologies beyond those of materials and structures. It provides a software tool that facilitates evaluation of composite materials for various applications; as well as providing a mechanism for acceptance by primary users of the system. And the program provided validation of the methodology, and toolsets by those responsible for certification of those applications in which new materials are used.

This paper presents the key elements of the methodology, their content, how they are applied, and how they each contribute to the acceleration of insertion defined by the process. Before summarizing these key elements of the methodology there are some important concepts and relationships that must be defined.

Qualification and Certification Definitions

Throughout this document, the words qualification and certification will be used frequently. In general, unless the context provides a different interpretation, qualification will be used to mean the knowledge base developed on a material system, under particular process conditions, that demonstrates ability for meet a specific set of materials and process

specifications (Reference 2). Certification will be used to refer to that knowledge base for a material system, fabrication process, and assembly procedure that meets the design requirements for a given component of a DoD system. In this definition set, qualification refers to the general acceptability and limitations of a material and process and certification refers to the ability of the material and process to perform as required in a specific application (Reference 3). These definitions are depicted in Figure 1 to show that the DKB developed by the AIM-C methodology consists of both data sets and while there is much shared between these datasets, specific applications often do require more data focused toward that application than is contained in the qualification dataset.

The design knowledge base developed by the AIM-C system includes both qualification data and certification data for a specific application. This was intentionally done because accelerated qualification does not necessarily ensure accelerated insertion. The development of the DKB must go beyond qualification data to the certification data for the given application in order to ensure insertion.

The Design Knowledge Base

The Design Knowledge Base (DKB) for AIM-C is that knowledge that qualifies the materials for use and certifies the material for use in specific components of the aerospace system being to which it is applied. In general terms the elements of a design knowledge base for aerospace systems was defined by a set of experienced leaders of integrated product development teams as shown in Figure 1. This figure identifies everything that the IPT desired in the DKB, a portion of which was the focus of the AIM-C Phase 1 effort.

It should be noted that while the AIM-C team focused on the materials and processing, manufacturing, and structural aspects of this DKB, we did address some elements of the supportability and miscellaneous categories. In general, the methodology in AIM-C was developed at high levels for the majority of the categories shown in Figure 1 and in depth for only the highlighted elements shown. This allowed us to address the broad issues surrounding accelerated insertion, while still allowing us to focus on a few for more complete development. Those few that are more fully



Figure 1. Integrated Product Team's View of the Design Knowledge Base

developed will pave the way toward the understanding required to extend the methodology to those elements that were addressed at only the higher levels.

Approach Overview

The foundational practice used in the development of the AIM-C approach was the Building Block approach to structural maturity that has been used since the introduction of composite materials into aircraft structure before we had the kind of accurate and comprehensive toolset that we now have for these materials. Faced with the need to be able to certify such structures from a single static and fatigue test as had been done with metallic structures (and because the airframes were then primarily metallic), application development teams, in conjunction with certification agents, developed a method based on increasing complexity of testing that linked the final airframe test through component tests, subcomponent tests, critical detail tests, element tests, to the coupon level tests which could be used to wring out the performance limits of the materials under various service environments. The basic Building Block Approach is shown in Figure 2.

The Basic Building Block Approach as presented in Figure 2 is a solid and secure foundation for certification of aircraft structures and makes no assumptions about the level of analytical capability available since it was developed when

composite analysis techniques were unproven. However, AIM-C also applies validated analysis tools that can radically reduce the amount of testing required to achieve the same level of confidence demonstrated in the Building Block Approach in an accelerated manner as shown in Figure 3. Here instead of relying on test data from each level of complexity to feed the next, the focus is on developing the database needed to support the fabrication and test of a full-scale key feature test article. This test article is used to ascertain readiness for certification of the application of the material, processes, fabrication technique, assemble, and the design.

The AIM-C approach differs from the conventional Building Block approach in two ways to accelerate insertion of a new material system. First, and most obviously, the multi-disciplinary, integrated product team concept develops the DKB much more rapidly than the sequential Building Block approach. This is true even without acknowledging the effect of analysis capability, but is dependent only on the ability to cover a number of needs with a few tests when they are jointly planned. Second, the focus on the key features fabrication and test article provides a focus for the early knowledge

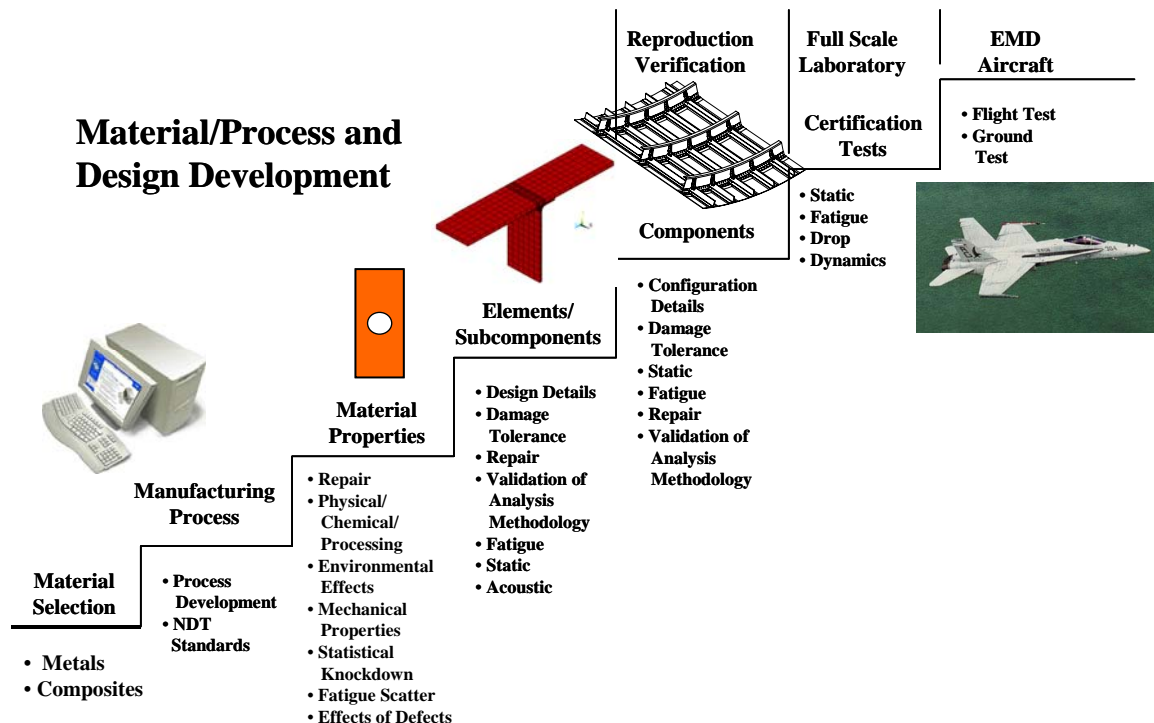
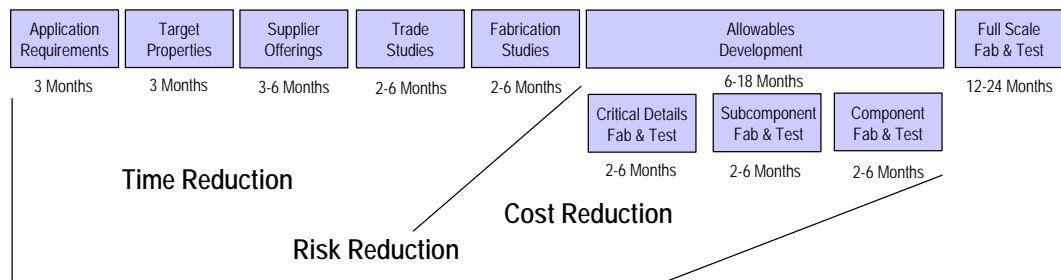


Figure 2. Conventional Building Block Approach to Airframe Certification

development, a gate for the technology into certification, and a source of failure mode and repair information that can help focus and reduce

Conventional Building Block Approach to Insertion



The AIM Focused Approach to Insertion

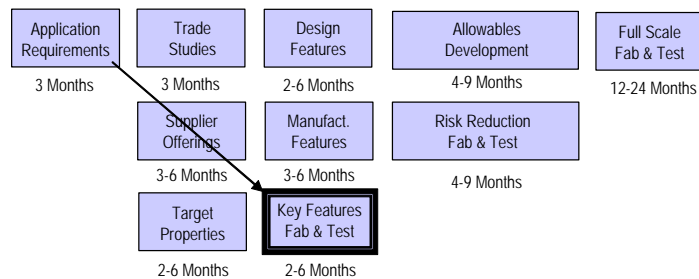


Figure 3. Comparison of the Conventional Building Block Approach with the AIM-C Approach

certification testing. The disciplines involved in the plans developed under the AIM-C Program are identified in Figure 4.

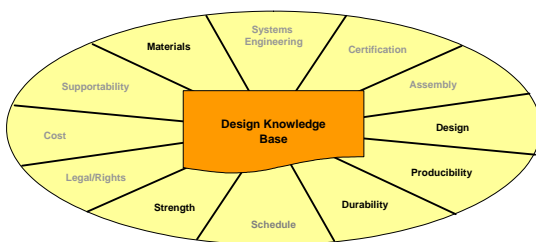


Figure 4. The Disciplines Involved in Developing the Design Knowledge Base take Data from It and Contribute to It

The AIM-C approach is a multi-faceted plan to achieve safe, reliable, and rapid insertion of a material system into a DoD application with minimum risk of failure as the application approaches certification. The approach consists of assembling an integrated product team of the technology and application development members, assessing the readiness of the material for insertion, determining the requirements for the application, determining how the IPT will determine conformance with those requirements, gathering the knowledge by existing knowledge, test, and analysis to fulfill the requirements, assessing the conformance to requirements to determine if the knowledge gathered can be committed to the design knowledge base, or

whether there are elements of the knowledge that require a different approach to ensure robustness.

There are gates at each step denoted by technology readiness level throughout the maturation process; however, there are two primary gates which are impacted most by AIM-C methodology. The first is the technology readiness review (TRL= 0) in which the IPT reaches the consensus that the material, its support materials, and its processes can be obtained with sufficient reproducibility that materials evaluated can be obtained using rudimentary requirements sheets to achieve the same pedigree. Another key review (TRL= 3) is at the time of the decision to proceed with the key features fabrication and test article(s). The materials, processes, and fabrication techniques must be capable of producing full-scale parts consistent with the designs for this application. Moreover, the key features article should demonstrate predictable geometry, response, strength, failure modes, and repair capabilities so that parts subsequently fabricated are not outside of tooling, processing, analysis, and repair capabilities.

As the AIM-C methodology is expressed in this report, please note that it is also applicable to the insertion of other technologies.

Baseline Best Practices

There were a number of Best Practices that were used in the development of the AIM-C methodology. These Boeing Best Practices include: Integrated Product Teams, Quality Function Deployment, Technology Readiness Levels, and ISO 9000. These practices and methods are defined here and their use within the AIM-C System is examined so that as the methodology is presented the use of these practices will be evident.

First, Integrated Product Teams are multi-disciplinary teams used throughout much of industry so that the knowledge base resident within each discipline can be brought to bear on the solution of a problem. Design solutions are a known compromise among affected disciplines and must not result in a design having a weakness overlooked by a discipline that is not represented. IPTs have been so successfully applied to design, build, and test of high performance products that they are now being introduced into manufacturing and most recently into technology development to reap similar

gains to those achieved in design. The benefit of a multi-functional team to develop a DKB is the rapid assessment of the requirements imposed by affected disciplines in the development and evaluation of a new materials system even before it is ready for evaluation in trade studies.

One of the key points encountered during the course of the AIM-C Program was that IPTs doing technology development are usually separate from those doing product development. If these teams are going to successfully and rapidly insert a new material into an application, these two teams must become one team throughout the course of the insertion process. There are some very good arguments for maintaining the tie between the groups even after this point in the maturation process, but the key is that the applications team must know what the technology development team knows about the material and processes that are proposed and the technology team must know what the requirements, environments, and expectations of the materials will be in the proposed application. Neither team can be successful without this information and neither team can share it well enough to be excluded from the design discussions. They must be made into one team.

Evaluations of the applicability of a material or process to a specific component are best performed at the component level. But often it is difficult to interpret component level performance or benefit at the systems level. The house of quality process offers a tie between systems level requirements and payoffs to component level requirements and payoffs. But the relationship is not one to one. There are often component level requirements that limit how a material can perform or what processes can be used that impact the application of the material to the component. These are often requirements not defined at the systems level, but are part of the disciplinary knowledge base that comes through the IPT. Documenting these requirements is just as important as documenting the system level requirements and priorities.

The AIM-C Methodology used Technology Readiness Levels to track the maturation of the technology (material) through the insertion process. It did not take long as we formulated IPTs under the AIM-C Program to realize that although various disciplines used Technology Readiness Levels (TRLs) to track technology

maturity, they did not interpret their TRLs consistently. Technology developers tended to start their TRLs with the discovery and

Technology Readiness Levels										
Technology Development	1	2	3	4	5	6	7	8	9	
Application Development				1	2	3	4	5	6	7

Figure 5. The Discrepancy Between Technology Based TRLs And Application Based TRLs

documentation of a new capability. Application developers tended to start their TRLs at the stage when the technology was reproducible and when they could receive a specified product using an initial definition or specification. As shown in Figure 5, these TRL definitions are out of phase with one another.

This discrepancy in definition between these two TRL definitions, led to confusion between the technology development teams and the application development teams. This discrepancy was not unique to AIM-C but has existed since the formation of the Readiness Level definitions. The Air Force has always focused on a more applications oriented set of TRLs fostered by Dr. Jack Lincoln the specialist in airframe certification for so many years (References 4 and 5). At the same time NASA used a set of TRLs that was more closely aligned with the technology development TRLs, since TRL of 0, an IPT between the technology development team and the application development team is formed and a Technology Readiness Review is held to determine that its properties and projected costs are attractive, that the technology (or material) is reproducible, and that the system ready to begin the AIM-C insertion process. If that review is positive for the material, then that team continues to work toward maturation of the system to insertion. While the process works through all TRL levels, it is really most focused on levels 0-4 for the AIM-C program because that is where most of the risk reduction is done that eliminates the showstoppers and risks for insertion to the application. Levels 5-8 deal with design certification and readiness for production, and levels 9-10 deal with production and support for the product. they were so often looking at embryonic technologies at the research level (Reference 6).

Once the discrepancy was realized, a single set of Technology Readiness Levels was determined focused on the application as shown in Figure 6. Technology Readiness Level 0 was defined to encompass all the development work from discovery to the development of a reproducible process at the laboratory or pilot plant scale.

Technology Readiness Levels										
Technology Development	0.25	0.50	0.75	1	2	3	4	5	6	
One Team										
Application Development				0	1	2	3	4	5	6

Figure 6. The Common TRL Numbering Scheme Adopted by AIM-C

A common maturity tracking method certainly helps an IPT, but it is not sufficient to ensure a successful insertion of a new material into an aerospace application. Lessons learned from previous material systems gave us some rather specific do's and don'ts that can spell the difference between successful insertion and insertions stopped without recourse. Some of these lessons learned are identified and categorized in Figure 7. In that Figure, we have segregated the lessons into particular disciplines so that the lead for that discipline can review and refresh the understandings that drive designs in particular directions (away from one fabrication method, toward another for example).

Once a common definition for the meaning of each TRL was defined, then the progress of the entire IPT could be tracked according to a single TRL-based chart. This chart is shown in Figure 8, but its use is described in greater detail in later sections of this report. This chart became the IPT's primary means of assessing the maturation of a material, or technology, through insertion.

Customer / Stakeholders	IPT	Design	Allowables
Regulatory agency understands and approves methods used to insert materials	Full time focus of development team	Design teams can make design decisions before design guidelines were established	Testing for allowables costs too much
Customers are ready for 1) price, 2) service level, 3) maintenance & inspection reqs, and 4) repair requirements	Development maturity in one area that outstrips the general maturity can be detrimental to the overall process	Preliminary design values can be developed with very few tests in prototype. How do we move into this paradigm with reduced risk for operational vehicles?	Must establish the requirements for the material
Customer is part of IPT in good and bad times	If materials development lags product development, the product is at risk	Concept development is done without regard to materials - this imposes limitations on designs, concepts, and costs	Early specs did not address the variables which impacted the process downstream
When customer changes, the tolerance for risk, vision, and technical criteria change	Has the material been used on other products or is it currently in use on other products?	Multifunctional parts require different designs than we traditionally look at.	Must test durability, aging, and environmental effects
Identify stakeholders early	Is an industry database available?	Design criteria that are late in being developed or established can eliminate new materials from the design space.	Moisturization takes a long time
Need to resolve conflicting requirements	IPTs need to be much larger than is currently perceived. They must include more administrative disciplines.	When designers do not follow composite design guidelines, there will be problems manufacturing parts.	Must understand long term environmental exposure effects
Material decisions must be made with the head and not with the heart.	Must demonstrate the ability to manufacture parts as designed	Design capabilities for composite parts and tools are required.	The impact of proof testing on certification and risk reduction must be determined.
Government programming - large scale demos instead of basic materials and structural data. These programs leave many unaddressed issues and uncertainties	Need an On-the-Floor support staff capable of identifying problems and resolving them.	Conceptual design tools impose load paths that make composites a tough sell.	Due to miscommunication, the entire materials qualification program was run with an incorrect posture - autoclave cycles used in the lab were not validated.
	Material form not compatible with design requirements and manufacturing process (K-3 wing, tow vs slit tape, fabric types, large T/castings)	Incorrectly stacking design or lay-up sequence	Lower performance of the materials in design details
	Lack of interface between design, materials, and manufacturing	Product design requirements and objectives must be met	Coupon data doesn't translate into elements

Figure 7. A Portion of the Lessons Learned from the AIM-C Design Team and the Certification Team

TRL	0	1	2	3	4	5	6	7	8	9	10
IPT Reviews	Technology Readiness Review	System Requirements Review	Initial Design Review	Preliminary Design Review	Critical Design Review	Ground Test Readiness Review	Flight Test Readiness Review	Operational Readiness Review	Production Readiness Review	Production Support	Recycle or Dispose
Application/ Design	Concept Exploration	Concept Definition	Proof of Concept	Preliminary Design (Elements)	Design Maturation (Revised by Subcomponent Testing)	Revised by Component Testing	Revised by Ground Testing	Revised by Flight Test	Production Support	Recycle or Dispose	Design Support
Certification	Qualification Plan Assessment	Certification Elements Documented	Certification Plan Approved	Elements	Subcomponent Testing	Full Scale Component Testing	Full Scale Airframe Tests	Flight Test Eval	Op Eval	Production Approval	Disposal Plan Approval
Assembly/ Quality	Preliminary Assembly Concept Assessed	Assembly Concept	Assembly Plan Definition	Key Features/Assembly Detail Definitions	Subcomponents Assembled	Airframe Assembled	Flight Vehicles Assembled	EMD Assembly	Low Rate Initial Production (LRIP)	Production	Disassembly for Disposal
Survivability	General Requirements Assessed	Requirements Definition	Concept Definition	Preliminary Design Data and Guidelines	Critical Details Testing	Design Allowables and Guidelines Defined	Ground Test	Flight Test	Operational Testing	Production Support	Operations Support & Disposal
Fabrication/ Quality	Fabrication Capability Demonstrated	Unfeatured-Panel Fabrication	Feature Based Generic Small/Subscale Parts Fabricated	Property-Fab Relationships Tested/ Target Application Pilot Production of Generic Full Size Parts	Process Specs/ Effects of Fab Variations Tested/ Elements Fab'd/ Production Representative Parts Fab'd	Full Scale Components Fabricated	Full Scale Vehicle Components Fabricated	EMD Fabrication	Low Rate Initial Production (LRIP)	Production	Recycle or Disposal
Supportability	Repair Requirements Assessed	Repair Items/Areas Identified	Repair Materials & Processes Identified	Repair Materials & Processes Documented	Fab Repairs Identified	Fab Repair Trials/ Subcomponent Repairs	Component Repairs	Production Repairs Identified	Flight Qualified Repairs Documented	Repair-Replace Decisions	Support for Recycle or Disposal Decisions
Structures & Durability	Preliminary Properties-Characteristics Assessed	Preliminary Properties-Characteristics	Initial Properties	Design To Properties Developed	Preliminary Design Allowables	Final Design Allowables	Allowables for Critical Design Features	Production and Test Support	Certified Allowables	Flight Tracking/ Production Support/ Fleet Support	Retirement for Cause
Materials	Lab-Prototype Materials	Lab-Prototype Materials Reproducible	Pilot Production Materials	Pre-Production Materials	Production Scaleability Validated	EMD Material Supplied	EMD Material Supplied	EMD Material Supplied	LRIP Material Supplied	Production Material Supplied	Support for Recycle or Disposal Decisions
Cost/Schedule/Benefits	Cost Benefit Elements ID'd & Assessed	Cost Benefit Elements ID'd & Projected	ROM Cost Benefit Analysis	Cost Benefit Analysis Reflect Size Lessons Learned	Cost Benefit Analysis Reflect Element and Production Representative Part Lessons Learned	Cost Benefit Analysis Reflect Subcomponent Fab & Assembly Lessons Learned	Cost Benefit Analysis Reflect Component Fab & Assembly Lessons Learned	Cost Benefit Analysis Reflect EMD Lessons Learned	Cost Benefit Analysis Reflect LRIP Lessons Learned	Cost Benefit Analysis Reflect Production Lessons Learned	Cost Benefit Analysis Reflect Disposal Lessons Learned
Intellectual Rights	Concept Protection Plan Developed	Protection Plan Documentation	Patent Disclosure Filed	Proprietary Rights Agreements	Data Sharing Rights	Vendor Agreements	Material and Fabrication Contracts	Production Rate Contracts	Vendor Requal Agreements	Post-Production Agreements	Liability Termination Agreements

Figure 8. Technology Readiness Chart for a Materials Insertion IPT

While these lessons learned and the subsequent Technology Readiness chart were developed by the AIM-C Design Team, they were reviewed, revised, and added to, in some cases by the Certification Team, which is identified in Figure 9. This is where the work of Jim Starnes and Jack Lincoln and a number others was so important to the AIM-C team. Their experience with certifying and maturing composite technologies over the years was a crucial element in the development of the AIM-C Methodology.

Agency	Integration	Structures	Materials	Producibility
Air Force	Tim Jennewine & <i>Jack Lincoln</i>	Dick Holzwarth	Katie Thorp	Bob Reifenberg
Army	Mark Smith	Jon Schuck	Marc Portanova	Steve Smith
Boeing	Charley Saff	S. Eric Cregger	Pete George	John Griffith
FAA	Curt Davies	Larry Ilcewicz	David Swartz	David Ostrodka
NASA	Mark Shuart	<i>Jim Starnes</i>	Tom Gates	Tom Freeman
NAVAIR	Don Polakovics	David Barrett	Denise Wong	Steve Claus

Figure 9. The AIM-C Certification Team

ISO 9000 concepts were used to ensure that in each discipline at each TRL, there was an approach and a plan for how the IPT was going to achieve conformance with the requirements for the application and an assessment of the conformance of the knowledge (existing data, analysis, heuristic data, or test data) with the requirements before the data was committed to the Design Knowledge Base (DKB). Each discipline develops its own approach to meeting the requirements of the component, but the IPT has to approve the integrated plan including the approach to achieving conformance and assuring that each discipline will get knowledge consistent with its needs at each stage. The IPT must also validate conformance was achieved prior to committing the data to the DKB. Therefore, the approach for each element of IPT plan for conformance with

requirements, there was an approach defined, data gathered, an assessment of the data gathered against the requirements and a committal to the DKB or a rework (or changed approach) in order to achieve conformance for that element of the plan.

Methodology Ground Rules - Methodology provides the disciplined process that captures the designer's problem statement, communications the problem to the integrated technology/product team via the AIM-C system, and provides solutions for the designer with confidence levels, risks/drivers, risk mitigation options, and links to further detail. Our methodology is built on the following ground rules:

- a. Integrate the building block approach to insertion.
- b. Involve each discipline in maturation.
- c. Focus tests on needs identified by considering existing knowledge and analyses.
- d. Target long lead concerns, unknowns, and areas predicted to be sensitive to changes in materials, processing, or environmental parameters

The methodology is imparted to users via the following formats:

- a. User interface screens/prompts
- b. Linked text files
- c. Software documentation
- d. Training
- e. Methodology/process definition and change procedures document

AIM-C Features to Accelerate Insertions – A summary of the features introduced in the AIM-C approach is given in Figure 10.

The software system developed to aid the IPTs in applying the AIM-C methodology was embodied in a modular software package, for which the main menu page is shown in Figure 11.

Accelerated Insertion of Materials Is Achieved in AIM-C Methodology by

- Focusing on Real Insertion Needs (Designer Knowledge Base)
- Approach for coordinated use of
 - Existing Knowledge
 - Validated Analysis tools
 - Focused Testing
- Application of Physics Based Material & Structural Analysis Methods
- Use of Integrated Engineering Processes & Simulations
- Uncertainty Analysis and Management
 - Early Feature Based Demonstration
 - Tracking of Variability and Error Propagation Across Scales
- Rework Avoidance
- Disciplined approach for pedigree management

Orchestrated Knowledge Management to efficiently tie together the above elements to DKB

Figure 10. AIM-C Features to Accelerate Insertion

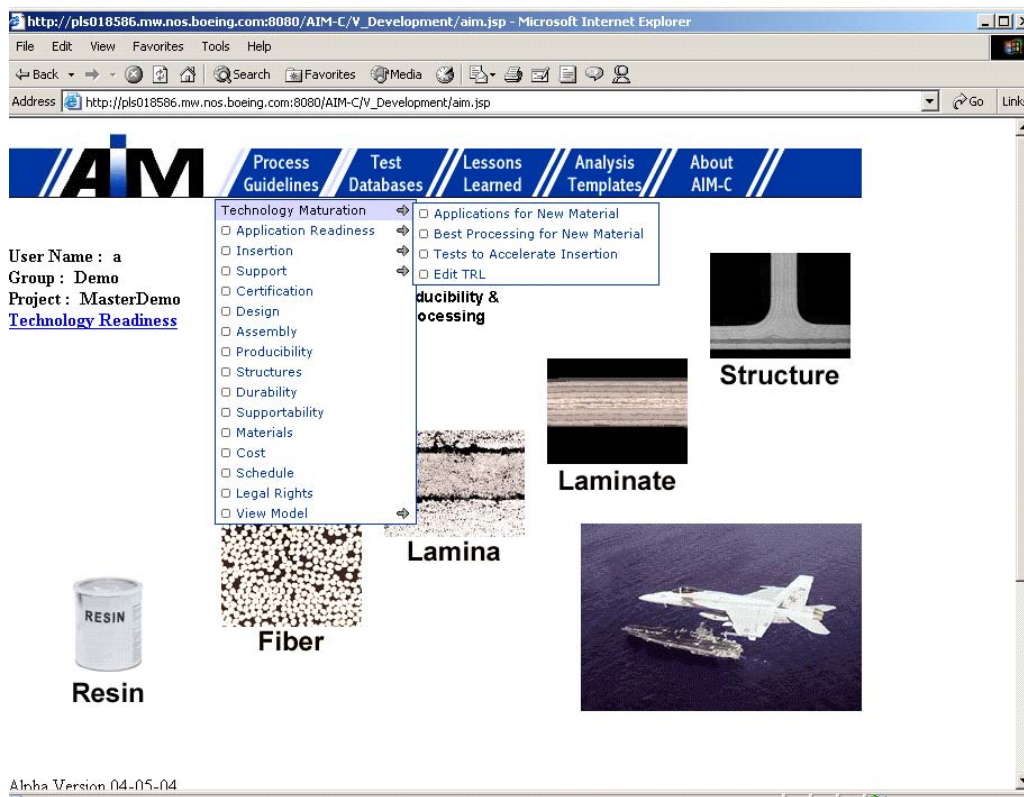


Figure 11. Main Menu for AIM-C Software System

The basic system is described in Figure 12. The system was developed to be web-based and machine independent using the latest Java and open source codes for the backbone of the system and for the object-oriented relational database used within it. There are numerous lessons learned from this attempt to embed a methodology guide into software. Some of the major lessons were: 1) The software must allow for IPT manipulation to adjust the methodology to fit the need. The current methodology embedded in the software is old and cannot be updated readily because too much of it was hardwired to get it working for immediate needs. 2) Software that houses large datafiles must be resident at one location accessible via the web from any location and be capable of additions or modification from here according to strict enforcement of editing protocols. Distributed computing is certainly possible and was demonstrated in this program, but the time required to pass large databases across the internet is too great for efficiency. It is far better to allow access and modification and provide exceptional computing power at the host location. 3) The AIM-C software acts well as a host and repository of the tools used, and does provide version control those tools, but it does not perform the guidance function for users that we had originally sought.

System v 1.4.1

Architecture / Backbone

Database

Logic Engine

GUI

Help

Utilities

Post_SFT v1_0_2

Post_Thermal v1_0_2

Rdcs2file v_1_0_0

Spring in and Deflection V1.0.0

Modules

Fiber v_1_0_0

Resin_and_Adhesive v_1_0_0

Lamina v_1_0_0

Laminate v 1.3.0

Processing v_3_1_3

Prepreg v_1_0_0

Durability

Integrated Durability Tool v1.0.0

Delamination Durability Tool v_1.1.0

Stanford Durability v_1.0.1

 Super Mic Mac.xls v 1.0.1

 Micromechanics.xls v_1_0_0

DURASOFT-HTM v_3.0.0

Thermal Degradation v_1_0_0

Producibility v_1.0.0

ResinMan, v_1_0_0

WinASCOM Public Version 1.0

ISAAC, Boeing, V_1.0.0 (Template 21)

ISAAC, Boeing, V 2.0.0

Figure 12. The Basic AIM-C System

The Methodology

The overall approach applied for each element of the plan is shown in Figure 13. This approach to DKB development used in AIM-C is entirely consistent with the concepts of ISO 9000. To have an approach defined prior to application, to monitor the application of the process, measure results to ascertain conformance, and to apply corrective measures if conformance is not achieved are all consistent with ISO 9000 concepts. The serendipitous product of this approach is that any DKB developed by the AIM-C approach is readily documented as ISO 9000 compliant.

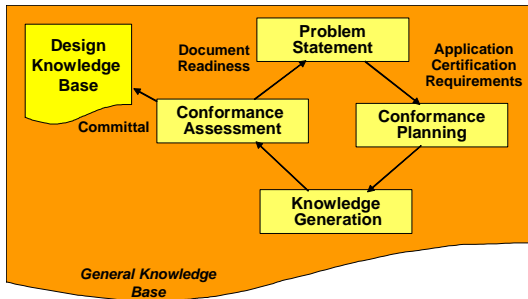


Figure 13. The AIM-C Process for Design Knowledge Base Development

The Problem Statement Generation - The problem statement bounds the qualification program by providing a clear statement of the desired outcome and success criteria. It delineates responsibilities for appropriate aspects of the program to the material supplier, processor, test house, prime contractor and the customer. It serves as the foundation for many decisions and as the basis of the business case as well as divergence and risk analyses on which the technical acceptability matrix is built. When the problem statement is found to be deficient in specificity, or to be so specific as to limit approaches, or to have a clear technical error, modifications must be made with the agreement of the qualification participants and stakeholders.

Problem Statements can take many forms: they can be statements of the desire to determine what material fits a given application best, they can be

statements of determining what application fits a given material system best. Most often it is a combination of materials and potential applications that are being examined to determine where the greatest payoff for a match of material system and application lies. Note that when we refer to a material system we are including the processing involved in fabricating a part from that material. If either the material or the fabrication process change, then the system has changed.

The first step in developing the Problem Statement is to determine the level of risk that can be tolerated for the match of application and material system. The level of risk that can be tolerated depends on the maturity of the system to which it is to be applied. Production aircraft can accept little to no risk, development aircraft more, and experimental aircraft more still, and conceptual aircraft can accept the greatest risks. Figure 14 shows that the scope of the effort required to overcome these risks is greater for higher risk conditions and lesser for lower risk conditions. But the scope is not always determined by the risk, it is sometimes dictated by the limits of schedule and costs of the effort. In these cases this chart can identify the disparity between the risk, the scope of the effort required to reduce risk, and the scope being allowed to accommodate that risk.

	New Application	Existing Application
New Material New Process	Greatest Scope	Moderate to High Scope
New Material Existing Process	Moderate to High Scope	Moderate Scope
Existing Material New Process	Moderate Scope	Low to Moderate Scope
Existing Material Existing Process	Low to Moderate Scope	Least Scope

Figure 14. Selecting the Scope of the Effort Allowed

Once the team understands the relationship between the scope of the effort allowed they are allowed to perform and the choices in technology that can be applied to the application, then they can go down another level in detail and address individual material systems and their potential applications to determine which fall within the bounds of the risk reduction scope they have been afforded. This is done using a chart like that shown in Figure 15.

required to meet those needs from the technology development point of view. A simple assessment of the scope of the effort is mapped across this assessment. The scope definitions are a complete development (100%) which goes from initial process development, to properties development, to Key Features article fabrication to allowables development. To the ability to insert the material system with out testing, based on current experience with similar or more rigorous applications, that have already produced the database required to certify the application.

		New Application					Existing Application				
		Primary wo Cert.	Primary W. Cert	Secondary wo Cert	Secondary with Cert.	Tertiary wo Cert	Primary wo Cert.	Primary W. Cert	Secondary wo Cert.	Secondary with Cert.	Tertiary wo Cert.
New Mat'l or Process	No Proof of Reproducible Props.	100%	100%	100%	100%	90%	80%	70%	60%	50%	40%
	Proof of Reproducible Properties	100%	100%	100%	90%	80%	70%	60%	50%	40%	30%
	Producer Spec	100%	100%	90%	80%	70%	60%	50%	40%	30%	20%
	Company Spec	100%	90%	80%	70%	60%	50%	40%	30%	20%	10%
Existing Material or Process	Tertiary Application without Cert.	90%	80%	70%	60%	50%	40%	30%	20%	10%	0%
	Secondary Application without Cert.	80%	70%	60%	50%	40%	30%	20%	10%	10%	0%
	Secondary Application with Cert.	70%	60%	50%	40%	30%	20%	10%	0%	0%	0%
	Primary Application with Cert	60%	50%	40%	30%	20%	10%	10%	0%	0%	0%
	Multiple Certified Applications	50%	40%	30%	20%	10%	0%	0%	0%	0%	0%

Figure 15. Detailed Problem Statement Definition

Here the applications are broken down into the scope of the effort required to meet certification requirements and the level of development

Finally, the problem statement itself is prepared which simply states the material system selected and the application selected and the key objectives being sought in the combination. Once the Problem Statement has been formulated it is checked using a list of questions like those that follow.

- Is the problem statement (or application requirements documentation) captured in writing like a story problem?
- • Is the objective clearly identified?
- Has the information necessary to solve the problem been identified?
- Has extraneous information been identified as such?
- Is this statement an identification of the problem or erroneously identification of a desired or anticipated solution?
- Are the critical checks/issues being captured for the next stage of the qualification/certification process, conformance planning?
- Are all of the appropriate stakeholders (including customers) involved and concurring to the statement?
- Have applicable assumptions, compromises, and contingencies been identified in writing?
- Is the problem statement in a useable form for a Strengths, Weaknesses, Opportunities, Threats (SWOT) analysis?
- Was a check made of past showstoppers/major issues related to problem statements of a similar nature? (This will be addressed in more detail in planning for conformance, but should also be addressed in the problem statement to help achieve early understanding among stakeholders.)
- Does the problem statement consider the applicable inputs needed from the following readiness level categories?
 - Application
 - Certification
 - Legal Considerations
 - Design
 - Assembly
 - Design Allowables
 - Development/Structures
 - Materials and Process Development
 - Fabrication/Producibility
 - Supportability
 - Business Case

Requirements Definition - Quality Functional Deployment, via a House of Quality concept is used in the AIM-C Program to simply document the relationship of requirements from the systems level to the component and technology levels. Insertion cannot be successful without meeting the requirements. Unsuccessful insertions have most often been stopped, not by a lack of knowledge about potential show stoppers, but because people did not carefully document and share the requirements for the

component or material or manufacturing process or did not address the issues they knew existed. Without documentation these issues can be ignored to the peril of the insertion. An example of Quality Function Deployment is shown in Figure 16.

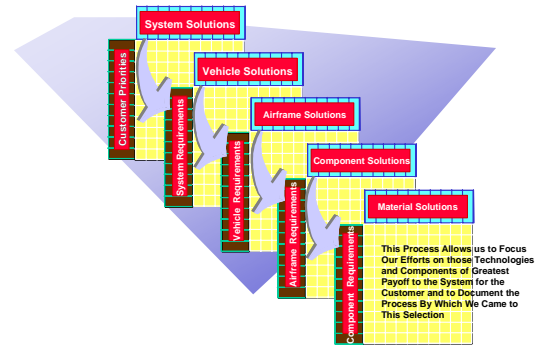


Figure 16. Quality Function Deployment Is Used in AIM-C to Document the Linkage between System Level Requirements and Technology Requirements

The primary advantage of the House of Quality System is that it ties the System level requirements to the component or part level requirements at which materials system are applied. It also allows us to roll up the benefits of a given technology to determine its effect on the system level capabilities or benefits. The primary benefit of the activity is to document the link between the system, vehicle, airframe, component, and part level requirements and benefits so that application trade studies can be performed in a knowledge rich environment.

Another key element of the requirements definition process is to determine the requirements imposed by the AIM-C process. The overall TRL definition, previously shown in Figure 8, can be drilled down to the individual disciplines for each TRL level to form what we term xRL sheets which guide the functional leads toward the data required to support other disciplines at each step of the process. These xRL Worksheets give:

- Detailed multiple discipline perspective of information needed to address the problem statement;
- Identification of *why* conformance activities need to be done
- Exit criteria guide established for creating lower level xrls, that deal with specific
- Disciplinary problems

- Covers all disciplines involved in the process
- Provide an application perspective along with materials perspective
- Exit criteria guide established for creating materials and processing/producibility
- xrls
- Covers technical areas and production readiness

At the lower level xrl level, the guide is generic, addressing technical and production readiness areas. The guide has been exercised with composite materials, hand layup processing/producibility, and analytical tools. The generic guide is used to establish specific readiness charts according to the technologies being addressed. And the guide was used to establish specific composite material xrl examples and hand layup/autoclave cure examples. Some examples of these lower level guides are shown in Figure 17.

Application Information		Application/ Material Information		Material Information		
Indicate Ultimate Strength - Uniaxial Compression	Bonded Interface Joint Strength-Damage Initiation	Durability/Life- Microcracking	Durability/Life- Delamination Growth	Material Mechanical Properties - Primary (Tension, Compression, Shear, Bearing/Bypass)		
Indicate Ultimate Strength - Uniaxial Tension	Bonded Interface Joint Strength- First Failure			Material Mechanical Properties - Secondary (CTE, Poisson's, Fracture Toughness)		
Ultimate Strength- Combined Loads	Bulk Joint - Bearing/Bypass			Material Mechanical Properties - Other ()		
Indicate Ultimate Strength - Open Hole Compression	Medium Diffusion			Material Durability/Life Properties - Environmental Impact on Properties		
Indicate Ultimate Strength - Open Hole Tension	Residual Strength - BMD Compression	Durability/Life- Stiffness Degradation	Durability/Life- Bearing Strength Degradation	Material Durability/Life Properties - Impact Resistance and Fatigue		
Ultimate Strength- Open Hole Combined Loads	Residual Strength- Penetration, Tension			Material Durability/Life Properties - Solvent Resistance		
Stability- Global Panel	Residual Strength- Penetration, Compression					
Stability- Skin Buckling	Residual Strength- Penetration, Combined Loads					
Stability- Stringer Crimping	Local Stability- Free warping (Stretch/Chy)					
Stability- Stringer Column Buckling	Local Stability- Inboard Buckling (Stretch/Chy)					
	Local Stability- Shear Crimping (Stretch/Chy)					

Figure 17. Lower Level Readiness Level for specific Elements of Disciplines
Conformance Definition – Requirements
 definiton and the TRL, XRL, and xRL spreadsheets help the team to determine what must be done and why. These sheets lead to what were termed Conformance Check Sheets, like that shown in Figure 18. These sheets were a simple way to assure the team that once they had determined what path they would take to fulfill the requirements, that they had a plan that

was consistent with those requirements and the needs for accelerated knowledge gathering. The conformance check sheets define for the team what is to be done to meet requirements, how they will be done (whether by analysis, existing data, or knowledge generation), who is responsible from the functional standpoint for what data, and when that data was required by the team in order to accelerate the insertion process.

RESIN - THERMOSET	0	1	2	3	4	5	6	7	8	9	10	How Obtained, Test or Analysis	Test/Analysis Identification
Uncured Resin												Test	ASTM D 4473
Viscosity	x	x	x	x	x							Test	ASTM D 4473
Reaction Rate	x	x	x	x	x							Test	DSC via ASTM D 3418 and ISO 11357
Heat of Reaction	x	x	x	x	x							Test	DSC via ASTM D 3418 and ISO 11357
Volatiles Content/evolution temperature	x	x	x	x	x							Test	TGA
Volatiles Type	x	x										Test	Test/product knowledge FTIR/Formula access
Volatiles Vapor Pressure												Test	Test
Density	x	x	x	x	x							Analysis	Specified Value
Resin Cure Shrinkage		x	x	x	x							Analysis	Based on vendor input
Thermal Conductivity		x										Analysis	Based on calculated test data
CTE		x										Analysis	Based on TMA or linear dilatometer data
Specific Heat		x										Analysis	Assumed to be that of cured resin
Kinetics Model		x	x									Analysis	Based on Reaction Rate
Viscosity Model		x	x									Analysis	Based on Kinetics Model, Test Data
Intellectual Property Issues	x	x	x	x	x							Test	
HF/LC	x	x	x	x	x							Test	
FTIR	x	x	x	x	x							Test	
Health and Safety Information	x	x										MSDS	
Morphology	x												
Impurities Suppliers	x	x	x	x									
Cured Resin													
Tensile Strain to Failure	x	x										Test	ASTM D638
Young's Modulus - Tensile	x	x										Test	ASTM D638
Tensile Strain to Failure	x	x										Test	ASTM D638
Glass Transition Temperature	x	x										Test	ASTM D3418
Volatiles Content	x	x	x	x	x							Test	ASTM D3550
Density	x	x	x	x	x							Test	ASTM D-792
Modulus as a Function of Temp		x										Test	Function of Temp and Degree of Cure
CTE		x										Test	ASTM E831 or linear dilatometry
Thermal Conductivity		x										Test	ASTM C177
Solvent Resistance		x										Test	ASTM D545
Specific Heat		x										Test	ASTM E-1269 or Modulated DSC
Bulk Modulus		x										Analysis	ASTM E143
Shear Modulus		x										Test	ASTM E143 (Room Temp)
Poisson's Ratio		x										Test	No Standard
Coefficient of Moisture expansion		x										Test	ASTM D695
Compression Strength		x										Test	ASTM D695
Modulus Transfer Properties		x										Test	right gain vs time, Fick's Law and models
Viscoelastic Properties		x	x	x								Analysis	
Toughness Properties		x	x	x								Test	ASTM D3418
To Wet		x	x									Test	
CME		x										Test	
Solvent (Moisture) Diffusivity		x										Test	
Solvent Resistance		x										Test	

Figure 18. Planning Check Sheets Help the Team Plan the Maturation Process

As noted in the above checksheet, some of the required information can be developed using analytical tools and elementary data. Some can be developed using analysis tools and existing data, and some will have to be gathered by test. The team is encouraged to review these conformance checklists and reconfigure them to fit their needs, their scope, and their timeframe for knowledge gathering. They are a guide based on the generic readiness level requirements defined previously and so they will not match every insertion specifically. It is the team's job to make these conformance checklists match the plan they have determined to use to meet their requirements.

It should be noted that not all knowledge is gathered by analysis, test, or existing data. Process and producibility information can really only be developed by fabricating parts, and so there is within the AIM-C process a guide for manufacturing toward a very efficient and rapid knowledge gathering process that can lead to first time quality parts. Still, the knowledge

must be developed or verified using fabrication of detailed parts as shown in Figure 19, and the process by which one develops these parts is reviewed and revised as necessary by the team.

predictions in three dimensions. Still these predictions must be validated using element and

Producibility Item Assessments

- Producibility Items/Areas
 - Manufacturing/Processing
 - Cutting
 - Layup
 - Debulking
 - Bagging
 - Cure
 - Unbagging
 - NDE
 - Tooling
 - Quality
 - In-Process
 - Final Part

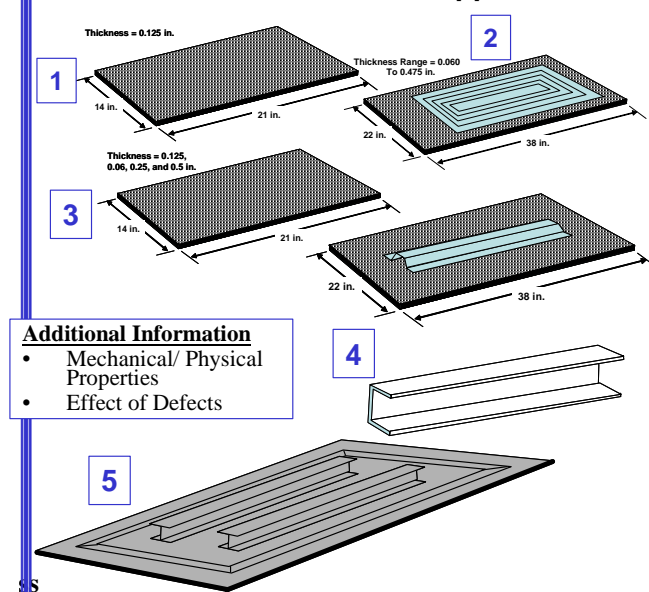
Feature Based Part Producibility Methodology/Process Steps

1. Flat Panel, Constant Thickness
2. Ramped Panel
3. Flat Panel, Multiple Thicknesses
4. Elements (Hats, C's, I's, etc.)
5. Scale-up, Size

and Producibility

All facets of the conformance planning process are enhanced by today's analytical tools. The ability to predict the response of both the tool and the part as it is processed and as it consolidates is key to the acceleration of the development of composite material systems that can meet today's stringent and aggressive goals on risk reduction. Some of these models and their use are described in Figure 20. The ability to model both tooling and the part in its unconsolidated state and then as it consolidates is the key to determining the state of the part, geometrically as well as chemically and physically, at the end of any process. The ability of today's tools to handle gapping between parts in addition to the pressures applied by the tooling to the part help us get a better knowledge of what tooling is required to achieve complex parts for tomorrow's applications. Consolidation models like COMPRO (a commercial software code from CMT, Inc in Vancouver) make these kinds of calculations in two dimensions and will potentially have capability to make such

Feature Based Part Approach



panel level component fabrication in order to ensure that the input parameters reflect accurately the behavior of the materials as it cures as well as the interaction of the part with the tool during that curing process.

Knowledge Gathering – Once the conformance plan has been developed by the team, then the knowledge gathering takes place. Here again the TRL, XRL, xRL guides the each discipline toward the exit criteria for each element of the plan. The Conformance Sheets help define how the team planned to achieve the requirements for each exit criterion. The first step consists of gathering existing knowledge on the problem statement at hand as well as related relevant knowledge on similar systems. The team works to determine the divergence of the new case at hand from previous similar experiences to assess the applicability of such “knowledge” to both

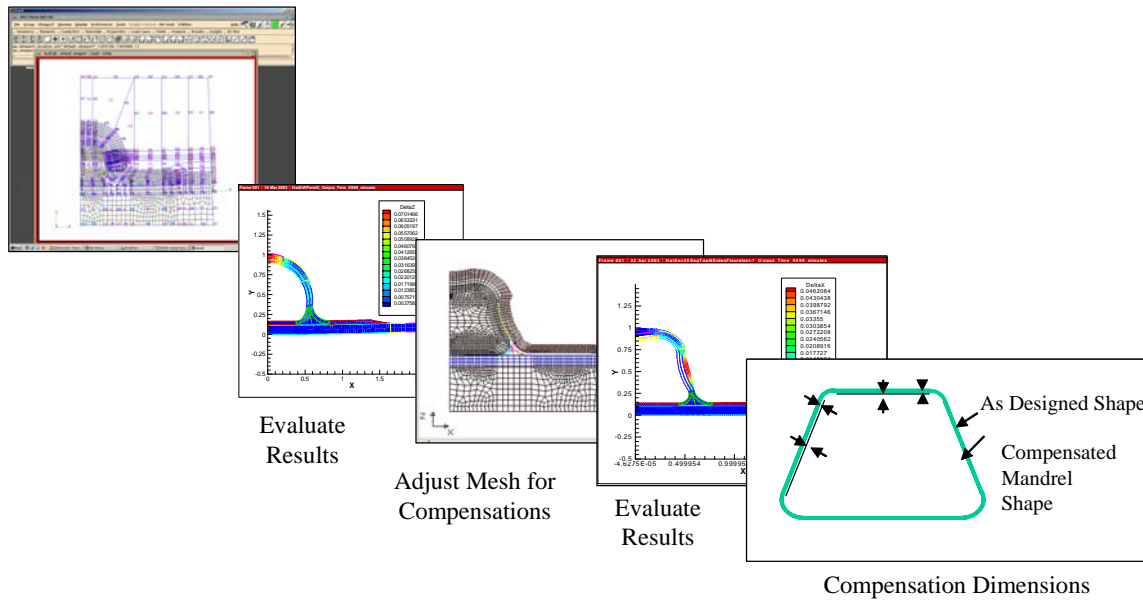


**Figure 20. AIM-C Analysis Tools Guide
Fabrication Maturation**

accelerate insertion while mitigating the risk of using understanding that might not be as directly relevant to the new problem statement as initially thought. Figure 21 illustrates the linkage and flow of readiness level criteria and knowledge generated.

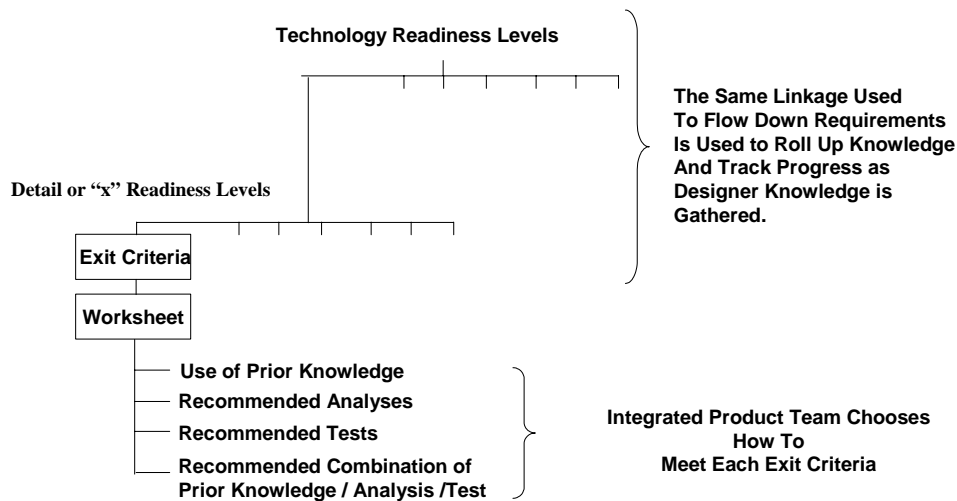


**Figure 21. Linkage of TRLs, XRLs and Exit
Criteria for Knowledge Gathering**

It is very important to reveal concerns early – cost, schedule, and technical – so that unknowns can be addressed and risk mitigation plans can be exercised if necessary. As such, it is good to ask *and document*, the handling of questions which interrogate every aspect of the material, process,

application, threat, and opportunity. Performing this type of assessment requires different perspectives – assembly personnel, business personnel, customers, designers, fabricators, manufacturing personnel, system maintainers, suppliers, technologists, etc.

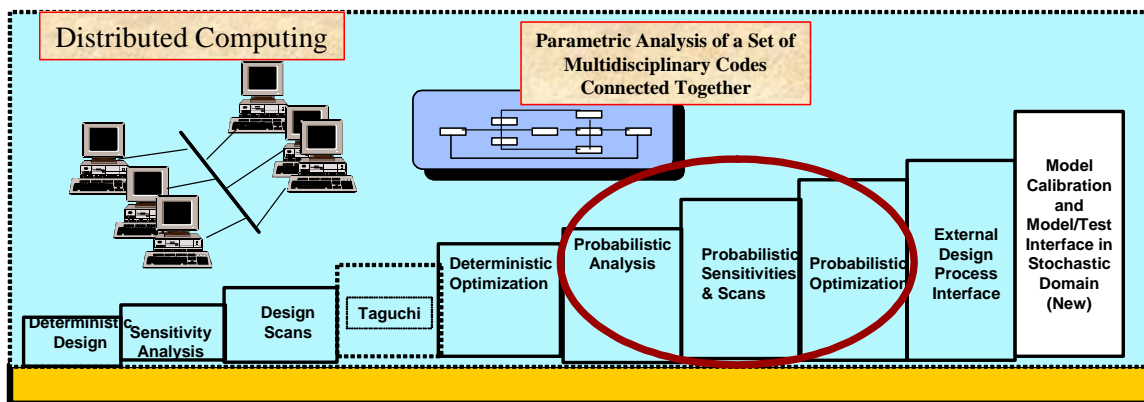
The information in this methodology and in the AIM-C system is helpful to performing strength, weakness, opportunities, and threats (SWOT) analyses on the materials, processes, and applications considered.

- Sensitivity analysis on mixed space and constrained design space exploration
- Integration of external uncertainty analysis plug-ins with RDCS

Advanced design of experiments – Design Explorer

- Probabilistic (Robust) Optimization
A capability to define statistical parameters as design variables

A Domain Independent Comprehensive Tool Set to Analyze the Design Space



Major challenges exist to ensure broad adoption of detailed uncertainty analysis across, not only data gathering and analysis, but to the understanding of the role of hierarchy in the integration of random variations into the final prediction of the variations expected from design, fabrication, and test events. But the benefits are potentially very large. These include reducing the cost and schedule associated with testing, and developing tools and approaches which make analytical statistical studies fast, accurate, easy to use, and produce understandable results. The emergence of new physically-based analysis methods and the continued enhancement of RDCS have made great inroads toward this goal, but the determination of appropriate approaches and procedures for differing applications is still under study.

Recent RDCS improvements, Figure 22, greatly expand the operating space of uncertainty analysis. These improvements include:

- Continuous, discrete and enumerated variable types

Figure 22. Robust Design Computational System Tools for Quantifying Variation

One simple example on AIM-C is the use of RDCS Probabilistic Analysis to assess the effect of constituent properties, prepreg properties, and geometric variables on the strength of open hole tension (OHT) coupons. The results of this Monte-Carlo Simulation are shown in Figure 23.

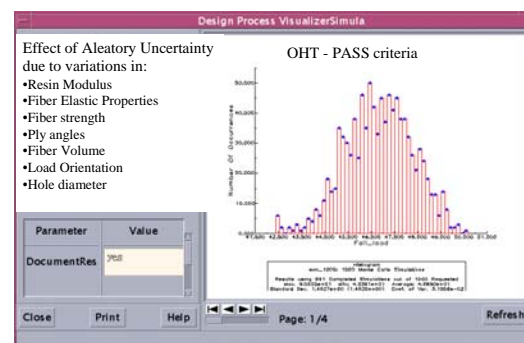
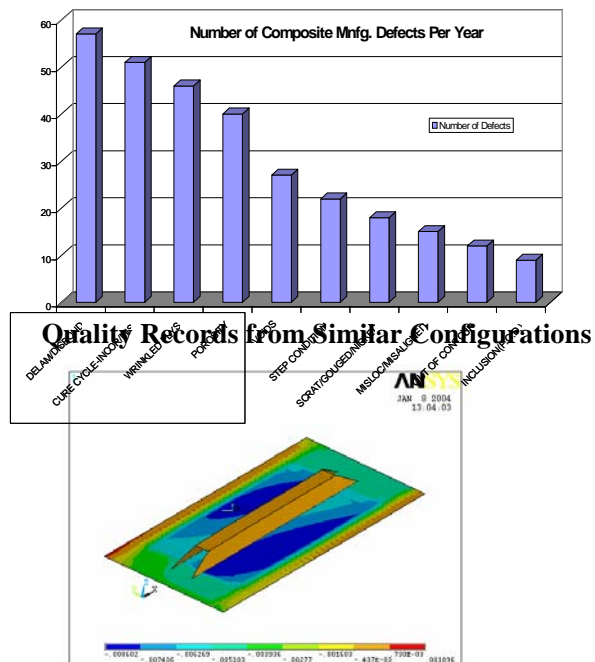


Figure 23. Monte Carlo Simulation Result for Open Hole Tension Strength

As shown in Figure 24, knowledge can consist of existing data or processing guides, analysis or simulation, or test data. Existing knowledge includes customer and supplier

validation case to the particular application of the analysis method at the time of use for maturing technology/applications for insertion.



Single Stiffener Shear Laminate Analysis

references, related quality records, previous databases, and lessons learned. It is important when using existing knowledge in an insertion assessment to understand and document the pedigree of the data (the source and the details surrounding the situation in which the knowledge was first generated or understood). It is also important to identify the difference between opinion and scientific observation. There are several sources for designers of composite airframes available today. One of the foremost is the DoD/FAA sponsored MIL-HDBK-17 (Reference 7). But, when evaluating how closely a new material might match these data, one should certainly review the equivalency criteria developed by Tomblin, et.al., (Reference 8) for the FAA general aviation segment.

When using analysis to mature technology, one must understand the pedigree of the algorithms used, the assumptions made, the uncertainties introduced, the pedigree of the input files, and the validation performed to date. Similar to distance from experience expressed in Figure 1 for previous knowledge, is the assessment of the similarity of the analysis

Single Stiffener Shear Test (front and back)

Figure 24. Knowledge of Materials Can come from Existing Data, Analysis, or Test

As with heuristic knowledge and with test data, it is imperative to document the input, the analytical method configuration control, the operating system used, and any validation planned or completed.

When establishing the qualification test matrix, the plan should be sequenced to identify critical design and manufacturing properties early so that testing and analysis can be modified or discontinued if success criteria are not met. This will minimize qualification costs and risk by eliminating inadequate alternate materials and/or processes early in the test program before more expensive qualification tests are performed. Key elements of the plan include specimen traceability of material, processing, and fabrication.

All testing has variability. It is very useful to have a list of expected test results and typical coefficients of variability (COV) based on previous testing with similar materials. When doing a second-source qualification, the COV's

are available for the existing material based on the quality control data and the original test matrix. When generating data by analysis (analogy, interpolation or extrapolation), the statistical approach to generating COV's must be clearly stated along with assumptions and a statement regarding the validity of that approach.

Conformance Assessment – Once knowledge gathering begins, conformance assessments can also start. The primary elements of conformance assessment are:

- Review available knowledge: heuristics, lessons-learned, information on similar problems or applications, public literature, analyses, and test results.
- Address every question/requirement. Address functional/disciplinary issues. Address interdisciplinary issues/assumptions/decisions as an IPT with all stakeholders involved.
- Determine divergence risk on existing information.
- Evaluate the handling of error and uncertainty.
- Assess the conformance of existing knowledge with requirements.
- Determine additional knowledge needed based on knowledge gaps, unacceptable risk, etc.
- Audit documentation, marking, completeness of information, version controls, etc.
- Secure agreement from all stakeholders. Note differences, concerns, assumptions, and highlight critical information to the committal gate at the next level of maturity.
- Commit appropriate files to the master database.
- Make a plan for corrective action on that data which did not meet committal criteria, marking, uncertainty management, etc.
- Make the committals of maturity advancement in the readiness level files. Include all required documentation at the time of committal.
- Address the business case as appropriate.
- Make the decision to continue maturing on the problem statement or

revise the problem statement as appropriate.

- If the problem is not continued, prepare and commit the decision and rationale to the knowledge base for archival purposes and future lessons learned.

Some key lessons learned from the AIM-C program was the necessity for producibility maturation to keep pace with design maturation. Whenever these two functions were disconnected and not feeding each other lessons learned and solutions, the opportunities for needless rework increased proportionately. Figure 25 is an example of how lessons learned from initial fabrication of the hat stiffeners developed under the AIM-C Program fed the eventual design. Finding that cap geometry was very tough to control, the team had the structures discipline analyze the effect of the rounded cap. Finding that this geometrical inaccuracy had no negative influence on the strength of the stiffener, the team was released to address those geometrical issues that did impact strength and durability of the panel.

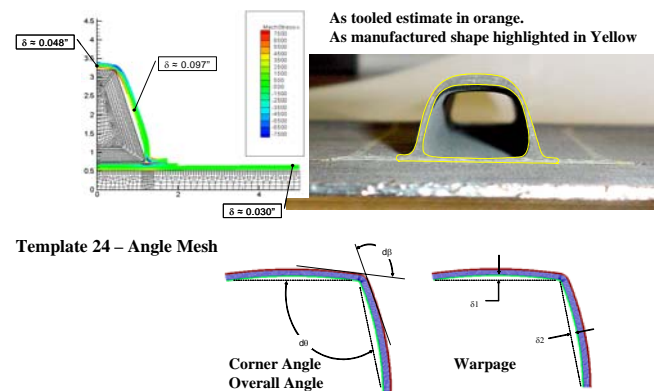


Figure 25. Processing and *Producibility Assessments Must Keep Pace with Design Development and Highlight Concerns*

The ability of the AIM-C process to highlight non conformance of all kinds and assess them from a performance impact perspective is a strength of the system. Figure 26 shows the results of a set of measurements of key conformance characteristics from one of the hat

stiffened panels fabricated under the AIM-C Program. The highlighted areas of the figure indicate locations in which measured geometries deviated from those predicted by more than acceptable limits. These were each analyzed and, as shown, some were not critical to the performance of the panel (dashed line), but some were (solid line). Those which were deemed necessary to remove from the panel, the heuristical knowledge in the system was used to develop a process that would remove the imperfection. Thus the knowledge based developed in the AIM-C methodology also helps with rework when such rework is necessary. The great savings comes when the system can determine that rework is not necessary, of course.

loading conditions that control the design of the component. At the IPT level, and for each of the disciplines that make up the IPT, the approach revolves around problem definition to focus the team, conformance planning to determine as a team how they will pursue the DKB required to fulfill the requirements of the application being considered, knowledge gathering, conformance assessment, and committal of the data to the DKB and documentation of a remaining issues for maturity cycles or other approaches applied to meet the conformance criteria. As shown in Figure 26, the approach allows the IPT team (and its leader) to have a constant visual representation of the progress the team is making through the insertion process – based on hard data that assures the team that the exit criteria

Net Defects	Tooling Cuts						Productibility								Facing
	Material	None (Bag)	Flexible	Semi Rigid	Rigid	Machined Metal	End Stream	Casting	Lump	Decubing	Bugging	Cure	Unweighting	Trimming	
Center															
Top Crown	x	< .060	< .060	< .015	< .005	< .005					x	x			
Side Crown	x	< .060	< .060	< .015	< .005	< .005					x	x			
Top Thinning	x	< .015	< .015	< .015	< .015	< .015					x	x			
Bottom Thinning	x	< .01	< .01	< .015	< .015	< .015					x	x			
Upper Radii Thickening				< .010	< .010	< .010					x	x			
Upper Radii Thinning	< .01	< .010	< .010	< .01	< .010	< .010			x	< .006	< .01				
Upper Radii Fiber Waviness		< .015	< .01							< .006	< .006				
Lower Radii Thickening	< .01	< .010	< .010	< .010	< .010	< .010			x	< .006	< .006	x			
Lower Radii Thinning	< .01	< .010	< .010	< .010	< .010	< .010			x	x	x	x			
Flange Thickening				< .01	< .01	< .01			x	x				x	
Flange Thinning		< .01	< .01	< .005					x	x				x	
Flange Edge Fiber Volume		+5% - 60%	+5% - 60%						± .02	± .05	x				
Flange Edge Fiber Waviness		< .03	< .03	< .015							x	x	x		
Nugget/Noodle Porosity/Voids		< 3% - 5 in2	< 3% - 5 in2	< 3% - 5 in2	< 3% - 5 in2	< 3% - 5 in2					x	x	x		
Nugget/Noodle Fiber Waviness	< .015	< .015	< .015	< .015	< .015	< .015					x	x	x		
Surface Finish/Roughness	< .01	± .003 to ± .015	± .003 to ± .015	< .01	< .002	< .002				± .003 to ± .015	± .003 to ± .015				
Ends															
SAME AS ABOVE															
Net - Fiber Variation		+5% - 60%	+5% - 60%						± .02	± .05	x	x	x		
Excess - Trimming Defects Determination	x							< .125 in2						< .5 in2	
Along Length															
Spacing		< .125	< .125	< .06	< .06	< .03									
Straightness		< .125	< .125	< .09	< .09	< .09									

Encoded Heuristics

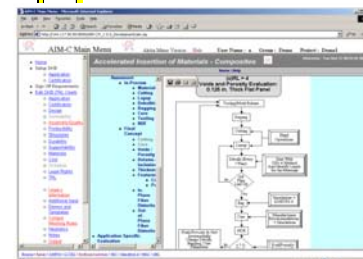


Figure 26. Ability of the AIM-C Process to Highlight Concerns for the IPT is Key to Its Success

Summary - The AIM-C approach integrates best practices, critical ground rules, and accelerated analysis and test methodologies into a process that can accelerate the risk reduction required to safely insert new materials into applications.

AIM-C methodology accelerates the insertion of materials providing a disciplined approach toward developing the design knowledge base as rapidly as possible to enable the fabrication of a key features test article that focuses the certification testing on the failure modes and

they have established have been met. In this chart green means the exit criteria have been met, yellow means that work is moving toward completing the exit criteria, and red means that there is a problem finding a plan that will meet the exit criteria as currently defined. This team is working toward the Systems Requirements Review knowledge base.

TRL	0	1	2	3	4	5	6	7	8	9
	Technology Readiness Review	System Requirements Review	Initial Design Review	Preliminary Design Review	Critical Design Review	Ground Test Readiness Review	Flight Test Readiness Review	Operational Readiness Review	Production Readiness Review	Recycle or Dispose
IPT Reviews										
Application/ Design										
Certification										
Assembly/ Quality										
Survivability										
Fabrication/ Quality										
Supportability										
Structures & Durability										
Materials										
Cost/Schedule/ Benefits										
Intellectual Rights										

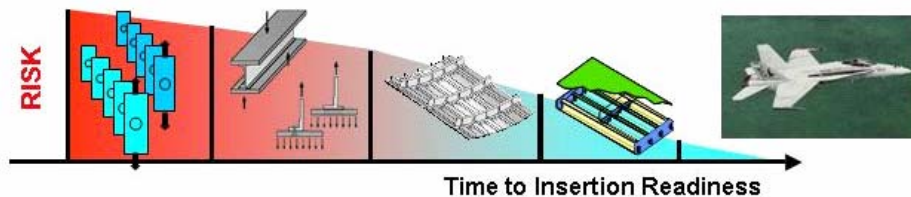
Figure 27. The AIM-C Process Gives the IPT a Clear Picture of the Porgress Toward Insertion Being Made

The AIM-C philosophy, with its focus on the key features fabrication and test article to guide development toward those features which drive design requirements, has embodied in it a planned rework cycle. In fact the Problem Statement to Conformance Planning, to Knowledge Development, to Conformance Assessment, to Committal or refinement has embedded within it a planned cycle, while

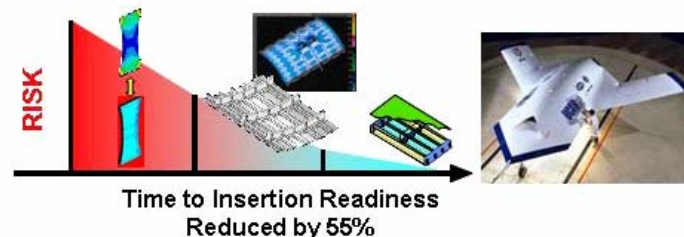
standards. The objective of this philosophy is to provide a gate for the technology at the key features test article to evaluate and mitigate the risks associated with successful certification. This is crucial. In examining past insertion failures, we found that the most expensive failures came when the technology could not be scaled-up to the sizes, or geometric requirements for the design. These lessons, learned the hard expensive way, led to incorporation of the key features full scale test article early in the development process and to evaluate risks before going further with certification.

The AIM-C methodology has been used in several exercises that demonstrate its capability to accelerate the rate at which knowledge of a technology can be gathered and used for qualifying the technology and certifying its application. The results of each of these Design Knowledge Base generation exercises has reinforced the acceleration benefits that can come from an orchestrated approach to meeting the needs for technology insertion. Figure 28 shows the results we have achieved under a number of such exercises. And it is the team's perception that the disciplined approach could reap similar gains for technologies beyond those of materials and processing as well.

Traditional Test Supported by Analysis Approach



AIM Provides an Analysis Approach Supported by Experience, Test and Demonstration



working to minimize the reliance on that “rework” cycle in certification. This philosophy is consistent with that used in the ISO 9000

figure 28. Benefits of the AIM-C Methodology Are Schedule, Cost, and Risk Reductions

Acknowledgments: This effort was conducted under the Accelerated Insertion of Materials – Composites (AIM-C) Program, N00421-01-3-0098. The team gratefully acknowledges the guidance and support of Dr. Leo Christodoulou of DARPA/DSO and Dr. Ray Meilunas of NAVAIR.

References:

1. Hahn, Gail, H., et.al., “Accelerated Insertion of Materials – Composites, Vol. 1 – Methodology,” Boeing Report No. 2004P0020, dated 12 May 2004.
2. Banisaukas, J., Office of Naval Research, Contract No. N00014-97-C-0417, “New Materials, New Processes and Alternate Second Source Materials Data Base Generation and Qualification Protocol Development,” Enclosure 4 to the Final Report dated 31 August 2000.
3. Lincoln, J. W., “USAF Experience in the Qualification of Composite Structures,” Composite Structures: Theory and Practice, ASTM STP 1383, P. Grant, Ed., American Society for Testing and Materials, West Conshohocken, PA, 2000, pp. 1-11.
4. Technology Transition for Affordability. A Guide for S&T Program Managers, <http://www.dodmantech.com/PUBS/TechTransGuide-Apr01.pdf>, April 2001.
5. Interim Defense Acquisition Guidebook, AP6. Appendix 6 – Technology Readiness Levels and Their Definitions, October 30, 2002
6. Mankins, John C. Technology Readiness Levels, <http://advtech.jsc.nasa.gov/downloads/TRLs.pdf>, 6 April 1995.
7. The Composites Materials Handbook-MIL17, MIL-HDBK-17E, Technomic Publishing Company, Inc., Lancaster, Pennsylvania, 1997.
8. Tomblin, J.S., Ng, Y.C., and Raju, K.R., DOT/FAA/AR-00/47, “Material Qualification and Equivalency for Polymer Matrix Composite Material Systems,” Final Report Dated April 2001.

This page left blank intentionally.

Increasing Design Load and Reducing Weight of Structures by Error Reduction

Erdem Acar^{*} and Raphael T. Haftka.[†]
University of Florida, Gainesville, FL, 32611-6250

Bhavani V. Sankar[‡]
Business University of Florida, Gainesville, FL, 32611-6250

and

Xueshi Qiu[§]
South West United Machinery Corporation, China

In this paper we analyze tradeoffs of design load, weight and safety of structures via probabilistic design methodology. We first perform the probabilistic analysis of a sandwich panel used in aerospace structures. We explore the effect of using a more accurate prediction technique for interfacial fracture toughness that combines interfacial fracture toughness with mode-mixity instead of using the traditional model that disregards mode-mixity. We find that the use of this more accurate model allows on average 12% increase in design load. Next, we consider structural failure due to point stress without damage propagation in a representative aircraft structure. We find that reducing errors from 50% to 10% provides up to 27% weight savings.

Nomenclature

C and R	=	Capacity and response of the structure, respectively.
e_C and e_R	=	Error factors for C and R , respectively
e^A and e^{MM}	=	Errors in fracture toughness assessment corresponding to the traditional (averaging) method and the method with mode-mixity, respectively
G	=	Strain energy release rate
G_c	=	Interfacial fracture toughness of the sandwich structure
K_I and K_{II}	=	Mode I and mode II stress intensity factors, respectively
P_{design} , W_{design} and t_{design}	=	Design load, weight and thickness of the structure, respectively
S_F	=	Safety factor of 1.5
VAR_C and VAR_R	=	Variabilities of C and R , respectively
w and σ_a	=	Width and allowable stress for the representative structure
ψ	=	Mode-mixity angle

^{*} Research Assistant, Department of Mechanical and Aerospace Engineering.

[†] Distinguished Professor, Department of Mechanical and Aerospace Engineering.

[‡] Ebaugh Professor, Department of Mechanical and Aerospace Engineering.

[§] Senior Engineer, Structural Mechanics Department

I. Introduction

STRUCTURAL design of aerospace structures is still performed with deterministic design philosophy. Researchers are constantly improving the accuracy of structural analysis and failure prediction. This improvement in accuracy reduces uncertainty in aircraft design and can therefore be used to enhance safety. However, since the record of structural safety in civilian transport aircraft is very good, it makes sense to ask how much the design load can be increased or the weight can be reduced if safety is to be maintained at a specified level. Currently, there is no accepted way to translate the improvement in accuracy to weight savings or increased design loads. The objective of this paper is to take a first step in this direction by utilizing probabilistic design methodology. Qu et al. (2003) showed that for fixed probability of failure small reductions in variability can be translated to substantial weight savings. Here we seek to investigate the potential of reduction in errors.

Sandwich structures are used in aerospace vehicles due to their low areal density and high stiffness. However, debonding of core from the face sheet is a common failure mode in sandwich construction, and the interfacial fracture is traditionally characterized by a single fracture toughness parameter. However, in reality the fracture toughness is a function of the relative amount of mode II to mode I (mode-mixity) acting on the interface (Suo, 1999). Stiffness of sandwich structures depends very much on the integrity of the face sheet/core bonding. Even a small disbond can significantly reduce the load carrying capacity, especially when the structure is under compressive loads (Avery and Sankar, 2000; Sankar and Narayanan, 2001). Grau et al. (2005) measured the interfacial fracture toughness as a function of mode-mixity to characterize the propagation of the disbond between the face sheet and the core. They performed asymmetric double cantilever beam fracture tests to determine the interfacial fracture toughness of the sandwich composite, and then demonstrated its application in predicting the performance of a sandwich structure containing a disbond. The use of mode-mixity dependent fracture toughness led to improvement in the accuracy of failure prediction of debonded structures. In this paper we perform probabilistic analysis of the debonded sandwich structure analyzed by deterministic approach by Grau et al. (2005) to explore a possible increase in the design load of the structure.

Next, with the question of trading weight for accuracy improvement in mind, we analyze structural failure of a representative aircraft structure due to point stress failure. Here we do not model damage propagation in the structure, for example, due to fatigue, corrosion, impact damage, etc. We make use of our previous work (Kale et al., 2004, Acar et al., 2004), which explored the effects of errors, variability and safety measures on the probability of failure of aircraft structural components. We utilize probabilistic design methodology to translate reductions in error bounds to weight reduction for fixed probability of structural failure.

The following section discusses the structural design of a sandwich structure and a representative aircraft structure. Section 3 presents the analysis of structural uncertainties with the main perspective of how to control uncertainty. Section 4 gives the general form of probability of failure in terms of loading, weight and uncertainty. Section 5 discusses the tradeoffs of accuracy against increasing design load or reducing weight of structures. Section 6 presents the quantification of errors and variability for the sandwich structure and the representative aircraft structure. Section 7 shows the results of increase in the design load of the sandwich structure and the weight savings from the representative aerospace structure by reducing errors. Finally, concluding remarks are given in the last section.

II. Structural Analyses of a Sandwich Structure and a Representative Aircraft Structure

In this section, we introduce the structural design analysis of the two structures that we analyzed in this paper. First, we introduce the structural design analysis of a sandwich structure, for which we explore the effects of error reduction on increasing the design load of the structure in the following sections. Next, we introduce a representative aircraft structure designed for point stress failure. For this representative structure we investigate the effects of error reduction on the weight savings from the structure in the following sections.

A. Structural Analysis of a Sandwich Structure

Sandwich panels are susceptible to debonding of the face sheet from the core. This is similar to the phenomenon of delamination in laminated composites. Disbonds could develop due to poor manufacturing or during service, e.g., foreign object impact damage. Evaluation of damage and prediction of residual strength and stiffness of debonded sandwich panels is critical because the disbonds can grow in an unstable manner and can lead to catastrophic failure. Stiffness of sandwich structures depends very much on the integrity of the face sheet/core bonding. Even a small disbond can significantly reduce the load carrying capacity, especially when the structure is under compressive loads (Avery and Sankar, 2000; Sankar and Narayanan, 2001). Under compressive loads the debonded face sheet can buckle and create conditions at the crack tip that are conducive for unstable propagation of the disbond.

Fracture at the interface between dissimilar materials is a critical phenomenon in many multi-material systems including sandwich construction. Traditionally, in engineering practice, the interfacial fracture was characterized by a single fracture toughness parameter obtained by averaging the interfacial fracture toughness, hereinafter termed as “average G_c ” or \bar{G}_c , obtained for some number of K_I and K_{II} combinations, where K_I and K_{II} are the mode I and mode II stress intensity factors, respectively. Later, studies have indicated, e.g., Suo (1990), that for these multi-material systems, the interfacial fracture is a strong function of the relative amount of mode II to mode I acting on the interface, hereinafter termed as “ G_c with mode-mixity” or simply G_c . The criterion for initiation of crack advance in the interface can be stated as

$$G_c = G_c(\psi), \quad \psi = \tan^{-1}(K_{II} / K_I) \quad (2.1)$$

where G is the strain energy release rate and G_c is the interfacial fracture toughness that depends on the mode-mixity angle ψ . In bimaterial fracture, K_I and K_{II} are the real and imaginary parts of the complex stress intensity factor K . The toughness of interface $G_c(\psi)$ can be thought of as an effective surface energy that depends on the mode of loading.

Grau et al. (2005) analyzed a debonded sandwich panel, and determined the maximum internal gas pressure in

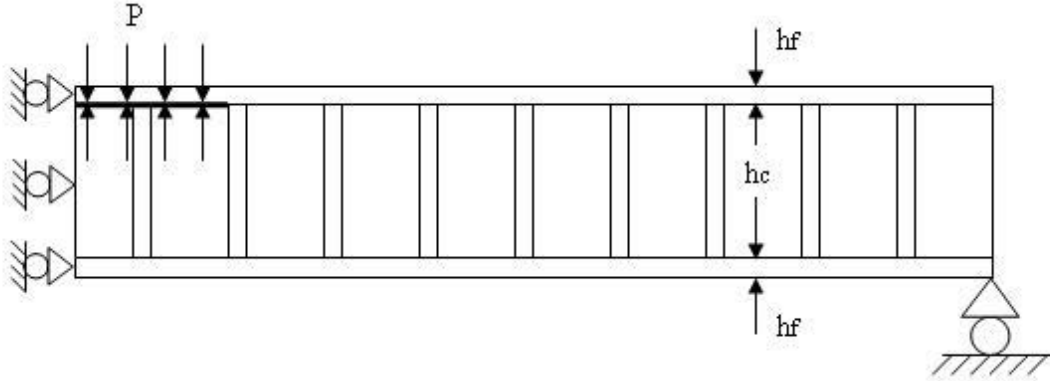


Figure 1. The model of face-sheet/core debonding in a one-dimensional sandwich panel with pressure load. Note that half of the structure is modeled.

the core before the disbond could propagate. They used interfacial fracture mechanics concepts to analyze this problem. The main premise here is that the crack will propagate when the energy release rate equals the fracture toughness for the core/face-sheet interface. This problem has become very significant after the historic failure of X-33 vehicle fuel tank made of a sandwich design of PMC face sheets and honeycomb core. The load and boundary conditions for the model problem are depicted in Figure 1.

The maximum allowable pressure for a given disbond length is calculated from the energy release rate for a unit applied pressure p . The energy release rate G is proportional to the square of the applied load or

$$G = G_0 p^2 \quad (2.2)$$

where G_0 is the energy release rate due to unit pressure for a given sandwich panel and disbond configuration and p is the applied pressure. The critical pressure p_{\max} can be obtained using

$$p_{\max} = \sqrt{\frac{G_c}{G_0}} \quad (2.3)$$

where G_c is the interfacial fracture toughness of the sandwich material system obtained from testing and G_0 is the energy release rate corresponding to the unit pressure obtained from Eq. (2.3).

Grau (2003) conducted asymmetric Double Cantilever Beam (DCB) tests to determine the interfacial fracture toughness of the sandwich composite (The face sheet material was A50TF266 S6 Class E, Fiber designation

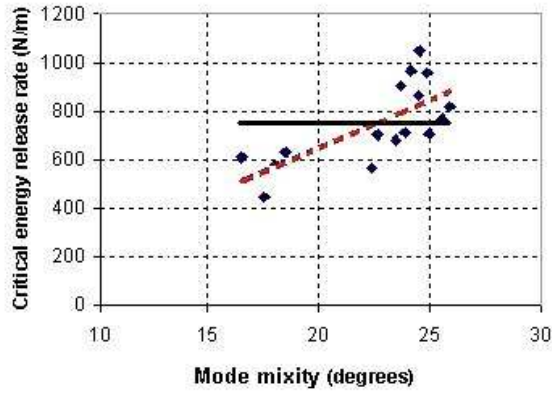


Figure 2. Critical energy release rate as a function of mode mixity. Continuous line denotes average G_c (\bar{G}_c) and the dashed line denotes a linear least square to fit to G_c as a function of mode-mixity angle.

ture.

B. Structural Analysis of a Representative Aircraft Structure

As noted earlier, aircraft structural design is still done by using code-based design rather than probabilistic approaches. Safety is improved through conservative design practices that include use of safety factors and conservative material properties. FAA regulation FAR-25.303 states that aircraft structures need to be designed with a safety factor to withstand 1.5 times the limit-load without failure. For use of conservative material properties, FAR-25.618 states that A-basis** or B-basis** material properties should be used in the design. If there is redundancy, B-basis value is used, otherwise A-basis value is used. In this work, we do not include redundancy in the analysis. The A-basis property is determined by calculating the value of a material property exceeded by 99% of the population with 95% confidence. Besides safety factor and conservative material properties, the safety of structures is also improved by tests of components and certification tests that can reveal inadequacies in analysis or construction. Certification tests improve the safety mainly by updating the distribution of errors in a conservative way. The effect of certification tests on the probability of failure of aircraft structures and the details of probability of failure calculations can be found in our previous papers (Kale et. al. 2004, Acar et al, 2004).

We consider a representative element (with representative length w and thickness t) in an aircraft structural component such as an element of wing skin, fuselage or engine blades such that the design variable for the element is the thickness. For this element, the stress is calculated from

$$\sigma = \frac{P}{wt} \quad (2.4)$$

where P is the applied on the small element. The design thickness is determined so that the calculated stress in the element is equal to material allowable stress for a design load P_d multiplied by a safety factor S_F , hence the design thickness of the representative element is calculated from Eq. (2.4) as

$$t_{design} = \frac{S_F P_d}{w \sigma_a} \quad (2.5)$$

σ_a is the allowable stress, i.e., A-basis value for the failure stress.

** A-basis value is the value exceeded by the 99% of the population with 95% confidence. B-basis value is the value exceeded by 90% of the population with 95% confidence. If there is redundancy, B-basis value is used, otherwise A-basis value is used.

T800HB-12K-40B, matrix 3631 and the core sheet material was Euro-Composites aramid (ECA) fiber type honeycomb.). Grau et al. (2005) performed finite element analyses to compute the mode-mixity angle corresponding to designs tested in experiments. The average interfacial fracture toughness prediction and the fracture toughness in terms of mode-mixity angle are presented in Fig. 2.

As shown in Fig.2, a simple way of determining the interfacial fracture toughness parameter is to perform tests over a range of mode-mixity values and to take the average. However, as seen from Fig. 1 that the critical energy release rate is assessed better as a function of mode-mixity. Grau et al. (2005) represent the critical energy release rate as a linear function of the mode-mixity that improves the accuracy of estimate of G_c . In the following sections, we explore the effect of improvement in accuracy of G_c estimation on the design load of a sandwich structure.

After the element has been designed by Eq. (2.5), we assume that for certification the element is loaded with the design axial force of (S_F times P_d). If this stress exceeds the failure stress then the design is rejected, otherwise it is certified for use. That is, the element is certified if the following inequality is satisfied

Table 1. Uncertainty Classification

Type	Spread	Cause	Remedies
Error (mostly epistemic)	Departure of the average fleet of an aerospace structure model (e.g. Boeing 737-400 from an ideal)	Errors in predicting structural failure, construction errors, deliberate changes	Testing and simulation to improve math model and the solution.
Variability (aleatory)	Departure of an individual structure from fleet level average	Variability in tooling, manufacturing process, and flying environment	Improve tooling and construction. Quality control.

III. Analysis of Structural Uncertainties

A good review of different sources of uncertainty in engineering modeling and simulations is provided by Oberkampf et al. (1999, 2000). We simplify the classification as shown in

Table 1 to distinguish between uncertainties that apply equally to the entire fleet of a structural component and uncertainties that vary for an individual structure. In addition, this simple classification makes it easy to analyze the effects uncertainty control. The uncertainties that affect the entire fleet are called here errors. They reflect inaccurate modeling of physical phenomena, errors in structural analysis, errors in load calculations, or use of materials and tooling in construction that are different from those specified by the designer. The aleatory uncertainty reflects variability in material properties, geometry, or loading between different copies of the same structure.

IV. Assessment of Probability of Failure

Probability of failure of a structural component can be expressed in terms of its structural response R (e.g., stress) and its capacity C corresponding to that response (e.g., failure stress) by

$$P_f = \Pr(C \leq R) \quad (4.1)$$

The structural response R is usually a function of several parameters such as the applied load P and the geometric parameters (and hence weight W). The capacity C is generally a material property, for instance failure strength. Both the response R and the capacity C have variability that needs to be included in the calculation of the probability of failure. Therefore, the response R and the capacity C can be represented in compact form as

$$R = R(VAR_R, P, W), \quad C = C(C_0, VAR_C) \quad (4.2)$$

where C_0 is the nominal value of the capacity C , VAR_R and VAR_C represent the variability (i.e. randomness) in structural response and capacity, respectively. Due to errors in assessing R and C (e.g., errors in load, stress and material property calculations), the calculated values of R and C are different from their actual values. The calculated values of the response R and capacity C can be expressed in terms of the actual values by introducing error parameters e_R and e_C

$$R_{calc} = (1 + e_R)R_{act}, \quad C_{calc} = (1 - e_C)C_{act} \quad (4.3)$$

The error parameter e_R stands for all errors related to the calculation of structural response such as errors in stress calculation, load calculation and geometry parameters. For the details of combining different sources of errors into a single error parameter, the reader is referred to Acar et al (2004). Similarly, e_C represents the error in predicting the capacity of the structure. Note that Eqs. (4.3) are formulated in such a way that a positive error leads to a conservative design.

The general equation for probability of failure given in Eq. (4.1) can be expressed as

$$P_f = \text{Prob}\left(\frac{1}{1-e_C} C_{calc}(C_0, VAR_C) - \frac{1}{1+e_R} R_{calc}(VAR_R, P, W) \leq 0\right) \quad (4.4)$$

Then, the probability of failure can be written in compact form as

$$P_f = P_f(e_C, C_0, VAR_C, e_R, VAR_R, P, W) \quad (4.5)$$

V. Tradeoffs of accuracy and design load and weight

We propose in this paper that the improvements in accuracy can be traded for increasing the design load of the structure or alternatively the weight of the structure can be reduced as discussed in the following two sub-sections.

A. Tradeoff of accuracy and design load

As seen from Eq. (4.5) that the probability of failure depends on the nominal value of capacity C_0 , error parameters e_R and e_C , the variabilities VAR_C and VAR_R , the weight W and the applied load P . This indicates four distinct ways to increase the design load of a structure

- (a) Use different material to increase C_0 .
- (b) Develop new techniques yielding more accurate solutions that reduce the error parameters e_R and e_C .
- (c) Improve quality control and manufacturing processes to reduce variability between nominally identical structural components.
- (d) Use a higher safety factor (S_F) leading to more conservative and heavier design.

We see from Eq. (4.5) that it is possible to use (b) or (c) to increase the design load of the structure while still keeping the weight unchanged. The FAA specifies the use of A-basis or B-basis properties that add a safety factor on material allowables that depends on variability. For example, a standard deviation of 10% in failure stress translates to more than 20% reduction in the allowable design stress using A-basis properties. Similarly, Qu et al. (2001) found that the application of quality controls to detect and reject material with low failure stress reduces the probability of failure significantly. Here we propose that we can similarly increase the design load of structures by improving accuracy.

For a target probability of failure $(P_f)_{\text{target}}$, the design load can be calculated from

$$\text{Prob}\left(\frac{1}{1-e_C} C_{calc}(C_0, VAR_C) - \frac{1}{1+e_R} R_{calc}(P_{\text{design}}, W, VAR_R) \leq 0\right) = (P_f)_{\text{target}} \quad (5.1)$$

We will illustrate this with sandwich structure design problem, for which the structural response is $R=G_0 p^2$, and the capacity is $C=G_c$. Here, we consider only the error in the capacity G_c of the structure. In addition, the variability in both the structural capacity and response is taken into account. We consider the use of a more accurate model (the method that uses mode-mixity) for the interfacial fracture toughness prediction of sandwich structures that will reduce e_C . Thus, given the target probability of failure, the design loads corresponding to different error factors can be calculated from Eq. (5.2).

$$P_f(e_{C_1}, P_{\text{design}_1}) = P_f(e_{C_2}, P_{\text{design}_2}) = (P_f)_{\text{target}} \quad (5.2)$$

The design load P_{design} of the sandwich structure can be also assessed using deterministic design philosophy. In that case, the safety factor of 1.4 (commonly used for space applications) for loads and conservative material properties (B-basis values) are used. For the sandwich structure, we approximate the probability of failure by considering the system failure of two parallel connected structures to simulate redundancy with normally distributed limit-state functions. The sandwich panels do not have normally distributed limit-state function, so that the use of Eq (5.3) provides only an approximation.

$$\beta_S = \beta_C \sqrt{\frac{n}{1 + \rho(n-1)}} \quad (5.3)$$

In Eq. (5.3), β_S is the reliability index for the system made of n components, β_C is the reliability index for the components (here $n=2$) and ρ is the correlation coefficients (here it is assumed to be 0.5) of the limit states of the components. The details of calculation of component probability of failure by analytical means are given in Appendix I. Recall that the relationship between the reliability index β and the probability of failure is given as

$$P_f = \Phi(-\beta) \quad (5.4)$$

where Φ is the cumulative distribution function of the standard normal distribution.

B. Tradeoff of accuracy and weight

Alternatively, for a given probability of failure, it is possible to reduce the safety factor, i.e., reduce the weight by either reducing the error or reducing the variability. We propose that we can trade changes in the safety factor (hence the weight) against changes in accuracy, while still maintaining the same probability of failure level. The changes in the safety factors may require changes to FAA mandated safety factors that will allow flexible safety factors based on accuracy, or they may require changes in company practices that enforce additional conservative design practices above the formal requirements.

The calculation of weight savings is similar to the calculation of the increase in design load. For weight savings, we consider the design of a representative aircraft structure that we discussed earlier. For this problem, the structural response is $R=P/wt$ and the capacity is $C=\sigma_f$. In the composite structure example, we consider the error in the capacity of the structure, e_C . However, for this problem we consider the error in the structural response, e_R . The variability in both the structural capacity and response are also taken into account. We calculate the weight savings from the structure corresponding to different error factors from Eq. (5.5). The details of calculation of probability of failure for this problem are given in Appendix II.

$$P_f(e_{R_1}, W_1) = P_f(e_{R_2}, W_2) = (P_f)_{\text{target}} \quad (5.5)$$

VI. Analysis of Error and Variability

A. Quantification of Variability and Errors for the Sandwich Structure

As noted earlier, one way of controlling errors is improving the accuracy of analysis by using more sophisticated analysis techniques. Grau et al. (2005) consider the problem of a pressure vessel similar to the liquid hydrogen tank of the X-33 reusable flight demonstration vehicle to demonstrate the usefulness of fracture mechanics approach for debonded sandwich structures. They explored the effect of mode mixity on the interfacial fracture toughness of sandwich composites, and study the effects on the residual strength of a debonded structure. In the present work we analyze the same problem by probabilistic approach and investigate the effect of improved accuracy associated with using mode-mixity on the design load.

1. Variability

We consider that the mode-mixity dependent G_c accurately represents the physical phenomenon. However, we notice in Fig. 2 that the G_c values obtained from experiments (performed by Grau et al., 2005) are different than mode-mixity dependent G_c . We assume that this deviation represents the variability. It is given in the third column of Table 2. Each row of Table 2 corresponds to a different design having a different mode-mixity angle, which is calculated through finite element analysis. Approximate probability density function for this variability is obtained by using ARENA software, which is a product of Systems Modeling company. The distribution parameters and goodness of fit statistic are given in Fig. 3. The corresponding p-value given in Fig. 3 is a measure for goodness of the fit. The p-values fall between 0 and 1 and larger p-values indicate better fits (Kelton et al., 1998). The p-values less than about 0.05 indicate that the distribution is not a good fit. In our case, the p-values are larger than 0.15, so we have good fits for probability density functions.

In addition to variability in G_c predictions, there is also variability in P . We assume that the maximum lifetime loading P follows lognormal distribution with mean value of P_{design} and coefficient of variation (*c.o.v.*) of 10%.

2. Errors

The fourth column of Table 2 presents the deviations of G_c values obtained through experiments from their average values. These deviations combine variability and error. Errors are due to neglecting the effect of mode-mixity in

G_c . Here, we do not perform a separate quantification for error and variability. Instead, we concentrate on total uncertainty. The distribution of uncertainty for this case is given in Figure 4.

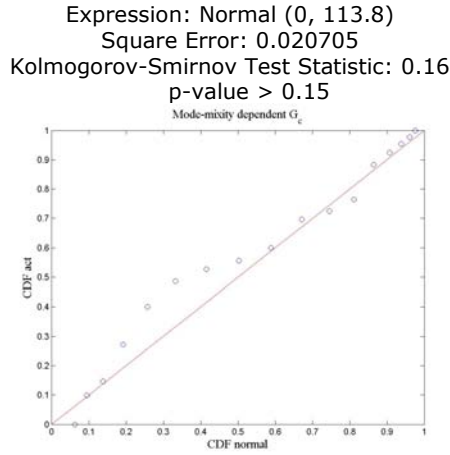


Figure 3. Probability density function fitted to variability of G_c by using ARENA.

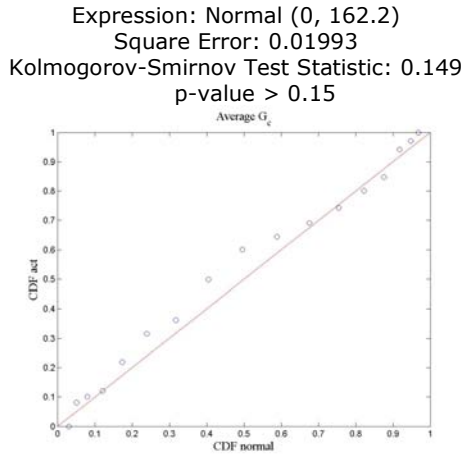


Figure 4. Probability density function fitted to variability of G_c by using ARENA.

Comparing the standard deviation of *error & variability* (u^A) to that *variability only* (u^{MM}) given in the last row of Table 2, we see that the improvements in the accuracy of G_c prediction (that is, reducing errors) leads to reduction of the total uncertainty by 30%. In the next section, we analyze the effect of this reduction on the design load.

B. Quantification of Errors and Variability for Representative Structural Element

1. Variability

Here we have variability in loading, material properties and geometric parameters. As we noted earlier, variability reflects departure the properties between different copies of the same structure. A summary of the distributions for these random variables listed in Table 3, which is taken from Kale et al. (2004).

2. Variability

For the representative structural element, we condense errors in load calculation, stress calculation, material properties and geometry parameters into a representative single error parameter e_R . So, the calculated stress is expressed as

Table 2. Quantification of Uncertainty in the “average G_c ” and “ G_c with mode mixity” for different designs. The superscript ‘A’ denotes the use of average fracture toughness and ‘MM’ indicates the use of mode-mixity dependent fracture toughness and ‘u’ represents the uncertainty.

Design	ψ (deg)	% u^A	% u^{MM}
1	16.52	-137.1	-3.7
2	17.53	-303.5	6.3
3	18.05	-168.7	1.2
4	18.50	-117.9	13.1
5	22.39	-180.9	-14.9
6	23.89	-35.6	13.3
7	24.50	116.8	-5.5
8	24.89	209.6	-22.5
9	23.48	-67.1	8.8
10	24.98	-39.1	-0.7
11	25.55	20.5	-10.3
12	25.90	71.3	-25.1
13	22.65	-44.3	-11.0
14	23.69	157.1	2.5
15	24.15	218.4	-18.3
16	24.54	300.7	-16.6
Std. Dev.		162.2	113.8

* Table 3 of Grau et al. (2005) is used to calculate the errors

$$\sigma_{calc} = (1 + e_R) \sigma_{true} = (1 + e_R) \frac{P}{wt} \quad (6.3)$$

where P is the applied load on the small element. Because of the error e_R , the design thickness formulated in Eq. (2.5) is replaced by

$$t_{design} = (1 + e_R) \frac{S_F P_d}{w \sigma_a} \quad (6.4)$$

Certification testing described earlier updates the probability distribution of error, which is initially assumed to be uniform distribution. The simplicity of the error distribution helps us to perform a detailed analysis by utilizing the derivatives of probability of failure with respect to error bound, safety factor and the design thickness as illustrated in Appendix III.

Table 3. Variability and Error for the representative aircraft structure

Variables	Distribution	Mean	Scatter
Length (w)	Uniform	1.0	(1%) bounds
Thickness (t)	Uniform	t_{design}	(3%) bounds
Failure stress (σ_f)	Lognormal	150.0	10 % c.o.v.
Service Load (P)	Lognormal	100.0	10 % c.o.v.
Error factor (e_R)	Uniform	0.0	0% to 50%

VII. Results

The percent increase in design load of the sandwich structure and weight savings from the representative aircraft structure as a result of error reduction are presented in the following sub-sections.

A. Increase in Design Load of the Sandwich Structure

We first compute the design load P_{design} by deterministic design philosophy. As noted earlier, the safety factor of 1.4 for loads and conservative material properties (B-basis values) are used. For the sandwich structure, we calculate the probability of failure by considering the system failure of two parallel connected structures. Since we impose redundancy, B-basis value for G_c is used. The correlation coefficient between the two components is taken as 0.5. The design load and the probability of failure values are presented in Table 4.

Table 4. Design load and corresponding probabilities of failure of the sandwich panels designed via deterministic approach. The superscript 'A' denotes the use of average fracture toughness of experiments and 'MM' indicates the use of mode-mixity dependent fracture toughness.

Design	Design Load			Probability of Failure	
	(P_{design}) ^A (kPa)	(P_{design}) ^{MM} (kPa)	% Δp	(P_f) ^A (10^{-4})	(P_f) ^{MM} (10^{-4})
1	65.6	58.0	-11.7	54.73	26.18
2	342.2	311.4	-9.0	54.74	16.72
3	203.3	195.3	-3.9	54.74	6.88
4	98.8	100.5	1.7	54.74	2.47
5	58.0	60.7	4.8	54.74	1.43
6	316.8	298.8	-5.7	54.74	9.38
7	197.5	196.3	-0.6	54.74	3.79
8	93.7	98.2	4.8	54.73	1.43
9	54.8	59.0	7.6	54.74	0.86
10	316.8	298.5	-5.8	54.74	9.56
11	187.4	184.7	-1.5	54.73	4.42
12	89.9	92.6	3.0	54.74	1.97
13	52.3	55.1	5.3	54.74	1.30

Average	-0.8	54.74	6.65
---------	------	-------	------

The second and third columns of the Table 4 show the design loads of the panels designed by using average G_c and by using G_c with mode-mixity, respectively. The fourth column shows the percent change of the design load if the use of G_c with mode-mixity is preferred over the use of average G_c . We see that the average over 13 designs is only -0.8%. That is the design load of the structure remains nearly the same. However, when we compare the probabilities of failure of the structures, we see that the average probability of failure reduced by more than a factor of eight.

Because the deterministic design is performed with fixed safety factors, improvements in accuracy reduce the probability of failure. Probabilistic analysis permits increasing instead the design load. Table 5 shows the comparison of design load for the average G_c and mode-mixity dependent G_c approaches.

Table 5. Design loads of the sandwich panels calculated via probabilistic approach. The superscript 'A' denotes the use of average fracture toughness of experiments and 'MM' indicates the use of mode-mixity dependent fracture toughness.

Design	$P_f = 5.47 \times 10^{-3}$		
	$(P_{\text{design}})^A$ (kPa)	$(P_{\text{design}})^{MM}$ (kPa)	% Δp
1	65.7	61.1	-7.0
2	342.0	335.7	-1.9
3	203.3	217.9	7.2
4	98.7	115.3	16.8
5	58.0	70.6	21.7
6	316.7	329.8	4.2
7	197.6	223.0	12.8
8	93.7	114.0	21.6
9	54.8	69.1	26.1
10	316.7	329.4	4.0
11	187.4	208.9	11.5
12	89.8	106.7	18.8
13	52.3	64.1	22.6
Average			12.2

We see in Table 5 that the design load for the sandwich panels designed using ' G_c with mode-mixity' are larger on average than loads obtained by using 'average G_c ' by about 12%.

B. Weight Savings from the Representative Element

Similar to the sandwich structure problem, we use probabilistic design methodology to calculate weight savings from the representative aircraft structure. The saving from the weight (i.e. the thickness) is calculated from Eq. (5.4) and plotted with respect to error bound is plotted in Figure 5. It is seen that reducing the error bound from 50% to 10%, provides about 24% savings in weight.

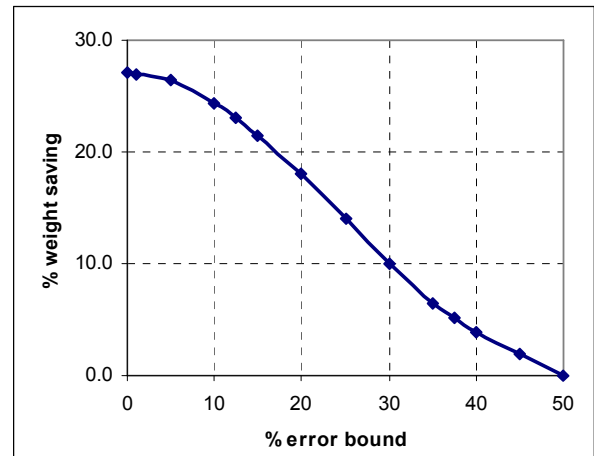


Figure 5. Weight savings from the representative element by error reduction

VIII. Concluding Remarks

The effect of error control on tradeoffs of design load, weight and safety of structures are analyzed by using probabilistic design methodology. We first analyzed the effect of error control on design load of structural components. The example is a sandwich structure analyzed by Grau et al. (2005). The error control mechanism here is the use of a more sophisticated failure (the use of mode-mixity dependent fracture toughness) over the simpler failure model (average fracture toughness). It is found that the design load of the structure can be increased by 12% by using G_c with mode-mixity instead of average G_c .

Next, we consider structural failure due to point stress without damage propagation, and illustrate by using a representative aircraft structure that improving the accuracy of structural analysis can allow weight reduction. The ef-

fects of the use of safety factor, conservative material properties and certification testing are taken into account in the analysis. The sensitivities of probability of failure and design thickness with respect to safety factor and error bound are calculated. It is found that reducing errors from 50% to 10% provides up to 24% savings in weight of the representative structure.

Appendix I

Calculation of F_G and P_f for the sandwich structure

The distribution of a function Z of two random variables X and Y , $Z=h(X, Y)$ can be calculated as (Ang and Tang, 1975, p.170)

$$f_Z(z) = \int_{-\infty}^{\infty} f_{X,Y}(x,y) \left| \frac{\partial x}{\partial z} \right| dy \quad (A1.1)$$

where $f_{X,Y}(x,y)$ is joint probability distribution function of $x = h^{-1}(z,y)$ and Y and.

We can write the limit-state function for the sandwich panel problem as

$$g = (G_c)_{calc} - G_0 p^2 \quad (A1.2)$$

We calculate probability density function (PDF) of the limit state function g from PDF's of $(G_c)_{calc}$. Therefore, in Eq. (A1.1) we replace Z with g , X with $(G_c)_{calc}$, Y with p , and also we have $(G_c)_{calc} = g + G_0 p^2$. After performing these changes, we get from Eq. (A1.1) that

$$f_G(g) = \int_0^{\infty} f_{G_c,p}(g + G_0 p^2, p) dp \quad (A1.3)$$

Here we assume that G_c and p are statistically independent, hence the joint distribution in Eq.(A1.3) is calculated as

$$f_{G_c,p}(G_c, p) = f_{G_c}(g + G_0 p^2) f_p(p) \quad (A1.4)$$

and also we have $\left| \frac{\partial x}{\partial z} \right| = \left| \frac{\partial G_c}{\partial g} \right| = 1$

Then, the cumulative distribution function (CDF) of g is calculated as

$$F_G(g) = \int_{-\infty}^g f_G(g) dg \quad (A1.5)$$

which yields us to compute the probability of failure simply as $P_f = F_G(0)$.

Appendix II

Probability of failure calculation for the representative element

Failure is predicted to occur when the structural response R is greater than carrying capacity of the structure C . Then, the probability of failure is given as

$$P_f = \Pr(C \leq R) \quad (A2.1)$$

where

$$R = \frac{P}{wt(e)} \text{ and } C = \sigma_f \quad (A2.2)$$

Since the coefficient of variations of t and w is small compared to the coefficient of variation of P (see Table 3 in the main text), R can be approximated as lognormal to take advantage of the properties of lognormal distribution for calculating the distribution parameters. Hence, both C and R are lognormally distributed random variables with distribution parameters λ_C , ζ_C , λ_R and ζ_R . Then, from Eqs. (A2.2) the distribution parameters can be obtained as

$$\lambda_R(e) = \lambda_P - \lambda_t(e) - \lambda_w \text{ and } \zeta_R^2 = \zeta_P^2 + \zeta_t^2 + \zeta_w^2 \quad (\text{A2.3})$$

where

$$\lambda_t(e) = \ln(t_{design}(e)) - 0.5\zeta_t^2 = \ln\left((1+e)\frac{S_F P_d}{w\sigma_a}\right) - 0.5\zeta_t^2 \quad (\text{A2.4})$$

and λ_R and ζ_R are the distribution parameters of the failure stress.

Then, P_f can be calculated as

$$P_f = P(C \leq R) = \Phi\left(\frac{\lambda_R(e) - \lambda_C}{\sqrt{\zeta_R^2 + \zeta_C^2}}\right) = \Phi(-\beta(e)) = \int_{-\infty}^{-\beta(e)} \frac{1}{\sqrt{2\pi}} \exp\left(-\frac{x^2}{2}\right) dx \quad (\text{A2.5})$$

Appendix III

Sensitivity Analysis for Probability of Failure of the representative structural element

For the case of a uniformly distributed errors between $(-b_e, b_e)$ we can use the following simple derivation to obtain the effect of error reduction on the design thickness of the representative structural element for fixed probability of failure. To attain the probability of failure at a specified level, we equate the total derivative of probability of failure to zero. Recall that probability of failure is expressed in compact form as

$$P_f = P_f(e_C, C_0, VAR_C, e_R, VAR_R, P, W) \quad (4.5)$$

For the representative structure, we keep variables except e_R and W unchanged. The weight W is a function of safety factor S_F used in the design and the probability distribution of error e_R is only dependent on the error bound b_e . So, probability of failure is a function of error bound b_e and safety factor S_F . Thus, the total derivative of probability of failure can be expressed as we have

$$d\bar{P}_f = \frac{\partial \bar{P}_f}{\partial b_e} db_e + \frac{\partial \bar{P}_f}{\partial S_F} dS_F = 0 \quad (\text{A3.1})$$

So, given the change in error bound and safety factor, the change in failure probability can be calculated. Similarly, the total derivative of design thickness is

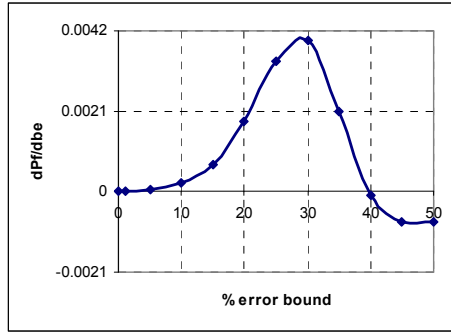
$$dt_{design} = \frac{\partial t_{design}}{\partial b_e} db_e + \frac{\partial t_{design}}{\partial S_F} dS_F \quad (\text{A3.2})$$

Imposing the condition that the failure probability to be attained at the same value (i.e. Eq. (A3.1)) we obtain the thickness change depending on the bound of error

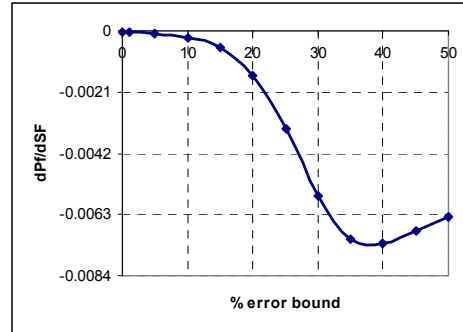
$$dt_{design} = \left(\frac{\partial t_{design}}{\partial b_e} - \frac{\partial t_{design}}{\partial S_F} \frac{\partial \bar{P}_f / \partial b_e}{\partial \bar{P}_f / \partial S_F} \right) db_e \quad (\text{A3.3})$$

which gives the saving from the structural weight of the aircraft component. Since we choose a representative component and a simple failure mode, the derivatives are calculated by analytical means, which is given in the next subsection of this appendix. For a more complex geometry and complex failure model, numerical differentiation can be employed.

We calculate the partial derivatives of probability of failure with respect to the error bound b_e and with respect to the safety factor. Hence, given the change in error bound and safety factor, the change in failure probability can be calculated. These derivatives are shown as function of the error bound in Figure A3.1.



(a)

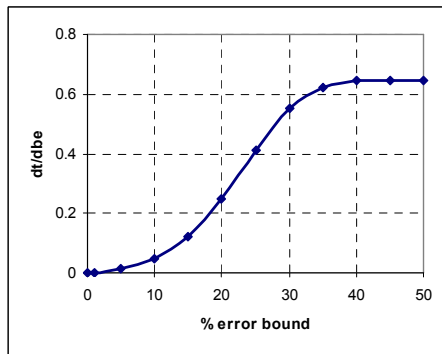


(b)

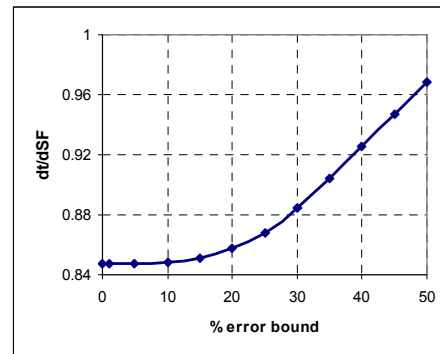
Figure A3.1. Variation of Partial Derivatives of \bar{P}_f with error bound b_e (for $S_F=1.5$)

(a) derivative with respect to error bound b_e (b) derivative with respect to S_F

Next, we calculate the partial derivatives of design thickness with respect to the error bound b_e and with respect to the safety factor. The derivatives as function of the error bound are presented in Figure A3.2.



(a)

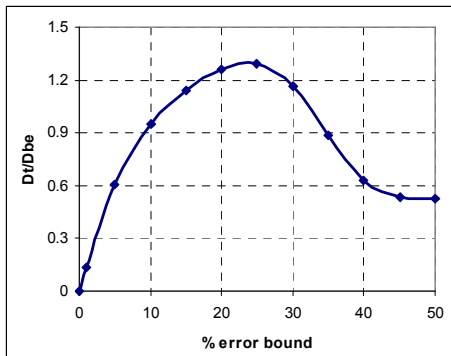


(b)

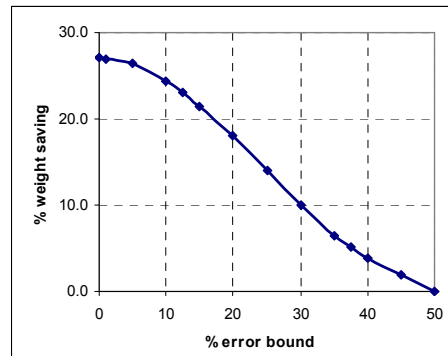
Figure A3.2. Variation of Partial Derivatives of design thickness with error bound b_e

(a) derivative with respect to error bound b_e (b) derivative with respect to S_F

Finally, we use Eq. (A3.3) to calculate the total derivative dt_{design} by using the partial derivatives that we calculated before. The variation of this total derivative with error bound is shown in Fig. A3.3(a). Integration of this expression over bound of error gives the reduction of thickness by error reduction. The saving from the thickness (i.e. the weight) with respect to error bound is plotted in Fig. A3.3(b). It is seen that reducing the error bound from 50% to 10%, provides about 24% savings in weight.



(a)



(b)

Figure A3.3. Effect of error bound on weight saving

(a) the effect on total derivative of thickness (b) the effect on the thickness

Analytical calculation of partial derivatives of probability of failure

For the representative structural element, the capacity of the structure is $C=\sigma_f$ while the response of the structure is $R=P/wt$. Since we assume that w and t are also lognormally distributed, then R also has lognormal distribution. Since capacity C and resistance R both have lognormal distributions, then the probability of failure is easily calculated by analytical means as

$$P_f = \Phi \left(-\frac{\lambda_C - \lambda_R}{\sqrt{\zeta_C^2 + \zeta_R^2}} \right) \quad (A3.4)$$

where

$$\lambda_R = \lambda_P - \lambda_w - \lambda_t \quad (A3.5)$$

and

$$\zeta_R^2 = \zeta_P^2 + \zeta_w^2 + \zeta_t^2 \quad (A3.6)$$

The terms involved in Eqs. (A3.5) and (A3.6) are all constant except λ_t . Given the mean and standard deviation of the distributions, these distribution parameters are calculated from

$$\zeta = \sqrt{\ln \left(1 + \frac{\sigma^2}{\mu^2} \right)} = \sqrt{\ln(1 + \delta^2)} \quad (A3.7)$$

where δ is the coefficient of variation and

$$\lambda = \ln(\mu) - \frac{1}{2} \zeta^2 \quad (A3.8)$$

However, since design thickness t_{design} is a function of error e_R , t_{design} is itself a random variable. Since we do not take the error in capacity e_C into account, we represent e_R simply as e . Recall from Eq. (6.49) that t_{design} is defined as

$$t_{design} = (1 + e) \frac{S_F P_d}{w \sigma_a} \quad (A3.9)$$

Therefore, the term λ_t is not constant but a function of t_{design} as given below.

$$\lambda = \ln(t_{design}) - \frac{1}{2} \zeta_t^2 \quad (A3.10)$$

The probability of failure can be re-written as

$$P_f = \Phi \left\{ - \left[a \ln(t_{design}) + b \right] \right\} \quad (A3.11)$$

where a and b are positive constants defined in terms of distribution parameters of w , t , σ_f and P given by

$$a = \frac{1}{\sqrt{\zeta_{\sigma_f}^2 + \zeta_w^2 + \zeta_t^2 + \zeta_P^2}} = \frac{1}{\sqrt{\ln(1 + \delta_{\sigma_f}^2) + \ln(1 + \delta_w^2) + \ln(1 + \delta_t^2) + \ln(1 + \delta_P^2)}} \quad (A3.12)$$

$$b = a \left[\lambda_{\sigma_f} + \lambda_w - \frac{1}{2} \zeta_t^2 - \lambda_P \right] = a \left[\ln(\mu_{\sigma_f}) - \frac{1}{2} \ln(1 + \delta_{\sigma_f}^2) + \ln(\mu_w) - \frac{1}{2} \ln(1 + \delta_w^2) - \frac{1}{2} \ln(1 + \delta_t^2) - \ln(\mu_P) + \frac{1}{2} \ln(1 + \delta_P^2) \right] \quad (A3.13)$$

Inserting Eq. (A3.9) into (A3.11) yields

$$P_f = \Phi \left\{ - \left[a \ln \left((1+e) \frac{S_F P_d}{w_d \sigma_a} \right) + b \right] \right\} \quad (\text{A3.14})$$

Since error factor e is a random variable, probability of failure P_f is also random. An estimator for P_f is defined as

$$\bar{P}_f = \int_{e_{low}}^{e_{upp}} P_f f_e de \quad (\text{A3.15})$$

where f_e is the probability density function of error factor e , e_{low} and e_{upp} are lower and upper bounds for e , respectively. To maintain the same \bar{P}_f value, the total derivative of \bar{P}_f should be zero.

$$d\bar{P}_f = \frac{\partial \bar{P}_f}{\partial e_{low}} de_{low} + \frac{\partial \bar{P}_f}{\partial e_{upp}} de_{upp} + \frac{\partial \bar{P}_f}{\partial a} da + \frac{\partial \bar{P}_f}{\partial b} db + \frac{\partial \bar{P}_f}{\partial S_F} dS_F \quad (\text{A3.16})$$

and for finite changes Eq.(A3.13) can be written as

$$\Delta \bar{P}_f = \frac{\partial \bar{P}_f}{\partial e_{low}} \Delta e_{low} + \frac{\partial \bar{P}_f}{\partial e_{upp}} \Delta e_{upp} + \frac{\partial \bar{P}_f}{\partial a} \Delta a + \frac{\partial \bar{P}_f}{\partial b} \Delta b + \frac{\partial \bar{P}_f}{\partial S_F} \Delta S_F \quad (\text{A3.17})$$

As a starting point, we assume $e_{upp} = -e_{low} = b_e$ and also assume no change in variability ($\Delta a = \Delta b = 0$) which yields

$$\Delta \bar{P}_f = \frac{\partial \bar{P}_f}{\partial b_e} \Delta b_e + \frac{\partial \bar{P}_f}{\partial S_F} \Delta S_F \quad (\text{A3.18})$$

where

$$\bar{P}_f = \int_{-b_e}^{b_e} \Phi \left\{ - \left[a \ln \left((1+e) \frac{S_F P_d}{w_d \sigma_a} \right) + b \right] \right\} f_e de = \int_{-b_e}^{b_e} \Phi \{h(e, S_F)\} f_e de \quad (\text{A3.19})$$

and

$$h(e, S_F) = - \left[a \ln \left((1+e) \frac{S_F P_d}{w_d \sigma_a} \right) + b \right] \quad (\text{A3.20})$$

$$\Phi(x) = \frac{1}{\sqrt{2\pi}} \int_{-\infty}^x \exp \left(-\frac{t^2}{2} \right) dt = \frac{1}{2} \left[1 + \text{erf} \left(\frac{x}{\sqrt{2}} \right) \right] \quad (\text{A3.21})$$

The updated distribution of error factor is obtained through Bayes' theorem as

$$f^U(e) = \frac{\Pr(\text{Passing Certification} | e) f^I(e)}{\int_{-b_e}^{b_e} P(C | e) f^I(e) de} \quad (\text{A3.22})$$

where $f^I(e)$ is the initial distribution of the error factor e , and

$$\Pr(\text{Passing Certification} | e) = \Pr(C > R) = \Phi \left(\frac{\lambda_C(e) - \lambda_R}{\zeta_C^2 + \zeta_R^2} \right) = \Phi[h_c(e, S_F)] \quad (\text{A3.23})$$

is the probability that the structure passes the certification testing. In Eq. (A3.23), the term h_c is similar to h defined earlier in (A3.20) and is expressed as

$$h_c(e, S_F) = \left[a_c \ln \left((1+e) \frac{S_F P_d}{w \sigma_a} \right) + b_c(S_F) \right] \quad (\text{A3.24})$$

where the subscript ‘c’ stands for certification. Similarly, the terms a_c and b_c are expressed as

$$a_c = \frac{1}{\sqrt{\ln(1 + \delta_{\sigma_f}^2) + \ln(1 + \delta_w^2) + \ln(1 + \delta_t^2)}} \quad (\text{A3.25})$$

$$b_c(S_F) = a_c \left[\ln(\mu_{\sigma_f}) - \frac{1}{2} \ln(1 + \delta_{\sigma_f}^2) + \ln(\mu_w) - \frac{1}{2} \ln(1 + \delta_w^2) - \frac{1}{2} \ln(1 + \delta_t^2) - \ln(S_F P_d) \right] \quad (\text{A3.26})$$

Then, we can re-write the updated distribution of the error factor as

$$f^U(e, b_e, S_F) = \frac{\Phi[h_c(e, S_F)] \frac{1}{2b_e}}{\int_{-b_e}^{b_e} \Phi[h_c(e, S_F)] \frac{1}{2b_e} de} = \frac{\Phi[h_c(e, S_F)]}{\int_{-b_e}^{b_e} \Phi[h_c(e, S_F)] de} \quad (\text{A3.27})$$

Thus we can write probability of failure as

$$\bar{P}_f = \int_{-b_e}^{b_e} \left(\Phi[h(e, S_F)] \frac{\Phi[h_c(e, S_F)]}{\int_{-b_e}^{b_e} \Phi[h_c(e, S_F)] de} \right) de = \int_{-b_e}^{b_e} (u(e, b_e, S_F)) de \quad (\text{A3.28})$$

where

$$u(e, b_e, S_F) = \frac{1}{\int_{-b_e}^{b_e} \Phi[h_c(e, S_F)] de} \Phi[h(e, S_F)] \Phi[h_c(e, S_F)] \quad (\text{A3.29})$$

Partial derivative with respect to error bound b_e

To calculate $\frac{\partial \bar{P}_f}{\partial b_e}$ we use Leibniz rule given in Eq. (A3.30)

$$\frac{\partial}{\partial z} \int_{a(z)}^{b(z)} f(x, z) dx = \int_{a(z)}^{b(z)} \frac{\partial f}{\partial z} dx + f(b(z), z) \frac{\partial b}{\partial z} - f(a(z), z) \frac{\partial a}{\partial z} \quad (\text{A3.30})$$

Then, the partial derivative $\frac{\partial \bar{P}_f}{\partial b_e}$ is calculated from

$$\frac{\partial \bar{P}_f}{\partial b_e} = \int_{-b_e}^{b_e} \frac{\partial u}{\partial b_e} de + u(b_e, b_e, S_F) + u(-b_e, b_e, S_F) \quad (\text{A3.31})$$

where

$$\frac{\partial u}{\partial b_e} = \Phi[h(e, S_F)]\Phi[h_c(e, S_F)]\frac{\partial}{\partial b_e}\left\{1/\int_{-b_e}^{b_e}\Phi[h_c(e, S_F)]de\right\} \quad (\text{A3.32})$$

and the last term of Eq. (A3.32) can be re-written as

$$\frac{\partial}{\partial b_e}\left\{1/\int_{-b_e}^{b_e}\Phi[h_c(e, S_F)]de\right\} = \frac{-\frac{\partial}{\partial b_e}\left\{\int_{-b_e}^{b_e}\Phi[h_c(e, S_F)]de\right\}}{\left[\int_{-b_e}^{b_e}\Phi[h_c(e, S_F)]de\right]^2} \quad (\text{A3.33})$$

where the numerator is evaluated by using the second fundamental theorem of calculus given in Eq. (A3.34)

$$\frac{d}{dx}\left[\int_a^x f(t)dt\right] = f(x) \quad (\text{A3.34})$$

Hence, the numerator in Eq. (A3.33) reduces to

$$\frac{\partial}{\partial b_e}\left\{\int_{-b_e}^{b_e}\Phi[h_c(e, S_F)]de\right\} = \Phi[h_c(e, S_F)] + \Phi[h_c(-e, S_F)] \quad (\text{A3.35})$$

Then, Eq. (A3.32) becomes

$$\frac{\partial u}{\partial b_e} = -\frac{\Phi[h_c(e, S_F)] + \Phi[h_c(-e, S_F)]}{\left[\int_{-b_e}^{b_e}\Phi[h_c(e, S_F)]de\right]^2}\Phi[h(e, S_F)]\Phi[h_c(e, S_F)] \quad (\text{A3.36})$$

Finally, the desired partial derivative $\frac{\partial \bar{P}_f}{\partial b_e}$ is then obtained as

$$\begin{aligned} \frac{\partial \bar{P}_f}{\partial b_e} = & -\frac{\Phi[h_c(e, S_F)] + \Phi[h_c(-e, S_F)]}{\left[\int_{-b_e}^{b_e}\Phi[h_c(e, S_F)]de\right]^2}\int_{-b_e}^{b_e}[\Phi[h(e, S_F)]\Phi[h_c(e, S_F)]]de \\ & + \Phi[h(b_e, S_F)]\frac{\Phi[h_c(b_e, S_F)]}{\int_{-b_e}^{b_e}\Phi[h_c(e, S_F)]de} + \Phi[h(-b_e, S_F)]\frac{\Phi[h_c(-b_e, S_F)]}{\int_{-b_e}^{b_e}\Phi[h_c(e, S_F)]de} \end{aligned} \quad (\text{A3.37})$$

Partial derivative with respect to safety factor S_F

Partial derivative $\frac{\partial \bar{P}_f}{\partial S_F}$ for updated probability of failure is calculated as follows.

$$\frac{\partial \bar{P}_f}{\partial S_F} = \int_{-b_e}^{b_e} \frac{\partial u(e, b_e, S_F)}{\partial S_F} de \quad (\text{A3.38})$$

where $u(e, b_e, S_F)$ is defined earlier in Eq. (A3.28). The derivative of u with respect to S_F can be written as

$$\begin{aligned} \frac{\partial u}{\partial S_F} = & \frac{\partial}{\partial S_F} \left\{ 1 / \int_{-b_e}^{b_e} \Phi[h_c(e, S_F)] de \right\} \Phi[h(e, S_F)] \Phi[h_c(e, S_F)] \\ & + \left\{ 1 / \int_{-b_e}^{b_e} \Phi[h_c(e, S_F)] de \right\} \left\{ \frac{\partial \Phi[h(e, S_F)]}{\partial S_F} \Phi[h_c(e, S_F)] + \Phi[h(e, S_F)] \frac{\partial \Phi[h_c(e, S_F)]}{\partial S_F} \right\} \end{aligned} \quad (\text{A3.39})$$

The first partial derivative in Eq. (A3.39) is calculated as follows.

$$\frac{\partial \Phi[h(e, S_F)]}{\partial S_F} = \frac{1}{\sqrt{2\pi}} \frac{\partial}{\partial S_F} \left[\int_{-\infty}^{h(e, S_F)} \exp\left(-\frac{z^2}{2}\right) dz \right] \quad (\text{A3.40})$$

Now, utilizing the chain rule and the second fundamental theorem of calculus given in Eq. (A3.34) we obtain

$$\frac{\partial \Phi[h(e, S_F)]}{\partial S_F} = \frac{1}{\sqrt{2\pi}} \left\{ \frac{\partial}{\partial h} \left[\int_{-\infty}^{h(e, S_F)} \exp\left(-\frac{z^2}{2}\right) dz \right] \right\} \frac{\partial h}{\partial S_F} = \frac{1}{\sqrt{2\pi}} \left[\exp\left(-\frac{h^2(e, S_F)}{2}\right) \right] \frac{\partial h(e, S_F)}{\partial S_F} \quad (\text{A3.41})$$

where

$$\frac{\partial h}{\partial S_F} = \frac{\partial}{\partial S_F} \left(- \left[a \ln\left((1+e) \frac{S_F P_d}{w_d \sigma_a} \right) + b \right] \right) = - \frac{a}{S_F} \quad (\text{A3.42})$$

Then, Eq. (A3.40) reduces to

$$\frac{\partial \Phi[h(e, S_F)]}{\partial S_F} = - \frac{a}{\sqrt{2\pi} S_F} \left[\exp\left(-\frac{1}{2} h^2(e, S_F)\right) \right] \quad (\text{A3.43})$$

The first partial derivative in Eq. (A3.39) is calculated as follows. The first term is easily obtained by noticing the similarity to Eq. (A3.42) as

$$\frac{\partial}{\partial S_F} \left(a_c \ln\left((1+e) \frac{S_F P_d}{w_d \sigma_a} \right) \right) = \frac{a_c}{S_F} \quad (\text{A3.44})$$

and also Eq. (A3.26) reveals that

$$\frac{\partial}{\partial S_F} (b_c(S_F)) = - \frac{a_c}{S_F} \quad (\text{A3.45})$$

Then, we have

$$\frac{\partial h_c}{\partial S_F} = \frac{\partial}{\partial S_F} \left(- \left[a_c \ln\left((1+e) \frac{S_F P_d}{w_d \sigma_a} \right) + b_c(S_F) \right] \right) = - \left(\frac{a_c}{S_F} - \frac{a_c}{S_F} \right) = 0 \quad (\text{A3.46})$$

That leads to

$$\frac{\partial \Phi[h_c(e, S_F)]}{\partial S_F} = \frac{\partial}{\partial h_c} \left[\int_{-\infty}^{h_c} \frac{1}{\sqrt{2\pi}} \exp\left(-\frac{z^2}{2}\right) dz \right] \frac{\partial h_c}{\partial S_F} = 0 \quad (\text{A3.47})$$

And thus we also get

$$\frac{\partial}{\partial S_F} \left\{ 1 / \int_{-b_e}^{b_e} \Phi[h_c(e, S_F)] de \right\} = - \frac{\int_{-b_e}^{b_e} \frac{\partial \Phi[h_c(e, S_F)]}{\partial S_F} de}{\left[\int_{-b_e}^{b_e} \Phi[h_c(e, S_F)] de \right]^2} = 0 \quad (\text{A3.48})$$

Then, Eq. (A3.38) becomes

$$\frac{\partial u}{\partial S_F} = \left\{ 1 / \int_{-b_e}^{b_e} \Phi[h_c(e, S_F)] de \right\} \left\{ - \frac{a}{\sqrt{2\pi} S_F} \left[\exp\left(-\frac{h^2(e, S_F)}{2}\right) \right] \right\} \Phi[h_c(e, S_F)] \quad (\text{A3.49})$$

And finally we have

$$\frac{\partial \bar{P}_F}{\partial S_F} = \left\{ 1 / \int_{-b_e}^{b_e} \Phi[h_c(e, S_F)] de \right\} \int_{-b_e}^{b_e} \left\{ - \frac{a}{\sqrt{2\pi} S_F} \left[\exp\left(-\frac{h^2(e, S_F)}{2}\right) \right] \right\} \Phi[h_c(e, S_F)] de \quad (\text{A3.50})$$

Acknowledgments

This work has been supported by the NASA Constellation University Institute Program (CUIP), Ms. Claudia Meyer program monitor.

References

- Acar, E., Kale, A. and Haftka, R.T. (2004). Effects of Error, Variability, Testing and Safety Factors on Aircraft Safety. *NSF workshop on Reliable Engineering Computing*, Savannah, Georgia, 15-17 September, 2004.
- Ang, A., H-S. and Tang, W.H. (1975). Probability Concepts in Engineering Planning and Design, Volume I: Basic Principles. *John Wiley & Sons*.
- Avery, J.L. and B.V. Sankar (2000). Compressive failure of sandwich beams with debonded face-sheets. *Journal of Composite Materials*, Vol. 34, No. 14, pp. 1176-1199.
- Grau, D. (2003). Relating Interfacial Fracture Toughness to Core Thickness in Honeycomb-core Sandwich Composites. M.S. Thesis, University of Florida.
- Grau, D.L., Qiu, S., Sankar, B.V. (2005) Relation between Interfacial Fracture Toughness and Mode-mixity in Honeycomb Core Sandwich Composites. To appear in *Journal of Sandwich Structures & Materials*.
- Kale, A., Acar, E. Haftka, R.T., and Stroud, W.J. (2004). Why Airplanes are so Safe Structurally? Effect of Various Safety Measures on Structural Safety of Aircraft. 45th Structures, Structural Dynamics and Materials Conference, AIAA Paper No. 2004-1629, 19-22 April 2004, Palm Springs California.
- Kelton, W.D., Sadowski, R.P. and Sadowski, D.A. (1998). Simulations with Arena. *WCB McGraw Hill*.
- Oberkampf, W. L., DeLand, S. M., Rutherford, B. M., Diegert, K. V. and Alvin, K. F. (1999). A New Methodology for the Estimation of Total Uncertainty in Computational Simulation. *AIAA Non-Deterministic Approaches Forum*, St. Louis, MO, Paper No. 99-1612, April, 1999.
- Oberkampf, W.L., DeLand, S.M., Rutherford, B.M., Diegert, K.V., and Alvin, K.F. (2000). Estimation of Total Uncertainty in Modeling and Simulation, *Sandia Report SAND2000-0824*, 2000.
- Qu, X., Haftka, R.T., Venkataraman, S., and Johnson, T.F. (2003). Deterministic and Reliability-Based Optimization of Composite Laminates for Propellant Tanks. *AIAA Journal*, 41(10), pp. 2029-2036.
- Sankar, B.V. and M. Narayanan (2001). Finite Element Analysis of Debonded Sandwich Beams under Axial Compression. *J. Sandwich Structures & Materials*, Vol. 3, No. 3, pp. 197-219.
- Suo, Z., (1999), Singularities, interfaces and cracks in dissimilar anisotropic media. *Proc. R. Soc. Lond.* A427, 331-358.

This page left blank intentionally.

Overview of the Structures Investigation for the American Airlines Flight 587 Investigation

B. Murphy*, J. O'Callaghan†, and M. Fox‡
National Transportation Safety Board, Washington, D.C. 20594

L. Ilcewicz§
Federal Aviation Administration, Seattle, Washington 98055

and

James H. Starnes, Jr.**
National Aeronautics and Space Administration, Langley, Virginia

On November 12, 2001, about 9:16 a.m., American Airlines flight 587, an Airbus Industrie A300-605R, N14053, crashed into a neighborhood in Belle Harbor, New York, after taking off from John F. Kennedy International Airport (JFK), Jamaica, New York. The airplane was on a scheduled flight to Santo Domingo, Dominican Republic. Two pilots, seven flight attendants, 251 passengers, and five persons on the ground were killed. The airplane crashed after a loss of control resulting from the separation of the vertical stabilizer from the fuselage. The separation of the vertical stabilizer from a transport-category airplane was unprecedented. As a result, the National Transportation Safety Board conducted an extensive structures investigation. For this effort, the Safety Board enlisted the assistance of the Federal Aviation Administration; the National Aeronautics and Space Administration's Langley Research Center; and the airplane manufacturer, Airbus Industrie. The Board's final report on the American Airlines flight 587 accident was issued in October 2004.††

I. Introduction

The vertical stabilizer of the A300-600 is primarily made of a carbon/epoxy composite material and is attached by six lugs and six lateral yokes to the aluminum fuselage. Figure 1 shows the major components of the vertical stabilizer including the fin, rudder, and lugs. The fin and lugs are solid angle ply laminated composites of variable thicknesses and ply lay-ups, and the rudder is a sandwich composite made of composite facesheets over a honeycomb core. Figure 2 shows the details of the fin box near the right rear lug, including the ribs, stringers, rear spar, and yoke attachment.

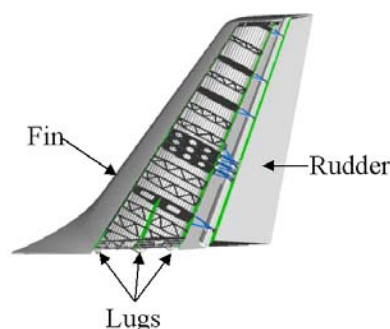


Figure 1. Vertical stabilizer

* Aircraft Structures Engineer, Office of Aviation Safety, 490 L'Enfant Plaza, Washington, DC 20594

† National Resource Specialist—Aircraft Performance, Office of Research and Engineering, 490 L'Enfant Plaza, Washington, DC 20594

‡ Materials Engineer, Office of Research and Engineering, 490 L'Enfant Plaza, Washington, DC 20594

§ Chief Scientific and Technical Advisor – Advanced Composite Materials, Seattle, Washington 98055

** Dr. James H. Starnes passed away during the investigation of the American Airlines flight 587 accident.

†† National Transportation Safety Board, 2004, In-Flight Separation of Vertical Stabilizer, American Airlines Flight 587, Airbus Industrie A300-605R, N14053, Belle Harbor, New York, November 12, 2001, Aircraft Accident Report NTSB/AAR-04-04 (Washington, DC: NTSB, 2004).

Investigative work included the inspection and characterization of the failed structure, a review of the manufacturer's design and certification procedures, numerical analyses to simulate the accident event, and structural tests to verify the most likely failure scenarios. The accident investigation team developed in-depth photographic records of the vertical stabilizer and rudder and mapped the failure sites. A fault tree analysis and failure scenarios were developed. Specimens were cut from the flight 587 vertical stabilizer and rudder for chemical analyses, tests, and nondestructive evaluations (NDE). In-depth NDE surveys were also made of the entire vertical stabilizer and rudder. Fractographic analyses of failed metallic and composite parts were conducted to determine if fatigue was a contributor. Mechanical property tests and chemical analyses of the composite parts were conducted to determine if the composite structure was manufactured as designed and if the properties of the material had not degraded with time. To determine the external loads acting on the vertical stabilizer and rudder, computational fluid dynamics analyses were conducted for the accident conditions. Flutter analyses of the vertical stabilizer and rudder were conducted, and the effects of wake vortex encounters were also determined. Structural analyses of the vertical stabilizer and rudder and structural design details were conducted to determine the external loads necessary to cause the vertical stabilizer and rudder to fail. Detailed finite element models that incorporated progressive failure methods were developed and used to simulate failure for certification test and accident conditions. Structural tests were conducted, and large-scale tests were developed to help verify the most likely failure scenarios.

With the use of these investigative methods, the Safety Board analyzed the circumstances of the flight 587 accident and determined that the vertical stabilizer attachment lugs (see fig. 2) were subjected to in-flight forces and associated stresses above those that they were designed to carry and were capable of withstanding. The overload resulted from the aerodynamic loads on the vertical stabilizer produced principally by the combination of sideslip angle, rudder deflection, and dynamic pressure. These aerodynamic loads were about 2 times the "design limit load," that is, the maximum load the airplane was expected to encounter in service. For certification, the vertical stabilizer is only required to support loads of 1.5 times design limit load without failure. The Safety Board determined that the failure of the right rear lug (see fig. 3) precipitated the failure of the other lugs and the yokes and then the separation of the entire vertical stabilizer. The Board also determined that the vertical stabilizer separation was the result of the loads beyond ultimate design that were created by the pilot's unnecessary and excessive rudder pedal inputs.

This paper presents the Safety Board's findings concerning the accident airplane's structure, including the aerodynamic loading that was placed on the vertical stabilizer in response to the wake turbulence that the airplane encountered just before the accident and the development of stresses in the right rear main attachment lug as a result of this loading. A comparison of this in-flight loading with the certification requirements is also presented.

II. Design Loads for the A300-600 Vertical Stabilizer

The Safety Board's final report on the flight 587 accident included the following information about the design loads for the A300-600 vertical stabilizer (the figure numbers have been changed to reflect the numbering in this paper):

Airbus performed a loads assessment of the A300-600 using a theoretical model that involved aerodynamic, mass, structural stiffness, engine, and systems data. The model was validated by data generated during ground and flight tests.

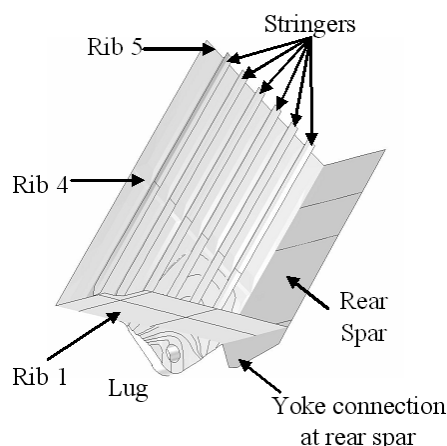


Figure 2. Details of the Fin Box Near the Right Rear Lug

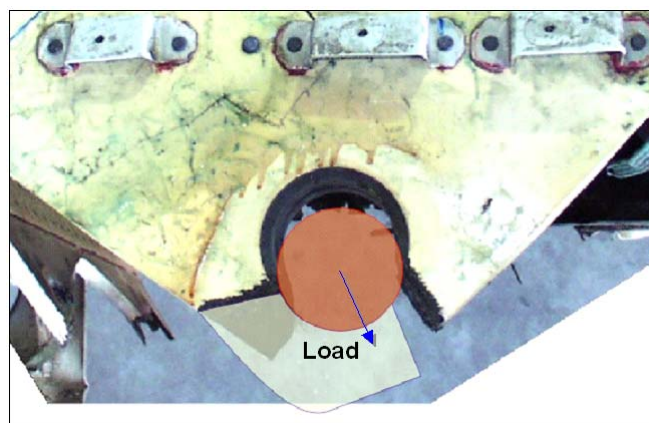


Figure 3. AA 587 Right Rear Lug – Observed Failure

With the use of this model, airplane movements resulting from yawing maneuvers, gusts, and engine failures were simulated, and the associated internal forces induced by the external aerodynamic and mass inertial loadings (the net external loading) on the vertical stabilizer were calculated. These internal forces are transmitted to the fuselage through the six main attachment fittings and the six transverse load fittings. The internal forces within each lug are characterized by the local stress (force per unit area of material), which can be compared directly with measured material strength values.

The external aerodynamic and mass inertial loadings on the vertical stabilizer can also be quantified as a net shear (a side load), a net bending (a moment about the longitudinal axis), and a net torsion (a moment about the vertical axis), as shown in fig. 4. The correlated shear force diagram, which is used to define the limit and the ultimate load design envelopes, consists of one diagram plotting net shear versus net torsion and, as shown in fig. 5, one diagram plotting net torsion versus net bending.

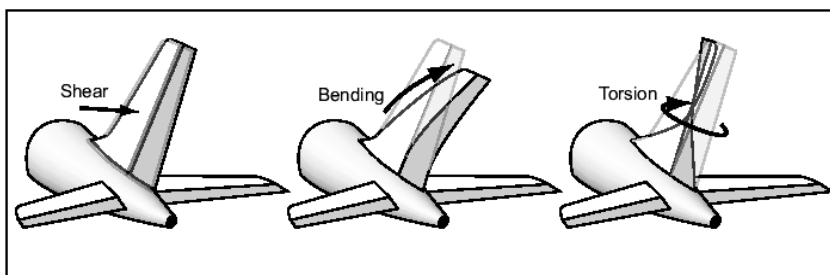


Figure 4. Shear, Bending, and Torsion

Source: National Transportation Safety Board.

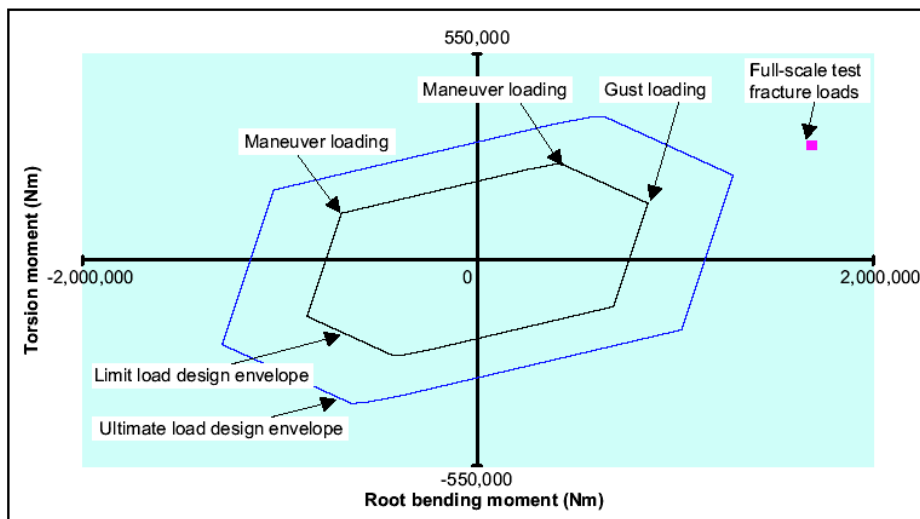


Figure 5. Net Torsion Versus Net Bending

Source: National Transportation Safety Board.

III. Loads on the Flight 587 Vertical Stabilizer

The Safety Board's final report on the flight 587 accident included the following information about the loads on the accident airplane's vertical stabilizer (the figure numbers have been changed to reflect the numbering in this paper):

At any given altitude and airspeed, many parameters affect the loads on the vertical stabilizer; the most significant of these parameters are sideslip angle and rudder angle. During the design of the A300-600, Airbus developed a model of the loads on the vertical stabilizer based on linearized wind tunnel data that described the effects of sideslip angle and rudder angle on the vertical stabilizer structural loads. With the use of this linear loads model, the Safety Board calculated the shear, bending, and torsion loads on the vertical stabilizer during the final seconds of flight 587's recorded FDR data (before the sound of the loud bang at 0915:58.5). Figure 6 shows the calculated bending moment about the root chord in the vertical stabilizer axis system.

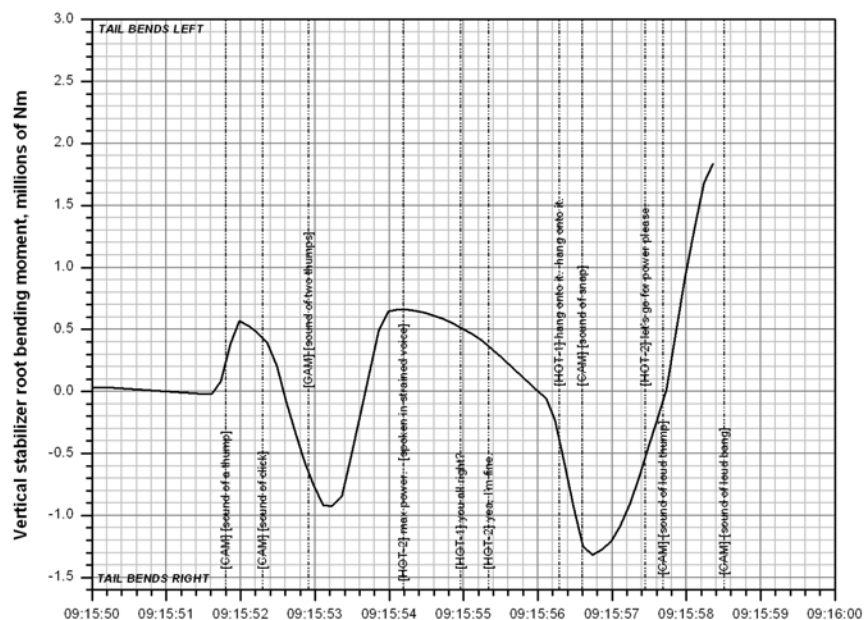


Figure 6. Bending Moment About the Root Chord in the Vertical Stabilizer Axis System

Source: National Transportation Safety Board.

The rudder and sideslip angles about the time of the lug fracture were large enough that portions of the vertical stabilizer began to exhibit aerodynamic stall behavior, that is, regions of separated flow. This separated flow affected the loads such that the linear loads model (which does not account for flow separation) could overestimate the loads in those conditions (high sideslip and rudder angles) in which separated flow is present. As a result, a CFD analysis was performed to calculate directly the effects of the separated flow at the high sideslip and rudder angles of interest. Specifically, the Safety Board asked Airbus to perform a CFD analysis of the flowfield about the entire A300-600 airplane and to provide the aerodynamic pressure loads over portions of the vertical stabilizer. The conditions at which these calculations were made reflected the flight conditions and airplane orientation at the time that the vertical stabilizer separated from the aft fuselage. Because of uncertainties in the sideslip angle, rudder angle, and the absolute load values computed by CFD, the final estimate of loads at the time of the lug fracture were expressed as a range of values. At the time that the vertical stabilizer separated from the airplane, the range of the shear, bending, and torsion loads on the vertical stabilizer were as follows:

shear force: 353,000 to 436,000 N \pm 5 percent
 bending moment: 1,580,000 to 1,840,000 Nm \pm 5 percent (see fig.7)
 torsion moment: 18,600 to 48,100 Nm \pm 5 percent

The bending moment load ranges shown in fig.7 are presented along with the “effective sideslip angle” range and the rudder range at the time that the vertical stabilizer separated from the airplane. Figure 8 compares the estimated aerodynamic loads with the A300-600 design envelopes (as defined by the torsion versus bending correlated shear force diagram).

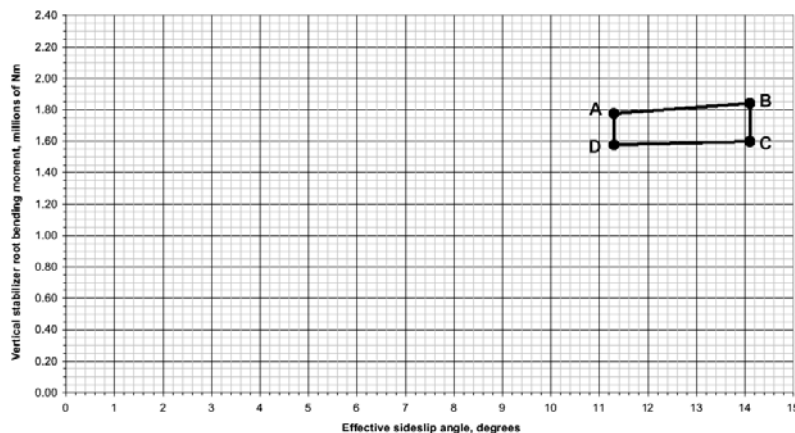


Figure 7. Bending Moment Load Range at the Time of Vertical Stabilizer Separation

Note: The calculated range of the root bending moment is defined by points A through D, which are described in addendum 2 to the airplane performance study. See the public docket for this accident for more information.

Source: National Transportation Safety Board.

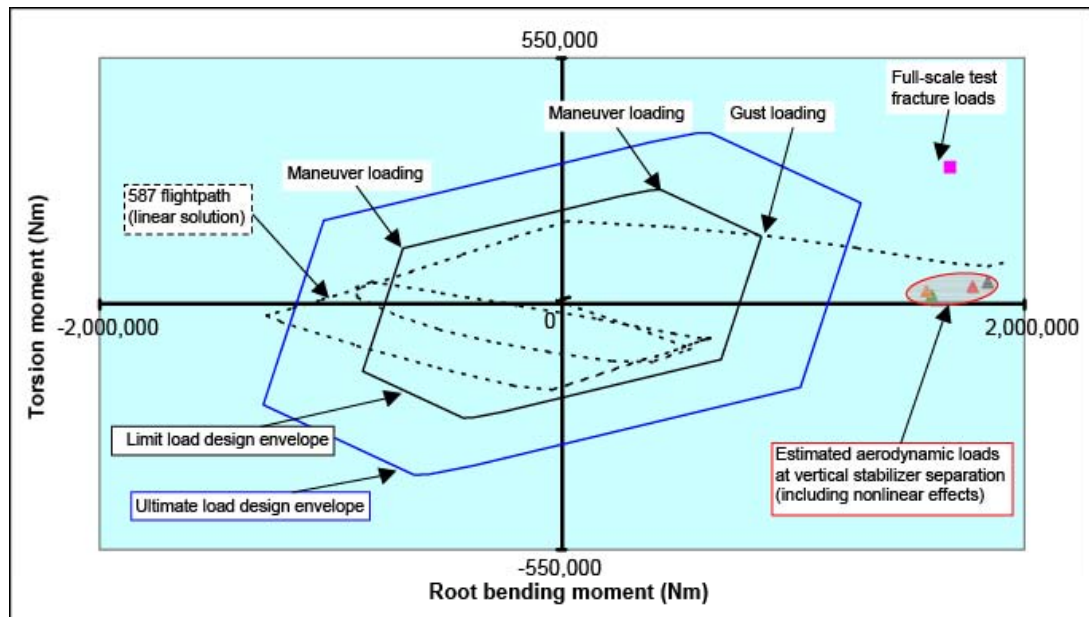


Figure 8. Estimated Aerodynamic Loads in Relation to the Torsion Versus Bending Correlated Shear Force Diagram

Note: The four triangles correspond to the four points in fig. 7. Specifically, the red triangle is point A, the gray triangle is point B, the green triangle is point C, and the orange triangle is point D.

Source: National Transportation Safety Board.

IV. Vertical stabilizer Structures Analysis

A. Design Methods

The Airbus design methods were assessed as comprehensive after a review of the A300-600 certification documentation. The design methods were based on a building-block approach for coupon, subcomponent, and full-scale testing. Further review of certification documents did not reveal any faulty methods or invalid assumptions, although the following three points of concern surfaced during the investigation:

1. Validity of the Full-Scale Fin Certification Test

The validity of the full-scale fin certification test conducted in 1985 was questioned. During the full-scale test, the fin was tested separate from the fuselage, and there was concern that the loading applied at the main attachment lugs might not have represented the fin-on-aircraft condition. The fitting loads applied during the fin test were prescribed exactly from finite element analysis (FEA) of the fin-on-aircraft condition, and thus the validity of the test loading was dependent on the validity of the global (vertical stabilizer, rudder, and aft fuselage) finite-element model. The structures group demonstrated the validity of the global finite-element model through a combination of test/analysis correlation and sensitivity studies and concluded that the applied forces in the full-scale test were representative of the fin-on-aircraft condition. The insensitivity of attachment lug forces to stiffness variations suggested that the attachment lug forces were primarily dictated by the aerodynamic load distribution and the overall geometry of the structure rather than by the local stiffness representation.

Another concern was that the load introduction structure used during the test did not produce attachment lug local bending moments that represented the fin-on-aircraft condition. Safety Board staff did not think that this concern was substantiated because all FEA indicated the bending moments at the attachment lugs were predominantly the result of stiffness eccentricity in the fin structure and the lateral load on the fittings, both of which were represented in the full-scale fin test.

2. Airbus Lug Strength Allowables for Design and Certification

During the investigation, it was recognized that non-trivial local bending moments were reacted at the attachment lugs and that the magnitudes of the moments computed were sensitive to the finite-element idealization of the attachment region. In addition, detailed strength analysis of subcomponent models using progressive failure

analysis (PFA) showed that the magnitude of the bending moment applied to the attachment lug influenced the failure strength of the fitting. The lug strength (force) allowables^{††} applied by Airbus during design and certification were expressed in terms of a resultant force and did not explicitly represent the effect of local bending moments on the strength of the fittings.

The structures group determined that the fact that Airbus did not express the strength allowables in terms of force and moment values did not indicate fault in the certification procedure for two reasons. First, the FEA demonstrated that the local bending moment at the lug was directly related to the force on the lug and was not an independent quantity. Second, the Airbus strength (force) allowable for the lug attachment was based on a building-block test sequence that ultimately incorporated local bending moment effects. Unlike the 1985 certification subcomponent test, the full-scale fin test article generated a representative local bending moment in response to applied fitting forces and, as a result, ruptured at a lower resultant force than the subcomponent test. When Airbus reduced the lug strength (force) allowable for certification based on the full-scale test result, the effect of a representative bending moment on the lug strength was captured, even though the magnitude of the bending moment was never computed or measured.

3. Accident Aerodynamic Loading (External Loads)

A review of the digital flight data recorder (DFDR) data for the last 12 seconds of the accident flight indicated that the first officer performed a series of maneuvers for which the A300-600 was not designed or certificated to perform. The rudder movements immediately before the accident were cyclical and rapid, with full, abrupt, stop-to-stop reversal deflections. The regulations at the time of certification did not require that the analysis of alternating full rudder inputs. Additionally, the current regulations do not require the analysis or demonstration of alternating full rudder inputs during a certification program.

During the accident investigation, Airbus and the Safety Board computed the loads on the vertical stabilizer during the last 12 seconds of the flight, as indicated by the DFDR data. The analysis indicated that the rudder movements created vertical stabilizer loads greatly exceeding those required by the certification standards. The loads were computed from the time history of the control surfaces and associated motion of the airplane, as obtained from the DFDR and subsequent analysis. The time of failure, as determined by the Board and Airbus for the vertical stabilizer, was correlated to a shift/jump in the lateral acceleration.

The bending loads on the vertical stabilizer were the result of the combined sideslip angle (β) and rudder deflection during the flight. At the time of tail separation, the bending loads were extremely high and well above the ultimate load of 129,248 daN-m, which the structure is certified to carry. Additionally, the calculated root bending moment (M_xQ) was nearly equivalent to the bending moment applied during the full-scale certification rupture test. During the 1985 certification test, the vertical stabilizer was loaded to approximately two times the A310-300 limit net shear (Q_y) load of -22,339 daN and the limit fin root bending (M_xQ) moment of 88,300 daN-m. When scaled^{§§} to the design loads for A300-600, this would be approximately two times design limit shear load (Q_y) of -21,580 daN and the bending moment (M_xQ) of 86,165 daN-m. During the test, the vertical stabilizer left rear main attachment lug failed in cleavage mode as a result of a tensile static overload. The measured resultant (F_{xz}) force for the A310-300 rear main attachment at rupture was 904,660 N, which was approximately two times the limit resultant lug force (F_{xz}) of 471,115 kN for the A300-600. The calculated resultant lug force (F_{xz}) at rupture for the accident flight is 925,300 kN. Table 1 summarizes this information.

Table 1. A300-600 Design Loads, 1985 Rupture Test Loads, Flight 587

	A300-600 Design Limit Load	A310-300 Rupture Test	A300-600 Flight 587
Q_y (daN)	-21,580	42,444	-41,577
M_xQ (daN-m)	86,165	-167,770	184,676
M_zQ (N)	15,268	34,072	9,6530
F_{xz} (N)	471,115	904,660	925,300

^{††} Airbus defined the “strength (force) allowable” as the “tested lug rupture load.” Airbus referred to this value, when divided by the applied lug ultimate load or lug limit load in the case of a failsafe analysis, as the “reserve factor.”

^{§§} During the development of the A310-300 and A300-600 airplanes, the gust load levels for the A300-600 decreased below those of the A310-300. The major reason for the decrease in the lateral gust design loads was a reduction to the design speed V_b for the A300-600.

4. Structural Analysis

An FEA was conducted to assess the most likely final failure scenarios. The analysis determined that failure of the right rear main attachment lug was the most probable initial failure. The analysis results indicated that, after the rear main attachment lug ruptured, all the remaining attachment lugs would fail sequentially, with no increase in external loading required. Thus, initial failure of the rear main attachment lug would initiate nearly instantaneous separation of the vertical stabilizer from the airplane.

Both Airbus and NASA evaluated the failure of the right rear main attachment lug using global and local (lug area only) models. The right rear main attachment lug was analyzed, including the neighboring fin region between ribs 1 and 5 and near the rear spar. Detailed FEA with contact was used to determine contact areas, contact pressures and both the lug stress state and strain profile under a loading representative of the accident condition, and the 1985 subcomponent and full-scale certification tests. A PFA was also performed for these conditions to determine the load, mode, and location of failure in the right rear main attachment lug. The FEA results indicated that the contact areas, contact pressures, and the lug stress and strain profile as well as the predicted failure loads, failure mode, and location of failure initiation in the right rear main attachment lug were in excellent agreement with each other for all conditions.

The following conclusions were drawn from the FEA:

- Failure initiated at the right rear main attachment lug followed by an unstable progression of failure of all fin-to-fuselage attachments and separation of the vertical stabilizer from the aircraft.
- The global fin root bending moment M_{xQ} showed a direct relationship to the lug forces F_z and F_{xz} (resultant force) and the lug local bending moment M_x and the associated lug stresses.
- The contact areas, contact pressures, and the lug stress states and strain profiles of the 1985 certification testing and the accident condition were in very good agreement, which suggested that the 1985 static tests represented the accident condition.
- The predicted load, mode, and location of the failure of the 1985 certification tests, and the accident condition were in very good agreement, which suggested that the 1985 tests represented the accident condition.
- The failure mode of the right rear main attachment lug for the 1985 tests and the accident were both cleavage-type failures.
- For the accident case, the predicted failure load for the right rear main attachment lug from the PFA was approximately two times the limit load of the lug.
- The local lug moment, M_x (moment about the fuselage longitudinal axis) had an effect on the failure load of the lugs. Higher absolute values of M_x gave lower failure loads.
- The local bending moment at the lug was directly related to the force on the lug and was not an independent quantity. These bending moments at the attachment lugs were predominantly the result of stiffness eccentricity in the fin structure and the lateral load on the fittings.
- The values of the computed local bending moments were affected by the FEA idealization used during the analysis (rigid versus flexible pin). Accordingly, the associated stresses and strains in the lug varied depending on the idealization.

5. Safety Board Subcomponent Testing

The most likely failure scenario was validated by conducting subcomponent tests on three rear main attachment lugs, with loading based on analysis of the aircraft configuration at the final observed maximum fin loading condition.

Of the three lugs tested, the lugs used in the second and third tests contained nonvisible damage created by a flight excursion^{***} outside the ultimate design envelope. Preliminary strength analyses conducted by the structures group indicated that subcomponent strength was a function of the global fin root bending moment (M_{xQ}), the lug resultant force, and lug local lateral bending moment applied at the lug pin. To increase the fidelity of the computed pin loading, global and local models were coupled to tune the global model, and a global/local iterative procedure was applied to effectively embed a refined 3-D lug ABAQUS model into the global model for both rear main attachment fitting regions. The computed pin loading from the global/local analysis for the airplane model and accident condition was used to prescribe loading conditions for the subcomponent tests conducted at the Airbus facility in Hamburg, Germany. Strength analyses were conducted for the subcomponent test and the airplane configurations.

^{***} American Airlines flight 903, May 1997.

The strength analyses and test results for the subcomponent tests produced a failure load, failure mode, and failure initiation location that were consistent with the predicted accident loading and the physical evidence of the right rear main attachment lug from the accident.

a) Subcomponent Test No. 1

During subcomponent test No. 1 the F_y -load application control commanded a shutdown during damage initiation. The shutdown was caused by a change in lateral stiffness of the lug caused by damage propagation. The test fixture (without lateral yokes) did not allow for load redistribution and subsequent load transfer to the lateral yoke, and thus the test was terminated. For this reason, tests Nos. 2 and 3 were conducted with displacement control versus load control in the y-axis. However, the damage initiation (visible fiber cracks) that was visible on the outboard surface of the lug was typical for the beginning of fracture in the cleavage mode. Additional delaminations within the specimen were also visually similar to those observed in the accident lug. The fracture initiation location was also consistent with the FEA and PFA performed and was similar to the location physically observed in the flight 587 accident lug and FEA and PFA. The final resultant (F_{xz}) load level achieved during the test was 907 kN.

The associated measured strains compared well with the predicted strain values and thus validated the test fixture FEA model and methods. Additionally, the strain level comparison between the subcomponent test No. 1 FEA model and the right-hand-side airplane configuration FEA model indicated that the test performed was representative of the lug behavior during the accident.

b) Subcomponent Test No. 2

During subcomponent test No. 2, the F_y -load application control was changed to displacement control to prevent a premature test shutdown resulting from a reduction in the lateral stiffness caused by damage propagation. This test proceeded to complete rupture of the specimen. The type and location of the fractures and delaminations were consistent with those observed in test No. 1 and the accident lug. The fracture initiation location was also consistent with the FEA and PFA performed and was similar to the location physically observed in the flight 587 accident lug and the flight 587 FEA and PFA. The final resultant (F_{xz}) load level at rupture was 893 kN. The associated measured strains compared well with the predicted strain values and thus validated the test fixture FEA model and methods. Additionally, the strain level comparison between the test No. 2 and the right-hand-side airplane configuration FEA models indicated that the test performed was representative of the lug behavior during the accident.

c) Subcomponent Test No. 3

During subcomponent test No. 3, the F_y -load application control was displacement control to prevent a premature test shutdown resulting from a reduction in the lateral stiffness because of damage propagation. This test proceeded to complete rupture of the specimen. The type and location of the fractures and delaminations were consistent with those observed in test No. 1, test No. 2, and the accident lug. The fracture initiation location was also consistent with the FEA and PFA performed and was similar to the location physically observed in the flight 587 accident lug and flight 587 FEA and PFA. The collected test data showed that the failure initiated at a resultant load level of 953 kN. However, the test stopped at this point (before rupture) because the maximum-programmed load level had been achieved and maintained. Upon removing the load limitation, the final resultant (F_{xz}) load level at rupture was 1,093 kN. Further examination of the test data revealed that significant damage and/or significant changing of the boundary conditions occurred when the 953 kN resultant load was reached, which caused the validity of the data for the final rupture test to be suspect. Overall, the associated measured strains compared well with the predicted strain values up to 953 kN and thus validated the test fixture FEA model and methods. Additionally, the strain level comparison between the test No. 3 and the right-hand-side airplane configuration FEA models indicated that the test performed was representative of the lug behavior during the accident.

The following conclusions were drawn from the testing and analyses:

- The contact areas, contact pressures, and the lug stress states and strain profiles of the subcomponent tests and the accident condition were in very good agreement, which suggested that the subcomponent tests represented the accident condition accurately.
- The predicted load, mode, and location of the failure initiation of the subcomponent tests and the accident condition were in very good agreement, which suggested that the subcomponent tests represented the accident condition accurately.
- The strain level comparison between the subcomponent tests and the airplane configuration FEA model indicated that the tests performed represented the lug behavior during the accident.

6. Summary of Vertical stabilizer and Lug Analysis

All analysis results indicated that the failure initiated at the final observed maximum fin root bending condition during the accident flight, which is when the vertical stabilizer was subjected to a global root bending moment of two times the design limit load of 86,165 daN-m calculated during certification. Relative to the certification limit

load, the resultant lug force from linear global static analysis, local nonlinear contact, and progressive failure strength analyses corresponded to load factors of approximately twice the limit load of 471 kN. For certification, the vertical stabilizer is only required to support loads of 1.5 times design limit load without catastrophic failure. The maximum loading during the accident was shown to significantly exceed the certification requirement. The associated lug stresses were equivalent to the 1985 full-scale and subcomponent certification analysis and the Safety Board's subcomponent analysis and testing. The stresses developed were critical for the material system being used, and thus the lug failed because of a tensile static overload in the cleavage mode. The predicted load, mode, and location of the failure observed during the original full-scale and subcomponent certification tests, as well as the Board's subcomponent analysis and testing, were consistent. Additionally, the observed fracture features and detailed fractography for the accident lug and the subcomponent tests were all consistent. On the basis of the analysis performed by the structures group, it was demonstrated that the large aerodynamic loading produced by the accident scenario caused the right rear main attachment lug to experience reaction forces and associated stresses of approximately twice limit load and that the structure did not fail prematurely but instead performed in a manner consistent with its design and certification. Thus, failure was attributed to vertical stabilizer loads that were greater than expected.

V. Vertical stabilizer Materials Analysis

The Safety Board's final report on the flight 587 accident included the following information about the accident airplane's vertical stabilizer:

No deviations from the original design and materials specifications were found in the vertical stabilizer (including the repair to the left center lug area that was made during manufacturing) that would have contributed to the vertical stabilizer separation. Also, a detailed inspection of flight 587's wreckage, including an extensive examination of the vertical stabilizer main attachment fitting fractures, revealed that each main attachment fitting had features that were consistent with overstress fracture and exhibited no evidence of fatigue features or other preexisting degradation. Fracture features and damage patterns on the right forward, center, and rear lugs were consistent with overstress failure under tensile loading. The right rear lug, in particular, had fracture features that were consistent with failure in the cleavage-tension mode. Fracture features and damage patterns on the left forward, center, and rear lugs had features that were consistent with the vertical stabilizer bending to the left after separation of the lugs on the right side.

VI. Summary of Vertical stabilizer and Lug Analysis

All analysis results indicated that the failure initiated at the final observed maximum fin root bending condition during the accident flight, which is when the vertical stabilizer was subjected to a global root bending moment of two times the design limit load of 86,165 daN-m calculated during certification. Relative to the certification limit load, the resultant lug force from linear global static analysis, local nonlinear contact, and progressive failure strength analyses corresponded to load factors of approximately twice the limit load of 471 kN. For certification, the vertical stabilizer is only required to support loads of 1.5 times design limit load without catastrophic failure. The maximum loading during the accident was shown to significantly exceed the certification requirement. The associated lug stresses were equivalent to the 1985 full-scale and subcomponent certification analysis and the Safety Board's subcomponent analysis and testing. The stresses developed were critical for the material system being used, and thus the lug failed because of a tensile static overload in the cleavage mode. The predicted load, mode, and location of the failure observed during the original full-scale and subcomponent certification tests, as well as the Board's subcomponent analysis and testing, were consistent. Additionally, the observed fracture features and detailed fractography for the accident lug and the subcomponent tests were all consistent. On the basis of the analysis performed, it was demonstrated that the large aerodynamic loading produced by the accident scenario caused the right rear main attachment lug to experience reaction forces and associated stresses of approximately twice limit load and that the structure did not fail prematurely but instead performed in a manner consistent with its design and certification. Thus, failure was attributed to vertical stabilizer loads that were greater than expected.

The structural analysis was incorporated into the overall analysis of the accident. Based on the analysis of the facts learned during the course of the nearly 3-year-long investigation, the Safety Board determined that the probable cause of the accident was as follows:

the in-flight separation of the vertical stabilizer as a result of the loads beyond ultimate design that were created by the first officer's unnecessary and excessive rudder pedal inputs. Contributing to these rudder pedal inputs were characteristics of the Airbus A300-600 rudder system design and elements of the American Airlines Advanced Aircraft Maneuvering Program.

References

All of the following references can be found in the NTSB Public Docket for the American Airlines flight 587 accident investigation.

- ¹O'Callaghan, J., "Group Chairman's Aircraft Performance Study", October 2002, NTSB
- ²O'Callaghan, J., "Group Chairman's Aircraft Performance Study Addendum #1", October 2003, NTSB
- ³O'Callaghan, J., "Group Chairman's Aircraft Performance Study Addendum #2", August 2004, NTSB
- ⁴Fox, M.R., "Materials Laboratory Factual Report 02-077", September 2002 (overall exam report), NTSB
- ⁵Fox, M.R., "Materials Laboratory Factual Report 02-078", October 2002 (NDI report), NTSB
- ⁶Fox, M.R., "Materials Laboratory Factual Report 02-082", July 2003 (materials testing report), NTSB
- ⁷Fox, M.R. and Schultheisz, C.R., "Materials Laboratory Factual Report 02-083", October 2002 (fractography report), NTSB
- ⁸Fox, M.R., "Materials Laboratory Factual Report 03-018", July 2003 (left forward porosity report), NTSB
- ⁹Fox, M.R., "Materials Laboratory Factual Report 03-033", July 2003 (CT scanning report), NTSB
- ¹⁰Young, R. D., Hilberger, M., Moore, D., and Lovejoy, A. E., "NASA Structural Analysis Report on the American Airlines Flight 587 Accident- Part 2," NASA TMX-xxxx, 2003.
- ¹¹Raju, I.S., Dávila, C.G., Glaessgen, E.H., Krishnamurthy, T., Mason, B.H., "NASA Structural Analysis Report on the American Airlines Flight 587 Accident- Part 3", NASA TMX-xxxx, 2003.
- ¹²Airbus Report "A300B4-605R MSN420 - New York Accident - Loads Assessment"
- ¹³Airbus Report TN-EGLG-A00ME0316813, "AA587 Investigation A300-600R Fin Root CSF Diagrams"
- ¹⁴Airbus Report, "AAL587 Accident Investigation: Side-Slip Computation with Integration Method"
- ¹⁵Airbus Report, "AAL587 Handling Qualities Investigation"
- ¹⁶Airbus Report TN-ESGC-1017/03, "AAL587 Investigation, Accident Analysis - FEM Global model VTP & Rudder"
- ¹⁷Airbus Report TN-ESGC-1018/03, "AAL587 Airbus Structure Investigation, Accident Analysis - FEM RHS local rear lug model"
- ¹⁸Airbus Report TN-ESGC-1019/03, "AAL587 Airbus Structure Investigation, FEM Global to Local analysis details"
- ¹⁹Airbus Report TN-ESGC-1020/03, "AAL587 Airbus Structure Investigation, LHS Lug sub-component test #1 FEM analysis"
- ²⁰Airbus Report TN-ESGC-1021/03, "AAL587 Airbus Structure Investigation, Lug sub-component test #1 - Results Test/FEA Comparison", Issue 4
- ²¹Airbus Test Requirement, "Test program Rear Main Fitting A300-600R (Lug Test #1)"
- ²²Airbus Report, "AAL 587 Study of Aeroelastic Scenarios"
- ²³Airbus Report, "AAL587 Investigation – Study on potential Effect of Rudder Delamination"
- ²⁴Airbus Report, "Engine loads calculation for the A300-600R (flight number 587)"
- ²⁵Airbus Report, "A300/A310, Rear Fin Box Attachment - Sub-component Test Summary"
- ²⁶Airbus Report, "A300/A310 Composite Fin Box, Full-Scale Certification Test Summary"
- ²⁷Airbus Test Requirement, "Test program Rear Main Fitting A300-600R (Lug Test #2 and #3)"
- ²⁸Airbus Report TN-ESGC-1020/04 Is1, "AAL587 Airbus Structures Investigation, Lug Test #2 – Results/FEA Comparison"
- ²⁹Airbus Report, TN-ESGC-1021/04 Is1 "AAL587 Airbus Structures Investigation, Lug Test #3 – Results/FEA Comparison"
- ³⁰Airbus Report TN-ESGC-0001/04, "AAL587 Airbus Structure Investigation, Validation of Sub-component Test Principles"
- ³¹Airbus Report "Incoming inspection of the rear lug cut-outs LH side shell of the fin box from the aircraft MSN 513 of the American Airlines"
- ³²Airbus Report "Incoming inspection of the rear lug cut-outs RH side shell of the fin box from the aircraft MSN 513 of the American Airlines"

Fractographic Examination of the Vertical Stabilizer and Rudder from American Airlines Flight 587

Matthew R. Fox* and Carl R. Schultheisz†
National Transportation Safety Board, Washington D.C.

James R. Reeder‡
NASA Langley Research Center, Hampton, VA 23681

The first major structural component failure of a composite part on a commercial airplane occurred during the crash of American Airlines Flight 587. The fractured composite lugs that attached the vertical stabilizer to the aircraft tail and the fractured composite honeycomb rudder were examined as part of the National Transportation Safety Board investigation of the accident. In this paper the composite fractures are described and the resulting clues to the failure events are discussed.

I. Introduction

On November 12, 2001, shortly after taking off from Kennedy International Airport, the composite vertical stabilizer and rudder separated from the fuselage of American Airlines Flight 587, rendering the airplane uncontrollable. The Airbus A300-600 airplane crashed into a neighborhood in Belle Harbor, New York, killing all 260 persons aboard the airplane and 5 persons on the ground. This accident was unique partly in that it was the first time a major structural component fabricated out of composite material failed in flight on a commercial airplane.

Analysis of the flight data recorder revealed the airplane had performed a series of yawing maneuvers in the seconds before separation of the vertical stabilizer, and the separation of the vertical stabilizer occurred while the airplane was pointed to the left of its flight path. This orientation would have produced a bending moment on the vertical stabilizer leading to tension on the right-side attachments and compression on the left.

The separated pieces of the vertical stabilizer and rudder were recovered away from the main crash site mainly from the water of Jamaica Bay. The vertical stabilizer was largely intact, and had separated from the fuselage by fractures at the lower end where it had attached to the fuselage. Many fractured pieces of the rudder were recovered near, but mostly fractured from, the vertical stabilizer. As part of the overall investigation into the accident, a detailed examination of the fractures in the vertical stabilizer and rudder was conducted in order to determine the failure mechanism and direction of fracture propagation where possible, including assessing the possibility of any pre-existing damage or fatigue cracking.

In addition, three subcomponent tests were conducted on aft lugs from an unused skin panel and from another airplane using accident loads derived from analysis of recorded flight data. Fracture patterns for these three test specimens were compared to the corresponding structure on the accident airplane.

In this paper, the structures of the vertical stabilizer and rudder are described. Next, results of the fractography of the vertical stabilizer and rudder are presented and the interpretation of the results toward understanding the failure is discussed. Finally, fractographic examination results of the three subcomponent tests are presented and significance of the fracture features are discussed.

II. Description of Structures

Development of the Airbus A300-600 model began in 1980, and certification occurred in 1984. The vertical stabilizer and rudder for the accident airplane, delivered new in 1988, had a symmetric airfoil shape. The vertical stabilizer and rudder were 27 feet 3 inches tall. From leading edge to trailing edge the width of the vertical stabilizer and rudder was 25 feet at the base and 10 feet 2 inches at the tip.

*Senior Materials Engineer, Materials Laboratory Division

†Materials Research Engineer, Materials Laboratory Division

‡Research Engineer, Mechanics of Structures and Materials Branch.

A. Vertical Stabilizer Structure

The vertical stabilizer for the Airbus A300-600 airplane was a stiffened box with removable leading edge fairings and trailing edge panels. An internal view drawing of the vertical stabilizer is shown in Figure 1. The stiffened box consisted of two integrally stiffened skin panels for the left and right sides, spars for the forward and aft sides, and closure ribs at the upper and lower ends. The integral stiffeners in the skin panels consisted of 24 "I"-shaped stringers that extended spanwise parallel to the aft spar, numbered from the aft to forward. Internal stiffeners for the box consisted of a center spar at the lower end of the span and 16 ribs, not including the two closure ribs. The ribs were numbered from the lower end upward starting with the lower closure rib. The components of the box were riveted together, and the leading edge fairings and trailing edge panels were attached with threaded fasteners.

Except for the fasteners, lightning protection strips, and trailing edge panel support frames, the vertical stabilizer was made entirely of composite materials. The stiffened box of the vertical stabilizer was a solid carbon-fiber reinforced polymer (CFRP) laminate composed of T300 carbon fibers in a CIBA 913 epoxy matrix. The laminate included both unidirectional tape and eight-harness satin fabric layers in the construction. The zero-degree fibers of the fabric and tape layers in the composite were oriented parallel to the stringers and aft spar, which was at an angle of 33.3 degrees aft of vertical. The leading edge fairings and the trailing edge panels for the vertical stabilizer were sandwich composites having a Nomex honeycomb core and glass-fiber reinforced polymer (GFRP) facesheets on the leading edge fairings and both GFRP and CFRP facesheets for the trailing edge panels.

The main attachment locations for the vertical stabilizer were six CFRP lugs (main lugs) that connected by bolts approximately 2 inches in diameter to six metal clevis fittings on the fuselage. A schematic view of the typical assembly cross-section is shown in Figure 2 (drawing of lug cross-section). After the assembly was cured, the lug attachment bolt holes were core-drilled out. Three main lugs extended from the lower end of each of the two vertical stabilizer skin panels. At the thickest point, the main lugs were approximately 1.62 inches, 2.48 inches, and 2.17 inches thick for the forward, center, and aft lugs, respectively. The aft lugs alone each had more than 170 layers composed of approximately 50 percent ± 45 -degree fabric, 25 percent 0/90-degree fabric, and 25 percent 0-degree tape. The thickness of each lug decreased as plies were dropped in the lug-to-skin transition area. The skin layers were made of ± 45 -degree fabric. The I-shaped stiffeners had 0-degree tape at the caps and ± 45 -degree fabric in the web.

Each lug contained two separate pieces that were cured separately before the final assembly. In the final assembly, the outer precured half was laid down, followed by the skin layers, then the inner precured half, the compensation layers, the rib 1 attach flange, the stringer outer flange (tape) layers, and the stringer module layers.

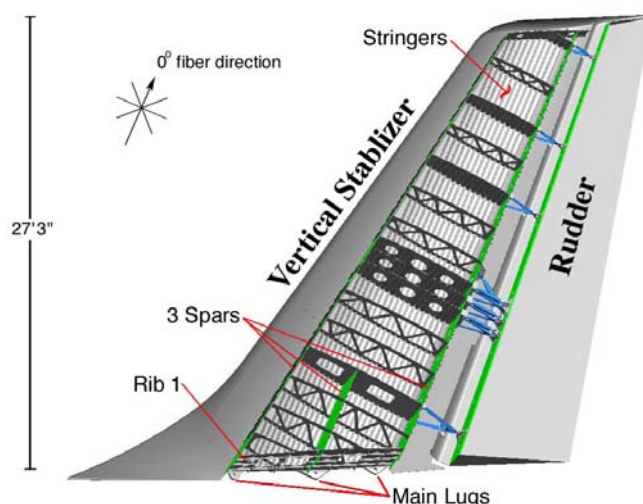


Figure 1. Airbus A300-600 vertical stabilizer construction.

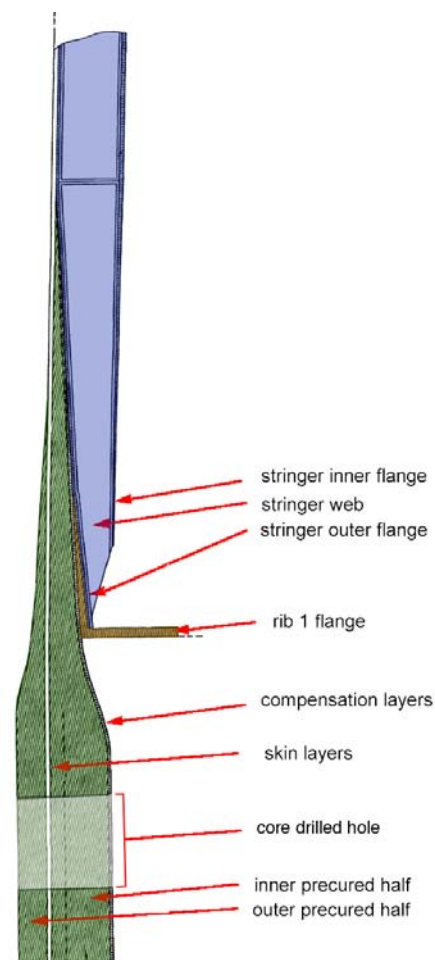


Figure 2. Drawing of main lug cross-section.

Six smaller composite lugs (transverse lugs) attached the vertical stabilizer to the fuselage by lateral yokes. Two of these transverse lugs extended from the lower end of each of the three spar webs. These lugs were approximately 0.47 inch thick.

B. Rudder Structure

The rudder was a single-segment wedge-shaped box design with removable leading edge fairings. The wedge consisted of left and right skin panels with a single spar at the forward side. The skin panels were fastened together at the trailing edge by rivets with a metallic strip on each side. Threaded through-bolts near the trailing edge also helped fasten the two skin panels. At the lower end, a metal strap, which retained the rubber lower sealing strip, was attached by threaded fasteners that also connected the skin panels to the lower rib. The spar was riveted to the skin panels. Pieces of the leading edge fairings were attached to the skin panels with threaded fasteners and to each other with threaded fasteners through metal support flanges. There were no internal stiffeners in the wedge. Closure ribs cap the upper and lower ends of the rudder.

The rudder skin panels and spar were sandwich composite panels. Each panel had a Nomex honeycomb core and GFRP and CFRP face sheets. The leading edge fairings were sandwich composites with GFRP facesheets.

The rudder was attached to the vertical stabilizer by seven hinges, numbered from the lower end upward. There were three rudder position actuators that control the rotation of hinges 2, 3, and 4. Each hinge was composed of two aluminum alloy fittings pinned together at the hinge line. The forward fittings were attached to the vertical stabilizer with bolts that fastened to CFRP flanges on the vertical stabilizer aft spar. Spherical bearings were located at each attach point for the forward fitting. The aft fittings were attached to the rudder spar using bolts that threaded into barrel nuts located in fiberglass blocks embedded in the rudder skin panels aft of the rudder spar.

III. Fractographic Examination Procedures and Challenges

For most common airplane structural metals, visual inspection or low-power magnification is often sufficient to determine fracture mechanism and direction. For metals, the fracture plane, surface roughness, radial marks, chevrons, shear lips, and general deformation when present all provide macroscopic clues to the fracture mechanisms, direction of fracture propagation, and relative motion of mating surfaces. Preexisting cracks in metals often show staining or changes in color associated with corrosion¹. Using these clues, large areas of damaged structure can be examined relatively quickly by an experienced investigator to identify fracture origins and areas requiring closer inspection.

The fractographic examination of the composite fractures in the accident vertical stabilizer presented a challenge in that it was more extensive than what is typically required for an overstress fracture of a similar metal structure. Visual clues to preexisting fractures, such as flat fracture features with curving boundaries or staining from corrosion that can be readily observed in structural metals, generally are not readily visible in composites. Furthermore, the visual cues to fracture propagation directions that are sometimes apparent in composite structures, such as crack branching in translaminar fractures (fractures that break fibers) or banding in delaminations (fractures between layers), were not apparent in many of the fractures of interest. In determining the failure mechanism and directions in the vertical stabilizer and rudder during the accident investigation, fine fracture features were examined at high magnification across relatively large areas of the fracture surfaces in order to determine fracture mechanisms and propagation directions, a time-consuming process for the failure investigation. However, since fatigue fractures and other preexisting cracks may appear similar during a macroscopic examination, the detailed inspection using high magnification was required to complete the fractographic analysis.

The fractographic examination of the translaminar fractures and delaminations of the vertical stabilizer and rudder incorporated visual examination and scanning electron microscopy (SEM). The visual examination included the documentation of the macroscopic fracture features. The documentation included mapping of fractures, which could be used to aid in identifying fracture propagation directions from crack branching patterns. Also, macroscopic indications of translaminar fracture under tension or compression were documented. On delaminations, surfaces were examined for changes in reflectivity, which could indicate changes in fracture mechanism or mode². However, for most of the fracture surfaces, SEM was required to determine the fracture mechanism and fracture propagation direction.

SEM examination of translaminar fracture surfaces was used to determine the fracture mechanism and propagation directions, and SEM examination of delamination surfaces was used to identify the layers involved, fracture mechanisms, modes of fracture, and propagation directions. Additionally, results of the examination were

used to check the construction against the manufacturing drawings and to determine how the fractures related to the loading of the overall structure.

Over 300 SEM photographs were taken of translaminar fractures in the main attachment areas of the vertical stabilizer, and more than 150 square inches of delamination surface areas were examined at high magnification. Examined fracture surfaces were coated with a conductive layer of gold and palladium. For translaminar fractures intersecting the lug attachment hole, the entire fracture surfaces were examined at high magnification, and for translaminar fractures above the lug holes, several inches of the fracture were examined at high magnification. Samples for the SEM examination of the delamination surfaces were typically approximately two inches square and were taken from widely spaced areas on the exposed fracture surfaces in an effort to identify the overall trends. Samples were also taken across areas where the delamination surface morphology changed (mostly as a result of the ends of plies in the lay-up) to explore for local differences in stress state or crack propagation direction. Two samples, one from each of the two large delaminations, were not cleaned and were the first ones examined in order to explore the surface for matrix rollers, which would have been an indication of fatigue³. Since uncleaned samples were covered in debris, all other fracture surfaces were ultrasonically cleaned in water before coating.

Another challenge for the fractographic analysis was the relatively small amount of fractographic reference material dealing specifically with fabric-reinforced composites. Most of the literature describing fractography of composites focused on unidirectional tape lay-ups. However, fabrics have unique characteristics that lead to features such as more variation in resin content on delamination surfaces and less fiber pullout in translaminar fractures relative to tape-reinforced materials. The presence of woven fabric in the construction led to some interesting phenomena that could be useful in better analyzing composites failures. In the unidirectional lay-ups, river marks were typically only observed in Mode I loading. However, in the fabric construction, river marks also could be found in matrix-rich areas in the vicinity of the bundle crossings, and could be seen in the base of hackles in the transition from a bundle at one orientation to a perpendicular crossing bundle. The river marks in the matrix-rich bundle crossings were used to identify a general direction of fracture propagation upward and aftward for both of the large delaminations (at the forward left and aft left attachments). The use of the river marks at the base of the hackles was explored in the examination of the delaminations at the forward right lug. As composites with fabric reinforcements are being increasingly used in airplane structures, more research is needed in characterizing these fracture surfaces generated under controlled laboratory conditions to assist the failure analyst in interpreting fractographic details.

IV. Fracture Surface Observations and Discussion

A. Stabilizer Damage

The vertical stabilizer was largely intact with no significant areas of skin buckling. An overall view of the vertical stabilizer as it was being recovered from the water of Jamaica Bay is shown in Figure 3. At the lower end, each of the six attachment locations were separated either by fractures that intersected the lug attach hole or by fractures through the structure above the hole. A schematic drawing of the lower end of the vertical stabilizer is shown in Figure 4, where a general fracture location for each lug is shown with overall views of each of these lug fractures. Portions of rib 1, the rib 1 rib-to-skin attach angle, and the lower end of the forward spar also were fractured. Along the trailing edge, the trailing edge panels were damaged in several locations. A more detailed description of the damage is presented in reference 4.



Figure 3. Vertical stabilizer as recovered from Jamaica Bay.

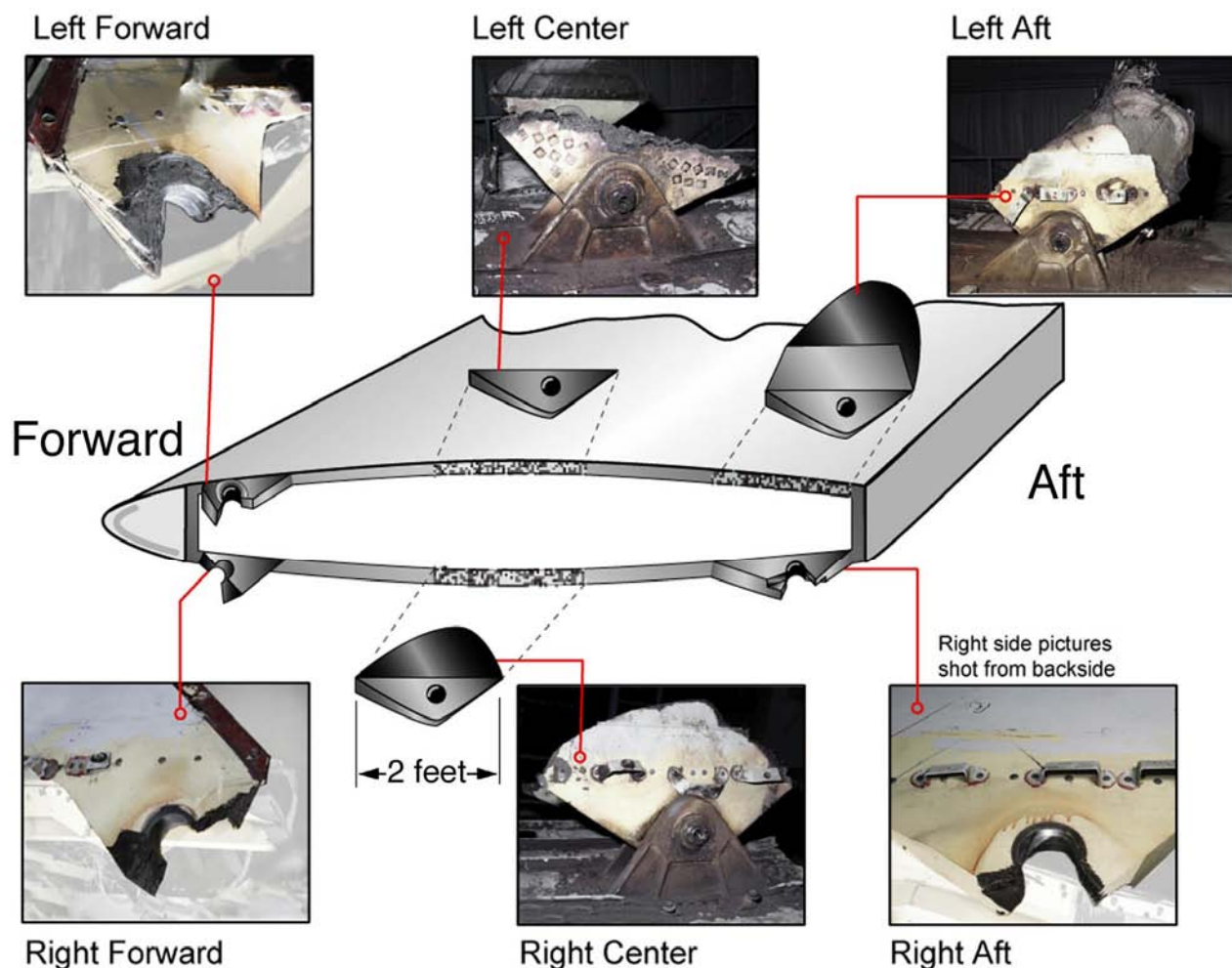


Figure 4. Overall views of main lug fractures with relative locations on vertical stabilizer.

B. Description of main lug fractures

The right aft, right forward, and left forward main lugs had translamellar fractures that intersected the attachment hole, and the remaining lugs had translamellar fractures in the structure above the lug. Each of the lugs had delaminations in the lug area and/or in the structure above the lug. Details of the fractographic examination are presented in references 5 and 6. Some of the delaminations extended into the main portion of the vertical stabilizer, and the extents of these delaminations were determined using nondestructive inspection (NDI), including ultrasonic inspection and x-ray-computed tomography scanning and imaging. Results of the NDI of the vertical stabilizer are presented in references 7 and 8.

1. Macroscopic fracture features

The main lug translamellar fractures on the right side of the vertical stabilizer generally had rough fracture features consistent with overstress fracture in primarily tensile loading. Delaminations were observed at the edges of each of the lugs on the right side. The extent of the delaminations as determined using NDI was limited to within the fractured lugs or within approximately four inches of a translamellar fracture.

The right aft lug failed by translamellar fracture through the bolt hole as shown in Figure 5. The translamellar fracture surfaces had a rough appearance consistent with fracture primarily under tensile loading. Fractures on each leg of the lug were on different translamellar planes, and the change in planes occurred near the center of the lug thickness. On the aft side of the bolt hole, the outboard side of the fracture was in a plane nearly perpendicular to the zero-degree fiber direction, and the inboard side of the fracture was in a plane approximately parallel to the 45-degree fiber direction. On the forward side of the bolt hole, the outboard side of the fracture was in a plane approximately parallel to the zero-degree fiber direction, and the inboard side of the fracture was in a plane nearly

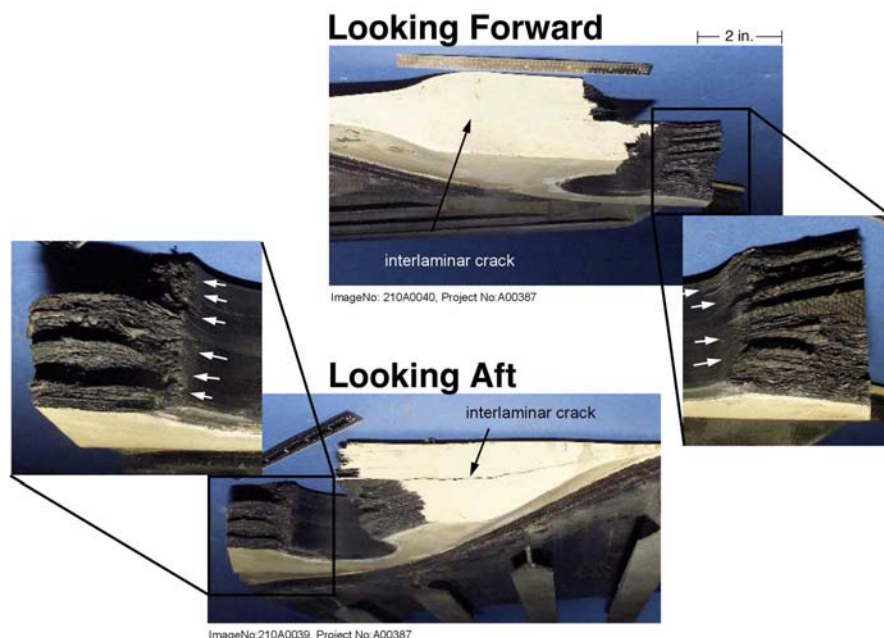


Figure 5. Right aft lug translaminar fractures (pictured from below the lug).

indicating that fracture occurred at the forward side first, and then the lower ligament hinged about the aft side.

The main lug translaminar fractures on the left side of the vertical stabilizer also generally had rough fracture features consistent with overstress fracture in primarily tensile loading, but they also showed indications of bending to the left. The left forward lug had multiple delaminations in the lug area and an impression on the left side corresponding to contact with the fuselage attachment clevis. The impression indicates the left skin panel of the vertical stabilizer bent to the left and in order to obtain the bending displacement required, the right side skin panel must have separated from the fuselage first. The left forward lug also had a delamination extending upward into the structure up to 43 inches from the lower end. The left center lug had an area with compression fracture features at the outboard side of the translaminar fracture, consistent with bending loads to the left. The left aft lug had delaminations extending up to 37 inches from the lower end. Multiple delaminations through the thickness were present in the lug-to-skin transition area, allowing layers associated with lug to separate from the rest of the structure.

2. Microscopic fracture features

On translaminar fractures, the ends of some fibers were oriented roughly perpendicular to the fracture plane. A typical SEM view of these fiber ends on one of the translaminar fracture surfaces is shown in Figure 6. Fiber ends such as those shown in Figure 6 were examined using SEM to help determine the fracture mechanism and propagation direction. For fibers having radial patterns indicative of tensile fracture, the local fracture propagation direction could be determined from the direction of the radial pattern of several fibers^{9,10}. Then, general directions of fracture propagation for the translaminar fractures could be determined by averaging the directions indicated by the

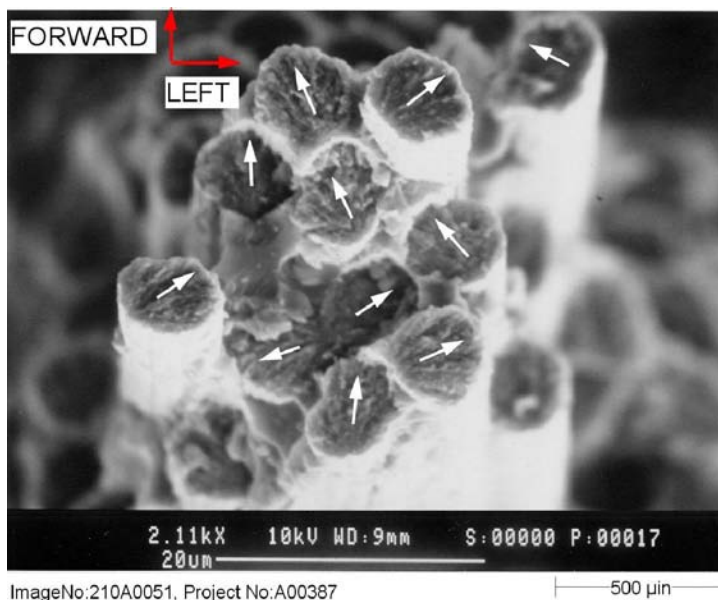


Figure 6. Fractured carbon fibers showing crack growth directions.

parallel to rib 1. Bearing damage was observed at the bore surface near both fracture surfaces, as indicated by white unlabeled arrows in Figure 5.

The right center lug failed above the bolt hole in the lug-to skin transition above rib 1. Translaminar fracture features were relatively rough, consistent with overstress fracture under tensile loading.

Fractures on the right forward lug intersected the lug hole. Translaminar fracture features were relatively rough, consistent with overstress fracture under tensile loading. Some evidence of local compressive loading was observed near the aft side of the lug,

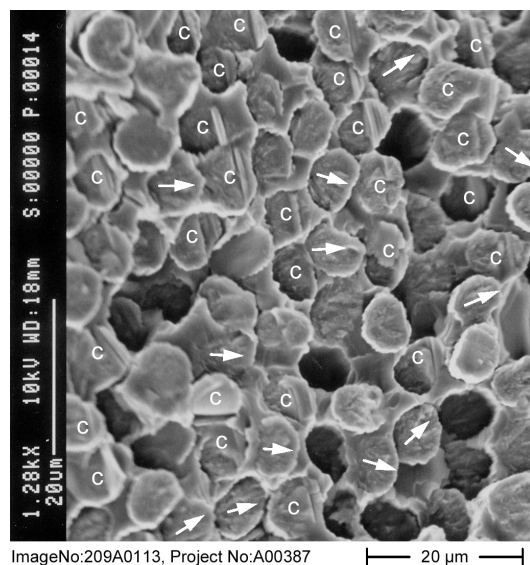


Figure 7. Fractured carbon fibers showing compression chop marks (C).

Samples of the delamination fracture surfaces were examined in the scanning electron microscope to determine the orientation of the shear stress at the fracture and to identify the direction of crack propagation. Fracture features that were used to make these determinations included hackles (thin plates of fractured matrix material between fibers oriented perpendicular to the fiber axis, with free edges that point in a general direction opposite to the local shear applied at the fracture surface)^{13,14} and river marks (related to the initiation of matrix cracks that coalesce into larger cracks, indicating the direction of propagation)². A typical view of hackles and river marks observed on one of the delaminations is shown in Figure 8. The samples also were carefully examined for indications of fatigue crack propagation, such as striations in the fiber impressions in the matrix^{3,10}, matrix rollers (pieces of fractured matrix material rolled into cylindrical shapes by the relative motion of the fracture surface during cyclic loading)^{3,10}, or rubbed hackle formations³, however no evidence of fatigue was observed on any of the delamination surfaces.

When hackles form in CFRP's, the hackles orient perpendicular to the fiber axes, so the hackles in the orthogonal bundles of the woven fabric would generally point in two orthogonal directions. In some cases, the superimposed imprints of unidirectional tape at 45° to those bundles also added hackles at a third direction. Hackles also point generally opposite the locally applied shear at the fracture surface, so the multiple orientations of hackles from the different fiber bundles bound the direction of the local shear within an angle of 90°.

River marks were observed in matrix-rich areas in the vicinity of the bundle crossings, and could be seen in the base of hackles in the transition from a bundle at one orientation to a perpendicular crossing bundle. The river marks in the matrix-rich bundle crossings were used to identify a general direction of fracture propagation upward and aftward for both of the large delaminations (at the forward left and aft left attachments). The use of the river marks at the base of the hackles to determine delamination growth direction was explored in the examination of the delaminations at the forward right lug.

radial patterns across many areas of the fracture surfaces. Also, since fatigue and overstress fractures can appear similar from a macroscopic view, the microscopic examination of the fracture surfaces included looking for evidence of fatigue such as rounded edges on fiber ends¹¹ or striations in the matrix^{3,10,12}, however, no evidence of fatigue was observed on any of the translaminar fracture surfaces.

At high magnification, fiber end fractures for fibers oriented perpendicular to the fracture plane generally showed radial fracture features consistent with fracture under tensile loading. In an area near the outboard surface of the left center lug, fiber ends showed chop marks (lines across the fiber ends), indicative of local compressive loading. Examples of these chop marks can be seen in Figure 7 on the fiber ends marked with a "C". The combination of tension on the inside edge and compression on the outboard surface is associated with an overall lug bending to the left. Using the radial patterns on the lug translaminar fractures, fracture propagation directions were determined to be extending from the lug holes for the right aft, right forward, and left forward lugs (all lugs that had fractures intersecting the lug hole). For the right center lug, fracture propagated from aft to forward, and for the left center and left aft lugs, fracture propagated from forward to aft.

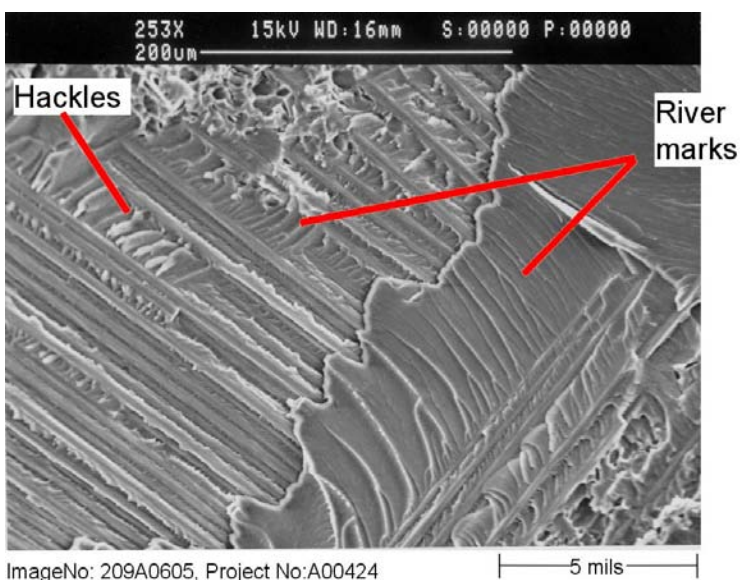


Figure 8. Delamination fracture features.

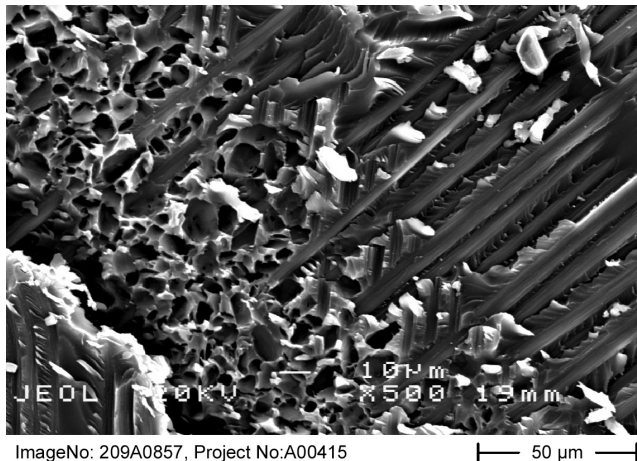


Figure 9. Porosity in matrix rich regions where bundles cross.

lug layers, and on average pointed upward and aft on the mating sides, consistent with the lug pieces moving downward relative to the remaining structure. In the portion of the delamination above the lug-to-skin transition, hackles generally pointed downward and forward on the outboard side and upward and aft on the mating side, indicating a shear direction consistent with fracture under bending to the left. River patterns generally coalesced upward and aft, indicating crack propagation extending upward from the lower end. No evidence of fatigue, such as striations in the matrix or edge rounding of the fiber ends on the translaminar fracture surfaces or matrix rollers or striations on the delamination surfaces, was observed on any of the fractures.

A summary of the observed fracture patterns is shown in Figure 10. The schematic drawing represents a horizontal cross-section of the vertical stabilizer through the main attachment lugs as viewed from above. Lug cross-sections with a light band at the center represent the lugs that failed through the bolt hole. Solid lug cross-sections represent fractures above the bolt holes. Arrows on the lug surfaces indicate the approximate direction of fracture observed on the translaminar surface. On the left center lug, the area of compression fracture features near the outboard side is indicated. The results showed that the failure pattern of fracture in tension on the right side was consistent with an overall bending of the vertical stabilizer to the left. On the left side, the failure pattern of tension and bending to the left was consistent with an overall bending of the vertical stabilizer to the left after fracture of the lugs on the right side.

It was noted that the only compression translaminar failure features were present on the vertical stabilizer at the outboard side of the center aft lug. Typically, composites have less strength in compression than tension. However, the design of the vertical stabilizer was such that the magnitude of the lug failure loads in tension were less than in compression. Furthermore after failure of the lugs on the right side, the curvature of the panel would cause tension loading in the forward and aft lug and compression in the center lug with continued bending to the left. Other unknown factors, such as changes in air loading as the vertical stabilizer deflected after the initial fractures on the right side, would further influence the failure patterns on the left side.

At the matrix-rich areas where bundles crossed, some porosity was observed having a somewhat angular appearance as shown in Figure 9. These pores were identified as arising from excess curing agent that had crystallized within the matrix. Such crystals could have been physically removed in the fracture process or dissolved by the water from which the vertical stabilizer was recovered.

On the delamination surfaces at the left forward lug, hackles on average pointed downward and forward on the outboard side of the delamination and upward and aft on the mating side, indicating a shear direction consistent with fracture under tensile loading and/or bending to the left. River patterns coalesced upward and aft, indicating crack propagation extending upward from the lower end.

On the delamination surfaces at the left aft lug, hackles on average pointed downward and forward on the side of the delamination associated with the

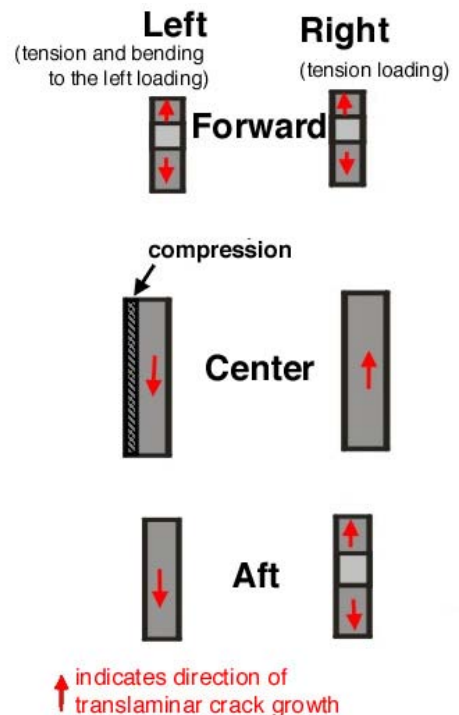


Figure 10. Main lug fracture pattern summary (viewed from above).

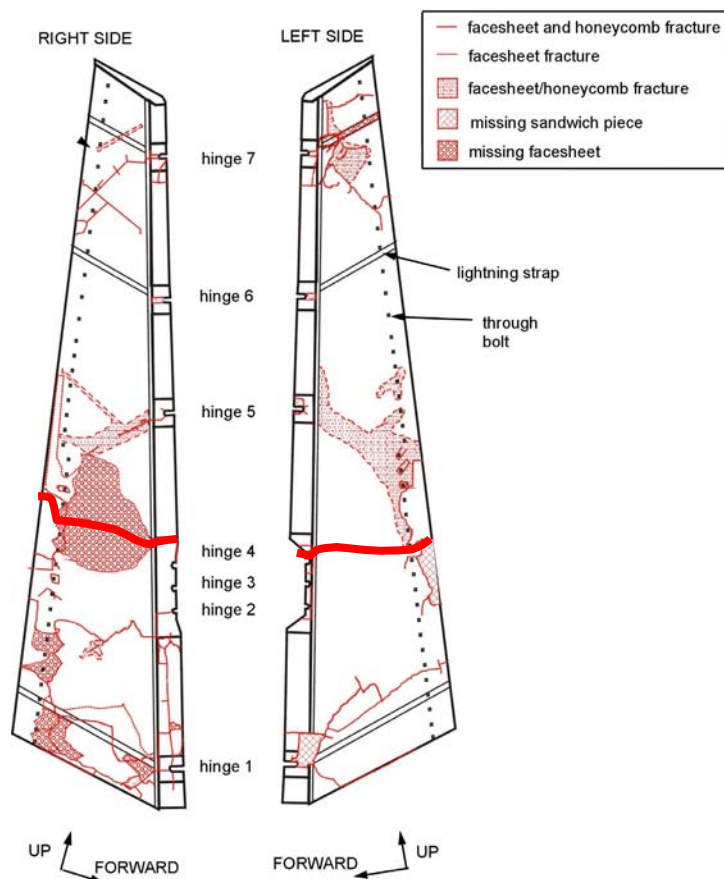


Figure 11. Rudder visible damage.

including x-ray radiography, Lamb wave imaging, thermography, ultrasonic inspection, and tap testing. Generally, no evidence of debonding or water ingress was observed in areas away from visible fracture locations.

The rudder had a chordwise fracture through the skin panels on both sides of the rudder near hinge 4 as highlighted in Figure 11. The fractured facesheets of the honeycomb panels in this region were examined. The only fibers running perpendicular to the fractured surface were glass fibers in the adhesive layer that bonded the facesheet to the Nomex core. Chop marks indicating compression failure were found on some of the glass fibers on the inner and outer facesheet on the left side of the rudder and were also found on the inner facesheet on the right hand side. No compression markings were found on the outside facesheet of the right side. An explanation of how these failures occurred would be that the left side failed first due to a bending moment to the left. Once the left side failed the right side sandwich panel would carry the bending moment putting the inside facesheet in compression.

A large section of facesheet was peeled from the Nomex core in the area of hinges 2, 3, and 4. The facesheet was not recovered, but the fractured adhesive attached to honeycomb was examined and found to have step and scalloping features as seen in Figure 12 that indicated a fracture direction. River markings found in the scalloped region supported this interpretation of the

C. Description of the rudder damage

Approximately 95% of the rudder was recovered in numerous pieces. Two pieces of the rudder leading edge fairing and one piece of the rudder right skin panel were recovered on land. The remaining pieces of the rudder were recovered from Jamaica Bay. An overall view of the damage patterns on the rudder is shown in Figure 11. Detailed description of the visible damage is presented in reference 4. Results of NDI on the rudder are presented in reference 7.

Many areas of the rudder had facesheets that fractured from the honeycomb core. The facesheet-to-honeycomb fractures had features consistent with laboratory peel test fracture features. A description of the laboratory peel tests is presented in reference 15. Metal strips at the leading and trailing edges of the skin panels had features consistent with overstress fracture with no evidence of fatigue.

All but one (the hinge 1 aft fitting) of the 14 rudder-to-stabilizer hinge fittings were recovered, either attached to the vertical stabilizer or to the rudder. Forward pieces of several fractured attachment bolts were not recovered. Hinge and attachment bolt fractures at the rudder hingeline were consistent with overstress fracture, and no evidence of fatigue was observed.

Portions of the rudder skin panels were examined using several NDI techniques

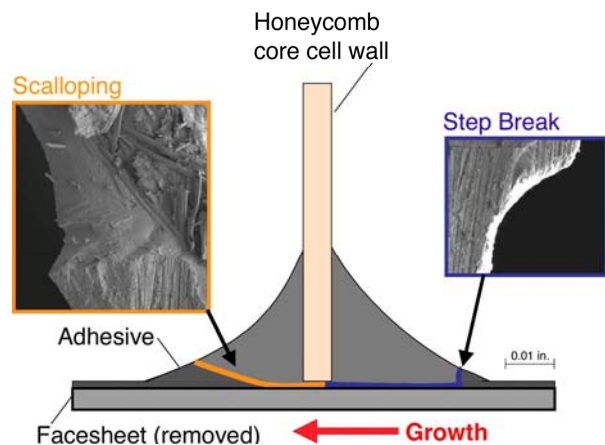


Figure 12. Fracture of the rudder honeycomb core from the facesheet.

fracture growth direction. From samples taken from three separate regions, the facesheet appeared to have been peeled from the forward side of the rudder skin panel toward the trailing edge.

In summary, no evidence of significant preexisting damage was observed on the rudder. Furthermore, airplane performance analysis based on information from the flight data recorder showed the rudder performed as expected until the vertical stabilizer separated from the fuselage. Also, a structural analysis showed that the aerodynamic loads on the rudder prior to separation of the vertical stabilizer from the fuselage were insufficient to cause failure. Therefore, damage to the rudder was considered secondary to the failure of the vertical stabilizer.

V. Subcomponent Tests

Structural analysis indicated that under accident loading conditions, fracture of the vertical stabilizer would have initiated at the right aft lug. Three aft lugs were obtained for mechanical testing using applied loads that were derived from recorded flight data from the accident. The lug for the first test was obtained from a production left skin panel that had sections cut from it for destructive testing, but the aft lug had been left undisturbed. The lugs for the second and third tests were obtained from a vertical stabilizer that had been removed from service after experiencing loads exceeding design limit loads. The three vertical stabilizer aft lug specimens were tested at Airbus Industrie under National Transportation Safety Board supervision in a loading fixture that applied prescribed forces and moments to the lugs. Testing of each lug continued until a translamina fracture was observed. The fracture loads for these three tests were consistent with calculated accident loads and with earlier tests completed by Airbus Industrie during certification. Details of the test procedures and results are documented in references 16-20. A fractographic examination of each of the lugs was conducted after completing the tests as documented in reference 21.

Before testing, each lug was examined for non-visible defects or damage using ultrasonic inspection. Results of these inspections are documented in reference 21. No defects were observed in the first test lug. Some damage was detected in each of the second and third test lugs near the lug attachment hole and in some areas in the lug fitting assembly transition area above the lowermost rib, however these lugs had experienced in-service loads exceeding design limit loads. Following the tests, the lugs were examined again using ultrasonic inspection. The post-testing ultrasonic inspection showed that the preexisting damage in these lugs grew in size during the testing.

Overall views of the lugs from each test are shown in Figure 13 (outboard surface view). A similar view of the accident right aft lug also is shown in Figure 13. Unlabeled red arrows indicate where translamina fractures intersected the outboard surfaces of the lugs, and an unlabeled large green arrow indicates loading direction (the force vector for the horizontal and vertical loading components for each lug). The lugs from the first and second tests were left aft lugs, and as such, the orientations are mirror images of the accident right aft lug and the third test lug.

Results from the fractographic examination showed that fractures in the test lugs occurred at locations similar to those on the accident right aft lug. In the first test, loading was interrupted after fracture occurred as shown in Figure 13. The translamina fracture was located at a position on the forward part of the lug in a plane nearly parallel to the resultant

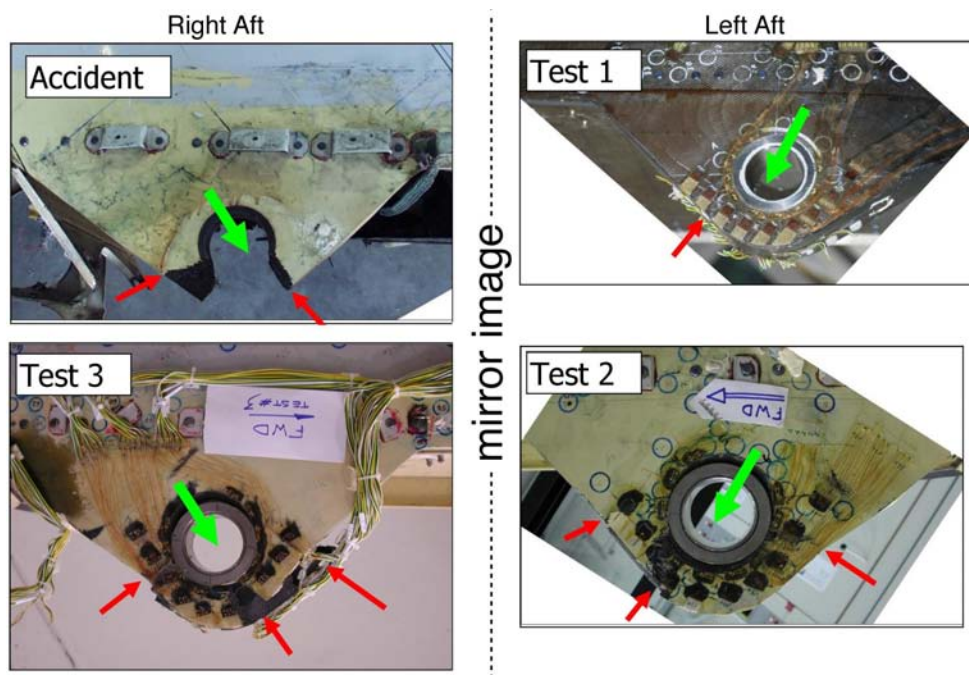


Figure 13. Aft lugs from accident and subsequent subcomponent tests.

force direction, similar to one of the translaminal fractures in the accident right aft lug. Fracture features for the lugs from tests 2 and 3 were similar to each other. The outboard side of each of these lugs had a translaminal fracture on the forward sides of the holes in a plane nearly parallel to the loading direction and another translaminal fracture at the aft side of the hole in a plane approximately perpendicular to the loading direction, fractures similar to that of the accident lug. In addition on the outboard sides, a compression buckling fracture was observed on the forward sides of each lug above the fracture parallel to the loading direction, which is different from features on the accident lug but was attributed to constraints of the loading fixture. On the inboard sides of lugs 2 and 3, fracture locations were on translaminal planes different from that of the outboard side of the lug. This change in fracture planes was similar to that of the accident right aft lug.

A delamination was present within the first test lug having an extent similar to that of the accident right aft lug and in a location through the thickness slightly outboard of that of the accident right aft lug. Delaminations also were detected above the translaminal fractures in lugs 2 and 3. In lugs from tests 2 and 3, the locations of the delaminations through the thickness were similar to that of the accident right aft lug, but the extents of the delaminations in the test lugs were slightly less.

Each subcomponent test lug had translaminal fractures that intersected the lug hole and had delaminations that were located within the lug, features similar to the accident right aft lug. Each lug had a translaminal fracture at the forward lower side of the hole on the outboard side of the lug, including the first test, which was interrupted and had no other translaminal fractures. The fracture at the forward lower side of the hole corresponds to one of the translaminal fracture locations on the accident lug. The second test lug showed changes in translaminal fracture planes that were qualitatively similar to that of the accident right aft lug. These results indicated that the accident right aft lug had fracture features consistent with being the first lug fracture from a substantially intact vertical stabilizer and rudder under accident load conditions.

VI. Concluding Remarks

The fractographic examination revealed no evidence of pre-existing damage or fatigue cracking in the vertical stabilizer or rudder, supporting the conclusion that the separation of the vertical stabilizer and rudder was a result of high aerodynamic loads. The fractographic results of examination of the main attachment lugs for the vertical stabilizer showed that failures on the right side of the vertical stabilizer were overstress failures under tension loading, consistent with an overall bending of the vertical stabilizer to the left. Fractographic results for the main lugs on the left side of the vertical stabilizer showed overstress failure in tension and bending to the left, consistent with bending of the vertical stabilizer to the left after failure of the main lugs on the right side. The structural analysis of the vertical stabilizer and rudder also conducted as part of the overall investigation indicated that under accident loads, fracture of the vertical stabilizer would initiate at the right aft main lug, which was consistent with the fractographic analysis.

The failure mode in the accident was further confirmed by a series of three aft lug subcomponent tests. The failure loads for these three tests were consistent with predicted failure loads and with earlier tests completed by Airbus Industrie during certification. Fracture patterns for the three test specimens were compared to the corresponding structure on the accident airplane, and good correlation was observed.

The analysis of the fractographic evidence was incorporated into the overall analysis of the accident. As a result of the analysis of the facts learned during the course of the nearly 3-year long investigation of the accident, the Safety Board determined that the probable cause of the accident was, “the in-flight separation of the vertical stabilizer as a result of the loads beyond ultimate design that were created by the first officer’s unnecessary and excessive rudder pedal inputs. Contributing to these rudder pedal inputs were characteristics of the Airbus A300-600 rudder system design and elements of the American Airlines Advanced Aircraft Maneuvering Program²².”

References

- ¹Mills, K., et al., ed. *Fractography*, *ASM Handbook Vol. 12*. 1987, ASM International: Metals Park, Ohio.
- ²Kar, R.J., *Atlas of Fractographs*, in *Composite Failure Analysis Handbook Volume 2: Technical Handbook*. 1992, Northrop Corp, Aircraft Div.
- ³Sjögren, A., L.E. Asp, and E.S. Greenhalgh, *Interlaminar Crack Propagation in CFRP: Effects of Temperature and Loading Conditions on Fracture Morphology and Toughness*, in *Composite Materials: Testing and Design, and Acceptance Criteria*, *ASTM STP 1416*, Nettles and Zureick, Editors. 2002.
- ⁴NTSB, *Materials Laboratory Factual Report 02-077*, NTSB Public Docket, 2002.
- ⁵NTSB, *Materials Laboratory Factual Report 02-083*, NTSB Public Docket, 2002.
- ⁶NTSB, *Materials Laboratory Factual Report 03-018*, NTSB Public Docket, 2003.
- ⁷NTSB, *Materials Laboratory Factual Report 02-078*, NTSB Public Docket, 2002.

- ⁸NTSB, *Materials Laboratory Factual Report 03-033*, NTSB Public Docket, 2003.
- ⁹Purslow, D., *Matrix Fractography Of Fibre-Reinforced Thermoplastics, Part 2. Shear Failures*. Composites Vol. 19, 1988.
- ¹⁰Stumpff, P.L., *Fractography*, in *ASM Handbook, Vol. 21: Composites*. 2001. p. 977-987.
- ¹¹Stumpff, P.L., *personal communication*. 2002.
- ¹²Mandell, J.F., *Fatigue Behavior of Short Fiber Composite Materials*, in *Fatigue and Fracture of Composite Materials*, K.L. Reifsnider, Editor. 1990, Elsevier. p. 231-337.
- ¹³Singh, S. and E. Greenhalgh. *Micromechanisms of Interlaminar Fracture in Carbon-Epoxy Composites at Multidirectional Ply Interfaces*. in *4th International Conference on Deformation & Fracture of Composites*. 1998. Manchester, UK: UMIST.
- ¹⁴Hibbs, M.F. and W.L. Bradley, *Correlations Between Micromechanical Failure Processes and the Delamination Toughness of Graphite/Epoxy Systems*, in *Fractography of Modern Engineering Materials: Composites and Metals*, ASTM STP 948, J.E. Masters and J.J. Au, Editors. 1987, American Society for Testing and Materials: Philadelphia. p. 68-97.
- ¹⁵NTSB, *Materials Laboratory Factual Report 02-082*, NTSB Public Docket, 2002.
- ¹⁶NTSB, *Structures 7 Addendum 17, Airbus Report, Flight AA587 Structure Accident Investigation, Validation of Subcomponent Test Principles*, NTSB Public Docket, 2004.
- ¹⁷NTSB, *Structures 7 Addendum 16, Airbus Report, AAL587 Airbus Structure Investigation, Lug Test#3 – Results Test/FEA Comparison*, NTSB Public Docket, 2004.
- ¹⁸NTSB, *Structures 7 Addendum 15, Airbus Report, AAL587 Airbus Structure Investigation, Lug Test#2 – Results Test/FEA Comparison*, NTSB Public Docket, 2004.
- ¹⁹NTSB, *Structures 7 Addendum 8C, NASA Report NASA/TMX-2003-XXX, Structural Analysis Report on the American Airlines Flight 587 Accident – Part 3*, NTSB Public Docket, 2003.
- ²⁰NTSB, *Structures 7 Addendum 6 (Rev A), Airbus Report, AAL587 Airbus Structure Investigation, Lug sub-component test #1 –Results Test/FEA Comparison*, NTSB Public Docket, 2003.
- ²¹NTSB, *Materials Laboratory Factual Report 04-065*, NTSB Public Docket, 2004.
- ²²NTSB, *Aircraft Accident Report, In-Flight Separation of Vertical Stabilizer, American Airlines Flight 587, Airbus Industrie A300-605R, N14053, Belle Harbor, New York, November 12, 2001*, NTSB/AAR-04/04, 2004.

NASA Langley Inspection of Rudder and Composite Tail of American Airlines Flight 587

William P. Winfree^{}, Eric Madaras[†], K. Elliott Cramer[‡], and Patricia A. Howell[§]*
Langley Research Center, Hampton, Virginia

*Kenneth Hodges^{**}, Jeffrey Seebo^{††}, and John Grainger^{‡‡}*
Lockheed-Martin, Hampton, Virginia

Abstract

This paper presents nondestructive evaluation (NDE) results of the American Airlines Flight 587 vertical stabilizer and rudder. The composite vertical stabilizer was tested with both ultrasonic and lamb-wave imaging techniques to thoroughly document the damage to the structure. The rudder was examined using three NDE technologies: x-ray radiography, lamb-wave imaging, and thermography.

A compilation of all ultrasonic imaging of the vertical stabilizer delineated two notable delaminations at the lower end near the forward and aft spars on the left side of the tail. No notable delaminations were detected on the right side of the tail. Lamb-wave data was acquired along the leading edges, trailing edges and along the centerline of both the left and right side of the tail. Aside from stiffness changes associated with thickness variations, there was no apparent evidence of any change in stiffness in the data.

Lamb wave measurements were also recorded on the composite rudder. A “V” shaped region of lower structural stiffness was found above the rudder hinge attachment point on the right side of the rudder. On the left side of the rudder, a diagonal section of lower stiffness going from the rudder hinge attachment point toward the bottom outboard of the rudder was measured.

X-ray radiographs of the rudder clearly delineate the rudder structure, including the walls of the honeycomb composite, and water entrapped in the honeycomb cells. It is clear that the entrapped water is at the lower half of the rudder section. Thermographic NDE tests confirm these regions of entrapped water.

^{*} Branch Head, Nondestructive Evaluation Sciences Branch.

[†] Senior Research Scientist, Nondestructive Evaluation Sciences Branch.

[‡] Senior Research Scientist, Nondestructive Evaluation Sciences Branch.

[§] Research Scientist, Nondestructive Evaluation Sciences Branch.

^{**} Research Engineer, Nondestructive Evaluation Sciences Branch.

^{††} Electronics Technician, Nondestructive Evaluation Sciences Branch.

^{‡‡} Electronics Technician, Nondestructive Evaluation Sciences Branch.

Introduction

The Nondestructive Evaluation Sciences Branch at NASA Langley Research Center in Hampton, VA was tasked with fully documenting the damage to the composite tail and rudder of American Airlines flight 587. The facilities and equipment available for testing include a variety of both standard, well documented and tested NDE technologies (e.g. x-ray) and emerging new technologies for composite NDE (e.g. lamb-wave imaging). Four applicable techniques were chosen for the inspection based on the size of the structures, the kinds of defects or anomalies being sought and the resolution required. These four techniques included ultrasonic imaging, thermography, x-ray radiography, and lamb-wave imaging. These techniques have been successfully used for NDE of composites in previous work, and each was chosen for their particular strengths. References listed at the end of this paper include general texts on the techniques and articles and papers with greater detail.

The ultrasound imaging utilized a contact technique, where a scanner is placed on the structure's surface, and a transducer is translated over the surface with computer control, to enable measurement of the ultrasonic response of the structure within the area of the scanner. A more detailed discussion of the basics of ultrasonic NDE can be found in Fundamentals of Ultrasonic Nondestructive Evaluation (Schmerr, L.W.) For this case, an ultrasonic transducer is coupled to the composite using a closed tapered latex tube, filled with water. The surface of the region of the composite being inspected is kept moist, to ensure the ultrasound is able to couple from the tip of the latex tube into the composite. The same transducer is used to both generate and receive the ultrasonic wave. The output of the transducer is digitized and stored to enable post processing of the responses.

One of the primary data reductions performed on the responses is a determination of the time of flight in the composite layer - the delay time between the echo of the front surface of the composite and the echo off the back surface of the composite. A significant reduction in this delay time between a front and back surface echo is an indication of a delamination in the composite. Amplitude changes in the response signal can also be indicative of porosity or delaminations and were included in the data analyses.

Among the emerging new technologies being developed for the inspection of composites is guided acoustic waves (Lamb waves). Studies have been conducted which show a reduction in Lamb wave velocity due to a loss of stiffness caused by matrix cracking (Seale and Madaras, 2000). The system used for this test was the Lamb Wave Imager™ (LWI); a commercial ultrasonic scanner developed by Digital Wave Corporation (DWC) in Englewood, Colorado. It is capable of measuring the elastic properties for isotropic as well as anisotropic materials. Lamb wave testing was done on both the vertical stabilizer and the rudder.

X-ray radiography is a common technique for the detection of entrapped water in honeycomb structures (Bryant, 1985). The water absorbs the x-rays reducing the intensity of the x-rays that expose the film. The reduction in the number of x-rays exposing the film results in a light spot on the film behind the water locations. This is a measurement through the entire thickness of the structure, so it is not possible to delineate where within the thickness water is present.

The final inspection technology used was thermography. Thermography is a fast non-contacting inspection technique, particularly useful for inspection of complex geometries (Cramer *et al.*, 1995). Subsurface variations in thermal properties change the pattern of the heat flow in the structure. These changes are detectable from the changes in temperature at the surface. By analyzing the pattern, it is possible to image subsurface features. This technique is particularly useful for imaging water in the rudder, where the thermal mass of the water acts as a thermal sink for the heat. These Thermographic tests were conducted in a single-sided measurement scenario, where heat was applied and images recorded on the same side of the structure. As the useful information for these thermal measurements occurs at a fairly shallow depth, water detected in the honeycomb cells on one side of the rudder may not appear on the other side. Therefore, while x-ray radiographic has a higher resolution and better image detail than thermography, thermal NDE offers information through the thickness of the honeycomb.

Experimental Procedure

Ultrasonic Measurement

Ultrasonic data was acquired by using a contact technique. An immersion transducer (5Mhz, 2" foc, 0.5" dia) was mounted in an acrylic tube filled with water, and coupled to the surface of the vertical stabilizer with a thin rubber nitrile sleeve. The surface was coated with a thin layer of water/glycol mixture in order to promote acoustic coupling between the transducer assembly and the composite. Ultrasonic imaging was accomplished by using a scanner, which was placed on the vertical stabilizer (tail) surface, and a transducer is translated over the surface, to enable measurement of the ultrasonic response of the structure within the area of the scanner. For this case, an ultrasonic transducer is coupled to the composite using a closed tapered latex tube, filled with water. The surface of the region of the composite being inspected is kept moist, to ensure the ultrasound is able to couple from the tip of the latex tube into the composite. The same transducer is used to generate and receive the ultrasonic wave. The output of the transducer is digitized at 100 MHz and stored to enable post processing of the responses.

Lamb Wave Measurement

The Lamb Wave scanner consists of a scan frame, a scan bridge, and a scan head. The scan frame dimensions are 20 inches wide by 24 inches long. The scan frame incorporates guide rods, a motor, and drive screw to control the motion along the y-axis. The scan bridge uses guides, a motor, and drive screw to govern the motion along the x-axis. The scan head is comprised of the ultrasonic transducers as well as a z-axis motor and a delta-x motor. The z-axis motor is used to raise and lower the transducers. Coupling between the article under test and the transducers is achieved through a thin rubber faceplate, which is attached to the bottom of the transducers. Bicycle tire patch material proved to be a convenient source for the rubber faceplate and provided a good coupling between the test specimen and the transducers. A delta-x motor regulates the spacing between the stationary sending transducer and the movable receiving transducer.

The scanner control unit incorporates a receiver, a high-voltage amplifier, and a motor controller. The receiver has an amplification range from 0 to 66 dB. The high-voltage amplifier is used to amplify the pulse used to drive the sending transducer. It has a bandwidth of 12 kHz to 1 MHz and a maximum output of 350 volts peak-to-peak. The motor controller is capable of

independently controlling the motion of each of the scanner motors. The computer contains a function generator card that produces a sinusoidal pulse and an 8-bit A/D board that digitizes the received signals.

X-ray Radiography

To perform the X-ray inspection, the rudder section was mounted vertically in two padded wooden yokes. Before the inspection, lead markers were taped to back side of the rudder. The lead markers are highly attenuative to x-rays and are clearly visible on the exposed film. By taking a picture of the position of the markers on the rudder, it is possible to determine the relative position of each piece of film with respect to the rudder.

An x-ray source was placed 8 feet from one side of the specimen, and four pieces of x-ray film are taped to the other side of the specimen. The x-ray source was turned on with a 30-kV acceleration voltage and a 2-minute exposure time. Following the exposure, the film was developed and examined to determine the location of water in the rudder.

Thermography Measurement

Measurement of the thermal response of the rudder was performed by impulse heating of one side of the specimen. The impulse heating was supplied by commercial photographic flash lamps. The duration of the flash was typically less than 3 msec. The time was much shorter than the data acquisition rate of the measurement system. The duration of the pulse is therefore inconsequential and can be considered as an impulse. A computer that controlled the measurement process triggered the application of the heat pulse.

Detection of the thermal response of the layer to impulse heating was performed with an infrared imager. The infrared imager used a detector array for the full field of view. The detector operated in the 3-5 μm range and is cooled to near liquid nitrogen temperatures with a closed cycle electric microcooler. The output of the imager was captured with a real time image processor. The sampling rate was variable down to 1/60 sec in steps of 1/30 sec. Variable length time records up to 300 time samples were obtainable with the system. User input into a computer, which controlled the measurement process, controlled the sampling time and the number of time samples. The computer typically recorded the infrared image of the specimen immediately prior to the firing of the flash lamps, then the thermal response of the specimen at a user-defined sampling rate and for a user-defined duration. Real time averaging of the thermal response also could be preformed to improve the signal-to-noise ratio. The thermal response was saved for post processing of the data to obtain a diffusivity map.

Results

Ultrasonic Measurement of Rear Stabilizer

One of the primary data reductions performed on the responses is a determination of the time of flight in the composite layer. The time of flight is delay time between the echo of the front surface of the composite and the echo off the back surface of the composite. In a homogenous material, the time of flight is proportional to the thickness of the material. Therefore a significant reduction in the time of flight is an indication of a delamination in the composite. If the composite thicknesses and velocity are known, it is possible to compare the time of flight

measurements to calculations of the time of flight and be confident of the existence of delaminations. For this case there are two issues that make this determination difficult. First the thicknesses shown in the schematic drawings are significantly less than the thicknesses in the actual part. Second the velocity is not a constant in the part, but rather varies between the regions with and without stiffeners. Delaminations therefore are called out only when there is a significant relative change in the time of flight relative to the surrounding region that is not consistent the qualitative information in the schematics.

Another of the primary data reductions performed on the data is a determination of the relative amplitudes of the echoes from the front and back surfaces. Reduction in the relative amplitude can be a factor of many parameters such as porosity in the composites, variations in coupling between the transducer and front surface of the composite and material mounted on the back surface of the composite. Since every variation in amplitude does not reflect a flaw in the composite, not all reductions in relative amplitude are noted in this documentation. However, for all significant changes in amplitude, the ultrasonic responses at that point were examined. A typical ultrasonic response from an anomaly-free region is shown in figure 1(a). A typical response that indicates an anomaly in the composite is shown in figure 1(b). For this point, there is clearly an echo between the front and back surface as noted in the figure. Where such echoes are clearly visible, the relative amplitudes of the region of are shown in detail.

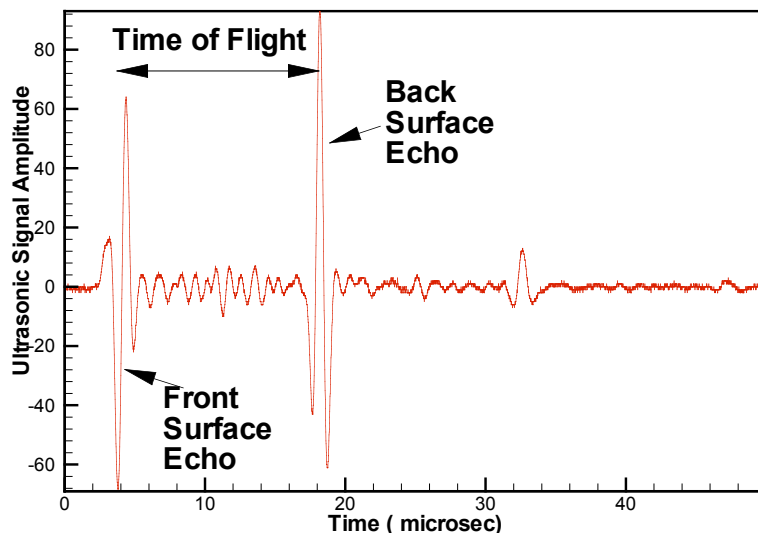


Figure 1(a). A typical time response of an ultrasonic wave propagating in an undamaged composite layer.

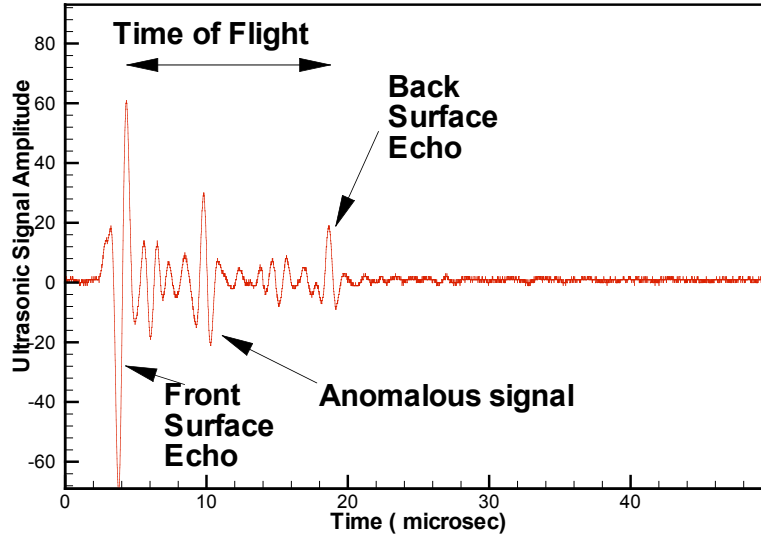


Figure 1(b). A typical time response from a region with an anomalous signal.

Figures 2, 3, 4, and 5(a)-5(r) are the results obtained from measurements on the left side of the tail. Figure 2 is the compilation of all the time of flight measurements performed on the left side. Two notable delaminations were detected at the lower end near the forward and aft spars. Enlarged images of the data with a designation of the extents of these two delaminations are shown in figure 3. Figure 4 designates the regions shown in figures 5(a)-5(r). These are the images of regions with anomalies in the relative attenuation, with responses typical of those found in figure 1(b).

Figures 6, 7, 8(a)-8(o) are the results obtain from measurements on the right side of the tail. Figure 6 is the compilation of all the time of flight measurements performed on the left side. No notable delaminations were detected on the right side of the tail. Figure 7 designates the regions shown in figures 8(a)-8(o). These are the images of regions with anomalies in the relative attenuation, with responses typical of those found in figure 1(b).

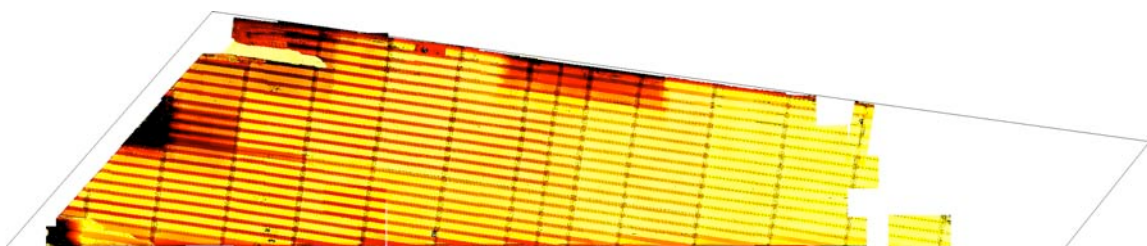


Figure 2. Ultrasonic time of flight measurements performed on the left side of the composite tail.

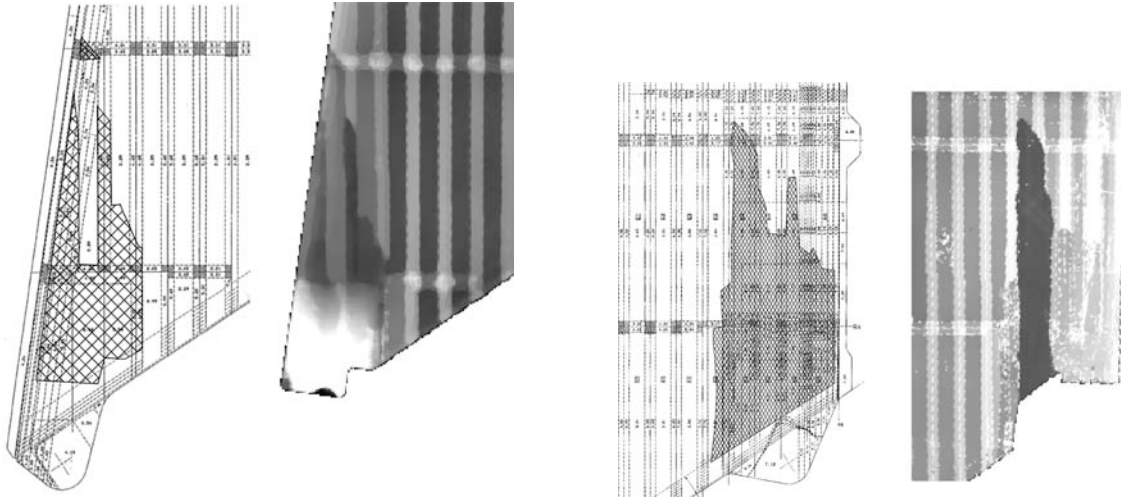


Figure 3. Expanded view showing delaminations at the lower end near the forward and aft spars.



Figure 4. Region definitions used in subsequent images for the left side of tail. These are the regions with significant anomalies in ultrasonic attenuation responses.

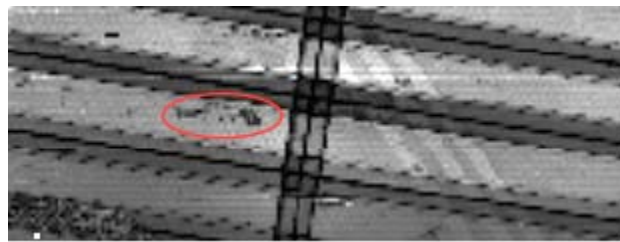


Figure 5(a). Ultrasonic attenuation image of left side tail region A.

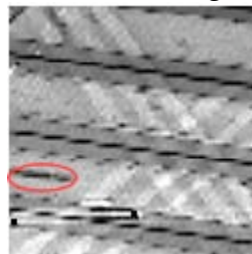


Figure 5(b). Ultrasonic attenuation image of left side tail region B.

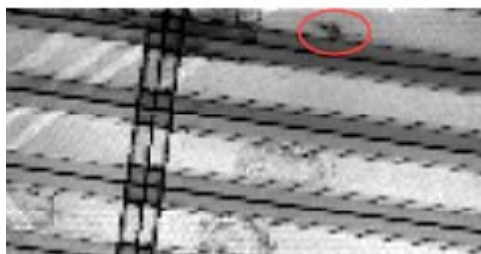


Figure 5(c). Ultrasonic attenuation image of left side tail region C.

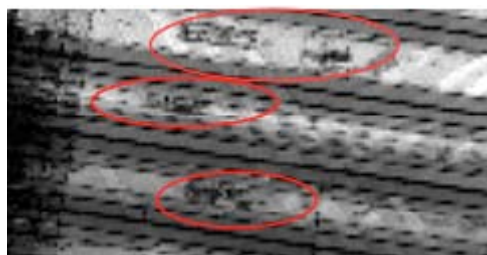


Figure 5(d). Ultrasonic attenuation image of left side tail region D.



Figure 5(e). Ultrasonic attenuation image of left side tail region E.



Figure 5(f). Ultrasonic attenuation image of left side tail region F.

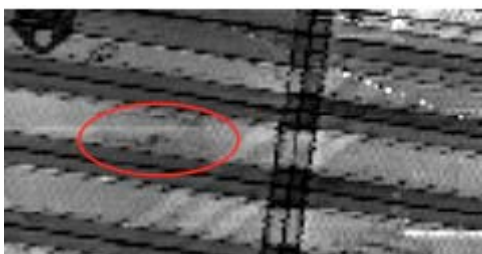


Figure 5(g). Ultrasonic attenuation image of left side tail region G.

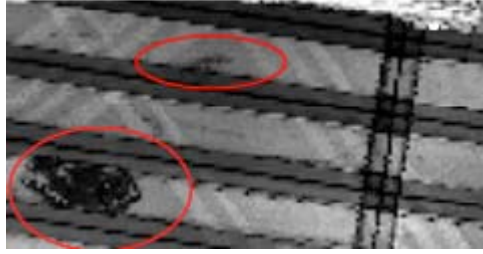


Figure 5(h). Ultrasonic attenuation image of left side tail region H.

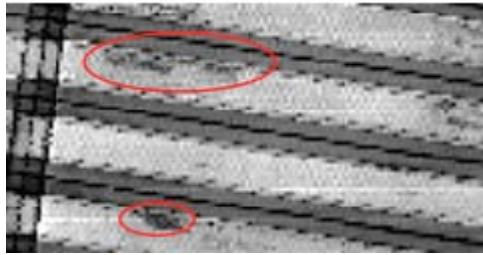


Figure 5(i). Ultrasonic attenuation image of left side tail region I.

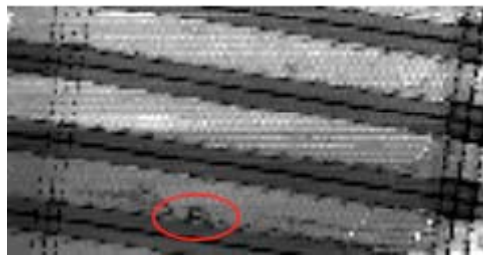


Figure 5(j). Ultrasonic attenuation image of left side tail region J.

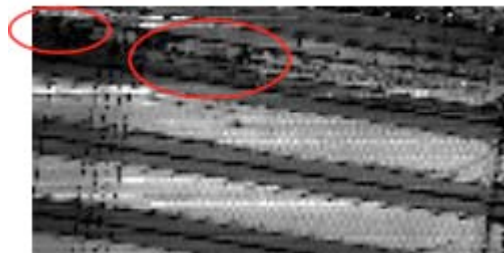


Figure 5(k). Ultrasonic attenuation image of left side tail region K.

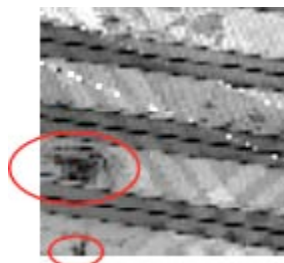


Figure 5(l). Ultrasonic attenuation image of left side tail region L.

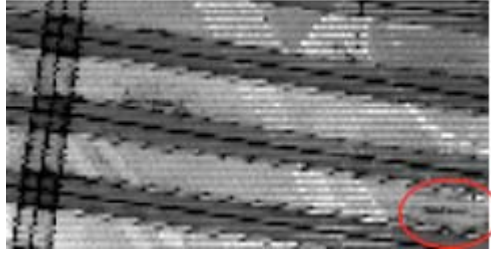


Figure 5(m). Ultrasonic attenuation image of left side tail region M.

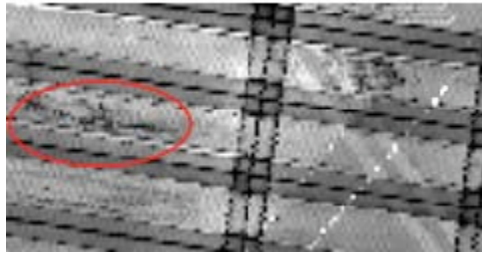


Figure 5(n). Ultrasonic attenuation image of left side tail region N.

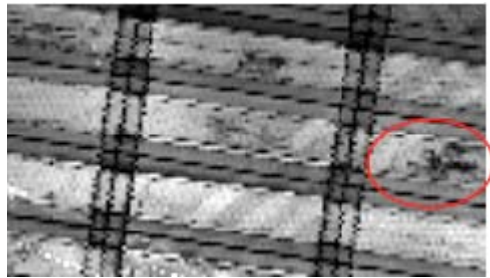


Figure 5(o). Ultrasonic attenuation image of left side tail region O.

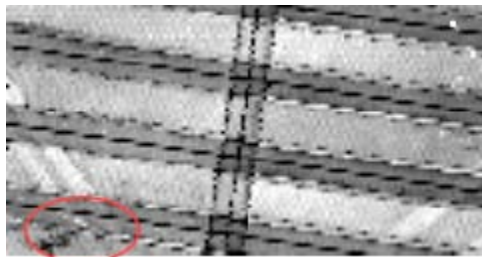


Figure 5(p). Ultrasonic attenuation image of left side tail region P.

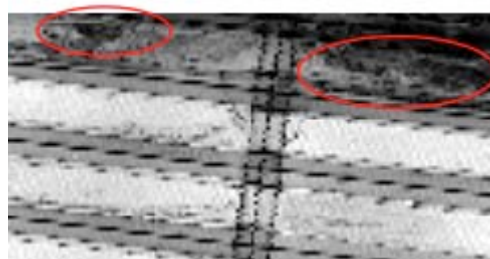


Figure 5(q). Ultrasonic attenuation image of left side tail region Q.

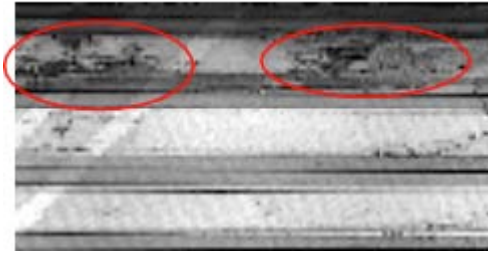


Figure 5(r). Ultrasonic attenuation image of left side tail region R.

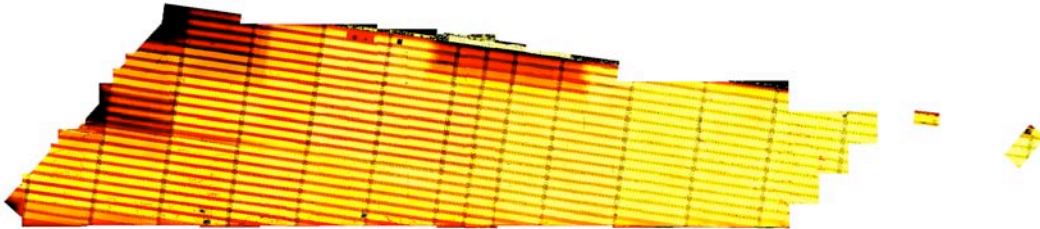


Figure 6. Ultrasonic time of flight measurements performed on the right side of the composite tail.

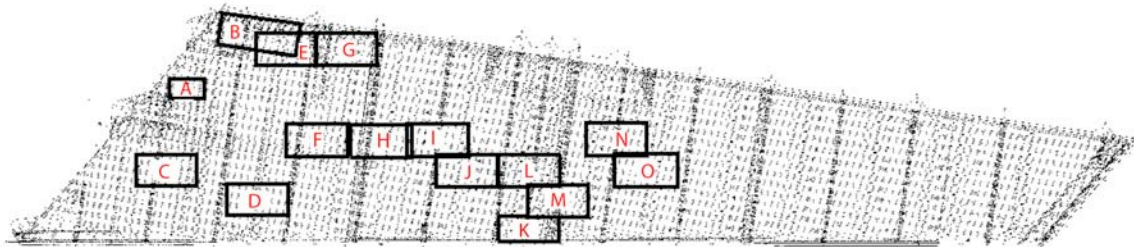


Figure 7. Region definitions used in subsequent images for the right side of tail. These are the regions with significant anomalies in ultrasonic attenuation responses.



Figure 8(a). Ultrasonic attenuation image of right side tail region A.

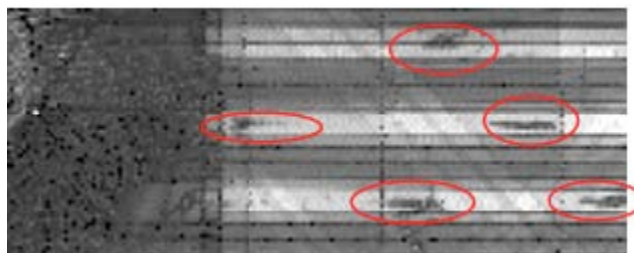


Figure 8(b). Ultrasonic attenuation image of right side tail region B.

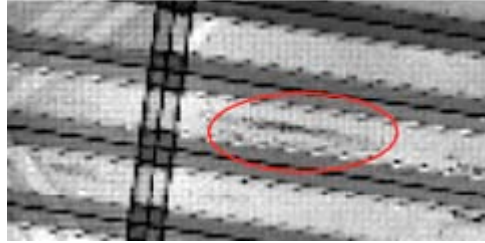


Figure 8(c). Ultrasonic attenuation image of right side tail region C.

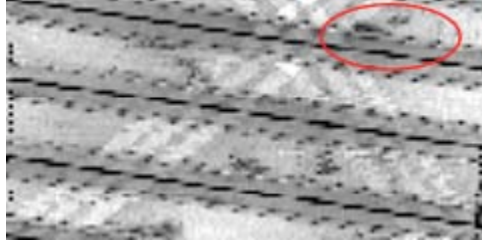


Figure 8(d). Ultrasonic attenuation image of right side tail region D.

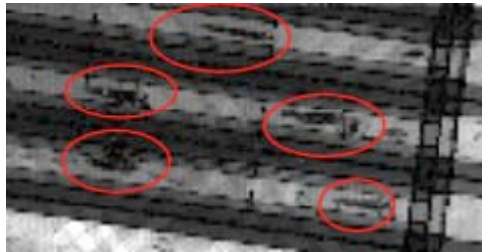


Figure 8(e). Ultrasonic attenuation image of right side tail region E.

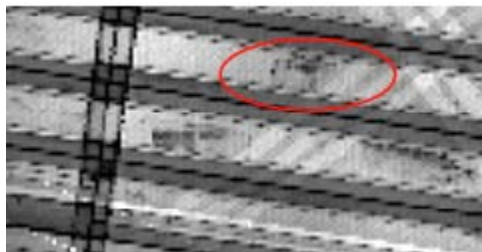


Figure 8(f). Ultrasonic attenuation image of right side tail region F.

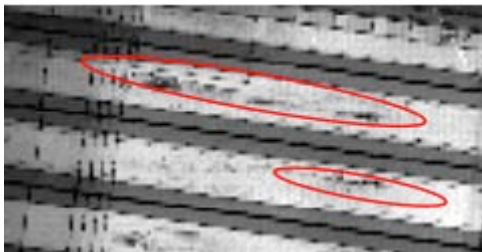


Figure 8(g). Ultrasonic attenuation image of right side tail region G.

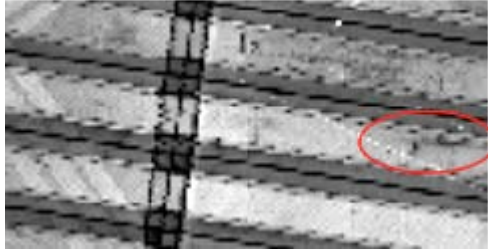


Figure 8(h). Ultrasonic attenuation image of right side tail region H.

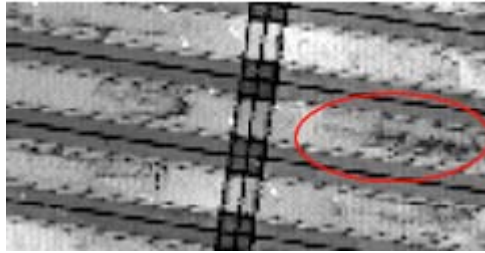


Figure 8(i). Ultrasonic attenuation image of right side tail region I.

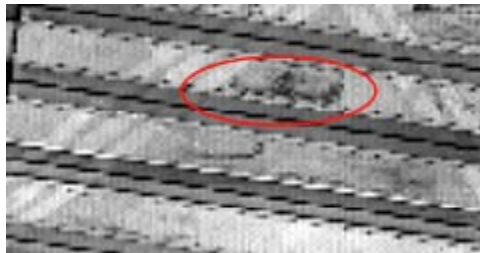


Figure 8(j). Ultrasonic attenuation image of right side tail region J.

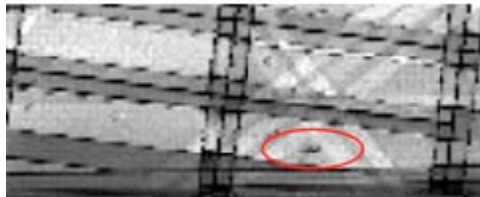


Figure 8(k). Ultrasonic attenuation image of right side tail region K.

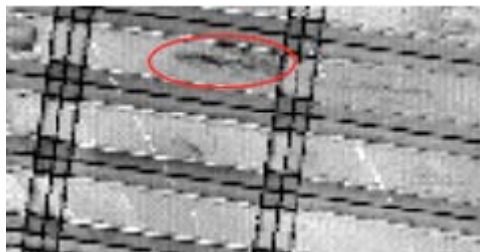


Figure 8(l). Ultrasonic attenuation image of right side tail region L.

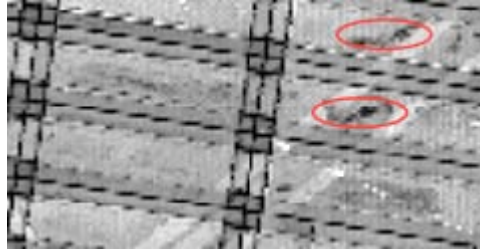


Figure 8(m). Ultrasonic attenuation image of right side tail region M.

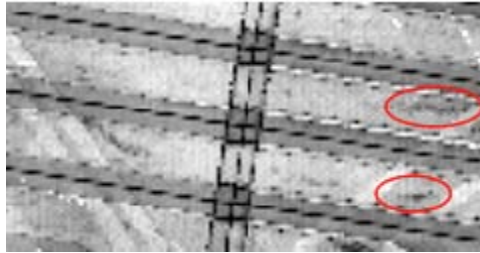


Figure 8(n). Ultrasonic attenuation image of right side tail region N.

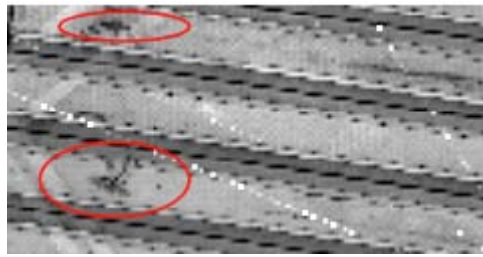
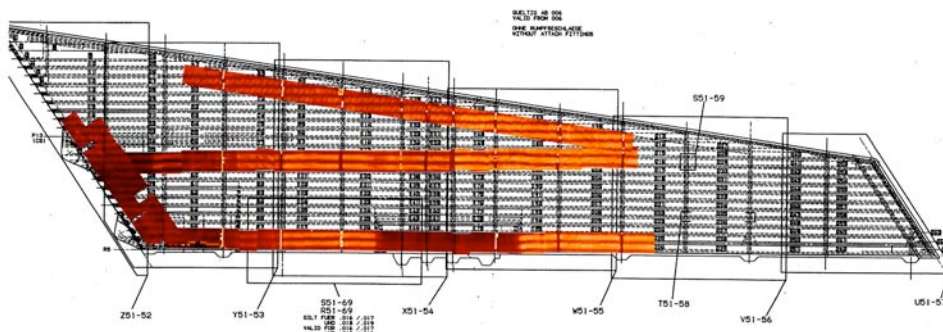
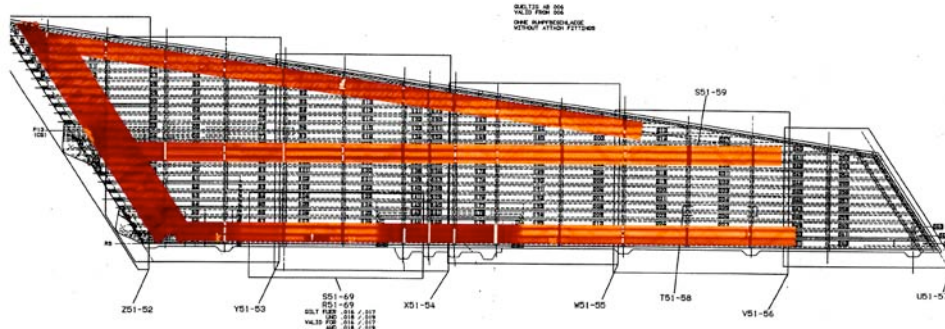


Figure 8(o). Ultrasonic attenuation image of right side tail region O.

Lamb Wave Measurement of Rear Stabilizer and Rudder

Strips of data were acquired along the leading edges, trailing edges and along the center-line of both the left and right side of the tail. Measurements were performed with a transducer separation of approximately 1 inch. The scan area for each scan was approximately 12 by 12 inches, and acquiring the data for each scan area required about 30 minutes.

A compilation of all the data from the right side superimposed on a schematic of the tail is shown in figure 9(a). The data from the left side is shown in figure 9(b). Regions of higher stiffness appear red, and lower stiffness regions appear orange in the figures. The most significant characteristics in the images are the variations in thickness of the composites tail. Aside from stiffness changes associated with thickness variations, there is no apparent evidence of any change in stiffness in the data.



For the rudder, measurements were performed with a transducer separation of approximately 2 inches. Measurements were only performed on portions of the rudder with enough residual strength to easily support the weight of the scan frame. A compilation of all the data from the right side of the rudder superimposed on a picture of the right side of the rudder is shown in figure 10(a). The data from the left side superimposed on the same picture is shown in figure 10(b). In regions with consist face sheet thickness, the areas with lower stiffness appear as lighter regions. Where there is an increase in ply thickness due to ply overlaps, these regions appear darker in the image. The system has difficulty tracking the delay time in the ultrasonic pulse in regions with significant addition subsurface support such as the lightning strip and rudder hinge attach blocks. For these regions, the stiffness maps are not meaningful. Figure 11 indicates typical responses in these regions.

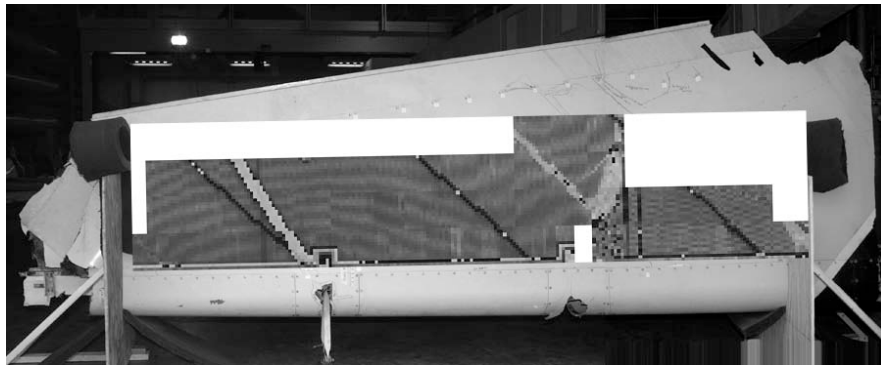


Figure 10(a). Lamb wave results from the right side of the rudder (superimposed on a picture of the right side of the rudder).



Figure 10(b). Lamb wave results from the left side of the rudder (superimposed on a picture of the right side of the rudder).

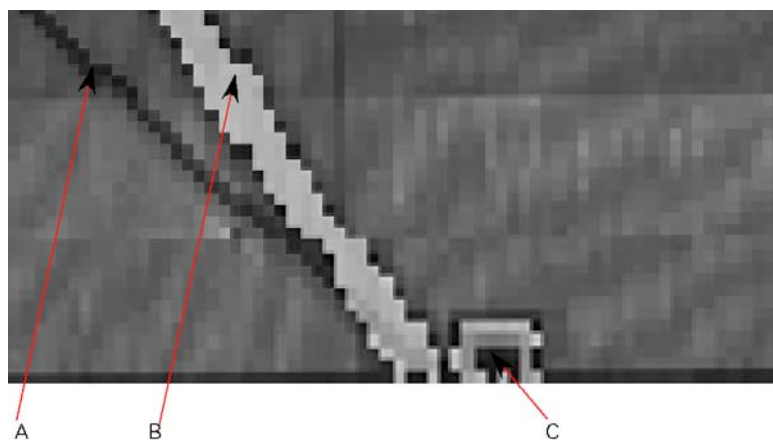


Figure 11. Typical structural features in the Lamb wave image. A) Ply overlap, B) lightning strip and C) rudder hinge attach block.

X-ray radiography of Rudder

A typical x-ray image is shown in figure 12. In the image, the entrapped water is clearly visible. Also visible in the image are the lead markers and the walls of the honeycomb. A compilation of all the photos is shown in figure 13. In the figure it is clear that the entrapped water is at the lower half of the rudder section.

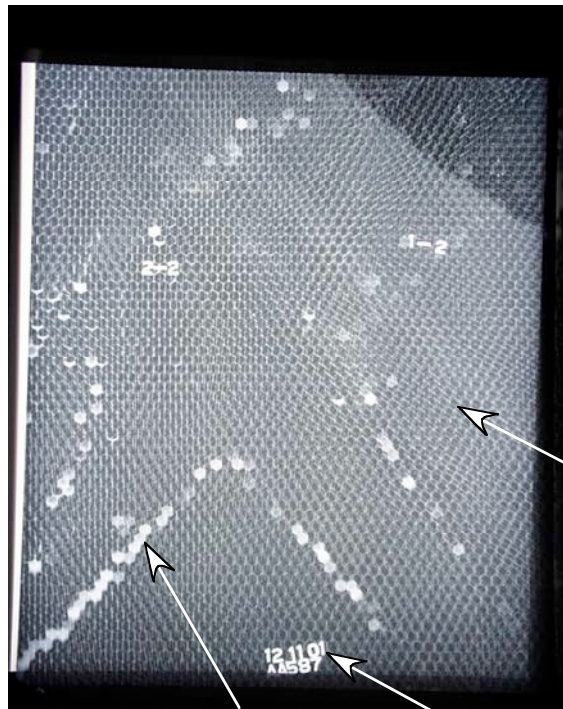


Figure 12. Radiographic image of water in the rudder honeycomb structure.

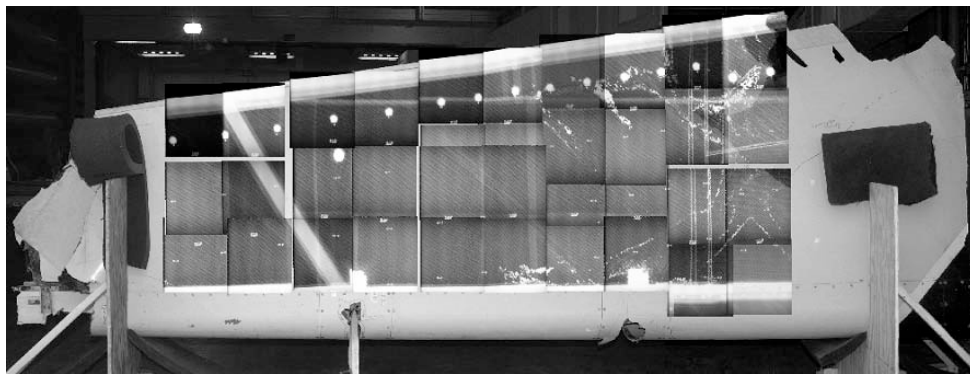


Figure 13. Compilation of radiography results (superimposed on picture of the section of rudder examined).

Thermography Measurement of Rudder

The thermal time response for a region of the rudder with and without entrapped water in the honeycomb is shown in figure 14. It is clear from the figure that there is significantly more cooling occurring in the region with entrapped water. The regions that appear darker in the data are indications of water. Other substructures, such as potting in the honeycomb also caused significant additional cooling relative to the unbacked face sheet. A compilation of all the data from the right side of the rudder superimposed on a picture of the right side of the rudder is shown in figure 15(a). The data from the left side superimposed on the same picture is shown in figure 15(b). Figures 16(a) and 16(b) show the same data with the locations of water highlighted in red.

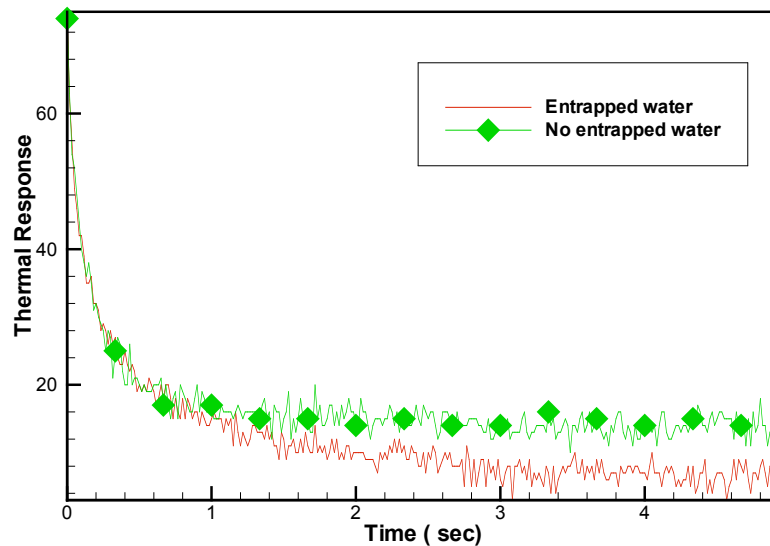


Figure 14. The thermal time response for a region of the rudder with and without entrapped water in the honeycomb



Figure 15(a). A compilation of thermal data from the right side of the rudder (superimposed on a picture of the right side of the rudder).

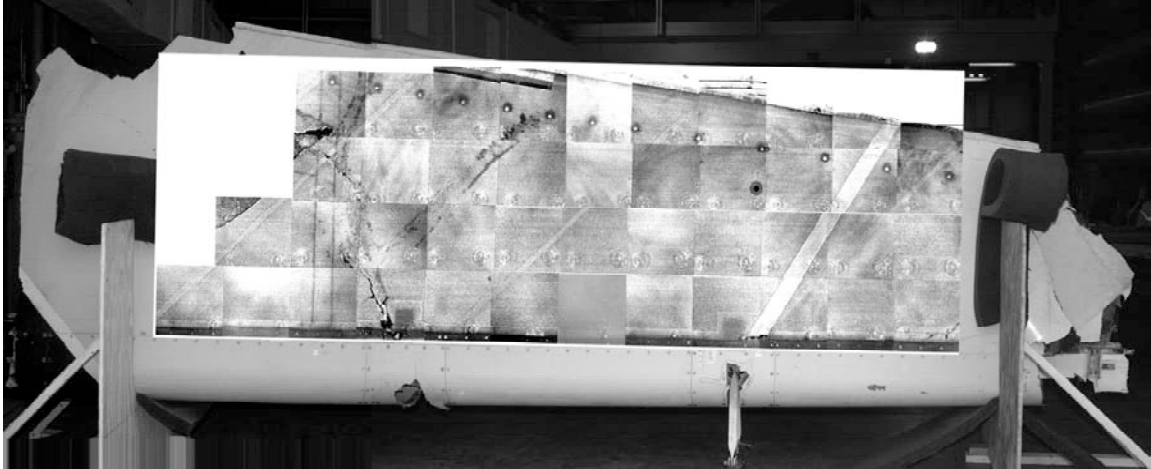


Figure 15(b). A compilation of all the data from the left side of the rudder superimposed on a picture of the right side of the rudder

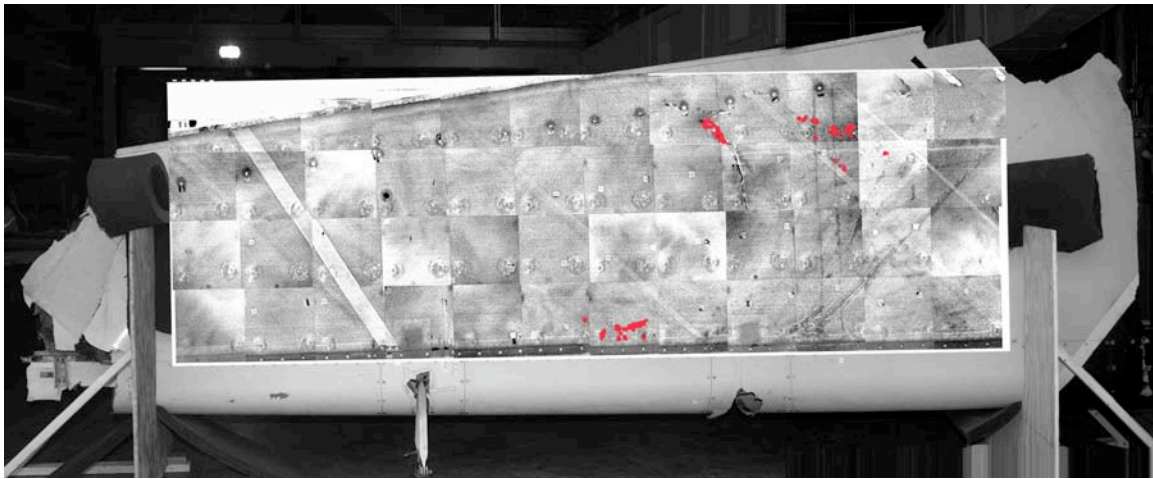


Figure 16(a). A compilation of all the data from the right side of the rudder superimposed on a picture of the right side of the rudder with water highlighted in red

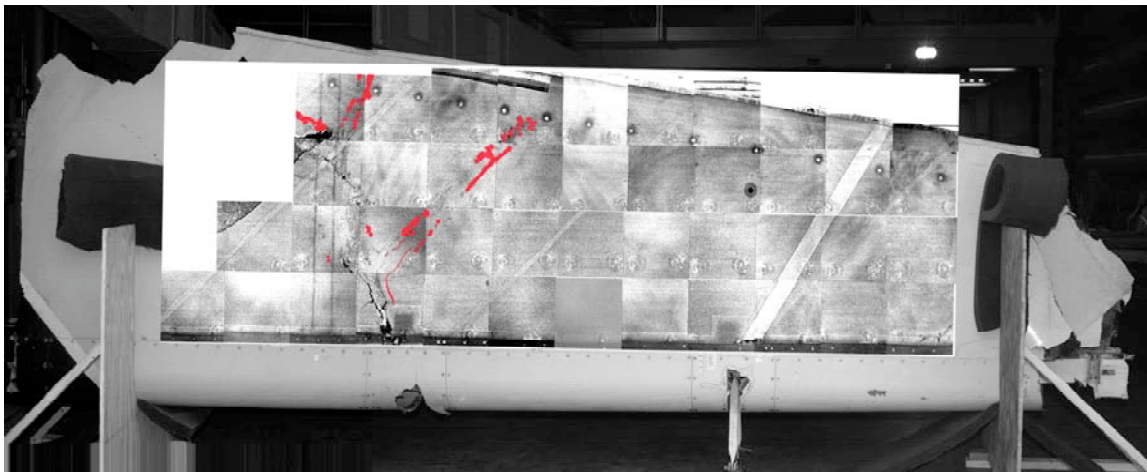


Figure 16(b). A compilation of all the data from the left side of the rudder superimposed on a picture of the right side of the rudder with water highlighted in red

Conclusions

Nondestructive evaluation results of the American Airlines Flight 587 vertical stabilizer and rudder document the details of damage to the structures. The composite vertical stabilizer was tested with both ultrasonic and lamb-wave imaging techniques. The rudder was examined with three NDE techniques: x-ray radiography, lamb-wave imaging, and thermography.

A compilation of all ultrasonic imaging of the vertical stabilizer delineated two notable delaminations at the lower end near the forward and aft spars on the left side of the tail. No notable delaminations were detected on the right side of the tail. Lamb-wave data was acquired along the leading edges, trailing edges and along the centerline of both the left and right side of the tail. Aside from stiffness changes associated with thickness variations, there was no apparent evidence of any change in stiffness in the data.

Lamb wave measurements were also recorded on the composite rudder. A “V” shaped region of lower structural stiffness was found above the rudder hinge attachment point on the right side of the rudder. On the left side of the rudder, a diagonal section of lower stiffness going from the rudder hinge attachment point toward the bottom outboard of the rudder was measured.

X-ray radiographs of the rudder clearly delineate the rudder structure, including the walls of the honeycomb composite, and water entrapped in the honeycomb cells. It is clear that the entrapped water is at the lower half of the rudder section. Thermographic NDE tests confirm these regions of entrapped water.

References

- Bryant, L.E.: *Radiography and Radiation Testing*. (Nondestructive Testing Handbook, Vol. 3.) Second Ed., American Society for Nondestructive Testing, 1985.
- Carslaw, H.S.; AND Jaeger, J.C.: *Conduction of Heat in Solids*, Clarendon Press, Oxford, 1959, pp. 266-267.
- Cramer, K.E.; Howell, P.A.; and Syed, H.I.: *Proceedings SPIE - Thermosense XVII*, Vol. 2473, ed. S. A. Semanovich (SPIE, Bellingham, 1995), p. 226.
- Cramer, K.E.; Howell, P.A.; and Syed, H.I.: "Quantitative Thermal Imaging of Aircraft Structures," *Proceedings SPIE - Thermosense XVII*, Vol. 2473, April 1995, pp. 226-232.
- Cramer, K.E.; Winfree, W.P.; Generazio, E.R.; Bhatt, R.; and Fox, D.S.: *Review of Progress in Quantitative Nondestructive Evaluation*, Vol. 12, ed. D.O. Thompson and D.E. Chimenti (Plenum Press, New York, 1993), p. 1305.
- Davis, C. W.; Fulton, J. P.; Nath, S.; and Namkung, M.: Combined Investigation of Eddy Current and Ultrasonic Techniques for Composite Materials NDE , Review of Progress in Quantitative Nondestructive Evaluation, Vol. 14B, Snowmass, Colorado, July 1994, pp. 1295-1301.
- Hellier, C.J.: *Handbook of Nondestructive Evaluation*. First Ed., McGraw-Hill, Inc., 2001
- Madaras, E.I.: Highlights of NASA's Role in Developing State-of-the-Art Nondestructive Evaluation for Composites, *AHS International Structures Specialists' Meeting*, Williamsburg, Virginia, October 30-November 1, 2001.
- Madaras, E.I.: Ultrasonic Attenuation Results From Thermoplastic Resin Composites Undergoing Thermal and Fatigue Loading, *25th Annual Review of Progress in Quantitative Nondestructive Evaluation Conference, Snowbird, Utah, July 19-24, 1998*, published in Review of Progress in Quantitative Nondestructive Evaluation, 1999, pp. 1329-1336.
- Madaras, E.I.; Winfree, W.P.; and Johnston, P.H.: Ultrasonic Studies of Composites Undergoing Thermal and Fatigue Loading, *24th Annual Review of Progress in Quantitative Nondestructive Evaluation*, San Diego, California, July 27--August 1, 1997, also appears in Review of Progress in QNDE, Volume 17.
- Maldague, X.P.V.: *Nondestructive Evaluation Of Materials By Infrared Thermography*, Springer-Verlag, London, 1993, pp. 45-60, 83-93.
- Maldague, X.P.V.; and Moore, P.O.: *Nondestructive Testing Handbook: Infrared and Thermal Testing*. Third Ed., American Society for Nondestructive Testing, 2001

Plotnikov, Y.A.; and Winfree, W.P.: Thermographic Imaging of Defects in Anisotropic Composites , *24th Annual Review of Progress in Quantitative Nondestructive Evaluation, San Diego, California, July 27--August 1, 1997*, p. 8, Also appeared in Review of Progress in QNDE, Vol. 17 A, 1998, pp. 457-464.

Schmerr, L.W.: *Fundamentals of Ultrasonic Nondestructive Evaluation* (A Modeling Approach.) Plenum Publ. Co., 1998.

Seale M.D.; and Madaras, E.I.: *Lamb Wave Evaluation of the Effects of Thermal-Mechanical Aging on Composite Stiffness*, J. Composite Materials, vol.43, no. 1, 2000, Pt. 1, pp. 27-38

Shull, P. J.: *Nondestructive Evaluation* (Theory, Techniques, and Applications.) First Ed., Marcel Dekker, 2002.

Structural Analysis for the American Airlines Flight 587 Accident Investigation – Global Analysis

Richard D. Young*

NASA Langley Research Center, Hampton, VA 23681-2199

Andrew E. Lovejoy†

Analytical Services & Materials, Inc., Hampton, VA 23666-1340

Mark. W. Hilburger‡ and David F. Moore§

NASA Langley Research Center, Hampton, VA 23681-2199

NASA Langley Research Center (LaRC) supported the National Transportation Safety Board (NTSB) in the American Airlines Flight 587 accident investigation due to LaRC's expertise in high-fidelity structural analysis and testing of composite structures and materials. A Global Analysis Team from LaRC reviewed the manufacturer's design and certification procedures, developed finite element models and conducted structural analyses, and participated jointly with the NTSB and Airbus in subcomponent tests conducted at Airbus in Hamburg, Germany. The Global Analysis Team identified no significant or obvious deficiencies in the Airbus certification and design methods. Analysis results from the LaRC team indicated that the most-likely failure scenario was failure initiation at the right rear main attachment fitting (lug), followed by an unstable progression of failure of all fin-to-fuselage attachments and separation of the VTP from the aircraft. Additionally, analysis results indicated that failure initiates at the final observed maximum fin loading condition in the accident, when the VTP was subjected to loads that were at minimum 1.92 times the design limit load condition for certification. For certification, the VTP is only required to support loads of 1.5 times design limit load without catastrophic failure. The maximum loading during the accident was shown to significantly exceed the certification requirement. Thus, the structure appeared to perform in a manner consistent with its design and certification, and failure is attributed to VTP loads greater than expected.

I. Introduction

On November 12, 2001, an Airbus 300-600R being operated as American Airlines Flight 587 crashed soon after take-off from John F. Kennedy airport in New York City, killing all 260 persons aboard and 5 on the ground. The plane's composite vertical stabilizer and rudder (referred to herein as the Vertical Tail Plane or VTP) separated from the aircraft before it impacted the ground. Initial analyses indicated that this accident was the first commercial aircraft crash that involved the failure of a primary structure made from composite materials. NASA Langley Research Center (LaRC) was requested by the National Transportation Safety Board (NTSB) to support the accident investigation because of LaRC's expertise in high-fidelity structural analysis and testing of composite structures and materials. In coordination with the NTSB and under the technical guidance of Dr. James H. Starnes, Jr. of NASA LaRC, technical expertise was provided for several aspects of the investigation that included global analysis of the composite vertical tail fin and rudder. This paper presents a summary of the NASA AA587 Global Analysis Team results for the American Airlines Flight 587 accident investigation.¹

The charter established by the NTSB for the NASA Global Analysis Team was as follows:

The team shall address the following objectives:

- *Review of Airbus certification process: testing, analysis and design procedures*

*Senior Research Engineer, Mechanics of Structures and Materials Branch

†Research Scientist

‡Aerospace Engineer, Mechanics of Structures and Materials Branch

§Aerospace Engineer, Structural & Thermal Analysis Branch

- *Develop and interrogate failure scenarios*
- *Provide loads to Local Analysis Team to perform strength analyses*
- *Conduct failure sequence analyses for most likely failure scenario (and correlate predicted damage with the physical evidence)*
- *Provide evidence to assess whether the structure performed as intended*

To address this charter, the NASA Global Analysis Team reviewed the manufacturer's design and certification procedures, developed finite element models and conducted structural analyses, and participated jointly with the NTSB and Airbus in subcomponent tests conducted at Airbus in Hamburg, Germany. Throughout the investigation, the NASA team worked closely with the investigation teams at the NTSB and Airbus. Several of the investigation analysis efforts were developed independently by the NASA and Airbus teams and had common objectives. However, in some cases, different analysis approaches were used and served to verify the predicted results. The NASA team received initial finite element models from Airbus. These initial models were modified by the NASA team, as deemed necessary, and then verified to the point that the NASA team felt confident in the validity of the models. For the analysis efforts that were common between the NASA and Airbus teams, the NASA team's efforts may be used to independently verify Airbus results. In addition to conducting standard linear analyses for the most likely failure scenario, the NASA team also considered variations in analysis procedures and model details to determine if alternative failure scenarios would be indicated. The following text outlines the sequence of activities conducted by the NASA Global Analysis Team, and the findings of the team are reported in the body of this paper.

The NASA team conducted a review of Airbus design and certification documents and the results of this review are described in Section II. The team also conducted a review of the Airbus fin and rudder NASTRAN² models that were delivered to NASA, and made a number of model modifications that were implemented in an attempt to improve model fidelity, enable geometrically nonlinear analysis, and enable dynamic analysis (see Section III). Failure scenarios were developed based upon the physical evidence^{3,4} and an initial assessment of the predicted critical reserve factors of the VTP subjected to accident load conditions (Section IV). The most likely failure scenario was identified and validated by conducting a subcomponent test with loading based on analysis results of the VTP at the final observed maximum fin loading condition, as described in Section V. The analysis included a global/local iterative procedure to effectively embed a refined, local three-dimensional finite element model into the global model.⁵ In Section VI, the VTP hardware failure sequences associated with the most likely failure scenario that are predicted using both static and dynamic analyses are described, and these results are compared to the physical evidence.

II. Review of Airbus A300-600 Certification

One of the first tasks of the NASA Global Analysis Team was to review the Airbus certification and design methods used in the design of the composite VTP of the A300-600 Airplane. Specific goals of the review included a review of the Airbus models and analysis methods, reserve factor calculations, and supporting test data used to develop the design allowables. Airbus design justification documents were reviewed to obtain familiarity with the design process and reserve factor calculations, and selected reserve factors were recalculated to verify the Airbus results. This review was conducted to look for errors in modeling, analysis, or testing that would have resulted in an unconservative design.

The NASA Global Analysis Team possesses expertise in high-fidelity analysis and testing of composite structures. The team utilized this expertise to review the Airbus design and certification documents. The certification review included examination of the procedures used for establishing design allowables through coupon and subcomponent tests that were validated using full-scale structural tests to failure (see Fig. 1, that shows typical document content). The review also fostered an understanding of the Airbus allowable calculations, e.g., material failure criteria and reserve factor calculations, in order for the team to calculate meaningful reserve factors and failure predictions for the accident loading conditions. Specifically, material failure criteria and reserve factors were used during the investigation to determine regions that may exhibit failure. It should be noted that these failure allowable and reserve factors are, in general, very conservative, are used during the design process to indicate satisfaction of design requirements, and do not necessarily indicate the presence of failure. Furthermore, these allowables and factors were used in the investigation to identify the most likely locations of failure.

NASA's examination of the Airbus design allowable and reserve factor processes determined that the Airbus analysis, design and testing procedures were complete and comprehensive, utilizing a well-defined building block approach. Because no significant or obvious deficiencies were identified, the NASA team felt confident using the design allowables, failure calculations and reserve factor calculations to conduct the accident investigation.

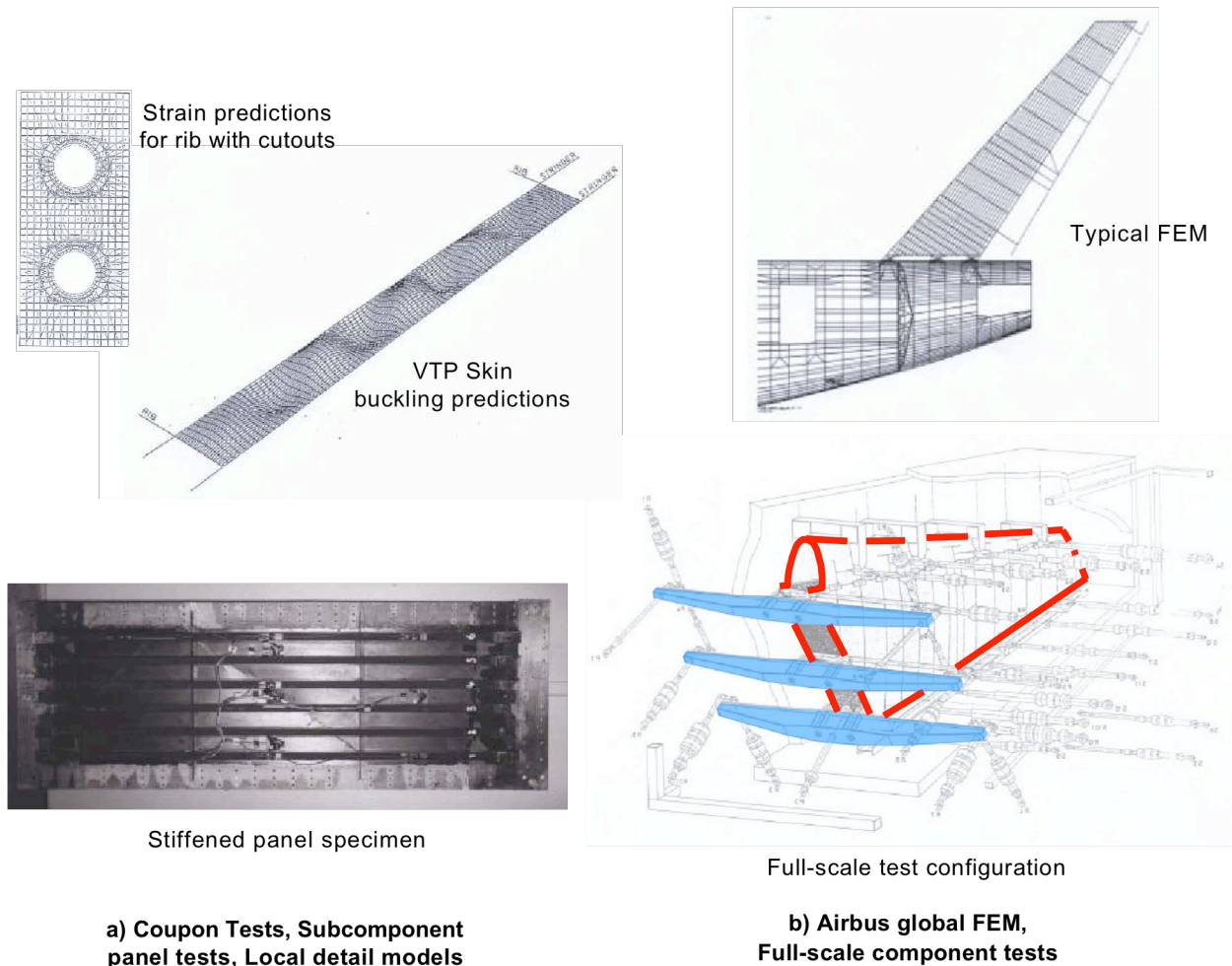


Figure 1: Airbus building-block approach to design allowable development.

However, during the review process, two items of concern with the certification process were identified that were subsequently addressed within the investigation. These certification concerns were as follows:

- 1) The validity of the full-scale fin certification test was questioned as to whether the loading applied in the full-scale fin test was representative of the actual aircraft loading. The full-scale fin test was conducted with the fin off the aircraft and the distribution of applied loads was prescribed exactly from the analysis. Thus, the validity of the test loading was dependent on the validity of the global finite-element model. In addition, the load-introduction structure may have introduced bending moments at the main-attachment fittings, or lugs, that are different than what the fuselage frames would have introduced.
- 2) The lug-strength allowables applied during design and certification were resultant forces, and did not take into consideration directly the effect of bending moments on the strength of the fin-to-fuselage attachments, and certification analyses were not detailed enough to quantify the bending moments at the lugs. Detailed strength analysis conducted by the NASA AA587 Local Analysis Team has shown that the bending moment at the rear lug attachment influences the failure strength of the lug.

The first concern was addressed during the model verification activities (see Section III) by conducting sensitivity analyses to validate the test load conditions. The second concern was addressed by examining the global attachment pin moment and rotation results and the local progressive failure analysis results.⁵ The team determined that pin moments are not an independent parameter, and therefore, the Airbus method for establishing the strength allowables inherently included moment effects.

III. Model Development and Validation

A. Model Modification and Convergence

The NASA team conducted detailed model refinement and model validation activities. Airbus provided NASA with a finite element model for the tail structure in March of 2002, which is shown in Fig. 2. This model included changes incorporated by Airbus after the AA587 accident, such as mesh refinement, particularly in the rudder. The Airbus tail structure model comprises three major components; the fuselage section, the vertical stabilizer (fin), and the rudder. Together, the fin and rudder make up the VTP that is connected to the fuselage via 12 attachment fittings (6 lugs and 6 shear yokes). Descriptions of these components are provided in Ref. 1. The finite element model was reviewed to gain familiarity with the model, and then the model was compared to design drawings supplied by Airbus. Comparison was limited to regions of interest, such as areas of observed failure in the accident

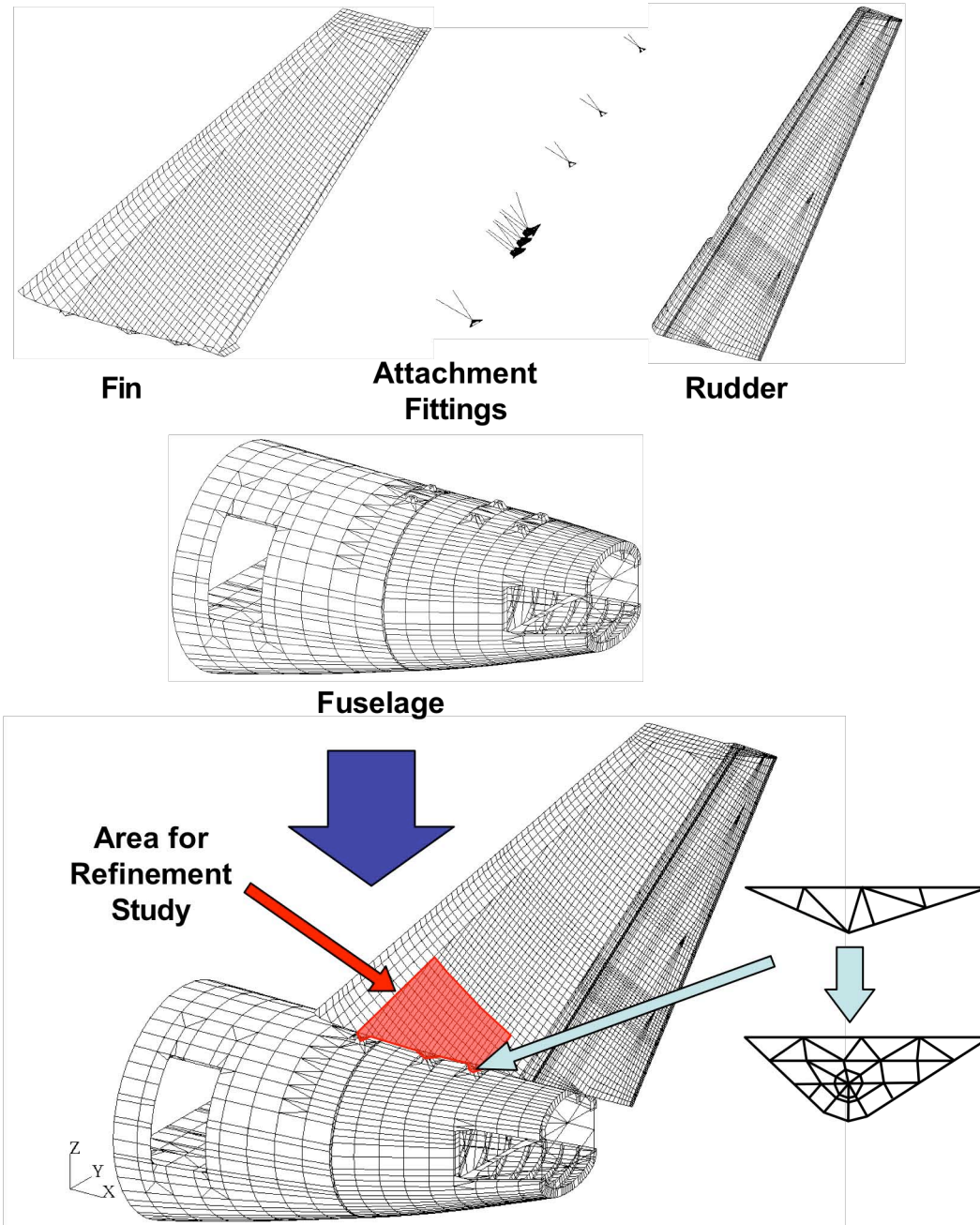


Figure 2: Finite element model of the A300-600 tail section (minus horizontal stabilizer).

aircraft and in regions where detailed modeling was present, and included the lugs, spar attachment points and the rudder skins. The Airbus model appeared to accurately represent the as-designed structure. An understanding of the Airbus analysis model and method was established by replicating the results for 15 load cases supplied by Airbus, providing a baseline from which model modifications were made to conduct further studies.

A number of model modifications were implemented to improve model accuracy in specific regions and to enable additional analyses, including enabling nonlinear analysis capability, mass adjustment, and lug mesh refinement. The original model supplied by Airbus was not able to support nonlinear analyses in NASTRAN, therefore, a major effort was expended to introduce nonlinear capability into the model. To enable the nonlinear analysis, numerous PATRAN⁶ Command Language (PCL) functions were written to automatically incorporate all necessary changes. The nonlinear capable model mesh remained the same as that for the linear model, however, many elements were changed to elements that are formulated to run in a NASTRAN nonlinear analysis. Next, the mass definitions of the global model were adjusted to permit accurate modal and transient analyses since the model supplied by Airbus was not intended for analyses requiring accurate mass modeling. Modifications were also made to the FEM of the VTP lugs to allow more accurate representation of the thickness distributions and to capture bending response. Additionally, the lug was modified to introduce loads through multiple nodes instead of one. The original Airbus FEM and the final NASA FEM for the right rear lug are shown in Fig. 2. Model modifications were implemented, and then the results from the modified models were interrogated and their convergence and accuracy were assessed.

The response of the lower portion of the fin was examined for convergence through a mesh refinement study in which a large lower portion of the fin was refined. The location of this refinement region is shown in Fig. 2. The region was refined from the baseline model consisting of approximately 21600 nodes and 40000 elements to a refined model consisting of approximately 50600 nodes and 75600 elements. Refinement encompassed all fin components from the lugs up to Rib 5, and was bounded by the front and rear spars, which were included in the refinement. The results of the refinement study were used to demonstrate convergence of the predicted attachment loads and skin strains. It was observed that the mesh refinement has very little effect on the VTP response and it was concluded that the coarse model was sufficient to provide converged results for the required accident loading conditions. Details about all model modifications and the convergence study can be found in Ref. 1.

B. Linear vs. Nonlinear Analysis

There was a concern that geometrically nonlinear behavior would affect the response of the VTP under the accident loading, particularly at the maximum loading condition. Therefore, using the nonlinear capable model, geometrically linear and nonlinear analysis results were examined to determine if the VTP exhibited geometrically nonlinear behavior when subjected to the maximum accident loading condition. In particular, VTP deformations, fin skin stress resultants, and main attachment forces and moments predicted for linear and nonlinear analyses were compared. The tip deflections were 608.11 mm and 606.95 mm for the linear and nonlinear analyses, respectively, a difference of -0.2%. Similarly, the right rear lug forces predicted with the linear and nonlinear analyses showed a difference of approximately 5%, and the fin skin force resultants for the two analyses were within 3%. For the most part, there were no other appreciable differences found between the results for the linear and nonlinear analyses. Therefore, linear analysis was deemed sufficient to examine the general response of the VTP structure.

C. Model Validation

Airbus conducted a finite element model validation study as a part of their design justification process by comparing results from several full-scale VTP tests with their analysis results. The full-scale test results from a test conducted in 1985 were used to validate the fin portion of the FEM used in the investigation. A sketch of the test setup is illustrated in Fig. 3, with the fin edges outlined in red and the lug load introduction beams highlighted in blue. The main objective was to verify that the FEM accurately predicts the over-all global response (e.g., global deformations) and local response characteristics in the acreage of fin skin panel (e.g., local strains to ensure structural stiffnesses and load paths were accurately modeled. Predicted and measured displacements that characterize the front and rear spar bending response indicated good correlation as shown in Fig. 4. In addition, predicted and measured chordwise strain distributions were compared (see Fig. 5), as were bending strains in the fin skin panels determined from back-to-back strain gage pairs (see Fig. 6). The predicted attachment point reaction forces at the test rupture load showed that the left rear lug load F_{xz} (the resultant in-plane load in the lug) is 917,070 N, as compared to 902,000 N for the tension rupture load as measured in the test, an error of less than 2%. In general, all results showed good correlation between the test and analysis, and indicate that the overall character of load distribution and stiffness in the fin was accurately predicted by the finite element model.

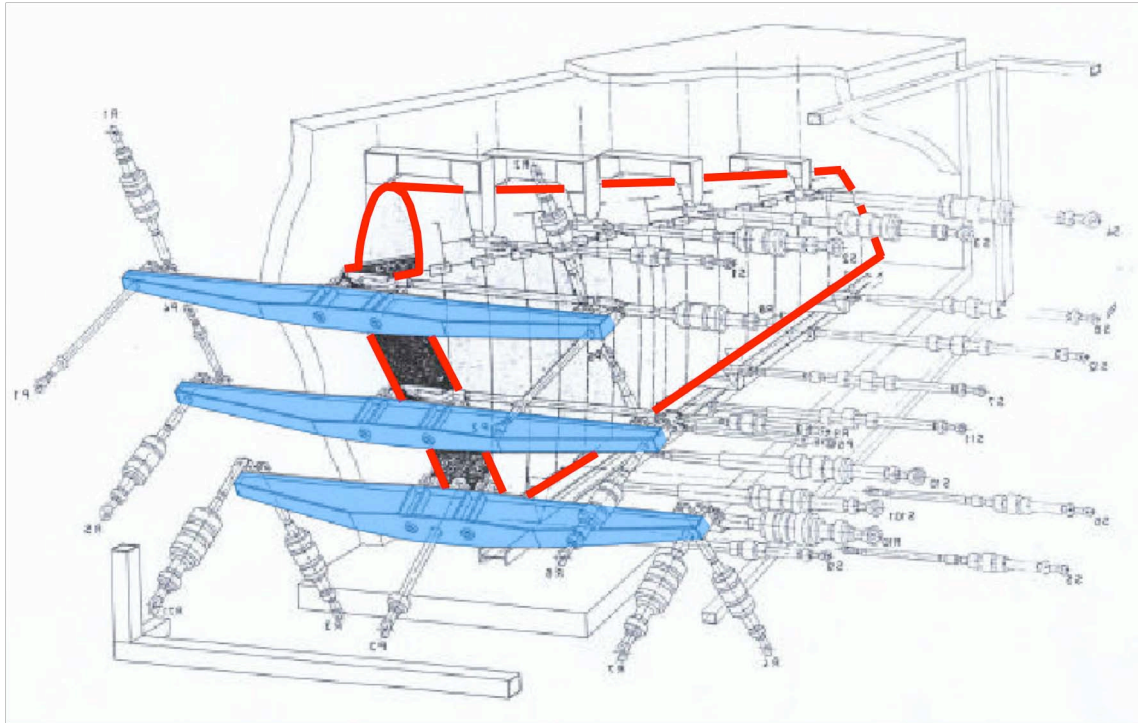


Figure 3: Airbus fin test setup (fin outlined in red, load introduction beams highlighted in blue).

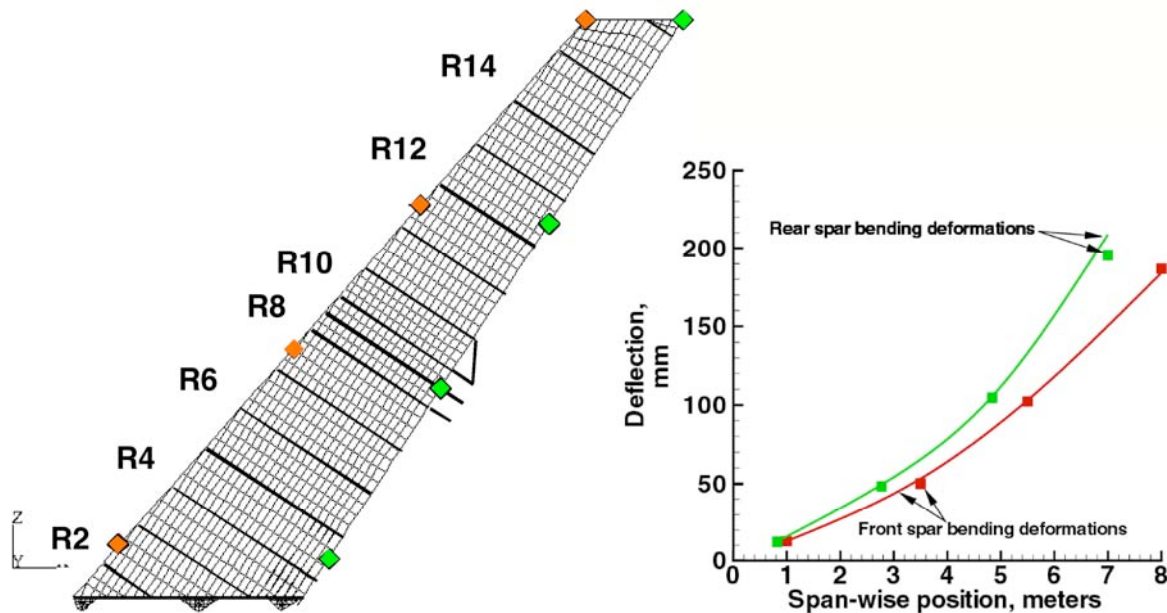


Figure 4: Comparison of full-scale test and analysis fin spar bending lines.

The main attachment loads that were used in the full-scale test were prescribed based on global finite element analysis results. However, the fin/fuselage attachment represents a statically-indeterminate structure. Therefore, the load distribution at the connection points will be dependent upon the geometry and stiffness of the structure. The stiffness of the fin model was demonstrated by comparison of fin responses to the full-scale test, as described above. Sensitivity studies were conducted to examine the dependency of the attachment loads on the fin lug and fuselage stiffnesses. One study focused on the stiffness variations in the lug region of the fin, and the other on stiffness variations in the fuselage. For the regions shown in Fig. 7, the fin stiffness was decreased by 20% for each region independently, then simultaneously. The fuselage stiffness was studied with the fuselage locally rigidized between the clevis pairs to represent the load introduction beams in the full-scale test (see Fig. 3) and with a fully rigid

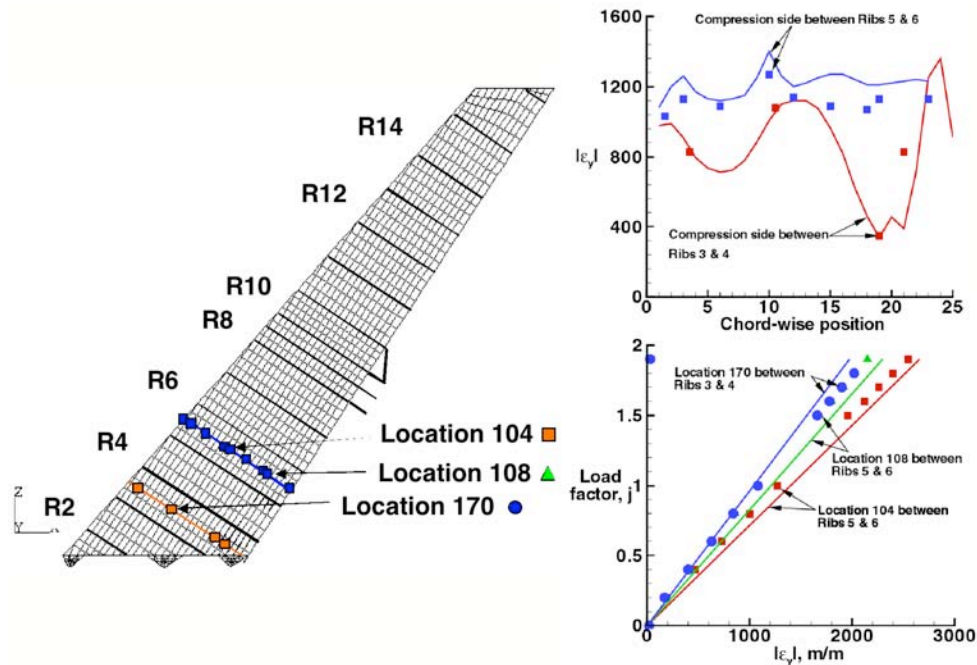


Figure 5: Comparison of full-scale test and analysis chordwise strains.

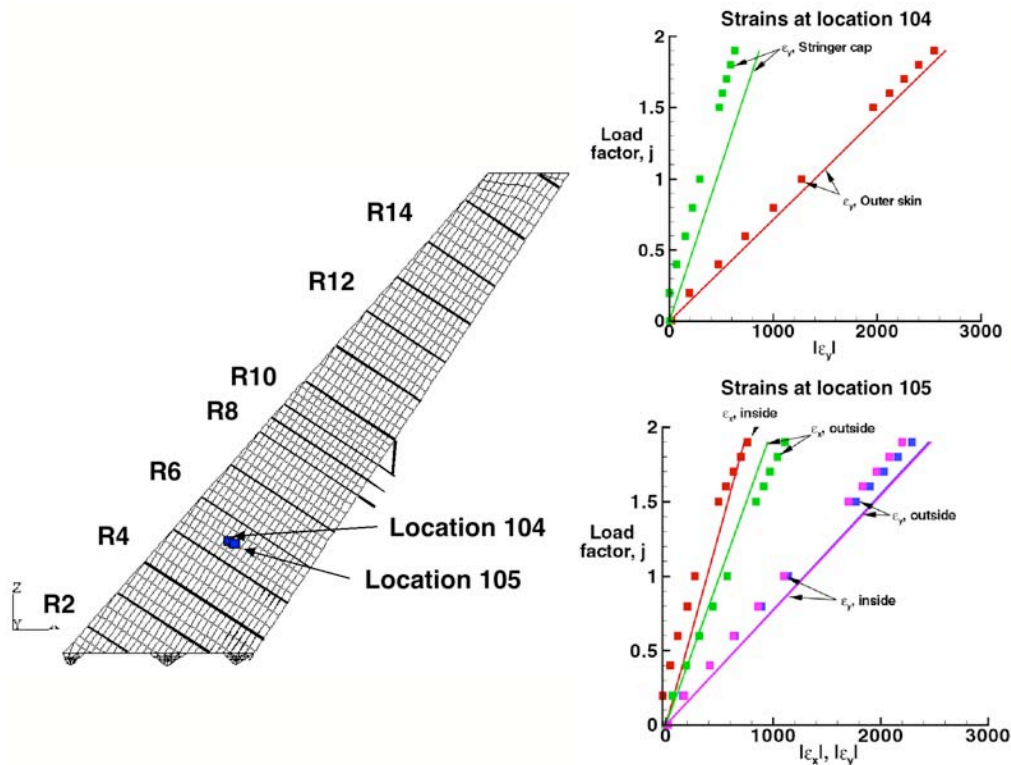


Figure 6: Comparison of full-scale test and analysis back-to-back gage strains.

fuselage. These studies indicated that while there were significant changes in local strains and in tip deflection, as a result of changes in VTP rigid body motion, the attachment loads changed very little. Therefore, it was determined that the load distribution at the attachments is primarily geometry driven so that use of the attachment loads from the global analysis for the off-fuselage full-scale fin test is valid.

Based upon the convergence and validation efforts, it was determined that the finite element model could be used to accurately evaluate the response of the VTP for the accident load conditions to interrogate failure scenarios.

IV. Failure Scenario Development and Validation

Five failure scenarios were defined based on the physical evidence and the initial assessment of the critical reserve factors. The critical reserve factors were calculated from the analysis results of the pristine VTP subjected to the accident maximum upset load condition using the modified model described in Section III. Accident flight loads used in the failure scenario investigation were derived from the flight data recorder (FDR) data by Airbus through a procedure verified by the NTSB, and were provided to NASA. The physical evidence of the AA587 VTP has been photographed and documented by the NTSB. Two of these documents were submitted as part of the public docket; Exhibit No. 15-A designated with Docket No. SA-522 and submitted on October 7, 2002,³ and the Structures Group Chairman's

Factual Report DCA02MA001 that was included in the public docket and revised on December 16, 2002.⁴ Figs. 8 and 9 show pictures of typical fin and rudder damage, and Fig. 10 shows a sketch of the rudder damage. The five

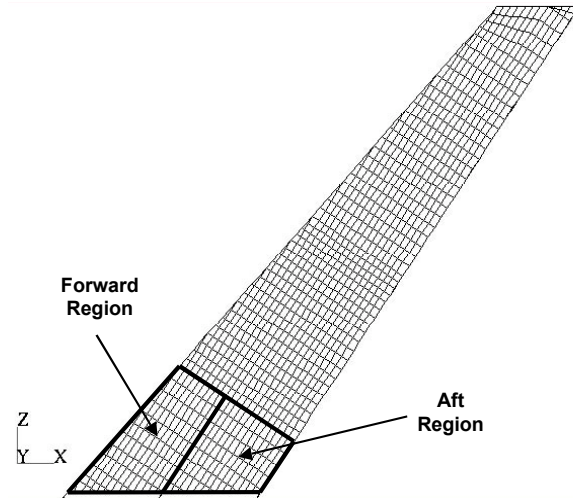


Figure 7: Regions of stiffness reduction for fin stiffness sensitivity study.



Figure 8: Fin and rudder hinge line damage of AA587.

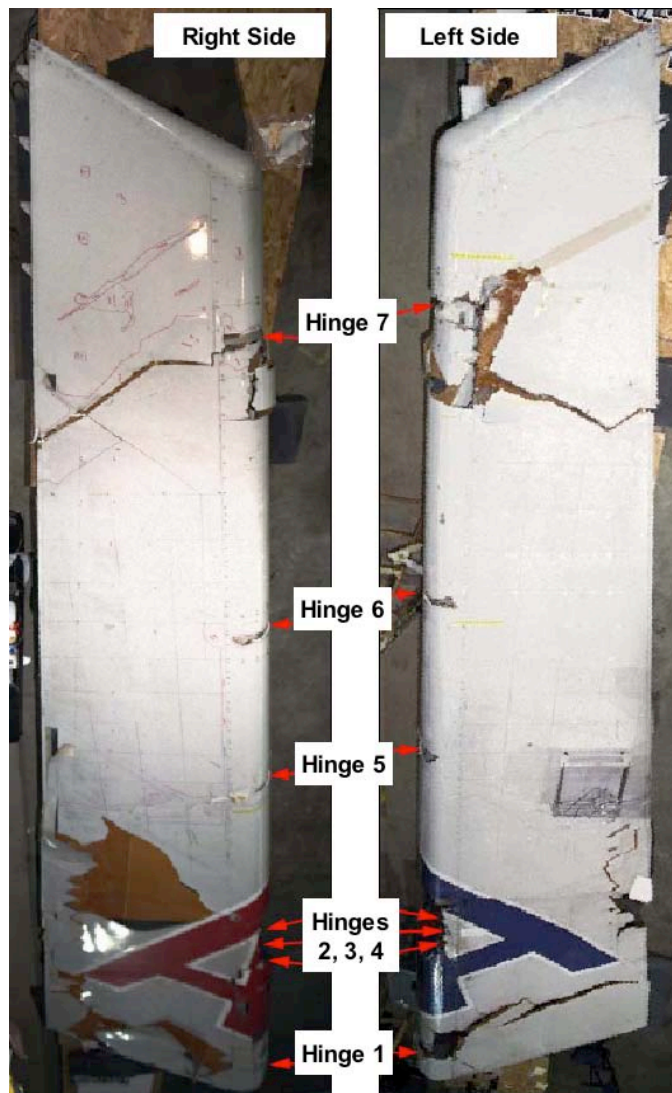


Figure 9: Rudder damage of AA587.

3) rudder skin failure at the ply-drop detail near the reinforced actuator region, 4) actuation of the bent hinge line that causes rudder fracture or rudder hinge line failure, 5) flutter of the VTP that results from delamination of the rudder skin. The five failure scenarios considered herein were evaluated using various analyses, and the models, analysis methods used and conclusions for these scenarios are discussed in the following subsections.

A. Main Attachment Fitting: Pristine and Pre-existing Damage

Main attachment fitting failure was examined using the full tail structure model. Flight simulation based upon FDR data was used to generate a time history of the fin root bending moment, torsion and shear loads during the accident event. The loads used in the study cycled the VTP through several maximum root bending moment load points on the FDR curve, and linear static analyses were performed at each point. Specifically, the pristine structure was analyzed for three critical load cases. Additional analyses were also performed to examine the effects of hypothetical pre-existing lug failure on the main attachment fitting failure scenario. The lug and shear yoke strength allowables provided by Airbus were used in both studies, and are listed in Table 1.

Three linear analyses were conducted and attachment fitting results for the pristine VTP under these load conditions were predicted. Figure 11 shows the root bending moment as a function of time, with the three analysis points identified as Max A, Max B and Max C. The fin/rudder icons illustrate the rudder deflection and the orientation of the VTP with respect to the free stream direction, indicated by a thick horizontal arrow). The locations of the six lugs are indicated by hatches on the icon. The results indicated that the right rear lug is most

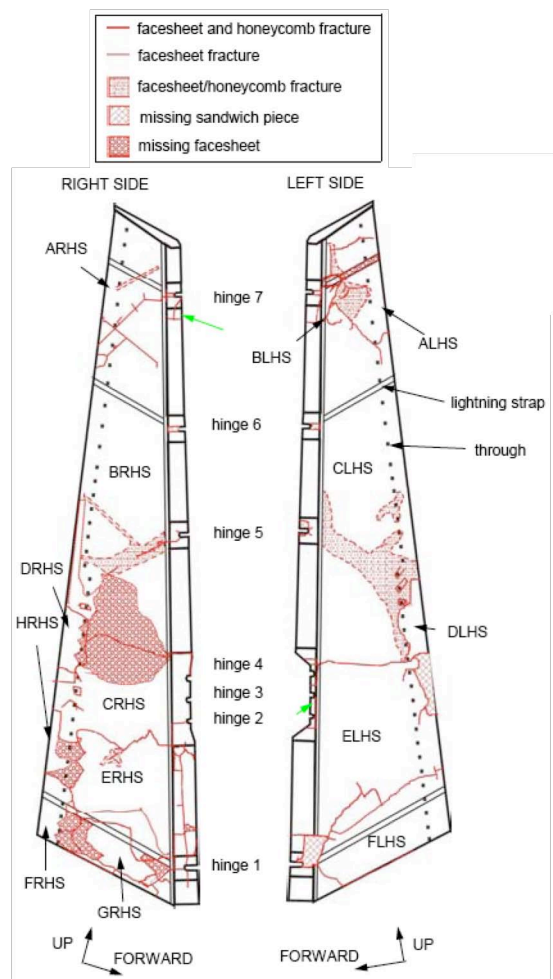


Figure 10: Sketch of rudder damage of AA587.

scenarios that were identified and examined are: 1) main attachment fitting failure, 2) buckling of fin box structure that causes main attachment fitting failure, rudder hinge line failure, or rudder failure,

Table 1: Lug and shear yoke allowable strengths.

Component	Tension Strength (N)	Compression Strength (N)
Front Lug	730,000	> 730,000 ^a
Center Lug	1,040,750	> 1,040,750 ^b
Rear Lug	902,000	1,003,000
Front Shear Yoke	73,700	73,700
Center Shear Yoke	90,900	90,900
Rear Shear Yoke	152,000	152,000

a) Provided by Airbus to be greater than 520,360 from test, but taken to be at least equal to tension as per rear lug.

b) Provided by Airbus to be greater than 761,640 from test, but taken to be at least equal to tension as per rear lug.

critical with a reserve factor of only 1.10 at the Max C location, and indicated the possibility of this scenario as being the most likely to have occurred (see Fig. 11)

Next, a limited study was conducted to examine the response of the VTP subjected to AA587 flight conditions where selected main lug fittings were prescribed to have pre-existing failure. It was assumed that a failed lug was not able to sustain a tension load, but that it could sustain a compressive load due to bearing of the lug on the fitting pin. Based on the ability of the failed lugs to sustain compressive loads, analyses were performed only for load cases for which the lug with pre-existing failure is placed in tension. Therefore, right lug pre-existing failures were analyzed at Max A and Max C which produce right side tension loads, while left lug pre-existing failures were analyzed at Max B which produces left side tension loads, as seen in Fig. 12. The blue dot on the fin/rudder icon marks the location of the pre-existing failure, and the red dots on the curve indicate the point when the analysis predicts the VTP will exhibit catastrophic failure and separate from the fuselage. The conclusions for the six pre-existing damage failure scenarios are as follows:

- 1) Pre-Existing Right Front Lug Failure: The analysis results indicate that catastrophic progressive failure would initiate at a level similar to the undamaged structure, at Max C. Therefore, pre-existing failure of the

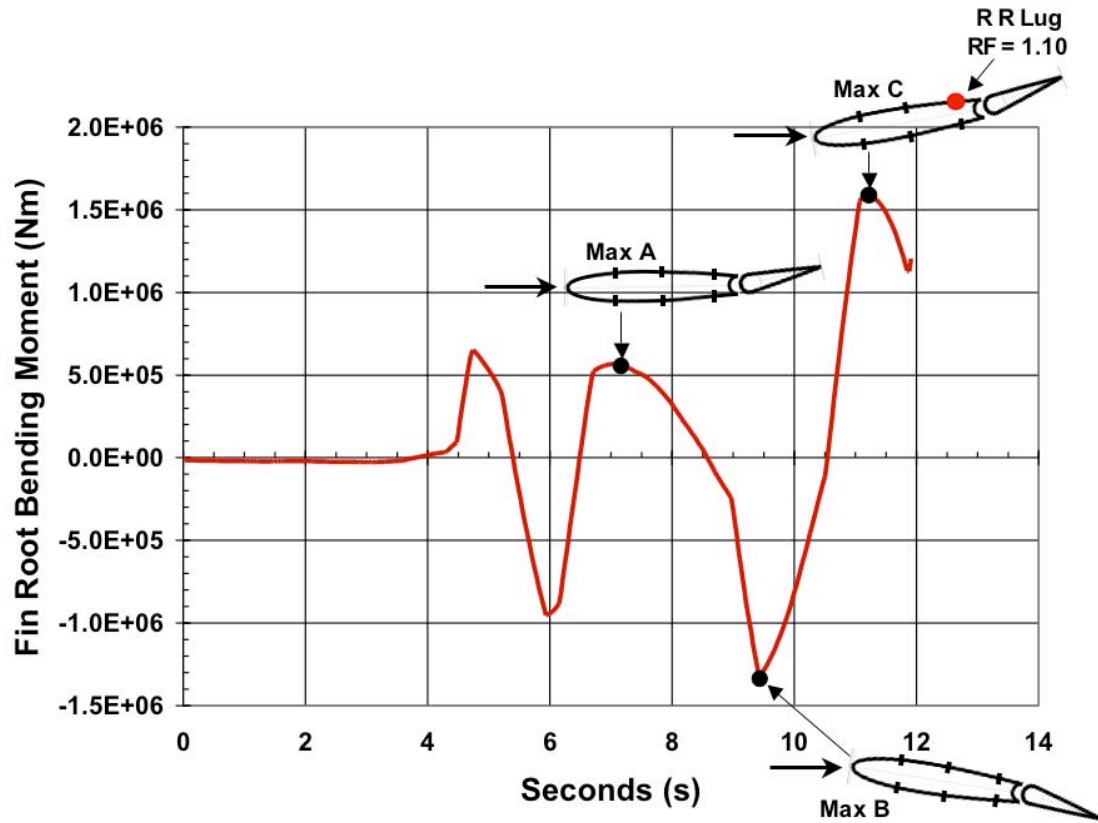


Figure 11: Pristine lug VTP response.

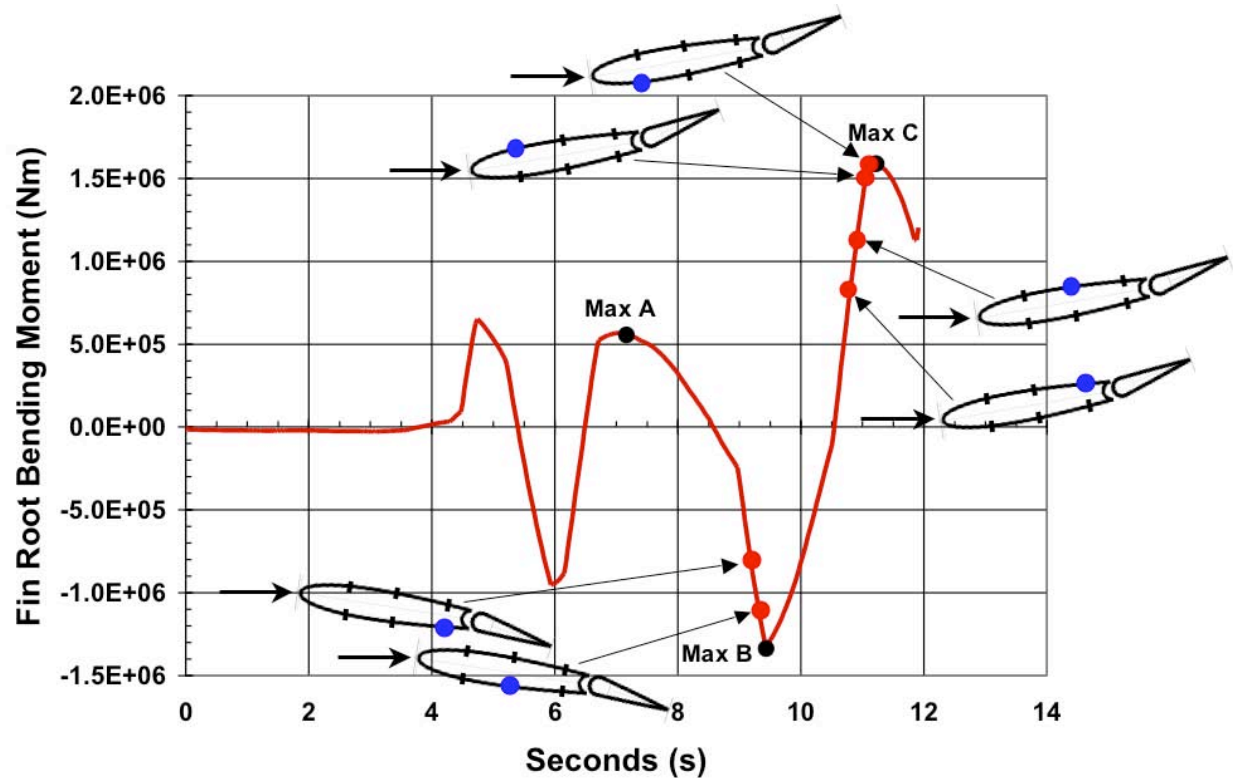


Figure 12: Pre-existing lug failure VTP response.

- right front lug is possible, but would have very little effect on the final static failure of the VTP attachments.
- 2) Pre-Existing Right center Lug Failure: The analysis results indicate that it would not be possible for the aircraft to encounter a later load condition since catastrophic progressive failure would occur for loads approximately 73% of the Max C load condition. Therefore, a pre-existing failure of the right center lug is not possible.
 - 3) Pre-Existing Right Rear Lug Failure: The analysis results indicate that the aircraft could not have reached the Max C load condition since catastrophic progressive failure would have occurred at approximately 60% of the Max C load condition. Therefore, a pre-existing failure of the right rear lug is not possible.
 - 4) Pre-Existing Left Front Lug Failure: The analysis results indicate that no progressive failure of the VTP attachment fittings would have occurred prior to load condition Max C. Therefore, it is possible that a pre-existing failure of the left front lug could have been present and still permitted the aircraft to encounter the latest load condition. However, the AA587 VTP physical evidence does not support the existence of a pre-existing left front lug failure.
 - 5) Pre-Existing Left Center Lug Failure: The analysis results indicate that catastrophic progressive failure of the VTP attachment fittings will occur at accident load levels prior to reaching the Max B load condition, thus not permitting the aircraft to encounter successive load conditions. Therefore, a pre-existing failure of the left center lug is not possible.
 - 6) Pre-Existing Left Rear Lug Failure: The analysis results indicate that catastrophic progressive failure of the VTP attachment fittings would have occurred at accident load levels prior to reaching the Max B load condition, thus not permitting the aircraft to encounter successive load conditions. Therefore, a pre-existing failure of the left rear lug is not possible.

B. Buckling of Fin Box Causing Failure Elsewhere

The results of preliminary analyses conducted during the investigation indicated that sections of the fin box could exhibit buckling response when the fin was subjected to the accident loading conditions, e.g., buckling of the fin skin, shear web rib and spars. Recall that buckling does not necessarily indicate failure, and the physical evidence does not indicate any failure in the regions that indicate the possibility of buckling. However, since buckling can have a significant influence on the stiffness and the load distribution of the structure, which could lead

to failures elsewhere, an attempt was made to approximate the effects of buckling on the response of the fin structure. This section describes the theory of the approach, assumptions, limitations, and results of the buckling analysis.

In general, when a panel buckles, there is a substantial reduction in the panel's stiffness. One approach to simulate the stiffness reduction is to introduce a secant stiffness that depends on the extent of postbuckling. Figure 13 illustrates the nonlinear stress-strain response of a postbuckled skin panel or shear web that is approximated using a bi-linear stress-strain curve where the stiffness of the buckled region is approximated by the secant stiffness S' . In the NASA

buckling analysis, the sections of the skin and shear web that indicated potential buckling were modified to include a reduced stiffness (secant stiffness) that was 50% of the prebuckling stiffness and is considered to be a worst-case situation. Specifically, the secant stiffness was applied to all elements that were at or above 90% of the allowable buckling load. This lower buckling threshold was used because it was assumed that elements adjacent to the buckled elements would have load redistributed to them, and thus, these elements could potentially buckle as well.

Results indicate that localized regions of the skin near the buckled regions show some differences in the strains. In particular, the maximum tension and compression strains are different by approximately 46% and 6.4%, respectively. Similarly, shear strains can increase by as much as 74% in the LHS fin skin (see Fig. 14, buckled regions outlined). In addition, load redistribution occurs near the buckled regions of the skin. The results indicate that there is a significant reduction in the load carried by the buckled region of the skin and the load is redistributed to the adjacent regions of the skin and into the stringer webs and stringer flanges, as expected. This load redistribution response is a typical response characteristic of a locally buckled stiffened panel where the load path is redirected to adjacent unbuckled skin and stiffeners, and thus, this result represents a physically meaningful result. However, the results indicate that the buckling of the fin skin, shear web ribs and rear spar have a very small effect on the global VTP response. In particular, the tip deflection of the fin in the "buckled" condition was increased approximately 0.8% as compared to the "unbuckled" condition. Similarly, the buckling of the structure has a relatively small (at most +/- 2.5% difference) effect on the loads transmitted to the rudder and to the main lug fittings and spar fittings. Overall, the global response characteristics and strain distributions for the buckled fin are similar to those results exhibited by the corresponding pristine unbuckled fin. There are a few localized regions of the fin skin where the results do indicate the largest failure indices and suggest material failure, but these results are very conservative because of the conservative design allowables combined with the large stiffness reductions applied in the analysis. Furthermore, the physical evidence does not indicate material failures of the fin skin or stringers in the areas where it is predicted to occur. Therefore, it was determined that local buckling of the fin skin does not appear to affect the failure load or mode for the AA587 VTP.

C. Rudder Skin Failure Near Ply Drop

Physical evidence indicated that significant failure of the rudder occurred at some time during the accident, either before, during or after the VTP departed from the fuselage. One of the more prominent failures in the rudder was located in the left-hand and right-hand side sandwich panels near the transition from the reinforced actuator region (booster region) to the unreinforced region of the rudder skin. This transition region is referred to herein as the rudder skin ply-drop region. The region of interest is illustrated in Fig. 15, where reinforcement plies in the actuator region are indicated as shaded areas in part a) of the figure. Three ply-drop regions were studied, and the most critical cross-section is shown in the Fig. 15b, which indicates the ply orientation and the ply drop-off schedule. The response phenomenon of interest is a localized bending response near the ply-drop when subjected to a span-wise bending load that causes elevated stresses in the face sheets. Localized bending may develop a peel stress between the skin and core material and can locally elevate the skin strains or cause a local skin buckling

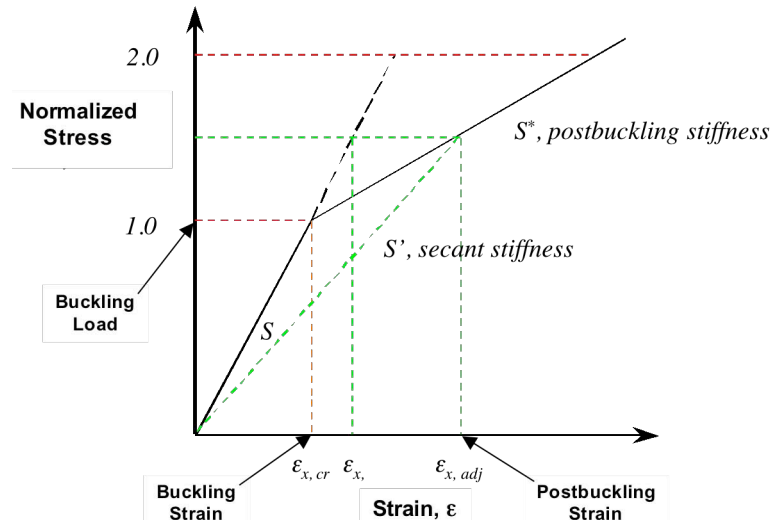


Figure 13: Bi-linear approximation of the stress-strain response of a postbuckled panel and secant stiffness model.

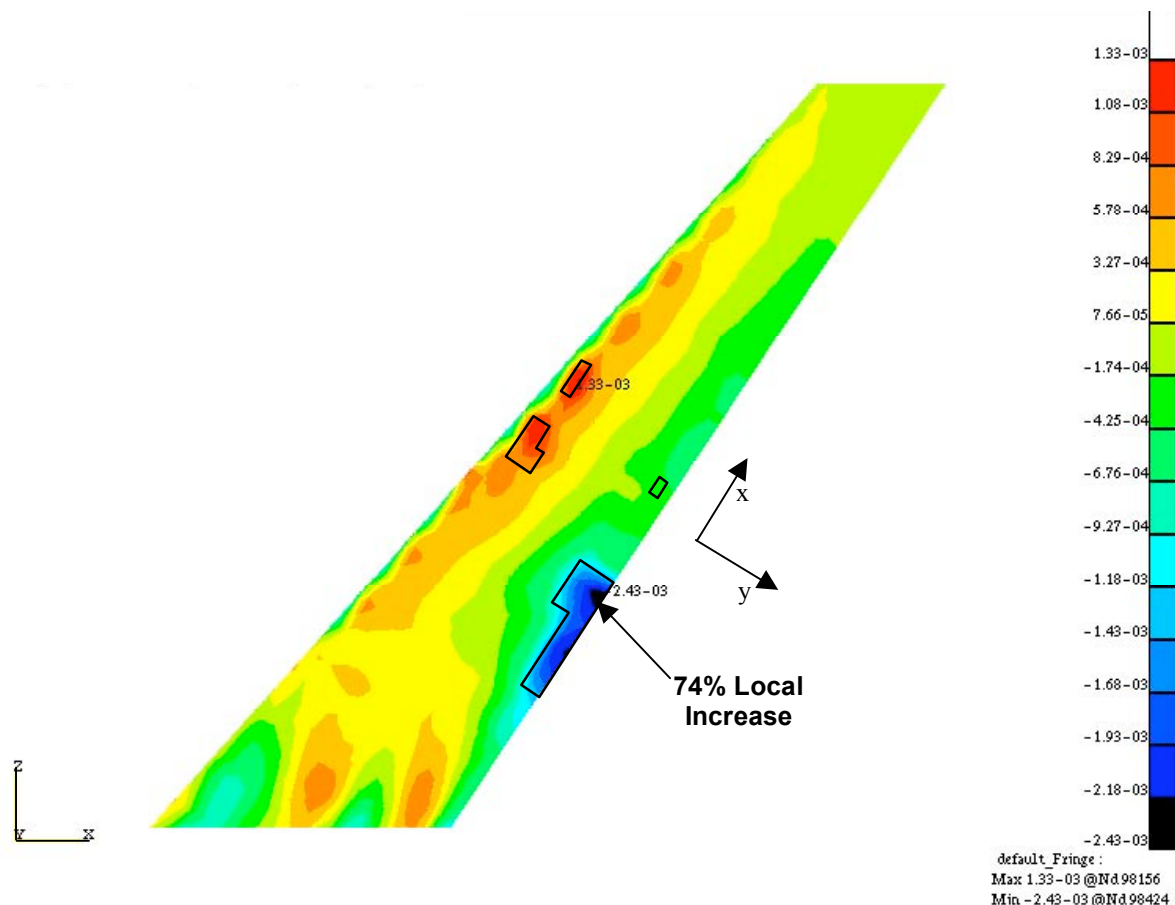


Figure 14: Left-hand fin skin shear strain, γ_{xy} , including buckling effects, Max C.

response. The rudder allowables presented in the Airbus design documentation did not specifically address the ply-drop feature in the rudder skin. Thus, to determine if the ply-drop details could have contributed to failure of the rudder, NASA generated analysis-based failure allowables and applied them to the accident loading conditions.

Detailed finite element analyses were conducted to establish far-field strain allowables that correspond to failure near ply-drops in the rudder skin. The STAGS (S_{TR}uctural Analysis of General Shells)⁷ finite element analysis code was used to model selected ply-drop regions of the rudder sandwich panels subjected to a span-wise bending load. Specifically, the model was used to investigate the effects of the ply-drops on the skin buckling response, the stresses that develop between the skin and the core material, and elevated strains that develop as a result of a localized bending response near the ply-drop. The effects of chord-wise compression loads and in-plane shear loads were neglected in the analysis since they would have a negligible effect on the localized span-wise bending response

associated with the ply-drop when subjected to compression. The finite element model used solid elements to represent the sandwich panel skin and core material. Each layer of the skin is modeled with a single layer of solid elements through its thickness and the core is modeled with 6 to 12 elements through its thickness. The material properties for the core and the face sheet material were taken from the NASTRAN model. A convergence study was performed on the models to verify their accuracy in predicting the deformation response, skin buckling

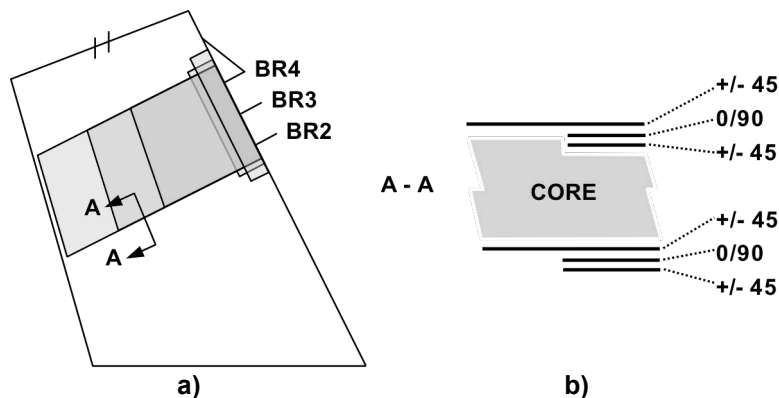


Figure 15: Rudder skin reinforcement in the actuator (booster) region and selected span-wise ply drop-off patterns.

load and selected stress and strain quantities. The allowables for several ply-drop regions were established through a series of analyses in which the finite element model was subjected to uniform end shortening (see Ref. 1). Specifically, the results from these analyses were compared to standard material allowables for the rudder structure, then effective global strain allowables that correspond to local ply-drop failures were determined.

Fig. 16 shows the local deformation and shear stress contours at the location of the 3-to-1 ply-drop, where significant local bending is observed. Analyses indicate that skin fiber failure at the ply-drop was the most likely failure mode rather than facesheet-to-core delamination. Allowables were established for three rudder ply-drop cross-sections and were compared to the static analysis results for the VTP under accident loading. Predicted rudder strains under accident loading indicate that global strains in regions of the ply drops do not exceed the predicted allowables. Therefore, failure at the ply-drop region of the rudder is not a likely candidate for initiation of the AA587 VTP failure. However, ply-drop failure was revisited during subsequent sequential failure evaluations, both static and dynamic, in an attempt to explain the presence of the physical evidence.

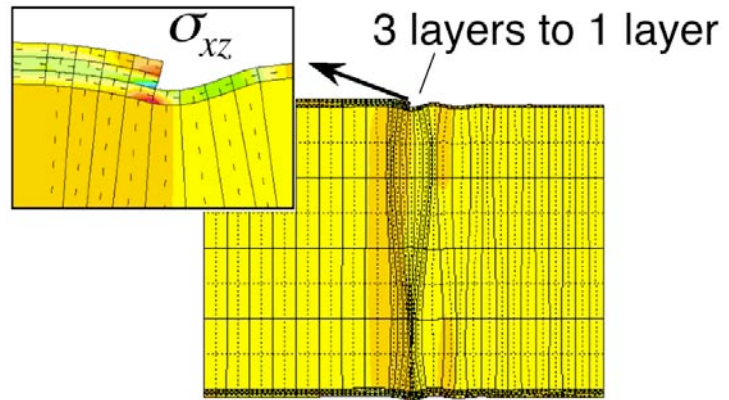


Figure 16: Local shear stress and deformation at ply-drop.

D. Actuation of Bent Rudder

A series of analyses were conducted to determine if the bending response of the VTP during the accident could cause the rudder motion to stiffen as the rudder was actuated through the neutral position. This type of response is exhibited when hinges become misaligned, a condition that could exist due to bending of the VTP, as suggested by the rudder position at high root bending moments as seen in Fig. 17. Notice that as the root bending moment traverses from Max B to Max C, when the root bending moment becomes zero the rudder is still in a tail-left

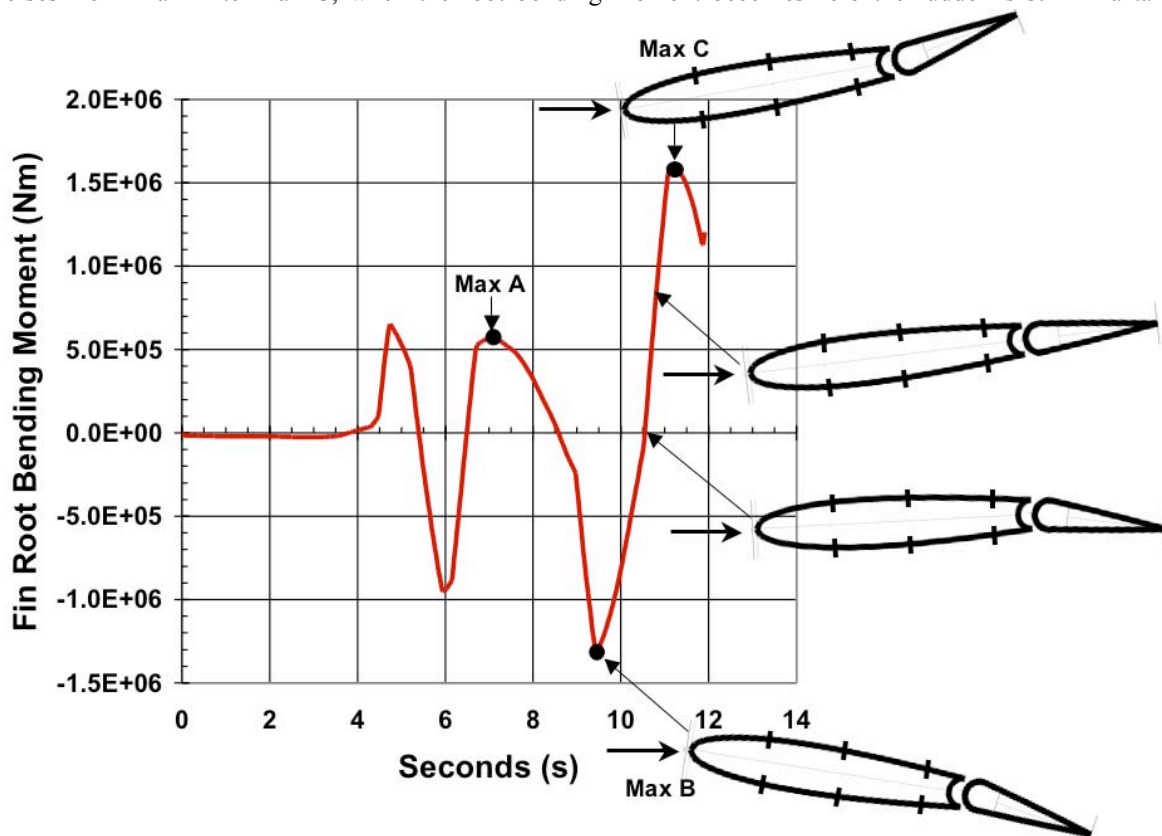


Figure 17: Rudder deflection in sweep from Max B to Max C.

position. When the rudder position is reversed and is passing through the rudder-neutral position, the root bending moment has already increased to approximately half of the Max C value due to aircraft sideslip. Therefore, the VTP would be bent in the same direction as seen at Max C when the rudder is actuated from the neutral position to the Max C position, which could potentially cause bending in the pivots and result in elevated hinge loads. The aerodynamic loads for points on the curve between Max B and Max C are lower in magnitude than those at the extreme points (Max B and Max C). However, in order to simplify the analysis and to more easily identify changes in hinge line loads, the Max C aerodynamic loads were applied during the bent hinge line study.

The NASA nonlinear model was used and a procedure was developed to determine whether a deflected VTP could cause a nonlinear increase in the rudder fitting actuator loads and/or strains in the rudder when the rudder is actuated. In the procedure, the actuator elements were lengthened or shortened by applying thermal load, thereby deflecting the rudder. Since the deflection of the rudder can be accomplished via temperature actuation, the initial rudder position chosen was the neutral (undeflected) position, and temperatures were then assigned accordingly such that the actuator obtains the required actuation displacements for each load case examined.

In order to reduce the problem size, the fuselage was eliminated and the VTP was restrained at the attachment points (lugs and yokes). This approach is valid since it was shown that there is little effect on the VTP response with this boundary condition when compared to the VTP attached to the fuselage (recall Section III.C). Nonlinear analyses were conducted on this model as follows:

- 1) The aerodynamic loading of Max C was applied in conjunction with an actuator thermal load set that deflects the rudder to 9.35 degrees (see Fig. 18) and a nonlinear analysis was conducted.
- 2) The nonlinear analysis was restarted from the final solution of step 1) where the aerodynamic loads are maintained, and a new actuator thermal load set is applied to deflect the rudder to -9.35 degrees (see Fig. 18)
- 3) Fin deflection, rudder fitting forces and rudder strains are compared at 1 degree increments and at the 9.35 and -9.35 degree rudder positions.

For these analyses, the loads are follower-type, and the loads remain perpendicular to the rudder chord as it is rotated. Little difference is observed in the strains throughout the entire actuation sequence of the rudder.

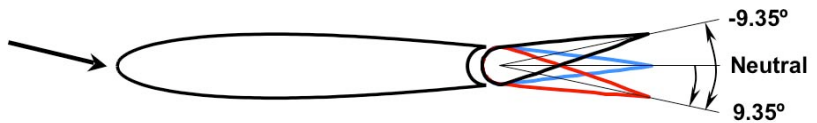


Figure 18: Rudder deflection definition for bent hinge line analysis

The rudder structure is designed to be stiff in torsion, and fairly compliant in bending. Thus, the rudder fitting forces required to bend the rudder to conform to the shape of the deflected fin are small compared to the fitting strength and the rudder fitting forces required to react the aerodynamic load. The significance of a bent hinge line depends on the stiffness of the components that are hinged, and for the VTP the effect was negligible. Therefore, it was concluded that rudder binding was not an issue and would not affect the VTP response during the incident.

E. Flutter of VTP from Delamination of Rudder Skin

One of the potential modes of failure of the fin involved the initial failure of the rudder, which could then lead to a flutter instability causing an eventual overload condition in the fin. Delamination of the rudder skin is seen as the most likely mode of failure in the rudder based on the visual evidence of the failed hardware. Therefore, the effects of a delamination in the rudder skin on the flutter response of the rudder was studied. Specifically, the NTSB recommended that the team consider two different sized delaminated regions in the LHS rudder skin; a 1075 mm by 350 mm chordwise strip located above hinge 4, and a 1000 mm by 2000 mm region that extends from hinge 4 to hinge 5 (see Fig. 19). The smaller delamination region is referred to herein as *delam1*, and the larger delamination is referred to as *delam2*. Since delamination of a sandwich panel significantly reduces the shear and compression stiffness of the panel, the intent was to compute a reduced membrane stiffness associated with the delamination, and then simulate an equivalent reduced stiffness in the global shell model of the VTP and conduct a modal analysis.

Finite element models of rectangular sandwich panels with facesheet delaminations were developed and analyzed using STAGS. In the model, the panel was clamped around the edges and the edges were subjected to a uniform compression or shear displacement. The sandwich construction was modeled using plate elements for each facesheet laminate, separated by a solid element core. One facesheet was fully delaminated from the core except at the edges of the plate. Contact elements were utilized between the delaminated face sheet and the core to prevent interpenetration of the two parts of the structure (see Fig. 19). The analyses indicate that for all cases the unsupported facesheet buckles at a very low strain ($<15 \mu\epsilon$ for *delam1* and $<3 \mu\epsilon$ for *delam2*) when subjected to uniform compression or shear. When the unsupported facesheet buckles, the effective in-plane stiffness K of the

panel immediately reduces to 80% of the stiffness of the original undelaminated sandwich panel (see Figs. 19 and 20). When the load is increased, the second facesheet with the core attached also buckles, and the membrane stiffness of the panel reduces to 20% of the stiffness of the original intact sandwich panel.

The nonlinear stiffness reduction of a buckled, delaminated sandwich panel was simulated in NASTRAN analyses by defining new material and laminate constructions with reduced stiffness in the model. In the delaminated regions, the in-plane stiffness of the face sheet material was reduced to 20% of its original value, and the core material was eliminated from the sandwich structure laminate (most conservative model). The reduced stiffness of the face sheets reflects the reduced membrane stiffness of the delaminated structure, and the elimination of the core simulates the reduced bending stiffness of two independent face sheets compared to the bending stiffness of the intact structure. Previously, the Airbus approach to simulating a delamination has been to eliminate the core, but to maintain full membrane stiffness of the face sheets.

A set of modal analyses have been conducted using the global VTP model. Comparison was made between the pristine structure and the structure with a stiffness reduction incorporated into the left-hand-side rudder skin. Modal results were compared for the two models, and included the frequency, the type of mode (full VTP or rudder dominated) and the percent difference. The results indicated that a reduction in rudder stiffness due to the delaminations had very little effect on the modal frequencies associated with full VTP response. For the rudder dominated modes, the delamination produces larger frequency reductions but the differences are still

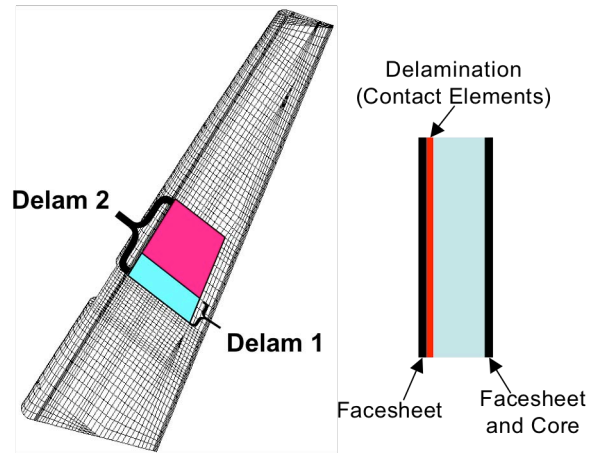


Figure 19: Rudder delamination regions studied and delamination definition.

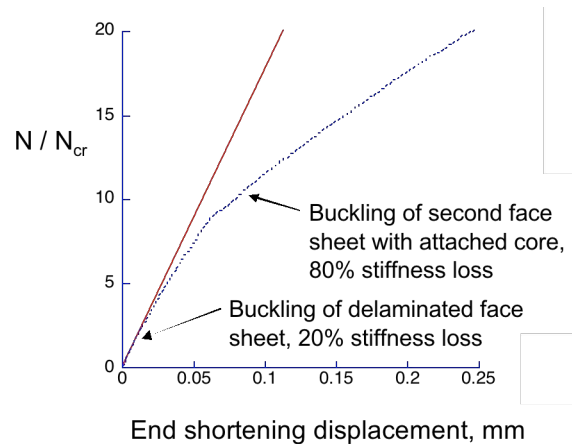


Figure 20: Normalized load versus end shortening response curve for a typical delaminated sandwich panel.

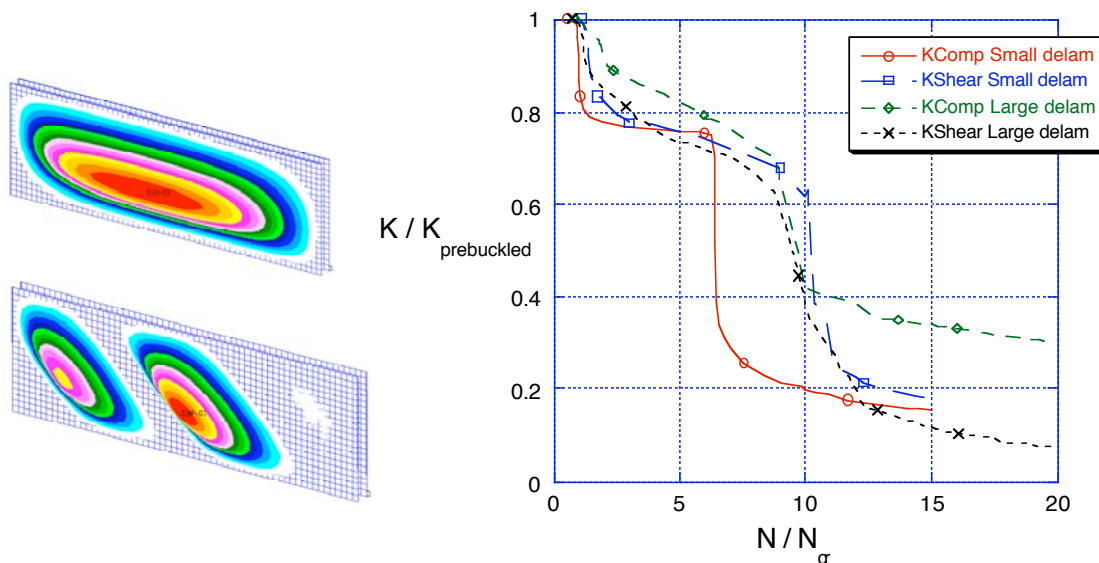


Figure 21: Normalized effective axial stiffness as a function of normalized load.

relatively small (less than 8%). These modal results were transferred to NASA's aeroelasticity group for use in a flutter analysis and subsequent results indicated that the delaminations had very little effect on the overall flutter response of the VTP and rudder. Therefore, it was concluded that the presence of a large delamination in the rudder skin causing flutter was not likely, and hence, flutter-induced failure was not a likely initiator of the AA587 VTP failure.

Therefore, after interrogating these five failure scenarios, the conclusion was that failure of the right rear lug was the most likely failure scenario. This most likely failure scenario is studied further in the following section.

V. Confirmation of Most Likely Failure Scenario

Failure of the right rear lug was determined to be the most probable failure scenario, and thus, more detailed analyses of the lug was undertaken. The NASA Local Lug Analysis Group developed a detailed ABAQUS model of the right rear lug, and used this model to conduct progressive failure analysis (PFA) of the lug subjected to accident loads to predict the lug failure load. The local group analysis methods, results, and validation against subcomponent tests are presented in Ref. 5. The global group provided boundary condition information to the local group to enable local analysis of the right rear lug under accident conditions. To facilitate the passing of this boundary information between the global and local analysis groups, the global model was modified to more closely match the local lug model stiffness, and then a global/local procedure was developed to ensure proper loading in the local model based on global model inputs. The global/local approach permitted passing of boundary information (displacements and tractions) to the local analysis group for conducting local lug analyses (see Fig. 22).

During the accident, the right rear lug ruptured at the pin location, so detailed local modeling was conducted at the pin-to-lug connection area to simulate the state of stress at the lug hole.⁵ The local model was established with the intent of applying the displacements from the global shell model to the edges of the local model and conducting progressive failure analyses. However, analyses indicated that the local model needed to be incorporated into the

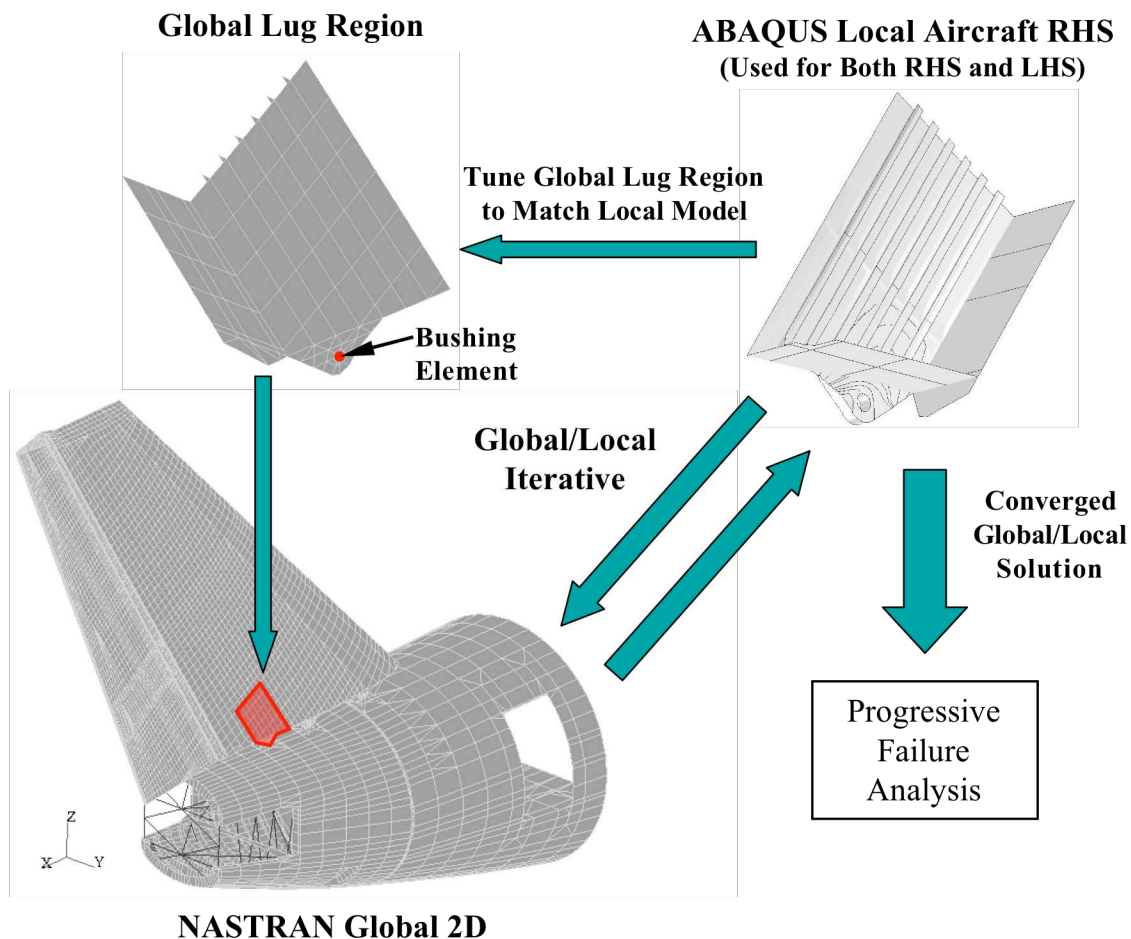


Figure 22: Model refinement and analysis process.

global model to ensure that the stiffness of this region was reflected in the global analysis. A global/local approach was developed that effectively embedded the local model in the global model, so that the local lug region stiffness was accurately reflected in the global model. The converged global/local displacements were applied to the local model to perform the progressive failure analysis of the lug. Throughout this process, the pin connecting the VTP lug to the fuselage clevis was assumed to be rigid, that is, pin flexibility was ignored.

The NASA local model was derived from a solid NASTRAN lug model provided by Airbus and is shown in Fig. 23. The model has solid elements modeling the lug and doubler region, and shells and beams modeling the remainder of the structure. The lug region, which is defined as that portion below Rib 1, is composed of the skin extension that is sandwiched between two doublers. The local model encompasses Rib 1 from the centerline to the skin, the skin from Rib 1 to Rib 5 that is bounded by the rear spar and the 7th stringer forward of the rear spar, the rear spar from the centerline to the skin, the stringers between Rib 1 and Rib 5, and the lug/doubler region. The red region, partially hidden by the shell elements that comprise the stringer flanges, marks the solid FEM portion that represents the lug/doubler region. Contact surfaces were defined to allow “bearing” on the compression side of the pin surface, and “gapping” on the tension side of the pin surface. The local model interfaces with the global model at 9 boundary edges and 17 boundary point locations, and is used for global/local analyses and subsequent progressive failure analyses.

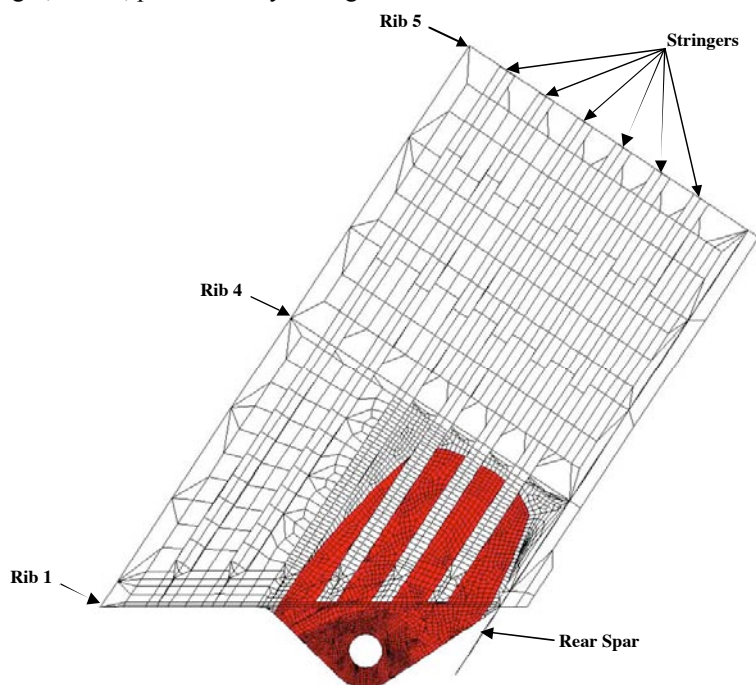


Figure 23: Local right rear lug finite element model.

The global model was modified to more accurately represent the local model stiffness. Specifically, because the global shell model is more stiff than the refined local model that utilizes solid elements and transfers load via a contact surface, modifications were made to the global shell model to reduce the stiffness of the lug region. The global model was “tuned” to the local model by reducing the effective stiffnesses of the rear lug regions through the use of NASTRAN bushing elements (see Fig. 22). The process for tuning the global model with bushing elements is described in Ref. 1. Tuning resulted in less stiffness on the tension side, which was reflected by the lower stiffness values assigned to the bushing element.

Although the global model was modified to more accurately represent the stiffness of the local lug model, it was found that when the boundary and pin displacements were applied to the local model, the pin reactions and boundary forces from the local model were not completely consistent with the pin reactions and boundary forces from the global model. That is, the local model was not in equilibrium with the global model. Therefore, an iterative global/local approach was developed by which a refined local lug representation was effectively embedded in the global model. The global/local process was necessary because the pin/lug interaction (specifically, force transfer) was modeled with a contact surface in the local model and is analyzed using ABAQUS. The global model was analyzed using NASTRAN, so a direct connection of the coarse (global) model and the refined (local) model was not possible.

The global/local procedure is depicted in Fig. 24, was implemented for both the right and left rear lugs, and is defined as follows:

- 1) An initial global analysis is performed and displacements are extracted along the global/local interface boundary to act as input boundary conditions for the local model. Additionally, aerodynamic loads within the local region are also passed to the local model.

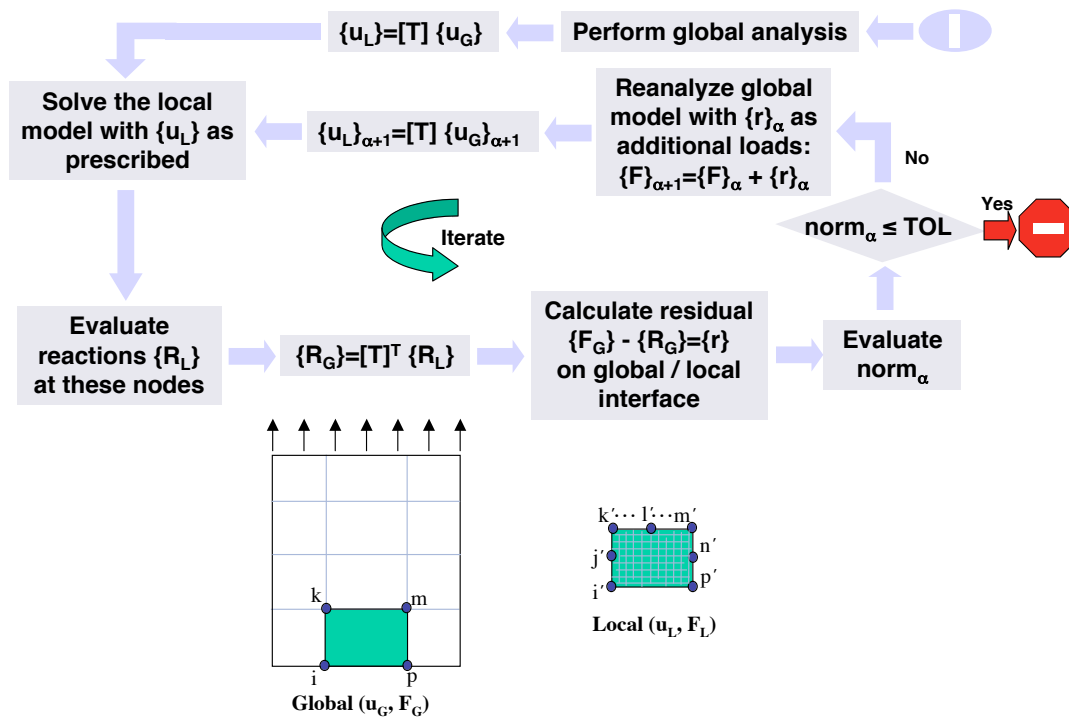


Figure 24: NASA global/local analysis procedure.

- 2) The local model is analyzed and the boundary reaction loads (forces/moments) are computed at the global boundary points.
- 3) The boundary load residual is computed by subtracting the boundary reaction loads of the local model from the boundary reaction loads of the global model.
- 4) The boundary load residual is calculated and the solution is checked for convergence. If convergence has been obtained, the process is complete.
- 5) If convergence has not been obtained, then the residual vector is introduced to the global model as an additional load set. That is, the total load set for the next iteration is the load set of the previous iteration plus the boundary residual load.
- 6) A global analysis is performed and displacements are extracted along the global/local interface boundary to act as input boundary conditions for the local model. Return to step 2) above.

Convergence for this investigation was examined by using a total boundary work residual. The total boundary work residual was used to ensure that the displacement and traction compatibility was maintained across the entire global/local interface. It represented the integrated work done at the interface between the global and local models and assessed the solution convergence in an overall energy sense. The total boundary work residual was normalized by the boundary work from the initial global analysis.

Four analysis steps were carried out to confirm the most likely failure scenario, three of which included global/local analysis. The sequence of steps used to confirm the most likely failure scenario is listed in order in Table 2. Adjacent to each step in the process is an explanation for the purpose for that step. The table outlines the validation of the progressive failure analysis and global/local analysis procedures. Linear Global/local analyses were conducted and the local group performed progressive failure analysis using the converged global/local values. The most likely failure scenario was confirmed where the failure is simulated to be within 3% of the accident loading condition.

The load level to which the VTP was subjected during the accident for the most likely failure scenario was evaluated to determine if the VTP performed in accordance with certification. Load factors for the accident Max C load condition were calculated based upon design limit load certification values. The certification values used were for a gust loading condition that is very similar to the accident loading condition in terms of VTP root reactions. Calculated accident load factors for the Max C load condition are presented in Table 3, and are based upon several load case parameter values for defining the failure initiation load factor. The load factor based on the right rear lug in-plane force was calculated using NASA model results for both the design gust and accident loading conditions.

Table 2: Steps used to confirm failure of right rear lug as most likely failure scenario.

Step	Purpose
Global/Local for Accident Condition	Provide Representative Loads for Subcomponent Test
Subcomponent Test/Progressive Failure Analysis (PFA)	Validate PFA with Representative Loads (Failure Load and Mode)
Global/Local with PFA, Full-Scale Test	Validate Global/Local/PFA Process (Results within 1%)
Global/Local with PFA, Accident Condition	Confirmation of Most Likely Failure Scenario (Results within 3%)

Load factor values in the table indicate that the load level at failure is at minimum 1.92 times limit load based upon the VTP root shear load. Since the certification requirement is that the component must be able to attain 1.5 times limit load without catastrophic failure, it is clear that the AA587 VTP reaches loads that are significantly above the certification requirements before catastrophic failure led to departure of the VTP from the aircraft.

Table 3: VTP failure load factors of AA587.

Calculation Parameter	Max C
Root Shear, Q_y	1.92
Root Bending Moment, M_x	2.13
Right Rear Lug In-Plane Force	2.03

VI. Failure Sequence Analysis

The failure scenario investigations indicated that the most likely failure scenario is the result of failure initiation at the right rear lug. Because the largest right rear lug forces resulted when the Max C load condition was applied, failure sequence development was carried out using this load case. Additionally, the progressive failure analysis presented in Ref. 5 indicated that the Airbus allowables for the lug were reasonable for use in developing a final failure sequence. For the purpose of failure sequence development, the Airbus design allowables were used to predict component failures. Both static and transient failure sequences were developed to determine if most of the observed physical damage could be sufficiently explained.

A. Static

The static failure sequence was evaluated through a series of linear static analyses with failed components represented in the model. During development of the failure sequence, it was seen that there were times when multiple attachment fittings simultaneously exceed their allowable values. In these cases, there are two possible methods to propagate failure: 1) consider that all components fail simultaneously or 2) consider that only the component that exceeds its allowable value the most fails. The second analysis method is used herein. With these guidelines set forth, the static failure sequence was established.

Component failure was modeled by removing the connection, thus separating the components. Details on the method for removing the connections can be found in Ref. 1. Typical main attachment fitting force values are shown in Table 4 for the case with failed right rear lug, left rear shear yoke and right center lug. Values for components exhibiting failure are highlighted. In this case, the next component that indicated failure was the right center shear yoke. Therefore, using the Airbus allowable values and method described, and considering only main attachment fitting failures, the predicted AA587 VTP main attachment fitting failure sequence based upon linear static finite element analyses is shown in Fig. 25. The numbers indicate the failure sequence, which is:

- 1) Right Rear Lug
- 2) Left Rear Shear Yoke
- 3) Right Center Lug
- 4) Right Center Shear Yoke
- 5) Left Center Shear Yoke
- 6) Right Front Lug
- 7) All Remaining Attachment Fittings

Note that the sequencing is carried out while maintaining the load level as constant, which may not be a physically meaningful response. However, assumptions made during the static sequencing will only affect the sequence of subsequent failures after initial failure of the right rear lug. Additionally, notice that the static failure sequence does

Table 4: Linear analysis lug/yoke forces, failed right center lug, left rear yoke and right rear lug.

	Main Fittings (Lugs)					
	Front		Center		Rear	
	LHS	RHS	LHS	RHS	LHS	RHS
F_x (N)	925041	-1373929	395967	0	114974	0
F_y (N)	113761	92983	303899	0	502796	0
F_z (N)	1468629	-1772700	761736	0	-342070	0
F_{xz} (N)	1735676	2242799	858505	0	360875	0
F_{res} (N)	1739400	2244725	910706	0	618898	0
M_x (N*m)	-15808	-13420	-49358	0	-55849	0
M_z (N*m)	-438	232	9011	0	15559	0

	Shear Fittings (Yokes)					
	Front		Center		Rear	
	LHS	RHS	LHS	RHS	LHS	RHS
F_x (N)	-2646	5019	-5892	-42264	0	-25802
F_y (N)	35624	67561	80553	-577832	0	-211988
F_z (N)	-3013	5714	-8976	-64387	0	-39369
F_{res} (N)	35848	67988	81265	582942	0	217151

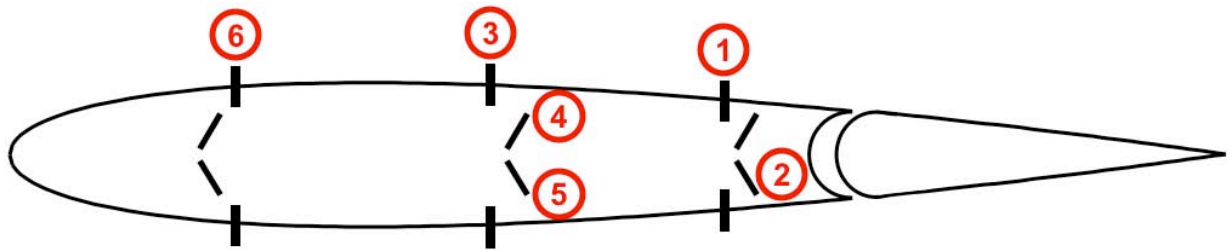


Figure 25: Static failure sequence.

not include any failures in the rudder. In fact, the rudder strains and hinge line loads remain nearly constant during the static failure sequence analysis.

B. Transient

Dynamic analysis was considered because including inertial effects potentially causes higher loads to develop in the VTP. Several types of dynamic analyses can be conducted in NASTRAN including normal modes, frequency response and transient. Of particular interest for the AA587 VTP is the time-dependent response of the VTP as various components fail, which can be simulated using transient analysis. The procedure for conducting the geometrically linear transient analyses is outlined below, results from the transient analysis are presented, and the transient failure sequence is summarized.

In general, the procedure begins with a static analysis, then failures are introduced through a transient analysis where the connection forces that occur are replaced by a time-dependent loading history that simulates the release of the connection. A load history is developed for each failure that is assumed to occur, and the process begins from the static analysis each time a new failure is identified. Each load history is defined using a separate load set so that the failure can be introduced sequentially at the proper time. The analysis was carried out until the first possible rudder failure was identified. Additional details for the transient analysis procedure can be found in Ref. 1.

The transient failure analysis was carried out at the Max C load condition, and as with the static failure sequencing, this load condition is held constant throughout the transient analysis. Allowables were examined as a function of time and successive failures were determined. Figure 26 shows a typical main attachment fitting force-time history plot, in this case for the left rear yoke, which was identified as the second failure in the sequence, i.e., the first failure after the right rear lug. Figure 27 shows a typical rudder skin strain plot after multiple failures have

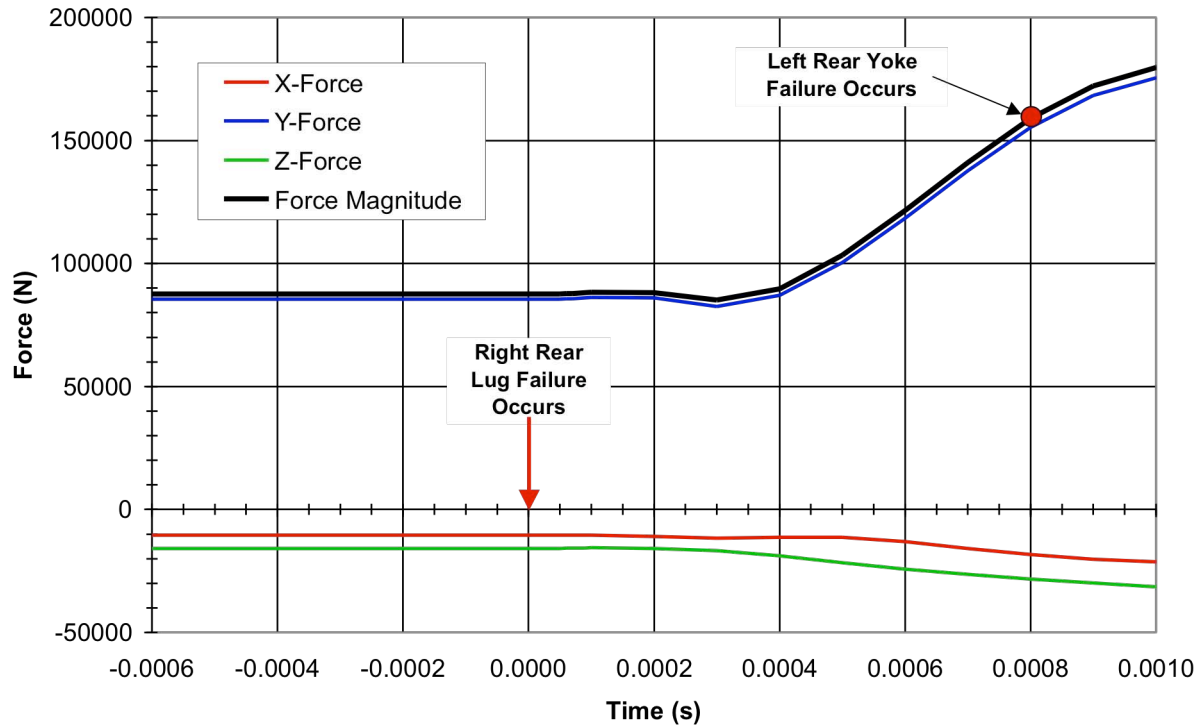


Figure 26: Left rear yoke forces.

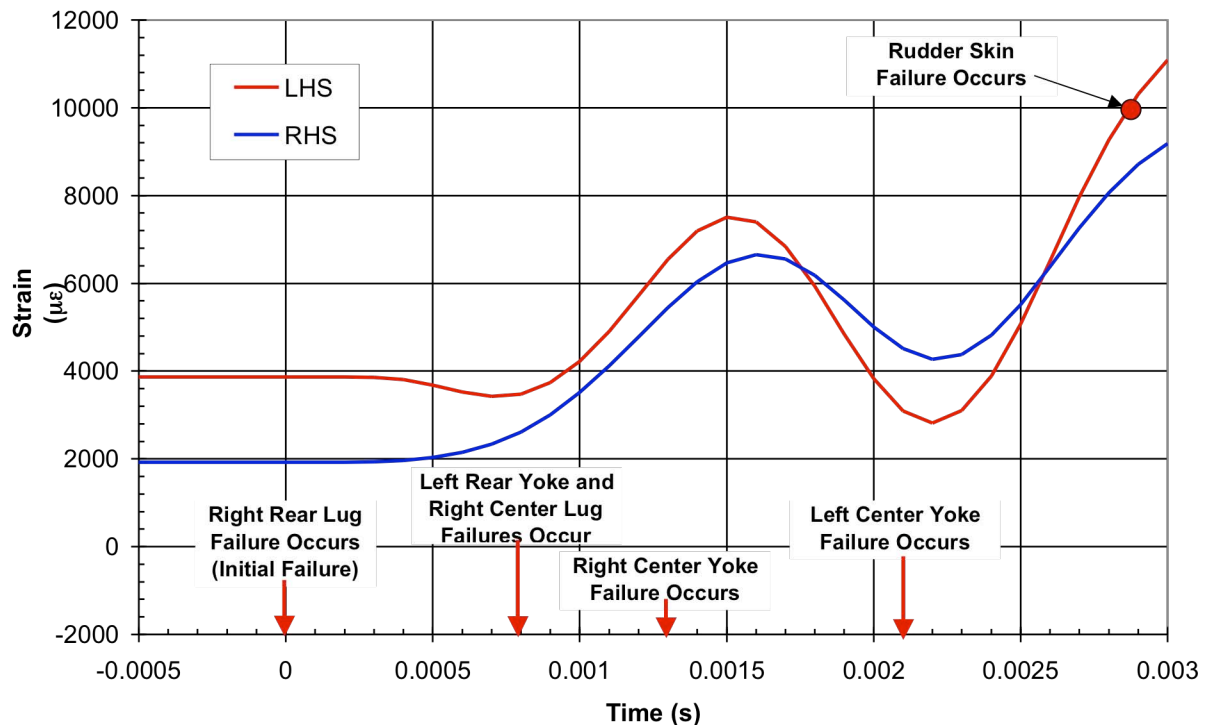


Figure 27: Inner surface rudder skin strains, ϵ_{xx} , in region of hinge fitting #1.

occurred. Various types of failure, such as main fitting failure, fin or rudder skin failure, rudder fitting failure, bolted connection failure, etc., were examined, and the transient failure sequence was established.

The possible failure sequence determined using the transient analyses is identical to the static sequence through the fifth failure as shown in Fig. 28. However, the transient analysis suggests that the sixth failure is a possible first rudder failure in the form of skin failure in the region of hinge fitting #1 (recall Fig. 27). The transient analyses also

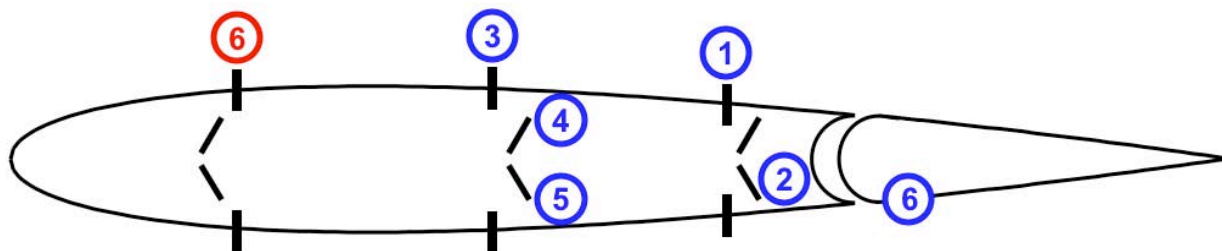


Figure 28: Transient failure sequence (red number indicates static sequence).

showed that there were many locations in the rudder that exhibited significant load variation due to dynamic effects, contrary to what was seen in the sequential static analyses in which the rudder and rudder hinge line forces remained nearly constant. The significant changes to the rudder response observed in the transient analyses, in conjunction with the physical evidence of the rudder damage, suggests that dynamic effects were present and contributed to the observed damage. Based upon the transient analyses conducted, skin failure at the rudder hinge fitting #1 region may have been the first rudder failure that leads to the remaining rudder failures. Additionally, it was seen that dynamic effects can significantly increase the rudder attachment fitting/hinge arm/actuator forces at numerous other fittings. Therefore, a reasonable possibility exists that the dynamic effects, post first failure at the right rear lug, could cause subsequent failure in the rudder, and thus explain the presence of the observed rudder damage. However, accurate determination of the first rudder failure would likely require higher-fidelity modeling and analysis

VII. Summary and Conclusions

NASA LaRC supported the NTSB in the AA587 accident investigation due to LaRC's expertise in structural analysis and testing of composite structures and materials. As part of this support, a Global Analysis Team was formed to address several aspects of the investigation. The Global Analysis Team reviewed the manufacturer's design and certification procedures, developed finite element models and conducted structural analyses, and participated jointly with the NTSB and Airbus in subcomponent tests conducted at Airbus in Hamburg, Germany.

The findings of the NASA AA587 Global Analysis Team indicate that the most-likely failure scenario was failure initiation at the right rear main attachment fitting, followed by an unstable progression of failure of all fin-to-fuselage attachments and separation of the VTP from the aircraft. The outcome of all analysis results indicates that failure initiates at the final observed maximum fin loading condition in the accident, when the VTP was subjected to loads that were at minimum 1.92 times the design limit load condition for certification. For certification, the VTP is only required to support loads of 1.5 times design limit load without catastrophic failure. The maximum loading during the accident was shown to significantly exceed the certification requirement. Thus, the structure appeared to perform in a manner consistent with its design and certification, and failure is attributed to VTP loads greater than expected.

Acknowledgement

The NASA Global Analysis Team would like to acknowledge the leadership and guidance provided by Dr. James H. Starnes, Jr. Dr. Starnes was our friend and colleague who led the NASA Langley AA587 investigation team and passed away before the completion of the investigation. We dedicate this paper to his memory.

References

- ¹Young, R. D., Lovejoy, A. E., Hilburger, M. W., and Moore, D. F., "NASA Structural Analysis Report for the American Airlines Flight 587 Accident Investigation: Part 2 – Global Fin/Rudder Structural Analysis and Assessment", NASA/TM 2005-213744 (in preparation).
- ²MSC.NASTRAN 2001 Reference Manual, 2002.
- ³Materials Specialists' Submission - Selected Photographs and Drawings of the Damage Areas on the Vertical Stabilizer and Rudder, Docket No. SA-522, Exhibit No. 15-A.
- ⁴Structures Group Chairman's Factual Report DCA02MA001.
- ⁵Raju, I. S., Davila, C. G., Glaessgen, E. H., Krishnamurthy, T., and Mason, B. H., "NASA Structural Analysis Report for the American Airlines Flight 587 Accident Investigation: Part 3 – Local Analysis of the Right Rear Lug", NASA/TM 2005-213745 (in preparation).
- ⁶MSC.PATRAN 2001 Reference Manual, 2001.
- ⁷Rankin, C. C., Brogan, F. A., Loden, W. A., and Cabiness, H. D., Stags User Manual, Version 5.0, March 2003.

This page left blank intentionally.

NASA Structural Analysis Report on the American Airlines Flight 587 Accident— Local Analysis of the Right Rear Lug

I. S. Raju^{*}, E. H. Glaessgen[†], B. H. Mason[†], T. Krishnamurthy[†], and C. G. Dávila[†]
NASA Langley Research Center, Hampton, Virginia, 23681

A detailed finite element analysis of the right rear lug of the American Airlines Flight 587 - Airbus A300-600R was performed as part of the National Transportation Safety Board's failure investigation of the accident that occurred on November 12, 2001. The loads experienced by the right rear lug are evaluated using global models of the vertical tail, local models near the right rear lug, and a global-local analysis procedure. The right rear lug was analyzed using two modeling approaches. In the first approach, solid-shell type modeling is used, and in the second approach, layered-shell type modeling is used. The solid-shell and the layered-shell modeling approaches were used in progressive failure analyses (PFA) to determine the load, mode, and location of failure in the right rear lug under loading representative of an Airbus certification test conducted in 1985 (the 1985-certification test). Both analyses were in excellent agreement with each other on the predicted failure loads, failure mode, and location of failure. The solid-shell type modeling was then used to analyze both a subcomponent test conducted by Airbus in 2003 (the 2003-subcomponent test) and the accident condition. Excellent agreement was observed between the analyses and the observed failures in both cases. From the analyses conducted and presented in this paper, the following conclusions were drawn. The moment, M_x (moment about the fuselage longitudinal axis), has significant effect on the failure load of the lugs. Higher absolute values of M_x give lower failure loads. The predicted load, mode, and location of the failure of the 1985-certification test, 2003-subcomponent test, and the accident condition are in very good agreement. This agreement suggests that the 1985-certification and 2003-subcomponent tests represent the accident condition accurately. The failure mode of the right rear lug for the 1985-certification test, 2003-subcomponent test, and the accident load case is identified as a cleavage-type failure. For the accident case, the predicted failure load for the right rear lug from the PFA is greater than 1.98 times the limit load of the lugs.

I. □ Introduction

ON November 12, 2001, American Airlines Flight 587 (AA 587) crashed shortly after take-off killing all 260 people on board and 5 on the ground. The composite vertical tail of the aircraft separated from the fuselage resulting in loss of control and ultimately the loss of the aircraft.

Several teams at the NASA Langley Research Center were assembled to help the National Transportation Safety Board with this investigation. The internal NASA team was divided into several discipline teams including a structural analysis team that consisted of a global analysis team and a detailed lug analysis team. The global analysis team considered global deformations, load transfer, and failure modes within the composite vertical tail as well as failure of the composite rudder. The detailed lug analysis team focused on failure of the laminated composite lugs that attach the tail to the aluminum fuselage. This paper describes the analyses conducted by the detailed lug analysis team.

^{*} Structures Discipline Expert, NASA Engineering and Safety Center, MS 155, AIAA Fellow.

[†] Aerospace Engineer, Computational Structures and Materials Branch, MS 155, AIAA Senior Member.

First, an overview of the problem, including the vertical tail plane (VTP) structure, is presented. Second, the various models developed for the right rear lug are described. Third, details of the material modeling, contact modeling, and progressive failure analysis (PFA) for solid-shell type modeling are presented. Fourth, a brief discussion of an alternative modeling approach, layered-shell modeling, is presented. Fifth, the global-local connection processes used to virtually embed the local lug model within a global model of the VTP are described. Sixth, the results of the analyses are presented. Finally, the results and lessons learned are discussed.

II. Description of the Problem

The vertical tail plane (VTP) of an Airbus A300-600R is connected to the fuselage with 6 lugs (3 on the right-hand side and 3 on the left-hand side) through a pin and clevis connection (see Figures 1a to 1d). Six yokes (not shown in figures) also connect the VTP to the fuselage and take some of the lateral loads. The air loads on the VTP during the 12 seconds before the VTP separated from the fuselage were evaluated and were supplied to the NASA structures teams by the National Transportation Safety Board (NTSB) and Airbus. The air loads were derived from digital flight data recorder (DFDR) data obtained after the accident.

The NASA global analysis team and the Airbus team evaluated the loads on each of the lugs and determined that the right rear lug (see Figure 1d) carried the largest loads compared to the design allowable. The lug analysis team, therefore, focused on the detailed analysis of the right rear lug. The objectives of the lug analysis team were to predict the failure load, mode, and location in the right rear lug for the loading conditions that the right rear lug experienced during the accident.

The lug analysis team considered the right rear lug region shown in Figure 1d. The lug is a continuation of the skin of the vertical tail with two pre-cured fitting halves cured to either side of the skin in the vicinity of the lug hole (the fitting extends to rib 4, as shown in Figure 1d). The region modeled consists of the right rear lug, rib 1, the rear spar, and 6 stringers from rib 1 to rib 5. Two different modeling approaches were used. The first modeling approach involved the development of a finite element (FE) model of the region shown in Figure 1d using three-dimensional (3D) elements in the region of the two pre-cured fitting halves of the lug and shell elements for the rest of the model and is termed the solid-shell model. The second modeling approach involved the development of an

FE model of the region shown in Figure 1d using shell elements throughout and is termed the layered-shell model. In the layered-shell model, the 3D region of the first approach is modeled as shell layers that are connected by decohesion elements representing multi-point constraints. The results obtained by these approaches were validated by comparison with reference solutions for simplified configurations. The two approaches were also verified by comparing the finite element results with Airbus experimental results.

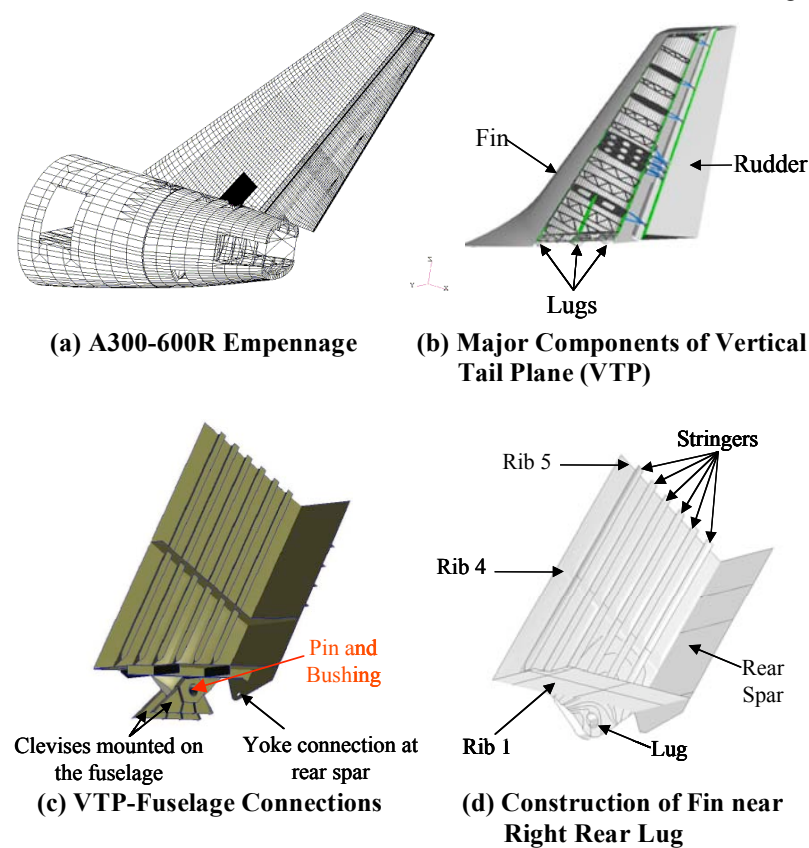


Figure 1. Vertical Tail Plane Mounted on the Fuselage.

III. Modeling

The coarse 3D model (part of the solid-shell series of models) and layered-shell model were developed by modifying an Airbus-developed model of the same region. The damage modeling applied to each modeling approach was developed independently, which provided a degree of independent verification of the results from both methods. During the course of the investigation, two other solid-shell models were also

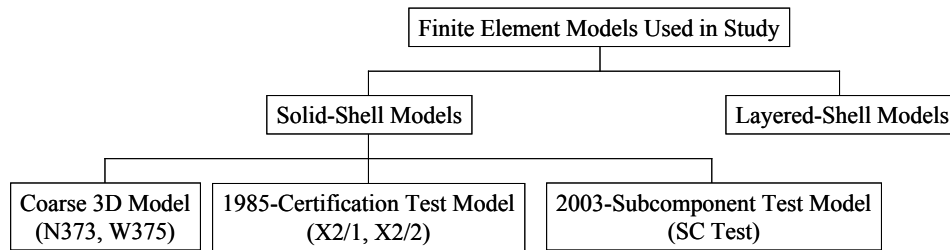


Figure 2. Various Finite Element Models Used.

developed. These models are the 1985-certification test model and the 2003-subcomponent (SC) test model. Figure 2 presents a summary of all the models used in the analyses – N373 and W375 denote different

loading conditions; X2/1 and X2/2 represent two different specimens that were tested as part of an Airbus certification test conducted in 1985 (the 1985-certification test).

In the NASA-developed models, the clevises and the elastic pin with the bushing were not modeled. Rather, the pin is represented as a rigid analytical cylinder with a diameter equal to the diameter of the lug hole. This analytical cylinder is rigidly connected to an FE node at the location of the center of the pin. In the models, the pin is loaded by applying displacements or tractions to this single node. The pin loads are assumed to be reacted in the contact region between the lug hole and the pin.

The solid-shell and layered-shell analyses were performed using the commercial finite element code, ABAQUS [ABAQUS, 2000]. The code was chosen because it allows the user to implement specialized elements and material constitutive relationships while taking advantage of the features of a general-purpose code.

The progressive failure algorithms used to predict failure within the solid-shell and layered-shell models were defined as user defined material (UMAT) and user field (USFLD) algorithms, respectively. In the implementation of the UMAT and USFLD routines, material properties are degraded to small but nonzero values either in a single step or in several steps in each damaged element. To maintain stability of the system of equations, the values cannot be degraded to zero-values. Further, although some specialized codes allow failed elements to be removed from a model (element extinction), this capability is not available in ABAQUS. In the present implementation, the small stiffness contributions that remain in the degraded elements after failure allow a very small amount of load transfer across the damaged region. Therefore, in the present implementation of failure, complete separation of the lug is not possible.

A. Coarse 3D Model

A coarse 3D model (part of the solid-shell series of models) of the lug was developed using thickness contours extracted from the reference Airbus model. The coarse 3D model, shown in Figure 3a, has 25931 nodes and 21519 elements. The axial (x -) coordinate is along the fuselage axis and is directed toward the rear of the airplane. The y -axis is parallel to the axis of the pin in the lug hole, and the z -axis is normal to the x - and y -axes. The lug fittings and skin are modeled with up to 14 layers of solid (8-node hexahedral) elements with 10 layers of elements in the vicinity of the hole. The thickness of each of the layers of solid elements was adjusted in order to match the volume of the lug fittings in the Airbus model. All other regions of the model were converted to shell elements. Multi-point constraint (MPC) equations were used at the solid-to-shell transition locations to ensure compatible translations and rotations along the interface.

B. Layered Shell Model

A layered-shell model of the lug was constructed using the same thickness contours as the coarse 3D model. The pin assembly was modeled as a rigid surface with a diameter equal to that of the lug hole. Frictionless contact equations were prescribed between the edge of the layered-shell elements around the bolt hole and the rigid surface. A discussion of the approximations caused by using a rigid frictionless pin can be found in Camanho and Matthews [Camanho and Matthews, 1999]. The lug fittings were modeled with 14 layers of shell elements, which were connected with 3D decohesion elements [Dávila *et al.*, 2001a]. All other regions of the model were modeled with a single layer of shell elements. In addition, the model is used for progressive failure analyses in which the matrix and fiber damage is simulated by degrading the material properties. The analyses used for modeling the progressive delamination and intra-ply damage were developed within ABAQUS with user defined element (UEL) and USFLD user-written subroutines, respectively. This model, shown in Figure 3b, has 20886 nodes with 34524 elements.

The ability of the coarse 3D and layered-shell models to predict the same displacements as the original Airbus model was verified. Both the magnitude and spatial distributions of the displacement components predicted by the two NASA models were in very close agreement with those predicted by the Airbus model.

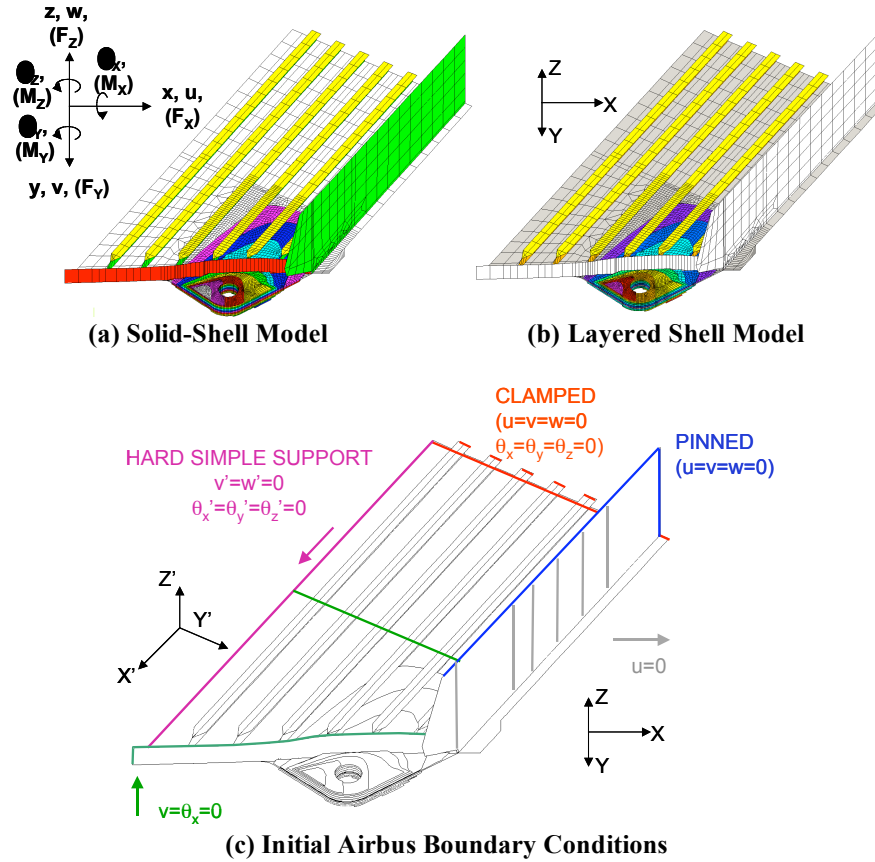


Figure 3. Finite Element Models of Right Rear Lug (colors are for visualization purposes only).

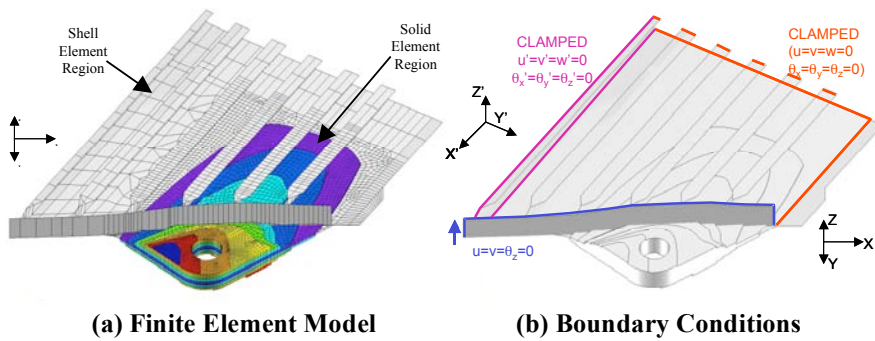


Figure 4. 1985-Certification Test Model of X2/2 Specimen (colors are for visualization purposes only).

C. 1985-Certification Test Model

Two test specimens (called X2/2 and X2/1) were tested by Airbus in 1985. One FE model was used to represent both test specimens. To simulate the configurations of the X2/2 and X2/1 test specimens, an FE model was created from the coarse 3D model by deleting all the elements above rib 4 and forward of stringer 6 as shown in Figure 4a. This model had 23216 nodes and 19149 elements. The boundary conditions used with this model are shown in Figure 4b.

D. 2003-Subcomponent Test Model

As part of the investigation, a subcomponent test was conducted during 2003 on a *left rear* lug made of the same material as the accident aircraft. A left rear lug was used because this was the only rear lug (with the same material as the accident aircraft) that was available at the time of the test. Airbus modeled this left rear lug (see Figure 5a) including the support structure and supplied the model to the lug analysis team. This Airbus model then became part of the solid-shell series of models. The boundary conditions for this model are shown in Figure 5b. When this model is used to represent the *right rear lug*, the loads and boundary conditions are mirrored about the global xz -plane; i.e. the sign of F_Y , M_X , M_Z , v , θ_X , and θ_Z are reversed.

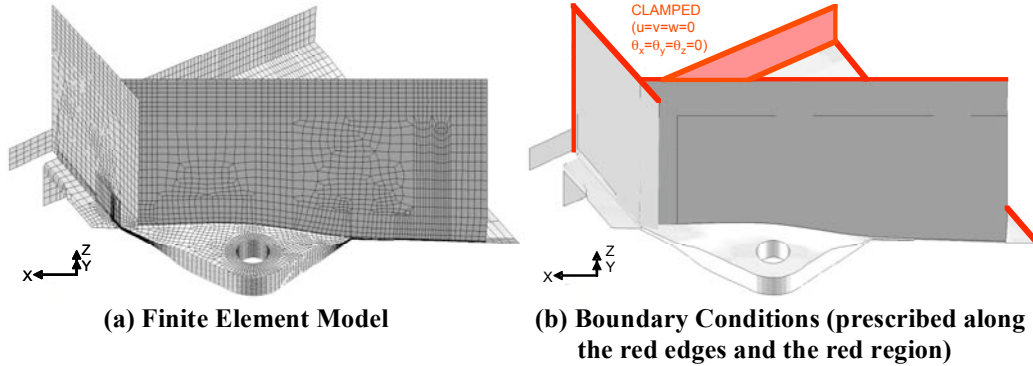


Figure 5. 2003- Subcomponent Test Model.

IV. □ Solid Element Models

A. Material Modeling

The right rear lug consists of two pre-cured fitting-halves, the vertical tail plane (VTP) skin and several compensation layers. The inner fitting-half, skin, and outer fitting-half are made from T300/913C in the form of $\pm 45^\circ$ fabric, $90^\circ/0^\circ$ fabric, and 0° tape and are approximately 55 mm thick in the vicinity of the pin.

Table 1 shows the elastic, strength, and toughness parameters for T300/913C from the recent World Wide Failure Exercise (WWFE, Soden and Hinton, 1998a and Soden and Hinton, 1998b). The subscripts 1, 2, and 3 denote the fiber direction, in-plane transverse direction, and out-of-plane direction, respectively, and the subscript “c” denotes a compressive property. Also, X_T , X_C , Y_T , and Y_C denote the fiber-direction tensile strength, fiber-direction compressive strength, transverse-direction tensile strength, and transverse-direction compressive strength, respectively. Finally, G_{IC} is the mode-I interlaminar fracture toughness.

1. Homogenization of Material Properties

The right rear lug contains numerous plies of T300/913C in the form of tape and fabric. Although a finite element model that explicitly modeled each of the plies and each of the numerous curvilinear ply drops within the lug could be developed, doing so would have required a finite element model with millions of elements. Such a detailed finite element model would be too cumbersome to use in progressive failure analyses. To maintain a reasonable number of elements and yet accurately account for failures in each of the plies, a two-level procedure is followed. In the first level, within each finite element, the material properties of the plies are homogenized. In the second level, within the progressive failure analysis, the stress and failure state of each ply is evaluated. The details of this procedure are described below.

Table 1. Material Properties for T300/913C Tape.

Property	WWFE [Hinton and Soden 1998]
E_1 (GPa)	138
E_{1C} (GPa)	--
E_2 (GPa)	11
E_{2C} (GPa)	--
ν_{12}	0.28
ν_{23}	0.4
μ_{12} (GPa)	5.5
X_T (MPa)	1500
X_C (MPa)	900
Y_T (MPa)	27
Y_C (MPa)	200
S_{xy} (MPa)	80
G_{IC} (KJ/m ²)	220

Elements of classical lamination theory (CLT) were used to construct and deconstruct the homogenized material properties and to evaluate ply-level values in a manner that is suitable for the PFA, but its use for this problem requires several assumptions:

- 1) Nominal percentages and uniform spatial distribution of 0° , $\pm 45^\circ$, and $90^\circ/0^\circ$ plies at every quadrature point in each element of the model
- 2) No non-zero coupling (i.e., the 16, 26, and B -matrix) terms after ply failure
- 3) Bending deformations that are inherent in the CLT are not explicitly modeled. Rather, the deformations are modeled using solid elements
- 4) Independent material properties at each quadrature point in the element that can be degraded independently
- 5) Woven fabric can be treated as 2 plies of tape

Ply of each of the orientations are distributed nearly uniformly throughout the lug adding credibility to the assumption of a uniform spatial distribution of plies. Additionally, the large number of plies in the lug tends to reduce the effect of the coupling terms. The assumption of piecewise constant bending is reasonable given the number of integration points through the thickness of the lug and the relatively low bending gradient. The assumption of independence of properties at each quadrature point has been explored extensively for PFA analyses [Averill, 1992].

Prediction of failure within textile-based composite materials has been a topic of considerable attention for two decades [Poe and Harris, 1995; Glaessgen *et al.*, 1996]. However, there is no accurate method for predicting the micromechanical details of damage progression in textile-based composites that has the computational efficiency needed to predict failure in structural models of the size used in this accident investigation. This deficiency in the state-of-the-art led to the approximation of the 8-harness satin weave material as plies of “equivalent” tape as shown in Figure 6. Hashin’s failure criteria was used to predict failure of the equivalent tape.

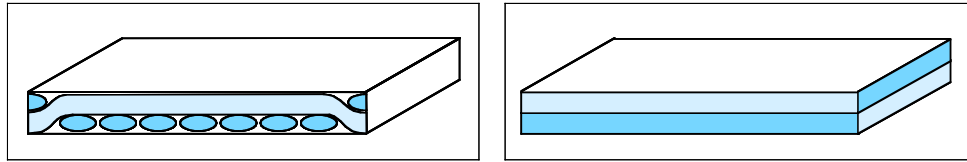


Figure 6. Eight-Harness Satin Weave and Tape Approximation.

V. □ Contact

Although most of the load transfer between the pin and lug is normal to the interface (initially, the global xz -plane), only friction prevents the pin from sliding (rigidly translating) in the global y -direction. Because of the proximity of the location of the material failures to the location of the pin-lug interface, considerable effort was taken to accurately model the details of the load transfer between the pin and lug.

Although the ABAQUS code correctly models the normal contact between the pin and lug, the modeling of friction along the pin-lug contact region was not straightforward. The lug analysis team did not have access to friction data about the lug, so the following approach was developed. A multi-point constraint (MPC) equation was generated to prevent sliding of the pin. In the MPC equation, the displacement of the pin in the global y -direction (v_p) is set equal to the average of the global y -displacements of all of the nodes in the two rings on the lug hole (v_l and v_o for average displacements of the inner and outer rings, respectively) shown in Figure 7. This MPC equation, referred to as Y-MPC #1, was used for all analyses prior to the 2003-subcomponent test. Differences were found between the global-local moments computed by NASA using Y-MPC #1 and the moments computed by Airbus using their global-local analysis process. The NASA lug team re-evaluated the MPC equation and concluded that it was not accurately simulating the global y -force

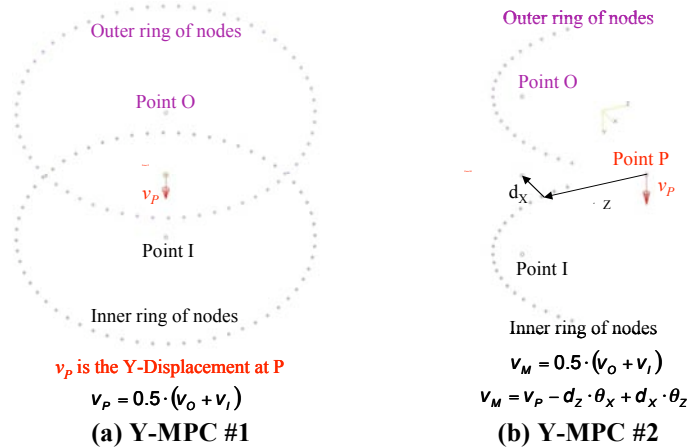


Figure 7. Multi-Point Constraint Formulation.

reacted by the pin because the y -force can only react on the contact surface, and Y-MPC #1 effectively treated the y -force as reacting around 360° of the hole. In order to improve the simulation, another MPC equation, Y-MPC #2, was developed.

For equation Y-MPC #2, two 120° arcs ($\pm 60^\circ$ relative to the load vector) were used instead of the 360° rings, as shown in Figure 7b. The average displacement of these two arcs is represented by the displacement (v_M) at Point M. The displacement at Point M is related to the pin displacement (v_P) by an equation that includes the global x - and z -rotations of the pin, as shown in Figure 7b. All lug results generated before the 2003-subcomponent test used Y-MPC #1; all later analyses used Y-MPC #2.

A. Progressive Failure Analysis (PFA)

1. Background to Failure Theories

Strength-based approaches for the prediction of initial and progressive failure in polymeric matrix composites are founded on a continuum representation of ply-level failure mechanisms. The comparative simplicity of applying strength-based criteria for the prediction of failure events within common analysis frameworks such as finite element procedures has led to this approach becoming increasingly accepted as a method for predicting the onset and development of material failure in composite structures.

Active research is directed towards representing micromechanical-level damage mechanisms in macroscopic, continuum-based failure criteria. These investigations have commonly elicited controversial discussions regarding the theoretical validity of developed failure criteria [Soden and Hinton, 1998a and b]. At issue is the difficulty of simulating the complexity of underlying failure mechanisms in terms of a discrete set of fixed strength parameters and the validity of using these parameters determined for individual lamina in the elastically constrained environment of an assembled laminate. The need to develop computationally efficient methodology to avoid detailed micromechanical analyses is aptly expressed by a passage by Hashin [Hashin, 1980]: “The microstructural aspects of failure are of such complexity that there is little hope of resolution of this problem on the basis of micromechanics methods. Such methods would require analytical detection of successive microfailures in terms of microstress analysis and microfailure criteria and prediction of the coalescence of some of them to form macrofailures which is an intractable task.”

A large number of continuum-based criteria have been derived to relate internal stresses and experimental measures of material strength to the onset of failure [Rowlands, 1984; Nahas, 1986]. However, the use of any of these criteria for predicting failure beyond initiation may become theoretically invalid due to the underlying physics of interacting failure mechanisms that are implicitly neglected in the experimental determination of critical strength parameters.

2. Failure Theory Used in the PFA

In the analysis of the right rear composite lug, the Hashin criterion [Hashin, 1980] was chosen. Hashin's criterion assumes that the stress components associated with the plane of fracture control the failure. This consideration leads to the following equations expressing fiber and matrix failure written for general three-dimensional states of stress.

Tensile fiber mode

$$\left(\frac{\sigma_{11}}{X_T}\right)^2 + \frac{1}{S_{xy}^2}(\sigma_{12}^2 + \sigma_{13}^2) = 1 \quad (1)$$

or

$$\sigma_{11} = X_T \quad (2)$$

Compressive fiber mode

$$|\sigma_{11}| = X_C \quad (3)$$

Tensile matrix mode ($\sigma_{22} + \sigma_{33} > 0$)

$$\frac{1}{Y_T^2}(\sigma_{22} + \sigma_{33})^2 + \frac{1}{\tau_T^2}(\sigma_{23}^2 - \sigma_{22}\sigma_{33}) + \frac{1}{S_{xy}^2}(\sigma_{12}^2 + \sigma_{13}^2) \geq 1 \quad (4)$$

Compressive matrix mode ($\sigma_{22} + \sigma_{33}) < 0$

$$\frac{1}{Y_c} \left[\left(\frac{Y_c}{2\tau_T} \right)^2 - 1 \right] (\sigma_{22} + \sigma_{33}) + \frac{1}{4\tau_T^2} (\sigma_{22} + \sigma_{33})^2 + \frac{1}{\tau_T^2} (\sigma_{23}^2 - \sigma_{22}\sigma_{33}) + \frac{1}{S_{xy}^2} (\sigma_{12}^2 + \sigma_{13}^2) \geq 1 \quad (5)$$

In equations 1 to 5, the strength values (X_T , X_C , Y_T , Y_C , and S_{xy}) are defined in Table 1. Note that both the normal stress in the fiber-direction, σ_{11} , and the shear stress components parallel to the fiber direction, σ_{12} and σ_{13} , are considered in equation 1. In equations 1-5, τ_T is the transverse shear strength corresponding to the σ_{23} stress component, while S_{xy} is the shear strength corresponding to the σ_{13} and σ_{12} components.

3. Internal State Variable Approach

Once failures are detected at a quadrature point, the material properties are degraded using an internal state variable approach. This approach degrades the properties from their original values to very small but non-zero values in a pre-determined sequence over several load steps. Material properties are degraded according to the particular active failure mode as determined by the Hashin criterion. For example, a compressive matrix mode failure requires that the matrix-dependent properties be degraded, but that the fiber-dependent properties, e.g. E_{11} , remain unchanged. In these analyses, the strength values presented in Table 1 are used.

4. Progressive Failure Analysis Algorithm

Figure 8 shows the algorithm that is implemented as a user defined material (UMAT) subroutine within ABAQUS. Note that this algorithm consists of a preprocessing phase in which ply-level stresses are computed, an evaluation phase in which failures are determined, a material degradation phase in which ply level properties are degraded, and a post-processing phase in which updated laminate properties are computed. This algorithm is called for every quadrature point of every hexahedral element within the model, and updated material properties are evaluated at the quadrature points when the ply failure criteria are satisfied.

There are two adjustable parameters in this algorithm: the degradation schedule and the load (or displacement) increment. Studies undertaken by the authors have shown that a degradation factor of 0.7 (instead of 1.0 or 100%) appears to be ideal for the stability of the algorithm. Rather than incrementing the loads, the current PFA increments

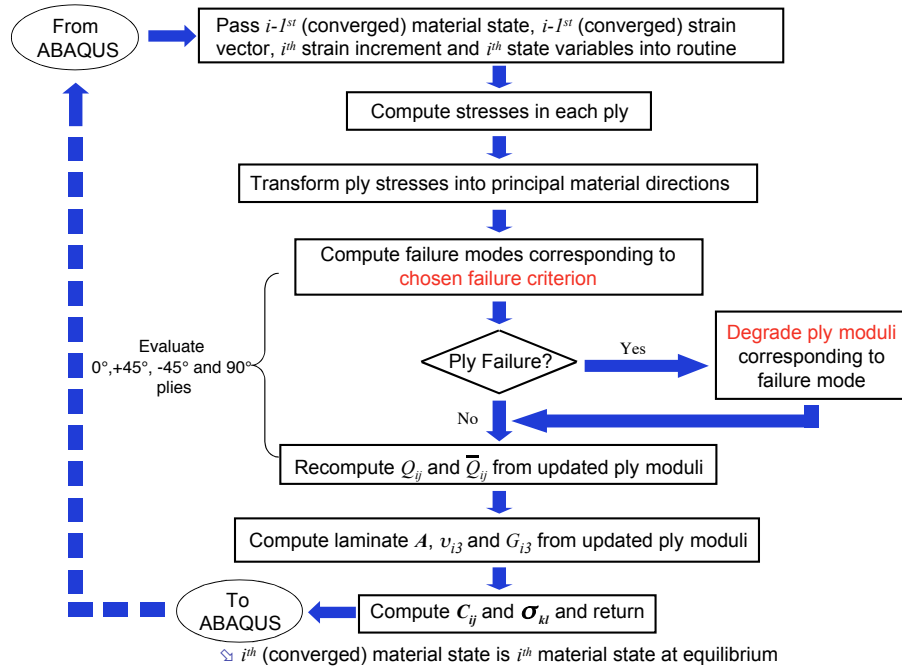


Figure 8. PFA Algorithm Used as a UMAT Subroutine in ABAQUS (Note: Stop is executed in ABAQUS and hence is not shown in this figure).

the displacements and hence simulates displacement-controlled tests. This approach simplifies the process of simulating unloading past the peak load as discussed in the following section.

5. "Load-Increment in the PFA"

Displacement control is used in the current implementation of the progressive failure analysis to ensure that both the loading and unloading are traced by the algorithm. A load control procedure will encounter convergence difficulties after damage occurs because the monotonically increasing load applied to the damaged structure will cause abrupt failure. In contrast, a displacement-controlled procedure has fewer convergence difficulties after damage initiates because the load can decrease as damage forms, and the material becomes more compliant.

In cases where the maximum linear load, P_{max} , carried by the specimen is known, the corresponding maximum linear displacement, d_{max} , is calculated from a linear analysis. If P_{max} is unknown, a projected value is assumed and the corresponding maximum linear displacement, d_{max} , is also calculated from a linear analysis. The displacements are incremented using the d_{max} as a guide and are termed here as load factor (d/d_{max}). A schematic of the load vs. load factor curve is shown in Figure 9. The solid line with symbols and dashed line represent a hypothetical PFA load-displacement curve and a linear load-displacement curve, respectively. Note that the load factor of unity will intersect the dashed line at P_{max} , the maximum linear load, and corresponds to the maximum linear displacement, d_{max} (i.e. at load factor equal to unity). Once damage is determined and the corresponding material properties are degraded, the actual load-displacement curve will begin to deviate from the linear curve. The load continues to increase monotonically until a peak value, the failure load, $P_{failure}$, is reached. Then, P decreases until a zero-value of load is reached or the analysis can no longer converge.

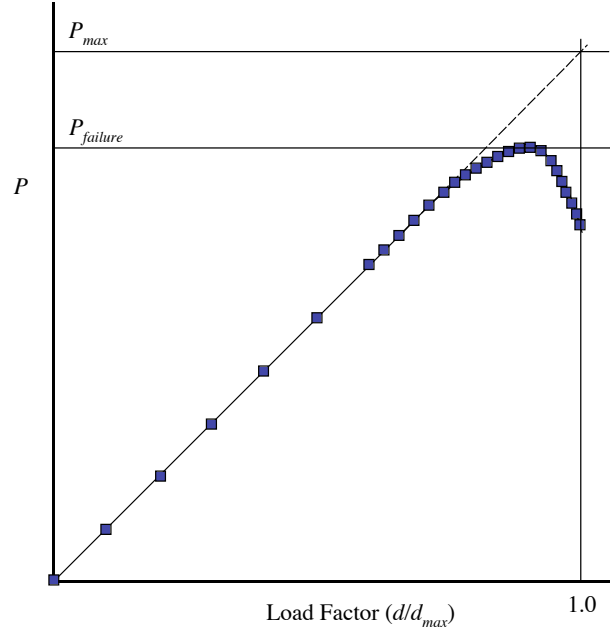


Figure 9. Schematic of Load vs. Load Factor Curve.

Note that in the PFA implementation, large displacement increments are chosen to start the algorithm, and shortly before damage initiates, the increment size is scaled down. As the damage accumulates, near the failure load, the increment size is scaled down further. The determination of the load factor increments is an art and requires the insight of an experienced analyst.

VI. □ Layered-Shell Model

In addition to the coarse 3D element analyses of the AA 587 right rear lug described in the previous section, an analysis based on a layered-shell model was developed. The layered-shell analyses were developed as an alternate means of predicting the failure of the lug. The term layered-shell signifies that the thickness of the lug is modeled by several layers of shell elements rather than a number of layers of solid elements. The layered-shell analyses lend themselves to the evaluation of delamination initiation or propagation through the addition of decohesion elements between the shell layers. The analysis was developed in ABAQUS, and UEL and USFLD user-written subroutines were used for modeling the progressive delamination and intra-ply damage, respectively.

As with the solid-shell models, the layered-shell model was developed by modifying the original Airbus model of the right rear lug. The original Airbus model used 3D solid elements in the lug region and solid and shell elements in the remainder of the model. To develop the ABAQUS model, the faces of the solid elements in the xz -plane were converted into quadrilateral shell elements, and then the solid elements were converted into decohesion elements. The layered-shell model had 21000 nodes involving approximately 130000 equations.

A. Material Modeling

1. Modeling Damage with Superimposed Shell Elements

The layered-shell models use a novel and computationally efficient element superposition technique that separates the failure modes for each ply orientation and does not rely on the computation of the $[A]$, $[B]$, and $[D]$ matrices [Dávila *et al.*, 2000]. The modeling is performed such that the elements in the region around the bolt hole,

where a potential for damage growth is anticipated, are constructed of four superposed layers of shell elements that share the same nodes. No centroidal offset is applied to any of the elements. Each layer of elements represents one ply orientation (0 or 45 or -45 or 90 degrees), and each element spans the entire thickness of the laminate as shown in Figure 10. It is implied that the plies for each orientation are uniformly distributed and can be smeared over the thickness of the laminate. The elements used in the analyses consist of the ABAQUS four-node reduced-integration shear deformable S4R element [ABAQUS, 2000].

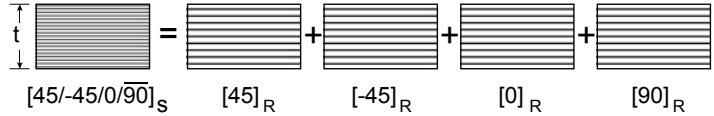


Figure 10. The Thick Laminate Modeled With Four Layers of Superposed Shell Elements.

To model the appropriate stiffnesses corresponding to a given damage state, reduced engineering properties are applied to each layer. A reduced material property for a given orientation is simply the product of the engineering property and the sum of the thicknesses of all the plies in that orientation divided by the total laminate thickness. Reduced material properties are denoted by the notation $[\]_R$, as illustrated in Figure 10. Bending effects are taken into account by the use of five integration points through-the-thickness of the laminate.

B. Progressive Failure Analysis for the Layered-Shell Model

A progressive damage model for notched laminates under tension was first proposed by Chang et al. [Chang and Chang, 1987] and accounts for all of the possible failure modes in each ply except delamination. Chang and Lessard [Chang and Lessard, 1991] later investigated the damage tolerance of composite materials subjected to compressive loads. The present analysis, which also deals with compression loads, is largely based on the work by Chang and Lessard. However, the present analysis extends Chang's method from two-dimensional membrane effects to a shell-based analysis that includes bending.

The failure criteria applied in the present analysis are those for unidirectional fiber composites as proposed by Hashin [Hashin and Rotem, 1973], with the elastic stiffness degradation models developed for compression by Chang and Lessard [Chang and Lessard, 1991]. Unidirectional failure criteria are used, and the stresses are computed in the principal directions for each ply orientation. The failure criteria included in the present analysis are summarized below. In each, failure occurs when the failure index exceeds unity.

- *Matrix failure* in tension and compression occurs due to a combination of transverse stress σ_{22} and shear stress σ_{12} . The failure index e_m can be defined in terms of these stresses and the strength parameters $Y_{T/C}$ and the shear allowable S_{xy} . The matrix allowable $Y_{T/C}$ takes the values of Y_T in tension and Y_C in compression. Failure occurs when the index exceeds unity. Assuming linear elastic response, the failure index has the form:

$$e_m = \sqrt{\left(\frac{\sigma_{22}}{Y_{T/C}}\right)^2 + \left(\frac{\sigma_{12}}{S_{xy}}\right)^2} \quad (6)$$

- *Fiber buckling/tension failure* occurs when the maximum compressive stress in the fiber direction exceeds the fiber tension or buckling strength $X_{T/C}$, independently of the other stress components. The failure index for this mechanism has the form:

$$e_b = \frac{|\sigma_{11}|}{X_{T/C}} \quad (7)$$

- *Fiber-matrix shearing failure* occurs due to a combination of fiber compression and matrix shearing. The failure index has the form:

$$e_f = \sqrt{\left(\frac{\sigma_{11}}{X_{T/C}}\right)^2 + \left(\frac{\sigma_{12}}{S_{xy}}\right)^2} \quad (8)$$

The finite element implementation of this failure analysis was developed in ABAQUS using the USFLD user-written subroutine. The program calls this routine at all material points of elements that have material properties

defined in terms of the field variables. The routine provides access points to a number of variables such as stresses, strains, material orientation, current load step, and material name, all of which can be used to compute the field variables. Stresses and strains are calculated at each incremental load step and evaluated by the failure criteria to determine the occurrence of failure and the mode of failure.

VII. □ Global-Local Analysis

A. Global-Local Connection Procedure

The aerodynamic loads on the vertical tail at failure (during the accident) were computed by Airbus and provided to NASA. This load case, referred to as W375, was directly applied only to the global model. The local region of the global NASTRAN (MSC/NASTRAN, 1997) model is shown in Figure 11a. Because the global model is a MSC/NASTRAN model and the local lug model (the coarse 3D model) is an ABAQUS model, it was not possible to embed the local model in the global model. Conversion of the NASTRAN model to ABAQUS was not feasible due to time constraints. Additionally, the version of NASTRAN used for the global model was not capable of modeling contact. The details of the global model and global analysis are discussed by Young *et al.* [Young *et al.*, 2005].

Along the interfaces between the global and local models, the continuity of the displacements and the reciprocity of tractions need to be satisfied. An iterative process was developed to ensure satisfaction of these requirements. This process is illustrated in Figure 12 and is implemented as follows:

- 1) Perform the global analysis using the global model and evaluate the displacements at all the nodes in the global model. Let $\{u_G\}$ represent the displacements of the global nodes along the global-local boundary and $\{u_L\}$ represent the displacements of the local nodes along the global-local boundary. Evaluate the tractions at the global nodes, $\{F_G\}$, from the elements that are entirely in the global region. That is, evaluate the tractions that do not include the elements that occupy the local region of the global model.
- 2) Establish a transformation matrix, $[T]$, between $\{u_G\}$ and $\{u_L\}$, and use this matrix to compute $\{u_L\}$ using

$$\{u_L\} = [T] \{u_G\} \quad (9)$$

- 3) Solve the local model with $\{u_L\}$ as prescribed displacements.
- 4) Because of the prescribed displacements, reactions at the interface nodes in the local model $\{R_L\}$ are produced.
- 5) Local reactions are mapped back to the global nodes using

$$\{R_G\} = [T]^T \{R_L\} \quad (10)$$

Equation 10 is obtained by requiring that the work done on the global-local boundaries in the local model $(\frac{1}{2}) \cdot (\{u_L\}^T \cdot \{R_L\})$ and the global model $(\frac{1}{2}) \cdot (\{u_G\}^T \cdot \{R_G\})$ are identical. The $\{R_G\}$ reactions represent the stiffness of the local model in the global model.

- 6) The global tractions $\{F_G\}$, in general, will not be identical to the reactions mapped from the local model, $\{R_G\}$, as the reciprocity of tractions is not imposed. Thus, a residual, $\{r\}$, is left on the global-local boundary:

$$\{r\} = \{F_G\} - \{R_G\} \quad (11)$$

- 7) Evaluate a norm $\|r\|$ for the residual $\{r\}$ using

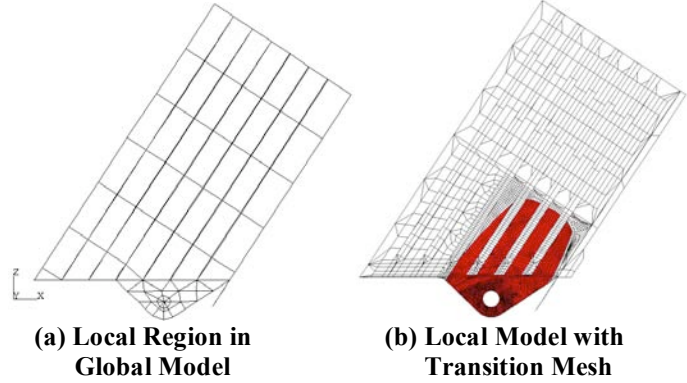


Figure 11. Models of Region Near Right Rear Lug.

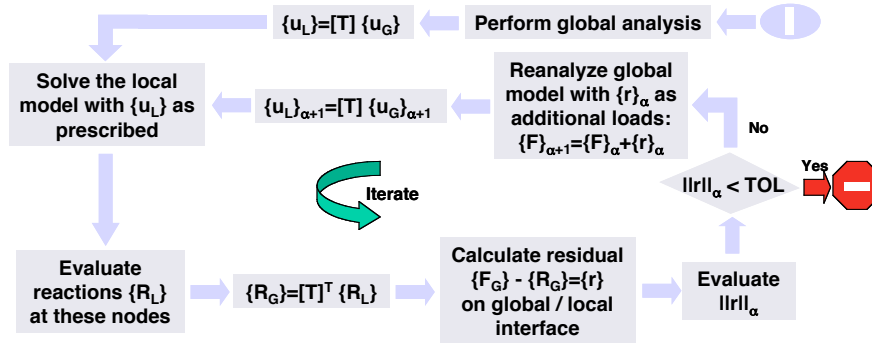


Figure 12. Global-Local Iterative Analysis Process.

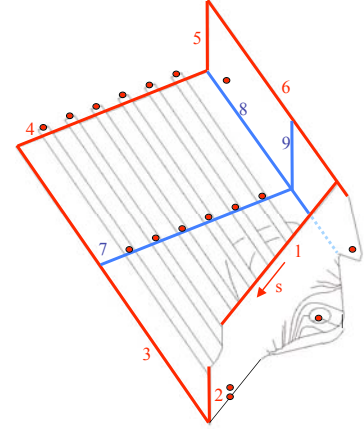


Figure 13. Interfaces Between the Global and Local Models.

$$\|r\|_{\alpha} = \frac{\sum_{Boundary} |(F_{G_i})_{\alpha} (u_{G_i})_{\alpha} - (u_{G_i})_{\alpha-1}|}{\sum_{Boundary} |(F_{G_i})_{Initial} (u_{G_i})_{Initial}|} \quad (12)$$

where α is the current iteration number in the convergence process and the Σ implies accumulation at all nodes on the global-local boundary.

- 8) If the normalized residual is less than a prescribed tolerance, then this procedure is stopped, and the system has converged. If the normalized residual is higher than the prescribed tolerance, then the residual vector is added as an initial load set in the global model and the global analysis is executed again (i.e. return to step 1).

The interfaces between the global and local model are defined on 9 edges (shown as red and blue lines in Figure 13) and at 17 discrete locations (shown as red dots in Figure 13). The coarse 3D model was modified so that the local edge nodes matched the global edge nodes exactly as shown in Figure 11b. Therefore, the mapping from the global and local models can be accomplished with a unit $[T]$ matrix.

To maintain symmetry of the global model, the stiffness of both the right rear and left rear lugs was updated by the global-local process. Thus, during the global-local process, two local analyses were performed during each iteration. Instead of creating another FEM, one local FEM was used for both the right rear and left rear lug. For the left rear lug, the loads and boundary conditions were mirrored about the global xz -plane (i.e. the sign of F_y , M_x , M_z , v , θ_x , and θ_z are reversed).

B. Global-Local Analysis and PFA

The global-local process described in the previous section assumes that the stiffness of the local model does not change in the iterative procedure. Similarly, the PFA assumes that the boundary conditions on the local model do not change as the PFA continues. The most rigorous analysis of the VTP requires that damage determined in the local model be returned to the global model. That is, at step 2 of the global-local process, the PFA needs to be performed to determine the current damage state of the lug. After convergence is obtained (and equilibrium is established), the global-local process is continued with step 3.

Such a rigorous procedure involving both the global model and the local model and with the current large degree of freedom model is impractical. Therefore, the global-local procedure is performed first to determine the boundary conditions on the global-local interfaces and the loads at the pin. With these boundary conditions and loading, the PFA is performed on the local model. The verification of this decoupling assumption is provided in the *Results* section.

Convergence of the forces and moments in the right rear lug for the W375 load case are plotted in Figures 14a and 14b, respectively. In these figures, the reactions are normalized by the average of the global and local results at the end of the sixth iteration. At the sixth iteration, the difference between the global and local forces is less than 1 kN, and the difference between the corresponding moments is approximately 0.03 kN-m.

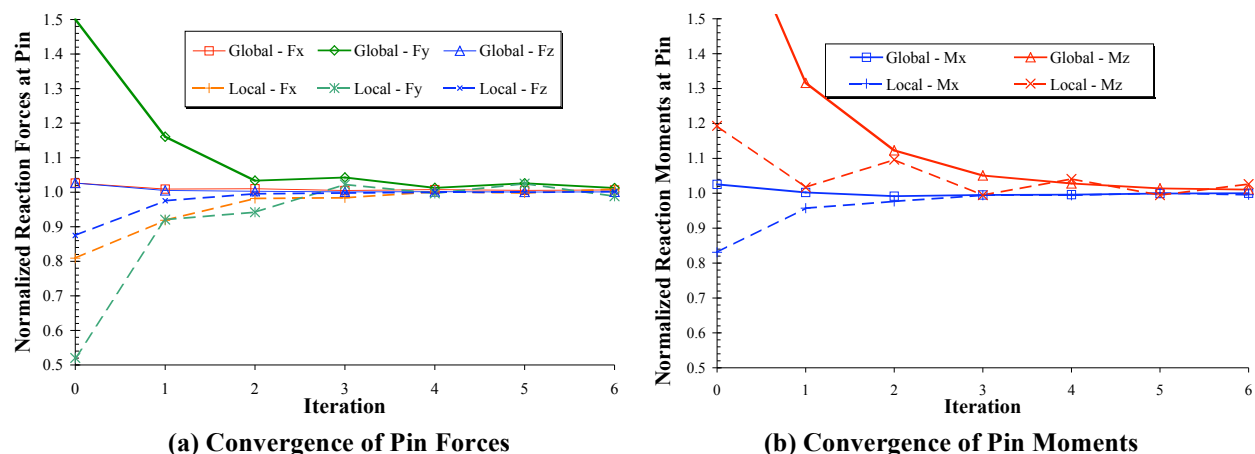


Figure 14. Convergence in Global-Local Analysis (Load Case W375).

VIII. □ Results

The PFA results are compared with available experimental results for the 1985-certification test (X2/1 and X2/2 specimens) and the 2003-subcomponent (SC) test. In addition, the load case corresponding to W375 is analyzed using the coarse 3D model. Table 2 presents various load cases analyzed and the corresponding models used in the analysis. Note that all of the PFA analyses shown in Table 2 were performed considering both geometric non-linearity and pin-lug contact.

Table 2. Various Load Cases Analyzed and Finite Element Models Used.

Finite Element Models		Load Cases Analyzed				
		X2/1	X2/2	PFA Studies	SC Test	W375
Solid-Shell Model	Coarse 3D Model			X		X
	1985 Test Model		X			
	SC Test Model				X	
Layered-Shell Model		X	X	X		

A. 1985-Certification Test (X2/2 Specimen)

1. Configuration

As part of the certification process for the composite lugs on the A300-600R aircraft, Airbus developed the certification test configuration shown in Figure 15. In this configuration, a hydraulic piston and lever were used to apply an in-plane load to the lug as shown in Figure 15a. The test specimen was fixed around the perimeter of the skin as shown in Figure 15b, and the constraint due to rib 1 was simulated using the transverse girder shown in Figure 15c. Because all of the loading was in the plane of the specimen, the M_X at the lug in this test was entirely due to the combination of F_X , F_Z , and the eccentricity. A boundary condition of $\theta_X=0$ at the pin is hypothesized and is used in the analysis.

The instrumentation on the X2/2 test specimen consisted of 16 strain gauges as shown in Figure 16. There are two sets of back-to-back rosettes on the tapered portion of the lug immediately above rib

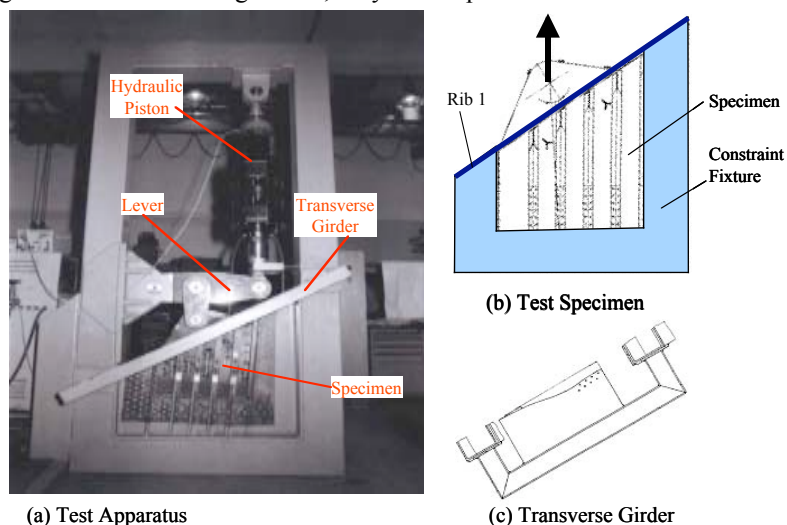


Figure 15. 1985-Certification Test Configuration.

1 (gauges 1-12) and four uniaxial gauges along the profile of the lug (gauges 13-16). During the test, all 16 gauges were monitored. The load vs. strain data from all these 16 gauges was available and was used in the PFA validation.

2. Results

Figure 17 shows the strain gauge results obtained from Airbus as open red circle symbols and NASA's finite element predictions made using the solid-shell model as solid blue lines. Applied load is shown in kN on the ordinate, and measured or predicted strain is shown (in thousands of microstrain) on the abscissa.

Because gauges 13 and 16 are located near large changes in stiffness, they are not shown in Figure 17. In general, the predicted values agree very well with the strain gauge results. However, the predicted values do not agree well with strains from gauges 3 and 10. The reasons for these two deviations is unknown. Also, because the location of gauges 14 and 15 through-the-thickness was not known, finite element predictions of strain on the outboard side and stringer side of the lug are shown. These predictions bound the strain gauge results. From this figure, it was concluded that the present PFA represents accurately the behavior of the lug over the complete loading range.

The computed values of F_{Res} (resultant of F_X , F_Y , and F_Z force components) and M_X vs. load factor are shown in Figure 18. In Figure 18, the load factor is a non-dimensional scaling factor that is applied to the displacements during the PFA analysis. A load factor of 1.0 corresponds to the displacements produced from a linear analysis. The curve for resultant force (F_{Res}) vs. load factor is shown as a solid blue line with open circle symbols and the curve of M_X vs. load factor is shown as a solid red line with open square symbols. The linearly projected values of M_X and F_{Res} are shown as closed diamonds. The failure load from the X2/2 test specimen is shown as a thick horizontal red line. Peak values of M_X and F_{Res} are shown on the graph and in the tabular insert as points A and B, respectively. The load factor for the linear case and points A and B are shown with vertical dashed lines. The F_{Res} at the maximum moment (Point A) agrees extremely well

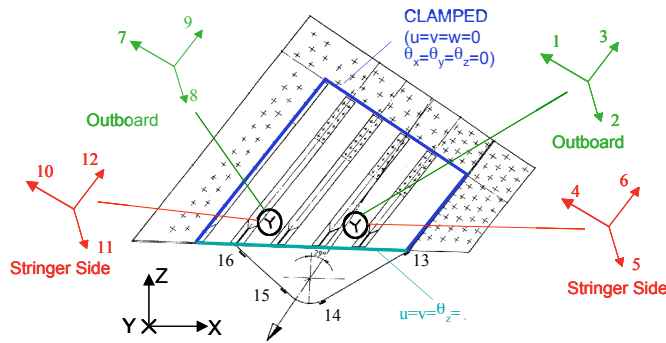


Figure 16. Strain Gauges on X2/2 Test Specimen.

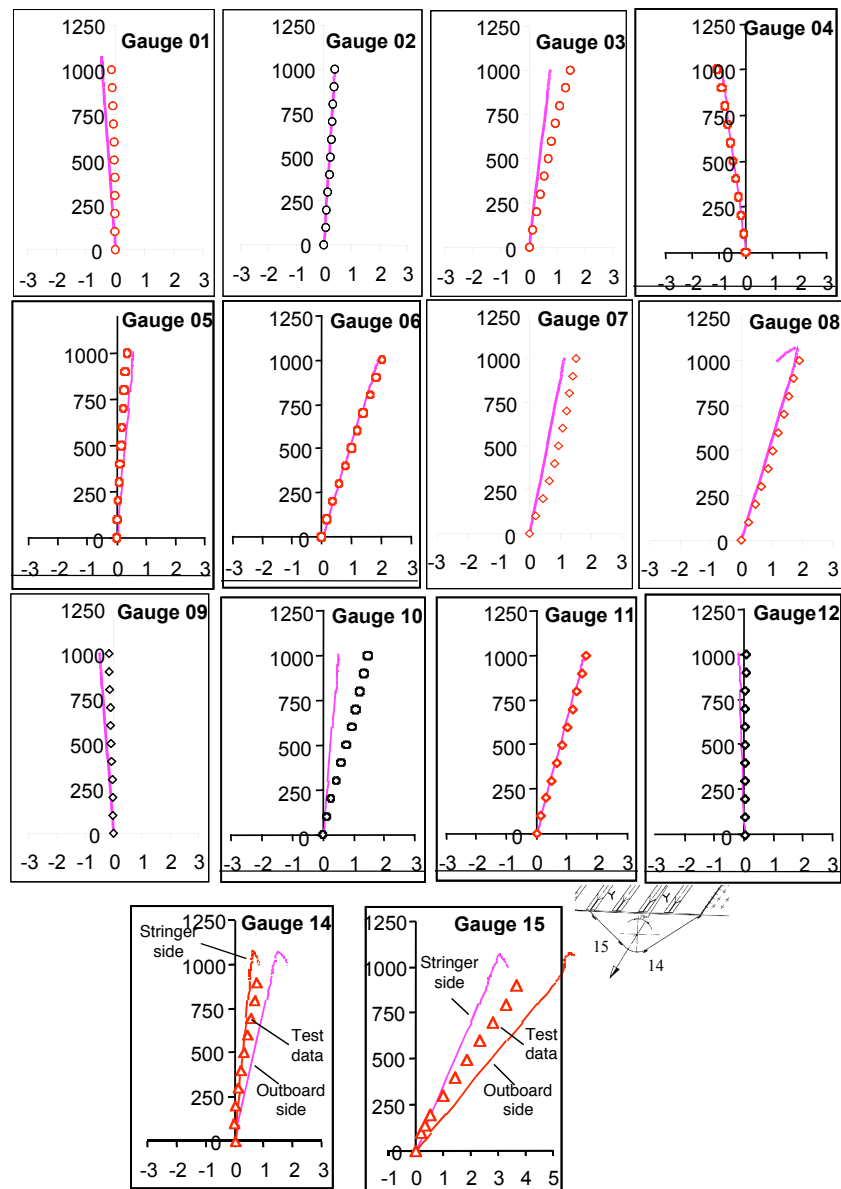


Figure 17. Strain Gauge and Finite Element Results.

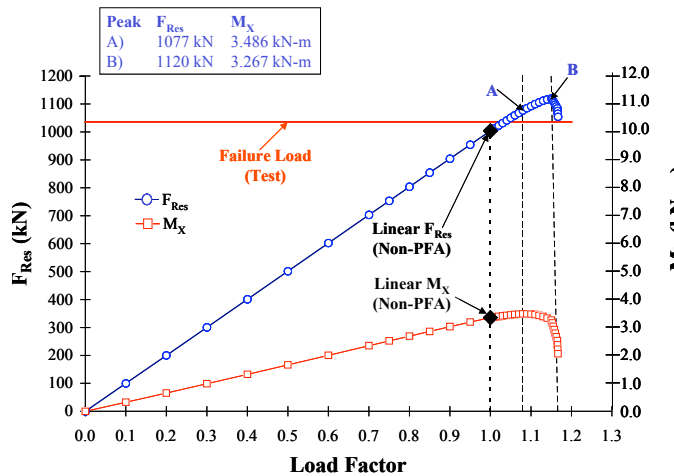


Figure 18. Load and Moment vs. Load Factor for 1985-Certification Test.

with the experimentally determined value for this configuration. The extent of the damage predicted by the PFA in Figure 19 agrees well with that observed during the 1985-certification test shown in Figure 20. Note that Figure 19 is based on superposition of all active failure modes within all ply types at each Gauss point in the model.

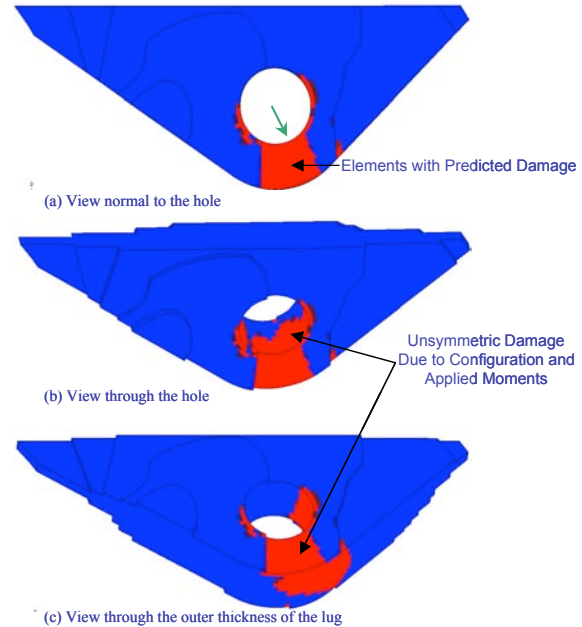


Figure 19. Damage Prediction from PFA for 1985-Certification Test.



Figure 20. X2/2 Test Specimen – Observed Failure.

B. 2003-Subcomponent Test

As part of the AA 587 accident investigation, Airbus developed a new certification test configuration to more accurately simulate the load introduction and boundary conditions near the lug. The 2003-subcomponent (SC) test model and the PFA algorithm shown in Figure 8 were used to predict the response of the 2003-subcomponent test specimen with boundary conditions shown in Figure 5b. Because the exact value of the M_X to be applied was unknown prior to the test, several values were considered as shown in Table 3. Note that in Table 3, because the SC test model is a left rear lug, the loads and moments are mirrored from their corresponding right rear lug load cases (i.e. the sign of F_Y , M_X , M_Z , v , θ_X , and θ_Z are reversed). The pin forces in all cases in Table 3 correspond to the global-local analysis with Y-MPC #1 (with F_Y reversed). Case (C) was analyzed before the 2003-subcomponent test and corresponds to an M_X value of 6.537 kN-m. Cases (D) and (E) were analyzed after the subcomponent test. Cases (D) and (E) correspond to the actual θ_X value of 0.51° applied in the test with 360° friction contact (Y-MPC #1) and 120° friction contact (Y-MPC #2), respectively. Post-test linear analyses gave the M_X values of 6.67 and 6.27 kN-m for cases (D) and (E), respectively.

Because the PFA is implemented as a displacement- (translation and rotation) controlled process, a linearly projected target value of M_X based on an assumed linear relationship between applied rotation and the resulting

Table 3. Pin Moments and Rotations for Subcomponent Test Model (left rear lug).

Loading Case	M_X	M_Z	θ_X	θ_Y	θ_Z
SC Test W375 (C)	+6.537	-1.000	0.487	0.000	-0.065
SC Test W375 (D)	+6.670	-0.379	0.510	0.000	0.000
SC Test W375 (E)	+6.270	-0.508	0.510	0.000	0.000

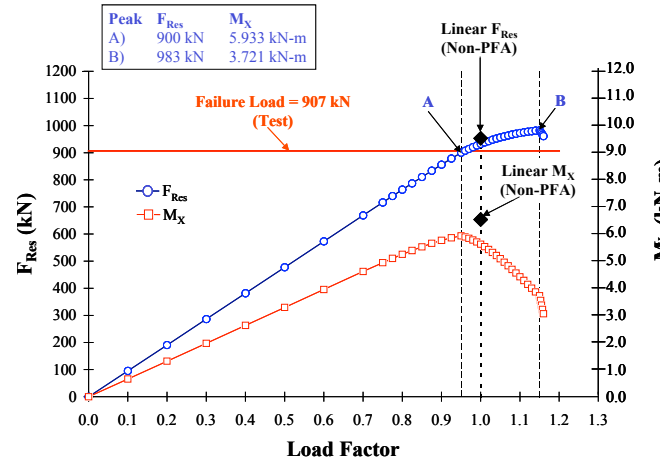
moment was used. Note that as damage develops, the specimen loses its stiffness and hence will not carry the moment that is predicted by the linear relationship.

The computed values of F_{Res} and M_X vs. load factor are shown for load cases SC (C), SC (D), and SC (E) in Figures 21a to 21c, respectively, for applied rotations resulting from linearly projected load and moment values as given in Table 3. The curves for resultant force (F_{Res}) vs. load factor are shown as solid lines with open circles, and the curves of M_X vs. load factor are shown as solid lines with open square symbols. The linearly projected values of M_X and F_{Res} are shown as closed diamonds. The failure load observed during the test is shown as a thick horizontal red line in Figures 21a to 21c. Peak values of M_X and F_{Res} are shown on the graph and in the tabular insert as points A and B, respectively. The load factor for the linear case and points A and B are shown with vertical dashed lines.

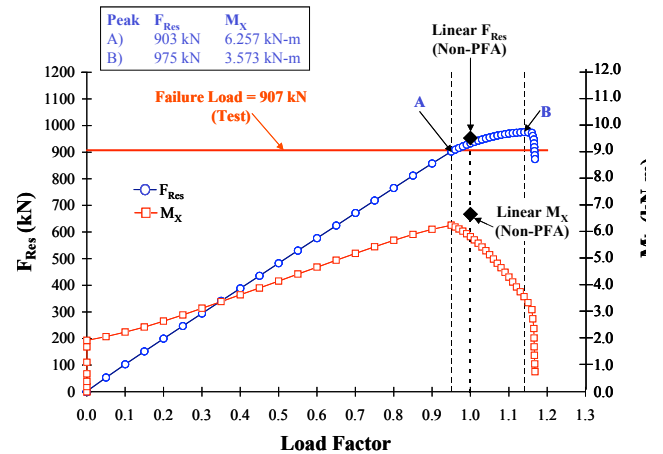
Two entirely different loading sequences are represented by the sets SC (C) (Figure 21a) and SC (D) and (E) (Figures 21b and 21c). In load case SC (C), the translations and rotations were applied simultaneously and proportionally starting from zero values to develop the F_{Res} and M_X shown in the figures. For load cases SC (D) and (E), θ_X was applied initially until the desired initial rotation (θ_X) was reached, and then the translations and rotations were increased proportionally. These later cases (D and E) represent more accurately the loading sequence during the 2003-subcomponent test.

While the curves in Figures 21a to 21c show the same general trends, increased values of M_X result in lower values of F_{Res} at failure. Also, larger values of M_X decrease the difference between F_{Res} at peak moment (point A) and maximum F_{Res} (point B). The difference between the values of points A and B is largest for load case SC (E) in which an initial value of θ_X is applied, and then is held constant. The constant rotation contributes to an artificial stiffening of the lug in load case SC (E) and results in higher peak F_{Res} than for load case SC (C).

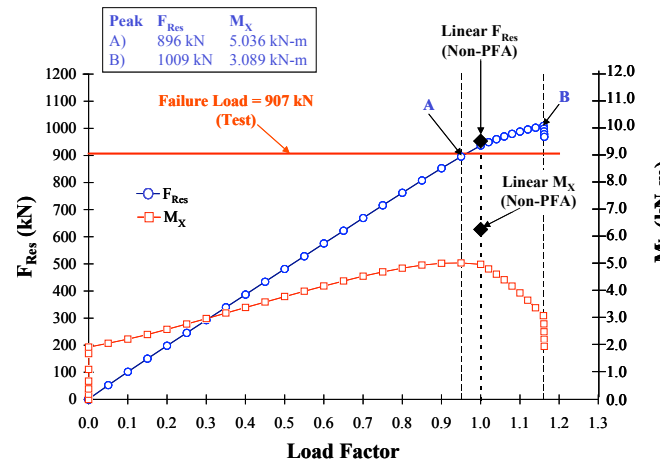
The damage predictions for the lug under load case SC (C) at peak moment and peak force are shown in Figures 22a and 22b, respectively. The mode of damage (cleavage type failure) is the same as seen previously in the 1985-certification test. The extent of the damage predicted by the PFA (Figures 22a and 22b) also agrees well with that observed during the SC test shown in Figure 23. These damage surfaces are consistent with the damage surfaces seen in the other cases.



(a) SC (C) Load Case

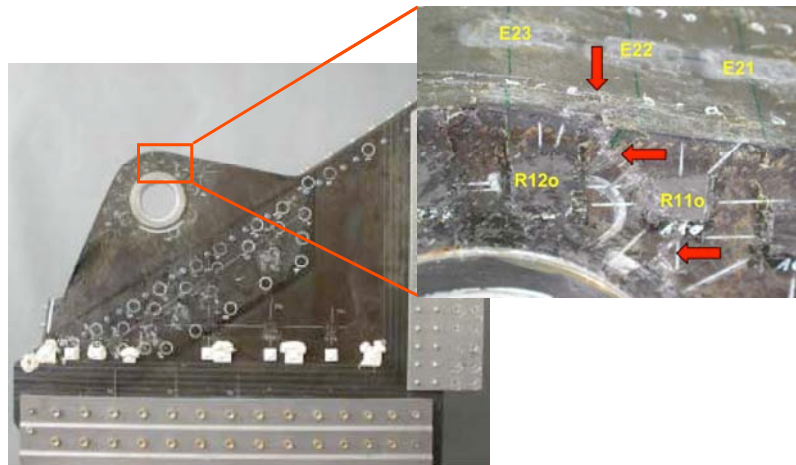
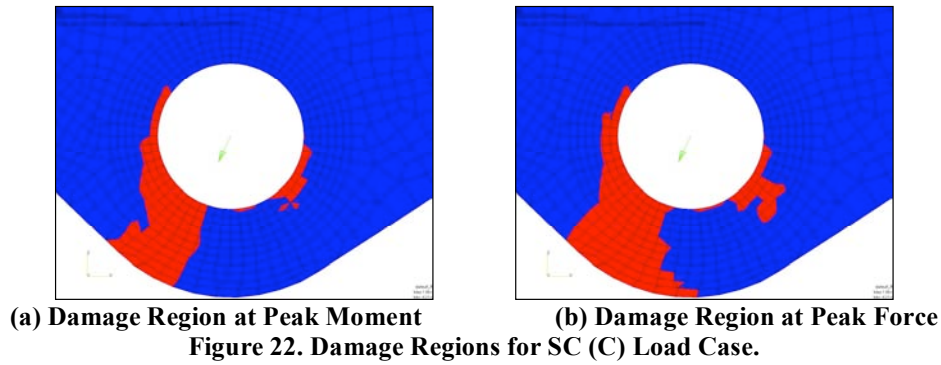


(b) SC (D) Load Case



(c) SC (E) Load Case

Figure 21. Load and Moment vs. Load Factor.



C. W375 Accident Case PFA Analysis

The forces and moments at the pin and the boundary conditions on the global-local interfaces for W375 accident case were obtained from the global-local analysis. The corresponding pin rotations predicted from global-local analysis are given in Table 4 and are 48% higher than those used in the Airbus 2003-subcomponent test because they represent global rotations and include the effect of the rotation of the fuselage; the boundary conditions during the test did not consider the deformation of the fuselage and corresponded to a fixed condition at the base of the VTP.

The computed values of F_{Res} and M_X vs. load factor are shown for the W375 accident case in Figure 24, using

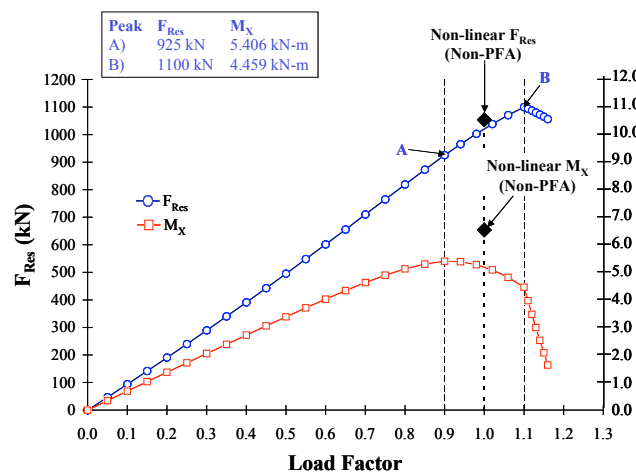


Figure 24. Load and Moment vs. Load Factor for W375 Load Case.

Table 4. Pin Rotations for Load Case W375 in Accident Model (RHS).

CASE	θ_X	θ_Z
Accident W375	0.756	0.286

applied translations and rotations resulting from linearly projected load and moment values. The curve for resultant force (F_{Res}) vs. load factor is shown as a solid blue line with open circle symbols, and the curve of M_X vs. load factor is shown as a solid red line with open square symbols. The linearly projected values of M_X and F_{Res} are shown as closed diamonds. Peak values of M_X and F_{Res} are shown on the graph and in the tabular insert as points A and B, respectively. Further, the extent of the damage predicted by the PFA for the W375 accident case (Figure 25), again a cleavage type failure, generally agrees with the damage seen in a photograph of the failed AA 587 right rear lug in Figure 26. These damage predictions are similar to those obtained for the 1985-certification test and the 2003-subcomponent test.

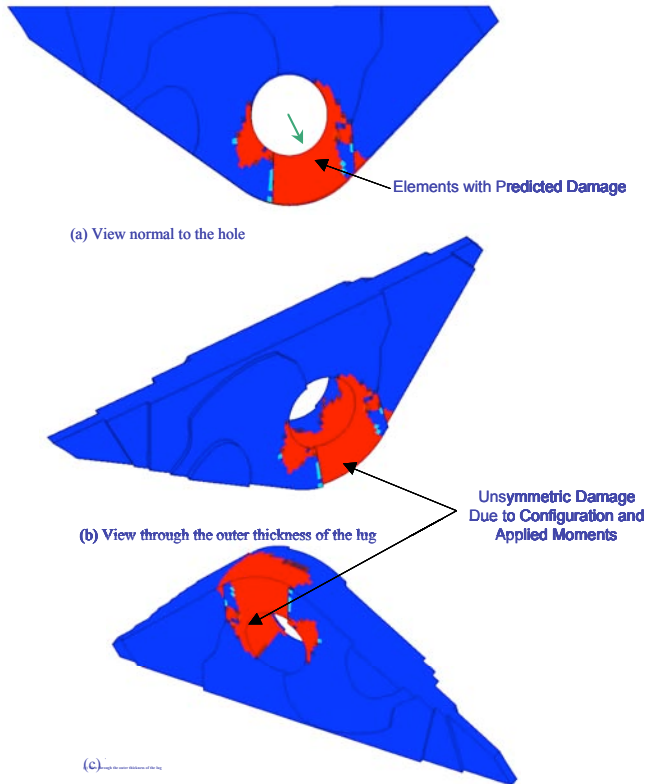


Figure 25. Damage Prediction for W375 Accident case from PFA.

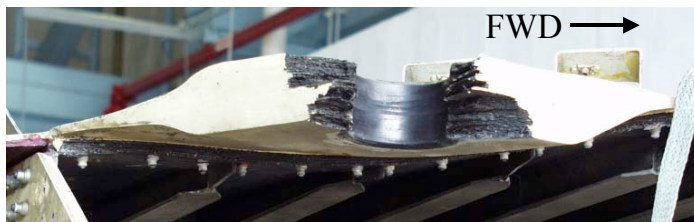


Figure 26. AA 587 Right Rear Lug – Observed Failure.

as those on the failed part. However, several issues in the analysis make the determination of the fracture sequence difficult. The first issue pertains to the convergence of the numerical solution. Once the ultimate strength of the lug is exceeded, the lug is no longer in equilibrium and the numerical procedure fails to yield a converged solution. Secondly, models assume that all the applied loads and boundary displacements are incremented proportionally to each other during the analysis. The proportionality is a reasonable assumption until the ultimate strength is exceeded. After the peak force, the stiffness of the lug changes dramatically, and the assumption of load proportionality is no longer valid. Finally, damage is modeled as a softening of the material continuum rather than as a stress free surface or crack. Consequently, fracture surfaces that are plainly observable in the failed part are not as clearly represented in the model.

C. Test and Accident Case Comparisons

Figures 27 and 28 compare the failure loads and M_X variation predicting with the solid-shell model and PFA for the three cases: the 1985-certification test, 2003-subcomponent (SC) test, and the W375 accident condition. The stiffnesses of the lug (represented by the slope of the F_{Res} vs. Load Factor curve in Figure 27) for the three cases and the maximum moment M_X (Figure 28) for the SC test and the W375 accident case agree very well.

The failure loads (Figure 29) and the damage regions (Figure 30) obtained using the solid-shell model and PFA for the three cases are compared in these figures. The failure loads for the 1985-certification test and the 2003-subcomponent test are included in Figure 29. Table 5 presents the individual load components in the lug at failure

IX. Discussion

This section discusses the results and lessons learned during the course of the analysis of the failure of the AA 587 right rear lug.

A. Effect of M_X and M_Z on Experimentally Determined Failure Load

As discussed in the *Results* section, the moment M_X has a significant effect on the failure loads during the tests. Larger absolute values of M_X result in lower failure loads for the lugs. For example, an observed increase in M_X of 45 percent from the 1985-certification test (Figure 18) to the 2003-subcomponent test (Figure 21c) caused a 17 percent decrease in the failure load. In contrast, the moment M_Z was determined to have a marginal effect on the failure load.

B. Failure Modes

The classical failure modes of a bolted joint are bearing failure, net tension failure, and shear-out failure. In addition to these three classical modes of failure, a failure identified as cleavage failure is also common [Camanho and Matthews, 1999]. The progressive failure analysis showed that the right rear lug failures are very similar to the cleavage type, but do not show separation of the failed piece from the remainder of the lug. Ideally, the progressive failure analysis of a lug should reproduce the entire sequence of failure events and should end with an analysis result exhibiting the same fracture surfaces

for the 2003-subcomponent test and W375 accident condition. The experimentally determined failure loads agree very well with the PFA predicted values, thus validating the present PFA methodology for the lug configuration. Further, all three configurations showed cleavage type failures. The failure load for the lug for the W375 accident condition (925 kN) is greater than 1.98 times the limit load (467 kN) [Hilgers and Winkler, 2003].

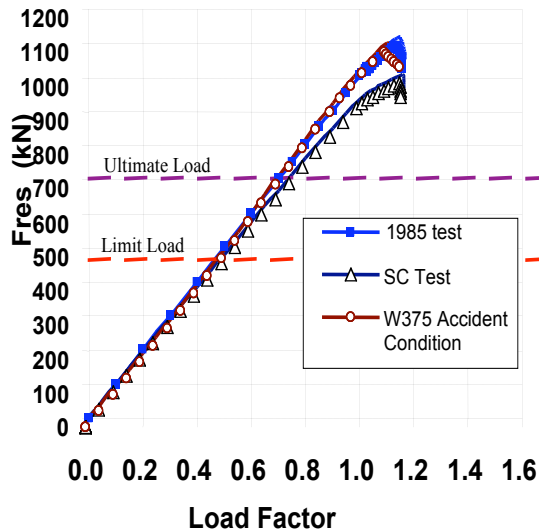


Figure 27. F_{Res} vs. Load Factor Variation for 1985-Certification Test, 2003-Subcomponent Test, and W375 Accident Case.

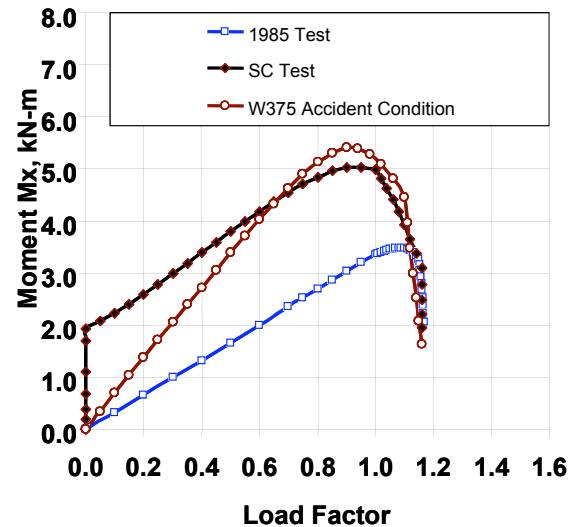


Figure 28. Bending Moment M_x Variation 2003-for 1985-Certification Test, Subcomponent Test, and W375 Accident Case.

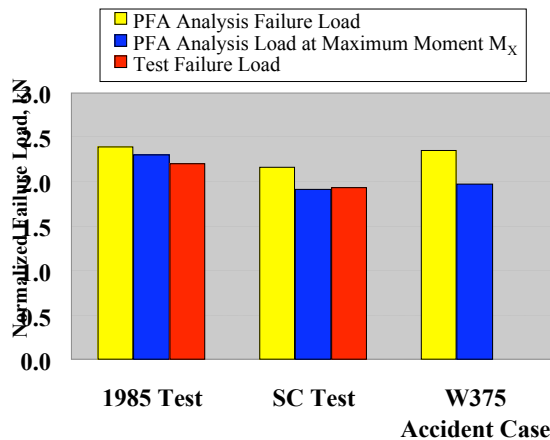


Figure 29. Failure Loads Normalized by Limit Load for 1985-Certification Test, 2003-Subcomponent Test, and W375 Accident Case.

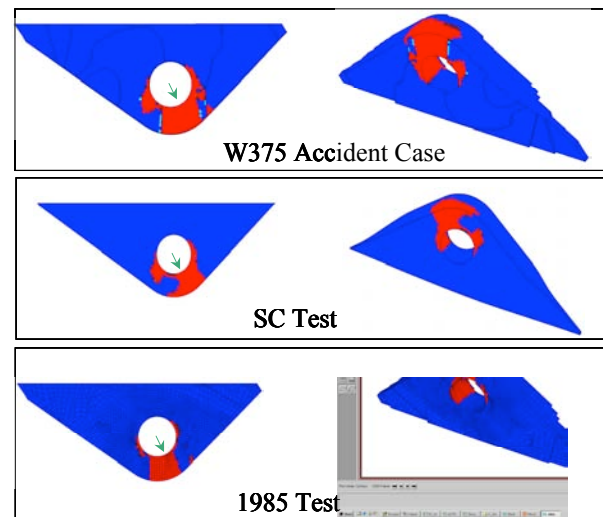


Figure 30. Comparison of Damage Predictions 1985-Certification Test, 2003-Subcomponent Test, and W375 Accident Case.

Table 5. Load Components (Normalized by Limit Load) in the Lug at Failure.

Test Case	F_x	F_y	F_z	F_{Res}	M_x
SC Analysis (PFA)	-374.8	-40.39	-812.7	895.9	-5.04
2003-Subcomponent Test	-381.6	-39.10	-822.5	907.0	Not measured
W375 Analysis (PFA)	-359.9	-40.35	-851.5	925.3	-5.41

X. □ Concluding Remarks

An analysis of the failure of the composite vertical tail of the American Airlines Flight 587 - Airbus A300-600R was performed as part of the National Transportation Safety Board's failure investigation of the accident that occurred on November 12, 2001. Two structural analysis teams, the global analysis team and the detailed lug analysis team, analyzed the vertical tail. The global analysis team evaluated the loads on each of the six lugs that attach the tail to the aluminum fuselage and determined that the right rear lug carried the largest loads compared to the design allowable. The detailed lug analysis team developed and verified user defined material and user field algorithms within the ABAQUS general-purpose finite element code. The team then performed progressive failure analyses (PFA) to predict the failure of the right rear composite lug. A global-local connection procedure was developed and validated to ensure the satisfaction of the continuity of displacements and reciprocity of tractions across the global-local interfaces and connection regions.

The right rear lug, including the neighboring fin region near the rear spar, was analyzed using two modeling approaches. In the first approach, solid-shell type modeling was used, and in the second approach, layered-shell type modeling was used. To validate the models, the solid-shell and the layered-shell modeling approaches were used in conjunction with the PFA to determine the load, mode, and location of failure in the right rear lug under loading representative of a certification test conducted by Airbus in 1985 (1985-certification test). Both analyses were in excellent agreement with each other and with the experimentally determined failure loads, failure mode, and location of failure. The solid-shell type modeling was then used to analyze a subcomponent test conducted by Airbus in 2003 as part of the failure investigation (2003-subcomponent test). Excellent agreement was observed between the PFA analyses and the experimentally determined results from the 2003-subcomponent test. Excellent agreement was also observed between the analyses of the 2003-subcomponent test and the accident condition.

From the analyses conducted and presented in this report, the following conclusions were drawn:

- The moment, M_X (moment about the fuselage longitudinal axis) had significant effect on the failure load of the lugs. Higher absolute values of M_X give lower failure loads. For example, an observed increase in M_X of 45 percent from the 1985-certification test to the 2003-subcomponent test caused a 17 percent decrease in the failure load. Therefore, to properly test a lug under a loading condition that is representative of the flight loads, it is important to apply to the lug an accurate moment, M_X . The predicted load, mode, and location of the failure of the 1985-certification test, 2003-subcomponent test and the accident condition were in very good agreement. This similarity in results suggests that the 1985-certification and 2003-subcomponent tests represented the accident condition accurately.
- The failure mode of the right rear lug for the 1985-certification test, 2003-subcomponent test, and the accident load case was identified as a cleavage-type failure.
- For the accident case, the predicted failure load for the right rear lug from the PFA and solid-shell models was greater than 1.98 times the limit load of the lugs.

References

- ABAQUS User's Manual, Vol. III, Version 6.1, Hibbitt, Karlsson & Sorensen, Pawtucket, RI, 2000.
- Averill, R.C., Non-linear Analysis of Laminated Composite Shells Using a Micromechanics-Based Progressive Damage Model, Ph.D. Thesis, Virginia Polytechnic Institute and State University, 1992.
- Camanho, P.P., and Matthews, F.L., "A Progressive Damage Model for Mechanically Fastened Joints in Composite Laminates," *Journal of Composite Materials*, Vol. 33, No. 24, 1999, pp. 2248-2280.
- Chang, F.-K., and Chang, K.Y., "A Progressive Damage Model for Laminated Composites Containing Stress Concentrations," *Journal of Composite Materials*, Vol. 21, 1987, pp. 834-855.
- Chang, F.-K., and Lessard, L.B., "Damage Tolerance of Laminated Composites Containing an Open Hole and Subjected to Compressive Loadings: Part I-Analysis," *Journal of Composite Materials*, Vol. 25, 1991, pp. 2-43.
- Dávila, C.G., Ambur, D.R., and McGowan, D.M., "Analytical Prediction of Damage Growth in Notched Composite Panels Loaded in Compression," *Journal of Aircraft*, Vol. 37, No. 5, 2000, pp. 898-905.
- Dávila, C.G., Camanho, P.P., and de Moura, M.F.S.F., "Mixed-Mode Decohesion Elements for Analyses of Progressive Delamination," *Proceedings of the 42nd AIAA/ASME/ASCE/AHS/ASC Structures, Structural Dynamics and Materials Conference*, Seattle, Washington, April 16-19, 2001(a).
- Glaesgen, E.H., Pastore, C.M., Griffin, O.H., Jr. and Birger, A., "Geometrical and Finite Element Modeling of Textile Composites," *Composites Part B*, Vol. 27B, No. 1, 1996, pp. 43-50.
- Hashin, Z., and Rotem, A., "A Fatigue Criterion for Fiber-Reinforced Materials," *Journal of Composite Materials*, Vol. 7, 1973, pp. 448-464.
- Hashin, Z., "Failure Criteria for Unidirectional Fiber Composites," *J. Appl. Mech.*, Vol. 47, 1980, pp. 329-334.
- Hilgers, R. and Winkler, E., "AAL587 Investigation Lug Sub Component Test #1 – Results Test / FEA Comparisons," TN-ESGC – 1014/03, November 2003.

- MSC/NASTRAN Quick Reference Guide, Version 70, the MacNeal-Schwendler Corporation, Los Angeles, CA, 1997.
- Nahas., M.N., "Survey of Failure and Post-Failure Theories of Laminated Fiber-Reinforced Composites," J. Composites Technology and Research, Vol. 8, No. 4 , 1986, pp. 138-153.
- Poe, C.C., Jr. and Harris, C.E., "Mechanics of Textile Composites Conference," NASA CP 3311, Parts 1 and 2, October 1995.
- Rowlands, R.E., Strength (Failure) Theories and Their Experimental Correlation. In Handbook of Composites, Vol. 3. Failure Mechanics of Composites, ed. G.C. Sih and A. M. Skudra. North-Holland, 1984, pp. 71-125.
- Soden, P.D., Hinton, M.J. and Kaddour, A.S., "A Comparison of the Predictive Capabilities of Current Failure Theories for Composite Laminates," Composites Science and Technology, Vol. 58, 1998(a), pp. 1225-1254.
- Soden, P.D., Hinton, M.J. and Kaddour, A.S., "Lamina Properties, Lay-Up Configurations and Loading Conditions for a Range of Fibre-Reinforced Composite Laminates," Composites Science and Technology, Vol. 58, 1998(b), pp. 1011-1022.
- Young, R.D., Hilberger, M., Moore, D. and Lovejoy, A.E., "Structural Analysis for the American Airlines Flight 587 Accident Investigation - Global Analysis," Proceedings of the 46th AIAA/ASME/ASCE/AHS/ASC Structures, Structural Dynamics, and Materials Conference, AIAA-2005-2254-CP, AIAA, Austin, TX, April 18-21, 2005.

This page left blank intentionally.

Appendix

List of Publications Authored or Co-authored by Dr. James H. Starnes, Jr.

Books

1. Starnes, James H., Jr., *The Effects of a Circular Hole on the Buckling of Cylindrical Shells*, PhD Dissertation, California Institute of Technology, 1970, Pasadena, CA.
2. Elishakoff, Isaac; Lin, K. K.; and Starnes, James H., Jr.: *Nonclassical Problems in the Theory of Elastic Stability*, Cambridge University Press, New York. January 2001.

Book Chapters

1. Stein, Manuel; and Starnes, James H., Jr.: Numerical Analysis of Stiffened Shear Webs in the Postbuckling Range. *Numerical Solutions of Nonlinear Structural Problems*, edited by R. F. Hartung, AMD-Vol. 6, ASME, New York, 1973, pp. 211-223.
2. Starnes, James H., Jr.: The Effects of Cutouts on the Buckling of Thin Shells. *Thin Shell Structures. Theory, Experiment and Design*, edited by Y. C. Fung and E. E. Sechler, Prentice-Hall, Inc., 1974, pp. 289-304.
3. Starnes, James H., Jr.; Rhodes, Marvin D.; and Williams, Jerry G.: Effect of Impact Damage and Holes on the Compressive Strength of a Graphite-Epoxy Laminate. *Nondestructive Evaluation and Flaw Criticality for Composite Materials*, ASTM STP 696, R. B. Pipes, Ed., American Society for Testing and Materials, 1979, pp. 145-171.
4. Williams, Jerry G.; Anderson, Melvin S.; Rhodes, Marvin D.; Starnes, James H., Jr.; and Stroud, W. Jefferson: Recent Developments in the Design, Testing and Impact-Damage Tolerance of Stiffened Composite Panels. *Fibrous Composites in Structural Design*, E. M. Lenoe, D. W. Oplinger, and J. J. Burke, Eds., Plenum Press, New York, 1980, pp. 259-291.
5. Starnes, James H., Jr.; and Williams, Jerry G.: Failure Characteristics of Graphite-Epoxy Structural Components Loaded in Compression. *Mechanics of Composite Materials – Recent Advances*, Z. Hashin and C. T. Herakovich, Eds., Pergamon Press, 1983, pp. 283-306.
6. Knight, Norman F., Jr.; and Starnes, J. H., Jr.: Postbuckling Behavior of Compression-Loaded Graphite-Epoxy Cylindrical Panels with Circular Holes. *Collapse Analysis of Structures*, L. H. Sobel and K. Thomas, Eds., ASME PVP-Vol. 84, 1984, pp. 153-168.

7. Card, Michael F.; and Starnes, James H., Jr.: Current Research in Composite Structures at NASA Langley Research Center. *Composite Materials and Structures*, K. A. V. Pandalai, Ed., Indian Academy of Science, Bangalore, Vol. II, 1988, pp. 5-26. Also in Sadhana- Academy Proceedings in Engineering Science, Indian Academy of Science, Vol. II, 1987, pp. 273-294.
8. Perry, Christine A.; Gurdal, Zafer; and Starnes, James H., Jr.: Minimum Weight Design of Compressively Loaded Stiffened Panels for Postbuckling Response. *Mechanics of Composite Materials - Nonlinear Effects*, Hyer, M. W., ed., ASME AMD-Vol. 159, June 1993, pp. 71-80.
9. Koiter, W. T.; Elishakoff, I.; Lin, T. W.; and Starnes, J. H., Jr.: Buckling of an Axially Compressed Cylindrical Shell of Variable Thickness. *Recent Advances in Structural Mechanics*, ASME PVP-Vol. 269/NE-Vol. 13, 1993, pp. 23-28.
10. Librescu, L.; Lin, W.; Nemeth, M. P.; and Starnes, J. H., Jr.: Effects of Tangential Edge Constraints on the Postbuckling Behavior of Flat and Curved Panels Subjected to Thermal and Mechanical Loads. *Buckling and Postbuckling of Composite Structures*, ASME AD-Vol. 41/PVP-Vol. 293, 1994, pp. 55-71.
11. Fuchs, H. P.; Starnes, J. H., Jr.; and Hyer, M. W.: Numerical and Experimental Investigation of the Collapse Response of a Quasi-Isotropic Graphite-Epoxy Cylindrical Shells Subjected to Bending and Internal Pressure Loads. *Buckling and Postbuckling of Composite Structures*, ASME AD-Vol. 41/PVP-Vol. 293, 1994, pp. 73-94.
12. Elishakoff, I.; Cai, G. Q.; and Starnes, James H., Jr.: Probabilistic and Convex Models of Uncertainty in Buckling of Structures. *Structural Safety & Reliability*, Schueller, G. I.; Shinozuka, M. and Yao, J. T. P., Editors, A. A. Balkema, Rotterdam, The Netherlands, 1994, pp. 761-766.
13. Li, Y. W.; Elishakoff, I.; and Starnes, J. H., Jr.: Axial Buckling of Composite Cylindrical Shells with Periodic Thickness Variation. *Buckling and Postbuckling of Composite Structures*, ASME AD-Vol. 41/PVP-Vol. 293, 1994, pp. 95-114.
14. Elishakoff, I.; Li, Y. W.; and Starnes, J. H., Jr.: Localization Phenomenon of Buckling Mode in Stiffened Multi-Span Elastic Plates. *Recent Advances in Solids and Structures - 1995*, ASME PVP-Vol. 321/NE-Vol. 18, 1995, pp. 153-164.
15. Ambur, Damodar R.; Starnes, James H., Jr.; and Prasad, Chunchu B.: Influence of Impact Parameters on the Response of Laminated Composite Plates. *Composite Materials: Fatigue and Fracture - Fifth Volume*, ASTM STP 1230, R. H. Martin, Ed., American Society for Testing and Materials, 1995, pp. 389-404.
16. Starnes, James H., Jr.; and Ambur, Damodar R.: Composite Structures Research and Development Experiences at NASA Langley Research Center. *Mechanics of*

Composite Materials and Structures, C. A. Mota Soares; C. M. Mota Soares; and M. J. M. Freitas, Eds., NATO Science Series E: Applied Sciences - Vol. 361, Kluwer Academic Publishers, 1999, pp. 489-508.

17. Starnes, James H., Jr.; Hilburger, Mark, W.; and Nemeth, Michael P.: The Effects of Initial Imperfections on the Buckling of Composite Shells. *Composite Structures: Theory and Practice*, P. Grant and C. Q. Rousseau, Eds., American Society for Testing and Materials, October 2000, pp. 529-550.
18. Simitses, George J.; Starnes, James H., Jr.; and Rezaeepazhand, J.: Structural Similitude and Scaling Laws for Plates and Shells: A Review. *Advances in the Mechanics of Plates and Shells (The Avinoam Libai Anniversary Volume)*, D. Durban, D. Givoly and J. G. Simmons, Eds., Kluwer Academic Publishers, 2001, pp. 295-310.
19. Arbocz, Johann; and Starnes, James H., Jr.: On a High-Fidelity Hierarchical Approach to Buckling Load Calculations. *Calladine Festschrift*, S. Pellegrino, Ed., Wolters Kluwer Academic Publishers. Dordrecht, The Netherlands, 2002.

NASA Conference Publications

1. Noor, A. K.; Shuart, M. J.; Starnes, J. H., Jr.; and Williams, J. G. (Editors): Failure Analysis and Mechanisms of Failure of Fibrous Composite Structures. NASA CP 2278, August 1983.
2. Starnes, J. H., Jr.; Bohon, H. L.; and Garzon, S. B.: Eighth DOD/NASA/FAA Conference on Fibrous Composites in Structural Design, NASA CP-3087, September 1990.
3. Noor, A. K.; Housner, J. M.; Starnes, J. H., Jr.; Hopkins, D. A.; and Chamis, C. C. (Compilers): Computational Structures Technology for Airframes and Propulsion Systems. NASA CP-3142, May 1992, 527 p.

NASA Contractor Reports

1. Knauss, J. F.; Starnes, J. H., Jr.; and Henneke, E. G., II; The Compressive Failure of Graphite/Epoxy Plates with Circular Holes. NASA CR-157115, February 1978.
2. Boitnott, R. L., Johnson, E. R.; and Starnes, J. H., Jr.: Nonlinear Response and Failure Characteristics of Internally Pressurized Composite Cylindrical Panels. NASA CR-176148, June 1985,
3. Swanson, G. D.; Gurdal, Z.; and Starnes, J. H., Jr.: Structural Efficiency Study of Composite Wing Rib Structures, NASA CR-183004, September 1988.

4. Stoll, F.; Gurdal, Z.; and Starnes, J. H., Jr.: A Method for the Geometrically Nonlinear Analysis of Compressively Loaded Prismatic Composite Structures, NASA CR-184846, February 1991.
5. Ley, R.; Gurdal, Z.; Johnson, E. R.; and Starnes, J. H., Jr.: Analysis and Optimal Design of Pressurized, Imperfect, Anisotropic Ring-Stiffened Cylinders. NASA CR-191375, November 1992.
6. Fuchs, J. P.; Hyer, M. W.; and Starnes, J. H., Jr.: Numerical and Experimental Investigation of the Bending Response of Thin-Walled Composite Cylinders. NASA CR-195730, September 1993.
7. Ragon, S. A.; Gurdal, Z.; and Starnes, J. H. Jr.: Optimization of Composite Box-Beam Structures Including Effects of Subcomponent Interactions, NASA CR-199667, July 1995.

NASA Technical Publications

1. Davis, R. C.; and Starnes, J. H., Jr.: Design Detail Verification Tests for a Lightly Loaded Open-Corrugation Graphite-Epoxy Cylinder, NASA TP-1981, March 1982.
2. Nemeth, M. P.; Britt, V. O.; Collins, T. J.; and Starnes, J. H., Jr.: Nonlinear Analysis of the Space Shuttle Superlightweight External Fuel Tank. NASA TP-3616, December 1996, 27 p.
3. Nemeth, M. P.; and Starnes, J. H., Jr.: The NASA Monographs on Shell Stability Design Recommendations—A Review and Suggested Improvements. NASA TP-1998-206290, January 1998, 21 p.
4. Hilburger, M. W.; Nemeth, M. P.; and Starnes, J. H., Jr.: Effective Widths of Compression-Loaded Plates With a Cutout. NASA TP-2000-210538, October 2000, 24 p.

NASA Technical Memorandums

1. Haftka, R. T.; and Starnes, J. H., Jr.: WIDOWAC (Wing Design Optimization with Aeroelastic Constraints): Program Manual. NASA TM-X-3071, October 1974.
2. Rhodes, M. D.; Williams, J. G.; Starnes, J. H., Jr.: Effect of Low-Velocity Impact Damage on the Compressive Strength of Graphite-Epoxy Hat-Stiffened Panels, NASA TM-X-73988, December 1976.
3. Starnes, J. H., Jr.: Rhodes, M. D.; and Williams, J. G.: The Effect of Impact Damage and Circular Holes on the Compressive Strength of a Graphite-Epoxy Laminate. NASA TM-78796, October 1976.
4. Rhodes, M. D.; Williams, J. G.; Starnes, J. H., Jr.: Effect of Low-Velocity Impact Damage on the Compressive Strength of Graphite-Epoxy Hat-Stiffened Panels, NASA TN-D-8411, April 1977.
5. Williams, Jerry G.; Anderson, Melvin S.; Rhodes, Marvin D.; Starnes, James H., Jr.; and Stroud, W. Jefferson: Recent Developments in the Design, Testing and Impact-Damage Tolerance of Stiffened Composite Panels. NASA TM 80077, April 1979.
6. Starnes, James H., Jr.; and Williams, Jerry G.: Failure Characteristics of Graphite-Epoxy Structural Components Loaded in Compression. NASA TM 84552, September 1982.
7. Bonanni, D. L., Johnson, E. R.; and Starnes, J. H., Jr.: Local Buckling and Crippling of Composite Stiffener Sections. NASA TM-101133, June 1988.
8. Ambur, D. R.; Starnes, J. H., Jr.; and Prasad, C. B.: Influence of Transverse-Shear and Large-Deformation Effects on the Low-Speed Impact Response of Laminated Composite Plates. NASA TM-107753, April 1993, 31 p.

9. Harris, C. E.; Starnes, J. H., Jr.; and Newman, J. C., Jr.: Development of Advanced Structural Analysis Methodologies for Predicting Widespread Fatigue Damage in Aircraft Structures. NASA TM-110187, August 1995, 25 p.
10. Harris, C. E.; Newman, J. C., Jr.; Piascik, R. S.; and Starnes, J. H., Jr.: Analytical Methodology for Predicting the Onset of Widespread Fatigue Damage in Fuselage Structure. NASA TM-110293, November 1996, 26 p.
11. Nemeth, M. P.; Young, R. D.; Collins, T.J.; and Starnes, J. H., Jr.: Nonlinear Analysis of the Space Shuttle Superlightweight LO₂ Tank. NASA TM-1998-207287, 1998.
12. Harris, C. E.; Starnes, J. H., Jr.; and Shuart, M. J.: An Assessment of the State-of-the-Art in the Design and Manufacturing of Large Composite Structures for Aerospace Vehicles. NASA TM-2001-210844, April 2001, 50 p.
13. Harris, C. E.; Starnes, J. H., Jr.; and Shuart, M. J.: Advanced Durability and Damage Tolerance Design and Analysis Methods for Composite Structures—Lessons Learned From NASA Technology Development Programs. NASA TM-2003-212420, June 2003, 36 p.
14. Hilburger, M. W.; Nemeth, M. P.; and Starnes, J. H.: Shell Buckling Design Criteria Based on Manufacturing Imperfection Signatures. NASA TM-2004-212659, May 2004, 25 p.
15. Hilburger, M. W.; and Starnes, J. H., Jr.: Buckling and Failure of Compression-Loaded Composite Cylindrical Shells with Geometric and Material Imperfections, NASA TM-2004-212677, September 2004.
16. Hilburger, M. W.; and Starnes, J. H., Jr.: Parametric Study on the Response of Compression-Loaded Composite Cylindrical Shells with Geometric and Material Imperfections. NASA TM-2004-212676, September 2004.

Refereed Journal Papers

1. Starnes, James H., Jr.: Effect of a Slot on the Buckling of a Cylindrical Shell with a Cutout. *AIAA Journal*, Vol. 10, No. 2, February 1972, pp. 227-229.
2. Starnes, James H., Jr.: Effect of a Circular Hole on the Buckling of Cylindrical Shells Loaded by Compression. *AIAA Journal*, Vol. 10, No. 11, November 1972, pp. 1466-1472.
3. Stephens, Wendell B.; Starnes, James H., Jr.; and Almroth, B. O.: Collapse of Long Cylindrical Shells Under Combined Bending and Pressure Loads. *AIAA Journal*, Vol. 13, No. 1, January 1975, pp. 20-25.
4. Haftka, Raphael T.; Starnes, James H., Jr.; Barton, Furman W.; and Dixon, Sidney C.: A Comparison of Two Types of Structural Optimization Procedures to Satisfy Flutter Requirements. *AIAA Journal*, Vol. 13, No. 10, October 1975, pp. 1333-1339.
5. Almroth, B. O.; and Starnes, James H., Jr.: The Computer in Shell Stability Analysis. *Journal of the Engineering Mechanics Division*, ASCE, Vol. 101, No. EM6, December 1975, pp. 873-888.
6. Haftka, Raphael T.; and Starnes, James H., Jr.: Applications of a Quadratic Extended Interior Penalty Function for Structural Optimization. *AIAA Journal*, Vol. 14, No. 6, June 1976, pp. 718-724.
7. Starnes, James H., Jr.; and Haftka, Raphael T.: Preliminary Design of Composite Wings for Buckling, Strength and Displacement Constraints. *Journal of Aircraft*, Vol. 16, No. 8, August 1979, pp. 564-570.
8. Rhodes, Marvin D.; Williams, Jerry G.; and Starnes, James H., Jr.: Low-Velocity Impact Damage in Fiber-Reinforced Laminated Epoxy Structures. *Polymer Composites*, Vol. 2, No. 1, January 1981, pp. 36-44.
9. Haftka, Raphael T.; Starnes, James H., Jr.; and Nair, Sudhakar: Design for Global Damage Tolerance and Associated Mass Penalties. *Journal of Aircraft*, Vol. 20, No. 1, January 1983, pp. 83-88.
10. Starnes, James H., Jr.; Knight, Norman F., Jr.; and Rouse, Marshall: Postbuckling Behavior of Selected Flat Stiffened Graphite-Epoxy Panels Loaded in Compression. *AIAA Journal*, Vol. 23, No. 8, August 1985, pp. 1236-1246.
11. Knight, Norman F., Jr.; and Starnes, James H., Jr.: Postbuckling Behavior of Axially Compressed Graphite-Epoxy Cylindrical Panels with Circular Holes. *ASME Journal of Pressure Vessel Technology*, Vol. 107, No. 4, November 1985, pp. 394-402.

12. Gurdal, Zafer; Haftka, Raphael T.; and Starnes, James H., Jr.: The Effect of Slots on the Buckling and Postbuckling Behavior of Laminated Plates. *Journal of Composites Technology and Research*, Vol. 7, No. 3, Fall 1985, pp. 82-87.
13. Haftka, Raphael T.; and Starnes, James H., Jr.: Use of Optimum Stiffness Tailoring to Improve the Compressive Strength of Composite Plates with Holes. *AIAA Journal*, Vol. 26, No. 1, January 1988, pp. 72-77.
14. Knight, Norman F., Jr.; and Starnes, James H., Jr.: Postbuckling Behavior of Selected Curved Stiffened Graphite-Epoxy Panels Loaded in Axial Compression. *AIAA Journal*, Vol. 26, No. 3, March 1988, pp. 344-352.
15. Hyer, Michael W.; Loup, Douglas C.; and Starnes, James H., Jr.: Stiffener/Skin Interactions in Pressure-Loaded Composite Panels. *AIAA Journal*, Vol. 28, No. 3, March 1990, pp. 532-537.
16. Bonanni, David L.; Johnson, Eric R.; and Starnes, James H., Jr.: Local Crippling of Thin-Walled Graphite-Epoxy Stiffener Section. *AIAA Journal*, Vol. 29, No. 11, November 1991, pp. 1951-1959.
17. Swanson, Gary D.; Gurdal, Zafer; and Starnes, James H., Jr.: Structural Efficiency Study of Graphite-Epoxy Rib Structures. *Journal of Aircraft*, Vol. 27, No. 12, December 1991, pp. 1011-1020.
18. Nagendra, S.; Haftka, R. T.; Gurdal, Z.; and Starnes, James H., Jr.: Design of a Blade-Stiffened Composite Panel with a Hole. *Composite Structures*, Vol. 18, 1991, pp. 195-219.
19. Curry, James M.; Johnson, Eric R.; and Starnes, James H., Jr.: Effect of Dropped Plies on the Strength of Graphite-Epoxy Laminates. *AIAA Journal*, Vol. 30, No. 2, February 1992, pp. 449-456.
20. Noor, Ahmed K.; Starnes, James H., Jr.; and Waters, W. Allen, Jr.: Numerical and Experimental Simulations of the Postbuckling Response of Laminated Anisotropic Panels. *Journal of Aerospace Engineering*, ASCE, Vol. 5, No. 3, July 1992, pp. 347-368.
21. Wieland, Todd M.; Morton, John; and Starnes, James H., Jr.: Scale Effects in Buckling, Postbuckling, and Crippling of Graphite-Epoxy Z-section Stiffeners. *AIAA Journal*, Vol. 30, No. 11, November 1992, pp. 2750-2757.
22. Sridharan, Srinivasan; Zeggane, Madjid; and Starnes, James H., Jr.: Postbuckling Response of Stiffened Composite Cylindrical Shells. *AIAA Journal*, Vol. 30, No. 12, December 1992, pp. 2897-2905.

23. Reddy, J. N.; and Starnes, James H., Jr.: General Buckling of Stiffened Circular Cylindrical Shells According to a Layerwise Theory. *Computers & Structures*, Vol. 49, No. 4, November 1993, pp. 605-616.
24. Noor, Ahmed K.; Starnes, James H., Jr.; and Peters, Jeanne M.: Thermomechanical Buckling and Postbuckling of Multilayered Composite Panels. *Composite Structures*, Vol. 23, 1993, pp. 233-251.
25. Elishakoff, I.; Cai, G. Q.; and Starnes, J. H., Jr.: Non-Linear Buckling of a Column with Initial Imperfections via Stochastic and Non-Stochastic Convex Models. *International Journal of Non-Linear Mechanics*, Vol. 29, No. 1, January 1994, pp. 71-82.
26. Nagendra, S.; Gurdal, Z.; Haftka, R. T. and Starnes, J. H., Jr.: Buckling and Failure Characteristics of Compression-Loaded Stiffened Composite Panels with a Hole. *Composite Structures*, Vol. 28, 1994, pp. 1-17.
27. Elishakoff, I.; Li, Y. W.; and Starnes, James H., Jr.: A Deterministic Method to Predict the Effect of Unknown-But-Bounded Elastic Moduli on the Buckling of Composite Structures. *Computer Methods in Applied Mechanics and Engineering*, Vol. 111, 1994, pp. 155-167.
28. Koiter, W. T.; Elishakoff, I.; Lin, T. W.; and Starnes, J. H., Jr.: Buckling of an Axially Compressed Cylindrical Shell of Variable Thickness. *International Journal of Solids and Structures*, Vol. 31, No. 6, 1994, pp. 797-805.
29. Prasad, Chunchu B.; Ambur, Damodar R.; and Starnes, James H., Jr.: Response of Laminated Composite Plates to Low-Speed Impact by Different Impactors. *AIAA Journal*, Vol. 32, No. 6, June 1994, pp. 1270-1277.
30. Noor, Ahmed K.; Starnes, James H., Jr.; and Peters, Jeanne M.: Thermomechanical Buckling of Multilayered Composite Panels with Cutouts. *AIAA Journal*, Vol. 32, No. 7, July 1994, pp. 1507-1519.
31. Sridharan, Shrinivasan; Zeggane, Majid; and Starnes, James H., Jr.: Mode Interaction Analysis of Stiffened Shells Using "Locally Buckled" Elements. *International Journal of Solids and Structures*, Vol. 31, No. 17, 1994, pp. 2347-2366.
32. Elishakoff, I.; Cai, G. Q.; and Starnes, James H., Jr.: Non-linear Buckling of a Column with Initial Imperfection via Stochastic and Non-stochastic Convex Models. *International Journal of Non-Linear Mechanics*, Vol. 29, No. 1, 1994, pp. 71-82.
33. Ambur, Damodar R.; Starnes, James H., Jr.; and Prasad, C. B.: Low-Speed-Impact Damage-Initiation Characteristics of Selected Laminated Composite Plates. *AIAA Journal*, Vol. 33, No. 10, October 1995, pp. 1919-1925.

34. Elishakoff, I.; Marcus, S.; and Starnes, J. H., Jr.: On Vibrational Imperfection Sensitivity of Augusti's Model Structure in the Vicinity of a Nonlinear Static State. *International Journal of Non-Linear Mechanics*, Vol. 31, No. 2, 1996, pp. 229-236.
35. Librescu, Liviu; Lin, W.; Nemeth, Michael P.; and Starnes, James H., Jr.: Frequency-Load Interaction of Geometrically Imperfect Curved Panels Subjected to Heating. *AIAA Journal*, Vol. 34, No. 1 January 1996, pp. 166-177.
36. Noor, A. K.; Starnes, J. H., Jr.; and Peters, J. P.: Mechanics of Postbuckling of Multilayered Composite Panels with a Cutout. *Composite Structures*, Vol. 30, No. 4, 1995, pp. 369-388.
37. Rezaeepazhand, J.; Simiteses, G. J.; Starnes, J. H., Jr.: Use of Scaled-Down Models for Predicting Vibration Responses of Laminated Plates. *Composite Structures*, Vol. 30, No. 4, 1995, pp. 419-426.
38. Rezaeepazhand, J.; Simiteses, G. J.; Starnes, J. H., Jr.: Design of Scaled Down Models for Stability of Laminated Plates. *AIAA Journal*, Vol. 33, No. 3, March 1995, pp. 515-519.
39. Boitnott, Richard L.; Starnes, James H., Jr.; and Johnson, Eric R.: Nonlinear Response and Failure Characteristics of Pressurized Composite Curved Panels. *Journal of Aerospace Engineering*, ASCE, Vol. 8, No. 3, July 1995, pp. 129-138.
40. Madenci, E.; Ileri, L.; and Starnes, J. H., Jr.: Analysis of Pin-Loaded Holes in Composite Laminates under Combined Bearing-Bypass and Shear Loading. *International Journal of Solids and Structures*, Vol. 32, No. 14, 1995, pp. 2053-2062.
41. Li, Y. W.; Elishakoff, I.; Starnes, J. H., Jr.; and Shinozuke, M.: Nonlinear Buckling of a Structure with Random Imperfection and Random Axial Compression by a Conditional Simulation Technique. *Computers & Structures*, Vol. 56, No. 1, 1995, pp. 59-64.
42. Li, Y. W.; Elishakoff, I.; and Starnes, J. H., Jr.: Axial Buckling of Composite Cylindrical Shells with Periodic Thickness Variation. *Computers & Structures*, Vol. 56, No. 1, 1995, pp. 65-74.
43. Librescu, Liviu; Lin, W.; Nemeth, Michael P.; and Starnes, James H., Jr.: Thermomechanical Postbuckling of Geometrically Imperfect Flat and Curved Panels Taking into Account Tangential Edge Constraints. *Journal of Thermal Stresses*, Vol. 18, 1995, pp. 465-482.
44. Noor, Ahmed K.; Starnes, James H., Jr.; and Peters, Jeanne M.: Nonlinear and Postbuckling Responses of Curved Composite Panels with Cutouts. *Composite Structures*, Vol. 34, No. 2, February 1996, pp. 213-240.

45. Librescu, L.; Lin, W.; Nemeth, M. P.; and Starnes, J. H., Jr.: Vibration of Geometrically Imperfect Panels Subjected to Thermal and Mechanical Loads. *Journal of Spacecraft and Rockets*, Vol. 33, No. 2, March-April 1996, pp. 285-291.
46. Li, Y. W.; Elishakoff, I.; and Starnes, J. H., Jr.: Buckling Mode Localization in a Multi-span Periodic Structure with a Disorder in a Single Span. *Journal of Chaos, Solutions and Fractals*, Vol. 5, No. 6, 1995, pp. 955-969.
47. Elishakoff, I.; Li, Y. W.; and Starnes, J. H., Jr.: Buckling Mode Localization in Elastic Plates due to Misplacement in the Stiffener Location. *Journal of Chaos, Solutions and Fractals*, Vol. 5, No. 8, 1995, pp. 1517-1531.
48. Rezaeepazhand, J.; Simiteses, G. J.; Starnes, J. H., Jr.: Scale Models for Laminated Cylindrical Shells Subjected to Axial Compression. *Composite Structures*, Vol. 34, No. 4, April 1996, pp. 371-379.
49. Li, Y. W.; Elishakoff, I.; Starnes, J. H., Jr.; and Shinozuke, M.: Prediction of Natural Frequency and Buckling Load Variability Due to Uncertainty in Material Properties by Convex Modeling. *Fields Institute Communications*, American Mathematical Society, Vol. 9, 1996, pp. 139-154.
50. Rezaeepazhand, J.; Simiteses, G. J.; Starnes, J. H., Jr.: Design of Scaled Down Models for Predicting Shell Vibration Response. *Journal of Sound and Vibrations*, Vol. 195, No. 2, 1996, pp. 301-311.
51. Zhu, L. P.; Elishakoff, I.; and Starnes, J. H., Jr.: Derivation of Multi-Dimensional Ellipsoidal Convex Model for Experimental Data. *Mathematical Computing and Modeling*, Vol. 24, No. 2, 1996, pp. 103-114.
52. Elishakoff, I.; Li, Y. W.; and Starnes, J. H., Jr.: Imperfection Sensitivity Due to the Elastic Moduli in the Roorda-Koiter Frame. *Journal of Chaos, Solutions and Fractals*, Vol. 7, No. 8, 1996, pp. 1179-1186.
53. Qiu, Zhiping; Elishakoff, I.; and Starnes, James H., Jr.: The Bound Set of Possible Eigenvalues of Structures with Uncertain But Non-Random Parameters. *Journal of Chaos, Solutions & Fractals*, Vol. 7, No. 11, 1996, pp. 1845-1857.
54. Elishakoff, I.; Li, Y. W.; and Starnes, James H., Jr.: Passive Control of Buckling Deformation Via Anderson Localization Phenomenon. *Journal of Chaos, Solutions & Fractals*, Vol. 8, No. 1, 1997, pp. 59-75.
55. Perry, Christine A.; Gurdal, Zafer; and Starnes, James H. Jr.: Minimum-Weight Design of Compressively Loaded Stiffened Panels for Postbuckling Response. *Engineering Optimization*, Vol. 28, 1997, pp. 175-197.

56. Hilburger, M. W.; Waas, A. M.; and Starnes, J. H., Jr.: Modeling the Dynamic Response and Establishing Post-buckling/Post Snap-thru Equilibrium of Discrete Structures via a Transient Analysis. *Journal of Applied Mechanics*, Vol., 64, No. 3, September 1997, pp. 590-595.
57. Noor, Ahmed K.; Starnes, James H., Jr.; and Peters, Jeanne M.: Curved Sandwich Panels Subjected to Temperature Gradient and Mechanical Loads. *Journal of Aerospace Engineering*, Vol. 10, No. 4, October 1997, pp. 143-161
58. Barut, A.; Madenci, E.; Britt, V. O.; and Starnes, J. H., Jr.: Buckling of a Thin, Tension-Loaded, Composite Plate with an Inclined Crack. *Journal of Engineering Fracture Mechanics*, Vol. 58, No. 3, October 1997, pp.233-248.
59. Li, Yi-Wei; Elishakoff, Isaac; Starnes, James H., Jr.; and Bushnell, David: Effect of the Thickness Variation and Initial Imperfection on Buckling of Composite Cylindrical Shells: Asymptotic Analysis and Numerical Results by BOSOR4 and PANDA2. *International Journal of Solids and Structures*, Vol. 34, No. 28, 1997, pp. 3755-3767.
60. Noor, Ahmed K.; Starnes, James H., Jr.; and Peters, Jeanne P.: Thermomechanical Buckling and Postbuckling Responses of Composite Panels with Skewed Stiffeners. *Finite Elements in Analysis and Design*, Vol. 27, 1997, pp.193-214.
61. Harris, Charles E.; Newman, James C., Jr.; Piascik, Robert S.; and Starnes, James H., Jr.: Analytical Methodology for Predicting the Onset of Widespread Fatigue Damage in Fuselage Structure. *Journal of Aircraft*, Vol. 35, No. 2, March-April 1998, pp. 307-317.
62. Venter, Gerhard; Haftka, Raphael T.; and Starnes, James H., Jr.: Construction of Response Surface Approximations for Design Optimization. *AIAA Journal*, Vol. 26, No. 12, December 1998, pp. 2242-2249.
63. Hilburger, Mark W.; Waas, Anthony M. and Starnes, James H., Jr.: Response of Composite Shells with Cutouts and Subjected to Internal Pressure and Axial Compression Loads. *AIAA Journal*, Vol. 37, No. 2, February 1999, pp.232-237.
64. Nemeth, Michael P.; Britt, Vicki O.; Young, Richard D.; Collins, Timothy J.; and Starnes, James H., Jr.: Nonlinear Behavior of the Space Shuttle Superlightweight Liquid-Oxygen Tank Under Prelaunch Loads. *Journal of Spacecraft and Rockets*, Vol. 36, No. 6, November-December 1999, pp. 788-803.
65. Nemeth, Michael P.; Young, Richard D.; Collins, Timothy J.; and Starnes, James H., Jr.: Effects of Welding-Induced Imperfections on the Behavior of the Space Shuttle Superlightweight Tank. *Journal of Spacecraft and Rockets*, Vol. 36, No. 6, November-December 1999, pp. 812-819.

66. Young, Richard D.; Nemeth, Michael P.; Collins, Timothy J.; and Starnes, James H., Jr.: Nonlinear Behavior of the Space Shuttle Superlightweight Tank under Booster Ascent Loads. *Journal of Spacecraft and Rockets*, Vol. 36, No. 6, November-December 1999, pp. 820-827.
67. Nemeth, Michael P.; Young, Richard D.; Collins, Timothy J.; and Starnes, James H., Jr.: Nonlinear Behavior of the Space Shuttle Superlightweight Tank under End-of-Flight Loads. *Journal of Spacecraft and Rockets*, Vol. 36, No. 6, November-December 1999, pp. 828-835.
68. Noor, Ahmed K.; Starnes, James H., Jr.; and Peters, Jeanne M.: Uncertainty Analysis of Composite Structures. *Computer Methods in Applied Mechanics and Engineering*, Vol. 185, Nos. 2-4, May 2000, pp. 413-432.
69. Librescu, L.; Nemeth, M. P.; Starnes, J. H., Jr.; and Lin, W.: Nonlinear Response of Flat and Curved Panels Subjected to Thermomechanical Loading. *Journal of Thermal Stresses*, Vol. 23, No. 6, August 2000, pp. 549-582.
70. Noor, Ahmed K.; Starnes, James H., Jr.; and Peters, Jeanne M.: Uncertainty Analysis of Stiffened Composite Panels. *Composite Structures*, Vol. 51, No. 2, February 2001, pp. 139-158.
71. Park, Oung; Haftka, Raphael T.; Sankar, Bhavani V.; Starnes, James H. Jr.; and Nagendra, Somanath: Analytical-Experimental Correlation of a Stiffened Composite Panel Loaded in Axial Compression. *Journal of Aircraft*, Vol. 38, No. 2, March-April 2001, pp. 379-387.
72. Nemeth, Michael P.; Young, Richard D.; Collins, Timothy J.; and Starnes, James H., Jr.: Effects of Initial Geometric Imperfections on the Non-linear Response of the Space Shuttle Superlightweight Liquid-Oxygen Tank. *International Journal of Non-Linear Mechanics*, Vol. 37, Issues 4-5, June 2002, pp. 723-744.
73. Hilburger, Mark W.; and Starnes, James H., Jr.: Effects of Imperfections on the Buckling Response of Compression-Loaded Composite Shells. *International Journal of Non-Linear Mechanics*, Vol. 37, Issues 4-5, June 2002, pp. 623-643.
74. Corona, Edmundo; Waters, W. Allen, Jr.; and Starnes, James H., Jr.: Collapse of Rectangular Aluminum Plates with Axial Cracks. *AIAA Journal*, Vol. 40, No. 8, August 2002, pp. 1665-1672.
75. Harris, Charles E.; Starnes, James H., Jr.; and Shuart, Mark S.: Assessment of the State-of-the-Art for the Design and Manufacturing of Large Composite Structures. *Journal of Aircraft*, Vol. 39, No. 4, July-August, 2002, pp. 545-560.
76. Arbocz, Johann; and Starnes, James H., Jr.: Future Directions and Challenges in Shell Stability Analysis. *Journal of Thin-Walled Structures*, Vol. 40, 2002, pp. 729-754.

77. Noor, Ahmed K.; Starnes, James H., Jr.; and Peters, Jeanne M.: Thermomechanical Response Variability of Stiffened Composite Panels. *ASCE Journal of Aerospace Engineering*, Vol. 15, No. 4, October 2002, pp. 154-164.
78. Keesecker, Amy L.; Davila, Carlos G.; Johnson, Eric R.; and Starnes, James H., Jr.: Crack Path Bifurcation at a Tear Strap in a Pressurized Shell. *Computers and Structures*, Vol. 81, No. 16, 2003, pp. 1633-1642.
79. Hilburger, Mark W.; and Starnes, James H., Jr.: Buckling Behavior of Compression-Loaded Composite Cylindrical Shells with Reinforced Cutouts. *International Journal of Non-Linear Mechanics*, Vol. 40, No. 7, 2005, pp. 1005-1023.

Referenceable Oral Presentations and Conference Papers

(*Indicates presenter of paper)

1. Haftka, Raphael T.; Starnes, James H., Jr.*; and Barton, Furman W.: A Comparison of Two Types of Structural Optimization Procedures for Satisfying Flutter Requirements. Presented at the AIAA/ASME/SAE 15th Structures, Structural Dynamics, and Materials Conference, Las Vegas, Nevada, April 17-19, 1974. AIAA Paper No. 74-405, 1974.
2. Stephens, Wendell B.*; Starnes, James H., Jr.; and Almroth, B. O.: Collapse of Long Cylindrical Shells under Combined Bending and Pressure Loads. Presented at the AIAA/ASME/SAE 15th Structures, Structural Dynamics, and Materials Conference, Las Vegas, Nevada, April 17-19, 1974. AIAA Paper No. 74-407.
3. Haftka, Raphael T.; and Starnes, James H., Jr.*: Application of a Quadratic Extended Interior Penalty Function for Structural Optimization. Presented at the AIAA/ASME/SAE 16th Structures, Structural Dynamics, and Materials Conference, Denver, Colorado, May 27-29, 1975. AIAA Paper No. 75-764, 1975.
4. Starnes, James H., Jr.*; and Haftka, Raphael T.: Preliminary Design of Composite Wings for Buckling Strength and Displacement Constraints. Presented at the AIAA/ASME 19th Structures, Structural Dynamics, and Materials Conference, Bethesda, Maryland, April 3-5, 1978. AIAA Paper No. 78-466, 1978.
5. Rhodes, Marvin D.; Williams, Jerry G.; and Starnes, James H., Jr.: Effect of Impact Damage on the Compression Strength of Filamentary-Composite Hat-Stiffened Panels. The Science of Advanced Materials and Process Engineering Series, Vol. 23, *Selected Applications of Materials for Products and Energy*, pp. 300-319, SAMPE, 1978. Proceedings of the 23rd National SAMPE Symposium and Exhibition, Disneyland Hotel, Anaheim, CA, May 2-4, 1978.
6. Starnes, James H., Jr.: Compression Strength of Graphite-Epoxy Structural Components with Cutouts. Proceedings of the Fifth Annual Mechanics of Composites Review, AFWAL-TR-80-4020, U.S. Air Force, January 1980, pp. 125-133.
7. Starnes, James H., Jr.*; and Haftka, Raphael T.: Preliminary Design of Composite Wing-Box Structures for Global Damage Tolerance. Proceedings of the AIAA/ASME/ASCE/AHS 21st Structures, Structural Dynamics, and Materials Conference, Seattle, Washington, May 12-14, 1980. AIAA Paper No. 80-0755.
8. Starnes, James H., Jr.: Buckling and Postbuckling Research on Flat and Curved Composite Panels. Proceedings of the Second Industry Review of the NASA

Aircraft Energy Efficiency (ACEE) Composites Program, Seattle, WA, August 11-13, 1980. NASA CP 2142, August 1980, pp. 35-78.

9. Starnes, James H., Jr.*; and Rouse, Marshall: Postbuckling Strength of Stiffened Flat 24-Ply Graphite-Epoxy Panels Loaded in Compression. Proceedings of the Sixth Annual Mechanics of Composites Review, AFWAL-TR-81-4001, U.S. Air Force, February 1981, pp. 106-112.
10. Starnes, James H., Jr.; and Rouse, Marshall*: Postbuckling and Failure Characteristics of Selected Flat Rectangular Graphite-Epoxy Plates Loaded in Compression. Proceedings of the AIAA/ASME/ASCE/AHS 22nd Structures, Structural Dynamics, and Materials Conference, Atlanta, Georgia, April 6-8, 1981. AIAA Paper No. 81-0543.
11. Starnes, James H., Jr.; Knight, Norman F., Jr.*; and Rouse, Marshall: Postbuckling Behavior of Selected Flat Stiffened Graphite-Epoxy Panels Loaded in Compression. Proceedings of the AIAA/ASME/ASCE/AHS 23rd Structures, Structural Dynamics, and Materials Conference, New Orleans, LA, May 10-12, 1982. AIAA Paper No. 82-0777.
12. Starnes, James H., Jr.*; and Williams, Jerry G.: Failure Characteristics of Graphite-Epoxy Structural Components Loaded in Compression. Presented at the 1st International Union of Theoretical and Applied Mechanics Symposium on Mechanics of Composite Materials, Blacksburg, VA, August 16-19, 1982.
13. Starnes, James H., Jr.*; Rouse, Marshall; Stein, Manuel; and Knight, Norman F., Jr.: Postbuckling Behavior of Graphite-Epoxy Panels Loaded in Compression. Eighth Annual AFWAL Mechanics of Composites Review, Dayton, OH, October 5-7, 1982. AFWAL-TR-83-4005, April 1983, pp. 1-12.
14. Boitnott, R. L.*; Starnes, J. H., Jr.; and Johnson, E. R.: Nonlinear Response of Internally Pressurized Graphite-Epoxy Cylindrical Panels. Proceedings of the AIAA/ASME/ASCE/AHS 25th Structures, Structural Dynamics and Materials Conference, Palm Springs, CA, May 14-16, 1984. AIAA Paper No. 84-0955.
15. Knight, Norman F., Jr.*; and Starnes, J. H., Jr.: Postbuckling Behavior of Compression-Loaded Graphite-Epoxy Cylindrical Panels with Circular Holes. Invited Paper in honor of B. O. Almroth for the ASME Joint Pressure Vessels and Piping/Applied Mechanics Conference, San Antonio, TX, June 17- 21, 1984.
16. Starnes, James H., Jr.*; Dickson, John N.; and Rouse, Marshall: Postbuckling Behavior of Graphite-Epoxy Panels. Presented at the NASA ACEE Composite Structures Technology Conference, Seattle, WA, August 13-16, 1984. In NASA CP-2321, August 1984, pp. 137-159.

17. Haftka, Raphael T.*; and Starnes, James H., Jr.: Use of Optimum Stiffness Tailoring to Improve the Compressive Strength of Composite Plates with Holes. Presented at the AIAA/ASME/ASCE/AHS 26th Structures, Structural Dynamics and Material Conference, Orlando, FL, April 15-17, 1985. AIAA Paper No. 85-0721-CP.
18. Knight, Norman F., Jr.; and Starnes, James H., Jr.*: Postbuckling Behavior of Selected Curved Stiffened Graphite-Epoxy Panels Loaded in Compression. Presented at the AIAA/ASME/ASCE/AHS 26th Structures, Structural Dynamics and Materials Conference, Orlando, FL, April 15-17, 1985. AIAA Paper No. 85-0768-CP.
19. Boitnott, Richard L.*; Johnson, Eric R.; and Starnes, James H., Jr.: A Nonlinear Analysis of Infinitely Long Graphite-Epoxy Cylindrical Panels Loaded with Internal Pressure. Presented at the AIAA/ASME/ASCE/AHS 26th Structures, Structural Dynamics and Materials Conference, Orlando, FL, April 15-17, 1985. AIAA Paper No. 85-0770-CP.
20. Dickson, John N.*; Biggers, Sherrill B.; and Starnes, James H., Jr.: Stiffener Attachment Concepts for Graphite-Epoxy Panels Designed for Postbuckling Strength. Presented at the 7th DoD/NASA Conference on Fibrous Composites in Structural Design, Denver, CO, June 17-20, 1985. AFWAL-TR-85-3094, June 1985, pp. v(a)95-v(a)109.
21. Knight, Norman F., Jr.; Starnes, James H., Jr.; and Waters, W. Allen*: Postbuckling Behavior of Selected Graphite-Epoxy Cylindrical Panels Loaded in Axial Compression. Presented at the AIAA/ASME/ASCE/AHS 27th Structures, Structural Dynamics and Materials Conference, San Antonio, TX, May 19-21, 1986. AIAA Paper No. 86-0881-CP.
22. Loup, Douglas C.*; Hyer, Michael W.; and Starnes, James H., Jr.: Stiffener-Skin Interactions in Pressure-Loaded Composite Panels. Presented at the AIAA/ASME/ASCE/AHS 27th Structures, Structural Dynamics and Materials Conference, San Antonio, TX, May 19-21, 1986. AIAA Paper No. 86-0917-CP.
23. Curry, James M.*; Johnson, Eric R.; and Starnes, James H., Jr.: Effect of Dropped Plies on the Strength of Graphite-Epoxy Laminates. Presented at the AIAA/ASME/ASCE/AHS 28th Structures, Structural Dynamics and Materials Conference, Monterey, CA, April 6-8, 1987. AIAA Paper No. 87-0874-CP.
24. Card, Michael F.*; and Starnes, James H., Jr.: Current Research in Composite Structures at NASA Langley Research Center. International Conference on Composite Materials and Structures, Indian Institute of Technology, Madras, India. In Composite Materials and Structures, K. A. V. Pandalai, Ed., Indian Academy of Science, Bangalore, Vol. II, 1988, pp. 5-26. Also in Sadhana-

- Academy Proceedings in Engineering Science, Indian Academy of Science, Vol. II, 1987, pp. 273-294.
25. Swanson, Gary D.*; Gurdal, Zafer; and Starnes, James H., Jr.: Structural Efficiency Study of Graphite-Epoxy Aircraft Rib Structures. Presented at the AIAA/ASME/ASCE/AHS/ASC 29th Structures, Structural Dynamics and Materials Conference, Williamsburg, VA, April 18-20, 1988. AIAA Paper No. 88-2218-CP.
 26. Bonanni, David L.*; Johnson, Eric R.; and Starnes, James H., Jr.: Local Crippling of Thin-Walled Graphite-Epoxy Stiffener Sections. Presented at the AIAA/ASME/ASCE/AHS/ASC 29th Structures, Structural Dynamics and Materials Conference, Williamsburg, VA, April 18-20, 1988. AIAA Paper No. 88-2251-CP.
 27. Noor, Ahmed K.*; Starnes, James H., Jr.; and Waters, W. Allen, Jr.: Numerical and Experimental Simulations of the Postbuckling Response of Laminated Anisotropic Panels. Presented at the AIAA/ASME/AHS/ASC 31st Structures, Structural Dynamics, and Materials Conference, Long Beach, CA, April 2-4, 1990. AIAA Paper No. 90-0964.
 28. Starnes, James H., Jr.: Comparison of Analysis and Test Results for Composite Structures. Presented at the AGARD 70th Structures and Materials Panel Meeting Workshop on Analytical Qualification of Aircraft Structures, Sorrento, Italy, April 2-6, 1990.
 29. Davis, John G., Jr.*; Starnes, James H., Jr.; and Johnston, Norman J.: Advanced Composite Research and Development for Transport Aircraft. Presented at the 17th Congress of the International Council of the Aeronautical Sciences, Stockholm, Sweden, September 10-14, 1990.
 30. Weiland, T.*; Morton, J.; and Starnes, James H., Jr.: Scale Effects in Buckling, Postbuckling and Crippling of Graphite-Epoxy Z-Section Stiffeners. Presented at the AIAA/ASME/ASCE/AHS/ASC 32nd Structures, Structural Dynamics and Materials Conference, Baltimore, MD, April 8-10, 1991. AIAA Paper No. 91-0912.
 31. Starnes, James H., Jr.* and Shuart, Mark J.: Behavior of Composite Structures Subjected to Compressive Loading. Presented at the AGARD 73rd Structures and Materials Panel Meeting Workshop on the Utilization of Advanced Composites in Military Aircraft, San Diego, CA, October 7-8, 1991.
 32. Starnes, James H., Jr.* and Camarda, Charles J.: Analysis and Design Technology for High-Speed Aircraft Structures. Presented at the NASA/UVA Specialty Workshop on Computational Structures Technology for Airframes, Hampton, VA, September 4-5, 1991. NASA CP 3142, 1992, pp. 137-172.

33. Starnes, James H., Jr.* and Shuart, Mark J.: Composite Fuselage Shell Structures Research at NASA Langley Research Center. Presented at the Ninth DoD/NASA/FAA Conference on Fibrous Composites in Structural Design, Lake Tahoe, NV, November 4-7, 1991. NASA CP 3154, 1992, pp. 57-83.
34. Starnes, James H., Jr.* and Britt, Vicki O.: Nonlinear Stiffened Shell Research at NASA Langley Research Center for Damaged Fuselage Structures. Presented at the International Conference on Aging Aircraft and Structural Airworthiness, Washington, DC, November, 19-21, 1991. NASA CP 3160, 1992, pp. 203-220.
35. Noor, Ahmed K.*; Starnes, James H., Jr. and Peters, Jeanne M.: Thermomechanical Buckling and Postbuckling of Multilayered Composite Panels. Presented at the AIAA/ASME/ASCE/AHS/ASC 33rd Structures, Structural Dynamics and Materials Conference, Dallas, TX, April 13-15, 1992. AIAA Paper No. 92-2541.
36. Elishakoff, Isaac*; Arbocz, Johann; and Starnes, James H., Jr.: Buckling of Stiffened Shells with Random Initial Imperfections, Thickness and Boundary Conditions. Presented at the AIAA/ASME/ASCE/AHS/ASC 33rd Structures, Structural Dynamics and Materials Conference, Dallas, TX, April 13-15, 1992. AIAA Paper No. 92-2233.
37. Starnes, James H., Jr.* and Britt, Vicki O.: Nonlinear Analysis of Stiffened Fuselage Shells with Local Damage. Presented at the International Workshop on Structural Integrity of Aging Airplanes, Atlanta, GA, March 31- April 2, 1992.
38. Starnes, James H., Jr.: Advanced Composites Technology Research at NASA Langley Research Center. Presented at the American Society For Composites Seventh Technical Conference on Composite Materials, University Park, PA, October 13-15, 1992.
39. Nagendra, S.; Gurdal, Z.; Haftka, R. T.*; and Starnes, J. H., Jr.: Buckling and Failure Characteristics of Compression Loaded Stiffened Composite Panels with a Hole. Proceedings of the American Society for Composites Seventh Technical Conference, University Park, PA, October 13-15, 1992, pp. 650-661.
40. Prasad, C. B.; Ambur, D. R.*; and Starnes, James H., Jr.: Response of Laminated Composite Plates to Low-Speed Impact by Airgun-Propelled and Dropped-Weight Impactors. Presented at the AIAA/ASME/ASCE/AHS/ASC 34th Structures, Structural Dynamics and Materials Conference, La Jolla, CA, April 19-21, 1993. AIAA Paper No. 93-1402.
41. Noor, Ahmed K.; Starnes, James H., Jr.*; and Peters, Jeanne M.: Thermomechanical Buckling of Multilayered Composite Panels with Cutouts. Presented at the AIAA/ASME/ASCE/AHS/ASC 34th Structures, Structural

- Dynamics and Materials Conference, La Jolla, CA, April 19-21, 1993. AIAA Paper No. 93-1336.
42. Librescu, L.*; Chandiramani, N.; Nemeth, M. P.; and Starnes, J. H., Jr.: Postbuckling of Laminated Flat and Curved Panels under Combined Thermal and Mechanical Loadings. Presented at the AIAA/ASME/ASCE/AHS/ASC 34th Structures, Structural Dynamics and Materials Conference, La Jolla, CA, April 19-21, 1993. AIAA Paper No. 93-1563.
 43. Ambur, Damodar R.*; Starnes, James H., Jr.; and Prasad, Chunchu B.: Influence of Impact Parameters on the Response of Laminated Composite Plates. Presented at the ASTM Fifth Symposium on Composite Materials, Atlanta, GA, May 4-7, 1993.
 44. Ambur, Damodar R.*; Starnes, James H., Jr.; and Prasad, Chunchu B.: Influence of Large Deformations and Transverse Shear Effects on the Low-Speed Impact Response on Graphite-Epoxy Plates. Presented at the Ninth International Conference on Composite Materials, Madrid, Spain, July 12-16, 1993. *Composites Properties and Applications*, Vol. 5, July 1993, pp. 456-464.
 45. Fuchs, Hannes P.*; Starnes, James H., Jr.; and Hyer, Michael W.: Prebuckling and Collapse Response of Thin-Walled Composite Cylinders Subjected to Bending Loads. Presented at the Ninth International Conference on Composite Materials, Madrid, Spain, July 12-16, 1993. *Composites Properties and Applications*, Vol. 6, July 1993, pp. 410-417.
 46. Shridharan, Srinivasan*; and Starnes, James H., Jr.: Mode Interaction in Stiffened Composite Panels. Presented at the First Joint ASCE/ASME/SES Meeting, Charlottesville, VA, June 6-9, 1993.
 47. Perry, Christine A.*; Gurdal, Zafer; and Starnes, James H., Jr.: Minimum Weight Design of Compressively Loaded Stiffened Panels for Postbuckling Response. Presented at the First Joint ASCE/ASME/SES Meeting, Charlottesville, VA, June 6-9, 1993. *Mechanics of Composite Materials - Nonlinear Effects*, Hyer, M. W., ed., ASME AMD-Vol. 159, June 1993, pp. 71-80.
 48. Librescu, L.*; Lin, W.; Nemeth, M. P.; and Starnes, J. H., Jr.: Classical Versus Non-Classical Postbuckling Behavior of Laminated Composite Panels Under Complex Loading Conditions. Presented at the First Joint ASCE/ASME/SES Meeting, Charlottesville, VA, June 6-9, 1993.
 49. Harris, Charles E.*; and Starnes, James H., Jr.: Analytical Methodology to Predict the Residual Strength and Fatigue Life of Stiffened Shell Structures. Presented at the 5th International Conference on Structural Airworthiness of New and Aging Aircraft, Hamburg, Germany, June 16-18, 1993. Published in *Advanced Structural Integrity Analysis Methodology for Airframe Structures*,

- proceedings of the 5th International Conference on Structural Airworthiness of New and Aging Aircraft, DGLR-Bericht 93-02, Hamburg, Germany, 1993, pp. 151-156.
50. Koiter, W. T.; Elishakoff, I.*; Lin, T. W.; and Starnes, J. H., Jr.: Buckling of an Axially Compressed Cylindrical Shell of Variable Thickness. Presented at the 1993 ASME Winter Annual Meeting, New Orleans, LA, November 28-December 3, 1993. PVP-Vol. 269/NE-Vol. 13, Recent Advances in Structural Mechanics, ASME 1993, pp. 23-28.
 51. Elishakoff, I.*; Cai, G. Q.; and Starnes, James H., Jr.: Probabilistic and Convex Models of Uncertainty in Buckling of Structures. Proceedings of ICOSSAR'93 - The 6th International Conference on Structural Safety and Reliability, Innsbruck, Austria, August 9-13, 1993.
 52. Young, Richard D.*; Starnes, James H., Jr.; and Hyer, Michael W.: Effects of Skewed Stiffeners and Anisotropic Skins on the Response of Compression-Loaded Composite Panels. Proceedings of the Tenth DoD/NASA/FAA Conference on Fibrous Composites in Structural Design, Hilton Head, SC, November 1-4, 1993. Naval Air Warfare Center Report No. NAWCADWAR-94096-60, Vol. I, April 1994, pp. II-109 to II-123.
 53. Davis, John G., Jr.*; Starnes, James H. Jr.; and Dexter, H. Benson: NASA ACT Status and Plans. Proceedings of the Tenth DoD/NASA/FAA Conference on Fibrous Composites in Structural Design, Hilton Head, SC, November 1-4, 1993. Naval Air Warfare Center Report No. NAWCADWAR-94096-60, Vol. I, April 1994, pp. IV-3 to IV-58.
 54. Librescu, L.*; Lin, W.; Nemeth, Michael P.; and Starnes, James H., Jr.: Vibration of Geometrically Imperfect Laminated Flat and Shallow Curved Panels Subjected to Heating and to a System of Mechanical Loadings. Proceedings of the Tenth DoD/NASA/FAA Conference on Fibrous Composites in Structural Design, Hilton Head, SC, November 1-4, 1993. Naval Air Warfare Center Report No. NAWCADWAR-94096-60, Vol. II, April 1994, pp. IX-51 to IX-66.
 55. Sridharan, Shrinivasan*; and Starnes, James H., Jr.: Mode Interaction Analysis of Stiffened Shells Using "Locally Buckled" Elements. Presented at the AIAA/ASME/ASCE/AHS/ASC 35th Structures, Structural Dynamics and Materials Conference, Hilton Head, SC, April 18-20, 1994. AIAA Paper No. 94-1338.
 56. Koiter, Warner T.; Elishakoff, Isaac*; Li, Y. W.; and Starnes, James H., Jr.: Buckling of an Axially Compressed Imperfect Cylindrical Shell of Variable Thickness. Presented at the AIAA/ASME/ASCE/AHS/ASC 35th Structures, Structural Dynamics and Materials Conference, Hilton Head, SC, April 18-20, 1994. AIAA Paper No. 94-1339.

57. Librescu, Liviu*; Lin, W.; Nemeth, Michael P.; and Starnes, James H., Jr.: Effects of a Thermal Field on Frequency-Load Interaction of Geometrically Imperfect Shallow Curved Panels. Presented at the AIAA/ASME/ASCE/AHS/ASC 35th Structures, Structural Dynamics and Materials Conference, Hilton Head, SC, April 18-20, 1994. AIAA Paper No. 94-1342.
58. Noor, Ahmed K.*; Starnes, James H., Jr.; and Peters, Jeanne M.: Thermomechanical Postbuckling of Multilayered Composite Panels with Cutouts. Presented at the AIAA/ASME/ASCE/AHS/ASC 35th Structures, Structural Dynamics and Materials Conference, Hilton Head, SC, April 18-20, 1994. AIAA Paper No. 94-1367.
59. Ambur, Damodar R.*; Starnes, James H., Jr.; and Prasad, C. B.: Low-Speed-Impact Damage-Initiation Studies for Selected Laminated Composite Plates. Presented at the AIAA/ASME/ASCE/AHS/ASC 35th Structures, Structural Dynamics and Materials Conference, Hilton Head, SC, April 18-20, 1994. AIAA Paper No. 94-1402.
60. Ambur, Damodar R.*; Starnes, James H., Jr.; and Waters, W. Allen, Jr.: Effects of Low-Speed Impact Damage on the Compression Strength of a Graphite-Epoxy Laminated Plate with a Skewed Thickness Taper. Presented at the AIAA/ASME/ASCE/AHS/ASC 35th Structures, Structural Dynamics and Materials Conference, Hilton Head, SC, April 18-20, 1994. AIAA Paper No. 94-1403.
61. Ragon, Scott A.*; Gurdal, Zafer; and Starnes, James H., Jr.: Optimization of Composite Box-Beam Structures Including the Effects of Subcomponent Interaction. Presented at the AIAA/ASME/ASCE/AHS/ASC 35th Structures, Structural Dynamics and Materials Conference, Hilton Head, SC, April 18-20, 1994. AIAA Paper No. 94-1410.
62. Fuchs, Hannes P.*; Starnes, James H., Jr.; and Hyer, Michael W.: Numerical and Experimental Investigation of the Collapse Response of Thin-Walled Graphite-Epoxy Cylindrical Shells Loaded in Bending. Presented at the AIAA/ASME/ASCE/AHS/ASC 35th Structures, Structural Dynamics and Materials Conference, Hilton Head, SC, April 18-20, 1994. AIAA Paper No. 94-1608.
63. Starnes, James H., Jr.*; Britt, Vicki O.; Young, Richard D.; Rankin, Charles C.; Shore, Charles P.; and Bains, Nancy Jane B.: Nonlinear Analysis of Damaged Stiffened Fuselage Shells Subjected to Combined Loads. Presented at the FAA/NASA International Symposium on Advance Structural Integrity Methods for Airframe Durability and Damage Tolerance, Hampton, VA, May 4-6, 1994. NASA CP 3274, Part 2, pp. 1045-1075, September 1994.

64. Finn, S. R.; Dickson, J. N.; Vause, R. F.; Carbery, D. J.; Bowman, L. M.; Dost, E. F.; and Starnes, J. H., Jr.*: Analysis of a Pathfinder Shell Subjected to Internal Pressure and Mechanical Loads. Presented at the 5th NASA/DoD Advanced Composites Technology Conference, Seattle, WA, August 22-25, 1994. NASA CP 3294, Vol. 1, Part 1, May 1995, pp. 33-72.
65. Ambur, D. R.; Rouse, M.; Starnes, J. H., Jr.*; and Shuart, M. J.: Facilities for Combined Loads Testing of Aircraft Structures to Satisfy Structural Technology Development Requirements. Presented at the 5th NASA/DoD Advanced Composites Technology Conference, Seattle, WA, August 22-25, 1994. NASA CP 3294, Vol. 1, Part 1, May 1995, pp. 73-91.
66. Li, Y. W.; Elishakoff, I.*; and Starnes, J. H., Jr.: Axial Buckling of Composite Cylindrical Shells with Periodic Thickness Variation. Presented at the 1994 ASME Winter Annual Meeting, Chicago, IL, November 6-11, 1994. AD-Vol. 41/PVP-Vol. 293, Buckling and Postbuckling of Composite Structures, ASME 1994, pp. 95-114.
67. Librescu, L.*; Lin, W.; Nemeth, M. P.; and Starnes, J. H., Jr.: Effects of Tangential Edge Constraints on the Postbuckling Behavior of Flat and Curved Panels Subjected to Thermal and Mechanical Loads. Presented at the 1994 ASME Winter Annual Meeting, Chicago, IL, November 6-11, 1994. AD-Vol. 41/PVP-Vol. 293, Buckling and Postbuckling of Composite Structures, ASME 1994, pp. 55-71.
68. Fuchs, H. P.*; Starnes, J. H., Jr.; and Hyer, M. W.: Numerical and Experimental Investigation of the Collapse Response of a Quasi-Isotropic Graphite-Epoxy Cylindrical Shells Subjected to Bending and Internal Pressure Loads. Presented at the 1994 ASME Winter Annual Meeting, Chicago, IL, November 6-11, 1994. AD-Vol. 41/PVP-Vol. 293, Buckling and Postbuckling of Composite Structures, ASME 1994, pp. 73-94.
69. Librescu, L.*; Lin, W.; Nemeth, M. P.; and Starnes, J. H., Jr.: Postbuckling of Shear Deformable Laminated Doubly Curved Shallow Panels Under Combined Thermal and Mechanical Loadings. Presented at the First University/Industry Symposium on High Speed Civil Transport Vehicles, Greensboro, NC, December 3-7, 1994.
70. Harris, C. E.; Starnes, James H., Jr.; and Heyman, Joseph S.: Advanced Analysis Methods and Nondestructive Inspection Technology under Development in the NASA Airframe Structural Integrity Program. Presented at the SAE Finishing, Maintenance and Repair Conference and Exposition, Paper No. 941247, 1994.
71. Perry, Christine A.*; Gurdal, Zafer; and Starnes, James H. Jr.: Minimum-Weight Design of Compressively Loaded Stiffened Panels for Postbuckling Response.

- Presented at the AIAA/ASME/ASCE/AHS/ASC 36th Structures, Structural Dynamics and Materials Conference, New Orleans, LA, April 10-13, 1995. AIAA Paper No. 95-1162.
72. Starnes, James H., Jr.*; Britt, Vicki O.; and Rankin, Charles C.: Nonlinear Response of Damaged Stiffened Shells Subjected to Combined Internal Pressure and Mechanical Loads. Presented at the AIAA/ASME/ASCE/AHS/ASC 36th Structures, Structural Dynamics and Materials Conference, New Orleans, LA, April 10-13, 1995. AIAA Paper No. 95-1462.
 73. Noor, Ahmed K.*; Starnes, James H., Jr.; and Peters, Jeanne M.: Nonlinear and Postbuckling Responses of Curved Composite Panels with Cutouts. Presented at the AIAA/ASME/ASCE/AHS/ASC 36th Structures, Structural Dynamics and Materials Conference, New Orleans, LA, April 10-13, 1995. AIAA Paper No. 95-1412.
 74. Ambur, Damodar R.*; Starnes, James H., Jr.; Stourmbos, T.; and Kapania, Rakesh: Effects of Large Deformations on the Impact Response of Flat and Curved Graphite-Epoxy Panels. Presented at the AIAA/ASME/ASCE/AHS/ASC 36th Structures, Structural Dynamics and Materials Conference, New Orleans, LA, April 10-13, 1995. AIAA Paper No. 95-1205.
 75. Harris, Charles E.; Starnes, James H., Jr.*; and Newman, James C., Jr.: Development of Advanced Structural Analysis Methodologies for Predicting Widespread Fatigue Damage in Aircraft Structures. Presented at the FAA/NASA Sixth International Conference on Continued Airworthiness of Aircraft Structures, Atlantic City, NJ, June 26-29, 1995. DOT/FAA/AR-95-86, Catherine A. Bigelow, Editor, December 1995, pp. 139-164. Also, NASA TM 110187, August 1995.
 76. Harris, Charles. E.*; Newman, James C., Jr.; Starnes, James H., Jr.; and Piascik, Robert S.: Analytical Methodology to Predict the Onset of Widespread Fatigue Damage in Airframe Structure. Presented at the Air Force 3rd Aging Aircraft Conference, Wright-Patterson AFB, OH, September 26-28, 1995. Proceedings of the 1995 USAF Structural Integrity Program Conference, WL-TR-96-4093, Waggoner, G. K.; Lincoln, J. W.; and Rudd, J. I., eds. August 1996, pp. 279-306.
 77. Harris, Charles E.*; Newman, James C., Jr.; and Starnes, James H., Jr.: Analytical Methodology to Predict the Onset of Widespread Fatigue Damage in Airframe Structure. Presented at the 1995 USAF Structural Integrity Program Conference, San Antonio, TX, November 28-30, 1995.
 78. Elishakoff, I.*; Li, Y. W.; and Starnes, J. H., Jr.: Localization Phenomenon of Buckling Mode in Stiffened Multi-Span Elastic Plates. Presented at the 1995 ASME International Mechanical Engineering Congress and Exposition, San

- Francisco, CA, November 12-17, 1994. PVP-Vol. 321/NE-Vol. 18, Recent Advances in Solids and Structures - 1995, ASME 1995, pp. 153-164.
79. Starnes, James H., Jr.*; Britt, Vicki O.; Rose, Cheryl A.; and Rankin, Charles, C.: Nonlinear Response and Residual Strength of Damaged Stiffened Shells Subjected to Combined Loads. Presented at the AIAA/ASME/ASCE/AHS/ASC 37th Structures, Structural Dynamics, and Materials Conference, Salt Lake City, UT, April 15-17, 1996. AIAA Paper No. 96-1555.
 80. Rose, Cheryl A.*; and Starnes, James H., Jr.: Interlaminar Stresses in Composite Stiffened Panels. Presented at the AIAA/ASME/ASCE/AHS/ASC 37th Structures, Structural Dynamics, and Materials Conference, Salt Lake City, UT, April 15-17, 1996. AIAA Paper No. 96-1497.
 81. Nemeth, Michael P.*; Britt, Vicki, O.; Collins, Timothy J.; and Starnes, James H., Jr.: Nonlinear Analysis of the Space Shuttle Super-Lightweight External Fuel Tank. Presented at the AIAA/ASME/ASCE/AHS/ASC 37th Structures, Structural Dynamics, and Materials Conference, Salt Lake City, UT, April 15-17, 1996. AIAA Paper No. 96-1552.
 82. Noor, Ahmed K.*; Starnes, James H., Jr.; and Peters, Jeanne M.: Thermomechanical Buckling and Postbuckling Responses for Composite Panels with Skewed Stiffeners. Presented at the AIAA/ASME/ASCE/AHS/ASC 37th Structures, Structural Dynamics, and Materials Conference, Salt Lake City, UT, April 15-17, 1996. AIAA Paper No. 96-1636.
 83. Harris, Charles E.; Newman, James C., Jr.*; Piascik, Robert S.; and Starnes, James H., Jr.: Analytical Methodology for Predicting the Onset of Widespread Fatigue Damage in Fuselage Structure. Presented at the FAA-NASA Symposium on Continued Airworthiness of Aircraft Structures, Atlanta, GA, August 28-30, 1996. DOT/FAA/AR-97/2, Vol. I, Compiled by Catherine A. Bigelow, July 1997, pp.63-88.
 84. Starnes, James H., Jr.*; Rose, Cheryl A.; and Rankin, Charles C.: Effects of Combined Loads on the Nonlinear Response of Stiffened Shells with Long Cracks. Presented at the FAA-NASA Symposium on Continued Airworthiness of Aircraft Structures, Atlanta, GA, August 28-30, 1996. DOT/FAA/AR-97/2, Vol. I, Compiled by Catherine A. Bigelow, July 1997, pp.183-196.
 85. Venter, Gerhard; Haftka, Raphael. T.*; and Starnes, James H., Jr.: Construction of Response Surfaces for Design Optimization Applications. Presented at the 6th AIAA/USAF/NASA/ISSMO Symposium on Multidisciplinary Analysis and Optimization, Bellevue, WA, September 4-6, 1996. AIAA Paper No. 96-4040.
 86. Starnes, James H., Jr.*; and Rose, Cheryl A.: Nonlinear Response of Thin Cylindrical Shells with Longitudinal Cracks and Subjected to Internal Pressure

- and Axial Compression Loads. Presented at the AIAA/ASME/ASCE/AHS/ASC 38th Structures, Structural Dynamics, and Materials Conference, Kissimmee, FL, April 7-11, 1997. AIAA Paper No. 97-1144.
87. Mikulas, Martin M.*; Card, Michael F.; Peterson, James P.; and Starnes, James H., Jr.: Manuel Stein's Five Decades of Structural Mechanics Contributions (1944-1988). Presented at the AIAA/ASME/ASCE/AHS/ASC 38th Structures, Structural Dynamics, and Materials Conference, Kissimmee, FL, April 7-11, 1997. AIAA Paper No. 97-1073.
 88. Nemeth, Michael P.*; and Starnes, James H., Jr.: The NASA Monographs on Shell Stability Design Recommendations - A Review and Suggested Improvements. Presented at the AIAA/ASME/ASCE/ AHS/ASC 38th Structures, Structural Dynamics, and Materials Conference, Kissimmee, FL, April 7-11, 1997. AIAA Paper No. 97-1302.
 89. Ambur, Damodar R.*; and Starnes, James H., Jr.: Nonlinear Response and Damage-Initiation Characteristics of Curved Composite Plates Subjected to Low-Speed Impact. Presented at the AIAA/ASME/ASCE/AHS/ASC 38th Structures, Structural Dynamics, and Materials Conference, Kissimmee, FL, April 7-11, 1997. AIAA Paper No. 97-1058.
 90. Noor, Ahmed K.*; Starnes, James H., Jr.; and Peters, Jeanne M.: Analysis of Curved Sandwich Panels Subjected to Combined Temperature Gradient and Mechanical Loads. Presented at the AIAA/ASME/ASCE/AHS/ASC 38th Structures, Structural Dynamics, and Materials Conference, Kissimmee, FL, April 7-11, 1997. AIAA Paper No. 97-1246.
 91. Knight, Norman F., Jr.*; and Starnes, James, H., Jr.: Developments in Cylindrical Shell Stability Analysis. Presented at the AIAA/ASME/ASCE/AHS/ASC 38th Structures, Structural Dynamics, and Materials Conference, Kissimmee, FL, April 7-11, 1997. AIAA Paper No. 97-1076.
 92. Breivik, Nichole L.*; Hyer, Michael W.; and Starnes, James H., Jr.: Thermal and Mechanical Buckling and Postbuckling of Selected Curved Composite Panels. Presented at the AIAA/ASME/ASCE/AHS/ASC 38th Structures, Structural Dynamics, and Materials Conference, Kissimmee, FL, April 7-11, 1997. AIAA Paper No. 97-1247.
 93. Ambur, Damodar R.*; Starnes, James H., Jr.; and Phillips, Eric A.: Response of Composite Panels with Stiffness Gradients due to Stiffener Terminations and Cutouts. Presented at the AIAA/ASME/ASCE/AHS/ASC 38th Structures, Structural Dynamics, and Materials Conference, Kissimmee, FL, April 7-11, 1997. AIAA Paper No. 97-1386.

94. Fuchs, Hannes P.*; Starnes, James H., Jr.; and Hyer, Michael W.: Collapse of Composite Cylinders in Bending. Presented at the AIAA/ASME/ASCE/AHS/ASC 38th Structures, Structural Dynamics and Materials Conference, Kissimmee, FL, April 7-11, 1997. AIAA Paper No. 97-1241.
95. Starnes, James H., Jr.*; Rose, Cheryl A.; Young, Richard D.; and Rankin, Charles C.: Effects of Combined Loads on the Nonlinear Response of Stiffened Shells with Long Cracks. Presented at the 1997 International Committee on Aeronautical Fatigue (ICAF), Edinburgh, Scotland, June 16-20, 1997. Proceedings of the 19th Symposium of the International Committee on Aeronautical Fatigue, ICAF 97, Fatigue in New and Aging Aircraft, P. Poole and R. Cook, Eds., Engineering Materials Advisory Services Ltd., EMAS Publishing, West Midlands, UK, Vol. II, 1997, pp. 967-978.
96. Starnes, James H., Jr.*; and Rose, Cheryl A.: Effects of Initial Crack Length on Stable Tearing and Buckling of Selected Unstiffened Aluminum Shells Subjected to Internal Pressure and Axial Compression. Presented at the First Joint DoD/FAA/NASA Conference on Aging Aircraft, Ogden, UT, July 8-10, 1997.
97. Young, Richard, D.*; Rose, Cheryl A.; Davila, Carlos G.; Starnes, James H., Jr.; and Rankin, Charles C.: Crack Growth and Residual Strength Characteristics of Selected Flat Stiffened Aluminum Panels. Presented at the First Joint DoD/FAA/NASA Conference on Aging Aircraft, Ogden, UT, July 8-10, 1997.
98. Barut, A.; Madenci, E.*; Starnes, J. H., Jr.; and Tessler, A.: Stiffened Curved Panel with an Inclined Crack under Tension. Presented at the Fourth U. S. National Congress on Computational Mechanics, San Francisco, CA, August 6-8, 1997.
99. Librescu, L.*; Lin, W.; Nemeth, M. P.; and Starnes, J. H., Jr.: Nonlinear Response of Geometrically Imperfect Flat and Curved Panels under Thermomechanical Load Systems. Presented at the 1997 International Mechanical Engineering Congress and Exposition, Dallas, TX, November 16-21, 1997.
100. Starnes, James H., Jr.*; and Rose, Cheryl A.: Buckling and Stable Tearing Responses of Unstiffened Aluminum Shells with Long Cracks. Presented at the AIAA/ASME/ASCE/AHS/ASC 39th Structures, Structural Dynamics and Materials Conference, Long Beach, CA, April 20-23, 1998. AIAA Paper No. 98-1991.
101. Nemeth, Michael P.*; Young, Richard D.; Collins, Timothy J.; and Starnes, James H., Jr.: Effects of Welding-Induced Initial Geometric Imperfections on the Nonlinear Behavior of the Space Shuttle Superlightweight LO₂ Tank. Presented at the AIAA/ASME/ASCE/AHS/ASC 39th Structures, Structural Dynamics and

- Materials Conference, Long Beach, CA, April 20-23, 1998. AIAA Paper No. 98-1840.
102. Young, Richard D.*; Nemeth, Michael P.; Collins, Timothy J.; and Starnes, James H., Jr.: Nonlinear Analysis of the Space Shuttle Superlightweight LO₂ Tank: Part I - Behavior Under Booster Ascent Loads. Presented at the AIAA/ASME/ASCE/AHS/ASC 39th Structures, Structural Dynamics and Materials Conference, Long Beach, CA, April 20-23, 1998. AIAA Paper No. 98-1838.
 103. Nemeth, Michael P.*; Young, Richard D.; Collins, Timothy J.; and Starnes, James H., Jr.: Nonlinear Analysis of the Space Shuttle Superlightweight LO₂ Tank: Part II - Behavior Under 3g End-of-Flight Loads. Presented at the AIAA/ASME/ASCE/AHS/ASC 39th Structures, Structural Dynamics and Materials Conference, Long Beach, CA, April 20-23, 1998. AIAA Paper No. 98-1839.
 104. Ambur, Damodar R.*; and Starnes, James H., Jr.: Effect of Curvature on the Impact Damage Characteristics and Residual Strength of Composite Panels. Presented at the AIAA/ASME/ASCE/AHS/ASC 39th Structures, Structural Dynamics and Materials Conference, Long Beach, CA, April 20-23, 1998. AIAA Paper No. 98-1881.
 105. Hilburger, Mark W.*; Starnes, James H., Jr.; and Waas, Anthony M.: The Response of Composite Cylinders with Cutouts and Subjected to Internal Pressure and Axial Compression Loads. Presented at the AIAA/ASME/ASCE/AHS/ASC 39th Structures, Structural Dynamics and Materials Conference, Long Beach, CA, April 20-23, 1998. AIAA Paper No. 98-1768.
 106. Hilburger, Mark W.*; Starnes, James H., Jr.; and Waas, Anthony M.: A Numerical and Experimental Study of the Response of Selected Compression-Loaded Composite Shells with Cutouts. Presented at the AIAA/ASME/ASCE/AHS/ASC 39th Structures, Structural Dynamics and Materials Conference, Long Beach, CA, April 20-23, 1998. AIAA Paper No. 98-1988.
 107. Breivik, Nicole L.*; Hyer, Michael W.; and Starnes, James H., Jr.: Response of Curved Composite Panels Subjected to Combined Thermal and Mechanical Loads. Presented at the AIAA/ASME/ASCE/AHS/ASC 39th Structures, Structural Dynamics and Materials Conference, Long Beach, CA, April 20-23, 1998. AIAA Paper No. 98-1773.
 108. Arbocz, Johann.*; Starnes, James H., Jr.; and Nemeth, Michael P.: Towards a Probabilistic Criterion for Preliminary Shell Design. Presented at the AIAA/ASME/ASCE/AHS/ASC 39th Structures, Structural Dynamics and

- Materials Conference, Long Beach, CA, April 20-23, 1998. AIAA Paper No. 98-2051.
109. Starnes, James H., Jr.*; and Ambur, Damodar R.: Composite Structures Research and Development Experiences at NASA Langley Research Center. Proceedings of the NATO Advanced Studies Institute Conference on Mechanics of Composite Materials and Structures, Tróia, Portugal, July 12-24, 1998.
 110. Starnes, James H., Jr.*; and Rose, Cheryl A.: Stable Tearing and Buckling Response of Unstiffened Aluminum Shells with Long Cracks. Presented at the Second Joint NASA/FAA/DoD Conference on Aging Aircraft, Williamsburg, VA, August 31-September 3, 1998. NASA/CP-1999-208982/Part 1, pp. 610-626, January 1999.
 111. Young, Richard D.; Rouse, Marshall; Ambur, Damodar R.; and Starnes, James H., Jr.*: Residual Strength Pressure Tests and Nonlinear Analyses of Stringer- and Frame-Stiffened Aluminum Fuselage Panels with Longitudinal Cracks. Presented at the Second Joint NASA/FAA/DoD Conference on Aging Aircraft, Williamsburg, VA, August 31-September 3, 1998. NASA/CP-1999-208982/Part 1, pp. 408-426, January 1999.
 112. Ambur, Damodar R.*; and Starnes, James H., Jr.: Influence Of Curved Composite Plate Nonlinear Response On The Low-Speed Impact Damage Tolerance. Presented at the AIAA/ASME/ASCE/AHS/ASC 40th Structures, Structural Dynamics and Materials Conference, St. Louis, MO, April 12-15, 1999. AIAA-99-1324, April 1999.
 113. Rose, Cheryl A.; Young, Richard D.*; and Starnes, James H., Jr.: Nonlinear Bending Response of Pressurized Aluminum Shells with Long Cracks. Presented at the AIAA/ASME/ASCE/AHS/ASC 40th Structures, Structural Dynamics and Materials Conference, St. Louis, MO, April 12-15, 1999. AIAA-99-1412, April 1999.
 114. Noor, Ahmed K.*; Starnes, James H., Jr.; and Peters, Jeanne M.: Uncertainty Analysis of Composite Structures. Presented at the AIAA/ASME/ASCE/AHS/ASC 40th Structures, Structural Dynamics and Materials Conference, St. Louis, MO, April 12-15, 1999. AIAA-99-1584, April 1999.
 115. Arbocz, Johann*; Starnes, James H., Jr.; and Nemeth, Michael P.: A Hierarchical Approach to Buckling Load Calculations. Presented at the AIAA/ASME/ASCE/AHS/ASC 40th Structures, Structural Dynamics and Materials Conference, St. Louis, MO, April 12-15, 1999. AIAA-99-1232, April 1999.

116. Corona, Edmundo*; and Starnes, James H., Jr.: Collapse of Cracked Flat Plates under Biaxial Loading. Presented at the AIAA/ASME/ASCE/AHS/ASC 40th Structures, Structural Dynamics and Materials Conference, St. Louis, MO, April 12-15, 1999. AIAA-99-1302-wip, April 1999.
117. Elishakoff, Isaac*; and Starnes, James H., Jr.: Safety Factor and the Non-Deterministic Approaches. Presented at the AIAA/ASME/ASCE/AHS/ASC 40th Structures, Structural Dynamics and Materials Conference, St. Louis, MO, April 12-15, 1999. AIAA-99-1614, April 1999.
118. Starnes, James H., Jr.*; Hilburger, Mark, W.; and Nemeth, Michael P.: The Effects of Initial Imperfections on the Buckling of Composite Shells. Invited paper for the ASTM Symposium on Composite Structures: Theory and Practice, Seattle, WA, May 17-18, 1999. ASTM STP 1383, P. Grant and C. Q. Rousseau, Eds., American Society for Testing and Materials, October 2000, pp. 529-550.
119. Starnes, James H., Jr.; Ambur, Damodar R.; Young, Richard D.; and Harris, Charles E.*: Experimental Verification of the Analytical Methodology to Predict the Residual Strength of Metallic Shell Structures. Proceedings of the SEM Annual Conference on Theoretical, Experimental, and Computational Mechanics, Cincinnati, OH, June 7-8, 1999. pp. 776-780.
120. Newman, James C., Jr.*; Harris, Charles E.; Dawicke, David S.; Piascik, Robert S.; Young, Richard D.; and Starnes, James H., Jr.: Methodology for Predicting the Onset of Widespread Fatigue Damage in Fuselage Structure. Presented at the Seventh International Fatigue Conference, Beijing, People's Republic of China, June 8-12, 1999.
121. Nemeth, Michael P.; Starnes, James H., Jr.; Librescu, Liviu*; and Lin, W.: Nonlinear Response of Flat and Curved Panels Subjected to Thermomechanical Loads. Presented at the ASME Mechanics and Materials Conference, Blacksburg, VA, June 27-30, 1999.
122. Dawicke, David S.*; Newman, James C., Jr.; Starnes, James H., Jr.; Rose, Cheryl A.; Young, Richard D.; and Seshadri, B. R.: Residual Strength Analysis Methodology: Laboratory Coupons to Structural Components. Presented at the Third Joint FAA/DoD/NASA Conference on Aging Aircraft, Albuquerque, NM, September 20-23, 1999.
123. Young, Richard D.*; Rose, Cheryl A.; and Starnes, James H., Jr.: Nonlinear Local Bending Response and Bulging Factors for Longitudinal and Circumferential Cracks in Pressurized Cylindrical Shells. Presented at the Third Joint FAA/DoD/NASA Conference on Aging Aircraft, Albuquerque, NM, September 20-23, 1999.

124. Elishakoff, Isaac; Duan, Dehe; Qiu, Zhipung; and Starnes, James H., Jr.: How to Find the Range of Eigenvalues Due to Uncertain Elastic Modulus and Mass Density? In *Whys and Hows in Uncertainty Modeling, Probability, Fuzziness and Anti-optimization*, International Centre for Mechanical Sciences, Courses and Lectures - Number 388, Springer-Verlag, 1999, pp. 341-355.
125. Noor, Ahmed K.*; Starnes, James H., Jr.; and Peters, Jeanne M.: Uncertainty Analysis of Composite Structures. Presented at the European Conference on Computational Mechanics (ECCM'99), Munich, Germany, August 31-September 3, 1999.
126. Noor, Ahmed K.*; Starnes, James H., Jr.; and Peters, Jeanne M.: Uncertainty Analysis of Composite Structures. Presented at the 1999 ASME International Mechanical Engineering Congress and Exposition, Nashville, TN, November 14-19, 1999.
127. Arbocz, Johann*; Starnes, James H., Jr.; and Nemeth, Michael P.: A Comparison of Probabilistic and Lower Bound Methods for Predicting the Response of Buckling Sensitive Structures. Presented at the AIAA/ASME/ASCE/AHS/ASC 41st Structures, Structural Dynamics and Materials Conference, Atlanta, GA, April 3-6, 2000. AIAA-2000-1382, April 2000.
128. Hilburger, Mark W.; and Starnes, James H., Jr.*: Effects of Imperfections on the Buckling Response of Compression-Loaded Composite Shells. Presented at the AIAA/ASME/ASCE/AHS/ASC 41st Structures, Structural Dynamics and Materials Conference, Atlanta, GA, April 3-6, 2000. AIAA-2000-1387, April 2000.
129. Hilburger, Mark W.; Nemeth, Michael P.*; and Starnes, James H., Jr.: Effective Widths of Compression-Loaded Plates with a Cutout. Presented at the AIAA/ASME/ASCE/AHS/ASC 41st Structures, Structural Dynamics and Materials Conference, Atlanta, GA, April 3-6, 2000. AIAA-2000-1658, April 2000.
130. Young, Richard D.*; Rose, Cheryl A.; and Starnes, James H., Jr.: Nonlinear Bulging Factors for Longitudinal and Circumferential Cracks in Cylindrical Shells Subjected to Combined Loads. Presented at the AIAA/ASME/ASCE/AHS/ASC 41st Structures, Structural Dynamics and Materials Conference, Atlanta, GA, April 3-6, 2000. AIAA-2000-1514, April 2000.
131. Young, Richard D.*; Hyer, Michael W.; and Starnes, James H., Jr.: Prebuckling and Postbuckling Response of Tailored Composite Stiffened Panels with Axial-Shear Coupling. Presented at the AIAA/ASME/ASCE/AHS/ASC 41st Structures, Structural Dynamics and Materials Conference, Atlanta, GA, April 3-6, 2000. AIAA-2000-1459, April 2000.

132. Cowan, Amy L.*; Davila, Carlos G.; Johnson, Eric R.; and Starnes, James H., Jr.: Crack Path Bifurcation at a Tear Strap in a Pressurized Shell. Presented at the AIAA/ASME/ASCE/AHS/ASC 41st Structures, Structural Dynamics and Materials Conference, Atlanta, GA, April 3-6, 2000. AIAA-2000-1517, April 2000.
133. Simitses, George J.*; Starnes, James H., Jr.; and Rezaeepazhand, J.: Structural Similitude and Scaling Laws for plates and Shells. Presented at the AIAA/ASME/ASCE/AHS/ASC 41st Structures, Structural Dynamics and Materials Conference, Atlanta, GA, April 3-6, 2000. AIAA-2000-1383, April 2000.
134. Ambur, Damodar R.*; and Starnes, James H., Jr.: Influence of Target and Impactor on the Nonlinear Response and Residual Strength of Curved Thin Composite Plates. Presented at the AIAA/ASME/ASCE/AHS/ASC 41st Structures, Structural Dynamics and Materials Conference, Atlanta, GA, April 3-6, 2000. AIAA-2000-1591, April 2000.
135. Young, Richard D.*; Rose, Cheryl A.; and Starnes, James H., Jr.: The Effect of Stiffeners on Bulging Factors for Longitudinal Cracks in Pressurized Cylindrical Shells. Presented at the Fourth Joint DoD/FAA/NASA Conference on Aging Aircraft, St. Louis, MO, May 15-18, 2000.
136. Starnes, James H., Jr.*; and Hilburger, Mark W.: Effects of Imperfections on the Buckling Response of Compression-Loaded Composite Shells. Invited paper presented at the 20th International Congress of Theoretical and Applied Mechanics, Chicago, IL, August 27-September 2, 2000.
137. Harris, Charles E.; Shuart, Mark J.*; and Starnes, James H., Jr.: Composite Materials and Structures for Aerospace: Past, Present and Future. Presented at the 22nd SAMPE Europe International Conference, Paris, France, March 27-29, 2001.
138. Hilburger, Mark W.; and Starnes, James H., Jr.*: High-Fidelity Nonlinear Analysis of Compression Loaded Composite Shells. Presented at the AIAA/ASME/ASCE/AHS/ASC 42nd Structures, Structural Dynamics and Materials Conference, Seattle, WA, April 16-19, 2001. AIAA Paper No. 2001-1394, April 2001.
139. Rose, Cheryl A.*; Young, Richard D.; and Starnes, James H., Jr.: Numerical Study of the Nonlinear Response of Cracked Aluminum Shells Subjected to Combined Loads. Presented at the AIAA/ASME/ASCE/AHS/ASC 42nd Structures, Structural Dynamics and Materials Conference, Seattle, WA, April 16-19, 2001. AIAA Paper No. 2001-1395, April 2001.

140. Arbocz, Johann*; Starnes, James H., Jr.; and Nemeth, Michael P.: On a High-Fidelity Hierarchical Approach to Buckling Load Calculations. Presented at the AIAA/ASME/ASCE/AHS/ASC 42nd Structures, Structural Dynamics and Materials Conference, Seattle, WA, April 16-19, 2001. AIAA Paper No. 2001-1392, April 2001.
141. Hilburger, Mark W.*; Nemeth, Michael P.; and Starnes, James H., Jr.: Nonlinear and Buckling Behavior of Curved Panels Subjected to Combined Loads. Presented at the AIAA/ASME/ASCE/AHS/ASC 42nd Structures, Structural Dynamics and Materials Conference, Seattle, WA, April 16-19, 2001. AIAA Paper No. 2001-1392, April 2001.
142. Young, Richard D.*; Rose, Cheryl A.; and Starnes, James H., Jr.: Skin, Stringer and Fastener Loads in Buckled Fuselage Panels. Presented at the AIAA/ASME/ASCE/AHS/ASC 42nd Structures, Structural Dynamics and Materials Conference, Seattle, WA, April 16-19, 2001. AIAA Paper No. 2001-1398, April 2001.
143. Arbocz, Johann*; Starnes, James H., Jr.; and Nemeth, Michael P.: On the Accuracy of Probabilistic Buckling Predictions. Presented at the AIAA/ASME/ASCE/AHS/ASC 42nd Structures, Structural Dynamics and Materials Conference, Seattle, WA, April 16-19, 2001. AIAA Paper No. 2001-1236, April 2001.
144. Noor, Ahmed K.*; Starnes, James H., Jr.; and Peters, Jeanne M.: Uncertainty Analysis of Stiffened Composite Panels. Presented at the AIAA/ASME/ASCE/AHS/ASC 42nd Structures, Structural Dynamics and Materials Conference, Seattle, WA, April 16-19, 2001. AIAA Paper No. 2001-1326, April 2001.
145. Hilburger, Mark W.*; Rose, Cheryl A.; and Starnes, James H., Jr.: Nonlinear Analysis and Scaling Laws for Noncircular Composite Structures Subjected to Combined Loads. Presented at the AIAA/ASME/ASCE/AHS/ASC 42nd Structures, Structural Dynamics and Materials Conference, Seattle, WA, April 16-19, 2001. AIAA Paper No. 2001-1335, April 2001.
146. Starnes, James H., Jr.*; Dexter, H. Benson; Johnston, Norman J.; and Ambur, Damodar R.: Composite Structures and Materials Research at NASA Langley Research Center. Presented at the NATO Research and Technology Organization Applied Vehicle Technology Panel Specialists' Meeting on Low Cost Composite Structures, Loen, Norway, May 7-11, 2001.
147. Deo, Ravi B.*; Holzwarth, Richard A.; and Starnes, James H., Jr.: Low Cost Composite Structures for Aircraft Applications. A plenary session paper presented at the NATO Research and Technology Organization Applied Vehicle

- Technology Panel Specialists' Meeting on Low Cost Composite Structures, Loen, Norway, May 7-11, 2001.
148. Starnes, James H., Jr.*; Newman, James C., Jr.; Harris, Charles E.; Young, Richard D.; Rose, Cheryl A.; and James, Mark A.: Advances in Residual Strength Analyses from Laboratory Coupons to Structural Components. Proceedings of the 21st Symposium on the International Committee on Aeronautical Fatigue, Vol. 1, J. Rouchon, ed., Toulouse, France, June 25-29, 2001, pp. 401-427.
 149. Harris, Charles E.*; Starnes, James H., Jr.; and Shuart, Mark S.: Assessment of the State-of-the-Art for the Design and Manufacturing of Large Composite Structures. Presented at the National Space & Missile Materials Symposium, Monterey, CA, June 25-28, 2001.
 150. Starnes, James H., Jr.*; Hilburger, Mark W.; and Waters, W. Allen: Effects of Imperfections on the Buckling Response of Composite Shells. Invited presentation at the EUROMECH 424 Colloquium on Buckling Predictions of Imperfections Sensitive Shells, Kerkrade, The Netherlands, September 3-5, 2001.
 151. Arbocz, Johann*; Starnes, James H., Jr.; and Nemeth, Michael P.: On a High-Fidelity Hierarchical Approach to Buckling Load Calculations. Invited presentation at the EUROMECH 424 Colloquium on Buckling Predictions of Imperfections Sensitive Shells, Kerkrade, The Netherlands, September 3-5, 2001.
 152. Young, Richard D.*; Rose, Cheryl A.; and Starnes, James H., Jr.: Nonlinear Response of Fuselage Panels with Cracks and Subjected to Combined Loads. Presented at the Fifth Joint NASA/RAA/DoD Conference on Aging Aircraft, Kissimmee, FL, September 10-13, 2001.
 153. Starnes, James H., Jr.*; Newman, James C., Jr.; Harris, Charles, E.; Piascik, Robert S.; Young, Richard D.; and Rose, Cheryl A.: Advances in Structural Integrity Analysis Methods for Aging Metallic Airframe Structures with Local Damage. Proceedings of the NATO Research and Technology Organization Applied Vehicle Technology Panel Specialists' Meeting on Life Management techniques for Aging Air Vehicles, Manchester, UK, October 8-11, 2001.
 154. Starnes, James H., Jr.*; Harris, Charles E.; and Shuart, Mark J.: Pathways to the Future Enabled by Revolutionary Materials. Presented at the International Flight Symposium, The North Carolina First Flight Centennial Commission, Raleigh, NC, October 22-25, 2001.
 155. Wu, Chauncy*; Gurdal, Zafer; and Starnes, James H., Jr.: Buckling and Postbuckling of Tow-Placed, Variable Stiffness Panels. Presented at the AIAA/ASME/ASCE/AHS/ASC 43rd Structures, Structural Dynamics and

- Materials Conference, Denver, CO, April 22-25, 2002. AIAA Paper No. 2002-1512, April 2002.
156. Arbocz, Johann*; and Starnes, James H., Jr.: Buckling Load Calculations of the Isotropic Shell A-8 using a High-Fidelity Hierarchical Approach. Presented at the AIAA/ASME/ASCE/AHS/ASC 43rd Structures, Structural Dynamics and Materials Conference, Denver, CO, April 22-25, 2002. AIAA Paper No. 2002-1513, April 2002.
 157. Hilburger, Mark W.*; and Starnes, James H., Jr.: Buckling and Failure of Compression-Loaded Composite Cylindrical Shells with Reinforced Cutouts. Presented at the AIAA/ASME/ASCE/AHS/ASC 43rd Structures, Structural Dynamics and Materials Conference, Denver, CO, April 22-25, 2002. AIAA Paper No. 2002-1516, April 2002.
 158. Noor, Ahmed K.*; Starnes, James H., Jr.; and Peters, Jeanne: Nonlinear Response of Composite Panels Subjected to Combined Mechanical and Thermal Loading. Presented at the AIAA/ASME/ASCE/AHS/ASC 43rd Structures, Structural Dynamics and Materials Conference, Denver, CO, April 22-25, 2002. AIAA Paper No. 2002-1518, April 2002.
 159. Starnes, James H., Jr.*; and Hilburger, Mark W.: Using High-Fidelity Analysis Methods and Experimental Results to Account for the Effects of Imperfections on the Buckling Response of Composite Shell Structures. Presented at the NATO Research and Technology Organization Applied Vehicle Technology Panel Specialists' Meeting on Reduction of Military Vehicle Acquisition Time and Cost through Advanced Modeling and Virtual Product Simulation, Paris, France, April 22-25, 2002.
 160. Starnes, James H., Jr.*; and Hilburger, Mark W.: Effects of Reinforced Cutouts on the Buckling of Composite Shells. Invited paper, Proceedings of the Fifth World Congress on Computational Mechanics (WCCM5), July 6-12, 2002, Vienna, Austria, Eds. Mang, H. A., Rammesdorfer, F. G., and Eberhardstein, J., Publisher, Vienna University of Technology, Austria (ISBN 3-9501554-0-6).
 161. Rose, Cheryl A.*; and Starnes, James H., Jr.: The Nonlinear Response of Damaged Composite Shells Subjected to Internal Pressure. Presented at the AIAA/ASME/ASCE/AHS/ASC 44th Structures, Structural Dynamics and Materials Conference, Norfolk, VA, April 7-10, 2003. AIAA Paper No. 2003-1593, April 2003.
 162. Hilburger, Mark W.*; Nemeth, Michael P.; and Starnes, James H., Jr.: Shell Buckling Design Criteria Based on Manufacturing Imperfection Signatures. Presented at the AIAA/ASME/ASCE/AHS/ASC 44th Structures, Structural Dynamics and Materials Conference, Norfolk, VA, April 7-10, 2003. AIAA Paper No. 2003-1843, April 2003.

163. Arbocz, Johann*; and Starnes, James H., Jr.: A Hierarchical High-Fidelity Analysis Procedure for Buckling Critical Structures. Presented at the AIAA/ASME/ASCE/AHS/ASC 44th Structures, Structural Dynamics and Materials Conference, Norfolk, VA, April 7-10, 2003. AIAA Paper No. 2003-1844, April 2003.

REPORT DOCUMENTATION PAGE					Form Approved OMB No. 0704-0188	
<p>The public reporting burden for this collection of information is estimated to average 1 hour per response, including the time for reviewing instructions, searching existing data sources, gathering and maintaining the data needed, and completing and reviewing the collection of information. Send comments regarding this burden estimate or any other aspect of this collection of information, including suggestions for reducing this burden, to Department of Defense, Washington Headquarters Services, Directorate for Information Operations and Reports (0704-0188), 1215 Jefferson Davis Highway, Suite 1204, Arlington, VA 22202-4302. Respondents should be aware that notwithstanding any other provision of law, no person shall be subject to any penalty for failing to comply with a collection of information if it does not display a currently valid OMB control number.</p> <p>PLEASE DO NOT RETURN YOUR FORM TO THE ABOVE ADDRESS.</p>						
1. REPORT DATE (DD-MM-YYYY)		2. REPORT TYPE			3. DATES COVERED (From - To)	
01- 02 - 2006		Technical Memorandum				
4. TITLE AND SUBTITLE Collected Papers in Structural Mechanics Honoring Dr. James H. Starnes, Jr.				5a. CONTRACT NUMBER		
				5b. GRANT NUMBER		
				5c. PROGRAM ELEMENT NUMBER		
6. AUTHOR(S) Knight, Norman F., Jr.; Nemeth, Michael P.; and Malone, John B. (Compilers)				5d. PROJECT NUMBER		
				5e. TASK NUMBER		
				5f. WORK UNIT NUMBER 732759.07.11		
7. PERFORMING ORGANIZATION NAME(S) AND ADDRESS(ES) NASA Langley Research Center Hampton, VA 23681-2199				8. PERFORMING ORGANIZATION REPORT NUMBER L-19190		
9. SPONSORING/MONITORING AGENCY NAME(S) AND ADDRESS(ES) National Aeronautics and Space Administration Washington, DC 20546-0001				10. SPONSOR/MONITOR'S ACRONYM(S) NASA		
				11. SPONSOR/MONITOR'S REPORT NUMBER(S) NASA/TM-2006-214276		
12. DISTRIBUTION/AVAILABILITY STATEMENT Unclassified - Unlimited Subject Category 39 Availability: NASA CASI (301) 621-0390						
13. SUPPLEMENTARY NOTES An electronic version can be found at http://ntrs.nasa.gov						
14. ABSTRACT This special publication contains a collection of structural mechanics papers honoring Dr. James H. Starnes, Jr. presented at the 46th AIAA/ASME/ASCE/AHS/ASC Structures, Structural Dynamics, and Materials Conference held in Austin, Texas, April 18-21, 2005. Contributors to this publication represent a small number of those influenced by Dr. Starnes' technical leadership, his technical prowess and diversity, and his technical breath and depth in engineering mechanics. These papers cover some of the research areas Dr. Starnes investigated, which included buckling, postbuckling, and collapse of structures; composite structural mechanics, residual strength and damage tolerance of metallic and composite structures; and aircraft structural design, certification and verification. He actively pursued technical understanding and clarity, championed technical excellence, and modeled humility and perseverance.						
15. SUBJECT TERMS Aircraft Design; Buckling; Composites; Structures						
16. SECURITY CLASSIFICATION OF:			17. LIMITATION OF ABSTRACT	18. NUMBER OF PAGES	19a. NAME OF RESPONSIBLE PERSON	
a. REPORT	b. ABSTRACT	c. THIS PAGE			STI Help Desk (email: help@sti.nasa.gov)	
U	U	U	UU	817	19b. TELEPHONE NUMBER (Include area code) (301) 621-0390	